



# ОТЕН 2024

11<sup>TH</sup> INTERNATIONAL SCIENTIFIC CONFERENCE  
ON DEFENSIVE TECHNOLOGIES

## *PROCEEDINGS*

### TOPICS

AERODYNAMICS AND FLIGHT DYNAMICS

AIRCRAFT

WEAPON SYSTEMS AND COMBAT VEHICLES

AMMUNITION AND ENERGETIC MATERIALS

INTEGRATED SENSOR SYSTEMS AND ROBOTIC SYSTEMS

TELECOMMUNICATION AND INFORMATION SYSTEMS

MATERIALS AND TECHNOLOGIES

QUALITY, STANDARDIZATION, METROLOGY, MAINTENANCE AND EXPLOITATION



# OTEH 2024

**11<sup>TH</sup> INTERNATIONAL SCIENTIFIC CONFERENCE  
ON DEFENSIVE TECHNOLOGIES**  
Serbia, Tara, 9-11 October 2024



**Pavle Savic  
(1909-1994)**

### **Publisher**

The Military Technical Institute  
Ratka Resanovića 1, 11030 Belgrade

### **Publisher's Representative**

Col Asst. Prof. Ivan Pokrajac, PhD Eng

### **Editors**

Col Aleksandar Kari, PhD Eng  
Prof. Ljubica Radović, PhD Eng

### **Technical Editing**

Aida Jeremić  
Jelena Petrović

### **Printed by**

The Military Technical Institute  
Ratka Resanovića 1, 11030 Belgrade

CIP - Каталогизација у публикацији  
Народна библиотека Србије, Београд

NAUČNO-stručni skup iz oblasti odbrambenih  
tehnologija (11 ; 2024 ; Beograd)  
Proceedings [Elektronski izvor] / 11th  
International Scientific Conference on  
Defensive Technologies, ОТЕН 2024, Belgrade,  
9-11 October 2024 ; [organized by] Military  
Technical Institute, Belgrade ; [editors Aleksandar Kari,  
Ljubica Radović]. - Belgrade : Military Techni-  
cal Institute, 2024 (Beograd : Military Technical Institute) 1 USB  
memorija.

Sistemska zahtevi: Nisu navedeni. - Nasl. sa  
naslovne strane dokumenta. -  
Bibliografija uz svaki rad.

ISBN 978-86-81123-94-2

1. Vojnotehnički institut (Beograd)  
a) Војна техника - Зборници  
b) Технички материјали – Зборници  
c) Телекомуникациони системи - Зборници

11th INTERNATIONAL SCIENTIFIC CONFERENCE  
ON DEFENSIVE TECHNOLOGIES

# ОТЕН 2024

SUPPORTED BY



MINISTRY OF DEFENCE  
[www.mod.gov.rs](http://www.mod.gov.rs)

Organized by



MILITARY TECHNICAL INSTITUTE  
1 Ratka Resanovića St., Belgrade 11000, SERBIA  
[www.vti.mod.gov.rs](http://www.vti.mod.gov.rs)

SUPPORTED BY



MINISTRY OF SCIENCE TECHNOLOGICAL DEVELOPMENT AND INNOVATION  
[www.nitra.gov.rs](http://www.nitra.gov.rs)

## ORGANIZATIONAL COMMITTEE

**Nenad Miloradović**, PhD Eng, Assistant Minister of Defense for Materiel Resources, *President of the Organizational Committee*

Bg Asst. Prof. **Slavko Rakić**, PhD Eng, Head of the Department for Defense Technologies

Col Asst. Prof. **Ivan Pokrajac**, PhD Eng, Acting Director of the Military Technical Institute

**Marina Soković**, PhD Eng, Assistant Minister for Science - Ministry of Science, Technological Development and Innovations

**Vladimir Popović**, PhD Eng, Dean of the Faculty of Mechanical Engineering, Belgrade

Bg **Milan Popović**, Head of the Department for Planning and Development GS SAF

Col **Dejan Stojković**, PhD, Head of the Department for Strategic Planning

Bg Prof. **Boban Đorović**, PhD Eng, Rector of the University of Defense

Col Prof. **Srdan Blagojević**, PhD, Head of the Military Academy

Col **Nebojša Svjetlica**, Head of the Department for International Military Cooperation

Col **Saša Veselinović**, PhD Eng, Director of the Technical Test Center

Col Prof. **Slobodan Ilić**, PhD Eng, Director of Directorate for Standardization, Codification and Metrology

Col **Ivica Marjanović**, PhD Eng, Director of Military Quality Control

Col **Dejan Đorđević**, PhD Eng, Director of Military Geographical Institute

Prof. **Jovanka Šaranović**, PhD Eng, Institute for Strategic Research

**Vladimir Radovanović**, Assistant Minister for Innovation, Transfer of Technology and Technological Development – Ministry of Science, Technological Development and Innovations

Prof. **Dejan Gvozdić**, PhD Eng, Dean of the Faculty of Electrical Engineering, Belgrade

Prof. **Petar Uskoković**, PhD Eng, Dean of the Faculty of Technology and Metallurgy, Belgrade

**Boris Dumnić**, PhD Eng, Acting Dean of the Faculty of Technical Sciences, Novi Sad

Prof. **Danijela Milošević**, PhD Eng, Dean of the Faculty of Technical Sciences, Čačak, University of Kragujevac

Prof. **Vladimir N. Cvetković**, PhD Eng, Dean of the Faculty of Security Studies, Belgrade,

Prof. **Goran Bošković**, PhD Eng, University of Criminal Investigation and Police Studies, Belgrade

**Predrag Ćulibrk**, Director, IRITEL, Belgrade

**Vladimir Cizelj**, PhD Eng, Vlatacom Institute, Belgrade

**Nikola Tomašević**, PhD Eng, Director, Mihajlo Pupin Institute

**Jugoslav Petković**, Director, Yugoimport SDPR, Belgrade

**Jovanka Andrić**, Director, Krušik, Valjevo

**Zoran Stefanović**, Director, Sloboda, Čačak

**Predrag Ilić**, Acting Director Milan Blagojević - Namenska A.D. Lučani

**Dobrosav Andrić**, Director, Prvi Partizan, Užice

**Stanoje Biočanin**, Director, Prva Iskra - namenska, Barič

**Saša Milošević**, Director, Zastava - oružje, Kragujevac

**Andelka Atanasković**, Director, Prva Petoletka – namenska, Trstenik

**Stefan Đurić**, Director, Zastava Tervo, Kragujevac

**Časlav Kljajić**, Director, PPT-TMO A.D., Trstenik

## SECRETARIAT

**Elida Vasiljević**, Military Technical Institute, *Secretary*

**Mirjana Krstović**, Military Technical Institute, *Deputy Secretary*

**Jelena Pavlović**, Military Technical Institute

Lt Col **Nebojša Grebović**, Military Technical Institute

Asst. Prof. **Tihomir Kovačević**, PhD Eng, Mili-

tary Technical Institute

**Srdjan Živković**, PhD Eng, Military Technical Institute

Col **Branko Medan**, Department for Defensive Technologies

Lt Col **Slobodan Malbašić**, Department for Defensive Technologies

Lt Col **Igor Đorić**, Military Technical Institute

**Ljiljana Obradović**, Military Technical Institute  
**Suzana Vuković**, Military Technical Institute  
**Dobrivoje Granžan**, Military Technical Institute

tute  
**Irina Ulanova**, Military Technical Institute  
**Aida Jeremić**, Military Technical Institute  
**Jelena Petrović**, Military Technical Institute

## SCIENTIFIC COMMITTEE

Col **Aleksandar Kari**, PhD Eng, Military Technical Institute, Belgrade, Serbia,  
*President of the Scientific Committee*  
Prof. **Ljubica Radović**, PhD Eng, Military Technical Institute, Belgrade, Serbia  
Col **Bojan Pavković**, PhD Eng, Military Technical Institute, Belgrade, Serbia  
Prof. Emeritus **Taek Lyul Song**, PhD Eng, Hanyang University, South Korea  
**Evgeny V. Sudov**, PhD Eng, R&D Applied Logistic Centre, Moscow, Russia  
Prof. **Stevan Berber**, PhD Eng, Auckland University, New Zealand  
**Srećko Stopić**, PhD Eng, RWTH University Aachen, Germany  
**Zbyšek Korecki**, PhD Eng, University of Defense, Brno, Czech Republic  
**Radi Ganev**, PhD Eng, “Lyuben Karavelov” University of Structural Engineering and Architecture, Sofia, Bulgaria  
Prof. **Tomaž Vuherer**, PhD Eng, Faculty of Mechanical Engineering, Maribor, Slovenia  
Prof. **Biljana Marković**, PhD Eng, Faculty of Mechanical Engineering, East Sarajevo, Republic of Srpska (Bosnia and Herzegovina)  
Prof. **Milan Tica**, PhD Eng, Faculty of Mechanical Engineering, Banja Luka University, Republic of Srpska (Bosnia and Herzegovina)  
Prof. **Dženana Gačo**, PhD Eng, University in Bihac, Bosnia and Herzegovina  
Prof. **Strain Posavljak**, PhD Eng, Faculty of Mechanical Engineering, Banja Luka, Republic of Srpska (Bosnia and Herzegovina)  
Prof. **Mersida Manjgo**, PhD Eng, Faculty of Mechanical Engineering Mostar, Bosnia and Herzegovina  
Prof. **Kemal Delijić**, PhD Eng, Faculty of Technology and Metallurgy, Podgorica, Montenegro  
Col **Predrag Rakonjac**, PhD Eng, University of Defense, Belgrade  
Col Prof. **Dragan Trifković**, PhD Eng, Military Academy, Belgrade, Serbia  
Col Prof. **Damir Jerković**, PhD Eng, Military Academy, Belgrade, Serbia

Col Prof. **Branimir Krstić**, PhD Eng, Military Academy, Belgrade, Serbia  
Col Prof. **Boban Pavlović**, PhD Eng, Military Academy, Belgrade, Serbia  
Col Prof. **Boban Bondžulić**, PhD Eng, Military Academy, Belgrade, Serbia  
Col Prof. **Milenko Andrić**, PhD Eng, Military Academy, Belgrade, Serbia  
Col Prof. **Slobodan Simić**, PhD Eng, Military Academy, Belgrade, Serbia  
Col Prof. **Zoran Bajić**, PhD Eng, Military Academy, Belgrade, Serbia  
Col Prof. **Radovan Karkalić**, PhD Eng, Military Academy, Belgrade, Serbia  
Col **Saša Bakrač**, Military Geographical Institute, Belgrade, Serbia  
**Jasmina Stevanović**, IHTM Belgrade, Belgrade, Serbia  
**Srećko Manasijević**, PhD Eng, LOLA Institute, Belgrade, Serbia  
**Dragana Perić**, PhD Eng, Vlatacom Institute, Belgrade, Serbia  
Prof. **Srećko Nijemčević**, PhD Eng, Vlatacom Institute, Belgrade, Serbia  
**Miroslav Sokić**, PhD Eng, Institute for Technology of Nuclear and Other Mineral Raw Materials, Belgrade, Serbia  
Prof. **Stevica Graovac**, PhD Eng, Mihajlo Pupin Institute, Belgrade, Serbia  
**Nikola Zogović**, PhD Eng, Mihajlo Pupin Institute, Belgrade, Serbia  
**Violeta Nikolić**, PhD Eng, Vinča – Institute of Nuclear Sciences, Belgrade, Serbia  
Prof. **Vladimir Mladenović**, Faculty of Engineering, Čačak, University of Kragujevac, Serbia  
Asst. Prof. **Dušan Arsić**, Faculty of Engineering, University of Kragujevac, Serbia  
Prof. **Vladimir Arsovski**, PhD Eng, Faculty of Electrical Engineering, Belgrade, Serbia  
Prof. **Dragan Milčić**, PhD Eng, Faculty of Mechanical Engineering, University of Niš, Serbia  
Prof. **Dragan Šešlija**, Faculty of Technical Sciences, Novi Sad, Serbia

Prof. **Predrag Elek**, PhD Eng, Faculty of Mechanical Engineering, Belgrade, Serbia

Prof. **Aleksandar Simonović**, PhD Eng, Faculty of Mechanical Engineering, Belgrade, Serbia

Prof. **Jelena Svorcan**, PhD Eng, Faculty of Mechanical Engineering, Belgrade, Serbia

**Vencislav Grabulov**, PhD Eng, IMS Institute, Belgrade, Serbia

Prof. **Ivan Kostić**, PhD Eng, Faculty of Mechanical Engineering, Belgrade, Serbia

Prof. **Slađana Vujičić**, PhD, Faculty of Business Economy and Entrepreneurship, Belgrade, Serbia

Prof. **Aleksandar Marinković**, PhD Eng, Faculty of Technology and Metallurgy, Belgrade, Serbia

Prof. **Melina Kalagasidis Krušić**, PhD Eng, Faculty of Technology and Metallurgy, Belgrade, Serbia

Asst. Prof. **Marija Samardžić**, PhD Eng, Military Technical Institute, Belgrade, Serbia

**Dijana Damljanović**, PhD Eng, Military Technical Institute, Belgrade, Serbia

Asst. Prof. **Jelena Gržetić**, PhD Eng, Military Technical Institute, Belgrade, Serbia

Prof. **Maja Vitorović-Todorović**, PhD Eng, Military Technical Institute, Belgrade, Serbia

**Željko Bulatović**, PhD Eng, Military Technical Institute, Belgrade, Serbia

**Miloš Pavić**, PhD Eng, Military Technical Institute, Belgrade, Serbia

Lt Col Asst. Prof. **Saša Brzić**, PhD Eng, Military Technical Institute, Belgrade, Serbia

Asst. Prof. **Danica Bajić**, PhD Eng, Military Technical Institute, Belgrade, Serbia

Col **Rade Pavlović**, PhD Eng, Military Technical Institute, Belgrade, Serbia

Col Asst. Prof. **Mihajlo Ranisavljević** PhD, Military Technical Institute, Belgrade, Serbia

## PREFACE

Military Technical Institute, the first and the largest military scientific-research institution in the Republic of Serbia with over 75 years long tradition, has been traditionally organizing the OTEH scientific conference, devoted to defense technologies. The Conference is supported by the Ministry of Defense and it takes place every second year.

Its aim is to gather scientists and engineers, researchers and designers, manufactures and university professors in order to exchange ideas and to develop new relationships.

The 11th International Scientific Conference OTEH 2024 is scheduled as follows: lecture on the occasion of “Pavle Savic”, given by Vladimir Cizelj, PhD, and two plenary lectures: “Energetic Materials“, given by Prof. Thomas M. Klapoetke, PhD Eng, and “Anti-Drone Combat“ given by Boban Sazdic Jotic, PhD , as well as working sessions according to the Conference topics.

The papers which will be presented at the Conference have been classified into the following topics:

- Aerodynamics and Flight Dynamics
- Aircraft
- Weapon Systems and Combat Vehicles
- Ammunition and Energetic Materials
- Integrated Sensor Systems and Robotic Systems
- Telecommunication and Information Systems
- Materials and Technologies
- Quality, Standardization, Metrology, Maintenance and Exploitation.

The Proceedings contain 130 reviewed papers which have been submitted by the authors from 11 different countries. I would also like to emphasize that we have 14 papers with authors from abroad. The quality of papers accepted for publication achieved very high standard. I expect stimulated discussion on many topics that will be presented online, during two days of the Conference.

On behalf of the organizer I would like to thank all the authors and participants from abroad, as well as from Serbia, for their contribution and efforts which made this Conference possible and successful.

I would also like to thank the Ministry of Science, Technological Development and Innovations of the Republic of Serbia for its financial support.

Finally, dear guests and participants of the Conference, I would like to wish you a pleasant and successful work during the Conference. I am looking forward to see you again at the Conference. All the best and stay healthy.

Belgrade, October, 2024

Col. Aleksandar Kari PhD Eng  
President of the Scientific Committee  
OTEH 2024





# OTEH 2024

11<sup>TH</sup> INTERNATIONAL SCIENTIFIC CONFERENCE  
ON DEFENSIVE TECHNOLOGIES

*PLENARY LECTURE*

***Thomas Matthias Klapötke***



## NEW SECONDARY EXPLOSIVES AND OXIDIZERS DEVELOPED AT LMU

THOMAS M. KLAPÖTKE

LMU Munich, Department of Chemistry, Energetic Materials Research, 81377 Munich, Germany,

[tmk@cup.uni-muenchen.de](mailto:tmk@cup.uni-muenchen.de)

**Abstract:** The energetic materials research group at LMU has been interested in the synthesis and energetic properties of new explosives and rocket propellant ingredients for many years. Out of the many interesting compounds which we have prepared over the years, the most promising candidate compound for use in real-life applications is the secondary explosive TKX-50. An overview of the synthesis and properties of TKX-50 will be given, as well as recent aspects we have investigated. The progress and development of new CHNO-based oxidizers will also be discussed, focusing predominantly on 2,2,2-trinitroethyl formate (TNEF) and bis(trinitroethyl) oxalate (BTNEO).

### 1. INTRODUCTION

Many new secondary explosives are synthesized each year and reported in the scientific literature, however, very few of these compounds are of interest for actual real-life applications<sup>[1]</sup>. The steps necessary for investigating whether a new secondary explosive is suitable for translation from being a pure laboratory-scale compound to one which has potential for upscaling and being investigated as a serious potential candidate for use in real-life applications are rarely described in the literature. Since these post-initial considerations are rarely reported for new secondary explosives, the process from initial laboratory report to scale-up remains poorly described<sup>[2]</sup>.

Initial reports on new explosive substances generally follow a relatively standard structure nowadays. Namely, the compound is synthesized on a less than 200 mg scale (for secondary explosives, considerably less for primary explosives), it is then characterized using standard characterization techniques used in the research laboratory for any class of compound, such as multinuclear NMR spectroscopy (typically <sup>1</sup>H, <sup>13</sup>C, <sup>14</sup>N), IR spectroscopy and C/H/N analysis. Usually, but not always, the solid-state structure of the compound is determined using single crystal X-ray diffraction, which also provides a value for the density. For energetic compounds, additional factors are important and usually determined before the compound is reported in the scientific literature. These values are usually the decomposition temperature ( $T_{dec}$ ) using DSC or TGA, density from pycnometry, and in particular, the sensitivity of the energetic compound towards external stimuli such as impact, friction and electrostatics<sup>[3]</sup>. These values, combined with the calculated energetic performance parameters ( $VoD$ ,  $PC-J$ ,  $V_0$ ,  $Q_{ex}$ ,  $T_{ex}$ ) which are usually calculated using the program EXPLO5<sup>[4]</sup>, provide a very good initial insight into an energetic compound. Inspection of the properties at this stage helps to drastically reduce the pool of reported compounds to a selected group

of compounds which are still of interest as energetic compounds for possible applications. Most reported secondary explosive compounds don't make the cut for further consideration, either because the decomposition temperature is too low (it should be at least 200°C), or the sensitivity of the compound to external stimuli such as impact or friction is too high, or the calculated energetic performance parameters predicts a detonation velocity the same as or lower than HMX and RDX, which would therefore suggest that there would be no advantage to be gained in replacing HMX or RDX by the compound<sup>[2]</sup>.

The very few compounds which meet these strict criteria require further, more specialized testing, in order to establish whether they are still of interest as an HMX/RDX replacement, or whether they too fail the cut at this second stage of testing. At this stage, there are a number of tests which can be performed. However, there are perhaps two main reasons why only very few compounds that pass the initial selection get investigated further. The first is that some testing equipment is very specialized and therefore not available to all synthetic energetic chemists<sup>[2]</sup>. A second aspect sounds trivial, but is a particularly tricky issue in synthetic energetic materials chemistry, and that is the necessity of handling only safe quantities, while at the same time, many of the more advanced, specialized tests require larger quantities than 200 mg of the compound, sometimes even several g<sup>[2]</sup>. Both of these issues strongly contribute to the trend of new energetic materials only being reported as far as the stage 1 characterization mentioned above, but then not further.

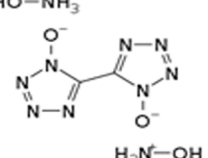
One result of this situation is that illustrative examples of energetic compounds being developed past the initial stages of characterization are relatively few and far between. Perhaps the most well-known examples of compounds which have in the recent past made the transition from initial testing to specialized testing and scale-up for applications are the secondary explosives Fox-7<sup>[5]</sup>, LLM-105<sup>[6]</sup> and CL-

20<sup>[7]</sup>. Another secondary explosive which has undergone this transition is dihydroxylammonium-5,5'-bistetrazolyl-1,1'-diolate, TKX-50. Published for the first time in 2012<sup>[8]</sup>, initial characterization immediately showed its potential for use<sup>[8]</sup>. The advances in research into TKX-50 have been rapid, and fueled by the large interest it has generated from groups around the world, such that in little over 10 years, TKX-50 is undergoing up-scaling by a company<sup>[9]</sup>.

## 2. RESULTS AND DISCUSSION

TKX-50 is one of a large number of tetrazole compounds which have been synthesized with the aim of discovering a new secondary explosive<sup>[10]</sup>. The introduction of the N-oxide functional group to the tetrazole ring helps to improve the oxygen balance of the compound, while the resonance stabilization of the tetrazole rings increases the stability of the NN bonds with relatively low bond order<sup>[2]</sup>. The low sensitivity to impact, friction and electrostatics of TKX-50 combined with the high decomposition temperature and relatively high density at TMD (table 1) were initial positive indicators that TKX-50 was a particularly promising compound<sup>[8]</sup>. The enthalpy of formation of TKX-50 was initially overestimated<sup>[8]</sup>, but the value of 194 kJ/mol corresponding to the average value from several independent measurements<sup>[11]</sup>, combined with the high density, results in a calculated detonation velocity of 9649 ms<sup>-1</sup>, which is higher compared to that of HMX and RDX<sup>[12]</sup>.

**Table 1.** Physical, sensitivity and energetic performance data for TKX-50<sup>[8], [11]</sup>

Formula	C <sub>2</sub> H <sub>8</sub> N <sub>10</sub> O <sub>4</sub>
Connectivity	HO-NH <sub>3</sub> <sup>+</sup>  H <sub>3</sub> N <sup>+</sup> -OH
MWt. / g mol <sup>-1</sup>	236.2
IS / J	8 - 18
FS / N	120
ESD / J	0.1
Ω(CO <sub>2</sub> ) / %	-27.1
T <sub>dec</sub> / °C	crude: 221 recryst. from water: 237
ρ / g cm <sup>-3</sup>	1.918 @ 100 K 1.877 @ room temperature
ΔH <sub>f</sub> <sup>o</sup> / kJ mol <sup>-1</sup>	194 ± 20 kJ mol <sup>-1</sup>

The original report on TKX-50 already contained data on many specialized energetic properties of TKX-50, such as the behavior of TKX-50 in the Trauzl test, ESD sensitivity, as well as toxicity data<sup>[8]</sup>. Possibly the most problematic initial aspect of TKX-50 was its synthesis, which required the synthesis and isolation of the explosive diazidoglyoxime, and which used chemicals which are not REACH conform. These two factors could have relegated

TKX-50 to being an explosive compound which failed to pass stage 1 selection criteria<sup>[8]</sup>. However, an improved synthetic route was established which not only excluded the isolation of the explosive intermediate diazidoglyoxime, but also conformed to REACH guidelines and – equally important – was possible to scale-up safely<sup>[9]</sup>.

Establishing the detonation velocity of TKX-50 was important to confirm the value predicted using EXPLO5. A value for the detonation velocity lower than that determined experimentally for RDX or HMX would also render TKX-50 to be of no significant improvement. As a consequence of the large critical diameter of TKX-50 (40 - 60 mm), determination of the detonation velocity requires a relatively large quantity of material, highlighting the importance of being able to prepare significant quantities of the compound. The VoD value of 8927 m s<sup>-1</sup> determined experimentally for TKX-50 with a loading density of 1.73 g cm<sup>-3</sup> agrees well with the calculated value and makes it higher in terms of detonation velocity than RDX or HMX and comparable with CL-20 (table 2)<sup>[12], [13], [14]</sup>.

**Table 2.** Calculated performance parameters of TKX-50 and other secondary explosives<sup>[4], [12]</sup>

Explosive	ρ / g cm <sup>-3</sup>	HE : wax	VoD / m s <sup>-1</sup>	pC-J / GPa	Q <sub>det</sub> / kJ kg <sup>-1</sup>
TKX-50	1.74	97 : 3	8919	30.0	4627
	1.877 (TMD)	100 : 0	9649	37.1	4791
RDX	1.74	97:3	8490	30.2	5561
	1.82 (TMD)	100	8877	34.5	5745
HMX	1.74	97:3	8472	29.9	5502
	1.905 (TMD)	100	9192	37.8	5699
CL-20	1.74	97:3	8506	31.4	5855
	2.038 (TMD)	100	9773	44.7	6231

A huge number of other investigations involving many aspects of TKX-50 by a large number of international research groups have been summarized recently in reviews<sup>[15]</sup>.

One interesting recent aspect of TKX-50 is the possibility of using TKX-50 as the secondary explosive in thermobaric formulations<sup>[16]</sup>. Thermobaric explosives are a current important area of energetic materials, due to the improved incendiary and blast effects they produce in comparison to only the secondary explosive. Thermobaric explosives (TBXs) generally consist of a high explosive, polymeric binder, fuel (which is usually a metal powder such as Al or Mg or the Magnalium alloy) and an oxidizer (which is usually AP or AN)<sup>[17]</sup>. Recently, we have investigated the performance of TBXs in which two components of the thermobaric explosives were changed<sup>[16]</sup>. In one, the use of TKX-50 as the secondary explosive instead of the commonplace RDX or HMX was investigated both under a normal air atmosphere as well as under an inert atmosphere and in the second investigation, the performance of a TBX

in which the oxidizer AP was replaced by the chlorine-free C, H, N, O oxidizer TNEF was determined in an experimental study<sup>[18]</sup>.

The performance of TKX-50 in the TBX formulations TKX-50/Al (90/10) and TKX-50/Al/Paraffin (70/27/3) was recently investigated<sup>[16]</sup>. The idea behind these TBXs was to investigate whether it would be possible to prepare TBXs free of additional oxidizer (i.e. AP or AN) in which a nitrogen-rich secondary explosive such as TKX-50 is used instead of the conventional choices of secondary explosive, HMX and RDX. By doing this, it was hoped that this would mean that the amount of additional oxidizer which is required for a traditional TBX could be reduced, meaning that the charge would be able to contain more secondary explosive by mass. It was hoped that the Al present would react with the nitrogen present in the nitrogen-rich TKX-50 to form aluminum nitrides, instead of the aluminum oxides formed when additional oxidizer is present in commonly used TBX formulations.

Experimental calorimetry measurements performed under an argon atmosphere found that the addition of 10% micron-sized Al powder to TKX-50 reduced the heat of detonation by around 90 J/g compared to pure TKX-50. However, the exothermic reaction of Al with the detonation products of TKX-50 is an exothermic process, contributing approximately 375 J/g<sup>[16]</sup>. The initial detonation products of TKX-50 mainly consists of N<sub>2</sub>, CO<sub>x</sub>, H<sub>2</sub>O and smaller quantities of NO<sub>2</sub> and O<sub>2</sub>. All of which can react with Al in the post-detonation stage in an exothermic reaction. Thermodynamically, the reactions between Al and O<sub>2</sub> or CO<sub>x</sub> are preferred, however kinetically, reactions between Al and nitrogen are preferred due to the fact that the concentration of nitrogen is highest in the detonation products. Calculations predict that increasing the Al content of the TBX should result in an increase in the heat of detonation of the mixture, however it was found that initiation with a standard detonator was insufficient to cause detonation of TBX mixtures of TKX-50 with Al content of greater than 10%<sup>[16]</sup>. It was found for the TKX-50, 90/Al, 10 mixture that when the detonation was performed in an inert argon atmosphere (i.e. air is absent), the solid phase which was predominant was that corresponding to the formula Al<sub>2.811</sub>N<sub>0.435</sub>O<sub>3.565</sub>, whereas this was not the case if the detonation was performed in an air atmosphere, whereby aluminum oxynitrides were essentially not observed<sup>[16]</sup>. For the detonations performed in an air atmosphere, it was found that the addition of Al to TKX-50 (TKX-50<sub>ph</sub>/Paraffin/Al, 70/3/27) resulted in a 30% higher maximum overpressure value than for TKX-50<sub>ph</sub> (TKX-50/Paraffin, 97/3) without aluminum metal, an increase in the maximum temperature of the explosion products in the chamber by 700 K, and the duration of time at which the temperature exceeds 1600 K was found to be three times longer (table 3)<sup>[16]</sup>. Therefore, it could be included that the addition of micron-sized aluminum powder to TKX-50 in a thermobaric mixture resulted in an improvement in the important performance values in comparison with the Al-free TKX-50 in an air atmosphere, and that due to the absence of aluminum oxynitrides in the

solid phase detonation product for detonations performed in an air atmosphere, in the presence of oxygen (air), Al present reacts preferentially with oxygen present rather than nitrogen, even if the nitrogen content is high<sup>[16]</sup>.

**Table 3.** Measured and calculated values for the maximum overpressure in the chamber for TKX-50 and TKX-50/Al mixture<sup>[16]</sup>

	TKX-50		TKX-50/Al	
	air	Ar	air	Ar
$\Delta p_{\max}$ [MPa]	0.63	0.48	0.81	0.58
$\Delta p_{\text{cal}}$ [MPa]	0.97	0.70	1.14	0.92
$\frac{\Delta p_{\max}}{\Delta p_{\text{cal}}}$ [%]	65	69	71	64

As mentioned above, generally thermobaric mixtures contain an oxidizer which is usually AP and AN. AN and particularly AP are well-known and the most commonly used oxidizers. Not only does AP have an excellent oxygen balance ( $\Omega_{\text{CO}} = 34\%$ ), it can be mass produced in an economically viable process, has a high density, high thermal stability good compatibility and can be stored for prolonged periods of time<sup>[2]</sup>. Furthermore, so much information has been accumulated over the years with respect to almost every aspect relevant to APs behavior as an oxidizer, it makes it a reliable and convenient oxidizer to use. However, it does have some drawbacks such as its more negative enthalpy of formation (-2536 kJ kg<sup>-1</sup>) than other oxidizers, as well as its heat of combustion (4587 kJ kg<sup>-1</sup>) which is lower than that of, for example, its “greener” rival ammonium dinitramide, ADN (5145 kJ kg<sup>-1</sup>)<sup>[19]</sup>. ADN has one major advantage over AP, and that is the fact that it is an H, N, O oxidizer, whereas AP is a H, N, O, Cl oxidizer containing chlorine. Not only does AP contain chlorine, it is also water soluble, meaning that the perchlorate ion has been found in drinking water, and is suspected of interfering with thyroid gland function<sup>[2], [20]</sup>. Another health and environmental issue linked to AP is also due to the presence of chlorine, since on combustion, highly toxic and corrosive HCl is produced which forms acid rain. Despite these health and ecological concerns, AP is still the oxidizer of choice, but work is on-going to find halogen-free alternatives<sup>[2], [20]</sup>.

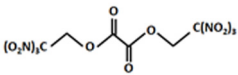
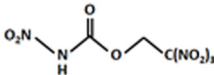
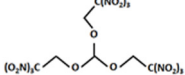
This is however, not an easy task, since the list of requirements for a compound to be considered a future, halogen-free, green oxidizer is long. A very high oxygen balance is obviously essential, good thermal stability, economical and easy synthesis on a large scale, low sensitivity to external stimuli, non-toxic, non-hygroscopic, halogen-free and ideally smokeless, as well as not showing phase changes in the solid state within the relevant temperature range. The latter issue along with the hygroscopic nature of AN are arguably its two major drawbacks for use – as well as the dangers in its storage<sup>[2]</sup>.

Ammonium dinitramide is another compound under scrutiny for use as a green oxidizer, since in addition to

being halogen-free and possessing a high oxygen balance, it shows a high enthalpy of formation, burning rate and does not have the phase change issues in the solid-state which plague AN<sup>[20]</sup>. However, it is highly hygroscopic, has issues with thermal stability and also compatibility and cost of production. Hydrazinium nitroformate (HNF) has also been a forerunner in the race to replace AP, since it is non-hygroscopic, more endothermic enthalpy of formation than AP, high density and easy synthesis<sup>[20]</sup>. HNF has been known for over 70 years, however, issues still surround its thermal stability, as well as its sensitivity to external stimuli, as well as the health concerns surrounding compounds which could be release hydrazine which is carcinogenic<sup>[20]</sup>.

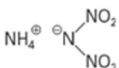
It is interesting to note that all of the above-mentioned compounds – AP, AN, ADN and HNF – are all salts. However, recently we have investigated three neutral compounds with high oxygen balances for their suitability for use as oxidizers. The three compounds which were found to be of most interest from this work are bis(2,2,2-trinitroethyl)oxalate [BTNEO] (1), 2,2,2-trinitroethyl-nitrocarbamate [TNENC] (2) and 2,2,2-trinitroethyl formate [TNEF] (3) (table 4)<sup>[21]</sup>. Each of these compounds contains at least one -C(NO<sub>2</sub>)<sub>3</sub> group and are halogen-free, C, H, N, O oxidizers.

**Table 4.** Relevant data for the neutral C, H, N, O oxidizers bis(2,2,2-trinitroethyl)oxalate [BTNEO] (1), 2,2,2-trinitroethyl-nitrocarbamate [TNENC] (2) and 2,2,2-trinitroethyl formate [TNEF] (3)<sup>[21d]</sup>

	BTNEO (1)	TNENC (2)	TNEF (3)
Formula	C <sub>6</sub> H <sub>4</sub> N <sub>6</sub> O <sub>16</sub>	C <sub>3</sub> H <sub>3</sub> N <sub>5</sub> O <sub>10</sub>	C <sub>7</sub> H <sub>7</sub> N <sub>9</sub> O <sub>21</sub>
MWt. / g mol <sup>-1</sup>	416	269	553
Connectivity			
IS / J	10	10	5
FS / N	> 360	96	9
ESD / J	0.7	0.1	0.2
Ω(CO) / %	+15.4	+32.7	+30.4
Ω(CO <sub>2</sub> ) / %	+7.7	+14.9	+10.1
m.p. / °C	115	109	128
T <sub>dec</sub> / °C	186	153	192
ρ / g cm <sup>-3</sup>	1.84	1.73	1.81
ΔH <sup>o</sup> f / kJ mol <sup>-1</sup>	-688	-366	-519

An overview of the properties of these three compounds as well as those of HNF, ADN, AN and AP is given in tables 3 and 5. Common to BTNEO and TNEF are high densities and decomposition temperatures, whereas TNENC suffers from a relatively low decomposition temperature. Conversely, TNENC shows the highest oxygen balance followed closely by TNEF. TNEF has been scaled-up to produce 100 g, which was a necessary step in order to explore the possibility of TNEF being able to replace AP in a model thermobaric formulation<sup>[21d]</sup>.

**Table 5.** Relevant data for the oxidizers HNF, AND, AN and AP<sup>[1],[20]</sup>

	HNF	ADN	AN	AP
Formula	CH <sub>5</sub> N <sub>5</sub> O <sub>6</sub>	H <sub>4</sub> N <sub>4</sub> O <sub>4</sub>	H <sub>4</sub> N <sub>2</sub> O <sub>3</sub>	H <sub>4</sub> NO <sub>4</sub> Cl
MWt. / g mol <sup>-1</sup>	183.08	124.06	80.04	117.49
Connectivity	N <sub>2</sub> H <sub>5</sub> +C(NO <sub>2</sub> ) <sub>3</sub> -		NH <sub>4</sub> +NO <sub>3</sub> -	NH <sub>4</sub> +ClO <sub>4</sub> -
IS / J	4	4	40	15
FS / N	28	64	>360	>320

$\Omega$ / %	+13.11	+25.8	+19.99	+27.2
m.p. / °C	128	91.5	170	>220 (values vary)
T <sub>dec</sub> / °C	131	135 (values vary)	210	389 (values vary)
$\rho$ / g cm <sup>-3</sup>	1.88	1.812	1.722	1.95
$\Delta H^{\circ}_f$ / kJ mol <sup>-1</sup>	-71	-149	-367.5	-295.8

The thermobaric formulation investigated consisted of HMX as the high explosive, Al, binder and TNEF (40% HMX, 20% Al, 20% TNEF, 20% binder (TBX-2)) and was directly compared with the same mixture but in which the 20% TNEF oxidizer was replaced by 20% of the conventional oxidizer AP (TBX-1). Initial results show that TBX-1 and TBX-2 show very similar performance, even though AP in TBX-1 has been completely replaced by TNEF in TBX-2 (table 6)<sup>[18]</sup>.

**Table 6.** Performance parameters of two TBX formulations (calculated with EXPLO5\_V6.05.02)<sup>[4],[18]</sup>.

	TBX-1	TBX-2
oxidizer	AP	TNEF
VoD / m s <sup>-1</sup>	6699	6593
pC-J / GPa	18.2	17.6
-Q <sub>ex</sub> / kJ kg	8202	8355
T <sub>ex</sub> / K	4371	4451

Although there is much more work to be undertaken to assess whether TNEF has a future as an oxidizer in applications, initial investigations show that it has promising properties and is worth investigating further.

### Acknowledgments

The author is indebted to and thanks Dr. Danica Simic (Military Technical Institute, Belgrade) and Prof. Dr. Muhamed Suceška (University of Zagreb) for a year-long great collaboration.

### Literature

- [1] T. M. Klapötke, *Energetic Materials Encyclopedia*, 2th Edition, De Gruyter, Berlin/Boston, 2021.
- [2] T. M. Klapötke, *Chemistry of High Energy Materials*, 6th Edition, De Gruyter, Berlin/Boston, 2022.
- [3] J. Köhler, R. Meyer, A. Homburg, *Explosivstoffe*, 9th edn, Wiley-VCH, Weinheim, 2008.
- [4] M. Suceška, EXPLO5, version V6.06.01, Zagreb, 2021.
- [5] H. Östmark, H. Bergman, U. Bemm, P. Goede, E. Holmgren, M. Johansson, A. Langlet, N. V. Latypov, A. Pettersson, M.-L. Pettersson, N. Wingborg, C. Vörde, H. Stenmark, L. Karlsson, M. Hihkiö, 2,2-Dinitroethene-1,1-diamine (FOX-7) – Properties, Analysis and Scale Up, Proc. Int. Conf. ICT, 2001, Karlsruhe, Germany, pp. 26-1–26-21.
- [6] a) D. S. Donald, Tetraaminopyrazine, 2,3,5-Triamino-6-nitropyrazine, 2,6-Diamino-3,5-dinitropyrazine, US Patent 3808209, 30th April 1974. b) T. D. Tran, P. F. Pagoria, D. M. Hoffman, J. L. Cutting, R. S. Lee, R. L. Simpson, Characterization of 2,6-Diamino-3,5-Dinitropyrazine-1-Oxide (LLM-105) as an Insensitive High Explosive Material, Proc. 33rd Int. Conf. ICT, 25th – 28th June 2002, Karlsruhe, Germany.
- [7] A. T. Nielsen, A. P. Chafin, S. L. Christian, D. W. Moore, M. P. Nadler, R. A. Nissan, D. J. Vanderah, *Tetrahedron*, 1998, 54, 11793–11812
- [8] N. Fischer, D. Fischer, T. M. Klapötke, D. G. Piercey, J. Stierstorfer, *J. Mater. Chem.*, 2012, 22 (38), 20418 – 20422.
- [9] T. Alaime, M. Bölter, A. Delage, G. Eck, T. Klapötke, F. Lacemon, J. Stierstorfer, Method for Sequential One-Pot Synthesis of TKX-50, World Intellectual Property Organization, WO2022129724 A1 2022-06-23 and FR3118034 A1 2022-06-24.
- [10] H. Gao, J. M. Shreeve, *Chem. Revs.*, 2011, 111, 7377 – 7436.
- [11] A. L. R. Silva, A. R. R. P. Almeida, M. D. M. C. Ribeiro da Silva, J. Reinhardt, T. M. Klapötke, *Prop. Explos. Pyrotech.*, 2023, 48, e202200361.
- [12] T. M. Klapötke, S. Cudziło, W. A. Trzciński, *Prop. Explos. Pyrotech.*, 2022, 47, e202100358.
- [13] J. L. Gottfried, T. M. Klapötke, T. G. Witkowski, *Prop. Explos. Pyrotech.*, 2017, 42, 353 – 359.
- [14] T. M. Klapötke, New Secondary Explosives and Oxidizers Developed at LMU, 53rd Intl. Annual Conf., Proc. Int. Conf. ICT, Karlsruhe, Germany, June 25th – 28th, 2024, V1.
- [15] a) TKX-50: A highly promising secondary explosive, T. M. Klapötke, in: *Materials Research and Applications (Select Papers from JCH8-2019)*, D. Trache, F. Benaliouche, A. Mekki (eds.), Springer, Singapore, 2021. b) X. Wang, G. Hao, L. Xiao, Y. Hu, G. Zhang, S. Wang, J. Yang, W. Jiang, *Thermochim. Acta*, 2023, 719, 179393. c) D. Liu, J. Chen, R. Yang, L. Xiao, G. Zhang, X. Feng, K. Zhang, W. Jiang, G. Hao, *Chem. Mater.*, 2024, 36, 3496 – 3535.
- [16] T. M. Klapötke, S. Cudziło, W. A. Trzciński, J. Paszula, L. Bauer, C. Riedelsheimer, J. T. Lechner,

- Prop. Explos. Pyrotech., 2023, 48, e202300010.
- [17] D. Simic, U. Andjelic, D. Knezevic, K. Savic, V. Draganic, R. Sirovatka, J. Tomic, *Centr. Eur. J. Energet. Mater.*, 2016, 13, 161 – 182.
- [18] D. Simic, T. M. Klapötke, Manuscript in preparation.
- [19] Y. Wang, X. Song, F. Li, *ACS Omega*, 2019, 4, 214 – 225.
- [20] D. Trache, T. M. Klapötke, L. Maiz, M. Abd-Elghany, L. T. DeLuca, *Green Chem.*, 2017, 19, 4711 – 4736.
- [21] a) M. B. Frankel, *J. Chem. Eng. Data*, 1962, 7, 410. b) Process for acetal preparation, M. E. Hill, K. G. Shipp, US Patent US3526667, 1970. c) A. B. Sheremetev, I. L. Yudin, *Mendeleev Commun.*, 2005, 15, 204 – 205. d) D. E. Dosch, K. Andrade, T. M. Klapötke, B. Krumm, *Prop. Explos. Pyrotech.*, 2021, 46, 895 - 898.

## TABLE OF CONTENTS

### PLENARY LECTURE

- NEW SECONDARY EXPLOSIVES AND OXIDIZERS DEVELOPED AT LMU,**  
IX Thomas M. Klapötke, LMU Munich, Department of Chemistry, Energetic Materials  
Research, 81377 Munich, Germany  
**10.5937/OTEH24001K**

### 1. SECTION : AERODYNAMICS AND FLIGHT DYNAMICS - AFD

- 2 **THE NA-DEL AIRFOIL MODIFICATIONS FOR GENERAL AVIATION AND UAV APPLICATIONS,** Zorana Z. Dančuo, Ivan A. Kostić, Olivera P. Kostić, Aleksandar Č. Bengin, Goran S. Vorotović  
**10.5937/OTEH24002D**
- 8 **AERODYNAMIC OPTIMIZATION OF WINGLETS FOR AN UNMANNED AERIAL VEHICLE,** Dušan Ivković, Ivan Kostić, Olivera Kostić, Mirko Dinulović, Aleksandar Simonović  
**10.5937/OTEH24003I**
- 15 **COMPUTATIONAL ANALYSIS OF ROCKET-ASSISTED PROJECTILE TRAJECTORY,** Abdellah Ferfour, Damir D. Jerković, Aleksandar V. Kari, Saša Živković  
**10.5937/OTEH24004F**
- 24 **COMPUTING AERODYNAMIC DAMPING IN ROLL AND PITCH OF A SUPERSONIC FINNER MODEL,** Jelena Svorcan, Toni Ivanov, Ognjen Peković, Aleksandar Simonović  
**10.5937/OTEH24005S**
- 28 **DESIGN AND EXPERIMENTAL EVALUATION OF A MISSILE LATERAL THRUSTER,** Toufik Allouche, Saša Živković, Marko Karić, Abdellah Ferfour, Damir Jerković, Nebojša Hristov  
**10.5937/OTEH24006A**
- 34 **NUMERICAL INVESTIGATION OF THICKNES, ASPECT AND TAPER RATIO INFLUENCE ON DIVERGENCE VELOCITIES OF COMPOSITE PLATES AT SUBSONIC MACH NUMBERS,** Aleksa Maljević, Mirko Dinulović, Nemanja Deura  
**10.5937/OTEH24007M**
- 39 **EVALUATION OF THE INFLUENCE OF POWER SETTING ON AIRCRAFT PERFORMANCE IN A SPIN,** Jelena Šobot, Đorđe Jankuloski, Miša Živković, Jasminka Jelisavac, Ivan Vesić  
**10.5937/OTEH24008S**
- 43 **EXPERIMENTAL RESULTS FROM THE MISSILE MODEL TEST CAMPAIGN IN THE VTI T-38 WIND TUNNEL,** Marija Samardžić, Nataša Vujić, Biljana Ilić, Goran Ocokoljić  
**10.5937/OTEH24009S**



- 50 **CONTROL DERIVATIVE ESTIMATION OF NONCONVENTIONAL UAV DESIGN**, Miodrag Milenković-Babić, Branislav Ostojić, Biljana Dovatov, Ilija Nenadić  
**10.5937/OTEH24010M**

## **2. SECTION : AIRCRAFT - A**

- 56 **USAGE OF MULTI-HOLE PROBE ON UAV WITH WARHEAD**, Ilija Nenadić, Dijana Damljanović, Biljana Dovatov, Marko Bek-Uzarov  
**10.5937/OTEH24011N**
- 60 **DESIGN AND VERIFICATION OF A PNEUMATIC LAUNCH SYSTEM FOR A SINGLE-USE UAV WITH A WARHEAD**, Marko Bek-Uzarov, Ilija Nenadić, Stefan Rašić  
**10.5937/OTEH24012B**
- 65 **THE EFFECTIVNES OF THE USE OF DRONES IN MODERN CONFLICT**, Stevan Jovičić, Jasminka Jelisavac, Ljubiša Tomić, Ivo Obradovic  
**10.5937/OTEH24013J**
- 70 **AIRCRAFT PROTECTION AGAINST LIGHTNING AND STATIC ELECTRICITY**, Marina Ostojić, Tamara Nikolić, Radoje Zarubica, Nikola Bogavac  
**10.5937/OTEH24014O**
- 74 **FAILURE ANALYSIS OF AIRCRAFT STRUCTURAL ELEMENTS**, Stevan Maksimović, Katarina Maksimović, Ivana Vasović Maksimović, Mirjana Đurić, Mirko Maksimović  
**10.5937/OTEH24015M**
- 80 **SMALL FIXED-WING UAV PRECISION AERIAL DROP CAPABILITY DEVELOPMENT**, Vuk Antonić, Milenko Trifković, Vojimir Molović,  
**10.5937/OTEH24016A**
- 86 **ANALYSIS OF THE RESCUE SYSTEM IMPLEMENTATION IN THE MEDIUM RANGE UAV**, Vanja Stefanović Gobeljić, Miodrag Milenković Babić, Mihailo Zdravković  
**10.5937/OTEH24017S**
- 91 **ANALYSIS OF THE MASS AND AERODINAMICAL CHANGES DUE TO IMPLEMENTATION OF AN EXTERNAL RESCUE SYSTEM ON A MEDIUM RANGE UAV**, Branislava Ostić, Miodrag Milenković-Babić, Vanja Stefanović-Gobeljić, Branislav Ostojić  
**10.5937/OTEH24018O**

## **3. SECTION : WEAPON SYSTEMS AND COMBAT VEHICLES – WSCV**

- 96 **ANALYSIS OF THE BEHAVIOUR OF THE MOBILE PLATFORM DURING FIRING**, Milan Simonović, Marko Simonović, Aleksandra Živković, Ana Gačić, Aleksandar Kari  
**10.5937/OTEH24019S**

- 103 **THE CONCEPT OF REMOTE CONTROLLED WEAPON STATION FOR SELF-PROPELLED MORTARS**, Aleksandra Živković, Milan Simonović, Goran Dragović, Marija Milovanović, Nina Mitričević  
**10.5937/OTEH24020Z**
- 109 **DESIGN OF MORTAR BARREL 82 mm ON BASIS OF ANALYSIS OF INTERNAL BALLISTICS PARAMETERS**, Marija Milovanović, Nikola Radovanović, Nebojša Hristov, Lazar Arsić, Aleksandra Živković  
**10.5937/OTEH24021M**
- 114 **SIMULATION MODEL OF TANK COMBAT**, Marko Simonović, Milan Simonović, Lazar Arsić, Ana Gačić, Dušan Božić  
**10.5937/OTEH24022S**
- 120 **SIMULATION MODEL OF PRIORITIZED THREAT SELECTION IN DEFENSIVE MULTITARGET MILITARY SWARMING**, Radomir Janković  
**10.5937/OTEH24023J**
- 126 **PROBABILITY OF HITTING AND DESTROYING A SURFACE TARGET FOR ARTILLERY ROCKETS**, Katarina Nestorović, Marina Simović – Pavlović, Miloš Pavić, Srđan Stojković, Slobodan Bosiljčić  
**10.5937/OTEH24024N**
- 131 **ACTIVE GYRO-DUMPING FOR MISSILE WITH PITCH/YAW DISTURBANCE SENSITIVE HOMING HEAD**, Miloš Pavić, Ivan Marić  
**10.5937/OTEH24025P**
- 135 **OPTIMIZATION OF AUTOMATIC SAFETY ALGORITHMS FOR GUIDED MISSILES TO MEET TESTING RANGE BOUNDARIES**, Ivana Todić, Luka Miličić, Vladimir Kuzmanović, Miloš Marković, Dejan Jevtić  
**10.5937/OTEH24026T**
- 140 **OPTIMIZATION OF SINGLE STAGE PLANETARY GEARBOX PARAMETERS USING GENETIC ALGORITHM**, Miloš Sedak, Maja Rosić  
**10.5937/OTEH24027S**
- 147 **TESTING OF TECHNICAL SOLUTION FOR ACHIEVING THE OPTIMAL DURATION OF THE ACTIVATION CADENCE OF THE FRONT AND MAIN WARHEAD IN THE TANDEM CUMULATIVE WARHEADS**, Slobodan Bosiljčić, Miroslav Gluvačević, Rade Stančić, Marinko Ugrčić, Katarina Nestorović  
**10.5937/OTEH24028B**
- 152 **A NEW APPROACH TO MUZZLE CLIMB REDUCTION IN ASSAULT RIFLES**, Ranko Babić  
**10.5937/OTEH24029B**
- 159 **PERSPECTIVES ON THE DEVELOPMENT OF THE ARTILLERY BRANCH OF THE SERBIAN ARMY**, Katarina Janković, Nenad Komazec  
**10.5937/OTEH24030J**

- 166 **ANALYSIS OF THE USE OF MODERN FIRE GUIDANCE SYSTEMS AND THEIR IMPLEMENTATION IN INFANTRY UNITS**, Marko Radovanović, Aleksandar Petrovski, Aner Behlić, Rexhep Mustafovski, Kristijan Ilievski, Željko Jokić, Sofija Ackovska  
**10.5937/OTEH24031R**
- 172 **ANALYTICAL AND NUMERICAL ANALYSIS OF AXIAL STRESSES IN A HIGH EXPLOSIVE ROCKET ASSISTED PROJECTILE BODY DURING ITS LAUNCH**, Svetlana Stojnović, Abdellah Ferfour, Nikola Radovanović, Miloš Pešić, Srećko Manasijević, Vladimir Milovanović  
**10.5937/OTEH24032S**
- 177 **EFFECT OF EROSIVE BURNING IN ROCKET MOTOR ON THE BALLISTICS OF ROCKET FLIGHT**, Srđan Stojković, Nikola Gligorijević  
**10.5937/OTEH24033S**
- 186 **ASSESSMENT OF EXPOSURE TO PHYSICAL HAZARDS IN THE WORKING ENVIRONMENT DURING TESTING OF PROTOTYPES**, Snežana Jovanović, Dragan Stojadinović, Martin Jovanović, Aleksandar Đurić  
**10.5937/OTEH24034J**
- 191 **PRESENTATION OF THE USE OF MODERN FIRE CONTROL SYSTEMS AND THEIR IMPLEMENTATION IN INFANTRY UNITS**, Marko Crnogorac, Marko Radovanović  
**10.5937/OTEH24035C**
- 196 **PREDICTION OF ARTILLERY CORRECTION ELEMENTS BY SOFTWARE FOR BALLISTICS MODULE OF FIRE CONTROL SYSTEMS**, Dragoslav R. Petrović  
**10.5937/OTEH24036P**
- 202 **CHANGE OF SPEED OF COMFORT PARAMETERS IN THE ARMORED COMBAT VEHICLES OF THE SERBIAN ARMY DUE TO ENVIRONMENTAL CONDITIONS**, Snežana Mališić, Milica Ivanović, Filip Stanić  
**10.5937/OTEH24037M**

#### **4. SECTION : AMMUNITION AND ENERGETIC MATERIALS - AEM**

- 207 **MODELING OF SHAPED CHARGE JET PENETRATION DEPTH: ANALYTICAL AND NUMERICAL APPROACH**, Predrag Elek, Miloš Marković, Dejan Jevtić, Radovan Đurović  
**10.5937/OTEH24038E**
- 213 **MONITORING PLASTICIZER'S MIGRATION IN THE HMX/DOA MIXTURE UNDER ELEVATED TEMPERATURES**, Mirjana Krstović, Danica Bajić, Teodora Stančić, Mladen Timotijević, Fidanovski Bojana  
**10.5937/OTEH24039K**
- 222 **INFLUENCE OF DIFFERENT HMX/RDX CONTENTS IN COMPOSITE ROCKET PROPELLANTS ON THE VACUUM STABILITY TEST RESULTS**, Bojana Fidanovski, Slavko Mijatov, Mirjana Krstović, Marica Bogosavljević, Mirjana Dimić  
**10.5937/OTEH24040F**

- 228 **PARTICLE SIZE SENSITIVITY IN SMOOTH PARTICLE HYDRODYNAMICS NUMERICAL SIMULATION OF NATURAL FRAGMENTATION PHENOMENA**, Miloš Marković, Predrag Elek, Ivana Todić, Dejan Jevtić, Martin Macko  
**10.5937/OTEH24041M**
- 235 **NUMERICAL MODELING OF EXPLOSIVELY FORMED PROJECTILES FORMATION**, Andjela Mitrović, Saša Savić, Milan Vučković, Nebojša Hristov, Damir Jerković, Mladen Josijević  
**10.5937/OTEH24042M**
- 241 **CARBON BLACK VS CHARCOAL. INFLUENCE ON COMBUSTION PROPERTIES OF SELECTED PYROTECHNIC COMPOSITIONS**, Jelena Mojsilović, Ivan Dimitrijević, Mirjana Krstović, Stevan Stupar, Veselin Živanović  
**10.5937/OTEH24043M**
- 246 **CALCULATION OF SAFE DIAMETER OF PROPELLANTS USING HEAT FLOW MEASUREMENTS**, Vesna Petrović, Slaviša Stojiljković, Jelena Šultans  
**10.5937/OTEH24044P**
- 252 **INFLUENCE OF GUNPOWDERS AND ROCKET PROPELLANTS SAMPLE PREPARATION ON TEST RESULTS**, Jelena Šultans, Slaviša Stojiljković, Vesna Petrović  
**10.5937/OTEH24045S**
- 258 **DEVELOPMENT OF LINER FOR CASE-BONDED GRAIN WITH END-BURNING CONFIGURATION**, Tihomir Kovačević, Slavko Mijatov, Alen Crnalić, Jelena Gržetić, Darko Kuprešak, Saša Brzić  
**10.5937/OTEH24046K**
- 263 **BLAST PERFORMANCE OF ISOPROPYL NITRATE - BASED THERMOBARIC EXPLOSIVES VS. CAST-CURED PBX**, Danica M. Bajić, Slavica Terzić, Mladen Timotijević, Radoslav Sirovatka, Dragan Knežević, Igor Blagojević, Maja Radmanovac  
**10.5937/OTEH24047B**
- 268 **UNSTEADY INTERNAL BALLISTIC CALCULATION OF ATYPICAL PROCESSES IN ROCKET MOTOR**, Saša Živković, Saša Antonović, Miloš Filipović, Mirko Karić, Marko Karić  
**10.5937/OTEH24048Z**

## **5. SECTION : INTEGRATED SENSOR SYSTEMS AND ROBOTIC SYSTEMS – ISSRS**

- 276 **IMPLEMENTATION OF AN ALGORITHM FOR AUTONOMOUS MOVEMENT ON A ROBOTIC PLATFORM**, Nina Mitričević, Rade Pavlović  
**10.5937/OTEH24049M**
- 281 **THE IMPORTANCE OF PINHOLE SIZE TARGET IN THERMOGRAPHIC AND RADIOMETRIC MEASUREMENT**, Katarina Mišković  
**10.5937/OTEH24050M**

- 284 **IMPROVEMENT OF THE SIGNAL-TO-NOISE RATIO BY USING A STATISTICAL FILTER**, Miodrag Vračar, Stevo Vračar  
10.5937/OTEH24051V
- 289 **DESIGN OF A SERVO MECHANISM FOR CONTROLLING MISSILE FINS IN PITCH AND YAW PLANES**, Nebojša Jovičić, Aleksandar Stefanović, Marijana Stojanović, Miloš Pavić  
10.5937/OTEH24052J
- 293 **TESTING THE ROLL STABILIZATION OF A SUPERSONIC SURFACE-TO-AIR GUIDED MISSILE**, Marijana Stojanović, Aleksandar Stefanović, Nebojša Jovičić, Ivan Marić  
10.5937/OTEH24053S
- 298 **AZIMUTH ANGLE ERROR DEPENDING OF THE INERTIAL NAVIGATION SYSTEM MOUNTING ERROR**, Vladimir Vukmirica Phd, Ivana Trajkovski Msc, Nada Asanović Eng, Adrijana Jovanović Msc  
10.5937/OTEH24054V
- 301 **UWB SENSOR PERFORMANCE IN UGV ‘FOLLOW ME’ APPLICATIONS WITH OBSTACLE INTERFERENCE**, Rade Pavlović, Nina Mitričević, Srđan Savić  
10.5937/OTEH24055P
- 307 **FRACTIONAL ORDER ITERATIVE LEARNING CONTROLLER WITH PSO-BASED PARAMETERS TUNING FOR ROBOTIC SYSTEMS**, Nikola Živković, Mihailo Lazarević, Jelena Vidaković, Stjepko Pišl  
10.5937/OTEH24056Z
- 313 **HIGH ACCURACY WEAPONS**, Dragan Knežević, Milan Popović, Miloš Simić, Goran Marjanović  
10.5937/OTEH24057K
- 319 **MULTISENSOR IMAGE FUSION: DATASET, METHODS AND PERFORMANCE EVALUATION**, Mohammed Zouaoui Laidouni, Boban Bondžulić, Dimitrije Bujaković, Touati Adli, Milenko Andrić  
10.5937/OTEH24058Z
- 326 **COMPARATIVE ANALYSIS OF YOLO ALGORITHMS FOR AIRCRAFT DETECTION IN REMOTE SENSING IMAGES**, Touati Adli, Dimitrije Bujaković, Boban Bondžulić, Mohammed Zouaoui Laidouni, Milenko Andrić  
10.5937/OTEH24059A
- 332 **NOVEL INSTRUMENT FOR AERODYNAMIC PRESSURE MEASUREMENTS WITH EXCHANGEABLE MULTISENSOR MODULES**, Miloš Frantlović, Miloš Vorkapić, Žarko Lazić, Milče M. Smiljanić, Ivana Jokić, Predrag Poljak, Dušan Nešić, Dragan Tanasković  
10.5937/OTEH24060F

336 **ANALYSING USAGE OF COMMERCIAL GRADE SINGLE ANTENNA INERTIAL NAVIGATION SYSTEM IN COMBAT UNMANNED GROUND VEHICLES FOR ESTIMATING ORIENTATION AND POSITION**, Goran Dragović, Nedeljko Dučić, Stefan Jovanović, Marko Simonović, Dušan Božić  
**10.5937/OTEH24061D**

343 **APPLICATION OF SCREW THEORY AND ITS IMPLEMENTATION IN PYTHON FOR CONTROLLING A NIRYO ONE MANIPULATOR**, Vuk Todorović, Milan Blagojević, Nikola Nešić  
**10.5937/OTEH24062T**

## **6. SECTION : TELECOMMUNICATION AND INFORMATION SYSTEMS - TIS**

353 **EXAMINATION OF THE PROTECTION FACTOR WITH A LASER PHOTOMETER**, Miljan Miletić, Marina Ilić, Tatjana Marković  
**10.5937/OTEH24063M**

357 **CASE STUDY: IMPLEMENTATION PERSPECTIVES OF END-TO-END ENCRYPTION IN MILITARY IOT**, Kristina Živanović, Dimitrije Kolašinac, Stefan Ivanović, Jovana Mihailov, Marija Šekler  
**10.5937/OTEH24064Z**

361 **OPTIMAL SOURCE LOCALIZATION IN A REAL RADIO CHANNEL BASED ON TDOA APPROACH USING THE HYBRID DIFFERENTIAL EVOLUTION ALGORITHM**, Maja Rosić, Miloš Sedak  
**10.5937/OTEH24065R**

369 **SIMPLE ENERGY DETECTOR FOR TWO-STAGE CLASSIFICATION FOR ANTIDRONE SYSTEMS**, Snežana Zurovac, Nikola Petrović, Vasilija Joksimović, Ivan Pokrajac, Darko Mikanović, Boban Sazdić-Jotić  
**10.5937/OTEH24066Z**

376 **CONTEMPORARY CRYPTOGRAPHY: RECENT ACHIEVEMENT AND RESEARCH PERSPECTIVES**, Boriša Jovanović, Ivan Tot, Silvana Ilić  
**10.5937/OTEH24067J**

381 **AN EXAMPLE OF VHF RADAR SIGNAL PROCESSING**, Darko Pijević, Aleksandar Ristić, Dragan Nikolić, Dejan Ivković, Zvonko Radosavljević  
**10.5937/OTEH24068P**

386 **THE POWER CONSUMPTION OF EMBEDDED GPU COMPUTERS FOR DEEP LEARNING APPLICATIONS**, Boban Sazdić-Jotić, Snežana Zurovac, Nikola Petrović, Dragana Bojić  
**10.5937/OTEH24069S**

392 **PROPOSITION OF LABORATORY EQUIPMENT AND ITS UTILISATION FOR COMPLEX BATTLEFIELD IP NETWORK SIMULATION**, Đorđe Nešković, Marko Marković, Lara Kašca, Stefan Stanković, Miroslav Perić, Mladen Koprivica, Dejan Drajić  
**10.5937/OTEH24070N**

- 397 **PERFORMANCE CHARACTERIZATION OF SECURE IP COMMUNICATION SYSTEMS FOR VARIOUS INTERACTIVITY LEVEL APPLICATIONS**, Lara Kašca, Đorđe Nešković, Marko Marković, Stefan Stanković, Miroslav Perić  
**10.5937/OTEH24071K**
- 403 **GRE TUNNEL UTILIZATION FOR MINIMIZING MULTI-VENDOR NETWORK EQUIPMENT ISSUES FOR VARIOUS TRANSMISSION CHANNELS**, Marko Marković, Lara Kašca, Đorđe Nešković, Stefan Stanković, Miroslav Perić, Mladen Koprivica, Goran Marković  
**10.5937/OTEH24072M**
- 409 **THE USE OF GEOGRAPHIC INFORMATION SYSTEMS (GIS) IN THE TEACHING OF MILITARY TOPOGRAPHY**, Marko Stojanović, Nenad Galjak, Jasmina M. Jovanović, Marko Simić, Vladimir Vučenov  
**10.5937/OTEH24073S**
- 415 **STANDARD CUMULANTS- BASED AUTOMATIC MODULATION CLASSIFICATION PERFORMANCE UNDER COLORED NOISE CHANNEL CONDITIONS**, Rade R. Božović, Vladimir D. Orlić  
**10.5937/OTEH24074B**
- 420 **SENTINEL-1 SAR INTERFEROMETRY FOR TERRAIN MONITORING: A CASE STUDY OF MINE DYNAMICS**, Miloš Basarić, Dušan Jovanović  
**10.5937/OTEH24075B**
- 427 **ANALYSIS OF TRAFFIC ACCIDENTS IN NOVI SAD USING GIS TECHNOLOGY**, Dejan Djordjević, Miloš Basarić, Ivan Garić  
**10.5937/OTEH24076D**
- 433 **DETERMINATION OF ELECTROMAGNETIC FIELD STRENGTH IN AREAS OF INCREASED SENSITIVITY AROUND RADIO TRANSMITTERS**, Ana Matović, Elmedin Biberović, Milan Gligorijević  
**10.5937/OTEH24077M**
- 439 **DIGITAL RADIO SYSTEM FOR REMOTE MONITORING AND CONTROL ON THE MEDIUM VOLTAGE DISTRIBUTION NETWORK USING THE PDR 300 RADIO DEVICE AS A TRANSMITTER**, Marija Matović, Ana Matović, Ivica Marjanović  
**10.5937/OTEH24078M**
- 444 **THE LEVEL CROSSING RATE OF THE NAKAGAMI-M RANDOM PROCESS**, Ivica Marjanović, Ana Matović, Marija Matović  
**10.5937/OTEH24079M**

## **7. SECTION : MATERIALS AND TECHNOLOGIES - MT**

- 449 **PORTABLE RAMAN SPECTROSCOPY FOR DETECTION OF AMMONIUM NITRATE–FUEL OIL EXPLOSIVE PRECURSORS**, Denis Dinić, Branislav Stojković, Dijana Aksentijević, Milan Tanić, Negovan Ivanković, Nemanja Jovanović, Marko Anđelković  
**10.5937/OTEH24080D**

- 452 **INFLUENCE OF TEMPERING TEMPERATURE ON MECHANICAL PROPERTIES OF G42CrMo4 CAST STEEL**, Đorđe Ivković, Dušan Arsić, Anđela Mitrović, Vladimir Milovanović, Dragan Adamović, Vesna Mandić, Marko Delić  
**10.5937/OTEH24081I**
- 457 **THE INFLUENCE OF THE PHASE TRANSFORMATION: Fhyd → FE3O4, OCCURS DURING THE ANNEALING TREATMENT OF SOL-GEL SYNTHESIS, ON THE ABSORPTION PROPERTIES OF THE FINAL SYNTHESIS PRODUCT (Fe3O4/C HOLLOW-SPHERE NANOPARTICLES)**, Violeta Nikolić, Zoran Ivić, Jose F. M. L. Mariano  
**10.5937/OTEH24082N**
- 463 **THE DESIGN AND PREPARATION OF CERIUM-DIOXIDE AND ZIRCONIUM(IV) HYDROXIDE-INCORPORATED NANOFIBERS FOR THE DEGRADATION OF CHEMICAL WARFARE AGENTS**, Maja Vitorović-Todorović, Tamara Vujatović-Velimirov, Stevan Stupar, Danica Bajić  
**10.5937/OTEH24083V**
- 469 **THE INFLUENCE OF DESIGN CONDITIONS ON THE FAILURE OF THE UNIVERSAL CROSS JOINT (UCJ) OF THE CARDAN COUPLING**, Saša Spasenić, Mileta Ristivojević, Vladimir Milovanović, Aleksandar Dimić, Stefan Dikić, Sreten Spasenić  
**10.5937/OTEH24084S**
- 475 **ADSORPTION OF ORGANOPHOSPHATE PESTICIDES ON NITROGEN-DOPED CARBON CRYOGELS AND THE ASSESSMENT OF THEIR NEUROTOXIC EFFECTS**, Vladan J. Anićjević, Tamara Tasić, Vedran Milanković, Dalibor B. Jovanović, Radovan M. Karkalić, Miloš Baljuzović, Biljana M. Babić, Igor A. Pašti, Tamara D. Lazarević-Pašti  
**10.5937/OTEH24085A**
- 480 **PRELIMINARY INVESTIGATION OF BAMBOO FIBRE METALLIZATION VIA CHEMICAL/ELECTROCHEMICAL METHODS**, Ivana Mladenović, Dušan Nešić, Marko Obradov, Miloš Vorkapić, Marija Vuksanović, Nebojša Nikolić, Dana Vasiljević Radović  
**10.5937/OTEH24086M**
- 486 **THE DESIGN AND SYNTHESIS OF THE FOUR NOVEL DUAL REVERSIBLE INHIBITORS OF ACETYLCHOLINESTERASE BASED ON THE TACRINE AND AROYLACRYLIC ACID PHENYLAMIDE SUBSTRUCTURES**, Tamara B. Vujatović-Velimirov, Milan R. Nikolić, Maja D. Vitorović-Todorović  
**10.5937/OTEH24087V**
- 493 **SIGNIFICANT CHARACTERISTICS OF LEAD AND ALLOYS WITH ANTIMONY IN THE PRODUCTION OF SMALL ARMS AMMUNITION**, Miroslav Papović  
**10.5937/OTEH24088P**



- 499 **ADSORBING DANGER: CARBON MATERIAL COMBATTING ORGANOPHOSPHATE**, Tamara Tasić, Vedran Milanković, Vladan Anićijević, Igor Pašti, Tamara Lazarević-Pašti  
**10.5937/OTEH24089T**
- 504 **ORGANOPHOSPHORUS NEUROTOXINS REMEDIATION IN DYNAMIC CONDITIONS**, Vedran Milanković, Tamara Tasić, Vladan Anićijević, Igor Pašti, Tamara Lazarević-Pašti  
**10.5937/OTEH24090M**
- 509 **INVESTIGATION OF THE DEPENDENCE OF PRESSURE DROP AND PARTICLES FLOW RATE ON THE PARTICLE DIAMETER IN SPOUT-FLUIDIZED BED**, Teodora Stančić, Mihal Đuriš, Tatjana Kaluđerović Radoičić  
**10.5937/OTEH24091S**
- 515 **MICROSTRIP DC-BLOCK ON TEXTILES USING ONLY SELF-ADHESIVE COPPER TAPE**, Dušan Nešić, Dragan Tanasković, Miloš Vorkapić  
**10.5937/OTEH24092N**
- 518 **DETERMINATION OF NATURAL BACKGROUND RADIATION IN AN URBAN AREA AS AN ASPECT OF NUCLEAR SECURITY DETECTION ARCHITECTURE: AN EXAMPLE FROM THE CITY OF KRUŠEVAC, SERBIA**, Milan Tanić, Denis Dinić, Stevan Stupar  
**10.5937/OTEH24093T**
- 524 **INVESTIGATION OF THE POSSIBILITY OF APPLICATION OF BIOINDICATORS IN REDUCTION LEVEL CONCENTRATIONS OF RADIOLOGICAL CONTAMINANTS**, Nataša Pajić, Željko Senić, Sonja Bauk  
**10.5937/OTEH24094P**
- 531 **DETERMINATION OF THE TEMPERATURE PROFILE OF SELECTED MOBILE PHONE CHARGERS AS A SAFETY FACTOR IN TERMS OF THERMAL RADIATION**, Ljubiša Tomić, Saša Veselinović, Marina Simović Pavlović, Katarina Nestorović, Darko Janković, Darko Vasiljević  
**10.5937/OTEH24095T**
- 535 **INFLUENCE OF SMALL ARMS AMMUNITION ON TARGETS MADE OF GRANULAR MATTER**, Marina Simović Pavlović, Vladimir Obradović, Darko Janković, Maja Pagnacco, Ljubiša Tomić, Darko Vasiljević  
**10.5937/OTEH24096S**
- 539 **CATALYTIC PROPERTIES OF PAPER-IMMOBILIZED HORSE SERUM BUTYRYLCHOLINESTERASE**, Sonja Bauk, Marina Ilić, Nataša Pajić, Tatjana Marković  
**10.5937/OTEH24097B**
- 545 **MAGNETOIMPEDANCE EFFECT OF NANOCRYSTALLINE FeNiSiB and FeCuVSiB RIBBONS**, Radoslav Surla, Milica M. Vasić, Dragica M. Minić, Ljubica Radović, Nebojša Mitrović, Pavel Crnomarković  
**10.5937/OTEH24098S**

- 550 **ALTERNATIVES TO CADMIUM PROTECTION IN DEFENSE AND AEROSPACE INDUSTRY**, Konstantin Komatina, Milan Ignjatović, Stefan Tomić, Dunja Crnogorac  
**10.5937/OTEH24099K**
- 553 **Cu -DECORATED TIO<sub>2</sub> NANOPARTICLES AS THE PHOTOCATALYTIC MATERIAL FOR CIPROFLOXACIN DEGRADATION**, Marija Kovačević, Sanja Živković, Miloš D. Milović, Dragana Vasić Anićijević  
**10.5937/OTEH24100K**
- 557 **SELECTIVE ELECTRODEPOSITION TO EXTRACT COBALT AND NICKEL FROM LEACHING SOLUTION**, Jonas Mitterecker, Milica Košević, Marija Mihailović  
**10.5937/OTEH24101M**
- 560 **INFLUENCE OF PROCESS PARAMETERS IN ADDITIVE MANUFACTURING ON THE QUALITY OF PRODUCED METAL PARTS**, Maja Mladenović, Jovana Mandić, Aleksandar Ćitić, Vesna Pejović, Aleksa Grubić, Srđan Živković  
**10.5937/OTEH24102M**
- 567 **FAILURE ANALYSIS OF WELDED JOINT BETWEEN ROCKET MOTOR CASE AND FINS**, Aleksandar Ćitić, Nada Ilić, Maja Mladenović, Vesna Pejović  
**10.5937/OTEH24103C**
- 572 **EFFECTS OF DIFFERENT SURFACE PREPARATIONS ON BONDING PROPERTIES OF ALUMINIUM ALLOY EN AW-5754**, Nataša Zdravković, Damjan Klobčar, Dragan Milčić, Miodrag Milčić, Vukašin Pavlović, Aleksija Đurić  
**10.5937/OTEH24104Z**
- 578 **CAVITATION EROSION MONITORING OF 42CrMo4 STEEL SAMPLES USING THE IMAGE AND MORPHOLOGICAL ANALYSIS**, Ana Alil, Stanica Nedović, Sanja Martinović, Tatjana Volkov Husović  
**10.5937/OTEH24105A**
- 582 **CAVITATION EROSION MONITORING OF MULLITE CERAMIC SAMPLE USING IMAGE ANALYSIS**, Sanja Martinović, Ana Alil, Tatjana Volkov Husović  
**10.5937/OTEH24106M**
- 586 **CORROSION OF 42CrMo4 STEEL IN MARINE ENVIRONMENT USING SEM/EDS ANALYSIS**, Stanica Nedović, Ana Alil, Sanja Martinović, Tatjana Volkov-Husović  
**10.5937/OTEH24107N**
- 590 **ADHESIVE JOINING OF 3D PRINTED PARTS**, Aleksija Đurić, Biljana Marković, Dragan Milčić, Srđan Samardžić, Miodrag Milčić, Nataša Zdravković  
**10.5937/OTEH24108D**
- 596 **CORROSION PROPERTIES OF LOW-CARBON STEEL WELDED JOINT IN SYNTHETIC SEA WATER ENVIRONMENT**, Mihael Bučko, Milan Jovanović Sreten Perić, Dragana Lazić, Jelena Marinković, Radovan Radovanović  
**10.5937/OTEH24109B**

- 600 **ENHANCED METHOD FOR MEASURING MATERIAL RESISTANCE TO BURNING NAPALM MIXTURE**, Tatjana Marković, Marina Ilić, Željko Senić, Sonja Bauk, Miljan Miletić  
**10.5937/OTEH24110M**
- 605 **STRUCTURAL AND MAGNETIC PROPERTIES OF CoFeSiB AMORPHOUS WIRE GMI ELEMENT**, Nebojša Mitrović, Jelena Orelj, Borivoje Nedeljković, Radoslav Surla, Vladimir Pavlović  
**10.5937/OTEH24111M**
- 610 **EXAMINING FATIGUE OF FIBER REINFORCED POLYMER: A COMPREHENSIVE REVIEW**, Amer. Alsammarraie, Muraja S. Slman  
**10.5937/OTEH24112A**
- 616 **REVIEW ON GRAPHITE PLUGGED BRONZE BUSHINGS**, Amir Alsammarraie, Bmaki H. Zaidan, Cali K. A. Aljboury  
**10.5937/OTEH24113A**
- 622 **IMPACT OF ACTIVE FILLER COMPOSITION MODIFICATION ON THE SORPTION CHARACTERISTICS OF FILTERS**, Biljana Mihajlović, Marina Ilić, Tatjana Marković, Vukica Grković  
**10.5937/OTEH24114M**
- 627 **EFFECT OF TEMPERING PARAMETERS ON MICROSTRUCTURE AND HARDNESS OF A LOW ALLOY ARMOR STEEL**, Gvozden Jovanović, Dragomir Glišić, Stefan Dikić, Esmail Ali Salem Ahmed, Nenad Radović  
**10.5937/OTEH24115J**

## **8. SECTION: QUALITY, STANDARDIZATION, METROLOGY, MAINTENANCE AND EXPLOITATION - QSMME**

- 632 **ANALYSIS OF RESULTS OBTAINED DURING CALIBRATION OF FORCE TRANSDUCERS**, Igor Goršić, Saša Antonović, Violeta Brnin, Saša Gundelj  
**10.5937/OTEH24116G**
- 636 **COORDINATE METROLOGY DATA MANAGEMENT OF MACHINE PARTS MADE BY METAL ADDITIVE MANUFACTURING**, Srđan Živković, Slobodan Malbašić, Miloš Stepanović  
**10.5937/OTEH24117Z**
- 643 **RELIABILITY OF ARTIFICIAL INTELLIGENCE**, Slavko Pokorni  
**10.5937/OTEH24118P**
- 647 **TEST SETUP FOR QUALIFICATION OF POWER SUPPLY FOR GENIII NIGHT VISION IMAGE INTENSIFIERS**, Slobodan Petričević, Peđa Mihailović, Petar Atanasijević  
**10.5937/OTEH24119P**

- 652 **IMPLEMENTATION OF ZIGBEE TECHNOLOGY IN THE PROCESS OF SENSOR CALIBRATION IN WIRELESS SENSOR NETWORK SYSTEMS**, Igor Medenica, Miloš Jovanović, Slobodan Subotić, Dragan Lazić  
**10.5937/OTEH24120M**
- 656 **THE ROLE OF INTELLECTUAL CAPITAL REPORTING IN THE PROCESS OF SUPPLY CHAIN INTEGRATION OF THE MILITARY TECHNICAL INSTITUTE**, Aleksandar Savić, Mihajlo Ranisavljević, Milan Mihajlović  
**10.5937/OTEH24121S**
- 662 **GROUNDWATER AS AN IMPORTANT RESOURCES IN EMERGENCY SITUATIONS OF THE REPUBLIC OF SERBIA**, Boris Vakanjac, Radoje Banković, Vesna Ristić Vakanjac, Saša Milanović, Ljiljana Vasić, Saša Bakrač, Nikola Kozić  
**10.5937/OTEH24122V**
- 668 **RISK MANAGEMENT IN INDUSTRIAL SECURITY IN THE FIELD OF PRODUCTION AND TRADE OF WEAPONS AND MILITARY EQUIPMENT**, Nenad Komazec, Katarina Janković, Milica Mladenović  
**10.5937/OTEH24123K**
- 673 **IMPROVEMENT OF PRODUCT QUALITY BY IMPLEMENTATION QFD METHODS**, Branko Vujatović, Marija Vujatović, Darko Grubač, Nenad Stojanović  
**10.5937/OTEH24124V**
- 679 **COMPARATIVE ANALYSIS OF INFORMATION SECURITY STANDARDS APPLICATION IN DIFFERENT IT SECTOR REGIONS**, Predrag Ranitović, Siniša Mitić  
**10.5937/OTEH24125R**
- 684 **BENFORD'S LAW IN SERVICE OF DATA QUALITY: TWO CASES OF NATURAL NUMBERS**, Igor Đorić, Slađana Vujičić, Mihajlo Ranisavljević  
**10.5937/OTEH24126D**
- 688 **THE NEW METHOD FOR SOLVING GAMMA-GAMMA, X-X, X-GAMMA COINCIDENCE SUMMING IN GAMMA SPECTROSCOPY**, Dragana Jordanov, Laslo Nadjdjerdj, Milena Rosić  
**10.5937/OTEH24127J**
- 692 **THE IMPACT OF DIVERSIFICATION STRATEGY ON COMPANY PERFORMANCE IN DEFENSE INDUSTRY**, Srđan Mirković, Mihajlo Ranisavljević, Igor Đorić  
**10.5937/OTEH24128M**
- 698 **STUDY AND ANALYSIS THERMAL PERFORMANCE OF TAZA GAS POWER PLANT IN KIRKUK –IRAQ**, H. J. Khalafa, M. I. Qaddouri  
**10.5937/OTEH24129K**
- 704 **DEFENSE ACQUISITIONS AND INTERNATIONAL POLITICS**, Marko Jovanović, Goran Vukadinović  
**10.5937/OTEH24130J**



# **OTEH 2024**

**11<sup>TH</sup> INTERNATIONAL SCIENTIFIC CONFERENCE  
ON DEFENSIVE TECHNOLOGIES**

*SECTION I*

**Aerodynamics and flight dynamics - *AFD***



## THE NA-DEL AIRFOIL MODIFICATIONS FOR GENERAL AVIATION AND UAV APPLICATIONS

ZORANA Z. DANČUO

University of Belgrade - Faculty of Mechanical Engineering, Innovation Center, Kraljice Marije 16, Belgrade, Serbia,  
[zdancuo@mas.bg.ac.rs](mailto:zdancuo@mas.bg.ac.rs)

IVAN A. KOSTIĆ

University of Belgrade - Faculty of Mechanical Engineering, Kraljice Marije 16, Belgrade, Serbia,  
[ikostic@mas.bg.ac.rs](mailto:ikostic@mas.bg.ac.rs)

OLIVERA P. KOSTIĆ

University of Belgrade - Faculty of Mechanical Engineering, Kraljice Marije 16, Belgrade, Serbia,  
[okostic@mas.bg.ac.rs](mailto:okostic@mas.bg.ac.rs)

ALEKSANDAR Č. BENGIN

University of Belgrade - Faculty of Mechanical Engineering, Kraljice Marije 16, Belgrade, Serbia,  
[abengin@mas.bg.ac.rs](mailto:abengin@mas.bg.ac.rs)

GORAN S. VOROTOVIĆ

University of Belgrade - Faculty of Mechanical Engineering, Kraljice Marije 16, Belgrade, Serbia,  
[gvorotovic@mas.bg.ac.rs](mailto:gvorotovic@mas.bg.ac.rs)

---

**Abstract:** This paper presents the NA-DEL geometric method for modifications of the so-called Dolphin family airfoils. Based on the original mathematical concept for Dolphin airfoils by Iosif Taposu, a new modification method was developed by the authors of this paper to achieve better aerodynamic efficiency than the original Dolphin airfoils and also their NACA geometrical counterparts. Bionic airfoils represent cutting-edge aerodynamic research. After the creation and integration of the natural optimization method - the semi-elliptical method, a new concept was introduced. The concept proposed that changing the shape of the leading edge of the original Dolphin airfoils could produce favorable outcomes in terms of aerodynamic efficiency. This method involves merging the two corresponding NACA and Dolphin airfoils to create a new hybrid airfoil in the leading edge zone. The NA-DEL method was tested both numerically and experimentally, and it showed noticeable improvements by modifying the airfoils of the 2410, 2412, and 2415 series. By numerical analyses, the NA-DEL 2410, 12, and 15 hybrid airfoils have been found to increase lift and lift-to-drag ratio, while also reducing drag in cases of standard roughness and  $MRe=6.0$ , which corresponds to the general aviation category. Through wind tunnel tests performed at the Belgrade University – Faculty of Mechanical Engineering, it has been discovered that the hybrid NA-DEL 2415 is also aerodynamically more effective than NACA and original Dolphin counterparts at a Reynolds number of 400.000. Results for this Reynolds number indicate that the NA-DEL airfoils are a suitable choice for fixed-wing UAVs and in that sense have potential military applications as well.

**Keywords:** NA-DEL, geometrical modification, Dolphin airfoils, CFD, wind tunnel tests, general aviation, UAV.

### 1. INTRODUCTION

The study of airfoils remains a fascinating area in aviation. Despite extensive research and analysis of different geometric shapes in aerodynamics, as well as established practices of airfoil modification, special individuals push the boundaries and redefine our understanding of this scientific field. Bionic research in aerodynamics has made a significant breakthrough in the development of technologies inspired by biological systems. Animals, such as birds and aquatic mammals, have inspired scientists to discover new aerodynamic

shapes.

In a recent study in [1], researchers introduced a new bionic airfoil inspired by the sturgeon. It has superior aerodynamic characteristics compared to the symmetric NACA 0015 airfoil, particularly in terms of the lift coefficient. The study involved the development of three bionic airfoils, followed by a Large Eddy Simulation (LES) to evaluate their performance. The results indicated a significant improvement in aerodynamic efficiency for the bionic airfoils showcasing their potential for enhancing the performance of various applications.

Researchers in [2] traced the wing geometry, angle of

attack (AoA), camber, and other bionic and flight parameters of a three-dimensional flapping wing of a barn owl. They studied the kinematics of a single flight, providing valuable insight into the bionic mechanisms and paving the way for future bionic design. In a study conducted by scientists in [3], the leading edge of a long-eared owl's wing served as the basis for the design of a bionic airfoil. This innovative airfoil was developed using reverse engineering techniques. The research findings indicated that the bionic airfoil contributed significantly to aerodynamic enhancements, particularly in deep stall conditions.

In a study in [4], researchers drew inspiration from a seagull's wing to design a bionic airfoil resembling the classical NACA 4412 airfoil. The bionic airfoil showed improved aerodynamic performance at low Reynolds numbers compared to the NACA 4412. The authors suggested its suitability for use in UAVs. In a similar study in [5], the NACA 4412 airfoil was compared to an airfoil designed to mimic the shape of a swallow's wing. After conducting numerical calculations and experimentation in a wind tunnel, the results showed that the bionic airfoil outperformed the NACA 4412 in terms of lift coefficient, lift-to-drag ratio, and stall angle.

The study of aquatic mammals, such as humpback whales, porpoises, and dolphins, which fall under the classification of Cetacea, has become a focal point in the field of aerodynamics. The shape of the dolphin has fascinated many aerodynamicists, although this topic is not yet fully explored. In [6], a bionic airfoil was examined. This airfoil was inspired by the shape of a porpoise *Phocoenoides dalli*, which is a mammal from the same family as the dolphin. Based on the streamlined profile of the *Phocoenoides dalli*'s head, the airfoil was modified into a new design with a leading edge similar to the streamlined profile of the porpoise's head. Minor adjustments were made to this new airfoil, resulting in three bionic dolphin airfoils: the Original Dolphin Airfoil, the Smooth Transition Dolphin Airfoil, and the Deflected Dolphin Airfoil.

Romanian scientist Taposu [7] developed a mathematical model to create an airfoil with a shape inspired by a dolphin. While this airfoil is not a replica of a dolphin's body in biological terms, the mathematical model offers the advantage of generating a variety of airfoils, allowing for the creation of entire families of airfoils. The authors of this paper have made several modifications to various specific Dolphin airfoils constructed using this mathematical model in [8, 9, 10, 11]. In the following sections of this paper, the NA-DEL geometrical modification of Taposu's Dolphin airfoils (referred to as "the original Dolphin airfoils" in the rest of the paper) will be explained, which is the main focus of this study.

## 2. DOLPHIN AIRFOILS

### 2.1. The original Dolphin airfoil

The original Dolphin airfoil in Figure 1. [7] is defined by piecewise mathematical functions that encompass four primary functions: the semi-thickness distribution

function, the skeleton line function, the suction and pressure surface functions.

The designer specifies the constructive parameters governing the position of maximum thickness and maximum camber to facilitate the generation of a specific airfoil from the broad spectrum of airfoils that can be derived using this mathematical model.

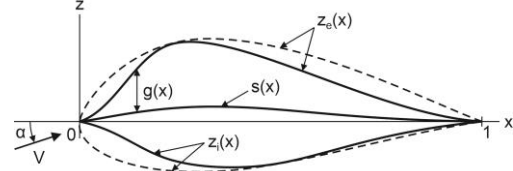


**Figure 1.** The original Dolphin airfoil geometry [7]

The functions of the semi-thickness distribution  $g(x)$  and skeleton line  $s(x)$  are given in Equations (1) and (2):

$$g(x) = \varepsilon \begin{cases} F_1(x), & 0 \leq x \leq x_1 \\ F_2(x), & x_1 < x \leq x_\varepsilon \\ F_3(x), & x_\varepsilon < x \leq x_2 \\ F_4(x), & x_2 < x \leq 1 \end{cases} \quad (1)$$

$$s(x) = \begin{cases} \Phi_1(x), & 0 \leq x \leq \zeta_1 \\ \Phi_2(x), & \zeta_1 < x \leq x_\zeta \\ \Phi_3(x), & x_\zeta < x \leq \zeta_2 \\ \Phi_4(x), & \zeta_2 < x \leq 1 \end{cases} \quad (2)$$

For an airfoil to be classified as a Dolphin-type, it must satisfy the condition given in Equation (3):

$$g'(0) = g'(1) = 0 \quad (3)$$

along the unit chord on the  $x$ -axis for the interval  $x \in [0, 1]$ . In other words, the airfoil must have zero thickness at the leading and trailing edge, i.e. without any radius. Parameters in Equations (1) and (2) represent:  $\varepsilon$  – half-thickness,  $\zeta$  – camber,  $\zeta_1$  – local camber at position  $x_1$  (along the  $x$ -chord),  $\zeta_2$  – local camber at position  $x_2$ ,  $x_\zeta$  – position of the maximum camber,  $x_\varepsilon$  – position of the maximum thickness,  $x_1$  and  $x_2$  positions of the local half-thicknesses  $\varepsilon_1$  and  $\varepsilon_2$ . The functions of the suction surface  $z_e(x)$  and pressure surface  $z_i(x)$  are given in Equations (4) and (5):

$$z_e = s(x) + g(x) \quad (4)$$

$$z_i = s(x) - g(x) \quad (5)$$

### 2.2. The NA-DEL airfoil modification method

The NA-DEL modification in [10] was developed to potentially enhance the hybrid Dolphin airfoils obtained through the semi-elliptical method using a geometric approach instead [10, 11]. While the semi-elliptical method can be described as a form of "natural modification" inspired by the contours of the velocity field at specific angles of attack and the flow field,

leading to the creation of a new airfoil shape, the NA-DEL method differs as it is entirely based on geometric principles. The term NA-DEL was derived from the combination of NACA - NA and Delfin - DEL (Serbian for "Dolphin"). Upon careful consideration, it was determined that the NACA geometric counterparts would be connected tangentially to the original Dolphin airfoils in the leading edge zone. Specifically, the suction surface of the NACA geometric counterpart would be added up to the maximum thickness on the suction surface of the original Dolphin airfoil. Similarly, the pressure surface of the NACA geometric counterpart would be added up to the maximum thickness on the bottom, i.e. pressure surface of the original Dolphin airfoil. Subsequently, from those points to the trailing edge, the original Dolphin airfoil would be maintained. A geometrical counterpart in this sense is an airfoil that has the same relative maximum thickness in the same position on the unit chord, and the same maximum relative camber and position. This means that an airfoil like the NACA 2410 has its geometrical counterpart in the original Dolphin airfoil family with the Dolphin 2410. These airfoils have parameters according to the four-digit NACA series airfoil convention [12].

### 3. NA-DEL AIRFOILS

In this particular section, the NA-DEL Dolphin airfoils will be presented. Significant advancements have been made in modifying the NA-DEL 2410, 2412, and 2415 airfoils. Furthermore, experimental testing of the NA-DEL 2415 was conducted within the wind tunnel facilities at the University of Belgrade - Faculty of Mechanical Engineering [10]. The NA-DEL 2410, 2412, and 2415 were obtained through modifications of the following geometrical counterparts respectively: the NACA 2410 - and Dolphin 2410, the NACA 2412 - and Dolphin 2412, and the NACA 2415 - and Dolphin 2415 airfoils. All the aforementioned airfoils underwent numerical analyses in ANSYS FLUENT. The RANS equations with SST  $k-\omega$  turbulent model were used for all calculations at Reynolds number of  $6 \times 10^6$  (or  $MRe = 6$ ; corresponds to the general aviation category), assuming standard roughness cases. A structured C-mesh was generated with a 2D control volume of  $25 \times 25m$ . All analyzed airfoils had a unit chord of  $1m$  in length. The Sutherland viscosity equation

was used with a density-based model for subsonic flow. A standard roughness case involves an early forced boundary layer transition. The temperature was set to  $T=288.15 \text{ K}=\text{const}$ , and an operating pressure  $p=101325 \text{ Pa}$ . The study employed the Full Multi-Grid method for initialization, as well as solution steering to optimize the Courant number. The mesh consists of 115600 elements. The number of iterations was set to 1000. The convergence criteria were set to absolute, with residuals set to a value of  $1e-07$ . Convergence conditions were set to "All conditions met," and second-order discretization was used [8, 9, 10, 11].

#### 3.1. The NA-DEL 2410 airfoil

The NA-DEL 2410 airfoil is a hybrid Dolphin airfoil obtained, as previously mentioned, by merging the two corresponding geometric counterparts, the NACA 2410 and the original Dolphin 2410 airfoils. These airfoils have a maximum camber of 2% positioned at 40% of the unit chord, and a relative maximum thickness of 10% positioned at 30% of the unit chord. The NA-DEL 2410 airfoil is presented in Figure 2, along with the original Dolphin 2410. The airfoil was obtained by merging the NACA and original Dolphin at coordinates for the upper surface: at  $x=0.35$ ,  $z=0.069200655$ , and lower surface at  $x=0.29$ ,  $z=0.031850023$ , assuming unit chord length. The results obtained by CFD calculations are given in Table 1.

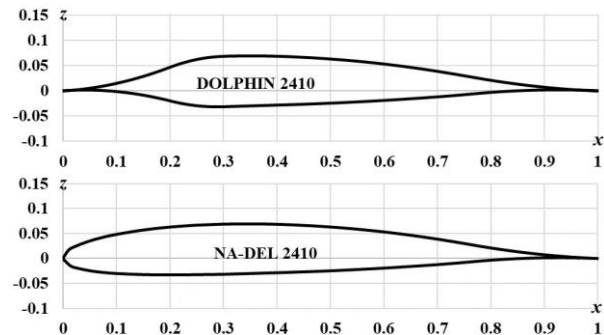


**Figure 2.** The original Dolphin airfoil geometry and hybrid NA-DEL 2410 counterpart

**Table 1.** The AoA, lift and drag coefficients, and the lift/drag ratio for the 2410 series

NACA 2410				DOLPHIN 2410				NA-DEL 2410			
$\alpha$ [°]	CL	CD	CL/CD	$\alpha$ [°]	CL	CD	CL/CD	$\alpha$ [°]	CL	CD	CL/CD
-6	-0.42	0.01132	-37.10	-6	-0.44	0.04950	-8.89	-6	-0.49	0.01150	-42.61
-4	-0.22	0.00943	-23.33	-4	-0.25	0.02625	-9.52	-4	-0.27	0.00919	-29.38
-2	-0.01	0.00863	-1.16	-2	-0.02	0.01285	-1.56	-2	-0.03	<b>0.00821</b>	-3.65
0	0.19	<b>0.00861</b>	22.07	0	0.20	<b>0.00778</b>	25.71	0	0.20	0.00824	24.27
2	0.40	0.00922	43.38	2	0.42	0.01144	<b>36.71</b>	2	0.43	0.00906	47.46
4	0.61	0.01059	57.60	4	0.63	0.02257	27.91	4	0.67	0.01080	62.04
6	0.81	0.01280	<b>63.28</b>	6	0.79	0.03858	20.48	6	0.89	0.01360	<b>65.44</b>
8	1.01	0.01636	61.74	<b>8</b>	<b>0.86</b>	0.06356	13.53	8	1.11	0.01810	61.33
10	1.18	0.02149	54.91	10	0.75	0.11994	6.25	10	1.30	0.02500	52.00
12	1.31	0.02929	44.73	/	/	/	/	<b>12</b>	<b>1.42</b>	0.03640	39.01
<b>14</b>	<b>1.39</b>	0.04654	29.87	/	/	/	/	14	1.40	0.06000	23.33
16	1.32	0.18530	7.12	/	/	/	/	16	/	/	/



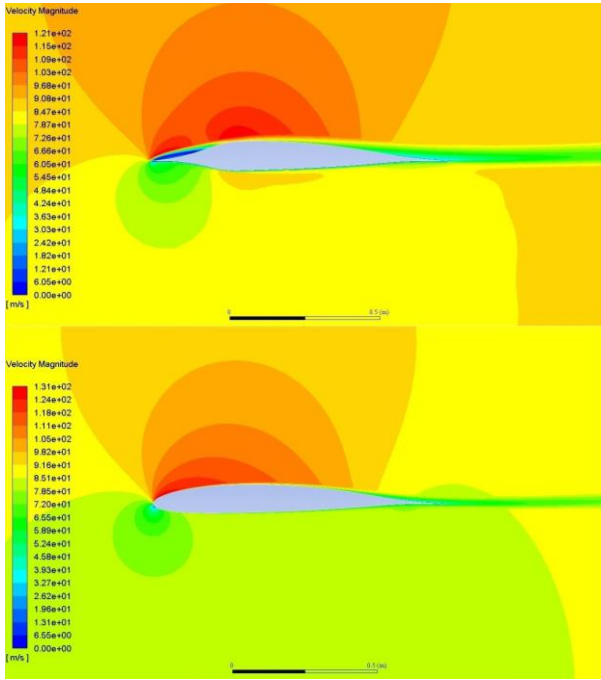


**Figure 3.** The velocity contours of the original Dolphin 2410 and hybrid NA-DEL 2410 airfoils at  $\alpha=4^\circ$

The velocity contours indicate that, in the case of the original Dolphins, as well as the 2410 airfoil, separation occurs at the leading edge (blue bubble in Figure 3).

This occurs even at low AoA, resulting in a significant loss of aerodynamic efficiency. Conversely, the smooth flow patterns over the NA-DEL 2410, without leading edge separation, indicate favorable aerodynamic characteristics of the airfoil design, Figure 3. The NA-DEL 2412 and 2415 exhibited similar behavior compared to their original Dolphin counterparts.

### 3.2. The NA-DEL 2412 airfoil

The NA-DEL 2412 airfoil is a hybrid Dolphin airfoil obtained by merging the NACA 2412 and the original Dolphin 2412 airfoils. The airfoil was obtained by merging the two airfoils at coordinates for the upper surface at  $x=0.35, z=0.0791241$ , and the lower surface at  $x=0.29, z=-0.0418166$  unit chord. The flow patterns, i.e. velocity contours, show the same tendencies as in Figure 3 for the NA-DEL 2410. The original Dolphin 2412 airfoil exhibits a strong separation bubble on the leading edge at AoAs lower than 4 degrees. In contrast, the hybrid NA-DEL 2412 airfoil displays a smooth pattern, which is expected for airfoils at such AoAs. In Table 2, the numerical results of the CFD analysis are provided. Maximum values for each column are highlighted in bold. The values indicate that the Dolphin 2412 stalls at an AoA of 8 degrees, whereas the NACA 2412 and the NA-DEL 2412 at an AoA of 14 degrees. The NA-DEL 2412 lift, polar curves, and lift/drag ratios are given in Figures 4 and 5.

**Table 2.** The AoA, lift and drag coefficients, and the lift/drag ratio for the 2412 series

NACA 2412				DOLPHIN 2412				NA-DEL 2412			
$\alpha$ [°]	CL	CD	CL/CD	$\alpha$ [°]	CL	CD	CL/CD	$\alpha$ [°]	CL	CD	CL/CD
-6	-0.41	0.01128	-36.35	-6	-0.44	0.06460	-6.81	-6	-0.50	0.01098	-45.54
-4	-0.21	0.00978	-21.47	-4	-0.26	0.03674	-7.08	-4	-0.27	0.00926	-29.16
-2	-0.01	<b>0.00910</b>	-1.10	-2	-0.04	0.01692	-2.36	-2	-0.02	<b>0.00853</b>	-2.34
0	0.18	0.00911	19.76	0	0.18	<b>0.00931</b>	19.33	0	0.21	0.00865	24.28
2	0.38	0.00970	39.18	2	0.40	0.01225	<b>32.65</b>	2	0.44	0.00948	46.41
4	0.59	0.01097	53.78	4	0.61	0.02455	24.85	4	0.67	0.01118	59.93
6	0.79	0.01300	60.77	6	0.78	0.04155	18.77	6	0.90	0.01375	<b>65.45</b>
8	0.98	0.01607	<b>60.98</b>	<b>8</b>	<b>0.86</b>	0.06807	12.63	8	1.12	0.01759	63.67
10	1.15	0.02055	55.96	10	0.84	0.10528	7.98	10	1.32	0.02312	57.09
12	1.29	0.02706	47.67	/	/	/	/	12	1.47	0.03176	46.28
<b>14</b>	<b>1.37</b>	0.03875	35.35	/	/	/	/	<b>14</b>	<b>1.54</b>	0.04576	33.65
16	1.28	0.06767	18.92	/	/	/	/	16	1.48	0.07227	20.48

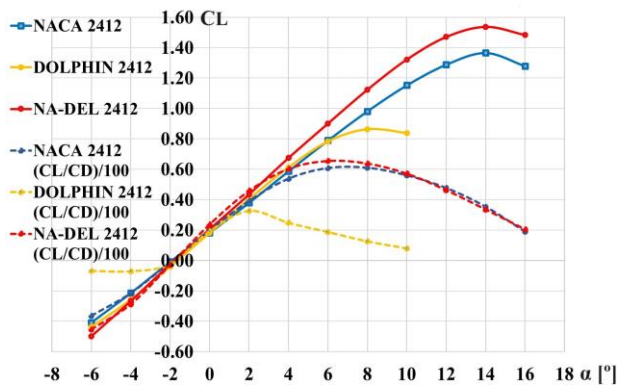


**Figure 4.** The lift and lift/drag curves for the 2412 airfoils

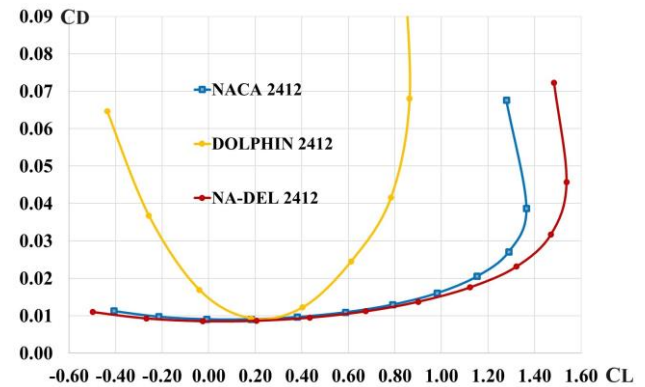


**Figure 5.** The polar curves for the 2412 airfoils

### 3.3. The NA-DEL 2415 airfoil

The NA-DEL 2415 airfoil is a hybrid Dolphin airfoil obtained by merging the NACA 2415 and the original

Dolphin 2415 airfoils. The airfoil were merged at  $x=0.34$ ,  $z=0.09403$  coordinates for the upper surface, and at  $x=0.29$ ,  $z=-0.05677$  for the lower surface. The results obtained by CFD calculations are given in Table 3.

**Table 3.** The AoA, lift and drag coefficients, and the lift/drag ratio for the 2415 series

NACA 2415				DOLPHIN 2415				NA-DEL 2415			
$\alpha$ [°]	CL	CD	CL/CD	$\alpha$ [°]	CL	CD	CL/CD	$\alpha$ [°]	CL	CD	CL/CD
-6	-0.41	0.01135	-36.12	-6	-0.38	0.04045	-9.39	-6	-0.51	0.01144	-44.58
-4	-0.21	0.01008	-20.83	-4	-0.24	0.02409	-9.96	-4	-0.27	0.00978	-27.61
-2	-0.02	<b>0.00953</b>	-2.10	-2	-0.02	0.01384	-1.45	-2	-0.03	<b>0.00909</b>	-3.30
0	0.18	0.00962	18.71	0	0.21	<b>0.00936</b>	22.44	0	0.21	0.00925	22.70
2	0.38	0.01038	36.61	2	0.44	0.01253	<b>35.12</b>	2	0.45	0.01020	44.12
4	0.59	0.01183	49.87	4	0.64	0.02118	30.22	4	0.69	0.01199	57.55
6	0.79	0.01408	56.11	6	0.76	0.03520	21.59	6	0.92	0.01477	<b>62.29</b>
8	0.98	0.01727	<b>56.75</b>	<b>8</b>	<b>0.81</b>	0.05452	14.86	8	1.14	0.01895	60.16
10	1.14	0.02176	52.39	10	0.80	0.08298	9.64	10	1.32	0.02566	51.44
12	1.28	0.02838	45.10	12	/	/	/	12	1.43	0.03599	39.73
<b>14</b>	<b>1.36</b>	0.03965	34.30	14	/	/	/	<b>14</b>	<b>1.46</b>	0.05194	28.11
16	1.32	0.06288	20.99	16	/	/	/	16	1.41	0.07802	18.07

The velocity contours show flow patterns as similar to those shown in Figure 3. In Table 4 a comparison of the experimental results was presented to validate the general trends of the previously obtained numerical findings. The experiments (Figure 6) were conducted at a relatively low average Reynolds number of  $MRe \approx 0.4$  (corresponding to

the UAV category) due to power plant limitations [10]. The NA-DEL 2415 showed noticeably better aerodynamic characteristics, compared to its counterpart airfoils NACA 2415 and Dolphin 2415 at this Reynolds number, as well.



**Figure 6.** The NA-DEL 2415 airfoil in the wind tunnel test section (left and center) at Belgrade University - Faculty of Mechanical Engineering, Aerospace Department; airfoil models used in these experiments (right).

**Table 4.** Relative differences in experimentally obtained maximum lift and minimum drag coefficients, and lift/drag ratios of the original Dolphin and NA-DEL 215, compared to the NACA 2415 airfoil, used as reference.

Airfoil	CLmax	Relative change [%]	CDmin	Relative change [%]	(CL/CD)max	Relative change [%]
NACA 2415	1.22	/	0.00540	/	58.21	/
DOLPHIN 2415	0.993	-18.60%	0.00418	-22.60%	54.73	-5.97%
NA-DEL 2415	<b>1.28</b>	<b>+4.91%</b>	<b>0.00362</b>	<b>-32.96%</b>	<b>73.13</b>	<b>+25.63%</b>

## 4. DISCUSSION

The new hybrid NA-DEL 2410 showed an increase in the maximum lift coefficient by 2.16% and a decrease in the minimum drag coefficient by 4.65%, according to Table 1., in comparison to the NACA 2410. It also exhibited an

increase in the maximum lift-to-drag ratio by 3.41%. The velocity field contours in Figure 3 displayed the expected appearance, with separation near the trailing edge at the critical AoA. On average, the NA-DEL 2410 is 3.41% more efficient than its NACA 2410 counterpart. When comparing a newly designed hybrid airfoil to a

benchmark NACA airfoil, the maximum lift, minimum drag, and maximum lift-to-drag coefficients are considered. To obtain an average value for comparison, these three values are added together and divided by three. If the result is greater than 100%, the hybrid airfoil is considered more aerodynamically efficient than the NACA counterpart. It is important to note the sign for the minimum drag coefficient, where a value less than 100% indicates an aerodynamic improvement.

The results for the hybrid NA-DEL 2412 in Table 2, in comparison to the NACA 2412 airfoil, show an increase in the maximum lift coefficient by 12.4% and a decrease in the minimum drag coefficient by 6.27%. Figures 4 and 5 illustrate that the NA-DEL 2412 polar curve is below the Dolphin 2412 and NACA 2412 airfoil polars (which is also a tendency observed in the NA-DEL 2410 and NA-DEL 2415 analyses). The maximum lift/drag ratio has increased by 7.33%. On the average, the NA-DEL 2412 is 8.67% more efficient than its NACA 2412 counterpart.

The results from Table 3 for the NA-DEL 2415 airfoil, in comparison to the NACA 2415 airfoil, show an increase in the maximum lift coefficient by 7.35%, a decrease in the minimum drag coefficient by 4.62%, and an increase in the maximum lift/drag ratio by 9.76%. The NA-DEL 2415 is on average more aerodynamically efficient than the NACA 2415 by 7.21%. Experimental results in Table 4 indicate that the NA-DEL 2415 has an increase in maximum lift coefficient by 4.91%, minimum drag coefficient decrease by 32.96%, and maximum lift-to-drag increase by 25.63% in comparison to the NACA 2415 airfoil.

## 5. CONCLUSION

The results outlined in this paper demonstrate obvious improvements in the aerodynamic performance of the new, and here presented airfoils NA-DEL 2410, 12, and 15 compared to the NACA counterparts, and significant improvements compared to the original Dolphin airfoils. The numerical calculations performed at  $MRe = 6$  and standard roughness case revealed a noticeable increase in maximum lift coefficients, lift-to-drag ratios, and minimum drag coefficient reductions, along with enhancements in lift curve slopes, stall delay, and the creation of smooth flow patterns around the leading edge, which was not the case with the original Dolphins. Experiments performed at  $MRe = 0.4$  and with natural boundary layer transition have confirmed all general improvement trends of NA-DEL airfoils. Consequently, the hybrid NA-DEL airfoils might be equally suitable both in general aviation designs ( $MRe = 6$ ), and for fixed-wing UAV applications ( $MRe = 0.4$ ), as suggested by the experimental results. Numerical results for the  $MRe=0.4$  confirming experimental findings in this paper will be provided in future studies.

## Acknowledgements

This research was supported by the Ministry of Science, Technological Development and Innovation of the Republic of Serbia under contract number 451-03-

66/2024-03/200213 dated 05.02.2024.

## References

- [1] YAN, H, SU, X., ZHANG, H., HANG, J., ZHOU, L., LIU, Z., WANG, Z.: *Design approach and hydrodynamic characteristics of a novel bionic airfoil*, Ocean Engineering, 216 (2020) 108076.
  - [2] WOLF, T., KONRATH, R.: *Avian wing geometry and kinematics of a free-flying barn owl in flapping flight*, Experiments in Fluids, 56 (2015) 1-18.
  - [3] XU, C. Y., QIAN, Z. H., LIU, Q. P., SUN, S. M., REN, L. Q.: *Aerodynamic performance of bionic coupled foils based on leading edge of long-eared owl wing*, Journal of Jilin University (Engineering and Technology Edition), 40(1) (2010) 108-12.
  - [4] LIMIN, Q., XUESHAN, L., YONGBO, Y., RUI, G., YONGJI, L.: *Performance Analysis of Bionic Airfoil on the Small Unmanned Plane*, Advanced Materials Research, 655-657 (2013) 24-7.
  - [5] TIAN, W., LIU, F., CONG, Q., LIU, Y., REN, L.: *Study on aerodynamic performance of the bionic airfoil based on the swallow's wing*, Journal of Mechanics in Medicine and Biology, 13(06) (2013) 1340022.
  - [6] HUANG, S., HU, Y., WANG, Y.: *Research on aerodynamic performance of a novel dolphin head-shaped bionic airfoil*, Energy, 214 (2021) 118179.
  - [7] TAPOSU, I.: *Profilele delfin. Un nou concept în aerodinamică (The Dolphin Profiles. A new Concept in Aerodynamics, in Romanian)*, S.C. Editura Technica S.A., Bucharest, Romania, 2002.
  - [8] DANČUO, Z.Z., KOSTIĆ, A. I., KOSTIĆ, P. O., BENGIN, Č. A., VOROTOVIĆ, S. G.: *Leading edge shape optimization of a novel family of hybrid dolphin airfoils*, Proceedings of the 9<sup>th</sup> International Congress of the Serbian Society of Mechanics, (2023) 35-45, Vrnjačka Banja, Serbia.
  - [9] DANČUO, Z. Z., KOSTIĆ, A. I., KOSTIĆ, P.O., BENGIN, Č. A., VOROTOVIĆ, S. G.: *Influence of Thickness Ratio on the Aerodynamic Characteristics of a Family of Hybrid Semielliptical Dolphin Airfoils*, Novel Techniques in Maintenance, Repair, and Overhaul, Proceedings of the International Symposium on Aviation Technology, MRO, and Operations, Belgrade, Serbia, 2022, publ. (2024) 1-7, by Springer Nature, Switzerland.
  - [10] DANČUO, Z. Z.: *Razvoj familije hibridnih Delfin aeroprofila (Development of a family of hybrid Dolphin airfoils, in Serbian)*, Doctoral Thesis, University of Belgrade - Faculty of Mechanical Engineering, Belgrade, 2023.
  - [11] DANČUO, Z. Z., KOSTIĆ, A. I., KOSTIĆ, P.O., BENGIN, Č. A., VOROTOVIĆ, S. G.: *Initial development of the hybrid semielliptical-dolphin airfoil*", Thermal Science, 26(3) (2022) 2199-2210.
- ABBOTT, I. H., VON DOENHOFF, A. E., STIVERS JR, L.: *Summary of airfoil data* (No. NACA-TR-824), National Advisory Committee for Aeronautics, 1945.



## AERODYNAMIC OPTIMIZATION OF WINGLETS FOR AN UNMANNED AERIAL VEHICLE

DUŠAN IVKOVIĆ✉

University of Belgrade, Faculty of Mechanical Engineering, Kraljice Marije 16 Belgrade, [dudiivko@gmail.com](mailto:dudiivko@gmail.com)

IVAN KOSTIĆ

University of Belgrade, Faculty of Mechanical Engineering, Kraljice Marije 16 Belgrade, [ikostic@mas.bg.ac.rs](mailto:ikostic@mas.bg.ac.rs)

OLIVERA KOSTIĆ

University of Belgrade, Faculty of Mechanical Engineering, Kraljice Marije 16 Belgrade, [okostic@mas.bg.ac.rs](mailto:okostic@mas.bg.ac.rs)

MIRKO DINULOVIĆ

University of Belgrade, Faculty of Mechanical Engineering, Kraljice Marije 16 Belgrade, [mdinulovic@mas.bg.ac.rs](mailto:mdinulovic@mas.bg.ac.rs)

ALEKSANDAR SIMONOVIĆ

University of Belgrade, Faculty of Mechanical Engineering, Kraljice Marije 16 Belgrade, [asimonovic@mas.bg.ac.rs](mailto:asimonovic@mas.bg.ac.rs)

**Abstract:** *The main aim of this paper was to determine the influence of different parameters of winglet design on overall Unmanned Aerial Vehicle (UAV) aerodynamics. Looking from an aerodynamicist's point of view, the main reason for using such wingtip devices is to reduce induced drag component, which noticeably contributes to total drag when flying both in cruising flight and on higher angles of attack at lower speeds. Significant benefits of using winglets on overall aircraft performance include reduced fuel burn, increased maximum range and endurance, and higher cruise altitude. Total drag of a simplified mock-up of an existing tactical UAV was calculated using hybrid approach. Parasite drag was obtained using analytical and semi empirical methods, while the induced drag and the lift in its linear domain were determined using inviscid CFD model based on a 3D vortex lattice method (VLM). Computational analyses were focused on determining the influence of winglet cant angle, root chord length, span, airfoil, and twist angle on lift-to-drag ratio of the UAV. Results obtained for different types of winglets (straight, blended and elliptical) were compared, and the best performing in the prescribed dimensions were the elliptical winglets. Their geometry was further optimized, finally providing an overall lift-to-drag ratio increase of 7% compared to the original UAV design without winglets, which represents quite remarkable improvement.*

**Keywords:** Aerodynamics, Hybrid calculation method, UAV, VLM, Optimization of winglets, CFD

**Topic:** Aerodynamics and Flight Dynamics

### 1. MOTIVATION BEHIND WINGLETS

Since the Wright brothers first flew their “Wright Flyer” in 1903, the main goal of aeronautical engineers has been to make airplanes stay in the air the longest and fly the furthest distances possible. Today there are aircraft capable to circumnavigate entire Earth without refueling. Such an example is Virgin Atlantic’s “Global Flyer” which in 2005. flew 36898 km in 67 hours, at an average speed of 550 km/h [1]. Difference in aerodynamic configurations between the Wright Flyer and the Global Flyer is obvious, and is best represented by comparing their maximum glide ratios, measuring 5.6 for the first [2], and 37 for the second [3].

Aerodynamic optimization became crucial in the last few decades because of the increasing jet fuel prices, and more and more rigorous ecological policies posted by the civil aviation authorities.

The use of wing tip devices in aviation is not a novelty. Inspiration for them came, like for a lot of other things in aviation, from birds. The first mention of winglet-like devices dates even before Wright brothers’ first flight. English engineer Frederick W. Lanchester (1868.-1946.) patented wing end plates, aimed to reduce the influence of wingtip vortices, and they were based on different physical principles compared to modern day winglets. While the end plates were aimed to simply prevent the secondary wing tip flow (and to fully succeed in that, they would have to be extremely large), winglets use the secondary flow to generate a wing tip force with propulsive, forward oriented component. In the 1970’s NASA scientists led by Richard Whitcomb worked on a scaled model of jet airplane, adding and optimizing for the first time the “real” winglets, which resulted in 9% [4] increase of lift to drag ratio. That is the moment airlines recognized benefits of adding winglets, starting to invest in their development, thus leading to their mass use.

According to industry, since first introduced to fleets, NASA-developed winglets have saved airlines approximately 4 billion gallons of jet fuel [5].

Looking from an aerodynamicist point of view, main motivation behind all wingtip devices is reduction of induced drag, which, at moderate and high angles of attack most often generates very remarkable or even the major part of the overall drag.

Another potential reason for adding winglets can also be optimization of aircraft stability as shown in [6] for jet transport model, and in [7] for a tandem wing UAV, although this is definitely not their primary role.

Together with reducing costs of fuel burn, winglets contribute to the reduction of carbon dioxide emissions and also reduce the aircraft noise on takeoffs and landings.

## 2. CHARACTERISTICS OF UAV

This paper is focused on determining the influence of different parameters of winglet design on the Pegasus Unmanned Aerial Vehicle (UAV) aerodynamic characteristics. For all here presented analyses only publicly available data were used, such as technical data available in [8] and 4 view drawing in [9]. All other data, such as the wing airfoil and its thickness ratio, were selected by the authors, based the available technical data and the intended UAV use.

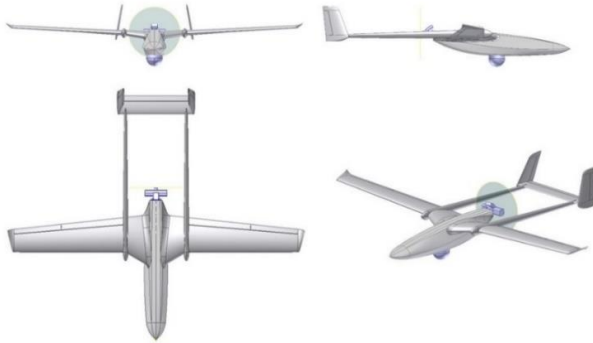


Figure 1. The UAV model [9]

Pegasus is a twin boom high wing UAV (Figure 1), with the following technical characteristics [8] and adopted airfoils:

Table 1. Characteristics of UAV model

Engine	2 stroke, horizontally opposed
Engine Power	32kw (43 hp)
Propeller	wooden, 2 blades
Wingspan	6.34 m
Wing Area	4.24 m <sup>2</sup>
Length	5.395 m
Empty Weight	120 kg
Payload	40 kg

MTOW	230 kg
Max. speed	200 km/h
Cruise speed	130-150 km/h
Cruising altitude	3000 m
Endurance	12 h +
Here adopted wing airfoil	FX-67-K-170/17
Here adopted tail airfoil	NACA 0010

## 3. HYBRID METHOD FOR DRAG COEFFICIENT ESTIMATION

Total drag was determined using hybrid approach, where parasite drag was determined using analytical and semi empirical methods, and induced drag was calculated using Vortex Lattice Method (VLM) software. Total drag formula can be written as [10]:

$$C_D = C_{Dmin} + k \cdot C_L^2 + C_{Di} \quad (1)$$

analytical + semi-empirical      VLM

First two members on the right side of (1) define the parasite drag,  $C_{Dmin}$  representing minimum drag coefficient of the entire UAV, and the second one  $k \cdot C_L^2$  representing position component dependent on the angle of attack of the UAV. Third member  $C_{Di}$  represents lift induced drag component of total drag.

### 3.1. Parasite Drag Calculation

Parasite drag consists of form, friction and interference drag. Using analytical and semi empirical methods for estimating parasite drag in initial design phases provide good balance between accuracy and speed of calculation. In this paper parasite drag was determined using methods from [10, 11] which, combined with the VLM calculations for the induced drag, have proven to provide trustworthy results [12-15].

Calculated value of UAV's minimum drag coefficient without winglets is  $C_{Dmin} = 0.0345$  [16]. Parameter  $k$  was determined using method from Douglas Aircraft Company [10] as  $k = 0.38 \cdot C_{Dmin}$ . Total drag equation (1) can now be written as:

$$C_D = 0.0345 + 0.013 \cdot C_L^2 + C_{Di} \quad (2)$$

VLM

Equation (2) represents total drag equation for UAV configuration without winglets, and was different for individual test cases, as a consequence of each winglet configuration having distinct parasite drag.

### 3.2. Induced Drag Calculation

Vortex lattice methods are used for 3D flow analyses over the lifting surfaces and entire aircraft configurations. They represent numerical methods based on inviscid CFD calculations and are mainly used in early stages of aircraft design. Software based on VLM are easy to use, provide fast solutions on modern computers, and even very

complex geometries can be modelled relatively quickly, compared to more complex viscous CFD software packages. For all calculations presented in this paper, VLAERO+ software was used.

As explained in [17] in VLM airplane configuration is represented by multiple surfaces on which a grid of horseshoe vortices is superimposed. Velocities induced on control points by horseshoe vortices are calculated using Biot-Savart law. Then the summation is performed for all control points (on each element, e.g. the wing), which produces sets of linear algebraic equations for determining strength of each vortex. Solution must satisfy boundary conditions which state that flow through the element must be equal to zero. Strength of vortices is dependent on circulation over lifting surface, and difference of pressures on top and bottom of it. Difference of pressures is integrated in order to acquire forces and moments acting on aircraft.

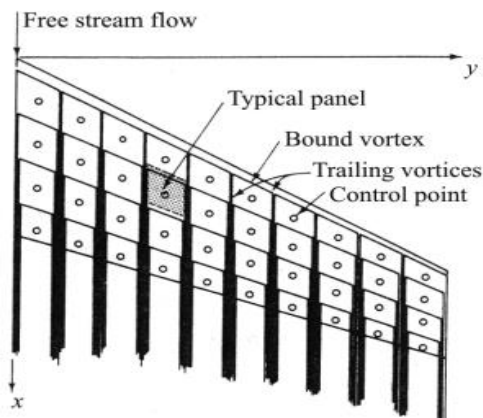


Figure 2. Coordinate system, elemental panels, and horseshoe vortices for a typical wing planform in the VLM [17].

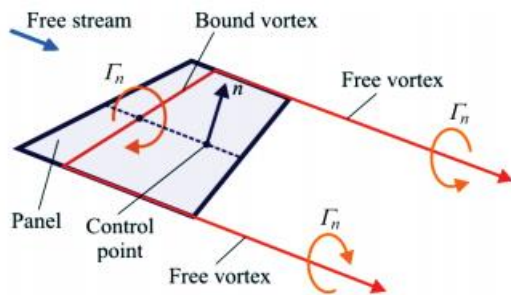


Figure 3. Representation of a single panel [14].

Horseshoe vortices are placed on trapezoidal panels. As shown in Figure 3, a horseshoe vortex consists of two semi-infinite free vortices and one bound vortex which coincides with the quarter-chord line of the panel, and is aligned with the local sweep angle. Control point is located on the three quarters chord position in the middle of the panel width.

Even though in VLM an airplane is formally represented by flat panels, this method accounts for the existence of airfoils, control surface deflections and fuselage cambers, by adding proper normals to each panel.

Vortex lattice methods can be used for the calculations of lift, moment and induced drag coefficients with remarkable precision considering their complexity. Since they are based on the potential flow model, obtained results are valid only in the domains of angles of attack and sideslip angles where separation effects are not immense.

Although performed analyses represent symmetrical flight cases, full model was created so further asymmetrical calculations can be performed in future. For VLM a relatively low number of panels is needed, only a single panel is required to predict the lift on a straight high-aspect ratio wing. Number of panels is chosen as to adequately define spanwise and chordwise lift distribution. In this particular case it was decided that adequate number of panels for the wing is 20 chordwise and 50 half-span wise, without winglets.

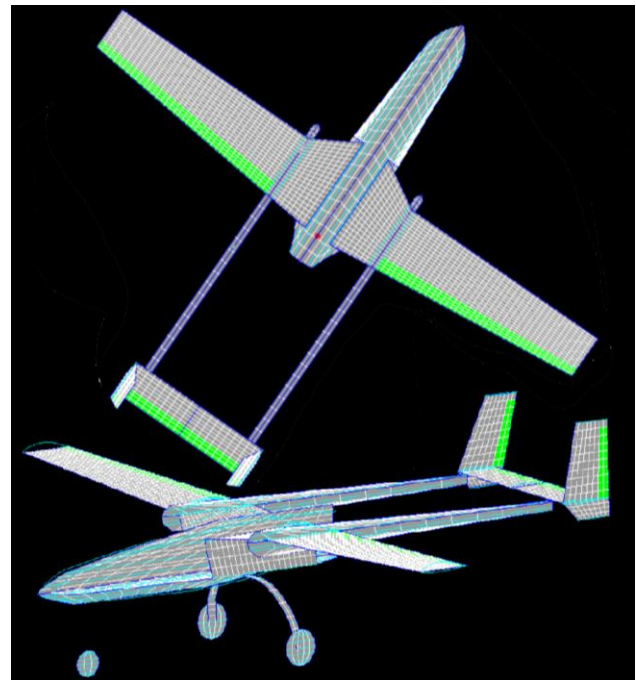


Figure 4. The UAV 3D model in VLAERO + software

#### 4. WINGLET DESIGN

The first stage in these analyses was to determine how different winglet design parameters influence the overall UAV aerodynamic characteristics. In order to quantify the benefits of different configurations, it was chosen to compare the UAV's maximum lift to drag  $C_L$   $f$   $C_D$  ratios. All configurations were compared to UAV's lift to drag ratios without winglets, (Table 2). The influence of winglet cant angle, root chord length, span, airfoil, and twist angle on  $C_L$   $f$   $C_D$  ratio of the UAV were calculated. Results obtained for different types of winglets (straight, blended and elliptical) were mutually compared, and the final winglet design was proposed and adopted.

**Table 2.** Characteristics of UAV without winglets

$\alpha$ [°]	$C_L$	$C_{Dmin}$	$C_L^2$	$k \cdot C_L^2$	$C_{Di}$	$C_D$	$C_L/C_D$
-6	-0.25	0.0345	0.062	0.00081	0.0239	0.0592	-4.196
-4	-0.06	0.0345	0.004	0.00005	0.0146	0.0492	-1.246
-2	0.13	0.0345	0.016	0.00021	0.0105	0.0452	2.781
0	0.31	0.0345	0.098	0.00128	0.0115	0.0473	6.613
2	0.50	0.0345	0.250	0.00327	0.0176	0.0554	9.022
4	0.69	0.0345	0.472	0.00619	0.0289	0.0696	9.877
6	0.87	0.0345	0.765	0.01003	0.0453	0.0898	9.737
8	1.06	0.0345	1.130	0.01482	0.0670	0.1163	9.140
10	1.25	0.0345	1.568	0.02056	0.0940	0.1491	8.400
12	1.44	0.0345	2.080	0.02726	0.1265	0.1882	7.661

**4.1. Influence of Winglet Cant Angle, Chord Length, Winglet Span, Airfoil and Twist Angle**

Initially, 13 straight winglets having the same span, chord length, taper ratio and airfoil were tested, with cant angle varying from 0 degrees (vertical, pointing upwards) to 180 degrees (vertical, pointing downwards) with 15 degrees steps (Figure 5). Obtained results are shown in Figure 6.

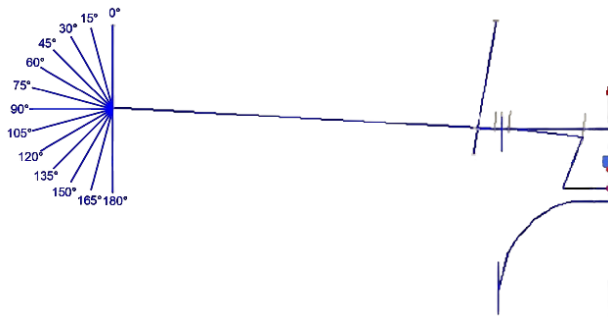


**Figure 5.** Tested variations of cant angle for straight winglets

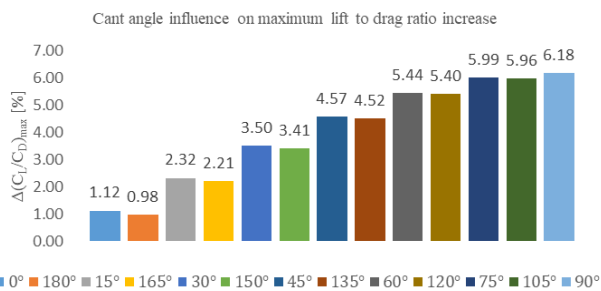


**Figure 6.** Cant angle influence on maximum lift to drag ratio increase (results shown in pairs symmetrical over horizontal axis).

Next the influence of winglet chord length was analyzed. For that purpose, three sets of straight winglets were designed, with same span and taper ratio, but with different chord lengths equal to 50%, 70% and 100% of wing tip chord, with cant angles varying from 0° to 90°, also with 15 degrees steps. Results are shown in Table 3.

**Table 3.** Results for winglets with different root chord lengths and same span

		0°	15°	30°	45°	60°	75°	90°
$\Delta \left( \frac{C_L}{C_D} \right)_{max} [\%]$	0.5c <sub>tip</sub>	1.1	2.3	3.5	4.6	5.4	6.0	6.2
	0.7c <sub>tip</sub>	1.5	2.9	4.3	5.6	6.6	7.2	7.4
	1.0c <sub>tip</sub>	1.9	3.5	5.2	6.6	7.8	8.5	8.8

These winglets have different aerodynamic areas, which obviously influences their apparent contributions (increases with winglet area). So in the next phase, winglets with different chord sizes were tested but all having the same areas, achieved by keeping taper ratios the same, but adjusting the winglet spans. Results for cant angle of 30° are presented in Table 4.

**Table 4.** Results for winglets with different root chord lengths and same area

Cant angle 30°	0.5c <sub>tip</sub>	0.7c <sub>tip</sub>	1c <sub>tip</sub>
$\Delta \left( \frac{C_L}{C_D} \right)_{max} [\%]$	3.5	3.47	3.11

Further analyses were focused on the influence of straight winglet’s span on maximum  $C_L f C_D$  ratio, and obtained results are graphically presented in Figure 7. They show that there is an obvious and progressive increase in maximum lift to drag ratio with the increase of winglet span, but this dependence is not linear, and for values above 1m it would be negligible.

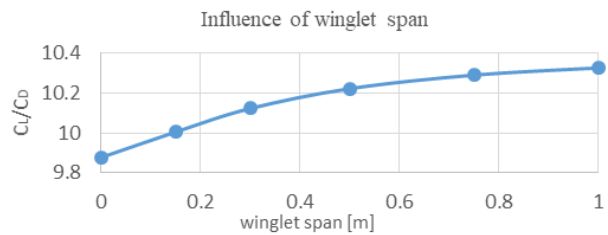


**Figure 7.** Influence of winglet span on UAV’s maximum lift to drag ratio

Next the influence of the winglet airfoil was tested. Two sets of straight winglets were compared, with same geometries consisting of 30° cant angle, 50% wing tip chord length, 0.5m span and 0.4 taper ratio winglet, but with different airfoils, in first case having symmetrical NACA 0010 airfoil, and in second the asymmetrical FX-67K-170/17 [18, 19]. Results shown in Figure 8. show that having asymmetrical airfoil provides additional increase of maximum  $C_L f C_D$  ratio.

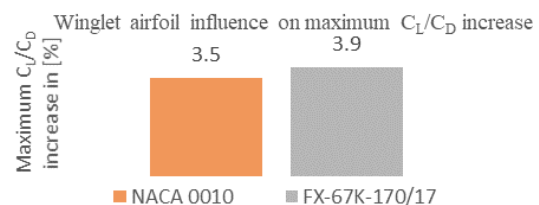


**Figure 8.** Influence of airfoil on maximum lift to drag ratio

The final winglet design parameter that was investigated was the twist angle. In this research, 7 different twist angles were analyzed on a straight winglet configuration described in the previous paragraph, showing relatively small influence of this parameter on maximum lift to drag ratio (Table 5).

**Table 5.** Influence of different twist angles on UAV’s maximum lift to drag ratio

$\left(\frac{C_L}{C_D}\right)_{max}$	Twist angle [°]						
	-3	-2	-1	0	1	2	3
	10.195	10.205	10.214	10.223	10.231	10.238	10.245

From this chapter it was concluded that winglets symmetrical over horizontal axis provide similar benefits, thus in the following analyses only winglets pointing upwards were used, since they do not lower wings ground clearance. Root chord length initially seemed to have a big influence on increase of  $C_L$  f  $C_D$  ratio when tested with same winglet span, but it was concluded that major contribution was indeed because of increased winglets surface area, which was proven in the next analysis where winglets areas were kept the same while different chord sizes were tested. Having in mind that in this scenario tested winglets have different spans, and that span also influences obtained results, and that it is very hard to compare just one parameter of winglets design while keeping others the same, influence of winglet span was tested showing increase of  $C_L$  f  $C_D$  ratio, but only up to a certain length. Use of asymmetrical airfoil winglet provided better results versus symmetrical airfoil winglet, and it was concluded that twist angle can be used to fine tune final winglet design, providing small benefits.

**4.2. Special Types of Winglets**

In the previous chapter influence of the different parameters of the straight winglet design were tested. In the next stage three different winglet types were compared, in order to select the best for the final optimizations. All winglets were designed with the requirements not to exceed UAV’s dimensions more than 30 cm horizontally from the wing tip, and more than 52 cm vertically from the wing tip, as shown in Figure 9. Requirements like this must be posted when designing winglets of a UAV that should be transported in predefined containers with strictly limited dimensions. The following winglet types were tested: two straight winglets, one designed to be the diagonal of a given rectangle and the other as a horizontal wing extension; two blended winglets, with different values of blending radius and cant angle, and the two elliptic winglets (Figures 9 and 10).

Blended winglets are designed with a radius blending the winglet with wing tip, and are designed with a smooth chord variation in the transition area where the wing joins the winglet minimizing vortex concentrations that produce drag.

Elliptic winglets are continuously curved from the joining point with the wing to its end tip, with curve representing

the curvature of an ellipse, achieving minimum interference between wing and winglet. Same as with blended winglets they are designed with a smooth chord variation in the transition area where the wing joins the winglet to avoid vortex shedding from the leading edge.

**Table 6.** Different types of winglets

Winglet	$\Delta\left(\frac{C_L}{C_D}\right)_{max}$ [%]
Straight-diagonal	3.8
Straight-wing ext.	4.1
Blended 1	5.4
Blended 2	6
Elliptic 1	5.9
Elliptic 2	6.17

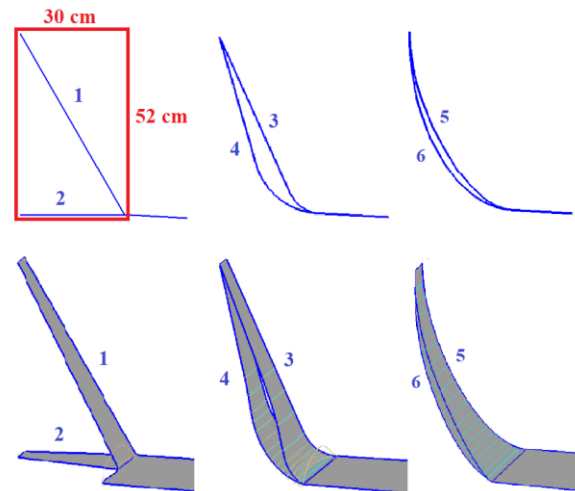


**Figure 9.** Winglet geometry limit box is marked red; 1 - straight diagonal type; 2 - straight horizontal wing extension type; 3 - blended 1 type; 4 - blended 2 type; 5 - elliptic 1 type; 6-elliptic 2 type

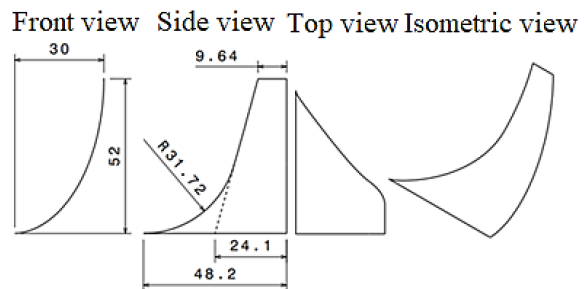


**Figure 10.** Elliptic 2 winglet type design parameters (all dimensions are in centimeters)

Initially all types of winglets were designed with no twist angle and symmetrical airfoil, in order to reduce number of test cases. From Table 6. it is obvious that the Elliptic 2 type winglet has given the best improvements in maximum lift to drag ratio, of 6.17%. Owing to that, it was selected for final optimizations. They were performed first by varying the twist angle, which provided best results when set at +3°, increasing UAV’s maximum lift to drag ratio for additional 0.33%. Finally, changing the winglet airfoil from NACA0010 to FX-67K-170/17 has provided further increase of the maximum lift to drag ratio to 10.572, giving 7% increase when compared to original 9.877 of the initially analyzed UAV without



winglets (Table 7.).

**Table 7.** UAV optimization results

Configuration of UAV	$\left(\frac{C_L}{C_D}\right)_{max}$	$\Delta\left(\frac{C_L}{C_D}\right)_{max}$ [%]
UAV without winglets	9.877	- - -
Elliptic 2 optimized winglets	10.572	7

## 5. CONCLUSION

In this paper different aspects of winglet design options were investigated, in order to evaluate their aerodynamic effectiveness and influence. For all calculations a hybrid approach was applied, where vortex lattice method was used to obtain the induced drag component for the entire UAV aerodynamic configurations, without and with the winglets. Parasite drag was calculated using analytical and semi empirical methods, and they were superimposed with induced drag obtained by VLM. Influence of winglet cant angle, chord length, span, airfoil, and twist angle was determined in order to better understand the influence of different design parameters and their combinations on overall UAV's aerodynamics. Additionally three different types of winglets were compared, with blended winglets showing better performance than straight winglets, and elliptic winglets outperforming both. Final winglet design was proposed, consisting of an optimized elliptic winglet, designed taking into consideration all results obtained during the research performed in this paper, increasing UAV's maximum lift to drag ratio by 7%. This methodology proved to be time efficient in providing valuable results when testing a vast number of different custom winglet designs.

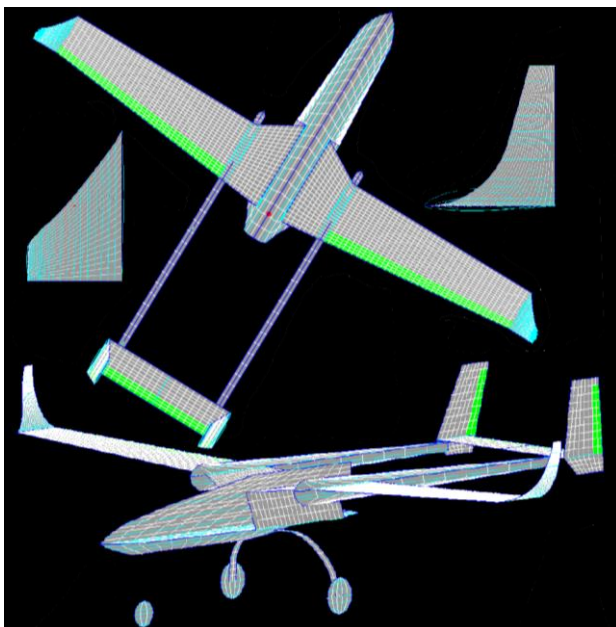


**Figure 11.** The UAV with Elliptic 2 optimized winglets

## References

- [1] World Air Sports Federation Records page, [https://www.fai.org/records?f%5B0%5D=field\\_type\\_of\\_record%3A779](https://www.fai.org/records?f%5B0%5D=field_type_of_record%3A779), last accessed 2021/03/20
- [2] ACKROYD, J.A.D.: *Aerodynamics as the Basis of Aviation: How Well Did It Do?*, Journal of Aeronautical History Paper No. 2018/01, 2018.
- [3] NOLAND, D.: *The Ultimate Solo*, Popular Mechanics, vol. 180, no. 2, 74-79, 114-115, 2005.
- [4] WHITCOMB, R.T.: *A Design Approach and Selected Wind-Tunnel Results at High Subsonic Speeds for Wing-Tip Mounted Winglets*, NASA TN D-8260, 1976.
- [5] NASA article, <https://www.nasa.gov/image-article/nasa-contribution-winglets/>, last accessed 2024/01/22.
- [6] JACOBS, P., Flechner, G.: *The effect of winglets on the static aerodynamic stability characteristics of a representative second generation jet transport model*, NASA TN D-8267, 1967.
- [7] KOSTIĆ, I., SIMONOVIĆ, A., KOSTIĆ, O., IVKOVIĆ, D., TANOVIĆ, D.: *Lateral-Directional Aerodynamic Optimization of a Tandem Wing UAV Using CFD Analyses*, Aerospace, 11(3):223, 2024.
- [8] VTI projects page, <http://www.vti.mod.gov.rs/index.php?view=actuality&type=projects&category=1&id=138>, last accessed 2024/01/22.
- [9] VELIMIROVIĆ, K., VELIMIROVIĆ, N.: *Tactical UAV Pegasus as a platform to carry missiles*, In: Proceedings from 4<sup>th</sup> International Scientific Conference on Defensive Technologies OTEH 2011, 133-136, 2011.
- [10] SHEVELL, R.S.: *Fundamentals of flight*, Stanford University - Prentice-Hall International Editions, Englewood Cliffs, New Jersey, 1983.
- [11] KOSTIĆ, I.: *Applied Aerodynamics*, handouts. University of Belgrade - Faculty of Mechanical Engineering, 2020.
- [12] STEFANOVIĆ, Z., KOSTIĆ, I., KOSTIĆ, O.: *Efficient Evaluation of Preliminary Aerodynamic Characteristics of Light Trainer Aircraft*, Engineering Review, Vol. 32, 1, 49-56, 2012.
- [13] STEFANOVIĆ, Z., KOSTIĆ, I., KOSTIĆ, O.: *Primary Aerodynamic Analyses of a New Light Aircraft in Symmetrical Flight Configurations*, Proceedings of the 7th International Symposium KOD 2012, 24-26.05.2012, Balatonfüred, Hungary, 97-104, 2012.
- [14] STEFANOVIĆ, Z., KOSTIĆ, I., KOSTIĆ, O.: *Hybrid Approach in the Initial Aerodynamic, Stability and Performance Calculations of a Light Aircraft*, Technical Gazette, Vol. 20, 4, 605-614, 2013.
- [15] KOSTIĆ, I., KOSTIĆ, O.: *Several Approaches in Contemporary Light Aircraft Aerodynamic Design*, Invited Presentation at The 3<sup>rd</sup> International Forum on Aerospace and Aeronautics AEROFORUM 2023, San Diego, USA, 2023.

- [16] IVKOVIĆ, D.: *Aerodinamička optimizacija vingleta za bespilotnu letelicu (Aerodynamic optimization of winglets for an Unmanned Aerial Vehicle)*, MSc Thesis, University of Belgrade, Faculty of Mechanical Engineering, Belgrade, 2021.
- [17] BERTIN, J., CUMMINGS, R.: *Aerodynamics for engineers*, 5th Edition, Pearson Prentice - Hall, Upper Saddle River, NJ., 2008.
- [18] STEFANOVIĆ, Z.: *Airfoils* (in Serbian), University of Belgrade, Faculty of Mechanical Engineering, Belgrade, 2005.
- [19] LEDNICER, D.: *The Incomplete Guide to Airfoil Usage*, Aeromechanical Solutions LLC, Redmond, WA, <https://m-selig.ae.illinois.edu/ads/aircraft.html>, last accessed 2024/01/23.



# COMPUTATIONAL ANALYSIS OF ROCKET-ASSISTED PROJECTILE TRAJECTORY

ABDELLAH FERFOURI

University of Defence Belgrade, Military Academy, [fer-abdel@hotmail.com](mailto:fer-abdel@hotmail.com)

DAMIR D. JERKOVIĆ

University of Defence Belgrade, Military Academy, [damir.jerkovic@va.mod.gov.rs](mailto:damir.jerkovic@va.mod.gov.rs)

ALEKSANDAR V. KARI

Military Technical Institute, Belgrade, [aleksandarkari@gmail.com](mailto:aleksandarkari@gmail.com)

SASA ŽIVKOVIĆ

Military Technical Institute, Belgrade, [sasavite@yahoo.com](mailto:sasavite@yahoo.com)

**Abstract:** A computational analysis was carried out in order to study the effect of solid rocket motor operating parameters on the trajectory elements of 155mm rocket-assisted projectile. Two numerical solutions have been programmed for this purpose. The first for the rocket motor internal ballistic calculation. The second is intended for the six degree-of-freedom (6-DOF) trajectory determination for both unpowered and powered flight. The effect of three operating parameters of the solid rocket motor on the trajectory elements was taken into account, namely: (1) thrust-time profile (neutral, regressive or progressive), (2) working time and (3) ignition delay. The results obtained following this analysis are helpful as a preliminary stage in the design of extended range projectiles in order to optimize flight performance.

**Keywords:** rocket-assisted projectile, trajectory elements, internal ballistic calculation, 6-DOF trajectory model.

## 1. INTRODUCTION

Extending the range of artillery projectiles is crucial to improve their effectiveness on the battlefield. This expansion helps maintain a strategic advantage to ensure successful operations in different combat scenarios. Projectile range can be extended by many methods, such as increasing muzzle velocity; boosted (rocket-assisted) projectile; or by improved ballistics, including drag reduction or using subcalibers [1]. The rocket-assisted projectile (RAP) is a type of shell that has a small solid propellant rocket motor at the base to extend its range [2]. The rocket motor ignites after a predetermined delay after muzzle exit and operates for a short time to quickly increase projectile velocity (powered flight). After that, the projectile flies as an unpowered artillery shell, achieving greater ranges than the conventional one. Its range depends on its initial velocity and ballistics, and also on the operating parameters of its rocket motor. Hence the need to study the rocket motor operating parameters that could impact the performance of this type of projectile. This constitutes the main purpose of the present work that aims to study the effect of three operating parameters of the solid rocket motor on the trajectory elements of a 155mm rocket-assisted projectile, namely: (1) thrust-time profile (neutral, regressive or progressive), (2) working time and (3) ignition delay. This work is divided into five sections: the second section

describes projectile motion model; the third section covers the internal ballistic theory of rocket motor. The fourth section includes the obtained results and their analysis and discussion. Finally, the fifth section contains the main conclusions.

## 2. PROJECTILE MOTION MODEL

The primary objective of external ballistics is to compute the trajectory of the projectile during its flight. In other words, the prediction of trajectory elements such as velocity, range, altitude, crossrange (deflection), spin, impact angle, etc. This objective is achieved by establishing an appropriate model of projectile motion in the form of a system of differential equations and solving them. The projectile mechanically represents a rigid body whose motion model requires the prior definition of certain physical parameters that determine: the structure of the body, the characteristics of the coordinate system in which the trajectory is considered, the forces acting on the body, the environment properties through which the body moves and the initial conditions of motion [3]. The motion of the projectile with respect to the Earth is relative. The projectile velocity in relation to the Earth denotes its relative velocity, while the time derivatives of its projections onto the axes of any coordinate system constitute the components of the relative acceleration.

The six degree-of-freedom (6-DOF) trajectory model of reference [4] was used for the purposes of determining the

trajectory elements of the projectile considered in this study. This model is formulated to solve the projectile pitching and yawing motion in terms of direction cosines of the projectile axis of symmetry, rather than the Euler-angle method used in several other 6-DOF models [4]. Only the starting vector equations of the model are mentioned in this section. The full development of the model leading to the system of differential equations which describe the projectile motion is detailed in references [4,5]. A right-handed, rectangular coordinate system, with its origin located at the gun muzzle was adopted. In this coordinate system the 1-3 plane is tangent to the earth surface at the launch point, the 1-axis points downrange, the 2-axis points vertically upward through the launch point, and the 3-axis points to the right, when looking downrange. The trajectory and the 6-DOF coordinate system used here are illustrated in Fig.1.

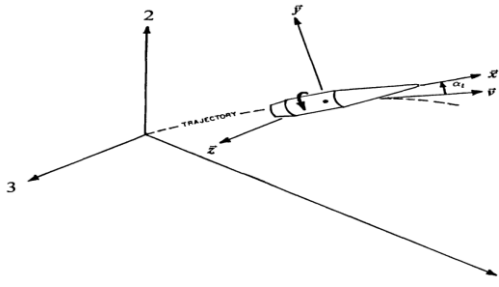


**Figure 1.** Coordinate system for 6-DOF trajectories [4]

Newton's laws of motion state that the rate of change of linear momentum must equal the sum of all the externally applied forces, and that the rate of change of angular momentum must equal the sum of all the externally applied moments. Newton's laws for a rocket-assisted projectile are:

- Vector equation for the relative motion of the center of gravity (CG) (Fig.2);

$$m \frac{d\vec{V}}{dt} = \sum \vec{R} + m\vec{g} + m\vec{a}_c + \vec{F} \quad (1)$$

- Vector equation of motion about the center of gravity (Fig.2);

$$\frac{d\vec{H}}{dt} = \sum \vec{M}_R + \vec{M}_F \quad (2)$$

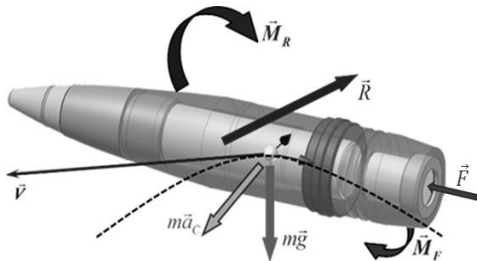


**Figure 2.** Forces and moments acting on the projectile

Where are:  $m$  projectile mass,  $\vec{V}$  vector velocity with respect to the ground-fixed coordinate axes,  $\sum \vec{R}$  vector sum of all aerodynamic forces,  $\vec{g}$  acceleration due to gravity,  $\vec{a}_c$  Coriolis acceleration due to the earth rotation,  $\vec{F}$  rocket thrust forces,  $\vec{H}$  total vector angular momentum

of the projectile,  $\sum \vec{M}_R$  vector sum of all aerodynamic moments (referenced to the CG),  $\vec{M}_F$  rocket thrust moments.

The aerodynamic forces and moments are calculated based on the prior determination of all their static and dynamic aerodynamic coefficients. This can be done via experimental (e.g., wind tunnel, aeroballistics spark facilities, and free-flight ranges) and computational methods, ranging from semi-empirical design codes to full three-dimensional Navier Stokes based computational fluid dynamics (CFD) codes.

### 3. INTERNAL BALLISTIC OF ROCKET MOTOR

All the rocket propulsion systems are explained by Newton's third law of motion which states that there is always an equal and opposite reaction for every action [6]. Accurate internal ballistic (IB) calculation of solid propellant rocket motor (SPRM) working parameters is very important process, in all design phases [7]. The combustion chamber of the rocket motor (RM) serves as a solid propellant reservoir, in which the chemical energy of the propellant is transformed into the kinetic energy of the combustion products. The chamber with cylindrical section is the most common SPRM case shape [8]. Geometry of propellant grain is various for every rocket motor and also variable during the operating period [7]. The RM operating regime calculation can be conducted using IB coefficients, which represent certain parameters or processes characteristic inherent to RM performance (Fig.3). These coefficients can be derived theoretically, experimentally or semi-empirically.

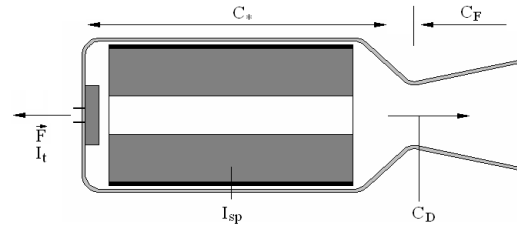


**Figure 3.** Internal ballistic coefficients and performance parameters scheme [7]

Thrust  $F(t)$  is total produced force by RM, in the axial direction, i.e. along the axis of symmetry of the projectile. It represents the integral of the pressure field acting on both internal and external surfaces of the RM, resulting in the overall reactive force known as thrust.

$$F = \dot{m} \cdot V_e + (p_e - p_a) \cdot A_e \quad (3)$$

Expanding pressure at nozzle exit, with respect to atmospheric pressure, can be differentiated into following flow conditions which depends on the difference  $(p_e - p_a)$  [9]:

- $p_e > p_a$ , under-expanded (the most favored and commonly used);
- $p_e = p_a$ , fully-expanded (adapted nozzle, higher exit velocity);

- $p_e < p_a$ , over-expanded (negative effect, flow detachment).

Where are:  $p_a$  atmospheric pressure,  $p_e$  nozzle exit pressure,  $\dot{m}$  mass flow rate,  $V_e$  nozzle exit velocity,  $A_e$  nozzle exit area.

Total impulse  $I_t$  is the integral of thrust curve over the total operating time period  $\tau$ . It is equivalent of energy amount, released from propellant charge mass. An average thrust  $F_{avg}$  could be taken to calculate the total impulse over the effective working time period  $t_e$ .

$$I_t = \int_0^\tau F(t) \cdot dt \quad (4)$$

$$I_t = F_{avg} \cdot t_e \quad (5)$$

The specific impulse  $I_{sp}$  represents the thrust per unit propellant “weight” flow rate  $\dot{m}$ , i.e. total impulse per one kilogram of propellant mass  $m$  [7,10]. It is an important figure of merit of the performance of any RM [10], which also depends from RM and nozzle geometry design quality [7].

$$I_{sp} = \frac{F}{\dot{m}} = \frac{I_t}{m} \quad (6)$$

The specific impulse  $I_{sp}$  can also be expressed as the ratio between the thrust coefficient  $C_F$  and the discharge coefficient  $C_D$ .

$$I_{sp} = \frac{C_F}{C_D} \quad (7)$$

The thrust coefficient  $C_F$  is dimensionless. It represents efficiency of thrust generation, regarding nozzle flow efficiency [7]. For specific nozzle throat area  $A_t$ , thrust coefficient defines amount of thrust generated from products pressure  $p_c$  in combustion chamber.

$$C_F = \frac{F}{p_c A_t} = \sqrt{\frac{2\kappa^2}{\kappa-1} \left(\frac{2}{\kappa+1}\right)^{\frac{\kappa+1}{\kappa-1}} \left[1 - \left(\frac{p_e}{p_c}\right)^{\frac{\kappa-1}{\kappa}}\right] + \frac{p_e - p_a}{p_c} \frac{A_e}{A_t}} \quad (8)$$

The ratio of the nozzle exit area  $A_e$  to the throat area  $A_t$  is called the nozzle area expansion ratio  $\varepsilon$ , and is given by the equation (8).

$$\varepsilon = \left[ \left(\frac{2}{\kappa+1}\right)^{\frac{1}{\kappa-1}} \cdot \left(\frac{p_c}{p_e}\right)^{\frac{1}{\kappa}} \cdot \left[ \frac{\kappa+1}{\kappa-1} \cdot \left(1 - \left(\frac{p_c}{p_e}\right)^{\frac{1-\kappa}{\kappa}}\right) \right] \right]^{-0.5} \quad (9)$$

Discharge coefficient  $C_D$  is measure of chamber and nozzle flow losses. It defines mass flow rate  $\dot{m}$  through throat area  $A_t$ , inducted with products pressure energy in chamber [7].

$$C_D = \frac{\dot{m}}{p_c A_t} = \sqrt{\frac{\kappa}{RT_c} \left(\frac{2}{\kappa+1}\right)^{\frac{\kappa+1}{\kappa-1}}} \quad (10)$$

The characteristic velocity  $C^*$  is a function of the propellant characteristics and combustion chamber

design, and it is essentially independent of the nozzle characteristics [6,7]. It is defined as the product of chamber pressure  $p_c$  and nozzle throat area  $A_t$  divided by the propellant mass flow rate  $\dot{m}$  [6].

$$C^* = \frac{p_c A_t}{\dot{m}} = \frac{1}{C_D} \quad (11)$$

Where are:  $\kappa$  heat capacity ratio,  $R$  gas constant,  $T_c$  chamber temperature.

In addition to the introduced coefficients and performance parameters, the RM operating regime is heavily influenced by the combustion products properties and combustion characteristics, such as the burning rate  $r$  [7]. The RM propellant grain burning regresses in a perpendicular way to the surface which characterizes the grain combustion [6]. The burning rate as a function of chamber pressure  $p_c$  could be determined for different types of propellants using empirical Saint Robert or Vieille law for a given burning rate coefficient  $b$  and pressure exponent  $n$ .

$$r = b \cdot p_c^n \quad (12)$$

The design of a SPRM typically starts with establishing the technical and tactical requirements that it must satisfy. The type of propellant can be selected, based on desired performances and special requirements [11].

The pressure change in the combustion chamber can be calculated using the mass conservation equation. Total pressure within the combustion chamber is nearly uniform across the entire free volume at certain moments. This pressure level can be determined based on products mass balance, accounting for generation, accumulation and discharging through nozzle. The production of products on burning surfaces equals the change in mass of the combustion products within the chamber and discharged through the nozzle throat [7].

For unsteady flow through the RM domain (Fig.4), continuity equation has the following form:

$$\dot{m}_b(t) = \dot{m}_c(t) + \dot{m}_t(t) \quad (13)$$

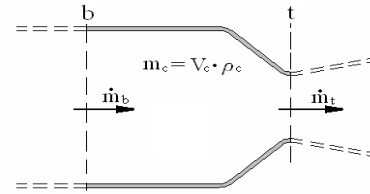


**Figure 4.** Combustion products mass balance in RM flow Domain [7]

The mass balance equation can be expressed as first order differential equation of unknown variable chamber pressure, which is nonlinear and inhomogeneous. The details of this equation extraction can be found in [12]. Nonlinearity of this ordinary differential equation manifests in the burning rate function, which dependent from chamber pressure. Some functions are defined in terms of the burned web  $x(t)$ , such as the burning area  $A_b(t)$  and the chamber free volume  $V_c(t)$ . Burned web is

also function of time, and can be derived from burning rate function. Those dependences can be written in form of system of two differential equations, one integral and two algebraic equations (equations 14-18). Solving this system we can obtain pressure-time and burned web-time curves.

$$A_b(t) = A_b[x(t)] \quad (14)$$

$$V_c(t) = V_c(t=0) + \int_0^t A_b[x(t)] \cdot r(t) \cdot dt \quad (15)$$

$$r(p_c, t) = r[p_c(t)] \quad (16)$$

$$\frac{d}{dt} p_c(t) = \frac{R \cdot T_c \cdot A_b(t) \cdot r(p_c, t) \cdot \rho_p}{V_c(t)} - \quad (17)$$

$$\varphi \cdot \frac{A_t}{V_c(t)} \cdot \sqrt{\kappa \cdot R \cdot T_c \cdot \left(\frac{2}{\kappa+1}\right)^{\frac{\kappa+1}{\kappa-1}} \cdot p_c(t) - \frac{A_b(t) \cdot r(p_c, t) \cdot p_c(t)}{V_c(t)}} \quad (18)$$

$$\frac{d}{dt} x(t) = r(p_c, t)$$

Using calculated real  $C_F$  and pressure-time curve, thrust-time curve can be also calculated, according to equation:

$$F(t) = C_F \cdot p_c(t) \cdot A_t \quad (19)$$

Where are:  $\rho_p$  propellant density,  $\varphi$  throat coefficient.

## 4. RESULTS AND DISCUSSIONS

### 4.1. Research model

The 155 mm rocket assisted projectile (RAP), shown in Fig.5, was chosen as the research model in this work. The projectile has the following characteristics: reference diameter (cal.) 155mm, total length ~ 5.61 cal., nose length ~ 3.37 cal., boattail length ~ 0.55 cal., center of gravity (CG) from nose ~ 3.53 cal., explosive charge mass ~ 7 kg, rocket motor propellant mass ~ 3 kg and projectile mass ~ 43 kg.

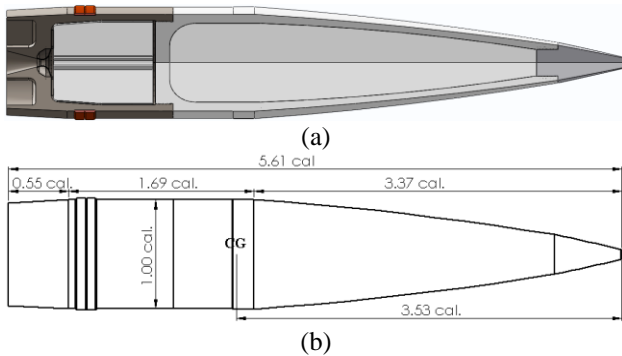


**Figure 5.** Projectile model, (a) CAD model, (b) dimensions in cal.

This projectile fired from 39 calibre howitzer with 19 litre chamber volume, should reach velocity of 830 m/s at the muzzle exit. The solid rocket motor, placed at the rear, must be ignited in the ascending part of the ballistic trajectory, after a predetermined ignition delay, and with a

short working time, to quickly increase projectile velocity.

### 4.2. Rocket motor internal ballistic calculation

The aim of the internal ballistic calculation is to determine the thrust-time variation of the solid rocket motor, which is subsequently used in the 6-DOF projectile motion model. Hence, this section does not include the presentation of all the outcomes from the intermediate stages of the calculation. The required propellant solid rocket motor characteristics are: total impulse ~ 6500 Ns, propellant mass ~ 3 kg and effective working time which takes values between 2s and 4s with a step of 0.5s, in order to analyze its effect on the projectile range. Table 1 specifies the necessary input data for the calculation.

**Table 1.** Input data for the internal ballistic calculation

Input data	Value
Temperature of combustion $T_c$	2900 [K]
Mean chamber pressure $p_{cm}$	200 [bar]
Propellant density $\rho_p$	1750 [kg/m <sup>3</sup> ]
Specific heat ratio $\kappa$	1.25 [ ]
Gass constant $R$	308.7 [J/kg·K]

Three distinct propellant grain configurations are selected (star, slot and tubular), as shown in Fig.6, to achieve the desired thrust-time profiles (neutral, regressive and progressive). The star configuration is inhibited at outer diameter and rear-end. The slot and tubular configurations are inhibited at entire outer surface. The burning area variations versus burning web for the three grain configurations are shown in Fig.7, labeled as follows: N (neutral), R (regressive) and P (progressive).

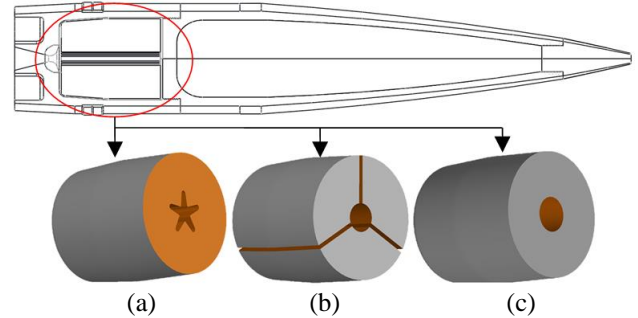


**Figure 6.** Propellant grain configurations, (a) star (neutral), (b) slot (regressive), (c) tubular (progressive)

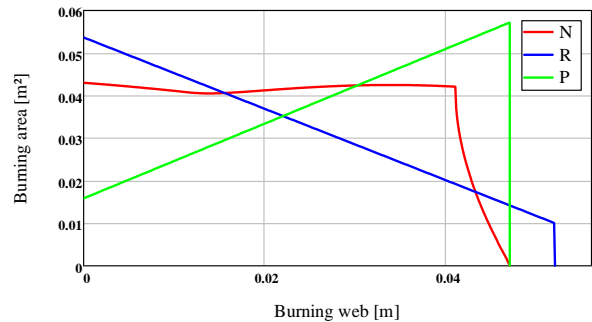


**Figure 7.** Burning area variations versus burning web for the three grain configurations

After having obtained the burning area variations as a

function of the burning web, it is possible to compute the pressure-time evolution  $p_c(t)$  in combustion chamber by solving the system of equations (14-18), which is composed of two differential equations, one integral and two algebraic equations. The differential equations were numerically integrated using the 4th-order Runge-Kutta method. In order to determine the thrust force of the rocket motor over time using equation (19), it is also essential to calculate the thrust coefficient  $C_F$  defined by equation (8). Thus, the nozzle exit pressure  $p_e$  must be determined by utilizing equation (9), which describes the nozzle area expansion ratio  $\varepsilon$ , taking into account the atmospheric pressure  $p_a$  which corresponds to the altitude at which the rocket motor ignites. The obtained thrust-time curves for an effective working time of 3s, calculated for the three grain configurations using equation (19), are shown in Fig.8.

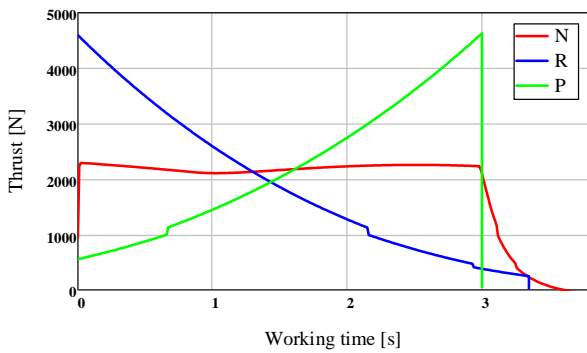


**Figure 8.** Thrust-time variations for the three grain configurations

The thrust-time curves were also calculated for the three cases of grain configuration considering other effective working times, as illustrated in Fig.9 for the neutral thrust profile. This was done to analyze the effect of this operating parameter on the range of the projectile.

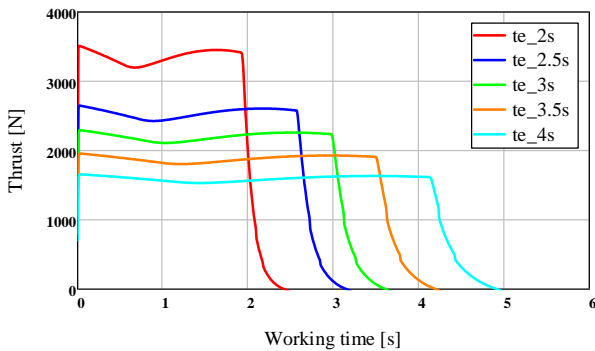


**Figure 9.** Thrust-time variations for different effective working times (neutral profile)

### 4.3. Analysis of trajectory elements

As mentioned before, the six degrees of freedom (6-DOF) trajectory model is used in this work for the purpose of determining the projectile trajectory elements. A 6-DOF trajectory program was built in OCTAVE software to implement the 6-DOF trajectory model, following the algorithm presented in the Fig.10. This program is designed to perform external ballistic calculation and

flight simulation for a rigid, rotationally symmetric projectile, acted on by all significant aerodynamic forces and moments, in addition to wind, gravity, Coriolis forces and rocket thrust. This program also includes an improved semi-empirical method for power-on base-drag prediction during rocket motor operating phase, developed by [13]. The differential equations of projectile motion were numerically integrated using the 4th-order Runge-Kutta method.

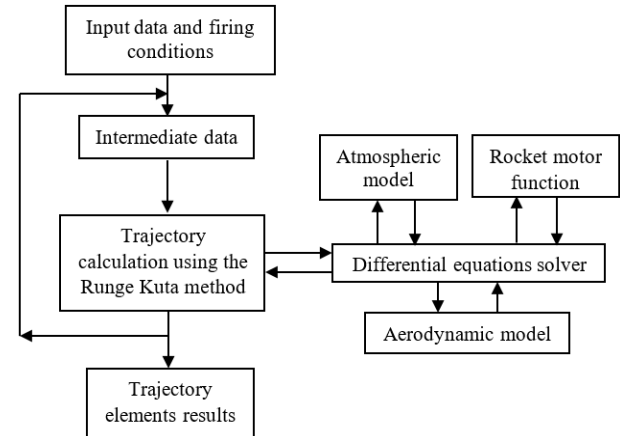


**Figure 10.** Numerical solution program algorithm

The atmospheric model is included to determine variations in air temperature, speed of sound and air density as a function of flight altitude, according to the ANA standard atmosphere [3]. The static and dynamic coefficients of aerodynamic forces and moments are determined via semi-empirical design codes (ADK0, ADK1 and ADK2), using aerodynamic prediction based on theories of reference [14-16]. The effect of wind velocity components was not included in the calculation of projectile trajectory elements.

To check the accuracy of the 6-DOF program, an existing projectile case was considered. This concerns the M101 155mm artillery projectile. The projectile input data and firing conditions are presented in Table 2. The comparison between the firing-tables data and results obtained by numerical calculation are illustrated in Table 3.

**Table 2.** Input data and firing conditions of the M101 projectile

Projectile input data	
Caliber $d$ [mm]	155
Length $l$ [mm]	704
Mass $m$ [kg]	43.25
Center of gravity from nose $x_{CG}$ [mm]	458.37
Moments of Inertia [kg·m <sup>2</sup> ]	
Axial $I_{xx}$	0.144
Lateral $I_{yy} = I_{zz}$	1.216
Firing conditions	
Muzzle velocity $V_0$ [m/s]	840
Firing altitude $Y_0$ [m]	500
Muzzle spin rate $p_0$ [rad/s]	1162
Firing elevation angle $\theta_0$ [°]	47.88

**Table 3.** Trajectory elements of the M101 projectile

	6-DOF calculation	Firing Tables data	Deviation [%]
Summit $Y_{max}$ [m]	9260	8963	+3.3
Range $X_{max}$ [m]	23532	23808	-1.2
Crossrange $Z_{max}$ [m]	911.6	982.3	-7.2
Impact angle $\theta_f$ [°]	65.68	65.03	+0.9
Impact time $t_f$ [s]	85.77	85	+0.9
Impact velocity $V_f$ [m/s]	337.3	337	+0.1

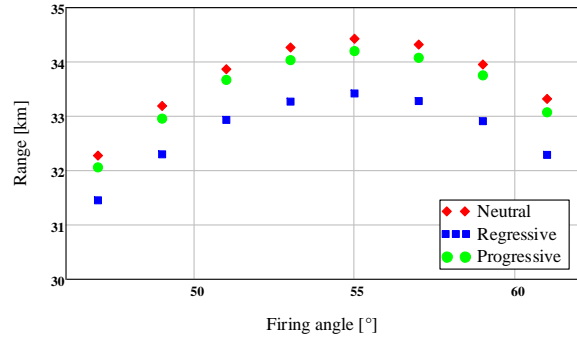
In Table 3, it can be seen that the percent deviations between the calculated results and firing-tables data are not significant, which confirms the accuracy of the 6-DOF program as a tool for predicting trajectory elements.

Once the program accuracy has been checked, it becomes feasible to investigate the effect of the solid rocket motor operating parameters on the trajectory elements of the 155mm rocket-assisted projectile (RAP), especially their effect on the projectile range. As mentioned before, these parameters are: (1) thrust-time profile (neutral, regressive and progressive), (2) working time and (3) ignition delay. The input data and firing conditions of the studied projectile are presented in Table 4.

**Table 4.** Input data and firing conditions of the rocket-assisted projectile

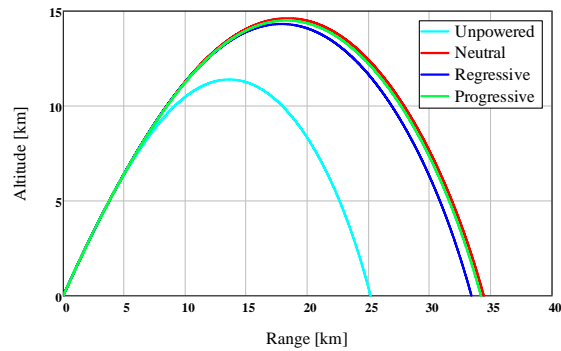
Projectile input data		
Caliber $d$ [mm]		155
Length $l$ [mm]		870
Before burnout	Mass $m_i$ [kg]	43
	Center of gravity from nose $x_{CGi}$ [mm]	548.7
	Axial Moment of Inertia $I_{xxi}$ [kg·m <sup>2</sup> ]	0.14
	Lateral Moment of Inertia $I_{yyi} = I_{zxi}$ [kg·m <sup>2</sup> ]	1.78
After burnout	Mass $m_f$ [kg]	40
	Center of gravity from nose $x_{CGf}$ [mm]	540
	Axial Moment of Inertia $I_{xxf}$ [kg·m <sup>2</sup> ]	0.13
Lateral Moment of Inertia $I_{yyf} = I_{zzf}$ [kg·m <sup>2</sup> ]		1.67
Firing conditions		
Muzzle velocity $V_o$ [m/s]		830
Firing altitude $Y_o$ [m] (sea level)		0
Muzzle spin rate $p_o$ [rad/s]		1148
Firing elevation angle $\theta_o$ [°]		Variable

Figure 11 shows the projectile range changes versus firing angle, for each of the three thrust-time profiles, with working time of 3s and ignition delay of 7s. The projectile range, as indicated in the Fig.11, changes with the thrust-time profile. For this configuration, the maximum range is achieved at a firing angle of 55° in the three profile cases with different values, while the neutral profile exhibiting the largest.



**Figure 11.** Projectile range changes versus firing angle (working time 3s, ignition delay 7s)

Altitude and crossrange versus range are shown in Figs. 12 and 13 for unpowered and powered flights (for each of the three thrust-time profiles), with working time of 3s, ignition delay of 7s and firing angle of 55°. These two Figs. 12 and 13 indicate that this trajectory parameters for powered flight exhibit the same variation patterns as those for unpowered flight. The trajectory does not have a symmetry axis that passes through its summit, which is due to the impact of total aerodynamic load on projectile motion. Compared to unpowered flight, Fig.12 illustrates the benefit of using the rocket motor to enhance the performance of artillery projectiles, with extensions of more than 35% for range and around 25% for summit altitude.



**Figure 12.** Altitude versus range (working time 3s, ignition delay 7s and firing angle 55°)

The projectile deflection (crossrange) in the horizontal plan, shown in Fig.13, is caused by the Magnus effect. For uncontrolled flight, this deflection expands as the projectile range increases.

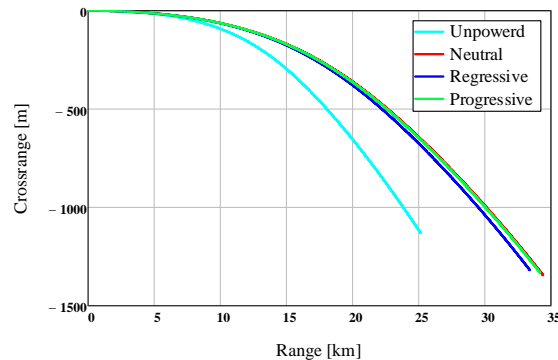


**Figure 13.** Crossrange versus range (working time 3s, ignition delay 7s and firing angle 55°)



Figure 14 illustrates the flight velocity versus flight time from launch to impact point for unpowered and powered flights (neutral, regressive and progressive), with working time of 3s, ignition delay of 7s and firing angle of 55°.

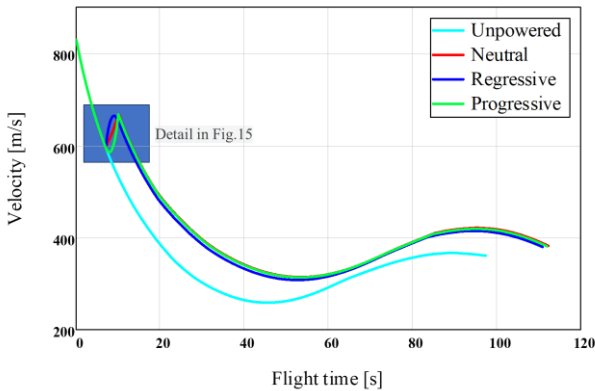


**Figure 14.** Flight velocity versus flight time (working time 3s, ignition delay 7s and firing angle 55°)

As depicted in Fig.14, it can be seen that the velocity decreases immediately after launch due the impact of total aerodynamic load. During rocket motor operating phase, which begins 7 seconds after launch continues for 3 seconds, the velocity quickly increases due to the thrust force. Following that, it begins to decrease again under the same aerodynamic impact until the projectile reaches the highest point of the trajectory, which is the summit point. At that highest point, the vertical velocity component becomes zero. After this, the velocity increases again under the influence of gravitational acceleration. Fig.14 further shows that the RAP projectile velocity at both the summit and impact points, as well as the total flight time, exceed those of the unassisted projectile (unpowered flight).

Velocity-time variations during rocket motor operating phase are shown in Fig.15, for each of the three thrust-time profiles, with working time 3s, ignition delay 7s and firing angle 55°.

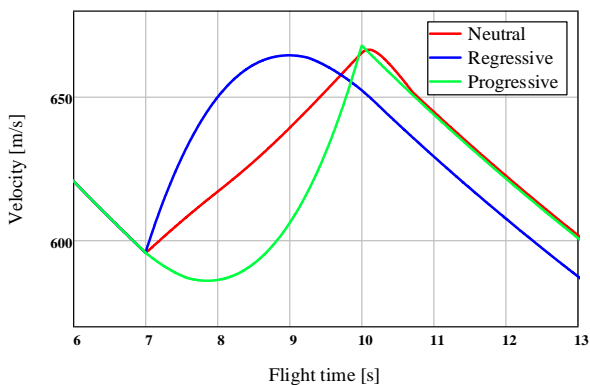
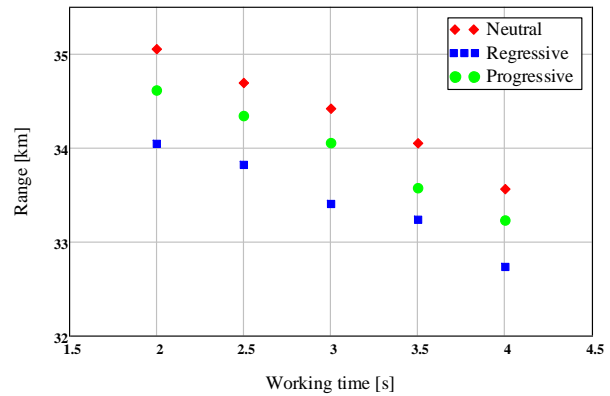


**Figure 15.** Velocity-time variations during rocket motor operating phase (working time 3s, ignition delay 7s and firing angle 55°)

It is evident from Fig.15 that the velocity-time profiles reflect the integrated form of the thrust-time profiles. In the case of neutral thrust, the integration produces a linear velocity-time profile, showing a steady rate of velocity change. Concerning the case of regressive thrust which decreases with time, the integration gives a concave-down

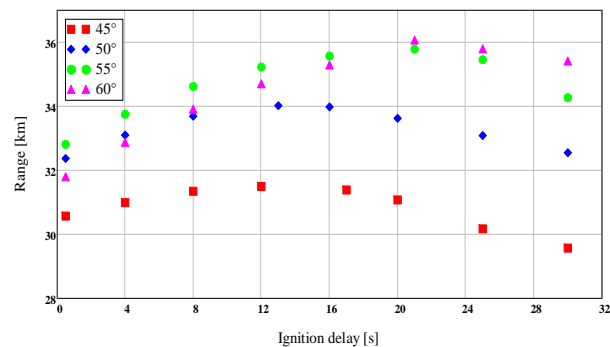
parabolic curve, indicating a decelerating rate of velocity increase. Finally, and for the progressive thrust that increases with time, the integration produces a concave-up parabolic curve, indicating an accelerating rate of velocity increase. These variations highlight the effects of the different thrust-time profiles on the projectile velocity.

Figure 16 shows the projectile range changes versus working time, for each of the three thrust-time profiles, with ignition delay of 7s and firing angle of 55°. The projectile range varies not only with the thrust-time profile, but also with the working time, where the range extension increases by using shorter working time, as shown in Fig.16. The maximum range for this configuration is reached at a working time of 2s in all three profile cases, each with distinct values, while the neutral profile shows the largest range. However, using shorter working times while maintaining the required total impulse leads to high thrust levels (as already shown in the Fig.9 for the neutral profile), which demands careful consideration of the effects of thrust on the projectile aerodynamic characteristics.



**Figure 16.** Projectile range changes versus working time (ignition delay 7s and firing angle 55°)

After illustrating the effect of the thrust-time profiles and working time on the trajectory elements, especially the projectile range, it remains to analyze the effect of the rocket motor ignition delay. This was done with working time of 3s and neutral thrust-time profile, as this profile has shown to be more effective than the other two profiles.



**Figure 17.** Projectile range changes versus ignition delay for different firing angles (neutral thrust profile, working time 3s)

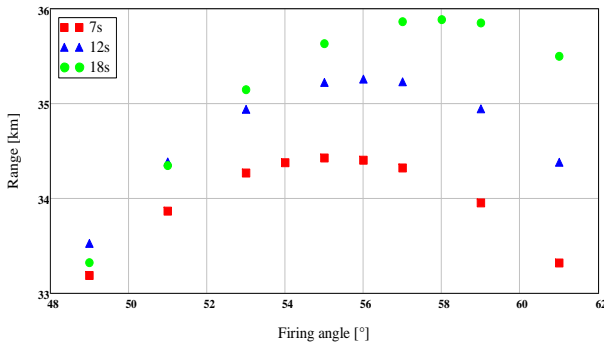


**Figure 18.** Projectile range changes versus firing angles for different ignition delays (neutral thrust profile, working time 3s)

Projectile range changes versus ignition delay for different firing angles are shown in Fig.17. The outcomes of this figure illustrate that the range varies with the ignition delay, and the projectile maximum range for each firing angle is associated with particular ignition delay. Fig.18 shows the projectile range changes versus firing angle for different ignition delays. Fig.18 also illustrates that the firing angle corresponding to the maximum range changes with the ignition delay.

## 5. CONCLUSION

In this work, computational analysis was performed to examine the influence of different operating parameters of solid rocket motor on the trajectory elements of 155mm rocket-assisted projectile, especially the projectile range. The six degree-of-freedom trajectory model and the solid rocket motor internal ballistic have been briefly explained. The selected operating parameters of solid rocket motor for this analysis are: (1) thrust-time profile, (2) working time and (3) ignition delay. Thrust-time variations of three selected propellant grain configurations (star, slot and tubular) were computed, in order to obtain the desired thrust-time profiles (neutral, regressive and progressive). The trajectory elements were calculated using a 6-DOF trajectory program, built for the purpose of this work.

The 6-DOF program results showed that the trajectory elements of rocket-assisted projectile are impacted not only by the projectile characteristics and firing conditions, but also by the operating parameters of the solid rocket motor. The results also illustrated the benefit of using the solid rocket motor, with extensions of more than 35% for range and around 25% for summit altitude, and with longer time of flight. Among the three thrust time profiles considered for this analysis, the neutral one enabled more range extension, with slight differences compared to the progressive profile. It has also been shown that the range extension increases using shorter working times, but with high thrust levels. Concerning the ignition delay, the results illustrated that the projectile range varies with this operating parameter. It was found that the projectile maximum range for each firing angle is related to a specific ignition delay.

For possible perspectives, this work can be extended to investigate the incorporation of base bleed unit and solid

rocket motor in the same artillery projectile, wherein each is used in its most effective part of the ballistic trajectory.

## Acknowledgement

This research has been supported by the University of Defence in Belgrade within the Project No. VA/TT/1/24-26.

## References

- [1] Gunners N. E., Andersson K. and Hellgren R., *Base-Bleed Systems for Gun Projectiles*, Gun Propulsion Technology, vol. 109, p. 537–562, 1988.
- [2] Guodong Z., *The Study of the Modeling simulation for the Rocket-Assisted Cartridge*, IOP Conference Series Materials Science and Engineering, vol. 439(4), 2018.
- [3] Regodić D., *Spoljna balistika*, Beograd, Vojna Akademija, 2006.
- [4] McCoy R. L., *Modern Exterior Ballistics*, Schiffir Publishing Ltd, ISBN: 978-0-7643-3825-0, 1998.
- [5] Carlucci D. E. and Jacobson S. S., *Ballistics: Theory and design of guns and ammunition*, Florida. United States: CRC Press, 2008.
- [6] Alazeezi M., *Design and Optimization of Dual-Propellant Grains of Solid Rocket Motors*, University of Belgrade – Faculty of Mechanical Engineering, 2024.
- [7] Živković S., Filipović M., Elek P., Milinović M., Gligorijević N. and Boulahlib M. A., *Experimental determination of rocket motor internal ballistic coefficients and performance parameters*, in 6th International scientific conference on defensive technologies OTEH, Belgrade, 2014.
- [8] Živković S., Savković M. and Grigorijević N., *Solid propellant rocket motor components initial design*, chez 4th International scientific conference on defensive technologies OTEH, Belgrade, 2011.
- [9] Jelić Z., *Optimization of design parameters for modular range enhanced projectile*, Cranfield University, Cranfield Defence and Security, Doctoral Dissertation, 2015.
- [10] George P. S. and Donald M. R., *Rocket Propulsion Element*, Hoboken, New Jersey, John Wiley & Sons, Inc., 2017.
- [11] Ocokoljić G., Živković S. and Subotić S., *Aerodynamic coefficients determination for antitank missile with lateral jets*, in 4th International scientific conference on defensive technologies OTEH, Belgrade, 2011.
- [12] Marjanović G., Živković S. and Gligorijević N., *Program SVOD for Solid Propellant Grain Design*, in 5th International scientific conference on defensive technologies OTEH, Belgrade, 2012.
- [13] Moore F. G. and Moore L. Y., *Improvements to Power-On Base Pressure Prediction for the Aeroprediction Code*, Journal of Spacecraft and Rockets, vol. 47(1), pp. 101-112, 2010.
- [14] Regodić D., *Zbirka rešenjih zadataka iz spoljne*

- balistike*, Beograd: Vojna Akademija, 2003.
- [15] Jerković D. and Samardžić M., *The aerodynamic characteristics determination of classic symmetric projectile*, in the 5th international symposium about design in mechanical engineering KOD, Novi Sad, 2008.
- [16] Ferfour A., Allouche T., Jerković D., Hristov N., Vučković M. and Benmeddah A., Prediction of drag aerodynamic coefficient of the 155mm projectile under axisymmetric flow using different approaches, *Journal of the Serbian Society for Computational Mechanics*, vol. 17(2), pp. 69-86, 2023.



## COMPUTING AERODYNAMIC DAMPING IN ROLL AND PITCH OF A SUPERSONIC FINNER MODEL

JELENA SVORCAN

University of Belgrade, Faculty of Mechanical Engineering, Belgrade, [jsvorcan@mas.bg.ac.rs](mailto:jsvorcan@mas.bg.ac.rs)

TONI IVANOV

University of Belgrade, Faculty of Mechanical Engineering, Belgrade, [tivanov@mas.bg.ac.rs](mailto:tivanov@mas.bg.ac.rs)

OGNJEN PEKOVIĆ

University of Belgrade, Faculty of Mechanical Engineering, Belgrade, [opekovic@mas.bg.ac.rs](mailto:opekovic@mas.bg.ac.rs)

ALEKSANDAR SIMONOVIC

University of Belgrade, Faculty of Mechanical Engineering, Belgrade, [asimonovic@mas.bg.ac.rs](mailto:asimonovic@mas.bg.ac.rs)

**Abstract:** Accurate aerodynamic coefficients and their derivatives are crucial for flight dynamics analysis and appropriate control definition. Even when the investigated geometry is simple (e.g. a revolution body, with simple control or stabilizing surfaces), determination of its aerodynamic derivatives, particularly at supersonic regimes, is rather challenging, and usually includes extensive computational and experimental campaigns. This paper computationally investigates quasi-steady or unsteady supersonic flows that include rigid body motion effects around the Army-Navy Finner geometry (a basic, revolution body with  $L/D = 10$  fineness, slender, conical nose section, and wedge-section fins in  $\times$  configuration). To elucidate the flow fields, the Reynolds-averaged Navier-Stokes equations are closed by  $k-\omega$  SST turbulence model. Roll and pitch damping are estimated by different approaches, and the obtained values are compared mutually, but also to the available experimental data. In addition, some representative flow visualizations are included.

**Keywords:** roll damping, pitch damping, supersonic finner model, CFD.

### 1. INTRODUCTION

The correct estimation of aerodynamic coefficients (both numerical and experimental) of objects flying at supersonic speeds is a prerequisite for their subsequent flight dynamics analyses and appropriate control definition, as well as their overall performance. For that reason, comparative numerical and experimental studies have been conducted for decades to ensure greater levels of detail, acquired knowledge and useful data [1-8]. While static aerodynamic coefficients can be computed and measured with acceptable accuracy, dynamic coefficients (assumed in the form of Taylor series) and their corresponding derivatives still pose quite a challenge to both experimental and computational aerodynamics (due to the increased complexity, expenses and sensitivity to outer instigations).

There are several different standard models (geometries), designed for higher velocities, that are typically used for validation of experimental set-ups and installations, but also numerical codes. One of them is Army-Navy Finner geometry, a simple revolution body with four aft stabilizing/control surfaces [1-5,8]. Here, it is chosen for its geometric simplicity and great amount of data available for comparison, and used to check the ability of

flow simulations performed in ANSYS FLUENT to accurately estimate aerodynamic damping, while keeping the numerical set-up as simple as possible, as will be demonstrated in the following sections.

### 2. MODEL DESCRIPTION

The Army-Navy Finner model comprises an axisymmetric body with four rear wedge-shaped stabilizing/control surfaces arranged in  $\times$  configuration, as illustrated in Fig. 1. Body-fixed coordinate system is used, attached to the model center-of-gravity (CG), where  $x$ -axis points forward,  $y$ -axis to the right side, and  $z$ -axis downward. Here, body length is  $L = 0.5$  m, and fineness is  $L/D = 10$ . More geometric details are available in [5].

Similarly to [5], experimentally-determined aerodynamic roll and pitch damping data from the Arnold Engineering Development Center (AEDC) Supersonic Wind Tunnel facility are used to validate the current numerical results.

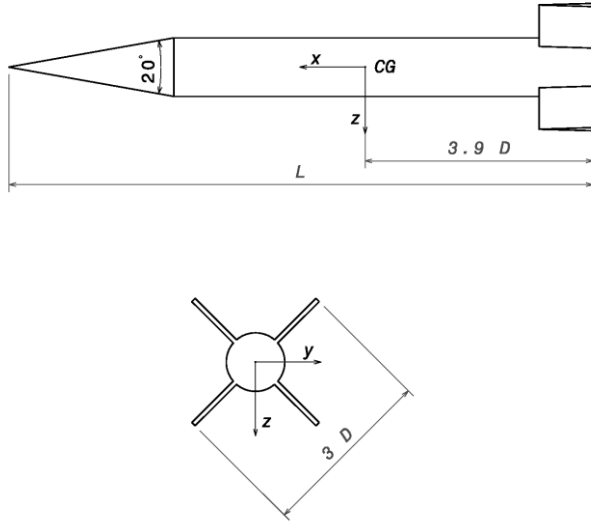


**Figure 1.** Investigated model and used coordinate system

### 3. FLOW SIMULATION

The following subsections describe all the steps of the performed flow computations, starting from the geometric model, formed computational meshes, to setting up the problems in ANSYS FLUENT.

#### 3.1. Geometry

The finner geometry is modeled completely in accordance with the previously mentioned geometric features. The surrounding computational domain is cylindrical, extending  $10L$  in axial direction, starting  $1.5$  m fore and ending  $3.5$  m aft of the coordinate beginning (where CG is located  $195$  mm from the base), and with the diameter of  $8L$ .

#### 3.2. Computational mesh

Since the starting geometry is rather simple, so are the generated unstructured, hybrid meshes. To ensure that grids do not significantly affect the results, two different meshes are generated (containing approximately  $1.4$  and  $2.4$  million control volumes, respectively) and analyzed (by comparing the coefficients of  $x$ -components of the computed aerodynamic force). In both cases, global sizing is prescribed (with limited maximal edge and face sizes, and with very fine minimal, proximity and defeature sizes) to adequately represent the model surfaces. Also, several layers of thin, prismatic cells encompass the walls to better capture considerable changes of flow quantities within the thin boundary layer. The first cell height is  $y_1 = 0.01$  mm resulting in the satisfactory value of dimensionless wall distance ( $y^+ < 5$ ).

Details of the generated finer computational mesh are given in Fig. 2.

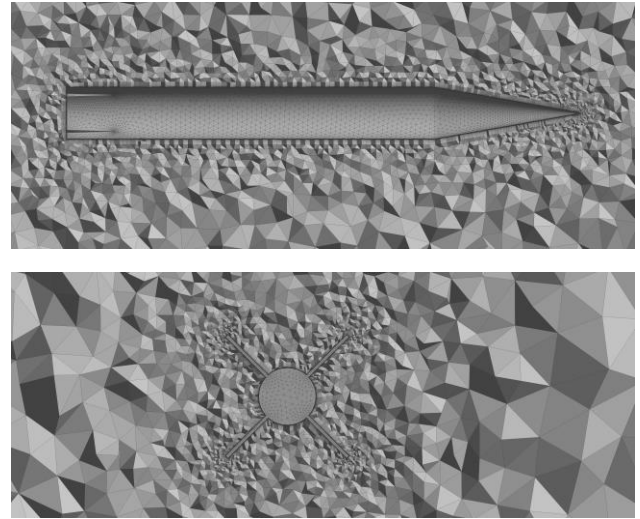


**Figure 2.** Details of the generated computational grid

#### 3.3. Initial, steady flow case

In both cases (for both roll and pitch damping), a converged steady case and solution are required. ANSYS FLUENT is employed for resolving the flow fields, i.e. solving the governing flow equations by finite volume method. In this initial case, the flow is considered steady, compressible (density-based solver is used), turbulent ( $k-\omega$  SST turbulence model is employed for closing the flow equations), fluid (air) is assumed as an ideal gas, where the viscosity changes with temperature are modeled according to the Sutherland law.

The following boundary conditions are defined along all the outer boundaries: Mach number is  $M = 2.49$ , angle-of-attack (AoA) is  $\alpha = 0^\circ$ , static pressure is  $p = 2664$  Pa, and static temperature is  $T = 139$  K. These static values are defined so that they match the total values in the wind tunnel during the experiments. The reference values used for the computation of aerodynamic coefficients are  $A_{ref} = 0.002$  m<sup>2</sup> and  $l_{ref} = 0.05$  m.

Implicit numerical formulation is employed, with Roe-FDS flux type, and all numerical schemes of 2nd order, where  $CFL = 2$ . Aerodynamic coefficients of forces ( $C_x$  and  $C_z$ ) and moments ( $C_l$  and  $C_m$ ) were monitored, and computations were performed until reaching their convergence (usually 1000 iterations). The expressions of interest are:

$$C_x = \frac{X}{\frac{1}{2}\rho V^2 A_{ref}} = \frac{X}{\frac{1}{2}\kappa p M^2 A_{ref}}, \quad (1)$$

$$C_z = \frac{Z}{\frac{1}{2}\rho V^2 A_{ref}} = \frac{Z}{\frac{1}{2}\kappa p M^2 A_{ref}}, \quad (2)$$

$$C_l = \frac{L_x}{\frac{1}{2}\rho V^2 A_{ref} l_{ref}} = \frac{L_x}{\frac{1}{2}\kappa p M^2 A_{ref} l_{ref}}, \quad (3)$$

$$C_m = \frac{M_y}{\frac{1}{2}\rho V^2 A_{ref} l_{ref}} = \frac{M_y}{\frac{1}{2}\kappa p M^2 A_{ref} l_{ref}}, \quad (4)$$

where  $X$  and  $Z$  are components of aerodynamic force along  $x$ - and  $z$ -axis respectively,  $L_x$  and  $M_y$  are roll and pitch moments respectively,  $\rho$  is fluid density and  $\kappa = 1.4$  is ratio of specific heat.

### 3.4. Forced continuous roll

To determine the damping in roll, it is possible to perform quasi-steady simulations assuming rotation of the complete computational domain. Here, frame motion is assumed, and additional inertial terms are simply added to the flow equations. This approach is computationally much less expensive than unsteady simulations with actual rotation of the portion of the computational domain. Otherwise, the numerical setting is quite similar to the previously described.

The flow is steady, compressible and turbulent, and air is considered as ideal gas. Frame motion around the axial,  $x$ -axis is defined with  $p = 353$  rad/s. Computations are performed until achieving the convergence of the roll coefficient  $C_l$ . The obtained results are then post-processed to determine the roll damping (roll derivative with respect to angle rate  $p$ ) according to the equations:

$$\frac{\partial C_l}{\partial p} \approx \frac{\Delta C_l}{\Delta p}, C_{l_p} = \frac{\frac{\partial C_l}{\partial p}}{\frac{l_{ref}}{2V}} \approx \frac{2V}{l_{ref}} \frac{\Delta C_l}{\Delta p}. \quad (5)$$

### 3.5. Forced harmonic pitch

To determine the damping in pitch, it is necessary to perform unsteady flow simulations. However, instead of rotating the model and portion of the domain closely surrounding it (which is computationally rather expensive), it is possible to assign variable conditions at the boundaries, in particular the harmonic (sine shaped) change of the angle-of-attack:

$$\alpha(t) = \alpha_0 + A \sin(\omega t), q = \dot{\alpha} = A\omega \cos(\omega t), \quad (6)$$

where  $\alpha_0 = 0^\circ$ ,  $A = 0.5^\circ$  and  $\omega = 3764$  rad/s.

By writing and including user-defined functions (UDFs) governing the change of velocity direction, in every timestep velocity components corresponding to the harmonic (sine) change of AoA are recomputed and assigned anew to the outer boundaries.

Other than this difference in BCs, the flow is compressible and turbulent, and the remainder of the numerical set-up is the same as before.

Again, during the computation, the periodic aerodynamic coefficients are monitored and registered, and afterwards, their derivatives are determined from the saved files/data:

$$\begin{aligned} C_m(t) &= C_{m_o} + Ak(C_{m_{\dot{\alpha}}} + C_{m_q})\cos(\omega t) \\ &= C_{m_o} + Ak\bar{C}_{m_q}\cos(\omega t), k = \omega D/2V, \end{aligned} \quad (7)$$

where  $D$  is the model diameter. We can assess the derivative of interest:

$$\bar{C}_{m_q} = \frac{2V}{n\pi AD} \int_{t_a}^{t_b} C_m(t) \cos(\omega t) dt, \quad (8)$$

by numerically computing this integral. The difference  $(t_b - t_a) = nT_t = 2\pi n/\omega$  is the integer ( $n$ ) number of time periods  $T_t$ . Usually, the computations were performed for at least 5-10 periods  $T_t$ , and the effect of time step  $dt$  was also investigated ( $dt = T_t/180$  and  $dt = T_t/360$ ).

## 4. RESULTS AND DISCUSSION

Illustrations of the computed steady, nearly axisymmetric flow at zero AoA by Mach number contours and vortical structures are given in Figs. 3 and 4. The initial oblique shock is apparent, as well as the smaller ones forming at the wedges, and the considerable wake induced by the model base.

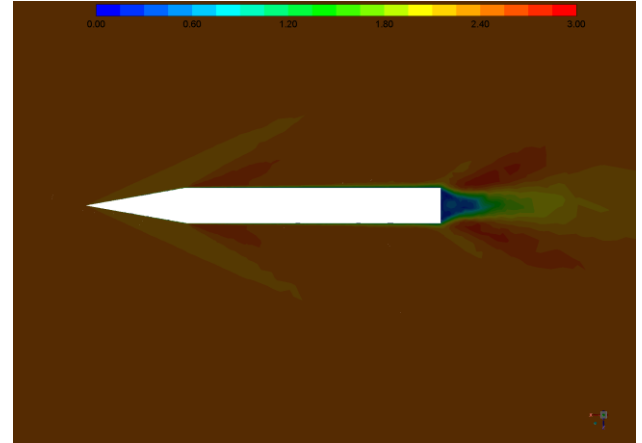


**Figure 3.** Computed velocity field in the symmetry  $xz$ -plane

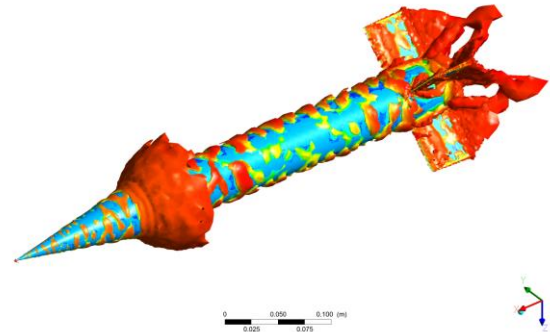


**Figure 4.** Computed vorticity structures originating from the model surfaces

The computed damping in roll and pitch are provided in Tables 1 and 2. Given the sensitivity of these derivatives and simplified computational set-ups, it can be concluded that rather satisfactory correspondence between the two

sets of data is achieved.

**Table 1.** Computed and measured damping in roll

Mode	$C_{l_p}$
Numerical (mesh 1)	-16.07
Numerical (mesh 2)	-16.05
Experimental	$-16.8 \pm 0.8$

**Table 2.** Computed and measured damping in pitch

Mode	$\bar{C}_{m_q}$
Numerical ( $dt = T_f/180$ )	-135
Numerical ( $dt = T_f/360$ )	-139
Experimental	$-180 \pm 45$

The registered (resulting periodic) change/output in aerodynamic pitch coefficients with respect to time and AoA is illustrated in Fig. 5.

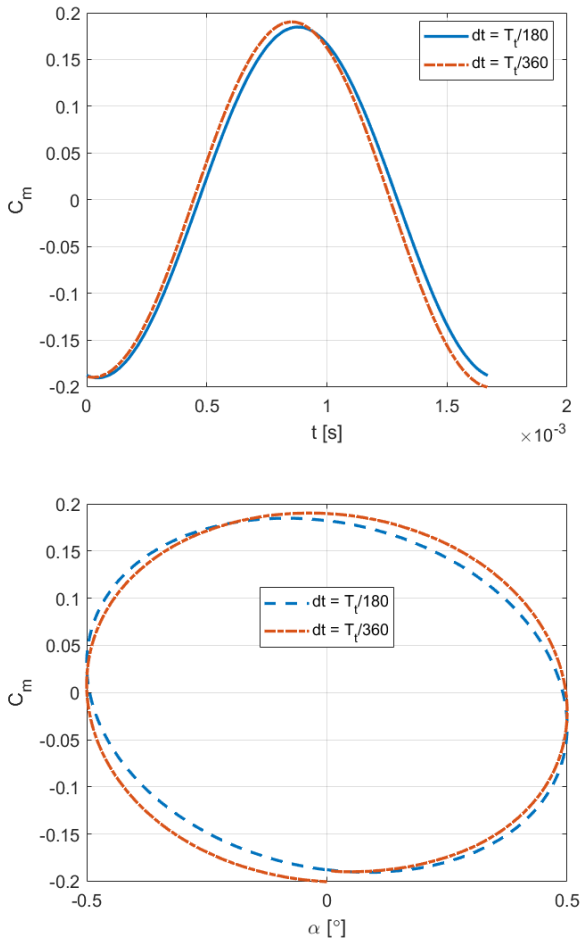


**Figure 5.** Periodic response to forced harmonic pitch motion

## 5. CONCLUSION

This study confirms the considerable sensitivity of aerodynamic derivatives in roll and pitch that

significantly change with Mach and Reynolds numbers, as well as angles-of-attack. Furthermore, their accurate determination, both experimental and numerical, is extremely difficult and costly (in both time and resources). For the time being, by employing standard numerical models, it is possible to estimate aerodynamic damping with approximate relative error amounting to 20%. In future studies, to achieve higher levels of accuracy, finer meshes and more advanced computational approaches should also be considered and tested.

## Acknowledgement

This research work was supported by the Ministry of Science, Technological Development and Innovation of the Republic of Serbia through contract No. 451-03-65/2024-03/200105 from 5 February 2024.

## References

- [1] BHAGWANDIN,V.A., SAHU,J.: *Numerical prediction of pitch damping stability derivatives for finned projectiles*, ARL-TR-6725, U. S. Army Research Laboratory, Aberdeen Proving Ground, 2013.
- [2] BHAGWANDIN,V.A., SAHU,J.: *Numerical prediction of pitch damping stability derivatives for finned projectiles*, Journal of Spacecraft and Rockets, 51(5) (2014) 1603-1618.
- [3] SAMARDŽIĆ,M., ISAKOVIĆ,J., MILOŠ,M., ANASTASIJEVIĆ,Z., NAUPARAC,D.B.: *Measurement of the direct damping derivative in roll of the two calibration missile models*, FME Transactions 41(3) (2013) 189-194.
- [4] SAMARDŽIĆ,M., ISAKOVIĆ,J., ANASTASIJEVIĆ,Z., MARINKOVSKI,D.: *Apparatus for measurement of pitch and yaw damping derivatives in high Reynolds number blowdown wind tunnel*, Measurement: Journal of the International Measurement Confederation 46(8) (2013) 2457-2466.
- [5] SHELTON,A., MARTIN,C., SILVA,W.: *Characterizing aerodynamic damping of a supersonic missile with CFD*, AIAA Aerospace Sciences Meeting, Kissimmee, 2018.
- [6] GUO,C., REN,Y.-X.: *The computation of the pitch damping stability derivatives of supersonic blunt cones using unsteady sensitivity equations*, Advances in Aerodynamics 1(1) (2019) 17.
- [7] TATAR,M., MASDARIM.: *Investigation of pitch damping derivatives for the Standard Dynamic Model at high angles of attack using neural network*, Aerospace Science and Technology 92 (2019) 685-695.
- [8] YAYLA,K.: *Numerical Prediction of Aerodynamic Stability Derivatives of a Projectile*, M.Sc. - Master of Science, Middle East Technical University, 2021.

## DESIGN AND EXPERIMENTAL EVALUATION OF A MISSILE LATERAL THRUSTER

TOUFIK ALLOUCHE

University of Defence – Military Academy, Belgrade, [toufik.allouche@gmail.com](mailto:toufik.allouche@gmail.com)

SAŠA ŽIVKOVIĆ

Military Technical Institute, Belgrade, [sasavite@yahoo.com](mailto:sasavite@yahoo.com)

MARKO KARIĆ

Military Technical Institute, Belgrade, [karicmarko83@gmail.com](mailto:karicmarko83@gmail.com)

ABDELLAH FERFOURI

University of Defence Belgrade; Military Academy [fer-abdel@hotmail.com](mailto:fer-abdel@hotmail.com)

DAMIR JERKOVIĆ

University of Defence Belgrade; Military Academy [damir.d.jerkovic@gmail.com](mailto:damir.d.jerkovic@gmail.com)

NEBOJŠA HRISTOV

University of Defence Belgrad; Military Academy, [nebojsahristov@gmail.com](mailto:nebojsahristov@gmail.com)

**Abstract:** Lateral thrusters are small, short-duration rocket motor mounted on the lateral side of the missile to provide a force able to change the missile's direction. In the present paper, a design and experimental evaluation of a solid propellant thruster is considered. The design starts from technical requirements, internal ballistic calculation, thruster prototype manufacturing and finally static tests on a static test bench to evaluate its internal pressure profile. In design, the propellant imperfections are considered. After tests and simulations, a comparative analysis between the analytical and the experimental results is done.

**Keywords:** Side thruster, solid rocket motor design, internal ballistic, static tests, missile control system.

### 1. INTRODUCTION

For guided missiles, control systems based on aerodynamic control surfaces present some physical limitations, particularly at low speed and at high altitudes where the air density is low. To improve maneuverability and overcome these limitations, thrusters are a very good addition which offer better agility, maneuverability as well as a much faster response time to the commands. For achieving higher precision, lower cost and better manoeuvrability, this alternative method of control has been integrated into several areas of missile systems as the trajectory tracking on artillery, or course refining on air defense interceptors as shown in Figure 1.

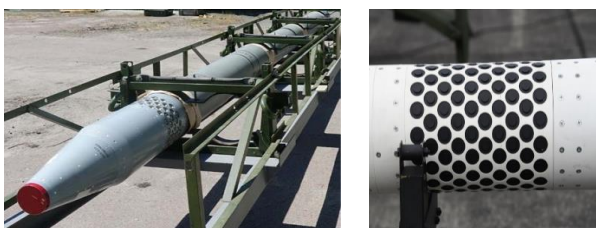


**Figure 1.** (a) Missile R624 [1], (b) Control section of PAC-3 [2]

Thrusters are small solid rocket, short-duration, high-force motor mounted in the lateral side of the missile to provide a force able to change/reorient the missile's direction. The thruster is composed of a metal structure (casing with an insulation), an igniter, a grain (solid propellant) and a nozzle as shown in Figure 2.

In missile systems, thrusters can be used in several areas of application, namely: Trajectory tracking [3,4], Anti-ballistic and air defense interceptors [5] and Anti-tank rockets [6].

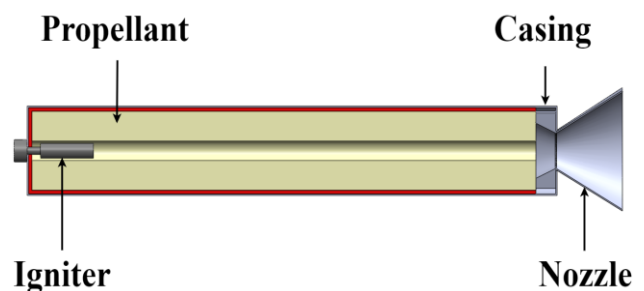


**Figure 2.** Components of solid rocket motor

The process of solid rocket motor design requires first to determine application field, input data as the thrust



(generated force), burning time and the total impulse then comes the second step where the propellant grain design and the propellant properties are chosen in such way that they respond to requirements. Numerical calculation allow to predict the thruster's performances.

In the field of SPRM (Solid Propellant Rocket Motor) design, significant researches are done and scientific papers are published; this concerns the design of the motor casing [7-9], grain propellant [10,11], experimental performance tests [12,13]. There are also works that encompass more than one aspect [14,15].

## 2. EXPERIMENTAL BENCH

The experimental part consists to conduct a static test on the designed motor in order to evaluate the pressure profile. These tests are essential to validate the theoretical curve predicted by the analytical model. Figure 3. presents a schema of the test bench used to measure the pressure of the combustion chamber of the motor using an adequate pressure transducer.

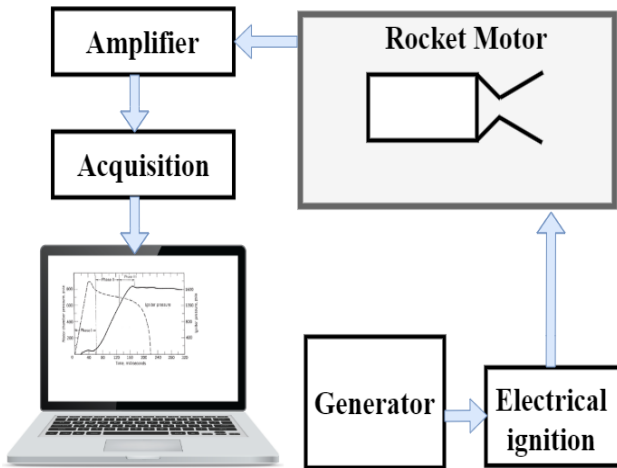


Figure 3. Experimental test bench

The test bench is composed of 3 systems: Motor installation, power alimentation, acquisition and processing.

- Motor installation: composed of a thruster prototype, a support where the thruster is fixed, a pressure transducer connected to combustion pressure and an electrical igniter.

- Power alimentation: the electric device needed to generate the ignition current as well as the control box and the associated wiring.

- Acquisition and processing: composed of an amplifier, an acquisition device and a laptop to process and display data.

## 3. ANALYTICAL CALCULATION

### 3.1. Flight requirements

Thrusters are employed to deliver a short-duration impulse then, the thruster must use a quick-burn propellant, this propellant has the ability to generate thrust in short operating time of the order of few milliseconds. For that:

- The propellant shown in table 1. is chosen;
- A multi-tubes propellant configuration with internal-external burning is chosen.

The propellant presented in Table 1 is used.

Table 1. Propellant characteristics

Characteristics	Value	Unit
Density	1620	[Kg/m <sup>3</sup> ]
Specific heat ratio	1.24	[ / ]
Temperature of combustion	2345	[K]
Molar mass	23.1	[ Kg/Kmol]
Specific impulse	2000	[ N.s/Kg]

The motor initial parameters are presented in Table 2.

Table 2. Motor characteristics

Characteristics	Value	Unit
Thrust force	600	[N]
Effective working time	10	[ms]
Internal pressure	125	[bar]
Throat diameter	3.5	[mm]

### 3.2. Internal ballistics equations

The motor's internal parameters are calculated using the internal ballistic mathematic model of rocket motors.

Solid propellant mass is defined as the ratio between the total impulse and the specific impulse of the propellant. It is given by equation (1):

$$m = \frac{F \cdot t_e}{I_{sp}} \quad (1)$$

The mass flow rate of combustion gases can be calculated with equation (2):

$$\dot{m} = \frac{m}{t_e} \quad (2)$$

Mass flow coefficient:

$$C_d = \sqrt{\frac{\kappa}{RT_0} \cdot \left(\frac{2}{\kappa+1}\right)^{\frac{\kappa+1}{\kappa-1}}} \quad (3)$$

The exit diameter of nozzle is related to the throat diameter and the product gases characteristics. It is given by equation (4):

$$D_e = D_{th} \sqrt{\frac{\left(\frac{2}{\kappa+1}\right)^{\frac{1}{\kappa-1}} \cdot \left(\frac{P_0}{P_a}\right)^{\frac{1}{\kappa}}}{\sqrt{\frac{\kappa+1}{\kappa-1} \cdot \left[1 - \left(\frac{P_0}{P_a}\right)^{\frac{1-\kappa}{\kappa}}\right]}}} \quad (4)$$

Burning rate [16]:

$$r = a \cdot P^n \quad (5)$$

Burning rate at different initial propellant temperature:

$$r_{T_i} = r_{T_0} \cdot e^{\sigma(T_i - T_0)} \quad (6)$$

The pressure-time curve can be predicted solving the system of differential equations presented as follow:

$$\frac{d}{dt} P(t) = \frac{R \cdot T_0 \cdot A_b \cdot (t) \cdot r(t) \cdot \rho}{V_0(t)} - \frac{A_b}{V_0(t)} \sqrt{\kappa \cdot R \cdot T_0 \left( \frac{2}{\kappa + 1} \right)^{\frac{\kappa + 1}{\kappa - 1}}} \cdot P(t) - \frac{A_b \cdot (t) \cdot r(t) \cdot P(t)}{V_0(t)} \quad (7)$$

$$\frac{d}{dt} x(t) = r(t)$$

Combustion chamber free volume

$$V_0(t) = V_0(0) + \int_0^t A_b(t) \cdot r(t) dt \quad (8)$$

The thrust is defined as the product of the chamber pressure, the thrust coefficient and the throat area [16]:

$$F = C_F \cdot P \cdot A_{th} \quad (9)$$

The throat area is given by:

$$A_{th} = \frac{\pi \cdot D_{th}^2}{4} \quad (10)$$

### 3.3. Propellant grain configuration

The multi-tubes configuration of the propellant used in the thruster is described in Figure 4.

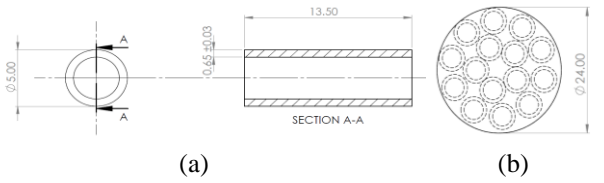


**Figure 4.** (a) Unit tubular propellant geometry,  
(b) propellant configuration

The burning surface area for an ideal propellant unit tube is done by equation (10):

$$A_b(x) = 15 \cdot \left[ 2 \cdot \frac{\pi}{4} \left[ (D - 2x)^2 - (d + 2x)^2 \right] + \pi(L - 2x) \cdot (D + d) \right] \quad (11)$$

The solid propellant is formed into the desired shape by extruding. The non-coaxiality tolerance of the extrusion machine is measured and equal to 0.1 mm. This inaccuracy in propellant manufacturing has an effect on the burning surface area so on the rocket motor's performances.

**Table 3.** Motor performances

Characteristics	Value	Unit
Mass of propellant	0.003	[Kg]
Mass flow	0.3	[Kg/s]
Mass flow coefficient	0.00071425	[/]
Thrust coefficient	1.45	[/]

Figure 5 presents the graphs of variations of the burning surface area as function of web distance for a grain of 15 ideal tubes and for a grain of 15 tubes with a non-coaxiality of 0.1mm.

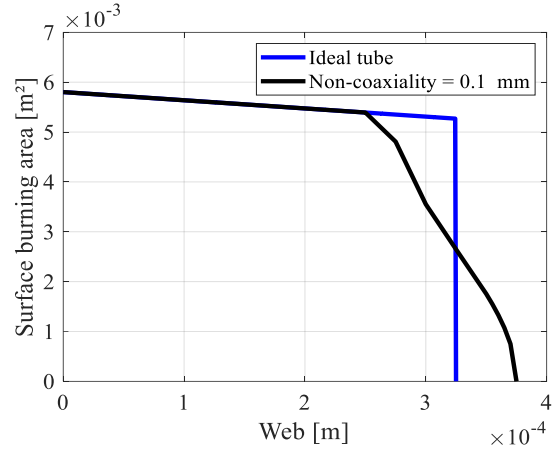


**Figure 5.** Total burning surface area versus web distance

### 3.4. Burning rate

**Table 4.** Burning rate  $r$  [mm/s] as a function of pressure  $P$  [bar] at different propellant initial temperatures  $T$  [°C]

	-30° C	20° C	50° C
Ambient pressure	22.2	23.9	26.1
50 bars	26.4	28.8	30.3
100 bars	27	29.5	31.3
150 bars	28	30	31.7
200 bars	28.5	30.7	32.2
250 bars	28.6	31.1	32.9
300 bars	28.7	31.5	33.5
350 bars	28.8	32.1	34
400 bars	29	32.5	34.3
450 bars	29.3	33	34.5
500 bars	29.5	33.5	34.9

In order to determine the variation of burning rate as a function of pressure, experiments were conducted on the solid propellant at various working pressures and initial propellant temperatures. The scatter plot obtained presented in Table 3. is fitted using regression to establish a mathematical relationship between the burning rate ( $r$ ), working pressure ( $P$ ), and the adjusted coefficients ( $a$  and  $n$ ) of the Saint-Robert and Vieille equation (5), defined as follows:

$$r_{20} = 23.684 \cdot P^{0.05} \quad (12)$$

Using equation (6) and data from table 4.

$$r_{T_i} = r_{20} \cdot e^{\sigma(T_i - 20)} \quad (13)$$

Where  $\sigma$  is the temperature sensitivity of the propellant and it is equal to 0.00175/°C.

Figure 6. presents the comparison between the predicted curves of the chamber pressure in time at different initial propellant temperatures at  $T = -30^\circ\text{C}$ ,  $20^\circ\text{C}$  and  $50^\circ\text{C}$ .

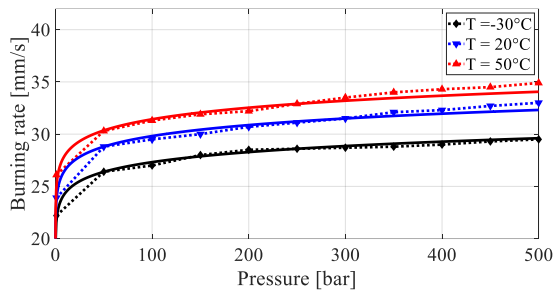


**Figure 6.** Burning rate at different initial propellant temperatures

For the same motor with the same propellant grain under different initial temperatures, from figure 6, there is a difference in the pressure curves. We notice that this initial propellant temperature has an effect on burning time and chamber pressure such that, the higher the initial propellant temperature, the higher-pressure chamber and lower is burning time and vice versa.

#### 4. RESULTS AND DISCUSSION

Simulation allowed to predict the pressure-time curve for different initial propellant temperatures, results are shown in Figure 7 and 8 for the two cases of grain state (ideal and imperfect).

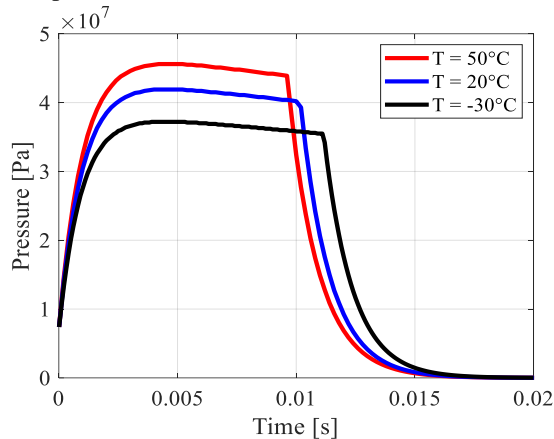


**Figure 7.** Predicted pressure vs. time at different temperatures for the ideal tubes.

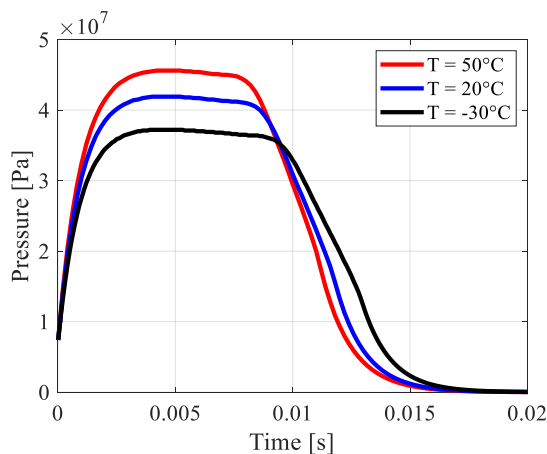


**Figure 8.** Predicted pressure vs. time at different temperatures for the imperfect tubes.

Comparison between the pressure vs. Time curves of simulations of the ideal and imperfect propellant allows to see the consequences of the manufacturing imperfections on performances of the thruster.

For the ideal propellant, the curves show an uniform profile of pressure, indicating an optimal combustion process, while the curves of the imperfect propellant grain present a deviation from the standard pressure-time profile, they exhibit longer burn duration, a quite higher peak of pressure but drop and decreases faster compared to the ideal propellant. The higher peak is caused by the rapid combustion due to the imperfections, these imperfections during combustion creates unburned fragments called *Sliver*. Slivers burn slower creating an additional burning time and this explain the longer burn duration of the imperfect propellant.

A thruster prototype is manufactured (Figure 9) and tested on the test bench described earlier in Figure 3.

The test was carried out at an initial propellant temperature of 20°C, Figure 10 presents the comparison between the analytic and the experimental curves of the chamber pressure in time.



**Figure 9.** The thruster prototype

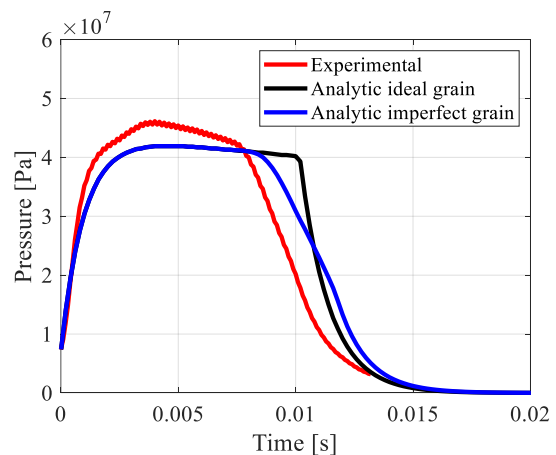


**Figure 10.** Predicted and experimental pressure curve versus time at 20°C

Data shows a good correspondence between the curves in terms of shape and values with a small error margins in values. The analytic curves show a constant work pressure of 418 bar, an effective working time of 10ms with an ideal propellant and 8ms with an imperfect propellant grain while the experimental curve shows higher quite constant pressure of 447 bar, it starts to decrease at  $t = 7.5\text{ms}$ .

Comparing the analytic curves with the experimental, the experimental curve is closer to the curve of the imperfect grain, this is due to the fact that the used propellant tubes presents some manufacturing imperfections (non-coaxial).

## 5. CONCLUSION

In this work, a lateral thruster is designed through internal ballistic calculations and rocket propulsion theory. A prototype model is manufactured and tested on a static test bench, in which the pressure-time variations is successfully measured. Results obtained by the analytic model and those obtained experimentally show a good agreement which demonstrates the reliability of the internal ballistic mathematical model of rocket motors.

The experimental approach showed that thrusters, as a rocket motor with a very short operating time, are very sensitive to many parameters which can influence their performances. From this, to design a thruster, many considerations must be carefully taken to reach the desired performances. Thrusters use a quick-burn propellant which is particularly the most sensitive parameter. Being susceptible to manufacturing imperfections, this can grossly affect the thruster performances.

## Nomenclature

### Latin symbols

$A_b$	-	Burning surface area, [m <sup>2</sup> ]
$A_{th}$	-	Nozzle throat area, [m <sup>2</sup> ]
$a$	-	Temperature constant, [-]
$C_d$	-	Mass flow coefficient, [-]
$C_F$	-	Thrust coefficient, [-]
$D$	-	Outer diameter of a unit propellant tube, [m]
$D_e$	-	Nozzle exit diameter, [m]
$d$	-	Inner diameter of a unit propellant tube, [m]
$F$	-	Thrust force, [N]
$I_{sp}$	-	Specific impulse, [ N.s/Kg ]
$I_{tot}$	-	Total impulse, [ N.s ]
$L$	-	Length of a unit propellant tube, [m]
$m$	-	Propellant mass, [Kg]
$\dot{m}$	-	Mass flow, [Kg/s]
$n$	-	pressure exponent, [-]
$P$	-	Chamber pressure, [Pa]
$P_a$	-	Atmospheric pressure, [Pa]
$R$	-	Gas constant, [J/(K.mol.K)]
$r$	-	Burning rate, [m/s]
$r_{T_i}$	-	Burning rate at $T_i$ , [m/s]
$T$	-	Propellant initial temperature, [K]
$T_0$	-	Temperature of combustion, [K]
$t$	-	Time, [s]

$t_e$	-	Thruster effective working time, [s]
$V_0$	-	Free volume in the combustion chamber, [m <sup>3</sup> ]
$x$	-	Web, [m]

### Greek symbols

$\kappa$	-	Specific heat ratio, [-]
$\rho$	-	Density, [Kg/m <sup>3</sup> ]
$\sigma$	-	Temperature sensitivity, [K <sup>-1</sup> ]

## Acknowledgements

This work was by Serbian Ministry of Defense and Serbian Ministry of Education, Science and Technological Development, Grant No 451-03-66/2024-03/200325.

## References

- [1] S. Mitzer and J. Oliemans , "Oryx," [Online]. Available: <https://www.oryxspioenkop.com/2021/05/novel-capabilities-ukraines-vilkha-mrl.html?m=1>. [Accessed 20 02 2024].
- [2] "Wikimedia," [Online]. Available: [https://upload.wikimedia.org/wikipedia/commons/5/58/JASDF\\_MIM-104\\_Patriot\\_PAC-3\\_Missile%28dummy\\_model%29\\_side\\_thruster\\_at\\_Hamamatsu\\_Air\\_Base\\_October\\_20%2C\\_2019.jpg](https://upload.wikimedia.org/wikipedia/commons/5/58/JASDF_MIM-104_Patriot_PAC-3_Missile%28dummy_model%29_side_thruster_at_Hamamatsu_Air_Base_October_20%2C_2019.jpg) [Accessed 27 06 2024].
- [3] Gupta, S.K., Saxena, S., Singhal, A. and Ghosh, A.K., «Trajectory Correction Flight Control System using Pulsejet on an Artillery Rocket,» *Defence Science Journal*, vol. 58 (1), pp. 15-33, 2008.
- [4] T. Jitraphai and M. Costello, «Dispersion Reduction of a Direct-Fire Rocket Using Lateral Pulse Jets,» *Journal of Spacecraft and Rockets*, vol. 38 (6), pp. 929-936, April 2001.
- [5] R. Głęboki and M. Jacewicz , «Sensitivity Analysis and Flight Tests Results for a Vertical Cold Launch Missile System,» *Aerospace*, vol. 7(12):168, 2020.
- [6] S. Živković, «Naučnotehničke informacije», Vol. LII, Br.4, Beograd, 2015.
- [7] D. Kumar et al., «Design and Structural Analysis of Solid Rocket Motor Casing Hardware used in Aerospace Applications,» *Journal of Aeronautics & Aerospace Engineering*, vol. 5(2), 2016.
- [8] Md Akhtar khan, B.K chaitanya and Eshwar Reddy cholleti, «Conceptual Design and Structural Analysis of Solid Rocket Motor Casing,» *International Journal of Computational Engineering Research (IJCER)*, vol. 7 (2), pp. 23-28, 2017.
- [9] Zhu, L.; Wang, J.; Shen, W.; Chen, L.; Zhu, «Design and Analysis of Solid Rocket Composite Motor Case Connector Using Finite Element Method,» *Polymers*, vol. 14(13), 2022.
- [10] M. ALAZEEZI, Nikola P. POPOVIĆ and Predrag M. ELEK, "Two-Component Propellant Grain For Rocket Motor Combustion Analysis And Geometric

- Optimization," *Thermal Science*, vol. 26 (2B), pp. 1567-1578, 2022.
- [11] Hainline, Roger, "Design Optimization Of Solid Rocket Motor Grains For Internal Ballistic Performance," University of Central Florida, Orlando, Florida, 2006.
- [12] S. Veerendra Prasad, Dr. B. V. R. Ravi Kumar and Dr. V. V. Subba Rao, "Static Testing Of Solid Fuel Rocket Engine," *Journal of Engineering Sciences*, vol. 11(2), pp. 863-866, Feb 2020.
- [13] F. Augusto, C. Fernandes, C. d'Andrade Souto and R. Pirk, "Static Firing Tests of Solid Propellant Rocket Motors: Uncertainty Levels of Thrust Measurements," *J. Aerosp. Technol. Manag*, 2022.
- [14] Yuan, Chung-I, «An interactive computer code for preliminary design of solid propellant rocket motors,» Monterey, California, 1987.
- [15] R. A. Nakka, Solid Propellant Rocket Motor Design and Testing, Department of Mechanical Engineering - The Faculty of Engineering - The University of Manitoba, 1984.
- [16] D. Mishra, «Fundamentals of Rocket Propulsion,» Taylor & Francis Group, 2017



# NUMERICAL INVESTIGATION OF THICKNES, ASPECT AND TAPER RATIO INFLUENCE ON DIVERGENCE VELOCITIES OF COMPOSITE PLATES AT SUBSONIC MACH NUMBERS

ALEKSA MALJEVIĆ<sup>1,2</sup>

<sup>1</sup>Vlatacom Institute of High Technologies, Belgrade, [aleksa.maljevic@vlatacom.com](mailto:aleksa.maljevic@vlatacom.com)

<sup>2</sup>University of Belgrade, Faculty of Mechanical Engineering, Belgrade, [d10-2023@studenti.mas.bg.ac.rs](mailto:d10-2023@studenti.mas.bg.ac.rs)

MIRKO DINULOVIĆ<sup>2</sup>

<sup>2</sup>University of Belgrade, Faculty of Mechanical Engineering, Belgradelatacom Institute, Belgrade, [mdinulovic@mas.bg.ac.rs](mailto:mdinulovic@mas.bg.ac.rs)

NEMANJA DEURA<sup>1</sup>

<sup>1</sup>Vlatacom Institute of High Technologies, Belgrade, [nemanja.deura@vlatacom.com](mailto:nemanja.deura@vlatacom.com)

**Abstract:** Within the scope of this research, the influence of different geometrical parameters on static aeroelastic instability of thin composite plates is analyzed. Design of the composite plate's geometry is aligned with design of modern subsonic missiles fins. Orthotropic material model is based on the classical laminate theory, mechanical properties of unidirectional laminae are calculated with composite micromechanics theories and laminates design is based on Tsai and Han quasi-isotropic composite lay-ups. Divergence velocities, the crucial static aeroelastic effect, are calculated numerically using commercial finite element method software. Calculation method is based on coupling subsonic aerodynamics models with structural models, and divergence effect on static stability loss is analyzed.

**Keywords:** Divergence, Composites, QI Laminates, Static stability loss.

## 1. INTRODUCTION

Since the early days of flying, the aircraft loss of structural stability has been imposed as primary design variable for achieving a safe flight. Starting with the initial design, aircraft's structure is tailored to optimally meet all necessary structural requirements within the flight envelope. Therefore, designers must enough accurately predict a wide scope of effects that arise from flexible airframe structure and aerodynamics load's coupling, at the early stages of design.

In this paper, the dependency of divergence velocity of thin composite plates of low speed flight vehicles on plates geometrical parameters in investigated. Torsional divergence is the most representative static aeroelastic effects that has crushing effect on airframe static structural stability. Airframe components are light and flexible, and therefore they are keen to both static and dynamic instability. During the flight, lifting surfaces deform in such way that leads them to entirely new, deformed shape which has completely new aerodynamic load. Lifting surfaces are being twisted around it's elastic axes, and therefore they "see" higher angle of attack that produces larger twisting moment. If the aerodynamic loads generated on the deformed surfaces are higher than airframe torsional stiffness, lifting surfaces are twisted of the flight vehicles, which usually leads to structural failure. Therefore, with the aim of achieving a safe and

designed flight trajectory, divergence velocity must be sufficiently higher than the aircraft operational speeds, at all time and under all flight conditions, within the flight envelope.

Investigated plates are designed accordingly to modern subsonic ASM and AGM missile control surfaces [1]. Divergence velocities and plates inertial characteristics are obtained with usage of analytical and numerical methods. Plates are designed from composite material *E-GLASS / Epoxy 3501 - 6*, in accordance with modern trend and overwhelmed application of composites in aerospace industry [2]. Material and lay-up designs are conducted within CLT theory and with respect to the well-known aerospace composite guidelines [3].

## 2. ANALYSIS MODEL

### 2.1. Theoretical model

Analytical model for evaluation of the torsional divergence of lifting surfaces is derived from the commonly used method – *Typical section* method [4], in the early design stages. For the typical section shown in Figure 1, steady state, aerodynamic loads are expressed as:

$$R_z = \frac{1}{2} \rho q \frac{dc_z}{d\alpha} \alpha_a l \quad M_{ac} = \frac{1}{2} \rho q C_{mac} c l \quad (1)$$

Typical section is twisted around its elastic axis, which is shown in Figure 2, and twisting moment is generated due to the aerodynamic loads:

$$M_t = M_{ac} + R_z \cdot (el) \quad (2)$$

Following the Saint-Venant's theory of pure twisting of beams, the twisting moment of typical section can be, in the domain of small and linear deformations as a function of its torsional stiffness:

$$M_t = C_{\theta\theta} \theta \quad (3)$$

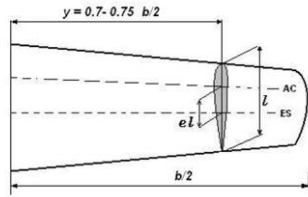


Figure 1. Lifting surface typical section.

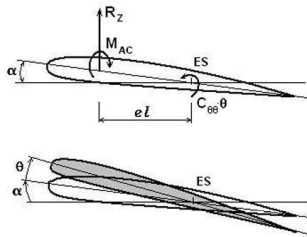


Figure 2. Deformation of typical section.

Since the lifting surface is flexible and it deforms upwards for the value of angle of twist  $\theta$ , the characteristic section is then exposed to new angle of attack  $(\alpha_a + \theta)$  and new aerodynamic loads. Therefore, based on this theoretical approach, and since the airframe torsional stiffness is independent of flight conditions, airframe will become neutrally stable at critical, divergence speed:

$$V_D = \sqrt{\frac{2C_{\theta\theta}}{\rho \frac{dC_z}{dx} S eI}} \quad (4)$$

In the above equation, it can be seen that divergence speed has proportional dependency to the torsional stiffness (airframe inertial characteristics) and disproportionately to the aerodynamic loads. Within this paper, lifting surfaces are thin, flat plates, for which the lift gradient is known as  $dC_z/d\alpha = 2\pi/rad$ . In order to evaluate divergence speed, structure's inertial characteristics are examined.

As mentioned in the above text, for the linearly elastic structure, torsional stiffness can be expressed analytically in terms of its inertial characteristics which is described in :

$$C_{\theta\theta} = GJ \quad (5)$$

In the above equation,  $G$  represents influence of material

design and  $J$  represents influence of structure's geometry design on the overall structure torsional stiffness. Within this research, in-plane shear modulus of QI laminates with long fibers is calculated following the conducted researches [6], [7]:

$$G_{xy} = \frac{1}{2} G_{12} + \frac{1}{8} \frac{E_1(E_1 + E_2 - 2\nu_{12}E_2)}{E_1 - 2\nu_{12}^2 E_2} \quad (6)$$

Individual laminae mechanical characteristics  $E_1$ ,  $E_2$ ,  $G_{12}$  and  $\nu_{12}$  are evaluated with composite micromechanics theory [8], for known mechanical characteristics of individual phases in aerospace composite *E-GLASS / Epoxy 3501 - 6* and fiber volume fraction  $V_f = 0.55$ . Afterwards, with the usage of identical analogy, material strength characteristics are calculated and shown in Table 1.

Table 1. Designed lamina mechanical properties.

E-Glass / Epoxy 3501 - 6; $V_f = 0.55$	
$E_1$ [GPa]	42.1
$E_2$ [GPa]	14.2
$G_{12}$ [GPa]	5.37
$\nu_{12}$ [ ]	0.284
$\rho$ [g/cm <sup>3</sup> ]	2.0015
$F_{1t}$ [MPa]	1100
$F_{2t}$ [MPa]	50
$F_{1c}$ [MPa]	520
$F_{2c}$ [MPa]	140
$F_6$ [MPa]	100

Finally, inertial characteristic of typical section  $J$  is derived from the closed form Prantl's torsional equation and it is simplified for the case of thin plate ( $a \gg b$ ) under pure shear loads [9], its valid approximation is as follows:

$$J \approx a^3 b \left( 0.333 - 0.21 \frac{b}{a} \left( 1 - \frac{1}{12} \left( \frac{b}{a} \right)^4 \right) \right) \quad (7)$$

## 2.2. Geometry and lay-up model

Design variables, thickness ( $t$ ), aspect ratio (AR) and taper ratio (TR) are varied in such way, that the plate geometry could always represent subsonic missile fins – presented in Figure 3, while the planform plate surface was maintained constant at  $S = 0.15 \text{ m}^2$ . Plate geometry is obtained with following equations:

$$C_r = \sqrt{\frac{4S}{AR(1+TR)^2}}$$

$$C_t = TR \cdot C_r \quad (8)$$

$$H = AR \frac{C_r}{2} (1 + TR)$$

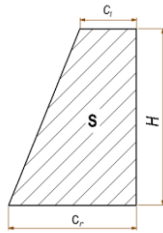


Figure 3. Fin planform geometry.

For the lay-up model, one of the most popular QI lay-up's in aerospace was used:  $[0^\circ, 45^\circ, -45^\circ, 90^\circ]_s$ . Designed geometries for this research are presented in the Table 2.

Table 2. Designed fin's planform geometries.

No.	t [mm]	AR [/]	TR [/]	C <sub>r</sub> [mm]	C <sub>l</sub> [mm]	H [mm]
1	0.5	0.4	2	391	156	548
2	1	0.4	2	391	156	548
3	1.5	0.4	2	391	156	548
4	2	0.4	2	391	156	548
5	1	0.2	2	456	91	548
6	1	0.6	2	342	205	548
7	1	0.8	2	304	243	548
8	1	1	2	274	274	548
9	1	0.4	0.5	782	313	274
10	1	0.4	1	553	221	387
11	1	0.4	1.5	452	181	474
12	1	0.4	2.5	350	140	612
13	1	0.4	3	128	128	671

### 2.3. Numerical model

The modern approach to structural stability loss predictions of airframe is to couple numerics and finite element methods. Within this research, commercial software *Nastran* was used to evaluate the divergence speed and verify theoretical methods. Based on the numerical simulations, two different methods are used for calculation. For both cases, plates were clamped at the root, which simulates fin-body connection. This approach, beside divergence velocity, also renders informations about structure stress-strain field.

First numerical model was based on experimental test and guidelines based on suggested literature for static aeroelastic experimental testing [10] and it is illustrative presented in Figure 4. Based on the equation (3) and in the field of small and linear deformations, twisting moment is applied at the wing tip and deformations

(twisting angle) are measured. For the known deformations and applied twisting load, lifting surface torsional stiffness is recalculated, and afterwards, divergence velocity is calculated on the basis of equation (9). Small and linear deformations are calculated as a function of leading and trailing edge displacements:

$$\theta = \frac{\Delta_{LE} + \Delta_{TE}}{l_{section}} \quad (9)$$

Second numerical model represents more realistic simulation of in-flight conditions with generation of three-dimensional aerodynamic loads, which is shown in Figures 5 and 6. Structural model is coupled with aerodynamic model with the usage of infinite plate splines, that transfer displacements and rotation between two models [11]. Steady aerodynamic model is based on VLM method for subsonic speeds [12] and it consists of large number of small aeropanel, that simulates potential flow for the given flight conditions. Divergence speed is adopted as the flight speed that generates such steady aerodynamic loads that leads to static failure of the structure.

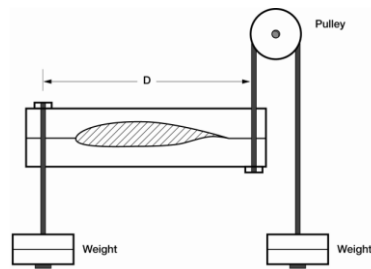


Figure 4. Simulated experimental test [10].

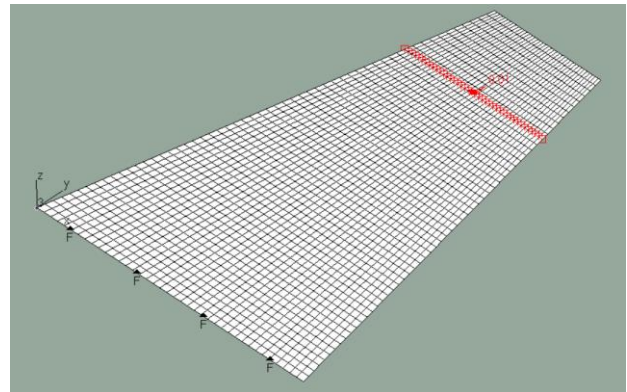


Figure 5. First numerical model setup.



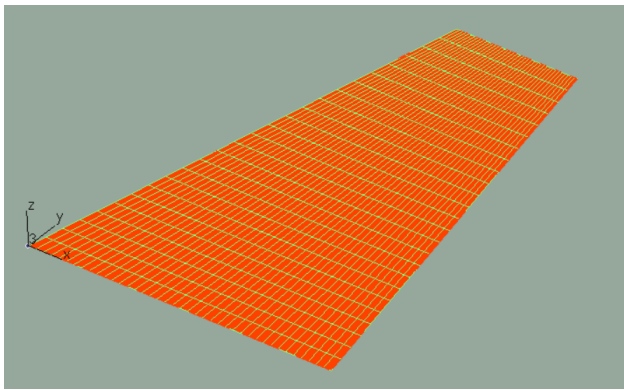


Figure 6. Aerodynamic model.

### 3. RESULTS AND DISCUSSION

Analytical approach is verified with numerical models, although the analytical approach overestimates the loss of static stability, because it doesn't take into consideration the structure stress – strain field and doesn't sufficiently enough capture the AR and TR influence on static instability. Therefore, it is appropriate to use the analytical approach at the early design stages in order to obtain an understanding of the order of magnitude of the static instability. The typical deformed shape of missile fin due to twisting is given in Figure 7.

The design variable of paramount importance for structure static stability is its thickness, because it directly and mostly influence the structures inertial characteristics. The influences of AR and TR are drastically lower, and the theoretical method isn't suitable for its prediction. Coupled influence of two or more design variables could be analyzed in the future work. Figure 8 shows the formed dependencies of the divergence speed on the plate thickness, obtained with theoretical and numerical approach.

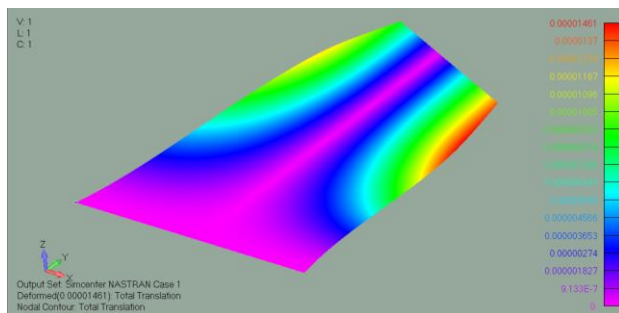


Figure 7. Deformed model, experimental testing simulated with numerics.

Table 3. Divergence velocities obtained theoretically.

Plate No. [/]	Divergence velocity [m/s]
1	4.05
2	11.44
3	21.00
4	32.30
5	11.42
6	11.44
7	11.45
8	11.45
9	11.45
10	11.44
11	11.44
12	11.44
13	11.43

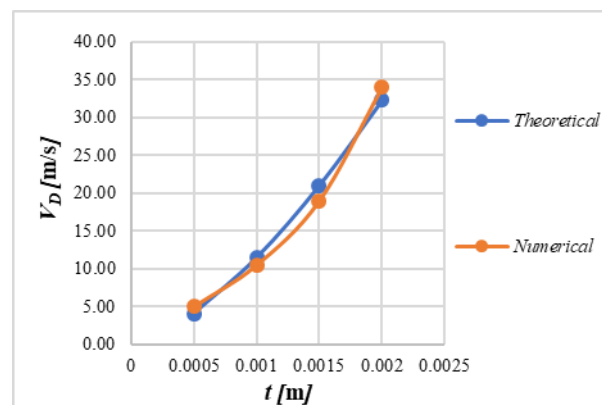


Figure 8. Dependence of divergence speed on plate thickness.

### 4. CONCLUSION AND FURTHER WORK

Within the content of this research, the influence of geometrical parameters on low speed missile fins static instability is analyzed. Results are obtained with theoretical method and afterwards verified with two different numerical methods. It was found out that designers could use either theoretical or experimental method simulated with FEM, in the early design stages, because they are fast, not expensive, and they render enough accurate preliminary results. Difference between theoretical and first numerical method is within 20% which is suitable in the preliminary design stage. In the detailed design phase, it is strongly suggested to use such numerical models that couple structural and aerodynamic effects. In the further work, aerodynamic modeling (panel AR) on the static instability will be investigated.

**Table 4.** Theoretical model verification.

Plate No. [/]	Model	Divergence velocity [m/s]
3	Analytical	21.0
	Experimental setup	19.2
	SOL 144	10.3
4	Analytical	32.3
	Experimental setup	29.2
	SOL 144	14.5

In the following research, complex and detailed theoretical methods will be used in order to predict the static and dynamic plates instability and further database of parameters that influence aeroelastic effects will be built that will be used to predict the aeroelastic instability with Machine Learning.

**References**

[1] T.Milligan: Peak of Flight, Issue 442, 2017. Available on:<https://apogeerockets.com/education/downloads/Newsletter442.pdf>  
 [2] A.Quilter: Composites in Aerospace Applications – White paper, IHS ESDU, USA

[3] NASA, Design and manufacturing guidelines for aerospace composites, No.GD-ED-220, Marshall Space Flight Center, USA, 1999.  
 [4] Y C, Fung.: An Introduction to the Theory of Aeroelasticity, Dover Books on Aeronautical Engineering, 1955.  
 [5] S.Timoschenko, J.N.Goodier: Theory of Elasticity, McGraw-Hill, Third Ed., Toronto, USA, 1970.  
 [6] Akkerman, R.: On the properties of quasi-isotropic laminates, Composites: Part B, Vol. 33 (2002) pp. 133-40  
 [7] Tsai SW, Hahn HT.: Introduction to composite materials. Lancaster: Technomic, 1980  
 [8]J.Aboudi, S.Arnold, B.Bednarczyk, Practical Micromechanics of Composite Materials, Butterworth – Heinemann, First Ed., 2021. ISBN: 978-0128206379.  
 [9] W.C.Young, R.G.Budynas: Roark’s formulas for stress and strain, McGraw-Hill, Eight Ed, Toronto, USA, 2021. ISBN: 978-0071742474.  
 [10] John K. Ramsey.: NASA Aeroelasticity Handbook Volume 2: Design Guides, NASA/TP—2006-212490/VOL2/PART2, 2006.  
 [11] Rodden, William P., and Johnson, Erwin H.: MSC/NASTRAN Aeroelastic Analysis User’s Guide, V68, The MacNeal-SchwendlerCorporation, 1994.  
 [12] NASA, Vortex-lattice utilization. NASA SP-405, NASA-Langley, Washington, 1976.



## EVALUATION OF THE INFLUENCE OF POWER SETTING ON AIRCRAFT PERFORMANCE IN A SPIN

JELENA ŠOBOT

Technical Test Centre, Belgrade, [jsobot@outlook.com](mailto:jsobot@outlook.com)

ĐORĐE JANKULOSKI

Technical Test Centre, Belgrade, [jankuloskidj@gmail.com](mailto:jankuloskidj@gmail.com)

MIŠA ŽIVKOVIĆ

Technical Test Centre, Belgrade, [misazivkovic89@gmail.com](mailto:misazivkovic89@gmail.com)

JASMINKA JELISAVAC

Technical Test Centre, Belgrade, [jjelisavac@gmail.com](mailto:jjelisavac@gmail.com)

IVAN VESIĆ

Technical Test Centre, Belgrade, [ivesic01@gmail.com](mailto:ivesic01@gmail.com)

**Abstract:** Aircraft spin is a critical flight regime that is strictly prohibited for the majority of airplanes. However, due to its critical nature, it is mandatory in military aerospace to carefully test and analyze different spin scenarios and observe all spin characteristics. This paper presents an analysis of the influence of varying power and thrust on aircraft performance during spin and spin recovery. The behavior of the aircraft was observed and analyzed during flight tests of a light airplane in a clear configuration with two different c.g. positions. Due to the gyroscopic effects of the propeller, the influence of power differs between left and right spins, necessitating tests for both spin directions in each configuration. The results reveal significant differences in spin dynamics based on power settings, highlighting the role of propeller-induced forces. Spins entered with full throttle exhibited more pronounced entry characteristics and pre-spin roll compared to spins entered at idle. Left spins were found to be less oscillatory and had a lower pitch angle, while right spins were more oscillatory and steeper. The data obtained provides valuable insights into spin dynamics, contributing to improved pilot training, flight safety protocols and aircraft design considerations related to spin performance. The findings from these tests are crucial for enhancing spin awareness and serve as a guide for both engineers and pilots.

**Keywords:** aircraft, flight test, power, spin recovery.

### 1. INTRODUCTION

Aircraft spin is a critical flight regime that is strictly prohibited for the majority of airplanes. After stalled aircraft begins autorotating in a helical path around its vertical axis we say it has entered spin. The spinning rotation can include variations in pitch, roll and yaw. The spin reaches its fully developed state when its path becomes vertical and its characteristics consistently repeat from one rotation to the next. [1] Some airplanes can continue autorotation for multiple turns, repeating their movement at regular intervals without stabilization. However, most airplanes do not achieve a fully developed spin within just one turn. Spin flight testing in some general aviation, aerobatic airplanes, trainers and highly maneuverable fighter aircraft is crucial for several reasons. Firstly, understanding and examining the spin characteristics of an aircraft is vital for improving aircraft safety by helping developing effective recovery procedures and training pilots for minimizing the risk of

accidents. Secondly, all regulatory authorities require spin testing as part of certification process. Thirdly, spin testing results provide valuable input in improving aircraft design and performance as well as increasing safety and knowledge. Comprehending the impact of various factors, such as weight distribution, control inputs and power setting on spin behavior provide guidance for both engineers and pilots.

#### 1.1. Spin Awareness

Even though for majority of aircraft spin is forbidden procedure, for some aircraft flight testing in spin is mandated by regulations and certification processes. The FAA (Federal Aviation Administration) recognizes airman certification process (ACS) [2] which goal is to ensure the applicant possesses the knowledge and ability to manage risk and demonstrate the skills consistent with the privileges of a Commercial Pilot Certificate and any associated ratings being exercised, in order to act as pilot-in-command (PIC). One part of testing is to test various airplane configurations, including relationship between

AOA, airspeed, load factor, power setting, airplane weight and center of gravity (c.g.) etc.

## 2. FLIGHT TEST

### 2.1. Flight test aircraft

Aircraft used for flight testing is light military trainer airplane UTVA LASTA 95 Prototype 1 (Figure 1). Lasta 95 is a low-wing, metal constructed airplane with two seats powered by single piston engine propeller group. This aircraft's aerobatic capabilities renders it suitable for conducting various spin tests. The aircraft Lasta has been analyzed in many scientific papers such as: Flight testing methodology and procedure of spin characteristic on basic training aircraft [3], Analysis of the impact of aileron deflection on aircraft spin [4], Power optimization of a single propeller Airplane take-off run on the basis of lateral maneuver limitations, stability characteristics of the single-engine tractor propeller airplane in climb, etc.

For this specific flight test, due to the sensitivity of spin test procedure, aviation regulations and potentially hazardous activities airplane was equipped with antispin parachute as external spin recovery device (Figure 2). [5]



Figure 1. Airplane Lasta 95, Prototype 1

Antispin parachute and parachute deployment system has been tested on ground in order to safely determine its reliability and susceptibility to unintentional or undesired deployment.



Figure 2. Antispin parachute system on airplane Lasta 95

### 2.2. Flight test equipment

To guarantee the successful execution of flight spin tests, a credible configuration management system is crucial. This system must ensure accurate time synchronization and data recording, enabling easy searches for specific events and ability to replay sections of the recordings when needed. For data acquisition the next equipment is

used: acquisition system, recorder and multiple transducers. Acquisition system used is Airborne acquisition and transmission system ACRA KAM-500 9U (Figure 3) and recorder NET-500 (Figure 4). [4] [6]

ACRA acquisition system and its transducers possess ability to record numerous flight parameters based of measuring sensors installed in airplane, from which essential parameters for this evaluation are, beside velocity and altitude, deflections of all three primary controls ( $\delta_l$ ,  $\delta_m$ ,  $\delta_n$ ), angular rates of yaw, roll and pitch ( $r$ ,  $p$ ,  $q$ ) and yaw, roll and pitch angles ( $\psi$ ,  $\phi$ ,  $\theta$ ). These parameters were later used to determine airplane behavior in spin and calculate spin recovery delay.

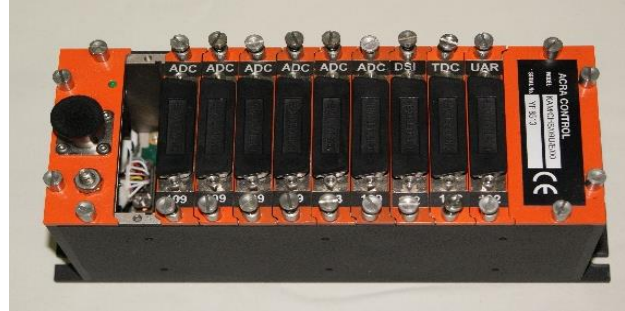


Figure 3. ACRA acquisition system KAM-500 9U



Figure 4. ACRA recorder NET-500

### 2.3. Flight test procedure

In order to achieve flight test conditions of evaluation of influence of power setting change on aircraft behavior during spin, two variants of c.g. positions have been tested:

- Single-seat with c.g. position of around 27%MAC (variant A).
- Twin-seat with c.g. position of around 31%MAC, with 50 kg weight used as balance in second pilot seat (variant B).

Flight test conditions were defined in two configurations for two variants of c.g., for both spin was entered from the altitude of 3000 m with different power setting:

- Spin entry with power reduced to idle and normal spin entry procedure. After two turns of the commanded spin, power was set to the maximum RPM.
- Spin entry with full engine power and normal spin entry procedure.

For both variants, after 4 spin turns power was reduced to idle, stopping of rotation and spin recovery were commanded via standard procedure, or stopping of rotation and spin recovery were commanded via standard procedure with full power setting. Due to the gyroscopic effects of the propeller, the influence of power differs between left and right spins, necessitating tests for both spin directions in each configuration.

### 3. RESULTS AND EVALUATION

Results obtained from flight test data during a spin show highly oscillatory motion in terms of angular velocity “p” (angular velocity around x-axis, roll), “q” (angular velocity around y-axis, pitch) and pitch angle “ $\theta$ ”.

It can be noted that angular velocity “p” (Figure 5) in right spin varies in interval between approximately 230°/s and approximately -50°/s in direction opposite to the commanded spin direction. In left spin (Figure 6), “p” varies in interval between approximately -140°/s and approximately -20°/s in direction opposite to the commanded spin direction.

During fully developed spin phase maximum value of angular velocity (pikes on diagram) is increased up to the fourth turn after which it changes slightly.

Angular velocity “q” in right spin varies in interval between approximately -50°/s and approximately 110°/s, and in left spin it varies between approximately -40°/s and approximately 80°/s. The maximum values of this speed occur after the second turn.

The change of pitch angle ( $\theta$ ) is oscillatory in accordance with the variation of angular pitch velocity. Value of pitch angle in right spin (Figure 7) varies from -20° to -80°, while in left spin (Figure 8) pitch angle varies from -25° to -50°. In both side of spins value changes synchronously with the angular velocity alteration around the “y” axis.

Left spins with full engine power display reduced oscillatory tendencies and show a lower pitch angle by absolute value (while angle of attack is higher).

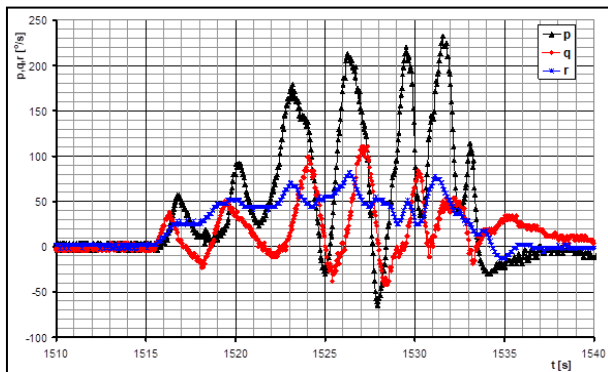


Figure 5. Angular velocities in right spin, full power

In order to effectively recover from the spin, the aircraft requires standard control inputs, which are full rudder deflection in the opposite direction and elevator deflection towards the approximately neutral position. If the elevator is controlled more aggressively, the aircraft exits the spin with a backward tumble.

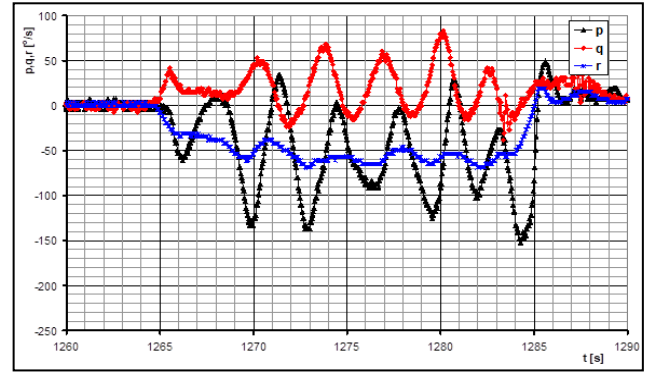


Figure 6. Angular velocities in left spin, full power

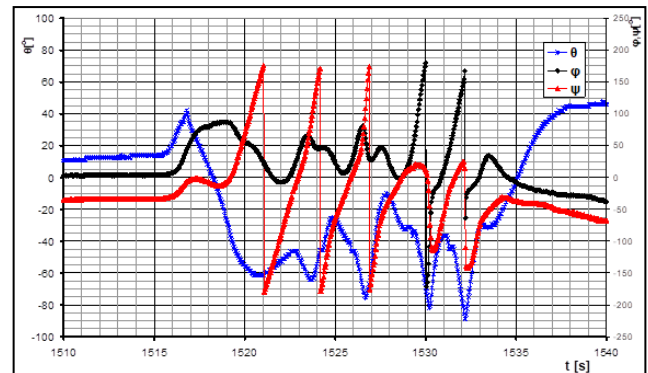


Figure 7. Angles of rotation in right spin, full power

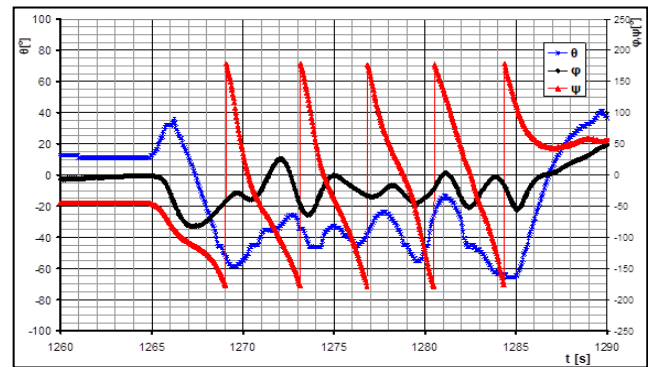


Figure 8. Angles of rotation in left spin, full power

In table 1. spin delay in both right and left spins for both c.g. variants and power setting is presented. As expected, B variant shows higher delay in turns. Rear c.g. position increases aircraft longitudinal stability, which with increased inertia reduces speed of control input change which is critical for spin recovery.

It is worth noting that the recovery delay is significantly shorter than the specifications outlined in the MIL-F-8785C aerospace technical regulations [7] (less than 1.5 turns).

Due to the higher angle of attack in left spins, the spin recovery delay is approximately  $\frac{1}{4}$  of a turn longer compared to right turns, but still less than allowable limit of 1.5 turns.

**Table 1.** Spin recovery delay

Power setting	c.g. variant	R/L spin	$\varphi$ [turns]	$\Delta\varphi$ [turns]	$\Delta H$ [m]	nz
Power at idle	A	L	4	0.66	140	3.4
Power at idle	B	L	4.6	0.7	150	4.6
Full power	A	L	4	0.43	140	3.5
Full power	B	L	4.4	0.6	170	4
Power at idle	A	R	4.4	0.45	160	3.5
Power at idle	B	R	4.6	0.35	135	3.6
Full power	A	R	4.2	0.3	180	3.5
Full power	B	R	3.9	0.3	100	4.2

#### 4. CONCLUSION

An experimental flight test was conducted in order to evaluate the influence of power setting on aircraft performance in spin. The results obtained from flight test data during a spin show that the airplane exhibits very similar behavior in all phases of the spin for both test variants. The only notable difference is that, in both left and right spins, when airplane enters spin with full engine power from a climb, airplane performs a pre-spin roll which is significantly slower than the pre-spin roll entered with power at idle.

Two different c.g. positions were tested and presented. Rearward position of c.g. resulted in a longer spin recovery delay because of reduced longitudinal stability, reduced efficacy of controls, higher inertia and less effective aerodynamic forces needed for spin recovery maneuvers compared to forward c.g. position.

The main characteristic of airplane performance in spin

with the influence of power setting lies in discrepancy between left and right spins. Left spin is significantly less oscillatory and has shallower descent angle compared to the right spin.

In left spins, the power setting (as a result trust) slightly increases airplane's angle of attack and decreases oscillatory behavior in spin. In right spins, the trust does not significantly affect the airplane's behavior.

Regardless of variant of power setting the airplane can be effectively recovered from the spin using standard control inputs, with delays in spin recovery well within the allowable limit of 1.5 turns. This study emphasizes the impact of power setting on airplane behavior in spin, highlighting distinctions between left and right spins, forward and rearward c.g. influence while confirming airplane's capability of effective spin recovery in tested cases.

#### References

- [1] Hurt, H., H., *Aerodynamics For Naval Aviators*, University of Southern California, 1965.
- [2] Airman Certification Standards, Federal Aviation Administration, Retrived May 17, 2024. from [https://www.faa.gov/training\\_testing/testing/acs](https://www.faa.gov/training_testing/testing/acs)
- [3] Pekmezović S., Jovanović M., Ilić Z.: *Flight Testing Methodology and Procedure of Spin Characteristic on Basic Training Aircraft*, Proceedings, 4<sup>th</sup> International Scientific Conference on Defensive Technologies OTEH 2011, 2011, pg (128-132)
- [4] ŠOBOT, J., JOVANOVIĆ, M.: *Analysis of the Impact of Aileron Deflection on Aircraft Spin*, Proceedings, The 7th International Congress of Serbian Society of Mechanics, 2019, pg (122-123)
- [5] EASA, *Flight Test Operations Manual Guide*, Initial Issue, 2018.
- [6] Curtiss-Wright Defense Solutions. (n.d.). KAM/CHS/09U Acra KAM-500 chassis - 9 user-slots. Retrieved June 16, 2024 from <https://www.curtisswrightds.com/products/flight-test/data-cquisition/acrakam500/kamchs09u.html>.
- [7] MIL-F-8785C, Military Specification Flying Qualities of Piloted Airplanes. 1980.

## EXPERIMENTAL RESULTS FROM THE MISSILE MODEL TEST CAMPAIGN IN THE VTI T-38 WIND TUNNEL

MARIJA SAMARDŽIĆ

Military Technical Institute, Belgrade, [marija.samardzic.vti@gmail.com](mailto:marija.samardzic.vti@gmail.com)

NATAŠA VUJIĆ

Military Technical Institute, Belgrade, [vujic.natasa45@gmail.com](mailto:vujic.natasa45@gmail.com)

BILJANA ILIĆ

Military Technical Institute, Belgrade, [biljana.ilic@vti.vs.rs](mailto:biljana.ilic@vti.vs.rs)

GORAN OCOKOLJIĆ

Military Technical Institute, Belgrade, [goran.ocokoljic@vti.vs.rs](mailto:goran.ocokoljic@vti.vs.rs)

**Abstract:** Testing of the missile model in the VTI T-38 trisonic wind tunnel is presented. Tests were carried out at Mach number range from 0.3 to 2.0. In the subsonic speed range tests were done at different values of the stagnation pressure, while the missile model was tested at nineteen values of Mach number in the transonic speed range. Aerodynamic loads were measured using six-component internal wind tunnel balance. The measured values of normal force, drag force and pitching moment obtained under varying conditions in the wind tunnel test section are shown.

**Keywords:** wind tunnel, missile model, strain gauge balance

### 1. INTRODUCTION

This paper presents the initial part of the supersonic projectile model test campaign within the new research project of the Experimental Aerodynamic Department of the Military Technical Institute (VTI) in Belgrade. The main goal of the project is experimental investigation of the side jet interactions in control of a supersonic projectile. The supersonic projectile model was tested in the VTI T-38 trisonic wind tunnel [1,2]. Within the initial part of the testing, wind tunnel measurements were conducted on the model without side jet system and with six-component internal wind tunnel balance. In the wind tunnel tests without side jet system aerodynamic characteristics of the model in the range of Mach numbers from 0.5 to 2.0 are obtained. The measured aerodynamic loads will be compared with the results obtained in the main, final, part of the experiential investigation with side jet system operating and with five-component internal wind tunnel balance.

### 2. SUPERSONIC PROJECTILE MODEL

Supersonic projectile model is shown in Figure 1. The model has a cylindrical body, ogive nose and wing section with four wraparound wings.

This projectile model is characterized with large slenderness ratio, so that the ratio of the model length to the model base diameter is  $L/D=21.78$ . The reference point for force/moment calculation is located a distance  $10.83D$  upstream of the model base.



Figure 1. Supersonic projectile model

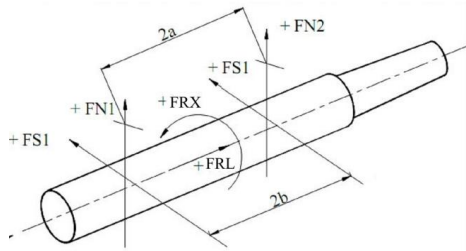
The projectile model mounted on the sting in the VTI T-38 wind tunnel test section is shown in Figure 2. Sting vs. model base diameter ratio was 0.75. The pressure in the cavity surrounding the sting at the model base (i.e. the base pressure) was measured by a single orifice at the end of a tube, which was routed through the sting to the sensor located in the model support.



Figure 2. Supersonic projectile model in the VTI T-38 test section

### 3. AERODYNAMIC LOAD MEASUREMENTS

Aerodynamic forces and moments acting on the model were measured by 2 inch ABLE internal six-component strain gauge balance. The six basic components of the balance consist of two normal force element (FN1 and FN2), two side force (FS1 and FS2), dual force element (FRX) and dual rolling moment element (FRL), Figure 3 [3-5]. Normal force (FRZ) and pitching moment (FRM) are determined from components FN1 and FN2, while side force (FRY) and yawing moment (FRN) are determined from FS1 and FS2.



a=0.092075 mm , b=0.0762 mm

Figure 3. Components of the 2 inch ABLE internal balance

The balance nominal operating load range and accuracy is shown in Table 1.

Table 1. Balance load ranges and accuracy

Component	FRX [N]	FRY [N]	FRZ [N]	FRL [Nm]	FRM [Nm]	FRN [Nm]
Load range	1800	8900	8900	170	820	680
Err. [N, Nm]	3.467	23.214	34.303	-0.406	0.887	1.114
P. Err. [%]	0.193	0.261	0.385	-0.239	0.108	0.164
Std.d. [%]	0.053	0.075	0.083	0.051	0.029	0.041

### 4. WIND TUNNEL MEASUREMENTS IN THE SUBSONIC SPEED RANGE

In the subsonic speed tests were done at different values of the stagnation pressure in the wind tunnel test section. Table 2-4 show the values of the stagnation pressure, dynamic pressure, as well as measured values of axial force, normal force and pitching moment. Results refer to Mach number 0.3 and 0.5 and angle of attack in the interval of -10° to +10°.

Table 2. Results for M=0.3 and FRX

FRX [N] M=0.3				
α [°]	RSN=1 p <sub>0</sub> =2.0 bar q=0.118 bar	RSN=2 p <sub>0</sub> =2.5 bar q=0.150 bar	RSN=3 p <sub>0</sub> =3.0 bar q=0.150 bar	RSN=4 p <sub>0</sub> =3.5 bar q=0.150 bar
-11.68	10.791	12.924	14.884	17.025
-10.06	10.810	13.006	14.980	17.251
-8.06	10.835	13.236	15.227	17.470
-6.05	10.788	13.301	15.278	17.596
-4.05	10.418	13.040	14.999	17.040
-2.05	10.331	12.907	14.865	16.773
-0.05	10.346	12.728	14.606	16.699
1.96	10.449	12.653	14.808	16.757
3.96	10.676	12.938	14.871	17.077

5.97	11.110	13.383	15.293	17.181
7.97	11.165	13.373	15.394	17.216
9.98	11.020	13.192	15.119	16.984
11.8	10.895	12.936	14.867	16.526

Table 3. Results for M=0.5 and FRZ

FRZ [N] M=0.5				
α [°]	RSN=6 p <sub>0</sub> =2.0 bar q=0.118 bar	RSN=7 p <sub>0</sub> =2.5 bar q=0.150 bar	RSN=8 p <sub>0</sub> =3.0 bar q=0.150 bar	RSN=14 p <sub>0</sub> =2.3 bar q=0.150 bar
-11.66	-213.055	-268.584	-325.821	-251.708
-10.03	-172.194	-218.170	-272.170	-208.920
-8.01	-129.528	-164.479	-200.762	-152.830
-6.00	-85.947	-113.568	-142.09	-107.152
-3.99	-52.088	-68.573	-89.635	-62.64
-1.99	-18.450	-27.569	-35.681	-23.783
-0.02	7.573	4.935	-3.645	7.161
2.04	32.092	36.223	40.523	36.490
4.04	67.164	76.640	88.012	75.112
6.05	104.277	124.559	143.695	115.907
8.06	144.380	171.249	201.282	160.155
10.07	188.047	224.675	262.211	210.739
11.92	231.416	282.919	323.930	261.015

Table 4. Results for M=0.5 and FRM

FRZ [N] M=0.3				
α [°]	RSN=6 p <sub>0</sub> =2.0 bar q=0.118 bar	RSN=7 p <sub>0</sub> =2.5 bar q=0.150 bar	RSN=8 p <sub>0</sub> =3.0 bar q=0.150 bar	RSN=14 p <sub>0</sub> =2.3 bar q=0.150 bar
-11.66	52.511	67.551	80.178	61.924
-10.03	43.485	54.551	69.471	53.603
-8.01	33.472	42.248	52.273	40.102
-6.00	22.183	29.391	37.718	28.547
-3.99	13.419	17.870	23.467	15.986
-1.99	3.469	5.830	7.910	4.791
-0.02	-2.687	-1.743	-1.108	-2.937
2.04	-8.170	-8.656	-9.185	-9.254
4.04	-18.260	-20.643	-22.654	-20.577
6.05	-28.245	-33.423	-38.087	-31.640
8.06	-38.716	-45.54	-53.305	-42.701
10.07	-48.460	-58.093	-66.861	-54.895
11.92	-57.990	-70.120	-80.597	-65.395

Nondimensional aerodynamic coefficients in the non-rotated axes system are calculated from the aerodynamic forces and moments according to the following equations:

$$C_A = \frac{FRX}{q \cdot S_{ref}}, C_N = \frac{FRZ}{q \cdot S_{ref}}, C_M = \frac{FRM}{q \cdot L_{ref} S_{ref}}$$

Compared graphs on Figures 4-9 show drag force coefficients, lift force coefficients and pitching moment coefficients in relation to the angle of attack for Mach number M=0.3 and M=0.5.

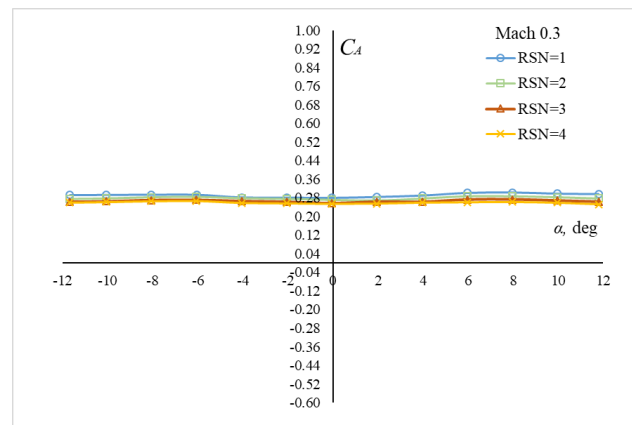


Figure 4. Drag force coefficient, M=0.3



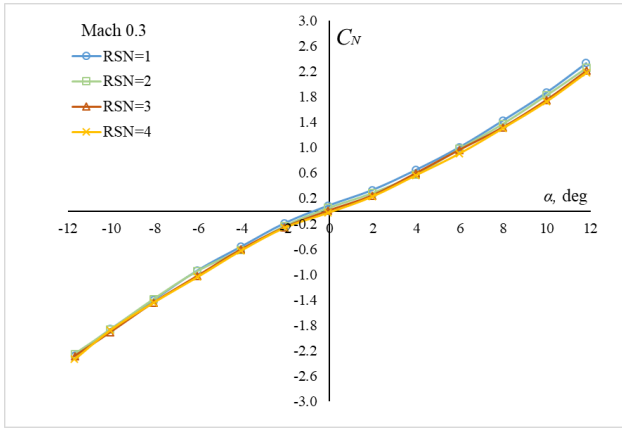


Figure 5. Normal force coefficient,  $M=0.3$

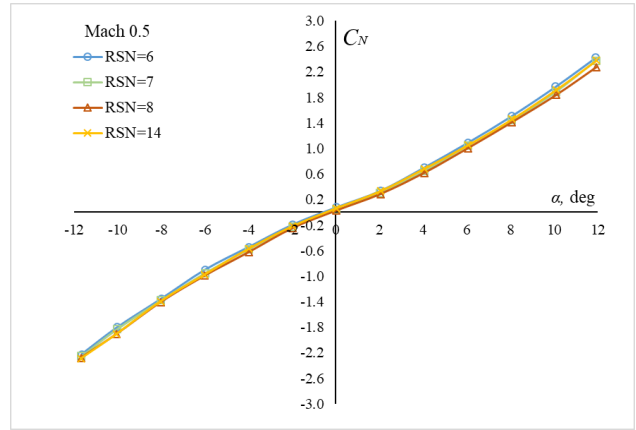


Figure 8. Normal force coefficient,  $M=0.5$

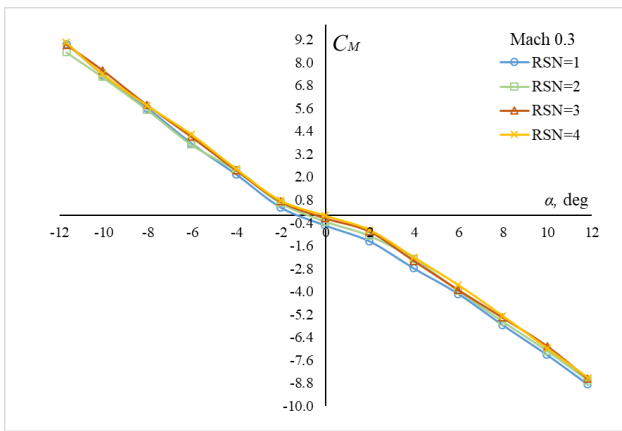


Figure 6. Pitching moment coefficient,  $M=0.3$

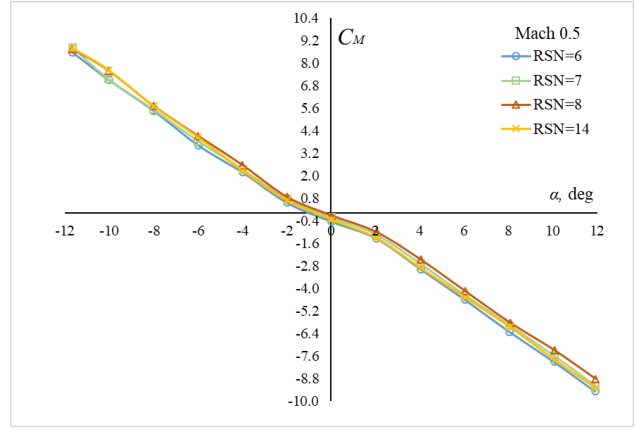


Figure 9. Pitching moment coefficient,  $M=0.5$

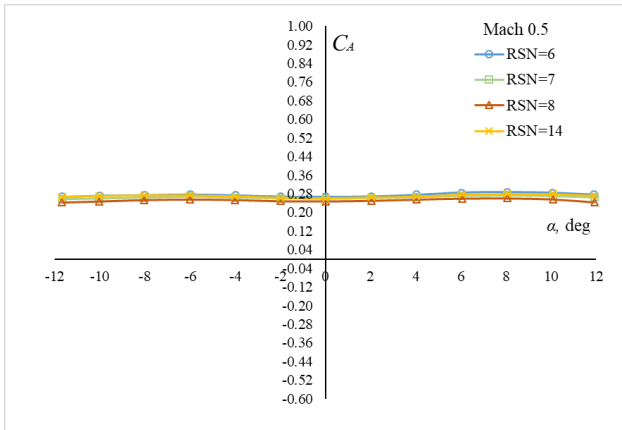
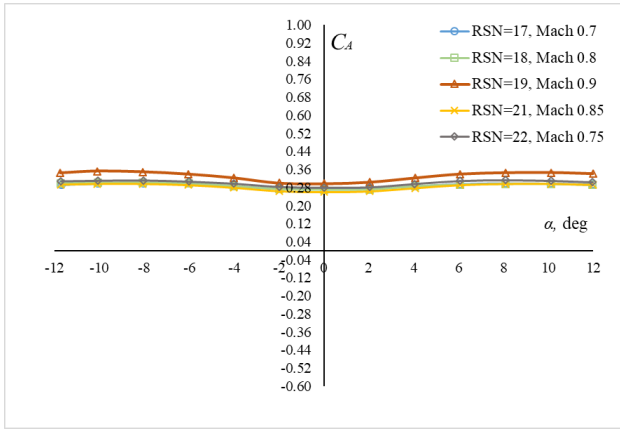


Figure 7. Drag force coefficient,  $M=0.5$

## 5. WIND TUNNEL MEASUREMENTS IN THE TRANSONIC SPEED RANGE

The supersonic projectile model was tested at nineteen values of Mach number in the transonic speed range. In the transonic speed range tests were conducted for one value of the stagnation pressure ( $2.3 \cdot 10^5$  Pa) and angle of attack in the interval of  $-10^\circ$  to  $+10^\circ$ . The angle of attack was covered by a continuous pitching movement of the model during the run with  $2^\circ/s$  rate of change. The results are presented through three groups of Mach numbers range. Drag force coefficients for each group of Mach numbers range are presented in Figures 10-12.



**Figure 10.** Drag force coefficient, Mach number range from 0.7 to 0.9

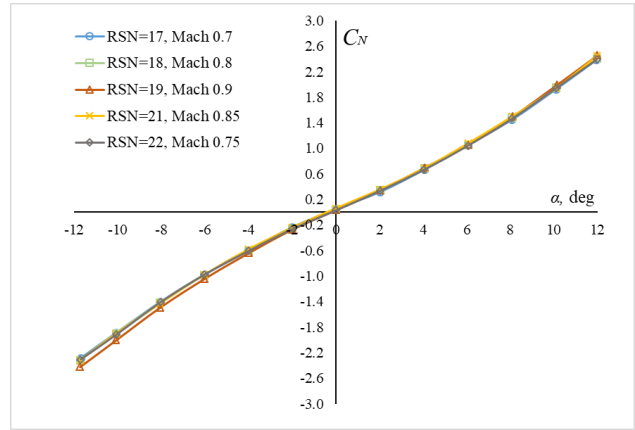


**Figure 13.** Normal force coefficient, Mach number range from 0.7 to 0.9

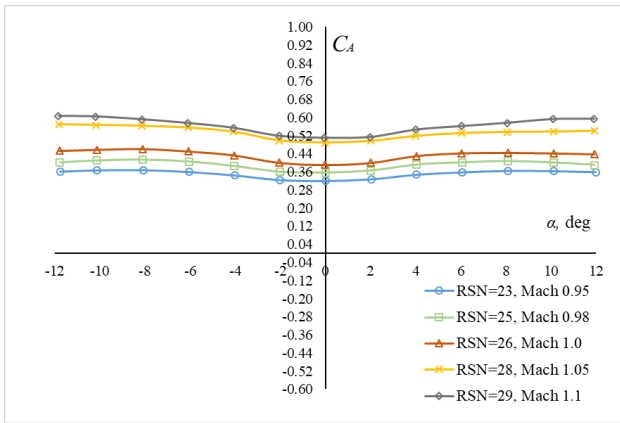


**Figure 11.** Drag force coefficient, Mach number range from 0.95 to 1.1

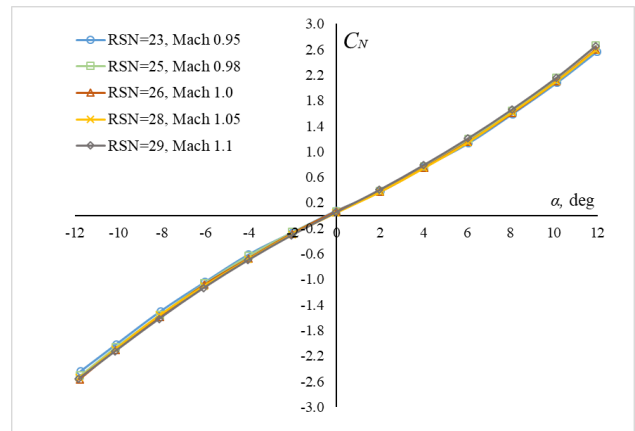


**Figure 14.** Normal force coefficient, Mach number range from 0.95 to 1.1

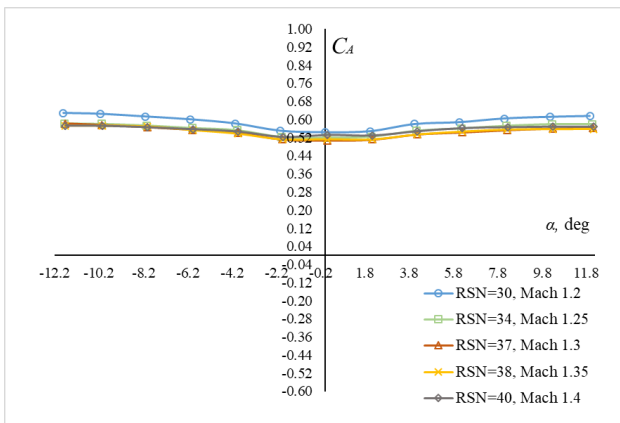


**Figure 12.** Drag force coefficient, Mach number range from 1.2 to 1.4

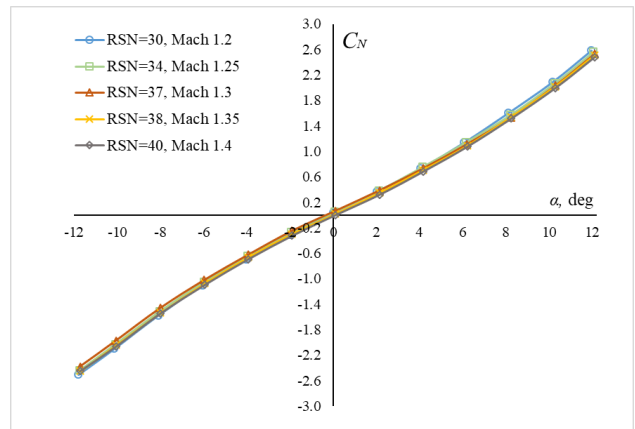


**Figure 15.** Normal force coefficient, Mach number range from 1.2 to 1.4

Normal force coefficients for each group of Mach numbers range are presented in Figures 13-15.

Pitching moment coefficients for each group of Mach numbers range are presented in Figures 16-18.

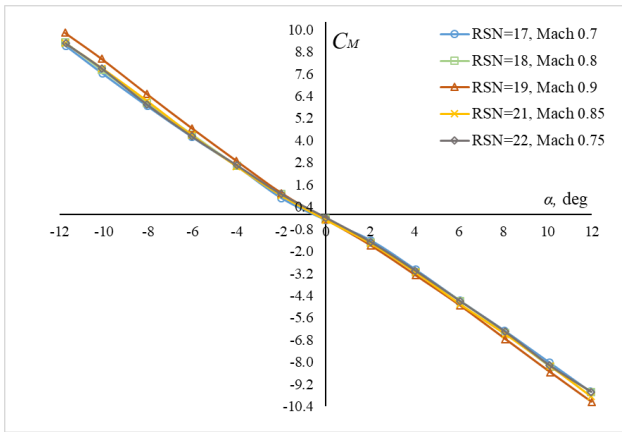


Figure 16. Pitching moment coefficient, Mach number range from 0.7 to 0.9

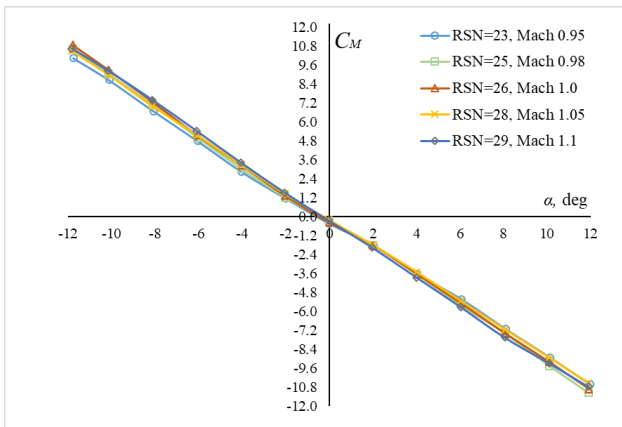


Figure 17. Pitching moment coefficient, Mach number range from 0.95 to 1.1

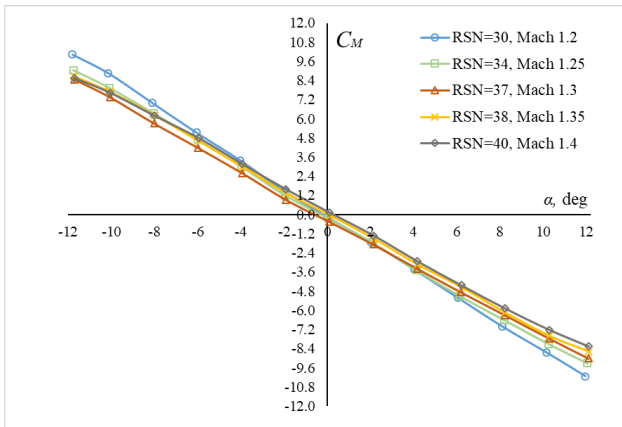


Figure 18. Pitching moment coefficient, Mach number range from 1.2 to 1.4

## 6. WIND TUNNEL MEASUREMENT IN SUPERSONIC SPEED RANGE

The results of the supersonic model testing on Mach number  $M=2.0$  are shown in Figures 19-21. Stagnation pressure in the wind tunnel test section was  $2.3 \cdot 10^5$  Pa, and angle of attack was in the interval of  $-10^\circ$  to  $+10^\circ$ . Base pressure coefficient and base drag force coefficient were calculated according to the following equations:

$$C_{pb} = \frac{p_b - p_{st}}{q} \quad C_{Ab} = -C_{pb} \frac{S_b}{S_{ref}}$$

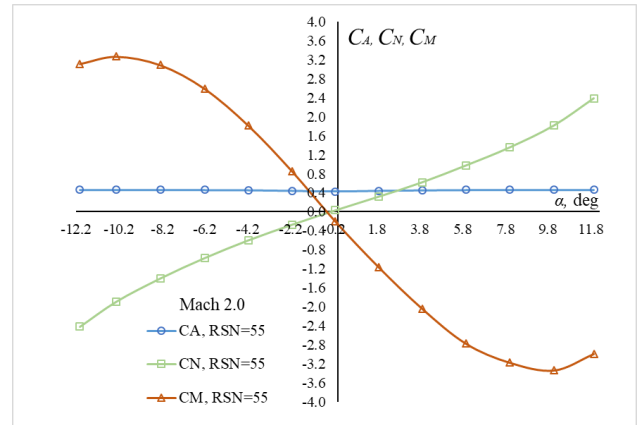


Figure 19. Drag force, normal force and pitching moment coefficients, Mach number 2.0

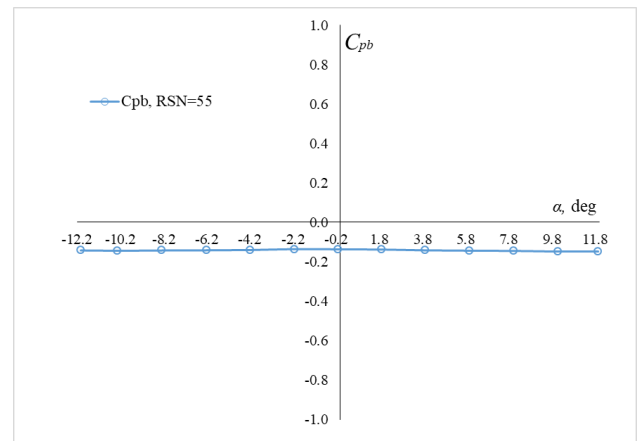


Figure 20. Base pressure coefficient, Mach number 2.0

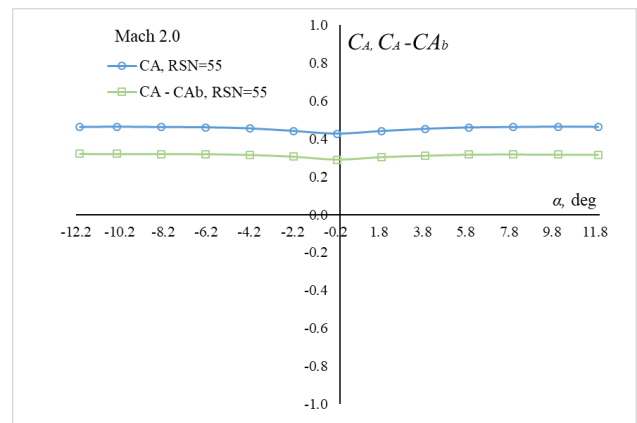


Figure 21. Drag force and total drag force coefficients, Mach number 2.0

On Mach number  $M=1.75$  short-time repeatability check was made. Short time repeatability in drag force, normal force and pitching moment measurements was checked on the basis of five repeated wind tunnel runs. Graphs, in Figures 22-24

, show comparisons of the measured drag force, normal force and pitching moment in relation to the model angle of attack.

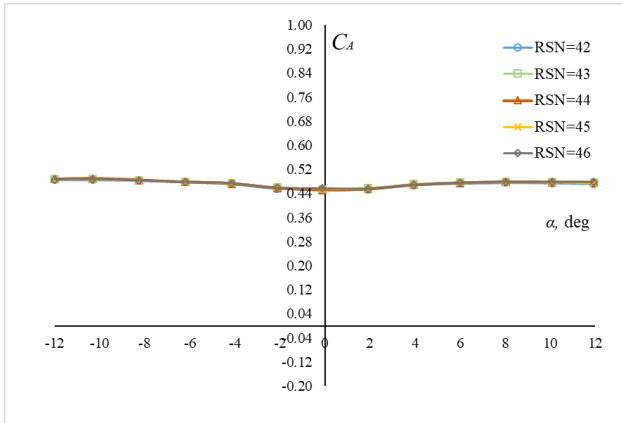


Figure 22. Drag force coefficient, Mach number 1.75

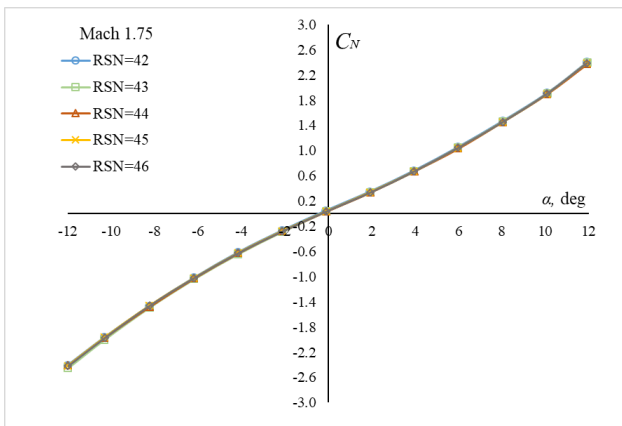


Figure 23. Normal force coefficients, Mach number 1.75

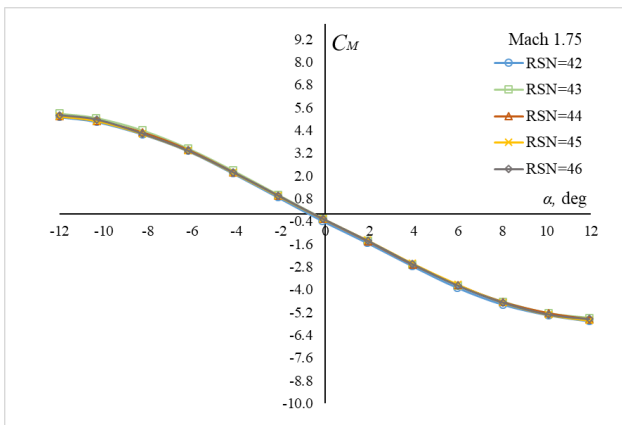


Figure 24. Pitching moment coefficient, Mach number 1.75

In Table 5 aerodynamic coefficient on certain angles of attack for respited wind tunnel runs are given.

Table 5. Aerodynamic coefficient for repeated runs

RSN	$\alpha$ [°]	$C_A$	$C_N$	$C_M$
42	-12.03	0.4856	-2.4031	5.1021
43	-12.04	0.4888	-2.4510	5.2870
44	-12.02	0.4878	-2.4062	5.1522
45	-12.03	0.4857	-2.4112	5.1413
46	-12.02	0.4862	-2.4191	5.2024
42	-0.110	0.4540	0.0510	-0.3771
43	-0.111	0.4539	0.0321	-0.2582
44	-0.109	0.4516	0.0342	-0.2842
45	-0.111	0.4548	0.0351	-0.2591
46	-0.109	0.4573	0.0341	-0.2611
42	11.93	0.4721	2.4070	-5.6620
43	11.92	0.4774	2.4011	-5.4981
44	11.93	0.4768	2.3742	-5.5621
45	11.92	0.4745	2.3878	-5.6313
46	11.93	0.4776	2.3912	-5.5580

7. CONCLUSION

Testing of the supersonic missile model in the VTI T-38 trisonic wind tunnel was conducted in subsonic, transonic and supersonic speed range. Subsonic data from measurements of drag force, normal force and pitching moment show a very good agreement in tests with different values of the stagnation pressure in the wind tunnel test section

The data in the transonic speed range show that internal six-component balance, used in the VTI T-38 wind tunnel tests, provide accurate determination of the increase in drag force coefficients for very small changes of the free stream velocity.

Analysis of the test data obtained through repeated wind tunnel runs showed the excellent agreement confirming high quality of the measurement repeatability. Short-term repeatability checks were done on the basis of five repeated supersonic wind tunnel runs.

Acknowledgements

This work was supported by the Ministry of Education, Science and Technological Development of the Republic of Serbia (Contract No. 451-03-66/2024-03/ 200325).

References

- [1] MEDVED, B., ELFSTROM, G.M.: The Yugoslav 1.5m trisonic blowdown wind tunnel, AIAA paper no. 86-0756-CP. American Institute of Aeronautics and Astronautics, Reston, Virginia, 1986.
- [2] ILIĆ B., MILOSAVLJEVIĆ M.: FPGA-Based Embedded System for Wind Tunnel Variable-Geometry Nozzle Positioning, *Scientific Technical Review*, Vol.69, No.1, 2019, pp. 3-9. DOI: 10.5937/str1901003I
- [3] SAMARDŽIĆ M., PETROVIĆ L., IVKOVIĆ U., ZUROVAC S.: *Measurement of hover performances for mini unmanned aircraft vehicle*, 10<sup>th</sup> International Scientific Conference on Defensive technologies, OTEH 2022, Belgrade, Serbia, 13-14 October 2022, pp.2-7.
- [4] HUFNAGEL K., SCHEWE G.: Force and moments

measurements, Springer Handbook of Experimental Fluid Mechanics, Part A Experiments in Fluid Mechanics, 2007, ISBN: 978-3-540-25141-5

- [5] ABLE Corporation, Document B-3181 (77482), S. Breunle, E.P. Ward, 10/13/81

### Notation

$C_A$	- drag force coefficient	$FRY$	- side force
$C_N$	- normal force coefficient	$FRZ$	- normal force
$C_M$	- pitching moment coefficient	$FRL$	- rolling moment
$C_{pb}$	- base pressure coefficient	$FRM$	- pitching moment
$C_{Ab}$	- drag force coefficient	$L$	- model length
$D$	- model diameter	$M$	- Mach number
$E_{rr}$	- maximum difference between applied and measured load in balance calibration	$P. E_{rr}$	- maximum difference between applied and measured load calculated in relation to the component full scale
$FN1$	- forward normal force	$p_0$	- stagnation pressure
$FN2$	- aft normal force	$p_b$	- base pressure
$FS1$	- aft side force	$p_{st}$	- static pressure
$FS2$	- backward side force	$q$	- dynamic pressure
$FRX$	- axial force	$RSN$	- Run sequence number
		$Std.d$	- standard deviation of the errors calculated in relation to the component full scale
		$S_b$	- model base area
		$S_{ref}$	- model reference area
		$L_{ref}$	- model reference length
		$\alpha$	- aerodynamic angle of attack



## CONTROL DERIVATIVE ESTIMATION OF NONCONVENTIONAL UAV DESIGN

MIODRAG MILENKOVIĆ-BABIĆ

Military Technical Institute, Belgrade, [miodragmmbm@yahoo.co.uk](mailto:miodragmmbm@yahoo.co.uk)

BRANISLAV OSTOJIĆ

Military Technical Institute, Belgrade, [branislavostojic1994@gmail.com](mailto:branislavostojic1994@gmail.com)

BILJANA DOVATOV

Military Technical Institute, Belgrade, [biljanadovatov@yahoo.com](mailto:biljanadovatov@yahoo.com)

ILIJA NENADIĆ

Military Technical Institute, Belgrade, [ilijanenadic98@gmail.com](mailto:ilijanenadic98@gmail.com)

**Abstract:** *The fast-moving technologies have enabled many new applications of Unmanned Aerial Vehicles for military and commercial purposes. This technology improvement has opened an incredible number of new opportunities for UAVs to be used for a variety of societal challenges. Despite the considerable investments and operational success, the nonconventional UAV design has not been well documented in the literature. In this paper, the nonconventional X-tail design will be evaluated. Control derivative estimation has been done by different methods.*

**Keywords:** UAV, CFD, derivative, flight control.

### 1. INTRODUCTION

During the last decade, Unmanned Aerial Vehicle (UAV) technology has seen a shift from military use to civil and commercial applications [1-6]. This shift has opened an incredible number of new opportunities for UAVs to be used for a variety of societal challenges. Different platforms [7-9] are used for different aspects of an event [10], such as surveying, search and rescue, crop analysis, environmental monitoring, infrastructure assessment, etc. The main advantage of fixed-wing UAVs is greater efficiency, longer endurance, and better performance. The greater range and endurance offered by fixed-wing designs lead to complexities in flight planning and approval, operator training, and licensing requirements, especially in use cases where a larger area needs to be covered (beyond visual line-of-sight operations). The main disadvantage of the fixed-wing UAVs is the need for a runway. This disadvantage can be reduced by implementing a parachute and airbag that will require less space for landing and launch from a catapult [11] or powered launcher. Despite some of the mentioned disadvantages, fixed-wing UAVs have been widely implemented for military applications. In the last 10 years, the number of nonconventional UAVs has increased significantly. Despite the considerable investments and operational success of Unmanned Aerial Systems, the nonconventional UAV design has not been well documented in the literature. The well-known aerodynamic principles that are given in the literature [12-14] apply to UAV design. The main drawback is that the

literature mentioned is primarily based on higher Reynolds numbers [15] that usually do not apply to UAVs. UAVs primarily operate at low Reynolds numbers and aerodynamic characteristics of airfoils at low Reynolds numbers are given in [16]. In the last few years combining vertical take-off and landing characteristics with fast-forward flight capabilities of fixed-wing UAVs is very popular [2-4, 7, 8]. By implementing vertical take-off and landing the UAVs can be easily operated in urban spaces.

In this paper, the nonconventional X-tail UAV design is analyzed and different methods have estimated control derivative. This UAV's tail configuration is very popular for the HERO family of loitering munitions [17]. According to the information in [17] the HERO series of high-precision loitering munition systems brings a unique design that enables maximum maneuverability with pinpoint strike accuracy and mission abort and reengage capability. This tail configuration has been used for the conceptual tail design of the loitering munition system Osica given in Figure 1. Osica is a fully autonomous UAS designed for attack missions. It is high-precision loitering munitions equipped with anti-tank warheads capable of destroying armored vehicles. UAVs' technical characteristics are given in Table 1. Osica is a project of the Military Technical Institute under development. The loitering munition systems [18] have reached high interest in the last few years.



Figure 1. UAV Osica in the take-off phase

Table 1. Technical characteristics

MTOW [kg]	8
Operative speed [km/h]	100
Operative altitude [m]	500
Endurance [min]	$\geq 30$
Link Range [km]	20
Engine	Electric BLDC
Take-off	Pneumatic launcher
Warhead weight [kg]	1.5

## 2. X-TAIL DESIGN

The well-known tail configuration as is conventional, T-tail, H-tail, V-tail, and inverted V have been documented in the literature [19] and the basic design steps are:

- Select tail configuration.
- Select tail location.
- Select tail volume coefficient.
- Calculate the tail moment arm.
- Calculate the tail planform area.
- Select tail geometry.
- Select the tail airfoil section.
- Determine tail lift curve slope.
- Calculate the aerodynamic moment coefficient.
- Calculate the tail desired lift coefficient.
- Calculated tail angle of attack at cruise.
- Estimate downwash angle at the tail.
- Calculate tail incidence angle.
- Calculated necessary tail angle of attack at different UAV speeds.
- Estimate UAV stability characteristics.
- Optimize the tail configuration if necessary.

To estimate aerodynamic coefficients and stability characteristics different tools are available. The most popular tools for airfoil analysis at low Reynolds numbers are probably XFOIL [20] and XFLR5 [21]. Additional data about airfoil characteristics can be found in [22]. For the tail, selecting a symmetric airfoil with the minimum profile drag coefficient is usual. Analysis of symmetric NACA airfoil characteristics has been done by XFLR5 software. Tail airfoils characteristic at cruise speed have been estimated and are given in Figures 2 and 3. According to the presented data in Figures 2 and 3 and the calculated tail incidence angle of attack at different airspeeds, it is possible to find adequate airfoils. For the preliminary X-tail design, the initial airfoil that is analyzed in this paper is the NACA 0012.

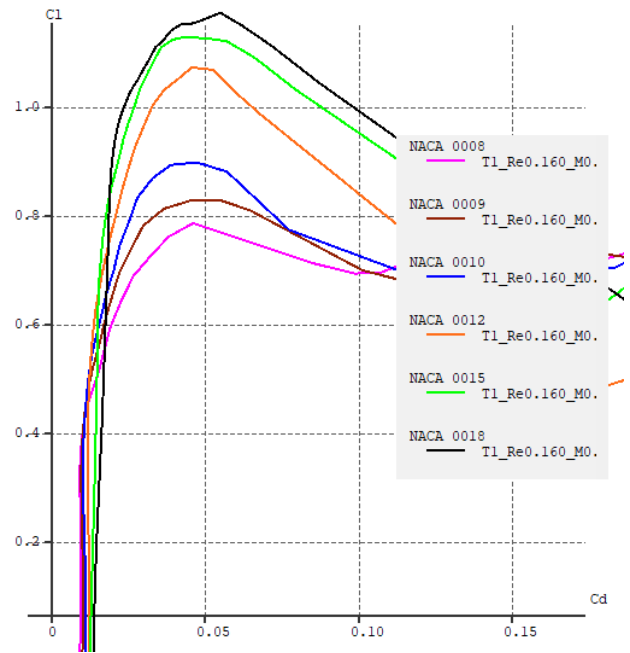


Figure 2. Airfoils polar

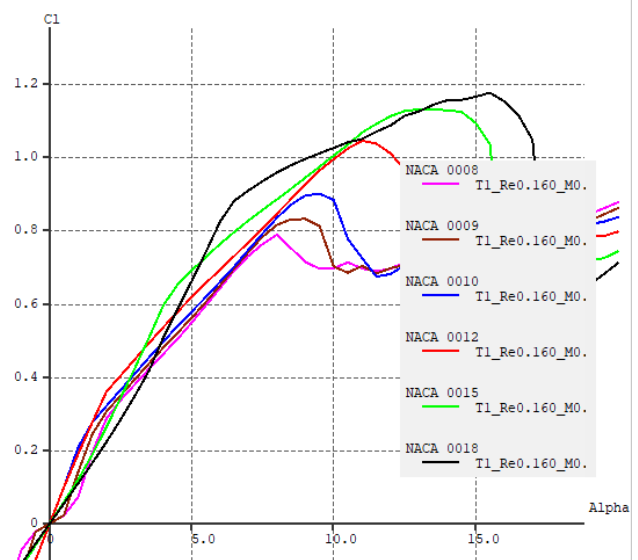


Figure 3. Airfoils coefficient of lift vs angle of attack

The procedure to define the X-tail area is defined in a few steps. First, the conventional empennage's vertical and horizontal tail areas are defined by a well-known tail volume coefficients method that can be found in textbooks [12]. In the next step, the data from [23, 24] have been used to estimate the equivalent X-tail area with the defined angle between the X-tail and the horizontal of 45 degrees.

## 3. CONTROL DERIVATIVE ESTIMATION

Equations for estimating stability and control derivatives are well known. These derivatives can be estimated by using empirical methods such as DATCOM [25] and ESDU [26], commonly available textbooks [11, 12, 27, 28], NACA reports, wind-tunnel testing [29-31], computational fluid dynamics (CFD) [32-33], estimated

from flight data or combination of just mention methods. Each of these approaches has some advantages and some disadvantages concerning cost, time consumption, range of applicability, and computational time. In this paper, the control derivative has been estimated by empirical methods given in [34], by vortex lattice method (VSPAERO) implemented in Open Vehicle Sketch Pad (OpenVSP) [35], and by CFD analysis [36]. OpenVSP is an open-source parametric aircraft geometry tool originally developed by NASA. VSPAERO is a useful tool for aerodynamic and flight dynamic analysis that consist of the vortex lattice and panel method. Additional useful information about stability derivative estimation can be found in [37]. To speed up the calculating process the aircraft or UAV geometry must be simplified. Simplified preliminary UAV geometry for vortex lattice analysis is given in Figure 4 and detailed information about UAV geometry and aerodynamic data can be found in [38].

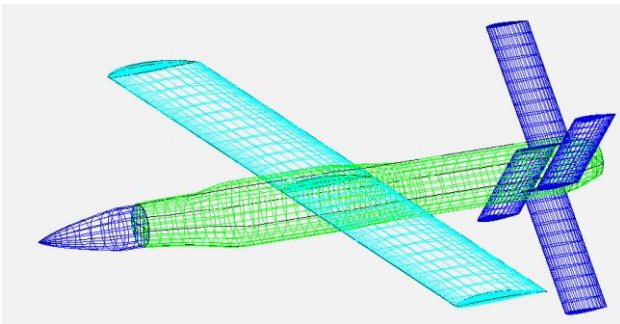


Figure 4. Simplified UAV geometry

It is important to mention that numerical methods OpenVSP and Ansys Fluent have been used indirectly to estimate the UAV control derivatives. First, it was calculated aerodynamic moment coefficient about the main axis at zero angle of attack, zero angle of sideslip, and zero deflection of the control surfaces. In the next steps, the aerodynamic moment coefficient was calculated at zero angle of attack, zero angle of sideslip, and deflection of control surfaces as it is given in Figure 5.

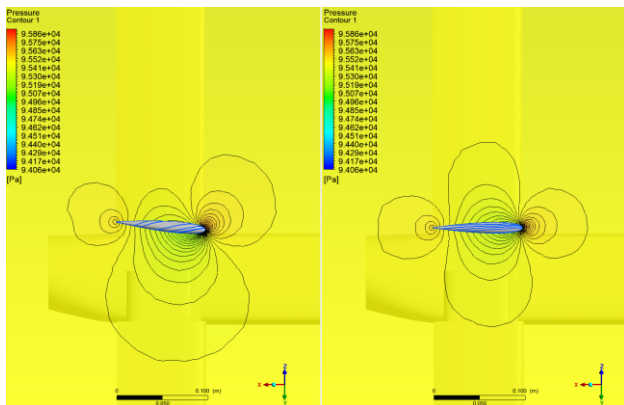


Figure 5. Control surface deflection

The control derivative about each axis has been estimated as the difference of moment coefficients divided by control angle deflection. CFD analysis was performed with unstructured tetrahedral mesh around the UAV. The resolution of a surface mesh is given in Figure 6. It was

done in commercial ANSYS Fluent software by the finite volume methods. The Reynolds average Navier Stokes system of equations was solved for compressible flow using a pressure-based solver. The mesh used for this case have 8.6 million cells.

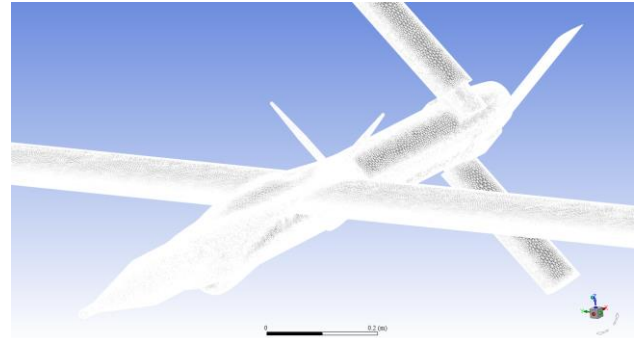


Figure 6. The resolution of a surface mesh on UAV

The Spalart-Allmars (S-A) turbulent model has been used with the second order approximation. The working fluid has been defined as ideal gas (air). The velocity inlet boundary conditions have been used for defining the velocity and direction of the free stream. The computations have been done until the convergence criteria have been achieved.

## 4. RESULTS AND DISCUSSION

According to the methods discussed above, in Table 2 the results for the UAV control derivative are presented. Those results have been calculated for standard atmospheric conditions at an altitude of 500 m.

Table 2. Calculated control derivatives

	Empirical methods [34]	OpenVSP	Fluent
$C_{m_{\delta_E}}$ [1/rad]	-1.841	-1.836	-2.172
$C_{n_{\delta_R}}$ [1/rad]	-0.229	-0.212	-0.250
$C_{l_{\delta_a}}$ [1/rad]	0.102	0.0829	0.0960

As it is shown in Table 2, the estimation of the pitching moment coefficient with elevator deflection angle deviates up to 15.5%. The empirical methods in general can be used for values of incidence and control deflection for which there is no separation of flow over the airfoil or control. Within these limitations, an accuracy of 15-20% is an acceptable value for preliminary design. Variation of the yawing moment coefficient with rudder deflection angle is up to 15.2%.

Variation of the rolling moment coefficient with the aileron deflection angle between Fluent and OpenVSP numerical methods is up to 13.6% and is acceptable for preliminary design. To estimate the rolling moment coefficient empirically slight coarse approximations have been used in the first iteration. It overestimates the rolling moment coefficient by almost 25%. This method is primarily developed for classical ailerons on the wings. To get a better estimation, a more precious approach has been used.



In the second iteration, the variation between empirical methods and Fluent was just 6.25%. In this case, the empirical methods overestimated numerical value but the difference in result is excellent.

## 5. CONCLUSION

Different methods have been used to estimate the control UAV derivatives of nonconventional X-tail UAV configurations.

Different methods have reached a good agreement. The results in this paper suggested that for nonconventional tail configuration, the numerical methods should probably give the best results for control derivative estimation.

To define the best method for estimating control derivative wind tunnel tests should be done or system identification based on flight test data.

## References

- [1] JANE'S.: All the World's Aircraft: Unmanned Yearbook 19/20, 2019/2020.
- [2] <https://threod.com/products/eos-c-vtol/>
- [3] <https://www.quantum-systems.com/project/scorpion/>
- [4] <https://www.c-astral.com/en/unmanned-systems/sqa-evtol>
- [5] <https://www.aeroexpo.online/prod/zala-aero/product-181291-63344.html>
- [6] MILENKOVIĆ-BABIĆ, M., IVKOVIĆ, D., OSTOJIĆ, B. et al.: *Take-off and Landing Performance of Tactical UAV*, Scientific Technical Review, Vol. 73, No. 2, Pages: 7-12, 2023.
- [7] GOETYENDORF-GRABOWSKI, T., TARNOWSKI, A., FIGAT, M. et al.: Lightweight unmanned aerial vehicles for emergency medical service - Synthesis of the layout, Part G: Journal of Aerospace Engineering, 2021, Vol. 235(1) 5-21.
- [8] SAEED, A.S., YOUNES, A.B., CAI, C. et al.: A survey of hybrid unmanned aerial vehicles. Progress in Aerospace Sciences 98 (2018) 91–105.
- [9] PASCUAL, M. and DA RONCH, A., *Advanced UAV Aerodynamics, Flight Stability and Control*, John Wiley and Sons, 2017.
- [10] VOSKUIJL, M., Performance analysis and design of loitering munitions: A comprehensive technical survey of recent developments, Defence Technology 18 (2022), 325-343.
- [11] PERKINS, C.D., and HAGE, R.E., *Airplane Performance Stability and Control*, John Wiley & Sons, New York, 1949.
- [12] RAYMER, D., *Aircraft Design: A Conceptual Approach*, Fifth edition, AIAA education series, 2012.
- [13] KHURULEV, A., Analysis of pneumatic catapult launch system parameters, taking into account engine and UAV characteristics. *Advanced UAV*, 3, (1), 10-24, 2023.
- [14] SNORRI, G., *General Aviation Aircraft Design: Applied Methods and Procedures*, Elsevier Inc, 2014.
- [15] USAF stability and control DATCOM, McDonnell Douglas Corporation, Douglas Aircraft Division, 1978.
- [16] MICHAEL, S. SELEG et al., *Summary of Low-Speed Airfoil Data, Volume 1-5, 1995-2012*.
- [17] <https://uvisionuav.com/>
- [18] WB GROUP, *WARMATE Loitering Munition System.pdf*, [www.wbgroup.pl](http://www.wbgroup.pl).
- [19] SADRAEY, M., *Design of Unmanned Aerial Systems*, John Wiley and Sons, 2020.
- [20] <https://web.mit.edu/drela/Public/web/xfoil/>.
- [21] <https://www.xflr5.tech/xflr5.htm>.
- [22] <http://airfoiltools.com/search/index>.
- [23] KHADKA, S., ABEYGOONWARDEN, J. and LIYANAGE, NP., Conceptual design of boom mounted inverted V-tail in the searcher MK 2 UAV, 13th International Research Conference General Sir John Kotelawala Defence University, 2020.
- [24] HELMUT STETTMAIER, *V-Tails for Aeromodels (pdf)*, 2001.
- [25] USAF Stability and Control DATCOM, McDonnell Douglas Corporation, Douglas Aircraft Division, 1978.
- [26] ESDU 86021B, *Introduction to aerodynamics derivatives, equations of motion and stability (with amendments a and B)*, 1987.
- [27] COOK, V.M., *Flight Dynamics Principles (Second edition)*, Elsevier, Amsterdam, The Netherlands, 2007.
- [28] ETKIN, B., *Dynamics of Atmospheric Flight (Third edition)*, John Wiley & Sons, New York, 1996.
- [29] SAMARDŽIĆ, M., ISAKOVIĆ, J., ANASTASIJEVIĆ, Z. and MARINKOVSKI, D., Apparatus for measurement of pitch and yaw damping derivatives in high Reynolds number blowdown wind tunnel, *Measurement*, Vol. 46, No. 8, pp. 2457-2466, 2013.
- [30] ANTON, N., BOTEZ R.M. and POPESCU D., Stability Derivatives for a Delta-Wing X-31 Aircraft Validated Using Wind Tunnel Test Data, *Proceeding of the Institution of Mechanical Engineers, Part G: Journal of Aerospace Engineering*, Vol. 225, Issue 4, pp. 403-416, 2011.
- [31] NASA TN D-5700, *Full Scale Wind-tunnel Investigation of the Static Longitudinal and Lateral Characteristics of a Light Single-engine Airplane*, 1970.
- [32] KOZIĆ, M., Comparison of the Navier-Stokes computations with the experiment for LASTA-95 wing at high angles of attack, *Scientific Technical Review*, ISSN 1820-0206, 2006, Vol.56, No.1, pp.41-44.
- [33] KOZIĆ, M., *Navier-Stokes Computations and Experimental Comparisons for Rudder Efficiency Analysis in the Moderately Steep Spin Part II:*

- Computation Method, Scientific Technical Review, ISSN 1820-0206, 2018, Vol.68. No.1, pp.61-65.
- [34] NAPOLITANO, M., Aircraft Dynamics: From Modeling to Simulation, John Wiley and Sons, 2011.
- [35] <https://openvsp.org/>.
- [36] <https://www.ansys.com/products/fluids/ansys-fluent/>.
- [37] KLAUSMAZER, S., FISHER, C., LAFIN, K. et al., Stability Derivative Estimation: Methods and Practical Considerations for Conventional Transonic Aircraft, Practical Considerations for Conventional Transonic Aircraft, Applied Aerodynamics Conference, 2018.
- [38] V3-0614-O-06, Analiza aerodinamičkih parametara – Proračun uzdužne statičke stabilnosti i upravljivosti, 2023.



# OTEH 2024

11<sup>TH</sup> INTERNATIONAL SCIENTIFIC CONFERENCE  
ON DEFENSIVE TECHNOLOGIES

*SECTION II*

**Aircraft - *A***

## USAGE OF MULTI-HOLE PROBE ON UAV WITH WARHEAD

ILIJA NENADIĆ

Military Technical Institute, Belgrade, [ilijanenadic98@gmail.com](mailto:ilijanenadic98@gmail.com)

DIJANA DAMLJANOVIĆ

Military Technical Institute, Belgrade, [didamlj@gmail.com](mailto:didamlj@gmail.com)

BILJANA DOVATOV

Military Technical Institute, Belgrade, [biljanadovatov@yahoo.com](mailto:biljanadovatov@yahoo.com)

MARKO BEK-UZAROV

Military Technical Institute, Belgrade, [markobekuzarov@gmail.com](mailto:markobekuzarov@gmail.com)

**Abstract:** This paper is about usage of multi-hole probes (MHPs) on unmanned aerial vehicle (UAV). Multi-hole probes are widely used in turbomachinery to determine angularity of velocity vector in unknown flow fields. New versions of UAV and the specter of their usage nowadays, request new solution in every area of their design. Strictly speaking, MHPs can be used on kamikaze UAV to determine sideslip angle in dive. This study present design of MHP with consideration the usage of UAV. Because this UAV is one-time use the goal is to get solution that is simple and easy to manufacture, but also precise to measure small sideslip angle. Precision of MHP measurements directly effect on epilogue if UAV hit the target or not. Computational Fluid Dynamics (CFD) are used to determine range of pressure difference created by probe head.

**Keywords:** Multi-hole probe, Five-hole probe, side slip angle, UAV, CFD.

### 1. INTRODUCTION

Unmanned aerial vehicles (UAV) with warhead have become the most common weapon for neutralization tanks and other large and slow moving vehicles. The goal is to get high success with cheap but reliable drones. That leads us to the fact that we are not able to use high quality and expensive equipment. To enhance the accuracy and performance of these UAV's, it is crucial to accurately measure aerodynamic parameters such as the angle of attack and side slip angle. These metrics are vital for ensuring that the UAV maintains optimal flight dynamics and precise targeting capabilities. A practical solution for this purpose is the five-hole probe, a relatively simple and inexpensive device used in aerodynamics.

The five-hole probe measures pressure differences at multiple points around the probe's surface, allowing for the determination of the direction and magnitude of airflow relative to the UAV [1-2]. By analyzing these pressure readings, the angle of attack and side slip angle can be calculated, providing essential data for flight control and stability. Despite its simplicity, the five-hole probe delivers reliable and accurate information crucial for the UAV's performance, making it an ideal choice for cost-sensitive applications [3].

### 2. GEOMETRY OF MHP AND PROBE HEAD

There are variety of possible configurations of a probe head. The most commonly employed probe head designs include conical, hemispherical, and pyramidal geometries, each tailored to different measurement needs and flow conditions, as shown on Figure 1 [4]. Each of these types has its advantages and disadvantages.

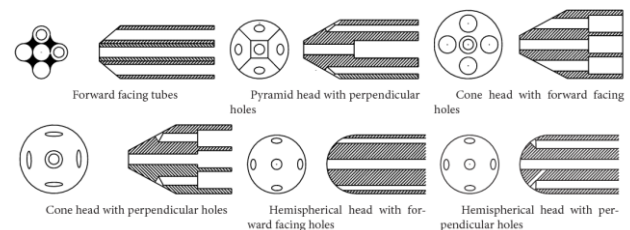
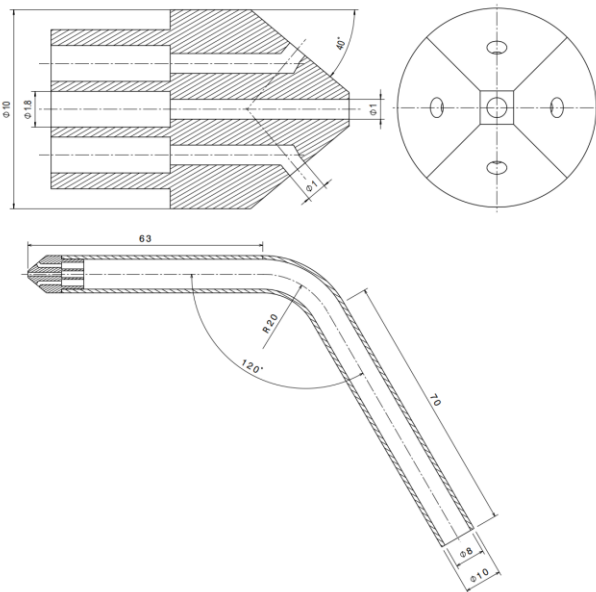


Figure 1. Types of five hole probe tip

For getting more resistible probe we choose pyramidal head with perpendicular holes. Reason for that is intentions to force flow separation along the corners of the head. This is very important since flow separation over holes gives us inaccurate pressure readings, as the separation causes turbulence and uneven pressure distribution.

As illustrated in Figure 2, we have selected a 40-degree apex angle for the probe tip, which represents an optimal compromise between sensitivity and measurement

accuracy. A sharper probe tip, with a smaller apex angle, generally provides higher sensitivity to changes in the angle of attack and side slip angle, which can be advantageous for detecting fine variations in flight angles. However, such a design is more prone to flow separation at high angles of attack. On the other hand, a blunter probe tip with a larger apex angle results in lower sensitivity. This design tends to produce smaller pressure differences between opposite measurement holes, which can be less responsive to subtle changes in airflow [5]. Despite this, the blunter geometry offers greater stability by maintaining more consistent flow over the probe head at high angles of attack.



**Figure 2.** Design of the probe

The outer diameter of the probe is designed to be 10 mm, which accommodates the necessary space for the five hoses that channel pressure to the sensors. Diameters of all five probe holes is 1 mm. To ensure stable and consistent flow through the probe, its length of straight part is set to 63 mm. This length is crucial for maintaining proper flow conditions and minimizing any potential disturbances that could affect the accuracy of the pressure measurements. To ensure accurate and timely pressure measurements, it is crucial to minimize the distance between the probe head and the sensors. A shorter distance allows the sensors to detect pressure changes more quickly, which is essential for capturing real-time data. The challenge lies in optimizing this distance while maintaining proper flow conditions within the probe's tubes. If the distance is too short, there may be issues with turbulence or interference, which can affect measurement accuracy [6]. Conversely, if the distance is too long, there could be delays in signal transmission and reduced responsiveness.

### 3. NUMERICAL SIMULATION

Numerical simulations are performed to analyze and get near value of the pressure differences generated by the Multi-Hole Probe (MHP). The computational fluid

dynamics (CFD) simulations are conducted using ANSYS Fluent software [7]. First step is to check MHP independently, without the UAV. As show at the Figure 3, the simulation focuses on the first segment of the probe, which contains five small tubes internally. The end of these tubes is used to get value of the pressure created by this MHP.



**Figure 3.** CAD model used for numerical simulation

An unstructured computational surface mesh is designed to accurately capture pressure variations at the probe head. To achieve this, a fine mesh is employed on the probe head surfaces and the internal walls of the tubes, ensuring detailed resolution where pressure changes are most critical. Coarser mesh is used further from the probe head, especially on the outer wall of the probe as it is shown at Figure 4. This mesh consists of 3,8 million cells.

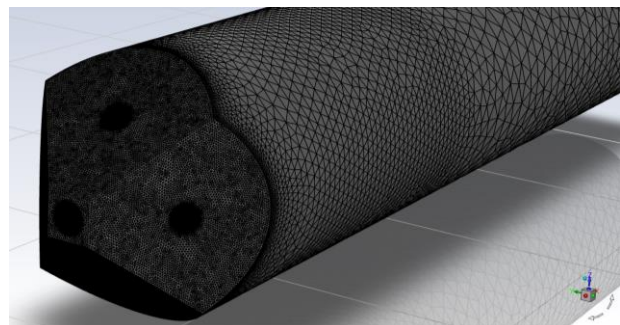


**Figure 4.** The resolution of a surface mesh on probe

Due to small Reynolds number, the simulation is calculated with laminar viscous model. The velocity inlet boundary conditions have been used for defining the velocity and direction of free stream. The simulation was carried out until the solution met the convergence criteria, ensuring that the numerical results were stable and precise.

### 4. RESULTS AND DISCUSSION

The simulation examines a range of angles from -15 to +15 degrees and only for both the angle of attack and the side slip angle. Due to the symmetrical design of the probe, the choice of which angle is used in the simulation does not affect the results. This range is determined because of limitation in maneuverability of this UAV in real flight.

As expected, when the side slip angle is zero, the difference in pressure is negligible. Figure 5, Figure 6 and Figure 7 shows the pressure differentials on the probe

head as a result of varying flow angles. In these figures, it is evident that the face of the probe head oriented directly into the flow experiences a higher local pressure in that specific region. The visual data from these figures demonstrate how the pressure distribution on the probe head is influenced by the angle of the incoming flow [8]. These observations are crucial for understanding the aerodynamic performance of the probe and for calibrating it to accurately measure pressure differences in various flight conditions.

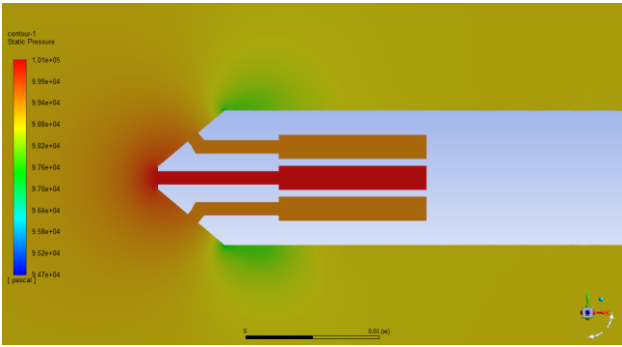


Figure 5. Pressure distribution at side slip angle  $\beta = 0^\circ$

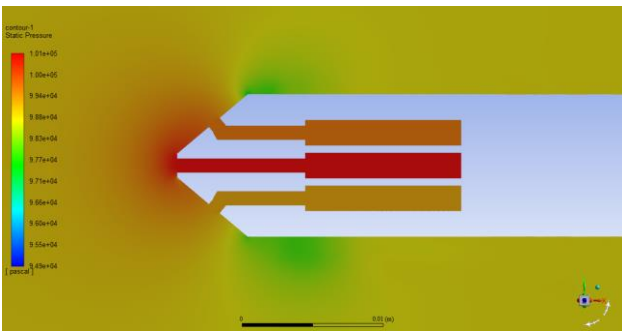


Figure 6. Pressure distribution at side slip angle  $\beta = 5^\circ$

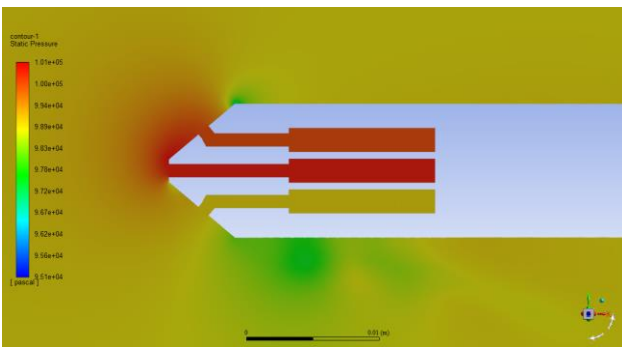


Figure 7. Pressure distribution at side slip angle  $\beta = 15^\circ$

Table 1 presents the pressure difference values obtained from the simulations, specifically for a velocity of 184 km/h at an altitude of 200 meters. These specific conditions are representative of the real flight scenario of the UAV. Figure 8 illustrates how, at the same altitude but with varying velocities, the pressure differences observed on the probe head change [9-10]. The data clearly show that as the velocity of the free stream increases, the pressure difference also increases. This correlation occurs because dynamic pressure, which is a function of the flow velocity, rises with higher speeds.

Table 1. Pressure difference values at V=184 km/h

Side slip angle $\beta$ ( $^\circ$ )	Pressure difference (Pa)
-15	-978.106
-10	-668.898
-5	-335.853
-2	-133.78
0	0.836
2	136.071
5	342.911
10	687.98
15	990.56

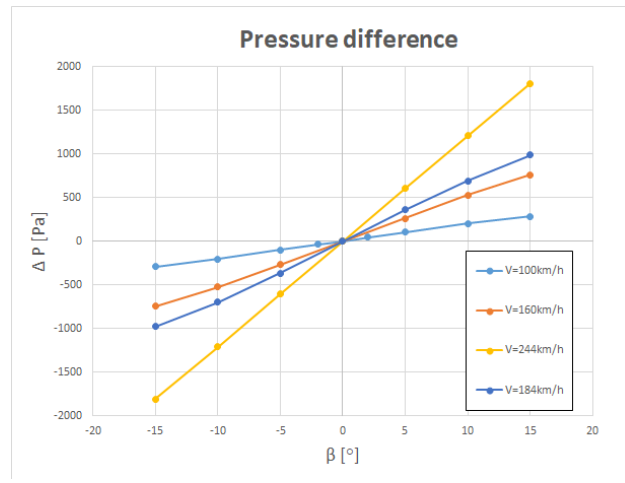


Figure 8. Pressure difference due to changes in velocity

### 5. CONCLUSION

Having gained an understanding of the pressure differences generated by the Multi-Hole Probe (MHP), we can effectively determine the side slip angle. Each specific angle of the probe corresponds to a distinct pressure difference measured by the probe head. However, it is important to consider that these pressure differences vary with different velocities. To solve this, the obtained results should be normalized with dynamic pressure. Selecting an appropriate pressure difference sensor is crucial. The sensor must be capable of covering the entire range of pressure values measured during flight. It should also have acceptable sensitivity to detect small pressure changes, enabling precise measurement of minor angles of the UAV.

One of the next steps involves conducting wind tunnel testing experiments to validate the results obtained from numerical simulations. These experiments are crucial for confirming the accuracy and reliability of the simulation data under controlled conditions. Additionally, it is essential to analyze the positioning of the probe on the UAV to understand how its placement affects the measurement outcomes. Evaluating the influence of the UAV itself on the obtained results during flight is also

necessary. This involves analyzing how the body of UAV interact with the probe and potentially impact the pressure measurements. By combining wind tunnel tests with in-flight analysis, we can ensure that the probe's performance and the data it provides are accurate and reliable under real-world conditions.

### Acknowledgements

This work was by Serbian Ministry of Defense and Serbian Ministry of Education, Science and Technological Development, Grant No 451-03-66/2024-03/200325.

### References

- [1] BRYER,D.W., PANKHURST,R.C.: *Pressure-probe methods for determining wind speed and flow direction*, Her Majesties Stationery Office, London, 1971.
- [2] Morrison, G.L., Schobeiri, M.T. and Pappu, K.R. (1998). 'Five-hole pressure probe analysis technique'. Flow Measurement and Instrumentation. Volume 9, Part 3: pp. 153-158.
- [3] Dobrowolski, B., Kabacinski, M. and Pospolita, J. (2005). 'A mathematical model of the self averaging Pitot tube. A mathematical model of a flow sensor'. Flow Measurement and Instrumentation. Volume 16: pp 251-265.
- [4] R.G. DOMINY, H.P. HODSON: *An Investigation of Factors Influencing the Calibration of 5-Hole Probes for 3-D Flow Measurements*, THE AMERICAN SOCIETY OF MECHANICAL ENGINEERS, New York, 1992.
- [5] SOLMOZ KATHLEEN AZARTASH-NAMIN: *Evaluation of low-cost multi-hole probes for atmospheric boundary layer investigation*, Oklahoma State University, 2017.
- [6] Akshoy Ranjan Paul, Ravi Ranjan Upadhyay, Anuj Jain.: *A novel calibration algorithm for five-hole pressure probe*, International Journal of Engineering, Science and Technology Vol. 3, No. 2, 2011, pp. 89-95
- [7] <https://www.ansys.com/products/fluids/ansys-fluent/>
- [8] CHRISTIAN SCHAFFER, KONSTANTIN SPECK, VOLKER GUMMER: *Numerical calibration and investigation of the influence of Reynolds number on measurements with five-hole probes in compressible flows*, Turbomachinery Technical Conference and Exposition, 2021.
- [9] Malviya, Vihar, Mishra, Rakesh, Palmer, Edward and Majumdar, Bireswar (2007) *Numerical analysis and optimisation of multi-hole pressure probe geometry*. In: Proceedings of Computing and Engineering Annual Researchers' Conference 2007: CEARC'07. University of Huddersfield, Huddersfield, pp. 1-8
- [10] Robert Sasse, Steve Borenstein, Radiance Calmer, Michael Rhodes, John Farnsworth, Gijs de Boer, and Brian M. Argrow.: *CFD-Assisted Calibration of a Multi-Hole Probe for a Small UAS*, AIAA SciTech Forum 2022, San Diego.



## DESIGN AND VERIFICATION OF A PNEUMATIC LAUNCH SYSTEM FOR A SINGLE-USE UAV WITH A WARHEAD

MARKO BEK-UZAROV

Military Technical Institute, Belgrade, [markobekuzarov@gmail.com](mailto:markobekuzarov@gmail.com)

ILIJA NENADIĆ

Military Technical Institute, Belgrade, [ilijanenadic98@gmail.com](mailto:ilijanenadic98@gmail.com)

CPT. STEFAN RAŠIĆ

Military Technical Institute, Belgrade, [rasha.soad@gmail.com](mailto:rasha.soad@gmail.com)

**Abstract:** The focus of this paper is the design of a pneumatic launch system (PLS) used for launching an unmanned aerial vehicle (UAV) and the verification of its mathematical model. Armed UAV systems without landing gears require a launch system for initiating the aircraft's take-off phase. Existing solutions typically work on a mechanical or pneumatic principle. Within this research, a pneumatically operated system was chosen as they have been proven to be more reliable during exploitation. Many existing pneumatic solutions function on the principle of a piston pulling a carriage on which the UAV rests, whereas this PLS is designed to have the UAV itself act as a piston. The mathematical model of the PLS is based on the principle of conversion of the potential energy of a pressurized gas into kinetic energy. The verification of the device was executed using a replica of the UAV's fuselage which was equipped with an inertial measurement unit (IMU). After multiple launch sequences, the data was analyzed and the final velocity of the UAV was calculated. The results proved to be sufficient as they deviated with less than a 10% error compared to the theoretical values.

**Keywords:** launcher, pneumatics, UAV, catapult

### 1. INTRODUCTION

During the early stages of development for the OSICA Loitering Munition, it was decided that the aircraft would need a standalone system for launching the aircraft into the air, which would eliminate the need for having personnel in its immediate vicinity during the take-off phase.

Since there are many existing solutions available, their working principles were considered during the initial phase of conceptual design. Most of the systems taken into consideration functioned either as mechanically spring-loaded mechanisms or utilized pneumatics for launching the aircraft. Based on previous experience and available evidence, it was decided to develop a pneumatic launch system as they were proven to be more reliable compared to their mechanical counterparts.

The pneumatic launch system (PLS) was designed in accordance to the technical requirements defined by multiple engineering departments. Although the end-goal was to design and construct a lightweight solution that could propel the aircraft to its desired take-off velocity, it was first of all necessary to verify the system's design and prove that it produced consistent and reliable results in regard to its governing equations. This meant that it was necessary to identify the parameters which affected the desired outcome and develop a design which would allow

for the controlling and constraining of these parameters. The focus of this paper will be the identification of those parameters, their relations and the design of the PLS.

### 2. WORKING PRINCIPLES AND GOVERNING EQUATIONS

Whether the design of a PLS is envisioned to be direct-acting or through an intermediary (as is the case with pneumatic launchers which rely on cables and pulleys) the working principles remain the same - the piston needs to move at a certain velocity (*Figure 1*) in order for the aircraft to take off, which is achieved by introducing a pressure differential within the system. The difference between the two aforementioned designs, mainly resides in the types of losses which need to be taken into consideration as well as the approach with which these losses need to be accounted for.



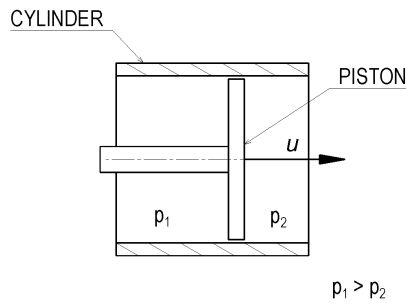


**Figure 1.** A representation of a piston moving inside a cylinder.

A PLS that relies on a system of cables and pulleys requires an orifice to be made in the launcher's cylinder in order for the cable to be connected to the piston. This type of design requires calculations of additional losses in the system caused by the orifice, whereas a design where the piston directly acts on the aircraft or carriage would only have to account for the losses caused by the forces of friction and the aircraft's drag. Aside from the elimination of the aforementioned losses, a PLS with a direct-acting piston opens up the possibilities of creating a lot simpler design.

Taking the advantages of a direct acting system into consideration as well as the fact that both the PLS and the UAV were being developed at the same time, the idea of having the aircraft itself act as a piston was adopted. This was achieved by integrating a tube inside that aircraft's fuselage which would slide over another tube on the launcher which would act as a cylinder (**Figure 2**).

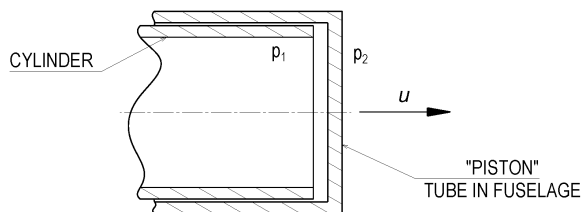


**Figure 2.** Representation of a "Direct acting" piston-cylinder assembly.

In order for the piston to move, it would be necessary to introduce a pressure differential in the system, that is, having the pressure at one side of the piston be greater than the pressure on the other. The creation of this pressure differential would be achieved by attaching the piston-cylinder assembly to a pressurized reservoir (**Figure 3**). The reservoir could be opened and closed using a valve.

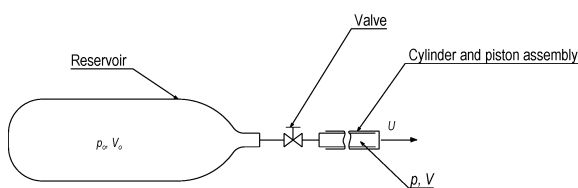


**Figure 3.** Depiction of the piston-cylinder assembly being attached to a pressurized reservoir.

Taking this into consideration, a need arose for defining the correlation between the pressure within the system and the piston's position along the cylinder (stroke) as well its velocity. The relation between the pressure inside the system and the piston's velocity was defined by taking into account that the change of energy inside a system is equal to the total work done by the forces inside it (1).

$$E = \int dE = \int dA = A \quad (1)$$

After further expanding the equation (1), the relation (2) was extracted. The change in the potential energy ( $E_p$ ) of the piston (aircraft), work done by the forces of friction ( $A_f$ ) and the drag experienced by the aircraft ( $A_{drag}$ ) are smaller by an order of magnitude compared to the change in kinetic energy as well as the work done by the change of pressure inside the system. It is important to note that the aforementioned factors were approximated in their most adverse form and as such were still expected to have a negligible contribution to the end results which further led to the assumption that they could be disregarded in further calculations.

These simplifications tremendously helped with defining the governing equations for the PLS. After simplifying, the following relation is acquired (2):

$$E = E_k = \underbrace{\frac{1}{2} mu^2}_{\text{Total energy}} = \underbrace{\int_{x_o}^x F dx}_{\text{Work done}} = \int_{V_o}^V p dV \quad (2)$$

Equation (2) was then further expanded in order to retrieve the final equation (eq. 3) which defined the relationship between the piston velocity in the function of the piston stroke.

$$u = \sqrt{\frac{2p_o V_o^\kappa A_p^{1-\kappa}}{m(1-\kappa)} (x^{1-\kappa} - x_o^{1-\kappa})} \quad (3)$$

Where;

$u$  – Piston velocity

$p_o$  – Initial reservoir pressure

$V_o$  – Initial system volume

$A_p$  – Piston area (*Area of the tube inside the fuselage*)

$m$  – Piston (aircraft) mass

$\kappa$  – Ratio of specific heats

$x$  – Piston (aircraft) stroke

$x_o$  – Initial piston position of the piston (eq. 4), if the initial acting volume ( $V_o$ ) was represented as a tube which had the same cross section as the tube on the launcher. Note that this value is indeed fictional and is derived from the initial acting volume (**Figure 4**).

$$x_o = \frac{V_o}{A_p} \quad (4)$$

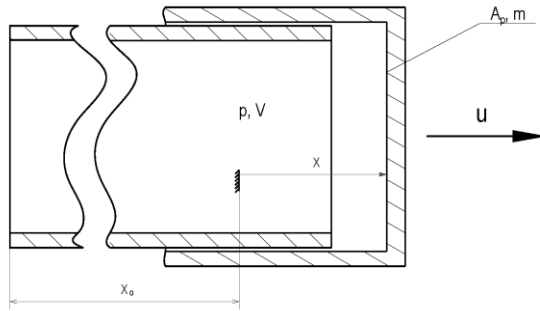


**Figure 4.** Depiction of the mathematical model

### 3. INITIAL DESIGN OF THE FUNCTIONAL MODEL

Aside from describing the approximate dynamic behavior of the system, equation (3) further defined the variables which affected the aircraft's velocity on the launcher. By having some of the variables defined by the technical requirements of the system, and the others by the limits imposed by the specifications of corresponding ready-made components, a more detailed design of the launcher was established. Having this in mind, a functional model (FM) was constructed for the purposes of verifying the aforementioned equations (*Figure 5*).

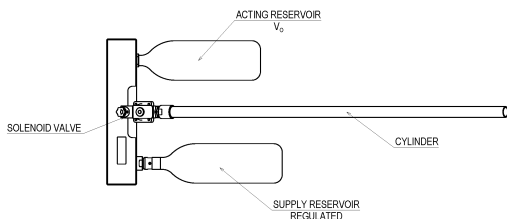


**Figure 5.** Top view of the functional model

The functional model consists of an acting pneumatic block which acts as a mounting point for all other components. Two refillable gas tanks were attached to the block, where one was equipped with a pressure regulator that regulated the pressure within the system, while the intent for the other tank was for it to be the acting volume ( $V_0$ ).

Because the pressure inside the tube on the launcher is filled up with pressure only when the solenoid valve opens up, it was necessary to equip the functional model with a high-flow valve in order to have the previously defined equation (eq. 3) be valid.

### 4. TESTING AND VERIFICATION

In order to confirm that equation (3) reliably describes the behavior of the system, it was necessary to conduct tests with known variables. For the verification of the functional model, a dummy fuselage was used which was modified to carry an inertial measurement unit (IMU). It was intended to use the IMU as a means to record and interpret the change of the aircraft's acceleration during the launch sequence, since the aircraft's acceleration correlated with the change in pressure within the system. The dummy model was also equipped with weights in order to have a total mass as close to the mass of the UAV.

The maximum initial pressure in the acting reservoir ( $p_0$ ) was imposed by the g-force limit of the IMU. Therefore, for the first test, an initial pressure value of  $p_0=20$  bar was chosen as it would ensure readability of the values recorded by the IMU. By assigning all the values to equation 3, an initial estimation of the aircraft's velocity during the launch sequence was obtained (*Figure 6*).

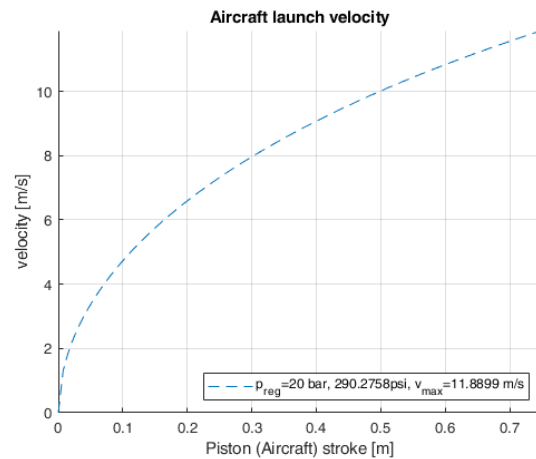


**Figure 6**

A total of three launch sequences were executed in order to prove that the results were consistent and that equation 3 was reliable. Considering the fact that the IMU's output variable was the acceleration along the aircraft's own axes (Body Frame  $F_b$ , *Figure 7* [1]), it was necessary to develop a method to convert the acceleration data to the dummy's velocity.

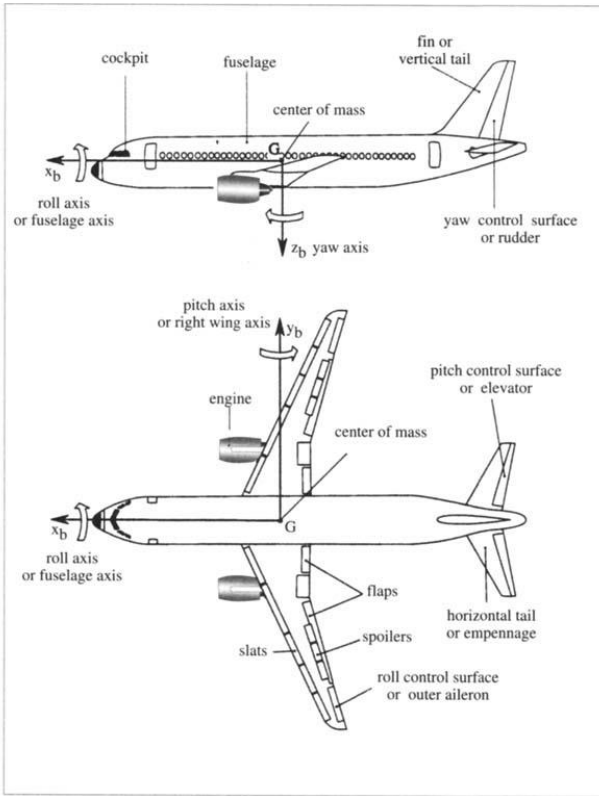


**Figure 7.** Depiction of the aircraft's IMU axis system

Considering the fact that during the launch sequence, the aircraft was intended to only move along its longitudinal axis ( $x_b$  on **Figure 6**), and that the axes were aligned with the aircraft's, it would only be necessary to convert one set of acceleration data per launch sequence which belonged to the corresponding axis.

The conversion of the acceleration data was achieved first by defining the already known and simple differential equation which defines acceleration (eq. 4).

$$a = \frac{dv}{dt} \quad (4)$$

Since the data recorded by the IMU was acceleration recorded in finite intervals of time, a simple finite difference model was implemented in order to linearize equation 4. This approach was chosen because the sampling rate of the IMU was high enough for the time between subsequent recordings ( $\Delta t$ ) to be less than the total time required for the whole launch sequence [2]. Taking all of this into consideration, equation 4 becomes:

$$a = \frac{dv}{dt} \approx \frac{\Delta v}{\Delta t} \approx \frac{v_i - v_{i-1}}{\Delta t} \quad (5)$$

$$\Rightarrow v_i = a\Delta t + v_{i-1} \quad (6)$$

Although equation 6 delivers an approximation for calculating the change of the velocity of the aircraft, it is represented as a time dependent variable. Whilst equation 3 is presented in such a way where the velocity is described as a function that's dependent on the aircraft's position along the PLS' tube ( $x$ ). Therefore, the equation (eq. 6) needed to be developed further in order to acquire

the approximation of the aircraft's position on the PLS' tube (Piston stroke).

The same methods were used to approximate the piston stroke as were used to approximate the aircraft's velocity. The difference being that this time, the relation between the piston stroke and the piston velocity were used (equations 4, 5 and 6)

$$v = \frac{dx}{dt} \quad (4)$$

$$v = \frac{dx}{dt} \approx \frac{\Delta x}{\Delta t} \approx \frac{x_i - x_{i-1}}{\Delta t} \quad (5)$$

$$\Rightarrow x_i = v\Delta t + x_{i-1} \quad (6)$$

Finally, after obtaining and converting all the necessary data, the recorded velocities were acquired in the function of the piston stroke and were compared to the theoretical values (**Figure 6**). The results can be seen on the diagram below (**Figure 8**).

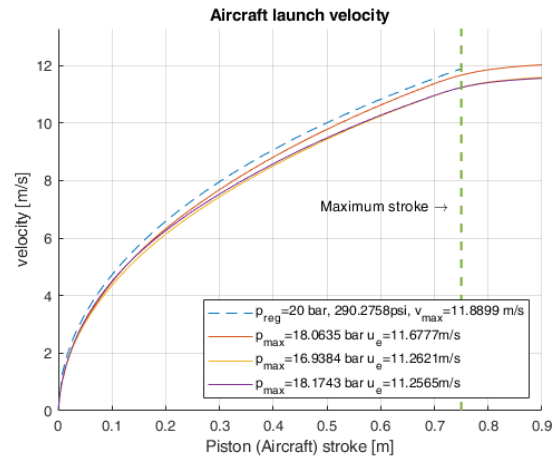


**Figure 8.** Aircraft launch velocity represented in the function of the piston stroke.

By visually inspecting the diagram it can be noted that the measured and approximated values of the velocities (Solid lines) closely follow the predicted (Dashed line) value. After further processing of the acquired data, the following values were acquired (**Table 1**):

**Table 1.** Recorded values of the aircraft's velocity

No.	$p_{max}$ [bar]	$\eta_{max}$ [*9.81 m/s <sup>2</sup> ]	$u_e$ [m/s]	$\epsilon$ [%]
1	18.06	10.78	11.68	2.57
2	16.94	10.11	11.26	6.38
3	18.17	10.85	11.26	6.39

Seeing the data presented in **Table 1** it can be concluded that the described governing equation for defining the aircraft's velocity during the launch sequence is satisfactory considering that the error rate ( $\epsilon$ ) is well below 10%.

## 5. CONCLUSION

By analyzing the acquired and approximated data, it can be concluded that the functional model of the PLS primary function performs as expected and in accordance to the primary governing equations (equation 3). It can also be concluded that the PLS' variables can be adjusted in order for the aircraft to reach a desired velocity in order for the take-off phase initiation. Although the PLS is designed primarily to suit the needs of the OSICA loitering munition and is fully compatible with that UAV, with further examination and development, it could be redesigned and repurposed for other smaller UAVs.

## Acknowledgements

This work was by Serbian Ministry of Defense and Serbian Ministry of Education, Science and Technological Development, Grant No 451-03-66/2024-03/200325.

## References

- [1] BOIFFIER, J., *The Dynamics of Flight: The Equations*, WILEY, 1998
- [2] MUNGAN, C., *Internal ballistics of pneumatic potato cannon*, European Journal of Physics, 2009
- [3] NOVAKOVIĆ Z., *Integration of tactical-medium range UAV and catapult launch system*, Scientific Technical Review, volume 66, issue 4 pp. 22-28, 2016.



## THE EFFECTIVNES OF THE USE OF DRONES IN MODERN CONFLICT

STEVAN JOVIČIĆ

Technical Test Center, Belgrade, [msmjovicic@gmail.com](mailto:msmjovicic@gmail.com)

JASMINKA JELISAVAC

Technical Test Center, Belgrade, [jelisavacjasminka@gmail.com](mailto:jelisavacjasminka@gmail.com)

LJUBIŠA TOMIĆ

Technical Test Center, Belgrade, [ljubisa.tomic@gmail.com](mailto:ljubisa.tomic@gmail.com)

IVO OBRADOVIC

Technical Test Center, Belgrade, [boki.deki@mts.rs](mailto:boki.deki@mts.rs)

**Abstract:** *We are witnessing armies participating in the conflict posting videos on social media depicting drones as cheap weapons that can effectively destroy expensive artillery pieces or tanks worth millions of dollars. Drones have transformed from performing specialized functions into one of the most important and widespread weapons on the battlefield. The deployment of smaller drones, which was inconsistent at the beginning of the war, has now become extremely organized. Almost every combat brigade has a company of attack drones, while most units have small reconnaissance drones. If we are at the beginning of the drone revolution, world politics will change dramatically in the near future. If the drone revolution is in the making, states will have to significantly revise their defense policies. Troops on the battlefield will become increasingly vulnerable and all states will have to restructure their armed forces away from expensive and complex military platforms in favor of new, less sophisticated and cheaper technologies such as drones. However, drone technology is most effective when used in conjunction with other types of weapons.*

**Keywords:** *drone, revolution, efectivnes, frontline*

### 1. INTRODUCTION

How do we remember all the wars of the 1990s, Middle East (certainly by names and abbreviations „BGM-109A Tomahawk”, „MQ-1 Predator”, „RQ-4 Global Hawk” or in 1991. Operation „Desert Storm” and 2003. Operation „Iraqi Freedom”, the former Yugoslavia NATO aggression on the strongholds of the VRS in BiH in 1995. and the NATO aggression on the FRY in 1999.). In all of the aforementioned conflicts, in addition to classic military aviation, drones and unmanned aerial vehicles were used. The price of that weaponry at the time was available only to the great powers and big military alliances. How its starts.

The economy and air defense of the attacked country first would be exposed to all kinds of sanctions and simply had no chance of sustaining against long-term conflict with the massive deployment of sophisticated smart missiles, guided bombs and drones.

However, a change was announced from the far East at the end of the eighties of the last century, microchips, semiconductors, micro electric motors... The commercial industry of entertainment and cheap electronic cameras, the application of a new type of batteries and reliable electric motors, the development of technology for the production and processing of composite materials and its

mass accessibility led to the mass production and civilian application of new aircraft that were cheap, easy to use, extremely agile, small in overall dimensions, undetectable by radars and, most importantly, there were lot of them on the market.

### 2. IN THE BEGINNING

The use of drones of all kinds is related to the conflict between Armenia and Azerbaijan in 2020, which ended with the victory of Azerbaijan. Without going into the tactical developments on the ground, the conflicting forces inflicted serious losses on each other using drones of various types . Drones of Russian, Turkish, Israeli, and indigenous designs performed both reconnaissance missions to support artillery use and strike missions. Unmanned aerial vehicle (UAV) and loitering munition attacks were able to destroy heavy ground units, including T-72 tanks and advanced S-300 air defenses [1]. The conflict's use of these various weapons provides important information and insights into how modern wars will employ the growing spectrum of missiles, drones, and artillery. At the end, the opponent who had more drones and unmanned aerial vehicles won the war.

The war in Ukraine began with a massive invasion of the Russian army, with hundreds of state-of-the-art tanks, armored personnel carriers, artillery dominated by VBR,

and a mass landing of helicopters bringing special forces deep into Ukrainian territory.

In a very short time, using the network of highways, the Russians broke out in the vicinity of Kiev, Kharkov and stopped, waiting for the surrender of Kiev.

But nothing like that were happened, motivated and determined to defend themselves, the Ukrainian forces inflicted heavy losses on the Russian army and forced the columns of combat vehicles to return to their starting positions.

Since then, for almost two years the frontline doesn't move, which is more and more reminiscent of the First World War. What has changed is that pictures from the ground have started coming in, showing drones, \$1,000 drones destroying radar equipment, missile systems, tanks with multimillions dollars value. Even the mighty Black Sea fleet was decimated and driven into ports by drone strikes from the sea and from the air.

### 3. TACTICAL DRONES – MILITARY DRONES DESIGNS

Various producers offer various types of Tactical Drones and Military Drones for emergency management and mission-critical operations. These rugged military drones are designed to meet the demanding needs of Border Security and Armed Forces and are optimal for a range of applications such as high-altitude logistics delivery, ISR, mine detection and neutralization, combat, and target decoys, among others. On the market can be found customized tactical drones based on user-specific requirements, to meet the varying demands of weight, flight altitude, payload capability, endurance, armament and ammunition integration, electro-optical features and ruggedness.

The advanced AI technologies and visual algorithms in tactical drones and tactical military drones aid intelligent mapping of defined geographical areas; detect and classify objects of interest at low light and harsh weather conditions. These cutting-edge features make tactical military drones ideal for cross-border surveillance and to gather crucial situational awareness during a conflict and gather intelligence on border activities. The rugged tactical drones are designed to transport in small SUVs and trucks and can be deployed in minutes from any terrain. These tactical military drones have a varying operational range of 3-10 km and can fly at an altitude of 1.500 m to 6.800 m, based on the payload, Electro-optical sensor specifications. [2]

Tactical military drones are equipped with advanced technology that enables them to perform a variety of functions, including surveillance, reconnaissance, target acquisition, and even weapon delivery. Producers offer Tactical military drones in a range of sizes and capabilities, from small quadcopters to large Octocopters.

The tactical drones usually come with three flight modes, Manual, fully Autonomous and pre-mapped Autonomous. The user can define the mode of flight based on perational needs in these rugged Military Drones. For instance, for

periodic cross-border surveillance at a defined area, a fully autonomous mode would be ideal. However, during a conflict wherein every second is crucial, Manual or semi-autonomous operation would provide quick insights to the operator. In case of link loss (loss of connectivity with GCS) due to signal jamming or extreme weather conditions, the Auto Return Home feature aids the drones to return to the launch safely. Producers also offers Tactical Military drones for distant surveillance with a range of up to 45 km, especially with stealth capabilities.

Rugged tactical drones come with ergonomically designed, user-friendly Ground Control Stations (GCS). The multi-layered safety protocols ensure secure communication between GCS and the drones. Based on the application and use case, the GCS can be designed to have single or dual displays to provide maximum usability and operational convenience to the operator on the field.

### 4. ANTI TANK DRONES

The AeroVironment Switchblade is a miniature loitering munition designed by Aero Vironment and used by US Army small enough to fit in a backpack, the Switchblade launches from a tube, flies to the target area, and crashes into its target while detonating its explosive warhead. The name Switchblade comes from how the spring-loaded wings are folded inside a tube and flipped out once released.

Introduced in 2011, the original Switchblade was rebranded the Switchblade 300 after the much larger and very different Switchblade 600 anti-armor variant was unveiled in 2020. The Blackwing is unarmed variant of the Switchblade 300, was released in 2015. More than 700 Switchblade 300 drones were sent to Ukraine by the United States as part of an arms package after the 2022 beginning Russian-Ukraine conflict.

#### 4.1 TYPICAL REPRESENTATIVE, SWITCHBLADE 300

The Switchblade 300 Block 20 is the next-generation successor to the Switchblade 300, Figure 1. Building on the Switchblade's battle-proven performance, the Switchblade Block 20 offers enhanced operational features including a high-resolution EO/IR panning camera suite, longer endurance, and a new touchscreen Fire Control Unit (FCU) allowing the operator to train, plan and execute missions with ease. Weighing just about (2-4) kg, this lightweight, miniature, precision-guided lethal missile can be deployed in less than 2 minutes via tube-launch from land, sea, or mobile platforms providing greater mission flexibility. Delivering 20-plus minutes of tactical reconnaissance, surveillance, and target acquisition (RSTA), the Switchblade 300 Block 20 provides real-time video for use against beyond-line-of-sight (BLOS) targets and its open architecture system allows it to interface with external C2 systems. Cursor-on-target GPS coordinates provide situational awareness, information collection, targeting and feature/object recognition, that together deliver the actionable

intelligence and precision firepower needed to achieve mission success across multiple domains [3].

Range: 30 km (with extended range antenna)

Endurance: 20+ min

Weight: munition 1,65 kg

AUR: 3,27 kg (Included payloads, launcher, transport bag)

Speed: Loiter 101 km/h, sprint 161 km/h



Figure 1. Drone Switchblade 300

#### 4.2 Lancet, Russian response

The Lancet-3's airframe and distinctive dual X-wing shape (see Figure 2) are built from composite materials enabling it to have a lightweight design. The drone is stored in a case that can be carried onto the battlefield, where the drone can be unfolded at the designated launch point. A crew of two trained soldiers operate the system. The drone is then launched via a catapult system and is controlled by a ground operator. The drone can be communicated with using an antenna or a mobile ground station. A camera at the front of the drone is used for visual identification of targets and guidance in the attack. According to ZALA-Aero Group, the Lancet-3 has a purported range of roughly 40 kilometers (km) and has an advertised maximum speed of 80-110 km/hour. The drone is powered by an electric motor. The drone system carries a warhead towards the front of the UAV weighing 1-3 kg.



Figure 2. Drone Lancet

The drone system has made a dramatic impact on the battlefield and has successfully targeted and destroyed or damaged a multitude of combat systems operated by the Ukrainian armed forces, including Western supplied armored vehicles and artillery. The Lancet-3 reportedly has the ability to identify and attack targets autonomously in groups with the help of AI processing modules embedded in the drone system. Lancet drone strikes

occur when reconnaissance UAVs are conducting operations, indicating that they operate in conjunction. Once the drone system has identified a target, it locks on to the target and explodes at a designated distance from the target using a rangefinder, enabling it to defeat anti-drone protection cages, which often confuse the impact fuses on other drone systems. Prior to the war in Ukraine, the Lancet had been tested in the combat theater of Syria against Turkish forces.

Newer versions of the drone, purportedly called "Product 53" or the "Izdeliye-53," can be launched from a four pneumatic tube launching system, which enables multiple next generation Lancet drones to be launched in short succession. According to the Institute for the Study of War, the Russian government claims that the new Izdeliye-53 had been used in combat missions in Ukraine, although no evidence of actual use has been found. Images of the Izdeliye-53 show that it is very similar in design to the Israeli Hero-120 loitering munition, produced by UVision. [4]

## 5. CONFLICT COSTS

Comparison the costs of employing various weapons against infantry and armor. Analysis shows incorporated data on the price of multiple weapons, the cost per shell, the probability of destroying the target, and the number of shots per unit required [Volodymyr Dacenko 2023.]. Furthermore comparison was done not only for the cost of utilizing various weapons but also for their efficiency. To do this, calculation was done including a cost ratio, which is derived by comparing the cost of eliminating a single target with a specific weapon – to the value of the target being destroyed.

Evaluation shows that the target cost for infantry is \$60,000. This represents the average compensation for a dead or seriously wounded soldier. Comparison was done for the cost of eliminating a single target using various weapons, such as a drone with a drop-down mechanism, a heavy drone, a Switchblade 300, mortar, and artillery. Figure 3, Figure 4.

Drones dropping grenades or an FPV drone are the cheapest and most effective way of destroying enemy infantry. Utilizing a drone proves to be almost seven times less costly than using the Switchblade 300, the most expensive infantry-targeting tool in his comparison. Additionally, using drones (FPV drones or drones equipped with a drop-down mechanism) are nearly three to four times cheaper than using mortars, artillery, or heavy drones to take out infantry targets.

However, the use of mortars and artillery on group targets in open terrain dramatically increases their effectiveness. But if the infantry is in the trenches, the effectiveness of traditional military means is drastically reduced. In this case, drones can have a much greater advantage. Also, estimation was made for the average cost of destroyin an armored unit at \$750,000. In this context, comparison of the FPV drone, heavy drone, Switchblade 600, ATGM Stugna, ATGM Javelin, and artillery augmented with the M982 Excalibur.

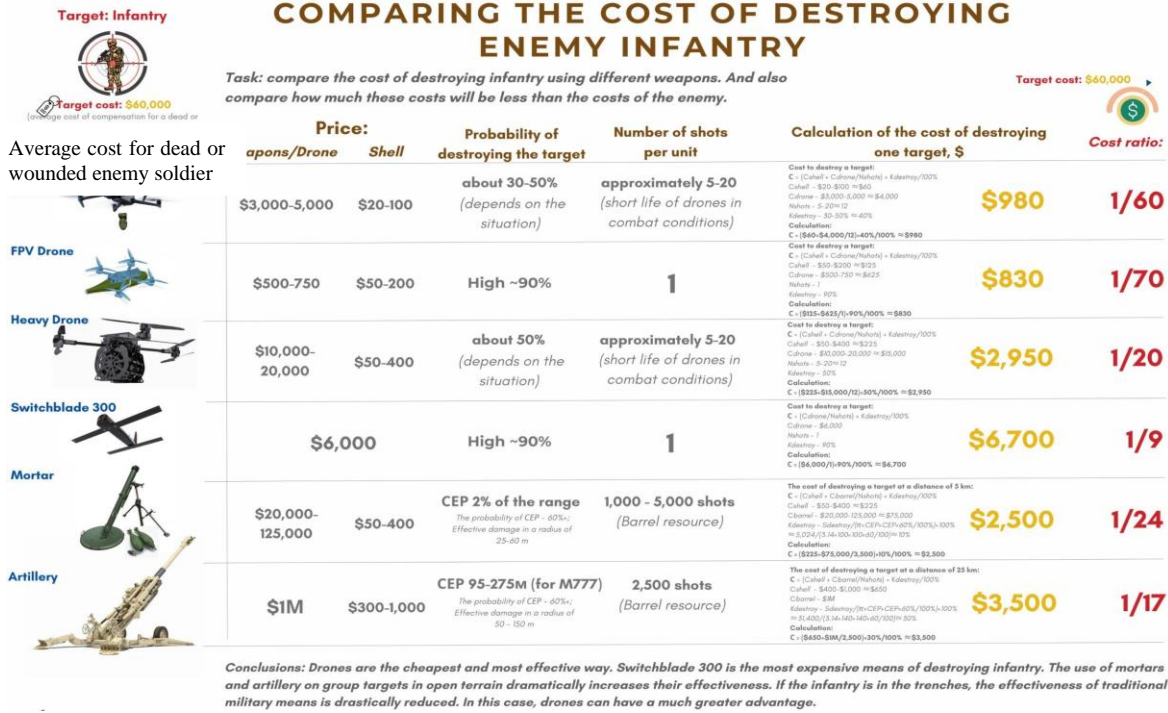


Figure 3. Cost comparison for destroying infantry with different weapons

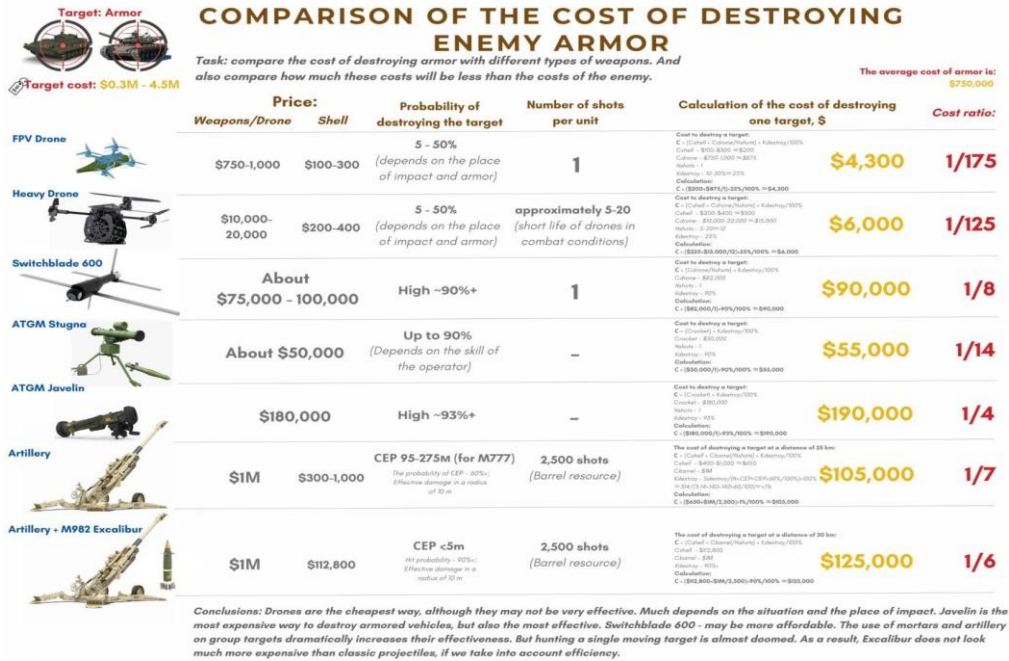


Figure 4. Cost comparison for destroying armored vehicles with different weapons



While it is recognized that drones to still be the cheapest method for eliminating a single target, they may not be very effective. Their effectiveness may vary considerably based on the terrain situation.

### 5.1 STUGNA-P (SKIF)

The **Skif**, also known as the **Stugna-P** or **Stuhna-P**, is a Ukrainian anti-tank guided missile (ATGM) system developed in the early 2010s by the Luch Design Bureau, a unit of UkrOboronProm. The initial guidance device PN-S (ПН-С) of the Skif was developed and manufactured by Belarusian design bureau Peleng based in Minsk.

The Skif is designed to destroy modern armored targets with combined carried or monolithic armor, including explosive reactive armor (ERA). The Skif can attack both stationary and moving targets. It can be used to attack from both long range (up to 5 km in the daytime) and close range (100 m). It can attack point targets such as weapon emplacements, lightly armored objects, and hovering helicopters. The Skif has two targeting modes: manually steered, and automated fire-and-forget that uses no manual tracking of a target, figure 5.



Figure 5. Stugna-P on tripod

The Javelin shoulder-fired anti-tank missile is the most expensive way to destroy armored vehicles, but also the most effective. The Switchblade 600 – may be more affordable. The use of mortars and artillery on group targets dramatically increases their effectiveness. But

hunting a single moving target is almost doomed. In particular, it can be pointed out that Excalibur is GPS-guided and is not effective against moving targets [5]

## 6. CONCLUSION

Just as it was said a long time ago: "There is no such thing as a perfect kill", so „There is no almighty weapon that will solve war". From the moment when atomic weapons ceased to be the property of only one country, they lost their meaning, the fear of mutual destruction remained. World peace on earth will last as long as the fear of self-destruction lasts. When someone thinks they can win a world war, civilization will come to an end as it has so many times before.

Drones have become the hit of limited-intensity conflict in the early 21st century. War has become a game again, and drones are the enforcers of punitive measures. However, the main drawback of drones as a perfect weapon for now is its limitations in terms of the payload it can carry and the possibility of electronic jamming. When these issues are resolved, we will be able to talk about weapons that can bring victory in the war and create the conditions for the penetration of larger army groups on the front line. For now, we can say that victory in the war cannot be achieved only through use of drones.

## References

- [1] <https://www.csis.org/analysis/air-and-missile-war-nagorno-karabakh-lessons-future-strike-and-defense>
- [2] <https://www.avinc.com/lms/switchblade-2024>
- [3] Moncourtois, Alyce; Hush, Brett (November 20, 2020). "Switchblade: From Gun-Launched UAV to Precision Strike Loitering Missile System". "Russian Kamikaze Drone "Lancet" Equipped With NVIDIA Jetson TX2 Computer And Xilinx Zynq Chip," SunDries, March 20, 2023, <https://sundries.ua/en/russian-kamikaze-drone-lancet-equipped-with-nvidia-jetson-tx2-computer-and-xilinx-zynq-chip/>
- [4] [twitter.com>Volodymyr\\_D\\_>status](https://twitter.com/Volodymyr_D_) Apr 17, 2023 · Comparison of the cost of destroying a target with different weapons Volodymyr Dacenko #RussiaUkraineWar #OSINT #javelin #UAV
- [5] Lessons learned and unlearned the drivers of US indirect-fire innovation / Brennan S. Deveraux. ISBN 9780578911588 (Adobe pdf) 2023.



## AIRCRAFT PROTECTION AGAINST LIGHTNING AND STATIC ELECTRICITY

MARINA OSTOJIĆ

UTVA Aircraft Industry, Pančevo, [majce74@yahoo.com](mailto:majce74@yahoo.com)

TAMARA NIKOLIĆ

UTVA Aircraft Industry, Pančevo, [tn.aircraft@yahoo.com](mailto:tn.aircraft@yahoo.com)

RADOJE ZARUBICA

MTU, Belgrade, [radoje.zarubica@gmail.com](mailto:radoje.zarubica@gmail.com)

NIKOLA BOGAVAC

UTVA Aircraft Industry, Pančevo, [bogavacnikola55@gmail.com](mailto:bogavacnikola55@gmail.com)

**Abstract:** *The aircraft safety is one of the most important things when thinking of designing and manufacturing the airplane. During the flight, there is a probability of lightning occurrence which may cause catastrophic consequences. In order to avoid potential aircraft damage, the aircraft must be protected against lightning effects. Metallic components should be bonded to the airframe, while the airplane design must secure that possible lightning strike would not endanger the plane, the crew and the passengers. In this paper, the compliance of „Sova“ aircraft design with certification requirements regarding lightning protection will be analyzed and shown.*

**Keywords:** *lightning, protection, airframe bonding, metallic components, safety.*

### 1. INTRODUCTION

The „Sova“ aircraft was designed by UTVA Aircraft Industry Research & Development team in compliance with certification specifications [1] and [2].

During designing and manufacturing of the aircraft, along with analyzing structure, controls, avionics and other systems, engineers must be aware of potential occurrences during the flight, such as lightning strike.

Certification specifications include requirements concerning aircraft protection against lightning effects.

In this paper, the compliance with requirements concerning electrical bonding and protection against lightning and static electricity, as well as fuel system lightning protection will be demonstrated.

### 2. CERTIFICATION

#### 2.1 Electrical bonding and protection against lightning and static electricity:

The paragraph CS 23.867 [1] defines the corresponding requirements:

(a) The aircraft must be protected against the catastrophic effects from lightning.

(b) For metallic components, compliance with sub-

paragraph (a) may be shown by bonding the components properly to the airframe; or Designing the components so that a strike will not endanger the aircraft.

(c) For non-metallic components, compliance with subparagraph (a) may be shown by Designing the components to minimise the effect of a strike; or Incorporating acceptable means of diverting the resulting electrical current so as not to endanger the aircraft.

On „Sova“ aircraft, metallization was carried out on the structure, control surfaces and all systems, so that protection of the aircraft and crew from lightning strikes is enabled, the stability and uninterrupted operation of electronic equipment is ensured, the risk of fire is prevented, and sparking caused by static electricity is eliminated.

„Sova“ is all metal structure except engine cowling, wingtips, rudder tips and elevator tips. Protection of the metal components of „Sova“ aircraft against lightning was achieved by bonding the components through mass in an appropriate manner to the aircraft structure.

The metallization of the metal elements of „Sova“ aircraft structure is defined in the technical documentation. Aircraft assemblies with number of bonding positions are specified in Table 1.

**Table 1.** Aircraft metallization

Assemblies	Quantity
Wing	32
Flaps	1
Empennage	6
Elevator controls	4
Flap controls	9
Aileron controls	6
Aileron Trimmer	1
Fuel installation	5
Hydraulic installation	14
Electrical installation	1
Antennas	2

Special screws for metallization are installed on the wings, and on the funnel for pouring fuel into the tanks there are defined points for attaching clips for metallization.

Also, the aircraft was successfully tested according to the Technical conditions for determining the quality of installation, testing and acceptance of electronic equipment and installation (insulation resistance of electronic equipment, transient resistance) and the Technical conditions for determining the quality of installation, testing and acceptance of electrical equipment and installation (electrical resistance of the insulation of the installation, ohmic resistance of the aircraft structure, transient resistances and metallization).

As for non-metallic aircraft parts, design ensures the protection of the following surfaces made of composite from the catastrophic consequences of a lightning strike:

- wingtips,
- rudder tips,
- elevator tips.

The redirection of the resulting electric current, which occurs as a result of a lightning strike, is carried out in such a way that the safety of the aircraft is not endangered:

- by applying an epoxy film LORD UltraConductive™ coating with high electro conductivity on the wingtips,
- by installing the Micropoint Trailing Discharger, P/N 11-16630, in the zone of the trailing edge of the tips.

The design solution for the protection of the tips zone on „Sova“ aircraft from the catastrophic consequences of a lightning strike demonstrates the compliance of the solution with certification requirements.

## 2.2 Fuel system lightning protection requirements

For the purposes of certification of „Sova“ aircraft in accordance with certification specifications [1] and [2], it

was necessary to design the fuel system so that it meets the corresponding requirements.

The paragraph CS 23.954 [1] defines the requirements concerning fuel system lightning protection:

The fuel system must be designed and arranged to prevent the ignition of fuel vapour within the system by –

(a) Direct lightning strikes to areas having a high probability of stroke attachment;

(b) Swept lightning strokes on areas where swept strokes are highly probable; and

(c) Corona or streamering at fuel vent outlets.

SWEPT - "sweeping" strikes occur when a lightning strike is deformed due to interaction with aerodynamic forces and is formed in a unique way due to the material and shape of aircraft surfaces. It is a series of continuous contact of lightning with the surface of the aircraft that is formed due to the aircraft movement through the air.

CORONA – light discharge that occurs as a result of the difference in electric potential between the aircraft and the external atmosphere.

STREAMERING – is a branch-like ionized path that occurs in the presence of a direct lightning strike or under conditions that prevail immediately before the strike.

ARC & SPARK – An arc and a spark are the same thing, but the spark usually lasts a very short time. However, when that spark remains continuous for a long time, then it is called an arc.

A lightning strike on aircraft can occur during flight and/or in the vicinity of a thunderstorm. In addition, due to flying in the vicinity of the lightning strike area, CORONA or STREAMER formation may occur on the aircraft. For this reason, it is necessary that the fuel vapors generated inside the fuel system are protected from ignition in the case of flight in conditions of a large difference in electrical potential between the aircraft and the atmosphere, as well as in the case of a direct lightning strike in zones with a high probability of a strike.

According to document [4], it is necessary to first define the zones on the aircraft that have a high probability of a direct lightning strike, as well as of a "Swept" strike. Figures 1 and 2 show the orthogonal and side projection of Sova aircraft with marked zones.

Zone 1B represents the surfaces that have a high probability of a direct lightning strike and are marked in yellow in figures 1 and 2. These are the extremities on the trailing edges of the control surfaces - wings, elevator, rudder, as well as the tips of the wings and the horizontal and vertical stabilizer. Since the trailing edge of the tip is made of composites (glass fibers) that are electrically conductive, then the 1B zone extends forward to the nearest electrically conductive surface. Also, this zone is extended laterally by 0.5 [m] due to possible "Swept" channels, and also in the event of a local scattering of points from a direct lightning strike.

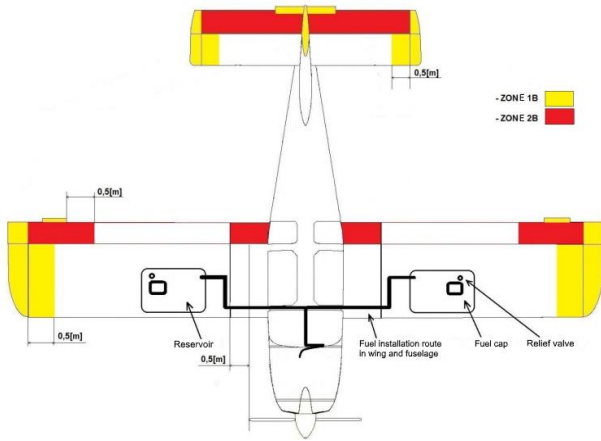


Figure 1. Sova aircraft top view

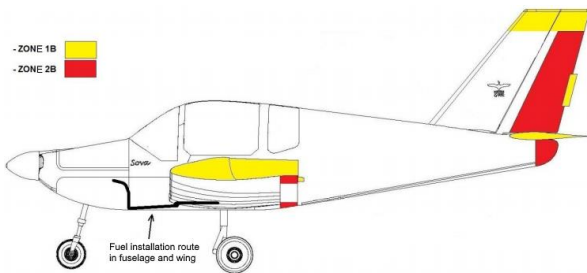


Figure 2. Sova aircraft side view

Zone 2B represents the surfaces that have a high probability of a "Swept" impact and are marked in red in figures 1 and 2. These are the trailing edges of the wings, horizontal and vertical control surfaces, as well as the top of the fuselage. Since the control surfaces of Sova aircraft are made of aluminum (electrically conductive materials), then the specified zone will not extend forward to the nearest electrically conductive surface. Since there is no fuel installation (pipelines and components) or reservoirs that could be exposed to a direct or "swept" lightning strike in the above-mentioned zones, it is concluded that Sova aircraft meets the certification requirements.

In order to meet the certification requirements, it is necessary to show that the fuel system is designed in such a way that the possibility of ignition of fuel vapors inside it is prevented in the event of the appearance of "Corona" or "Streamer" on the exhaust valves installed in the wings of Sova aircraft.

In manual [3], a Lockheed study examined three different types of exhaust valves. The testing concluded that the openings that are directed in the direction of the air flow have a more "diluted" mixture of fuel vapors at the exit, that is, the least flammable area compared to the other cases that were examined. The non-flammable mixture is 1D and more from the exhaust valve, which means that a lightning strike or "Streamer" must occur very close to the edge of the exhaust tube to ignite the fuel vapors. Tests have shown that it is only possible to ignite the vapors when the "Arc" is directly directed at the outlet of the exhaust valve.

It was also mentioned that during the reports collected until then, there was no record of a direct lightning strike on the exhaust valve, although on many aircraft these

openings are located on the winglets, which have a high probability of a direct lightning strike.

In Newman's test during 1966-1967, a 48kA ignition source was released on a Boeing 707 aircraft. During the test, a direct lightning strike on the vent occurred only once in 34 times at a wind speed of 90 knots. At a speed of 200 knots and 200 attempts, not once did a simulated direct lightning strike occur on the opening itself.

When the strikes last longer, so-called "swept" strikes are formed. During the above test out of 15 attempts, fuel vapors ignited 11 times. Based on this, it is concluded that exhaust valves should not be installed in 1B zones that have a high probability of "Swept" or direct impact.

The exhaust valve assembly on „Sova“ aircraft is shown in Figure 3. It is connected to the air deflector. Its position on the wing is shown in Figure 1 where it can be seen that the opening is far enough from the zones where there is a high probability of a strike that could ignite the fuel vapors.

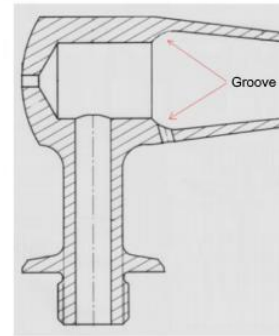


Figure 3. Exhaust valve air deflector

Positioning the vent in Zone 3 (where the exhaust valve is installed) will provide the highest level of protection, according to manual [3] point 7.3.4.(6). Since the air deflector directed directly in the direction of the air flow, then a much more diluted mixture of fuel vapors appears at its exit than usual, so the probability of ignition is minimal. Besides, the valve is made of aluminum which has good electrical conductivity. The pipe groove is recommended, because the pipe itself could later become a source of "Corona" or "Streamer" that can occur when the aircraft is flying in a strong electric field. For this reason, there is a groove on the air deflector, shown in Figure 3. In this way, the possibility of "CORONA" being transferred directly to the exhaust valve and igniting the fuel vapors was prevented.

Based on the above explanation, it is concluded that the exhaust valve on „Sova“ aircraft fulfills all the proposed recommendations from the used literature, and in this way the possibility of ignition of fuel vapors, and in the cases mentioned, also the lightning strike zone, is reduced to a minimum. Also, there are no fuel system components and pipelines in areas that have a high probability of lightning strikes, so it can be concluded that the fuel system on „Sova“ aircraft is designed to meet the certification requirements.

### 3. CONCLUSION

Utva Aviation Industry is approved by Civil Aviation Directorate of Republic of Serbia as a Design and Production organization under Part 21 regulations.

Also, „Sova“ aircraft is certified under CS-23 regulations.

Those approvals and certificates carry along high responsibility when designing and manufacturing the aircraft. There are plenty of certification requirements that the aircraft must comply.

Showing compliance of the aircraft with all those requirements meant hard work and effort. However, for some paragraphs, analyzing and testing were interesting, such as in the case of lightning protection.

### References

- [1] Certification Specifications for Normal, Utility, Aerobatic and Commuter Category Aeroplanes CS 23, Amendment 3 Book 1
- [2] Certification Specifications for Normal, Utility, Aerobatic and Commuter Category Aeroplanes CS 23, Amendment 3 Book 2
- [3] DOT/FAA/CT-89/22 Aircraft Lightning Protection handbook
- [4] DOT/FAA/CT-83/3 User's Manual for AC-20-53A Protection of Airplane Fuel System Against Fuel Vapour Ignition Due to Lightning



## FAILURE ANALYSIS OF AIRCRAFT STRUCTURAL ELEMENTS

STEVAN MAKSIMOVIĆ

Military Technical Institute, Belgrade, [s.maksimovic@mts.rs](mailto:s.maksimovic@mts.rs)

KATARINA MAKSIMOVIĆ

City of Belgrade – City Government, Belgrade, [kmaksimovic@mts.rs](mailto:kmaksimovic@mts.rs)

IVANA VASOVIĆ MAKSIMOVIĆ

Lola Institute, Kneza Višeslava 70, Belgrade, [ivanavvasovic@gmail.com](mailto:ivanavvasovic@gmail.com)

MIRJANA ĐURIĆ

Independent researcher, Belgrade, [minadjuric12@gmail.com](mailto:minadjuric12@gmail.com)

MIRKO MAKSIMOVIĆ

Belgrade Waterworks and Sewerage, Kneza Miloša 27, Belgrade, [maksimovic.mirko@gmail.com](mailto:maksimovic.mirko@gmail.com)

**Abstract:** The attention in the work is focused on the strength analysis of the vital elements of the aircraft structure. Special attention is focused on defining critical locations from the aspect of possible failures during exploitation. Then, initial damage in the form of initial cracking is assumed in the defined critical zone. The assumed crack sizes are in accordance with the recommendation on allowable damages. For the cracks defined in this way and the corresponding load spectrum, the propagation of the crack until the effective fracture is analyzed. Different crack propagation laws can be used for this purpose. In this paper, the various models were used. The finite element method (FEM) was used for the structural analysis, where special 6-node singular finite elements were used around the crack tip. Since there are always peaks within the real load spectrum, they are modeled using in-house software. This paper deals with research in the domain of estimating the failure of aircraft structures in critical locations under the effect of cyclic loads. The main goal is to provide an efficient computation method. The previous method is illustrated on the analysis of the failure of parts of vital connections of aircraft structures.

**Keywords:** aircraft, spectrum loading, overload effects, residual fatigue life estimation

### 1. INTRODUCTION

In general, failures occur when a component or structure is no longer able to withstand the stresses imposed on it during operation. Commonly, failures are associated with stress concentrations, which can occur for several reasons including:

- Design errors, e.g. the presence of holes, notches, and tight fillet radii;
- The microstructure of the material may contain voids, inclusions etc.;
- Corrosive attack of the material, e.g. pitting, can also generate a local stress concentration.

From our records and case histories data, an assessment can be made of the frequency of failure modes (Table 1). This reveals that the incidence of fatigue failure dominates the distribution in aircraft. This would suggest, therefore, that fatigue is the predominant failure mode in service. The detection and rectification of corrosion damage on in-service aircraft, however, consumes more effort than the repair of fatigue cracking. The high occurrence of fatigue failure observed probably reflects the destructive nature of this failure mode, while corrosive attack is generally slower than fatigue, and

usually more easily spotted and rectified during routine maintenance. Fatigue is a process whereby cracking occurs under the influence of repeated or cyclic stresses, which are normally substantially below the nominal yield strength of the material. Components that fail by fatigue usually undergo three separate stages of crack growth, which are described as follows:

- Initiation of a fatigue crack. This can be influenced by stress concentrations such as material defects or design.
- Propagation of the fatigue crack. This is progressive cyclic growth of the crack.
- Final sudden failure. Eventually, the propagating crack reaches a critical size at which the remaining material cannot support the applied loads and sudden rupture occurs. Fatigue failures generally leave characteristic markings on the fracture surface of cracks from which the failure investigator can deduce a great deal of information. The most obvious are the classic 'beach marks', which are commonly observed macroscopically. Beach marks indicate successive positions of the advancing crack front and are usually the first telltale signs that the mode of crack growth is fatigue. Fatigue fractures tend to be relatively smooth near the origin and show slight roughening of the surface as the

crack progresses. There tends to be little or no macroscopic ductility associated with fatigue cracking.

Detailed examination of the fracture surface in a scanning electron microscope (SEM) usually shows evidence of fatigue estimations (dependant on the material), which represent one cycle of load and crack propagation. If the magnitude of load cycle remains constant, the striations normally appear closer near the origin, gradually increasing in spacing as the crack front progresses due to the increasing stress at the crack tip.

By taking measurements of striation spacing at various distances from the origin to the end of the crack, it is possible to estimate the total number of load cycles to cause failure. If the cause of the loading can be determined, the number of cycles to failure can then be used to estimate the time required for crack growth.

Fatigue cracking is the most common cause of structural failure in aircraft, even though the laboratory fatigue behavior of most metals and alloys is well understood.

Materials and their design can be taken into consideration so that the probability of fatigue cracks occurring can be reduced, but it is often the case that the possibility cannot be removed completely. Therefore many aircraft structural components are designed with a safe or inspection-free life, below which fatigue cracking should not be a cause for concern. The fact that fatigue failures still occur, however, indicates the complex nature of this problem. There are many variables that influence fatigue, some of which are the mean stress, peak stress, frequency of loading, temperature, environment, material microstructure, surface finish, and residual stresses. Many of these factors are taken into account when determining the safe life of a component and, therefore, the majority of fatigue failures in aircraft causing catastrophic failure tend to be those that initiate as the result of unforeseen circumstances.

Material surface defects such as forging laps or surface cracking can increase the local stress, producing a concentration at these points that could initiate fatigue much quicker than would be expected. However, many aircraft components are thoroughly inspected by non-destructive techniques after manufacturing and these types of defects are usually detected and rectified. Stress concentrations caused by surface defects such as scratches and wear tend to be more common as these may not be present at build, but can be introduced during service. Another common cause of stress concentration is corrosion, which can lead to fatigue crack initiation.

Table 2 shows a summary of the common fatigue crack initiation sites observed in aircraft [1,2] that have led to accidents.

Ductile or overload failure occurs when a material has been exposed to an applied load at a relatively slow rate to the breaking point of the material. This results in a ductile fracture of the material, with the fracture surface exhibiting tearing of the metal and plastic deformation.

On rapid application of a load, fast fracture or brittle failure can occur. Microscopic examination of brittle fractures reveals intergranular or transgranular facets on the fracture surface.

Corrosion is the chemical degradation of metals as a result of a reaction with the environment. It usually results

in failure of components when the metal wastes to such an extent that the remaining material cannot support the applied loads or the corrosion renders the component susceptible to failure by some other mode (e.g. fatigue).

Extensive work has been carried out on the rates and types of corrosion observed in different materials so that selecting a suitable material in terms of corrosion resistance for a known environment is relatively straightforward. In aircraft structures, however, the strength to weight ratio can be a more desirable property than corrosion resistance and in these circumstances the most suitable material cannot always be used. In cases like this, measures must be taken to limit corrosion, which most commonly involve the use of a coating, such as a paint system, to act as a barrier to the environment. There are various forms of corrosion that exist, each of which poses different problems to aircraft structures.

The most common types of corrosion observed are discussed below:

- Uniform corrosion, as its name suggests, is corrosion that occurs without appreciable localized attack, resulting in uniform thinning.
  - Pitting corrosion is a localized form of attack, in which pits develop in a material causing localized perforation of the material. Pitting corrosion occurs when one area of a metal surface becomes anodic with respect to the rest of the surface of the material. The pits formed by this type of attack are generally very small and, therefore, difficult to detect during routine inspection. Pitting attack can cause failure by perforation with very little weight loss to the material.
  - Crevice corrosion occurs when localized changes in the corrosive environment exist and lead to accelerated localized attack. These changes in the localized corrosive environment are generated by the existence of narrow crevices that contain a stagnant environment, which results in a difference in concentration of the cathode reactant between the crevice region and the external surface of the material. Crevices can be formed at joints between two materials, e.g. riveted, threaded, or welded structures, contact of a metal with a nonmetallic material, or a deposit of debris on the metal surface.
  - Galvanic corrosion occurs when dissimilar metals are in direct electrical contact in a corrosive environment. This results in enhanced and aggressive corrosion of the less noble metal and protection of the more noble metal of the bimetallic couple. This type of corrosion can be recognized by severe corrosion near to the junction of the two dissimilar metals, while the remaining surfaces are relatively corrosion-product free. Galvanic corrosion is generally a result of poor design and materials selection.
  - Stress corrosion cracking is a mechanical-environmental failure process in which tensile stress and environmental attack combine to initiate and propagate a fracture. Failure by stress corrosion cracking is frequently caused by simultaneous exposure to an apparently mild chemical environment and to a tensile stress well below the yield strength of the material. The stress required for failure can originate from in-service conditions or from residual stress during component manufacturing.
- Hydrogen embrittlement is a failure process that results from the retention or absorption of hydrogen in metals,

usually in combination with applied tensile or residual stresses. It most frequently occurs in high-strength steels (>1100 MPa). For aircraft components, the common source of hydrogen embrittlement is hydrogen absorption during manufacturing processes such as pickling and electroplating.

## 2. ESTIMATION OF TOTAL FATIGUE LIFE

During exploitation, aircraft are exposed to cyclic loads of constant amplitude and spectrum. Basically, for life estimates during exploitation, life estimates are made until the appearance of initial damage from one side, as well as the remaining life estimate, i.e. In the presence of damage

### 2.1 Assessment of the age until the appearance of initial damage.

The Smith-Watson-Topper relation SWT relation was used to estimate the age until the appearance of initial damage. The Smith-Watson-Topper (SWT) relation for describing the low-cycle fatigue curve has the form:

$$P_{SWT} = \sqrt{\sigma_{max} \frac{\Delta \varepsilon}{2} E} = \sqrt{(\sigma'_f)^2 (N_f)^{2b} + E \sigma'_f \varepsilon'_f (N_f)^{b+c}} \quad (4)$$

whereby the influence of medium stress is included via dependence

$$\sigma_{max} = \sigma_m + \frac{\Delta \sigma}{2} \quad (5)$$

The notation  $P_{SWT}$  in (4) refers to the Smith-Watson-Topper parameter. The relation SWT (4) defines that there is no fatigue damage in situations where the value of the maximum stress,  $\sigma_{max}$ , is zero or has a negative value, which is not entirely true.

### 2.2 Estimation of remaining life using the strain energy density method

In this work fatigue crack growth method based on energy concept is considered and then it is necessary to determine the energy absorbed until failure [3-6]. This energy can be calculated by using cyclic stress-strain curve. As a result the energy absorbed until failure become [6]:

$$W_c = \frac{4}{1+n'} \sigma'_f \varepsilon'_f \quad (1)$$

where  $\sigma'_f$  is cyclic yield strength and  $\varepsilon'_f$  - fatigue ductility coefficient. Fatigue crack growth rate can be obtained in the next form [7]:

$$\frac{da}{dN} = \frac{(1-n')\psi}{4E I_n' \sigma'_f \varepsilon'_f} (\Delta K_I - \Delta K_{th})^2, \quad (2)$$

where  $\Delta K_I$  is the range of stress intensity factor,  $\psi$  -

constant depending on the strain hardening exponent  $n'$ ,  $I_n'$  - the non-dimensional parameter depending on  $\Delta K_{th}$  is the range of threshold stress intensity factor and is function of stress ratio i.e.

$$\Delta K_{th} = \Delta K_{th0} (1-R)^\gamma, \quad (3)$$

$\Delta K_{th0}$  is the range of threshold stress intensity factor for the stress ratio  $R = 0$  and  $\gamma$  is coefficient (usually,  $\gamma = 0.71$ ). Equation (2) enables us to determine crack growth life of different structural component. Very important fact is that equation (2) is easy for application since low cyclic material properties ( $n'$ ,  $\sigma'_f$ ,  $\varepsilon'_f$  are used as parameters.

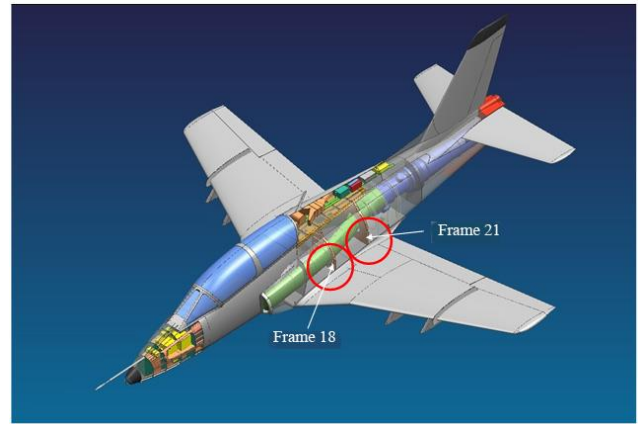


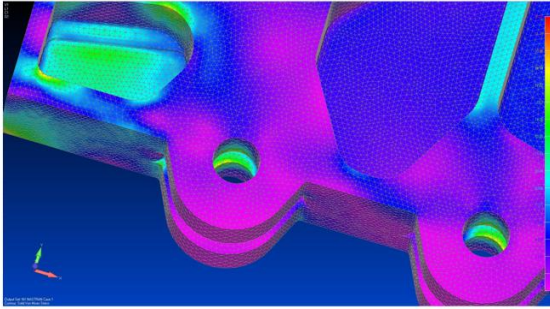
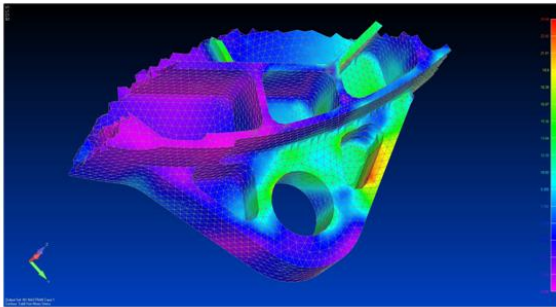
**Fig.1** Aircraft structure

Figures 2 and 3 show the results of the structural analysis, in this case the stress states, which were determined by the precise structural analysis based on FEM. These are basically the critical zones on the aircraft, the failure of which could lead to the effective breakage and even the loss of the aircraft itself.



**Table 1:** Wing-fuselage test results

Spec. No.	Experimental results		Numerical estimation of total life
1	788	$\bar{N}_{bl} = 806.85$  (Middle value )	$N_{bl,i}=505$ $N_{bl,p}=52$  $N_{bl,t}=557$
2	988		
3	946		
4	892		
5	686		
6	612		
7	736		

**Fig. 2** The stress state in the forward connection of the**Fig. 3** The stress state in the rear connection of the wing fuselage using FEM

### 3. VALIDATION OF CALCULATION RESULTS

In order to validate the results of the assessment of the total life under the influence of the load spectrum, a part of the connection of the wing fuselage of the ORAO aircraft is shown. On Fig. 4 shows part of the wing-fuselage connection of the aircraft. This part of the wing-fuselage connection was tested under static and dynamic loads.

**Fig. 4** Part of the wing fuselage connection**Fig. 5** The fracture appearance of the wing-fuselage connection part after the fatigue test

Table 1 shows the complete results of the examination of the part of the wing-fuselage connection of the aircraft, as well as comparisons with the results of the calculation assessment. In Table 2, for the experimental result for the number of blocks, the mean value of the number of blocks is taken, where one block corresponds to 50 hours of aircraft flight. In that case, the difference between the calculation estimate of the total lifetime and the experiment is about 18.6%, which can be considered that the calculation estimate of the lifetime is slightly conservative.

**Table 2:** Estimation of life to occurrence of wing-fuselage damage according to (SWT) and Morrow

Smear	Smear1	Smear2	Smear3	Smear4	Smear5	Smear6	Smear7	Smear8	Smear9	Smear10	Smear11	Smear12	Smear13	Smear14	Smear15	Smear16	Smear17	Smear18	Smear19	Smear20	Smear21	
58.800	147.200	n1	305																			
41.000	205.500	n2	245																			
28.000	279.800	n3	133																			
13.300	313.900	n4	58																			
6.150	356.500	n5	13																			
3.075	395.400	n6	7																			
1.538	436.500	n7	13																			
0.769	473.800	n8	50																			
0.385	509.500	n9	133																			
0.192	546.500	n10	245																			
0.096	584.000	n11	305																			
0.048	621.500	n12	0																			
0.024	659.000	n13	0																			
0.012	696.500	n14	0																			
0.006	734.000	n15	0																			
0.003	771.500	n16	0																			
0.0015	809.000	n17	0																			
0.00075	846.500	n18	0																			
0.00038	884.000	n19	0																			
0.00019	921.500	n20	0																			
0.000095	959.000	n21	0																			

$N_{bl, i} = 480$  (SWT) (Calculation estimate of the life until the appearance of initial damage.)

$N_{bl, i} = 505$  (Morrow) (Calculation estimate of the life until the appearance of initial damage.)

**3.1 Estimate of the remaining life**

In addition to the estimate of the life until the appearance of the initial damage, the results of which are for the part of the wing, under the influence of the load spectrum determined in the previous point and shown in Table 2, it is necessary to make a calculation assessment of the remaining life, that is, during the crack propagation. To estimate the remaining life, it is necessary to assume initial damage in the form of surface cracking. Based on the maximum stress value, determined by the elastic-plastic analysis of FEM, the critical position was defined during exploitation.

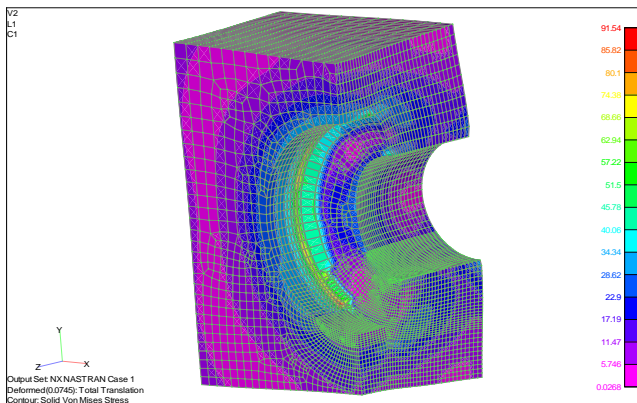


**Fig. 6** Distribution of the stress state [MPa] for a crack depth of 3.5 mm

Breakages of vital aircraft links during flight often lead to the loss of the aircraft itself. In order to avoid catastrophic breaks, it is necessary to pay special attention to the critical areas of the aircraft during the design, as well as the experimental verification of the strength of the aircraft structure itself. As a rule, these are vital connections such

as the wing-fuselage connection, fuselage-fuselage connection, tail-fuselage connection, and a number of others whose failures lead to catastrophic fractures. One of the important factors for prevention is a precise and detailed analysis of stress conditions in the aircraft structure. For this purpose, as illustrated in the paper, the finite element method (FEM) is used with one and precisely determined mechanical characteristics of the material. Due to efficiency and economy, the low-cycle fatigue characteristics of the material are used in the work, both for the assessment of the life until the appearance of initial damage and after the assessment of the remaining life.

**4. CONCLUSION**

The attention in the work is focused on the analysis of fractures in aircraft structures or, more precisely, how to prevent fractures during exploitation. Breakages of vital aircraft links during flight often lead to the loss of the aircraft itself. In order to avoid catastrophic fractures, it is necessary to pay special attention to the critical areas of the aircraft during the design, as well as the experimental verification of the strength of the aircraft structure itself. As a rule, these are vital connections such as the wing-fuselage connection, fuselage-fuselage connection, tail-fuselage connection, and a number of others whose failures lead to catastrophic fractures. One of the important factors for prevention is a precise and detailed analysis of stress conditions in the aircraft structure. For this purpose, as illustrated in the paper, the finite element method (FEM) is used with one and precisely determined mechanical characteristics of the material. Due to efficiency and economy, the low-cycle fatigue characteristics of the material are used in the work both for the assessment of the life until the appearance of initial damage and for the assessment of the remaining life. Figures 2 and 3 show the results of the structural analysis, in this case the stress states, which were determined by the precise structural analysis based on FEM. These are basically the critical zones on the aircraft, the failure of which could lead to the effective breakage and even the loss of the aircraft itself.

**Acknowledgement:**

This research has been supported by the research grant No. 451-03-66/2024-03/ 200066 of the Ministry of Science, Technological Development and Innovation of the Republic of Serbia.

**References**

- [1] Maksimovic S., Maksimovic K., Improved Computation Method in Residual Life Estimation of Structural Components, Theoretical and Applied Mechanics, Special Issue- Address to Mechanics, Vol. 40, No. 2, pp. 247-261, Belgrade, 2012.
- [2] Elber, W, in Damage Tolerance in Aircraft Structures, ASTM STP 486, ASTM, 1971, 230-242..
- [3] Maksimović S., Numerical analysis of aircraft structure strength from the standpoint of fatigue and fracture mechanics, Naučnotehnička informacija, Military Technical Institute, Vol. 38, No. 11, 2004 (ISSN: 1820-3418)
- [4] Boljanović S., Maksimović S., Carpinteri A., Fatigue-resistance evaluations for mixed mode damages under constant amplitude and overload, Theoretical and Applied Fracture Mechanics (2020), <https://doi.org/10.1016/j.tafmec.2020.102599>
- [5] Vasovic I., Maksimovic M., Maksimovic K., RESIDUAL FATIGUE LIFE ESTIMATION OF STRUCTURAL COMPONENTS UNDER MODE-I AND MIXED MODE CRACK PROBLEMS, International Conference of Experimental and Numerical Investigations and New Technologies – CNN TECH 2019, 02-05 July 2019, Zlatibor.
- [6] MSC/NASTRAN software code



## SMALL FIXED-WING UAV PRECISION AERIAL DROP CAPABILITY DEVELOPMENT

VUK ANTONIĆ

Military Technical Institute, Belgrade, [vukantonik@gmail.com](mailto:vukantonik@gmail.com)

MILENKO TRIFKOVIĆ

Military Technical Institute, Belgrade, [milenkot@gmail.com](mailto:milenkot@gmail.com)

VOJIMIR MOLOVIĆ

Military Technical Institute, Belgrade, [vojamolovic@gmail.com](mailto:vojamolovic@gmail.com)

**Abstract:** *Small fixed-wing unmanned aerial vehicles (UAVs) have proven themselves as invaluable assets for reconnaissance and surveillance missions. Their improvement and further development most often focuses on improved endurance, datalink range, camera capabilities etc. This paper presents a modular approach to “Vrabac” UAV improvement by integrating wing payload extensions, enabling precision aerial drop capabilities. This enables precise delivery of lethal or non-lethal payloads from the UAV at pre-determined coordinates or at a visually acquired target. Precision aerial drop software module is presented, focusing on the automated payload drop algorithm with continually calculated impact point prediction (CCIP) and UAV guidance to the continually calculated release point (CCRP). The chosen ballistics computation and control system implementation evaluates UAV flight parameters, wind direction and velocity, terrain profile etc. to achieve a precise target strike. Simulated results with a parameter sensitivity analysis, as well as field test results are presented.*

**Keywords:** *Unmanned Aerial Vehicle, Precision Drop, Control Design, Modular Design.*

### 1. INTRODUCTION

Small fixed-wing Unmanned Aerial Vehicles (UAVs) have proven themselves as invaluable assets for both military and civilian purposes in various missions such as reconnaissance, surveillance, target acquisition, search and rescue, surveys, mapping etc. Extending possible use cases consists of various performance improvements and new mission types. One of perspective mission types is payload delivery.

Payload drop use cases have been performed very successfully on an operational level for critical supply and medical deliveries in civilian use cases and are well proven [1]. The use of parachute delivery is useful for sensitive payload delivery (medical supplies etc.) but have a disadvantage of being relatively imprecise (parachute opening, wind effects etc.), with a total error, depending on dropping altitude of few tens of meters.

Precise payload delivery can be performed by utilizing either active payload guidance (GNSS or camera-guided) or precision delivery techniques and algorithms and non-guided payloads.

Non-lethal payloads such as ammunition, critical supplies (medical or technical) usually require soft-landing and parachute delivery. Depending on circumstances, precision of few tens of meters is usually sufficient. However, more precise delivery can be beneficial in time-

critical, urban or combat scenarios.

Lethal payloads that can be carried on a small fixed-wing UAV have to be very lightweight. Most attempts are based on regular 40 mm grenades or similar warheads (200g - 300 g), thus having a limited lethal radius of 5-8 m. This requires precise delivery of these non-guided munitions.

Use of hovering multi-rotor UAVs enables stable conditions and adjustment but have limitations, as they are relatively loud, vulnerable and slow to react, with much lower endurance, carrying capacity and range than fixed-wing systems.

Fixed-wing platforms present unique challenges for implementation, since these low-velocity munitions are greatly affected by wind, UAV speed and altitude above ground. The targeting software needs to account for all these factors in order to perform a successful strike. The implementation on the UAV needs to ensure safety, minimize effects on the primary reconnaissance role of the UAV and be flexible for further development and upgrades for various payload types.

This paper shows one such modular implementation on the Vrabac (Sparrow) reconnaissance UAV developed at the Military Technical Institute, Belgrade.

## 2. SYSTEM INTEGRATION

Sparrow UAV (shown on Fig. 1) is of conventional design with electric tractor propeller propulsion system. It is designed for hand-launch and parachute/airbag landing. It is the first UAV in service in Serbia to feature fully domestically developed avionics and software. Due to hundreds of flight tests performed and well understood UAV capabilities and limitations it was deemed easy for integration of additional payloads and modifications.

The requirements consisted of carrying four 40 mm bomblets, based on 40 mm grenade munitions. The bomblets feature custom designed arming mechanisms and the firing charge replaced with a simple 3D printed tail fin. The system needs to be safe and easy to use. It has to avoid compromising the basic unarmed mission capability. The required precision is 10 m, to ensure destruction of an unarmored target (light vehicle, infantry etc.) with the release of four bomblets, taking into account their dispersion.

### 2.1. Modular design

The “Sparrow” UAV is designed for easy transportation in a backpack-type case, with easy and quick toolless field assembly and disassembly. As such, it consists of 6 components (fuselage, tail boom with the vertical stabilizer, horizontal stabilizer, central and two outer wing sections). Wing-mounted weapon stores are an obvious choice due to the parachute landing and general UAV design.

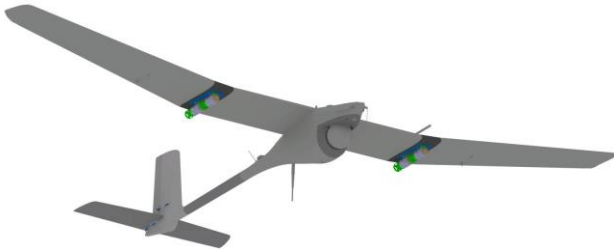


**Figure 1.** Sparrow UAV with wing extensions (marked in darker color) and bomblets

Wing extensions (shown with darker color on the UAV on Fig. 1 and independently on Fig. 2) were designed in order to facilitate pylon integration with minimal effect on the basic unarmed configuration. The extensions provide an increase in wing area from 0,75 m<sup>2</sup> to 0,87 m<sup>2</sup>, as such keeping most aerodynamic parameters unchanged (lift coefficient on cruise, stall speed, controls deflections etc.), which maintains good stability and efficiency with a significantly increased takeoff weight. The weight of the basic (unarmed) Sparrow UAV with the optoelectronic payload and battery is 8,3 kg. The armed configuration, with the wing extensions, weapon pylons and four 40 mm bombs weighs 9,9 kg (0,9 kg being the weapons themselves). The defined loiter, cruise and fast cruise speeds (15, 19 and 25 m/s, respectively) for the Sparrow UAV are kept the same as with the lighter reconnaissance configuration.

By mounting the wing extensions and bombs the UAV is

simply converted into the armed configuration. No other modifications, setup or setting changes are required.

### 2.2. Safety design

Safety is ensured by the newly designed arming mechanism and its integration with the wing pylons. The bomblet is secured for transportation with dual safety pins, ensuring that the mechanism cannot get to the armed position. One of these pins is removed when the bomblet is mounted on the pylon and interfaced with the pin on the pylon itself, thus maintaining the double-safety design. The second pin is removed just before takeoff. Thus, during flight, the bomblet is still secured by the safety pin interfaced with the wing pylon.

The system is robustly designed and tested for safety in the case of UAV crash on launch or other in-flight failure. In the case of any in-flight failure and crash of the UAV the bomblet remains unarmed and secured on the pylon. The pylon release mechanism is made of a combined plastic and metal design. All bomblet interfacing components are metal and the mechanism is robust and immune to acceleration-related bomb release.

The bomblets are mounted in pairs, two under each wing, one behind the other. The mechanism ensures that the rear bomblet is always released first, thus avoiding the possibility of in-flight collision.

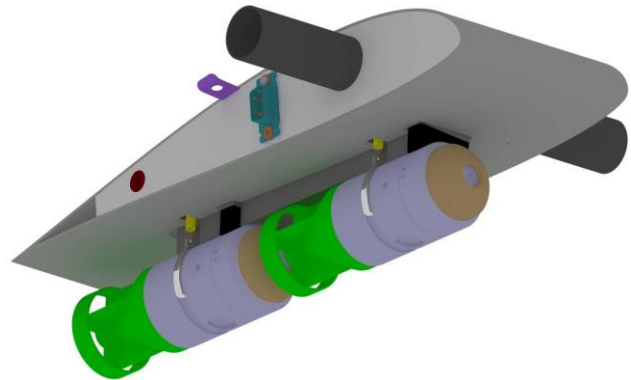


**Figure 2.** Wing extension with bomblets

The weapon pylon features micro-switches for payload release indication, with a secondary role of easier payload installation. It can be commanded to release bomblets sequentially, in pairs (with a defined delay) or independently, as such it can be considered as a smart weapon store solution. This way the required target area cover can be optimized.

The mechanism is servo-actuated, with known movement speed and delay, which is an important factor for achieving precision bomblet delivery, since a delay of 0.2 to 0.3 seconds leads to an additional 4 – 6 m of error. Thus, the system takes this delay into account when calculating impact point.

This way of integration is flexible and capable of supporting multiple different payload combinations, in addition to the presented ones, if their parameters are known and programmed into the system.

### 3. TARGETING AND SOFTWARE IMPLEMENTATION

The software component of the system consists of two components: the component running on the UAV flight control computer and the component running on the GCS (Ground Control Station).

The UAV flight control computer is developed at the Military Technical Institute (VTI) and based on dual ARM Cortex M7 series microcontrollers (STM32H743) running at 480 MHz, with independently developed sensor, navigation and flight control software (written in the C programming language). It has the capability to read a Digital Elevation Map (DEM) of the area surrounding the UAV, enabling the use of enhanced safety features (terrain avoidance), target coordinate acquisition (without the use of a laser rangefinder) and ballistics computation outlined in this paper. The flight control computer runs the guidance and control loops necessary for precise payload delivery. This is tied-in with regular waypoint or camera-guided navigation

The Ground Control Station is based on a ruggedized Windows laptop (Panasonic CF-33). The VTI-developed GCS software (written in the C++ programming language) is responsible for the graphical control interface, map, video display, communication, army C2 system integration etc.

Both software components for precision strike capability (on the UAV and GCS) run whenever the weapons subsystem is armed by the user. The system has two usage methods, semi-automated CCIP (Continuously Calculated Impact Point) and fully automated CCRP (Continuously Calculated Release Point).

The CCIP method does not need any target data, but only computes the bomblet impact point (if released at the current UAV position) and displays it to the user. The impact point is displayed on GCS map display and overlaid on the video feed from the camera (for visual targeting). In this mode it is the users responsibility to manually control the release of the bomblets and ensure proper guidance of the UAV (preferably in camera-guided mode or by moving the current waypoint position).

The CCRP method performs the same actions as CCIP, but requires the target coordinates, thus computing the geographic position the UAV needs to get to in order for the bomblets released there to hit the target. This position is then transferred to the flight control guidance and navigation algorithm and the UAV performs the attack autonomously. The bomblets are only dropped if the UAV gets within the predefined position envelope (acceptable position error envelope, settable by the user). The user can view the current estimated impact point in the same way as in CCIP mode and has the power, at any time, to command immediate payload drop manually or disarm the system (cancel the attack).

#### 3.1. Ballistics computation

The software implementation is based on continuous

bomblet flight path computation based on multiple variables:

- UAV flight speed
- UAV climb rate
- Wind speed
- Wind direction
- UAV course (track over ground)
- UAV altitude
- Terrain elevation profile
- Payload release delay
- Payload mass
- Payload aerodynamic coefficients

The ballistics software runs whenever the software is armed for an attack on the target (arming requires user action). The simple 3-degree-of-freedom (DOF) oblique shot calculation with drag and wind effects runs iteratively, calculating the bomblet flight path from the current position (obtained from the UAV navigation data), taking into account all the above defined variables. One similar approach can be seen in [2], more detailed model in [3].

The initial projectile position and velocity vectors are the UAV position and velocity. After release, an initial short transition period takes into account various non-linear effects, such as projectile stability, lift and pitch/sideslip moments etc. in order to improve precision and, simultaneously, simplify the computation (avoid the use of computationally intensive 6 degree-of-freedom models), since after the initial short period the angles of attack and sideslip are very small, as the bomblet velocity becomes dominant over the initial velocity. The wind velocity and direction is estimated by the UAV and is critical for precise delivery.

At every iteration the altitude of the bomblet above ground is checked (using DEM – Digital Elevation Model, i.e. 3D map). When the bomblet arrives to the ground (within the defined threshold) the final path parameters are output to the autopilot flight control logic and to the user interface.

A test of the software with real input data (release point, true impact point, aerodynamic and atmospheric parameters) is shown in Fig. 3 (made using MATLAB). The UAV flown path is shown in pink, with the calculated bomblet path shown in light blue color. Actual bomblet impact photo corresponding to this is shown in Fig. 4, showing excellent agreement between the prediction and result.

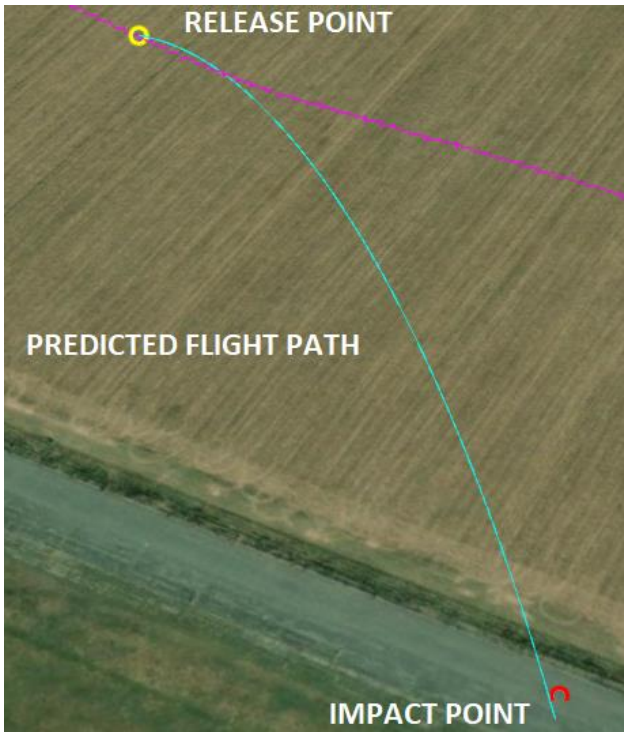


Figure 3. Flight test result with bomb predicted flight path



Figure 4. Actual impact for Fig. 5 (2-5 m error)

**3.2. Parameter sensitivity and precision**

Precision can only be achieved under correct circumstances. The best computation method will fail if incorrect data is input. Thus, sensor precision and computation parameter sensitivity need to be compared in order to assess the reliability of the computation. In accordance with this, correct computation iteration loop times have to be chosen (in order to maintain precision and minimize computational time and cost). The table below shows calculated bomblet flight path distance (X) and cross-track (Y) for changing UAV airspeed, climb rate, altitude, and wind speeds.

From this data we can estimate the required precision of input data for the calculation. UAV altitude above ground is not overly critical, with path length being around 20 times less sensitive than with regard to changes in airspeed (as shown on Fig. 5) or wind. The reason for this is the fact that, for the usable altitudes (150 m and above), the final flight path angle is already quite large, thus reducing the sensitivity to these parameters. This means that acceptable precision can be kept even when used

from higher altitudes (300-500 m) above ground.

In contrast, knowing airspeed, wind direction and velocity with enough precision is essential, since even a weak wind (1-2 m/s), if unaccounted for, has a very significant contribution and can cause the bombs to miss the target completely.

Table 1. Parameter sensitivity

Parameter	Values	X[m]	Y[m]
V <sub>x</sub> Airspeed	19 ± 1 m/s	113.8 ± 5.8 m	0 m
V <sub>z</sub> Climb rate	0 ± 1 m/s	113.8 ± 1.7 m	0 m
W <sub>x</sub> Headwind	0 ± 1 m/s	113.8 <sup>+3</sup> -7.9 m	0 m
W <sub>y</sub> Crosswind	0 ± 1 m/s	113.8 - 1.6 m	0 ± 3.9 m
H Altitude	200 ± 1 m	113.8 ± 0.25 m	0 m

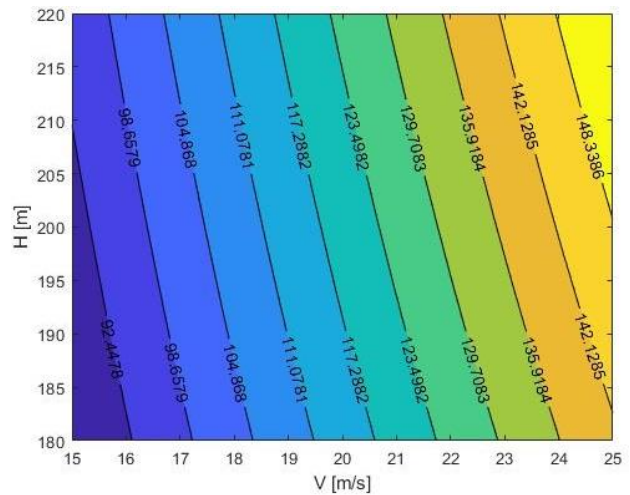


Figure 5. Flight path distance with changing airspeed and altitude

**3.3. User interface implementation**

The user has control of the targeting and bomb release at all times. The user control panel displays relevant data and enables the user to arm and disarm the system, release the payload on command, set the payload release threshold for the automated mode. The control panel also facilitates individual bomblet control, where they can be released independently. This feature is also used for pre-flight preparation and weapon loading.

The map displays all the regular information for the operation of the “Sparrow” UAV system. The target is defined as a special waypoint, with two possible modes (waypoint actions).

The bombing mode performs all the computations

mentioned previously, while the payload drop mode simply releases the payload when reaching the waypoint.

While the weapons system is armed the impact point position on the map is continuously updated and saved in the targets list with a CCIP designation. This list can be saved for post-flight analysis.

The video feed display takes in additional data, such as camera attitude relative to the UAV (azimuth, elevation), camera fields of view (horizontal and vertical, dependent of zoom level) and performs the world-to-screen coordinate transformation (geographic position transformation into video display pixel coordinates).

At the moment of payload release, a screenshot of the map and video feed is saved automatically for post-flight analysis (Fig. 6) and comparison with actual strike locations (Fig. 7).

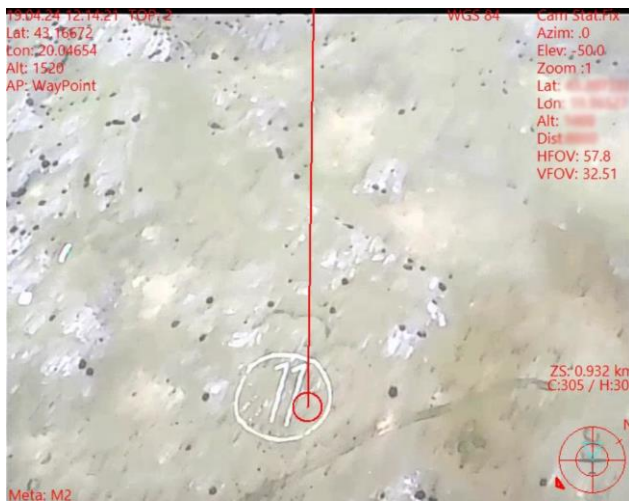


**Figure 6.** Computed impact point video display



**Figure 7.** Actual impact point for Fig. 6

#### 4. FLIGHT TESTING

The system was extensively tested in flight, as well as for safety in case of launch failure. A launch failure test with a catapult launch system with a mockup is shown in the figure below.

Flight testing was performed on the Kovin airfield (with dummy and shock bomblets), Nikinci and Pasuljanske Livade test and training ranges (dummy, shock-flash and live rounds).

The initial tests with dummy munitions were performed using the hand-launch method, proving the capability to successfully hand-launch the aerial vehicle even with a weight of 10 kg.

For safety reasons, for tests with shock-flash and live

munitions, the Sparrow test UAV was equipped with catapult interface pins and a bungee catapult launcher was used (Fig. 8). The catapult used was from a significantly larger and faster UAV and thus much bigger than needed for the Sparrow. However, based on launching process analysis (similar to that in [4]) bungee cords were replaced and a Sparrow UAV adapter constructed. On two of such tests the UAV survived (with minor damage) two unsuccessful launch attempts, both due to the flaws in the catapult itself. On both occasions, the bomblets remained on their pylons and were secured and removed properly, thus further proving the correct approach with regards to the safety of the system.



**Figure 8.** Sparrow UAV catapult launch

The UAV was also flown with the release of only two bomblets (one wing remaining) and it successfully compensated for the asymmetric loading [5].

UAV landings were performed with the two or all four bomblets remaining on the wing, with good results. However, this should be avoided, since a higher probability of damage is to be expected, especially in more difficult terrain conditions.

Dummy bomblet tests were performed with a colored pigment marker infill. After initial tests, modification of the system were made in order to improve precision, reliability and practical usage, after which, the system was mostly tested with shock-flash munitions, with some live munition tests performed (Fig. 9).



**Figure 9.** Live munitions test

In total more than 30 test flights were performed, dropping bombs from altitudes of 150 – 250 m, with bombs falling within the required 10 m area. The dispersion was in the range of 2 - 4 m. The path calculation was proven as accurate, with most deviations from target being correctly predicted by the algorithm and caused by wind gusts and UAV movement in the lateral direction (as seen in Fig. 3 and 4).

The system was tested with wind speeds ranging from 0



m/s to 7 m/s at altitude, with the system compensating correctly, but the dispersion increasing with increased wind speeds. With further improvement in the wind estimation algorithm (improved crosswind estimation) and lateral flight control compensation (gusts), it is possible to improve these results further.

## 5. CONCLUSION

The results of the tests have proven the viability of the concept. The UAV with the added weight and wing extensions performed excellently and the catapult integration, after some initial problems were corrected, was successful and reliable.

The targeting software and path estimation have proven reliable and practical. The results of the tests have demonstrated the required precision and accuracy.

Safety of the system was proven both for the bomblets independently and as part of the system, with intentionally mis-launching a dummy structure and during two mishaps in early development.

Future work will aim to further improve the algorithm and lateral control to better correct for cross-wind and to prepare the system for series production as an add-on kit for equipping already produced and future Sparrow UAV systems.

Further development of additional payload types and integration on larger UAVs, capable of carrying heavier payloads, is also possible.

[6]

## References

- [1] P.KREMER, A.LEYZEROVSKAYA, S.DUBOIS, J.LIPSITT, F.HARUNA, O.LEBED: *Bringing underserved communities life-saving aid through aerial logistics*, Science Robotics, Volume 8, No. 85 (2023)
- [2] SIRI H. MATHISEN, VEGARD GRINDHEIM, TOR A. JOHANSEN: *Approach Methods for Autonomous Precision Aerial Drop from a Small Unmanned Aerial Vehicle*, 20th IFAC World Congress, Volume 50, Issue 1 (2017)
- [3] G.KOWALECZKO, K.GRAJEWSKI, S.KOBIELA, R.KAZIMERCZAK, The Impact of standard deviation of wind on the bomb flight in atmospheric turbulence, Journal on KONBiN 2021, Vol. 51, Issue 2 (2021)
- [4] Z.NOVAKOVIĆ, Z.VASIĆ, I.ILIĆ, N.MEDAR, D.STEVANOVIĆ, *Integration of Tactical – Medium Range UAV and Catapult Launch System*, Scientific Technical Review, Vol. 66, No.4 (2016)
- [5] STOJAKOVIĆ, P.: *Analysis of the External Stores and Asymmetric Loads Influence on the Airplane Flight Dynamics*, PhD Thesis, University of Belgrade, Faculty of Mechanical Engineering, 2012.

## ANALYSIS OF THE RESCUE SYSTEM IMPLEMENTATION IN THE MEDIUM RANGE UAV

VANJA STEFANOVIĆ GOBELJIĆ  
Military Technical Institute, Belgrade, [vti@vti.vs.rs](mailto:vti@vti.vs.rs)

MIODRAG MILENKOVIĆ BABIĆ  
Military Technical Institute, Belgrade, [miodragmbm@yahoo.co.uk](mailto:miodragmbm@yahoo.co.uk)

MIHAILO ZDRAVKOVIĆ  
Military Technical Institute, Belgrade, [vti@vti.vs.rs](mailto:vti@vti.vs.rs)

### Abstract:

Modern approach to the aircraft design implies more often rescue system application to the aircrafts with human crew like gliders, ultra-light and trainer aircraft. Likewise different class of the UAVs is more commonly designed with the parachute, or parachute/airbag landing system. Whether the aim is to land UAV in a usual mission or to rescue the aircraft/UAV system and the crew, integration of the parachute system is the solution. This paper represents implementation analysis of the different rescue systems in the medium range UAV with the diverse aspects of limitations like minimum mass increase, limited free space in the UAV to place the system and minimum increase of the aerodynamic load.

**Keywords:** rescue system implementation, composite structure modification, aerodynamic load.

### 1. INTRODUCTION

Today's designers of aircrafts and unmanned aerial vehicles (UAV) are more than ever considering safety in the early stages of preliminary design. It can refer to minimal take-off weight which can guarantee the adherence to the levels of safety required by the airworthiness design requirement [1]. The easiest way to cover possible malfunction of any system is to integrate a parachute rescue system. It has become usual that we have in every newly design gliders, ultralights or trainer aircrafts and UAVs a recovery system. It can also be implemented later on in it. It is not a secret that there are plenty of research on subject to place a recovery system in a commercial airplanes [2]. Despite the parachute systems that are included within the UAVs for everyday landing at the end of the missions, we can confront, during exploitation, the situations that the aircraft is uncontrollable and you cannot, in many cases, prepare the aircraft for landing or to choose the position of the aircraft for activation of the rescue system. The parachute systems should be reliable, well integrated in the system and in the aircraft or UAV, in order to protect and rescue people's lives and to protect or minimize damage of expensive equipment of cutting-edge technology within it. Subject of this paper is medium range UAV Pegasus (figure 1), a multi-functional intelligence and reconnaissance UAV system with operational radius of 200 km and more.



Figure 1. Medium range UAV Pegasus

Table 1. UAVs technical characteristics

UAV Pegasus	
Power	38 KW (52 BHP) two-cylinder, two-stroke boxer
Propeller	wooden two blades, pusher
Wing span	7,068 m
Length	5,580 m
Max. payload weight	54 kg
Max. takeoff weight	265 kg
Max. speed	160 - 180 km/h+
Operational altitude	2000 -3000 m

Technical characteristics of Pegasus are given in Table 1. UAV can be used for intelligence, surveillance and reconnaissance missions, striking ground targets, target laser designation, damage effect assessment, etc. With 2

precision guided weapons, it is able of conducting air-to-ground accurate strike on the ground targets.

## 2. ANALYSIS OF THE RESCUE SYSTEM IMPLEMENTATION

Medium-range UAV *Pegasus* is fully composites structure with back position of an engine, to make it easy to service the UAV and to place the payload in the front part of the fuselage. Centre section of the wing is the integral part of the fuselage and, in the first phase of the project, it was reserved for integral tanks. In early phase of design, parachute rescue system was planned to be in the fuselage centre, rear of the fuel tanks. With a change of the concept and putting second tank in a fuselage, the space for integral tanks left empty, and the parachute system was left aside. Firstly idea for rescue system integration was replaced with a need for more fuel to increase endurance during two different missions. Expected endurance for the first reconnaissance mission is from 8-10 hours, and for the armed mission from 4-6 hours. With the new request for rescue system, we have analysed two different direction of parachute integration:

- 2.1 First version- the aim was to find a solution from our own capacity with collaboration between subcontractors from our country and
- 2.2 Second version-the aim was to find certified solution (ballistic parachute system) from abroad which is in use in many UAV and ultralight aircrafts.

Both versions demanded investigation of the market and parachute companies with certified systems that are already in use. In Table 2, data were presented for reviewed companies and products that were considered and analysed, and the depending on availability shortlist are marked with green.

**Table 2.** Considered solutions

Name of the system Characteristic	UAVOS 350 Parachute Systems	BRS BRS-6 System 600 Softpack	BRS BRS-6 System 600 VLS	Galaxy GRS GRS 4 270 60m2	Galaxy GRS GRS 4 270 60m2	PR 03-1 Kluz
Maximal UAV mass [kg]	360	272	272	270	270	
Type of the system	ballistic system	ballistic system	ballistic system	ballistic system	ballistic system	
Type of the package	hard	soft	hard	soft	OUT unit	soft
Mass of the system [kg]	5.7	9 (8.2)	11 (10.4)	8.8	9.6	6
Dimension of the system [mm]	210 x 210 x 510	280 x 250 x 150	460 x 293 x 191	195 x 245 x 305 (B1-B12)	Ø185x500 mm	420 x 240 x160
Maximal operational opening dynamic shock at VNE and MTOW				14.5	14.5	
Average UAV horizontal speed [m/s]	up to 6			6.6	6.6	
Average UAV vertical speed [m/s]						
Nominal parachute diameter [m]		8.2	8.2	7.2	7.2	
Maximal airspeed for usage [km/h]		222		230	230	
Parachute surface area [m <sup>2</sup> ]	56	53.1		60	60	45.5
System volume [l]	22.5	10.50		14.6		16.2
System life-cycle (repacking)	10 usage- (12 months)	24 years		6 years for ballistic system	6 years for ballistic system	

### 2.1. First approach

Knowing that maximum descending speed should be less than 7 m/s for the safe landing of the aircraft, and for the mass of 265 kg, it was necessary to ensure parachute with diameter at least 60 m<sup>2</sup>. There was no enough free space inside the UAV for a parachute, with that area, to be placed. First approach lead us to consider the only free space in the UAV, which is centre section of the wing, with free volume two times of 15 l (figure 2).

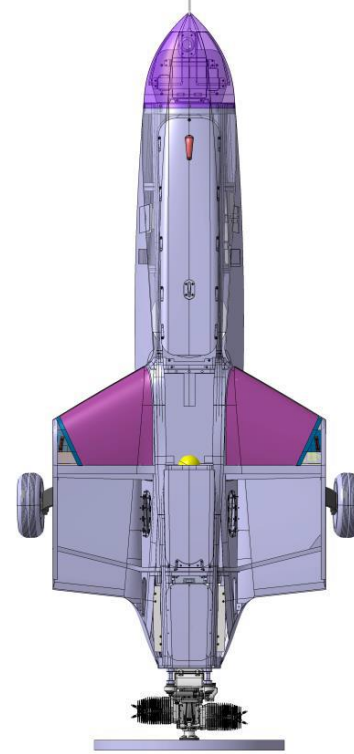


**Figure 2.** Free space for parachutes (purple)

We decided to start first analysis with two smaller parachutes that are available in short time for us. It was just enough space to place two reserve parachutes PR03-1 with area of 45.5 m<sup>2</sup> in a center sections of the wing. The mentioned parachutes were immediately available to be installed and tested. The system consists of two initial pilot parachutes with springs and two main parachutes which will be connected together. Center section of the wing will be modified making the cover on the upper skin of the wing and the inner place of the center section will be rearranged for easy opening and launching the pilot parachute with its reserved parachute. There will be one method to verify this type of opening in the wind tunnel where we will analyze the opening of the cover and launching the parachutes in the similar flow like in a real time rescue mission (figure 3). The pilot parachutes will be thrown high enough to jump over the tails and empennage of the UAV and to carry out main parachutes with it. In this case there will not be additional numerical and flying tests regarding change of aerodynamics because all parts of the system can be placed inside of the fuselage. Considering mass aspects, increase of the mass will be 10 kg for this type of system. Parachutes will be installed near the center of the mass so the correction of the center of the mass position will be minimal (center of

the mass – yellow sphere in figure 2). Carrying parachute system in a UAVs mission would have compensation like decreasing fuel that you take in the different missions.

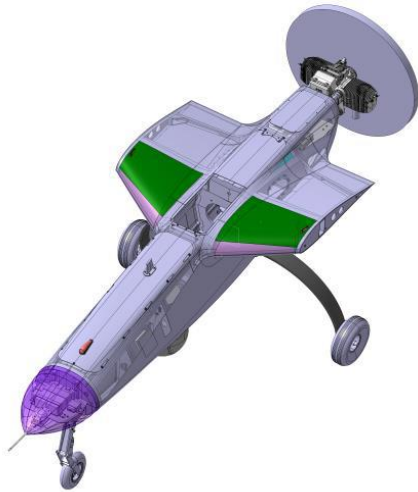


**Figure 3.** Cover on the upper skin (green)

## 2.2. Second approach

Second approach was to investigate foreign market and to find best rescue system for this type of UAV. We considered different types of systems and make contact with different firms. Companies that we found interested were mentioned in a table 2. The leading companies in this field were contacted like *BRS Aerospace*, *Junkers Magnum Rescue System* and *Galaxy rescue system*. For this type of the UAV the only *Galaxy rescue system (GRS)* could meet the requirements for this category of the UAV, and the other two have withdrawn production or don't have products for this type of UAV because *GRS* take primacy on the market for this category. We were considering two types of *GRS* parachute systems, soft pack system and OUT unit. There were many limitations because every system has rocket as a part of parachute launching system and the best solution was to put it at the top of the fuselage but there are front and back tanks, and it was not allowed for rocket to be installed near the fuel. Because we have already pylons under the reinforced wings, and installation was already prepared for the weapons, there will be a little work to put OUT unit under the wing (figure 4).



**Figure 4.** OUT unit attached to the wing pylon

Second option was to make integral container for soft pack and to mount rocket on it and with aerodynamically shaped cover the system will be well attached to the wing

pylon (figure 5). Integral container is weather-resistant pack as well as OUT unit, so the choice will be made based on availability of the mentioned systems, simplicity of use, and the drag force that system make, because the mass of the systems is approximately the same. In the same way as in the case of armed UAV, when the external parachute unit is part of the mission fuel reduction must be calculated to ensure that maximum UAV s mass not exceed 265 kg. Advantage is that center of the mass will not be compromised with the any of the rescue systems integration. System has electronic activation and its unit has to be installed inside the UAV, in the left wing.



**Figure 5.** Integral container with soft pack and rocket attached to the wing pylon

In a both variants hanging points will be in three points on a fuselage (two in a front of a center of a gravity a one behind). Figure 6 represent position of hanging points marked with purple line and center of gravity marked with yellow sphere.

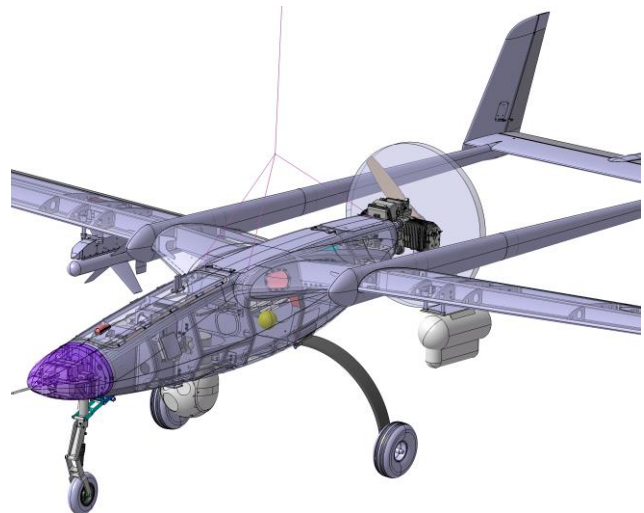


**Figure 6.** Hanging points and centre of the gravity

Before test with launching the rocket and parachute take place, some numerical calculations should be performed. Because the masses of the systems is less than weapons mass that already has been calculated for static strength of the wing with pylon, the verification of the static strength will be not necessary. Calculation of aerodynamic drag that are occurring with attaching any of these rescue systems described in second approach has been presented in the next chapter.

## 3. AERODYNAMIC DRAG NUMERICAL CALCULATIONS

To decide which system has minimal influence on mass, performance and any kind of change in the system of the UAV we need to consider both of discussed rescue systems. An aspect of aerodynamic drag that different

shapes make are presented in this chapter. Data, which were used for simulations, are presented in Table 3.

**Table 3.** Data for simulation

Data for simulation	
Altitude	3000 m
Flight speed	42 m/s
Pressure	70109 Pa
Density	0.909 kg/m <sup>3</sup>
Kinematic viscosity	1.861 x 10 <sup>-5</sup> m <sup>2</sup> /s

Computational fluid dynamic (CFD) has been performed in the commercial ANSYS Fluent software by the finite element methods. Calculated reference surface area is 4.24 m<sup>2</sup> and it has been used K-omega-SST turbulence model. We have analyzed model of integral container with aerodynamically shaped cover and OUT unit of parachute rescue system (figure 7).

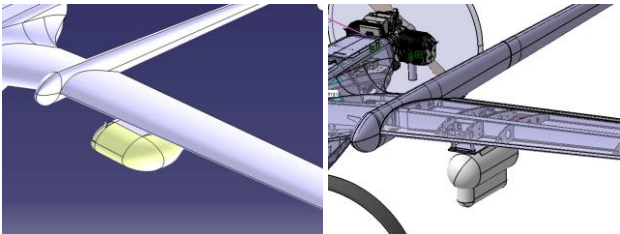


**Figure 7.** Integral container with soft pack (left) and OUT unit (right)

Computational surface mesh of aerodynamically shaped cover of integral container with rocket and OUT unit is presented in Figure 8.

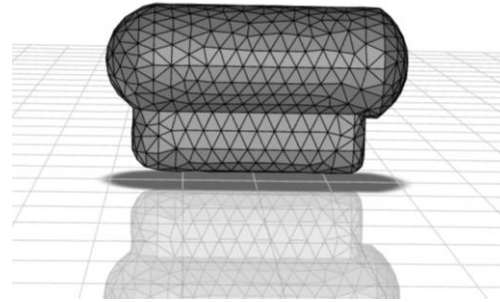
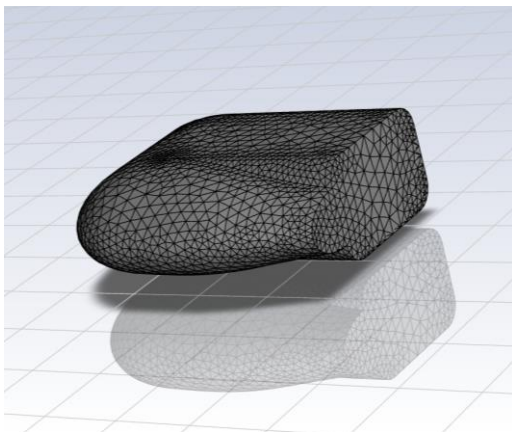


**Figure 8.** Mesh of integral container (upper) and OUT unit (lower)

Dynamic pressure values on the surface of the OUT unit is lower intensity than the pressure on the surface of integral container (figure 9).

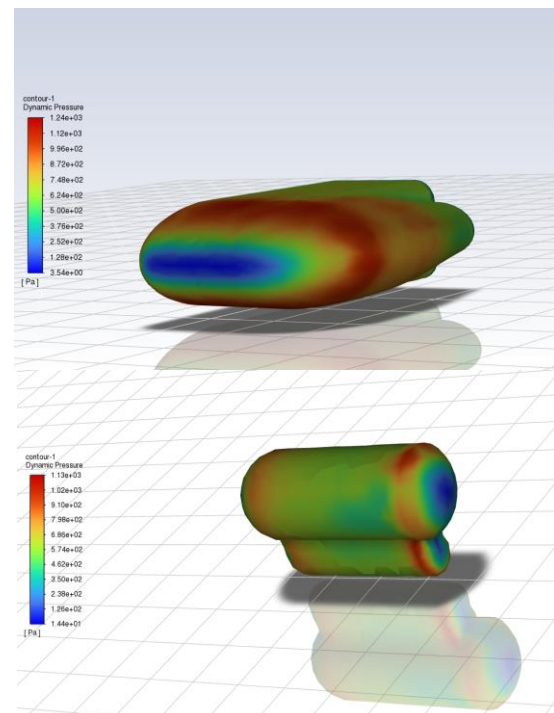


**Figure 9.** Dynamic pressure distribution of integral container (upper) and OUT unit (lower)

Vectors of velocity around the cover directly influence the total pressure distribution on the surfaces (figure 10).

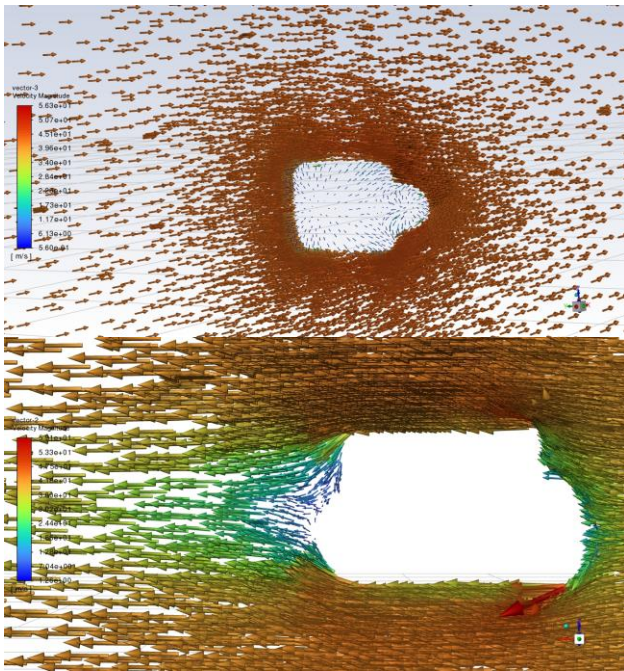


**Figure 10.** Vector of velocity around integral container (upper) and OUT unit (lower)

Total pressure values on the surface of the integral container is lower intensity than the pressure on the surface of OUT unit (figure 11), which is causing lower drag force.

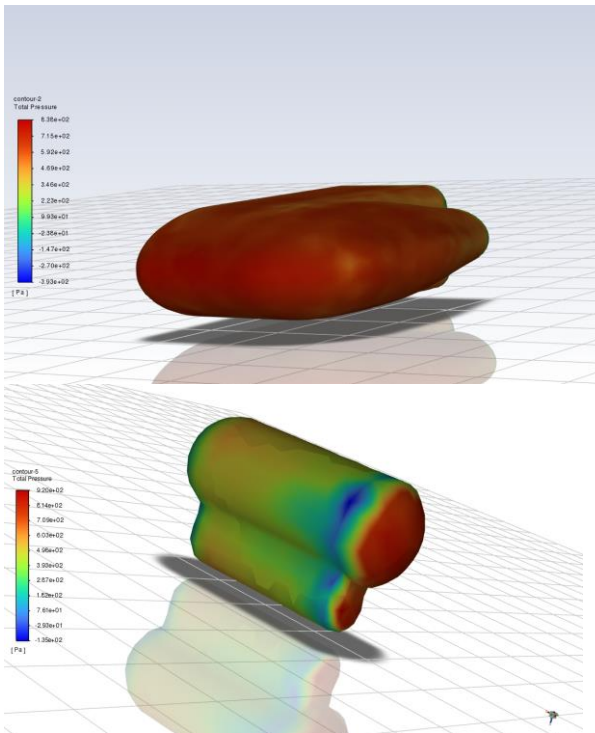


**Figure 11.** Total pressure distribution of integral container (upper) and OUT unit (lower)

Acquired data by simulation are given in table 4.

**Table 4.** Calculated data

Calculated data	Integral container	OUT unit
Form drag	12.778 N	16.411 N
Skin friction drag	1.216 N	0.505 N
General drag force	13.994 N	16.917 N
Form drag coefficient	0.00367	0.00484
Skin friction drag coefficient	0.00035	0.00015
General drag force coefficient	0.00402	0.00499

## 5. CONCLUSION

Parachute systems, today as inevitable part of almost every flying objects, and its integration were analyzed. Both variants of parachute systems that are presented in this paper will be subject of testing in order to decide whether systems are applicable for this purpose and which system is more reliable or available on the market. In a second variant, two different packs are presented and analyzed with the aspect of aerodynamic drag, mass, availability, easiness of application.

Based on data gain with numerical simulation, the integral container has a lower general drag force, but not in an amount that is substantial. So the other factors will decide the final choice for purchasing. Masses of the mentioned systems are similar but the integration and the time that is needed for systems to be functional suggested that OUT unit has advantage over integral container with aerodynamically shaped cover. In the first case we need to produce the container and the cover, to purchase a parachute and the rocket, and to do verification of the system. The faster and easier way is to get OUT unit with cover and packed system that needs minimal tests to perform for approval of its application. Anyhow further research and tests will make more clear which choice is more efficient.

## References

- [1] CASAROSA,C., GALATOLO,R., MENGALI,G., QUARTA,A.: *Impact of safety requirements on the weight of civil unmanned aerial vehicles*, Aircraft Engineering and Aerospace Technology, Volume 76, Number 6 600–606, 2004.
- [2] BOLONKIN, A: *Passenger life-saving in a badly damaged aircraft scenario*, Aircraft Engineering and Aerospace Technology, 80/6, 613-119, 2008.

# ANALYSIS OF THE MASS AND AERODINAMICAL CHANGES DUE TO IMPLEMENTATION OF AN EXTERNAL RESCUE SYSTEM ON A MEDIUM RANGE UAV

BRANISLAVA OSTIĆ

Military Technical Institute, Belgrade, [brankaostic@yahoo.com](mailto:brankaostic@yahoo.com)

MIODRAG MILENKOVIĆ-BABIĆ

Military Technical Institute, Belgrade, [miodragmbm@yahoo.co.uk](mailto:miodragmbm@yahoo.co.uk)

VANJA STEFANOVIĆ-GOBELJIĆ

Military Technical Institute, Belgrade, [vti@vti.vs.rs](mailto:vti@vti.vs.rs)

BRANISLAV OSTOJIĆ

Military Technical Institute, Belgrade, [vti@vti.vs.rs](mailto:vti@vti.vs.rs)

**Abstract:** Upgrading process of any aircraft or UAV system leads to a new design verification in almost every aeronautical field and at the end to an accepted compromise between all design points with the aim of reaching a light, reliable, durable and economical aircraft. A change in the center of aircraft mass position is in a direct correlation with aircraft performance and stability. Any additional change on the existing aircraft or UAV (implementation of a new system or a component) requests analysis of the aircraft mass, position of the center of mass and aircraft performances. This paper presents an analysis of the change in the center of mass position of the medium range UAV due to the integration of the aircraft rescue system at the wing hardpoint, and comparison of the aircraft performances before and after that integration.

**Keywords:** mass, center of mass position, aircraft performances, UAV, external aircraft rescue system

## 1. INTRODUCTION

The implementation of external rescue systems, such as parachutes, aims to enhance the UAV's survivability, reduce the possibility of damage other's property and protect valuable payloads. However, these systems introduce additional weight, potentially compromising flight efficiency and operational capabilities. Upgrading process of any aircraft or UAV system leads to a new design verification in almost every aeronautical field and at the end leads to an accepted compromise between all design points with the aim of reaching a light, reliable, durable and economical aircraft. In the presented paper the medium-range UAV shown in Figure 1 has been analyzed with the UAV characteristics given in Table 1.



Figure 1. Medium-range UAV

Table 1. Medium range UAV characteristics

Wing span (with winglet)	7.025 m
Wing aspect ratio	9.08
Length	5.556 m
Mean aerodynamic chord	0,736 m
Wing area	4.33 m <sup>2</sup>
Engine power	38.8 KW
Propeller diameter	0.86 m
Maximal mass of UAV	265 kg
Center of mass	2080 ±50 mm

## 2. THE MASS AND CENTER OF MASS POSITION CHANGE

To assess the impact of an external rescue system on UAV mass and center of mass position, a comprehensive analysis was conducted using a medium-range UAV model.

Several different possibilities of installing a rescue system were analyzed.

It was not possible to install it in the rear part of the fuselage due to the significant change in the center of gravity position. That would cause the center of the mass to move too far back. In this case, the rescue system

would also be at a relatively small distance from the engine and propeller.

Space was the main limitation for installing the system in front part of the fuselage.

The third analyzed possibility, the centroplane part of the wing, was acceptable in terms of centering but it required major changes to the UAV, which would lead to high costs and repeated or additional testing.

For the above reasons, the adequate position of the center of gravity will be provided with an underwing installation of a rescue system.

Two different types of a rescue system were identified as a possible solution, Soft pack system (Figure 2a) and OUT unit (Figure 2b). Soft pack system requires the construction of an integral container, mounting rocket on it and covering them with an aerodynamically shaped cover (Figure 2c). OUT unit only requires the creation of an adapter for installation on the existing support. Since the masses and positions of both systems are almost the same, due to the better availability of the Soft pack system, this is the system that will be presented in this paper.



**Figure 2a.** Medium-range UAV with external rescue system – Soft pack with container and rocket



**Figure 2b.** Medium-range UAV with external rescue system – OUT unit

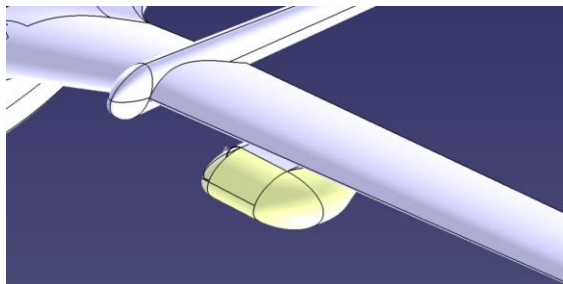


**Figure 2c.** Soft pack system with an aerodynamically shaped cover

External rescue system – Soft pack system with an aerodynamically shaped cover at the left wing hardpoint is selected for analysis and given on Figures 2a and 2c. The system is mounted on the existing weapons carrier and together weights 6.5% to the UAV's total weight. So, as it was in the case of armed UAV, the UAV equipped with rescue system also needs reduction of the available amount of fuel, which will ensure that the maximum permissible UAV's mass of 265 kg as shown in Table 1., is not exceeded.

The implementation of external rescue system on this UAV reduces usable fuel from 70 to 59 kg.

Table 2. shows the UAV's mass and center of the mass position before and after the system integration on the UAV with reduced amount of fuel. Total take-off mass fulfills the condition from the Table 1. regarding maximum UAV mass.

Change in the center of mass position from 2.069 to 2.067 m is insignificant and does not compromise the given range in Table 1.

Table 2. also shows the change in the relative position of the center of mass in relation to the length of the mean aerodynamic cord from 34.4 to 34.15% of MAC which is also negligible.

**Table 2.** The mass and center of mass position change

Configuration	m	X <sub>c.m.</sub>	X <sub>c.m.</sub>
	(kg)	(m)	(%MAC)
1 UAV with 59 kg of fuel and without weapon carriers	244.6	2.069	34.40
2 Weapon carriers	6.7	2.214	
3 Parachute	11.0	2.088	
4 Total take-off mass	262.3	2.067	34.15

### 3. ESTIMATION OF PERFORMANCE

The integration of the aircraft rescue system has multiple effects on UAV endurance as the most important flight characteristic and the most important effects are:

- Reduction of the maximum fuel weight as the UAV's maximum mass could not be exceeded.
- Additional drag due to the integration of the rescue system.
- Influence on stability and control and trim drag.

The integrated rescue system will have the same effect as weapons carriage. The additional parasitic drag can be estimated by the components build-up method that is summarized in Raymer's book [1] or by using software like OpenVSP [2]. The OpenVSP is conceptual design software developed by NASA. This tool enables detailed and precise parasitic drag calculations by leveraging the existing model components and a variety of atmospheric, skin friction, and form factor equations.

As mentioned in [1], the most important factor affecting



skin friction drag is the extent to which the aircraft has laminar flow over its surfaces. The skin-friction drag can be doubled if the flow is turbulent rather than laminar. In many real aeronautical cases, the boundary layer transitions from laminar to turbulent flow will happen at the front of the body and this will increase drag force.

Any flight can be divided into several segments, each clearly distinguished by its nature. In this paper, the evaluation of the medium-range UAV endurance will be analyzed. The endurance is one of the most important UAV characteristics. Starting from the well-known equation explained in [3]:

$$dt = \frac{-1}{c_t T} dW, \quad (1)$$

the endurance equation can be solved through numerical integration. The limits are the final and initial weight during the analyzed segment. In the well-known "Breguet" endurance equation  $t$  represents time,  $c_t$  represents thrust-specific fuel consumption [1/sec],  $T$  represents thrust [N], and  $W$  represents the UAV's weight [N]. To solve the endurance equation it is necessary to find the specific fuel consumption, that is given in [4]. Finally, some assumptions must be made and in the presented paper the constant airspeed/constant attitude cruise has been assumed with the equations:

$$R_{cScA} = \frac{V}{c_t} \frac{C_L}{C_D} \ln \left( \frac{W_{initial}}{W_{final}} \right). \quad (2)$$

In the equation 2 the  $C_L$  is UAVs lift force coefficient,  $C_D$  is the UAVs drag force coefficient and  $W_{initial}$  and  $W_{final}$  represents initial and final UAVs weight. By implementation of the Component build-up method, the additional drag of the integrated rescue system can be estimated by the data given in Table 12.6 from [1]. The assumption that an integrated rescue system has a similar drag force coefficient as the Bullet shape (blunt back) has been made. The parasite drag force coefficient of the integrated rescue system has been estimated to have a value of  $C_D=0.3$  based on the reference frontal area. The additional fuel weight reduction has been estimated at 11 kg. This value is equivalent to the parachute rescue system weight. The results of the just mentioned analysis are given in Table 3. as a function of UAV airspeed.

**Table 3.** Estimated endurance results

$V$ [km/h]	$t_{cScA}$ [h]	$t_{cScA}$ [h]
135	12.92	9.89
150	12.03	9.14

## 4. RESULTS AND DISCUSSION

In order to find the adequate position for integration of the rescue system the different possibilities have been analyzed. The rear and front position was inadequate due to the unacceptable position of UAVs center of gravity and restricted space for integration of the rescue system. The central part of the wing section possesses an adequate volume for the integration of the rescue system. The main drawback is the fact that it is divided in the left- and right-wing section and request two small independent parachutes and additional wing modification. This modification and implementation would require significant work to be done. It would require the change in the UAVs geometry and tooling for UAVs production. It is the main reason why this option has not been deeply analysed in this paper.

On the other hand, the wing attaching point has been the other possible solution. This position would not affect the change of the center of gravity position significantly. The attaching points on the wing are near the center of gravity of the UAV. As a consequence of all mentioned the attaching point under left-wing has been chosen as the optimal solution that was deeply analyzed in the presented paper.

The results indicate a noticeable decrease in usable fuel mass due to integration of external rescue systems. A parachute-based rescue system adds 4.2% to the UAV's total weight. So, integration of the rescue system requires a reduction in the available amount of fuel.

In order to verify the estimated results for the rescue system drag force coefficient, the computational fluid dynamics (CFD) was performed in the commercial ANSYS Fluent software by the finite volume methods. The K-omega-SST turbulence model has been used. The working fluid was defined as ideal gas-air. Computations have been done until the convergence criteria have been achieved. The computational surface mesh and dynamic pressure distribution on the design rescue system has been given on Figure 3.

Computational fluid dynamics estimated the drag force on value 13.994 N. The reference surface area was defined as 4.24 m<sup>2</sup> and it was assumed that UAV is flying on altitude of 3000 m with the airspeed of 42 m/s. The estimated drag force coefficient based on the reference rescue system frontal area is  $C_D=0.29091$ . The excellent agreement with the results from reference [1] has been achieved ( $C_D=0.3$ ). The error is up to 3%. This small error will not affect the performance estimated results.

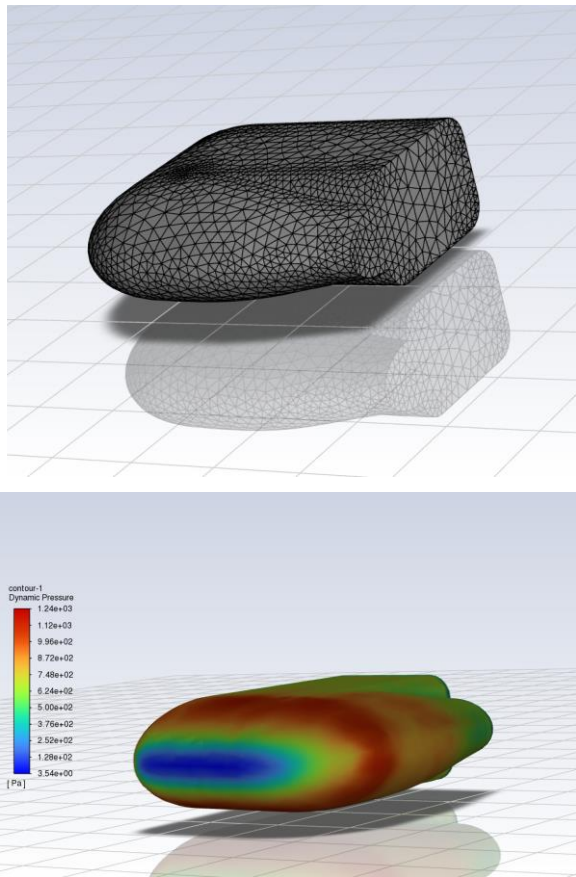


**Figure 3.** The resolution of a surface mesh on rescue system and dynamic pressure distribution

The effect of the reduction of usable fuel from 70 kg to 59 kg will produce an endurance reduction of 17.8%. The additional endurance reduction of 5.6-6.2% has been a consequence of the additional drag of the integrated parachute rescue system. If the UAV could have the same amount of fuel and the integrated rescue system attached under the left-wing pylon the flight endurance would be just 6% reduced.

The presented approach for estimating UAVs flight performance has been successfully implemented during medium range UAV flight performance estimation and verification that is given in the reports [5, 6].

## 5. CONCLUSION

Integrating an external rescue system on a medium-range UAV has been given in the presented paper. The possibility to integrate rescue system on existing UAV required comprehensive UAV mass and weight analysis.

In the presented paper a parachute-based rescue system adds 4.2% to the UAV's total weight and requires reduction in the amount of usable fuel.

In the presented paper effect of an integrated parachute rescue system on UAV endurance has been presented. The integrated rescue system will have a similar effect as the integration of one additional air-to-ground missile. It has been shown that the biggest effect would be the consequence of fuel weight reduction. Additional endurance reduction of 5-6% will be the price for additional drag of the integrated system as one payload under the wing.

The method provided fast and precise results of flight endurance characteristics that can be easily estimated in the preliminary design phase. The obtained data are in good agreement with the flight test data. The presented method will be used in future aircraft and UAV projects in VTI.

## References

- [1] RAYMER, D., Aircraft Design: A Conceptual Approach, Fifth edition, AIAA education series, 2012.
- [2] <https://openvsp.org/>.
- [3] Snorri, G. General Aviation Aircraft Design: Applied Methods and Procedures. Elsevier Inc, 2014.
- [4] Zanzottera Engines. 630HS Engine. Retrieved from <https://www.zanzotteraengines.com/engines/630hs-engine/>.
- [5] Даљински пилотирани ваздухоплов ПЕГАЗ–перформансе. VTI report No. В3–602-П-06, 2020.
- [6] Даљински пилотирани ваздухоплов ПЕГАЗ – извештај о земаљским и летним испитивањима. VTI report No. В3–602-И-06, 2022.



# OTEH 2024

11<sup>TH</sup> INTERNATIONAL SCIENTIFIC CONFERENCE  
ON DEFENSIVE TECHNOLOGIES

*SECTION III*

**Weapon systems and combat vehicles - *WSCV***



## ANALYSIS OF THE BEHAVIOUR OF THE MOBILE PLATFORM DURING FIRING

MILAN SIMONOVIĆ

Military Technical Institute, Belgrade, [milan.simonovic@mod.gov.rs](mailto:milan.simonovic@mod.gov.rs)

MARKO SIMONOVIĆ

Military Technical Institute, Belgrade, [marko.simonovic@mod.gov.rs](mailto:marko.simonovic@mod.gov.rs)

ALEKSANDRA ŽIVKOVIĆ

Military Technical Institute, Belgrade, [aleksandra.b.zivkovic@mod.gov.rs](mailto:aleksandra.b.zivkovic@mod.gov.rs)

ANA GAČIĆ

Military Technical Institute, Belgrade, [ana.gacic@mod.gov.rs](mailto:ana.gacic@mod.gov.rs)

ALEKSANDAR KARI

Military Technical Institute, Belgrade, [aleksandarkari@gmail.com](mailto:aleksandarkari@gmail.com)

**Abstract:** This paper describes the problem of the behavior of the truck 6x6 during the firing process from an anti-aircraft gun 40 mm, which is integrated on this vehicle. The calculation of the center of gravity coordinates and the reactions of the supports of the vehicle with an integrated gun is shown. Internal ballistic calculation determines the maximum recoil force. The behavior of the mobile platform is presented using a mathematical-mechanical model of platform oscillation, which was formed on the basis of the classical principles of the theory of vehicle dynamics. With the adopted simplifications, the system with a large number of degrees of freedom is reduced to a system with three degrees of freedom, whose generalized coordinates are: vertical position of the system  $T$ , rotation around the transverse axis (galloping) and rotation around the longitudinal axis (rolling). MATLAB software package was used for calculation. Generalized coordinates changes over time, as well as the velocity of these coordinates, were determined. The analysis determined that the position of the anti-aircraft gun on the vehicle is favorable, because the system easily supports all the loads caused by the firing and the weight of the weapons, and it also allows obtaining small oscillation values, which are easily damped by the elastic suspension system.

**Keywords:** Truck 6x6, anti-aircraft gun 40 mm, armaments integration, the mathematical-mechanical model of the oscillation.

### 1. INTRODUCTION

Mobile platforms, which are used for military purposes, represent any system on which weapons can be integrated. For example, a fighter plane represents a platform for the integration of machine guns, aerial bombs or automatic cannons, while machine guns, automatic cannons, rocket launchers, mortars, cannons, howitzers etc. can be integrated on the platforms of trucks, combat vehicles and various other commercial vehicles. In order for a commercial vehicle to be used for the integration of weapons, it is necessary to adapt its characteristics beforehand to the loads that it will have to withstand during its lifetime, such as: the impact of the mass of the weapon on the platform, recoil and recoil forces, the impact of the mass of the combat kit, oscillations of the weapon after firing, movement of recoiling masses, etc. One of the main problems is the construction of an elastic support system, which should have the appropriate stiffness to absorb all the forces that

are transferred to it and reduce oscillations to the smallest possible extent, in order to prevent the occurrence of resonance. Resonance is a physical phenomenon that occurs in a strongly oscillating system, when the maximum oscillation amplitude is reached at a certain excitation frequency. This phenomenon depends of damping, i.e. the energy of losses and the total energy of the system. For the selected vehicle and weapon, it is necessary to collect data on their performance. One of the most important steps in designing is the internal ballistic calculation, which determines the distribution of pressure inside the barrel as a function of time and its maximum value. This calculation also determines the initial speed of the projectile, achieved at the mouth of the barrel. It is very important to calculate the recoil force and recoil resistance force during the average firing, because it is transferred to a large extent to the mobile platform. Based on the calculation of the previously mentioned forces and structural characteristics of the vehicle, which include the elastic suspension system, as well as the chosen place for the integration of weapons, a dynamic model with certain

simplifications is set up. After this, a mathematical-mechanical model of the oscillation of the platform during the firing process, which contains the differential equations of motion, is set up. Based on the obtained data and by solving differential equations, concrete equations of platform oscillation, i.e. change of generalized coordinates over time, can be obtained, such as system generally cannot be solved analytically, and therefore it is necessary to solve it numerically, using modern computer software. Based on the obtained results, it is possible to correct the set mathematical-mechanical model, the place of integration, the method of connection, the characteristics of the elastic suspension system, the appropriate rate of fire, which would achieve the determination of the configuration of the vehicle-armament system, which is able to withstand the resulting loads [1].

## 2. STATIC DISTRIBUTION OF WEIGHT ON THE AXLES AND COORDINATES OF THE CENTER OF GRAVITY OF THE MOTOR VEHICLE

The position of the cannon integration on the vehicle, as well as the static weight distribution on the axles, is shown in Figure 1. The weight of the vehicle is transferred to the ground via the wheels of the front and rear axles. The substrate acts on them with normal reactions. The dynamic characteristics of the vehicle largely depend on the size of these forces (traction forces, stability, controllability, rolling resistance, braking forces, etc.) [2].

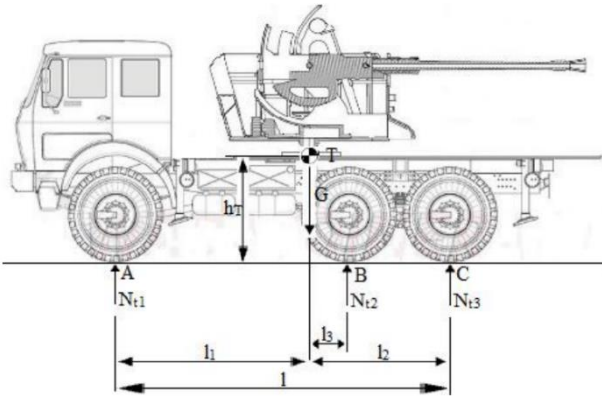


**Figure 1.** Armament integration position and static weight distribution

Calculation of support reactions is shown by the following equations:

$$\sum M_A = 0; N_{i2} * (l_1 + l_2) + N_{i3} * l - G * l_1 = 0 \quad (1)$$

$$\sum M_B = 0; -N_{i1} * (l_1 + l_2) + N_{i3} * (l_3 - l_2) - G * l_2 = 0 \quad (2)$$

$$\sum Z = 0; N_{i1} + N_{i2} + N_{i3} - G = 0 \quad (3)$$

By analyzing the previous equations, it can be seen that the load distribution on the axles is highly dependent on the position of the center of gravity T in relation on the vehicle axles and the base ( $l_1, l_2, l_3, h_T$ ).

Knowing the weight and disposition parameters of individual assemblies, by applying the analytical settings of theoretical mechanics, the position of the center of gravity in space and the normal reaction of the ground to the wheels of a motor vehicle can be determined. The analytical procedure for determining the center of gravity of a motor vehicle is shown in Figure 2.

The marks in the picture are:  $G$  – total weight of the vehicle/weapon system,  $G_M$  – engine weight,  $G_K$  – cabin weight,  $T$  – center of gravity and  $N_{i1}, N_{i2}, N_{i3}$  – reactions of supports.

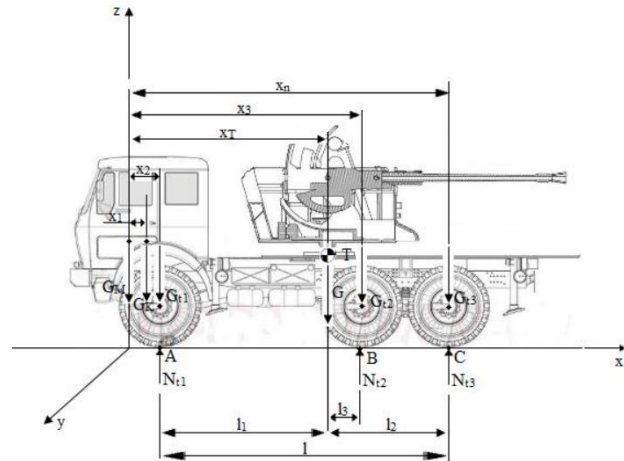


**Figure 2.** Analytical procedure for determining the center of gravity

$$G * x_T = G_K * x_1 + G_{i1} * x_2 + G_{i2} * x_3 + G_n * x_n = \sum_{i=1}^n G_i * x_i \quad (4)$$

X-axis coordinates of the center of gravity:

$$l_1 = x_T = \frac{\sum_{i=1}^n G_i * x_i}{G} = \frac{\sum_{i=1}^n G_i * x_i}{\sum_{i=1}^n G_i} \quad (5)$$

If the same forces  $G_i$  directed parallel X-axis are observed and an analogous procedure is applied, the coordinates of the center of gravity along the Z-axis are obtained:

$$h_T = z_T = \frac{\sum_{i=1}^n G_i * z_i}{G} = \frac{\sum_{i=1}^n G_i * z_i}{\sum_{i=1}^n G_i} \quad (6)$$

where  $h_T$  is the height of the center of gravity.

The deviation of the center of gravity from the longitudinal axis of the vehicle is obtained in the same way:

$$e_y = y_T = \frac{\sum_{i=1}^n G_i * y_i}{G} = \frac{\sum_{i=1}^n G_i * y_i}{\sum_{i=1}^n G_i} \quad (7)$$

The correct arrangement of aggregates aims to reduce the deviation of the center of gravity from the longitudinal axis of the vehicle [2].

### 3. CALCULATION OF THE MAXIMUM RECOIL FORCE

The internal ballistics calculation was done according to the Runge-Kutt method. This method belongs to the numerical methods. The essence is that system of differential equations is transformed into a form suitable for numerical integration [3]. During the firing process, the reactive force of the powder gas pressure  $P_{kn}$ , acts on the artillery tool, i.e. recoil force. This force occurs as a result of the accelerated movement of the projectile in the barrel channel and the powder gases in the direction towards the rear section of the barrel. According to the law on the amount of movement, the size of this force increases with the increase in the mass of the projectile and the velocity of its movement. The resistance of the weapon and its stability during firing depend on the magnitude of the recoil force.

The maximum recoil force is calculated according to the formula:

$$P_{kn\max} = P_{\max} * S_c \quad (8)$$

where are they:  $P_{\max}$  – maximum pressure of gunpowder gases and  $S_c$  – cross-sectional area of the barrel.

### 4. MATHEMATICAL-MECHANICAL MODEL OF MOBILE PLATFORM OSCILLATION UNDER THE EFFECT OF FIRING FORCE

The mathematical-mechanical model serves to mathematically represent the movement of the physical system, including all influential parameters, while maintaining the simplicity of the application of simplification. The model was formed based on the classical principles of the vehicle dynamics theory.

With the adopted simplifications, the system with an infinite number of degrees of freedom was reduced to a system with three degrees of freedom, which is shown in Figure 3, and the following quantities were chosen as generalized coordinates:  $z_T$  – vertical position of the center of gravity of the system T (distance from base),  $\varphi$  – rotation around the transverse axis  $y'$  (galloping) and  $\theta$  – rotation around the longitudinal axis  $x'$  (rolling).

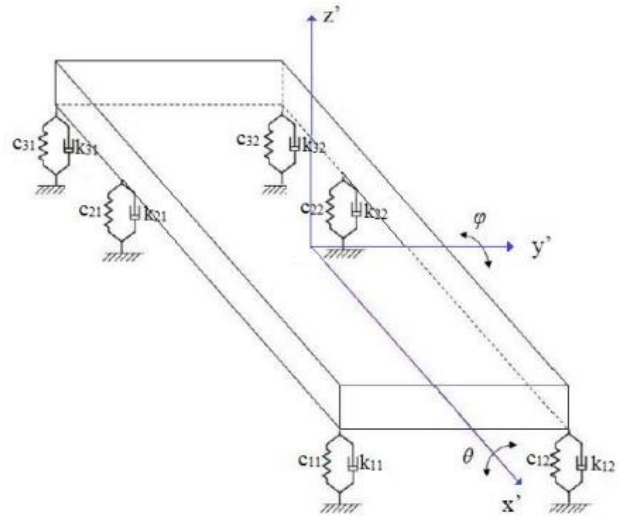


Figure 3. Three-dimensional representation of the dynamic model of the platform

The motion of the platform model with integrated weapons, excited by the force due to firing, can be described by Lagrangian equations of the second kind:

$$\frac{d}{dt} \left( \frac{\partial E_k}{\partial \dot{q}_i} \right) - \frac{\partial E_k}{\partial q_i} = - \frac{\partial E_p}{\partial q_i} - \frac{\partial \Phi}{\partial q_i} + Q'_{q_i} \quad (9)$$

where are they:

- $i = 1, n$  ( $n$  is the number of degrees of freedom of movement of the system, in this case  $n = 3$ ),
- $E_k$  – kinetic energy of the system,
- $E_p$  – potential energy of the system,
- $\Phi$  – dissipation function,
- $\left( - \frac{\partial E_p}{\partial q_i} \right)$  – a generalized conservative force,
- $\left( - \frac{\partial \Phi}{\partial q_i} \right)$  – a generalized dissipative force and
- $Q'_{q_i}$  – arbitrary non-conservative generalized force.

Since the system is considered as a whole, the total kinetic energy of the model consists of the kinetic energies of translation of the center of mass and rotation about the center of mass of the system:

$$E_k = \frac{1}{2} * m * \dot{z}_T^2 + \frac{1}{2} * J_y * \dot{\varphi}^2 + \frac{1}{2} * J_x * \dot{\theta}^2 \quad (10)$$

where are they:

- $J_y$  – moment of inertia of the mass of the system in relation to the longitudinal axis  $y'$  and
- $J_x$  – moment of inertia of the mass of the system in relation to the transverse axis  $x'$ .

To define the potential energy, it is necessary to geometrically determine the expressions for the relative deformations of the tire springs and the displacement of the shock absorber pistons. One of the simplifications of the elastic suspension system is the use of equivalent suspension stiffness, which takes into account the tire

stiffness. It is also considered that the displacements of springs and shock absorbers are equal [2].

Figure 4 shows a sketch of the suspension from the side, and Figure 5 shows the suspension from the front. The mark  $l_{st}$  represents the length of the support that deforms at the initial moment, and  $l_{kj}$  at an arbitrary moment ( $k = 1,2,3$ ).

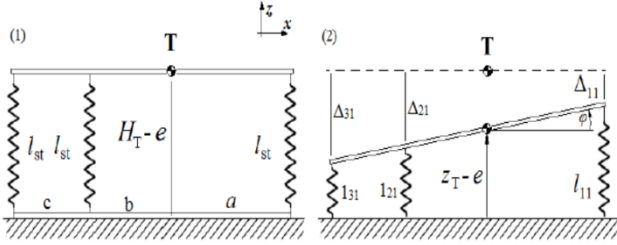


Figure 4. Support seen from the side

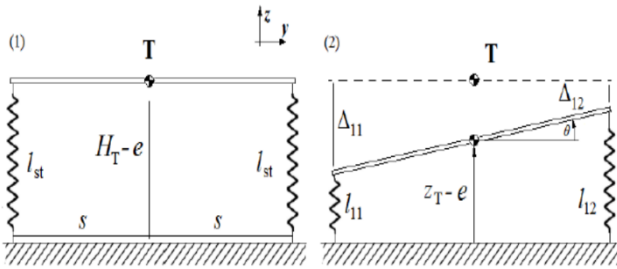


Figure 5. Support seen from the front

In these pictures, the mark  $\Delta$  represents the ultimate deformations of the shock absorber springs, namely:  $\Delta_{11}$  and  $\Delta_{12}$  for the wheels of the first axle,  $\Delta_{21}$  and  $\Delta_{22}$  for the wheels of the second axle, and  $\Delta_{31}$  and  $\Delta_{32}$  for the wheels of the third axle [2].

For the same stiffness values of the left and right elastic elements of the same axle, the following follows:

$$C_{11} = C_{12} = C_1, \quad C_{21} = C_{22} = C_2, \quad C_{31} = C_{32} = C_3$$

so the expression for the potential energy of the system is:

$$E_p = \frac{1}{2} * c_1 * (\Delta_{11}^2 + \Delta_{12}^2) + \frac{1}{2} * c_2 * (\Delta_{21}^2 + \Delta_{22}^2) + \frac{1}{2} * c_3 * (\Delta_{31}^2 + \Delta_{32}^2) \quad (11)$$

For the same damping values of the left and right shock absorbers of the same axle, the following follows:

$$k_{11} = k_{12} = k_1, \quad k_{21} = k_{22} = k_2, \quad k_{31} = k_{32} = k_3$$

so the expression for the dissipative function is:

$$\Phi = \frac{1}{2} * k_1 * (\Delta_{11}^2 + \Delta_{12}^2) + \frac{1}{2} * k_2 * (\Delta_{21}^2 + \Delta_{22}^2) + \frac{1}{2} * k_3 * (\Delta_{31}^2 + \Delta_{32}^2) \quad (12)$$

The force of pressure of the powder gases on the front of the bolt is opposed by the resistance force of the return springs and the friction force, which together form the recoil resistance force  $R(t)$ . The components of the shear resistance force in the direction of the three axes are:

$$\begin{aligned} - R_x(t) &= R * \cos\beta * \cos\alpha \\ - R_y(t) &= R * \sin\beta * \cos\alpha \end{aligned}$$

$$- R_z(t) = R * \cos\beta * \sin\alpha$$

Differential equations of motion of the system are set for each of the generalized coordinates:

- For vertical movement of the center of gravity of the system T,  $z_T$ :

$$\frac{d}{dt} \left( \frac{\partial E_k}{\partial \dot{z}_T} \right) - \frac{\partial E_k}{\partial z_T} = - \frac{\partial E_p}{\partial z_T} - \frac{\partial \Phi}{\partial z_T} + Q'_{z_T} \quad (13)$$

- For rotation around the transverse axis  $y'$  (galloping),  $\varphi$ :

$$\frac{d}{dt} \left( \frac{\partial E_k}{\partial \dot{\varphi}} \right) - \frac{\partial E_k}{\partial \varphi} = - \frac{\partial E_p}{\partial \varphi} - \frac{\partial \Phi}{\partial \varphi} + Q'_{\varphi} \quad (14)$$

- For rotation around the longitudinal axis  $x'$  (rolling),  $\theta$ :

$$\frac{d}{dt} \left( \frac{\partial E_k}{\partial \dot{\theta}} \right) - \frac{\partial E_k}{\partial \theta} = - \frac{\partial E_p}{\partial \theta} - \frac{\partial \Phi}{\partial \theta} + Q'_{\theta} \quad (15)$$

## 5. SIMULATION MODEL OF MOBILE PLATFORM OSCILLATION

Solving the previous differential equations is done numerically, using the MATLAB software package. The input data are shown in table 1, and they consist of vehicle data (technical data, position of the vehicle's elastic suspension system, moments of inertia), tool data (tool mass, integration position in relation to the system's center of gravity, elevation angles and azimuth) and data on the excitation force (maximum value of the recoil resistance force R). The initial data were adopted on the basis of several compared vehicles, whose platform is 6x6.

Table 1. Input data for the software solution

Num.	Characteristic size	Value
1.	Vehicle mass – $m_v$ [kg]	9000
2.	Mass of weapons – $m_o$ [kg]	3500
3.	Mass of the system – $m$ [kg]	12500
4.	Moment of inertia – $J_y$ [kg*m <sup>2</sup> ]	57950,2
5.	Moment of inertia – $J_x$ [kg*m <sup>2</sup> ]	12048,7
6.	Center of gravity height – $H_T$ [m]	1,2
7.	Distance from the front axle – $a_v$ [m]	2,517
8.	Distance from the rear axle – $b_v$ [m]	1,845
9.	Half the wheelbase – $s$ [m]	2,39
10.	Damping coefficient – $k$ [Ns/m <sup>2</sup> ]	16000
11.	Return spring force – $F_p$ [N]	15435
12.	Curve – $f_1$ [m]	0,002
13.	Maximum recoil force – $R$ [N]	17150
14.	Vertical distance to the weapon – $h$ [m]	0,5

15.	Horizontal distance to the weapon – d [m]	0
-----	---	---

In the initial data, the vehicle mass value is reduced by the crate mass value, because in this case of weapon integration, the crate must be dismantled. The weight of the weapon is reduced by the weight of the wheeled base, which is used in the case of the towing variant, but for better protection, armor weighing slightly less than 1000 kg has been added. Since the middle and rear axles behave as if they are coupled, they have an equivalent stiffness coefficient of the shock absorber springs, so the system is further viewed as a vehicle with two axles, i.e. four wheels. The position where the center of gravity of the vehicle is located was chosen for the place of integration of the weapon, so that the horizontal distance from the center of mass of the truck to the center of mass of the cannon is equal to zero, while the vertical distance is assumed to be at a height of 0.5 m from the center of gravity of the vehicle.

Under the effect of the weight of the weapon and its force of resistance to recoil, a deflection occurs, which in this case has a small value, because the mass of the cannon is much smaller than the mass of the vehicle, so when the force of the weight of the cannon is added to the force of resistance to recoil, there is no great impact on the chassis, which is very important for the whole system.

Due to the lack of exact data, it is assumed that the damping coefficient has a value of 16000 Ns/m<sup>2</sup>. Figure 6 shows the place of integration with the distances from the shafts and the base. The impact of the recoil force R is also shown. The output data is obtained in the form of diagrams, which represent the changes of the following components over time:

- Displacement of the center of gravity in height,
- galloping,
- rolling,
- velocity of moving the center of gravity in height,
- galloping velocity and
- rolling velocity.

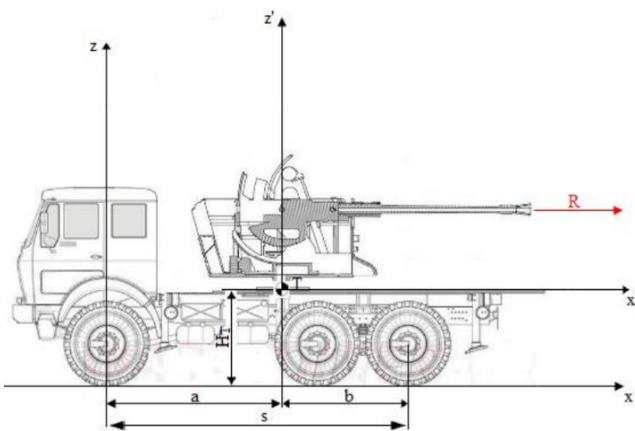


Figure 6. Weapon integration site

The diagrams of the output data are shown in the Figures 7-12. In the diagrams, the red line shows the damping of the oscillations.

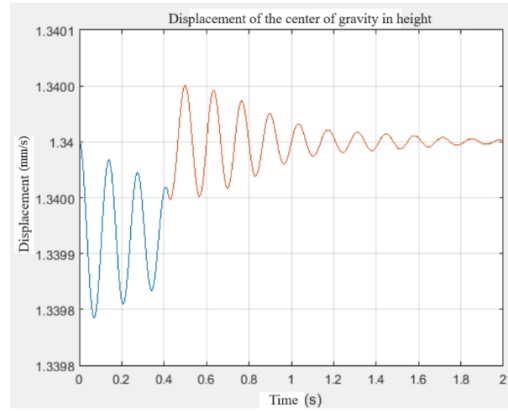


Figure 7. Displacement of the center of gravity in height

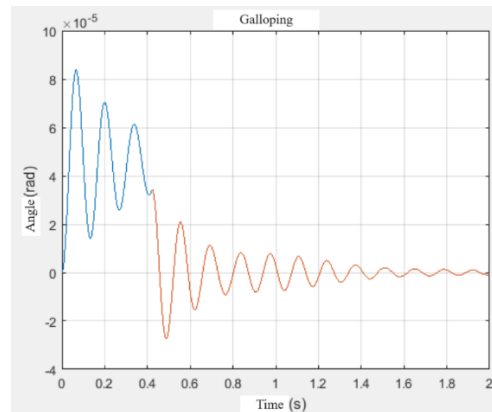


Figure 8. Galloping

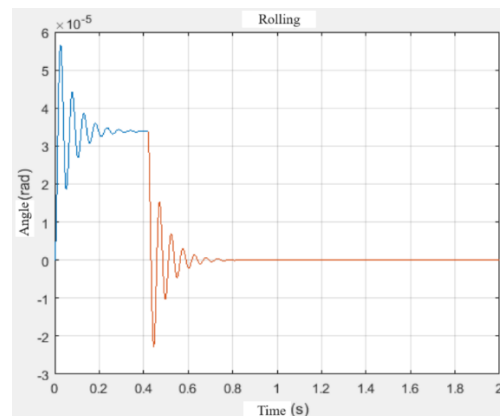


Figure 9. Rolling

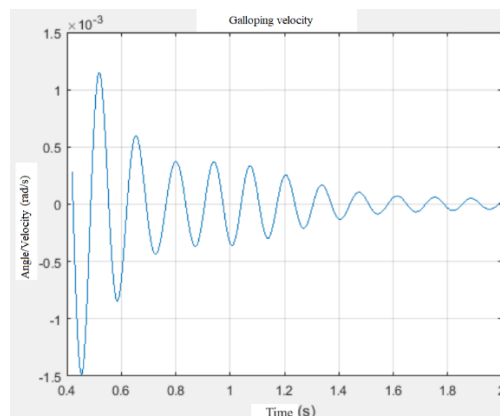


Figure 10. Galloping velocity



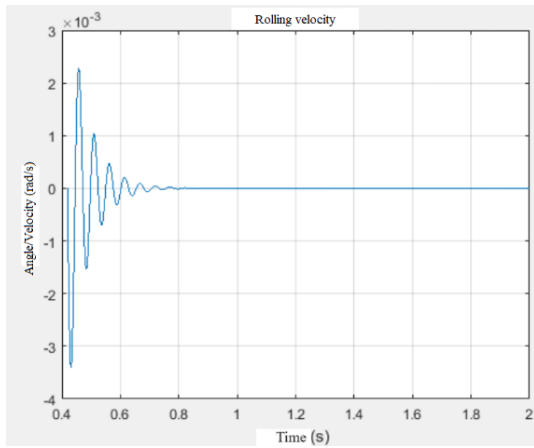


Figure 11. Rolling velocity

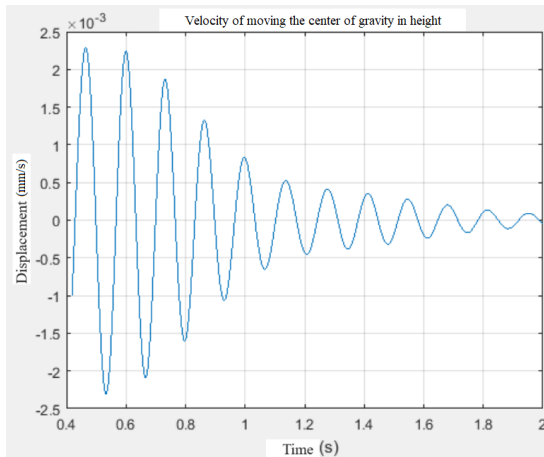


Figure 12. The velocity of moving the center of gravity in height

In the diagram showing the displacement of the center of gravity by height, it can be seen that the amplitude of the oscillation of the center of gravity is very small and amounts to less than 1 mm. The end of the oscillation period occurs after 2 s. Based on this, it can be seen that the system is very stable during the firing process, but for the accuracy, it is desirable to act in short bursts (up to 10 rounds), when it comes to land targets, so that there is not too much scattering of hits. By moving the center of gravity of the weapon in the horizontal direction along the axis of the vehicle, small amplitude oscillations are also obtained, which is a consequence of the much larger mass of the armored vehicle compared to the gun, so the integration can be done in other places on the chassis.

Galloping also contains an oscillation period lasting 2 s, with an amplitude of 0.085 mrad. After 0.6 s the amplitude decreases and the system returns to the equilibrium position. In this case, rolling lasts much shorter than galloping. The period of oscillation lasts slightly less than 0.8 s, and what is noticeable on the diagram is a sudden change in the angle of rotation. The change occurs already after 0.4 s, and soon after that, the system returns to the equilibrium position.

The velocity of galloping is expressed by the change of angle with time. The highest peak is reached at an angle of 1.5 mrad, after 0.45 s, after which there is a gradual decrease in the galloping angle, until the system returns to

its pre-firing state. Rolling velocity is also expressed as a change in angle over time, but it drops to zero very quickly, due to rolling itself takes less time than galloping. In this plot, the largest peak is reached at an angle of 3.4 mrad after approximately 0.45 s. The maximum velocity of moving the center of gravity in height is 2.3 m/s, after which it gradually decreases, until the center of gravity stops in the initial position at a height of 1.2 m.

The place of integration of weapons greatly affects the change of generalized coordinates. In this case, where the cannon is integrated above the center of gravity of the truck, acceptable values of the generalized coordinates are obtained. Changing the place of integration will certainly lead to an increase in one and a decrease in the other generalized coordinate. For example, moving the tool towards the rear of the vehicle will give a higher galloping value than the current position. If the cannon is not integrated to the left or right of the vehicle axis, but remains on it alone, there will not be much change in the amount of roll, whether the cannon is located just behind the cabin, above the truck center of gravity, or closer to the rear of the chassis..

## 6. CONCLUSION

When transforming a commercial vehicle into a combat vehicle, it must be taken into account that it must withstand all the loads that occur due to the effect of the weight of weapons with combat equipment and armor, primarily the loads caused by firing. In order to dampen the oscillations of the vehicle-weapon system in a short time, the elastic support system must be carefully constructed, which plays a key role in absorbing the energy created by firing. The shortcoming of the calculation is that only the maximum value of the force transmitted to the platform was used, instead of using its actual change. In order to present a more realistic picture of the impact of integrated weapons on the platform, it is necessary to set up a more realistic mathematical model, which includes more degrees of freedom and the movement of more masses. Regarding the elastic suspension system, the stiffness and damping coefficients can be varied, in order to show their influence on the oscillations of the system, or an already existing system can be used, which has been tested several times in practice.

## Acknowledgements

This paper is a part of the research done within the project of the University of Defence in Belgrade, No. VA-TT/1/24-26.

This work was supported by the Ministry of Science, Technological Development and Innovations of the).

## References

- [1] RISTIĆ, Z., JAKOVLJEVIĆ, M.: *Osnovi naoružanja-konstrukcija artiljerijskog oruđa*, Knjiga, Beograd, 2001.
- [2] KALEZIĆ, M.: *Projektovanje artiljerijskih sistema*, Knjiga, Beograd, 2010.

- [3] TANČIĆ, LJ.: *Zbirka zadataka iz unutrašnje balistike*, Sektor za školstvo, obuku, naučnu i izdavačku delatnost, Beograd, 1999. Republic of Serbia (Contract No. 451-03-66/2024-03/200325)



## THE CONCEPT OF REMOTE-CONTROLLED WEAPON STATION FOR SELF-PROPELLED MORTARS

ALEKSANDRA ŽIVKOVIĆ

Military Technical Institute, Belgrade, [aleksandra.b.zivkovic@mod.gov.rs](mailto:aleksandra.b.zivkovic@mod.gov.rs)

MILAN SIMONOVIC

Military Technical Institute, Belgrade, [milan.simonovic@mod.gov.rs](mailto:milan.simonovic@mod.gov.rs)

GORAN DRAGOVIĆ

Military Technical Institute, Belgrade, [goran.dragovic@mod.gov.rs](mailto:goran.dragovic@mod.gov.rs)

MILOVANOVIĆ MARIJA

Military Technical Institute, Belgrade, [marija.milovanovic@mod.gov.rs](mailto:marija.milovanovic@mod.gov.rs)

NINA MITRIČEVIĆ

Military Technical Institute, Belgrade, [nina.mitricevic@mod.gov.rs](mailto:nina.mitricevic@mod.gov.rs)

**Abstract:** This paper aims to contribute to the development of advanced military systems by presenting an innovative algorithm for the efficient operation of RCWS tailored for self-propelled mortars. The design process of a remote-controlled weapon station (RCWS) algorithm for a sophisticated artillery system, specifically a self-propelled mortar, was described. It was highlighted the significance of projectile flight kinematics in the design of a RCWS for artillery systems, delving into the theoretical challenges of targeting with weapon systems. It also analyses the components that make up the RCWS, focusing on the integration and functionality of these elements. Furthermore, examines the self-propelled mortar as a complex artillery system, discussing its purpose and unique characteristics. A key objective outlined is the development of an operational algorithm tailored for RCWS equipped self-propelled mortars, aiming to enhance their efficiency and effectiveness in deployment. The concept of the RCWS for self-propelled mortars, envisaged as a future modern system potentially applicable in the Serbian Armed Forces.

**Keywords:** RCWS, self-propelled mortar, algorithm, fire control system (FCS).

### 1. INTRODUCTION

The prevailing trend in the development of weaponry worldwide, including in our region, is the advancement of self-propelled mortars with calibers ranging from 60 mm to 240 mm. A primary characteristic of mortars is the smooth bore of the barrel, although there are examples of self-propelled mortars with rifled barrels. The most commonly utilized mortars are those with a caliber of 120 mm. In the design of self-propelled mortars, as well as in self-propelled artillery support weapons, there are two main conceptual approaches:

1. Open Mount Systems (without a turret): These weapons are mounted on the chassis of tracked or wheeled lightly armored vehicles without an enclosing turret. This configuration typically provides a simpler, lighter, and more cost-effective solution, allowing for rapid deployment and ease of maintenance. However, it may offer less protection for the crew and equipment compared to turreted systems.

2. Turreted Systems: These weapons are integrated into turrets mounted on the chassis of tracked or wheeled lightly armored vehicles. This approach offers better protection for the crew and the weapon system, enhancing

operational survivability in hostile environments. Turreted systems are often equipped with advanced targeting and

FCS, aligning them more closely with modern self-propelled artillery support weapons in terms of capability and performance.

Both concepts aim to enhance the mobility, responsiveness, and firepower of military units, making self-propelled mortars a critical component of modern artillery forces. The ongoing development in this field focuses on improving automation, accuracy, and ease of use, ensuring that these weapons systems remain effective in diverse and challenging combat environments. The turreted systems, in particular, are evolving to closely resemble contemporary self-propelled artillery support weapons, bridging the gap between traditional mortar systems and advanced artillery solutions.

The main trends in the development of self-propelled mortars globally are:

1. Primary Caliber: The 120 mm mortar, mounted in a turret on the chassis of lightly armored tracked or wheeled vehicles, is likely to become the standard.

2. Increased Range: Achieved by improving the internal ballistic characteristics of the weapon, enhancing the aerodynamic design of the mortar shell, and incorporating

additional propulsion systems.

3. **Enhanced Efficiency:** This includes improvements in the effectiveness of the mortar shell on target, as well as increased accuracy and rate of fire.

4. **Mobility and Maneuverability:** Enhancing the mobility, maneuverability, and ballistic protection of the systems both in firing positions and during movement.

5. **Reduced Reaction Time:** Utilizing new devices and systems for topographic, ballistic, and meteorological measurements to decrease the weapon's response time.

6. **Integration into Fire Control Systems (FCS):** Incorporating the mortars into higher-level fire control management systems to ensure coordinated and efficient operations.

## 2. RCWS FOR SELF-PROPELLED MORTARS

This section outlines the operational concept of RCWS designed specifically for self-propelled mortars, representing a future advanced system with potential application in the Serbian Armed Forces.

The RCWS is a sophisticated remotely operated weapon system for fire control, capable of being mounted on land combat vehicles, as well as on maritime and aerial platforms. These systems are employed on modern military vehicles because they provide the advantage of keeping personnel protected from direct enemy fire. The RCWS enhances operational effectiveness by enabling precise targeting and engagement from a protected position, thus increasing the survivability and combat capability of the vehicle and its crew.

Modern RCWS consist of a range of interconnected components that together form a complete system. The RCWS includes a weapon with an ammunition load, a stabilized weapon mount, a FCS and an electro-optical system for observation, targeting, and orientation.

The FCS constitutes a functionally integrated set of devices and measurement equipment connected by dependencies in mechanics, mathematics, and meteorology, ensuring the successful engagement of targets using weapons and artillery. The FCS is used to position the weapon in a manner that ensures the projectile reliably reaches the target, regardless of the movement of the RCWS or the target. The specific configuration of an FCS depends on the type of weapon, its specifications, and the degree of automation. The components forming an FCS can be divided into three main groups based on their functions within the system:

1. Components for information gathering and parameter measurement – sensors,
2. Components for information processing – computers and
3. Components for transmitting and executing processed information on the control object – actuators.

The first group includes various sensors for timely

detection, acquisition, identification, tracking of targets, and measuring their coordinates. This group of sensors is developing rapidly, being improved and applied across all types of FCS. It can be divided into active and passive sensors.

Passive sensors discreetly track the target. These sensors operate on the principle of detecting energy emitted by the target.

Active sensors operate on the principle of reflected energy from an irradiated object, providing information about the position or distance of the sensor from the target. Active sensors include radars (surveillance and targeting) and laser rangefinders. These sensors act as sources of radiation and can, therefore, be detected and jammed.

The second group of sensors is intended for measuring all parameters that influence the calculation of firing elements for stationary and moving targets. This includes sensors for measuring:

1. Angular velocities of the target,
2. Wind speed and direction,
3. Air temperature,
4. Air pressure,
5. Initial projectile velocity,
6. Temperature ranges for gunpowder and fuel and
7. Terrain inclination, among others.

## 3. FUNDAMENTAL KINEMATIC QUANTITIES REQUIRED FOR RCWS OF SELF-PROPELLED MORTARS

The type of weapon or artillery piece that serves as the executive element of the RCWS defines the various initial quantities needed to calculate the two fundamental firing elements. The primary advantage of RCWS is the inclusion of a system with sensors that automatically read data and store it in a computer, which then performs calculations and sends signals for aiming the weapon's barrel in both direction and elevation. When calculating the firing elements, it is necessary to consider and measure the values provided in the tables as well as the information about the target. The following values are read using the sensors on the RCWS:

1. Actual distance to the target,
2. Target height,
3. Local angle at which the target is being engaged,
4. Meteorological parameters,
5. Air temperature,
6. Barometric pressure,
7. Wind speed (lateral and longitudinal),
8. Horizontal angle at which the target is tracked and
9. Target speed (if the target is moving).

Based on the obtained target information, using a computer that already contains firing tables for a specific weapon, the firing elements are calculated. The computer's task is to perform calculations and determine the following values based on the received information:

1. Time of flight of the projectile to the target,
2. Range corrections due to differences in external temperature and barometric pressure compared to tabulated values,
3. Range corrections due to longitudinal wind,
4. Elevation angle with the included local angle and correction of the local angle and
5. Lead angle due to the target's movement.

The results of these calculations are the basic firing parameters:

1. Elevation angle ( $\phi$ ) and
2. Azimuth angle ( $\epsilon$ ).

The primary task of the FCS is to provide the most accurate values for these angles to ensure the target is hit by the mortar shell. Additionally, in the case of a moving target, continuous calculations and fire adjustments must be performed, similar to traditional artillery [1].

### 3.1. Firing elements in the vertical plane

The primary task of defining firing elements is determining all necessary initial conditions in the firing plane. The firing plane represents the vertical plane in which the ideal trajectory, free of lateral deviation, is located. The flight of the projectile in the vertical plane is defined by the following initial parameters:

1. Initial velocity,
2. Launch angle,
3. Time of flight of the projectile and
4. Range corrections due to atmospheric effects.

The design of the FCS for elements in the vertical plane must include the following conditions:

1. Target dimensions and
2. Target mobility.

### 3.2. Target dimensions as a condition for determining the elevation angle

The RCWS, using its sensors, determines the distance and height of the target. Based on these two parameters, the type of projectile trajectory is determined. The choice is made between two conditions:

1. The target height is above the apex of the trajectory and
2. The apex of the projectile trajectory is above the target height.

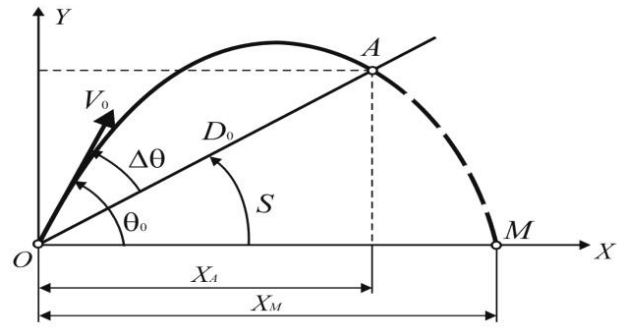


Figure 1. Projectile flight trajectories

In the case where the target height is greater than the apex of the projectile trajectory, a direct trajectory is adopted and the initial elevation angle is calculated [2]. This type of trajectory places the target within direct range. The basic formula for calculating the elevation angle of a direct trajectory is given by expression 1:

$$\theta_0 = S + \Delta\theta \cong S + \theta_{0T} \cdot \cos S \quad (1)$$

Where: S - local angle at which the target is observed,  $\theta_{0T}$  - tabulated angle from the firing tables.

In the case where the target height is lower than the apex of the trajectory, the calculation of the initial elevation angle differs from the previous one and will be applied for a parabolic trajectory.

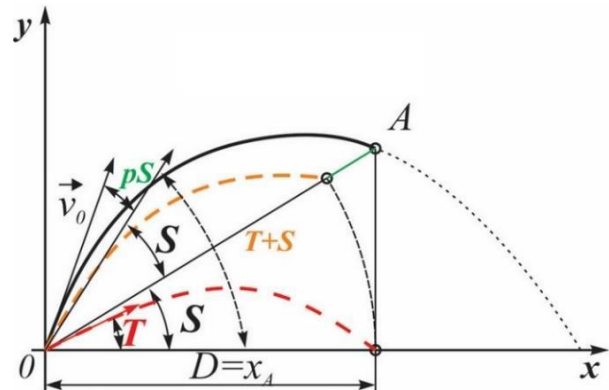


Figure 2. Projectile flight trajectories with local angle corrections

The main difference between these two firing methods is the introduction of a new variable called the local angle correction due to the local angle [2]. The formula for calculating the elevation angle in this case is as follows:

$$E = T + S + pS \quad (2)$$

Where: T - tabulated elevation angle, S - local angle at which the target is observed and pS - local angle correction.

The local angle correction is calculated using the recurrent formula given by expression 3:

$$\sin pS = \frac{\sin S \cdot \sin^2 T}{\cos(2T + S + pS)} \quad (3)$$

When calculating the firing elements, deviations in the projectile's flight range due to environmental parameters compared to normal conditions must be taken into account.

The normal environmental conditions adopted are:

1. Normal temperature:  $t = 15^{\circ}\text{C}$ ,
2. Barometric pressure:  $h = 1000$  mbar, and
3. Longitudinal wind:  $Wz = 0$ .

In the case of deviations from normal conditions, a range correction to the target must be made based on expression 4:

$$D = D_{so} \pm \Delta D_t \pm \Delta D_h \pm \Delta D_{wx} \quad (4)$$

Where:  $D_{so}$  - measured distance to the target,  $\Delta D_t$  - range correction due to temperature change,  $\Delta D_h$  - range correction due to pressure change and  $\Delta D_{wx}$  - range correction due to longitudinal wind.

When adopting the tabulated elevation angle, the range corrections are calculated first, and only then is the angle adopted, followed by determining the final elevation angle of the barrel.

### 3.3. Target mobility as a condition for determining the elevation angle

Determining the barrel elevation angle for a stationary target is a straightforward task during firing. However, for a moving target, additional variables are introduced to calculate the elevation angle. The primary task is to determine the lead angle [3]. The new variables introduced in the calculation for a moving target are:

1. Target movement speed:  $V_c$ ,
2. Angular velocity of barrel rotation in the vertical plane:  $\omega_{cy}$  and
3. Projectile flight time:  $T$ .

The target moves at a speed  $V_c$  and is tracked at a range  $X$ , which is continuously measured by a laser rangefinder, and with an angular velocity of the barrel  $\omega_{cy}$ . The vertical component of the target's movement speed  $V_c'$  is determined. Based on all this, the final elevation angle is determined using expression 5:

$$\theta_0 = \frac{6400}{2\pi} \left( \frac{g}{2V_0} \right) \cdot T \cdot \frac{V_0}{V_0 + \Delta V_0} + \omega_{cy} T \quad (5)$$

Where: 6400 - Eastern division of radians (Western division of radians is 6000),  $\theta_0$  - elevation angle,  $g$  - Earth's gravitational force,  $V_0$  - initial projectile velocity,  $\Delta V_0$  - change in initial projectile velocity,  $\omega_{cy}$  - angular velocity of the mortar barrel and  $T$  - time.

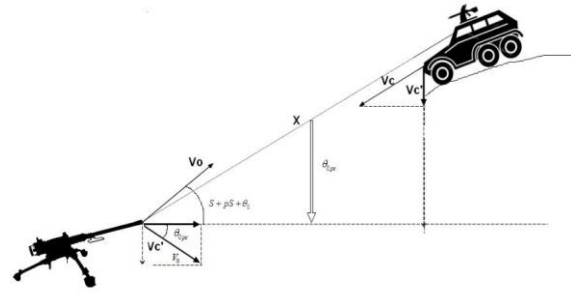


Figure 3. Diagram of firing at a moving target at a specific local angle and height

### 3.4. Firing elements in the horizontal plane

When firing at a target and determining the firing elements in the horizontal plane, the following characteristics are considered:

1. Derivation (deflection of the projectile during flight),
2. Presence of crosswind relative to the barrel axis and
3. Target mobility.

Derivation represents the deflection of the projectile along its path due to its rotation during flight. It is a calculated quantity that always occurs regardless of the type and size of the projectile, typically provided in firing tables. As with vertical angles, crosswind significantly influences aiming. When calculating this, it is assumed that the crosswind is normal to the aiming axis [5]. In the design process of self-propelled artillery systems, crosswind values are taken from firing tables and adopted as such in calculations. During targeting, the target can be in three basic positions, as shown in Figure 5 in relation to the direct aiming line, which aims at:

1. Frontal ( $0^{\circ}$ - $180^{\circ}$ ),
2. Oblique ( $45^{\circ}$ - $135^{\circ}$ ) and
3. Lateral ( $90^{\circ}$ - $90^{\circ}$ ).

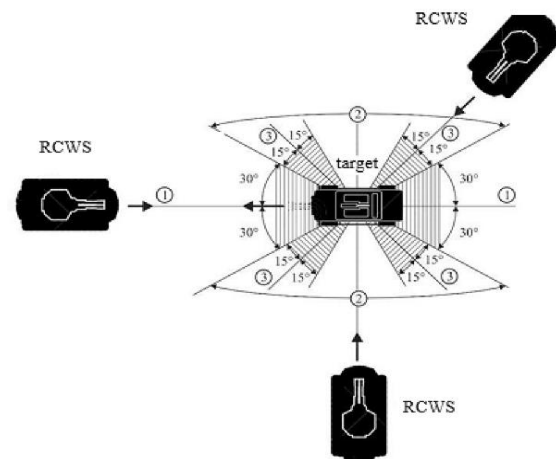


Figure 4. The position of the target relative to the RCWS

Each of these positions corresponds to a specific group of angles in the horizontal plane. The primary reason for this division is the design of the FCS, which is inherently linked to the principles of firing theory. Each of these procedures involves simplified kinematics, where certain targeting errors can be neglected to facilitate faster FCS operation [6].

The correction value for range  $\Delta D$  when targeting a moving target with a stationary DUBS is depicted in Figure 4 and can be determined by expression 6:

$$\Delta Dc = V_c \cdot \Delta t \cdot \cos q_c \tag{6}$$

Where:  $\Delta t$  is the time elapsed between the moment of measuring the distance  $X$  and the moment the projectile reaches the target, and can be approximated as the sum of preparation time  $t_{pr}$  and flight time of the projectile  $T$ .

$$\Delta t = t_{pr} + T \tag{7}$$

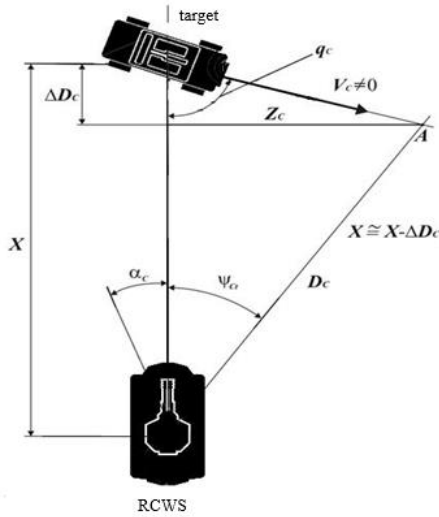


**Figure 5.** Horizontal elements to the target in the case of a moving target

Based on Figure 5, the deflection of the projectile at the point of intercept can be determined and described by the following expression:

$$Z_c = V_c \cdot \Delta t \cdot \sin q_c \tag{8}$$

The interception achieved by the projectile meeting the moving target is illustrated by expression 9:

$$\psi_c = \frac{6400}{2\pi} \cdot \frac{Z_c}{X \pm \Delta Dc} \tag{9}$$

It should be noted that when the target is moving, continuous tracking of the target and adjustment of the aiming line are performed throughout. It is assumed that the weapon is loaded and ready to fire, so the preparation time can be neglected. Therefore, the time  $\Delta t$  is solely the flight time of the projectile  $T$  [7].

#### 4. FCS ALGORITHM FOR SELF-PROPELLED MORTARS

The core of this seminar paper is designing algorithms for the operation of the FCS for self-propelled mortars. Figure 7 illustrates the general FCS operation algorithm.

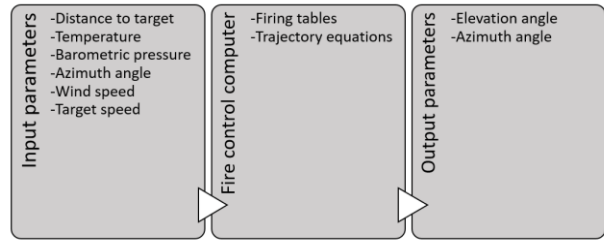


**Figure 6.** General algorithm of FCS operation

In this system, the computer plays the most critical role, which is to calculate the elevation and azimuth angles based on the firing tables and trajectory equations. Then, using actuators, the executive elements, the desired position of the mortar barrel is achieved.

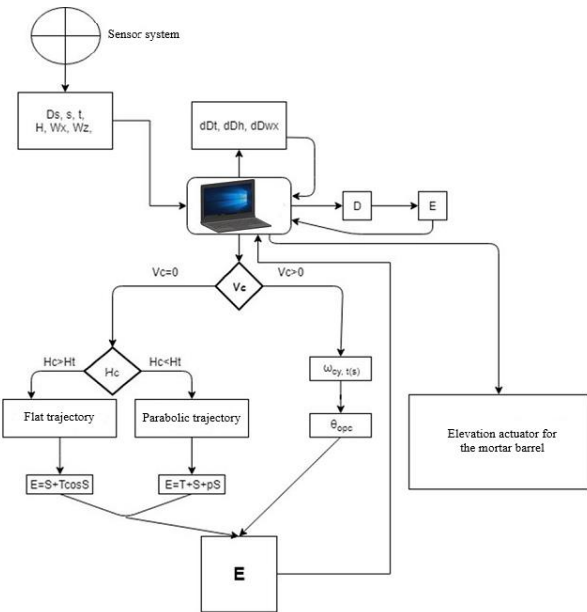


**Figure 7.** Algorithm for determining the elevation angle

Explanation of the algorithm in figure 7:

1. Target detection.
2. Determination of distance, local angle, and environmental conditions.
3. Sending information to the computer, which automatically calculates range corrections for the given distance to the target.
4. Based on the calculated distance, the computer selects the elevation angle.
5. When adopting the initial elevation angle, a series of conditions are set: Moving target YES - NO.
6. Target height ABOVE - BELOW the apex of the trajectory.
7. Depending on the conditions met, the computer automatically determines the type of trajectory and the elevation angle.
8. If the target is moving, the computer determines the elevation angle correction and adds or subtracts it from the already calculated elevation angle.
9. Finally, the final elevation angle  $E$  is obtained, whose value is converted into a signal for the actuator to adjust the barrel to the specified angle.

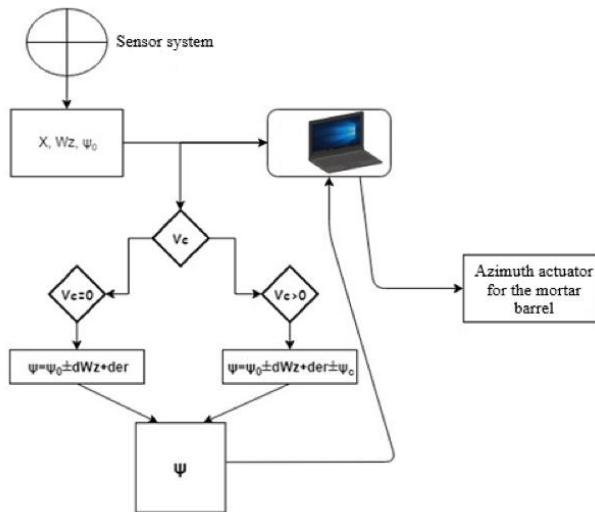


**Figure 8.** Algorithm for determining the azimuth angle

Explanation of the algorithm in figure 8:

1. Target detection.
2. Determination of the distance to the target, target speed and position, and environmental conditions.
3. Data is sent to the computer, which automatically calculates the azimuth correction due to derivation and crosswind.
4. A condition is set depending on whether the target is stationary or moving.
5. Based on known formulas for both conditions, the computer determines the angle at which the target should be engaged.
6. The obtained angle is converted into an impulse, which is sent to the actuator to apply corrections in the horizontal plane.

## 5. CONCLUSION

The development of self-propelled mortars represents a trend in the global military industry, including in our region. The mentioned modern artillery systems, which are already in use, are satisfactory in terms of construction and battlefield efficiency. Therefore, the emphasis and tendency of further development are directed towards improving the RCWS and FCS. In the Serbian Armed Forces, there is no self-propelled mortar, and the development of such an artillery system with an adequate RCWS would bring significant advantages over conventional mortars:

- Protection and safety of crew members,
- Better fire engagement,
- Automation of control functions,
- Increased measurement accuracy,
- Reduction of errors in achieving the desired effect on the target.

## ACKNOWLEDGEMENTS

This paper is a part of the research done within the project of the Univeraity of Defence in Belgrade, No. VA-TT/1/24-26.

This work was supported by the Ministry of Science, Technological Development and Innovations of the Republic of Serbia (Contract No. 451-03-66/2024-03/200325).

## References

- [1] DODIĆ, N.: *Target position measurement during automatic tracking*, Scientific Technical Review, vol. XLIX, no. 1, Serbia, 1999.
- [2] DODIĆ, N.: *Fighter plane trajectory generation*, Scientific Technical Review, vol. XLIX, no. 2, Serbia, 1999.
- [3] DODIĆ, N.: *Error analysis in the target tracking process*, Technical Review, vol. XLIX, no. 3, Serbia, 1999.
- [4] MILINOVIĆ, M., DODIĆ, N.: *Dynamic testing of the drive system for target tracking devices*, Technical Review, vol. L, no. 1, Serbia, 2000.
- [5] ŽIVANOVIĆ, M.: *Mathematical forms and methods for solving guidance problems of mechanical systems along a trajectory*, Technical Review, vol. L, no. 6, Serbia, 2000.
- [6] DODIĆ, N., MILINOVIĆ, M.: *A new concept of fire control for anti-aircraft guns*, Vojnotehnički glasnik, vol 47, no. 6, Serbia, 1999.
- [7] MILINOVIĆ, M., JEREMIĆ N.: *The problrm of the encounter between the projectile and the target in the automatic fire control system of an anti-aircraft turret*, Vojnotehnički glasnik, vol 44, no. 5, Serbia, 1996.





## DESIGN OF MORTAR BARREL 82 mm ON BASIS OF ANALYSIS OF INTERNAL BALLISTICS PARAMETERS

MARIJA MILOVANOVIĆ

Military Technical Institute, Belgrade, [marija.milovanovic@mod.gov.rs](mailto:marija.milovanovic@mod.gov.rs)

NIKOLA RADOVANOVIĆ

Military Technical Institute, Belgrade, [nikola.radovanovic@mod.gov.rs](mailto:nikola.radovanovic@mod.gov.rs)

NEBOJŠA HRISTOV

University of Defence Belgrade, Military Academy, [nebojsa.hristov@va.mod.gov.rs](mailto:nebojsa.hristov@va.mod.gov.rs)

LAZAR ARSIĆ

Military Technical Institute, Belgrade, [lazar.arsic@mod.gov.rs](mailto:lazar.arsic@mod.gov.rs)

ALEKSANDRA ŽIVKOVIĆ

Military Technical Institute, Belgrade, [aleksandra.zivkovic@mod.gov.rs](mailto:aleksandra.zivkovic@mod.gov.rs)

**Abstract:** The aim of this work was to obtain mortar with a higher initial velocity and lower pressure of powder gases. A analysis of the Internal ballistics (IB) parameters in the design phase of the 82 mm M69 mortar was performed using mathematical model of the Serebryakov method. In order to see the influence of certain parameters on the pressure of the gunpowder gases in the barrel and the initial velocity were first calculated with unchanged IB parameters, and then the influential parameters were varied in a certain range. A comparative method of calculating IB parameters is presented in a tabular way.

By optimally varying IB parameters in the range of  $\pm 5\%$ , the maximum pressure was reduced while the initial velocity was increased, which was the aim of this work.

**Key words:** Internal ballistics, mortar, internal ballistics design, method of Serebryakov, optimization.

### 1. INTRODUCTION

A mortar is a type of artillery weapon intended for immediate and general fire support. It is a weapon, usually with a smooth, less often rifling barrel, from which a non-rotating projectile is fired, at low initial speeds (less than 400 m/s) at relatively short ranges (up to 13 km).

The main characteristic of mortars is that they fire with the upper group of elevation angles (most often from 45° to 85°) with the possibility of smaller starting angles fire [1].

The projectile is self-stable, and the additional principle of stabilization of the projectile in flight is realized by wings on the rear part, because the barrel is smooth and there is no possibility of rotation after leaving the mouth of the barrel. The walls of the projectile are relatively thin, and therefore provide the possibility of installing a larger amount of explosive charge. The barrel of the mortar is usually 15 to 20 calibers long, which is breech-loaded at the back.

The highest working pressure of powder gases in the mortar tube does not exceed 1250 bar. The breechblock is wound on barrel and in it there is a mechanism for triggering and firing.

**Table 1.** Technical data for the 82 mm M69 mortar [2]

The main technical data	Mortar 82 mm M69
Horizontal field of action with fixed bipod	$\pm 7^\circ$
Caliber	82 mm
Internal barrel length	1200 m
Barrel length with breech	1347 mm
Mortar mass in firing position	45 kg
Barrel mass with breech	14,5 kg
Bipod mass	14 kg
Base plate mass	15 kg
Elevation	45° - 85°
Horizontal field of action with displacement of bipod	360°
Rate of fire	20-25 proj/min

### 2. IB CALCULATION OF THE 82 MM MORTAR M69

The internal ballistics calculation obtained by the Serebryakov method for the 82 mm M69 mortar is organized so that the calculation is carried out by periods of the firing process. First, the initial data is loaded, and then the constants and characteristics of the previous

period are calculated.

IB calculation was done using the know physico-chemical characteristics of double-base gunpowder, in the form of a flake. Characteristics of gunpowder for the base charge are:  $W_a=0.16$  mm;  $a=1.5$  mm;  $L=1.5$  mm,  $Q_v=5133$  J/g.

In the first period, the initial conditions and the interval of the independent variable are defined. Based on the interval of the independent variable and the number of points in the first period, the calculation step is defined. The program calculates the following characteristics for each step:  $p(y)$ ,  $X(y)$ ,  $V(y)$  and  $t(y)$ . For the second period, the procedure is the same. The initial conditions, the interval and the step of the independent variable are defined and calculated:  $p(X)$ ,  $V(X)$  and  $t(X)$ .

Additional data on the basis of which the other values needed to form the input file in the program for calculating the pressure of gunpowder gases in the barrel are calculated are shown in table 2.

**Table 2:** Calculation data

Half diameter of the propellant solid	0,00005 m
Volumetric propellant mass	1600 kg/m <sup>3</sup>
Amount of heat at constant volume BC	5133 J/kg
Amount of heat at constant volume IC	5108 J/kg
Initial volume of the powder chamber	0,000266 m <sup>3</sup>
Cross-sectional area of the gap	0,000079 m <sup>2</sup>
Total path of the projectile in the barrel	1,2 m
Specific heat ratio	1,2

**2.1. Results of IB calculations using the Serebryakov method**

**Table 3:** Input data for IB calculation

Label	Value	Unit
<i>Sc</i>	0.005281	<i>m</i> <sup>2</sup>
<i>Sz</i>	0.000082	<i>m</i> <sup>2</sup>
<i>W0</i>	0.00101	<i>m</i> <sup>3</sup>
<i>Xu</i>	1.2	<i>m</i>
$\xi$	0.95	/
<i>m</i>	3.05	<i>kg</i>
<i>Spr</i>	0.005199	<i>m</i> <sup>2</sup>
<i>fb</i>	1.1·10 <sup>6</sup>	<i>Jkg</i> <sup>-1</sup>
$\alpha$	0.00089	<i>m</i> <sup>3</sup> <i>kg</i> <sup>-1</sup>
$\rho_b$	1600	<i>kgm</i> <sup>3</sup>
<i>uz0</i>	1.37·10 <sup>-9</sup>	<i>msPa</i> <sup>-1</sup>
$\theta$	1,269	/
<i>r0</i>	0,00008	<i>M</i>
$\kappa_1$	1,2077	/
$\lambda_1$	-0,17198	/
<i>fb0</i>	5.98·10 <sup>5</sup>	<i>Jkg</i> <sup>-1</sup>
$\alpha_0$	0.00089	<i>m</i> <sup>3</sup> <i>kg</i> <sup>-1</sup>
<i>mb</i>	0.0798	<i>kg</i>
<i>mb0</i>	0.0078	<i>kg</i>

The IB calculation was performed using the Serebryakov method for mortars. The images below show the results,

i.e. the graphical dependence of one parameter on another [3].

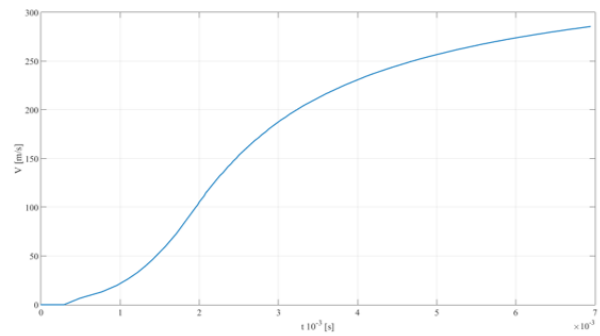


**Figure 1.** Velocity-time curve

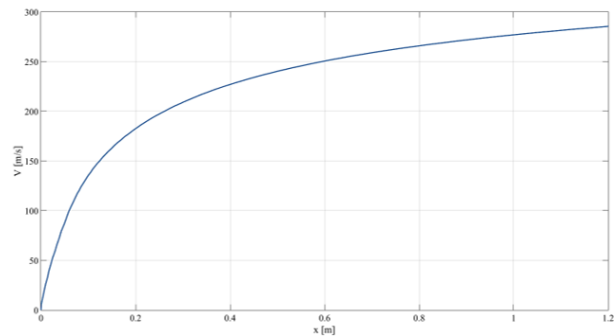


**Figure 2.** Velocity-travel curve

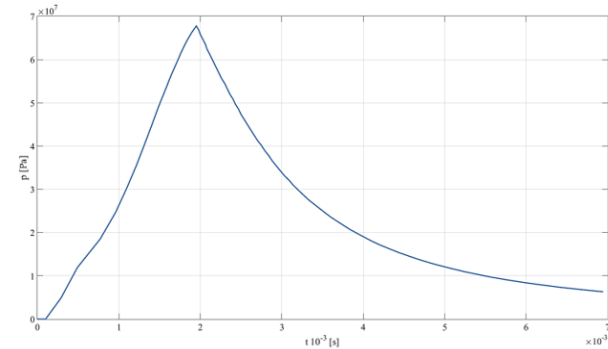


**Figure 3.** Pressure-time curve

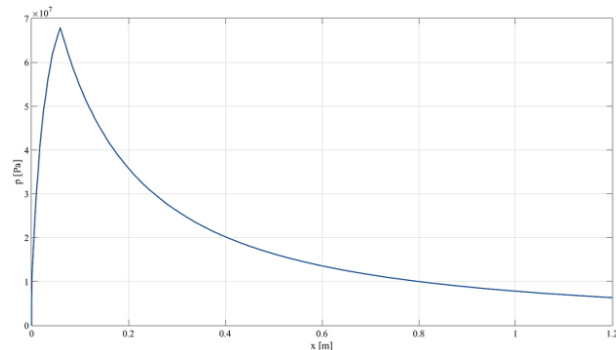


**Figure 4.** Pressure-travel curve

The characteristic data obtained by the calculation, important for further optimization, are the maximum pressure of powder gases  $p_m = 67.77$  MPa and the initial velocity of the projectile  $V_0 = 285.54$  m/s.

### 3. ANALYSIS THE INFLUENCE OF THE PARAMETERS ON THE PRESSURE OF GAS IN THE BARREL AND ON THE INITIAL SPEED OF THE MORTAR BOMB

In order to determine the influence of certain parameters on the pressure of powder gases in the barrel and the velocity of the projectile, they will be varied in a certain range. One parameter at a time will be varied in the range of  $\pm 5\%$ , while the other parameters will keep the basic value.

The parameters to vary are: the mass of the basic charge, the mass of the increment charge, the length of the projectile path in the barrel, the mass of the projectile, the "force" of the powder, the covolume of the powder gases, the unit burning rate, varying the thickness of the powder, the length of the powder grain and the initial volume of the combustion chamber.

By increasing the length of the projectile's path in the barrel by 5%, the velocity of the projectile increased by 1.3%, while the pressure of the powder gases in the barrel remained unchanged.

**Table 4.** Varying the parameter  $X_u$

$X_u$ [ m ]	$V_o$ [m/s]	$p_{max}$ [ bar ]
1,3	289.23	677
1,23	286.76	677
1,2	285.55	677
1,17	284.49	677
1,14	283.30	677

By varying the mass of the projectile, i.e. reducing it by 5%, the speed of the projectile increased by 2.5%, while the pressure of the gunpowder gases in the barrel decreased by 1.6%.

**Table 5.** Varying the parameter  $m$

$m$ [ g ]	$V_o$ [m/s]	$p_{max}$ [ bar ]
3,2	278,89	689
3,13	281,98	684
3,05	285.55	677
2,97	289,44	672
2,90	292,90	666

By varying the length of the projectile path from 1.2 m to 1.3 m and reducing the weight of the projectile from 3.05 kg to 2.90 kg, varying the other parameters did not have a significant impact on the basic internal ballistic characteristics or had an unfavorable influence.

By introducing the changed parameters into the calculation, an increase in the initial speed is obtained from 285.55 m/s to 296.48 m/s, with a decrease in the pressure of the powder gases from 67768304 Pa to 66542016 Pa.

### 4. DIMENSIONING OF BARREL

The resistance of the barrel is determined by the maximum stress and deformations in the walls under the influence of forces during firing. The basic force, on which the resistance of the barrel depends, is the force that arises from the pressure of the powder gases on its walls.

After defining the structural pressure diagram, the material for making the barrel is chosen with its elastic limit  $\sigma_e$ , and then, according to one of the theories of resistance, the outer radius of the barrel is determined in individual sections:

- according to the first resistance theory:

$$r_{2i} = r_{1i} \sqrt{\frac{\sigma_e + p_{1i}}{\sigma_e - p_{1i}}} \quad (1)$$

- according to the second resistance theory:

$$r_{2i} = r_{1i} \sqrt{\frac{\frac{3}{2}\sigma_e + p_{1i}}{\frac{3}{2}\sigma_e - p_{1i}}} \quad (2)$$

- according to the third resistance theory:

$$r_{2i} = r_{1i} \sqrt{\frac{3\sigma_e + 2p_{1i}}{3\sigma_e - 4p_{1i}}} \quad (3)$$

- according to the fourth resistance theory:

$$r_{2i} = r_{1i} \sqrt{\frac{\sigma_e^2 + p_{1i}\sqrt{4\sigma_e - p_{1i}^2}}{\sigma_e^2 - p_{1i}^2}} \quad (4)$$

In this way, the calculated values This paper showed the method of designing a mortar tube based on the optimization of UB parameters. The Serebryakov method was used for the UB calculation and was applied to the 82 mm mortar. of the outer diameter of the barrel  $r_{2pr}$  are obtained. When determining the actual values of  $r_{2stv}$ , it is necessary to take into account the installation of the barrel in the device as well as the elements that are attached to the barrel (muzzle brake, return mechanism, anti-recoil parts, etc.)

After determining the actual values of the outer diameter of the barrel  $d_{2stv}$ , a calculation is made and the real resistance of the barrel is determined, that is, the resistance of the barrel whose outer route is defined by the radiuses  $r_{2stv}$  according to one of the resistance theories mentioned above. The obtained pressure values indicate how much pressure a barrel of given dimensions can withstand. By dividing that pressure  $p_1$  with the corresponding pressure from the design pressure diagram  $p_{1k}$ , the actual safety coefficient is obtained:

$$n(n_i) = \frac{p_1}{p_{1k}} \quad (5)$$

In order to obtain the design pressure curve, first the pressure of the powder gases at the bottom of the chamber has to be determine. Since the ratio of the mass of the

powder charge to the mass of the projectile is small and the fictitiousness coefficient  $\varphi \approx 1$ , it can be assumed that the maximum pressure on the bottom of the powder gas chamber is equal to the maximum pressure of the powder gases on the bottom of the projectile  $p_{dm} \approx p_{pm}$ .

The point of maximum pressure of gunpowder gases on the graph  $p(x)$  moves by  $(2 \div 3) d$  towards the mouth of the barrel. This part continues with the "torment pressure" diagram of gunpowder gases in the barrel  $p_{tor}(x) = (1.12 \text{ to } 1.20) p(x)$ .

The structural pressure curve is defined on the basis of the chosen safety coefficient, most often for light mortars ( $d \leq 120$  mm) we take the strength coefficient to be 1.35 to 1.45 along the entire length of the barrel.

As the maximum pressure in the basic data for the IB calculation is higher than the pressure with optimized filling conditions, barrel sizing will be done based on the powder gas pressure curve for the basic data.

The maximum pressure of the powder gases was obtained from the IB calculation of the mortar:

$$p_m = 67768304 \text{ [Pa]} \quad (6)$$

Let's assume that the degree of safety is 1.4 for the entire length of the barrel. Elastic limit of the material from which the barrel is made  $\sigma_e = 1200 \text{ N/mm}^2$ .

Figures 5 and 6 show pressure changes for the design of the barrel and changes in the outer diameter of the barrel along the trajectory of the projectile.

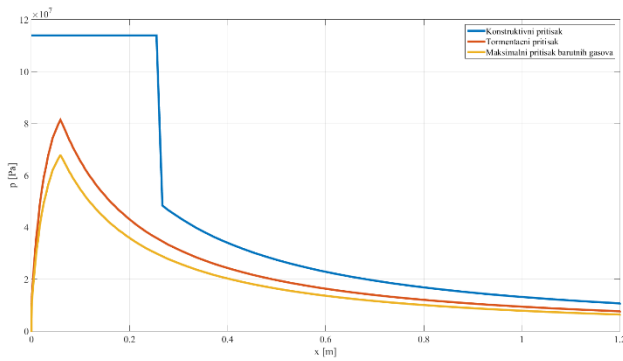


Figure 5. Pressure change graph for barrel design.

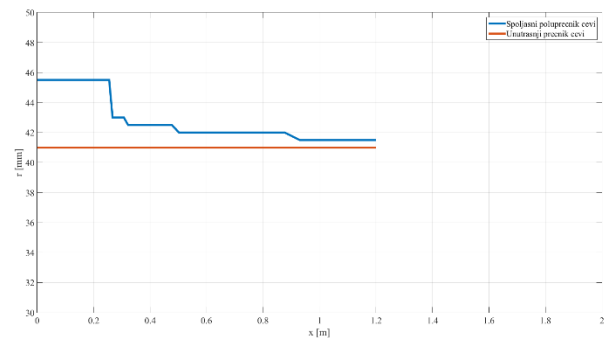


Figure 6. Graph of the change of the outer diameter of the barrel along the path of the projectile.

The maximum pressure of the powder gases was obtained from the IB calculation of the mortar for the optimized

solution:

$$p_m = 66542016 \text{ [Pa]} \quad (7)$$

Figures 7 and 8 show pressure changes for barrel design and barrel outer diameter changes along the projectile trajectory for the optimized solution.

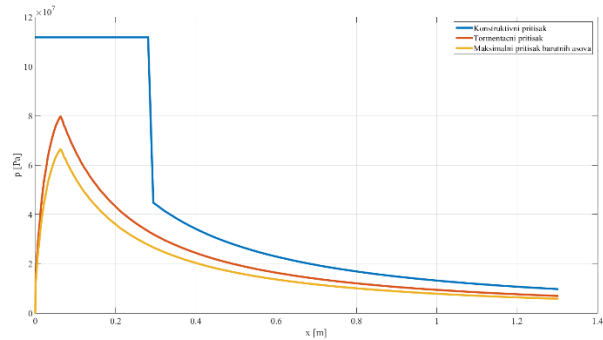


Figure 7. Graph of pressure change for barrel design - optimal solution.

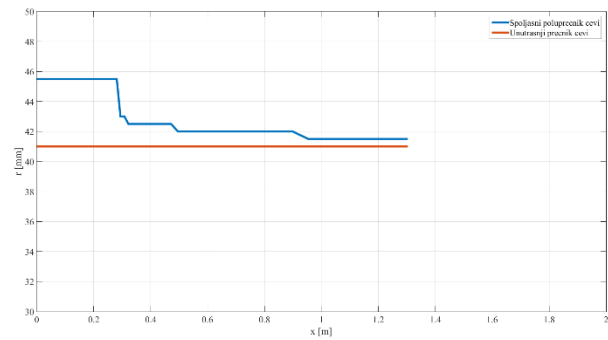


Figure 8. The graph of the change of the outer diameter of the barrel along the path of the projectile - the optimal solution

As the difference in the pressure of powder gases for the basic solution and the optimal solution is 1226288 [Pa], after rounding the diameter value to the first standard number, barrels of the same dimensions are obtained for the basic and optimal solution with an increase in the initial speed and thus an increase in the maximum range of the mine.

Figures 9 and 10 show a 3D model of an optimized mortar barrel made in the Solid Works software package. Designing the barrel and adding material resulted in a barrel mass of 5455.57 g. The barrel of the optimized solution is lighter by 344 g compared to the existing 82 mm barrel solution. Which led to a reduction in mass by approximately 6%.



Figure 9. 3D barrel model 82 mm



Figure 10. 3D model of the barrel section 82 mm

## 5. CONCLUSION

This paper showed the method of designing a mortar barrel based on the optimization of IB parameters. The Serebryakov method was used for the IB calculation and it was applied to the 82 mm mortar.

The influence of certain parameters on the magnitude of the pressure of powder gases in the barrel and the initial velocity (velocity at the mouth of the barrel) was examined. First, the pressure of gunpowder gases in the barrel and the initial velocity were calculated with unchanged IB parameters, and then the influential parameters were varied in a certain range in order to reach the optimal solution.

When varying, special care was taken to ensure that all initial data meet the Product Quality Regulation, which defines the permitted tolerances for certain parameters. Variation was made in the range of  $\pm 2\%$  to  $\pm 5\%$ . One parameter at a time was varied while the other parameters kept their basic value. The internal ballistic calculation resulted in a maximum pressure of powder gases in the barrel of  $67.77 \text{ MPa}$  and an initial velocity of  $285.54 \text{ m/s}$ . By varying the IB parameters in the range of  $\pm 5\%$ , the maximum pressure was reduced to  $66.54 \text{ MPa}$ , while the initial speed increased to  $296.54 \text{ m/s}$ , which is the goal of this paper. The length of the mortar barrel in the optimized model has been increased from  $1.2 \text{ m}$  to  $1.3 \text{ m}$ .

After that, barrel dimensioning was carried out according to the third theory of solidity and the external route of the barrel was obtained.

## Acknowledgements

This paper is a part of the research done within the project of the Univeraity of Defence in Belgrade, No. VA-

TT/1/24-26.

This work was supported by the Ministry of Science, Technological Development and Innovations of the Republic of Serbia (Contract No. 451-03-66/2024-03/200325).

## References

- [1] BUDISALIĆ, M.: *Internal ballistics 2*, Zagreb, 1971.
- [2] TANČIĆ, Lj.: *Internal ballistics design, textbook*, Military Academy, Belgrade, 2014.
- [3] *Corrected firing tables for the 82 mm light mortar with current projectile 82 mm M74A*.
- [4] MICKOVIĆ, D., JARAMAZ, S.: Solving interior ballistic problems using a two-phase model, *Scientific Technical Review*, vol. LI, br. 6, Serbia, 2021.
- [5] ABACI, W. B., KARI, A., HRISTOV, N.: *The Influence of the Internal Ballistic Pressure on the Rifled Barrel Stress Response*. *Scientific Technical Review*, vol. 70, no. 2, Serbia, 2020.
- [6] TANČIĆ, Lj.: *Collection of internal ballistics tasks*, Sector for education, training, scientific and publishing activities, Military technical academy of the army of Yugoslavia, Belgrade, 1999.
- [7] BUDISALIĆ, M.: *Internal ballistics 1*, Zagreb, 1971.

## SIMULATION MODEL OF TANK COMBAT

MARKO SIMONOVIĆ

Military Technical Institute, Belgrade, [marko.simonovic@mod.gov.rs](mailto:marko.simonovic@mod.gov.rs)

MILAN SIMONOVIC

Military Technical Institute, Belgrade, [milan.simonovic@mod.gov.rs](mailto:milan.simonovic@mod.gov.rs)

LAZAR ARSIĆ

Military Technical Institute, Belgrade, [lazar.arsic@mod.gov.rs](mailto:lazar.arsic@mod.gov.rs)

ANA GAČIĆ

Military Technical Institute, Belgrade, [ana.gacic@mod.gov.rs](mailto:ana.gacic@mod.gov.rs)

DUŠAN BOŽIĆ

Military Technical Institute, Belgrade, [dusan.bozic@mod.gov.rs](mailto:dusan.bozic@mod.gov.rs)

**Abstract:** In this paper, the fire control system for tanks (FCS) is presented, as a complex system, by means of which the target is detected, the necessary elements are occupied and shooting is carried out. The components of the FCS, the way in functions, and the way it is maintained are presented. The essence of FCS is presented in the form of algorithms, which includes all events, from the moment of target detection, to the firing order. The concept of direct fire is explained, as a model, which is characteristic in tank battles, with the problems and errors that may appear. Mathematical models for solving the problem of shooting in the horizontal and vertical planes have been set up. Also, the problem of shooting from a tank, when it is under a certain lateral inclination, in relation to the horizontal plane, where the shoulder of the cannon cradle is tilted, is explained. The mathematical model in this situation, which is presented in the paper, refers to the calculation of corrected angles of direction and elevation. In addition to FCS, in tank combat, one of the main factors for the success of the mission is the training of the crew. Based on all the set mathematical models, an example of a tank battle, consisting of two tanks, is shown. Tank combat is presented in the form of an algorithm, which includes all activities from target detection, through determining the necessary elements, to shooting.

**Keywords:** Tank, Fire control system, Tank combat

## INTRODUCTION

The Fire control system is a complex system, with the help of which the weapons detect the target, take the necessary elements for shooting, and hit it. The creation of the system, made it possible to relieve the crew and increase the probability of hitting. The Fire control system consists of: sensors, computers and executive bodies. The problems of the Fire control system can be presented in the form of an algorithm. [1]



Figure 1. Fire control system procedure

represent the procedure of the Fire control system. [1]

## SHOOTING IN DIRECT TANKS COMBAT

Direct firing from a tank is used in situations where it is necessary to complete the task with at least one direct hit on the target or where it is necessary to complete the task with as little consumption of ammunition as possible, in the shortest possible period of time. This is the basic mode of operation of the tank. Direct shooting can be divided into:

- shooting moving targets,
- shooting at stationary targets.

Hitting moving targets is most effective if shooting is done at distances of 1.5 to 2 swept ranges, because at longer distances the dispersion of hits increases sharply, the speed of the projectile decreases, its penetration of the target's armor decreases and errors occur in determining the elements for shooting. [1]

All members of the algorithm are interconnected and

## PROBLEMS OF SHOOTING IN DIRECT TANK COMBAT

Shooting from a tank requires complete concentration and training of the crew, correct measuring equipment and other parameters, which ensure the successful realization of shooting in all combat conditions. The problem of preparing elements for shooting comes down to solving two problems:

- calculation of the azimuth angle (horizontal shooting plane);
- calculation of the elevation angle (vertical shooting plane). [2]

## SHOOTING IN THE HORIZONTAL PLANE

The angle characteristic of this plane is the azimuth angle. It represents the angle, which is measured in relation to the direction of north, in the clockwise direction. If direct shooting is carried out, where both the tank and the target are stationary, the azimuth is equal to the table angle of the derivation. Derivation is the deflection of the projectile in the horizontal plane.

$$\psi = \psi_{der} = Der \quad (1)$$

In order to determine the azimuth, it is necessary to know two items. The first refers to whether it is shot with or without overtaking. The second relates to how the target moves relative to the tank it is targeting. There are three basic types of target movement: frontal, side and oblique movement. Each type of movements is characterized by a certain group of angles in the horizontal plane:

- frontal movement –  $0^\circ$  i  $180^\circ$ ;
- side movement – at an angle of  $90^\circ$  to the target;
- oblique movement –  $45^\circ$  i  $135^\circ$ . [2]

The types of mutual position of the tank and the target can be seen in figure 2.

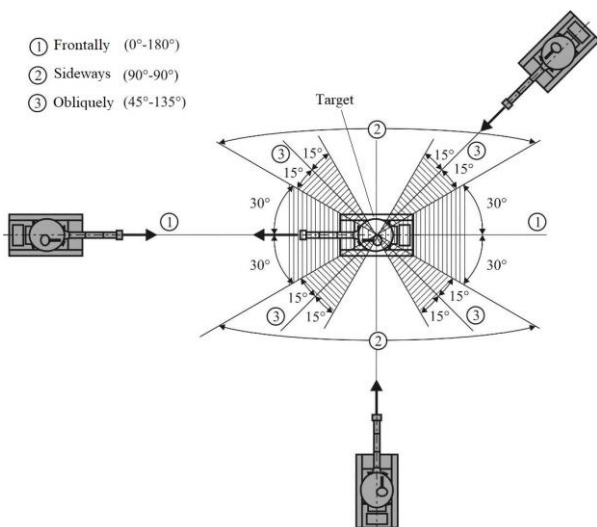


Figure 2. Mutual position of the tank and the target [2]

Figure 3 shows three cases of the relationship between the tank and the target in the horizontal plane. These cases are actually approximations in the course of shooting. The first case is when tanks move in straight lines in the horizontal plane, during aiming and shooting. The second case represents the rest of the tanks, where they have taken up a position. The third case represents the measurement of the distance to the target and shooting, where four subcases can arise:

- a stationary tank and a moving target – this case corresponds to shooting with sharp trajectories during direct shooting (1-1);
- a moving tank and stationary target – here the target lag behind the tank is characteristic (2-2);
- a stationary tank and moving target – a case where the target can be shot from rest or a short standstill (1-3);
- a moving tank and a moving target – the same case as shooting from rest (2-3). [2]

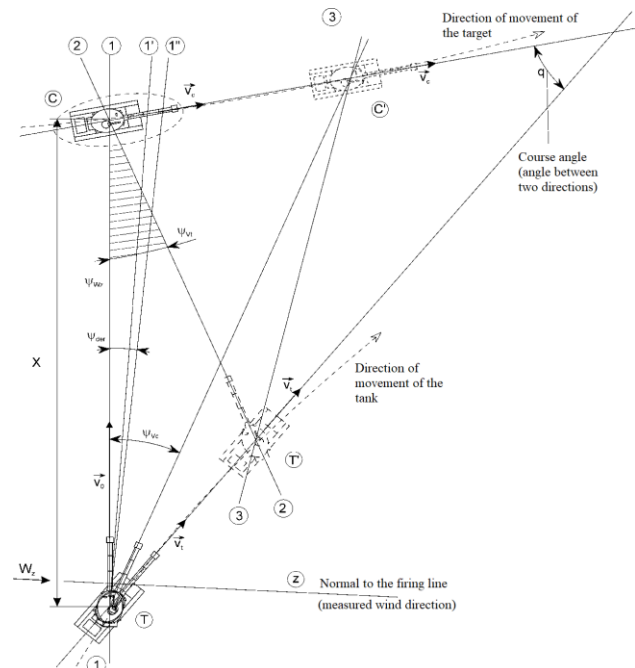


Figure 3. The relationship between the tank and the target in the horizontal plane [2]

Each of these cases includes a corresponding overtaking or lagging angle:

- $\psi_{vt}$  – the overtaking angle when the tank is moving and the target is stationary;
- $\psi_{vc}$  – overtaking angle, when the tank is stationary and the target is moving;
- $\psi_{vtvc}$  – collective angle, when both the tank and the target are moving;
- $\psi_{der}$  – missile derivation angle – this is the tabular value of the expected deflection of the projectile at the target in the horizontal plane;
- $\psi_{Wz}$  – the deflection angle of the projectile, due to the influence of the side wind, which results in a change in the relative speed of the projectile. [2]

The total overtaking angle is determined from the following expression, based on the speed of the firing tank:

$$\psi_{V_c V_t} = \frac{6000(6400)}{2\pi} V_t \sin \alpha_c \left( \frac{1}{\dot{X}} - \frac{1}{V_{0M}} \right) + \frac{6000(6400)}{2\pi} \frac{\Delta V'}{\dot{X}} T \quad (2)$$

$$\psi_{V_c V_t} = \frac{6000(6400)}{2\pi} (\Delta \psi_p + \omega_{cz} T) \quad (3)$$

$$\dot{X} = \frac{X}{T} = const \quad (4)$$

$V_t$  – projectile speed

$\alpha_c$  – the angle between the axis of the barrel of the cannon and the direction of movement of the tank in the horizontal plane

$X$  – range

$V_{0M}$  – the actual initial speed of the projectile

$\Delta V'$  – the relative speed of the target in the direction normal to the axis of the barrel of the cannon

$T$  – the flight time of the projectile

$\psi_p$  – overtaking angle without crosswind influence

$\omega_{cz}$  – angular speed of the target

The equation shows that the total overtaking angle, during the movement of both the tank and the target, is reduced to correction. This correction is determined by means of the component of the wind speed in the direction normal to the projection of the axis of the barrel of the cannon in the horizontal plane and the speed of the target, which is determined on the aiming device. [2]

### SHOOTING IN THE VERTICAL PLANE

Here, it is necessary to establish an adequate elevation angle of the barrel. If the target is moving, there must be an elevation angle correction at all times. If overtaking is present in the vertical plane, the elevation angle of the barrel must be determined by the speed of movement of the target and the firing tank. An additional complication is characterized by the fact that both the tank and the target move on terrain with arbitrary irregularities. []

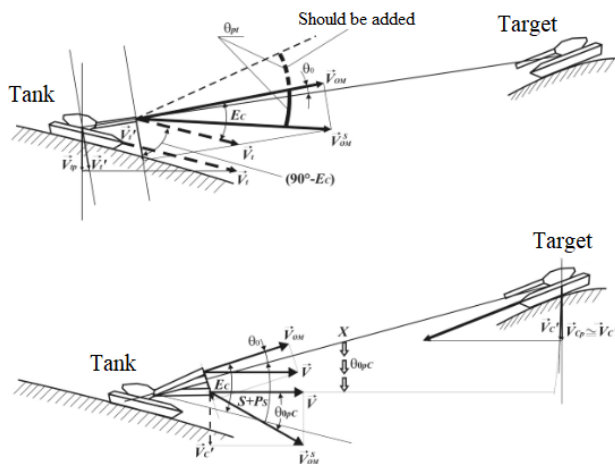


Figure 4. Overtaking during the movement of tanks in the vertical plane [2]

The elevation angle  $E_c$  represents the basic quantity for the dynamic correction of shooting moving target.

It contains the table angle  $\theta_0$  and the target angle  $S$ . Overtaking involves two questions. The first refers to overtaking due to the tank movement of the tank. The overtaking angle is calculated as:

$$\theta_{pt} = \frac{V_t'}{V_0} = \frac{V_t \sin E_c}{V_0} \approx 0 \quad (5)$$

The second refers to overtaking due to target movement. Then the overtaking angle is calculated as:

$$\theta_{0pc} \cong \frac{V_c' T}{X} \left( \frac{6000(6400)}{2\pi} \right) \quad (6)$$

$V_0$  – initial speed of the projectile with the appropriate ballistic correction

$V_c'$  – the speed of the change in the position of the target in the firing plane, in relation to the tank firing in the vertical plane

There is a problem that further complicates the entire shooting preparation, and that is the slope of the shoulder of the tank gun cradle. [2]

### INFLUENCE OF TANK CANNON CRADLE SHOULDER ANGLE

The simplest way to shoot from a tank is when it is standing on a flat surface, that is, when the cradle of its cannon is in a horizontal position. However, in practice, it often happens that the tank is located on the terrain, which is under some slope. One such example can be seen in figure 5. [1]

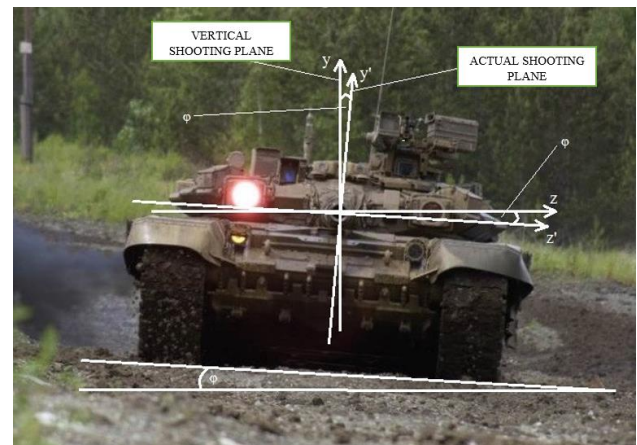


Figure 5. Position of the tank in an inclined plane

The z-y plane represents the horizontal position of the tank

The z'-y' plane represents its actual position

The corrected angle of direction and elevation of the barrel can be calculated as: [1]

$$\theta'_0 = \theta_0 \cos \varphi + \psi_0 \sin \varphi \quad (7)$$

$$\psi'_0 = \psi_0 \cos \varphi - \theta_0 \sin \varphi \quad (8)$$



### ALGORITHM OF TANK COMBAT

The tank battle begins the moment one of the tanks discovers the other, with its observation-aiming device. Then the preparation of elements for shooting begins, with the desire to neutralize the opponent's means as soon as possible. The battle of tanks lasts until that moment, when one tank hits another, and the hit is with a critical outcome for the opposing tank. There is another way to end the battle, and that is when both tanks run out of ammunition. In Figure 6, two tanks can be seen. The sighted tank (target) moves relative to the firing tank, in an oblique trajectory. The figure also show the parameters, which, using mathematical models, are used to calculate the necessary elements for shooting.

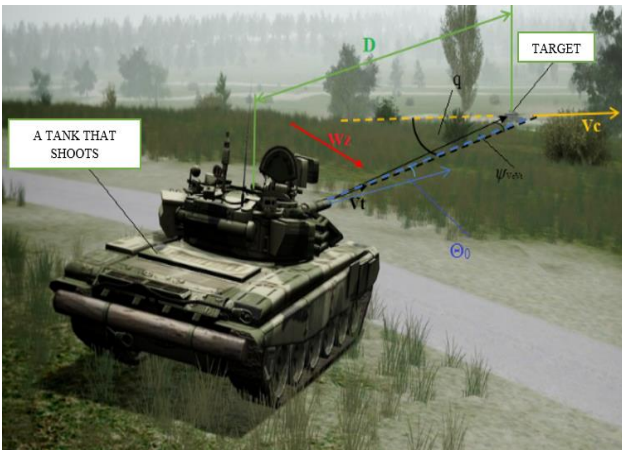
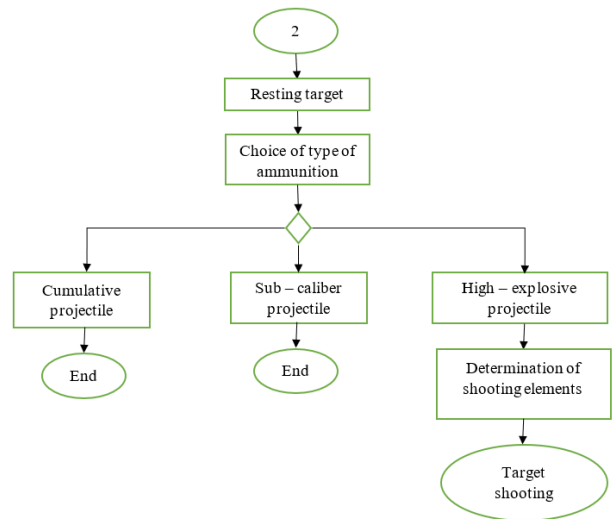
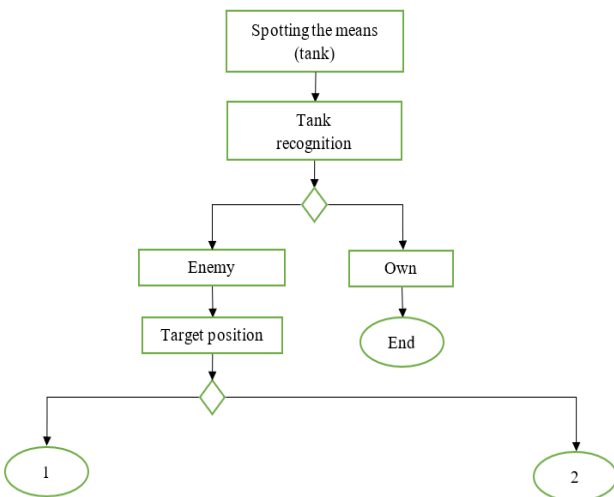
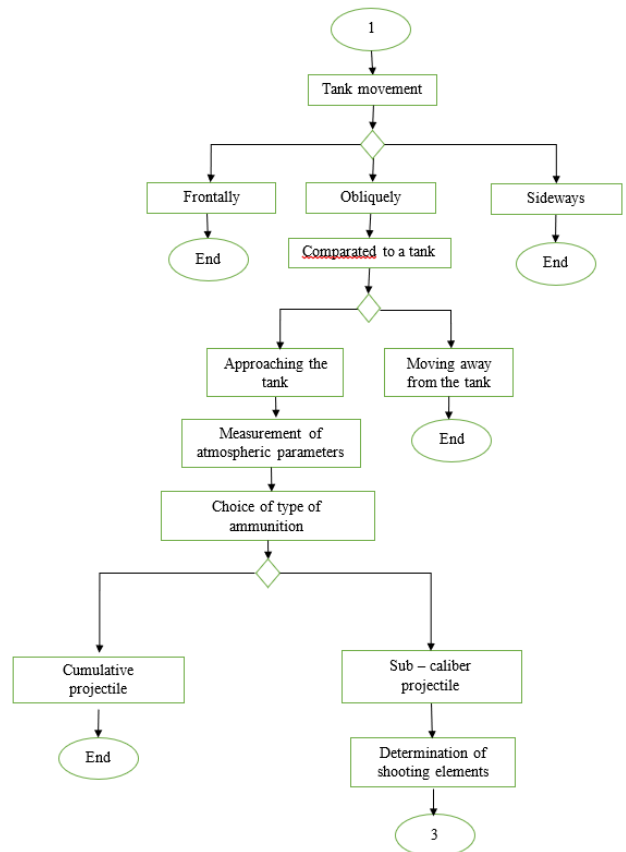


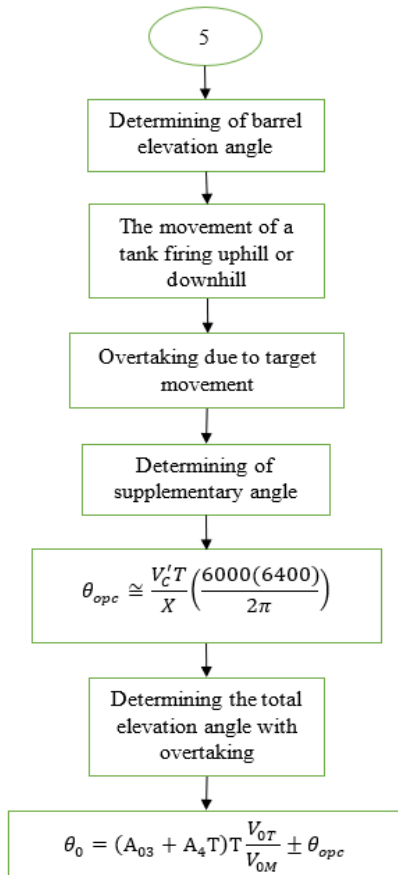
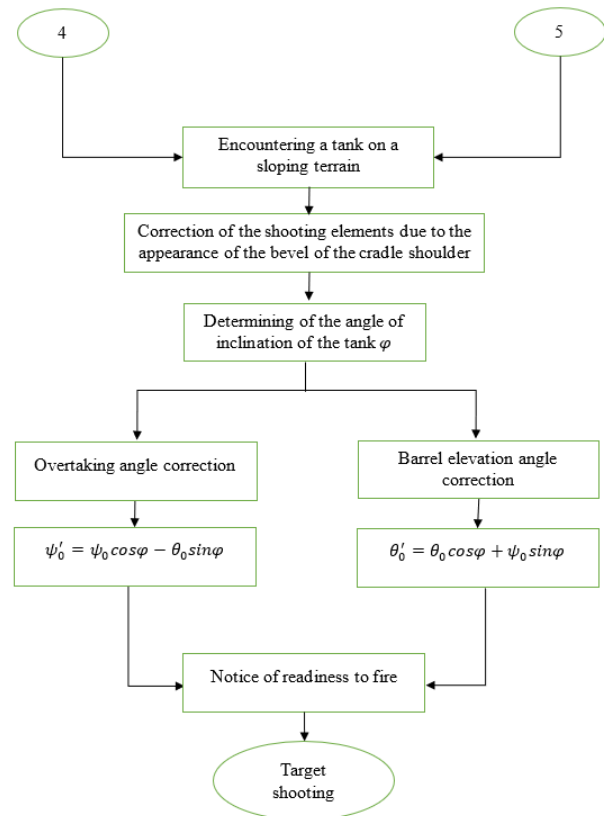
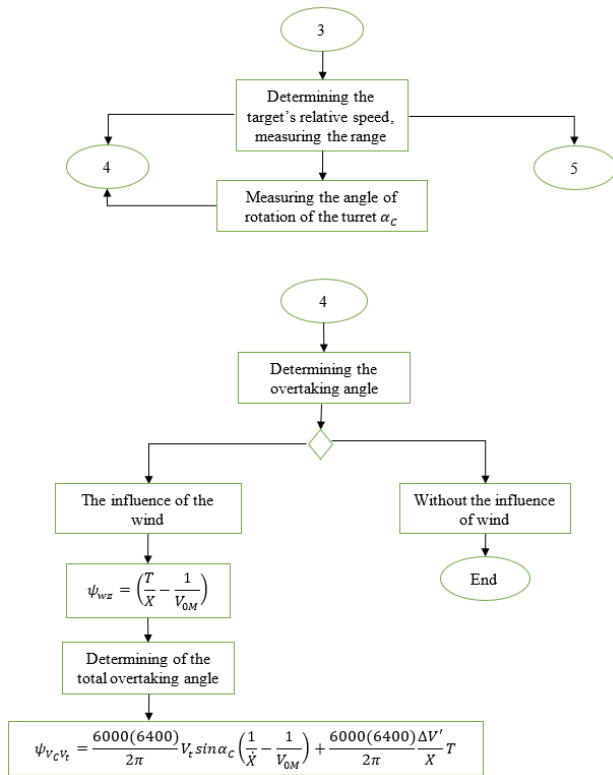
Figure 6. Tank battle with parameters for determining firing elements

The following is a presentation of the tank battle algorithm.



Note: The second case will be presented first, because it is much shorter than the first. Also, it is displayed informatively, so there won't be much lingering on it. For the selected projectile type, shooting elements are determined. After that, target shooting was done.





The algorithm starts with detecting the asset (tank). Immediately after sighting, it should be established whether it is one's own tank or an enemy tank. If it is its own, the tank continues its movement according to its predefined plan. In case the tank is enemy, the emergency mode of tank activity follows. By observing the target, the tank first collects information about whether the target is moving or stationary. The simplest way to fight is to shoot at a target at rest (case 2). A much more difficult situation is when both assets are in motion (case 1). When moving the target, the tank must see how the target is moving towards it (frontally, obliquely or sideways). The tank realizes that the target is moving obliquely, moving away from him. After that, the atmospheric parameters are measured. The combat kit of the tank consists of three types of projectiles: sub-caliber, high-explosive and cumulative. With the choice of ammunition, it was decided that the tank shoots sub-caliber projectile, because this ammunition is most often used to shoot moving targets, due to the high initial speed of the projectile. In the algorithm, the determination of the shooting elements was approached only for the selected type of projectile. Furthermore, the speed of movement of the target and the range are determined, which are necessary for determining the elements for shooting. After determining these parameters, the azimuth angle is determined. The influence of side wind, which further complicates the whole situation, is taken into account. Since the target is moving, it is necessary to determine the overtaking angle. The following is the determination of the elevation angle of the cannon barrel. Depending on the terrain, the firing tank can move uphill or downhill.

This type of movement requires a constant correction of the elevation angle, by supplementing it with a certain value of the supplemental angle.

After determining the requires angles, a new situation occurs, which further complicates the shooting process. A tank that is shooting encounters a steep plane, which forces it to move at a certain side slope, which results in the slope of the cradle shoulder by a certain angle. It is necessary to determine the angle at which the tank is now in relation to the horizontal plane, and then, using it, perform the correction of the azimuth and elevation angle. After determining the elements, there is a notification about readiness for shooting, and then the execution of the same. The tank must hit the target the first time, otherwise it becomes a target.

## CONCLUSION

The problem of shooting from a tank during a sudden tank battle, where both the tank and the target are moving in certain directions, is, by all accounts, a very complex and extremely inexhaustible topic for research and analysis. No two tank battles are the same, because each brings with it a different situation: the position of the target, the position of the firing tank, the range, the climatic conditions, the terrain on which it takes place and everything that goes with it. The role of the Fire control system is reflected in the fact that it solves all the

questions that the crew faces during the fight and reduces its solutions to successful shooting from the tank. The training of the crew plays a big role in all of this, because it means nothing if the Fire control system is functional and ready to use, and the crew is not prepared to apply it in the best away.

## Acknowledgements

This work was by Serbian Ministry of Defense and Serbian Ministry of Education, Science and Technological Development, Grant No 451-03-66/2024-03/200325.

## References

- [1] KARI A.: Skripta iz predmeta "Integracija naoružanja na mobilne platforme", 2018.
- [2] MILINOVIĆ M. ĐEDOVIĆ B.: Skripta „Sistemi za upravljanje vatrom“, Beograd 2018.
- [3] JANKOVIĆ R.: „Simulacioni model sukoba dve naoružane mobilne platforme“, YUINFO 2001, zbornik radova, Kopaonik, 2001.
- [4] DODIĆ N.: Target position measuring during automatic tracking, Schientific Technical Review, vol. XLIX, no. 1, Serbia, 1999.

# SIMULATION MODEL OF PRIORITIZED THREAT SELECTION IN DEFENSIVE MULTITARGET MILITARY SWARMING

RADOMIR JANKOVIĆ

Union University School of Computing, Belgrade, [rjankovic@raf.rs](mailto:rjankovic@raf.rs)

**Abstract:** A dynamic prioritized selection of threats and targets, as well as assignment of available resources, are important issues in discrete events simulation of defensive multitarget military swarming. An approach to simulation modelling of swarm counter swarm conflicts in a territory cell, where multiple mobile ground threats organized in swarms are attacking multiple objects defended by swarms of armed mobile platforms is presented in the paper.

**Keywords:** Simulation, Multitarget Swarming, Swarm vs Swarm Conflict, Selection, Priority.

military tactics research and development

## 1. INTRODUCTION

Swarm and derived concepts *swarming*, *swarming tactics*, or *swarm intelligence*, have become common words in contemporary research in various areas of science and technology, military applications in particular [1, 2, 3,4].

The majority of recent military research deals with drone swarming [5].

In Serbia, the research of swarming tactics, based on discrete events simulation, is underway for quite some time now [6]. It deals mainly with man-crewed armed mobile platform (AMP) group swarming, as a new armoured units' tactics, proposed in [7], where AMPs repeatedly attack an adversary threat from many different directions, and then regroup.

Some of the results of the research proved that swarming tactics of AMPs can have advantages, in both conventional and hybrid [8,9] conflicts, when swarmers are engaged in defence of one object counter one single threat.

However, an armoured battalion, as a basic tactical unit considered in the research, has opportunities to apply simultaneous multiple swarming against 2, 3 or even more different threats.

On the other hand, threats of a battalion size can also attack multiple defended objects, applying offensive multi swarming tactics. In such situations, there are multiple swarm versus swarm conflicts.

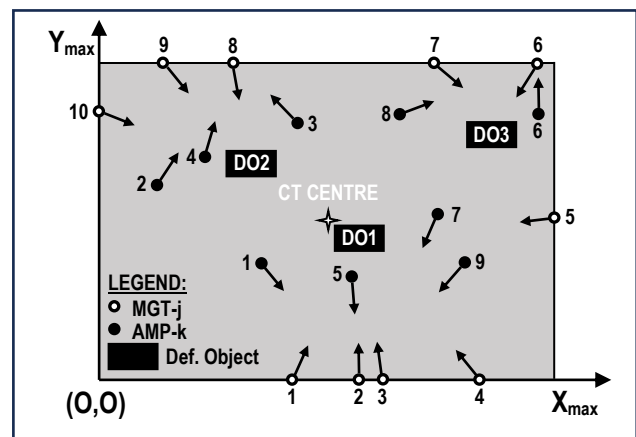
Computer simulations of such swarming systems impose important issues, such as dynamic prioritized selection of threats and targets, as well as assignment of available resources.

In this paper an approach to simulation modelling of swarming tactics application in such combat situations has been proposed.

It is expected that the approach will enable computer simulation of multiple swarm versus swarm combats, as one of the most challenging issues in contemporary new

## 2. THE SIMULATED SYSTEM

The simulated system (**Figure 1.**) considered in the model consists of: 2-dimensional territory cell (TC), D defended objects (ODs) in it, N defender armed mobile platforms (AMPs), and M mobile ground threats (MGTs), intended



to destroy ODs in TC.

**Figure 1.** Simulated system initial deployment

### 2.1 Territory cell

Territory cell (TC), actually the simulated battlefield, is a rectangle 2-dimensional space, with relative origin of coordinates in one of its base's corners. It is characterized by maximal values of its coordinates ( $X_{max}$ ,  $Y_{max}$ ).

In the proposed simulation model, the territory cell's terrain features are determined by possible average speeds of the moving components of the modelled system:

- $V_{AMP}$  for armed mobile platforms (AMPs);
- $V_{MGT}$  for mobile ground threats (MGTs).

### 2.2 Defended objects

In the beginning of any simulation pass,  $D_{OD}$  defended objects (ODs) are randomly deployed in TC.

The closer an OD is to the TC centre, the higher is its priority of defence (PoD).

Defended objects are immobile and unarmed, relying on AMPs to defend them of mobile ground threats (MGTs), with assigned priority of defence (PoD).

An OD is destroyed after receiving a defined number of hits ( $D_{HITS_{max}}$ ) from any MGT's main armament.

If some OD is destroyed, all of remaining AMPs or MGTs assigned to defend or attack it, are reassigned to defend or attack the remaining ODs, according to those ODs priority of defence.

### 2.3 Armed mobile platforms

In the beginning of any simulation pass,  $N_{AMP}$  armed mobile platforms (AMPs) are randomly deployed in TC.

AMPs mission is to defend ODs against  $M_{MGT}$  mobile ground threats (MGTs). For that, they are organized in multiple defending swarms, assigned to ODs, on priority basis, in number according to their PoD.

If an AMP or its OD is destroyed by some MGT, the other AMPs are dynamically reassigned to defence of remaining ODs, on the same priority basis.

AMPs use the defensive swarming tactics, attacking the swarms of MGTs.

The AMP priority is to attack the nearest MGT that appears in its main armament range.

AMP is destroyed if it is hit by 1 direct hit from any of MGTs main armaments.

AMPs dispose of main armaments, with maximal range  $R_{AMP_{max}}$ , reload time  $T_{rAMP}$ , and target hit probability  $p_{AMP}$ .

In the beginning of every simulation pass, all AMPs start with loaded main armaments.

AMPs can shoot and reload on the move, and are capable to move in TC area with an average speed of  $V_{AMP}$ .

### 2.4 Ground mobile threats

In the beginning of any simulation pass,  $M$  ground mobile threats (MGTs) are randomly deployed on TC outer edges.

MGTs mission is to destroy ODs in TC. For that, they are organized in multiple attacking swarms, assigned to ODs, on priority basis, in number according to their PoD.

MGTs use the swarming offensive tactics, attacking their assigned ODs as well as adversary swarms of AMPs, encountered in the process.

If an MGT is destroyed by some AMP, the other MGTs are dynamically reassigned to attack its assigned OD, on the same priority basis.

For MGT, a destruction of the closest encountered AMP, no matter to what defending swarm it belongs, is of

greater priority, in order to avoid being destructed itself by such an AMP. MGT is destroyed if it is hit by 1 direct hit from any of AMPs main armaments.

MGTs dispose of main armaments, with maximal range  $R_{MGT_{max}}$  and reload time  $T_{rMGT}$ . In the beginning of every simulation pass, all MGTs start with loaded main armaments.

MGTs can shoot and reload on the move, and are capable to move in TC area with an average speed of  $V_{MGT}$ .

## 3. THE SIMULATION MODEL BASICS

The proposed simulation model is discrete and dynamic, oriented to events in the system. The activities of the system components are represented in the model by means of pure simulation clock time delays.

The main events changing the state of the simulated system considered in the model are:

- Detection of some MGT in the range of some AMP's main armament;
- Detection of some AMP in the range of some MGT's main armament;
- Detection of some OD in the range of some MGT's main armament;
- Destruction of some MGT;
- Destruction of some AMP;
- Destruction of some OD.

The simulated system's moving parts in the model are:

- Mobile ground threats (MGTs);
- Armed mobile platforms (AMPs).

The simulation clock advancing takes place in these cases:

- After some time-consuming action in the system;
- After the model basic time interval  $\Delta t$ .

Time-consuming actions in the system are reloadings of main armaments of AMP ( $T_{rAMP}$ ) and MGT ( $T_{rMGT}$ ).

The model basic time interval is defined by:

$$\Delta t = \frac{P_{mod}}{\min(V_{AMP} \cdot V_{MGT})} \quad (1)$$

Where  $P_{mod}$  [m] is the model input, chosen by user.

## 4. PROPOSED MULTIPLE SVARM VS SWARM CONFLICT TACTICS

For both sides, MGTs or AMPs, it is proposed to shoot from their main armament at the nearest adversary swarmer that is encountered in one's own main armament range.

For the attacking side, for an MGT, that means that shooting at the nearest AMP has the priority even if a target OD is in its main armament range at the same time.

For the defending side, for an AMP, that means that shooting at the nearest MGT has the priority, no matter to what attacking swarm does the nearest MGT belongs.

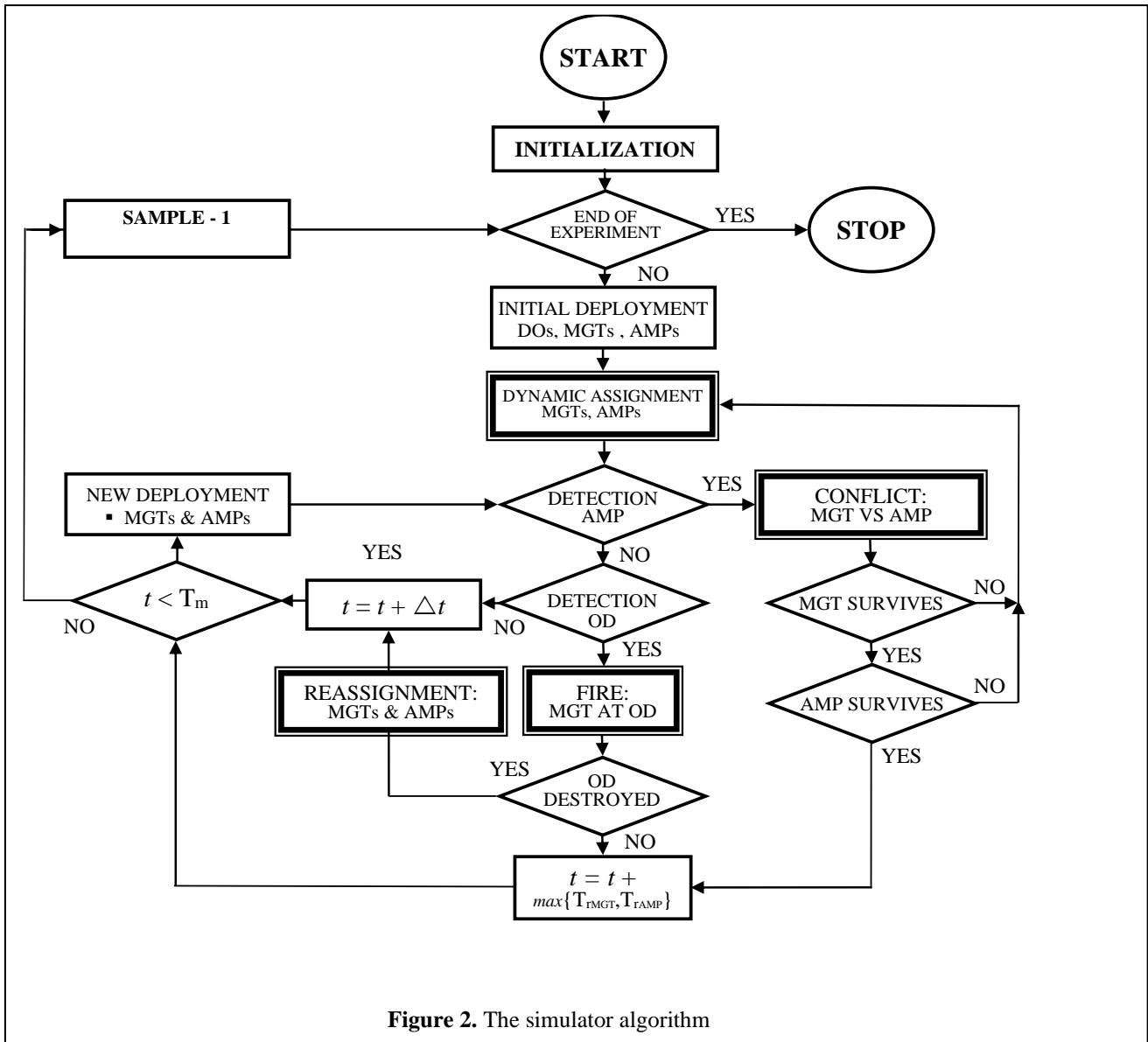


Figure 2. The simulator algorithm

The main reason for proposing such a tactics in a swarm versus swarm conflict is that both MGT and AMP can be destroyed with a single direct hit from the opponent's main armament. On the other hand, destroying an OD requires more hits, according to its predefined number  $D_{HITSmax}$ .

## 5. THE SIMULATOR ALGORITHM

The simulator algorithm is depicted in **Figure 2**.

INITIALIZATION of the simulator comprises the experiment parameters entering, such as:

- Number of completed simulation passes in the experiment (SAMPLE);
- Territory cell dimensions ( $X_{max}$ ,  $Y_{max}$ );
- Number and characteristics of defended objects ( $D_{OD}$ ,  $P_{OD}$ ,  $D_{HITS}$ );
- Number and characteristics of AMPs ( $N_{AMP}$ ,  $V_{AMP}$ ,  $R_{AMPmax}$  [m],  $T_{rAMP}$  [s],  $p_{AMP}$  [%]);
- Number and characteristics of MGTs ( $M_{MGT}$ ,  $V_{MGT}$ ,  $R_{MGTmax}$  [m],  $T_{rMGT}$  [s],  $p_{MGT}$  [%]);

- Initial distribution of MGTs for attacking ODs (fractions of  $M_{MGT}$  for each OD [%]);
- Initial distribution of AMPs for defending ODs (fractions of  $N_{AMP}$  for each OD [%]);
- MGTs to their assigned ODs motion laws or itineraries;
- Preciseness of the simulation model  $P$  [m];
- Lost ODs counter starting value: ( $L_{OD} = 0$ );
- Lost AMPs counter starting value: ( $L_{AMP} = 0$ );
- Lost MGTs counter starting value: ( $L_{MGT} = 0$ );
- Maximal simulated time of MGTs mission ( $T_m$  [s]).

END OF EXPERIMENT condition is met when the count-down counter of completed number of simulation passes reached 0 (SAMPLE=0). If the condition is met, the simulation stops and the report of results of interest is generated. If it is not, the simulation continues.

INITIAL DEPLOYMENT consists of:

- Random fixed positions of ODs on TC ground surface, the more OD- $i$  is close to the TC centre, the more it is important to be defended;
- Random positions of AMPs on TC ground surface;

- Random positions of MGTs on TC outer edges.

DYNAMIC ASSIGNMENT of MGTs and AMPs comprise prioritized selection of MGTs and AMPs, in order to form:

- Attack swarms of MGTs (ASW- $j$ ,  $j = 1, \dots, D_{OD}$ );
- Defence swarms of AMPs (DSW- $k$ ,  $k = 1, \dots, D_{OD}$ ).

MGTs are selected to be members of ASWs according to their distance from corresponding ODs, in numbers defined by the simulator input initial distribution of MGTs assignment.

For each ASW, MGT with minimal distance from its target OD is appointed as attacking swarm leader (ASL- $j$ ,  $j = 1, \dots, D_{OD}$ ). At the beginning of a simulation pass, every MGT as a member of attacking swarm is directed to the OD which is the target of that ASW.

AMPs are selected to be members of DSWs according to their distance from corresponding ODs, in numbers defined by the simulator input initial distribution of AMPs assignment. At the beginning of a simulation pass, every AMP as a member of defending swarm is directed to the ASL of the corresponding ASW.

A typical example of initial deployment and starting assignment is depicted in **Figure 1**.

The most important defended object is OD1, followed by OD2 and OD3.

Attacking swarms are:

- ASW-1: leader MGT-2, members MGTs 1, 2, 3, 4, 5;
- ASW-2: leader MGT-8, members MGTs 8, 9, 10;
- ASW-3: leader MGT-6, members MGTs 6, 7.

Defending swarms are:

- DSW-1: AMPs 1, 5, 7, 9, all directed to MGT-2;
- DSW-2: AMPs 2, 3, 4, all directed to MGT-8;
- DSW-3: AMPs 8, 6, all directed to MGT-6.

Initial deployment is subject of a change resulting in reassignments, as a consequence of different events that occur in simulation, such as destructions of ODs, MGTs and AMPs.

After initial deployment, for every attacking swarm and every MGT in it, starting from swarm leaders on, it is examined if some of defending AMP is detected to be in main armaments' range.

If there is one or more AMPs detected, MGT enters in conflict with the closest AMP.

Survival probability of MGT in conflict with  $k$  AMPs is:

$$P_{SURV\text{MGT}} = (1 - P_{AMP})^k \quad (2)$$

If MGT doesn't survive, the simulator enters in dynamic assignment, to reconfigure previous assignment of MGTs.

If MGT survives, it is examined whether its opponent AMP survived the conflict, which has the probability:

$$P_{SURV\text{AMP}} = (1 - P_{MGT}) \quad (3)$$

If AMP doesn't survive, the simulator enters in dynamic assignment, to reconfigure previous assignment of AMPs

If both MGT and AMP survive, the simulation clock is advanced by the maximal value between MGT and AMP reload times,  $t = t + \max\{T_{\text{MGT}}, T_{\text{AMP}}\}$ , which gives enough time to everybody who fired its main armament to reload it. It is examined if the new value of simulation clock  $t$  exceeds maximal time of MGT mission,  $T_m$ .

If  $t > T_m$ , that simulation pass is over, the experiment termination counter is decreased by 1 (SAMPLE-1), and it is examined whether the whole experiment is over. If is over (SAMPLE=0), the simulation stops, otherwise it continues, as described.

If  $t < T_m$ , all simulated MGTs and AMPs go to their new positions (NEW DEPLOYMENT), according to their targets, motion laws and the time elapsed from the last value of the simulation clock.

For every MGT, starting from swarm leaders, it is examined if some of defending AMPs is detected to be in their main armaments' range. If it is, the simulation proceeds as described.

If no adversary AMP is detected, it is examined if the target defended object (OD) is detected in range of the MGT's main armament.

If no OD is detected, the simulation clock is advanced by one of the simulation basic intervals  $\Delta t$ . Then, it is examined whether the simulation clock value is still less than the maximal time of MGT mission, ( $t < T_m$ ). If it is not, that simulation pass is over, and the simulation continues as described. If it is, all simulated MGTs and AMPs go to their new positions (NEW DEPLOYMENT).

If any OD is detected in some MGT's main armament range, MGT fires at it (FIRE).

If that OD is hit, its number of hits is increased by 1 ( $D_{\text{HITS}}+1$ ), and it is examined if that OD is destroyed.

If OD is destroyed, it is disabled for the current simulation pass, all MGTs and AMPs assigned to it are released, and assigned to attack or defend the remaining ODs, according to ODs priorities and current distances from them.

After reassignment of MGTs and AMPs, the simulation clock is advanced by one of the model's basic intervals  $\Delta t$ , and the simulation continues as described.

If OD is not destroyed, MGT reloads its main armament, ( $t = t + T_{\text{MGT}}$ ), and it is examined if the new value of the simulation clock exceeds maximal time of MGT mission,  $T_m$ . After that the simulation continues as described.

## 5.1. The simulator program implementation

The simulator program of the proposed algorithm is in course of development. GPSS World simulation language (Minuteman Software, [10]) has been chosen for the simulator algorithm implementation, due to its suitability for discrete events system simulation and easy availability of the tool on the Internet.

## 6. PROPOSED PERFORMANCE MEASURES

In order to quantify output results of the simulator, the following performance measures have been proposed:

- Primary performance measures, to estimate successes of attack or defense as a whole;
- Secondary performance measures, to estimate costs of successes of attack or defence.

### 6.1 Primary performance measures

The probability of attack success ( $p_{succATT}$ ) is defined as:

$$p_{succATT} = \frac{\sum_{i=1}^{D_{OD}} D_{HITS_i}}{\sum_{i=1}^{D_{HITSmax_i}} D_{HITSmax_i}} \quad (4)$$

Where  $D_{HITS_i}$  is the number of hits received by OD- $i$ , and  $D_{HITSmax_i}$  is a number of hits that destroys OD- $i$ .

Having in mind that primary performance measures are probabilities, double-sided and complementary ones, the probability of defence success ( $p_{succDEF}$ ) is defined as:

$$p_{succDEF} = 1 - p_{succATT} \quad (5)$$

### 6.2 Secondary performance measures

The costs of successes of attack ( $C_{ATT}$ ) or defence ( $C_{DEF}$ ) are expressed in terms of MGTs or AMPs losses during a simulation pass.

The costs of the attack success are defined as:

$$C_{ATT} = \frac{M_{destMGT}}{M_{MGT}} \quad (6)$$

Where  $M_{MGT}$  is the total number of MGTs, and  $M_{destMGT}$  is the number of MGTs destroyed during a simulation pass.

The costs of the defense success are defined as:

$$C_{DEF} = \frac{N_{destAMP}}{N_{AMP}} \quad (6)$$

Where  $N_{AMP}$  is the total number of AMPs, and  $N_{destAMP}$  is the number of AMPs destroyed during a simulation pass.

## 7. CONCLUSION

Selection of threats and targets, as well as assignment of available resources, are important issues in discrete events simulation of defensive multitarget military swarming systems.

A simulation model of a system consisting of several unarmed stationary objects, randomly situated over a limited two-dimensional territory cell, and defended by dozens of armed mobile platforms counter an attacking force of similar number of armed mobile ground threats has been presented.

Mobile ground threats, as attackers, are assigned to attack stationary objects according to their prescribed priority,

expressed in terms of number of hits to be received for destruction and dynamic distances changes of the system's moving components.

Armed mobile platforms, as defenders, are assigned to defend stationary objects according to their prescribed priority, expressed in terms of number of hits to be received for destruction and dynamic distances changes of the system's moving components.

Both mobile ground threats and armed mobile platforms are subject to destruction by a single direct adversaries' hit.

Both attackers and defenders are organized in swarms, so there are multiple swarm versus swarm combats in the simulation model.

A swarm versus swarm tactics is proposed. The priority for both sides is to immediately fire at the nearest member of any adversary swarm.

The simulator algorithm is presented and explained. The simulator program is in course of development, and the first experiments will follow soon.

Two-sided performance measures are defined: the primary measures are complementary ones, for estimation of defence or attack successes, and the secondary measures for estimation of their costs, expressed in both sides' losses.

It is expected that the proposed simulator can be a useful cost-effective tool for preliminary research of new tactical procedures, needed for application in contemporary or future conflicts, both hybrid or conventional ones.

## References

- [1] ARQUILLA, J., RONFELT, D. *Swarming and the Future of Conflict*, Rand Corporation, 1999.
- [2] EDWARDS, S.J.A. *Swarming and the future of warfare*, Rand Corporation, 2005.
- [3] HENKIN, Y. *On Swarming: Success and Failure in Multidirectional Warfare, from Normandy to the Second Lebanon War*, Defence Studies, 14, 3, 310–332, 2014.
- [4] RATIU, A. *Swarming – Doctrinary – Operational – Concept – Possible Solution to the Challenges of the Current Military Confrontations*, Scientific Bulletin, 21(2), 128–134, 2016.
- [5] GERGAL, E.K. *Drone Swarming Tactics using Reinforcement Learning and Policy Optimization*, United States Naval Academy, Annapolis, 2021.
- [6] JANKOVIC, R., MILINOVIC, M., JERICIC, O., NIKOLIC, N. *On Application of Discrete Event Simulation in Armoured and Mechanized Units Research*, Proceedings of the 1st International Symposium & 10th Balcan Conference on Operational Research, Thessaloniki, Greece, Vol.2, 28-35, 2011.
- [7] JANKOVIC, R. *Computer Simulation of an Armoured Battalion Swarming*, Defence Science Journal, 61(1), 36–43, 2011.



- [8] JANKOVIC, R., MILINOVIC, M. *Simulation Model of Territory Cell Defence Against Helicopter as a Hybrid Threat*, Proceedings of the 10th International Conference on Defensive Technologies (OTEH 2022), Belgrade, Serbia, 80-85, 2022.
- [9] JANKOVIC, R., *Computer Simulation of Conflict Between Self-Propelled Missile Artillery Systems and Helicopter as Hybrid Threat*, Proceedings of the 50th International Symposium on Operational Research (SYM-OP-IS 2023), Tara, Serbia, 751-756, 2023.
- [10] Minuteman Software, GPSS World.  
<http://www.minutemansoftware.com/simulation.htm>



## PROBABILITY OF HITTING AND DESTROYING A SURFACE TARGET FOR ARTILLERY ROCKETS

KATARINA NESTORVIĆ

Military Technical Institute, Belgrade, [katarina.nestorovic@mod.gov.rs](mailto:katarina.nestorovic@mod.gov.rs)

MARINA SIMOVIĆ - PAVLOVIĆ

Teleoptic Gyroscopes, Belgrade, [simovicmarina99@gmail.com](mailto:simovicmarina99@gmail.com)

MILOŠ PAVIĆ

Military Technical Institute, Belgrade, [meelos.pavic@gmail.com](mailto:meelos.pavic@gmail.com)

SRĐAN STOJKOVIĆ

Military Technical Institute, Belgrade, [ssrdjanvti@gmail.com](mailto:ssrdjanvti@gmail.com)

SLOBODAN BOSILJČIĆ

Military Technical Institute, Belgrade, [bobanbosiljcic@yahoo.com](mailto:bobanbosiljcic@yahoo.com)

**Abstract:** Artillery rockets of medium and long range are used on the battlefield for indirect firing of distant targets. Having a large dispersion of hits, they are used for targeting surface areas from multitube launchers. At the same time, the line of sight of the target does not exist, so the firing elements are taken based on the known geographical coordinates of the target and the launcher, using the ballistic computer and firing tables. Long ranges, low initial velocity and long duration of the flight to the target make such rockets very sensitive to the impact of disturbances on the accuracy of hitting. As the range increases, the accuracy of rocket systems decreases more and more. At the same time, for effective coverage of the target area, a large number of rockets is counted. Firing a target area with a large number of rockets involves a statistical approach to determining the efficiency of the firing. Thereby, statistical indicators of the distribution of impact points are used, such as the circular error probable, which represents the radius of the circle that contains half of all hits. In addition to the number of rockets with which an area is targeted, the probability of destroying all targets in the area also depends on the radius of the lethal effect of the warheads. This paper presents determination of the probability of hitting and destroying a surface target.

**Keywords:** artillery rockets, dispersion, probability, impact points, target

### 1. INTRODUCTION

Artillery rockets have significant place in the modern warfare based on the numerous advantages it achieves in comparison to classic artillery: longer range, higher concentration of firepower in a short time, low cost of launchers and their high mobility. On the other hand, the price of rockets is higher than the price of classic artillery ammunition and the accuracy of rocket systems is significantly lower.

The default standard for the accuracy of artillery rockets is that the circular error probable is about 1% of the range. In the case of targets (areas) at distances less than 20 km, the dispersion of impact points ensures an even distribution of hits throughout the target area. As firing ranges increase, the number of rockets needed to cover a given area increases quadratically, which makes the use of rocket artillery economically unprofitable.

Dispersion of impact points has a normal distribution so points with a large miss become a reality with the use of a

large number of rockets, which entails a high possibility of collateral damage.

The use of artillery rockets on the modern battlefield implies stricter requirements for accuracy, in order to minimize collateral damage. Also, longer ranges are required, so that the operating forces are as far as possible from the enemy. These two requirements are contradictory, because increasing the range has the effect of decreasing the accuracy.

On the other hand, there is a need to produce weapons with the lowest possible price. In the case of artillery rockets, this can be achieved by increasing accuracy and ensuring target destruction with fewer rockets. The task of these rockets is to achieve a circular error probable small enough so the impact points can be considered as point hits. [1]

In order to predict the dispersion of impact points and the effect on the target, this paper presents the probability of target destruction. Predicting the possible distribution of impact points and the probability of target destruction is

important in order to optimize the amount of ammunition and other resources used for a destruction of specific surface targets.

## 2. THEORETICAL BASIS

### 2.1 Distribution of unguided missile hits

Rockets are different from other artillery projectiles because they leave the launch tube at a low speed and after that in a relatively short flight phase, increase the speed by the action of the rocket motor. This phase is called the active phase of flight. [1]

Acceleration of the rocket under the action of the reactive force without limitation of the trajectory by the launcher causes the angular disturbances that are converted into a deviation of the position of the center of mass from the reference trajectory. [1] [3] [4]

The angular size of the deviation of the rocket axis from the velocity vector - angle of attack, occurs when the rocket descends from the launch device, but also during flight due to side wind.

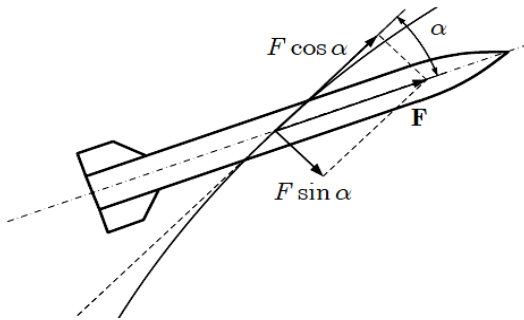


**Figure 1.** The influence of the angle of attack on the deviation of the rocket from the trajectory [1]

The angle at which the artillery rockets are launched is determined by ballistic calculation for the given position of the target and the launcher, as well as for the atmospheric conditions at the launch position and along the trajectory of the rocket. [1] [3] [4]

As artillery rockets are mostly fired from multitube launchers, the error of determination and positioning are constant for all rockets from a single salvo, while the error due to the oscillations of the launcher is an independent random variable.

The mean value of the error (standard deviation) occurred when positioning the firing elements and the error due to the oscillations of the launcher are conditioned by the quality of the launcher itself, while the error of determining the firing elements is conditioned by the quality of the fire control system. [1] [3] [4]

Observing a set of hits as a statistical sample, we can characterize it by mathematical expectation (desired impact point) and standard deviation as a measure of dispersion of hits. In external ballistics, instead of the standard deviation  $\sigma$ , as a measure of the dispersion of impact points, the size of the probable error is more often used, namely the probable error in the range  $V_x$  and the probable error in the direction  $V_z$ . [1] [3] [4]

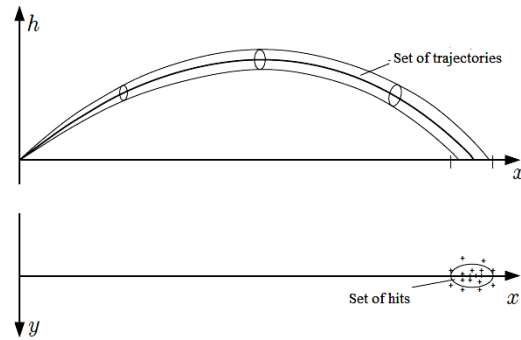


**Figure 2.** Dispersal of artillery projectiles [1]

Probable error is defined as:

$$\int_{-V}^V p(x) dx = 0,5 \tag{1}$$

where is:

$p(x)$  - the probability density function of the random variable  $x$ . [1]

In the case of a normal (Gaussian) distribution, we have:

$$p(x) = \frac{1}{\sigma\sqrt{2\pi}} e^{-\frac{(x-m)^2}{2\sigma^2}} \tag{2}$$

When firing rockets, two types of errors appear: errors of the mean hit of a group of rockets fired under the same conditions, and errors of the hit deviation from the average hit. The dispersion image of hit coordinates has the shape of an ellipse or a circle. The coordinates of the medium hit of the rocket are calculated as follows: [2]

$$\bar{x} = \frac{\sum_{i=1}^n x_i}{n} \quad \bar{z} = \frac{\sum_{i=1}^n z_i}{n} \tag{3}$$

where  $n$  is the number of launched rockets.

If we look at the set of impact points, the value of the probable error represents the limits of the interval that contains 50% of the hits. The relationship between standard deviation and probable error is given by: [2]

$$V = 0,6745\sigma$$

$$V_x = 0,6745\sigma_d = 0,6745 \cdot \sqrt{\frac{\sum (x_i - \bar{x})^2}{n-1}} \tag{4}$$

$$V_z = 0,6745\sigma_p = 0,6745 \cdot \sqrt{\frac{\sum (z_i - \bar{z})^2}{n-1}}$$

For the maximum deflection  $\pm 4V_x$  and  $\pm 4V_z$  are taken. The radius of the circular error probable can be calculated numerically as follows: [2]

$$\begin{aligned}
 V_x &= V_z \\
 r_{50} &= 1,1774\sigma = 1,746V \\
 \sigma &= \frac{\sigma_x + \sigma_z}{2} \\
 V &= \frac{V_x + V_z}{2}
 \end{aligned}
 \tag{5}$$

or:

$$\begin{aligned}
 V_x &\neq V_z \\
 r_{50} &= 0,615\sigma_x + 0,562\sigma_z \\
 r_{50} &= 0,589 \cdot (\sigma_x + \sigma_z)
 \end{aligned}
 \tag{6}$$

### 2.2 Probability of destroying the target

When firing a target with multiple rockets, system errors are repeated. It is assumed that firing is independent and that there is no correlation of hits. If the probability of destroying the target of individual rockets is  $P_{ui}$ , then the total probability is equal: [2]

$$P_{ut} = 1 - \prod_{i=1}^n (1 - P_{ui}) \tag{7}$$

Numerical analysis of the probability of destroying a surface target for artillery rockets was done for a surface target with dimensions of 150 x 100 m. Numerical calculations were performed with the assumption that the target destruction probabilities are as defined in the following statement. The following probabilities are assumed: if total area of the target is covered by all of the warheads declared lethality radius at their impact points in amount of 30% (0.3) - it is considered disabled, and if total area of the target is covered by all of the warheads declared lethality radius at their impact points in amount of 50% (0.5) - it is considered destroyed. Covering a target by all of the warheads declared lethality radius at their impact points over 50% is considered overkill and a waste of resources.

Under the condition that probability of destruction of all individual rockets is  $P$ , probability of destroying the target with  $n$  rockets is as follows:

$$P_{un} = 1 - (1 - P)^n \tag{8}$$

When firing with a circular dispersion in the center of a surface target, probability of destruction with  $n$  rockets is as follows: [2]

$$\begin{aligned}
 P_{un} &= 1 - e^{-\rho^2 \frac{nS_k}{\pi V_k^2}} \\
 S_k &= R_u^2 \pi
 \end{aligned}
 \tag{9}$$

where are:

- $\rho$  – constant with a value of 0.4769,
- $R_u$  – the radius of the destruction zone,
- $V_k$  - mean circular deviation,
- $S_k$  – surface of the destruction zone.

### 3. NUMERICAL ANALYSIS

Surface target with dimensions of 150 x 100 m represents a platoon in attack and it's a standard target for rocket artillery. Numerical analysis was done in two cases. In the first case, the probability of destruction of the mentioned surface target at a range of 20 km is presented, and in the second case, at a range of 40 km.

**1<sup>st</sup> case** - In the first case, at a range of 20 km, the required number of rockets to destroy a surface target was calculated using equation 9 for both assumed probabilities: 30% and 50%. Lethal effect of the warhead is 60 m. Probable dispersions by distance and direction as well as standard deviations are given in Table 1.

**Table 1:** Probable dispersions and standard deviations by range and direction at a range of 20 km

$V_x [m]$	239
$V_z [m]$	127
$\sigma_x [m]$	354
$\sigma_z [m]$	188

If the task is to disable the target with a probability of destruction of 30% ( $P_{un} = 0.3$ ), the following number of rockets is required at a range of 20 km:

$$\begin{aligned}
 P_{un} &= 1 - e^{-\rho^2 \frac{nS_k}{\pi V_k^2}} \Rightarrow \\
 \Rightarrow n &= -\frac{V_k^2 \cdot \ln(1 - P_{un})}{R_u^2 \cdot \rho^2} \\
 n &= -\frac{183^2 \cdot \ln(1 - 0,3)}{60^2 \cdot (0,4769)^2} = 14,58
 \end{aligned}
 \tag{10}$$

If the task is to destroy the target with a probability of destruction of 50% ( $P_{un} = 0.5$ ), the following number of rockets is required at a range of 20 km:

$$\begin{aligned}
 P_{un} &= 1 - e^{-\rho^2 \frac{nS_k}{\pi V_k^2}} \Rightarrow \\
 \Rightarrow n &= -\frac{V_k^2 \cdot \ln(1 - P_{un})}{R_u^2 \cdot \rho^2} \\
 n &= -\frac{183^2 \cdot \ln(1 - 0,5)}{60^2 \cdot (0,4769)^2} = 28,39
 \end{aligned}
 \tag{11}$$

Coverage of a surface with 15 rockets and a probability of destruction of 30% target is shown in Figure 3 and the coverage of the surface with 29 rockets and a probability of destruction of 50% target is shown in Figure 4. The dispersion of impact points is based on the normal distribution of hits in relation to the defined dispersions in Table 1. [3] [4] [5]

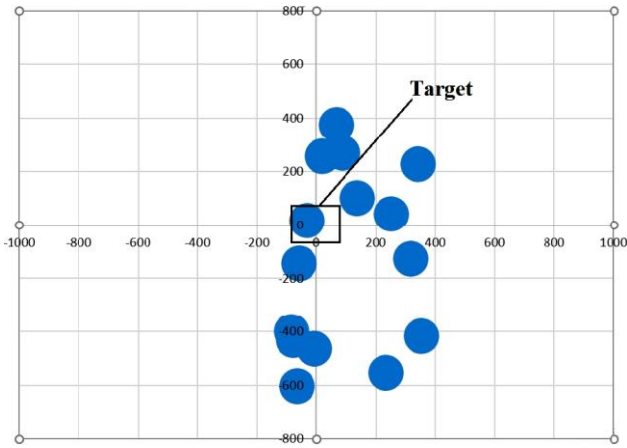


**Figure 3:** Dispersion of impact points with target destruction probability of 30% at range of 20 km

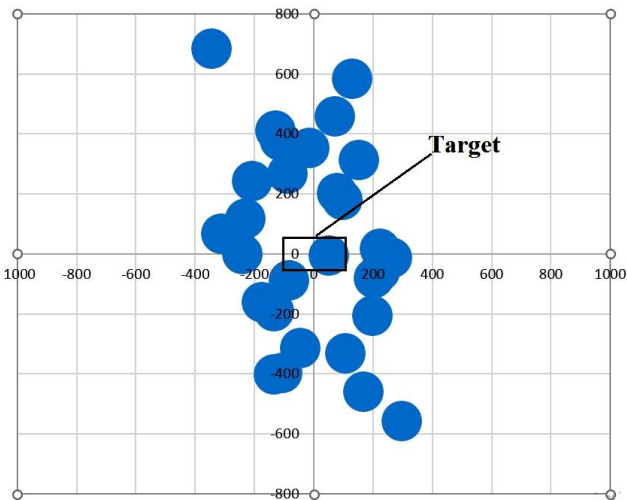


**Figure 4:** Dispersion of impact points with target destruction probability of 50% at a range of 20 km

**2<sup>nd</sup> case** - In the second case, at a range of 40 km, the required number of rockets to destroy a surface target was calculated using equation 9 for both assumed probabilities: 30% and 50%. Lethal effect of the warhead is 60 m. Probable dispersions by distance and direction as well as standard deviations are given in Table 2.

**Table 2:** Probable dispersions and standard deviations by range and direction at a range of 40 km

$V_x [m]$	411
$V_z [m]$	535
$\sigma_x [m]$	609
$\sigma_z [m]$	793

If the task is to disable the target with a probability of

destruction of 30% ( $P_{un} = 0.3$ ), the following number of rockets is required at a range of 40 km:

$$P_{un} = 1 - e^{-\rho^2 \frac{nS_k}{\pi V_k^2}} \Rightarrow \tag{12}$$

$$\Rightarrow n = -\frac{V_k^2 \cdot \ln(1 - P_{un})}{R_u^2 \cdot \rho^2}$$

$$n = -\frac{473^2 \cdot \ln(1 - 0,3)}{60^2 \cdot (0,4769)^2} = 97,45$$

If the task is to destroy the target with a probability of destruction of 50% ( $P_{un} = 0.5$ ), the following number of rockets is required at a range of 40 km:

$$P_{un} = 1 - e^{-\rho^2 \frac{nS_k}{\pi V_k^2}} \Rightarrow \tag{13}$$

$$\Rightarrow n = -\frac{V_k^2 \cdot \ln(1 - P_{un})}{R_u^2 \cdot \rho^2}$$

$$n = -\frac{473^2 \cdot \ln(1 - 0,5)}{60^2 \cdot (0,4769)^2} = 189,41$$

Coverage of a surface with 98 rockets and a probability of destruction of 30% target is shown in Figure 5 and the coverage of the surface with 190 rockets and a probability of destruction of 50% target is shown in Figure 6. The dispersion of impacts points is based on the normal distribution of hits in relation to the defined dispersions in Table 2. [3] [4] [5]

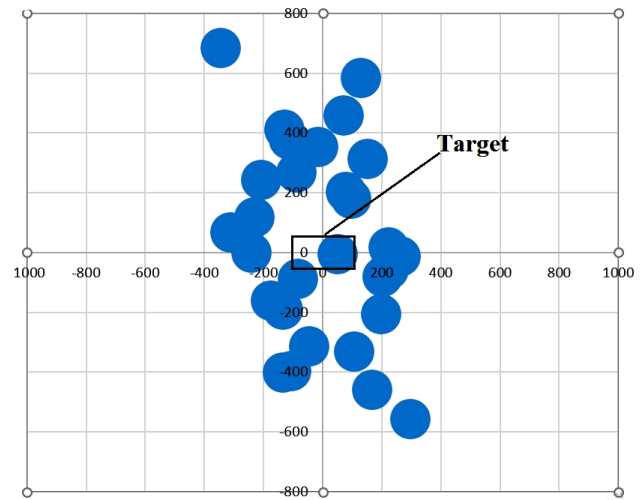


**Figure 5:** Dispersion of impact points with target destruction probability of 30% at a range of 40 km

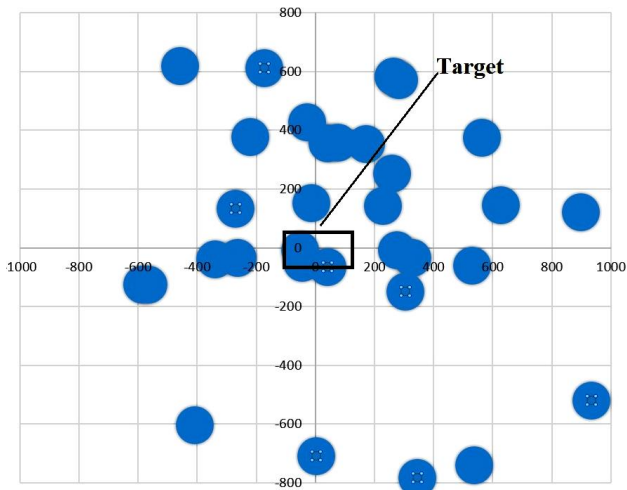


**Figure 6:** Dispersion of impact points with target destruction probability of 50% at a range of 40 km

The lethality circles of the warheads are shown with the assumption that the probability of destruction within the circle is 100%, while the probability of destruction outside the circle is 0%. In a practical case, the distribution of the probability of destruction in the circle and outside the circle is variable.

#### 4. CONCLUSION

In this paper, a numerical and comparative analysis of the probability of destruction of a surface target with dimensions of 150 x 100 m by rocket artillery was performed. Numerical analysis is performed assuming that the target destruction probabilities are known and that the number of rockets required in order to neutralize the target is unknown. There were two cases at different ranges under the same conditions. For both cases, the assumption is that probable deviations and standard deviations in range and direction are known (determined by flight experiments in the field, equation 4).

In the first case, at a range of 20 km, the required number of rockets was calculated in order to achieve a probability of destroying the target of 30% and 50%. To disable a target at 30% coverage 15 rockets are required and to destroy it at 50% coverage 29 rockets are required (equations 10 and 11). The normal distribution of impact points of the required number of rockets for both probabilities is shown in Figures 3 and 4.

In the second case, at a range of 40 km, the required

number of rockets was calculated in order to achieve a probability of destroying the target of 30% and 50%. To disable a target at 30% coverage 98 rockets are required and to destroy it at 50% coverage 190 rockets are required (equations 12 and 13). The normal distribution of impact points of the required number of rockets for both probabilities is shown in Figures 5 and 6.

Simulations and comparative analyzes were performed in order to optimize ammunition consumption and reduce collateral damage for the same target at a different range. As the range of artillery rockets increases, the probability of destroying the target decreases and the number of rockets required to disable the target increases exponentially.

A proposal for further research is to focus on increasing the accuracy of artillery rockets at longer ranges. One way to do this is to install special precision guidance kit (PGK) correction modules.

#### Acknowledgments

This work was supported by the Ministry of Science, Technological Development and Innovations (Serbia), Contract No. 451-03-66/2024-03/200325.

M.S.P. acknowledges the support of the EU: the EIC Pathfinder Challenges 2022 call through the Research Grant 101115149 (project ARTEMIS).

M.S.P. also acknowledges the support of the Office of Naval Research Global through the Research Grant N62902-22-1-2024.

#### References

- [1] PAVKOVIĆ, B.: *Research of projectile trajectory Correction Methods in Function of Their Range and precision enhancement*, PhD Thesis, Faculty of Mechanical Engineering University of Belgrade, Belgrade, 2012.
- [2] VUČUREVIĆ, O.: *Osnovi projektovanja raketa*, Faculty of Mechanical Engineering University of Belgrade, Belgrade, 2003.
- [3] REGODIĆ, D.: *Spoljna balistika*, Military Academy Belgrade, 2006.
- [4] JERKOVIĆ, D.: *Aerodinamika projektila*, Military Academy Belgrade, 2010.
- [5] JERKOVIĆ, D., REGODIĆ D.: *Praktikum iz spoljne balistike*, Military Academy Belgrade, 2007.

## ACTIVE GYRO-DUMPING FOR MISSILE WITH PITCH/YAW DISTURBANCE SENSITIVE HOMING HEAD

MILOŠ PAVIĆ

Military Technical Institute, Belgrade, Ratka Resanovic 1, Serbia, [meelos.pavic@gmail.com](mailto:meelos.pavic@gmail.com)

IVAN MARIĆ

Military Technical Institute, Belgrade Ratka Resanovic 1, Serbia, [ivanmaric094@gmail.com](mailto:ivanmaric094@gmail.com)

**Abstract:** The Missile with an imperfect pitch/yaw rate disturbance sensitive homing head will have oscillatory rudder deflection during the homing phase of a missile without a lateral autopilot. Implementing only one body-fixed velocity gyro sensor in internal negative feedback loop, the presented active gyro-damping method, will stabilize the whole homing loop and eliminate missile rudder oscillations.

**Keywords:** homing, homing head, missile, guidance, proportional navigation, active gyro-damping, disturbance sensitive.

### 1. INTRODUCTION

In the practical realization of the homing missile, one of the main guidance system components, the gimballed homing head can experience some great imperfection such as pitch/yaw rate disturbance sensitivity.

This means that its useful output measurement signal (line of sight rate) will be contaminated (superimposed) with another unwanted signal due to its pitch/yaw rate disturbance sensitivity.

In case when homing head designers, don't want or do not know how to improve the homing head and eliminate this problem (unwanted disturbance sensitivity), the overall guidance system designer can overcome this situation by reducing the disturbance i.e. reducing the missile pitch/yaw rate by increasing the dumping ratio of a missile.

This can be done by introducing the full lateral acceleration autopilot (with accelerometers for lateral specific force measurements), but there is one simple solution implementing only a body-fixed velocity-gyro sensor in internal negative feedback loop.

The presented active gyro-damping method, will stabilize the whole homing loop and eliminate missile rudder oscillations.

### 2. ACTIVE GYRO-DAMPING METHOD

The Missile aerodynamics transfer function from rudder deflection  $\eta$  to angular velocity  $q$  is [1]:

$$W = \frac{q}{\eta} = \frac{K_q \omega_n^2 (T_q s + 1)}{s^2 + 2\zeta_n \omega_n s + \omega_n^2} \quad (1)$$

, where the parameter values are: the missile

maneuverability gain  $K_q = 1$ ; dumping ratio  $\zeta_n = 0,1$ ; undamped natural frequency  $\omega_n = 7 \text{ rad}^{-1}$ ; and incidence lag time constant  $T_q = 1,2 \text{ s}$ .

As one can see the missile dumping ratio is very low and will cause the rudder oscillations in the guidance loop due to the disturbance sensitive homing head.

In order to increase the damping ratio of a missile, an additional negative feedback loop was added, as shown in Fig.1

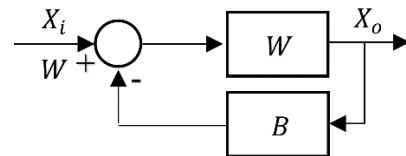


**Figure 1.** Additional negative feedback loop

The output signal from this system is:

$$X_o(s) = W(s)(X_i(s) - B(s)X_o(s)) \quad (2)$$

From Eq.2 the new transfer function for this system is

$$W_B = \frac{X_o}{X_i} = \frac{W}{1 + WB} \quad (3)$$

Using Eq.3 and Eq.1, after regrouping members, the new system transfer function is:

$$W_B = \frac{X_o}{X_i} = \frac{K_q \omega_n^2 (T_q s + 1)}{s^2 + (2\zeta_n \omega_n + K_q \omega_n^2 T_q B)s + \omega_n^2 (1 + K_q B)} \quad (4)$$

Comparing the denominator of Eq.4 with Eq.1, one can conclude that the new undamped natural frequency of this system has changed to:

$$\omega_{nB} = \omega_n \sqrt{1 + K_q B} \quad (5)$$

The new maneuverability gain of this system has also changed to:

$$K_{qB} = \frac{K_q}{1 + K_q B} \quad (6)$$

In order to determine gain  $B$  for desired damping ratio  $\zeta_{nB}$ , the Eq.4 was formally rewritten as:

$$W_B = \frac{K_q \omega_n^2 (T_q s + 1)}{s^2 + 2 \frac{2\zeta_{nB} \omega_n + K_q \omega_n^2 T_q B}{2\omega_n \sqrt{1 + K_q B}} \omega_n \sqrt{1 + K_q B} s + \omega_n^2 (1 + K_q B)} \quad (7)$$

Comparing the denominator of Eq.7 with Eq.1, one can conclude that the new damping ratio of this system has changed to:

$$\zeta_{nB} = \frac{2\zeta_n \omega_n + K_q \omega_n^2 T_q B}{2\omega_n \sqrt{1 + K_q B}} \quad (8)$$

The Eq.8 can be rearranged and squared like:

$$4\zeta_{nB}^2 \omega_n^2 (1 + K_q B) = (2\zeta_n \omega_n + K_q \omega_n^2 T_q B)^2 \quad (9)$$

Finally the square equation for loop gain  $B$  was:

$$(K_q \omega_n^2 T_q)^2 B^2 + (4\zeta_n K_q \omega_n^3 T_q - 4\zeta_{nB}^2 \omega_n^2 K_q) B + 4\zeta_{nB}^2 \omega_n^2 - 4\zeta_n^2 \omega_n^2 = 0 \quad (10)$$

This Eq.10 can be written as:

$$aB^2 + bB + c = 0 \quad (11)$$

, where:

$$a = (K_q \omega_n^2 T_q)^2 \quad (12)$$

$$b = 4\zeta_n K_q \omega_n^3 T_q - 4\zeta_{nB}^2 \omega_n^2 K_q$$

$$c = 4\zeta_{nB}^2 \omega_n^2 - 4\zeta_n^2 \omega_n^2$$

The loop gain  $B$  was determined as a solution:

$$B_{1,2} = \frac{-b \pm \sqrt{b^2 - 4ac}}{2a} \quad (13)$$

The positive loop gains  $B$  was determined for a few desired values of damping ratios as shown in Table 1.

**Table 1.** Loop gains  $B$  for desired damping ratios  $\zeta_{nB}$

$\zeta_{nB}$	0,4	0,5	0,6	0,7	0,8
$B$	0,075	0,101	<b>0,128</b>	0,155	0,183
$\omega_{nB}$	7,26	7,35	7,43	7,52	7,61
$K_{qB}$	0,93	0,91	0,89	0,87	0,85

The step responses for original missile and missile with active-damping was presented in Fig.2 for different values of closed loop gain  $B$ .

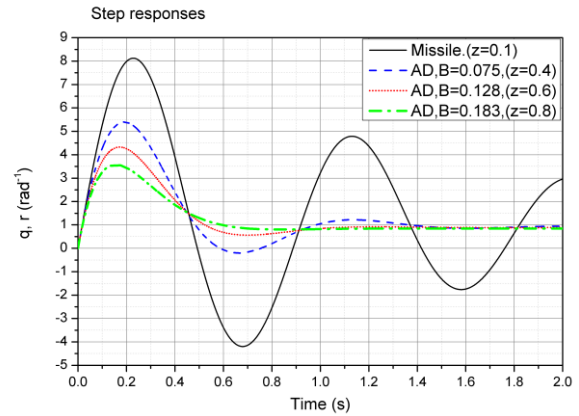


**Figure 2.** Missile rate ( $q, r$ ) step responses w/o active gyro-dumping (in fig.2,  $\zeta \equiv z$ )

The internal closed loop gain value  $B = 0,128$  was chosen to use in later homing simulations.

### 3. HOMING SIMULATION RESULTS

Due to the positive sign convention in [1], where positive rudder deflection produces negative missile deflection, i.e. missile will go down/left, looking from behind, the value of maneuverability gain was obtained as negative

$K_q = -1$ , so the formal sign-change gain (-1) was added in front of the missile aerodynamic transfer function in later homing simulations block diagram shown in Fig.4.

The relation between lateral acceleration  $a_{ny}$ , flight path rate  $\dot{\chi}$  and body rate  $r$  was given after neglecting small numerator terms in [1] (in Fig.4.6-2). This relation was rearranged and shown in Fig.3 and Eq.14.

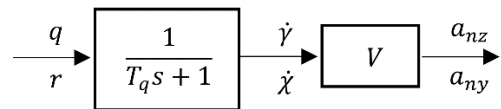


**Figure 3.** The relation between missile body rate and lateral acceleration

$$a_n = \frac{V}{T_q s + 1} \quad (14)$$



The nonlinear homing simulation was performed using the proportional navigation as guidance law, where the navigation constant was chosen from intervals 3-5 to be  $N = 4$ . Collision time was set to 10 s and the missile closing velocity was  $V = 200$  m/s.

The homing head (HH) transfer function was identified as a second-order system with unity gain, damping ratio  $\zeta_{nHH} = 1.3$  s and undamped natural frequency  $\omega_{nHH} = 5$  rad<sup>-1</sup>.

The homing head disturbance transfer function was also identified as a second-order system with the negative gain  $K_{HHd} = -0.09$  and the same damping ratio  $\zeta_{nHHd} = 1.3$  s and undamped natural frequency  $\omega_{nHHd} = 5$  rad<sup>-1</sup>.

The Dynamics of the rudder actuator system presented in [2] were neglected because it is one order faster than other components  $\omega_{nActuator} = 50$  rad<sup>-1</sup>. Only the nonlinearity of rudder angle deflection  $\pm 20^\circ$  was used in the homing simulation.

Chosen internal loop gain  $B = 0.128$  will reduce the

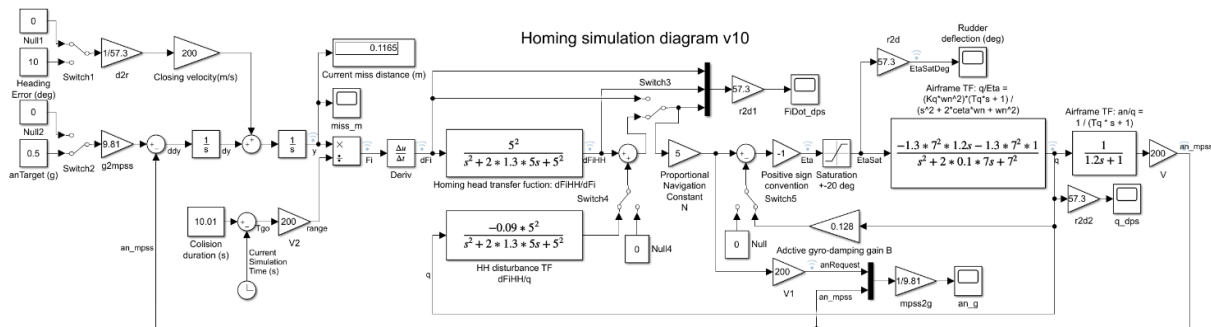


Figure 4. Block diagram of nonlinear homing simulation

### The effect of target lateral acceleration

Equivalent lateral target acceleration considered was 0,5 g and collision duration was 10 s.

Results of homing simulations are shown in Fig.5 and it was done for homing head with and w/o disturbance and in each case with and w/o active gyro-damping.

missile maneuverability gain  $K_q$  by 11% to the value  $K_{qB}$  as shown in Table 1. The result is that overall proportional navigation constant was no longer  $N = 4$  as it was chosen, but  $N = 3.56$  instead (reduced by 11%). It is still in the recommended range 3-5, but strictly speaking it should be increased by the same factor to the value  $N = 4.49$ .

Nevertheless, uncertainties during the identification of homing head gain can be up to 20% and that way the effective value of chosen navigation constant will increase its value up to  $N = 5$ , so this value was taken in homing simulations.

There also can be some uncertainties for the value of missile maneuverability gain which changes during the flight so despite the numerical calculations and wind-tunnel experiments, this value was increased by 30 % and in homing simulations was taken as  $K_q = -1.3$  as “worst case”.

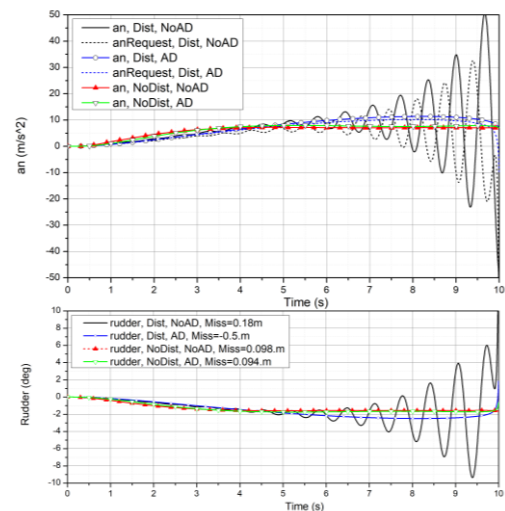


Figure 5. Equivalent lateral target acceleration effect on homing loop, (a) Missile lateral acceleration, (b) Rudder deflection

From Fig.5 it can be seen that disturbance sensitive HH leads the whole guidance system to instability (oscillations) as the missile approaches the target.

It does not affect much miss distance, but greater target maneuvers could lead to rudder angle saturation of  $\pm 20^\circ$ .

The presented active gyro-damping method successfully eliminates guidance instability and interestingly, makes the greater miss distance (from 0,18 m to 0,5 m) which is acceptable.

### The effect of missile heading error

The Heading error considered was  $10^\circ$  and homing simulations results are shown in Fig.6

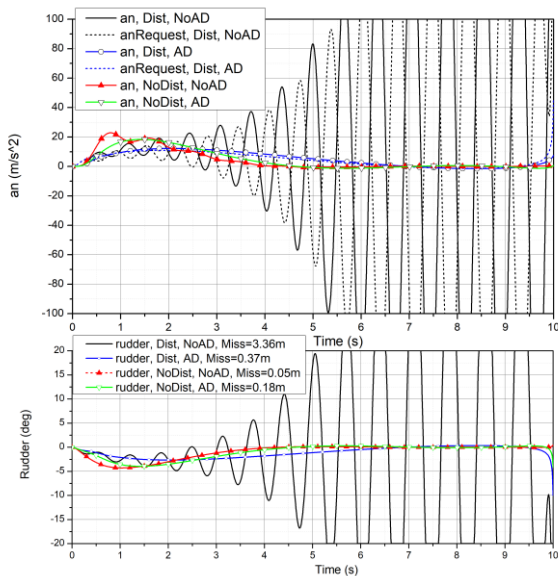


**Figure 6.** Heading error effect on homing loop, (a) Missile lateral acceleration, (b) Rudder deflection

From Fig.6 it can be seen that disturbance sensitive HH makes even more guidance system instability, causing rudders to saturate on  $\pm 20^\circ$  resulting a miss distance of 3,36 m.

In this case the presented active gyro-damping method successfully eliminates guidance instability and reduces the miss distance to 0,37 m.

## 4. CONCLUSION

If the homing head is not heading rate disturbance sensitive the guidance system will be stable (oscillations free), and the missile can achieve small miss distances.

Disturbance sensitivity of the homing head induces guidance loop instability that can result in large miss distance, missile heading oscillations, rudder oscillation and saturation.

Guidance system designer can overcome this situation by reducing the disturbance i.e. reducing the missile pitch/yaw rate by increasing the dumping ratio of a missile, implementing only body-fixed velocity-gyro sensor in an internal negative feedback loop.

The presented active gyro-damping method is simple to implement and it will stabilize the whole homing loop to eliminate the missile rudder/heading oscillations.

## References

- [1] GARNEL,P. & EAST,D.J. : *Guided weapon control systems*, Pergamon Press, Oxford, 1977.
- [2] ADAMOVIC,P., PETRONIJEVIC,Z., JOVICIC,N., STEFANOVIC,A., PAVIC.M.: *Lead compensator design for DC motor driven electromechanical fin actuator*, Scientific technical review, 2022 Vol.72, No.2, 44-49.



## OPTIMIZATION OF AUTOMATIC SAFETY ALGORITHMS FOR GUIDED MISSILES TO MEET TESTING RANGE BOUNDARIES

IVANA TODIĆ

University of Belgrade, Faculty of Mechanical Engineering, Belgrade, [itodic@mas.bg.ac.rs](mailto:itodic@mas.bg.ac.rs)

LUKA MILIČIĆ

University of Belgrade, Faculty of Mechanical Engineering, Belgrade, [lmilicic@mas.bg.ac.rs](mailto:lmilicic@mas.bg.ac.rs)

VLADIMIR KUZMANOVIĆ

University of Belgrade, Faculty of Mathematics, Belgrade, [vladimir\\_kuzmanovic@matf.bg.ac.rs](mailto:vladimir_kuzmanovic@matf.bg.ac.rs)

MILOŠ MARKOVIĆ

University of Belgrade, Faculty of Mechanical Engineering, Belgrade, [mdmarkovic@mas.bg.ac.rs](mailto:mdmarkovic@mas.bg.ac.rs)

DEJAN JEVTIĆ

University of Belgrade, Faculty of Mechanical Engineering, Belgrade, [djevtic@mas.bg.ac.rs](mailto:djevtic@mas.bg.ac.rs)

**Abstract:** This paper presents the rigorous protocols implemented to ensure the integrity of the missile's guidance and control system and the efficacy of its safety procedures. It outlines the safety zone parameters, emphasizing the criticality of adhering to safety protocols in the event of system malfunctions. Special attention is given to hypothetical scenarios, like the failure of steering channels and imposing proactive measures to prevent potential risks. Focusing on the guidance law and decision algorithms, the study delves into the core subsystems of the small cruise missile. Detailed procedures for verifying the functionality of the onboard computer are provided, covering data processing from inertial measurement units, navigation, autopilots, and communication interfaces. Furthermore, Software-in-the-loop (SIL) and Hardware-in-the-Loop (HIL) testing are elucidated, showcasing the robustness of the navigation and control algorithm under diverse scenarios, including sensor errors and communication failures. The study underscores the importance of meticulous testing to ensure the reliability and safety of the missile's guidance navigation and control system. The paper presents a comprehensive overview of safety procedures integrated into the guidance logic, highlighting the fail-safe mechanisms employed to mitigate risks during the missile's flight trajectory. This study offers valuable insights into the intricate process of ensuring safety and reliability in guided missile systems and enhancing operational security in defense applications.

**Keywords:** algorithm verification, safety algorithm, guidance, flight testing, fail-safe mechanisms.

### 1. INTRODUCTION

The optimization of automatic safety algorithms for guided missiles is a critical component in ensuring the effective and secure operation of these advanced systems. The primary objective is to ensure that the missiles operate within predefined testing range boundaries, preventing any unintended deviations that could pose safety and mission success risks. This paper focuses on the small cruise missile system, analyzing the safety procedures, decision algorithms, and the necessary optimizations to ensure adherence to testing range limitations.

Risk management and safety assessment frameworks developed for UAVs provide valuable methodologies and insights applicable to missiles. The comprehensive overview of risk management techniques for UAVs, including sensor integration and collision avoidance

strategies, highlights essential practices that can be adapted for missile safety [1][2]. Moreover, established frameworks like the Specific Operations Risk Assessment (SORA) for UAVs emphasize the importance of systematic risk assessment and mitigation, which are critical for optimizing missile safety protocols [3].

The optimization of automatic safety algorithms for small cruise missiles involves sensor calibration, scenario simulation, and algorithm testing to ensure that the missile operates safely within the designated range boundaries [4][5]. This paper has focused on various aspects, including sensor integration, real-time decision-making, and failure scenario simulations.

Furthermore, the integration of communication protocols between the missile and ground control station has been a critical development. These protocols enable real-time data transmission and reception, allowing for continuous monitoring and intervention if necessary.

## 2. RISK ASSESSMENT

Risk assessment is critical in developing and optimizing automatic safety algorithms for missiles. It involves identifying potential hazards, evaluating the risks associated with these hazards, and implementing strategies to mitigate them. The goal is to ensure the safe operation of guided missiles within predefined testing range boundaries.

The first step in risk assessment is to identify all potential hazards that could impact the safe testing of the missile. These hazards can be categorized into several types:

1. **Technical Failures:** Failures of key components such as sensors (IMU, GPS, altimeters), actuators, subsystems processors, and communication systems between them can lead to loss of control or deviation from the intended flight path.

2. **Environmental Factors:** electromagnetic interference, and other environmental variables that could affect sensor accuracy and missile performance.

3. **Human Errors:** Mistakes made during the pre-launch phase and in-flight monitoring. These can include errors in data entry, calibration, and decision-making processes.

4. **Systemic Risks:** Issues related to software bugs, algorithm malfunctions, and integration problems between different subsystems of the missile.

This study primarily focuses on the algorithms in the main computer and other subsystems to reduce risks due to technical failures or human errors.

### 2.1. Case study

The case study is a small cruise missile with a range of up to 25km. The main subsystems of the missile include a solid rocket booster, a turbojet engine, the aircraft structure, the navigation and control system, and a communication system via fiber optic link or radio link as a backup. The missile's mission is set from the ground station. After launch, the missile autonomously follows the designated path towards the target zone. The operator has a live image feed from the homing head. When the operator recognizes the target, they need to mark it in the image, after which the missile autonomously directs itself towards the target. If the operator does not lock onto the target within a range of 800 meters from the target, the missile begins a guidance maneuver towards the target point (sent from the ground station).

Functions of the "main computer" include

- Reading and processing data from the inertial measurement unit (IMU), inclinometer, altimeter, and GPS sensor
- Navigation
- Roll, pitch, and yaw autopilots
- Trajectory guidance
- Terminal guidance

- Communication with the "Ground Station"
- Communication with other missile subsystems: actuators, homing head, turbojet engine control, and power management system

The power distribution block diagram and communication block diagram are shown in Figure 1. and Figure 2.

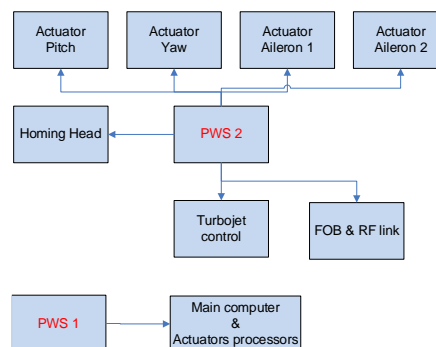


Figure 1. The power distribution

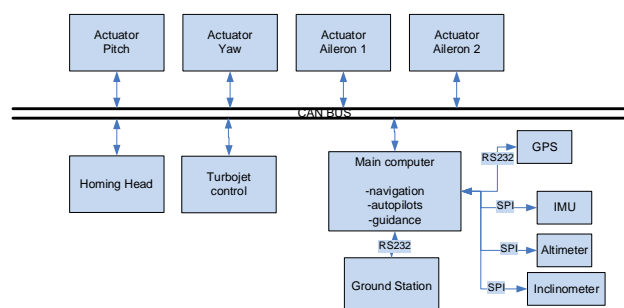


Figure 2. Block diagram of communication

Considering the object itself, it is essential to evaluate the possibilities for mission termination in the event of irregular operation. It should be noted that the warhead does not have a self-destruction capability, and not all tests at the testing range involve a live warhead. Therefore, in the case of an irregular operation that could lead to exiting the safe zone of the testing range, the only option is to bring down the missile through aerodynamic control. If the missile's main computer has not lost orientation, it is possible to bring down the missile using the maximum pitch-down command. However, if this is not the case or if the pitch control has failed, the most effective method is to apply the maximum roll command. This action would induce disturbances in all planes, causing the trajectory to transition into a disrupted ballistic path.

## 3. FAILURE RECOGNITION AND RISK MITIGATION

One of the fundamental safety procedures is that the main computer cannot enter the flight mission unless the mission has been set from the ground station beforehand. This situation could arise either due to human error or as a result of a reset of the main computer's processor. To

prevent this, there is a Watchdog Timer (WDT) as well as a byte indicating the status of the mission setting. The safety algorithm will activate if the missile launches without being set or if the main computer is reset. This algorithm includes the maximum roll command as a safety, turns off the turbojet engine, prevents the booster motor from being jettisoned, and ensures the warhead is not armed. This error will be signaled to the Ground Station.

The "main computer" communicates with the IMU, altimeter, and inclinometer via SPI communication. These sensors return digital data, which are further used in the navigation algorithm or during the missile's initialization (in the case of the inclinometer). Within the communication protocol of these sensors, the manufacturer defines a specific bit to indicate the validity of the sensor's readings. In addition to checking this manufacturer-defined bit, the algorithm verifies the sensors' presence or absence. If any condition is not met during the missile's mission, the missile initiates an automatic safety procedure, which is one of the main safety procedures, and each error is signaled to the operator at the Ground Station.

A satellite navigation module communicates with the "main computer" using the NMEA protocol over serial communication to obtain positioning data from the satellite navigation module. The NMEA protocol is defined by a header and a checksum, which unambiguously identify whether the received packets are valid or not. Besides communication verification, the software includes additional checks, such as:

- Checking for a fix from the GPS module
- Verifying the number of satellites, as the GPS module must use 5 or more satellites to utilize its data
- Checking the HDOP (Horizontal Dilution of Precision) to assess the quality and accuracy of the current fix

If any of these conditions are not met, the position data received from the GPS module is not used in the missile's navigation algorithm, and each error is signaled to the operator at the Ground Station.

The guidance algorithm includes the main part of safety procedures, which includes the testing range boundaries. Figure 3 presents a block diagram.

As illustrated in the block diagram, the guidance law subroutine starts after 0.5 seconds of flight. The timer begins counting after the missile leaves connectors. Subsequently, data from the homing head is checked to determine if the target is locked. If the target is not locked, the trajectory guidance subroutine is executed. Within this subroutine, it is verified whether the roll is stabilized, and if the missile's angular roll rate exceeds the permissible limit ( $50^\circ/\text{s}$ ), the roll is considered unstable, and the subroutine is not executed.

Next, safety procedures are checked to determine if the missile has deviated more than 500 meters from the

specified azimuth of the target or has exceeded the target range by more than 400 meters. If any of these conditions are met, the mission is terminated using the maximum roll command, i.e., maximum aileron deflections. Following this check, another safety procedure ensures that the missile's flight time does not exceed the permissible duration for the given target range. If it does, the mission is terminated using the maximum roll command.

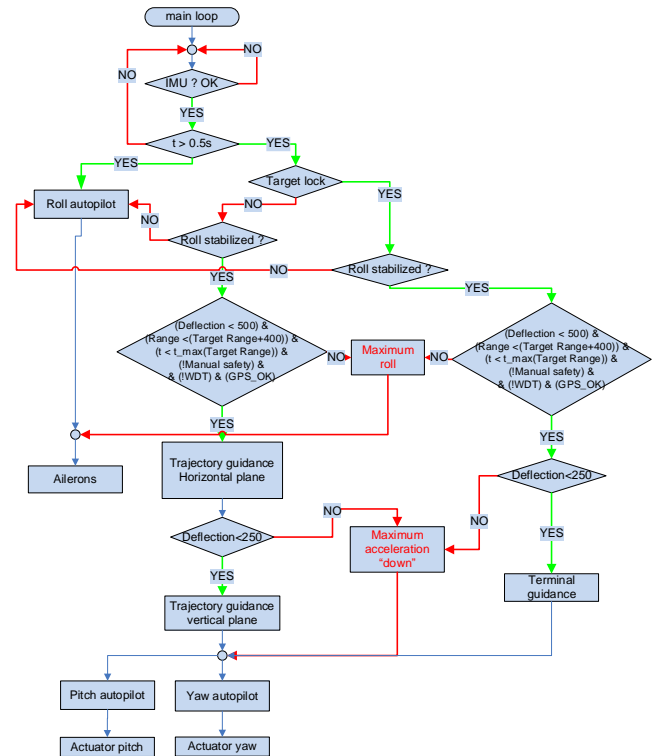


Figure 3. Block diagram of guidance and safety algorithm

Next, safety procedures are checked to determine if the missile has deviated more than 500 meters from the specified azimuth of the target or has exceeded the target range by more than 400 meters. If any of these conditions are met, the mission is terminated using the maximum roll command, i.e., maximum aileron deflections. Following this check, another safety procedure ensures that the missile's flight time does not exceed the permissible duration for the given target range. If it does, the mission is terminated using the maximum roll command.

It is also checked whether a manual termination command has been received from the Ground Station. If so, the mission is terminated using the maximum roll command. A final safety check verifies if the missile has deviated 250 meters from the specified azimuth if all previous conditions are not met. If the deviation exceeds this limit, the mission is terminated using the maximum downward normal acceleration command.

The additional condition of checking for a 500-meter deviation and 400-meter range overrun covers the possibility that the pitch actuators are not functioning, which would otherwise cause the mission to be terminated by rolling. The time-based safety condition ensures that in case of a navigation system error, where the missile is

unaware of its position, the mission is terminated after the set time limit expires.

If all safety checks are passed, the trajectory guidance algorithm and the target point guidance are executed. This subroutine is called every 16 ms, and all safety procedures are checked at the same frequency. At the end of this subroutine, the pitch and yaw autopilot subroutines are called based on the calculated values from the safety procedures or trajectory guidance.

As mentioned previously, the terminal guidance subroutine is executed if data from the homing head confirms that the target is locked. This subroutine is synchronized with the packets from the homing head, and if communication is lost for any reason, the trajectory guidance law is reactivated.

This subroutine also includes all the same checks and safety procedures as in the case of trajectory guidance.

Despite the calculated value from the roll autopilot, the actuators receive commands based on the safety protocol if it is active, as the trajectory guidance subroutine executes after the roll autopilot subroutine and before the desired commands are sent to the actuators.

**Table 1.** Failures and mitigation

Failure	Mitigation
WDT or failure to set mission	Maximum roll, Turbojet engine shutdown, booster motor jettison disabled, warhead not armed
IMU failure	Maximum roll
Altimeter failure	do not use it in the navigation algorithm
GPS failure	do not use it in the navigation algorithm
Manual safety	Maximum acceleration "down" or maximum roll
Deflection from the firing direction greater than 250m	Maximum acceleration "down"
Deflection from the firing direction greater than 500m	Maximum roll
Range greater than target range + 400m	Maximum roll
Time of flight greater than time to target	Maximum roll
The Pitch or Yaw actuator lost communication with the main computer	Neutral position
Roll actuators lost communication with the main computer	Maximum roll

An additional safety protocol exists for situations where

communication is lost between the "main computer" and the actuators. The software on the actuator side includes a Watchdog Timer (WDT). If the messages from the "main computer," which should arrive every 16ms during normal operation, fail to do so, the WDT initiates the safety procedure. In case of malfunction, the pitch and yaw actuators will move to the neutral position, and the roll actuators will engage the maximum roll command.

Table 1 presents all failure mitigation mentioned previously.

## 4. RESULTS

The flight paths in the case of normal system operation were considered with the following disturbances included: imperfections of the Inertial Measurement Unit (IMU) (particularly the effect of gyroscope misalignment and its impact on navigation errors when GPS is unavailable during the entire trajectory), permissible misalignment of the wings (stabilizers), permissible misalignment of the booster motor, and permissible crosswind  $\leq 5$  m/s.

Simulations were also conducted for the scenario where the turbojet engine fuel tank contains the amount of fuel necessary for the desired range, which remains in the tank after the startup procedure.

It is important to note that the maximum commands for pitch are  $[-7.5, 7.5]$  degrees, for yaw are  $[-6, 6]$  degrees, and for roll are  $[-14, 14]$  degrees. The actuators are designed based on self-locking worm gears, meaning that the control surface will remain in its last position in the event of a power loss.

In the event of a power failure, as seen in Figure 1, the control of the turbojet engine would also fail, resulting in the turbojet engine shutdown.

Cases of irregular operation were considered during the missile's "critical" flight phases: immediately after leaving the launcher and deploying the wings, during the phase of maximum yaw maneuver, at the beginning of cruising, at the midpoint of the planned trajectory, and during the phase after target lock-on (terminal guidance). All trajectories were simulated with disturbances within permissible limits [5] and shown in Figure 4.

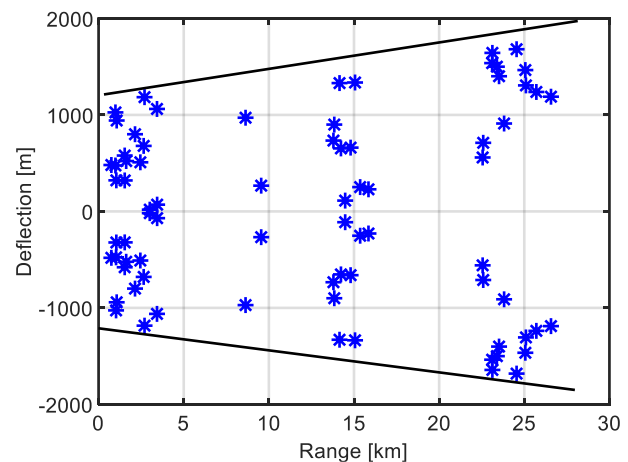


**Figure 4.** Irregular operation simulation results

Figure 4 shows a noticeable trend where the trajectories deviate more significantly as the range increases. This trend is due to the nature of the inertial navigation system (INS) when there is no correction from GPS. All errors in the INS grow exponentially over time and, consequently, with the increased range.

## 5. CONCLUSION

The automatic safety algorithms for missiles, such as small cruise missiles, are essential for maintaining operational integrity and ensuring that safety functions within predefined testing range boundaries. This paper has explored the approach required to achieve this optimization, incorporating sensor integration, real-time decision-making, and risk assessment frameworks. This process involves a detailed analysis of potential failures, environmental impacts, and human errors, along with the implementation of various safety protocols to minimize risks. Simulation results demonstrate different scenarios of irregular operation, highlighting the importance of precise navigation and timely safety measures.

The literature review highlighted the significance of risk management frameworks, such as the Specific Operations Risk Assessment (SORA), in providing systematic approaches to assessing and mitigating risks.

In conclusion, optimizing automatic safety algorithms for guided missiles involves a comprehensive approach that integrates advanced technology, structured risk assessment, and rigorous testing and validation. By leveraging insights from UAV safety and risk management, researchers and engineers can continue to enhance the reliability and performance of guided missile safety protocols. Integrating these safety procedures allows for safer and more reliable testing and use of guided missiles, reducing the likelihood of adverse events and enhancing mission effectiveness.

## Acknowledgments

This work was mainly supported by the company EDePro, Serbia, and partially supported by the Serbian Ministry of Education and Science under contract evidence number 451-03-65/2024-03/200105 from 05.02.2024.

## References

- [1] KUCHAR, J. K.: *Safety analysis methodology for unmanned aerial vehicle (UAV) collision avoidance systems*, 6th USA/Europe Air Traffic Management Research and Development Seminar, Baltimore, MD, 2005.
- [2] BALESTRIERI, E., DAPONTE, P., DE VITO, L., PICARIELLO, F., TUDOSA, I.: *Sensors and Measurements for UAV Safety: An Overview.*, Sensors. 2021; 21(24):8253.
- [3] NIKODEM, F., BIERIG, A., & DITTRICH, J. S.: *The New Specific Operations Risk Assessment Approach for UAS Regulation Compared to Common Civil Aviation Risk Assessment*, DLRK 2018.
- [4] OH, Y.-J., ROH, H., TAHK, M.-J.: *Fast Trajectory Optimization using Sequential Convex Programming with No-Fly Zone Constraints*, IFAC-PapersOnLine, Volume 52, Issue 12, 2019, Pages 298-303, ISSN 2405-8963
- [5] REARDON, B. E., LLOYD, J. M., & PEREL, R. Y.: *Tuning missile guidance and control algorithms using simultaneous perturbation stochastic approximation*. Johns Hopkins APL Technical Digest, 29(1), 85–100 (2010).



## OPTIMIZATION OF SINGLE STAGE PLANETARY GEARBOX PARAMETERS USING GENETIC ALGORITHM

MILOŠ SEDAK

Faculty of Mechanical Engineering, University of Belgrade, Belgrade, [msedak@mas.bg.ac.rs](mailto:msedak@mas.bg.ac.rs)

MAJA ROSIĆ

Faculty of Mechanical Engineering, University of Belgrade, Belgrade, [mrosic@mas.bg.ac.rs](mailto:mrosic@mas.bg.ac.rs)

**Abstract:** Planetary gearboxes are a mechanical devices consisting of multiple gears arranged in a circular configuration around a central sun gear. This layout enables an efficient gearbox with high torque in a compact design, thus making it well-suited for a wide range of industrial and military applications such as industrial motors, rotorcraft, vehicles, wind turbines, and more. However, when it comes to aircraft applications, weight and strength are essential considerations in the design process. Genetic algorithms are used to optimize the parameters of a single-stage planetary gearbox in order to achieve the necessary balance between weight, strength, and performance in aircraft applications. The study focuses on formulating the optimization problem in an appropriate way while also developing constraints that guarantee the effective functioning of the planetary gearbox. In order to effectively address this complex and multimodal constrained optimization problem, this paper suggests utilizing an enhanced genetic algorithm (NSGA-II), which is widely recognized as the most commonly employed evolutionary optimization technique. In comparison with conventional GA algorithm, the numerical simulation results demonstrate that the suggested method exhibits enhanced optimization performance in relation to the quality of the achieved solutions.

**Keywords:** Planetary gearboxes, optimization, efficiency, genetic algorithm.

### 1. INTRODUCTION

Planetary gearboxes, also known as epicyclic gear trains, are critical components in many mechanical systems due to their high power density, compact size, and versatility in providing a wide range of speed ratios. These gearboxes consist of a central sun gear, multiple planet gears rotating around the sun gear, and an outer ring gear that meshes with the planet gears. This configuration allows for efficient power transmission and torque distribution, making planetary gearboxes essential in various applications, including automotive transmissions, aerospace mechanisms, wind turbines, and industrial machinery [1], [2].

The optimization of planetary gearbox parameters, such as gear ratios, gear module, tooth number, and material properties, presents a significant engineering challenge. This complexity stems from the numerous interdependent variables that influence the overall performance of the gearbox, including efficiency, load distribution, noise levels, and reliability. Achieving an optimal balance among these factors requires sophisticated optimization techniques that can navigate the intricate trade-offs involved [1]. In this regard, the optimization of gearbox and gear transmission systems has traditionally focused on single-objective optimization. Single-objective optimization aims to improve a specific performance criterion such as minimizing weight or maximizing efficiency. However, these approaches often fail to meet the complex requirements of modern engineering

applications.

Single-objective optimization methods, while effective for specific criteria, do not suffice for the increasingly stringent and complex demands of modern engineering applications. Contemporary requirements often involve balancing multiple conflicting objectives, such as minimizing weight while maximizing efficiency and durability. Multi-objective (MO) optimization provides a more comprehensive approach by considering multiple performance criteria simultaneously. One exemplary study [3] explores a multi-objective optimization of a two-stage spur gearbox. This research incorporated constraints such as scuffing and wear, with objectives to reduce weight and power losses using a discrete version of the Non-Dominated Sorting Genetic Algorithm II (NSGA-II). The study demonstrated significant improvements in power loss reduction compared to single-objective optimization.

In [4] authors applied multi-objective optimization to vehicle drivetrains, aiming to improve fuel consumption, acceleration, and emissions. Using the Interactive Adaptive-Weight Genetic Algorithm, the study optimized gear ratios and other variables under various driving cycles, achieving a balanced enhancement in acceleration, fuel savings, and emission reductions. Additionally, in [5] researchers implemented a multi-objective optimization for gear unit design, targeting power loss and vibrational excitation minimization through a multi-scale approach.



The NSGA-II was used to optimize both macro and micro-geometry characteristics, resulting in reduced power loss and improved performance metrics compared to single-objective approaches.

To tackle the complexity of multi-objective optimization, evolutionary optimization algorithms (EAs) have been extensively employed. These algorithms are inspired by the principles of natural evolution and use mechanisms such as selection, crossover, and mutation to evolve solutions over successive generations. EAs are particularly effective in exploring large and complex solution spaces, making them suitable for solving multi-objective problems [6]. Several EAs have been developed for multi-objective optimization, including Differential Evolution (DE), Particle Swarm Optimization (PSO), and Ant Colony Optimization (ACO), each with its unique strengths and applications [6].

Among these, Genetic Algorithms (GAs) have proven to be particularly robust and flexible for solving complex optimization problems [7]. GAs encode potential solutions as chromosomes, which are then evolved through genetic operations to explore and exploit the solution space efficiently, enabling the finding of optimal or near-optimal global solutions. Since it is designed for single objective optimization, the application to MO problems requires specific modifications. The earliest advancements in the application of genetic algorithms to multi-objective optimization involved the weighted sum method. In this approach, each objective function is assigned a specific weight, and the weighted objectives are summed to transform the problem into a single-objective optimization task. Despite its simplicity, this method has significant limitations, particularly in the context of non-convex Pareto sets, where it often fails to identify global optimal solutions [8].

Genetic Algorithms for MO optimization, such as the NSGA-II [9] and the Strength Pareto Evolutionary Algorithm (SPEA2), have been specifically designed to handle multiple objectives. These algorithms maintain a diverse population of solutions and employ selection mechanisms that favor non-dominated solutions, ensuring a comprehensive exploration of the trade-offs between objectives [9].

In this study, the aim is to optimize the parameters of a single-stage planetary gearbox using a multi-objective genetic algorithm. By leveraging the strengths of GAs in handling complex optimization problems, the aim is to enhance the performance and efficiency of planetary gear systems through a rigorous and systematic approach. Our research focuses on the application of NSGA-II to identify optimal trade-offs among conflicting objectives, ultimately contributing to the advancement of gearbox design and performance. Furthermore, the performance of NSGA-II algorithm is compared to the more conventional GA using weighted sum method.

The structure of this paper is as follows: Section 2 formulates the optimization problem and introduces the penalty method used for handling constraints. Section 3 details the procedure of the multi-objective genetic

algorithm method. Section 4 presents the corresponding simulation results. Finally, conclusions are discussed in Section 5.

## 2. FORMULATION OF THE CONSIDERED OPTIMIZATION PROBLEM

The planetary gearbox considered in this study is a single-stage planetary gearbox. This gearbox includes three planet gears and two central gears. The sun gear, which is one of the central gears with external gearing, is directly connected to the input shaft. The other central gear, which has internal gearing, remains stationary and secures the assembly. Power is distributed from the input shaft and sun gear to the planet gears and subsequently transmitted to the carrier connected to the output shaft. The schematic representation of the gearbox under consideration is shown in Fig. 1.

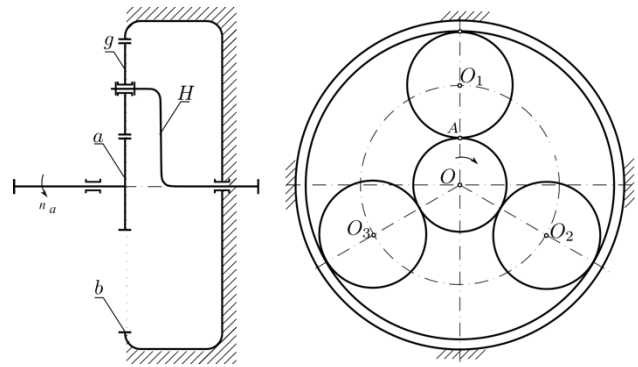


**Figure 1.** Schematic representation of a single-stage planetary gearbox considered in the optimization model

The primary goal of this study is to develop a reliable and lightweight planetary gearbox that maintains high efficiency. This necessitates creating a MO optimization model that integrates design variables, objectives, and constraints to optimize conflicting objectives, such as weight reduction, decreased power loss, and improved component reliability.

The general form of the multi-objective optimization problem can be expressed as:

$$\min f_m(\mathbf{x}), \quad m = 1, \dots, M \text{ and } i = 1, \dots, N_p \quad (1)$$

subject to:

$$g_k(\mathbf{x}) \geq 0, \quad k = 1, \dots, K \quad (2)$$

$$h_l(\mathbf{x}) = 0, \quad l = 1, \dots, L \quad (3)$$

$$x_{i,j} \in [x_j^{\text{Lower}}, x_j^{\text{Upper}}], \quad j = 1, \dots, n \quad (4)$$

where  $M$  represents the number of objectives ( $\geq 2$ ),  $g_k(x_i)$  represents the  $k$ -th inequality constraint out of a total of  $K$  inequality constraints,  $h_l(x_i)$  represents the  $l$ -th equality constraint out of a total of  $L$  equality constraints,  $\mathbf{x}$  is the vector of decision variables whose

components are  $x_{i,j}$  bounded by  $x_j^{\text{Lower}}$  and  $x_j^{\text{Upper}}$ , and  $N_p$  is the number of solutions in the population.

## 2.1 Objectives of the considered problem

The considered planetary gearbox optimization model takes into consideration a number of objective outlined in the following subsections the objectives are outlined.

### Volume of the Gears

One of the crucial requirements, especially in aerospace industry, is the requirement of mass minimization. Under the assumption of constant density, the problem can be reduce to the problem of minimizing the volume of the gears. The volume of the gears in the considered gearbox can be calculated as

$$W(\mathbf{x}) = \rho \frac{\pi}{4} b \left[ d_{(a)}^2 + n_w (d_{a(b)}^2 - D^2) + (d_{(g)}^2 - d_s^2) \right] \quad (5)$$

where  $V(x)$  denotes the volume of the gears,  $b$  is the gear face width, where  $d_{(a)}$  is the pitch circle of the sun gear,  $d_{a(b)}$  is tip diameter of the ring gear,  $d_s$  is outside bearing diameter,  $d_{(g)}$  is the pitch circle of the planet gear,  $n_w = 3$  is the number of planet gears,  $D$  denotes outside diameter of a ring gear.

### Contact Ratio

The contact ratio is introduced as an objective to ensure smooth and continuous gear operation by maintaining multiple teeth in contact, which distributes load evenly and reduces vibrations and noise, as follows

$$\varepsilon_\alpha = \frac{0.5 \left( \sqrt{d_{2a(a)} - d_{2a(b)}} + \sqrt{d_{2a(g)} - d_{2a(g)}} \right) - a \sin(\alpha_{wt})}{\pi m_t \cos(\alpha_t)} \quad (6)$$

where  $\varepsilon_\alpha$  denotes the contact ratio,  $a$  is the center distance,  $\alpha_{wt}$  and  $\alpha_t$  are appropriate pressure angles and  $m_t$  is the module of the gear.

### Safety Against Bending for Central Gears

Maximizing the safety against bending for the sun gear and other gears:

$$S_{F(a)(x)} = \frac{[\sigma_F]_{M(a)}}{\sigma_{F(a)}}, \quad (7)$$

$$S_{F(b)(x)} = \frac{[\sigma_F]_{M(b)}}{\sigma_{F(b)}}$$

where  $S_{F(a)(x)}$  and  $S_{F(b)(x)}$  are the safety factors against bending for gears  $(a)$  and  $(b)$ ,  $[\sigma_F]_{M(a)}$  and  $[\sigma_F]_{M(b)}$  are the allowable bending stresses, and  $\sigma_{F(a)}$  and  $\sigma_{F(b)}$

are the actual bending stresses for gears  $(a)$  and  $(b)$ , respectively.

### Safety Factor for Contact Stress

Minimizing the contact stress:

$$S_{H(a)(x)} = \frac{[\sigma_H]_{M(a)}}{\sigma_{H(a)}} \quad (8)$$

where  $S_{H(a)(x)}$  is the safety factor for contact stress,  $[\sigma_H]_{M(a)}$  is the allowable contact stress,  $\sigma_{H(a)}$  is the contact stress.

### Gearbox Efficiency

The second objective of the optimization issue pertains to the efficiency of the planetary gear box and can be mathematically expressed by the given statement

$$\eta_{aH}^b = \frac{1 - \eta_{ag}^H \eta_{gb}^H u_{ab}^H}{1 - u_{ab}^H} \quad (9)$$

where  $\eta_{ag}^H$  and  $\eta_{gb}^H$  denote relative efficiency of the sun-planet gears and relative efficiency of planet-ring gears, respectively. These efficiencies can be determined according to the numerical procedure given in [10]. Furthermore,  $u_{ab}^H$  denotes the relative gear ratio.

## 2.2 Constraints

### Bending Constraint

Ensuring the gear tooth bending strength:

$$g_{1,2,3} = \frac{[\sigma_F]_{M(a,g,b)}}{\sigma_{F(a,g,b)}} - S_F > 0 \quad (10)$$

where  $[\sigma_F]_{M(a,g,b)}$  is the allowable bending stress for gears  $a$ ,  $g$ , and  $b$ ,  $\sigma_{F(a,g,b)}$  is the actual bending stress for gears  $a$ ,  $g$ , and  $b$ , and  $S_F$  is the safety factor.

### Pitting Constraints

Ensuring resistance to surface fatigue:

$$g_4 = \frac{[\sigma_H]_{M(a,g)}}{\sigma_H} - S_H > 0,$$

$$g_5 = \frac{[\sigma_H]_{M(g,b)}}{\sigma_H} - S_H > 0 \quad (11)$$

where  $[\sigma_H]_{M(a,g)}$  and  $[\sigma_H]_{M(g,b)}$  are the allowable contact stresses for gear pairs  $(a,g)$  and  $(g,b)$ ,  $\sigma_H$  is the actual contact stress,  $S_H$  is the safety factor for pitting.

### Space Requirement

Ensuring appropriate clearance for gear assembly:

$$g_7 = 2a \sin\left(\frac{\pi}{n_w}\right) - f_z - d_{a-g} \geq 0 \quad (12)$$

where  $f_z$  is radial clearance and  $d_{a-g}$  is the addendum circle diameter of the sun gear.

#### Assembly Condition

Preventing teeth interference during meshing:

$$h_1 = \frac{z_a z_b}{n_w D(z_g, z_b)} - i = 0 \quad (13)$$

where  $z_a$  and  $z_b$  are the numbers of teeth on gears  $a$  and  $b$ ,  $D$  is the pitch diameter,  $z_g$  is the number of teeth on the planet gear,  $i$  is the gear ratio.

### 3. MULTI OBJECTIVE GENETIC ALGORITHM

Genetic algorithm is a metaheuristic optimization algorithm, inspired by the principles of natural genetics and natural selection. This algorithm is widely utilized to find optimal solutions to multimodal optimization problems at a global level. The process of utilizing a GA to identify the global optimum solution begins with the generation of a population of initial solutions. In traditional GAs, also known as single-objective GAs, each solution is evaluated based on a single objective function, and the algorithm aims to find the best solution according to that objective [8].

#### 3.1 Regular Genetic Algorithm

A GA operates through three primary evolutionary operators: selection, crossover, and mutation.

##### Selection

During the selection phase, the GA uses the objective function value of each individual to choose chromosomes from the population that have favorable mating qualities. Chromosomes with lower objective function values (for minimization problems) are more likely to be chosen. The selection probability of the  $i$  th individual is calculated as:

$$P_i = \frac{f_i}{\sum_{j=1}^N f_j}, \quad (14)$$

where  $f_i$  denotes the objective function value of the chromosome, and  $N$  is the population size. The cumulative probability  $C_i$  of the  $i$  th individual is determined by:

$$C_i = \sum_{j=1}^i P_j. \quad (15)$$

Individuals are then selected based on a random number  $r$  generated between 0 and 1, where:

$$C_{i-1} \leq r < C_i. \quad (16)$$

##### Crossover

The crossover operator combines the genetic information of two selected individuals to produce offspring that share important features from both parents. A common method is the two-point crossover, where two random points along the chromosome length are selected, and the segments between these points are exchanged between the two parents.

##### Mutation

Mutation introduces new genetic structures into the population by randomly altering some genes of selected chromosomes. This operator helps maintain genetic diversity within the population and prevents premature convergence to local optima. The mutation rate is typically kept low to avoid disrupting valuable genetic information. These operators are applied iteratively, evolving the population towards the global optimal solution until a termination condition is met, which is usually defined by a maximum number of iterations or a convergence threshold.

#### 3.2 Multi-objective Genetic Algorithm (NSGA-II)

In multi-objective optimization problems, multiple conflicting objectives must be optimized simultaneously. Unlike single-objective optimization, there is no single optimal solution but rather a set of solutions known as the Pareto front, where each solution is non-dominated with respect to the others. A solution is considered non-dominated if no other solution is better in all objectives simultaneously. To extend GAs for multi-objective optimization, non-dominated sorting and crowding distance mechanisms are introduced. One of the most widely used algorithms in this domain is the NSGA-II.

The NSGA-II [9] is an advanced version of the GA algorithm, designed to enhance the process of multi-objective optimization by focusing on non-dominated sorting. This method evaluates the quality of each solution  $\mathbf{x}$  based on a fitness function that considers not only the solutions dominating  $\mathbf{x}$  but also those that  $\mathbf{x}$  itself dominates. An essential aspect of NSGA-II is the crowding distance metric, which calculates the Euclidean distance of a solution from its neighboring solutions in the criterion space, thereby preserving solution diversity within the population.

##### Non-dominated Sorting

The NSGA-II algorithm classifies all chromosomes in the current population into different fronts based on their level of non-domination. Each solution  $\mathbf{x}_i$  is assessed for the number of solutions  $n_i$  that dominate it and the set  $S_i$  of solutions it dominates. Solutions not dominated by any

member of the population form the first non-dominated front (PF1). Subsequent fronts are formed by decrementing the dominance count  $n_j$  for each solution in  $S_i$  until all solutions are classified. This iterative sorting process ensures that all solutions are grouped into their respective non-dominated fronts, as illustrated in Fig.2, which depicts the maximization of two conflicting criterion functions.

After the non-dominated sorting, a new population for the next iteration is constructed by sequentially adding solutions from the highest-ranked fronts until the population size limit is reached. If adding an entire front would exceed the population limit, solutions from that front are sorted based on their crowding distance, and the top solutions are selected to fill the remaining slots. This method ensures that the new population maintains a balance between convergence and diversity.

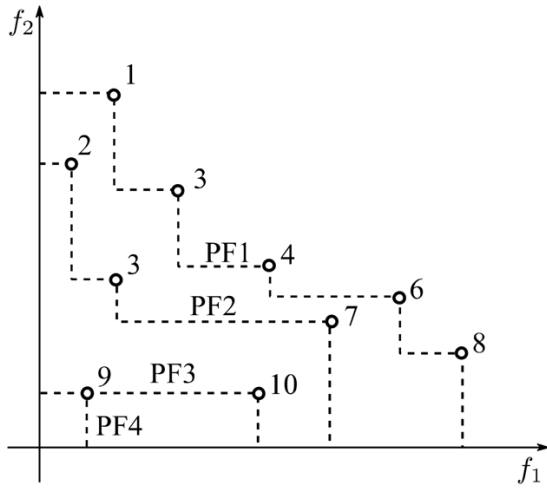


**Figure 2.** Illustration of the domination principle of NSGA-II algorithm

### Crowding Distance

The crowding distance metric in NSGA-II is calculated for each solution  $\mathbf{x}_i$  as the average Euclidean distance between the solution and its nearest neighbors along each criterion dimension. For a population of  $N_p$  chromosomes and a solution  $\mathbf{x}_a$  with a vector function value  $f(\mathbf{x}_a) = [f_1(\mathbf{x}_a), f_2(\mathbf{x}_a), \dots, f_m(\mathbf{x}_a)]^T$ , the maximum and minimum values of the nearest solutions in the population are determined. The crowding distance for solution  $\mathbf{x}_a$  is then computed using the formula:

$$d(\mathbf{x}_a) = \sum_{i=1}^m (f_{\max,i}(\mathbf{x}_a) - f_{\min,i}(\mathbf{x}_a))$$

Solutions located in densely populated regions of the criterion space have lower crowding distance values, while those at extreme values tend towards infinity. The crowding distance ensures a uniform distribution of solutions along the Pareto front, preventing premature convergence and maintaining diversity.

The NSGA-II algorithm effectively balances convergence and diversity by utilizing non-dominated sorting and crowding distance metrics. This approach results in a robust and efficient method for solving multi-objective optimization problems, and the pseudocode of this algorithm is shown in the Fig. 3

## 5. SIMULATION RESULTS

This section presents results of optimizing the parameters of planetary gearbox using the NSGA-II method compared to the conventional single objective GA method using the weighted sum method to apply to MO problems [8]. Table 1 shows the essential design characteristics of the planetary gearbox under consideration.

In the context of optimizing planetary gearboxes, the Pareto frontier serves as a critical tool for balancing multiple objectives. Therefore, firstly the combination of the contact ratio and gearbox efficiency as objectives have been analyzed, as shown in Fig. 4.

### Algorithm 1 NSGA-II

```

1: Initialize population  $P(0)$ 
2: Evaluate population  $P(0)$ 
3:  $t \leftarrow 0$ 
4: while termination criterion not met do
5:   Perform non-dominated sorting on  $P(t)$ , producing fronts  $F_i$ 
6:   for each front  $F_i$  do
7:     Calculate crowding distance  $d_i$  for each individual in  $F_i$ 
8:   end for
9:    $Q \leftarrow \emptyset$ 
10:  while  $|Q| < N$  do
11:    Select two parents from  $P(t)$  using tournament selection
12:    Perform crossover and mutation to produce offspring
13:    Evaluate offspring
14:    Add offspring to  $Q$ 
15:  end while
16:   $R(t) \leftarrow P(t) \cup Q$ 
17:  Perform non-dominated sorting on  $R(t)$ , producing fronts  $F_i$ 
18:   $P(t+1) \leftarrow \emptyset$ 
19:   $i \leftarrow 0$ 
20:  while  $|P(t+1)| + |F_i| \leq N$  do
21:    Calculate crowding distance  $d_i$  for each individual in  $F_i$ 
22:     $P(t+1) \leftarrow P(t+1) \cup F_i$ 
23:     $i \leftarrow i + 1$ 
24:  end while
25:  Sort  $F_i$  by crowding distance and select the first  $N - |P(t+1)|$  individuals
26:   $P(t+1) \leftarrow P(t+1) \cup$  selected individuals from  $F_i$ 
27:   $t \leftarrow t + 1$ 
28: end while

```

**Figure 3.** Pseudocode of NSGA-II algorithm

**Table 1.** Parameters of the planetary gear set used in this paper

Parameters	Symbol	Value
Input Power [kW]	$P_a$	180
Input speed [rpm]	$n_a$	2750

Parameters	Symbol	Value
Pressure angle [degree]	$\alpha_n$	20
Gear material		18CrNi8
Gear surface Roughness [ $\mu\text{m}$ ]	$R_a$	0.8
Factor of safety against bending	$S_{F\min}$	1.5
Factor of safety against pitting	$S_{H\min}$	1.25
Number of planet gears	$n_w$	3

From the Fig. 4 it can be seen that there exists a trade-off between contact ratio and gearbox efficiency as the objectives, where the increase in one, leads to the simultaneous decrease in the other.

Furthermore, regarding the optimization algorithms for a planetary gearbox optimization problem Fig. 4 showcases the effectiveness of NSGA-II in producing a more detailed Pareto frontier compared to a conventional Genetic Algorithm based on weighted sum method.

Next, the contact ratio and the contact stress are taken as the objectives, as shown in Fig. 5.

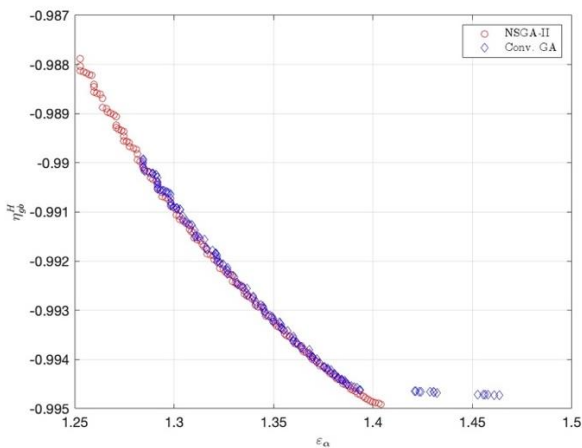


**Figure 4.** Pareto frontier for planetary gearbox for contact ratio and gearbox efficiency as objectives.

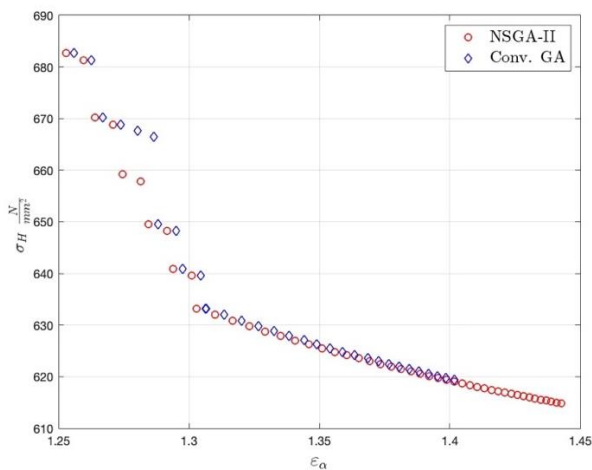


**Figure 5.** Pareto frontier for planetary gearbox for contact ratio and contact stress.

From the results depicted in Fig. 5 it can be observed that the considered objective functions are conflicting. Again the NSGA-II algorithm showed comparably better performance.

When compared to the industrial gearbox reference [11], it results in a 12% decrease in gearbox weight and a 0.3% increase in efficiency. The numerical simulations demonstrate that the gear optimization technique, which utilizes the NSGA-II algorithm, can yield superior design solutions in comparison to standard algorithms.

## 6. CONCLUSION

This study explores the development of a non-linear optimization model to find the best parameters for a planetary gearbox. The model is solved using a metaheuristic optimization technique. In order to determine suitable parameters for a planetary gearbox, the complex multimodal objective functions that involve multiple constraints have been minimized. In the paper, a comparative examination of the application of the widely recognized NSGA-II version of the GA and a more typical GA algorithm implemented using the weighted sum approach have been analyzed. In the given multi-objective optimization issue, the relevant objectives are formulated, including minimizing the weight of the gearbox and maximizing the efficiency of the gearbox. The NSGA-II optimization method enhances the characteristics of the planetary gearbox, resulting in superior performance.

Future research should extend the optimization framework to multi-stage planetary gearboxes and incorporate additional real-world constraints such as manufacturing tolerances and material properties variations. Additionally, combining NSGA-II with other optimization techniques and validating the results through experimental testing will enhance the robustness and practical applicability of the proposed method.

## Acknowledgment

The research of M. Sedak was supported by the Serbian Ministry of Education and Science under Grant No. TR35006. The research of M. Rosić was supported by the Serbian Ministry of Education and Science under Grant TR35029.

## References

- [1] N. Sen, S. Goutam, and S. K. Bairwa, "A Review Paper on Epicyclic Gear System," *Journal of Emerging Technologies and Innovative Research*, 2020.
- [2] Arnaudov, K. and Karaivanov, D.P., 2019. *Planetary gear trains*. CRC Press.
- [3] M. Patil, P. Ramkumar, and K. Shankar, "Multi-Objective Optimization of Spur Gearbox with Inclusion of Tribological Aspects," *Journal of Friction and Wear*, vol. 38, pp. 430-436, 2017.
- [4] J. Eckert, F. M. Santicioli, L. C. A. Silva, and F. Dedini, "Vehicle drivetrain design multi-objective optimization," *Mechanism and Machine Theory*, vol. 156, pp. 104123, 2021.
- [5] E. B. Younes, C. Changenet, J. Bruyere, E. Rigaud, and J. Perret-Liaudet, "Multi-objective optimization of gear unit design to improve efficiency and

- transmission error,” *Mechanism and Machine Theory*, vol. 167, pp. 104499, 2022.
- [6] T. Bäck, “Evolutionary Algorithms in Theory and Practice,” New York, NY: Oxford University Press, 1996.
- [7] D. E. Goldberg, *Genetic Algorithms in Search, Optimization, and Machine Learning*, Boston, MA: Addison-Wesley, 1989.
- [8] Wang, R., Zhou, Z., Ishibuchi, H., Liao, T., & Tao, Z. (2018). Localized weighted sum method for many-objective optimization. *IEEE Transactions on Evolutionary Computation*, 22(1), 3-18.
- [9] Deb, K., Agrawal, S., Pratap, A., & Meyarivan, T. (2002). A fast and elitist multiobjective genetic algorithm: NSGA-II. *IEEE Transactions on Evolutionary Computation*, 6(2), 182-197.
- [10] Sedak, M., & Rosic, B. (2021). Multi-Objective Optimization of Planetary Gearbox with Adaptive Hybrid Particle Swarm Differential Evolution Algorithm. *Applied Sciences*.
- [11] Standard, A.G.M.A., 2006. Design manual for enclosed epicyclic gear drives. Alexandria, VA: American Gear Manufacturers Association, pp.1-104.



## TESTING OF TECHNICAL SOLUTION FOR ACHIEVING THE OPTIMAL DURATION OF THE ACTIVATION CADENCE OF THE FRONT AND MAIN WARHEAD IN THE TANDEM CUMULATIVE WARHEADS

SLOBODAN BOSILJČIĆ

Military Technical Institute, Belgrade, [bobanbosiljcic@yahoo.com](mailto:bobanbosiljcic@yahoo.com)

MIROSLAV GLUVAČEVIĆ

MG Engineering, Belgrade, [mgluvacevic@gmail.com](mailto:mgluvacevic@gmail.com)

RADE STANČIĆ

MG Engineering, Belgrade, [radestancic@gmail.com](mailto:radestancic@gmail.com)

MARINKO UGRČIĆ

Mathematical institute SANU, [ugrcicmarinko@gmail.com](mailto:ugrcicmarinko@gmail.com)

KATARINA NESTOROVIĆ

Military Technical Institute, Belgrade, [katarina.nestorovic993@gmail.com](mailto:katarina.nestorovic993@gmail.com)

**Abstract:** *The production of modern armored vehicles through the use of new technologies and the development of additional active-reactive means of protection increase their toughness and resistance on the battlefield. Thus, increasing demands are placed on anti-tank missiles in order to achieve the required effect on the modern battlefield by using them. One of the directions of development of modern anti-armor missiles with high penetration is arming these missiles with tandem cumulative warheads (TKWH). In order to make the most of the effect of activating the TKWH, it is necessary to achieve very precise activation of the front and base warheads. The cadence between the activation of the front and main warheads in the TKWH depends on many factors, some of which are of constant value, while others are variable and depend on the speed of the missile at the moment of meeting the target, the angle of attack at which the missile hits the target and other factors. Due to all of the above, the control elements of the igniter that should activate the TKWH should meet many criteria, such as, first of all, absolute safety when manipulating the missile and/or TKWH, operational reliability, precision and repeatability of the dynamics of activating the front and main warhead.*

**Keywords:** *anti-tank missiles, tandem cumulative warhead, TKWH*

### 1. INTRODUCTION

Constant development, modernization and the use of modern technical solutions and modern technologies in production allow armored mechanized units to continue to be a significant, if not dominant, factor on the modern battlefield.

The development of new solutions that increase the active and passive protection of tanks, combined with the use of new materials that increase resistance to the effects of anti-armor means, increase the possibility of survival of tanks and armored vehicles on the battlefield, which on the other hand sets new requirements for the development of modern anti-armor means, with special emphasis on anti-armor guided missiles.

Due to all of the above, the control elements of the igniter that should activate the TKWH should meet many

criteria, such as, first of all, absolute safety when manipulating the missile and/or TKWH, operational reliability, precision and repeatability of the dynamics of activating the front and main warhead, first of all, those that rely on weapons used to arm aircraft platforms.

### 2. THEORETICAL BASIS

Anti-armor guided missiles are high-precision modern weapons that should represent one of the main answers to the directions of development of armored vehicles. The development of anti-armor guided missiles takes place in two basic directions: the first is increasing the range and accuracy of the missile, and the second is increasing the effectiveness of the missile's warhead. The warhead of an anti-armor guided missile, taking into account the development of elements of passive protection of armored vehicles, should have such characteristics that will enable it to effectively act on a target protected by explosive-

reactive armor (ERA). One of the effective ways to eliminate or significantly reduce the effect of explosive-reactive armor on the penetration of a cumulative warhead (KWH) is the use of the so-called tandem cumulative warhead (TKWH), composed of a front warhead (precursor) whose main task is to remove the explosively reactive armor by its action at the moment of the missile hitting the target, and the main cumulative warhead that has the task of effecting the target after removing the explosive-reactive armor.

The dynamics of activating precursors and main KWH mostly depends on:

- the mutual position of the precursor and the main warhead inside the rocket and
- relative speed of the rocket in relation to the target at the moment of encounter.

The time delay of the activation of the main warhead in relation to the precursor should ensure that there is no influence of the cumulative jet of the precursor on the cumulative jet of the main warhead on the one hand, and to prevent the influence of the effect of the explosive-reactive armor explosion on the formation of the cumulative jet of the main warhead on the other sides. By analyzing the mode of action of cumulative warheads, explosive-reactive armor, possible attack angles of the missile in relation to the target during the encounter, the new tandem cumulative warhead of increased penetration should meet the following requirements:

- the distance of the precursor from the explosive-reactive armor at the moment of activation of the igniter (the moment the rocket hits the target) should be at least 3 and at most 5 calibers (the diameter of the KWH copper funnel) of the precursor;
- the distance of the main warhead from the target at the moment of activation of the igniter should be at least 3 and at most 5 calibers of the main warhead;
- the time delay of the activation of the igniter of the precursor and the main warhead should be set in such a way as to prevent the influence of the effect of the precursor and the explosion of the ERA on the formation of the cumulative jet of the main KWH.

In order to meet these requirements, the following must be provided:

- the structural solution of the warhead and its position in the missile should be appropriate;
- the igniter that activates the TKWH should ensure the appropriate activation dynamics of the precursor and the main KWH.

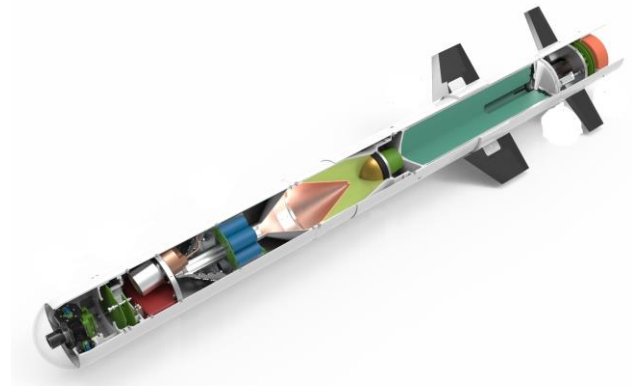


**Figure 1:** An example of a structural solution of TKWH inside of missile

The given example shows the performance of TKWH inside a missile with a homing head with an integrated IR camera on the gimbal. This configuration further complicates the effect of the precursor on the ERA because the homing head acts as an additional obstacle that the cumulative jet of the precursor needs to overcome before it acts on the ERA, which implies that the precursor in TKWH in this type of rocket must have a higher penetration than the precursor of TKWH rockets that are guided to the target in a different way and therefore do not need the existence of parts of the missile guidance system in front of the warhead.

### 3.INITIAL HYPOTHESES

In addition to the required characteristics of the warheads in TKWH, there was a need to develop a fuze with a safety arming mechanism that should provide:

- safe manipulation of the rocket with an emphasis on the safety of the employees who work with the rocket;
- multi-level protection against unwanted arming and activation of TKWH;
- arming the TKWH igniter only after the rocket is at a safe distance from the launch platform after launch;
- activation of the precursor and main warhead according to precisely defined dynamics with a cadence that can be adjusted in advance when preparing the missile for launch or during the flight of the missile to the target.

The technical solution that meets the stated requirements is an electromechanical assembly consisting of:

- a igniter with a safety arming mechanism for the precursor and the main BG, the design of which enables the establishment of a pyrotechnic chain for activating the igniter only under strictly defined conditions;
- the electronic part of the igniter that enables the control of the pyrotechnic elements of the mechanical part of the igniter.



Since the cadence of the activation of the precursor and the main warhead should be of exactly the same duration (200-500  $\mu\text{s}$ , which depends on the structural characteristics of the warhead and the speed of the missile when meeting the target) with as little deviation as possible (less than  $\pm 10 \mu\text{s}$ ), it is necessary that the igniter has a very reliable electro-mechanical-pyrotechnic system that will ensure absolute safety during exploitation and high accuracy of activation of TKWH warheads at the given moment.

The development of the electronic part of the igniter had to satisfy several basic requirements:

- it should have compact dimensions so that it can be installed in the relatively small available space inside the rocket;
- considering that the mechanical parts of the igniter are identical for the precursor and the base of the KWH, as well as due to the simplification of the future igniter manufacturing process, the electronic part of the igniter is also identical;
- the joint management unit should be realized so that it can be incorporated into the available one the space around the igniter housing on the main KWH;
- a reliable electromechanical mechanism should be provided in the front part of the missile – a signaler that provides unambiguous, reliable and unambiguous signaling that there has been contact between the target and the missile;
- provision of an electrical connection between the signaler of the contact of the missile and the target, electronics of the precursor, the main KWH with the control unit;
- the control unit should provide a self-test after connecting all the electronic elements of the igniter, as well as a lead to the appropriate connection on the rocket body through which the igniter will be connected to the control test station of the rocket in order to check the functional correctness of the igniter.

#### 4.EXPERIMENT

In order to successfully meet the stated requirements, tests were carried out in two directions:

1. using the already developed mechanical assembly of the securing-arming mechanism - the igniter for the air-to-ground non-guided missile, with electro-incendiary heads that use low voltage to activate all phases of the igniter, including the ignition of the pentrite transmitter that activates the KWH and
2. using the already developed mechanical assembly securing-executive mechanism - igniter for the surface-to-surface non-guided missile, with electro-incendiary heads that use low voltage to arm the igniter and with an electrode detonator that works at high voltage to activate the pentrite transmitter that activates the KWH.

#### 5.RESULTS DISCUSSION

Through experiments, it was determined that with the electro-ignition head that works at low voltage, there are excessive deviations in the dynamics of activation and ignition of the pentrite mixture that activates the KWH (up to 1ms), which does not meet the requirements for the speed of the igniter's reaction to the activation signal, so that model gave up. On the other hand, experiments with a high-voltage electro detonator have shown that the response speed of the electro detonator depends exclusively on the speed of establishment of the leading edge of the high-voltage electric pulse that triggers the electro detonator.

For the purposes of triggering the electro detonator (ED), a special electric circuit was developed that enables the formation of the leading edge of the trigger pulse lasting 1-2 $\mu\text{s}$ .

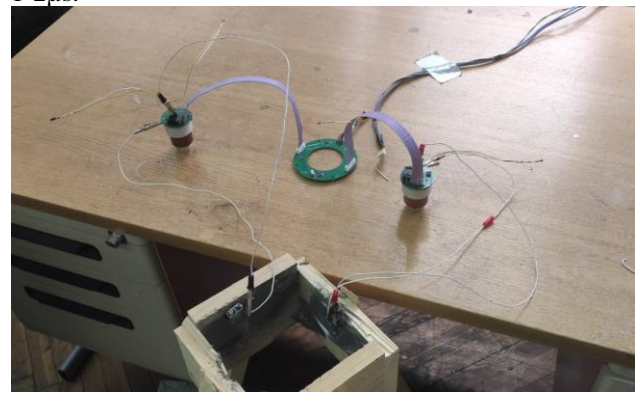


**Figure 2:** Test of regularity of the operation of the high-voltage electric circuit

Considering that the response of the electro detonator is high voltage pulse also around 1 $\mu\text{s}$ , the obtained total speed of the reaction, i.e. activation of the electro detonator, was reliably within 10 $\mu\text{s}$ , which were previously defined by calculation as satisfactory accuracy.

For the purposes of confirming the functionality and reliability of the circuit for triggering the high-voltage ED, a large number of ED activation experiments were performed, which were recorded with an ultra-fast camera (over 30 attempts), the recordings of which confirmed that in all attempts the ED was successfully activated and within one frame of the ultrafast camera (corresponding to a time interval of  $\pm 5\mu\text{s}$ ) and in the exact corresponding frame.

Table 1 shows the results of the cadence measurement carried out on March 21, 2024. when 8 measurements were made.

**Table 1:** Presentation of the results of measuring the activation cadence of electro detonators measured on 3/21/2024

Attempt	Set cadence [ $\mu\text{s}$ ]	Measured cadence [ $\mu\text{s}$ ]
1	300	300 $\pm 5$
2	300	300 $\pm 5$

3	450	450 ±5
4	600	600 ±5
5	100	100 ±5
6	150	150 ±5
7	200	200 ±5
8	400	400 ±5

For the purposes of these tests, MTI has developed a special test device that enables the realization of a wide range of tests for all phases of static tests, both individual elements of the igniter and the igniter as a whole, as well as precursors and main KWH, as well as TKWH as a whole. The device is shown in Figure 3.

In order to be able to fulfill all the above requirements, the control unit is relayed on a torus-shaped printed circuit board, which allows it to be installed in the space between the igniter body of the main KWH and the metal jacket of the main warhead.



**Figure 3:** Testing device for static tests of TKWH

The plate is fixed with screws to the tensioner of the explosive charge of the main KWH. The electronics itself and the software developed for it enable the testing of all electronic assemblies, as well as low-voltage electro-ignitable igniter heads. The basic self-test checks the electronic components and measures the internal resistance of all electro-incendiary heads, and if everything is correct, the green signal LED on the board itself is turned on, which is a sign that everything is correct and well connected. If there is a problem, the red one LED turns on, which is a sign that the control unit must be connected via the RS232 port to a computer with diagnostic software, which can be used to determine which individual part of the igniter has not passed the functional check. The set of electronics for one TKWH is shown in Figure 4

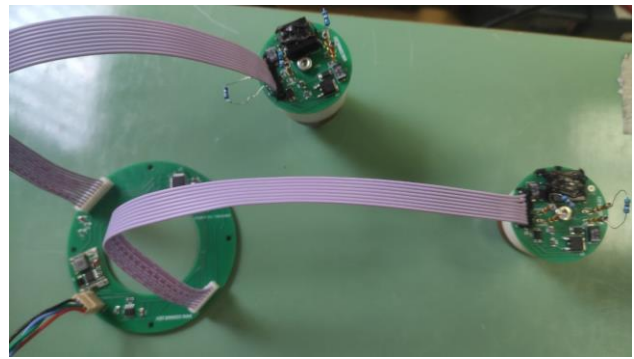


**Figure 4:** Set of electronics for TKWH

Through the same RS232 port, the cadence adjustment is performed between the activation of the precursor igniter and the igniter of the main KWH, with a minimum cadence adjustment step of 1µs. There is also the possibility that, if the missile is equipped with a device that measures the flight speed of the missile (or another platform - the carrier of this TKWH), based on that data during the flight, immediately before the meeting of the target and the missile, it will correct the size of the cadence and achieve optimal activation dynamics.

The VARNICA tester can also adjust the cadence between the activation of the precursor and the main KWH in the range of 50µs to 1500µs with a step of 1µs. Achieving the optimal duration of the cadence will be realized by an experimental method, with the adoption of initial conditions, which for a concrete example of a rocket are:

- Distance from the top of the rocket to the top of the precursor - 220mm;
- Distance from the top of the rocket to the top of the main KWH – 475mm;
- Theoretical minimum speed of the cumulative jet – 2,000 m/s;

We can calculate the working time of the precursor as:

$$t_p = t_u + t_M$$

Where it is:

- $t_u$  – the time of making the igniter
- $t_M$  – duration of the cumulative jet

The duration of the igniter is up to 5 µs, while the duration of the cumulative jet of the precursor is 250 ±20 µs, which was confirmed experimentally.

Based on the above, it can be concluded that the maximal cadence is theoretically around 275µs.

Choosing different cadence values will define the one at which the penetration of the main KWH is the highest.

## 6.CONCLUSION

After the successful development of a technical solution that will ensure proper activation of the TKWH and accurate and reliable adjustment of the activation cadence of the precursor and the mail KWH and theoretical calculations of the required cadence value, it is necessary

to realize the confirmation of the theoretically obtained values through experiments.

Testing will also determine the optimal cadence value for a specific configuration by finding the cadence value for which there is the greatest TKWH breakthrough.

**In this way, the optimal cadence value will be determined empirically.**

After the experimental determination of the optimal value of the cadence in static conditions, as a final part of confirming the overall technical solution and the achieved measurement results, a check of the obtained results would be carried out in the dynamic mode, i.e. by shooting and analyzing the penetration results of the main KWH achieved in this way.

## **Acknowledgements**

This work was by Serbian Ministry of Defense and Serbian Ministry of Education, Science and Technological Development, Grant No 451-03-66/2024-03/200325.

## **References**

- [1] UGRČIĆ, M.: Determination of the critical jet velocity during the penetration into the homogeneous steel obstacle, Belgrade, 2003.
- [2] KRSTIĆ, T., UGRČIĆ, M.: Computer Simulation and Experimental Testing of the Clock Safety and Arming Device Function, Belgrade, 2005.



# A NEW APPROACH TO MUZZLE CLIMB REDUCTION IN ASSAULT RIFLES

RANKO BABIĆ

Faculty of Technical Sciences, University of Pristina in Kosovska Mitrovica, Kosovska Mitrovica,  
[ranko.babic@pr.ac.rs](mailto:ranko.babic@pr.ac.rs)

**Abstract:** The paper addresses a crucial problem in assault rifle design and exploitation, the muzzle climb, proposing a new approach which relies on a combination of high-geometry butt stock and a foldable sighting periscope, which rise the line of sight to anatomically optimal height. A general frame of the issue is given through critical and comparative analysis of main existing assault rifles from this aspect. Also, a sufficiently thorough qualitative review of recoil process, preceding the climb, is presented in order to identify points and factors where one can intervene to reduce the effect. For both a broad reference list is provided. The solution is illustrated by a detailed design of optical system comprising an integral prism as the basic part, with the sighting openings, provided through several precise drawings, clearly explaining the idea. A few versions of the solution are given. In the conclusion pros and cons of the proposal are discussed.

**Keywords:** assault rifle, recoil, muzzle climb, butt stock, sight, periscope.

## 1. INTRODUCTION

The muzzle climb phenomenon is significant since it influences the directivity of fire, particularly of semi/automatic small arms. It is the result of the complex interaction of two systems, the firearm and the shooter.

The issue of muzzle climb reduction was recognised very early, but only since the WWI it got significance, with an idea to put a scaled down machine gun performance in hands of individual frontline soldier.

There are several aspects of muzzle climb, not separated but rather combined: the cartridge (energy, impulse), firearm system of operation, weapon geometry (in regard to recoil), muzzle attachments, shooter's training level etc.

To accommodate functional anatomy of the (military) rifle shooter, sighting line and its parallel at the top of the butt-stock foot, should be 40-50 mm apart. In conventional rifle configuration, the barrel axis is well above the said butt stock line, which produces a significant recoil torque, hence the muzzle climb.

This paper proposes a new approach to the reduction of muzzle climb by reshaping the butt stock and adding a foldable sighting periscope, intended to accommodate convenient sighting.

### 1.1. Aspects of muzzle climb

The muzzle climb, as interaction of two complex systems (firearm and shooter), is triggered by recoil, where the

free recoil [Free recoil]<sup>1</sup> is to be distinguished from the engaged recoil (the firearm firmly supported by the shoulder).

### 1.2. Firearm – the climb source

The recoil involves (bullet+gases) momentum and the system of transferring this impulse onto the shooter's body. The first means the total energy delivered to the system, while the other the rate of this delivery (impulse diagram) [1-4].

Two categories of firearms can be distinguished: (a) with fixed bottom, and (b) with movable bottom of the cartridge chamber, which means sharp and smoother transfer of recoil impulse.

The effect of recoil is best viewed in slow motion, for both of said basic categories of firearms [5-10], with an accent on the gas operation [9-11]. There are also subcategories of the movable bottom principle (blowback - simple, delayed, gas retarded (HK P7, Steyr GB), gas operated (usual for assault rifles), floating automatics (HK G11, AN94), balanced automatics (AEK-971, AK-107 [12]), balanced impacts in automatics (Russian smg Baksan RG-063, AN-94, Russian machine pistol Stechkin's Pernach), long recoil (GM6 Lynx) [13-15], which is of special interest to this research, etc.).

Since the Wikipedia is controversial reference, but often provides valuable information, it will be not quoted in References but only throughout the paper, according to the referencing scheme: [#/Free recoil](https://en.wikipedia.org/wiki/Free_recoil)

### 1.3. The shooter – response to recoil

In the said interaction, the shooter is more complex than the firearm, being a deformable and movable dynamic chain of mutually connected body parts from the hand down to the feet on the ground [16]. As before, participation of the shooter body can be seen in slow motion, in previous videos. It brings difficult to define factors, such as body size, strength of limb connections, level of training, psychological mood etc.). It is in contrast with fixed or movable (rails and carriage) laboratory firearm support.

The general factors of muzzle climb can be further detailed into: caliber/cartridge, firearm system of operation, firearm configuration (geometry and mass distribution in respect to recoil torque), muzzle breaks, compensators and silencers, contact surfaces between the firearm and the shooter, buffers in the firearm, butt stock geometry (with buffering supports and devices [17], [#Bump\_stock], [18]), burst limiters and cadence reducers, etc.

## 2. Muzzle climb: Excerpts from comparative chronology

Nearly the three centuries of military rifle evolution was crowned by bolt action rifles, with a typical example of Mauser model 98 (1898) [19]. The form of the butt stock in these rifles, with the butt foot and the neck as the grip, can be considered as optimal to shooter anatomy. The sights mounted just on the barrel are giving the rifle a slim and smooth outlook [19], [20]. The descendants of the Mauser two-lug-lock bolt are locking systems in AK47, and, as 7-lug lock, in M16 [21].

The center-fire cartridge (1866-70), with closely repeatable parameters in production, Maxim's patent of semiautomatic operation (1881/83), Lebel rifle (1886), first to use smokeless powder (with adjustable pressure diagram) set the stage for a wave of semiautomatic rifle designs (1885-1940), all that to finish with only two widely used models (SVT-38 Tokarev (7.62x54Rmm) and M1 Garand .30 (7.62x63mm)). In respect to butt stock configurations they followed manually operated counterparts.

Among all of them the Avtomat Fedorov (Fyodorov) is worth mentioning, developed in 1913 around Japanese 6.5x50mmSR Arisaka (6.5x51R by C.I.P.), official military cartridge (from 1897), because of lower energy than Russian 7.62x54R (3,140J vs. 3,550J of muzzle energy). Just to compare, the .30-06 (7.62x53mm) delivers 3820J for 151gr (10g), while 7.92x57mm 3934J with 181 gr (11.7g). Arisaka's 6.5mm is obviously related to small-stature Asian troops. Following this logic, the 7.62x54Rmm have similar considerations [#6.5% C3% 9750mmSR\_Arisaka], [#Fedorov\_Avtomat], [22].

The real corner stone was the StG44 ('StG' stands for 'sturm gewehr', eng. the 'assault rifle' - AR), gave the name to the whole class of weapons, and opened a new era in design [#List\_of\_battle\_rifles], [#List\_of\_assault\_rifles]. It is renamed from the German MP44 (MP - Maschinen

Pistole, eng. Submachine Gun - SMG), designed around a new cartridge 7.92x33mm, a scaled-down 7.92x57mm in size and energy. It was a new weapon system, introduced nearly the in-line configuration of the firearm, and iron sight raised above the weapon contours.

The Soviet 'answer' or, better to say, 'parallel work' was 7.62x39mm, M1943. Besides, the 7.62x39mm was not a simple follower of 7.92x33 but also stem from Soviet very good experience with PPS41 and PPS43, both in 7.62x25mm. Not to overlook the Japanese Type 95 cartridge 6.5x30 mm [22], as a shortened version of 6.5x50mmSR, proposed for the Experimental 1934 Model 2A submachine gun, 10 years before the StG44.

Prior to the StG44, Germans issued the FG42 (Fallschirm Jaeger Gewehr - paratroop machine rifle), a remarkable machine small arm, chambered by 7.92x57mm, which featured full in-line configuration, with coincidence of stock and barrel axes, huge and ergonomic foot of the butt stock, and, hence, both sticking-out foldable iron sights. It fires semiautomatic from the closed bolt and automatic from the open bolt. All these basic features, in combination with a very effective muzzle brake and compensator, reduction of recoil by the spring buffer in shoulder stock, yield a remarkable stability of semi- and automatic fire for a very powerful cartridge [23-26].

As for the pre war developments of semiautomatic military rifles, the post war period faced the flourishing developments of ARs [#List\_of\_assault\_rifles]. It seems that the AR design and the problem of muzzle climb are synonyms.

Accordingly, in this paper several designs are considered, conditionally divided into four categories, in respect to rifle configuration and butt stock geometry, recoil torque and sights, as explained above:

- conventional configurations (e.g. AK47 and its descendants),
- near-in-line configurations (e.g. StG44, FN FAL),
- in-line configurations (e.g. M16),
- true in-line configurations (e.g. FG42, SIG SG 510),

with the categorization parameter  $P$ , defined as the ratio (Figure 1)  $\Delta h/H$ , where the  $\Delta h$  is the distance between the stock spine (upper edge) line and the barrel axis, and the  $H$  is the stock foot height.

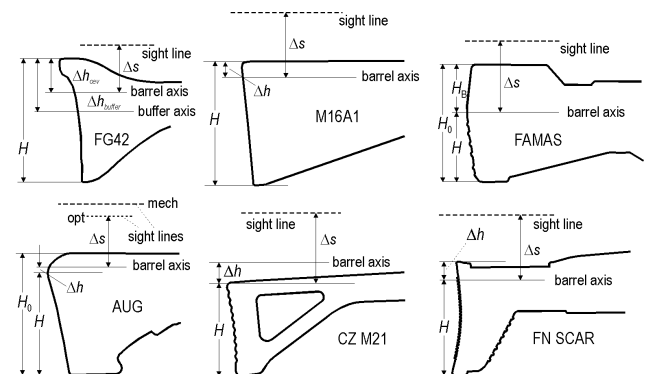


**Figure 1.** The geometry of butt stock in some ARs explains the idea of the categorization parameter  $P$ . Its meaning is unambiguous for FAMAS and AUG, and negative for CZ M21. Label  $\Delta s$  designates the distance between

barrel axis and sighting line. (The drawings are not in one scale; zoom in for details)

The magnitudes of the  $P$  for some ARs are: StG44 (1/10); FN FAL (0) (1/4 in prototype); HK G3 (0); SIG Type SG510-1 (1/3); SIG AM55 (1/3); SIG530-1 (0); AK47 (minus 1/4); AKM (0); M16A1 (1/11); IMI Galil (0); Valmet M76P (1/10); XL70E3/L85A1 (1/3) (XL64 prototype (6.5/28)); Madsen LAR (3/11); Japan Type 64 (3/23) (prototype 5/20); FN SCAR (10/45). Attention should be paid to SIG SG 510 and Stgw 57, in 7.5×55mm Swiss, and 7.62×51mm NATO [#wiki/SIG\_SG\_510].

Certain AR models are ambiguous, because the butt foot does not cover the whole butt height ( $H_0$  on Fig.1 for FAMAS and AUG). In the FAMAS, which stock appears to provide an excellent  $P=1/3$ , there seems to be an active part of foot, while the rest of  $H_0$ , labelled by  $H_B$ , is on other angle. In the standing firing posture, only the down part of the stock foot engages the shooter shoulder, giving  $P=0$  and convenient anatomy for aiming. Conversely, in the laying firing posture, the upper part of the stock foot is engaged against the shooter shoulder, providing  $P=1/3$  and still convenient anatomical position for aiming. This part of the stock, comprising the counter buffer with the hook, serves also as the suitable cheek support, and is instinctive in engagement. So, the FAMAS butt stock is designed with two values of the  $P$ . In the AUG, with a rounded corner on the stock, decreasing the foot height and lowering its up end, similar effect is not so clear, giving almost  $P=0$ .

The recoil and climb of certain ARs can be seen in [27]

Note how the bullpup configuration consequentllyz rises the sight line [#List\_of\_bullpup\_firearms].

The light machine gun (LMG), being automatic firearm based on powerfull cartridge, features a carefully designed butt stock. The magnitudes of parameter  $P$  for some models of LMG are: Steyr-Solothurn S2-200/MG 30 (10/23) [28]; FG42 (1/3); Madsen/Saetker (4,5/18); MG34 (6/19); MG42 (8/23); M60 (8/26 for barrel axis) (12/28 for buffer axis). The AR can be considered as smaller version of LMG, adapted to individual soldier. There is a tactical difference between AR and LMG, such that the AR should be portable and easy to carry, while the LMG is more stationary, and often with the assistant to machine gunner. But it does not mean that the LMG stock measures cannot be applied to the ARs. As a good and instructive example is the FG42 (not to be confused with MG42) [#FG\_42].

The risen geometry of butt stock, as significant factor for muzzle climb reduction, calls for consecutive rise of sighting line, i.e. placement the sights (iron or optical) on some platform or support, in firm (e.g. M16, FAMAS, HK G11 or G36, AUG, L85) or foldable manner (e.g. FG42, FN SCAR, QBZ-191, and in almost all LMG). It causes increase of firearm hight, sometimes with design compensation, such as unusual but comfortable and ergonomic forms of hand grips (in FN P90 and FN FS2000, firstly in FG42). These are low-profile pistol-hand grips, because the usual ones would make the firearm cumbersome in height. It is not applied in

FAMAS, because a sufficient length of AR better compensates increased hight than in the case of short FN P90 submachine gun.

It occasionally results in clumsy (as sighting bridge in L85 and in [29]) and bulky (as in FN FS2000) shapes, whatever it may look futuristic in appearance. Introduction and widespread use of Picatinny rail, combined with red dot reflex sights, enabled use of very flexible palette of mountable and foldable moduli of iron sights (B&T APC223/556, FN SCAR, APC9K, M4 carbine, HK MP7 etc.) red dots, holographic sights etc.

Here, iron sights and 1:1 optical sights (AUG A1 [30] [31], FN P90, HK G11 [32]) are considered as minimal sights, durable, with low maintainance, while all red dots and holographic ones, appart from being excellent, efective, fast acquisition, are sensitive to dust (particularly in urban combat areas) and moisture conditions.

On the other hand, in AN94, with high precision two-shot burst capability, there are fixed iron sights, with conventional stock configuration ( $P$ =minus 2/30-3/33) [#wiki/AN-94], [33-38].

The case of AN94 clearly confirms the methodology of considering the whole set of factors influencing the final climb effect. In order to study one of them the rest should be kept unchangeble. Namely this approach is applied in this paper.

### 3. Proposed solution for muzzle-climb reduction

Among all methods for reducing the flip effect, this paper considers rising the AR butt-stock axis (the line passing through the middle of the butt-stock foot) close to the barrel axis. This implays the rising of the sightline. As it was said above, it has been usually attained by foldable sighting posts or by placing the sights on a bridge. In the first case, the sights are exposed to impacts and damage, while in the second it increases vertical dimensions of the AR. Solution with foldable iron sights is only partially effective (e.g. HK MP7, with  $P=1/3$ , and B&T APC9 K Pro), where both sights pretty stick out of the weapon contours.

This paper proposes a high geometry stock, fixed or folding, on a new or existing firearm, primarily AR, with the parameter  $P$  magnitude between 0.3 and 0.5. Then, a foldable sighting periscopic module is installed on the firearm, which, in open position, allows the shooter to comfortably look along/through the iron sights, positioned low on the barrel or on the receiver (Figure 2). In the folded position, while in passive, marching or storing modes of the weapon use, the sighting periscope is completely into the firearm contour, and can be immediately stretched out prior to the action or at the alert mode.

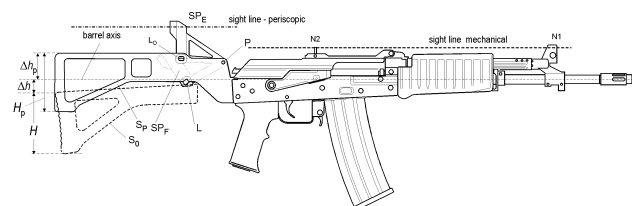


**Figure 2.** The concept of foldable sighting periscope (SP), installed in the neck of butt stock (here taken as fixed) with risen geometry, showing folded (SP<sub>F</sub>) and opened (SP<sub>E</sub>) positions, fixed by simple lock (L). (zoom in for details)

There are several variants of the proposal, clearly explained on Figures 2-6. In the basic one, the SP is installed in the cavity of the stock neck (Figure 2 and 3). The slanted wings (39) of the periscope module (SP) protect it from impacts in its open position. The simple lock (L) keeps the periscope firmly in both positions. The cavity shape follows the SP contours, preventing the penetration of dirt in folded position, but enables easy cleaning (in position A of fully opened SP). The periscope's eyepiece window (34) is shielded (33) against direct sunlight, while the objective window (35) by the periscope wings (32, 39).

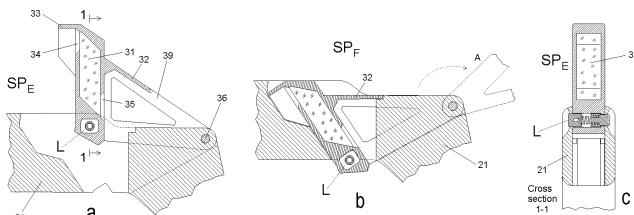


**Figure 3.** Details of SP simple design, shown in both positions, opened (a) and folded (b). The cross section (c) reveals the lock (L) function.

The compact version (V2 in Figure 4) keeps the basic idea but the placement of the SP is moved forward, providing to the shooter more room for comfortable aiming.

The SP can be also mounted on the receiver (dust cover if CZ M21 (AK) is considered, version V3 on Figure 4), either directly or on Picatinny rail. Positioning of rear sight on the AK47-type dust cover is applied in e.g. Galil, Valmet RK 62, M76F/P/T/W, RK 95TP) [#RK\_62], [#RK\_95\_TP]. Folded SP does not obstruct iron sights.

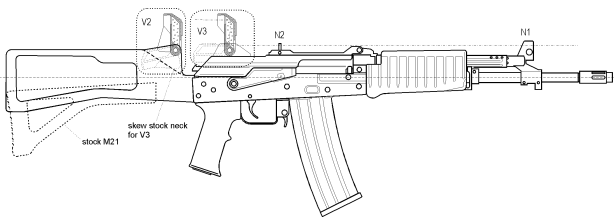


**Figure 4.** Dotline frames show folding SP in both variants (V2 and V3). Dash line show sighting line over iron sights N1 and N2, through the SP

In another version, the SP is combined with low magnifying optical sight, situated low on the dust cover (receiver) (Figure 5), and not on a high bridge, as in AUG, HK G11, HK G36 etc.

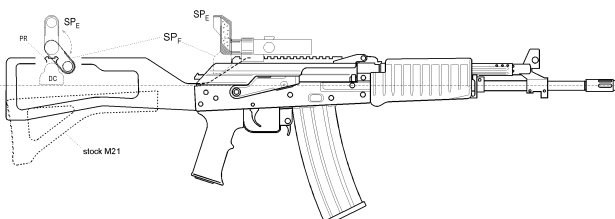


**Figure 5.** SP as an extension of optical sight mounted on

Picatinny rail, shown in extended (E) and folded (F) positions. Insert on the stock frame shows axial projection of SP, profile of dust cover (DC). The dashed line arc shows lateral rotation between two positions. (zoom-in for details)

Mechanical (iron) sights are the most resistant to dirt, dust and dewing. By inserting any glass surface in the sighting line adds a place for dust and/or dew catching. The proposed solution brings in this shortcoming not more than any other case. The designers admitted that fact by adding auxiliary crude iron sights besides the main optical one (as in AUG A1 and FN P90). In general, the designers admitted inadequacy of foldable iron sights by making them foldable.

This solution makes the rifle slimmer, which has positive effects on its design, production and mass. It also greatly improves overall manipulability (carrying, operation), suitability to place, store and transport. It is a well known rule in industrial design: effective design is elegant [39,40].

Apart from being prone to dust and moisture, each optical element in sighting line inserts attenuation of light. Even for iron sights the notion of sight transparency is valid, especially for aperture sights. Also, protective shields on front sight are not out of consideration, e.g. TV-like protective frame on AN-94, or the difference in size of protective cylindrical shield on AR Galil, versions for Israel and for South Africa. This solution provides a reserve for lateral broadening of sighting aperture in order to increase illuminance.

Optical sight, with the reticle (e.g. AUG A1, FN P90) provides one-point alignment with the target, which means far quicker acquisition than by aligning two iron sights with the target, parallax involved.

As for the butt stock, two versions are possible, fixed or foldable, with the latter in two variants: on the left, as in AK family, or on the right, as in this proposal. It is a loop-form stock, with long opening for easy reach of cocking handle, safety lever, not obstructive to cases ejection (Figure 4).

Some originally 'optical' firearms (Steyr AUG A1, FN P90) were converted into Picatinny-open platforms. The same is for AK74 successors, CZ M-21 included, used here as a platform for proposal illustration (Figure 5). But the foldable mechanical sights remain in, now just taking modular, accessory form (FN SCAR, HK MP7, B&T APC9 etc). Broad application of red dot reflex sights essentially changed this issue. Having necessary height, they allow the risen stocks, but such sights still are sticking out of the AR contour.

When applying (transferring) distinct linear configuration of LMGs to ARs, one should keep in mind that the LMG recoils mostly the lying-down gunner, with some percentage of exceptions of standing or kneeling posture (usually in the shelter). It seems that the LMG counteracts the shooter's whole mass, but it is rather a dynamic process, beginning with the jerk in the shoulder, starting a deformation shockwave which propagates along the gunner

lying body. On the other hand, the slow motion of the continuous fire from a LMG, with the gunner in standing posture, and not from the hip but from the shoulder, shows pretty narrow burst cone, giving the confirmation for the said transfer LMG – AR. This is why the consideration of LMGs is included in this research.

Speaking of the muzzle climb, it would be better to call it ‘flip’ than the ‘climb’, since there is a combination of vertical hop of the firearm and also a lateral one, as a consequence of recoil torque around the torso axis (spine) [23].

The LMG class of firearms is an obvious example what effect provides the butt stock with high geometry. Already mentioned German FG42 is possibly one of the most striking cases how to put heavy recoil under control. Here, one should not overlook contribution of very efficient muzzle break, and a spring buffer in the line of recoil, which, again, confirms combined and inseparable influence of all factors in climb reduction. Anyway, it is evidently that the butt stock high geometry is one of main factors. Similar effect can be noticed in SMG Walther MPL/K [7].

In general, the sliding mechanism (so-called long recoil), as with the cannon on its carriage, or in some small arms (e.g. HK G11 [42], AN94, GM6 Lynx, Hungarian heavy sniper rifle [13-15]) is able to transfer the recoil almost without disturbing the receiver (which mass includes (a part of) the shooter mass). What it demands is the length, a very precious resource in a firearm design. But it is a very obvious demonstration of recoil. In this context, it will be interesting to compare the 2-burst and 3-burst long recoils in AN94 and in HK G11, respectively, taking into account the energy of 5.45x39mm and of 4.73x33mm cartridges, through an multiaspect study (recoil length, complexity of mechanism, rifle vertical bulk etc.) [Heckler\_%26\_Koch\_G11], [32], [41-45].

Here a lot of attention has been paid to HK G11 and Russian AN94, though they both did not find their way to service ARs, but they are conceptualised right to muzzle climb reduction and are instructable cases which reveal basic ingredients of the phenomenon.

#### 4. CONCLUSION

The muzzle climb is the result of interaction firearm-shooter, comprising many factors. The reduction of this effect involves many aspects, which act in synergy. If certain is individually considered then the rest are assumed constant. Because of the said synergy, it is not easy to establish a hierarchy in the list of factors, but also it is not impossible.

This research has been focused on high geometry of butt stock as a means for the muzzle climb reduction. This imposes high sight line either through foldable sights or firmly raised sights (bridge, post).

The proposed solution is illustrated through several variants, thereby confirming the potential. It is actually not a part of the sight but rather an optical extension of existing low sightline. There is no need of zeroing of the

SP at each (un)folding. It is not a periscopic sight but the sighting periscope (SP).

It is easily applicable even on existing models, providing advantageous effects.

However, such solution brings glass surfaces into the sighting line, as spots susceptible to dust, dirt and dew, but nothing more than in other sights with optical elements (e.g. red dot, holographic, optical sights).

Speaking of e.g. red dots, they are fast-acquisition and easy-to-use, with one-point alignment. The SP, relying on existing iron sights, demands two-point alignment. The red dot is usually with wide window, either in ‘tube’ or ‘open’ designs, delivering a high sight transparency to the shooter’s eye. The periscope windows (apertures), although having modest openings, provide high transparency because its aperture is close to shooter eye. As for the maintenance of red dots (cleaning, battery replacement), the cleaning is more critical (two glass surfaces), but one battery enables run for hundreds and even tens of thousands of hours.

The iron sights are of minimalistic design, low profiled (do not stick off the firearm contour, not prone to impacts and damage), quite resistant to dust, dirt and moisture, reliable, no power consumption, low maintenance. In brief, the author’s intention has been to preserve such minimalistic and reliable design but to incorporate it in the high-profile butt stock. Therefore, the proposed solution keeps the firearm vertical compactness. The sighting periscope is only an optical extension of available iron sights.

One more point: the high-positioned butt stock goes off its line of joint to the AR receiver, which causes recoil torque at the joint. Anyway, such load is considered as modest, and easy to handle with proper design.

As the final line, the proposed solution can be considered as promising, giving the room and perspective for further research and application.

A part of it is implemented through a prototype, with a periscope having two little mirrors (instead of a prism). The periscope module (version for on-top receiver) has been mounted on several models of firearms (AUG A2, HK MP5, FN P90 (with Picatinny rail)) just to examine through-visibility of target, speed of instinctive target acquisition, parallax and double image effect in aiming with both eyes.

Because of obvious reasons the high profiled butt stock was not prototyped to examine the main issue of this research – muzzle climb reduction. These virtues of the proposal were left for further examination and verification by practical implementation.

#### References

- [1] Hall, M.: *Effects of breech bolt movement on felt recoil of a gas-operated semi-automatic sporting gun*, J Sports Engineering and Technology 2015, Vol. 229(3) 159–168, DOI: 10.1177/1754337114566664.



- [2] Qiang,L., Kedong,Z., Chao, S., Iei,H.: *Effect of an Internal Impact Balance Mechanism on the Perceptible Recoil of Machine Gun*, E3S Web of Conferences 231, 03001 (2021) PEEEE 2020, <https://doi.org/10.1051/e3sconf/202123103001>.
- [3] Burns,B.: *Recoil Considerations for Shoulder-Fired Weapons*, *Weapons and Materials Research Directorate*, Army Research Laboratory, ARL-CR-692 May 2012 (U.S. ARL, ATTN: RDRL-WM, Aberdeen Proving Ground, MD 21005-5066).
- [4] Алферов В.В.: *Конструкция и расчет автоматического оружия*, Машиностроение, Москва 1977, <http://dl.bookfi.org/genesis/3...o%20оружия.djvu>
- [5] Royal Armouries, Firearm Demonstration: Mauser Gewehr 98 Rifle, 25.6.2015., <https://www.youtube.com/watch?v=HkSMeAbwIGE&list=PL5nfBJWux0WppM3bSFB82R7tEAOZdijPL&index=10>
- [6] Warped En Espanol, Firing a .357 Magnum at 224,000 FPS in Ultra Slow Motion, 29.12.2017., <https://www.youtube.com/watch?v=QSILZeWLy3s>
- [7] Forgotten Weapons, Walther MPL Submachine Gun, 2015. <https://www.youtube.com/watch?v=tQSiilZnqdlA&t=16s>
- [8] The Oregonian, Super slow-motion video of bullets leaving a handgun (Sig Sauer SP2022), 1.12.2016., <https://www.youtube.com/watch?v=HElQk2wEY5w>
- [9] Royal Armouries, Firearm Demonstration: AK55 Assault Rifle, <https://www.youtube.com/watch?v=IACXi13IGUI&list=PL5nfBJWux0WppM3bSFB82R7tEAOZdijPL&index=20>
- [10] TAOFLEDERMAUS, AK-47 SLOW MOTION, 21. 12. 2009., <https://www.youtube.com/watch?v=iD7palHcaqE>
- [11] TAOFLEDERMAUS, Slow Motion FULL AUTO AK - Looks like RUBBER!, 15. 3. 2012., <https://www.youtube.com/watch?v=HGivoWD9OvQ>
- [12] <https://modernfirearms.net/en/assault-rifles/russia-assault-rifles/ak-107108-eng/>
- [13] <https://gm6lynx.com/>
- [14] Forgotten Weapons, GM6 Lynx: The Hungarian Long-Recoil .50-Caliber Bullpup, 24. 12. 2021., <https://www.youtube.com/watch?v=iRMfosCF4kQ>
- [15] Forgotten Weapons, GM6 Lynx .50 BMG Bullpup at the Range, [https://www.youtube.com/watch?v=cyx7TrZq\\_xI](https://www.youtube.com/watch?v=cyx7TrZq_xI)
- [16] Nishikawa,K, et al: *Neuromechanics: An Integrative Approach for Understanding Motor Control*, *Integrative and Comparative Biology* 47(1):16-54, July 2007, DOI: 10.1093/icb/icm024,
- [17] <https://bt-usa.com/product-category/apc223-apc556/>
- [18] <https://qph.cf2.quoracdn.net/main-qimg-f4c3a24ddf6fb42b5b6b8d396b7e3b46>
- [19] Smith, W.H.B.: *Small Arms of the World*, 10<sup>th</sup> ed (revised by J.E. Smith), A&W Visual Library, 1973
- [20] Ezell, E.C.: *Small Arms of the World*, 12<sup>th</sup> ed. (revised [19]), Barnes&Noble Books, New York 1993.
- [21] <https://thenewrifleman.com/the-enhanced-ar15-bolt-a-quick-reference-guide/>
- [22] Цвершиц, А.: *История развития пистолетов-пулеметов Японии. ч 1.* <https://web.archive.org/web/20220724081930/https://lautlesen.livejournal.com/89179.html>
- [23] Forgotten Weapons, Shooting the FG42: The Hype is Real, 2018., <https://www.youtube.com/watch?v=7x6LibuC4N0>
- [24] American Gangster, How a German FG 42 Works, 20. 10. 2022., <https://www.youtube.com/watch?v=2851VtWb42k>
- [25] PC Gaming Videos, World of Guns - FG42 | How It Works, <https://www.youtube.com/watch?v=7o1fdvbw5m8>
- [26] "New German Rifle for Paratroopers" Intelligence Bulletin, June 1944, <http://www.lonesentry.com/articles/fg42/index.html>
- [27] BigEyeTop10, 10 најбољих јуришних пушака на свету, <https://www.youtube.com/watch?v=Ср08Nkv7IHQ>
- [28] <https://modernfirearms.net/en/machineguns/switzerland-machineguns/steyr-solothurn-mg-30-eng/>
- [29] <https://en.topwar.ru/11060-eksperimentalnye-i-opytnye-obrazcy-oruzhiya-izhevskogo-mashinostroitelnogo-zavoda-avtomaty-i-vintovki.html>
- [30] Fechter,A., James, F.W.: *Der Dritte im Bund*, 20 Jahre AUG, Visier 12/1997, pp. 40-52.
- [31] WO 2008/137187 A2, SEMI-AUTOMATIC AND AUTOMATIC FIREARM, (13.11.2008)
- [32] [http://www.indaginibalistiche.it/utlities/manuali/hk\\_g11\\_EN.pdf](http://www.indaginibalistiche.it/utlities/manuali/hk_g11_EN.pdf)
- [33] Дегтярёв,М.: АН-94 «Абакан» –это просто, КАЛАШНИКОВ. ОРУЖИЕ, БОЕПРИПАСЫ, СНАРЯЖЕНИЕ 5/2007, стр.6-12, [https://web.archive.org/web/20131203041227/http://www.kalashnikov.ru/upload/medialibrary/e6e/006\\_012.pdf](https://web.archive.org/web/20131203041227/http://www.kalashnikov.ru/upload/medialibrary/e6e/006_012.pdf)
- [34] Lake,D.: *The Blackest Rifle: Avtomat Nikonova 94*, Small Arms Defense Journal, 9 August, 2023, <https://sdefensejournal.com/the-blackest-rifle-avtomat-nikonova-94/>
- [35] Forgotten Weapons, Rocket Surgery: Inside the Russian Nikonov AN94, 11. 4. 2017. <https://www.youtube.com/watch?v=gtMssTSnRHU>
- [36] American Gangster, How a AN-94 Rifle Works, 23. 10. 2023. <https://www.youtube.com/watch?v=D2CSrFB4O14>
- [37] Gun reviewer / how weapon works, How AN-94 Works. Animation Of Operation Of AN 94, <https://www.youtube.com/watch?v=vvfyDBItG6E>
- [38] Vickers Tactical, Russian AN-94, 16. 5. 2016., <https://www.youtube.com/watch?v=DJxpcKswEg> (from 1:13)
- [39] Domingo,M., Rams,D.: *10 Timeless Commandments for Good Design*, <https://www.interaction-design.org/literature/article/dieter-rams-10-timeless-commandments-for-good-design>
- [40] <https://www.vitsoe.com/us/about/good-design>
- [41] Babić,R.: *HK G11: Futuristička rešenja na 'kabastom' oružju*, Centurion br. 5, 2005, s. 25-29
- [42] <https://armourersbench.com/2017/11/19/an-introduction-to-the-heckler-koch-g11/>
- [43] <http://modernfirearms.net/en/assault-rifles/germany-assault-rifles/hk-g11-eng/>
- [44] DogSoldierToo, *HK G11 Assault rifle prototype firing*

*caseless ammunition*, 6. 1. 2020.,  
[https://youtu.be/1bE1JS\\_8KNw](https://youtu.be/1bE1JS_8KNw)  
[45] Military Archive, Abandoned US Weapons Prototypes -

AAI / H&K G11/ Steyr ACR / Colt ACR/ - Documentary,  
2016., <https://www.youtube.com/watch?v=sbSdjTBbMii>  
(7:58-10:05 HK G11 and Steyr ACR)



## PERSPECTIVES ON THE DEVELOPMENT OF THE ARTILLERY BRANCH OF THE SERBIAN ARMY

KATARINA JANKOVIĆ

Technical Test Center, Center For Testing Weapons and Military Equipment "NIKINCI",  
[jankovickatarina95@gmail.com](mailto:jankovickatarina95@gmail.com)

NENAD KOMAZEC

University of Defence Belgrad; Military Academy, [nenadkomazec@yahoo.com](mailto:nenadkomazec@yahoo.com)

**Abstract:** Artillery, as a branch of the Serbian Army, has made significant advancements in technological terms. Modern combat conditions require the synchronization of technological achievements with organizational, personnel, logistical, and operational needs. The introduction of new technological solutions has led to changes in the logic and practice of organizational structures, tactics, development strategies, logistical support, the method of securing combat positioning elements, methods of providing fire support to units, data collection, etc. Thus, the entire system of functioning of the artillery branch must be subject to changes. This paper analyzes the current capabilities and achievements of the artillery branch and the discrepancies relative to technological advancements. Given the ongoing progress in science and technology, it is crucial to analyze the real needs of the branch and the feasibility of their implementation within the temporal and financial dimensions of the Serbian Army.

**Keywords:** artillery, development perspectives, capabilities.

### 1. INTRODUCTION

The development of modern military technologies presents new demands for all branches of the Serbian Armed Forces. The role of artillery in contemporary combat operations is becoming increasingly complex, necessitating the integration of advanced technologies with traditional methods of employment. In this context, analyzing the current capabilities of the artillery branch of the Serbian Armed Forces is essential to identify areas requiring reform and enhancement.

The current doctrines governing the use of artillery rely on a combination of firepower, mobility, and precision. However, global trends indicate the need for greater automation of artillery combat systems, improvement of communication networks, and enhancement of logistical support. Modern combat conditions demand rapid response and adaptability, which also calls for changes in the organizational and structural framework of artillery units.

In addition to technological aspects, the study also addresses changes in the tactics of artillery employment. Traditional methods of fire support must be adapted to new scenarios that include asymmetric threats and urban warfare. At the same time, logistical support must be optimized to ensure the continuous operational capability of artillery units.

New technologies play a crucial role in enhancing the capabilities of the artillery branch. The development of autonomous artillery combat systems, the use of unmanned aerial vehicles for reconnaissance, and advanced methods of data collection and processing are significantly changing the way artillery operates.

Personnel training must also keep pace with these changes, ensuring that professional military personnel are equipped to command, operate, and maintain the artillery branch's combat systems.

The objective of this paper is to provide an analysis of the current capabilities of the artillery branch of the Serbian Armed Forces, identify discrepancies in relation to modern demands, and propose directions for future development. Through an analysis of organizational and structural frameworks, tactics of employment, logistical support, new technologies, and training, the paper offers a foundation for further strategic planning and the implementation of necessary reforms.

### 2. MODERN REQUIREMENTS FOR THE ARTILLERY BRANCH IN FUNCTION OF INCREASING OPERATIONAL CAPABILITIES

The artillery branch of the Serbian Armed Forces faces increasingly demanding requirements in modern military operations due to the evolution of contemporary warfare and the changing nature of conflicts. The growing complexity of threats, asymmetric warfare, and the need for rapid response in diverse combat conditions have necessitated the establishment of new demands. These demands include the enhancement of technological capabilities, the increase of operational efficiency, and the adaptation to various operational scenarios.

**Modern artillery combat systems must address several key needs [1]: increasing range, reducing the weight of artillery systems for improved mobility, enhancing precision and accuracy of targeting to reduce collateral damage, increasing rate of fire, shortening**

**preparation time for action, improving projectile effectiveness on target, simplifying and economizing maintenance, as well as ensuring the ability to conduct modernization throughout the system's entire life cycle.**

**Increasing range** has always been a fundamental requirement for the artillery branch since its inception. This requirement is primarily driven by the need for artillery units to provide fire support to supported forces at greater distances, thereby expanding the operational zone and enabling more efficient execution of assigned tasks. The development of new propellant technologies is central to achieving these extended ranges, allowing artillery systems to reach targets further away while maintaining or even enhancing the effectiveness and precision of their strikes, as improved propellants and advanced rocket motors, significantly contributes to increasing the range of artillery munitions [1]. Additionally, improving the aerodynamic characteristics of projectiles, such as reducing air resistance, further enhances efficiency and range. Moreover, **reducing the weight** of artillery systems becomes imperative due to the need for faster and easier mobility. Lighter artillery systems can be transported more easily and quickly, including the capability for helicopter transport, allowing new firing positions to be occupied in a shorter time. Weight reduction is achieved through the use of new materials, such as aluminum alloys and composite materials, which provide high strength with low mass. However, these are two contradictory requirements, as achieving greater ranges with traditional artillery systems typically demands larger caliber and heavier guns. Experts face the challenge of balancing these opposing needs and must determine what is more important based on specific operational requirements and tactical objectives.

**Improving the precision and accuracy of targeting** is also a necessary step toward increasing the efficiency of modern artillery combat systems. The introduction of advanced fire guidance and control systems, such as Global Navigation Satellite Systems (GNSS) and Inertial Navigation Systems (INS), enables more precise targeting and reduces collateral damage [1]. In addition, the use of sophisticated ballistic calculations, which precisely account for various meteorological and ballistic parameters, significantly increases the accuracy of firing compared to earlier manual calculations. The integration of these technologies enhances the effectiveness of artillery fire, thereby reducing the risk of unintended damage.

**Increasing the rate of fire and reducing preparation time** for action are two interrelated requirements in the modernization of the artillery branch. These requirements stem from the need to achieve short but intense fire strikes and to quickly change firing positions to avoid counter-battery fire. Technological advancements in automatic loading systems and automated targeting lines, compared to manual loading and setting of firing elements, allow for faster projectile firing. This reduces the time between shots and maintains a high rate of fire. As a result, the overall efficiency of artillery units increases. The practical application of the MRSI (Multiple Rounds Simultaneous

Impact) firing mode enables the firing of multiple projectiles with different propellant charges and varying firing elements, so that all projectiles hit the target simultaneously. This firing mode is sometimes referred to as a „single-gun volley“.

**Enhancing the effectiveness of projectiles** on target involves achieving maximum impact while optimally utilizing resources. This requirement can be met by integrating advanced technologies into ammunition, such as precision guidance systems (e.g., GPS or laser guidance), optimized warheads (e.g., tandem-charge warheads), improved aerodynamic characteristics of projectiles (e.g., recessed base, elongated jacket to reduce air resistance), and the use of "smart" fuzes that can automatically adjust the mode of action depending on the type of target (e.g., fuzes with multiple modes for different types of targets). These advancements reduce the need for repeated strikes on the same target. Additionally, increased effectiveness on target adds value in modern combat conditions by reducing collateral damage. In this way, missions are carried out in compliance with the provisions of International Humanitarian Law.

**Simplified and economical maintenance** means that the effectiveness of artillery combat systems depends not only on their firepower but also on their ability to remain operational under prolonged and intense conditions. Simplified maintenance involves the development of artillery combat systems with easily replaceable components that require minimal specialized tools or training for upkeep. Economical maintenance is achieved by reducing maintenance costs and increasing the reliability of artillery combat systems, thereby enabling continuous operation with minimal interruptions.

**The ability to implement modernization throughout the entire life cycle** of a system refers to the long-term sustainability and relevance of artillery combat systems. In a world of rapid technological change, the capability of an artillery combat system to be modernized over its life cycle ensures that it remains effective and capable of meeting new challenges [1]. Modernization may involve upgrades or the introduction of new technologies and components that enhance system performance. Maintaining compatibility with future innovations ensures that the artillery combat systems of the Serbian Armed Forces remain competitive and ready to respond to the demands dictated by the modern combat environment.

#### **Operational capabilities of the Serbian Armed Forces**

In the context of the operational capabilities of the Serbian Armed Forces, modern requirements for the artillery branch directly contribute to their enhancement. The Serbian Armed Forces define operational capabilities as the ability to achieve desired operational effects within a specified time frame and under certain standards and conditions by combining forces, resources, and methods of task execution [5]. According to the Doctrine of the Serbian Armed Forces (2010), operational capabilities include the capability of command, the capability for timely availability of forces, the capability for deployment and mobility within the operational zone, the capability to exploit the information space, the capability for effective use of forces, the capability of force resilience and protection, and force sustainability. Further analysis

examines how modern requirements for the artillery branch impact the operational capabilities of the Serbian Armed Forces, emphasizing their significance and practical application in military operations. To better understand the connection between modern artillery requirements and the enhancement of operational capabilities, it is necessary to explore individual aspects in greater detail and their implications for military practice.

**The capability of command** represents the ability to efficiently plan, organize, direct, and control the operations of the Serbian Armed Forces or their components to achieve set operational objectives and accomplish assigned missions and tasks [5]. Modern artillery combat systems, equipped with advanced communication and information technologies, enable faster decision-making and command transmission, as well as more efficient planning and execution of operations. Additionally, these advanced artillery systems allow commanders to more effectively monitor the situation on the ground and adjust their decisions in real-time, thereby increasing operational efficiency.

**The capability for timely availability of forces** reflects the ability of the Serbian Armed Forces or their components to form and sustain sufficient military forces within a given timeframe to respond to and conduct operations. This capability is determined by the size, structure, readiness level, stress level, and efficiency of the force integration process [5]. In other words, timely availability of forces represents the ability to form and support adequate military forces within a specified time for response. In the context of modern requirements for the artillery branch, this capability is directly enhanced through technological innovations that enable faster mobilization, deployment, and reduced preparation time for artillery units. As a result, artillery units are timely available to execute primary and assigned tasks and respond more swiftly to changes in complex combat conditions. These advancements allow the Serbian Armed Forces to efficiently manage their forces and respond to challenges more rapidly and effectively.

**The capability for deployment and mobility within the operational zone** refers to the ability of the Serbian Armed Forces or their components to deploy forces into the operational zone and maneuver them in accordance with the operational objectives within a specified timeframe [5]. Modern artillery combat systems, with reduced weight and enhanced mobility, enable artillery units to quickly adapt to changing conditions on the ground, occupy new firing positions or targeting elements, and provide the necessary fire support. Faster deployment and improved mobility of forces directly contribute to timely responses and the achievement of operational efficiency in dynamic combat conditions.

**The capability to exploit the information space** involves the ability of the Serbian Armed Forces or their components to collect, process, use, and exchange data on space, time, and both friendly and enemy forces [5]. Modern artillery combat systems utilize advanced technologies for data collection and processing, enabling precise location of targets and own positions. These systems allow artillery units to obtain accurate

information about targets, atmospheric conditions, and the terrain, significantly enhancing the accuracy and effectiveness of their actions. Additionally, the integration of automated fire control systems facilitates real-time data exchange between different units and commands, leading to better coordination and decision-making in line with the current situation on the ground.

**The capability for effective or efficient use of forces** refers to the ability of the Serbian Armed Forces or their components to successfully conduct operations and achieve combat and non-combat effects that support the accomplishment of operational objectives [5]. Enhancements in precision and accuracy of targeting, increased rate of fire, and improved effectiveness of projectiles on target directly contribute to the effective and efficient use of artillery units in combat operations. These improved performances allow artillery units to strike targets more accurately while reducing the need to fire multiple rounds, which in turn decreases the likelihood of revealing their own firing positions.

**The capability of force resilience and protection** refers to the ability of the Serbian Armed Forces or their components to reduce the likelihood of their forces being detected and to mitigate and eliminate the effects of enemy weaponry [5]. This capability is realized through the implementation of organizational, physical, and technical measures aimed at preserving personnel and equipment. Modern artillery combat systems, with their increased range and precision, enable operations from greater distances, reducing the risk of detection and counter-battery fire. Additionally, rapid changes in firing positions further enhance the resilience of forces against enemy attacks. These measures may also include improved camouflage techniques, protection against electronic jamming, and enhanced ballistic protection for crews, equipment, and machinery.

**The sustainability of forces** refers to the ability of the Serbian Armed Forces or their components to care for, maintain, supply, and relocate personnel and military equipment within a specified time frame, under certain conditions and with available resources, in order to ensure favorable conditions for the effective use of available forces and assets [5]. The sustainability of forces is directly linked to the requirements for simplified and economical maintenance of artillery combat systems. The use of artillery systems that allow for easy maintenance, as well as the optimization of logistical supply chains for spare parts and ammunition, are crucial for the long-term operational viability of artillery units. Additionally, the ability to modernize systems throughout their entire life cycle ensures that artillery combat systems remain relevant and functional, even during prolonged operations, thereby providing continuous and effective support to other forces.

Modern requirements for the artillery branch in the context of the operational capabilities of the Serbian Armed Forces emphasize the importance of continuous technological advancement and adaptation to new combat conditions. Technological innovations in artillery play a crucial role in enhancing the efficiency of military operations, enabling faster, more precise, and more flexible responses on the battlefield. Through these

innovations, artillery significantly contributes to the overall operational readiness of the Serbian Armed Forces, ensuring better command, availability, and mobility of forces, as well as more efficient information management and resilience against enemy threats. In this way, artillery becomes an even more critical factor in achieving operational objectives and maintaining combat readiness in the dynamic and complex environment of modern warfare.

### 3. ANALYSIS OF THE EXISTING CAPABILITIES OF THE ARTILLERY BRANCH AND IDENTIFICATION OF ISSUES AFFECTING THE PACE OF CAPABILITY DEVELOPMENT

The artillery branch of the Serbian Armed Forces has achieved significant technological advancements. Modern combat conditions require aligning technological achievements with organizational, personnel, logistical, and operational needs. The introduction of new technological solutions has led to changes in the logic and practice of organizational structures, tactics, development strategies, logistical support, methods of ensuring combat elements, fire support techniques, data collection methods, and more. Thus, the entire functioning system of the artillery branch must be subject to change. The following text provides an overview of the current capabilities and achievements of the artillery branch, as well as the discrepancies relative to technological advancements. Given the continuous progress in science and technology, it is crucial to analyze the actual needs of the branch and the possibilities of their implementation within the time and financial constraints of the Serbian Armed Forces.

#### 3.1. Current Capabilities

The Serbian Armed Forces are actively working on the modernization of the artillery branch through the introduction of new systems and the enhancement of existing ones [3]. One of the most significant projects is the operational deployment of the domestically produced 155 mm NORA B-52 self-propelled howitzer, which provides greater mobility, range, and firepower. Additionally, the modernization of the Oganj M77 self-propelled multiple rocket launcher into the digitized M17 system allows for more precise and efficient artillery use. The modernization of the 122 mm SH 2S1 Gvozdika self-propelled howitzer also contributes to the increased operational capabilities of the artillery branch.

Currently under testing are the modular self-propelled multiple rocket launcher LRSVM M18 "Oganj" and the modular self-propelled multiple rocket launcher LRSVM 262/122 mm „Tamnava," which will bring new capabilities to the Serbian Army's rocket artillery. Unlike the digitized M17 system, the modular M18 does not have a fixed launcher but uses a pre-loaded rocket launcher mounted on a truck, providing greater flexibility and faster readiness for action. This system can fire various types of rockets, both guided (such as the ALAS missile) and unguided (such as the 128 mm PLAMEN D rocket),

significantly enhancing its operational use and efficiency in modern military operations. The ALAS missile, also in the testing phase, represents the most ambitious development project of the Serbian defense industry. It is an anti-tank/multi-purpose self-guided missile system with a long range, capable of targeting a wide spectrum of threats such as tanks, infantry fighting vehicles, command posts, infrastructure, ships, industrial facilities, and low-flying helicopters. On the other hand, the LRSVM 262/122 mm „Tamnava" is also a fully automated system that uses launcher containers armed with 262 mm rockets and all variants of 122 mm rockets. This system enables the autonomous execution of combat missions, and its modularity ensures flexibility in the choice of rocket armament. The system is equipped with GPS and INS technologies for precise targeting, and the loading and unloading of the launcher system is performed using a crane mounted on the platform. "Tamnava" can launch rockets with a range of up to 70 km (262 mm) and 40 km (122 mm), significantly enhancing the firepower and range of the Serbian Army's rocket artillery.

New ammunition with a gas generator and recessed base improves the ballistic characteristics of projectiles, while the testing of long-range rockets allows for an expanded operational firing range [6]. The integration of drones for reconnaissance and fire guidance represents a significant step towards modernizing and increasing the efficiency of the artillery branch.

The artillery branch of the Serbian Armed Forces has made significant progress over the past decade. This development ensures that artillery units are better equipped and more prepared to respond to modern military challenges, risks, and threats with greater efficiency and reliability. Continuous modernization efforts ensure that artillery remains one of the key branches of the Serbian Armed Forces.

#### 3.2. Identification of issues affecting the pace of capability development

Although the Serbian Armed Forces are actively investing in the modernization and equipping of the artillery branch, there are significant discrepancies when compared to the latest technological advancements and the demands of modern warfare. These discrepancies can be identified in the following areas: **Lack of precision munitions; limited use of drones; outdated sensor systems; limited logistical support; training of personnel; lack of spare parts and accessories.**

The analysis of the current capabilities of the artillery branch and the identified discrepancies in relation to modern technological requirements reveals the necessity for continuous improvement to maintain a high level of operational capability. These discrepancies clearly indicate the development directions and strategies that should be implemented to achieve greater efficiency in military operations. By integrating advanced technologies, strengthening logistical support, and reforming the educational system, the Serbian Armed Forces can significantly enhance their artillery capabilities and better prepare for future military challenges.

## 4. DEVELOPMENT DIRECTIONS FOR THE CAPABILITIES OF THE ARTILLERY UNITS OF THE SERBIAN ARMED FORCES

In light of technological innovations and changes in modern warfare, the enhancement of the artillery units of the Serbian Armed Forces requires a strategic approach across various aspects. It is essential to focus on the organizational and structural framework, tactics of employment, logistical support, the introduction of new technologies, and the improvement of training. The following text analyzes these elements, with a review of current capabilities and the experiences of foreign military forces, in order to identify best practices and overcome existing challenges.

### 4.1. Organizational and structural framework

The organizational and structural framework of the artillery units of the Serbian Armed Forces serves as the foundation for efficient planning, organization, and execution of combat operations [2]. In the context of modern warfare, where speed of response, flexibility, and adaptability are considered key success factors, continuous adaptation of the organizational and structural framework is essential to meet the increasingly complex demands of combat conditions.

One possible aspect of improving the organizational and structural framework is increasing the level of autonomy for artillery units. This can be achieved through the formation of modular units capable of independently executing tasks at the tactical level with minimal support from other branches. These units would be equipped with modern artillery combat systems, advanced communication, and information technologies, enabling them to respond more quickly and effectively to changes in combat conditions. Additionally, it is necessary to consider increasing the number of specialized electronic warfare units to strengthen the artillery's ability to respond to contemporary threats. Integrating these specialized units into the existing structural framework would contribute to a more comprehensive and flexible response to various types of threats. Furthermore, enhancing vertical and horizontal coordination within artillery units, as well as between artillery and other branches of the Serbian Armed Forces, is crucial. Effective coordination and communication between different command levels and units in the field are vital for the successful execution of complex combat operations. By introducing advanced fire control systems, artillery units can achieve a high level of synchronization, further enhancing their combat effectiveness.

Improving the organizational and structural framework of the artillery units of the Serbian Armed Forces is essential to increase operational flexibility, autonomy, and efficiency in modern military operations, enabling the artillery to better respond to the complex and dynamic challenges of contemporary warfare.

### 4.2. Tactics of employment

The tactics employed by the artillery units of the Serbian Armed Forces play a significant role in achieving success and completing missions. However, the existing combat doctrines, shaped by traditional methods of artillery use, have not fully accounted for the integration of modern technologies and the modernization of artillery combat systems. This situation calls for an urgent reassessment and adaptation of current doctrines to ensure their relevance in modern warfare.

Modern artillery combat systems offer significantly greater precision, mobility, and autonomy for units. However, the integration of these systems into existing formations often encounters obstacles due to inconsistencies with current rules and tactics of employment. For instance, the current doctrines do not fully exploit the capabilities offered by advanced guidance systems, such as GNSS and INS, or the use of drones for reconnaissance and artillery fire guidance.

Therefore, it is essential to adapt combat doctrines to reflect the new capabilities brought by the modernization of artillery. This involves integrating new technologies into the techniques used in operations, from planning and reconnaissance to the execution of fire missions and rapid, efficient changes in firing positions. Beyond technological aspects, new tactics must also consider changes in the nature of conflict, including asymmetric threats and urban warfare. Artillery units must adapt to scenarios where the enemy employs unconventional methods, requiring greater flexibility and the ability to respond quickly. Adapting to these demands is essential for maintaining effectiveness and minimizing collateral damage. The reform of doctrines must also encompass better-coordinated actions with other branches of the military, particularly in the context of joint operations. The integration of artillery with the forces of other branches and services enhances overall capabilities and allows for more efficient use of resources on the battlefield.

Ultimately, the tactics employed by the artillery units of the Serbian Armed Forces must be adapted to new technological advancements and contemporary combat conditions.

### 4.3. Logistical support

The modernization of artillery requires adequate logistical support capable of sustaining new systems and technologies. This includes the procurement of specialized tools and spare parts, as well as the optimization of supply chains to deliver parts and ammunition to artillery units in the field. Beyond its importance for maintenance and supply, logistical support also impacts timely responses in critical situations, ensuring continuous readiness [4]. The introduction of new technologies in logistics, such as automated inventory management systems and advanced transportation methods, enhances the efficiency of logistical support. At the same time, it is necessary to ensure flexibility in logistical processes to quickly adapt to changing conditions in the field and maintain

continuity in supply and maintenance, even in complex combat conditions.

#### 4.4. New technologies

The integration of new technologies into the artillery units of the Serbian Armed Forces contributes to the enhancement of operational capabilities and the adaptation to modern combat conditions. Contemporary artillery combat systems increasingly rely on technological innovations that enable more precise, faster, and more flexible operations. One of the most important aspects of introducing new technologies is the development and implementation of advanced fire control systems, such as Global Navigation Satellite Systems (GNSS) and Inertial Navigation Systems (INS). These systems allow for precise targeting and increased accuracy in firing, reducing the need to launch a larger number of projectiles. Additionally, the introduction of unmanned aerial vehicles for reconnaissance and fire guidance represents a significant step forward in the modernization of artillery units, as it enables real-time intelligence gathering and faster decision-making in the field. Modern artillery also utilizes smart munitions capable of neutralizing targets with great precision. Firing fewer projectiles reduces the risk of revealing one's own positions. The introduction of automated loading and aiming systems significantly accelerates the firing process, enabling faster responses and adaptation to changes on the battlefield. By introducing new technologies, the Serbian Armed Forces ensure that their artillery units remain relevant and capable of responding to the increasingly complex challenges of modern warfare.

#### 4.5. Training

Training is a crucial element in the future development of the artillery units of the Serbian Armed Forces, particularly in the context of implementing new technologies and adapting the tactics of artillery use. To ensure that artillery personnel are prepared for the effective use of the latest systems, the curriculum at the Military Academy and the training programs at training centers must be continuously updated and aligned with the demands of modern warfare. Currently, the discrepancy between theoretical education and the practical application of new systems highlights the need for a reform of the educational process. In the future, training should focus on the integration of modern artillery systems into educational programs, thereby reducing the gap between theory and practice. Beyond training in handling and operation, future development should also include the enhancement of IT skills, given that modern artillery combat systems require advanced informatics competencies. These skills are crucial for the effective operation and maintenance of new systems. Through comprehensive training programs, similar to those implemented by advanced military forces, such as the Israeli Defense Forces, the Serbian Armed Forces can significantly improve the operational readiness of their artillery units. Emphasizing continuous training and adaptation to modern technologies will ensure that the

Serbian Armed Forces are prepared to meet the increasingly complex challenges of modern combat conditions.

Enhancing the capabilities of the Serbian Armed Forces' artillery units requires a strategic approach that encompasses various aspects. Contemporary warfare challenges and technological advancements necessitate the continuous adaptation of artillery units. By integrating new technologies, optimizing logistical processes, and reforming the educational system, the Serbian Armed Forces can significantly improve the operational capabilities of their artillery units and ensure they are capable of effectively responding to the demands of modern warfare. Such an approach enables the artillery to remain relevant in achieving operational objectives and maintaining national security.

### 5. CONCLUSION

The Artillery of the Serbian Armed Forces, faced with dynamic changes in the modern combat environment, demonstrates significant progress through the continuous modernization of its capabilities. The operational capacities of this branch ensure rapid and precise fire strikes against various targets. This paper provides an overview of the current capabilities of the artillery branch, identifies the challenges that affect the speed of capability development in relation to contemporary technological demands, and discusses the necessary development directions to enhance operational capabilities. The integration of new technologies, adaptation of organizational and structural frameworks, improvement of logistical support, and enhancement of training are key elements that enable artillery units to remain relevant and effective in confronting the complex challenges of modern warfare. To achieve a higher level of capability, the Serbian Armed Forces must continue their efforts in modernizing the artillery branch and ensure that all changes align with contemporary requirements and resource constraints. Continuous adaptation and improvement allow the artillery to remain a crucial component of the Serbian Armed Forces' firepower, capable of effectively executing tasks in combat operations.



**References**

- [1] KALEZIĆ, M. (2010). *Projektovanje artiljerijskih sistema*. Beograd: Vojnoizdavački zavod
- [2] JANKOVIĆ, K., KOMAZEC, N.: Osvrt na rizike autonomnog oružja, Zbornik radova 9. Međunarodna konferencija „Bezbednost i krizni menadžment – teorija i praksa”, Beograd, 2023.
- [3] JANKOVIĆ, K., KOMAZEC, N.: Upravljanje rizicima savremenog oružja, Zbornik radova međunarodni naučni skup „Savremeni izazovi i prijetnje bezbednosti”, Banjaluka, 2024.
- [4] MIRKOVIĆ, T. (2007): Naoružavanje i razvoj, Evropski centar za mir i razvoj (ECPD) Univerziteta za mir Ujedinjenih, Beograd
- [5] Doctrine of the Serbian Armed Forces, 2010.
- [6] Scharee, P. (2020): *Vojska bez vojnika*. Laguna, Beograd, 2020. (originalan naslov *Army of none: Autonomous Weapons and the Future of War*)



## ANALYSIS OF THE USE OF MODERN FIRE GUIDANCE SYSTEMS AND THEIR IMPLEMENTATION IN INFANTRY UNITS

MARKO RADOVANOVIĆ

University of Defense Belgrade, Military Academy, [markoradovanovicgdb@yahoo.com](mailto:markoradovanovicgdb@yahoo.com)

ALEKSANDAR PETROVSKI

‘Goce Delcev University’ Stip, Military Academy “General Mihailo Apostolski”, Skopje, [aleksandar.petrovski@ugd.edu.mk](mailto:aleksandar.petrovski@ugd.edu.mk)

ANER BEHLIĆ

‘Goce Delcev University’ Stip, Military Academy “General Mihailo Apostolski”, Skopje, [kadet.behlic.aner@gmail.com](mailto:kadet.behlic.aner@gmail.com)

REXHEP MUSTAFOVSKI

‘Goce Delcev University’ Stip, Military Academy “General Mihailo Apostolski”, Skopje, [rexhepmustafovski@gmail.com](mailto:rexhepmustafovski@gmail.com)

KRISTIЈAN ILIEVSKI

‘Goce Delcev University’ Stip, Military Academy “General Mihailo Apostolski”, Skopje, [kristijanilievski88@yahoo.com](mailto:kristijanilievski88@yahoo.com)

ŽELJKO JOKIĆ

University of Defense Belgrade, Military Academy, [antras1209@gmail.com](mailto:antras1209@gmail.com)

SOFIЈA ACKOVSKA

‘Goce Delcev University’ Stip, Military Academy “General Mihailo Apostolski”, Skopje, [sofija.velinovska@gmail.com](mailto:sofija.velinovska@gmail.com)

---

**Abstract:** This paper presents a novel system for accurately mapping military targets using a combination of trigonometry and computer vision, deployed through unmanned aerial vehicles (UAVs). The proposed system integrates a drone equipped with a camera and employs trigonometric principles to calculate target distances based on the drone's position, angles and elevation. Upon sighting a target, the system utilizes computer vision algorithms to precisely identify and localize it within the drone's field of view. Subsequently, leveraging the calculated distances and the drone's GPS coordinates, the system accurately maps the target's coordinates on a global positioning system (GPS). The integration of trigonometry and computer vision enhances target localization capabilities, facilitating efficient and precise mapping of military objectives in diverse operational environments. This system holds significant potential for enhancing situational awareness and operational effectiveness in military applications.

**Keywords:** Computer Vision, Target Localization, Military Surveillance, UAV, GPS, Angle

### 1. INTRODUCTION

The significance of cost-effective and portable military surveillance methods lies in their ability to provide critical intelligence and enhance situational awareness while optimizing resources. Compact and easily deployable equipment, like UAVs, enhances reconnaissance without burdening resources, offering flexibility and rapid deployment crucial in dynamic military environments [1,2]. These technologies improve situational awareness with real-time intelligence, reducing the need for soldiers in high-risk areas and increasing safety. Cost-effective methods are vital for military budgets, ensuring sustainable capabilities through advanced yet compact solutions like miniaturized sensors and lightweight UAVs. Integrating these methods enhances overall

military effectiveness, enabling informed decisions and strategic advantages in various scenarios.

Drone-based range detection is crucial in military operations, security systems, research, and other fields. It allows for safe distance assessments in military contexts, advanced area monitoring in security, and precise data collection in research. Drones are also pivotal in agriculture and energy industries for efficient process management. Various sensors, cameras, and data processing techniques enable accurate distance measurements in diverse conditions. Understanding this background highlights the technology's broad applications and potential for innovation across sectors.

The primary objective of this research is to develop a cost-effective methodology for high-precision range detection using commercial UAVs equipped with

cameras. The system integrates camera calibration, angle calculations, range determination, and GPS mapping to provide accurate target coordinates in real-time [3].

We hypothesize that by employing advanced image processing techniques for target identification and innovative methods for angle calculation, we can significantly enhance the accuracy of range detection. Specifically, we aim to demonstrate that:

- Accurate camera calibration and precise angle calculations can be achieved using commercial UAVs.
- The integration of these techniques with GPS mapping will result in real-time, high-precision target coordinates.
- Our methodology will provide a reliable and cost-effective solution for applications requiring pinpoint accuracy in range detection.

## 2. METHODOLOGY

The proposed methodology as seen in Figure 1 involves the multiple following steps to achieve accurate range detection and target identification using a UAV equipped with a camera and computer vision algorithms. The first step is Target Detection. The UAV's camera continuously scans the environment for potential targets. A computer vision algorithm processes the camera feed in real-time to identify and classify targets [4]. This algorithm is trained to recognize specific types of targets, such as military vehicles, and determine their exact model. The second step includes Target Identification and Dimension Retrieval [5]. Upon identifying the target, the algorithm retrieves the predefined dimensions of the target model. These dimensions are stored in a database and are used for subsequent calculations. Furthermore, the algorithm determines the target's size in the image, measured in pixels. By comparing the pixel size of the target in the image with its actual dimensions, the algorithm calculates the distance from the UAV to the target, based on its own position. With the distance known, the UAV's GPS coordinates, and the angle to the target, the precise GPS coordinates of the target are determined. The target's GPS coordinates are mapped in real-time, providing high-precision location data [6].

By integrating camera calibration, advanced image processing techniques, and precise mathematical calculations, this methodology ensures accurate range detection and target mapping. This approach leverages the capabilities of commercial UAVs, making it a cost-effective and reliable solution for high-precision reconnaissance [7,8].

The phases of development involved multiple steps necessary for full model development and integration.

The first step necessary was dedicated research and data gathering both for the identification and detection model, which includes several datasets of Military Targets (Tanks, APC's, Fortified positions, etc). Further followed, building dedicated datasets for model training and testing

and aligning the target's size descriptions with the target models. Additionally, a YOLOv8 model [9,10] was trained upon the produced datasets. Finally, a Target Mapping algorithm was developed and integrated alongside with the YOLOv8 vision model. The final product is a model capable of taking live feed, producing real-time target detection and accurate GPS mapping of the targets.

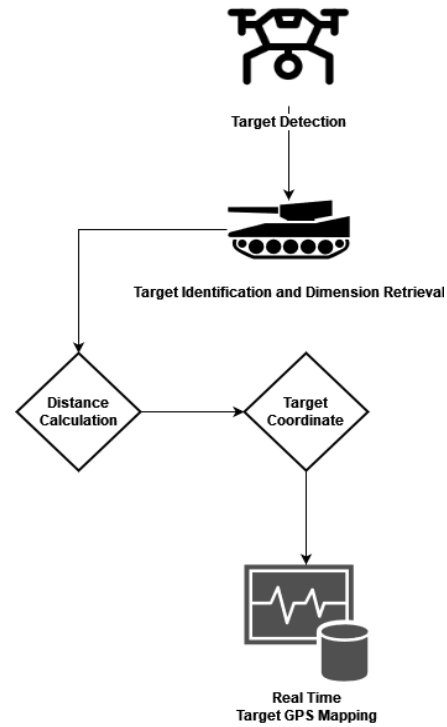


Figure 1: Proposed Methodology

## 3. ANGLE & RANGE CALCULATION

### 3.1 Calculating the angles between the camera's line of sight and the target

When the drone has an accelerometer, it can significantly facilitate the calculation of the angles of the camera in relation to the observed target [11]. The accelerometer can provide information about the acceleration affecting the drone in different directions, which can then be used to calculate orientation and angles. There are several models for calculating required elements. In the further part of the paper, one of the models is presented, in equation 1, the angle is calculated that refers to the pitch of the drone in relation to the horizontal plane (tilt forward-backward). The acceleration components from the accelerometer are used in the equation.

$$Pitch = \arctan \left( \frac{a_x}{\sqrt{a_y^2 + a_z^2}} \right) \quad (1)$$

Equation 2 shows the formula for calculating the angle related to the tilt of the drone (Roll) in relation to the horizontal plane (tilt left-right), the acceleration components from the accelerometer are also used:

$$\text{Roll} = \arctan\left(\frac{a_y}{\sqrt{a_x^2 + a_z^2}}\right) \quad (2)$$

To obtain the tilt values of the drone in specific directions, trigonometric formulas were used, utilizing acceleration data in three primary directions  $a_x, a_y, a_z$ . To calculate the pitch, roll, and azimuth angles, it is necessary to have specific acceleration values from the accelerometer and optionally data from the gyroscope and magnetometer.

To obtain the azimuth, data from the compass or gyroscope can be used. By integrating the angular velocity from the gyroscope, the azimuth angle can be determined. The azimuth represents the orientation of the drone relative to the direction of north.

The elevation angle refers to the vertical tilt of the camera up or down. If the target is on the horizon, the elevation angle will be approximately equal to the pitch angle. The formula for the elevation angle can be similar to the pitch formula (Equation 3), but the accuracy of this angle is directly related to the orientation of the camera relative to the horizon.

$$\text{Elevation angle} = \arctan\left(\frac{a_z}{\sqrt{a_y^2 + a_x^2}}\right) \quad (3)$$

This formula uses acceleration data in three dimensions to calculate the elevation angle of the camera relative to the horizon. It is important to note that this formula represents one approach and that accuracy can depend on the precision of the sensor data and the specific characteristics of the drone. For instance, if the target is on the horizon, the elevation angle will be approximately equal to the pitch angle.

### 3.2 Method for calculating the range from the drone to the target based on the angles obtained

To calculate the distance from the drone to the target based on the angles obtained, you can use trigonometry and geometry. This method relies on information about the pitch, roll, and yaw angles to determine the distance. Assume you have the elevation angle (pitch), azimuth, and, if necessary, the roll angle. Additionally, we will assume that the height of the drone above the ground is known.

If the values of the elevation angle (pitch) and the drone's height above the ground ( $h$ ) are known, it is possible to calculate the target's height above the ground using the tangent trigonometric function ( $\tan$ ). Assuming that  $d_{\text{pitch}}$  is the distance to the target in the direction of the elevation angle, by applying Equation 4, the target height ( $h_{\text{target}}$ ) can be determined.

$$h_{\text{target}} = h + d_{\text{pitch}} \times \tan(\text{pitch}) \quad (4)$$

When azimuth data is available and it's necessary to calculate the distance on the horizontal plane,

trigonometric functions cosine and sine can be used. If  $d_{\text{horizontal}}$  represents the horizontal distance to the target, it is calculated using Equation 5.

$$d_{\text{horizontal}} = d_{\text{pitch}} \times \cos(\text{pitch}) \quad (5)$$

Using the horizontal distance  $d_{\text{horizontal}}$  and the roll angle, it is possible to calculate the total distance to the target. When  $d_{\text{total}}$  represents the total distance, it is calculated using Equation 6.

$$d_{\text{total}} = \frac{d_{\text{horizontal}}}{\cos(\text{roll})} \quad (6)$$

The formulas provided offer a basic framework for calculating the distance to the target based on known angle values. It is important to note that the accuracy of these calculations largely depends on the precision of the angle information and other drone parameters.

### 3.3 Pythagorean theorem application for ground range calculation

There are several approaches to calculating the distance from the drone to the target based on the obtained angles. Another approach involves using trigonometric functions within the triangle formed by the drone, the target, and a point on the ground. The following section presents one calculation model.

If we have data for pitch and azimuth, it is possible to calculate the horizontal and vertical components of the distance to the target using trigonometric functions according to equations 7 and 8

$$d_{\text{horizontal}} = d_{\text{total}} \times \cos(\text{pitch}) \quad (7)$$

$$d_{\text{vertical}} = d_{\text{total}} \times \sin(\text{pitch}) \quad (8)$$

The calculation of the horizontal and vertical components on the ground can be performed using equations 9 and 10.

$$d_{\text{horizontal\_ground}} = d_{\text{horizontal}} \times \cos(\text{azimuth}) \quad (9)$$

$$d_{\text{vertical\_ground}} = d_{\text{horizontal}} \times \sin(\text{azimuth}) \quad (10)$$

The distance to the target on the ground is calculated using equation 11.

$$d_{\text{total\_ground}} = \sqrt{d_{\text{horizontal\_ground}}^2 + d_{\text{vertical\_ground}}^2} \quad (11)$$

This method uses the horizontal and vertical components of distance to calculate the total distance to the target on the ground.

Another additional model for calculating the distance to the target based on pitch and azimuth may involve using the drone's height above ground and the target's altitude. This model relies on trigonometry to form a right triangle between the drone, target, and point on the ground.

If we know the elevation angle ( $\text{pitch}$ ), the target's altitude ( $H$ ), and the drone's height above ground ( $h$ ), we can calculate the target's height above ground ( $h_{\text{target}}$ ) using equation 12.

$$h_{target} = h + \frac{H}{\tan(\text{pitch})} \quad (12)$$

To calculate the horizontal distance ( $d_{horizontal}$ ) when we have the azimuth angle, we compute it using equation 13.

$$d_{horizontal} = d_{total} \times \cos(\text{azimuth}) \quad (13)$$

The total distance to the target ( $d_{total}$ ) is calculated using equation 14.

$$d_{total} = \sqrt{d_{horizontal}^2 + h_{target}^2} \quad (14)$$

These formulas allow calculating the distance to the target using elevation angle, the altitude of the target, the altitude of the drone above ground level, and azimuth. When only the altitude of the drone above ground ( $h_{drone}$ ) and the altitude of the ground below the drone ( $h_{ground}$ ) are known, a simple model utilizing trigonometry can be used. This model is based on forming a right triangle between the drone, the point on the ground, and the target. We will assume that the distance to the target ( $d$ ) is the horizontal distance from the drone to the target.

The height of the target above the ground ( $h_{target}$ ) can be calculated as the difference between the altitude of the drone above ground and the altitude of the ground level, as shown in equation 15.

$$h_{target} = h_{drone} - h_{ground} \quad (15)$$

The horizontal distance ( $d_{horizontal}$ ) can be calculated using trigonometry, utilizing the height of the target above ground and the elevation angle (pitch), equation 16.

$$d_{horizontal} = \frac{h_{target}}{\tan(\text{pitch})} \quad (16)$$

The total distance to the target ( $d_{total}$ ) is the sum of the horizontal distance and the vertical distance to the target above ground, as shown in equation 14. This model uses basic trigonometric functions and allows you to calculate the distance to the target based on the drone's height above ground, the height of the ground below the drone, the elevation angle, and optionally the altitude above sea level.

#### 4. TARGET LOCALIZATION

Accurately determining the GPS coordinates of a target from a UAV requires combining the drone's GPS position with calculated ground range. This section explores the detailed methodology and mathematical principles involved in achieving this, along with a discussion on the practical implications and benefits of this approach. Traditional methods rely heavily on expensive sensors and complex setups, but advancements in computer vision and GPS technology offer more cost-effective and efficient solutions. GPS (Global Positioning System) coordinates provide a way to pinpoint a location on the Earth's surface using a combination of latitude, longitude, and altitude. UAVs equipped with GPS receivers can determine their own position accurately. However, determining the position of a ground target requires additional calculations, especially when the target is observed from an aerial perspective [12].

To achieve Target Localization in a real-world scenario, the following data are collected:

- UAV GPS Coordinates: Latitude, longitude, and altitude from the UAV's GPS receiver.
- Target Dimensions: Retrieved from a predefined database based on the target model identified by the computer vision algorithm.
- Image Analysis: The size of the target in the image, measured in pixels.

This data is processed in real-time by the onboard computer or a ground control station equipped with the necessary computational capabilities.

Once the target appears on the UAV's camera screen, and the algorithm measures its size in the image. Using the known actual length of the tank and its image size, we calculate the distance from the UAV to the target.

$$D = \frac{L}{l * IL/R} \quad (17)$$

Where; D - equals the distance from the target to the drone;

L - equals the actual length of the target in meters;

l - equals the length of the target in given image feed in pixels

IL/R - equals the Image to Length Ratio

Using the UAV's altitude and the direct distance to the target, Pythagorean theorem is applied to find the ground range. Next, the bearing from the UAV to the target is calculated based on the UAV's orientation and then the UAV's GPS coordinates are adjusted to find the target's coordinates. Using the ground range and bearing, the latitude and longitude are adjusted:

$$\Delta\text{Latitude} = \frac{\text{Ground Range} * \cos(\text{Bearing})}{\text{Conversion Factor}} \quad (18)$$

$$\Delta\text{Longitude} = \frac{\text{Ground Range} * \sin(\text{Bearing})}{\text{Conversion Factor}} \quad (19)$$

The algorithm then provides adjustment values which we add to the initial GPS coordinates of the UAV, to get Target's GPS coordinates.

$$\text{Target Latitude} = \text{UAV Latitude} + \Delta\text{Latitude} \quad (20)$$

$$\text{Target Longitude} = \text{UAV Longitude} + \Delta\text{Longitude} \quad (21)$$

This step-by-step process illustrates how the system works from spotting a target to determining its exact GPS coordinates using UAV's onboard systems and mathematical calculations [13].

#### 5. EQUIPMENT RESULTS & DISCUSSION

In this section, we present the experimental results of our methodology for determining target GPS coordinates

using a UAV's position and ground range calculations. The primary aim of this experiment is to validate the accuracy and effectiveness of our approach, leveraging computer vision, image processing, and precise mathematical computations. We provide detailed quantitative data and visual representations to illustrate the performance and reliability of the system.



**Figure 2.** Example of the systems Target Classification

To evaluate our methodology, we couldn't conduct a series of test flights using a commercial UAV equipped with a high-resolution camera and a GPS receiver. Therefore, the experiments were performed in a controlled environment with simulated known targets to ensure accurate measurement and validation. The computer vision algorithm demonstrated a high accuracy rate in identifying and classifying the targets. The overall identification accuracy across different target models was 95%, the complete breakdown can be viewed in the previous research paper related to this system (Petrovski et al., 2022).

The accuracy of GPS Transformation calculation was evaluated by comparing the calculated GPS coordinates with the actual known coordinates of the targets. The results showed an average error margin of  $\pm 2\%$ , indicating a high level of precision.

**Table 1.** Average GPS Transformation Error

Target Model	Average Error (meters)	Average Error (%)
Tank	15	+1.5%
Military Vehicles	30	+3%
Military Personnel	70	+5%

As seen, when it comes to positioning larger Military Targets such as vehicles and Tanks, the algorithm is fairly precise, however, when it comes to positioning live human targets such as soldiers or MG-nests, the algorithm derives in accuracy.

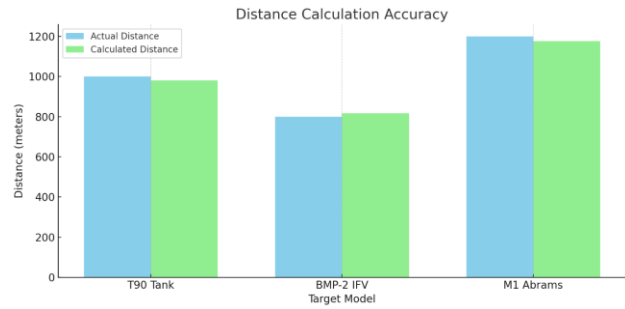


**Figure 3.** Comparison of Accuracy between three Military Target Tanks & IFV

That is because, military targets such as tanks and vehicles are detailed explained in the model and have precise lengths and widths which the model uses to calculate GPS coordinates, however, when it comes to live human targets, the height and width values are rather fixed to an average and do not interchange, therefore, based on the targets similarities to that coefficient the margin of error increases or decreases, however, the results are still fairly precisely mapped.

Overall, the computer vision algorithm achieved an overall identification accuracy of 95%, with slight variations among different target models. The average error margin in GPS mapping was  $\pm 3.1\%$ , indicating reliable measurements. Environmental Factors such as Lighting conditions, weather, and terrain variations can affect the accuracy of target detection and image analysis. Furthermore, the inherent accuracy limitations of commercial GPS receivers ( $\pm 10$  meter) can introduce minor errors in the final coordinate transformation. In all, the experimental results validate the proposed methodology for combining UAV GPS position with ground range calculations to determine target GPS coordinates. The high accuracy and reliability of the system make it a viable solution for various applications, including military reconnaissance, search and rescue operations, and environmental monitoring. Future work will focus on enhancing the robustness of the computer vision algorithm, and optimizing the computational efficiency for real-time applications.

## 6. CONCLUSION

This study introduces a novel system for accurate target mapping using unmanned aerial vehicles (UAVs) that combine trigonometry and computer vision. The proposed system utilizes a camera-equipped drone to identify and localize military targets, calculating distances through trigonometric principles based on the drone's position, angles, and elevation. The integration of computer vision algorithms enhances the precision of target identification, while GPS mapping ensures accurate localization of the targets in real time.

The research emphasizes the critical importance of cost-effective and portable surveillance methods in military operations. By leveraging compact, easily deployable UAVs, the military can significantly enhance reconnaissance capabilities, providing real-time

battlefield intelligence without overburdening resources. This agility and improved situational awareness are crucial for mission success in dynamic environments, where rapid setup and real-time data are vital.

The system's methodology involves advanced image processing techniques for target identification, angle calculation for range determination, and precise GPS mapping. Experimental results demonstrate high accuracy in identifying targets and calculating their GPS coordinates, with an overall identification accuracy of 95% and an average GPS transformation error margin of  $\pm 3.1\%$ . The system shows reliable performance, particularly in mapping larger military targets such as vehicles and tanks. However, there are challenges in accurately positioning smaller, dynamic targets like personnel due to the fixed height and width values used in the model.

Environmental factors, such as lighting conditions and terrain variations, as well as the inherent limitations of commercial GPS receivers, can affect the accuracy of target detection and mapping. Despite these challenges, the proposed system presents a viable and cost-effective solution for various military applications, including reconnaissance, search and rescue operations, and environmental monitoring.

Future work will focus on enhancing the robustness of the computer vision algorithm and optimizing computational efficiency for real-time applications. By addressing these areas, the system can further improve its accuracy and reliability, solidifying its potential as a critical tool for enhancing situational awareness and operational effectiveness in diverse and challenging military environments.

## References

- [1] PETROVSKI, A., BOGATINOV, D., RADOVANOVIĆ, M., ACKOVSKA, S.: *Application of Drones in Crises Management Supported Mobile Applications and C4IRS Systems*, Environmental Protection and Disaster Risks. EnviroRISKs 2022. Lecture Notes in Networks and Systems, 638. Springer, Cham, 2023, [https://doi.org/10.1007/978-3-031-26754-3\\_28](https://doi.org/10.1007/978-3-031-26754-3_28)
- [2] RADOVANOVIĆ, M., PETROVSKI, A., ŽNIDARŠIĆ, V., BEHLIĆ, A.: *The C5ISR System Integrated with Unmanned Aircraft in the Large-Scale Combat Operations*, Vojenski razgledi. 2023, 32(2), 098-118. <https://doi.org/10.3849/2336-2995.32.2023.02.098-118>
- [3] PETROVSKI, A., RADOVANOVIĆ, M.: *Application of detection reconnaissance technologies use by drones in collaboration with C4IRS for military interested*, Contemporary Macedonian Defence, 2021, 21(40), 117-126.
- [4] AHMAD, H., FARHAN, M., FAROOQ, U.: *Computer Vision Techniques for Military Surveillance Drones*, Wasit Journal of Computer and Mathematics Science, 2023, 2(2), 53-59. <https://doi.org/10.31185/wjcms.148>
- [5] LIN, T.Y., MAIRE, M., BELONGIE, S., HAYS, J., PERONA, P., RAMANAN, D., DOLLÁR, P., ZITNICK, C.L.: *Microsoft coco: Common objects in context*, Proceedings of the 13th European Conference on Computer Cision (ECCV 2014), Zurich, Switzerland, 2014, 740-755.
- [6] GAO, Z., LI, D., WEN, G., KUAI, Y., CHEN, R.: *Drone Based RGBT Tracking with Dual-Feature Aggregation Network*, Drones, 2023, 7(9):585. <https://doi.org/10.3390/drones7090585>
- [7] FU, X., WEI, G., YUAN, X., LIANG, Y., BO, Y.: *Efficient YOLOv7-Drone: An Enhanced Object Detection Approach for Drone Aerial Imagery*, Drones, 2023, 7(10):616. <https://doi.org/10.3390/drones7100616>
- [8] STOTT, E., WILLIAMS, R.D., HOEY, T.B.: *Ground control point distribution for accurate kilometre-scale topographic mapping using an RTK-GNSS unmanned aerial vehicle and SFM photogrammetry*, Drones, 2020, 4(3):55. <https://doi.org/10.3390/drones4030055>
- [9] CHENG, G., CHAO, P., YANG, J., DING, H.: *SGST-YOLOv8: An Improved Lightweight YOLOv8 for Real-Time Target Detection for Campus Surveillance*, Applied Sciences, 2024; 14(12):5341. <https://doi.org/10.3390/app14125341>
- [10] ZENG, Y., GUO, D., HE, W., ZHANG, T., LIU Z.T.: *ARF-YOLOv8: a novel real-time object detection model for UAV-captured images detection*, Journal of Real-Time Image Processing, 2024, 21: 107, <https://doi.org/10.1007/s11554-024-01483-z>
- [11] HARWIN, S., LUCIEER, A., OSBORN, J.: *The impact of the calibration method on the accuracy of point clouds derived using unmanned aerial vehicle multi-view stereopsis*, Remote Sensing, 2015, 7(9), 11933-11953, <https://doi.org/10.3390/rs70911933>
- [12] KAPLAN, E. D., HEGARTY, C. J.: *Understanding GPS: Principles and Applications*, Artech House, 2006.
- [13] SNYDER, J. P.: *Map Projections: A Working Manual*, U.S. Government Printing Office, 1987.
- [14] PETROVSKI, A., RADOVANOVIĆ, M., BEHLIĆ, A.: *Application of Drones with Artificial Intelligence for Military Purposes*, 10<sup>th</sup> International Scientific Conference od Defensive Technologies-OTEH, 2022, 92-100.

# ANALYTICAL AND NUMERICAL ANALYSIS OF AXIAL STRESSES IN A HIGH EXPLOSIVE ROCKET ASSISTED PROJECTILE BODY DURING ITS LAUNCH

SVETLANA STOJNOVIĆ

University of Defence in Belgrade, Military Academy, Serbia, [svetlanastojnovic@gmail.com](mailto:svetlanastojnovic@gmail.com)

ABDELLAH FERFOURI

University of Defence in Belgrade, Military Academy, Belgrade, Serbia, [fer-abdel@hotmail.com](mailto:fer-abdel@hotmail.com)

NIKOLA RADOVANOVIĆ

Military Technical Institute, Belgrade, Serbia, [nikola.radovanovic@mod.gov.rs](mailto:nikola.radovanovic@mod.gov.rs)

MILOŠ PEŠIĆ

University of Kragujevac, Institute for Information Technologies, Kragujevac, Serbia; [milospesic@uni.kg.ac.rs](mailto:milospesic@uni.kg.ac.rs)

SREĆKO MANASIJEVIĆ

Research and Development Institute Lola, Belgrade, Serbia, [srecko.manasijevic@li.rs](mailto:srecko.manasijevic@li.rs)

VLADIMIR MILOVANOVIĆ

University of Kragujevac, Faculty of Engineering, Kragujevac, Serbia [vladicka@kg.ac.rs](mailto:vladicka@kg.ac.rs)

**Abstract:** The paper presents analytical and numerical analysis of axial stresses in a novel designed high explosive rocket assisted projectile body during its launch. Classical theoretical approach and finite element method (FEM) were used for this purpose. The novel projectile design is based on the M107 and M549 projectiles, enhancing range and withstanding the barrel pressure from the propellant charges used. The goal of the research is to present that the obtained stresses results, in characteristic cross-sections, founded by the classical theoretical and numerical methods, give good agreement. The obtained results are helpful in a preliminary stage for the design of extended range projectiles. The analysis of axial stresses enables the selection of the rocket motor case material and its mechanical and thermal processing.

**Keywords:** Stress analysis, Finite Element Method analysis, High Explosive Rocket Assisted Projectile

## 1. INTRODUCTION

During the initial phases of projectile design, it is important to determine the state of stress in the projectile body. One of the major concerns is to ensure that projectile is capable of surviving gun launch conditions on the account of firing stresses [1,2].

The development of rocket assisted projectiles enabled to extend the range and improve the performance of traditional artillery projectiles. This research evaluates the axial stress conditions of projectile body and rocket motor case of the novel designed high explosive rocket-assisted (HERA) projectile using classical theoretical methods and finite element methods (FEM), aiming to provide a comprehensive and reliable analysis of the design's safety and performance.

The study's results offer valuable insights into the necessary mechanical and thermal processing treatments to ensure the projectile's durability and effectiveness.

## 2. ANALYTICAL STRESS ANALYSIS

Analytical stress analysis is a great tool for understanding projectile stress distribution, providing quick and exact solutions within the scope of its assumptions [3]. It serves as a critical step in the design and preliminary analysis of projectiles.

Until the appearance of modern computers, classical theoretical methods based on analytical calculation were the only way to determine the stress state of artillery projectile body. This paper deals with 155 mm novel designed rocket-assisted (HERA) projectile (shown in Fig.1).

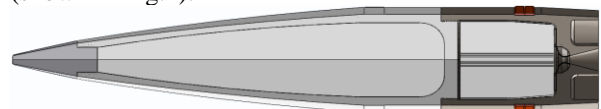


**Figure 1.** Newly designed 155mm HERA projectile

The projectile has the following characteristics: reference diameter (cal.) 155mm, total length ~ 5.61 cal., nose length ~ 3.37 cal., boat-tail length ~ 0.55 cal., center of gravity (CG) from nose ~ 3.53 cal., explosive



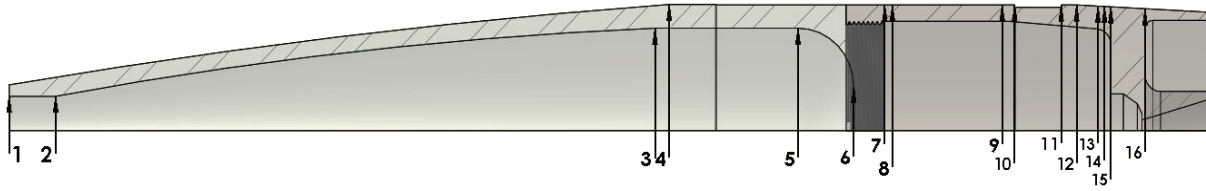


**Figure 2.** Cross-sections of the projectile body and rocket motor case

**Table 1.** Cross-sections characteristics

Location of $i^{\text{th}}$ section	Forward distance of $i^{\text{th}}$ section [mm]	Outer radius $r_o$ [mm]	Inner radius $r_i$ [mm]	Weight of parts forward of $i^{\text{th}}$ section $m_A$ [kg] ( $e_c = 6\text{mm}$ )	Weight of parts forward of $i^{\text{th}}$ section $m_A$ [kg] ( $e_c = 10\text{mm}$ )	Weight of parts forward of $i^{\text{th}}$ section $m_A$ [kg] ( $e_c = 12\text{mm}$ )
1	0	28	21	0.57		
2	30	32.75	21	1.16		
3	416.88	76.71	62.82	16.82		
4	426.05	77.37	62.82	17.45		
5	509.21	77.09	62.82	23.27		
6	545.21	77.09	26.83	26.36		
7	565.21	77.09	0	29.29		
8	570.21	77.09	71.09	29.5	29.57	29.6
9	641.11	77.09	71.09	32.66	33.7	34.19
10	649.05	77.09	70.77	33.02	34.16	34.7
10'	649.05	75.95	70.77	33.02	34.16	34.7
11	679.04	77.09	68.31	34.73	36.27	37.01
11'	679.04	75.95	68.31	34.73	36.27	37.01
12	689.05	77.09	67.49	35.26	36.94	37.73
13	702.95	76.36	66.35	36.02	37.87	38.75
14	706.95	76.15	64.69	36.23	38.12	39.05
15	711.21	75.93	22.5	36.49	38.44	39.37
16	733.21	74.78	7.05	39.41	41.37	42.29

charge mass  $\sim 7$  kg, rocket motor propellant mass  $\sim 3$  kg.

Changes in geometry can notably affect the stress distribution, making it required to analyze these points with higher precision. To calculate the stress state in a projectile body it is necessary to split the projectile body into cross-sections [4], as shown Fig.2. and summarized in Table 1. When calculating the stress of the rocket motor (RM), different casing wall thicknesses ( $e_c$ ) were taken into consideration as follows: 6, 10 and 12 mm, as well as two types of gun propellant charge with 9 kg (Zone 8) and 13 kg of propellant (Zone 9). This allows to consider different firing scenarios by combining the chosen thicknesses ( $e_c$ ) with the two types of gun propellant charge.

Based on knowledge of principal stresses and von Mises failure criteria, one can determine the equivalent stress [5]. The axial stresses  $(\sigma_p)_{i-i}$  in the zones of different cross-sections were calculated using different equations [4,6,7], as follows:

- Cross sections 1-10, the zone in front of driving band:

$$(\sigma_p)_{i-i} = \frac{m_A}{S_{i-i}} a_{\max} \quad (1)$$

- Cross sections 11-12, the zone behind of driving band, in front of rear cone:

$$(\sigma_p)_{i-i} = \frac{1}{S_{i-i}} (m_A a_{\max} + n F_{na}) \quad (2)$$

- Cross sections 13-16, the zone of rear cone:

$$(\sigma_p)_{i-i} = \frac{1}{S_{i-i}} [m_A a_{\max} + n F_{na} - P_{pr} (s_c - r_o^2 \pi)] \quad (3)$$

Where are:

$$a_{\max} = \frac{P_{pr} s_c}{m} \quad (4)$$

$$F_{na} = N (\sin \varphi + f \cos \varphi) \quad (5)$$

$$N = \frac{I_x}{n} \frac{4 \tan \varphi}{d^2 \cos \varphi} \frac{P_{pr}}{m} s_c \quad (6)$$

$$s_c = \frac{d^2 \pi}{4} + \frac{en}{2} (d_0 - d) \quad (7)$$

When designing a new projectile, the stress calculation is performed with a pressure  $P_{pr}$  [MPa] that is higher than the maximum pressure  $P_m$  [MPa] of the powder gases in the gun barrel under normal conditions:

$$P_{pr} = kP_m \quad (8)$$

The parameters in equations (1-8) are defined as follows:  $a_{max}$  [g] maximum acceleration in the barrel during launch,  $m_A$  [kg] mass of projectile's part left from cross section  $i-i$  (including mass of fuse, explosive charge filling and rocket motor propellant),  $m$  [kg] projectile total mass,  $s_c$  [mm<sup>2</sup>] bore area,  $F_{na}$  [N] axial force on one tooth of driving band,  $N$  [N] normal force on active surface of driving band's tooth,  $I_x$  [kg·mm<sup>2</sup>] axial moment inertia of projectile,  $n$  [/] number of grooves,  $d_o$  [mm] outer diameter,  $d$  [mm] inner diameter,  $\varphi$  [°] angle of groove's twisting,  $f$  [/] friction coefficient (steel – cooper),  $k$  [/] safety factor,  $e$  [mm] groove's width.  $S_{i-i}$  [mm<sup>2</sup>] represents area of projectile body in cross-section  $i-i$  which can be calculating using equation:

$$S_{i-i} = \pi(r_o^2 - r_i^2) \quad (9)$$

Input data for analytical calculation of the axial stresses for the 155mm newly designed HERA projectile are given in Table 2.

**Table 2.** Input data for calculation

Input data	Unit	Value
Number of grooves $n$	[/]	48
Inner diameter $d$	[mm]	155
Outer diameter $d_o$	[mm]	156.56
Groove's width $e$	[mm]	5.071
Angle of groove's twisting $\varphi$	[°]	8.9
Friction coefficient $f$	[/]	0.2
Safety factor $k$	[/]	1.3
Projectile total mass for each $e_c$ case ( $m_1, m_2, m_3$ )	[kg]	(40.72, 42.67, 43.6)
Axial moment inertia of projectile for each $e_c$ case ( $I_{x1}, I_{x2}, I_{x3}$ )	[kg.m <sup>2</sup> ]	(0.13, 0.14, 0.15)
Maximum pressure for each $e_c$ case ( $P_{m1}, P_{m2}, P_{m3}$ ) when using 9kg of propellant charge)	[MPa]	(160, 166, 169)
Maximum acceleration for each $e_c$ case ( $a_{max1}, a_{max2}, a_{max3}$ ) when using 9kg of propellant charge)	[·10 <sup>3</sup> g]	(9. 92, 9. 82, 9. 79)
Maximum pressure for each $e_c$ case ( $P_{m4}, P_{m5}, P_{m6}$ ) when using 13kg of propellant charge)	[MPa]	(258, 270, 275)
Maximum acceleration for each $e_c$ case ( $a_{max1}, a_{max2}, a_{max3}$ ) when using 13kg of propellant charge)	[·10 <sup>3</sup> g]	(16. 02, 15. 98, 15. 93)

In this study, the projectile rotation was not taken into account (generally, axial stresses are dominant during the launch phase of projectiles [6]). Additionally, the influence of other parts of the projectile, including high explosive charge, rocket motor propellant charge as well as stresses in all components of the projectile were

not included in the analysis also.

Graphic results with values of stresses in characteristic cross sections calculated by analytical method are shown in Figs.3 and 4, for each of the three casing wall thicknesses cases and for the two types of propellant charge.

The obtained values were compared with the material limits of the projectile components as it is high-fragmentation steel (HF-1) for the high explosive warhead and high-strength steel (AISI 4340) for the rocket motor case. The critical axial stress for these materials is 750 MPa [8] and 1500 MPa [9], respectively. Based on the analysis results, the rocket motor case wall thickness was decided to be 10 mm.

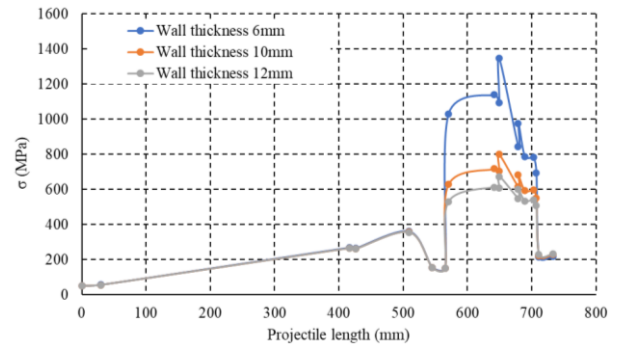


**Figure 3.** Values of stresses in characteristic cross-sections for 9 kg gun propellant charge

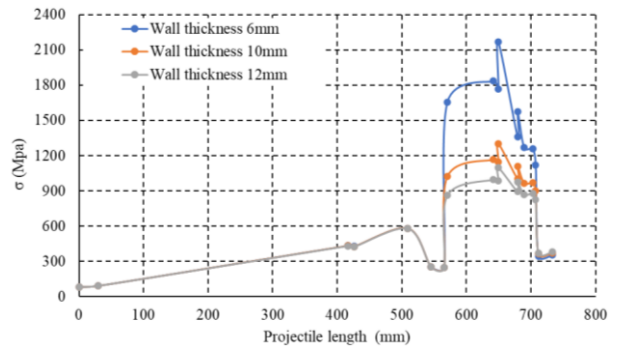


**Figure 4.** Values of stresses in characteristic cross-sections for 13 kg gun propellant charge

### 3. FINITE ELEMENT METHOD AND COMPARATIVE ANALYSIS

Finite Element Method (FEM) analysis involves a series of steps to model, simulate, and analyze the physical behavior of components and assemblies under various conditions [10]. Also, it includes defining loads and boundary conditions [10] (shown in Fig.5), which divides the model into smaller and simpler elements.

The projectile body model retains the same material and geometric properties in all cross sections along the longitudinal axis of symmetry, the fuze is not modelled

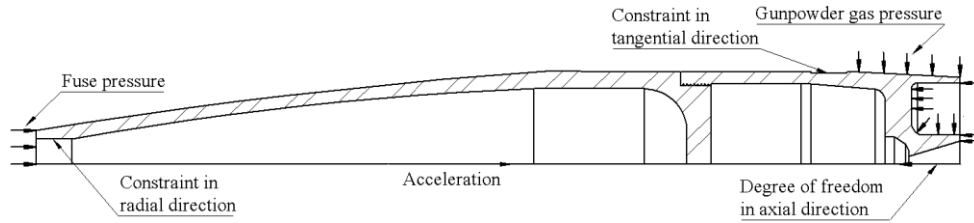


**Figure 5.** Loads and boundary conditions

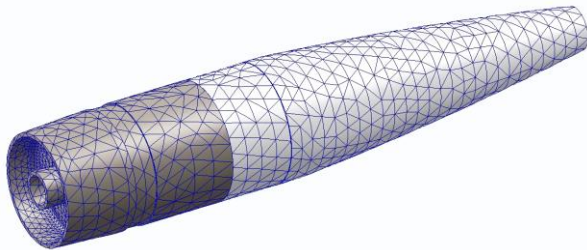


**Figure 6.** Numerical mesh for projectile model



**Figure 7.** Stress condition for a model with 9 kg propellant charge



**Figure 8.** Stress condition for a model with 13 kg propellant charge

[4]. The influence of fuze (weight 0.86 kg) is replaced by an equivalent pressure acting on the front area of the projectile body.

The structure is modelled with 19536 elements and 34402 nodes. Max size of element is about 22 mm and minimal size is about 4 mm. Numerical mesh for the given projectile model is shown in Fig.6.

The stress conditions based on the model with 10 mm of casing wall thickness are shown in Figs.7 and 8 for the both gun propellant charges with 9 kg. and 13 kg.

The maximum value of the stress in projectile body occurs at the place of the rocket motor, for the 9 kg propellant charge maximum value of the stress is 799,7 MPa, and for 13 kg propellant charge is 1249,2 MPa.

Stress distribution obtained using analytical and numerical methods are shown in Fig.9 for propellant charge with 9 kg and in Fig.10 for 13 kg.

It has been shown that the difference between results obtained using analytical and numerical methods is higher in the case with 9 kg of gun propellant charge. In both cases, the highest difference is observed for the maximum value of the stress. The general difference doesn't impact the choice of the material of the rocket motor body.

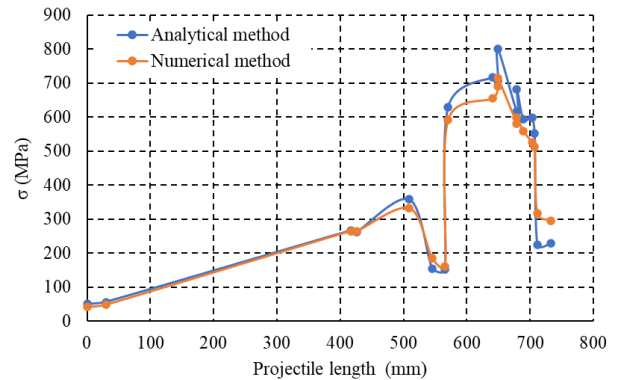


**Figure 9.** Stress distribution obtained using analytical and numerical methods with 9 kg propellant charge

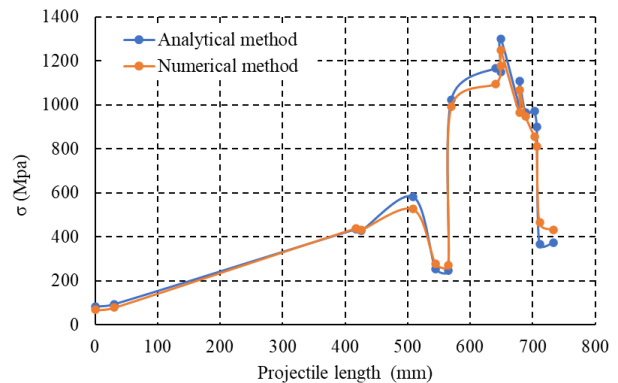


**Figure 10.** Stress distribution obtained using analytical and numerical methods with 13 kg propellant charge

## 4. CONCLUSION

The primary objective of this paper is to present that stress analysis enables the selection of the rocket motor case material for the newly designed rocket assisted projectile.

The general difference between results obtained using analytical and numerical methods shows that choice of method is not crucial for the choice of body materials of both the rocket motor and the high explosive warhead.

Compared to the analytical method, the numerical method provides visual distribution of projectile stress. Finally, this paper presents methodologies that helps in design of HERA projectiles or similar artillery shells.

## Acknowledgements

This work was by Serbian Ministry of Defense and Serbian Ministry of Education, Science and

Technological Development, Grant No 451-03-66/2024-03/200325.

## References

- [1] Rajesh B. Ohol, B.A. Parate, Dineshsingh G. Thakur: *Plastic Deformation of High Explosive Projectile 155 mm during Gun Launch Conditions using Finite Element Method*, Defence Science Journal, Vol. 72, No. 6, pp. 793-800 2022,
- [2] Ohol, R.B., Parshuramkar, T.N. & Thakur, D.G. 674–684, *Investigating the Effect of Abrupt Change in Geometry on Structural Failure of Artillery Projectile 155 mm*, J Fail. Anal. and Preven. 24, 2024
- [3] Nabil Ziane Ahmed, Damir D. Jerković, Nebojša P. Hristov, Walid Boukera Abaci; *Analytical and experimental investigation of the muzzle brake efficiency*, Facta universitatis, 2022
- [4] V. Milovanović, M. Živković, G. Jovičić: *Comparative Stress Analysis of an Artillery Projectile Body*, TEAM 9th International Scientific and Expert Conference, 2018
- [5] Walid Boukera Abaci, Nebojša Hristov, Igor Radisavljevic, Lazar Stojnic, Aleksa Anici-*Experimental and numerical investigation on the performances of a small weapon barrel during its life cycle*, Facta universitatis, 2022
- [6] D. E. Carlucci, S. S. Jacobson, *Ballistics - Theory and design of guns and ammunition*, CRC Press, 2018.
- [7] A. Stamatović.: *Konstruisanje projektila*, Iveys p.o., Beograd, 1995.
- [8] *Manufacture of projectiles, projectile components, and cartridge cases for artillery, tank main armament, and mortars*, MIL-HDBK-756(AR), 29 April 1991.
- [9] J. A. Cordes, D. E. Carlucci, J. Kalinowski, L. Reinhardt, *Design and development of reliable gunfired structures*, Technical Report ARAET-TR-06009, ARDEC, Picatinny Arsenal, New Jersey, 2006.
- [10] D. Đurđevac, *Possibility of the FEM application for a stress condition analysis of an artillery projectile body*. Scientific Technical Review 58(1) 2008

## EFFECT OF EROSIVE BURNING IN ROCKET MOTOR ON THE BALLISTICS OF ROCKET FLIGHT

SRĐAN STOJKOVIĆ

Military Technical Institute, Rocket Armament Sector, Belgrade, [ssrdjanvti@gmail.com](mailto:ssrdjanvti@gmail.com)

NIKOLA GLIGORIJEVIĆ

Institute Vlatacom, Belgrade, [nikola.gligorijevic@vlatacom.com](mailto:nikola.gligorijevic@vlatacom.com)

**Abstract:** Erosive burning in solid rocket motor is a phenomenon that occurs at the beginning of the motor operation and represents an increase in the burning rate in the motor compared to the designed rate. The result of increased burning rate is an unwanted pressure increase in the motor, and thus thrust, which changes the designed flight parameters of the rocket. During development of the rocket motor, this problem should be solved constructively, if possible, by changing the shape and dimensions of the propellant grain and motor elements. If it is not possible, the designer tries to make the system capable enough to withstand pressure and thrust jumps without major disturbances, and to provide to achieve the reproducibility of this phenomenon. The paper presents examples of the impact of erosive burning onto the flight of some small-caliber unguided rockets, and also for one short-range guided missile, where this phenomenon is clearly expressed, but reproducible and acceptable. In this paper, the results obtained on the basis of measurements carried out by researchers from MTI, HK Krusik, MB-Lucani and the Vlatacom Institute were used. Measurements were made in static and dynamic conditions, in the laboratories of the mentioned companies. For the analysed guided missile, the shape of the propellant grain was reconstructed to avoid guidance and structural problems. Some examples of design solutions of the rocket propellant grain in order to reduce the occurrence of erosive burning are also presented.

**Keywords:** Propellant, Grain, Erosive burning, Port/throat ratio, Thrust, Burning surface

### INTRODUCTION

In a solid rocket motor high-velocity flow of gaseous combustion products over the burning surface in the propellant grain channel, on their way towards the nozzle, causes an undesirable increase in the burning rate. The phenomenon is called erosive burning [1]. The increased burning rate affects the pressure increase in the motor, (Fig.1) and thus also the thrust increase, which can significantly affect the rocket cinematic and dynamic performances.

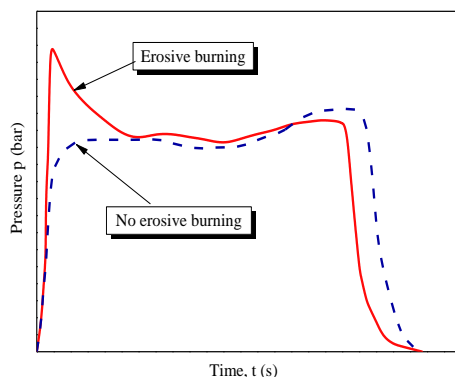


**Figure 1** – Erosive burning

Erosive burning is well known and much discussed in the literature [2,3], but in addition there is no clear pattern for defining the boundary conditions at which it occurs. Each case is different [4,5] and only some similar forms of propellant grains can be compared under recommended

criteria.

There are various methods of preventing or reducing erosive burning, and some of them are mentioned here. In addition, this paper discusses the possible effects of erosive burning on rocket flight.

Erosive burning occurs mainly at the start of rocket motor operation, most often in the central channel of the grain, but also in the gaps and perforations through which the combustion products flow towards the nozzle. This phenomenon usually lasts for a short time, until a certain layer of the propellant is burned out and until the channel for the passage of the gases are expanded. Sometimes this phenomenon can last even longer [6,7], depending on the design of the propellant grain and other motor elements.

Erosive burning is most reflected in the parts of the grain where the highest concentration of gases flowing towards the nozzle is present, in the rear portion of the channel, because the grain port is too small to accept a large amount of gases [8]. This happens when the port to throat ratio is less than 2, but the pressure overshoots of 100 % have been observed even with higher ratios of 4 to 6 [9].

This case often occurs with smaller-caliber rocket motors, which require a large thrust but the smallest possible mass, which implies a high propellant volumetric loading fraction [10] in the motor chamber. This is achieved by means of long propellant grain, usually with complex port shape. Designers often project propellant grain with low port-to-throat ratio, partially neglecting erosive burning or “controlling it to be reproducible from one motor to the next” [1].

In this paper some examples of the controlled erosive burning are shown, as well as some design details that prevent the high intensity of this phenomenon.

The influence of erosive burning process on the ballistic characteristics of the several well known rockets was also analysed. A few own-made softwares, developed in Military Technical Institute (MTI) were used for the analysis. Aerodynamic derivatives were calculated using the DMAC program [11]. On the basis of thrust distribution vs time curves and mathematical models of missile motions, the trimmed (equilibrium) trajectories in vertical plane were calculated using the GMTC-3D program [12]. Ballistic parameters of the rockets were used for calculation of their trajectory parameters using the program UMTC 3D [13].

### AN OVERVIEW OF INDIVIDUAL EXAMPLES

The S-8 is a rocket weapon cal.80 mm, developed by the Soviet Air Force in the 1970's for use by military aircraft [14]. There are two versions of this rocket, S-8 KO and S-8 KOM. Their motors are good examples of fairly strong but controlled erosive burning that is reproducible under the same conditions. Static tests in MB-Lucani, MTI and HK Krušik showed that during the design of these propellant grains the erosive burning was accepted, fully reproductive at elevated temperatures, but so that the system can withstand this without major disturbances.

The port to throat ratio of the propellant grain is generally a good criterion for the occurrence of erosive burning. If this ratio is greater than 4, it is considered that the basic construction of the propellant grain is good. This ratio also can be less than 2, if the propellant burning rate in standard conditions is less than 7-8 mm/s. However, with the S-8 KO and S-8 KOM motors, burning rates are around 11 mm/s and port to throat ratios are less than 2 [15]. It means that erosive burning could be predicted even in design phase. The only question was, which was later proven by experiments, whether the level of erosive burning was acceptable from the point of view of the motor elements safety factor, as well as from the point of view of external ballistics.

In the case of the WS-15, 122 mm Chinese-made rocket motor, which was tested by the Vlatacom Institute at the test laboratory in Egypt, this level of erosive burning should have been higher, but the designers prevented this by the grain shape. Similar logic was also applied for the Russian rocket motors Grad 122 mm and BUK 400 mm.

It is difficult to define the final rules during the design and development of a rocket motor, because each motor is a case for itself. In the case of special design, like for the sustainer for "Bumbar" ATGM guided missile [6,7], this port-to-throat ratio was even higher, about 4.50, which is a condition for less pronounced erosive burning, and yet this phenomenon was very high.

The reason for this was the specific design of the rocket motor with a central pipe, as a result of which there was a high turbulence in the gas flow towards the nozzle, causing a strong phenomenon of erosive burning. System "Bumbar" could not accept this level of erosive burning, so a redesign of the propellant grain and nozzle was carried out.

The port-to-throat ratio is only one in a series of different parameters for assessment for the occurrence of erosive burning. In the case of long propellant grains, like in the motors for unguided rockets S-8 KO and S-8 KOM, the ratio of the burning surface ( $A_b$ ) in the grain channel to the cross section of the channel ( $A_{port}$ ) is one of the very good parameters. In the examples given, this ratio ranges from 235 to 270. Preliminary calculations [15] show that erosive burning can be avoided if this ratio is reduced below 200 or even lower. Such is the case with the Chinese rocket WS-15, tested by Vlatacom institute. For the motors of this type, this parameter seems to be much better, because it takes into account the influence of the grain length. All gases produced by combustion, along the entire channel, go towards the nozzle and their highest concentration is at the rear end of the grain, where the greatest heat transfer from the gases to the surface of the propellant grain occurs. That means the greatest increase in burning rate, and thus the pressure and thrust.

In this paper, we analyzed the phenomena of erosive burning in the rocket motors of the unguided rockets "S-8 KO" and "S-8 KOM" with a diameter of 80 mm, the guided rocket "Bumbar", with a diameter of 136 mm, and their effects on the flight of these rockets. The examples are shown of solving the erosive burning problems in the motors of the rockets "Grad" and "WS-15" with a caliber of 122 mm, and BUK rockets with a diameter of 400 mm.

The S-8 KO rocket motor has a 7-wedges star perforated grain (Fig.2) with burning surface web-distribution like in Fig.3.



Figure 2 – Propellant grain S-8 KO

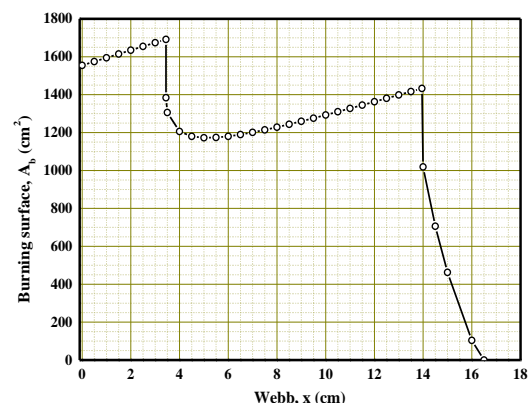


Figure 3 - Burning surface

It is known that the burning rate increases along with temperature, but erosive burning is also more pronounced at elevated temperatures.

Figure 4 shows the diagrams of the pressure vs. time in the S-8 KO rocket motor at characteristic temperatures.

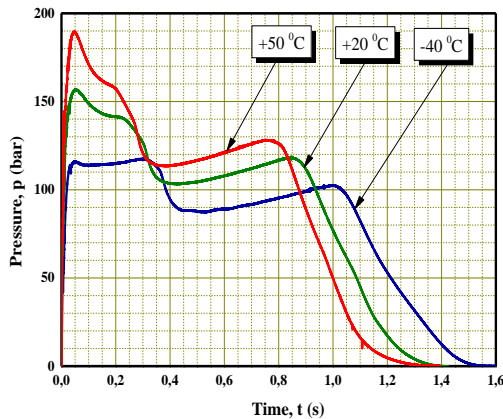


Figure 4 – Pressure distribution in the motor S-8 KO

By comparing the test diagrams (Fig.4) with the burning surface distribution (Fig.3), it is seen that the shape of the pressure curve at low temperature is very similar to the surface distribution. Considering the direct dependence of these two features, this correlation was expected at all temperatures.

However, with the increase in temperature, there is an obvious pressure augmentation in the initial period of motor operation, due to the erosive burning. An increase in pressure can already be seen at standard temperature. During a large number of static tests, it was determined that this phenomenon is reproducible in this motor.

How does it affect the missile's ballistic parameters? We analyzed the case when a rocket is launched from an aircraft that is at a height of 500 m, with an initial speed 200 m/s, and a launch angle of  $-10^{\circ}$ .

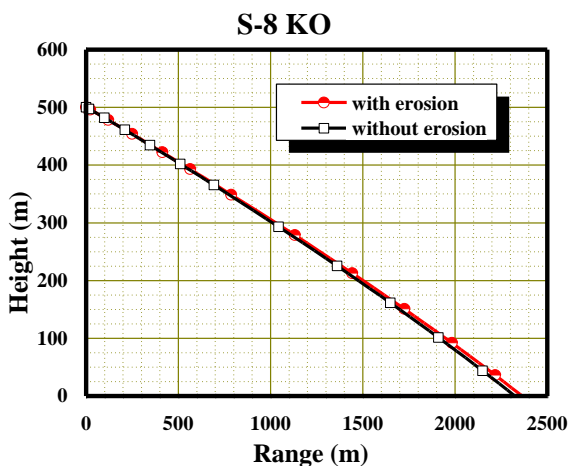


Figure 5 – Effect of erosive burning on missile range

Fig.5 shows two different cases of rocket trajectories, with and without erosive burning. Figs 6 and 7 compare the Range vs Time and Speed vs Time curves for the two cases. There is a big difference between the two operating modes of the motor, but there is no way to avoid this. The rocket designers considered that this impact can be ignored, because the calculation results have shown that

the dispersion of hits is very close to the prescribed standards.

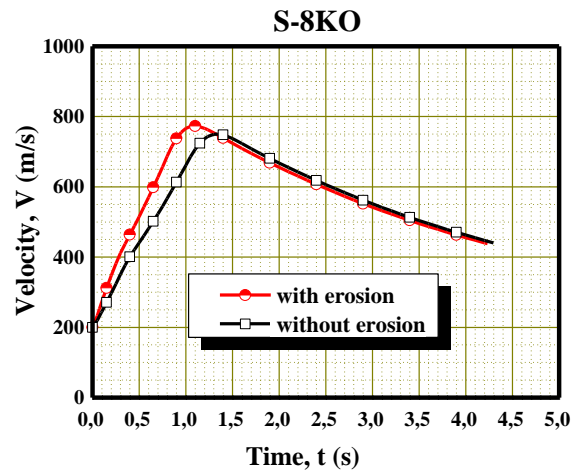


Figure 6 – Effect of erosive burning on rocket velocity

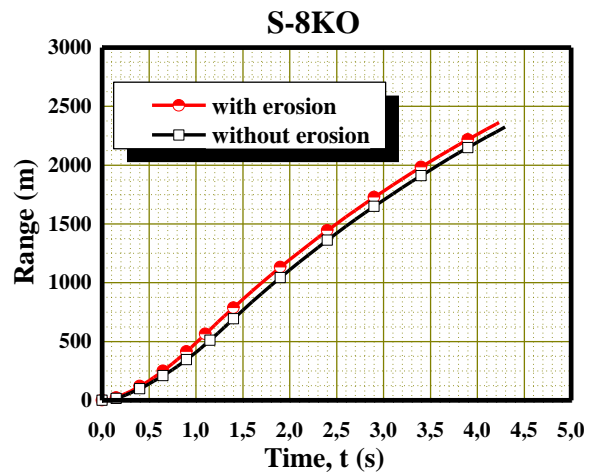


Figure 7 – The effect of erosive burning on the time of reaching the target

Big difference in the motor operating modes at different temperatures looks rather strange, but in this example it has no great effect on the missile's ballistic parameters. It is obvious that the rocket motor designer had experience how these differences affect the ballistic properties or he has solved this problem during development, through the tests, accepting a permissible level of erosive burning. Of course, each development is different and every assumption must be proven in experiments.

A similar analysis was done for the S-8 KOM missile. Propellant grain in the rocket motor, with three arms, burns radially from the outside and inside (Fig. 8).



Figure 8 - Propellant grain S-8 KOM

The propellant grain is very long (fig. 9), and during design it was immediately clear that there are conditions for the erosive burning occurrence.

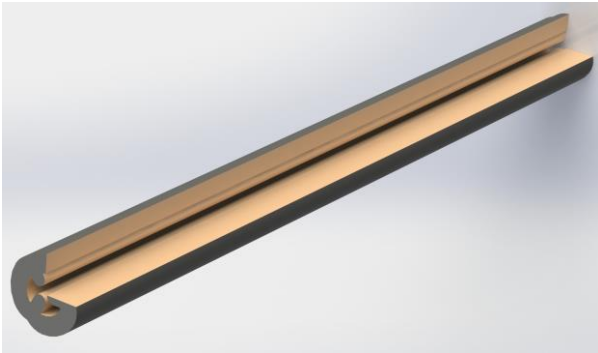


Figure 9 - S-8 KOM propellant grain

During most of the combustion process, the calculated burning surface is neutral, except at the end (Fig. 10).

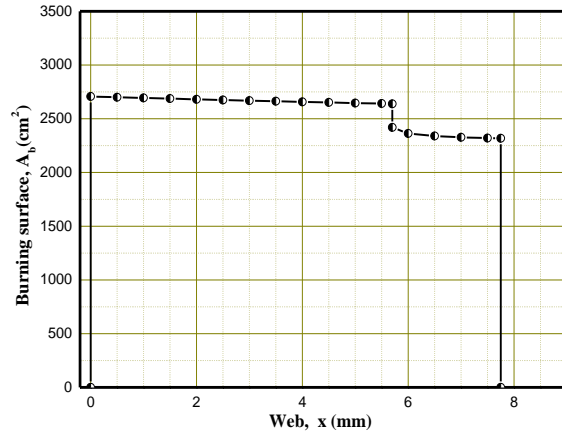


Figure 10 – S-8 KOM burning surface

However, since a large amount of gases hardly passes through the channel, erosive burning occurs in the rear part of the propellant grain, so the initial pressure at +60°C (225 bar) is much higher than the pressure at -60°C (90 bar). The pressure diagram at the extreme low temperature (-60 °C) completely follows the burning surface distribution. At higher temperatures, starting from standard one (+20 °C), pressure diagrams show pronounced erosive burning (Fig.11).

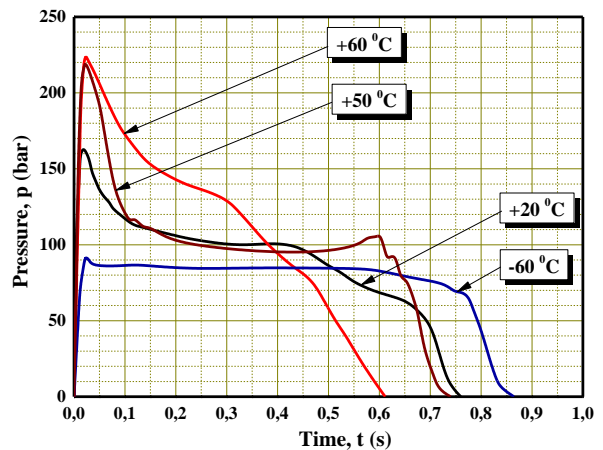


Figure 11 - Pressure distribution in the motor S-8 KOM

One gets the impression that the pressure difference between extreme temperatures is unacceptable. But we know following the practice that this rocket is reliable and in widespread use.



That's why we performed an analysis from the point of view of ballistics of the projectile, to make sure that this is still acceptable. It only means that the designer was able to accept this phenomenon when he achieved its reproducibility during the motor development.

As in the previous case, rocket trajectories were checked for two different cases, with and without erosive burning (Fig. 12). Figures 13 and 14 compare the Range vs Time and Speed vs Time curves for these two cases, in a similar way as for the S-8 KO rocket.

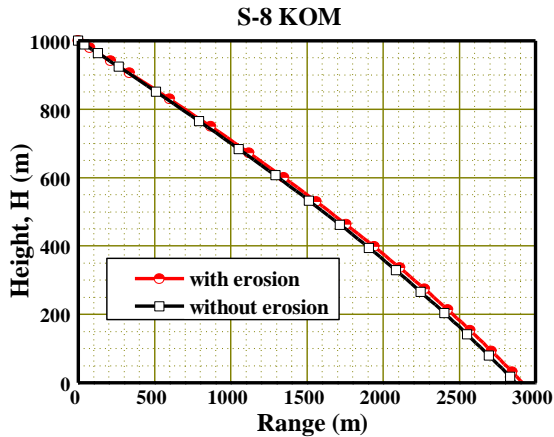


Figure 12- Effect of erosive burning on missile range

Here, the influence of erosive burning on ballistic parameters is also almost negligible, although there is a big difference in the motor operating modes (pressure vs time) with and without erosion (Fig. 11).

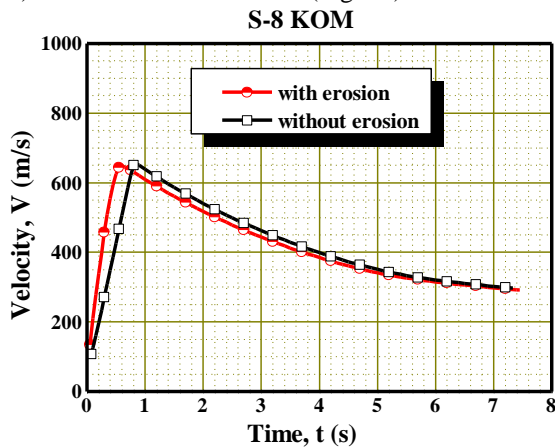


Figure 13- Effect of erosive burning on rocket velocity

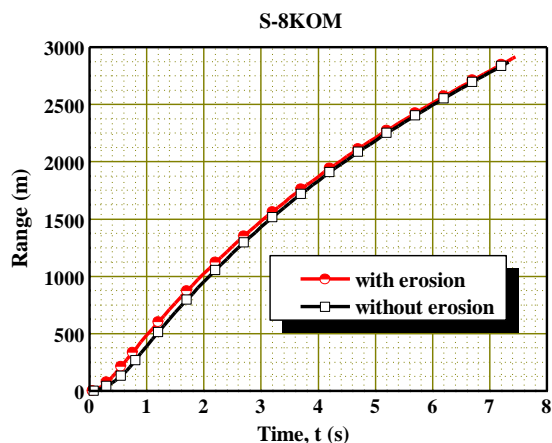


Figure 14 – The effect of erosive burning on the time of reaching the target

If it was determined during the motor development that the phenomenon is reproducible and acceptable from the ballistics point of view, then the pressure increase affects only the mechanical resistance of the motor elements, primarily the propellant grain itself and the motor case.

In the case of the aforementioned S-8 KO and S-8 KOM motors, the designer concluded that pressure increase due to erosive burning does not affect the final mission of the rocket, but the thickness of the motor chamber had to be increased, which affected the entire mass of the rocket. It was estimated that the mass increase was acceptable.

A special case is an example of erosive burning in the sustainer of Serbian-made "Bumbar" ATG missile.

Thrust vector control system is applied with interceptors that are going into and out of the stream of gaseous products at the exit of the nozzle (Fig.15 and 16).



Figure 15 – ATGM Bumbar

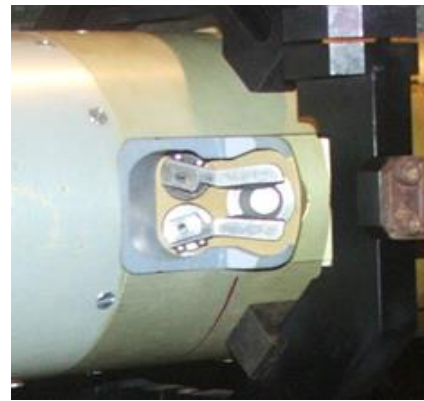


Figure 16 - Thrust vector control system with interceptors

A double based propellant grain in the simple form of internal-burning tube (Fig.17) have been designed for the use in the motor. The grain combines internal and double-end burning [1,8] with outer surface inhibited.

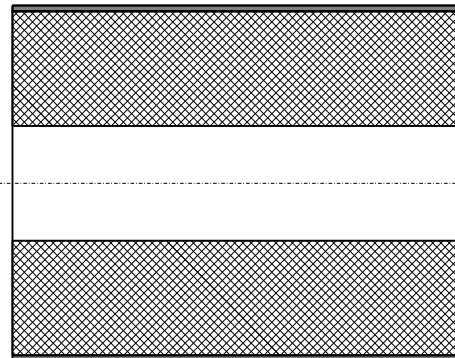


Figure 17- Propellant grain

With the small length to diameter ratio ( $L/D < 2$ ), a mildly progressive-degressive burning surface was expected with

a quite high degree of neutrality, in accordance with the calculations (Fig.18).

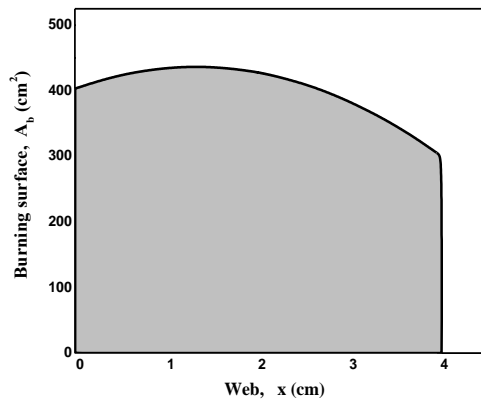


Figure 18 – Burning surface

It could be expected, during design, that both pressure and thrust curves have a slight increase in the central part of the motor operation, proportional to the burning area. Unfortunately, during the initial static tests of the propellant grain in experimental motor, in the temperature range between  $-30^{\circ}\text{C}$  and  $+50^{\circ}\text{C}$ , erosive burning as expected [4,5,9,16] appeared on higher temperatures (Fig. 19).

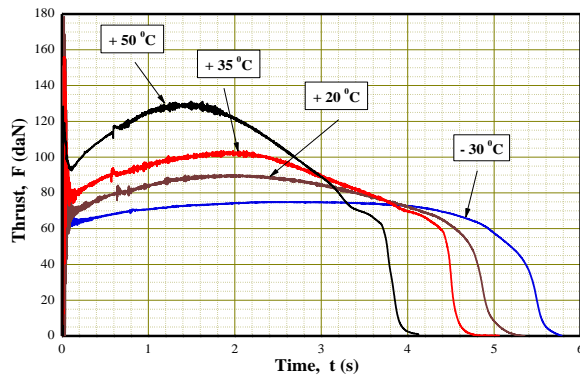


Figure 19 – Thrust vs. time

The main reason is central tube that passes through the grain channel reducing its cross section (Fig.21). Burning products are passing through significantly reduced channel port, in the form of a ring between the outer surface of the central tube and the inner surface of propellant grain. The small passage for the gases created conditions for increasing the flow-rate through the channel.

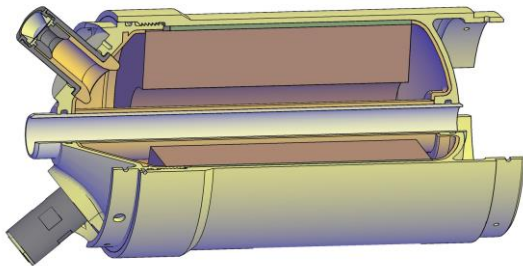


Figure 20 - Test motor intersection

A very good solution to this phenomenon was achieved by a relatively simple change of the propellant grain, by opening a part of the inhibited outer surface of the grain, (Fig 21), which equalized the amount of gases passing

through the channel and gases passing from the outside, through the gap between the grain and the chamber wall [6, 7, 17, 18].

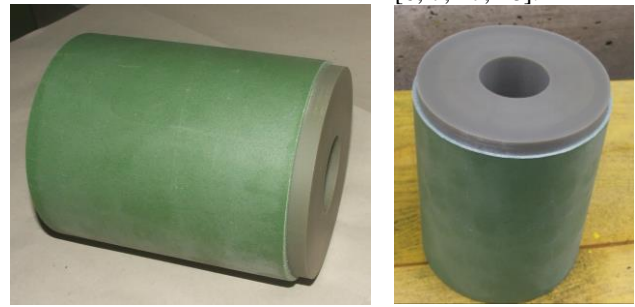


Figure 21 – Modified propellant grain

The tests have now produced the following results (Fig.22):

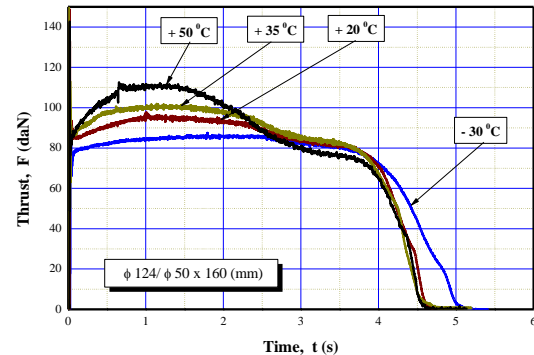


Figure 22 – Reduced thrust after changing the grain shape

Erosive burning is still present at  $+50^{\circ}\text{C}$ , but the thrust increase is much smaller than with the basic solution. This difference is best seen by comparing the two solutions at the same, upper extreme temperature (Fig 23).

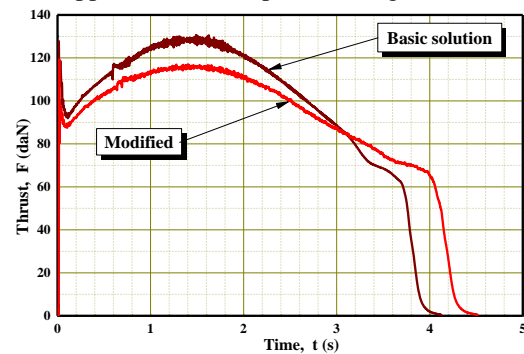


Figure 23 - Comparison of the test results at  $+50^{\circ}\text{C}$  for two different solutions

These two solutions were considered by ballistic analysis. As a consequence of the guidance system with thrust vector control, in the case with highly pronounced erosive burning, the rocket has a smaller effective range (Fig. 24).

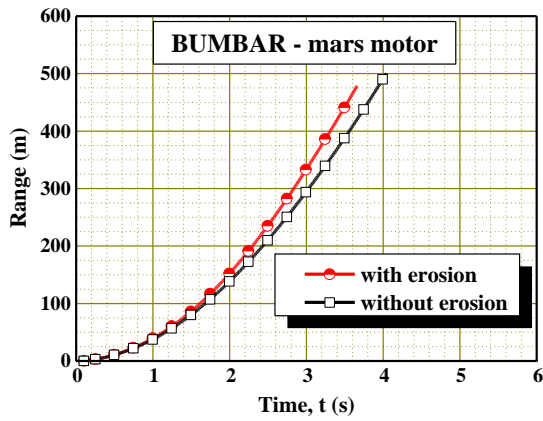


Figure 24 – Range vs Time

At the same time, a higher speed is not enough to reach the required range (Fig. 25).

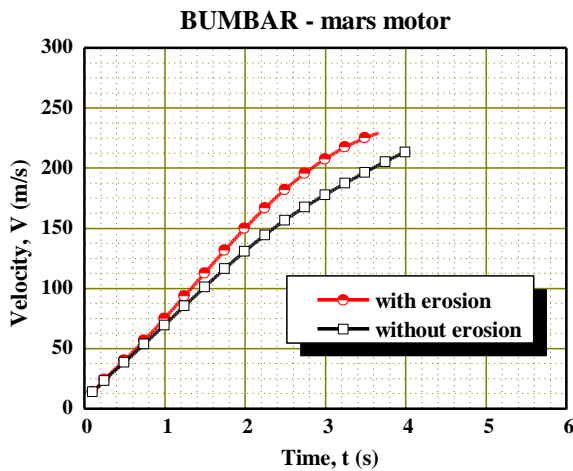


Figure 25 – Velocity vs Time

In the case of nonerosive (or less erosive) burning, in order to maintain trimmed horizontal flight we need 10% more command in pitch ( $\eta$ ) in the first phase of flight, but in the second phase, after 3.5 s, when it is much more convenient, we need 12% less command to achieve horizontal flight Fig.26)

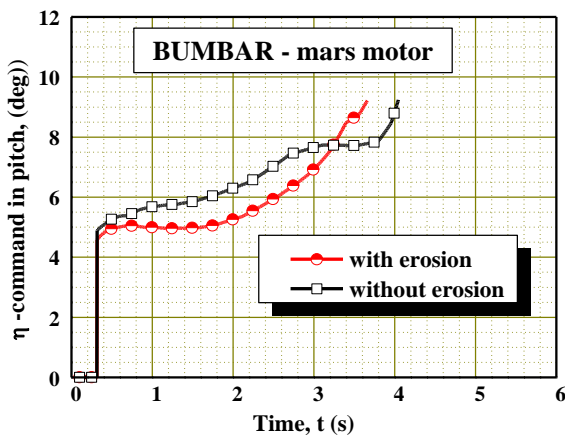


Figure 26 – Command in pitch

And finally, when there is no erosive burning in the motor, the thrust is lower and in the first phase of the flight, the maneuverability is lower. However, in the second phase of the flight, which is much more important, the maneuverability is greater (Fig. 27).

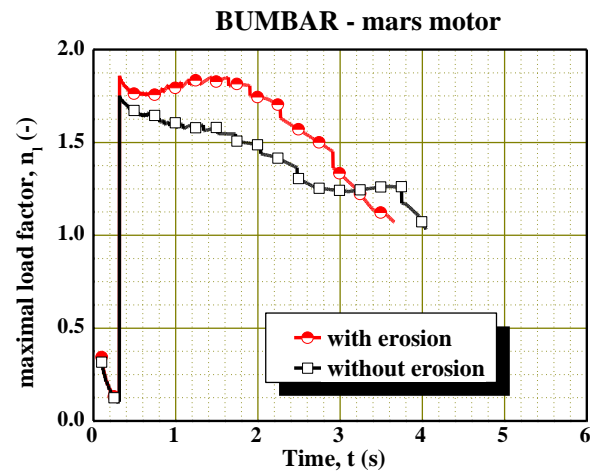


Figure 27 – Maximal load factor

The general conclusion is that in the Bumbar system, erosive burning led to a clearly pronounced weakening of the missile's ballistic properties.

In this particular case, there was another important reason to reduce erosive burning in a constructive way. The increase in pressure at the exit of the nozzle affected the appearance of greater obstacles for the entry of control elements (interceptors) into the stream of combustion products, as a result of which the thrust vector control system was not effective.

When the assumed intensity of erosive burning in the design phase and during development is not acceptable from a ballistic point of view, it is necessary to reduce this phenomenon with a suitable design of the propellant grain.

If neutral burning is desired, which is achieved by radial burning of cylindrical grains, both from the inner and outer side, then the propellant grain may be made in two parts, where the part of the grain that is closer to the nozzle is made with a wider channel that can accept the entire amount of gases from both parts of the grain (Fig. 28).

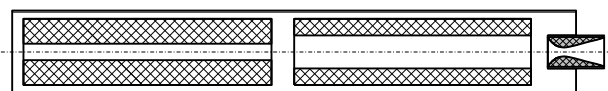


Figure 28 – Propellant grain with two different cylinders

We have such an example with the Grad 122 mm rocket motor, where the required burning surface is achieved by internal-external burning tube. Very high erosive burning is reduced to an acceptable level, although at +50°C the thrust at the start of motor operation is even 80% higher than the thrust in the steady state mode (Fig.29). The diagram shows that the phenomenon is reproducible. These tests were carried out in the laboratories in MB-Lučani and MTI.

Ballistic analysis showed in this case, as well, that erosive burning didn't affect the change in the total impulse of the motor, so it didn't have a great impact on the range and the rate of reaching the target.

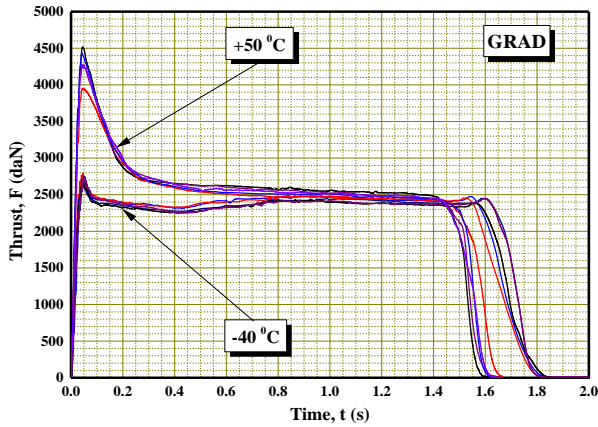


Figure 29 – GRAD, erosive burning

This type of solution is a kind of compromise, because the increase in the diameter of the grain channel reduced the volumetric loading fraction of the grain, and also the two parts of the grain increased the number of additional inert elements in the motor chamber.

Small-caliber motors can achieve high thrust and total impulse only by long propellant grain with radial burning, with a complex-shaped channel that has a large burning surface. This leads to a high production of gases that flow through the channel to the nozzle. The largest amount of gases is at the end of grain channel, where the erosive burning occurs.

This phenomenon is reduced in a similar way as in the previous case, by increasing the cross-section of the grain channel at the rear end. There are several examples in our practice where the front part of the channel is progressive with a small circle shaped cross-section, and the rear part of the channel is star shaped and degressive (Fig.30).

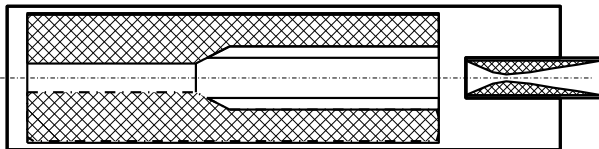


Figure 30 – Circle-Star propellant grain

Such an example is the propellant grain of the Chinese-made WS-15 122 mm rocket. The Vlatocom Institute tested these motors in its laboratory in Egypt. At elevated temperature, 5 motors were tested, whose Thrust vs Time diagrams are shown in Fig. 31.

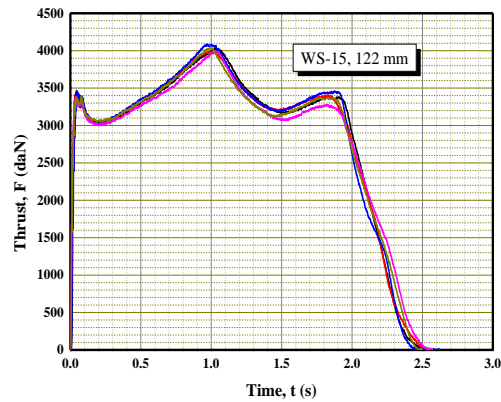


Figure 31 – Thrust vs time, WS-15

On the diagram (Fig. 31), one can recognize a very mild occurrence of erosive burning, which is completely reproducible, and then both progressive and degressive parts of the diagram.

It is important here that complete reproducibility of the erosive burning was achieved in all tested engines.

The Military Technical Institute in Belgrade produced a similar propellant grain (Fig.32) for its RLN rocket, popularly called "Franky", with an even better thrust diagram and with very little erosion at the start of the motor work, although the propellant grain is quite long.

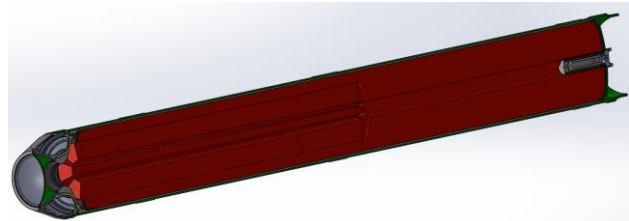


Figure 32 – RLN propellant grain

A similar principle of avoiding erosive burning was also applied to the Russian BUK motor 400 mm (Fig.33).

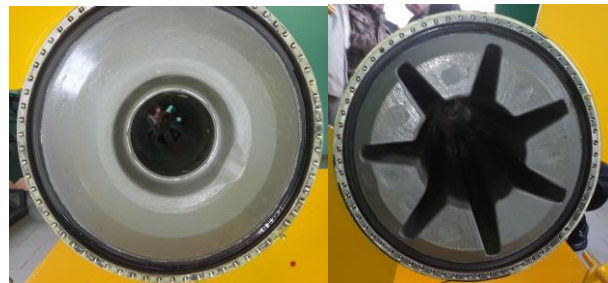


Figure 33 – BUK, The front and rear part of the propellant grain

Unfortunately, we did not have the opportunity to determine the operation mode of this motor through an experiment. The shape of the grain with two different channel ports has a double goal, first of all approximately achieving the desired operating mode, and then preventing erosive burning at the start of motor work.

#### 4. CONCLUSION

Erosive burning is a negative phenomenon in a rocket motor that leads to a change in designed properties.

The basic pressure dependence on the burning rate in rocket motor is usually used for standard ambient temperature. There are many attempts in the literature to theoretically describe erosive burning dependence. A large number of different criteria have been defined, but its true intensity is almost impossible to predict, except following previous experiences with similar solutions.

During this phenomenon, there is a pressure increase in the motor, causing double effects. It affects the strength of motor elements and the safety factor, which requires their increased mass. In addition, the change in the thrust distribution affects the ballistic properties of the rocket.

The experience with small unguided rockets says that this influence is not great until there is no a big difference in total impulse. Sometimes, but rare, this influence may be quite large, due to a big difference in motor operating modes, especially at different temperatures. That is why rocket motor designers for this type of rocket consciously accept the risk of erosive burning, in order to ensure that the volume of the motor chamber is filled with rocket propellant as much as possible. And yet, the intensity of this phenomenon must be controlled, so that it should be acceptable and reproducible.

Erosive combustion has a much greater impact in guided missiles and one such example is shown in this paper for our "Bumbar" missile. Ballistic analysis showed that the impact was not large enough to prevent the missile's mission, but it was enough to reduce its characteristics.

When there are similar experiences, this phenomenon can be included already during the initial design phase. In addition, there are various ways to reduce and control the intensity of this phenomenon. Some of them are presented in this paper.

#### References

- [1] George P. Sutton, Oscar Biblarz. 2010. Rocket Propulsion Elements. Eighth edition. John Wiley&Sons inc. ISBN: 978-0-470-08024-5.
- [2] R. Arora, X. Wu, F.X. White and K.K. Kuo, 23 May 2012, „Erosive Burning of Composite Solid Propellants: Mechanism, Correlation, and Grain Design Applications”, Journal of Spacecraft and Rockets.
- [3] M. K. King, "Erosive Burning of Solid Propellants," Journal of Propulsion and Power, Vol. 9, No. 6, November-December 1993.
- [4] Wimpres, R. N.: 1950. Internal Ballistics of Solid-Fuel Rockets. McGraw-Hill Book Company, New York-Toronto-London.
- [5] Marcel Barrere, Andre Jaumotte, Baudouin Fraeijs de Veubeke, Jean Vandekerckhove. 1960. Rocket Propulsion, Elsevier Publishing Company, Amsterdam-London-New York.
- [6] N. Gligorijević, S. Živković, S. Subotić, M. Nikolić, S. Kozomara, M.A. Boulahlib: „Solving an Irregular Burning Problem in a Small Rocket Motor“, Scientific Technical Review, 2014, Vol.64, No.2, pp.
- [7] M. A. Boulahlib, T. Radia, S.Živković, S. Subotić, N. Gligorijević: „An Example of a Successful Erosive Burning Reduction of a Small Rocket Motor“, OTEH 2014.
- [8] NASA. 1972. Solid propellant grain design and internal ballistics. NASA Space Vehicle Design Criteria SP-8076.
- [9] King K. Merrill. 1981. Erosive burning of composite solid propellants. Atlantic Research Corporation. Air Force Office of Scientific Research, AFOSR-TR-81-0395, AD A098088.
- [10] NASA Sp-8039: Solid Rocket Motor Analysis and Prediction, Space Vehicle Design Criteria, Monograph, May 1971.
- [11] Ćurčin M., Stojković S., Milošević M.: DMAC – Derivatives of Missile Aerodynamic Coefficient, MTI Beograd, 1995.
- [12] Ćuk D., Ćurčin M., Mandić S., Stojković S.: GMTC 3D: Guided missile Trajectory Calculation – 3 Degree of freedom motion model, MTI Beograd, 2002.
- [13] Ćurčin M.: UMTC 3D – Unguided missile Trajectory Calculation – 3 Degree of freedom Motion Model, MTI Beograd, 1996.
- [14] [https://en.wikipedia.org/wiki/S-8\\_\(rocket\)](https://en.wikipedia.org/wiki/S-8_(rocket))
- [15] N. Gligorijević: Proračun površine sagorevanja za pogonska punjenja S-8, Analiza mogućeg projekta raketnog motora R-70, Krušuk, 2022.
- [16] Landsbaum M. Ellis. 2005. Erosive Burning of Solid Rocket Propellants - A Revisit. Journal of Propulsion and Power, Vol. 21, No. 3, pp. 470-477. doi: 10.2514/1.5234.
- [17] Tehničko rešenje: Pogonsko punjenje Marš Motora Bumbar, Naučno veće VTI, Int.br.01/94-241, 28.09.2015.
- [18] Tehničko rešenje: Marš Motora Bumbar, Naučno veće VTI, Int.br.01/156-79, 18.05.2016.



## ASSESSMENT OF EXPOSURE TO PHYSICAL HAZARDS IN THE WORKING ENVIRONMENT DURING TESTING OF PROTOTYPES

SNEŽANA JOVANOVIĆ

Technical Test Center, Belgrade, e-mail: [sneza.jovanovic.toc@gmail.com](mailto:sneza.jovanovic.toc@gmail.com)

DRAGAN STOJADINović

Technical Test Center, Belgrade, e-mail: [dragan.stojadinovic@vs.rs](mailto:dragan.stojadinovic@vs.rs)

MARTIN JOVANOVIĆ

Institute of Public Health "Dr. M. J. Batut", Belgrade, e-mail: [martinjovanovic.arch@gmail.com](mailto:martinjovanovic.arch@gmail.com)

ALEKSANDAR ĐURIĆ

University of Defense Belgrade, Military Academy, e-mail: [aleksandar.djrc@gmail.com](mailto:aleksandar.djrc@gmail.com)

**Abstract:** This paper presents only a part of the risks and harmfulness to which the employees working in Serbian MoD and especially in Technical Test Center are exposed during tests on new armaments and various other equipment under development. In addition to the results of noise and vibration measurements in the working environment at the training grounds and the airport, the risks during laboratory and experimental-exploitation tests in the field are presented. Noise and vibration as harmfulness effects were measured and evaluated according to the relevant criteria, while far more dangerous risks of working with prototypes are immeasurable, unpredictable and not included in the regulations.

**Keywords:** work environment, noise, vibration, risk assessment.

### 1. INTRODUCTION

Activities in the army are characteristic of their specificity, numbers and diversity, as well as in civilian sector. The common motto of those employed in the army is respect for hierarchy and discipline as well as behavior in accordance with high moral values, which is often psychologically demanding and stressful. It is a known fact that being a soldier is one of the most stressful occupations, considering the factors of exposure to dangers, the expected level of mental and physical readiness and other specifics of military relations and life.

On the other hand, professional-technical staff, responsible for weapons and military equipment, are exposed to risks and dangers of the widest spectrum of harmfulness in the work environment: physical, mechanical, chemical, ergonomic, biological and previously stated psychosocial.

The strategic activity of preventing and reducing the occurrence of accidents is effective in certain domains such as military transport, but when performing many other tasks (and in order to successfully perform them), the exposure of the perpetrators to harm is inevitable.

The army is equipped with weapons and military equipment resources according to the model: own development, acquisition by license, procurement or donated final product, joint development with an international partner or a combined method of equipping. The advantages of own development from domestic

sources are numerous: independence from external factors, industrial progress of the country, strengthening the scientific research resources, etc.

Armament and military equipment (from domestic production, imported or after general overhaul) are put into operational use and exploitation based on and after testing and quality assessment.

An important, experimental phase in the armament and military equipment domestic development is the construction and testing of prototypes or small test batches. Prototypes are only the basis for the development of the finished product, therefore many technical and functional characteristics are unpredictable, which is the reason for possible serious accidents during their testing. The aim of the examination is to verify the fulfillment of the set tactical-technical requirements and the compliance of the asset with the technical regulations of defense.

When adopting and introducing new assets into the military systems, the satisfaction of the fulfillment the requirements of ergonomics, human engineering and adaptation of the asset to man, so one can operate and work efficiently, successfully and with quality.

The Technical Test Center is authorized to conduct final (from domestic development), verification and homologation (finished domestic and foreign products) tests of armament and military equipment. The following are examined: weapons (classical, aviation, naval), all types of vehicles, aircrafts and ships (combat, non-combat, special), engineering machines, means of nuclear, biological and chemical protection and electronic

(telecommunication, optoelectronic, fire control) means. For the needs of all types of tests, special measurements are performed in the laboratory, polygon and field (trial and operational tests). The Technical Test Center provides services of special measurements and polygon and other tests at the request of customers outside the Army, in order to test and evaluate their quality.

## 2. EXAMINATIONS ON PHYSICAL DAMAGE AND ERGONOMICS

As a part of the complex testing of assets that are expected to enter the military use, the fulfillment of requirements for the protection of the environment and the working environment is also checked. Possible harms are being measured, and after processing and analyzing the results, an assessment of the fulfillment of requirements that follow the latest standards is given.

In this paper, as an example, the results of noise and vibration measurements during the testing of the following prototypes are presented: on the military training ground – wheeled self-propelled gun-howitzers, on the military airport - school plane, during field test operation - vehicles with a superstructure for military equipment and armored vehicles. The results were evaluated according to health and comfort criteria: for noise, the Rulebook on preventive measures for safe and healthy work with exposure to noise (based on EU directive ES/10/03 and ISO 9612 standard), for vibrations, the Rulebook on exposure to vibrations (based on ES /44/02 and ISO 2631, 5349).

An example of immeasurable ergonomic hazards and risks when working with heavy loads during laboratory field tests of static and dynamic characteristics is also presented.

### 2.1. Noise and vibrations in the working environment of a Wheeled Mobile Howitzer on a military training ground

Shot noise measurements from a 155 mm howitzer were made with a NetdB12 measurement system (made by 01dB Metravib from France) with 1/4" microphones (free field, type 46AE G.R.A.S).

The measurement places were in the driver's cabin, the commander's place and the gunner's place, where the microphones are directed towards the shooting direction, and at a height corresponding to the position of the crew member's head.



**Figure 1.** Test object at the military training ground

The measurement results (Table 1) are expressed in  $dB_{C(peak)}$ , the unit for high-energy impulse noise, as well as in  $dB_{C(1)}$  related to impulse noise. Also an 1/3 octave noise analysis was also performed (Figure 1a).

**Table 1.** Noise levels of a 155 mm howitzer

Measuring point	Noise level $L_{peak,C}$ (dB)	Noise level $L_{impulse,C}$ (dB)
cabin	154.8	148
commander	158.5	149.6
gunner	159.6	150.9

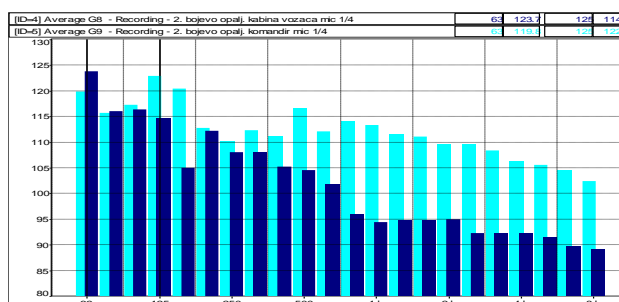


**Figure 1a.** 1/3 octave spectrum of firing at driver and commander position

Vibration testing when firing from a howitzer was performed with a dedicated vibrometer Maestro 01dB Metravib for workplace measurement, supported by software according to EC/44/02 and ISO 2631-1, 4, 5. The measuring device has a three-axis accelerometer built into the seat adapter to determine the vibrations transmitted to the whole body in the frequency range 0 ÷ 10,000Hz.

The results of triaxial vibration measurements are shown for the position of the gunner, from the point of view of the quality of health and comfort (Figure 2).

Whole body						
Quality	Health					
Body position	Seated					
Measurement location	Seat					
Type	aw					Exposure
Axis	X	Y	Z	Overall av	Overall A(8)	
Weighting	Wd	Wd	Wk			
Coefficient	1.4	1.4	1			
Level (m/s <sup>2</sup> )	1.52	0.70	5.87			
Corrected (m/s <sup>2</sup> )	2.12	0.97	5.87	6.31	5.87	8h
Warning level (m/s <sup>2</sup> )					0.50	3m29s
Maximum level (m/s <sup>2</sup> )					1.15	18m27s
Exposure level A(8) is above maximum level						
Type	Peak factor					Max.
Axis	X	Y	Z			
Peak factor	2.98	3.20	4.02		4.02	
Peak factor is smaller than 9						
According to Standard 2631-1, A(8) assessment is recommended						
Type	VDV					Exposure
Axis	X	Y	Z	Max. VDVeq		
Weighting	Wd	Wd	Wk			
Coefficient	1.4	1.4	1			
VDV dose (m/s 1.75)	4.37	2.09	19.47			
Corrected (m/s 1.75)	6.12	2.93	19.47	19.47	5s	
Warning level (m/s 1.75)				9.10		
Maximum level (m/s 1.75)				21.00		
VDV level is above warning level						

Whole body						
Quality	Comfort					
Body position	Seated					
Measurement location	Seat					
Type	aw					Overall av
Axis	X	Y	Z			
Weighting	Wd	Wd	Wk			
Level (m/s <sup>2</sup> )	1.52	0.70	5.87		6.10	
2.00 m/s <sup>2</sup> <= Aeq : extremely uncomfortable						

Figure 2. Vibration measurement report at the gunner's position according to criteria for health and comfort

### 2.2. Noise in the operating environment of a school plane at a military airport

In the working environment of the technical staff and crew of the school plane in ground mode, after warming up, the noise was measured with two directional 1/2" microphones (with the previously mentioned noise measurement system) at a height of 0.94 m, at a distance of 1.64 m from plane and at an angle of 90° and 45° placed left of the engine. The results are shown in Table 2.

Table 2. Noise level in the working environment around the school plane

Mode of work on the ground at:	Equivalent level, fast dB (A)	
	Measuring point of the microphone 45°	Measuring point of the microphone 90°
1800 rev	109.3	103.5
2200 rev	117.2	112.6
2400 rev	121.7	117.8
2700 rev	124	121
Add gas slowly (1200÷2610) rev	122.2	118.6
Checking the magnet 2 times with holding the work one of them for 10 seconds	114.5	108.9
Checking the regulator - easy	113.6	108.9

### 2.3. Noise and vibrations in the superstructures of military vehicles and armored vehicles during off-road driving

During the testing of military vehicles (mobile weapons and military equipment) in real conditions of exploitation, numerous parameters related not only to functionality, but also to working conditions and environmental protection are measured.

Of the many measurement results that affect health and comfort, the part related to noise and vibrations when driving in the superstructure of a vehicle with military telecommunications equipment (Table 3) and when driving in an armored military vehicle (Table 4) is shown.

Table 3. Results of oscillations measurements and noise at the operator's place in the cabin of a vehicle with a superstructure while driving at speeds adapted to the tracks

Track type	Eq. triaxial accelerat. for comfort a <sub>v</sub> (m/s <sup>2</sup> )	Comfort rating	Eq. triaxial speed up for health a <sub>v</sub> (m/s <sup>2</sup> )	Eq. noise level in the cabin (dB(A))
wasteland	1.40	very unconf.	1.72	78.4
macadam	1.26	very unconf.	1.47	79.8
asphalt	0.86	unconf.	0.95	77.5



**Table 4.** Results of noise measurements inside an armored vehicle during off-road driving at the driver's (passenger's) and crew's places

Track type	Speed (km/h)	Eq. noise level (dB(A)) driver / crew
asphalt	50	84.4 / 83.7
	60	85.6 / 85.1
wasteland	30	82.3 / 82.1
	40	86.1 / 85.4
plain macadam	30	81.7 / 80.8
	40	85.7 / 83.4
	50	84.0 / 83.2

## 2.4. Risks and dangers during experimental tests of static and dynamic characteristics of movable assets of armament and military equipment in laboratory and field conditions

Experimental methods of testing the characteristics of the support system and stability (load distribution and center of gravity of the dynamic system) of various types and types of military vehicles of various types and purposes are extremely risky for drivers and researchers and all other test participants too. Vehicles (wheelers, crawlers and amphibians) are lifted and overturned in laboratory conditions, in the field they overcome obstacles and limit angles of lateral, frontal and rearward inclination, while in strong rivers amphibians are tested for swimming.

The mentioned vehicles weigh up to 40 tons, so it can be assumed what kind of dangers they pose and what kind of accidents can happen. Regulations do not regulate all situations that can happen realistically and unexpectedly.

One of the common measurements of the center of gravity is shown in Figure 3, while Figure 4 shows the overcoming of the front slope obstacle in off-road conditions.



**Figure 3.** Working under a hanging vehicle - testing the center of mass



**Figure 4.** Vehicle tracking when moving down the front boundary slope

## 3. CONCLUSION

From the presented results of measurements at the training ground when firing from howitzers, it can be seen that the gunshot noise levels (expressed in  $\text{dB}_{\text{C(peak)}}$ ) at the crew positions are greater than  $140 \text{ dB}_{\text{C(peak)}}$ .

According to the EU Directive 2003/10/EC on minimum requirements for noise exposure, the limit value to which an employee can be exposed using personal protective equipment for impulse noise is  $140 \text{ dB}_{\text{C(peak)}}$ , and according to the Republic of Serbia Rulebook on preventive measures for safe and healthy work at exposure to noise, the limit value of exposure to noise is  $137 \text{ dB}_{\text{C(peak)}}$ , so the negative assessment of the noise in question is obvious. From the analysis of 1/3 octave spectra of the subject impulse noise, it can be seen that the characteristic frequencies are in the low-frequency range corresponding to large-caliber ammunition. Also, from the reports of the measured vibrations in the howitzer crew positions, extreme discomfort and time in that working position of 3.5 minutes to the warning value (or 18.5 minutes to the limit value) of health exposure can be seen.

The measured equivalent noise levels in the environment of the school plane during ground operation mode (airport) significantly exceed the limit value of daily exposure to noise of  $85 \text{ dB(A)}$  prescribed by the aforementioned noise regulations from the point of view of hearing protection from damage.

According to the measurement results, the oscillations in the cabin of the vehicle with a superstructure during off-road driving on asphalt are in the domain of uncomfortable driving, while when driving on wasteland and plane macadam road, they are in the domain of very uncomfortable driving. In relation to the criteria for harm to health, driving this off-road vehicle should be time-limited from the aspect of oscillations as in Table 3. The analysis of the measured noise in the cabin with military equipment (is in the range of  $77.5 \div 79.8 \text{ dB(A)}$ ) on asphalt and macadam results in a spectrum that is below

the limit norm NR80 (only physical work without mental strain is possible). Also, the noise levels measured in the armored vehicle in real operating conditions when driving on all types of tracks exceed the action (80 dB(A)) and mostly the limit level (85 dB(A)) of noise exposure, while the noise spectrogram in the closed space of the vehicle corresponds to the classification curve NR90, when only physical work is possible without mental strain.

The subjective feeling of discomfort while driving from the aspect of oscillations and noise is much worse than the measurement results due to the effect of combined health hazards (stiffness, lack of air conditioning, oscillations with impacts, noise or screeching from numerous racks with equipment, etc.).

The exposure limits given by unilateral directives are not sufficient for such workplaces. Also, you should keep in mind the problem of not being able to use ear protectors while driving due to monitoring the road situation.

All ergonomic harms cannot be predicted and counted, nor can they be defined by criteria. As these are assets under development, prototypes and various other samples which characteristics are still being tested, the probability of unpredictable and undesirable events is very high.

## References

- [1] Directive 2002/44/EC of the European parliament and the council-Minimum health and safety requirements regarding the exposure of workers to the risks arising from physical agents (vibration), June 2002.,
- [2] ISO 2631 - Mechanical vibration and shock-Evaluation of human exposure to whole-body vibration, May 1997.,
- [3] Directive 2003/10/EC of the European parliament and the council- Minimum health and safety requirements regarding the exposure of workers to the risks arising from physical agents (noise), 2003.,
- [4] ISO 9612 - Acoustics – Determination of occupational noise exposure – Engineering method, 2009.,
- [5] ISO 1999 – Acoustics - Determination of occupational noise exposure and estimation of noise-induced hearing impairment, 1990.,

Правилник о начину и поступку процене ризика на радном месту и у радној околини ("Службени гласник РС" бр. 30/10).



## PRESENTATION OF THE USE OF MODERN FIRE CONTROL SYSTEMS AND THEIR IMPLEMENTATION IN INFANTRY UNITS

MARKO CRNOGORAC

1<sup>st</sup> Army Brigade, Serbian Armed Forces, Novi Sad, [crnogorac.marko995@gmail.com](mailto:crnogorac.marko995@gmail.com)

MARKO RADOVANOVIC

University of Defense Belgrade, Military Academy, [markoradovanovicgdb@yahoo.com](mailto:markoradovanovicgdb@yahoo.com)

**Abstract:** *The implementation of fire control systems in infantry units represents a significant step towards modernizing and enhancing military operations. Integrating these systems enables infantry units to precisely and efficiently coordinate fire support from air, land, and sea, thereby reducing reaction time and increasing the accuracy of attacks. This paper presents the technology, training, and tactical procedures required for the successful integration of modern fire control systems into the infantry units of the Serbian Armed Forces. The focus is on contemporary tools such as laser rangefinders, advanced radio devices, and GPS systems that allow fire control operators to identify targets and direct fire with minimal collateral damage. Additionally, the paper examines the challenges in implementation, including the need for comprehensive training of infantry units. This study provides guidelines and recommendations for the optimal use of modern tools and fire control systems in operations, emphasizing the importance of technological advancement and coordination within the military system.*

**Keywords:** *Fire control Systems, JTAC (Joint Terminal Attack Controller), GPS, UAV, Infantry*

### 1. INTRODUCTION

Modern warfare has evolved due to intensive technology integration through all military systems. High precision ammunition, guided by complex navigation systems and integrated into unique command and control (C2) structure had a pivotal role in operational success, force protection and force support in critical moments.

Systems for fire control through last 20 years were developed with increased pace. Their use in operations enabled units to deploy high precision strikes, reducing collateral damage and optimizing costs of operation. Their effectiveness has been proven countless times in operations through Middle East, Africa, Ukraine [1] and Nagorno-Karabakh.

Complexity of these systems arises from their elements which include: observation equipment – land devices (optical, color camera, passive or thermal) or air systems (drones, aircrafts, helicopters, etc.) [2], communication equipment (radio systems), software with user interface (UI) to quickly gather, prepare, send data to command element and to distribute target package to fire support unit, fire support assets - artillery or close air-support (CAS) and human element – high performer in tactical thinking and accurate equipment usage.

Through this study, all of above mention elements will be presented in order to structure existing equipment in unique fire support system that will unite the actions of company forward observers (FO), tactical air control parties (TACP) and joint terminal attack controllers

(JTAC).

Additionally, this paper will analyze data required to standardize forms for requesting fire support in order to reduce time needed to analyze target, prepare and deploy fires. This standardization makes troop training easier, enables quick reaction, less time spent in radio transition and reduces risk of human-made mistakes.

Paper will present in-use equipment capabilities, how to integrate it in infantry tactics based on premium military experiences. Starting point will be targeting cycle and its implementation in military operations and units' organization. Literature analyzed represent both domestic and foreign academic researches on similar topics, foreign field manuals, tactical procedures and technical overviews, equipment user manuals and on-field usage analytical reviews. This comprehensive approach will offer insights into optimizing fire support systems for future military operations. The goal is to enhance the efficiency and effectiveness of military operations by leveraging advanced technology and standardized procedures. Ultimately, this study aims to contribute to the ongoing development and refinement of modern warfare tactics.

### 2. TARGETING PROCESS

A target is an entity or object that performs a function for the adversary, considered for possible engagement or other action [3]. Targeting is the process that matches the target with an adequate response to achieve desired effects. In an operational context, fire may be placed to

deceive, defeat, degrade, delay, deny, destroy, destruct, disrupt, divert, exploit, interdict, neutralize, or suppress a target. The targeting process includes a series of activities as shown in Figure 1.

- Joint Terminal Attack Controllers (JTAC) – experts in navigating both ground and air support. They are usually within special forces community and are attached to crucial operation elements [6,7].

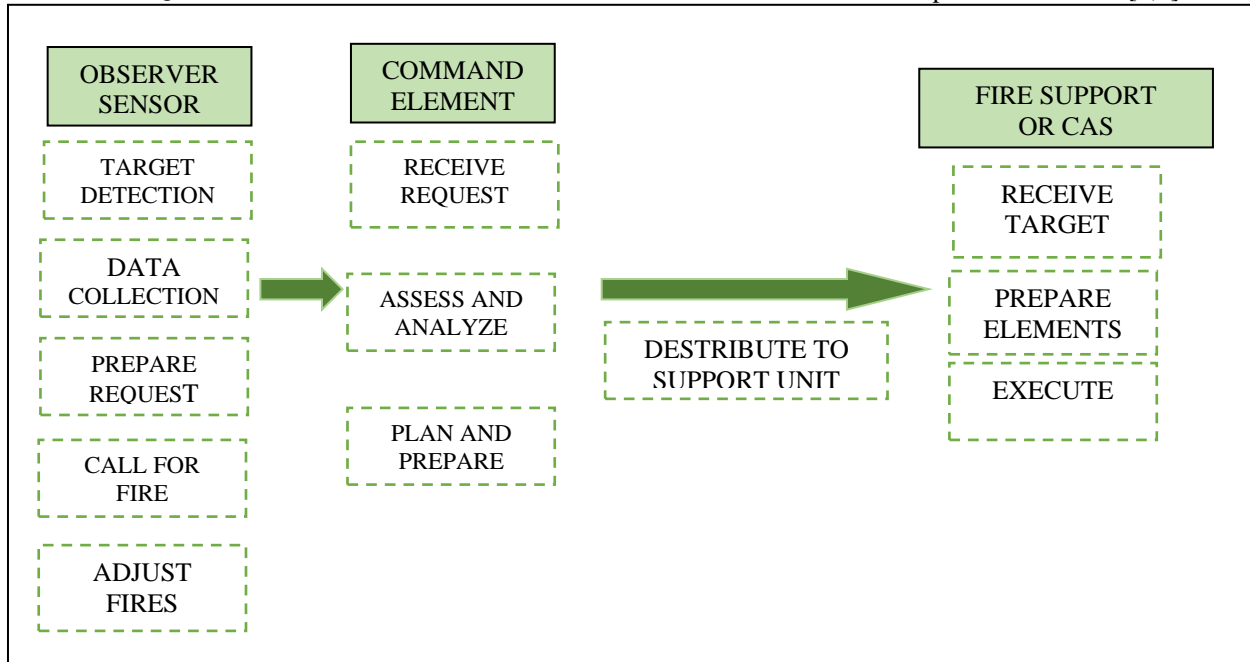


**Figure 1.** Targeting process

The first step for a unit in contact is to detect the target. The detection method depends on the tactics and equipment used, which can vary widely. Sensors used for detection can be either human or technical, each having its own advantages and limitations. Human sensors rely on trained personnel such as forward observers, TACPs, and JTACs, who use their skills and experience to identify and verify targets. Technical sensors, on the other hand, include a range of equipment such as optical instruments, camera systems, drones, and other reconnaissance technologies. These devices enhance the detection capabilities by providing real-time data and broader surveillance coverage. Effective detection is critical, as it sets the foundation for subsequent steps in the targeting process, including identification, tracking, and engagement of the target. The integration of both human and technical sensors ensures a comprehensive approach to targeting, enhancing accuracy and effectiveness in various combat scenarios.

### 3. OBSERVER ELEMENT

Human sensors are experts who completed extensive training in classic infantry tactics, weapons, observation equipment, fire support navigation tactics, communication systems, etc. Depending on asset they are guiding, these soldiers may be:

- Forward Observers – usually one on platoon or company level trained to guide fire support assets up to brigade level [4],
- Tactical Air Control Parties (TACP) – Airforce experts in navigating and guiding Close Air Support (CAS). They are usually attached to decisive operation battalion or brigade [5].

Technical sensors include following:

- Optical instruments (binoculars, spotters, etc.),
- Camera systems (color, thermal, passive),
- Various radars and
- Drone carried sensors for aerial air reconnaissance[8,9].

Besides listed, following equipment may be used for target data collection:

- Laser pointers (LP),
- Laser range finders (LRF) and
- Navigation systems (GPS, GLONAS, Bei Dou).

Additionally, target or own position marking can be done to distinct enemy and friendly units and setting fire limits and danger zones for Close Air Support with following gear:

- GPS devices,
- Active or IR markers (IR strobes, flashlights, etc.),
- Smoke grenades or
- Other improvised markers.

### 4. CALL FOR FIRE

Depending on target, call for fire can be planned or emergency. Well planned call is usually done after deliberate reconnaissance of area with purpose to display planned effect on target. It can be done through radio request or through software that supports data transition through sensor – computer – radio – Tactical Operations Center (TOC) [10].

On the other hand, emergency calls are usually made when unit is faced with danger that can cause mass

casualties (MASCAL) and can be put out of battle. These calls are made on moment, usually through standardized forms and protocols via radio communications.

Call for fire support form should minimally include:

- Observer location,
- Target location and
- Fire control measures.

Besides that, standard cards should enable giving as much details as possible about own position, target position, fire mission details in the fastest way possible. Analyzing forms for indirect fire support or close air support of foreign armies on one hand, and having in mind capabilities and procedures of Serbian Armed Forces (SAF) on the other hand, fire call form given below can be used when calling for fire in SAF.

**Table 1.** Fire support form

"Command call sign this is <u>Observer call sign</u> , FIRE MISSION – BREAK!"		
<b>My location coordinates</b>	a) MGRS b) POLAR c) OBJECTIVE CODE NAME	"BREAK!"
<b>My position marked with</b>	a) STROBE LIGHT b) IR LIGHT c) SMOKE d) REFLECTIVE PANEL e) NONE	"BREAK!"
<b>Target coordinates</b>	a) MGRS b) POLAR c) OBJECTIVE CODE NAME d) FRONT (LEFT COORDINATE, RIGHT COORDINATE)	"BREAK!"
<b>Target description</b>	a) PERSONEL b) VEHICLE c) OBJECT d) FORTIFIED	"BREAK!"
<b>Target marked with</b>	a) STROBE LIGHT b) IR LASER c) SMOKE d) TRACER ROUND e) NONE	"BREAK!"
<b>Fire control measures</b>	a) ON MY CALL b) ASAP c) CIVIL CLOSE d) DANGER CLOSE	"OVER" or "BREAK!"
<b>Adjust fires</b>	a) PROJECTILE COORDINATES b) VERTICAL DEVIATION (+-) c) HORIZONTAL DEVIATION (left-right) d) REPEAT e) HIT - STOP	"OVER" or "BREAK!"
"OVER!"		

This 9 – line form enables both calling for fires and adjusting fires. For example, call can be made like in example below:

- "1. **Star** this is **Chamber**, fire mission – BREAK!"
- "2. C) ALPHA 15, BREAK!"
- "3. A) BREAK!"
- "4. D) 34TDQ242344235, 34TDQ242344250 BREAK!"
- "5. A) BREAK!"
- "6. B) BREAK!"
- "7.B) BREAK!"

Adjusting fires can be one like in example:

- "1. **Star** this is **Chamber**, fire mission – BREAK!"
- "8. b) +30, c) L 20, d) BREAK!"

After adjusting fire, if target was destroyed, call will be made like in example:

- "1. **Star** this is **Chamber**, fire mission – BREAK!"
- "8. e) OVER!"

## 5. COMPARATIVE ANALYSIS OF COMMON INFANTRY TARGET ACQUISITION EQUIPMENT

The following table provides a comparative analysis of common infantry target acquisition equipment, focusing on three widely used systems: Vectronix Moskito, Sagem JIM, and DJI Matrice 30T. Each of these devices offers unique capabilities and features suited for different operational needs. This analysis aims to highlight the strengths and limitations of each system, providing a comprehensive overview for military personnel to make informed decisions regarding their deployment and use in various combat scenarios.

**Table 2.** Comparative analysis of common infantry target acquisition equipment

	VECTRONIX MOSKITO	SAGEM JIM	DJI MATRICE 30T
<b>Platform</b>	land	land	UAV
<b>Operators number</b>	1	1 regular, 2 for RC	2
<b>Observation method</b>	optical, passive NVG	day camera, thermal	day camera, thermal
<b>Thermal capabilities</b>	-	IR	IR
<b>LRF</b>	<4000 m	not restricted	not restricted
<b>LP</b>	no	yes	yes
<b>Navigation</b>	GPS	GPS	GPS, GLONAS, Bei Dou
<b>Digital compass</b>	64-00 360°	64-00 360°	360°
<b>Zoom</b>	none	x2, x4	5-16x optical
<b>Resolution</b>	-	standard and high	up to 8K
<b>Memory</b>	none	300 img with	adaptable to user needs

		standard resolution	
<b>AI integration</b>	none	none	flight assistance, tracking
<b>Remote control</b>	not available	available with RC station	operated from distance
<b>Data transfer capabilities</b>	none	RS 422 to RC-PC-radio	RC-PC-radio
<b>Jamming resilience</b>	resilient	resilient	high risk of jamming
<b>Versatilities</b>	not restricted	not restricted	open space required for takeoff and landing
<b>Mobility</b>	compact, easily carried	low restriction	need vehicle transport

Criteria given above are related to tactical requirements of infantry units. Additionally, few criteria can be added and considered, but should not be crucial. Those are:

- Ease of use,
- Training duration and
- Purchase and maintenance price.

These criteria are important, but compared to systems capabilities and their effect on operational success are minor.

All systems require technical knowledge. User interfaces of all three systems given in analysis are friendly oriented, easy to navigate and comprehensive. Users should not have any trouble navigating through menu and options in each one of them. Functions are well displayed, and user manuals are simple.

According to that, technical training should not be long, theoretical, but more practical oriented, short and intensive with hands-on principle.

Having in mind complexity of the system, its functions and capabilities, training should be recommended as following:

- SAFRAN VECTRONIX Moskito: up to 2 days,
- SAGEM JIM: up to 4 days and
- DJI MATRICE 30T: up to 7 days.

These recommendations are long enough to cover basic theoretical knowledge needed to display technical understanding of device on one hand and cover and rehearse all device functions on the other hand. It is important to emphasize that these recommendations are technology – wise, meaning that they not include tactics and system integration training, which are equally crucial for operational effectiveness and require additional dedicated training programs.

Complete training program for FOs (troop), TACPs (air force) and JTACs (special operations) usually vary from 5 days for FOs, up to 6 months for special operation forces JTACs [11].

Costs of given systems are divided into procurement costs and maintenance costs.

In order to maintain listed devices, armed forces should provide adequate training for their maintenance personnel, purchase tools and reserve part needed to function the system.

Procurement costs are given in table below:

**Table 3.** Commercial device prices

		PRICE (EUR)
<b>DEVICE</b>	<b>Moskito GPS XR5</b>	25.000 €
	<b>Sagem JIM</b>	27.000 €
	<b>MATRICE 30T</b>	9.888 €

All prices are collected from commercial store websites. Although DJI Matrice 30T provides better quality reconnaissance, detection and acquisition capabilities, its price is significantly lower than other two devices because its commercial purpose. Sagem JIM and Safran Vectronix Moskito are military devices that provide better characteristics in terms of materials used, durability, survivability and resilience.

This analysis support statement that all mentioned devices have large capacity when it comes to operational employment. Their limitations and needs of infantry units are determinators of fact in which unit these systems should be deployed.

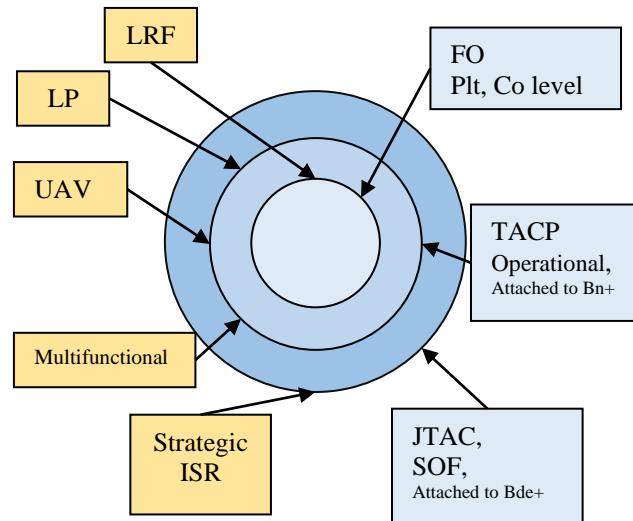


**Figure 2.** Fire control equipment deployment

As given in Figure 2, all platoon and company level fire observers should be equipped with at least GPS laser range finders. This provides them enough data to guide field indirect fires including mortar and artillery fires.

On battalion and above level, there should be at least one tactical air controller attached. Battalions that are conducting decisive operations should have at least 2 TACPs. If battalion is conducting shaping operations, and CAS is approved, at least one TACP should be attached to it. These airmen, among LRFs should be equipped with laser pointers to show enemy positions, strobes or other similar gear to mark own position in order to evade friendly fire.

JTACs are masters of all fire call disciplines and they are

proficient in guiding both indirect fires and CAS. These operators are attached to decisive operation brigade combat teams and similar operations, or they are just conducting special forces missions as guidance assets within their own teams. In support to their field activities, there should not be equipment restrictions.

When all of above fire control operators and equipment fail, strategic ISR assets should be deployed to deal with complexity of situation [12,13]. Additionally, incorporating real-time data analytics and machine learning algorithms could further enhance the accuracy and responsiveness of fire support operations, ensuring that units are better prepared to adapt to dynamic combat environments. This integration of advanced technologies will be crucial in maintaining a strategic edge in future conflicts.

Moreover, continuous training and adaptation to new technologies will be essential for maintaining operational readiness. Collaboration with technological industries to develop and refine these tools will also be a key factor in future advancements. Lastly, fostering interoperability between different branches of the military and allied forces can enhance the overall effectiveness and efficiency of fire support systems, leading to more coordinated and successful missions.

## 6. CONCLUSION

The evolution of modern warfare has been significantly influenced by the integration of advanced technology into military systems. Fire control as operational capability significantly contributes to the operational success. This paper highlights the fact that fire control as operational capability can be developed not only by using sophisticated equipment, but also necessarily by training professional operators to conduct various tasks related to targeting process.

A comparative analysis of common infantry target acquisition equipment highlighted the strengths and limitations of devices such as the Vectronix Moskito, Sagem JIM, and DJI Matrice 30T. Each system was evaluated based on tactical requirements, ease of use, training duration, procurement and maintenance costs. While commercial devices like the DJI Matrice 30T offer advanced capabilities at a lower cost, military-specific devices like the Moskito and JIM provide superior durability and resilience. All of presented systems have extensive potential in fire control missions when completed with precise tailored training.

Future research should focus on further refining of these systems in order to increase their resilience against jamming, improving the interoperability of different devices, and developing more intuitive user interfaces to cut training durations. Additionally, studies should explore the integration of emerging technologies such as artificial intelligence and machine learning to enhance the targeting process and decision-making capabilities of fire support units. Such advancements will ensure that military forces continue to maintain a strategic advantage in complex operational environments.

## References

- [1] ORKUSHPAEV, E.M., IBRAGIMOV, R.Z., ZHAMBIROV, R.M., ABDYBEKOV, D.M.: *Combat work of firing artillery units in modern armed conflicts*, ҚӘӘИ хабаршысы, 57(1), 2024, 27-34.
- [2] KOVALIUK, O., PETRYK, Y., MARCHENKO, V., KISHYANUS, I., NIKISHYN, V.: *Peculiarities of transformation of the concept of the infantry combat machine in modern conditions*, Collection of scientific works of Odesa Military Academy, 16 (2), 2021, 115-125.
- [3] *Army Techniques Publication ATP 3-60 Targeting*, Headquarters, Department of the Army Washington, DC, 2015.
- [4] *Tactics, Techniques and Procedures for Observed Fire - FM 6 - 30*, Headquarters Department of the Army, Washington, DC, 1991.
- [5] *Tactical Air Control Party - DIGITAL EDITION*, US Airforce, 2022.
- [6] *JP 3-09.3, Close Air Support (CAS)*, US Department of Defense, Washington, DC, 2014.
- [7] *JP 3-09 Joint Fire Support*, US Department of Defense, Washington, DC, 2019.
- [8] PETROVSKI, A., RADOVANOVIĆ, M.: *Application of detection reconnaissance technologies use by drones in collaboration with C4IRS for military interested*, Contemporary Macedonian Defense, 21(40), 2021, 117-126
- [9] PETROVSKI, A., BOGATINOV, D., RADOVANOVIĆ, M., ACKOSKA S.: *Application of Drones in Crises Management Supported Mobile Applications and C4IRS Systems*, In: Dobrinkova, N., Nikolov, O. (eds) Environmental Protection and Disaster Risks. EnviroRISKS 2022. Lecture Notes in Networks and Systems, 638, 2023, 321-334: Springer: Cham.
- [10] RADOVANOVIĆ, M., PETROVSKI, A., ŽNIDARŠIČ, V., BEHLIĆ, A.: *The C5ISR System Integrated with Unmanned Aircraft in the Large-Scale Combat Operations*, Vojenski rozhledy. 2023, 32 (2), 098- 118.
- [11] SHAND, P.M.: *JTAC AND FAC(A) Training: How Story Illustrates the Path to the Future*, MA thesis, Command and Staff Collage, US Marine Corps University, 2008.
- [12] RADOVANOVIĆ, M., SAMOPJAN, M., PETROVSKI, A.: *Possibility of Implementation of Drones in Mortar Units in Order to Increase the Efficiency of Fire Support Units*. 24. Međunarodna DQM konferencija Upravljanje kvalitetom i pouzdanošću ICDQM – 2021, Prijedor: ICDQM, 2021, 307-315.
- [13] RADOVANOVIĆ, M., PETROVSKI, A., JOKIĆ, Ž., ALEKSIĆ, A.: *Use of Unmanned Aerial Vehicles Integrated into the C4IRS System in Modern Combat Operations*, 8th International Forum "Safety for the Future", Belgrade, 2022, 88-98.



# PREDICTION OF ARTILLERY CORRECTION ELEMENTS BY SOFTWARE FOR BALLISTICS MODULE OF FIRE CONTROL SYSTEMS

DRAGOSLAV R. PETROVIĆ, PHD

Retired Colonel, former chief of Ballistic department MIT,  
Belgrade, Juriša Gagarina 146/50, 11070 N. Beograd, 064-2710883

**Abstract:** At present, by software for Ballistics Module –BM of Fire Control Systems -FCS can be calculated GUN elements - elevation in vertical plane and angle of its direction in horizontal plane. There is serious reason, say forced, for recording part of actual trajectory, not observing impact point of projectile fall, and on its values predict point of projectile fall, say only one. This method enables firing two projectiles for acceptable time period, firing second projectile with corrected GUN elements before first projectile is reached impact point - target. Finally, method for prediction artillery correction elements is based on comparing part of numerical data of actual path trajectory and corresponding data of nominal trajectory..

**Keywords:** Software, Ballistic Module extension, Artillery shooting

## 1. INTRODUCTION

The complexity of preparing data for opening artillery fire can be seen from the procedure for obtaining data that affects the flight of projectiles. The procedure is intended for complex formations of artillery units, and it is the same for an individual gun - howitzer. What characterizes the procedure is the time and means for collecting the necessary data in battle-field. It is enough to mention the determination of the initial speed of the projectile, as the most important factor affecting the flight of the projectile, and the elements of meteorological data in which the projectiles flight takes place, as the most important speed and direction of the air wind and temperature. Both meteorological elements are random quantities characterized by mean values and their dispersion. In other words, meteorological elements are statistical quantities whose determination requires a certain number of samples, far greater than one in order for the measured quantity to be faithfully presented. Today, the requirement is to hit the target with one projectile, and the statistical method of operation is applicable only during polygon tests in proving ground. In the past, and even today, a simplified method of preparing the elements for opening fire, called fire correction is used. With the initial elements, the projectile is fired, its fall position in relation to the target is recorded, and based on the distance difference in relation to the target and the shooting direction, previous elements for opening fire can be corrected. The time duration projectile flight today makes this fire correction procedure unacceptable. It is applicable only after time projectile ended is flight which is relatively long today and risk to be destroyed place of gun-howitzer on its position is certain. Another, important factor that makes correcting fire difficult is target position - enemy territory, notice its relation to the target and its delivery to the gun-howitzer position. The author see into

a partial way out of these difficulties in the process of predicting where the projectile will fall based on measured data on the position of the projectile at the beginning of its path trajectory. These measurements of the position of the projectile in flight are the basis for extending the author's software of the Ballistic Module – BM. Base calculations of BM are the initial elements for opening fire and performing their renewing. It goes without saying that there is designed original author suitable way of measuring the position of the projectile at the initial part of its trajectory and transferring the measured data to the computer running the authors BM extended software.

## 2. CALCULATION CORRECTIONS BASED ON FIRING TABLES DATA

Long time ago, Firing Tables –FT (collection on projectile trajectory data) exists as the only source of trajectory elements data. Nowadays, its frequency for using is reduced, for it is FCS are widely in use in army troops for Artillery preparation fire data. Range and Deflection corrections can be done for meteorological and ballistic conditions different from the FT nominal conditions, named meteorological and ballistic *deviations*. Their influence on the range and deflection and sign are given in auxiliary **Table P1** of FT (see NORA FT). Calculation total Deflection and Range corrections can be done as:

- a) For Deflection (mils)
- $$\Delta Z_{\Sigma} = Z \times K_{\Gamma} + 0.1 \times \Delta Z_W \times K_{\Gamma} \times W_Z + \Delta Z_{\Gamma\Phi} \quad (1)$$
- b) For Range (m) accordingly to Taylors expansion neglecting second terms  $f(x_i) = f_0 + \sum \frac{\partial f}{\partial x_i} \Delta x_i :$



$$\begin{aligned} \Delta X_{\Sigma} = & 0.1 \times \left[ (\Delta X_W \times K_{\Gamma} \times W_X) + \right. \\ & \left. + (\Delta X_H + 0.1 \times \Delta X_H \times \Delta H) \times \Delta H + \right. \\ & \left. + (\Delta X_{t_b} \times K_{\Gamma} \times \Delta t_b) + (\Delta X_T \times K_{\Gamma} \times \Delta T) + \right. \\ & \left. + (\Delta X_{V_o} \times K_{\Gamma} \times \Delta V_o) \right] + \Delta X_{\Gamma\Phi} \end{aligned} \quad (2)$$

Where:

GP – Altitude of GUN fire position (m)

$$K_{\Gamma} = 1.0 + GP(m) / 10000$$

Z - Drift (mils) –|12| –(Column 12, Table C1 of FT)

$\Delta Z_W$  – Correction (mils) for  $W_z=10(m/s)$  –|13|

$W_Z$  – Ballistic lateral wind component (m/s)

$\Delta Z_{\Gamma\Phi}$  – Defl. Dev. due to Earth rotation (mils) –|G1|

$\Delta X_H$  – Correction for  $W_x=10(m/s)$  –|14|

$W_X$  – Ballistic longitudinal wind component (m/s)

$\Delta X_H$  – Correction for 10mbar –|16|

$\Delta H$  – Ballistic atmospheric Pressure -mbar

$\Delta X_{t_b}$  – Corr. for powder temperature 10°C –|18|

$\Delta t_b$  – Powder temp. difference from Table  $t_b=21^{\circ}C$

$\Delta X_T$  – Corr. for air temp. diff. –|15|, for  $\Delta T=10^{\circ}C$

$\Delta T$  – Ballistic difference air temperature -°C

$\Delta X_{V_o}$  – Correction for  $\Delta V_o=10(m/s)$  –|17|

$\Delta V_o$  – Muzzle velocity difference -(m/s)

$\Delta X_{\Gamma\Phi}$  – Range deviation due to Earth rotation (m) –|G1|

$\Delta X_m$  – Corr. for proj. mass difference  $\Delta m=1$  mark –|19|

$n$  – Number of projectile mark –mass difference

According to the FT, GUN barrel angle – elevation ought to be determined for distance  $X_T$  calculated as

$$X_T = X_r + \Delta X_{\Sigma} \quad (3)$$

where  $X_r$  is geographic horizontal distance from GUN to the target.

This calculations can be automatized, and they are somewhere realized, but its validity is limited only to the nominal FT conditions, ie. for the same height level GUN

and target and other approximation to the used deviations data and its effects on projectile flight. For the mountain conditions can be used appropriate FT, but other auxiliary FT Tables complicate this calculations.

### 3. PROJECTILE MATHEMATICAL MODEL SOLUTION

By solving so called inverse External Ballistic -EB problem, the elevation angle  $\theta$  which should be given the barrel of the artillery GUN-HOWITZER is obtained in order to achieve the required range – distance from GUN to target  $X_C$ . The most significant part of the necessary ballistic calculations ought to be performed by the software of the Ballistic Module -BM of the Fire Control System -FCS.

The software of existing BM consists of two parts, first is mathematical model that describes the flight of the projectile in space – gives path trajectory elements. Modeled ballistic characteristics of the projectile and current flight conditions (the most important elements of the state of the atmosphere: pressure, temperature and wind with its strength and direction) serves to solve the direct EB problem. Another mathematical model is designed for resolving of inverse EB problem. They together make BM of FCS software and are coupled, so might not be isolated to work independently, except in case now introduced as extension of existing for correction range in advance. For the solution of the direct EB problem, a various mathematical models can be used that describes the motion of the projectile –its flight throw atmosphere. As example of complexity chosen projectile mathematical model, it is given Modified Point Mass and five degrees of freedom Model –|10|.

$$\begin{aligned} \frac{dx}{dt} &= V_x = V \cos \theta \cos \psi \\ \frac{dy}{dt} &= V_y = V \sin \theta \\ \frac{dz}{dt} &= V_z = V \cos \theta \sin \psi \end{aligned} \quad (4)$$

$$(V_R)_x = V_x - W_x, \quad (V_R)_y = V_y$$

$$(V_R)_z = V_z - W_z$$

$$V_R = \sqrt{(V_R)_x^2 + (V_R)_y^2 + (V_R)_z^2}$$

$$\theta = \arctg \frac{V_y}{V_x}, \quad \psi = \arctg \frac{V_z}{V_x}$$

$$\frac{dV_x}{dt} = a_x$$

$$\frac{dV_y}{dt} = a_y$$

$$\frac{dV_z}{dt} = a_z$$

$$\frac{d\omega}{dt} = k_7 + k_8 \frac{\omega}{V} \tag{5}$$

$$J = C_{et} \cdot K \cdot \xi(y) \cdot M_R^2 \cdot GAK(M_R)$$

$$\begin{bmatrix} b_1 \\ b_2 \\ b_3 \end{bmatrix} = \begin{bmatrix} a_{11}a_x + a_{12}a_y + a_{13}a_z \\ a_{21}a_x + a_{22}a_y + a_{23}a_z \\ a_{31}a_x + a_{32}a_y + a_{33}a_z \end{bmatrix}$$

$$a_{11} = 1 - C_1 \left( (V_R)_y^2 + (V_R)_z^2 \right)$$

$$a_{12} = C_1 (V_R)_x (V_R)_y + C_3 (V_R)_z$$

$$a_{13} = C_1 (V_R)_x (V_R)_z - C_3 (V_R)_y$$

$$a_{21} = C_1 (V_R)_x (V_R)_y - C_3 (V_R)_z$$

$$a_{22} = 1 - C_1 \left( (V_R)_x^2 + (V_R)_z^2 \right)$$

$$a_{23} = C_1 (V_R)_y (V_R)_z + C_3 (V_R)_x$$

$$a_{31} = C_1 (V_R)_x (V_R)_z + C_3 (V_R)_y$$

$$a_{32} = C_1 (V_R)_x (V_R)_y - C_3 (V_R)_z$$

$$a_{33} = 1 - C_1 \left( (V_R)_x^2 + (V_R)_y^2 \right)$$

$$b_1 = C_4 (V_R)_x - C_6 (V_R)_z$$

$$b_2 = C_4 (V_R)_y - C_5 (V_R)_z$$

$$b_3 = C_4 (V_R)_z + C_6 (V_R)_x$$

$$C_1 = k_3 \left( \frac{\omega}{V} \right) (\alpha_b - \alpha_a), \quad C_3 = -k_2 (\alpha_b - \alpha_a)$$

$$C_4 = -k_1 - k_9 (\alpha^2 + \beta^2) - k_3 \alpha_b \left( \frac{\omega}{V} \right) g (V_R)_y$$

$$C_5 = g \left( 1 - k_3 \left( \frac{\omega}{V} \right) \alpha_b \right), \quad C_6 = k_2 \alpha_b g$$

$$\alpha_b = k_6 \left( \frac{\omega}{V} \right) \frac{1}{k_2 k_4 + k_3 k_6 \left( \frac{\omega}{V} \right)^2}$$

$$\alpha_a = k_2 k_{11} \left( \frac{\omega}{V} \right) \frac{1}{k_2 k_4 + k_3 k_6 \left( \frac{\omega}{V} \right)^2}$$

$$k_i = k_0 \frac{p_0}{p_{0N}} \frac{m_0}{m_{0N}} k_i \xi(y) M^2 GAK(i)$$

$$GAK(1) = C_X$$

$$GAK(2) = C_Y^\sigma$$

$$GAK(3) = C_Z^{\omega, \sigma}$$

$$GAK(4) = m_Z^\sigma$$

$$GAK(5) = m_Z^{\Omega + \sigma}$$

$$GAK(6) = m_Y^{\omega, \sigma}$$

$$GAK(7) = m_X^\varepsilon$$

$$GAK(8) = m_X^{\omega_x}$$

$$GAK(9) = C_X^{\sigma^2}$$

$$k'_1 = k'_2 = k'_9 = \frac{d^2}{m} 10^3, \quad k'_3 = \frac{d^3}{m} 10^3$$

$$k'_4 = \frac{d^3}{mi_Y^2} 10^3, \quad k'_5 = k'_6 = \frac{d^4}{mi_Y^2} 10^3$$

$$k'_8 = \frac{d^4}{mi_X^2} 10^3, \quad k'_{10} = \frac{rtg\mu}{i_X^2} 10^3$$

$$k'_{11} = \frac{i_X^2}{i_Y^2} 10^3$$

Given mathematical model as equations of physical projectile with projectile characteristics incorporated as parameters in model, in fact form nonlinear system of differential and ordinary equations. It cannot be solved analytically, but its numerical solution for certain initial values -equation (6), for introduced kinematic parameters determines values projectile center of mass coordinate in space and other projectile characteristic.

Initial values and projectile characteristic are:

$$(V_{x,y,z})_0, (X, Y, Z)_0, (\theta, \psi, \omega)_0, a_{i,j=3}, k_{i=11}$$

$$W_{x,z} = f(Y), GAK(i), i = 1, 9 = f(M) \tag{6}$$

$M - \text{Mach number} = \frac{V}{a}, a - \text{speed of sound.}$

It is worth to notice that equation (6) determines derivation of high speed rotation projectiles, but step size for numerical integration is sufficiently acceptable great.

Sequences calculated values can serve to represent path trajectories as in Fig. 1, and the value of the distance  $X_C$  that is achieved for a given projectile and flight conditions.

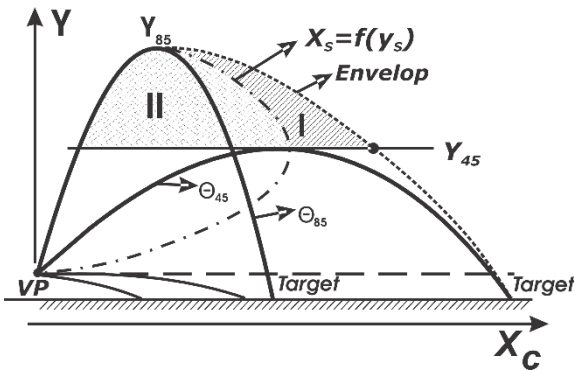


Figure. 1 Projectile path trajectories in plane X-Y

The solutions of the differential equations are obtained for known initial conditions, and one of them is an arbitrary value of the elevation angle  $\theta$  for which, after calculation, the size of the distance  $X_C$  is found, which is definitely not equal to the required distance  $X_C$  to impact point - target. Therefore, an algorithm for the solution of the inverse SB problem must be used, but regardless of its type, by intuition it can be concluded that there is no way to solve the set task after only one calculation: for the required distance to the target  $X_C$ , determine the required elevation angle  $\theta$ . In this, as well as in other similar cases, it is necessary to know the initial values  $\theta$  - predictions that serve as a starting point to achieve at the final solution through correction "if we are going in the right direction". In Fig. 1 are given two path trajectories for extreme angles  $\theta$ :  $-\theta_{45}$  which gives maximum range for lower angle fire -LAF, and  $-\theta_{85}$  maximum angle elevation for upper angle fire -UAF. Space occupied with path trajectory branches is at same time space where targets can be positioned.

#### 4. BM DISCRETE MODEL SOLUTION EXTENDING

By solving the direct SB problem, a series of discrete values  $\theta_i - X_i$  pairs is obtained, which, when plotted on the graph and connected to each other, have the shape as shown in Fig. 2. The shape of the curve shown in Fig. 2 is in relation on the mutual ratio of the altitudes of the firing position of the weapon  $Y_{VP}$  and the target  $Y_{CH}$ , and the given corresponds to the case when  $Y_{VP} = Y_{CH}$ . Having a discrete shape of the curve as in Fig. 2 a suitable prediction of the angle  $\theta_c$  can be found for any distance to the target  $X_C$  in range  $0 - X_{45}$ , where  $X_{45}$  is maximum range

obtained for  $\theta$  equal to 45 degrees. The value of the found  $\theta$  prediction should be corrected due to non-standard meteorological - ballistic conditions and due to errors caused by connecting the nodal points with straight lines and others. This correction is done by successive iteration solving direct EB problem.

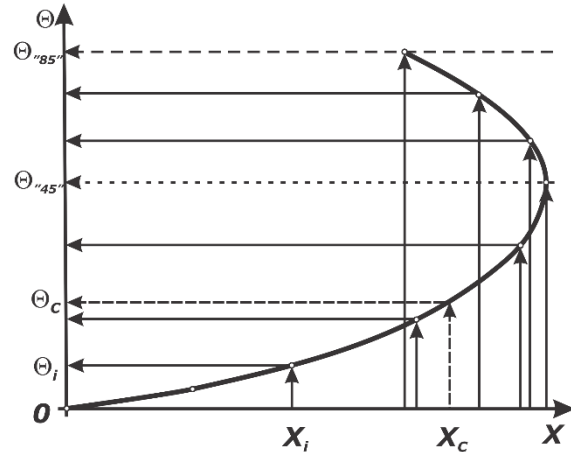


Figure. 2 Discrete form  $\theta = f(X)$  and  $X = f^{-1}(\theta)$

This is the most common and simplest case, and other forms of approximate polynomials are also possible to connect the nodal points.

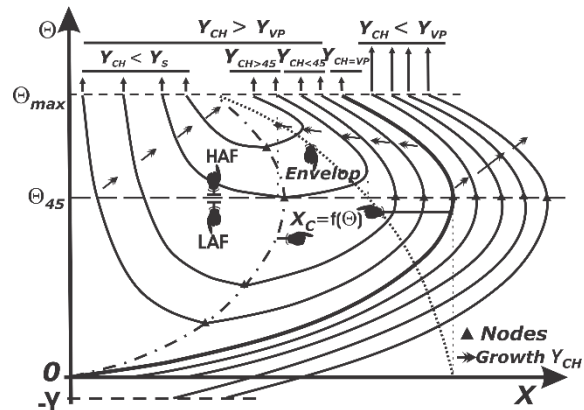


Figure. 3 Graph of discrete points - pairs  $\theta - X_C$

In [7], the space in plane  $\theta - X$  - Fig. 3 described by the projectile's path trajectories is divided into characteristic areas (domains), and for each of them, the affiliation of  $\theta = f(X)$  to the groups of angles - LAF-UAF is indicated, and it is indicated whether an increase in elevation also results in an increase or diminution the range.

As it is shown in Fig. 3, the discrete form  $\theta_i = f(X_i)$  or  $X = f^{-1}(\theta)$  depends from area to area (domain), and since there are a large number of them, the question arises as to how to form. That practically means, what data should be possessed in order to obtained various discrete forms  $\theta_i = f(X_i)$  that characterize certain areas. It was found that the generator (source) of all necessary curved paths lies in special partition trajectory path. Since it is not possible to have analytical form trajectory path that would define it, the starting - ascend and falling - descend trajectory path were discretized with straight segments. The discretization of the trajectory path is effective only if the

discretization points are foreseen in advance. Of the several possibilities, the most economical is the one that, for the selected value of the elevation angle  $\theta_i$  and the reached height of the vertex (summit) of the path  $Y_S$  at point "S", requires knowledge of the distances for the specified values  $Y_S$  of the height of the vertex of the path  $Y_S$ . The reason is simple, for the selected values  $\theta_i$  it is necessary to have only the  $Y_S$  value and a series of distances obtained at the intersection of the horizontal line at the specified heights. By more trials, it is found [7,8], that best approximation of the starting, ascent trajectory path ought to be at heights:  $0x Y_S$  (or  $Y_{GP}$ );  $0.6x Y_S$ ;  $0.9x Y_S$ ;  $Y_S$ , and on the falling -descent path:  $Y_S$ ;  $0.9x Y_S$ ;  $0.6x Y_S$ ;  $0.3x Y_S$ ;  $Y_{VP}=Y_{CH}$ ;  $0x Y_S$ .

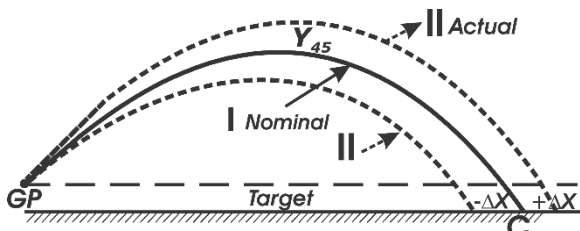


Figure. 4 Actual and nominal trajectory dispositions

After establishing a data generator (source) for construction graphics of type shown in Fig. 2 in the X-Y plane as it is showed in Fig. 1, served to form possible layouts for the observed characteristic areas - Fig. 3 - [7,8,9,11] transformed into the plane  $\theta$ -X.

Built-in algorithms in the software of the Ballistic Module -BM of the Fire Control System -FCS based on the interpolation of the nodal points  $\theta_i$  - $X_i$  proved to be very effective in determining the prediction of the elevation angle  $\theta_i$  that should be given by the barrel of the artillery GUN to achieve the required distance to the target  $X_C$  - [9,11].

There is one step to predict correction  $\pm\Delta X$  as it is signed in Fig. 4 for one condition:  $\pm\Delta X$  must be calculated earlier then projectile reached impact point "C" at appointed figure. Equation (2) cannot be used for it is not known data for its creation. On the very beginning of creation Ballistic model elements for the ARS prototype (Integral procedure) -[1-6], it is assumed that this data are known. Difficulties for its obtaining are well known for it is user obligated to collect them in battlefield and generally there is not its sources for user disposition.

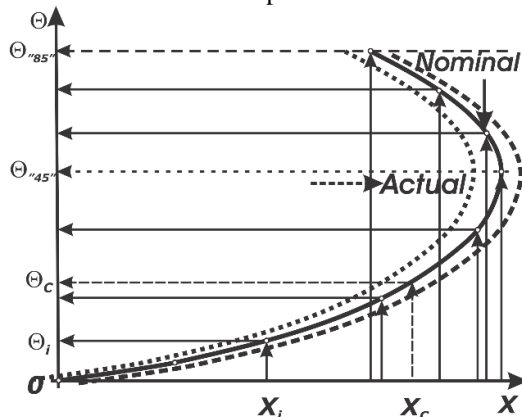


Figure. 5 Nominal and actual form  $\theta = f(X)$

There is sufficient software in existing BM to perform that job, except data of projectile coordinates from its flight and software for its processing. This software is based on recorded data of actual path trajectory at very beginning -GUN to same ascending trajectory point. It is assumed that recorded data ought to be sent to BM of FCS for processing with extended and modified present BM software on the basis created graph shown in Fig. 5.

### 5. CONCLUSION

By software for Ballistics module of Fire Control Systems -FCS can be calculated GUN elements - elevation -angle in vertical plane and its angle of direction in horizontal plane. Field artillery firing is done indirectly mainly on long distances and with various projectiles (unguided rockets, classical artillery projectiles and mines). Trajectories of this projectiles are various, from flat for direct fire and indirect (lower angle group -LAF) to mortar type trajectories (upper angle group -UAF). Ballistics module of FCS is based on method solution of inverse external ballistics problem for prediction firing elements and its successive corrections. Software for prediction artillery correction elements is not developed up to now. This software is based on recording data of actual path trajectory at very beginning GUN -ascending path to same trajectory point. It is assumed that recorded data ought to be sent to Ballistics Module -BM of FCS for processing with extended and modified present BM software. There is serious reason, say forced, for recording part of actual trajectory, not observing impact point of projectile fall, and on its values predict impact point of projectile fall, say only one. Target (impact point of projectile fall) is long away from GUN position and is situated in enemy land! If time of projectile flight is added to previous reason (say, 120 seconds), new situation is come to view - during that time gun will be eliminated from the air with airplane rocket or bomb. This method enables firing two projectiles for acceptable time period, firing second projectile with corrected starting gun elements before first projectile is reached impact point of fall - target. Finally, method for prediction artillery correction elements is based on comparing part of numerical data of actual path trajectory and corresponding data of nominal trajectory.

### References

- [1] Vasovic, P., Stojanovic, V., Gajic, M., Ballistic model elements for the ARS prototype (Integral procedure), Elaborat VTI-02-28-238, Belgrade, 1977.
- [2] Vasovic, P., Stojanovic, V., Gajic, M., Improvement of the ballistic model elements for the ARS prototype (Integral procedure), Elaborat VTI-02-28-238/I, Belgrade, 1978.
- [3] Petrovic, D., Creation TG (Firing Tables -Tablica gadjanja), Diploma thesis, Faculty of Mechanical Engineering, Belgrade, 1971
- [4] Petrovic, D., Procedure for making tables S-Ps and T-DTs using the interpolation method, Elaborat VTI-

- 02-27-101, Belgrade, 1983
- [5] Petrovic, D., Program TGMB for mortar firing tables, Elaborat VTI-02-28-235, Belgrade, 1984
- [6] Petrovic, D., TGOSV program for the production of firing tables of illuminating artillery projectiles, Elaborat VTI-02-27-175, Belgrade, 1985
- [7] Petrovic, D., Criteria for evaluating the quality of software of the ballistic module in the fire control system, Elaborat VTI-02-01-0862, Belgrade, 2004
- [8] Petrovic, D., Elements for software quality control of the ballistic module in the fire control system, Tehnicka dijagnostika, Belgrade, 2004
- [9] Petrovic, D., Algorithms for predicting the solution of the inverse external ballistic problem, Elaborat VTI-02-01-0866, Belgrade, 2004.
- [10] STANAG 4355, Modified Point Mass and five degrees of freedom Model
- [11] Petrovic, D., Prediction solution of inverse External Ballistics problem for Fire Control System Ballistic Module, 1. Naucni Skup Odbrambene Tehnologije u funkciji mira, Beograd, 6-7.12.2005.



# CHANGE OF SPEED OF COMFORT PARAMETERS IN THE ARMORED COMBAT VEHICLES OF THE SERBIAN ARMY DUE TO ENVIRONMENTAL CONDITIONS

SNEŽANA MALIŠIĆ

Technical test center of the Serbian Army, 11000 Belgrade, [snezana\\_malisc@yahoo.com](mailto:snezana_malisc@yahoo.com)

MILICA IVANOVIĆ

Faculty of Mechanical Engineering, University of Belgrade, 11000 Belgrade, [mivanovic@mas.bg.ac.rs](mailto:mivanovic@mas.bg.ac.rs)

FILIP STANIĆ

Faculty of Mechanical Engineering, University of Belgrade, 11000 Belgrade, [filipstanic75@gmail.com](mailto:filipstanic75@gmail.com)

**Abstract:** *This scientific paper refers to the conditions of the working environment of the crew members of the combat armored vehicle from the aspect of climate comfort and from the aspect of speed of the response of sensors (transducers).*

**Keywords:** *working environment, climate comfort, speed of the response of sensors.*

## 1. INTRODUCTION

The heating system was tested in real field conditions and warehouse conditions. The parameter that is considered the test standard is the temperature in the storage conditions of the armored combat vehicle (storage space temperature), and the speed of reaching the heating temperature of the crew cabin in storage conditions and in conditions without storage capacity is measured, as well as speed of the response of sensors (transducers).

This will be shown through a comparison of the achieved results of the heating and air conditioning system in real working conditions with the functional capability of the heating and air conditioning system in storage conditions on the armored combat vehicles of the Serbian Armed Forces. The system's response speed will show us the accuracy of the measured data in real time, that is, the testimony of the measured measurement results.

The environmental conditions that must be met, according to ISO 7730:2005 [1] and ANSI/ASHRAE 55-2020 [2] standards, are as follows: ( $-0.5 \leq PMV \leq +0.5$ ,  $PPD \leq 10\%$ ,  $\Delta t \leq 5^\circ S$ ,  $\tau \leq 60$  min), i.e. according to Fanger's criteria [3] for the thermal comfort of the working environment.

Measurements were made with calibrated measuring equipment, thermal comfort meter B&K 1212 and sensor MM0023 at ambient temperature and Tachymeter PeakTech type 5180.

The measurement was carried out at nine measuring points.

## 2. EXPERIMENTAL SETUP AND METHODOLOGY

The development of armored combat vehicles was realized through the development and integration of newly developed and improved subsystems. With the modernization of this armored fighting vehicle, the vehicle itself has been modernized with an air conditioning and heating system. This brought with it various challenges, both functional and technical, as well as the problem of how to meet the requirements of the ISO 7730:2005 and ANSI/ASHRAE 55-2020 standards.

By installing and integrating air conditioning and heating systems, the working environment of servers is improved.

The air conditioning system should be provided in the administrative and fighting compartment, while the heating system should provide heating in the same space, i.e. the administrative and combat area.

The difference that is particularly emphasized here between these two systems is that the air conditioning system is active only during engine operation, and the heating system has the possibility of overheating when the engine is not running with special systems installed just for that purpose.

The test was carried out at two locations. One location is a military training ground, and the other location is a storage area.

The examination was carried out in the summer period.

It's an all-male crew in an armored fighting vehicle.

There is nine measurement points in the vehicle. The

sketch is given in Figure 1. The length of the measurement response on the sensors (transducers) is ten seconds on three measurement channels.

The first measurement was within the storage space at an average outside temperature of 40 °C. At the ambient temperature in which the armored combat vehicle is located, the air conditioning system should achieve and maintain the temperature inside the working area of the armored combat vehicle in the range from 16 °C to 28 °C.

The temperature range is shown in Table 1, in which the bolded values are within the range of thermal comfort for crew members.

The second measurement was within conditions of the working environment space at an average outside temperature of 40 °C. At the ambient temperature in which the armored combat vehicle is located, the air conditioning system should achieve and maintain the temperature inside the working area of the armored combat vehicle in the range from 16 °C to 28 °C.

The temperature range is shown in Table 2, in which the bolded values are within the range of thermal comfort for crew members.

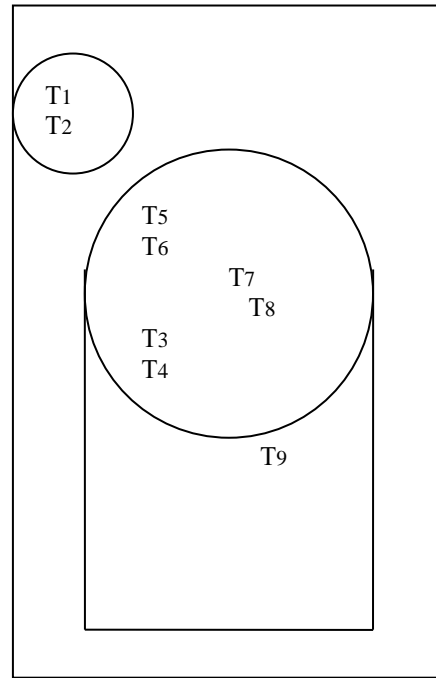


**Figure 1.** The positions of the measuring points

The characteristics of the air conditioning and heating system itself are as follows:

- Cooling system capacity.....14.2 kW
- Capacity of the heating system.....25.3 kW
- Coolant.....freon R 134 a
- Air flow.....3500 m<sup>3</sup> /h
- Fuel for heating.....diesel DIN EN 590
- Power supply.....24 V DC
- Nominal alternator current equation after the regulator.....200A

**Table 1.** Temperature range within the storage space in °C

time	T <sub>1</sub>	T <sub>2</sub>	T <sub>3</sub>	T <sub>4</sub>	T <sub>5</sub>	T <sub>6</sub>	T <sub>7</sub>	T <sub>8</sub>	T <sub>9</sub>	T <sub>10</sub>
11.35	41.9	39.2	42.5	40.2	41.5	40.8	42.3	39.5	40.3	43.6
11.45	34.9	38.2	39.1	32.2	36.6	34.6	35.8	32.9	35.8	42.3
11.55	33.1	37	37.2	29.9	34.6	32.5	33.1	30.6	33.6	41.7
12.05	32.1	36.4	35.5	28.1	33.2	30.9	31.6	29.1	32.1	
12.15	31.5	36.1	34.5	<b>27.3</b>	32.3	30.3	30.6	28.1	31.1	
12.25	31	35.6	33.6	<b>26.8</b>	31.7	29.5	29.6	<b>27.4</b>	30.3	
12.35	30.7	35.7	33.5	<b>26.1</b>	30.9	28.9	28.9	<b>26.7</b>	29.6	
12.45	30.6	35.7	32.3	<b>25.5</b>	30.2	28.5	28.2	<b>26.3</b>	29.1	
12.55	30.4	35.6	32.1	<b>25.3</b>	29.6	<b>27.9</b>	<b>27.7</b>	<b>25.8</b>	28.5	
13.05	30.2	35.5	31.5	<b>25</b>	29.4	<b>27.7</b>	<b>27.4</b>	<b>25.4</b>	28.3	
13.15	30.1	35.3	31	<b>24.8</b>	29	<b>27.2</b>	<b>26.7</b>	<b>25.2</b>	28.1	
13.25	32.1	36.4	35.5	28.1	33.2	30.9	31.6	29.1	32.1	

**Table 2.** Temperature range within of the working environment space in °C

time	T <sub>1</sub>	T <sub>2</sub>	T <sub>3</sub>	T <sub>4</sub>	T <sub>5</sub>	T <sub>6</sub>	T <sub>7</sub>	T <sub>8</sub>	T <sub>9</sub>
11.45	40.5	40.6	38.7	37.7	37.7	36.9	41.2	37.1	37.6
11.55	37.4	38.7	37.1	35.2	35.8	34.2	41.4	34.7	35.7
12.05	35.5	37.0	36	33.8	34.7	32.4	40.6	33.2	34.3
12.15	33.9	35.6	34.9	32.4	33.6	31	39.6	31.8	32.8
12.25	32.7	34.4	33.9	31.4	32.8	30	38.6	30.7	31.5
12.35	31.65	33.35	33.06	30.4	31.8	29	37.6	29.7	30.5
12.45	31.3	32.9	32.6	30	31.3	28.6	36.8	29.3	29.8
12.55	31.2	32.4	32	29.5	31	28.2	36.4	28.9	29.2
13.05	30.6	32.4	32.1	29.4	30.4	28.5	36	29.1	29.9
13.15	30.1	32	31.6	28.7	29.9	<b>27.7</b>	35.9	28.3	28.9
13.25	28.9	31.5	31.1	28.3	28.8	<b>27.3</b>	35.2	<b>27.6</b>	<b>28</b>
13.35	28.5	30.7	29.9	<b>27.1</b>	<b>27.9</b>	<b>26</b>	34.3	<b>26.2</b>	<b>26.2</b>

Monitoring and control systems have also been modernized in the form of various sensors that must provide:

- power supply of armored combat vehicles,
- determination of necessary and sufficient elements within armored combat vehicles,
- calculation of necessary and sufficient elements within armored combat vehicles,
- manual input within armored combat vehicles,
- information about an error within armored combat vehicles,
- supervision and management,
- reception and accurate detection of thermocouples,
- sending signals to activate electromagnetic valves.

### 3.RESULTS AND DISCUSSION

In order to determine the relationship and connection of the TSV readings, and to calculate the PMV factor, the following equation was used, which is part of the Fanger criteria for evaluating environmental parameters according to the ISO 7730:2005 standard, we calculated it with the following equation:

$$PMV = PMV (ta, tr, va, pa, M, Iclo) \quad (1)$$

It is also necessary to tabulate the instruments with which the measurement was performed, in order to clearly define the distribution of results when measuring the response speed of the sensor (transducer) table 3.

**Table 3.** dilation of the results during the test

Measuring device	Parameter	Measuring range	Measuring accuracy
Globus B&K 1212	Radiant temperature	±50 °C	±0.5 °C on ±15 °C ±2 °C on ±50 °C
PeakTech 5180	Air temperature	from -40 °C to +70 °C	±1 °C
	Relative humidity	from 0 to 100 %	±3 %

We will also show two diagrams, the first diagram of which refers to the first measurement in the storage conditions of armored combat vehicles figure 2.

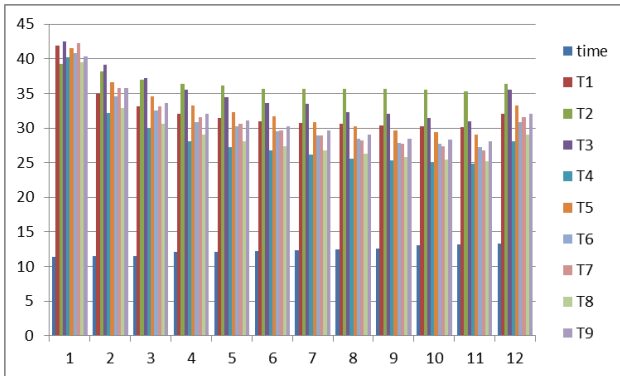


**Figure 4.** storage conditions of armored combat vehicles

Second diagram to the second measurement in real working conditions of armored combat vehicles figure 3.

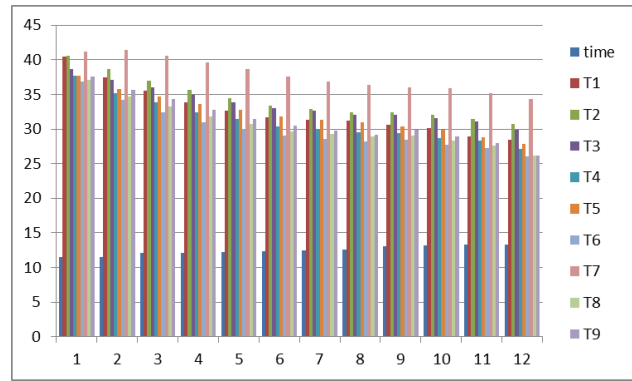


**Figure 3.** real working conditions of armored combat vehicles

### 4. CONCLUSION

Based on all the obtained results, we come to the following conclusions:

1. Thermal comfort of armored fighting vehicles depends on how the vehicle is handled when not in use.
2. The thermal comfort of the space for the crew is better and more pleasant if there is a possibility of storing armored combat vehicles, before they are put into use. This exactly means that one of the necessary and sufficient conditions to improve the crew's comfort is that tools that are not in use are adequately stored in a suitable space.
3. the fact that there are better results in the storage area is supported by the fact that in the first test of armored combat vehicles that were tested in storage conditions, we justify that four measuring points met the requirements of the set standards with an accuracy of seven results. While in the case of combat armored vehicles whose thermal comfort was measured in real working conditions, the same was achieved by four workplaces, but with an accuracy of two results within the required standards.
4. The response speed of the meters also varies by a full five minutes, which is a large delay in the response of the meters if you take into account that the transmitter is calibrated to respond for ten seconds.
5. It should be noted here that the examination could be improved if there were crew members of different grades, because in that case the parameters for evaluation according to Fanger's criteria would change.



## References

- [1] ANSI/ASHRAE Standard 55-2020, *American Society of Heating, Refrigerating and Air-Conditioning Engineers*, 2021.
- [2] ISO 7730:2005, *Ergonomics of the thermal environment — Analytical determination and interpretation of thermal comfort using calculation of the PMV and PPD indices and local thermal comfort criteria*, *The International Organization for Standardization*, 2005.
- [3] Fanger, P., *Thermal comfort: analysis and applications in environmental engineering*, *Danish Technical Press*, Copenhagen, Denmark, 1970.



# OTEH 2024

11<sup>TH</sup> INTERNATIONAL SCIENTIFIC CONFERENCE  
ON DEFENSIVE TECHNOLOGIES

*SECTION IV*

**Ammunition and energetic materials - *AEM***



## MODELING OF SHAPED CHARGE JET PENETRATION DEPTH: ANALYTICAL AND NUMERICAL APPROACH

PREDRAG ELEK

University of Belgrade – Faculty of Mechanical Engineering, Belgrade, [pelek@mas.bg.ac.rs](mailto:pelek@mas.bg.ac.rs)

MILOŠ MARKOVIĆ

University of Belgrade – Faculty of Mechanical Engineering, Belgrade, [mdmarkovic@mas.bg.ac.rs](mailto:mdmarkovic@mas.bg.ac.rs)

DEJAN JEVIĆ

University of Belgrade – Faculty of Mechanical Engineering, Belgrade, [djevtic@mas.bg.ac.rs](mailto:djevtic@mas.bg.ac.rs)

RADOVAN ĐUROVIĆ

University of Belgrade – Faculty of Mechanical Engineering, Belgrade, [rdjurovic@mas.bg.ac.rs](mailto:rdjurovic@mas.bg.ac.rs)

**Abstract:** Shaped charge is the most effective armor-piercing mechanism, harnessing explosive charge detonation energy to form and accelerate a hypervelocity metal penetrator known as a jet. The process entails intricate dynamics including detonation wave propagation, its interaction with the metal liner, and subsequent liner collapse leading to jet formation. While both analytical and numerical models offer insight into this complex process, each approach presents distinct challenges. Analytical models, while conceptually straightforward, often rely on simplifications that compromise accuracy. Conversely, uncertainty or even unavailability of relevant material properties and high computational cost are the most important drawbacks of numerical models. Notably, the jet penetration phase imposes significantly greater computational demands compared to preceding processes of jet formation. This research aims at providing a deeper understanding of the jet interaction with target, as well as on determining its influence on penetration depth. We revisit an analytical model based on the virtual origin concept and complement it with numerical simulations using Abaqus/Explicit in a pure Eulerian domain. Through comprehensive analysis, we explore various jet parameters – such as kinetic energy, diameter, length, velocity gradient, and effective standoff distance – and their impact on penetration depth. The insights derived from this study hold practical significance for the preliminary evaluation of the shaped charge's effectiveness and consequent refinement of the design of shaped charge projectiles or warheads.

**Keywords:** shaped charge, jet formation, jet penetration, penetration depth, numerical simulation.

### 1. INTRODUCTION

The shaped charge effect is still the most effective armor-piercing mechanism. Essentially, the working principle is based on focusing or directing the energy of explosion and its conversion in formation of a hypervelocity projectile, so-called shaped charge jet, from the metal liner [1-4]. Apart from its use in defense, it is also applied in other fields, such as petroleum and natural gas industry.

The main mechanism of a shaped charge (SC) is acceleration and collapse of metal liner by the gaseous products of detonation. The collapse of the liner to the symmetry axis is followed by its plastic deformation and formation of high-velocity penetrator, a process that can be seen in Fig. 1. This jet consists from a secondary part – the slug, which is relatively slow and significantly faster primary jet, which is responsible for target penetration.

The representative parameters of a shaped charge jet are presented in Table 1.

The focus of this research is the jet penetration modeling. Although both analytical and numerical models offer insight into this complex process, each approach presents distinct challenges. Analytical models, while conceptually straightforward, often rely on simplifications that compromise accuracy. On the other hand, uncertainty or unavailability of material properties and high computational cost are the most important disadvantages of numerical models. Notably, the jet penetration phase imposes significantly greater computational demands compared to preceding processes of jet formation. This research aims at providing a deeper understanding of the jet interaction with target, as well as on determining its influence on penetration depth.

**Table 1.** Characteristic values of a shaped charge warhead/projectile and jet [1,2]

SC cone diameter	$d = (40 \dots 700) \text{ mm}$
Detonation velocity	$D = (8.0 \dots 9.5) \text{ km/s}$
Jet diameter	$\approx d/20$ , variable
Jet length	$\leq 8d$ , variable
Hole diameter	$\approx d/6$
Jet tip velocity	$\approx D$ (up to 10 km/s)
Jet tail velocity	$(2 \dots 3) \text{ km/s}$
Penetration depth	$(5 \dots 10) d$

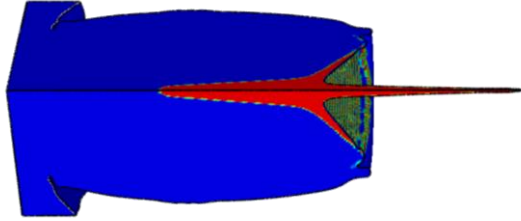


**Figure 1.** Numerical simulation of shaped charge effect: a sequence of the process of liner collapse and jet formation

## 2. ANALYTICAL MODELS

Two most prominent analytical models will be briefly described: the well-known density law and the model with variable jet velocity.

### 2.1. Density law

The main assumption of the density law model is that the jet velocity  $v_j$  is uniform, i.e. jet length is constant (Fig. 2). Additionally, a dominant penetration mechanism is erosion of both the target plate and jet, due to extremely high contact pressure which exceeds the material yield stress by two orders of magnitude. As a consequence, contact surface between the target and the jet moves with velocity  $u$  which is known as penetration velocity. Applying the pressure equilibrium equation in the moving coordinate system, the relation between the two aforementioned velocities can be established:

$$u = \frac{v_j}{1 + \gamma}, \quad \gamma = \sqrt{\frac{\rho_t}{\rho_j}}, \quad (1)$$

where  $\rho_t$  and  $\rho_j$  are the target and jet material densities, respectively. The density law is based on assumption that the penetration process is completed when the entire jet is consumed by erosion. The penetration depth  $P$  may be then calculated using Eq. (2), from which is evident that its value is proportional to the jet length and the ratio between densities of the jet and the target material:

$$P = l_j \sqrt{\frac{\rho_j}{\rho_t}} = \frac{l_j}{\gamma}. \quad (2)$$

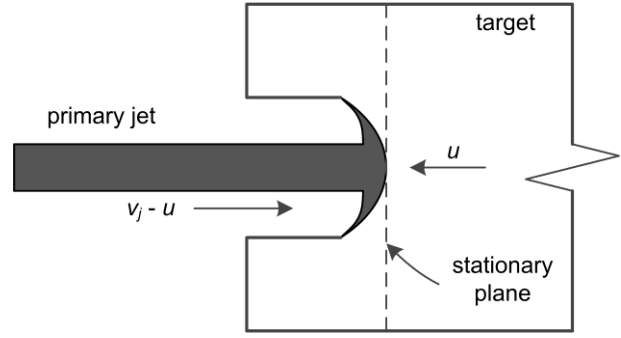


**Figure 2.** Hydrodynamic model of jet penetration

### 2.2. Penetration depth of variable velocity jet

The second, more complex model takes into account the fact that jet velocity is not uniform, due to which the jet gets elongated. This approach is based on the concept of the virtual origin [5], [6]. This concept abstracts the jet formation process, assuming that all jet particles are simultaneously ejected with different velocities from the virtual origin (Fig. 3). Similar treatment of equilibrium and erosion, and more complex approach to penetration dynamics lead to the final expressions for the current jet tip velocity

$$v_j = v_0 \left( \frac{s}{s + p} \right)^\gamma \quad (3)$$

and final penetration depth

$$P = s \left[ \left( \frac{v_0}{v_{\min}} \right)^{\frac{1}{\gamma}} - 1 \right]. \quad (4)$$

In previous equations  $v_0$  is the jet tip velocity,  $p$  is the current penetration depth,  $s$  is the effective standoff – the distance from the virtual origin to the target and  $v_{\min}$  designates the minimum jet velocity under which the penetration may be achieved through the mechanism of erosion. This value can be empirically calculated from:

$$v_{\min} = (1 + \gamma) u_{\min}, \quad u_{\min} = 0.44 + 0.00206 \cdot BHN. \quad (5)$$

where  $BHN$  is the Brinell hardness number for target material. (1)

This model takes also into account more complex cases when jet particulation occurs and the jet break-up time can be involved in corresponding variants of Eq. (4) [5], [6].

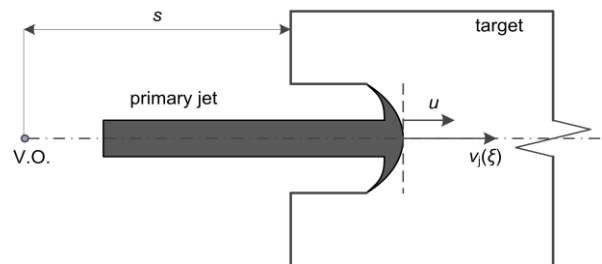


**Figure 3.** Penetration with variable velocity jet and virtual origin concept

### 2.3. Jet kinetic energy and crater volume

A well-know hypothesis in terminal ballistics about the link between the jet kinetic energy and the volume of the crater formed in the target [1], [4] will be investigated. Assuming a linear jet velocity profile in accordance with the virtual origin concept, the kinetic energy of the jet can be expressed as:

$$E_k = \frac{1}{2} m_j v_j^2 = \frac{1}{6} m_j v_0^2 \left[ 1 + \frac{v_t}{v_0} + \left( \frac{v_t}{v_0} \right)^2 \right] \quad (6)$$

where  $m_j$  is the mass of the primary jet, and  $v_0$ ,  $v_t$  and  $v_j$  are the jet tip, jet tail, and average jet velocities, respectively.

Assuming that the average representative value of the cylindrical crater radius is  $r_c$ , the crater volume is:

$$V_c = \pi r_c^2 P \quad (7)$$

The Szendrei-Held model [7-10] has been proposed to describe the radial expansion of the target material based on the equation of motion, alongside with previously considered axial crater growth. The dynamics of the crater radial expansion can be described by:

$$\frac{dr_c}{dt} = \sqrt{\frac{A}{r_c^2} - B}, \quad (8)$$

where parameters  $A$  and  $B$  are defined through:

$$A = \frac{1}{2} \frac{\rho_j}{\rho_t} \frac{\gamma^2}{(1+\gamma)^2} r_j^2 v_j^2, \quad B = \frac{\sigma}{\rho_t}. \quad (9)$$

In the previous equation  $r_j$  denotes the jet radius, while  $\sigma$  is the average dynamic plastic stress of the target material. Therefore, the maximum value of the crater diameter can be calculated:

$$r_c = r_{c,max} = \sqrt{\frac{A}{B}} = r_j \frac{1}{1+\gamma} \sqrt{\frac{\rho_t v_j^2}{2\sigma}}. \quad (10)$$

Using Eqs. (6) – (10) one can calculate the ratio between input kinetic energy of the jet and the resulting created crater volume in the form:

$$\frac{E_k}{V_c} = \left( \frac{1+\gamma}{\gamma} \right)^2 \frac{l_j}{P} \sigma = \frac{(1+\gamma)^2}{\gamma} \sigma = \left( 2 + \gamma + \frac{1}{\gamma} \right) \sigma. \quad (11)$$

It should be noted that for typical practical applications (e.g. copper jet and steel target) density ratio  $\gamma$  is close to unity, so the right-hand side of Eq. (11) is approximately equal to  $4\sigma$ . Obviously, the energy – volume ratio has the unit of pressure (or stress) and can be considered as a parameter of target resistance to jet penetration.

Referring to the well established Tate – Alekseevskii model [11] for jet penetration:

$$\frac{1}{2} \rho_j (v_j - u)^2 = \frac{1}{2} \rho_t u^2 + R, \quad (12)$$

target resistance  $R$  can be interpreted as the energy-

volume ratio calculated by Eq. (11) [10]. Therefore, we have the following relation between the measures of axial ( $R$ ) and radial ( $\sigma$ ) crater expansion resistance:

$$R = 4\sigma. \quad (13)$$

### 3. NUMERICAL APPROACH

Numerical investigation of shaped charge jet penetration is performed using the FEM-based platform Abaqus [12] with its explicit solver, which has been successfully applied for various problems related with transient, high-energy and high strain rates phenomena, including shaped charge formation and penetration [13-15].

Having in mind large plastic deformation of both the jet and the target materials, the Eulerian framework is preferred. In the present research, the focus was set on the penetration phenomena, so the jet formation phase was not considered. Instead, an already formed simplified jet of known material, geometric and kinetic properties was analyzed (Fig. 4). The target was considered to be semi-infinite and sufficiently large values of radius (60 mm) and thickness (from 800 mm to 1100 mm) were selected. The quarter-symmetry was utilized and the mesh which consists from about 2.5 million finite elements was created. Although the mesh was not uniform, the referent element size was equal to 0.75 mm.

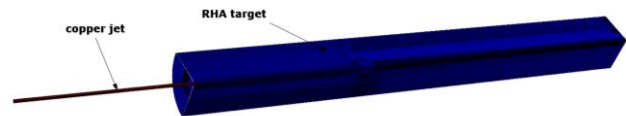


Figure 4. Model of the shaped charge copper jet impacting the RHA target

Definition of material behavior under the highly dynamic loads is of vital importance for the quality and precision of the numerical model. The considered shaped charge jet is made from copper and the target plate from rolled homogeneous armor steel (RHA). Dynamic plasticity of both metals is described by the Johnson-Cook plasticity model [16] and linear shock wave relation. Material failure is treated by the Johnson-Cook damage model [17]. The material properties used in Abaqus simulations have been summarized in Table 2.

Table 2. Material properties for jet material (copper) and target material (RHA) [16, 17]

	Copper	RHA
density (kg/m <sup>3</sup> )	8960	7850
<b>Johnson-Cook plasticity model</b>		
$A$ (MPa)	90	1400
$B$ (MPa)	292	1800
$C$	0.025	0.0049
$n$	0.31	0.768
$m$	1.09	1.17
$T_{melt}$ (K)	1356	1800
$T_{trans}$ (K)	300	300
<b>Linear <math>U_s - u</math> equation of state</b>		
$c_0$ (m/s)	6940	4578
$s$	1.49	1.33

$\Gamma$	2.0	1.67
<b>Johnson-Cook damage model</b>		
$d_1$	0.54	0.10
$d_2$	4.89	3.44
$d_3$	3.03	2.12
$d_4$	0.014	0.002
$d_5$	1.12	0.61

The nominal characteristics of the baseline jet in the moment of impact into the target are shown in Table 3. As the idea of the research was to investigate the influence of the jet properties on the penetration depth  $P$  and the volume of created crater  $V_c$ , the jet’s kinetic energy was held constant, while two effects have been considered: (i) variation of the jet velocity profile (gradient), and (ii) variation of the jet effective standoff.

**Table 3.** Main nominal properties of the benchmark jet-target system

Property (unit)	Value
Jet diameter (mm)	6
Jet length (mm)	250
Jet tip velocity (m/s)	9200
Jet tail velocity (m/s)	3000
Mass of the jet (g)	63.3
Kinetic energy of the jet (MJ)	1.279
Target thickness (mm)	800 ... 1100

#### 4. RESULTS AND DISCUSSION

Typical evolution of the baseline jet’s penetration into the RHA target is shown in Fig. 5. In this case, the penetration depth was equal to 536 mm, while the time of penetration (from jet impact to the completion of the process) had the value of 232  $\mu$ s.

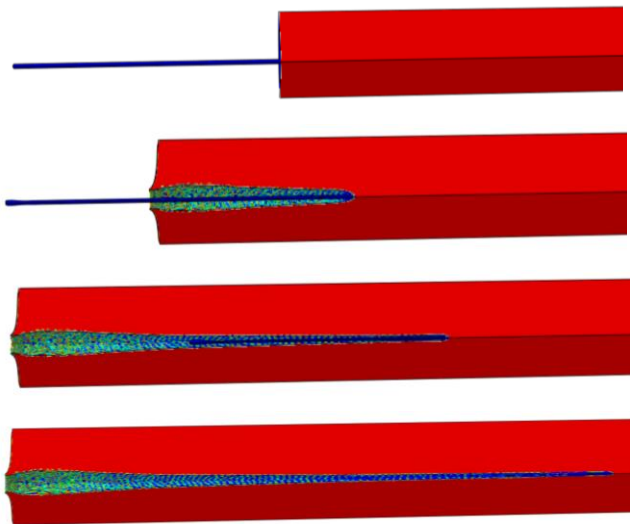


**Figure 5.** Evolution of the baseline jet’s penetration into the RHA steel target. Jet material is in blue and target material in red color. Sequences correspond to the following moments: 0  $\mu$ s, 40  $\mu$ s, 120  $\mu$ s and 232  $\mu$ s. Penetration depth is 536 mm.

Penetration depth is investigated for varying velocity

gradient of the jet – six variants of jet velocity profiles have been analyzed: from uniform velocity jet ( $v_0=v_t=6356$  m/s) to the jet with intense velocity gradient ( $v_0=10056$  m/s,  $v_t=2000$  m/s). Kinetic energy of the jet was kept constant for each variant. Results are presented in Fig. 6 where the abscissa  $\Delta v$  corresponds to the difference between the jet tip and jet tail velocity. It can be seen that penetration depth increases with the increase in jet velocity gradient, reaching the maximum for  $\Delta v \approx 5500$  m/s. Acceptable correspondence between numerical and analytical model results can be observed.

Relative penetration depth was also analyzed as a function of the effective standoff – the distance between the virtual origin and the target. Both numerical and analytical results indicate an increase of penetration depth with increasing standoff, as shown in Fig. 7. Models obviously fail to capture a well-known fact from experiments that there is an optimum standoff with maximum penetration capability of the jet. This is the consequence of the fact that both models assume ideal jets with perfect material homogeneity, geometric precision, symmetry and undisturbed break-up.

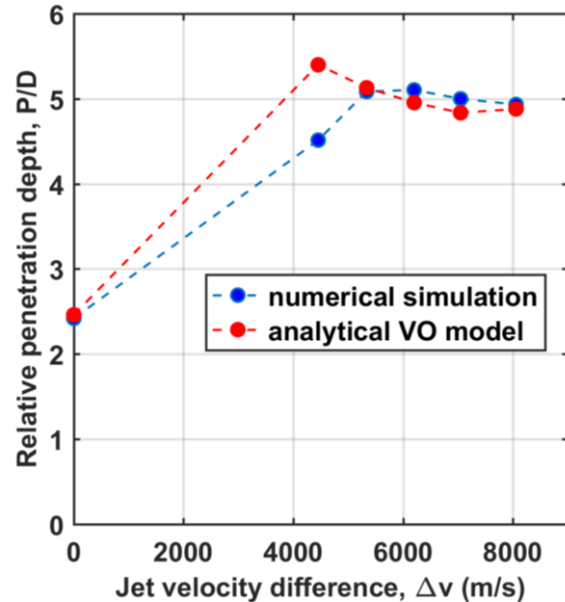


**Figure 6.** Relative penetration depth as a function of jet tip-to-tail velocity difference: comparison between results of numerical simulations and analytical model based on the virtual origin concept

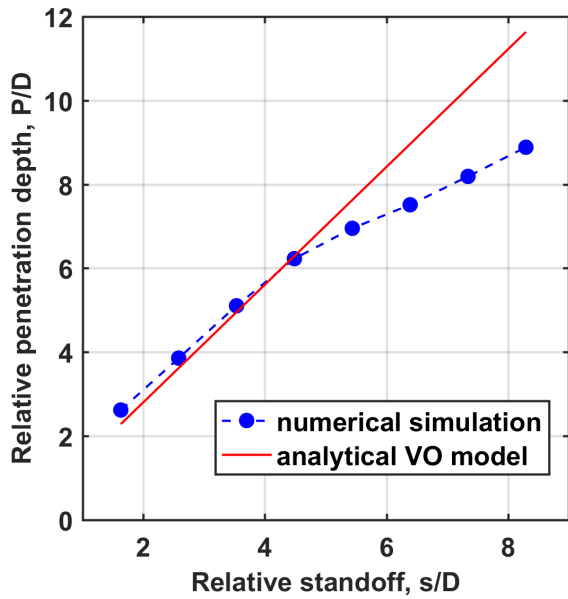


**Figure 7.** Relative penetration depth as a function of the effective standoff: comparison between simulations and analytical model

Volume of the crater created by the jet’s penetration can be presented in the similar manner, as a function of both jet gradient  $\Delta v$  and relative standoff distance, which is shown in Figs. 8 and 9, respectively. Although a scatter in the data is obvious, it is clear that the values of crater volume are within  $\pm 10\%$  deviation from the indicated average values. It should be noted that the exact values of crater volume cannot be obtained directly from the Abaqus output database due to the usage of Eulerian elements. Therefore, volumes are calculated through the use of a special image processing software ImageJ [18], which may be the source of additional discrepancies. Nevertheless, the hypothesis of approximately constant crater volume produced by the jets of the same kinetic energy is considered to be confirmed.

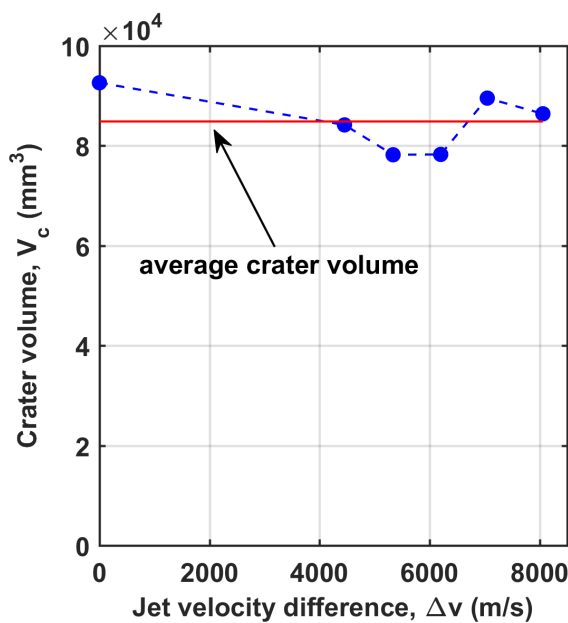


**Figure 8.** Crater volume vs. jet tip-to-tail velocity difference; average crater volume is indicated

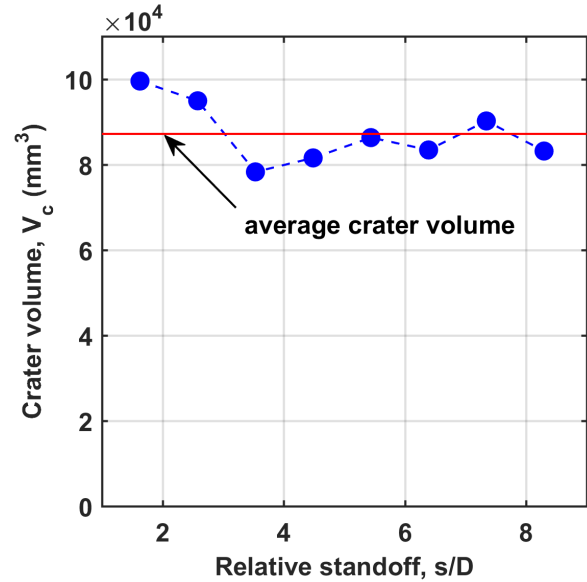


**Figure 9.** Crater volume vs. relative standoff distance; average crater volume is indicated

Moreover, the average crater volume from all simulations was equal to  $86181 \text{ mm}^3$ , and by applying the constant kinetic energy term from Table 3, one can determine the specific energy needed for cratering, i.e. characteristic material strength:

$$\frac{E_k}{V_c} = 14.833 \frac{\text{J}}{\text{mm}^3} = 14.833 \text{ GPa} . \tag{14}$$

On the other hand, the average representative value of the yield stress of the target material can be determined from the Johnson-Cook diagram (Fig. 10) using the data from Table 2. Having in mind that simulations indicate the maximum equivalent plastic strain of 2.8, and by neglecting the effects of strain rate hardening and thermal softening or considering them to be self-balancing, the average flow stress of  $\sigma=3.645 \text{ GPa}$  can be calculated. According to Eq. (13), the target resistance can be found:

$$R = 4\sigma = 14.580 \text{ GPa} . \tag{15}$$

The values obtained by Eqs. (14) and (15) are remarkably close, confirming the link between the specific energy required for cratering and the target material dynamic flow stress.

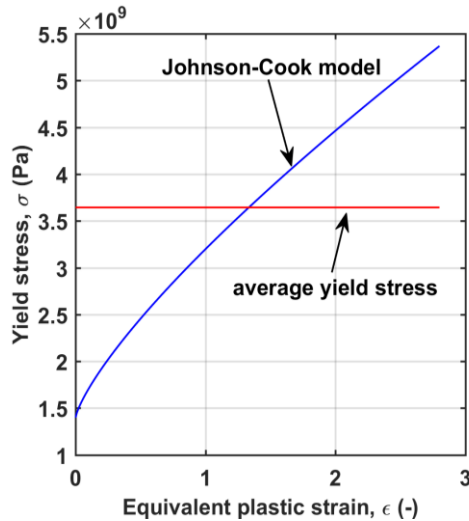


**Figure 10.** Flow stress vs. equivalent plastic strain for RHA steel according to the Johnson-Cook model; the average flow stress for the plastic strain of up to 2.8 is indicated

## 5. CONCLUSION

The paper considers various aspects of shaped charge jet penetration modeling. The following conclusions can be drawn:

- numerical simulations in Abaqus/Explicit provide detailed insight into the penetration process,
- jet characteristics, such as the velocity gradient and the standoff distance, significantly influence both the penetration depth and the volume of created crater,
- analytical penetration models exhibit limitations in terms of treatment of jet non-ideality (imperfect symmetry, break-up drift, etc.),
- crater volume created by the jet can be evaluated from the jet kinetic energy and the target material flow stress,
- further investigation can be focused on various issues, including jet break-up modeling and jet non-ideality.

## Acknowledgments

This work was supported by the Ministry of Science, Technological Development and Innovation, the Republic of Serbia, under contract evidence number 451-03-65/2024-03/200105 from 05.02.2024.

## References

- [1] WALTERS, W.P., ZUKAS, J.A.: *Fundamentals of shaped charges*, John Wiley & Sons, New York, 1989.
- [2] ZUKAS, J.A., WALTERS, W.P.: *Explosive effects and applications*, Springer, New York, 2002.
- [3] CARLUCCI, D.E., JACOBSON, S.S.: *Ballistics: Theory and design of guns and ammunition*, CRC Press, Boca Raton, FL, 2018.
- [4] ELEK, P.: *Terminal ballistics* (in Serbian), University of Belgrade – Faculty of Mechanical Engineering, 2018.
- [5] ALLISON, F.E., VITALI, R.: *A new method for computing penetration variables for shaped-charge jets*, Ballistic Research Laboratories, Aberdeen Proving Ground, Maryland, 1963.
- [6] DIPERSIO, R., SIMON, J., MERENDINO, A.: *Penetration of Shaped-Charge Jets into Metallic Targets*, BRL Report No. 1296, 1965.
- [7] SZENDREI, T.: *Analytical model of crater formation by jet impact and its application to calculation of penetration curves and hole profiles*, Proceedings of 7<sup>th</sup> International Symposium on Ballistics, The Hague, 1983, pp. 575-583.
- [8] SZENDREI, T.: *Analytical model for high-velocity impact cratering with material strengths: Extensions and validations*, 15<sup>th</sup> International Symposium on Ballistics, Jerusalem, 1983, pp. 123-131.
- [9] SZENDREI, T.: *Link between axial penetration and radial crater expansion in hypervelocity impact*, 17<sup>th</sup> International Symposium on Ballistics, Midrand, 1998, pp. 3-25-3-32.
- [10] HELD, M.: *Verification of the equation for radial crater growth by shaped charge jet penetration*, *International Journal of Impact Engineering*, Vol. 17, 1995, 387-398.
- [11] WALKER, J.: *Modern impact and penetration mechanics*, Cambridge University Press, Cambridge, 2021.
- [12] DSSC, *Abaqus Theory Manual*, Dassault Systemes, Simulia Corp, Providence, RI, USA, 2023.
- [13] DEHESTANI, P., FATHI, A., DANIALI, H.M.: *Numerical study of the stand-off distance and liner thickness effect on the penetration depth efficiency of shaped charge process*, *Proceedings of the Institution of Mechanical Engineers, Part C: Journal of Mechanical Engineering Science*, 233(3) (2019) 977-986.
- [14] ELEK, P., MARKOVIĆ, M., JEVTIĆ, D., ĐUROVIĆ, R.: *Modeling of penetration depth of a shaped charge jet*, 9<sup>th</sup> Congress of the Serbian Society of Mechanics, Vrnjačka Banja, Serbia, July 5-7, 2023.
- [15] ELEK, P., MARKOVIC, M., JEVTIC, D., DJUROVIC, R.: *Numerical and analytical modeling of a shaped charge penetration depth*, Proceedings of the 4<sup>th</sup> International Conference on Impact Loading of Structures and Materials, Freiburg, Germany, 13-17 May 2024, pp. 88-89.
- [16] JOHNSON, G.R., COOK, W.H.: *A constitutive model and data for metals subjected to large strains, high strain rates and high temperatures*, Proceedings of the 7<sup>th</sup> International Symposium on Ballistics, The Hague, 1983.
- [17] JOHNSON, G.R., W.H. COOK: *Fracture characteristics of three metals subjected to various strains, strain rates, temperatures and pressures*, *Engineering Fracture Mechanics*, 21 (1985) 31-48.
- [18] FERREIRA, T., RASBAND, W.: *ImageJ User Guide IJ 1.46r*, imagej.net (accessed: 10/07/2024)





## MONITORING PLASTICIZER'S MIGRATION IN THE HMX/DOA MIXTURE UNDER ELEVATED TEMPERATURES

MIRJANA KRSTOVIĆ

Military Technical Institute, Belgrade, [mirjana.krstovic@mod.gov.rs](mailto:mirjana.krstovic@mod.gov.rs)

DANICA BAJIĆ

Military Technical Institute, Belgrade, [danica.bajic@mod.gov.rs](mailto:danica.bajic@mod.gov.rs)

TEODORA STANČIĆ

Military Technical Institute, Belgrade, [teodorastancic@gmail.com](mailto:teodorastancic@gmail.com)

MLADEN TIMOTIJEVIĆ

Military Technical Institute, Belgrade, [mladen.timotijevic@gmail.com](mailto:mladen.timotijevic@gmail.com)

BOJANA FIDANOVSKI

Military Technical Institute, Belgrade, [bojana.fidanovski@mod.gov.rs](mailto:bojana.fidanovski@mod.gov.rs)

**Abstract:** Polymer-bonded explosives and plasticizer-coated nitramine based explosives represent a group of energetic materials that have been extensively manufactured in recent years in order to satisfy requirements ranging from boosters to the main charges of warheads. From the aspect of their production technology, physical-mechanical properties, and further detonation properties, it is important to properly select and incorporate specific functional additives into the explosive-polymer matrix. Dioctyl adipate (DOA) is the predominant plasticizer utilized in PBX formulations to enhance their processability. To enhance the safety of transporting HMX from the factory to the manufacturing facilities, it is not uncommon for HMX to be blended with DOA instead of using wetting explosives to make the highly reactive explosive less sensitive. This semi-product may be further incorporated in multi-component PBX formulations or pressed into booster charges. Occasionally, the HMX/DOA mixture is held for an extended period prior to utilization, which may be a problem, knowing the migration ability of DOA molecules. The aim of this paper is to monitor and measure the migration of DOA from the HMX/DOA mixture. The samples were exposed to slightly elevated temperatures for a certain period of time and compared with samples exposed to ambient temperatures. The content of DOA in the HMX/DOA system was monitored and determined using both classical and instrumental methods. The results indicate the migration of DOA is influenced by temperature, i.e. that the migration is more pronounced at a higher temperature, as well as the differences in the presence of DOA in the layers becomes more noticeable over time.

**Keywords:** HMX, dioctyl adipate, migration, plasticizer, polymer-bonded explosives.

### 1. INTRODUCTION

In recent decades, significant advance has been achieved in the synthesis and formulation of novel explosive compositions with the objective of enhancing fragmentation, penetration, and brisance. A particular field of focus for development has been, and continues to be, the formulation of polymer bound explosives (PBX's). PBX is an acronym that refers to an extensive variety of explosive materials that contain polymer binders. It encompasses not only plastic compositions that can be shaped by hand, but also formulations designed by pressing and solid compositions that are chemically cross-linked and can be produced using casting techniques [1].

This type of energetic materials has attracted a lot of attention due to the fact that they enable a very wide range of characteristics of the final product, depending on the choice of additives and their mass fractions in the

explosive composition. The initial PBX formulations were created in the 1950s, with the aim of developing formulations that had decreased sensitivity and increased safety during production and handling. Furthermore, PBX's have enhanced processability and mechanical characteristics [2-3]. The fundamental structure of PBX is comprised of high-explosive particles, polymers, with the inclusion of additives such as metal powder as a fuel component or the addition of oxidants to generate the desired effects, and the processing additives to the binder which make production easier.

Secondary explosives, such as PETN (pentaerythritol tetranitrate), RDX (hexogen), and HMX (octogen), are frequently integrated into PBX. Their distinctive attributes allow the final products to have a desirable impact on the target. Namely, PETN has detonation velocity of 8310 m/s at a density of  $\rho=1.77$  g/cm<sup>3</sup> [4], while RDX has detonation velocity of 8750 m/s at a density of  $\rho=1.76$  g/cm<sup>3</sup> [4]. Among the most common

secondary explosives HMX has highest possible efficiency due to detonation velocity of 9110 m/s at a density of  $\rho=1.89 \text{ g/cm}^3$  [4].

The selection of a binder has a substantial impact on the performance of the final product and the available production options. In general, polymer binders in energetic materials serve as matrices, binding all solid particles together into a cohesive structure. This allows the energetic material to possess the desired properties, and ensures that the resulting final product has the necessary geometric shape. While a multitude of polymers have been artificially created so far, only a limited number satisfy the stringent requirements to be considered a suitable matrix for energetic materials. More precisely, the chosen polymer must be compatible with other components, possess the desired mechanical properties, maintain its integrity within the operational temperature range, withstand various stresses during flight, and be suitable for the production process and technique. The extensive range of requirements imposed on polymers used in energetic materials significantly limits the selection of potential candidates for polymer matrices in ordnance.

Nowadays, the polymers utilized in energetic materials can be categorized as either inert or energetic, depending on whether they actively contribute their energy during the detonation process or not. In the context of inert polymers, the most commonly employed systems are those involving inert thermal cross-linking resin. These systems are primarily composed of polyurethane, specifically hydroxyl-terminated polyols that are crosslinked with isocyanates [5,6]. Hydroxyl-terminated polyols can be categorized into polyesters, polyethers, and polybutadienes based on their structural composition. Polyethers and polybutadienes are widely used compounds due to their extensive availability in the market, suitable viscosity, and rapid cross-linking speed. Furthermore, elastomers derived from these materials exhibit remarkable resistance to abrasion and favorable characteristics at low temperatures. The most commonly utilized polyurethanes are those derived from hydroxyl-terminated polyethers (HTPE), carboxyl-terminated (CTPB), and hydroxyl-terminated polybutadiene (HTPB). Each additive in energetic materials serves a distinct purpose. Metal powders enhance energy output; polymers enhance mechanical properties and bind all ingredients together into a dense structure. Curing agents initiate solidification of polymers providing the solid form of the charges, while plasticizers aid in the processing of the materials [7].

The utilization of plasticizers in energy materials offers several advantages: it enhances mechanical properties at low temperatures, softness, and has a direct influence on processability [8]. Incorporating this particular additive yields advantageous attributes in the final products (ammunition) in terms of preservation, application, and transporting [9]. Considering that plasticizers are responsible for achieving various desirable properties, they typically consist of low-viscosity liquid organic compounds that enhance viscosity control during mixing

and prolong the *pot life* during casting. Plasticizers, in general, are a frequent ingredient of all energetic materials. For example, powders and rocket fuels have had plasticizers for decades. Some of them, like nitroglycerin, can energetically participate in the combustion process, while certain are non-energetic. Some of them, including phthalates, have been utilized in gunpowder and rocket propellants for decades, while novel plasticizers are continually being developed.

Nevertheless, there might be a significant time lapse between the synthesis and implementation of novel plasticizers in complex structures like ammunition. Due to the relatively low mass percentage of plasticizer in energetic material formulations, the research on these additives is typically overlooked. The main reason for the preference of already tested plasticizers in new compositions is that they have been proven to be effective. In research, however, greater focus is given to modifying the other components that can result in a substantial boost in energy output.

A frequently employed composition for PBX, is consists of RDX or HMX as the secondary explosive, HTPB as the prepolymer, isophorone diisocyanate (IPDI) as the curing agent, and dioctyl adipate (DOA) as the plasticizer, along with the inclusion of different size of metal powder. The mentioned explosive compositions, with varying mass ratios have been widely recognized for a few years, with the possibility of modeling characteristics by varying the size and type of metal powder. However, the utilization of DOA as a plasticizer in energetic materials requires additional attention given its tendency for exudation i.e. migration. The issue of migration is not solely limited to DOA, but rather is a widespread problem that arises with the majority of plasticizers now in use. On the positive side, the addition of a small amount of this additive can improve the flow-ability of the energetic composition slurry by elongating the polymer chain structure. On the other hand, over time, it can lead to the infringe of the homogeneous structure due to migration [10].

The secondary explosives can only be stored or transported with a significant presence of moisture. This type of treatment of explosives requires its drying before their use in production facilities. One of the potential options that could enable the avoidance of wetting and thus drying of the explosive, involves coating the crystal particles with some phlegmatizing substance such as plasticizers, which itself is one of the ingredients of the PBX formulation. Applying a layer of DOA on explosive particles in production facilities and transporting them to factories for PBX production is an effective solution that significantly decreases the time required to prepare raw materials for mixing the mass used in casting PBX. However, considering the fact that specific plasticizers have a tendency to migrate, the question arises regarding the long-term behavior of this two-component composition under storage conditions, if it is not immediately used for the manufacturing of final products. The aim of this paper is to simulate the aging conditions of the HMX/DOA mixture and monitoring the plasticizer content in certain parts of its volume in order to determine

the behavior of DOA over time.

HMX - high melting point explosive (Fig.1) is known for its increased potency while remaining relatively resistant to various stimuli such as heat, impact, friction, and spark. These properties make them suitable for use as explosive fillings in bombs, shells, and other munitions [4,7].

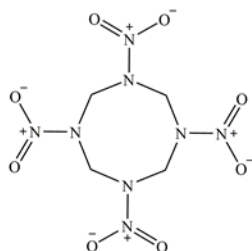


**Figure 1.** Octogen (HMX)

As it can be seen in Figure 1. HMX has a molecular structure that consists of an eight-membered ring made up of alternating carbon and nitrogen atoms. Each nitrogen atom in the ring is attached to a nitro group. HMX possesses a higher level of complexity in its manufacturing process compared to the majority of explosives, which limits its usage to specialized applications [10].

**Table 1.** HMX characteristics [3]

Characteristic	Value
Enthalpy of formation (kJ/kg)	252.8
Oxygen balance (%)	-13.51
Specific volume of gases (cm <sup>3</sup> /g)	927
Heat of the explosion (kJ/kg)	5679
Density (g/cm <sup>3</sup> )	1.91
Melting point (°C)	275
Auto-ignition temperature (°C)	240
Detonation velocity (m/s)	9120
Sensitivity to impact (Nm)	120
Sensitivity to friction (N)	7.4
Critical diameter (mm)	8

DOA (C<sub>22</sub>H<sub>42</sub>O<sub>4</sub>) is colorless, very faint, slightly greasy odor of its own, light resistance, transparent oily liquid known as a cold plasticizer commonly used in the production of polyvinyl chloride, polyethylene copolymers, polystyrene, nitrocellulose, ethyl cellulose, and synthetic rubber [11]. The extensive applicability of DOA (Figure 2.) as a plasticizer is attributed to its organic nature, which allows it to be compatible with all the aforementioned materials.

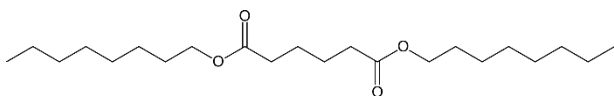


**Figure 2.** Dioctyl adipate DOA

Dioctyl adipate is a diester compound formed by the combination of adipic acid and octanol, as indicated by its

alternative name, adipic acid dioctyl ester. The core of the chemical consists of the remaining adipic acid, where the end carboxylic acid groups have been converted into esters by reacting with the hydroxyl groups of two molecules of 1-octanol. The symmetrical dioctyl adipate consists of two ester groups, each of which is sequentially connected to a regular and unbranched octyl radical [12]. Dioctyl adipate, with two functional groups, is capable of undergoing the standard reactions associated with an ester. These methods involve acid-catalyzed hydrolysis and saponification with a base, which reverts the octanol back to its original form and produces a salt of adipic acid. The solubility of the material is dictated by the extended, hydrophobic octyl chains. Due to the presence of polar ester groups, dioctyl adipate exhibits low solubility in polar solvents like water. It is common to combine DOA with other plasticizers such as dioctyl phthalate (DOP) and dibutyl phthalate (DBP) in various applications such as cold-resistant agricultural plastic film, frozen food packaging film, cables, electric wires, and more [13]. The utilization of DOA as a plasticizer in any industry, including the military, requires the acquisition of an already prepared commercial product available in the market. In Table 2. are shown some characteristics of commercial DOA.

**Table 2.** DOA characteristics [11]

Characteristic	Value
Molecular weight	370.57
Relative density	0.922
Boiling point	374.4 °C at 760 mmHg
Flash point	168.9 °C

DOA is a type of synthetic ester oil that is produced through the process of esterification, which involves combining adipic acid and 2-ethyl hexanol [14]. Because of its high thermal-oxidation stability, low carbon residue formation, outstanding viscosity index, strong thermal conductivity, and significant specific heat capacity, it is extensively used in different industry sectors [15-17].

## 2. MATERIALS AND METHODS

### 2.1. Materials

In this study, a blend of HMX/DOA was employed consisting of the following fundamental components:

- HMX Prva Iskra Namenska Barič and
- DOA provided by Traylor corporation.

The HMX/DOA mixture, as per the manufacturer's standard, consists of approximately 3wt.% commercial DOA, and 97wt.% HMX explosive.

Samples from the same batch of octogen coated with DOA were examined. All of the samples were evenly distributed among identical test tubes as it is shown in Figure 3.



**Figure 3.** a) Test tube for samples with its dimensions, b) sample exposed to light and ambient temperature, c) sample stored in a dark on ambient temperature

Two reference samples were kept at ambient temperature for 30 days, one sample stored in a dark and the other one exposed to natural light. The remaining ten test tubes were placed in a thermal blocks.

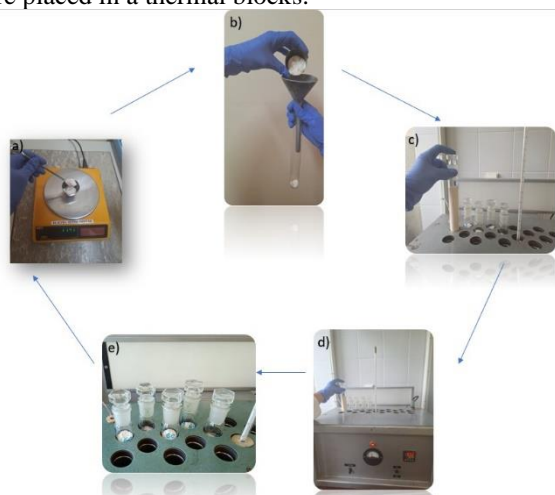


**Figure 4.** a) sample measurement, b) pouring the sample into the test tube, c) placing the test tube in the thermal block, d) thermal block with digital temperature gauge and control thermometer, e) five test tubes placed at a same temperature

Five of them were set at a temperature of 60°C and the other five were set at 80°C. At intervals of 5 to 10 days, a test tube was removed from the thermal blocks and the levels of DOA in three layers were analyzed.

## 2.2. Instrumental methods

The Fourier-transform infrared spectroscopy (FTIR) method was employed to analyze the raw ingredients used in the HMX/DOA mixture, as well as the filtrate produced after the rinsing process with organic solvents, while Differential scanning calorimetry (DSC) was used to investigate the melting behavior of crystalline explosives in order to experimentally verify the complete removal of DOA from the HMX particles.

## 2.3. Classical method

A classical method was employed to determine the DOA content in the HMX/DOA mixture relying on the solubility of these chemicals in specific solvents. Regarding DOA, it has excellent solubility in carbon tetrachloride, dichloromethane, alcohols and n-heptane. In this study, two appropriate solvents, dichloromethane, and n-heptane, were selected for separating the two-component mixture.

1 gram of the HMX/DOA mixture sample as well as 1 g of pure HMX was measured with a precision of 0.0001 g. The control sample, consisting of pure HMX, serves to quantify the amount of HMX wasted during the dissolution process in solvent and subsequent filtration. Every individual sample was placed inside graduated beakers and a volume of 20 cm<sup>3</sup> of dichloromethane was introduced to each sample. The samples were left during 30 minutes with intermittent agitation, after which they were subjected to filtration using a glass filter crucible, with a porosity level of 4. The beakers containing samples were thoroughly rinsed multiple times, using a total of 50 cm of liquid, to ensure the complete transfer of all insoluble material to the glass filter crucibles. Subsequently, the crucibles were placed in the oven and maintained at a temperature of 80°C until they attained a constant mass. After the drying process, the glass filter crucibles were measured, and the content of DOA was determined using the subsequent formula (1):

$$\%DOA = \left[ 1 - \frac{m_3(m_2 - m_1)}{m_0(m_5 - m_4)} \right] \cdot 100 \quad (1)$$

where:

$m_0$  – HMX/DOA mixture sample weight,  
 $m_1$  – weight of empty glass filter crucible for HMX/DOA mixture sample,  
 $m_2$  – weight of glass filter crucible with HMX/DOA mixture sample after the drying process,  
 $m_3$  – pure HMX sample weight,  
 $m_4$  – weight of empty glass filter crucible for pure HMX sample and  
 $m_5$  – weight of glass filter crucible with pure HMX sample after the drying process.

## 3. RESULTS AND DISCUSSION

The conventional gravimetric method is applied for all samples. The analysis was conducted in triplicate, and the results given encompassed the complete range of values obtained. Table 3. presents the measured mass loss of pure HMX in both solvents, taking into consideration even the slightest margin of error. The average value has been reduced to two decimal places.

**Table 3.** Pure HMX mass loss

Solvent	Mass loss [%]	Average [%]
Dichloromethane (CH <sub>2</sub> Cl <sub>2</sub> )	0.161	0.16
	0.153	
	0.172	
n-heptane	0.084	

$(\text{CH}_3(\text{CH}_2)_5\text{CH}_3)$	0.089	0.09
	0.093	

The gravimetric measurement of pure HMX clearly demonstrated that the selection of solvents was appropriate, with a minor quantitative advantage observed for n-heptane. But, in terms of safeguarding human health, n-heptane poses a higher risk due to its toxicity. Table 4. presents the results obtained from analyzing the HMX/DOA mixture sample. The examination was conducted before the samples were exposed to elevated temperatures and involved using formula (1) to calculate the loss of pure explosive during the filtering procedure using the chosen solvent.

**Table 4.** Quantification of DOA in the initial sample

Solvent	DOA [%]
Dichloromethane ( $\text{CH}_2\text{Cl}_2$ )	2.84±0.14
n-heptane ( $\text{CH}_3(\text{CH}_2)_5\text{CH}_3$ )	2.62±0.11

Using either solvent produces consistent measurements of the DOA content in the sample, with the findings deviating by 0.2% of the DOA content. When rinsing with n-heptane, the values obtained are 7.1% lower than those obtained when using dichloromethane.

Samples that were exposed to elevated temperatures, in order to simulate accelerated aging with the aim of observe and quantify DOA migration, were analyzed successively, with the dynamics that followed the removal test tubes with samples from the thermal blocks. Table 5. showed the results for both solvents by days and temperatures they were exposed to.

**Table 5.** Results of monitoring the DOA migration due to exposure of samples to elevated temperatures

day	Temp. [°C]	layer	Dichloromethane ( $\text{CH}_2\text{Cl}_2$ )	n-heptane ( $\text{CH}_3(\text{CH}_2)_5\text{CH}_3$ )
10	60	upper	2.82	2.42
		middle	2.84	2.45
		lower	2.98	2.49
	80	upper	2.83	2.32
		middle	2.93	2.42
		lower	3.09	2.53
15	60	upper	2.81	2.30
		middle	2.97	2.33
		lower	2.98	2.58
	80	upper	2.69	2.23
		middle	2.81	2.52
		lower	3.10	2.58
		upper	2.70	2.17

20	60	middle	2.85	2.40	
		lower	2.97	2.60	
	80	upper	2.70	2.12	
		middle	2.78	2.17	
	25	60	lower	2.88	2.31
			upper	2.44	1.99
middle			2.65	2.17	
80		lower	2.82	2.48	
		upper	2.31	1.61	
		middle	2.44	1.63	
30	60	lower	2.85	2.64	
		upper	2.41	1.94	
		middle	2.51	2.23	
	80	lower	3.06	2.68	
		upper	2.15	1.51	
		middle	2.34	1.54	
		lower	3.19	2.81	

Table 5. clearly demonstrates that DOA migration is detected within just 10 days of exposing the samples to increased temperatures. A temperature of 60°C resulted in a 0.16% disparity between the upper and bottom layers in samples treated with dichloromethane, but this disparity is half less (0.07%) in samples treated with n-heptane. After being subjected to a temperature of 80°C for a period of 10 days, the samples showed a larger migration of DOA, likely caused by the elevated temperature. Consequently, the dichloromethane-treated samples exhibited a disparity of 0.26% in the concentration between the upper and bottom layers of the HMX/DOA mixture, whilst the n-heptane-washed samples displayed a difference of 0.20%. Upon initial examination of the first samples, it is evident that there is a discernible alteration in the DOA content across different levels. Specifically, the plasticizer in question demonstrates a tendency to migrate towards the lower layers.

After a duration of 15 days, the samples that underwent tempering at 60°C and were treated with dichloromethane exhibit nearly equivalent outcomes to those subjected to the same temperature for 10 days. Notably, in this instance, the DOA value in the intermediate layer closely resembles that of the bottom layer. In the samples subjected to a temperature of 60°C during 10 days, the value of the middle layer closely approximated the values of the upper layer. These findings suggest that accelerated aging leads to a slow migration of DOA towards the lower layers. The values obtained after treatment with n-heptane result in a larger disparity between the layers, measuring 0.28%. Upon analyzing the obtained values of the sample that was exposed to a temperature of 80°C for 15 days, a significant difference between the upper and lower layers is observed. For samples treated with

dichloromethane, that difference is 0.41%, while for samples treated with n-heptane, that difference is 0.35%. It is an extremely high percentage, bearing in mind that DOA in the HMX/DOA mixture is present in a very small percentage (2.62-2.98%, Table 3). It means that about 1/8 of the total DOA migrated from the upper layers to the bottom of the test tube in first 15 days on higher temperature.

After subjecting the samples to heating at 60°C for a period of 20 days, the samples rinsed in dichloromethane showed a difference of 0.28% between the layers. On the other hand, the samples rinsed with n-heptane exhibited a higher difference between the layers, around 0.40%. However, samples that had been heated to a temperature of 80°C during 20 days yield data that suggest the absence of DOA in the sample. Simultaneously, while conducting the sampling process, two occurrences are noted. Firstly, a highly potent odor of DOA is detected, which is absent in the samples treated at 60°C. Secondly, the glass test tube retains a significant amount of grease, suggesting that a certain amount of the DOA adheres to the inner walls of the test tube.

After 25 days of being heated to high temperatures, the odor of DOA becomes detectable even in samples that have been exposed to the temperature of 60°C. Compared to the 20th day, there was a modest increase in the difference between the layers for samples in dichloromethane (0.38%) and in n-heptane (0.49%). There is a discernible decrease in the amount of DOA in the sample, indicating that some of the plasticizer adhered to the inner walls of the test tube.

After 25 days, two selected solvents yield significantly different values at a temperature of 80 degrees. Specifically, the analysis of the samples treated with dichloromethane reveals a discrepancy of 0.51% between the upper and bottom layers, whereas the samples treated with n-heptane exhibit a twofold difference of 1.03%. Both examples demonstrate a noticeable decrease in the overall concentration of DOA in the sample.

As anticipated, results were obtained after a period of 30 days, showing the highest migration of DOA. The samples subjected to a temperature of 60°C exhibited a disparity of 0.65% in the stratification between the upper and bottom layers for the samples treated with dichloromethane, whereas this discrepancy was 0.74% for the samples treated with n-heptane.

After being exposed to accelerated aging at 80°C for 30 days, the samples showed that over one-third of the initial amount of DOA had moved to the bottom of the test tube. The samples treated with dichloromethane exhibit a disparity of 1.04% between the upper and lower layers, whereas the samples subjected to n-heptane rinsing showed a disparity of 1.3% between the top and lower layers. Furthermore, it is apparent that the intermediate layer values closely resemble those of the upper layer for both solvents, indicating that DOA predominantly moved towards the bottom of the test tube.

**Table 6.** Results of monitoring the DOA migration for samples exposed to ambient temperature for 30 days

day	ambient temp.	layer	Dichloromethane (CH <sub>2</sub> Cl <sub>2</sub> )	n-heptane (CH <sub>3</sub> (CH <sub>2</sub> ) <sub>5</sub> CH <sub>3</sub> )
30	Exposed to light	upper	2.92	2.59
		middle	2.95	2.64
		lower	2.98	2.67
	Kept in dark place	upper	2.89	2.58
		middle	2.93	2.66
		lower	2.96	2.69

In order to evaluate the impact of temperature on the migration of DOA in the HMX/DOA composition, control samples were included. These samples were not subjected to accelerated aging due to high temperatures, but were instead kept in the test tubes at the same ambient temperature. Table 6 indicates a 30-day duration resulted in barely disparities between the upper and bottom layers. The results closely resemble those obtained after subjecting the samples to a temperature of 60°C during 10 days. Furthermore, it is noted that there are no substantial differences in the results regarding light exposure, aligning with the manufacturer's information about light resistance [11].

Considering that classical methods are less reliable than instrumental methods, the efficacy of separating two components - HMX and DOA was controlled using FTIR and DSC. Specifically, following each rinsing utilizing the DSC method, the residual content in the glass filter crucible was analyzed to confirm the absence of any residual DOA in the sample. In Figure 5 the respective DSC diagram is given, which corresponds to HMX without the presence of DOA.

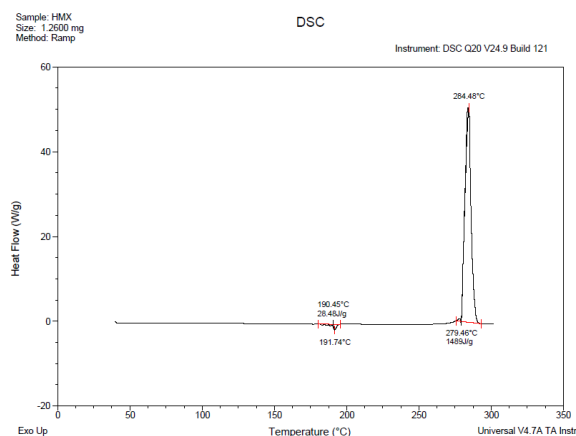


**Figure 5.** DSC diagram of HMX remaining in the glass filter crucible after solvent rinsing

Figure 6. shows the FTIR spectra for the HMX/DOA mixture, as well as the spectrum from the database for pure HMX and pure DOA.

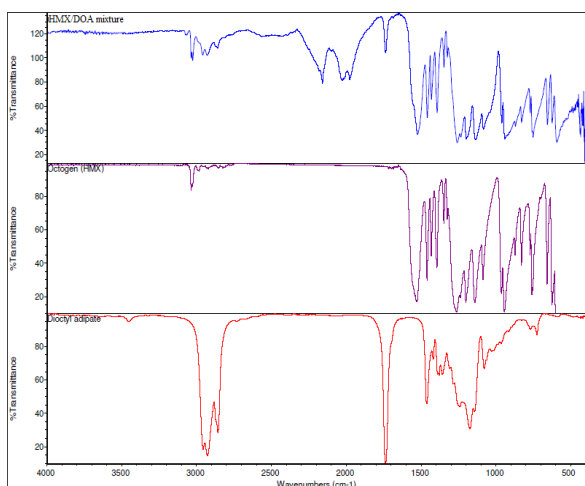


**Figure 6.** FTIR spectrum for HMX/DOA mixture, HMX and DOA

After the process of rinsing, the solvent was completely evaporated, leaving just the DOA that had been removed from the samples in the bottles. Figure 7 shows the FTIR spectrum of the remaining DOA after evaporation of dichloromethane. On the spectrum, peaks corresponding to DOA can be observed, attributed to the following groups:  $-\text{COOR}$ ,  $-\text{CH}_2$ ,  $-\text{CH}_3$  and  $\text{C}-\text{C}$ . predominantly at  $3000\text{ cm}^{-1}$ , then the stretching vibration  $\nu(\text{C}=\text{O})$  peak in ester group  $-\text{COOR}$  forming a strong absorption band in  $1750\sim 1735\text{ cm}^{-1}$ . The stretching vibration produced by  $-\text{C}-\text{O}-\text{C}-$  bond forms a wide range of absorption peak in the range of  $1300\sim 900\text{ cm}^{-1}$ .

Further, there are peaks due to HMX in the region of  $900$  to  $770\text{ cm}^{-1}$ , as well as from  $1500$  to  $1200\text{ cm}^{-1}$ . and

$1560\text{ cm}^{-1}$  ( $-\text{NO}_2$ ),  $1145\text{ cm}^{-1}$  ( $-\text{NO}_2$ , N-ring),  $965$  and  $945\text{ cm}^{-1}$  (ring stretching bands),  $830$  and  $760\text{ cm}^{-1}$  ( $-\text{NO}_2$ ), and  $625$  and  $600\text{ cm}^{-1}$  ( $-\text{NO}_2$ ).

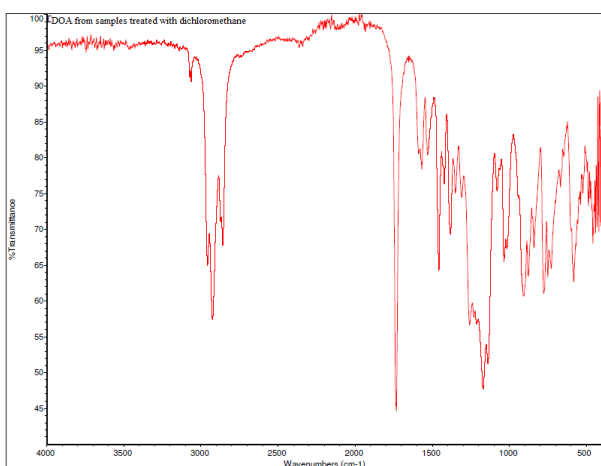


**Figure 7.** DOA spectrum from the samples treated with dichloromethane

This establishes the fact that when DOA is dissolved in dichloromethane and subsequently rinsed under vacuum, a portion of HMX is removed as well from the HMX/DOA mixture. In order to take into consideration for the loss of a minor quantity of HMX in the final calculation, it is essential to utilize formula (1) when determining the content of DOA in the sample (Table 3).

While analyzing the spectrum produced from the evaporation of n-heptane to identify DOA, distinct DOA peaks are readily recognized primarily at  $3000\text{ cm}^{-1}$ , exhibiting minimal overlap with HMX, which corresponds to the fact that a very small amount of pure HMX is removed by n-heptane, which can be seen in Figure 8.



**Figure 8.** DOA spectrum from the samples treated with n-heptane

The peaks observed at  $3300\text{ cm}^{-1}$  are a result of the presence of the OH group, indicating an inadequately matched sample. However, these peaks are not significant for the identification of DOA and HMX.

## 5. CONCLUSION

The monitoring of the migration of the plasticizer from the HMX/DOA mixture was analyzed. The samples were subjected to accelerated aging at two temperatures of  $60^\circ\text{C}$  and  $80^\circ\text{C}$  and were analyzed successively at intervals of 10, 15, 20, 25 and 30 days by the classic gravimetric method. The control of this approach was conducted using the instrumental methods of FTIR and DSC. Control samples were subjected to a 30-day period at room temperature, with one sample being exposed to natural sunlight and the other being kept in darkness.

Following conclusions can be made:

- regardless of the selection of solvents, it is important to consider the reduction in mass of pure HMX using formula 1,
- Within 10 days of being subjected to increased temperatures, the migration of DOA to the bottom layer commences gradually. This process becomes more pronounced at higher temperatures ( $80^\circ\text{C}$ ),
- After examining the data from the sample that was subjected to a temperature of  $80^\circ\text{C}$  for 15 days, a noticeable disparity between the top and bottom layers is detected. The discrepancy between samples treated with dichloromethane is 0.41%, but for those treated with n-heptane, the discrepancy is 0.35%. The percentage is remarkably high, considering that the presence of DOA in the HMX/DOA mixture is just a modest proportion (2.62-2.98%, Table 3). Approximately 12.5% of the total (DOA) moved

from the upper layers to the bottom of the test tube within the first 15 days at a higher temperature,

- The samples, which were subjected to a temperature of 80°C for a period of 20 days, produced results indicating the lack of DOA in the sample, followed by powerful smell of DOA, which is not present in the samples that were subjected to a temperature of 60°C and accumulation of DOA on the glass test tube,
- After being subjected to high temperatures for a period of 25 days, the scent of DOA becomes noticeable even in samples that have been exposed to a temperature of 60°C. After a period of 25 days, two specifically chosen solvents produce noticeably distinct values when exposed to a temperature of 80 degrees. Both cases exhibit a significant reduction in the total concentration of DOA in the sample,
- After a 30-day period, the statistics indicate the greatest migration of DOA in each sample. The samples exposed to a temperature of 60°C displayed a difference of 0.65% in the separation between the top and bottom layers for the samples treated with dichloromethane, while this difference was 0.74% for the samples treated with n-heptane, while the samples exposure to accelerated aging at a temperature of 80°C for a duration of 30 days, it was seen that more than one-third of the initial quantity of DOA had migrated to the lower portion of the test tube. The samples treated with dichloromethane display a difference of 1.04% between the upper and lower layers, whereas the samples submitted to n-heptane washing demonstrate a difference of 1.3% between the top and bottom layers,
- Control samples, stored in test tubes at the ambient temperature for 30 days, showed minimal differences between the top and bottom layers. The results closely reflect those obtained by exposing the samples to a temperature of 60°C for a period of 10 days. Moreover, it is seen that there are no significant disparities in the outcomes concerning light exposure, which is consistent with the manufacturer's claims on light durability.

The gravimetric method is highly efficient, as it is characterized by its rapidity and does not necessitate the use of costly equipment or the consumption of expensive chemicals. Within a brief timeframe, using only basic laboratory equipment, it yields quantitative data regarding the composition of the constituents. However, instrumental technique FTIR may provide some qualitative insight in this research, regarding the dissolving of HMX along with DOA in the selected selective solvents, and may help identify the presence of the remaining DOA on HMA after rinsing. The method used to determine the remaining pure explosive involves coloring the plasticizer, rather than directly detecting the plasticizer level.

Further work should encompass the influence of the total quantity of the sample (volume of the test tubes), the

influence of total DOA content on its migration, as well as effects of different temperatures and longer periods of time.

## ACKNOWLEDGEMENT

This work was supported by the Ministry of science, technological development and innovations (Serbia), Contract No. 451-03-66/2024-03/200325, and University of Defense, Military Academy, Proj. No. VA-TT/1/22-24.

## References

- [1] SZALA, M.: *Polymer-bonded secondary explosives*, High Energy Materials, 2021
- [2] KLAPÖTKE, M.T.: *Chemistry of high-energy materials*, 3<sup>rd</sup> edition, De Gruyter Graduate, Berlin, 2015.
- [3] SIMIĆ, D.: *Liveni termobarični PBX eksplozivi*, Kumulativna naučnotehnička informacija Vojnotehnički institut, Beograd, LIII (2) (2016.)
- [4] BAJIĆ, Z.: *Inicijalni i brizantni eksplozivi*, AGM knjiga, Beograd, 2015.
- [5] JEREMIĆ R., *Praktikum za raketna goriva*, Vojna akademija, Beograd, 2008.
- [6] ANTIĆ G.: *Livene eksplozivne smeše za podvodnu primenu*, Kumulativna naučnotehnička informacija, Vojnotehnički institut, Beograd, XXXIX (1) (2005.)
- [7] AGRAWAL, J.P.: *High energy materials, propellant, explosives and pyrotechnics*, Wiley-VCH, 2010.
- [8] Pinalia A., Prianto B., Setyaningsih H.: *Preliminary results of DOA plasticizer effect on AP/HTPB composite propellant characteristics*, AIP Conference Proceedings 2366, 040009 (2021); <https://doi.org/10.1063/5.0061303>, Published Online: 13 September 2021
- [9] Libardi J., Ravagnani S.P., Morais A.M.F., Cardoso A.R., Diffusion of Plasticizer in a Solid Propellant Based on Hydroxyl-Terminated Polybutadiene Polimeros 20, 241 (2010).
- [10] Yaacob I.N., Asli A.F., Norkhairunnisa M., Ahmad K.A., Ismail O., Salleh N.A., Shahedi: *A review on viscoelastic behaviour of plasticizers in ap/al/htpb based composite solid propellant*, Materials Today: Proceedings
- [11] [https://www.go-plasticizer.com/dioctyl-adipate-doa.html?google-network=g-campaignid=1768789814-adgroupid=70416065193-target=kwd-317041811721-creative=517586296988-device=c-placement=-keyword=dioctyl%20adipate&gad\\_source=1&gclid=Cj0KQCQjw\\_-GxBhC1ARIsADGgDjsh6sqGzu3DCVlISCojz\\_iZZpD0Y958eTvyEmCLXgm8bnJfQhQIQmoaAunvEALw\\_wcB](https://www.go-plasticizer.com/dioctyl-adipate-doa.html?google-network=g-campaignid=1768789814-adgroupid=70416065193-target=kwd-317041811721-creative=517586296988-device=c-placement=-keyword=dioctyl%20adipate&gad_source=1&gclid=Cj0KQCQjw_-GxBhC1ARIsADGgDjsh6sqGzu3DCVlISCojz_iZZpD0Y958eTvyEmCLXgm8bnJfQhQIQmoaAunvEALw_wcB)
- [12] <https://www.penpet.com/products/coatings-and-paints-printing-inks/dioctyl-adipate-doa>
- [13] <https://chemceed.com/products/dioctyl-adipate-doa/>
- [14] Stanisław G. Enzyme catalysed synthesis of some



- adipic esters. *J Mol Catal B-Enzym* 15: 9–13 (2001)
- [15] Kolwzan B, Gryglewicz S. Synthesis and biodegradability of some adipic and sebacic esters. *J Synthetic Lubric* 20:99–107 (2003)
- [16] He Y F, Zolper T J, Liu P Z, Zhao Y Z, He X L, Shen X J, Sun H W, Duan Q H, Wang Q. Elastohydrodynamic lubrication properties and friction behaviors of several ester base stocks. *Friction* 3(3): 243–255 (2015)
- [17] Sander J. The aspects of designing lubricants using an environmental product assessment. *NLGI Spokesman* 61(11): 18–27 (1998)
- [18] Sparkman DO, Penton Z, Kitson FG *Gas Chromatography and Mass Spectrometry: A Practical Guide*. Academic Press. (17 May 2011), ISBN 978-0-08-092015-3.



## INFLUENCE OF DIFFERENT HMX/RDX CONTENTS IN COMPOSITE ROCKET PROPELLANTS ON THE VACUUM STABILITY TEST RESULTS

BOJANA FIDANOVSKI

Military Technical Institute, Belgrade, [bojana.fidanovski@mod.gov.rs](mailto:bojana.fidanovski@mod.gov.rs)

SLAVKO MIJATOV

Military Technical Institute, Belgrade, [slavko.mijatov@yahoo.com](mailto:slavko.mijatov@yahoo.com)

MIRJANA KRSTOVIĆ

Military Technical Institute, Belgrade, [mbkrstovic@gmail.com](mailto:mbkrstovic@gmail.com)

MARICA BOGOSAVLJEVIĆ

Military Technical Institute, Belgrade, [marica.radusinovic@gmail.com](mailto:marica.radusinovic@gmail.com)

MIRJANA DIMIĆ

Military Technical Institute, Belgrade, [mirjanadimicjevtic@gmail.com](mailto:mirjanadimicjevtic@gmail.com)

**Abstract:** The stability control system for energetic materials during storage involves testing, which need to ensure their reliable performance and stability over time. Any change in these materials, due to compatibility or stability issues, can cause serious consequences. Therefore, rigorous testing using specific methods is essential during the development and initial testing phases to conform all required criteria. Composite solid propellants based on ammonium perchlorate (AP)/hydroxyterminated polybutadiene (HTPB)/isophorone diisocyanate (IPDI), including various contents of octogen (HMX) and hexogen (RDX), have been thoroughly investigated for their chemical stability. To achieve this, a highly effective modern method for testing the stability of pure explosives, explosive mixtures, solid rocket propellants and pyrotechnic mixtures the Vacuum Stability Test was employed. This test based on monitoring changes during gas diffusion, where vacuum conditions provide the highest sensitivity for the quantification of evolved gas, is another requirement for choosing this method within this research.

**Keywords:** Composite Rocket Propellants, RDX, HMX, Chemical Stability, Test Vacuum Stability Method.

### 1. INTRODUCTION

Under normal storage conditions, energetic materials (EMs) are placed in warehouses positioned at different locations with varying microclimatic conditions until their use. The storage period for EMs is often long, sometimes exceeding 20 years. Typically, storage facilities for explosive materials decreased in automatic heating and/or cooling systems, leading to temperature variations based on the microclimatic conditions of the location. This raises several questions and issues regarding the stability of the energetic materials, which require specific research and testing.

The concept of stability of energetic materials can be defined based on two aspects: safety (safe storage) and reliability (probability of functioning and retaining designed properties after storage). From a safety and reliability perspective, it is important that the stored energetic material remains unchanged (or partially changed within defined limits) for a certain period during storage and does not undergo chemical decomposition [1]. In general, safety refers to chemical stability, while reliability refers to mechanical and ballistic stability [2].

The stability of an energetic material implies a state in which the material retains its chemical, ballistic, and mechanical characteristics at a level that allows its use and storage under storage conditions without any risk.

Regarding composite rocket propellants (CRPs), mechanical stability involves maintaining shape, dimensions, homogeneity of composition and structure, while mechanical properties are crucial for ensure reliability and safety during use. Preserving the values of specific heat and burning rate parameters within specified limits represents the basis of ballistic stability. Chemical stability involves the ability to keep the chemical characteristics of the material during storage under varying temperature conditions, which includes monitoring the chemical decomposition of the energetic material that affects both ballistic and mechanical characteristics.

Composite rocket fuels are heterogeneous mixtures of organic fuel-binding components (binders), oxidizers, and additives (metal fuel components, inhibitors or combustion rate catalysts, stabilizers, etc.) [3]. To ensure stable operation during combustion, they need to release large quantities of low-molecular-weight gases at high temperatures, by directing the combustion products

through a nozzle opening, kinetic energy is provided for rocket propulsion.

The combustion of CRPs based on the oxidizer ammonium perchlorate (AP) and butadiene or polyol polyurethane prepolymers in a rocket engine yields the main combustion products: HCl, CO<sub>2</sub>, H<sub>2</sub>O, and N<sub>2</sub>. Considering HCl molecules, as a product of AP combustion, along with atmospheric moisture, formed undesirable visible white fog [4]. On the other hand, the use of rocket propellants based on ammonium perchlorate represented a great advancement in the field of energetic materials, but at the same time, these materials contribute to environmental pollution due to combustion products rich in chloride compounds. The dominance characteristic of ammonium perchlorate is its complete conversion into gaseous reaction products during combustion. One attempt to obtain compositions with lower chloride content, for less smokiness, pollution, and/or improvement of the characteristics of new composite rocket fuels, is the use of nitramine compounds as energetic components and oxidizers. Besides the aspect of environmental protection, there is also the possibility of achieving better energy performance (e.g., improving the specific impulse value to increase the range of rocket means). The elimination of chloride compounds also leads to smokeless (improved concealment of personnel and equipment) and non-corrosive combustion products (longer service life of launch tubes) [5].

Nitramines, such as cyclotrimethylenetrinitramine (RDX) and cyclotetramethylenetetranitramine (HMX), are used as an alternative to ammonium perchlorate, with the potential for obtaining better fuel energy performance. Due to the high concentration of hydrogen atoms, their combustion yields low-molecular-weight gases, resulting in an increase in the specific impulse value [5]. During the combustion of RDX, known as hexogen, a visible, defined liquid layer is formed, and it is assumed that the number of significant reactions contributing to the combustion process below the melting temperature is very small. The temperature of the melted layer is not determined, except according to literature data [6]. The higher burning rate of rocket fuel with RDX is a result of the larger amount of heat released from the combustion surface [7]. The increased amount of gases and the return heat flux from RDX are explained by the large temperature gradient near the combustion surface [8].

HMX, known as octogen, has a molar mass of 296.16 g·mol<sup>-1</sup>, a density of 1.91 g·cm<sup>-3</sup>, and a melting temperature between 276-286 °C [7]. It is a white powder, slightly soluble in water. Only a small amount of HMX evaporates into the surrounding environment. It develops a strong explosion at high temperatures. Due to its characteristics, it is in use in various types of explosives, rocket fuels, and booster charges.

Research in the field of CRPs containing certain amounts of RDX and HMX aims to determine the degree of influence of individual composition factors that can affect the aging process or decrease the stability of the fuel. To assess chemical stability, it is necessary to determine a parameter that best describes the aging process, as well as

an appropriate method for reliably determining the value and monitoring the change of that parameter over time. There are several methods for testing chemical stability. The most suitable one for examination the CRPs/explosives is instrumental method the Vacuum Stability Test. The instrumental method Vacuum Stability Test was developed in the USA and accepted in several countries, and that was modification of the W. Taliani Test, where the gaseous reaction products are determined volumetrically rather than using a manometer [9]. This test, conducted at 100°C, lasts for 40 hours, unlike the Taliani Test, which was terminated upon reaching a certain pressure or released gas volume. The Vacuum Stability Test is based on monitoring changes caused by gas diffusion into the surrounding environment during heating [10].

In addition, very important examination, before starting the Vacuum Stability Test, is analyzing the chemical structure of CRP with RDX and HMX by using the Fourier Transform Infrared Spectroscopy (FTIR). This instrument was applied to examine the chemical interaction between CRP and RDX, as well as between CRP and HMX compound.

## 2. EXPERIMENTAL SECTION

### 2.1. Composite rocket propellants with HMX and RDX

Samples of composite rocket propellants used for this research consist of oxidizer, which is a bimodal mixture of AP particles, pre-polymer hydroxyl-terminated polybutadiene, HTPB (manufacturer Arco), cross-linked isophorone diisocyanate (IPDI), plasticizer dioctyl adipate (DOA) and bonding agent triethylene-tetramine, TET. Titanium(IV) oxide, which in earlier research periods of similar compositions proved to be a favorable combustion stabilizer, affecting the reduction of the pressure exponent value in the combustion rate law, was also included in this CRP. [11, 12]. Compositions of CRP with different concentration of octogen and hexogen, which were the main subject of study in this paper, are presented in Table 1.

**Table 1.** Mixed composition formula of the CRP with HMX and RDX

No	Sample	HMX, %	RDX, %	TiO <sub>2</sub> , %
1.	CRP-H25	25	-	2.5
2.	CRP-H30	30	-	2.5
3.	CRP-R15	-	15	2.0
4.	CRP-R20	-	20	2.0

### 2.2. Vacuum Stability Test

#### Description of the apparatus and equipment

The tests were performed on a Vacuum Stability Test device, STABIL 20, OZM Research, used for testing the chemical stability of all type of energetic materials. The Vacuum Stability Test method is based on determining the volume of released gases that develop in

a closed controlled system, under vacuum, above the test samples [13]. All values of relisted gases were recorded during the measurement of chemical stability every minute, tabulated and graphically, as dependencies of pressure change of the gas over time.

### Sample preparation

Sample preparation involves so-called "coarse" and "fine" mechanical preparation. Coarse preparation involves reducing the samples to smaller dimensions, while fine preparation involves cutting with scalpels to the prescribed sample size of 2 mm. CRP samples, except for mechanical preparation, do not undergo additional preparation.

### Criterion of chemical stability

In the Vacuum Stability Test, the criterion of chemical stability is based on values of the volume of released gas, which is calculated using equation (1)

$$V = \left( V_c + V_t - \frac{m}{\rho} \right) \cdot \left( \frac{p_2 \cdot 273}{273 + t_2} - \frac{p_1 \cdot 273}{273 + t_1} \right) \cdot \frac{1}{1,013} \quad (1)$$

Where are:

- $V$  - volume of gas released from the sample,  $\text{cm}^3$
- $V_c$  - volume of the piezoelectric transducer,  $\text{cm}^3$
- $V_t$  - volume of the glass test tubes,  $\text{cm}^3$
- $m$  - mass of the sample, g
- $\rho$  - density of the test sample,  $\text{g} \cdot \text{cm}^{-3}$
- $p_1$  - calculated pressure measured at the beginning of the experiment, bar
- $p_2$  - calculated pressure measured at the end of the experiment, bar
- $t_1$  - room temperature at the beginning of the experiment,  $^{\circ}\text{C}$
- $t_2$  - room temperature at the end of the experiment,  $^{\circ}\text{C}$

The volume of released gas from the tested sample (expressed in  $\text{cm}^3$ ), calculated based on equation (5), is recalculated to a unit mass ( $\text{cm}^3 \cdot \text{g}^{-1}$ ) [13]. Based on the known criteria, Table 2., it can be determined whether the observed sample is chemically stable or not.

**Table 2.** Criteria for chemical stability for CRP samples

Sample	T, [ $^{\circ}\text{C}$ ]	m, [g]	Time of experiment, [h]	Criteria of stability, [ $\text{cm}^3 \cdot \text{g}^{-1}$ ], SPT*
CRP	100	2.5	40	$\leq 1.2$

\*SPT - Standard Pressure and Temperature

### 2.3. FTIR-ATR analysis

Fourier transform infrared spectroscopy method (FTIR) was employed to investigate and/or confirmed the chemical structure, according to characteristics peaks, of CRP samples with different proportions of two types of pure explosives. FTIR spectrometer, Thermo Nicolet iS10, with the Attenuated Total Reflectance (ATR)

measurement mode was used with the sample mounted on a diamond crystal. Absorption spectra were recorded in the range of  $4000$  to  $500 \text{ cm}^{-1}$ , with a resolution of  $4 \text{ cm}^{-1}$ .

## 3. RESULT AND DICUSION

The first steps after sample preparation, according to given percentage of ingredients Table 1., was to analyzed the characteristic FTIR spectra. Figure 1. and 2., shows the specific peaks for each of used organic compounds HMX and RDX.

The observed FTIR spectra for two CRP-HMX samples, Fig.1., showed presence of characteristic peaks corresponding to HMX [14], which is the main component of examined composite rocket propellants. The major bands can be assigned as follows: peaks corresponding to absorptions of the nitro group:  $1564 \text{ cm}^{-1}$  are from stretching vibrations of the nitro group;  $1145 \text{ cm}^{-1}$  are stretching vibrations of the nitro group and the ring; peaks  $830$ - $761 \text{ cm}^{-1}$  are from bending vibrations of the nitro group; and the praks at  $630 \text{ cm}^{-1}$  and  $600 \text{ cm}^{-1}$  are from vibrations of the nitro group, along with peaks characteristic for ring vibrations at:  $2996 \text{ cm}^{-1}$ ,  $1145 \text{ cm}^{-1}$ ,  $964 \text{ cm}^{-1}$  and  $946 \text{ cm}^{-1}$ . It can be concluded that characteristics peaks unmistakably indicates presents of HMX in examined samples, as well as the chemical interaction between CRP and HMX.

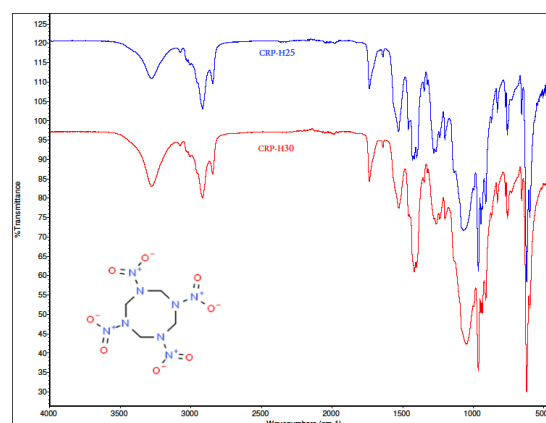


**Figure 1.** FTIR spectra of the samples CRP with HMX

FTIR spectra for the samples with RDX compound, Fig.2., also indicated existence of peaks corresponding to the absorptions of the nitro group [15]. More precisely: peaks at  $1590 \text{ cm}^{-1}$  and  $1308 \text{ cm}^{-1}$  correspond to stretching vibrations of the nitro group;  $1039 \text{ cm}^{-1}$  and  $910 \text{ cm}^{-1}$  are from in-plane bending vibrations of the nitro group, and the peak at  $1039 \text{ cm}^{-1}$  is characteristic for out-of-plane bending vibrations of the nitro group. In addition, ring vibration peaks were also registered at the following wavenumbers:  $3074 \text{ cm}^{-1}$ ,  $3065 \text{ cm}^{-1}$  (CH vibration stretching (doublet) in the chain);  $3003 \text{ cm}^{-1}$  (CH vibration stretching);  $1570 \text{ cm}^{-1}$  ( $\text{CH}_2$  out-of-plane stretching vibrations);  $1418 \text{ cm}^{-1}$  ( $\text{CH}_2$  in-plane stretching vibrations);  $1265 \text{ cm}^{-1}$  and  $1231 \text{ cm}^{-1}$  ( $\text{CH}_2$  group, deformation vibrations); and  $945 \text{ cm}^{-1}$  (CH vibration

stretching in the plane). All the examined peaks clearly indicate the presence of hexogen, and the chemical interaction between CRP and RDX.

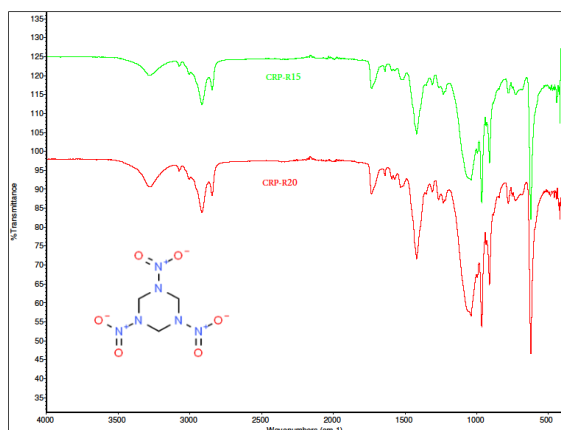


Figure 2., FTIR spectra of the samples CRP with RDX

The results of measurement and average value of the evolved gases, i.e. volume/volume per gram of the samples with HMX and RDX, as well as the density are given in Table 3. and Table 4. All measurements were performed on the Vacuum Stability Test instruments, and the mass of all examined samples was  $2.5 \pm 0.0001$  g.

Table 3. Results of the TVS method for CRP samples with different percentage of HMX

No	Sample name	$\rho$ [ $\text{g}\cdot\text{cm}^{-3}$ ]	V, [ $\text{cm}^3$ ]	V, [ $\text{cm}^3\cdot\text{g}^{-1}$ ]
1.	CRP-H25	1.642	0.144	0.057
2.			0.145	0.058
3.			0.148	0.059
4.	<b>Average value</b>		<b>0.146</b>	<b>0.058</b>
5.	CRP-H30	1.626	0.098	0.039
6.			0.099	0.039
7.			0.100	0.040
8.	<b>Average value</b>		<b>0.099</b>	<b>0.039</b>

Table 4. Results of the TVS method for CRP samples with different percentage of RDX

No	Sample name	$\rho$ [ $\text{g}\cdot\text{cm}^{-3}$ ]	V, [ $\text{cm}^3$ ]	V, [ $\text{cm}^3\cdot\text{g}^{-1}$ ]
1.	CRP-R15	1.620	0.246	0.098
2.			0.164	0.065
3.			0.207	0.083
4.	<b>Average value</b>		<b>0.205</b>	<b>0.082</b>
5.	CRP-R20	1.614	0.273	0.109
6.			0.302	0.121
7.			0.202	0.089
8.	<b>Average value</b>		<b>0.264</b>	<b>0.106</b>

The theoretical values of enthalpy of formation of HMX and RDX are positive ( $74.88 \text{ kJ}\cdot\text{mol}^{-1}$  vs.  $70.63 \text{ kJ}\cdot\text{mol}^{-1}$ ), which indicated that the resultant volume of released gases can be correlated with the existing bond energies and the enthalpies of formation of all input components. In addition, based on the united graphical time-pressure diagram of the separated gases, Figure 3., the character of

all the curves is specific and shows the same trend during the test time, regardless of the type of explosive or its share in the composition. Furthermore, throughout the entire testing period, there is a contribution to the increase in pressure, the curve shows a gradient of rise, and there is no difference in the levels of the curves, for either samples with RDX or samples with HMX.

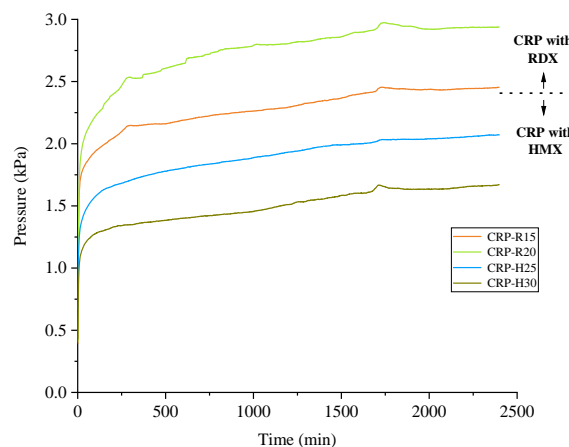


Figure 3., United time-pressure diagram for CRP samples with HMX and RDX

The values of released gases per gram for samples with RDX, Table 4. are similar  $0.082$  and  $0.106 \text{ cm}^3\cdot\text{g}^{-1}$ . The obtained values of released gases per gram for samples with HMX, Table 3. are also mutually similar  $0.058$  and  $0.039 \text{ cm}^3\cdot\text{g}^{-1}$ , and are much lower than the values for samples with RDX. Knowing the fact that, RDX has three nitramine bonds ( $-\text{C}-\text{N}-\text{NO}_2$ ) while HMX has four same molecule, it was expected that less energy is required for their dissociation. Therefore, the CRP with RDX compositions release more gaseous fragments, i.e. have increased in the value of evolved gases than CRP with HMX. Some data for the examination of pure substances for the quantities of gases record values for nitramine compounds ranging from  $0.1$  to  $0.4 \text{ cm}^3\cdot\text{g}^{-1}$  [16].

In terms of chemical stability and based on the requirements where the value who indicate chemical stability should be  $\leq 1.2 \text{ cm}^3\cdot\text{g}^{-1}$ , Table 2., and according to results, Tables 3. and 4., it can be seen that the corresponding values of the volumes of released gases for both examined compositions are below the set criteria. The evidence from given results implies that both compositions CRP are chemically stable.

The titanium(IV) oxide was added in amount range from 2.0 to 2.5 wt.% in all examined compositions. Based on previously published results, the volume of released gases decreases slowly but consistently, in both compositions, i.e. CRP with RDX and in those with HMX [11, 18, 19]. Thermochemical calculations indicate that the contribution of burn rate inhibitors (such as titanium(IV) oxide or lithium fluoride) is negative, meaning they reduce the energetic potential of the propellants [12]. These compounds indicated decreases in the combustion temperature of the fuel by consuming the energy generated during combustion. The enthalpies of formation of these compounds are always positive; the reactions are

endothermic and consume the heat needed for decomposition. If the same role of the inhibitor is analogously applied here, it appears that its presence reduces gas emissions, leading to the conclusion that it also serves as a stabilizer. The enthalpies of formation of these compounds are always positive; the reactions are endothermic and consume the heat needed for decomposition. If the same role of the inhibitor is analogously applied here, it appears that its presence reduces gas emissions, leading to the conclusion that it also serves as a stabilizer.

#### 4. CONCLUSION

The paper presents the results of tests conducted using the Vacuum Stability Test method on the composite rocket propellants (CRP) based on AP/HTPB/IPDI using the STABIL 20 instrument, while the chemical structure of the samples was examined using the "Thermo Nicolet iS10" FTIR spectrometer with ATR. The CRP compositions tested were made with nitramine explosives, hexogen, and octogen, added as energy components and oxidizers. The explosive was added at different mass content levels instead of oxidizer content, up to a total designed solid phase of 80 wt.%, and with titanium(IV) oxide as combustion stabilizer.

The chemical structure examination of the nitramine CRP compositions was performed by comparing characteristic peaks of the corresponding chemical groups of the tested samples, which indicated good matching of the characteristic peaks and thus confirmed the presence of the interaction between CRP and HMX/RDX.

The chemical stability test method for CRP is based on determining the volume of released gases during a standard prescribed heating period under vacuum. For various nitramine CRP compositions, and their contents, results as pressure-time diagram, as well as, values of gas-released volumes were obtained. The tested CRP HMX/RDX compositions exhibit high stability according to the chemical stability criterion applied to explosive charges and CRP, which is  $V \leq 1.2 \text{ cm}^3 \cdot \text{g}^{-1}$  [20]. However, analysis of the results indicated that in the increasing order of gas release volumes during the test (i.e., in the order of decreasing chemical stability of the composition), are nitramine CRP with RDX content compared to nitramine CRP with HMX.

In addition, regardless of the content of RDX in the composition, increase in the values of released gas volumes compared to compositions with HMX, indicated their significantly higher stability. The reason for the greater "instability" of CRP/RDX compositions compared to CRP/HMX is in the number of methyl nitramine groups (three versus four, respectively) and the overall energy required for the breaking the chemical bonds. The strength of chemical bonds within different molecules of the CRP components determines the amount of released gases, which is higher for less stable compositions whose molecules have lower total bond energy.

Furthermore, it is necessary to emphasize that, the determined results of the amount of released gases do not take into account the gases produced by AP degradation.

It is interesting that a higher amount of HMX gives a lower pressure and vice versa in the case of RDX. This phenomenon, in addition to the higher stability of HMX compared to RDX, can be also potentially attributed to AP (a bimodal mixture of AP particles present in the examined CRP), which will be our next steps in a further study of this topic.

The main conclusion of this work is that by altering part of the AP quantity with used nitramine explosives, compositions with favorable chemical stability can be obtained. Furthermore, since the current imperative is that the components that are in use, especially their decomposition products, are environmentally friendly, the obtained results supports the potential use of nitramine CRP in devices that are or will be in use in the Serbian Army.

#### Acknowledgement

The authors thank to the Ministry of Education, Science and Technological Development of Republic of Serbia for the support of the research through Contract No. 451-03-66/2024-03/200325.

#### Reference

- [1] AGRAWAL, J. P., *High Energy Materials - Propellants, Explosives and Pyrotechnics*, Wiley VCH Verlag, GmbH & Co KGaA Weinheim, ISBN 978-3-527-32610-5, 2010., 176-179.
- [2] BOBIĆ, N., *Primena nitramina i netoksičnih aditivnih jedinjenja u razvoju i proizvodnji savremenih eksploziva i baruta*, doktorska disertacija, TMF, Beograd, 2017.
- [3] TEASDALE, D., *Solid Propellant Microrocket*, Research project, (2000), pp. 8.
- [4] RODIĆ, V., BOGOSAVLJEVIĆ, M., MILOJKOVIĆ, A., BRZIĆ, S., FIDANOVSKI, B., GLIGORIJEVIĆ, N., *Preliminary Research of Composite Rocket Propellants Including Octogene*, Scientific Technical Review, ISSN 1820-0206, 67(1), (2017), pp.3-12.
- [5] KUBOTA, N., *Combustion of Composite Propellants: Combustion of Composite Propellants, in Propellants and Explosives, Thermochemical Aspects of Combustion*, Wiley-VCH Verlag GmbH & Co. KGaA, Weinheim, Germany. DOI: 10.1002/9783527693481.ch7, 2015.
- [6] BEHERA, S., *Effect of RDX on Elongation Properties of AP/HTPB Based Case Bonded Composite Propellants*, DRDO Science Spectrum, March 2009, pp 31-36.
- [7] KUBOTA, N., *Combustion Mechanisms of Nitramine Composite Propellants*, Symposium (International) on Combustion, 18(1):187-194, (1981), DOI: 10.1016/S0082-0784(81)80023-9.
- [8] BECKSTEAD, M., *Recent Progress in Modeling Solid Propellant Combustion*, Combustion, Explosion and Shock Waves, 42(6), 2006, pp 623-641.

- [9] STABIL, *Modernized Vacuum Stability Tester*, User`s Manual, OZM Research s.r.o., December 8, 2010.
- [10] FIDANOVSKI, B., DIMIĆ, M., MILOJKOVIĆ, A., RODIĆ, V., *Determination of chemical stability of propellants using the vacuum stability test method*, Scientific-Technical Review, Military Technical Institute, Beograd, 66(1), (2016), pp 18-22.
- [11] RODIĆ, V.: *The effect of titanium (IV) oxide on burning stability of composite solid propellants*, 4th International Scientific Conference on Defensive Technologies OTEH 2011, 06-07; October 2011, Belgrade, SERBIA, ISBN 978-86-81123-50-8, pp.354-360.
- [12] RODIĆ, V.: *Effect of titanium (IV) oxide on composite solid propellant properties*, Scientific Technical Review, ISSN 1820- 0206, 62 (3-4), (2012), pp.21-27
- [13] STANAG 4556: EXPLOSIVES: VACUUM STABILITY TEST Brussels (test 1, procedure B): North Atlantic Treaty Organization, Military Agency for Standardization, 1999.
- [14] JINTIAN, Z. , GUANGYUAN, Z., ZISHUAI, X., LUYAO, Z., LIZHEN, CH., JIANLONG, W., *Analysis of crystal purity of Octogen by Fourier transform infrared spectroscopy*, Vibrational Spectroscopy, 123, (2022), article 103461
- [15] MCNESBY, K.L.; PESCE-RODRIGUEZ, R.A., *Applications of vibrational spectroscopy in the study of explosives*, in Handbook of Vibrational Spectroscopy; Chalmers, J.M. and Griffiths, P.R., Ed.; John Wiley and Sons, Ltd.: Chichester, 2002.
- [16] BAYTOS, J.F.: *Vacuum Thermal Stability of Explosives Monitored Electronically*, LA-12173-MS, UC-706 and UC-741, Los Alamos University, New Mexico, USA, November 1991.
- [17] RODIĆ, V.: *The effect of titanium (IV) oxide on burning stability of composite solid propellants*, 4th International Scientific Conference on Defensive Technologies OTEH 2011, 06-07. October 2011, Belgrade, SERBIA, ISBN 978-86-81123-50-8, pp.354-360.
- [18] RODIĆ, V., FIDANOVSKI, B. *Burning Stability of Composite Solid Propellants Including Zirconium Carbide*, Scientific Technical Review, Belgrade, Vol. 63(3), (2013), pp. 33-40.
- [19] RODIĆ, V., BOGOSAVLJEVIĆ, M., MILOJKOVIĆ, A., *Composite solid propellants with hexogen*, 8th International Scientific Conference on Defensive Technologies OTEH 2018, 11-12; October 2018, Belgrade, SERBIA, ISBN 978-86-81123-50-8, pp.160-166.
- [20] BOHN, M. A., *NC-based energetic materials- Stability, decomposition and ageing*, Presentation on the meeting Nitrocellulose-Supply, Ageing and Characterization, England, 2007.



## PARTICLE SIZE SENSITIVITY IN SMOOTH PARTICLE HYDRODYNAMICS NUMERICAL SIMULATION OF NATURAL FRAGMENTATION PHENOMENA

MILOŠ MARKOVIĆ

University of Belgrade, Faculty of Mechanical Engineering, Serbia, [mdmarkovic@mas.bg.ac.rs](mailto:mdmarkovic@mas.bg.ac.rs)

PREDRAG ELEK

University of Belgrade, Faculty of Mechanical Engineering, Serbia, [pelek@mas.bg.ac.rs](mailto:pelek@mas.bg.ac.rs)

IVANA TODIĆ

University of Belgrade, Faculty of Mechanical Engineering, Serbia, [itodic@mas.bg.ac.rs](mailto:itodic@mas.bg.ac.rs)

DEJAN JEVTIĆ

University of Belgrade, Faculty of Mechanical Engineering, Serbia, [djevtic@mas.bg.ac.rs](mailto:djevtic@mas.bg.ac.rs)

MARTIN MACKO

University of Defence, Brno, Czech Republic, [martin.macko@unob.cz](mailto:martin.macko@unob.cz)

**Abstract:** Smoothed Particle Hydrodynamics (SPH), a computational method as part of ANSYS Autodyn software is widely employed for simulating natural fragmentation phenomena and all others process follow with large deformations. The goal of this study is to investigate the impact of particle size on key parameters such as fragment velocity and the total number of fragments. The research focused on the 105 mm M1 artillery projectile, aims to examine the relationship between particle size and fragmentation phenomena. The Johnson-Cook failure model was applied to the projectile case and Johnson-Cook strength model was applied to all metal parts of the artillery projectile. Furthermore, the research aims to underscore the importance of validation against available experimental data to ensure the reliability and applicability of SPH simulations. It is noted, however, that the available experimental results provide limited information. As a result, the comparison is restricted to the total number of fragments rather than a detailed analysis of fragment mass group numbers. Through systematic simulations with varying particle sizes, the study reveals a distinct trend: decreasing particle size correlates with increase of total number of fragments and no significant changes in fragment velocities within the specified material model behavior. By offering comprehensive insights into the relationship between particle size and fragmentation behavior, the study aims to emphasize the necessity of considering multiple factors in SPH simulations to enhance their accuracy and utility in predicting natural fragmentation phenomena.

**Keywords:** high explosive projectiles, natural fragmentation, numerical simulation, SPH simulation

### 1. INTRODUCTION

The determination of mass, number, and velocity of fragments during the development phase can be accomplished using a numerical method in ANSYS Autodyn software through the Smooth Particle Hydrodynamics (SPH) simulation. Nowadays, very few research papers can be found on the topic of numerical investigation on natural fragmentation of artillery projectiles larger than 57mm caliber. The topic of the present research on natural fragmentation using SPH solver is primarily based on a 105mm projectile, mainly due to the availability of information. The available information relates to the known geometry of the projectile and approximate characteristics of the material that could be found in [1]. However, the material Č1635VP intended for the casing is defined with a

minimal set of properties, where only the yield strength is known. Matching was done based solely on the yield strength, leading to the selection of AISI 1045 material, which is widely present in research papers dealing with natural fragmentation issues. The AISI 1045 material has approximately similar characteristics in the elastic zone as proposed by the author [1] and is well supported in available research papers [2-7], defined by Johnson-Cook strength model and various failure models. In the papers [2-7], the Johnson-Cook model was used as a strength model, describing the behavior of materials under high strain and high strain rate conditions. Regarding failure models, there are various approaches to modeling material fracture behavior using numerical analysis. Authors Luo et al. [8] conclude after testing various failure models available in ANSYS Autodyn that the principal strain failure model provides good results for thick cylindrical shells undergoing pure shear fracture. Additionally, some



authors have used the principal strain failure model and stochastic failure model [3,7,8] for the natural fragmentation of cylindrical shells, or just the principal strain failure model [4]. On the other hand, there are studies where the behavior of cylindrical shell is considered using the Johnson-Cook failure model, with satisfactory agreement with experimental data. Authors Ping et al. and Elshenawy et al. [6,9], for example, state that using SPH analysis eliminates the need to consider failure and erosion criteria for natural fragmentation problems of cylinders made of the same material previously mentioned, which is opposite conclusion to the findings of the aforementioned authors. When it comes to the influence of particle size on result convergence, completely opposite conclusions can be found from numerical simulations conducted using the same ANSYS Autodyn software. For example, in the study by Elshenawy et al. [9], it is concluded that decreasing particle size decreases the initial fragment velocity of a mortar shell sample until convergence is achieved. However, in the work of Wei Li et al. [3], it is found that the fragment velocity of a cylinder increases with decreasing particle size. Vignjević et al. [10] use the SPH solver for natural fragmentation purposes, based on well-known experiments conducted by Mock and Holt and the case of the MK82 bomb. The authors specify the number of particles per shell thickness, which is crucial for analyzing the influence of particle count on result convergence. For instance, for the MK82 bomb with an average shell thickness of 12.7mm, there are 6 particles per thickness, resulting in a total 1.2 million particles. The total number of particles is contained within a quarter of simulated models. Under these particle count conditions, the authors report that the results align with experimental findings within an acceptable margin of error. However, the authors Ugrčić et al. [11,12] demonstrate ANSYS Autodyn software's natural fragmentation capabilities with 105mm, 120mm mortar shells, and 128mm unguided artillery rocket warheads. Their approach combines Euler-Lagrange interaction: Lagrange solver for fragmentation and Euler solver for detonation modeling. Results cover fragment velocity, number, and mass distribution, but their solver focus diverges from this research paper's scope. Experimental results are available for the 105mm M1 artillery projectile [11,13], providing information on the total number and mass distribution of fragments. However, these studies lack sufficient detailed

information about the projectile material itself for numerical simulation and experimental testing. This limitation makes it challenging to verify the numerical model. The aim of this research is to study influence of the particle size (PS) on the convergence of results, such as fragment velocity and total number of fragments. Other phenomena are also included, such as shell interaction with the detonation products and kinetic energy of the detonation products. The paper also examines the sequences of shell expansion through a visual review of the fragmentation process. The work in this paper provides insights into the capabilities of SPH solvers within the ANSYS Autodyn software, emphasizing that result accuracy depends on precisely defined material behavior models and well-defined fragmentation properties in the simulation setup.

## 2. NUMERICAL MODEL

### *Artillery projectile configuration*

Based on the dimensions of the artillery projectile taken from [1], a 3D model of a quarter cross-section has been designed. The model includes a projectile case, a driving band, an explosive charge, and a fuze. The fuze, modeled as a solid part, is crucial in simulations, particularly at the start, to establish the detonation front and prevent early leakage of detonation products. Figure 1 shows a 3D quarter cross-section of the considered model with materials corresponding to each component of the projectile in ANSYS Autodyn environment.

### *Numerical setup*

The entire process of natural fragmentation is simulated using the SPH solver, where all components of the artillery projectile are simulated within the SPH domain. This research study does not go into the details of the SPH solver itself, where fundamental information can be found in [14]. Also, the same approach to modeling natural fragmentation phenomena can be found in research papers [2-10] involving the SPH solver. The study focuses on investigating the influence of PS on natural fragmentation phenomena. Reducing PS or increasing the total number of particles in the considered model directly affects computational requirements. Decreasing particle size leads to an increase in the number of nodes and significantly raises computation



**Figure 1.** Artillery projectile 105mm M1, 3D quarter numerical model with material assignment

time strongly affecting on the decreasing time step. Priority was given to the total number of particles and the number of cores used for parallel processing, and their impact on required RAM memory space. Figure 2 shows a 3D model with 10 subdomain decomposition, prepared according to the guidelines in the ANSYS Autodyn user manual [15] for parallel computation. Each simulation was set to record sequences every 25 μs within a total time interval of 350 μs. Several examples were run with the next properties:

- PS 5, case nodes 2940 and total nodes 6128,
- PS 2, case nodes 47004 and total nodes 97093,
- PS 1, case nodes 375799 and total nodes 778385,
- PS 0.7, case nodes 1096360 and total nodes 2163301,
- PS 0.6, case nodes 1742818 and total nodes 3605391,
- PS 0.5, case nodes 3010833 and total nodes 6232289.

**Material models**

The Johnson-Cook (JC) model was selected to characterize the behavior of a cylindrical casing made from AISI 1045 steel, a driving band made from Cu-OFHC2 and fuze made from AL 2024 - T4. This model is extensively employed to describe materials that undergo large strains, high strain rates, and thermal softening. Additionally, to enhance its capability in capturing the material's response under diverse conditions, the Gruneisen equation of state was integrated with the JC model,

$$\sigma = (A + B\varepsilon^n)(1 + C \ln \dot{\varepsilon}^*) (1 - T^{*m}) \quad (1)$$

Here, the constants A, B, n, C, and m are material properties, where ε represents the equivalent plastic strain, ε\* denotes the dimensionless effective plastic strain rate, and T\* signifies the dimensionless temperature, where all data are given in Table 1. Gruneisen EOS contains next parameters: Grun. Coeff. is 2.17, C1 is 4.569 km/s, S1 is 1.49 and specific heat is 452 J/kgK. The JC model for strain at fracture incorporates key parameters such as stress, strain rate, and temperature to predict the material's behavior under dynamic loading conditions. The higher stresses relative to a reference stress led to increased strain at fracture, assuming other factors remain constant.

The influence of strain rate sensitivity determines how the plastic strain rate affects fracture behavior. Additionally, the term for thermal softening indicates that higher temperatures relative to a reference temperature reduce the material's strength and ductility. The JC failure model which predicts the strain at fracture (ε<sub>f</sub>) using the following equation:

$$\varepsilon_f = [D_1 + D_2 \exp(D_3 \sigma^*)] \left[ 1 + D_4 \ln \left( \frac{\dot{\varepsilon}}{\dot{\varepsilon}_n} \right) \right] [1 + D_5 T^*] \quad (2)$$

where constants D<sub>1</sub>, D<sub>2</sub>, D<sub>3</sub>, D<sub>4</sub> and D<sub>5</sub> is given in Table 2. The JC failure model is applied only on AISI 1045, driving band and fuze are excluded. The Jones-Wilkins-Lee (JWL) equation of state serves as a widely adopted model in the explosives phenomena and is incorporated into ANSYS Autodyn software. It characterizes the detonation behavior of explosives, emphasizing the energy release and resulting pressure-volume relationship, expressed by the following equation:

$$p = A \left( 1 - \frac{\omega}{R_1 V} \right) e^{(-R_1 V)} + B \left( 1 - \frac{\omega}{R_2 V} \right) e^{(-R_2 V)} + \frac{\omega e}{V} \quad (3)$$

Here, p stands for pressure, V denotes relative volume, and constants A, B, R<sub>1</sub>, R<sub>2</sub>, and ω are given in the Table 3, with e representing the specific internal energy per cubic meter.

**Table 1.** Johnson-Cook strength model parameters

Material	A (MPa)	B (MPa)	n	C	m	T <sub>m</sub> (K)
AISIS 1045 [2-7]	507	320	0.28	0.064	1.06	1793
Cu-OFHC2	90	292	0.31	0.025	1.09	1356
AL 2024- T4	203	398	0.65	0.015	1.1	859

**Table 2.** Johnson-Cook failure model, damage constants for AISI 1045 [5]

D1	D2	D3	D4	D5

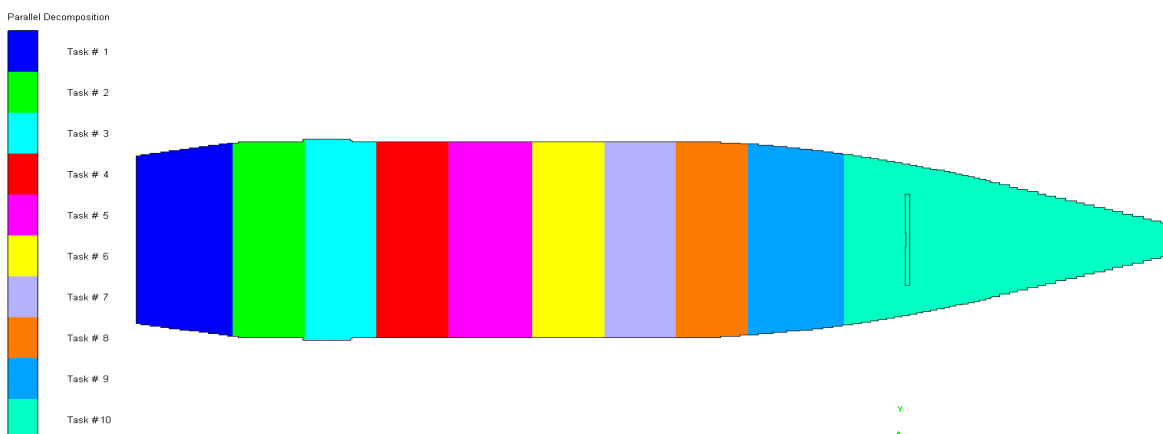


**Figure 2.** Artillery projectile 105mm M1, 3Dquarter numerical model (mirror function applied) with 10 subdomain parallel decomposition

0.1	0.76	-1.57	0.005	0.84
-----	------	-------	-------	------

**Table 3.** JWL equation of state model for TNT (from Autodyn material library)

$\rho$ (g/cm <sup>3</sup> )	$D_{c-j}$ (km/s)	$P_{c-j}$ (GPa)	A (GPa)	B (GPa)	$R_1$	$R_2$	$\omega$
1.63	6.93	21	373	3.747	4.15	0.9	0.35

### 3. NUMERICAL RESULTS AND ANALYSIS

The following section provides an analysis of the results obtained from numerical simulations based on six considered examples. The illustrated results from Figure 3, up to Figure 7 correspond to the example with the highest achieved convergence. The detonation front propagation can be observed in Figure 3, moving from right to left. The complete detonation process from the detonator to the bottom of projectile is completed in approximately 50  $\mu$ s. Figure 4 it is shown fragmentation process at 250  $\mu$ s and it is visible detonation products leaking and interaction with fragments. In accordance with findings from prior research papers, the fragmentation process of projectiles is typically considered complete when the projectile's lower section increases radially approximately twice its radius, observed to occur around 250  $\mu$ s, as visually depicted in Figure 5. Figure 5 serves to illustrate a comparative analysis between the resulting fragments and the initial configuration of the projectile casing.

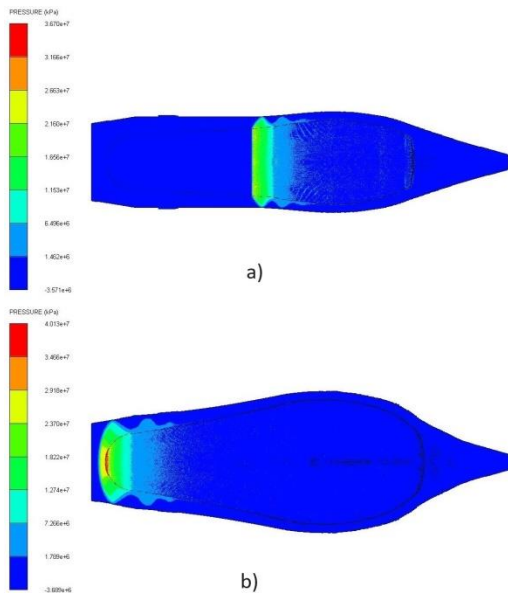


**Figure 3.** Detonation wave propagation in artillery projectile: a) 25  $\mu$ s and b) 50  $\mu$ s

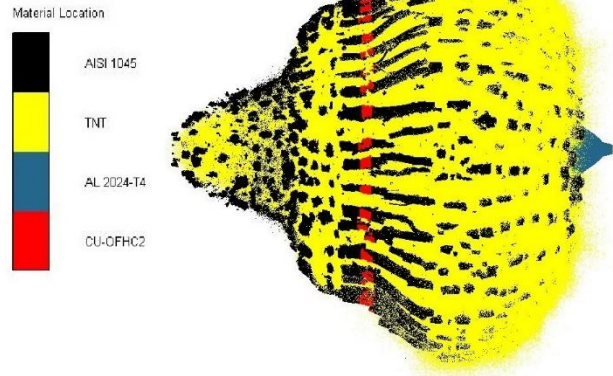


**Figure 4.** Completed fragmentation process with detonation products interaction 250  $\mu$ s

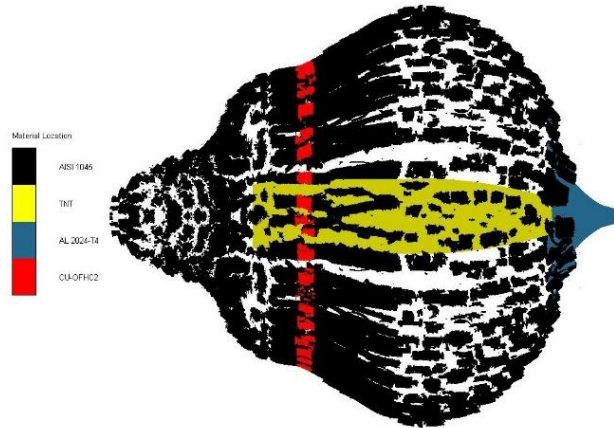


**Figure 5.** Completed fragmentation process compared to initial case volume (yellow color)

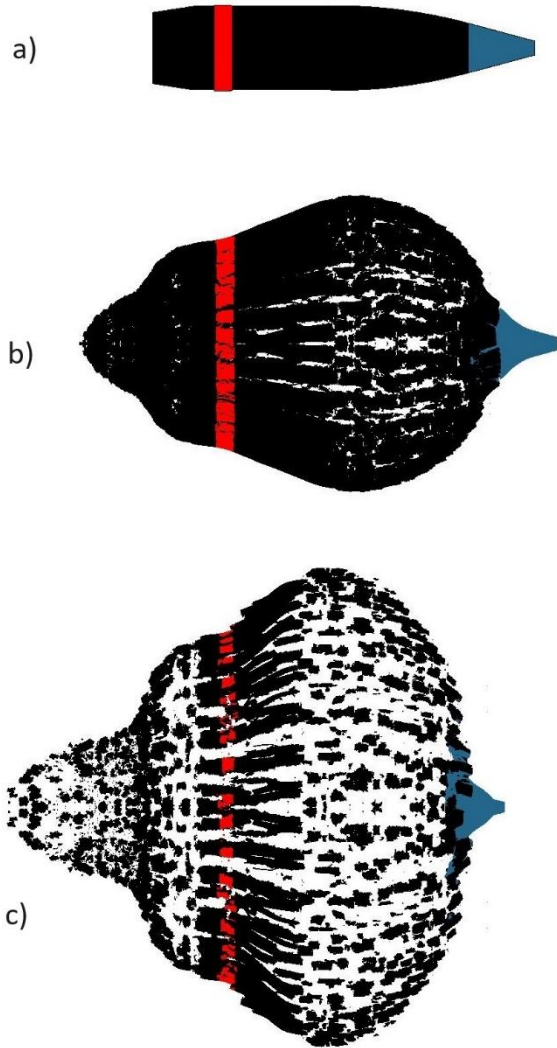


**Figure 6.** Fragmentation progression: a) 0  $\mu$ s, b) 125  $\mu$ s and c) 250  $\mu$ s

Figure 6 provides a detailed sequence showcasing the phases of both case expansion and fragment formation throughout the observed process. Specifically, it captures significant time points at 0  $\mu$ s, 125  $\mu$ s, and 250  $\mu$ s, offering a comprehensive view of the dynamic evolution of fragments. The entire fragmentation process was tracked until 350  $\mu$ s, with the determination of its completion grounded in the consistent total count of fragments observed up to approximately 250  $\mu$ s. Notably, the assessment also incorporates the structural dynamics involving the rupture of the driving band and the deformation of the fuze, both contributing to the overall fragmentation profile. Figure 7 further enhances the understanding by presenting a detailed velocity distribution across various fragment zones along the projectile casing. In the zones characterized by a higher ratio of explosive mass to metal mass, velocities peak at approximately 1200 m/s, underscoring the dynamic energy release during fragmentation. Conversely, velocities vary across other fragments, with velocities ranging from approximately 200 m/s to a minimum, with the fuze exhibiting an axial velocity of around 180 m/s,

reflecting the diverse kinetic outcomes across different components of the projectile.

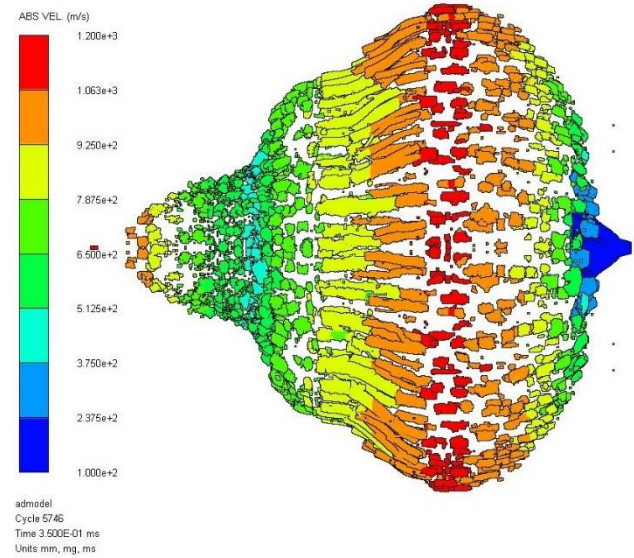


**Figure 7.** Absolute velocity distribution along axis of symmetry in 250  $\mu$ s

In Figure 8, it can be observed that the absolute velocities of fragments do not vary significantly when considering PS 2 decreasing to the value of PS 0.5. It can be concluded that convergence with velocity values is achieved already at PS 2.

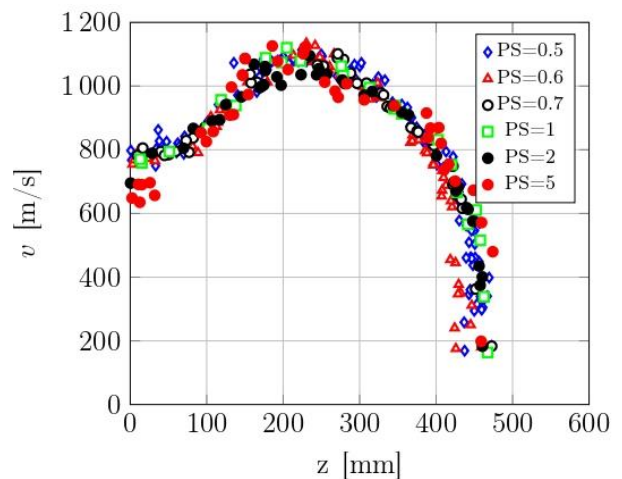


**Figure 8.** Absolute velocity of each fragment at 350  $\mu$ s along the axis of symmetry for different particle sizes (PS)

On the other hand, when PS is greater than 2 or exactly PS 5, scattered velocity distribution values can be seen, with some zones showing both lower and higher velocities of fragments compared with other obtained results. In all cases, the maximum velocity does not exceed 1200 m/s. Besides comparing the velocity results influenced by PS, the total number of fragments was also monitored. From Figure 9, it can be concluded that decreasing the PS has a significant impact on changing the total number of fragments. Each simulation was

compared with the experimental data, and it was found that numerical results converged at PS 0.7.

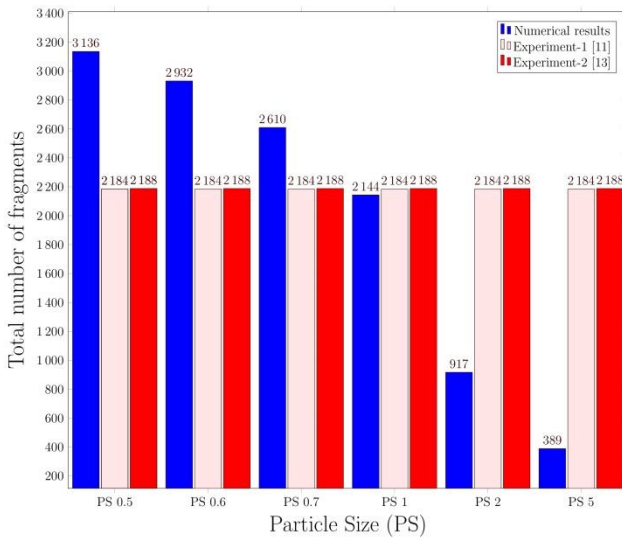


**Figure 9.** Comparison of the total number of fragments obtained by numerical simulation for various particle sizes (PS) with available experimental data.

Below value of PS 0.7, we have an increasing number of fragments compared with previous numerical results for 12.33%. It must be mentioned that additionally decreasing PS will strongly increase computation time, and the simulation will require more computational resources. For lower values of PS 0.7 it is notable that total number of fragments increases significantly. For example, for PS 0.5 compared to both available experimental results, the difference in achieving results is 30.4%. It can be concluded that a greater number of fragments obtained through simulation represents the number of fragments that could not be found after the experiment (pit test), due to very small dimensions and mass.

#### 4. CONCLUSION

Based on the research conducted and the numerical results obtained in this paper, focusing on the particle size (PS) influence and the capabilities of the Smoothed Particle Hydrodynamics (SPH) solver in ANSYS Autodyn software, the following conclusions can be drawn:

- The natural fragmentation process was analyzed using the Johnson-Cook strength model and the Johnson-Cook failure model to study the behavior of projectile cases under high strain rate deformation;
- The research reveals that considered PS values exhibit minimal changes in absolute fragment velocities, while the total number of fragments varies significantly. Below a PS 0.7 threshold, further simulation may not be necessary due to time constraints, as the outcomes show negligible deviation. A final conclusion can be drawn after characterizing the mass distribution for each simulation.
- Based on the results, it can be concluded that convergence cannot be followed based on a single parameter, as stated in some research papers. It

is necessary to consider multiple parameters, analyze them, and then draw a conclusion.

- Findings include the observation that the complete fragmentation process was done at approximately 200  $\mu$ s. The distribution of velocities among different fragment zones is calculated, with maximum velocities at approximately 1200 m/s in zones with a higher explosive-to-metal mass ratio. This comprehensive examination provides valuable insights into optimizing projectile design and enhancing understanding of fragmentation dynamics in ballistic applications;
- To effectively validate a numerical model for optimizing existing projectiles and designing new ones, it is crucial to accurately determine both the material properties of the projectile casing and the characteristics of the explosive material.

#### Acknowledgments

This work was supported by the Ministry of Science, Technological Development and Innovation, the Republic of Serbia, under contract evidence number 451-03-65/2024-03/200105 from 05.02.2024.

#### References

- [1] ĐURĐEVAC, D.: *Stress condition analyses of an artillery projectile*, Master thesis, University of Belgrade, Faculty of Mechanical Engineering, 2008.
- [2] ZHI-WEI, G., GUANG-YAN, H., WEI, Z., SHUN-SHAN, F.: *The fragmentation of D-shaped casing filled with explosive under eccentric initiation*, Defence Technology, Volume 14, Issue 5, 2018, 417-421.
- [3] WEI, L., GUANG-YAN, H., SHUN-SHAN, F.: *Effect of eccentric edge initiation on the fragment velocity distribution of a cylindrical casing filled with charge*, International Journal of Impact Engineering, Volume 80, 2015, 107-115.
- [4] YUEGUANG G., BO Z., XIAOMIN Y., TONG Z., XIANG X., SHUNSHAN F.: *Axial distribution of fragment velocities from cylindrical casing with air parts at two ends*, International Journal of Impact Engineering, Volume 140, 2020.
- [5] MA Y., HE Y., WANG C., HE Y., GUO Z. P., HU X.B.: *Dynamic fracture of the AISI 1045 steel cylinders under internal blast loading*, Journal of Physics: Conference Series, 2020, 1-12.
- [6] PING Y., QITIAN S., QIAN G., WEI H., XUANYI A., YONGXIANG D.: *Double casing warhead with sandwiched charge to produce multiple fragment groups for sequential hits: Concept and analysis of fragment velocity*, International Journal of Impact Engineering, Volume 158, 2021.
- [7] ZHI-YONG Y., XIAO-WEI C.: *Numerical study on the dynamic fracture of explosively driven cylindrical shells*, Defence Technology, Volume 27, 2023, 154-168.
- [8] LUO, Y., WEIBING, L., JUNBAO, L., WENBIN,

- L., XIAOMING, W.: *Crack propagation and damage evolution of metallic cylindrical shells under internal explosive loading*, Defence Technology, 2024.
- [9] ELSHENAWY, T., ZAKY, M.G., ELBEIH, A.: *Experimental and numerical studies of fragmentation shells filled with advanced HMX-plastic explosive compared to various explosive charges*, Brazilian JOURNAL OF Chemical Engineering, (2023), 481-492.
- [10] VIGNJEVIĆ, R., VUYST, T.D.: *SPH modelling of fragmentation of explosively driven metallic cylinders*, 4th International scientific conference on defensive technologies, 2011, 272-278.
- [11] UGRČIĆ, M. et al.: *Characterization of the natural fragmentation of explosive ordnance using the numerical techniques based on the FEM*, Scientific Technical Review, 65, (2015), 16-27.
- [12] UGRČIĆ, M. et al.: *Fem techniques in shaped charge simulation*, Scientific Technical Review, 59, (2009), 26-34.
- [13] MOHAMMED H.M.A., MOHAMMED A.A.: *Warhead fragments mass distribution using numerical combination of Mott's and Held's formulas*, 5<sup>th</sup> International conference on chemical and environmental engineering, Egypt, 2010, 1-9.
- [14] RANGLES, P.W., LIBERSKY, L.D.: *Smoothed Particle Hydrodynamics: Some recent improvements and application*, Comput. Methods Appl. Mech. Engrg., 139, 375-408.
- [15] Autodyn. (2023). *Autodyn User Manual*.



## NUMERICAL MODELING OF EXPLOSIVELY FORMED PROJECTILES FORMATION

ANDJELA MITROVIĆ

Military Technical Institute, Belgrade, [andjela.mitrovic@mod.gov.rs](mailto:andjela.mitrovic@mod.gov.rs)

SAŠA SAVIĆ

Military Technical Institute, Belgrade, [sasa.savic@mod.gov.rs](mailto:sasa.savic@mod.gov.rs)

MILAN VUČKOVIĆ

Military Technical Institute, Belgrade, [milan.vuckovic@mod.gov.rs](mailto:milan.vuckovic@mod.gov.rs)

NEBOJŠA HRISTOV

University of Defense, Military Academy, Belgrade, [nebojsahristov@gmail.com](mailto:nebojsahristov@gmail.com)

DAMIR JERKOVIĆ

University of Defense, Military Academy, Belgrade, [damir.d.jerkovic@gmail.com](mailto:damir.d.jerkovic@gmail.com)

MLADEN JOSIJEVIĆ

Faculty of Engineering University of Kragujevac, Kragujevac, [mladenjosijevic@gmail.com](mailto:mladenjosijevic@gmail.com)

**Abstract:** Within this study, the process of forming explosively formed projectiles is analyzed. This type of warhead is used for military purposes due to its excellent impact performance. The projectile is shaped like a metal disc which, during the action of the explosive, forms into a high-speed projectile. Such formed projectiles act on the target. The performance of the projectile is influenced by a large number of parameters, such as structural characteristics and material properties. Using a numerical program on the EFP model, various parameters influencing the final shape of the projectile and thus its performance on the target can be analyzed. The parameters considered within this study are the type of explosive filling and the thickness of the copper disc. The analyzed disc thickness was 1-4% of the explosive filling diameter. It was observed that reducing the thickness of the projectile results in higher values of projectile stable velocity. Specifically, reducing the initial thickness of the projectile can replace the use of more explosive explosives, thereby reducing the overall mass of the construction.

**Keywords:** Explosively formed projectile, EFP, High-speed projectile, Numerical modeling

### 1. INTRODUCTION

The explosively formed projectile (EFP) belongs to a group of warheads where explosive filling is used to accelerate the penetrator (formed disc) to high speeds. This type of warhead possesses a penetrator with a specific shape that is maintained until contact with the target [1].

Also, it belongs to the group of directed energy warheads, which focus explosive energy using the shape of a disc. EFP warheads can produce penetrators at speeds of 2-3 km/h [1]. In such cases, these warheads utilize most of casing for forming the penetrator.

The penetrator for the EFP is generally a bow-shaped metal part, called a self-forging fragment or ballistic disc. Warhead with shaped charge generally use a narrow cone-like geometry [2].

There is no clear line between shaped charge and EFP. A wide angle and a thick layer of shaped charge can form an EFP penetrator [1].

Most commonly, the shaped charge consists of an initial array with a detonator for forming a suitable circular detonation wave in the explosive filling, which, upon detonation, transforms the disc at the opposite end of the detonator.

After the explosive is initiated, a spherical detonation wave propagates forward from the initiation point. This high-pressure shock wave propagates at the detonation velocity of typical explosives (>8 km/s) and with a pressure equal to the Chapman-Jouget (CJ) pressure ( $P_{CJ} > 0.25$  Mbar) [1]. When the detonation wave reaches the material of the disc, it accelerates along the axis of symmetry and collapses towards the symmetry axis. The collapse of the disc material onto the central line forces the disc to move at high speed.

Due to this high speed, the penetrator can be transported to the target. Upon penetration of the penetrator into the target, the first element of the penetrator creates a hole. The second element impacts the target at the bottom of where the first element hit. Penetration continues as long as the penetrator has kinetic energy.

The entire process from explosive detonation to complete penetration occurs in less than half a millisecond, for short target distances. Due to the extremely high pressures, short duration, and harsh environment present in the penetrator/target interaction region, this is an exceptionally complex phenomenon.

The first publications related to this topic, i.e., to warheads similar to EFP, appeared in 1935 and 1936. However, research on this topic increased in the 1970s [3]. A large number of authors have presented various dependencies on the geometry of these projectiles, which can positively or negatively affect projectile performance. Among the significant parameters is the thickness of the casing, or the variability of its thickness, which is one of the more important factors, as well as the distance from the detonator center. Additionally, an important parameter is the ratio of the disc thickness to its diameter, which should be in the range of 4-7 %. [3] One of the most significant parameters is the ratio of width to height, or the ratio of length to diameter of the explosive before detonation. [4] A ratio of width to height can increase kinetic energy to a maximum of 1.5. [3]

The shape of the disc is an important parameter. The geometric shape can be hemispherical, hyperbolic, etc. In addition, the diameter and thickness of the disc are also crucial. According to data, the thickness of the disc occupies 1-4 % of the diameter of the explosive filling, while some projectiles can have a thickness of up to 8 % of the filling diameter. [5] The thickness of the disc can be variable, but care should be taken to ensure that the thickness does not change suddenly, as this can negatively impact disc performance [5]. Thinner discs may have a better effect than thicker ones and may achieve higher speeds [5]. It's essential to ensure that the disc thickness does not decrease infinitely, as this can cause the formed disc to rupture. The material of the disc plays a crucial role. It's necessary for the material to have a high melting point, high density, a closed crystal structure, good tensile characteristics, and to be free of impurities [5]. Additionally, the disc material should be easily deformable. The material of the disc is primarily copper because copper achieves maximum penetrations [6].

The height of the filling, i.e., the distance between the top of the explosive filling and the initiation point, represents an important factor. It's necessary

for this distance to be sufficient to ensure that the detonation wave becomes flatter when it reaches the disc [5]. If the wave reaching the disc has a spherical shape with a smaller radius, then the filling height is inadequate and does not uniformly transmit to the disc. Generally, the velocity, energy, and penetration depth of EFP increase with the increase in distance. However, the filling height should not be increased infinitely. The ideal filling height is from 1 to 1.5 times the filling diameter, without a deflector [5].

If a wave shaper is present in the construction of the EFP, its shape affects the shape of the detonation wave. The wave shaper is intended to redirect the detonation wave to more desirable, i.e., to reduce the angle of attack (the angle between the detonation wave and the disc), thereby more evenly transferring the wave energy to the disc. During initiation, the detonation wave "bypasses" the wave shaper, and then the detonation waves collide on the axis of the explosive filling. If the angle of incident is smaller than the critical Mach reflection angle, then regular reflection occurs, and the pressure at the collision point is 2.4 times greater than the CJ pressure [7, 8]. However, if the incident angle exceeds the critical angle, then Mach reflection occurs, where the pressure behind the Mach wave drops from four times the CJ pressure to normal pressure [7, 8]. It's essential to consider the shape of the wave shaper and its dimensions.

The explosive filling can be incorporated into the casing of the EFP through either casting or pressing processes. Regardless of the method, it's essential for the density and granulation of the explosive to be uniform to achieve the intended warhead effect.

## 2. NUMERIC MODEL

### 2.1. Material properties

The material of the disc is copper, which is described using the Johnson-Cook (JC) equation:

$$\sigma = (A + B\varepsilon^n)(1 + C \ln \dot{\varepsilon}) \left(1 - \left|\frac{T - T_r}{T_m - T_r}\right|^m\right) \quad (1)$$

Where are A, B, C, n, and m - material parameters;  $\varepsilon$  - the plastic strain;  $\dot{\varepsilon}$  - the strain rate;  $T_m$  - the reference temperature;  $T_r$  - the melting temperature of copper [3, 9]. The specified parameters for copper are shown in Table 1. The reason for using the Johnson-Cook constitutive method is that it provides better results for copper projectiles. This model accounts for thermal softening. Copper has a low melting temperature and a high thermal softening component [10]. The material of the casing is aluminum. Data for aluminum are provided in Table 2.



The explosive fillings are octogen (HMX), phlegmatized octogen (HMX-INERT), and explosive LX-10-1. The equation of state for the explosive is the Jones-Wilkins-Lee (JWL) equation of state:

$$P = A \left[ 1 - \frac{\omega}{R_1 V} \right] e^{-R_1 V} + B \left[ 1 - \frac{\omega}{R_2 V} \right] e^{-R_2 V} + \frac{\omega E_0}{V} \tag{2}$$

Where is P - the shock wave pressure; V - the volume ratio between the detonation products and the initial explosive; A, B, R<sub>1</sub>, R<sub>2</sub>, and ω - material parameters; E<sub>0</sub> - the specific internal energy of the explosive [3, 9]. The data are provided in Table 3.

**Table 1.** Characteristics of copper

COPPER	
Density [kg/m <sup>3</sup> ]	8960
Specific Heat [J/kgK]	383
Johnson Cook Strength	
Initial Yield Stress [Pa]	9E+07
Hardening Constant [Pa]	2.92E+08
Hardening Exponent	0.31
Strain Rate Constant	0,025
Thermal Softening Exponent	1.09
Melting Temperature [°C]	1082.9
Reference Strain Rate [1/sec]	1
Bulk Modulus [Pa]	1.29E+011
Shear Modulus [Pa]	4.6E+11

**Table 2.** Characteristics of aluminum

ALUMINUM (AL 6061-T6)	
Density [kg/m <sup>3</sup> ]	2703
Specific Heat [J/kgK]	885
Steinberg Guinan Strength	
Initial Yield Stress [Pa]	2.90E+08
Maximum Yield Stress	6.8E+08
Hardening Constant	125
Hardening Exponent	0.1
Strain Rate Constant	0.025
Melting Temperature [°C]	946.85
Shear Modulus [Pa]	2.76E+10
Shock EOS Linear	

Gruneisen Coefficient	1,97
Parameter C1 [m/s]	5240
Parameter S1	1,4
Parameter Quadratic S2 [s/m]	0

**Table 3.** Characteristics of selected explosives

Characteristic s	HMX	HMX-INERT	LX-10-1
Density [kg/m <sup>3</sup> ]	1891	1783	1865
Explosive JWL			
Parameter A [Pa]	7.7828E+11	9.4334E+11	8.807E+11
Parameter B [Pa]	7.0714E+09	8.8053E+09	1.84E+10
Parameter R1	4.2	4.7	4.62
Parameter R2	1	0.9	1.32
Parameter W	0.3	0.35	0.38
Detonation velocity [m/s]	9110	8730	8820
Energy per unit mass [J/kg]	5.55E+06	5.72E+06	5.58E+06
Pressure [Pa]	4.20E+10	3.35E+10	3.75E+10

The detonator material is explosive C4, the data for which are provided in Table 4. The wave shaper material is polyethylene, and its data are given in Table 5.

**Table 4.** Characteristics of C4 explosive

C4	
Density [kg/m <sup>3</sup> ]	1601
Explosive JWL	
Parameter A [Pa]	6.0977E+11
Parameter B [Pa]	1.30E+10
Parameter R1	4.5
Parameter R2	1,4
Parameter W	0.25
C-J Detonation Velocity [m/s]	8193

C-J Energy per unit mass [J/kg]	5.62E+06
C-J Pressure [Pa]	2.80E+10

**Table 5.** Characteristics polyethylene

POLYETHYLENE	
Density [kg/m <sup>3</sup> ]	915
Shock EOS Linear	
Gruneisen Coefficient	1.64
Parameter C1 [m/s]	2901
Parameter S1	1.481
Parameter Quadratic S2 [s/m]	0

**2.2. Calculation model**

The EFP model is shown in Figure 1. The Eulerian model describes the casing, detonator, wave shaper, and explosive filling. Meanwhile, the disc is described using the Lagrangian model. The Lagrangian model is used for "structural" elements, where the numerical mesh moves and deforms with the material motion. The Eulerian model is used for large movements and explosives, where the numerical mesh is fixed, and the fluid flows through the mesh. [1] The mesh size is 0.5 mm. Since the model is axisymmetric, only a quarter of the model is considered. The model is observed in 2D.

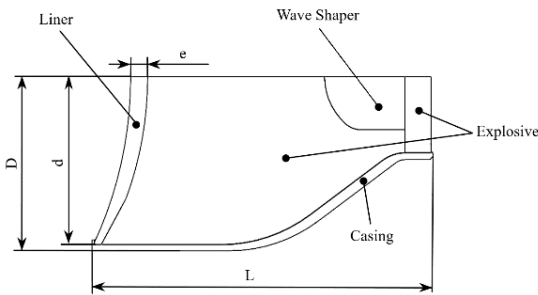


**Figure 1.** EFP, where are: D – casing diameter; d – disc diameter; e – disc thickness; L – casing length

**3. RESULTS**

The previously shown EFP model with different explosive fillings was analyzed in the corresponding numerical program. Additionally, the disc thicknesses were varied, starting from 5.3 mm and gradually reduced to 4.9 mm. Figure 2

illustrates the disc formation over time for an example of EFP with phlegmatized HMX explosive filling and a disc thickness of 5.3 mm.

The disc formation is a complex dynamic process primarily resulting from the interaction between various components of the warhead. The stability of flight velocity is achieved at approximately  $t = 400 \mu s$  [3]. In this case, it was observed that the stability of flight velocity occurs at around  $300 \mu s$ .

It is noticeable that the EFP with LX-10-1 explosive attains the highest disc velocity, slightly higher compared to the EFP with octogen. Conversely, the disc with phlegmatized octogen exhibits the lowest velocity. It is concluded that the EFP with LX-10-1 explosive causes the most significant elongation of the formed disc. Conversely, the EFP with phlegmatized octogen exhibits the shortest formed disc. It was observed that during the formation of the disc with stronger explosives (in this case, LX-10-1 and HMX), narrowing of the projectile's rear part occurs, which does not happen with the action of weaker explosives, such as phlegmatized octogen.

Based on Figure 3, it can be observed that reducing the disc thickness leads to an increase in its velocity during formation. Decreasing the disc thickness with weaker explosives can replace the use of stronger explosives. However, the disc thickness should not be reduced infinitely. Excessive reduction in disc thickness leads to the collapse of the disc structure during formation and results in irregular disc formation, which can cause projectile fragmentation and consequently irregular action on the target. The process of reducing disc thickness also contributes to reducing the overall mass of the construction.

The ballistic performance of the obtained projectile is evaluated based on criteria related to its kinetic energy. Ballistic parameters such as geometry, detonation type (number and position of detonators), and materials influence the stable flight velocity of the EFP and consequently its penetration stability (i.e., ballistic performance) [3].

Table 6 provides stable velocities, kinetic energy, and specific energy of the formed projectile for different disc thickness values. Based on the presented table, it is observed that the model of EFP with LX-10-1 explosive has the highest kinetic energy, which is expectedly proportional to the disc mass. However, the variant with the lowest mass also has significantly high kinetic energy due to the high disc velocity. The same applies to the specific energy of the formed projectile, which is significant for projectile penetration through obstacles.

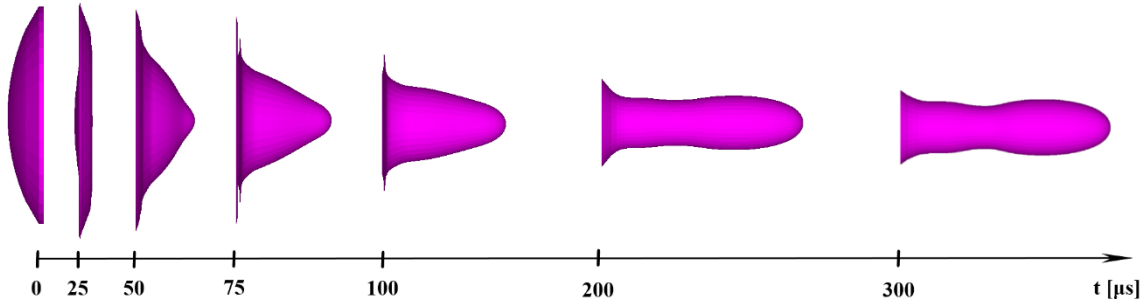


**Figure 2.** Display of disc formation over time, with an EFP containing HMX-INERT explosive fill and a disc thickness of 5.3 mm

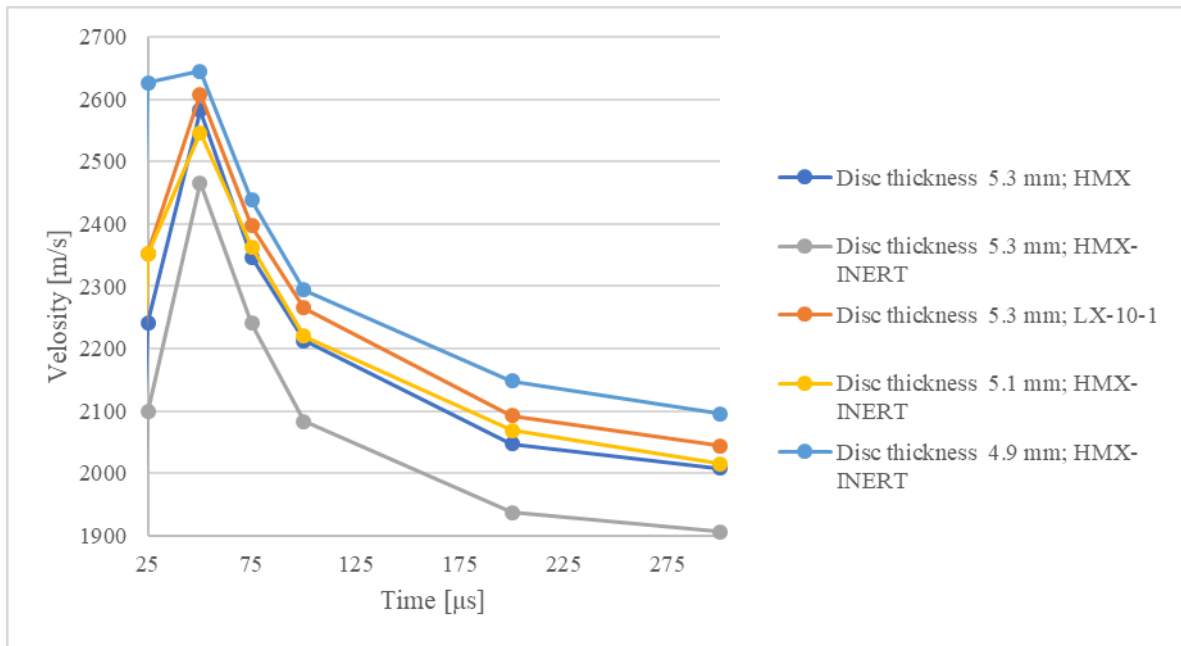


**Figure 3.** Diagram of the velocity change at the apex during disk formation

**Table 6.** Stable velocity and kinetic energy for different values of disk thickness

	Disc thickness 5.3 mm			Disc thickness 5.1 mm	Disc thickness 4,9.mm
	LX-10-1	HMX	HMX-INERT	HMX-INERT	HMX-INERT
<b>Disc mass [g]</b>	320	320	320	296.8	282.5
<b>Stable velocity [m/s]</b>	2044	2008	1906.3	2016	2095.6
<b>Kinetic energy [kJ]</b>	668469.8	645066	581436.7	603075.8	620304.9
<b>Formed penetrator diameter [mm]</b>	21.2	21.7	25.2	22	20.8
<b>Specific energy [kJ/mm<sup>2</sup>]</b>	473.4	434.4	291.4	396.6	456.4

#### 4. CONCLUSION

A large number of parameters affect the final shape of the penetrator. It's necessary to harmonize all parameters to achieve the desired effect on the target. Analyzing the presented EFP construction with different explosive fillings led to certain conclusions.

Firstly, when using explosives that are stronger according to their characteristics, penetrators of higher speeds are formed compared to the values of speeds when using weaker explosives. However, by reducing the thickness of the disk and using weaker explosives, higher values of stable speeds are obtained. These values are higher compared to the values of stable speeds when using stronger explosives.

Kinetic energy, as an indicator of ballistic performance, is greater in penetrators with stronger explosives and greater penetrator thickness, proportionally to the greater mass of the penetrator. However, using stronger explosives can lead to thinning of the rear part of the penetrator. This can cause the penetrator to break during flight and result in less kinetic energy reaching the target. Therefore, it is recommended to use weaker explosives with a smaller initial disk thickness to obtain a compact penetrator with high kinetic energy at the target. It is necessary to confirm the obtained data with experiments to validate numerical simulations, which represents the next step in this comprehensive topic.

Research related to this topic was partly done at the Military Academy (project VA/TT/1/24-26).

#### References

- [ 1] ESER GÜREL: *Modeling and simulation of shaped charges*, Middle East Technical University, 2009.
- [ 2] W. P. WALTERS, J.A. ZUKAS: *Fundamentals of shaped charges*, New York, 1943.
- [ 3] D. CARDOSO, F. TEIXEIRA DIAS: *Modelling the formation of explosively formed projectiles (EFP)*, International Journal of Impact Engineering 93, 2016
- [ 4] HUANG X., LI W., LI W., YIN G., WANG Y., GUO T.: *Energy spatial distribution of behind-armor debris generated by penetration of explosively formed projectiles with different length-diameter ratio*, Appl. Sci., 2023.
- [ 5] JUN WU, JINGBO LIU, YIXIN DU: *Experimental and numerical study on the flight and penetration properties of explosively-formed projectile*, International Journal of Impact Engineering, 2006.
- [ 6] SUNGRA MLK, ABDUL, QADEER. MALIK, A. HAMEED, KHAIRUDDIN SANAULLAH: *Analytical performance study of explosively formed projectiles*, Journal of Applied Mechanics and Technical Physics, 2003.
- [ 7] ZHENG XIANG HUANG, QIANG-QIANG XIAO: *Research on forming of EFP warhead with wave-shaper and center-hole Charge*, Dandao Xuebao/Journal of Ballistics, 2013.
- [ 8] XU DONG ZU, ZHENG XIANG HUANG, CHUAN SHENG YHU, QIANG QIANG XIAO: *Study of detonation wave contours in EFP warhead*, Defence Tehnology, 2016.
- [ 9] YAKUN LIU, JIANPING YIN, ZHIJUN WANG, XUEPENG ZHANG, GUANGJIAN BI: *The EFP formation and penetration capability of double-layer shaped charge with wave shaper*, Materials, 2020.
- [ 10] DONG YANG, JIAJIAN LIN: *Numerical Investigation on the Formation and Penetration Behavior of Explosively Formed Projectile (EFP) with Variable Thickness Liner*, Symmetry, 2021.



## CARBON BLACK VS CHARCOAL. INFLUENCE ON COMBUSTION PROPERTIES OF SELECTED PYROTECHNIC COMPOSITIONS

JELENA MOJSILOVIĆ

Military Technical Institute, Belgrade, [mojsilovic.jeca@gmail.com](mailto:mojsilovic.jeca@gmail.com)

IVAN DIMITRIJEVIĆ

Faculty of Technology and Metallurgy, University of Belgrade, [ivan.dimitrijaevic@mclabor.co.rs](mailto:ivan.dimitrijaevic@mclabor.co.rs)

MIRJANA KRSTOVIĆ

Military Technical Institute, Belgrade, [mbkrstovic@gmail.com](mailto:mbkrstovic@gmail.com)

STEVAN STUPAR

Military Technical Institute, Belgrade, [stevan.stupar13@gmail.com](mailto:stevan.stupar13@gmail.com)

VESELIN ŽIVANOVIĆ

Military Technical Institute, Belgrade, [veselin.zivanovic.best@gmail.com](mailto:veselin.zivanovic.best@gmail.com)

**Abstract:** Conventional black powder typically consists of charcoal, sulfur and potassium nitrate ( $KNO_3$ ). The use of other carbon-based substances instead of charcoal has been less common. Following the development of time delay pyrotechnic compositions in this research, the pyrotechnic properties of other carbon-based substances, particularly carbon black were studied. The use of charcoal has been widely spread due to its unique chemical composition and superior combustion properties. However, due to the specific production process and the selection of materials for producing charcoal, it is difficult to achieve the same quality, i.e., chemical composition of charcoal. The use of other carbon-based substances may suppress those problems. Quaternary compositions containing charcoal or carbon black as a fuel and  $KNO_3$ , sulfur and phenol-formaldehyde resin were prepared and tested. Commercially available charcoal and carbon black were obtained for this initial research. The as-received materials, charcoal and carbon black, were characterized by SEM, EDS and particle size analyzer. SEM and EDS analysis were used to obtain information about morphology and semi-quantitative determination of the chemical composition and particle size analyzer for obtaining information about particle size and its distribution. The experimental values of heat of reaction and linear burning rate were compared. The average linear burning rate for pyrotechnic composition with carbon black of 7.33mm/s showed increase of 28.5% comparing to pyrotechnic composition with charcoal. Observed behavior suggests that this compound may be useful for a variety of pyrotechnic applications.

**Keywords:** energetic materials, linear burning rate, heat of reaction, carbon black, charcoal.

### 1. INTRODUCTION

Pyrotechnic delays had been used since the first hand grenade has been made. They are used to provide a reproducible time interval between two energetic events. Until the mid-20<sup>th</sup> century black powder was materials of choice for delays [1,2]. Nowadays typically metals and other materials are used as fuels for delays since they have low production of gaseous products during the combustion and reproducible time intervals between two energetic events. Nevertheless, black powder can produce very reproducible intervals, but it must be vented due to the large amount of permanent gas generated during the combustion [3]. This disadvantage is prevented by adequate design of a fuze. Beside this, charcoal is both disadvantage and advantage of black powder. Charcoal is a natural solid fuel. It is produced by pyrolysis of wood. The physical and chemical properties are hard to define due to the nature of wood and technological parameters of

carbonization. Beside those non reproducible parameters, charcoal still has superior properties like large surface area, approximately  $1-3m^2/mg$ , heat conductivity and adsorption. It behaves like catalyst in combustion of black powder [4]. The chemical composition of charcoal is mainly carbon and in the small percentage there are also large number of different hydrocarbons, ash, moisture [5-6]. However, black powder is still in use nowadays and it has many modifications regarding its application.

The aim of this research was to overcome the disadvantage of non-reproducible parameters of charcoal. Knowing that charcoal consists mainly of carbon it came naturally to find substitute in a form of another carbon-based material. Nowadays, there are many carbon-based materials that have potential use in pyrotechnics. These are graphene, carbon nanotubes, carbon black etc. Carbon black is widely known for its use in different industries and as an additive in energetic materials, but it wasn't use in pyrotechnic compositions as a main fuel.

The term carbon black refers to an industrial product which essentially consists of elemental carbon in the form of near spherical particles of colloidal size, coalesced into particle aggregates and agglomerates. It is produced by the partial combustion or thermal decomposition of hydrocarbons. The production process nowadays can be precisely controlled, and in that manner produced carbon black has a clearly defined properties [7].

Carbon black has a wide range of applications like fillers to improve mechanical, electrical and optical properties, in elastomers, plastics, paint, inks etc. The primary carbon black characteristics that influence the properties of carbon black compounds are the particle size, aggregate size, the morphology of the carbon black aggregates and their microstructure.

For the aim of this study, quaternary compositions containing charcoal or carbon black as a fuel and  $\text{KNO}_3$ , sulfur and phenol-formaldehyde resin were prepared and tested.

## 2. EXPERIMENT

### 2.1. Materials

The used  $\text{KNO}_3$  powder, sulfur powder, willow tree charcoal, carbon black and phenolic resin were delivered by Traylor Corporation AD. Ethyl alcohol (96% v/v) was purchased from Sigma-Aldrich, USA. All used chemicals were analytical grade or higher and were used as received.

### 2.2. Preparation of charcoal and carbon black-based compositions

Pyrotechnic compositions were prepared by the following steps. First the fuels and oxidizer underwent a drying process in an oven for a duration of 3 hours at 60 °C and 5wt.% of phenolic resin was dissolved in ethanol to obtain solution. Then, dry homogenization was performed in two phases. The first phase consisted of mixing the fuels, charcoal or carbon black and sulfur, until all components were evenly dispersed. Then  $\text{KNO}_3$  was added, and all compounds were well mixed together. After that, phenolic resin solution was added into the dry oxidant-fuel composition and well mixed together in porcelain veneer. The as-prepared compositions were put in an oven for about 1 hour at 60 °C to partially remove solvent. After 1-hour, semi-dried composition was mashed through 100 mesh sieve and returned to an oven for 3 hours at 60 °C to remove remaining moisture content for further use in the following experiments.

Both pyrotechnic compositions have same weight ratios of  $\text{KNO}_3$ , sulfur, phenolic resin and depending on composition charcoal or carbon black, 75:5:5:15, respectively. Keeping the same ratio, it was possible to compare results depending on weather composition consisted of charcoal or carbon black as a main fuel.

### 2.3. Characterization of the raw materials

The surface morphology and semi-quantitative chemical element composition of charcoal and carbon black were employed by scanning electron microscope with Energy dispersive X-ray Spectroscopy (20 kV, JEOL 6610LV, Japan).

Particle size analysis of charcoal and carbon black was measured on Anton Paar PSA 1190 laser diffraction instrument in liquid mode. Water was used as carrier liquid, and Igepal CA-630 surfactant was used for improved wetting of particles. Particles were dispersed for 5 minutes with the use of stirring and 50 W power ultrasound. Particle size is determined according to Mie theory with values of refractive and absorption indexes of 2 and 1, respectively. The specific surface area (SSA) of samples was calculated with Anton Paar Kalliope software and represents the sum of the actual surfaces of each particle. For these calculations shape factor of 1 is used (which means that particles are like perfect spheres), and density determined on gas pycnometer Ultrapyc 5000 by Anton Paar.

### 2.4. Characterization of the pyrotechnic compositions

The heat of reaction measurements were conducted with isoperibolic calorimeter (IKA- Calorimeter C 2000 model). For this analysis samples were prepared in powder form, 3g in each polyethylene bag, with electric squib to initiate combustion. Three measurements of each composition are measured, and they were performed in an inert atmosphere of argon.

Linear burning rate was determined for both pyrotechnic compositions. Samples were measured and pressed into an aluminum alloy tube, with length 15mm, diameter 8mm and thickness of wall tube 2mm with 20 MPa of pressure on the hydraulic press. Five measurements of each composition were conducted to obtain more precise data. The data were collected by VOD 811 system with specially adjusted software for the correct display of lower combustion velocities.

## . RESULTS AND DISCUSSION

### 3.1. Preparation of pyrotechnic compositions

Preparation of selected pyrotechnic compositions was conducted as described in section 2.2.

While preparing charcoal/ $\text{KNO}_3$ /S/phenolic resin composition there were no difficulties regarding technique used to prepare this composition. On the other hand, composition containing carbon black as a main fuel had shown problems in dry homogenization and mashing phase. Due to the high tendency of agglomeration of carbon black it was difficult to achieve homogeneous dry mixture of fuels and oxidizer. One of the possible solutions was to separate dry homogenization into a few smaller batches. Also, a major problem appeared after wet homogenization. During the mashing phase, it was hard to put through a

sieve semi-dried mixture. The mixture was constantly “sticking” to a sieve. To untangle the problem, a limited amount of composition was put on a sieve and after all composition passed through the sieve, the sieve was cleaned with a brush to prevent sticking of next amount of semi-dried mixture.

### 3.2. SEM and EDS results

In Figure 1 and 2 SEM images with corresponding EDX spectra for charcoal and carbon black are shown, respectively.

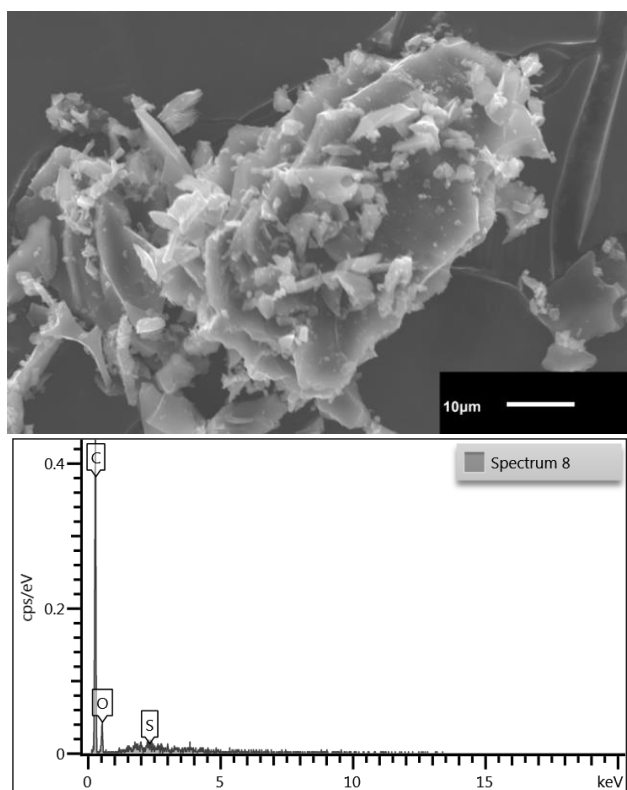


**Figure 1.** SEM image with corresponding EDS for charcoal

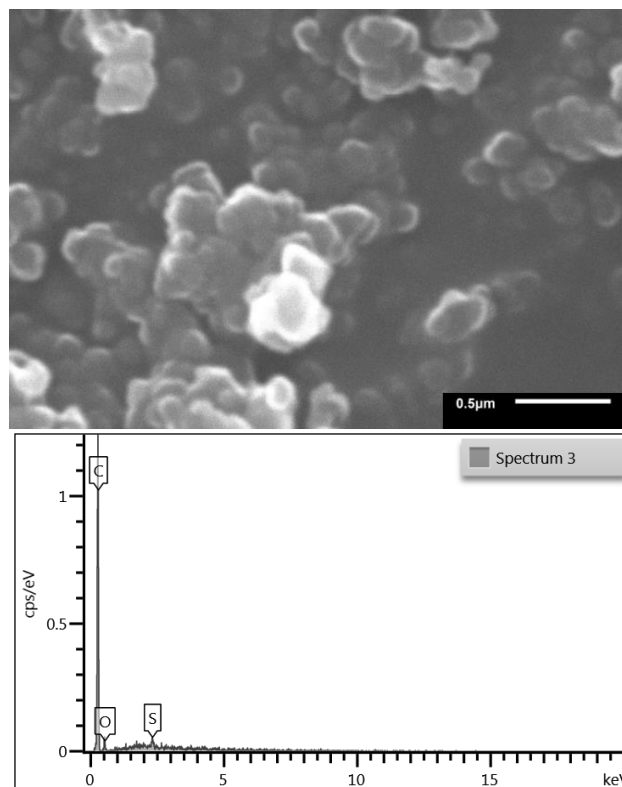
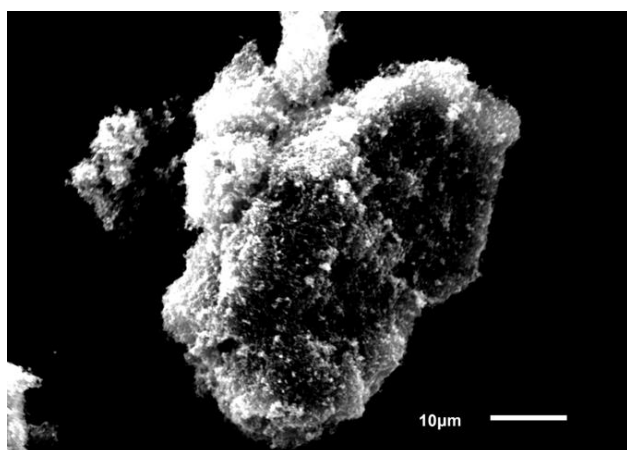


**Figure 2.** SEM images with corresponding EDS for carbon black

Figure 1 shows SEM image of charcoal where sample consist of broken pieces in different sizes and shapes. In Figure 2, are shown images of carbon black. First image, Figure 2, was captured with magnification of 1500, and it can be seen agglomerated sample of carbon black bigger than 10 µm compared to measurement bar of 10 µm on the image. On the image below, it's presented sample of carbon black magnified 45 000 time, and captured particles are much smaller, and they are more likely to be found in carbon black composition than large agglomerate.

Table 1 shows the results from the surface element analyses of the two samples determined by SEM-EDS.

**Table 1.** SEM-EDS analysis results of charcoal and carbon black

Element	Charcoal (wt%)	Carbon black (wt%)
C	79.80	95.83
O	19.94	3.21
S	0.26	0.96
Total	100	100

The analyzed EDX spectra, Table 1, shows that charcoal and carbon black consist mainly of carbon. The charcoal's degree of carbonization yields 79.80 wt% of element carbon and almost 20 wt% of other elements which are probably in the form of hydrocarbons, ash and moisture. Carbon black yields 95.83 wt% of carbon and in traces other elements like oxygen and sulfur.

### 3.3. Particle size analysis and specific surface area results

In Table 2 average volume weighted distribution results of five consecutive measurements and standard deviations are shown. Small standard deviations, which are in the range of less than one to a couple of percent compared to average values, indicate good dispersion of particles in carrier liquid and valid measurement results.

**Table 2.** Results of particle size and SSA analysis

Sample	D <sub>10</sub> ( $\mu\text{m}$ )	D <sub>50</sub> ( $\mu\text{m}$ )	D <sub>90</sub> ( $\mu\text{m}$ )	D[4,3] ( $\mu\text{m}$ )	Span	SSA ( $\text{m}^2/\text{g}$ )
Charcoal	4.96 $\pm 0.02$	18.66 $\pm 0.10$	52.50 $\pm 0.51$	25.48 $\pm 0.18$	2.55 $\pm 0.02$	0.45 $\pm 0.01$
Carbon black	0.48 $\pm 0.03$	1.74 $\pm 0.07$	8.58 $\pm 0.41$	3.54 $\pm 0.13$	4.65 $\pm 0.30$	3.29 $\pm 0.15$

In Figures 3 and 4 differential and cumulative particle size distributions are shown.

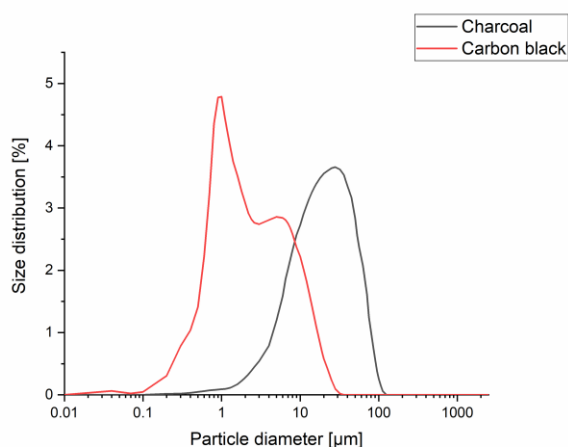


**Figure 3.** Differential particle size distribution of charcoal and carbon black

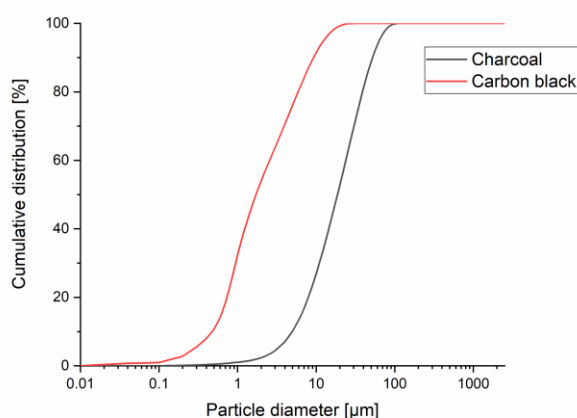


**Figure 4.** Cumulative particle size distribution of charcoal and carbon black

It is obvious that carbon black consists of much smaller particles than charcoal. Mean particle size of carbon black is more than 7 times smaller than of charcoal. Carbon black has a significant portion of particles smaller than 1  $\mu\text{m}$  (approximately 30% volume weighted), while

charcoal has only 1% of particles smaller than 1  $\mu\text{m}$ . The maximum particles size of carbon black is 20  $\mu\text{m}$ , and of charcoal is 100  $\mu\text{m}$ . This leads to a much higher specific surface area of carbon black (3.29  $\text{m}^2/\text{g}$ ) compared to charcoal (0.45  $\text{m}^2/\text{g}$ ), which is favorable parameter for fast burning pyrotechnic compositions. Also, width of particle size distribution is much wider for carbon black compared to charcoal, span is 4.65 versus 2.55. It can be seen from Figure 3 that particle size distribution of carbon black is bimodal, with main maximum distribution of particles around 1  $\mu\text{m}$  and 5  $\mu\text{m}$ , while particle size distribution of charcoal is monomodal, with main maximum distribution of particles around 30  $\mu\text{m}$ . Materials which have polydisperse particles usually can be pressed to a higher level due to more filled voids, and in that way higher densities can be achieved, which leads to more energy confined in the same volume.

### 3.4. Heat of reaction results

The heat of reaction values are presented in Table 3. Average values for charcoal-based and carbon black-based composition are 2774.0 J/g and 2650.2 J/g respectively. Standard deviation for charcoal-based and carbon black-based composition are 15.99 J/g, and 25.12 J/g, respectively. Standard deviation indicates that measurements were performed correctly. Slightly higher standard deviation for carbon black compositions of 25.12 J/g may be due to the difficulties regarding preparation technique described in section 3.1 that had brought to the less homogeneous mixture and may lead to the incomplete combustion as carbon black tends to agglomerate in composition.

Average value for charcoal-based composition is 123.83 J/g higher from average value for carbon black-based composition. Knowing from EDS analysis that charcoal contains O in 19.94 wt% and carbon black only 3.21 wt% of O shows that oxygen balance is higher for charcoal-based compositions. This indicates higher calorific value for charcoal-based compositions.

**Table 3.** Heat of reaction results for charcoal and carbon black-based compositions

Sample	Heat of reaction [ J/g ]	
	Charcoal based PC	Carbon black-based PC
1	2761.7	2648.4
2	2792.1	2626.5
3	2768.3	2676.6
Average value	2774.0	2650.2
Standard dev.	15.99	25.12

### 3.5. Linear burning rate results

The linear burning rate values are shown in Table 4. Standard deviation for linear burning rate for charcoal-based compositions is 0.26 mm/s and for carbon black compositions is 0.24 mm/s which indicates that measurements were performed correctly. It is obvious that carbon black composition has a higher value in linear burning rate than charcoal-based composition. Average values for charcoal-based and carbon black-based



compositions are 5.7 mm/s and 7.33 mm/s, respectively. There is an increase of 28.5% in linear burning velocity in favor of carbon black composition. Higher SSA, smaller mean particle size of carbon black and more energy confined in same volume resulted in faster burning of pyrotechnic composition with carbon black.

**Table 4.** Linear burning rate results for charcoal and carbon black-based compositions

Sample	Linear burning rate [mm/s]	
	Charcoal based PC	Carbon black-based PC
1	5.8	7.0
2	5.6	7.5
3	5.6	7.3
4	5.4	7.6
5	6.1	7.3
Average value	5.7	7.3
Standard dev.	0.26	0.24

## 4. CONCLUSIONS

Charcoal and carbon black-based delay pyrotechnic compositions were prepared and examined to research the possibility to incorporate other carbon-based materials instead of charcoal in pyrotechnic delay. Preparation technique showed difficulties regarding preparation of carbon black-based compositions due to the tendency of carbon black to agglomerate. EDS analysis of charcoal and carbon black offered different views on elemental semi-quantitative chemical composition. Charcoal has higher wt% of oxygen 19.94, probably in the form of moisture, hydrocarbons, ash etc., which directly increase an oxygen balance for charcoal-based composition. Also, charcoal-based composition showed higher values for heat of reaction of 2774.03 J/g compared to carbon black-based composition of 2650.2 J/g. Mean particle size of carbon black is more than 7 times smaller than of charcoal and it has approximately 30% of volume weighted of particles are smaller than 1  $\mu\text{m}$ . This implies higher SSA of carbon black and increase in average linear burning rate of 28.5% for carbon black-based composition compared to charcoal-based composition. Those attributes

suggest that particle size and its distribution are probably the most important physical properties of carbon black in terms of end-use applications. For some future study, this work provides an insight into difficulties regarding preparation of carbon black-based composition and a possible new idea for preparation of that composition in some different techniques.

## Acknowledgements

This work was supported by the Ministry of Science, Technological Development and Innovations (Serbia), Contract No. 451-03-66/2024-03/200325 and University of Defence, Belgrade, Serbia Research Project No. VA-TT/1/22-24.

## References

- [1] CONKLING, J. A.; MOCELLA, C. J.: *Chemistry of Pyrotechnics: Basic Principles and Theory*, 2nd ed.; CRC Press, Taylor & Francis Group: Boca Raton, 2011.
- [2] WILSON, M. A.; HANCOX, R. J.: *Pyrotechnic Delays and Thermal Sources" in Pyrotechnic Chemistry: Pyrotechnic Reference Series No. 4*, Kosanke, K.; Kosanke, B.; Journal of Pyrotechnics, Inc: Whitewater, CO, 2004.
- [3] Poret J.C. et al.: *Environmentally Benign Pyrotechnic Delays*, 38th International Pyrotechnics Seminar, Denver, Colorado, 10-15 June 2012, p. 494-500.
- [4] J.H. MC LAIN: *Pyrotechnic from the viewpoint of Solid-State Chemistry*, Franklin Institute Press, USA, 1980.
- [5] I. GLASSMAN: *Combustion*, 3rd Edition, 1996.
- [6] MOJSILOVIC J. et al.: *Design of suitable pyrotechnic delay composition with widely used components*, 10<sup>th</sup> International scientific conference on defensive technologies OTEH 2022, Belgrade, Serbia, 13.-14. October 2022. p.150 -154.
- [7] DONNET, J. B.: *Carbon Black: Science and Technology*, 2<sup>nd</sup> edition Revised and Expanded Marcel Dekker, inc., USA, 1993.



## CALCULATION OF SAFE DIAMETER OF PROPELLANTS USING HEAT FLOW MEASUREMENTS

VESNA PETROVIĆ

Technical Overhaul Facility Kragujevac, [lab@trzk.co.rs](mailto:lab@trzk.co.rs)

SLAVIŠA STOJILJKOVIĆ

Technical Overhaul Facility Kragujevac, [trzk@trzk.co.rs](mailto:trzk@trzk.co.rs)

JELENA ŠULTANS

Technical Overhaul Facility Kragujevac, [lab@trzk.co.rs](mailto:lab@trzk.co.rs)

**Abstract:** By using experimental and theoretical work, it has been made procedure in order to use microcalorimetric heat flow data to calculate safe diameter. For calculation of safe diameter two equations have been used. Calculated results were compared. If calculated value of safe diameter is compared with diameter of ammunition loading charge, one can make assessment whether ammunition storage is safe or not. This propellant testing has great importance for chemical stability evaluation of propellants. Microcalorimetric system, whether „TAM III“ or „TAM IV“ is used, gives heat flow data in terms of released heat quantity at elevated temperatures. Calculation of safe diameter is important in preventing accidents due to selfignition of propellants.

**Keywords:** chemical stability, safe diameter of propellants, microcalorimetry

### 1. INTRODUCTION

With the decrease of consumption of stock ammunition, and the increase of stock time, the safety problem of the ammunition in long stock becomes increasingly important. Gun powders and rocket propellants in long-term stock ammunition undergoes slow decomposition reaction and exothermic processes. If the heat can not be conducted away in time, its accumulation will lead to spontaneous combustion of propellants, which is a great threat to the safety of the stock and its surroundings. Specially, if the activation energy of the aging processes is low, degradation is fast. This will accelerate the degradation process, finally resulting in self-ignition or explosion [1]. This process is often called chemical aging.

The rate of spontaneous decomposition during storage the processes influencing property changes of the energetic materials during storage depends namely on:

- the external factors as geometry, storage temperature, thermal insulation and
- the intrinsic properties of the materials such as e.g. kinetic parameters of the decomposition processes, their specific heat, thermal conductivity.

In this paper the heat generation is measured for a non ground and grounded (cutted into appropriate size) propellant samples tempered during predetermined time at elevated temperatures [2]. Then, the maximum heat flow results are used to calculate the safe diameter of the

propellants, using two different equations. Then, two results are compared and estimated more accurate one.

#### 1.1. The theory of thermal explosion. Critical conditions.

The explosive regime is characterized by a rapid conversion of the initial reactant into the end products. The term “explosion” is often used alongside that of “self-ignition” due to thermal runaway reactions with serious consequences. Nikolay Semenov (sometimes Semyonov, Semionov or Semenov, Soviet physicist and chemist, awarded 1956 Nobel prize in Chemistry) was the first to mathematically analyse the heat balance equation and to lay foundation of the thermal explosion theory.

Semenov developed a model for thermal explosions, which demonstrated the principles of the thermal ignition phenomenon in a quantitative way.

Semenov diagram, in Figure 1, presents the relationship between heat and temperature, where the generated heat varies exponentially with process temperature, while the removed heat varies linearly with it.

The critical condition for thermal explosion is tangency between the heat generation curve and heat loss straight line. The rates  $q_{rel}$  and  $q_{rem}$  and their derivatives are equal in the tangency point  $T_*$ .

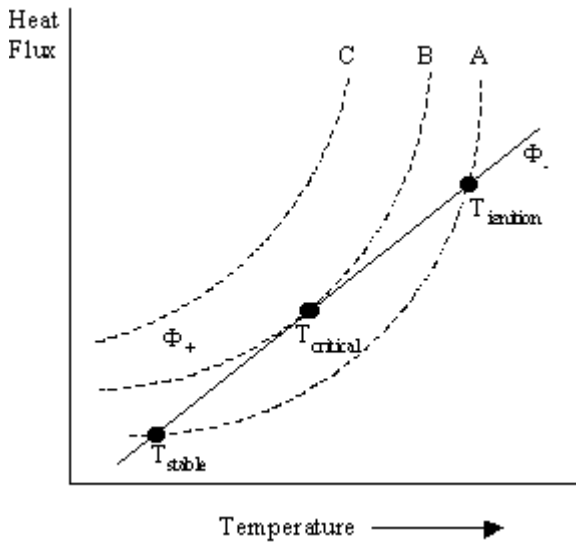


**Figure 1** - Plot of the thermal fluxes against temperature

To find this critical condition is the most important practical problem of thermal explosion theory.

Propellants has small heat conductivity coefficient due to good isolation properties, unfortunately. With the

**1.2. Safe diametar**

According to Serbian standard for assesment of chemical stability, safe diametar is criteria for chemical stability assesment revealing critical condition and possibility for selfignition. Also, safe diametar can be determined as the largest diametar of a cylindrical filled container with propellant for which selfignition is just excluded [3]. The definition is also valid for other sample geometry.

If a propellant has been stored, no self-ignition will occur as long as equilibrium exists between heat generation and heat transfer to the surroundings. Whether this equilibrium will establish or not, depends on the storage temperature, also. The other parameter that make influence is the resistance encountered by the heat flow on its way to the surroundings. This resistance depends on the heat conductivity of the propellant and the dimensions

$$D_{cr} = \sqrt{\frac{\lambda \cdot \delta_c \cdot R \cdot T^2}{E \cdot \rho_b \cdot q}} \tag{1}$$

where is:

- $\lambda$  – the heat conductivity coefficient [ Wm<sup>-1</sup>K<sup>-1</sup>],
- $\delta_c$  – constant denote critical value of thermal explosion, depends on propellant shape and for cylinder it's equal to 2,
- R – universal gas constant [kJmol<sup>-1</sup>K<sup>-1</sup>],
- E<sub>a</sub> – activation energy of reactions, depends on temperature [Jmol<sup>-1</sup>],
- $\rho_b$  – the bulk density [ kgm<sup>-3</sup>],

Table 1 Conductivity coefficients

Nº	Material	Heat conductivity coefficient [ Wm <sup>-1</sup> K <sup>-1</sup> ],
1.	diamant	1000-2600
2.	silver	406
3.	copper	385
4.	brass	109
5.	glass	0,8
6.	<b>propellant*</b>	<b>0,1</b>
7.	wood	0,04-0,12
8.	air(300 K, 100kPa)	0,026
9.	styrofoam	0,038

\*

According to Barendregt R.B.

respects to the heat gained during decomposition processes inside the propellant, it is obviously that it could be dangerous due to possible heat accumulation which can lead to critical values ( T<sub>critical</sub>) and selfignition at the end.

In Table 1 are given some examples of material conductivity coefficients.

of the propellants mass (package size). At a certain diameter the heat transfer will lag behind and the temperature will continue to rise, resulting in self-ignition.

Also the ageing of the propellant plays a role, because the heat generation depends on rections heat released and different reactons gives different heat quantities and heat summary gives appropriate safe diammeter calculated. In other words, stage of stabilizer depletion plays significant role in heat generation issue. According to Serbian standard for monitoring of chemical stability of gun powders and rocket propellants, there is mathematical dependence safe diametar of released heat and others and it looks like:

q – heat velocity coresponding to D<sub>cr</sub> and vessel with L equal to 40 mm

T – temperature for which D<sub>cr</sub> is calculated, [K].

According to Merzhanov [4] and Barendregt, formula to calculate the safe diameter, at 344 K (the worst case of ammunition storage temperature conditions), is as follows in Equation 2.

$$D_{cr} = \frac{2.7 \cdot \lambda}{2} + \sqrt{\frac{(2.7 \cdot \lambda)^2}{4} + \frac{4 \cdot RT_a^2 \cdot \delta_c \cdot \lambda \exp\left(\frac{E_a}{R} \left(\frac{1}{T_a} - \frac{1}{T_m}\right)\right)}{\rho_b \cdot E_a \cdot Q_{max}}} \quad (2)$$

where is:

$\lambda$  – the heat conductivity coefficient [ $\text{Wm}^{-1}\text{K}^{-1}$ ],

$R$  – universal gas constant [ $\text{kJmol}^{-1}\text{K}^{-1}$ ],

$\delta_c$  – constant denote critical value of thermal explosion, depends on propellant shape and for cylinder it's equal to 2,

$T_a$  - temperature for which  $D_{cr}$  is calculated, [K],

$T_m$ - teperature at which is measured heat flow, [K],

$E_a$  – activation energy of reactions, depends on temperature [ $\text{kJmol}^{-1}$ ], it is quit satisfied to take 120  $\text{Jmol}^{-1}$  for temperatures beyond 333 K, [5]

$Q_{max}$  – maximum heat flow during measurement [ $\text{Wkg}^{-1}$ ] and

$\rho_b$  – the bulk or loading density [ $\text{kgm}^{-3}$ ].

### 1.3. Equipment. Microcalorimeter.

To measure small heat effects microcalorimeters have been developed. For investigations of safe diameter, Heat Flow Calorimetry (HFC) results was used. The maximum heat flow results was obtained from experiments that was many years long performed. Tests were performed on TAM III and TAM IV device, made by TA Instruments Company.

HFC is very sensitive technique, with possibility to detect small quantities of heat, e.g. range of microwatts. With such a high sensitivity it is possible to investigate processes in early stages of decompositions.



Figure 2. Microcalorimeter TAM III

Data evaluation in HFC measurements consider:

- The data must be normalised to one gram of propellant.
- Determination of the maximum heat flow in the region between the time corresponding to a heat release of 5 J/g and the defined measuring time.
- Loading density 0,7-1,1  $\text{g/cm}^3$ ; for the porous propellants 0,4-0,6  $\text{g/cm}^3$ .

- Positive heat flow values means exothermic reactions.

## 2.EXPERIMENTAL

### 2.1.Experimental conditions

Several types of propellants were estimated from the thermally stability point of view. In this paper, there were used single and double based propellants with different formulations. Labels SB1, SB2 and SB3 identify diverse single base propellant compositions, while DB1, DB2, DB3 identify double base propellants. DB4S1, DB4S2, DB5S1, DB5S2 and LOVEX denotes samples of various types of double base propellants used for small caliber ammunition.

There are used heat flow measurements for propellants at several temperature profiles to calculate results for safe diameter. Temperatures used for thermal activity monitoring are 353, 356, 358 and 363 K.

Although, at elevated temperatures many processes are occurred in propellants, heat flow represents the heat summary of all reactions, whether exothermic or endothermic they are. So, we use final reaction heat to determine safe diameter by both equations.

It is assumed that for all elevated temperatures, reaction mechanisms are to be the same.

Activation energy of reactions is assumed like 120 kJ/mol.

Loading density,  $\rho_b$ , was calculated for every sample itself, for representativeness of the conditions.

Single base propellants were not grounded, to conduct experiments with „ammunition like“ conditions. Double base propellants were grounded, because of no possibility to test them in original shape. Double base propellants for small ammunition calibers were tested in original shape and size. Results are in tables below.

### 2.2.Results

Test results reveals slightly differences in calculated safe diameters by both equations. Safe diameter calculated by Serbian standard seems to be too harsh, regarding to fact that the biggest diameter of ammunition cartridge for SB1, SB2 and SB3 propellant is about 0,12 m and for DB1, DB2 and DB3 0,09 m. Therefore, it seems Equation 2 gives more appropriate and realistic values of safe diameter.

Also, results confirm that stage of stabilizer depletion plays significant role in heat generation issue, because during time heat flow value increases and safe

diammetar decreases. That is, the older propellant the released heat.  
greater number of exothermic reaction with lot of

**Table 2.** Experimental results for safe diametar obtained by two different equations for single base propellant samples

Propellant	Maximum Heat Flow $\mu\text{Wg}^{-1}$	Bulk Density ( $\text{kgm}^{-3}$ )	SAFE DIAMETAR (m) by Berendregt - Merzhanov	SAFE DIAMETAR (m) by Serbian standard	Testing Year	Testing Temperature (K)
SB1	67,1	0,70	0,64	0,13	2009	363
	128	0,72	0,21	0,092	2013	353
SB2	346	0,68	0,27	0,08	2012	358
	747.4	0,70	0,099	0,056	2013	353
SB3	385.3	0,71	0,35	0,077	2009	363
	350	0,71	0,17	0,081	2014	353
	374.6	0,80	0,15	0,074	2015	353

**Table 3** Experimental results for safe diametar obtained by two different equations for double base propellant samples

Propellant	Maximum Heat Flow $\mu\text{Wg}^{-1}$	Bulk Density ( $\text{kgm}^{-3}$ )	SAFE DIAMETAR (m) by Merzhanov-Berendregt	SAFE DIAMETAR (m) by Serbian standard	Testing Year	Testing Temperature (K)
DB1	205.3	0.63	0.34	0.11	2012	356
	207.2	0.74	0.31	0.10	2013	356
	453.7	0.63	0.34	0.075	2014	363
	397.9	0.66	0.36	0.079	2015	363
	114.3	0.60	0.41	0.15	2016	353
	360.7	0.80	0.34	0.075	2021	363
	141.3	0.76	0.38	0.12	2022	356
DB2	393.7	0,70	0,35	0,077	2014	363
	377,6	0,77	0,34	0,075	2015	363
	144,5	0,81	0,36	0,12	2016	356
DB3	143.3	0,71	0,64	0,13	2014	363
	35.95	0,71	0,74	0,25	2015	353
	25.76	0,96	0,73	0,28	2020	353
DB4S1	238.6	0.89	0.25	0.088	2022	356
	166.9	0.89	0.25	0.11	2022	353
DB4S2	501.7	0.88	0.25	0.088	2021	363
DB5S1	230.4	0.95	0.24	0.086	2022	356
DB5S2	539.3	0.94	0.23	0.057	2021	363
LOVEX	567.6	1.03	0.21	0.053	2021	363

### 2.3. Thermograms

In Figures 3, 4 and 5 diagrams heat flows against time is presented, for several propellants, for heat flow measurements.

It is evidentially that this samples can not meet criterion for chemical stability by STANAG 4582 but if it is used maximum heat flow information to calculate safe diameter, the prediction and evaluation of chemical stability can be slightly different. According to calculations in this paper, actually, it is possible to make conclusion as follows: propellant will remain chemically stable and safe if storage conditions are fulfilled, respectively, propellant is safe if diameter of ammunition charge - cartridge is less then calculated safe diameter.

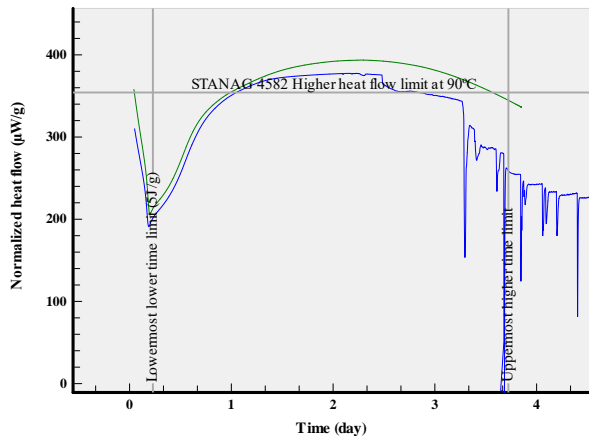


Figure 3. Heat flow against time for DB2 propellant

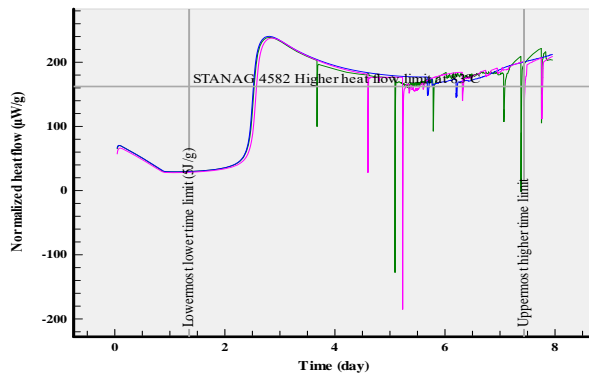


Figure 4. Heat flow against time for DB4S1 propellant

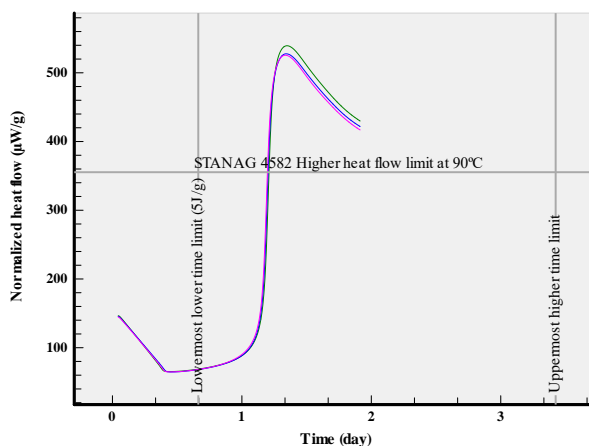


Figure 5. Heat flow against time for DB5S2 propellant

### 3. DISCUSSION

Calculated safe diameters by two different equations shows more appropriate seems to be equation of Berendregt-Merzhanov for their more realistic outcomes. When safe diameters are compared to diameter of ammunition cartridges the propellants service in, one more information about safety ammunition is easy to obtain.

It can be noticed that there is good reproducibility of results at different temperature regimes of heat flow measurements, and that confirms similarity of reaction mechanisms at different temperatures. Yet, it should avoid higher temperatures, like 363 K and carry out heat flow experiments at as lower temperatures as possible. Recommendation is to conduct experiments at 353 K.

Especially good illustration of the better mathematically interpretation of propellant stability by Berendregt-Merzhanov equation is given in Table 1. If SB kind of propellant is made for about approximately 0,12 m ammunition loading charges, for big span of years the propellant and ammunition would be on the border zone of stability criteria or even do not meet criterion at all, as showed in fifth column of the table.

For some propellants STANAG 4582 is unsuitable standard method to examine as though too strict stability criteria. Even brand new propellant can easily fail to meet criteria of stability. Calculating safe diameter is, in that case better and more comfortable choice for testing them and assess stability. Figure 3, 4 and 5 shows evidently exceeding heat flow upper limits by method mentioned. Calculated safe diameter for those samples gives the conditions in which the propellant would be safe to store and handle in, in a manner, propellant would be safe if its diameter of ammunition cartridge charge or storage vessel is not higher than those calculated. And for that purpose Equation 2 seems to be more appropriate than Equation 1.

### 4. CONCLUSION

Calculations of propellants safe diameter was made by using two different equations. Calculations were performed by using heat flow measurements conducted at elevated temperatures.

Benefits of calculating safe diameter are:

- Determination of safe diameter, described in paper is dedicated for stability testing of nitrate ester based propellants by use of Heat Flow Calorimetry method.
- Safe diameter determination contribute to chemical stability assessment of single base, double base and triple base propellants.
- It is possible to find all necessary conditions for ammunition to stay safe and chemically stable and conditions are different from one type of propellant to another.
- Using Equation 2 is more realistic than Equation 1.
- The procedure is equally applicable to propellants containing different types of stabilizers and even, for those without any.

- Beneficially method for those samples which falls the criteria of stability by STANAG 4582, with exact conditions recommended to be fulfilled.

## References

- [1] R.B.BARENDREGT: Thermal investigation of unstable substances, including different thermal analytical techniques.
- [2] STANAG 4582 (EDITION 1), EXPLOSIVES, NITROCELLULOSE BASED PROPELLANTS, STABILITY TEST PROCEDURE AND REQUIREMENTS USING HEAT FLOW CALORIMETRY, NATO, 2004
- [3] WIM P.C.de KLERK, JOS M. MUL,MARCO N.BOERS, Researchgroup, TNO Prins Laboratory: How critical the sample geometry could be in propellant research, TNO Prins Maurits Laboratory, Rijswijk, Netherlands.
- [4] A.G.MERZHANOV, V.G.ABRAMOV: Thermal explosion of explosives and propellants. A review, *Propellants and Explosives* 6, 130-148 (1981)
- [5] ULDIS TICMANIS,STEPHAN WILKER, GABRIELE PANTEL, MANFRED KAISER, PIERRE GUILLAUME, CORRINE BALES, NIELS VAN DER MEER, Working group: Principles of a STANAG for estimation of the chemical stability of propellants by heat flow calorimetry, 31<sup>st</sup> ICT Symposium.



## INFLUENCE OF GUNPOWDERS AND ROCKET PROPELLANTS SAMPLE PREPARATION ON TEST RESULTS

JELENA ŠULTANS

Tehnickal Overhaul Facility, Kragujevac, [lab@trzk.rs](mailto:lab@trzk.rs)

SLAVIŠA STOJILJKOVIĆ

Tehnickal Overhaul Facility, Kragujevac, [trzk@trzk.rs](mailto:trzk@trzk.rs)

VESNA PETROVIĆ

Tehnickal Overhaul Facility, Kragujevac, [lab@trzk.rs](mailto:lab@trzk.rs)

**Abstract:** Research, presented in this paper, deals with the influence of the different ways of preparation of gunpowders and rocket propellants, in terms of different granulations, on the results of microcalorimetric and chromatographic tests of the chemical stability of gunpowder. The samples were examined in their original form, where possible, as well as prepared in a way that requires certain defense standards of the Republic of Serbia and in this way their requirements regarding the preparation of the sample were also reviewed. The conclusion for the optimization of sample preparation for microcalorimetric testing are especially important, which reduces free oxygen to the smallest possible amount, which has a positive effect on the accuracy of sample test results. For comparison of results, methods based on thermal activity monitoring and changes in the chemical composition of samples were used.

**Keywords:** gunpowders and rocket propellants, chemical stability, preparation of samples

### 1. INTRODUCTION

Energetic materials such as propellants, pyrotechnics and explosives till nowadays are investigated from different points of view. The results are essential to safe production storage and handling. Nitrocellulose (NC) is main component of smokeless gunpowder and propellants. The spontaneous chemical degradation of nitrocellulose takes place over time, producing nitrogen oxides and excess of heat which causes its further autocatalytic degradation leading to critical conditions for possible self-ignition of propellant. To prevent autocatalysis and minimize degradation effects, components known as stabilizers are added to propellants composition. Diphenylamine (DPA) is one of those components usually used as a stabilizer. Besides diphenylamine, there are several substances that can be added to gun propellants composition like 1,3-diethyl-1,3-diphenylurea (centralite I) and 1,3-dimethyl-1,3-diphenylurea (centralite II). The consecutive nitration and nitrosation products of DPA, are formed over time [1] and some of them also have stabilizing effect.

Important information about behavior of energetic materials can be acquired by thermal methods and high-performance liquid chromatography.

Chemical stability is strongly influenced by storage conditions. After temperature, the most important atmospheric conditions for the stability of propellants is humidity. The measured heat flow increased with increasing relative humidity. In the past many studies were performed, to investigated the influence of oxygen, humidity etc. Less attention is paid to two other important aspects, namely the sample geometry and filling degree

during the microcalorimetric test and high-performance liquid chromatography (HPLC). The fact that the decomposition of nitrocellulose is influenced by the amount of oxygen, the best way to investigate the stability of gun propellants is to measure it "ammunition like". This means a combination of the propellant grains and the filling degree of the vessel.

Serveillance of nitrocellulose based propellants is performed without paying much attention to the enviromental conditions of the stored propellants, except for the storage temperature. Effect of the other major aspect like relative humidity (RH), amount of oxygen and the particle size are quite often discussed in the literature, but not adopted for test procedures [2].

The RH will vary with location and time. The relative humidity may change from day to day in coastal areas or from season to season, making incorporation in a standard test procedure complicated. During decomposition of propellants, NO<sub>x</sub> is released which reacts with water to nitric acid. Nitric acid accelerates decomposition reaction of NC propellants. In a serveillance procedure a sample preconditioning is not yet performed as a standard.

The effects of the oxygen content as well as the effects of grounding (cutting into appropriate size) to propellants stability will be discussed in this paper.

The methods used in this work, Heat Flow Calorimetry (HFC), High Performance Liquid Chromatography and Karl Fischer method. Test methods have been conducted on ten samples, single based (SB), single based with dinitrotoluene (DNT) and double based (DB) propellants.



## 2. EXPERIMENTAL

In this paper experiments with different preparation, in way of different particle size has been conducted. Also, for testing oxygen influence on degradation process, propellants were grounded.

For some propellants moisture was determined using Karl – Fischer titration method.

For purposes of influence sample size and oxygen on test results, Heat Flow Calorimetry was used.

Karl Fisher titration is a method in analytical chemistry that determines trace amounts of water in a sample using volumetric or coulometric titration. Table 1 shows the moisture content of propellant samples.

**Table 1.** Moisture content in the tested samples

Sample name	Humidity (%)
SB1DNT	0,97
Ballistite	0,70
SB2	1,34
SB8	0,75
SB9	1,03

### 2.1. HFC test

Microcalorimetry can yield information about the stability of propellants and high explosives because the heat flow is a measure of the decomposition rate – function of decomposition rate. It is powerful tool for assessment stability problems.

All experiments are carried out according to procedure of STANAG 4582 at 90°C using Heat Flow Calorimeter, TAM IV TA Instruments [3].

**Table 2.** Experimental data and results obtained in microcalorimetry tests

Sample name	Loading density (gcm <sup>-3</sup> )	Max Heat Flow (μWg <sup>-1</sup> )	Length of original propellant grain (mm)	Diameter of original propellant (mm)
SB1DNT grounded	0.81	55.7	7.00±1.00	1.05±0.15
SB1DNT original	0.69	73.8		
SB2 grounded	0.84	133.6	3.35±0.15	1.95±0.10
SB2 original	0.90	148.4		
SB3 grounded	0.88	135.4	4.35±0.15	4.60±0.30
SB3 original	0.85	126.5		
SB4DNT grounded	0.71	60.2	11.00±1.00	3.40±0.20
SB4DNT original	0.86	40.4		
SB5DNT grounded	0.74	134.2	9.00±1.00	5.60±0.35
SB5DNT original	0.76	136.8		
SB6 grounded	0.70	61.5	12.05±0.55	2.00±0.10
SB6 original	0.56	51.6		
SB7 grounded	0.94	50.5	4.00±0.10	3.35±0.10
SB7 original	0.90	55.2		
SB8 grounded	0.83	58.5	4.20±0.20	3.35±0.10
SB8 original	0.92	41.5		
SB9 grounded	0.84	73.9	3.10±0.40	2.32±0.10
SB9 original	0.92	72.0		
Ballistite grounded	0.76	74.1	5.00±0.05	0.52±0.04
Ballistite original	0.77	73.7		

Note: Max Heat Flow Calorimetry-test at 90°C is 350μWg<sup>-1</sup>



**Picture 1.** Microcalorimeter TAM IV

Heat flow calorimetric method for establishing chemical stability of single base, double base and triple base (TB) propellants for a minimum of 10 years when stored at 25°C or to an equivalent degree.

Model of TAM IV presented on Picture 1, contains 24 channel-minicalorimeters that are managed like four multicalorimeters consists of six minicalorimeters.

There were used samples of propellants prepared in two ways:

1. Original size
2. Cutted into appropriate size and took fraction as near as possible between 1-2 mm.

Loading density was calculated for each propellant itself and it is showed in Table 2. usually it is between 0.8-1.1 gcm<sup>-3</sup>.

— grounded sample    — grounded sample    — original sample    — original sample

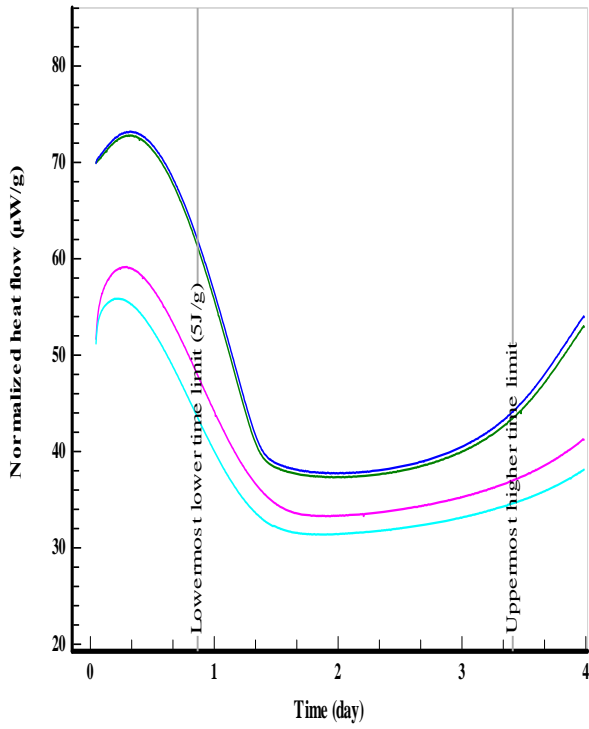


Figure 1. Heat flow against time for SB4DNT

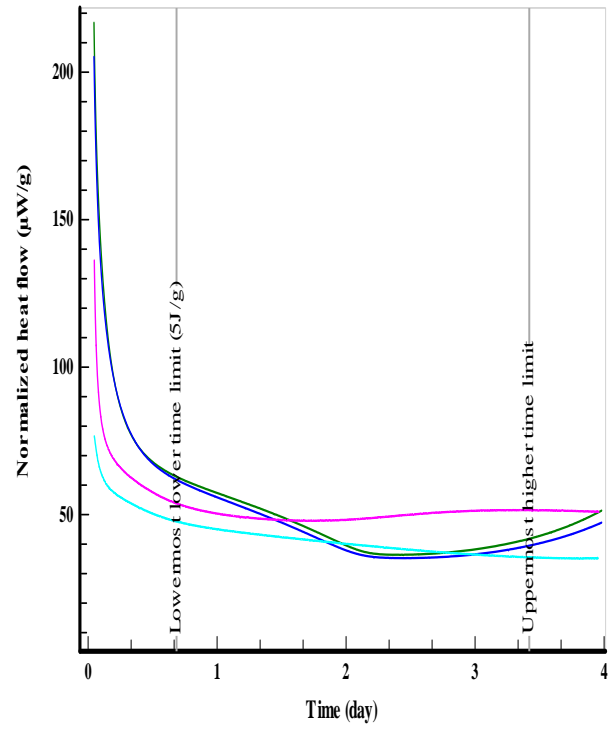


Figure 2. Heat flow against time for SB6

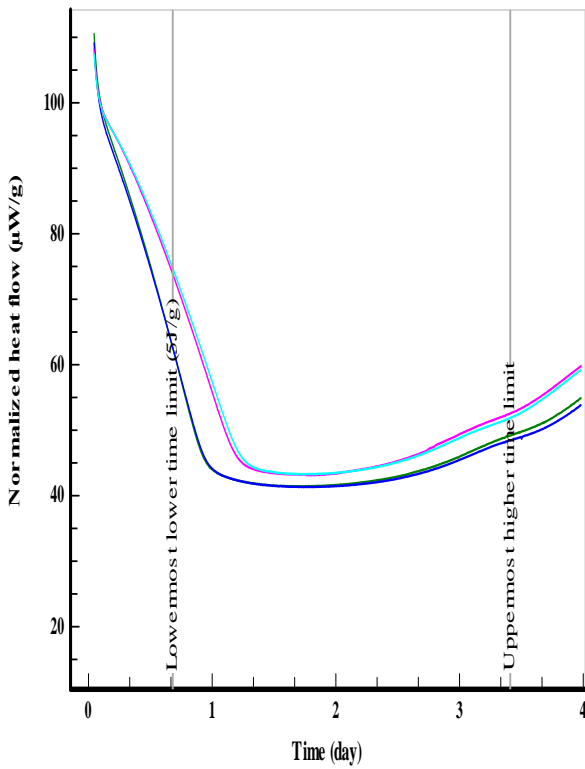


Figure 3. Heat flow against time for SB1DNT

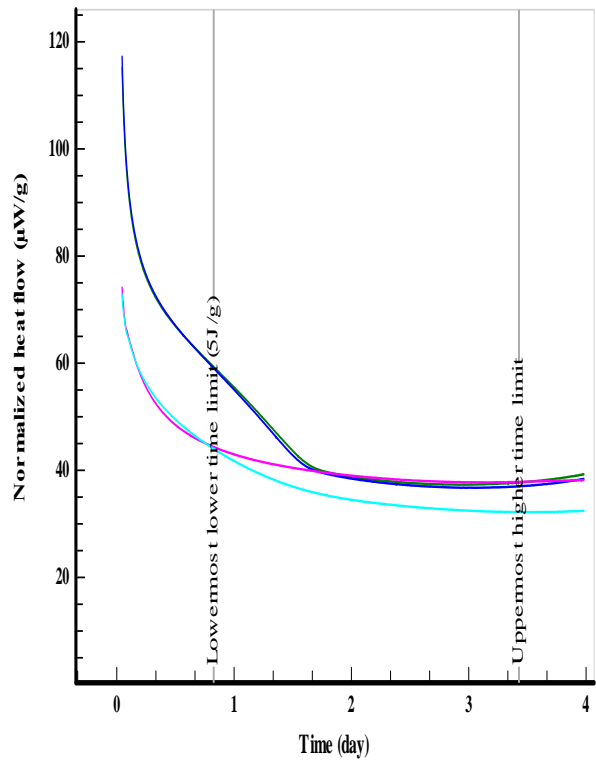


Figure 4. Heat flow against time for SB8

— grounded sample — grounded sample — original sample — original sample

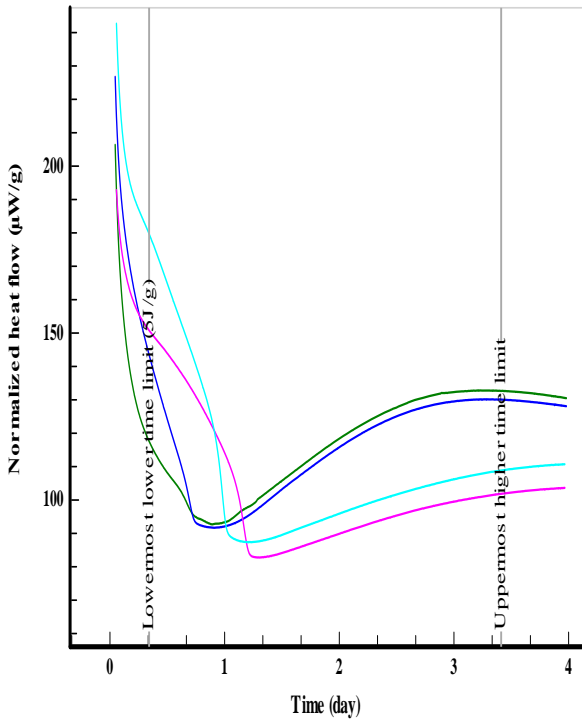


Figure 5. Heat flow against time for SB5DNT

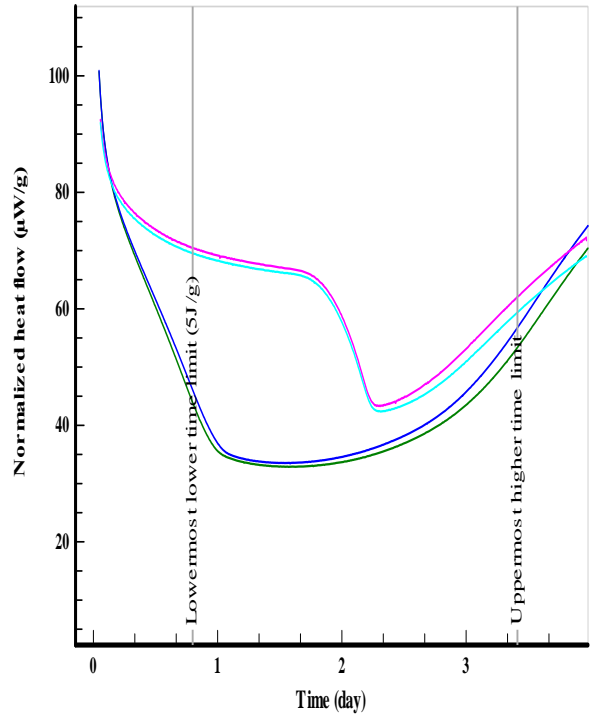


Figure 6. Heat flow against time for SB7

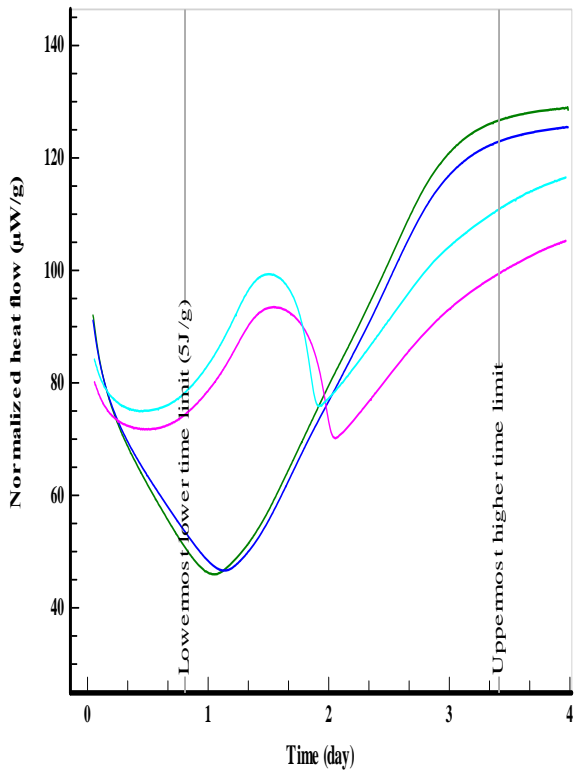


Figure 7. Heat flow against time for SB3

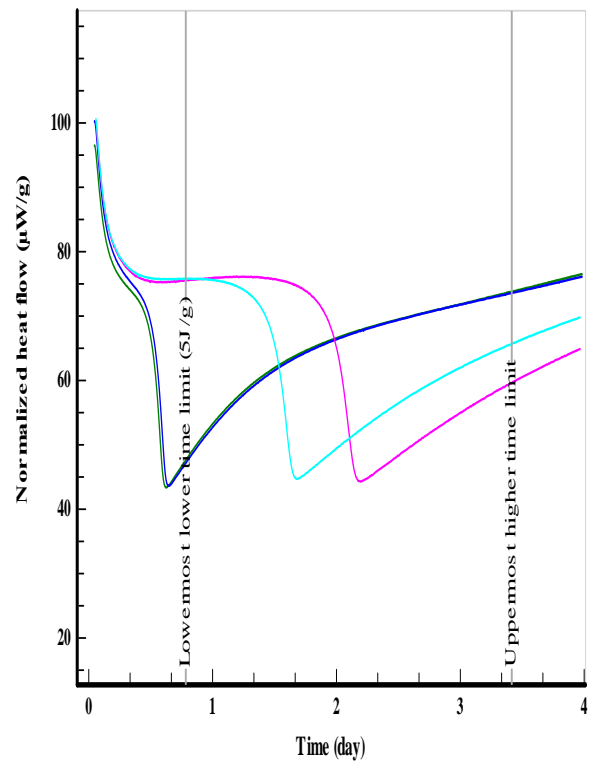


Figure 8. Heat flow against time for ballistite

## 2.2. Liquid chromatography tests

It has been used liquid chromatography for stabilizer content. Equipment was the Waters Alliance System 2695 with 2996 PDA detector.

High-performance liquid chromatography is analytical chemistry technique used to separate compounds in a chemical mixture. These separations utilize the pressure-driven flow of a mobile phase through a column packed with a stationary phase.

Propellant in original size or cutting in appropriate size were extracted in methylene chloride in a volumetric flask of 50 ml for 48 hours.

Sieves with 2 mm and 1 mm pore size and nylon membrane and syringe filters pores 0.20  $\mu\text{m}$  were used. C18 column 150\*4.6 mm with particle size of 3  $\mu\text{m}$  were used and column temperature 35°C and flow rate 1,2  $\text{mlmin}^{-1}$  were conducted in a method. Eluent is mixture of solvents acetonitrile and water in appropriate ratio.

**Table 3.** HPLC results for gun propellants of different granulation

Sample name	4 nitro DPA	N-NO-DPA	DPA	2 nitro DPA	C1
SB1DNT grounded	0.03	0.17	1.07	0.08	
SB1DNT original	0.03	0.17	1.05	0.09	
SB2 grounded	0.04	0.19	0.94	0.06	
SB2 original	0.03	0.18	0.93	0.06	
SB3 grounded	0.03	0.40	0.56	0.05	
SB3 original	0.03	0.38	0.55	0.05	
SB4DNT grounded	0.02	0.07	1.20	0.06	
SB4DNT original	0.02	0.07	1.20	0.06	
SB5DNT grounded	0.05	0.32	0.39	0.09	
SB5DNT original	0.07	0.33	0.38	0.10	
SB6 grounded	0.03	0.15	1.23	0.05	
SB6 original	0.03	0.15	1.20	0.05	
SB7 grounded	0.03	0.21	0.76	0.05	
SB7 original	0.03	0.21	0.76	0.05	
SB8 grounded	0.09	0.34	1.38	0.09	
SB8 original	0.05	0.17	0.81	0.05	
SB9 grounded	0.17	0.33	0.30	0.17	
SB9 original	0.16	0.28	0.28	0.16	
Ballistite grounded					1.48
Ballistite original					1.48

*Note: The results represents mean value of tree probes for each propellant sample.*

## 3. DISCUSSION

Table 2 shows the results of the HFC test, the samples were cutted in the appropriate size and in their original form. The loading density is shown, which is calculated from the volume of the appropriate vessel for the HFC test and the mass of propellant, grounded or original. Results shows impact of propellant sample preparation to heat flow results.

### 3.1. Influence of particle size

The Figure 1,2,3 and 4 show the influence of particle size. Besides experiments with original propellant grains also experiments were carried out with ground sample of varying particle size. There were investigated single base propellants, single base with dinitrotoluene and ballistite propellants. During the experimental program in Figure 1,2,3,4 it was observed that from the propellants the heat generation was relatively high during the first days of the experiment. The initial heat effect of original propellant is lower than that of grounded propellants. An explanation for the resulting effects is that due the grounding operation more oxygen reacts with the surface of the

propellants parts than with original propellant grains. It can be observed on Figure 1, single base propellant with DNT, with the loading density higher at original propellant has heat flow results lower and therefore it should be analysed in its original form. Figure 2 describes propellant with a long length, where the loading density is better when grounded, but the heat flow is greater due to the influence of oxygen, because of the opening of the grain itself. Figure 3 describes gunpowder with a small surface area, and during the preparation of gunpowder, oxygen does not have a large effect.

### 3.2. Influence of oxygen

Parameter that influence the chemical stability is oxygen. The presence of excess of oxygen is reported to increase the heat production of the propellant as NO can be oxidized to NO<sub>2</sub> which catalysis the decomposition of the propellant [4]. Indirectly the filling degree of the test vessel determines the amount of free oxygen. In case of a complete filled sample vessel, the amount of oxygen, available for the oxidation reaction is less, in correlation with amount of reaction surfaces. This will lead to decreased value of heat flow. In Figure 5,6,7,8 are shown

single base propellants, single base propellants with DNT and ballistite propellant. It can be observed the results of the HFC test, where the heat flow of grounded propellant with half-filled container was measured. The presence of free oxygen affects the course of reactions mechanism during the experiments.

In Table 3 is showed the HPLC results for gun propellants of different granulation. There is no difference in the stabilizer content except for propellant SB8 (foreign production propellant) which, probably has a sort of membrane around a grain that does not allow the stabilizer to be extracted by the solvent.

#### 4. CONCLUSION

In this paper it has been made conclusion, as follows:

- Whenever it is possible to obtain correct loading density of propellants in a testing vessel, either HFC or HPLC testing takes place, no preparation or grinding of samples should be carried out.
- The amount of available oxygen influence the reaction rate and as a results, the heat generation. Therefore, it is advisable to carry out the HFC tests as the propellant grains are originaly stored, so "ammunition like", if loading density is satisfied, meaning as high as possible to obtain

0.8 gcm<sup>-3</sup> at least.

#### References

- [1] E.o'N.ESPINOZA AND J.I.THORNTON, Characterization of smokeless gunpowders by means of diphenylamine stabilizer and its nitrated derivates, *Analytica Chimica Acta*, 288(1994) 57-69.
- [2] WIM P.C.de KLERK, JOS M. MUL, MARCO N.BOERS, Reasearchgroup, TNO Prins Laboratory: How critical the sample geometry could be in propellant research, TNO Prins Maurits Laboratory, Rijswijk, Netherlands. R.B.BARENDREGT: Thermal investigation of unstable substances, including different thermal analytical techniques.
- [3] STANAG 4582 (EDITION 1) EXPLOSIVES, NITROCELLULOSE BASED PROPELLANTS, STABILITY TEST PROCEDURE AND REQUIREMENTS HFC, NATO, Military Agency for Standardization, Brussels, 2004.
- [4] E. CAMERA, G. MODENA, B. ZOTTI, Propellants, Explosives, Pyrotechnics, 8, 70, 1983.



## DEVELOPMENT OF LINER FOR CASE-BONDED GRAIN WITH END-BURNING CONFIGURATION

TIHOMIR KOVAČEVIĆ

Military Technical Institute, Belgrade, [tkovacevic@tmf.bg.ac.rs](mailto:tkovacevic@tmf.bg.ac.rs)

SLAVKO MIJATOV

Military Technical Institute, Belgrade, [slavko.mijatov@yahoo.com](mailto:slavko.mijatov@yahoo.com)

ALEN CRNALIĆ

Military Technical Institute, Belgrade, [alen.crnalic@student.ni.ac.rs](mailto:alen.crnalic@student.ni.ac.rs)

JELENA GRŽETIĆ

Military Technical Institute, Belgrade, [jrusmirovic@tmf.bg.ac.rs](mailto:jrusmirovic@tmf.bg.ac.rs)

DARKO KUPREŠAK

Technical Test Center, Belgrade, [darkokvb7@gmail.com](mailto:darkokvb7@gmail.com)

SAŠA BRZIĆ

Military Technical Institute, Belgrade, [sasabrzc@gmail.com](mailto:sasabrzc@gmail.com)

**Abstract:** This paper deals with the potential to manufacture case-bonded propellant grain with the end-burning configuration. The end-burning configuration is not quite suitable for case-bonded architecture due to problems related to structural integrity. One approach to address this issue is to insert a liner between thermal insulation layer and the composite propellant, which absorbs stress generated during curing process and exploitation conditions. The prepared liner is a highly elastomeric material, based on hydroxyl-terminated polybutadiene (HTPB) and castor oil (CO). The amount of curing agent, isophorone diisocyanate (IPDI), is higher to establish a covalent bonding and thus good adhesion between the liner and the propellant/thermal insulation. CO provides more anchoring sites since it has higher functionality of HTPB and, in other hand, isotropy of the liner making it more able to withstand and reduce accumulated stress within the propellant grain. The molar ratio between prepolymer (HTPB and CO) and IPDI was varied and cured material was subjected to an uniaxial tensile test and examination of adhesion with propellant using a peel test.

**Keywords:** burning profile, adhesion, mechanical properties, grain configuration, OH:NCO ratio.

### 1. INTRODUCTION

Solid propellant grains appear in the two varieties: free-standing or cartridge-loaded and case-bonded. Case-bonded grain meets the requirements of long ranges and high payload-carrying capacity making it a favorable choice for spatial applications [1,2]. The case-bonded grain consists of a metallic motor case, a rubbery thermal insulator, an elastomeric liner and propellant as the energetic component which gives thrust upon burning. All of the mentioned sub-systems need to be securely fastened to avoid problems when the rocket motor starts. Even when the all integral parts of solid propellant grain appear to be tightly bonded to each other, separation and develop of uncontrolled burning surface may occur after ignition, especially during flight. This phenomenon is a consequence of the forces of acceleration and rotation which surpass established bonding strength between the integral parts within the propellant grain [3]. In addition,

the grain configuration has a great impact on the bond strength (adhesion), particularly between the thermal insulator or motor case and the propellant due to problems related to large differences in coefficients of linear thermal expansion. Polyurethane-based propellant is prone to dimensional changes due to external temperature and curing conditions, which create stress within the propellant and cause separation. An example of such a design is an end-burning configuration which is not entirely suitable for case-bonded architecture, particularly when the propellant grain is subjected to extremely low temperature (-40 °C). The main approach to deal with this issue is to insert a liner between thermal insulation and the composite propellant, which absorbs stress generated during the curing process and the exploitation conditions [4].

In most cases, propellant and thermal insulation are incompatible with each other and inserting a liner between them overcomes this issue, ensuring their good attachment. The liner is placed on the surface of the

thermal insulator surface and pre-cured prior to propellant casting, afterwards complete solidification of the prepared system is applied. During the solidification period, the liner is completely cured, establishing good adhesion with the propellant [1]. It is important to accomplish good bonding between the critical surfaces: motor case - thermal insulation, thermal insulation - liner and liner - propellant. Bond failure at the interfaces of integral parts within the propellant grain can form an increased burning surface resulting in improper ballistic properties or motor case cracking.

There are several mechanisms involved in the adhesion process where some of them act together and some of them are mutually exclusive [5]. Mechanisms include physical and chemical interactions (or combination) that are reflected in the following phenomena: adsorption, chemical linkage, electrostatic force attraction, interdiffusion and so on. The latter is most significant in a polymer/polymer system, such as the liner/propellant interface.

The major issue regarding good adhesion between the propellant and the liner or thermal insulation originates from the dissimilar materials used to prepare these two components of the case-bonded grain. This primary refers to thermal insulation obtained from rubbery-like materials such as ethylene propylene diene monomer (EPDM) or polybutadiene acrylonitrile (PBAN) [2]. Hereupon, the composition of the liner should be compatible with the polymer matrix of the propellant, which ensures good interaction between them, *i.e.* strong adhesion.

Since conventional composite propellants contain hydroxyl terminated polybutadiene (HTPB) as the polymer matrix, there are myriad studies which consider use of this material for liner preparation [6–9]. Liner as well as propellant contain a plasticizer which makes them easy to process and adjust the required mechanical properties. Conversely, the plasticizer can easily migrate and accumulate at the propellant/liner interface and affect the adhesion between them, resulting in debonding [10]. In addition, the plasticizer softens the propellant, leading the cohesive failure near the interface liner/propellant when good adhesion is established between them [4]. One of the approaches to address this issue is employing the reactive plasticizer that participates in the creation of polymer network, *i.e.* it is anchored to the main polymer backbone and cannot migrate [10].

In this study, several liner samples are prepared using HTPB as a polymer matrix and castor oil (CO) as a reactive plasticizer. CO, in addition to softening the propellant, has a multiple role as follows: it takes part in the curing reaction by including itself in the polymer network, acts as a chain extender and a cross-linking agent. The reference sample is prepared using a deficient amount of the curing agent, isophorone diisocyanate (IPDI), which produces a hydroxyl terminated product. Other samples possess an excess of IPDI giving the isocyanate terminated material capable to establish a covalent bonds with the propellant (NCO:OH ratio within the propellant is less than 1).

## 2. EXPERIMENTAL SECTION

### 2.1. Materials

HTPB, R-45M (USA, viscosity at 30 °C: 5500 mPa·s, OH value: 44-51 mg KOH·g<sup>-1</sup>, hydroxyl functionality: 2.4, average molecular weight, Mn: 2900 g·mol<sup>-1</sup>, glass transition temperature, T<sub>g</sub>: 80 °C) was used as a binder while Castor oil (CO-Interhem Ltd, Republic of Serbia, hydroxyl functionality: 3.0, Mn: 933 g·mol<sup>-1</sup>) was used as a reactive plasticizer. Curing agent, isophorone diisocyanate (IPDI) and antioxidant (2,2'-bis(4-methyl-6-tertbutyl) phenol (AO 2246) were supplied from Acros Organics, Belgium and Sigma Aldrich, Germany, respectively. Catalysts, ferric acetyl acetonate (FeAA)<sub>3</sub> was procured from Merck, Germany.

### 2.2. Sample preparation

The homogenization of liner compositions was performed using laboratory mixer (LR 1000 B S099, Ika, Germany) at a temperature of 30 °C in two-step procedure. Firstly, the premix excluding catalyst and curing agent was prepared by mixing HTPB, CO and AO22 for 1 hour under the reduced pressure (vacuum). After that, catalyst and curing agent were added in the obtained mixture and homogenization was carried on for 5 min under atmospheric pressure and 10 min under the vacuum. The obtained slurry was poured into two standard polytetrafluoroethylene (PTFE) molds and cured in the oven for the next 2 h (first mold) and 24 h (second mold) at 60 °C. In addition, liquid liner was applied on propellant surface and cured for 24 h at 60 °C to obtain sample for peeling test, *i.e.* determination of adhesion. Composition of the prepared liners is shown in Table 1.

**Table 1.** Composition of prepared liners in [%]

No.	HTPB	CO	AO22	(FeAA) <sub>3</sub>	IPDI	NCO/OH
L1	72.89	18.22	1.09	0.0255	7.760	0.59
L2	70.92	17.73	1.06	0.0248	10.26	0.80
L3	68.29	17.07	1.02	0.0239	13.59	1.10
L4	67.87	16.97	1.02	0.0238	14.12	1.15
L5	67.46	16.86	1.01	0.0236	14.64	1.20
L6	66.64	16.66	1.00	0.0233	15.67	1.30
L7	65.85	16.46	0.99	0.0230	16.68	1.40
L8	65.07	16.27	0.98	0.0228	17.66	1.50

L1 and L2 has NCO:OH ratio less than 1, *i.e.* these liners are hydroxyl terminated, while L3 – L8 are isocyanate terminated. The first group forms hydrogen bonding with the same terminated polymer matrix within the propellant. Second group is designed to enforce interaction between liner and propellant, *i.e.* to achieve good adhesion. Adhesion and mechanical properties of the prepared liners are determined using peeling and uniaxial tensile tests.

### 2.3. Characterization methods

The viscosity of the liquid liners was measured at the 60 °C by HBT type Brookfield viscometer with a T-C spindle at a rotation speed of 5 rpm.

The mechanical properties of the cured liner samples at

+20 °C were determined employing an Instron 1122 uniaxial tensile test machine. Dimension of the samples was as follows: initial length: 46.5 mm, width: 6 mm and thickness: 4.0 mm). The crosshead speed of the uniaxial tensile test machine jaws was 50 mm·min<sup>-1</sup>. Three samples were tested for each liner composition and the average value was calculated.

The specimen for determining the adhesive strength were obtained from samples of propellants and liners. The equipment for performing the peel test is shown in Figure 1.



Figure 1. Equipment for peel test

### 3. RESULTS AND DISCUSSION

#### 3.1. Viscosity measurements

It is important to obtain a fast-curing liner since the ultimate goal is to apply it to the inner surface of the cylindrical motor case. It is essential that the liner is quickly converted into a relatively solid form to avoid dripping and flowing (to achieve gel time). To achieve such curing kinetics, a catalyst is introduced composition of the liner, while amount of curing agent is varied. Table 2 shows the viscosity values for the prepared liner compositions.

Table 2. Viscosity of the tested liners

Sample	$\eta$ (Pa·s)					
	15	30	45	60	75	90

L1	19.2	56.0	176.0	664.0	cured	
L2	9.6	136.0	cured			
L3	16.0	78.4	160.0	cured		
L4	28.8	217.6	cured			
L5	22.4	401.6	cured			
L6	22.4	75.2	1600	cured		
L7	14.4	32.0	41.6	54.4	118.4	600.0
L8	40.0	46.4	41.6	52.2	73.6	94.4

L2 exhibits a higher reactivity compared to composition L1 due to greater presence of curing agent. The main disadvantage of L2 is the short pot life, which disables easy manipulation and application. L1 has an optimal pot life making it suitable for casting and distributing on the inner wall of the motor case. L4 and L5 liners behave similarly to the L2 regarding the pot life. The limit value for the NCO:OH ratio is 1.4 (L7) above which the amount of curing agent is too high, making the final product pasty and sticky (L8).

Most of the samples exhibit low a initial viscosity which increases rapidly. A slower curing rate is obtained when the amount of curing agent is too low (L1) whereas a significant number of macromolecule chains originating from HTPB and CO remain unbound. Another case is when the amount of curing agent is too high (L4 and L5) where remained IPDI makes particular liner too stretchy. Analysis of viscosity shows that the most prominent liner compositions are L1 and L7.

#### 3.2. Mechanical properties

The tensile characteristics of the analyzed liners, expressed as tensile strength ( $\sigma_t$ ), strain at maximum load ( $\epsilon_m$ ), strain at break ( $\epsilon_b$ ) as well as Young's modulus ( $E$ ), at +20 °C are shown in Table 3. The mechanical characteristics of the polymeric materials directly depend on the density of chemical bonds, *i.e.* on the content of hard segments of the resulting polymer network, which can be increased by adding diols/triols (CO), thus providing more sites for cross-linking [11]. CO provides more anchoring sites since it has higher functionality of HTPB and, in other hand, isotropy of the liner making it more able to withstand and reduce accumulated stress within the propellant grain.

Table 3. Average values of tensile properties of corresponding liners

No.	$\sigma_t$ /MPa	$\epsilon_m$ /%	$\epsilon_b$ /%	$E$ /MPa
L2	0.64	114.5	114.7	0.98
L3	0.57	130.0	130.1	0.73
L4	0.58	81.4	81.5	1.10
L5	0.99	75.4	75.5	1.92
L6	1.02	98.4	98.5	1.74
L7	0.29	247.2	247.6	2.47

Tensile test results for liner L1 is not shown because it has an elongation of more than 1000% and is beyond the measuring range of a uniaxial tensile test machine. In contrast, L2 is quite stiff compared to L1 and does not possess sufficient strain at maximum load to be a good candidate for liner application. L1 is deposited on the inner wall of the motor case and after that the propellant is cast, but separation occurs when the resulting grain is subjected to a temperature of -40 °C. That is the reason to



prepare an isocyanate terminated liner that can form a covalent bond with the polymer matrix from the propellant (L1 exhibits hydrogen bond interactions instead of covalent). The energy of the C-O covalent bond (allophanate linkage) is  $351 \text{ kJ}\cdot\text{mol}^{-1}$  compared to hydrogen bonds whose strength is  $18.8 - 31.8 \text{ kJ}\cdot\text{mol}^{-1}$  (O-H $\cdots$ O bond).

All liners behave as a highly cross-linked elastomeric material since there is no area of plastic deformation, which is reflected in a very close value of strain at maximum load and strain at break. Isocyanate terminated liners (L3 - L6) are very rigid materials, especially those containing a higher amount of IPDI. These characteristics exclude them as candidate for liner application where the strain at maximum load has to be at least 200%. The situation changes drastically when NCO:OH ratio is 1.4 (L7). Mentioned composition has sufficient elasticity to be applied as a liner in the case-bonded propellant grain. The analyzed liners have an effective polymer network where total amount of macromolecule chains are bound without the rest of the loose segments. The reason for the results obtained in the case of L7 may be the insertion of an increased amount of polar and relatively small IPDI molecules between non-polar polymer chains, which reduces their mutual interactions, *i.e.* the threshold for such a drastic change is reached. Results for the liner L8 are not shown because it is not completely cured and therefore not tested.

### 3.3. Peel test

The peel test is performed to quantify the adhesion strength between the prepared liners and the composite propellant. It is important to note that obtained results do not give a realistic picture of the bonding strength, which is a consequence of the nature of the resulting liners. Namely, most liners are stiff and tear during the test, *i.e.* adhesion between the liner and the propellant is much higher than the cohesion of the liner itself (Figure 2).



**Figure 2.** Collapse of the liner during the peel test

Each isocyanate terminated liner splits near the interface liner/propellant except L7 which breaks in a similar manner to the tensile test. The recorded value of the adhesion strength until breaking is  $5.55 \text{ N}\cdot\text{cm}^{-1}$  for L7 liner. Others has lower values, but the samples are stiffer and break easily, while, on the other hand, they are firmly attached to the propellant. Even L1 liner, which is hydroxyl terminated, exhibits good adhesion with the propellant, but the bond strength is not recorded due to great elasticity of such material which absorbs the stress generated during the test. These results are consistent with those obtained for tensile properties, where most of the analyzed liners break relatively quickly.

## 4. CONCLUSION

This research is performed to find a way to prepare a case-bonded propellant grain with the end-burning configuration. Such a motor has to contain thermal insulation, liner and propellant. The essential aspect to be fulfilled is to achieve good adhesion between the mentioned sub-systems. First attempt is focused on obtaining a highly elastic material capable to overcome the physical and chemical differences between those layers, *i.e.* receiving the generated stress and relaxing entire system. Consistency with this, a hydroxyl terminated liner with a loose polymer network (L1), which enables great flexibility, is prepared and analyzed. Since the L1 liner has great elasticity, it is applied to the inner wall of the motor case and after that propellant is cast, but separation occurs when the resulting grain is subjected to a temperature of -40 °C. This is the reason for the change of course toward preparation of isocyanate terminated liners. To achieve the given goal, several liner compositions are homogenized, cured and analyzed using viscosity, tensile and peel tests. All of the resulting liners are castable but solidify too fast, except composition L7.

Prepared liners are very tough materials, especially those containing a higher amount of IPDI. These characteristics exclude them as candidate for liner application where the strain at maximum load has to be at least 200%. The only one which is suitable for liner application is composition L7, since it has a strain of 247% at maximum load.

The peel test shows that all analyzed liners have good adhesion with the propellant, but break easily during the test. Again, L7 exhibits the best behavior, which, combined with viscosity values and tensile properties, makes it the best candidate for liner application in case-bonded propellant grain.

## Acknowledgement

The authors thank to the Ministry of Education, Science and Technological Development of Republic of Serbia for the support of the research through Contract No. 451-03-68/2024-14/200325.

## References

- [1] DE MORAIS AMF, HOLANDA S, PINTO J. Optimization of bondline's properties of solid rocket motors. *Inst. Fraunhofer Technol. Química*, 2006.
- [2] NAVALE SB, SRIRAMAN S, WANI VS, MANOHAR M V., KAKADE SD. Effect of Additives on Liner Properties of Case-bonded Composite Propellants. *Def Sci J* 2004;54:353–9. doi:10.14429/dsj.54.2049.
- [3] Byrd JD, Field L. Method of case bonding propellant. US 4,337,218, 1982.
- [4] RODIĆ V. Case Bonded System for Composite Solid Propellants. *Sci Tech Rev* 2007;LVII:11–21.
- [5] GRYPHE KF, HANSEN FK, OLSEN T. Adhesion in solid propellant rocket motors. *J Adhes* 2007;83:223–54. doi:10.1080/00218460701239059.
- [6] QUAGLIANO AMADO JC, ROSS PG, MATTOS SILVA MURAKAMI L, NARCISO DUTRA JC. Properties of Hydroxyl Terminal Polybutadiene (HTPB) and Its Use as a Liner and Binder for Composite Propellants: A Review of Recent Advances. *Propellants, Explos Pyrotech* 2022;47:e202100283. doi:10.1002/prep.202100283.
- [7] ZHOU Q-C, XU J-S, CHEN X, ZHOU C-S. Review of the Adhesively Bonded Interface in a Solid Rocket Motor. *J Adhes* 2016;92:402–28. doi:10.1080/00218464.2015.1040155.
- [8] ROSS P, ESCOBAR G, SEVILLA G, QUAGLIANO J. Micro and nanocomposites of polybutadienebased polyurethane liners with mineral fillers and nanoclay: thermal and mechanical properties. *Open Chem* 2017;15:46–52. doi:10.1515/chem-2017-0006.
- [9] LI H, WEI J, ZHANG Y, HU Y, JIANG W, ZHANG T. GO/HTPB composite liner for anti-migration of small molecules. *Def Technol* 2023;22:156–65. doi:10.1016/j.dt.2021.11.006.
- [10] KOVAČEVIĆ T, MIJATOV S, GRŽETIĆ J, CAKIĆ S, FIDANOVSKI B, BRZIĆ S. The effect of reactive plasticizer on viscoelastic and mechanical properties of solid rocket propellants based on different types of HTPB resin. *Def Technol* 2024;33:66–77. doi:10.1016/j.dt.2023.11.020.
- [11] BRZIC S, RODIC V, DIMIC M, SIMIC D, JELISAVAC L, BOGOSAVLJEVIC M. Influence of 1,4-butanediol on hydroxyl-terminated poly(butadiene) based composite propellant binder characteristics. *Sci Tech Rev* 2015;65:55–60. doi:10.5937/STR1503055B.



## BLAST PERFORMANCE OF ISOPROPYL NITRATE - BASED THERMOBARIC EXPLOSIVES VS. CAST-CURED PBX

DANICA M. BAJIĆ

Military Technical Institute, Belgrade, [danica.bajic@mod.gov.rs](mailto:danica.bajic@mod.gov.rs)

SLAVICA TERZIĆ

Military Technical Institute, Belgrade, [slavica@algodesk.com](mailto:slavica@algodesk.com)

MLADEN TIMOTIJEVIĆ

Military Technical Institute, Belgrade, [mladen.timotijevic@gmail.com](mailto:mladen.timotijevic@gmail.com)

RADOSLAV SIROVATKA

Military Technical Institute, Belgrade, [radesir@gmail.com](mailto:radesir@gmail.com)

DRAGAN KNEŽEVIĆ

Military Technical Institute, Belgrade, [dragankn@gmail.com](mailto:dragankn@gmail.com)

IGOR BLAGOJEVIĆ

Factory of explosives and pyrotechnics – TRAYAL Corporation, Kruševac,

MAJA RADMANOVAC

Factory of explosives and pyrotechnics – TRAYAL Corporation, Kruševac

**Abstract:** Thermobaric explosives are currently among most studied energetic formulations, due to their extraordinary combination of blast and thermal effects. They may be in the form of liquid explosive mixtures, often denoted as fuel-air explosives (FAE) or solid explosive charges, as solid fuel-air explosives (SFAE) or thermobaric explosives (TBE, TBX). This study compares the blast effect of selected formulations of the two types of thermobarics in field test. As FAE, compositions were prepared based on gelled isopropyl nitrate with metal particles as fuel component, and as TBE a multi-component polymer bonded explosive (PBX) was prepared, based on octogene, aluminium powder, ammonium perchlorate and a polymer binder. The selected explosive formulations were prepared as cylindrical charges of 5 kg and activated with electric detonator at 2 m height in open field test. The characteristics of the blast wave in air (maximum overpressure, duration of the positive phase of the pressure and impulse) were measured at different distances from the activation spot, using piezoelectric gauges. Also, the thermal effect of the explosions was observed with infra red imaging technique.

**Keywords:** thermobaric explosives, isopropyl nitrate, cast-cured PBX, blast performance, explosion.

### 1. INTRODUCTION

Thermobaric explosives represent a class of energetic materials highly regarded for their unique ability to produce devastating blast and thermal effects. They are distinguished by their formulation, which can either be in liquid form, such as fuel-air explosives (FAE), or in solid form, known as solid fuel-air explosives (SFAE) or simply as thermobaric explosives (TBE or TBX) [1-6]. These explosives harness a combination of fuel and oxidizer components that, when detonated, undergo rapid combustion in the surrounding atmosphere.

In the context of this study, researchers focused on comparing the blast effects of two specific types of thermobaric explosives through field tests. For the FAE

type, the compositions were developed using gelled isopropyl nitrate with added metal particles as the fuel component. On the other hand, the TBE variant consisted of a complex multi-component polymer bonded explosive (PBX) comprising octogene (HMX), aluminum powder, ammonium perchlorate, and a polymer binder [5, 7-10].

Isopropyl Nitrate (IPN) is a liquid fuel component commonly used in fuel-air explosive (FAE) formulations. FAEs are known for their ability to disperse a cloud of fuel in the air, which upon detonation creates a highly energetic blast and thermal effect. The basic principle involves the rapid vaporization and subsequent combustion of the dispersed fuel in the presence of atmospheric oxygen. IPN is a volatile liquid with a relatively low boiling point, which facilitates its rapid vaporization upon detonation. FAE formulations typically include additives such as metal particles or fine aluminum

or magnesium powder to enhance the combustion efficiency and increase the blast yield [8, 11]. Initiation is usually achieved via an electric detonator, triggering a rapid combustion process that propagates through the dispersed cloud of fuel. IPN-based FAEs are known for generating high-intensity blast waves characterized by significant overpressure and impulse. The blast wave's duration and spatial distribution of pressure are critical parameters measured to assess its effectiveness. In addition to the blast, IPN-based explosives produce intense thermal radiation due to the combustion of the fuel-air mixture, which can cause secondary damage and fires in surrounding structures.

Cast-Cured thermobaric PBX are often made of central core of high brisance and surrounding thermobaric charge of annular shape, or they can be monolithic charges. Explosive core typically includes high-energy materials like octogene (HMX) or other energetic compounds, often blended with aluminum powder for enhanced energy release. Polymer binder serves to bind the explosive particles together, providing structural integrity and allowing for casting into various shapes. The PBX mixture undergoes a curing process where the polymer binder solidifies around the explosive particles, forming a homogeneous composite. Cast-cured PBX explosives are designed to produce controlled and predictable blast effects, characterized by a well-defined shock front and relatively stable pressure profile. The energy release is efficient and tailored to specific applications. The polymer matrix enhances the mechanical properties of the explosive, making it suitable for shaped charges and other specialized configurations. PBX explosives are favored for their ability to be shaped and molded into various forms, allowing customization based on operational requirements [5].

IPN-based FAEs tend to have higher energy yields per unit mass due to the rapid vaporization and combustion of the liquid fuel, leading to more extensive blast effects over a larger area. Cast-cured PBX explosives offer greater precision and control over the blast wave characteristics, making them suitable for applications where a specific blast profile or shaped charge effect is required. The choice between IPN-based FAEs and cast-cured PBX depends on factors such as operational environment, target specificity, and desired blast effects (e.g., shockwave intensity, thermal impact). While IPN-based FAEs excel in generating widespread and intense blast effects through rapid fuel combustion, cast-cured PBX explosives offer enhanced precision and tailored blast profiles suitable for specialized applications. Understanding these differences allows for informed decision-making in selecting the appropriate explosive type based on operational requirements and tactical objectives.

## 2. EXPERIMENTAL PART – MATERIALS AND METHODS

### 2.1. Experimental charges preparation

The experimental setup involved preparing cylindrical explosive charges weighing 5 kg each, in thin plastic casings 150 mm in diameter. IPN-based charges were prepared by adding metal powder while intense steering using a propeller mixer. Gelation agent, fumed silica, was added to obtain the consistency of gel. Aluminium and Magnesium powders were used, with spherical particles. These experimental charges had a cylindrical central explosive core made of pressed explosive FH-5 (RDX/montan wax=95/5, Ø25 mm, 62.5 g in total). Regarding the TBE PBX, it was a solid charge of a multi-component composition HMX/AP/Al/HTPB, produced by casting technology, without central explosive core [5, 10].

### 2.2. Blast performance testing

The prepared experimental charges were detonated at a height of 2 meters in an open field environment. The detonation was initiated using an electric detonator. To assess the blast wave characteristics, air shock-wave parameters were measured at different distances from the detonation point using piezoelectric gauges – pencil probes PCB, including the maximum overpressure generated by the blast wave, the duration of the positive phase of the pressure wave, and the impulse generated by the explosion. In addition to blast effects, the study also investigated the thermal impact of the explosions using infrared imaging technique: IR camera FLIR SC7200 was applied in measuring range 1500-2500 °C, with 50 mm objective, emissivity 0.95 and recording frequency 1466 Hz. This aspect of the research aimed to capture and analyze the thermal signature produced by each detonation, and to compare the heat released depending on thermobaric composition. IR camera was placed at a safe distance of 50 m from the sample. High speed camera Phantom V2112 was used to observe the appearance of the thermobaric fireballs after the activation of the charges.

## 3. RESULTS AND DISCUSSION

### 3.1. Parameters of the shock wave in air

Blast parameters at different distances from the activation spot of the examined thermobaric charges, read from the registered pressure-time dependence diagrams,  $\Delta p = f(t)$ , are given in Tables 1-3.

**Table 1.** Maximum overpressure  $P_{\max}$ 

Composition	$P_{\max}$ [bar] at distance from explosive charge [m]				
	3 m	4 m	5 m	7 m	9 m
IPN	1.206	0.624	0.389	0.211	0.138
IPN/Al	3.520	1.697	1.104	0.516	0.438
IPN/Mg	3.064	1.718	1.134	0.571	0.461
TBE PBX	3.011	1.841	2.005	0.659	0.383

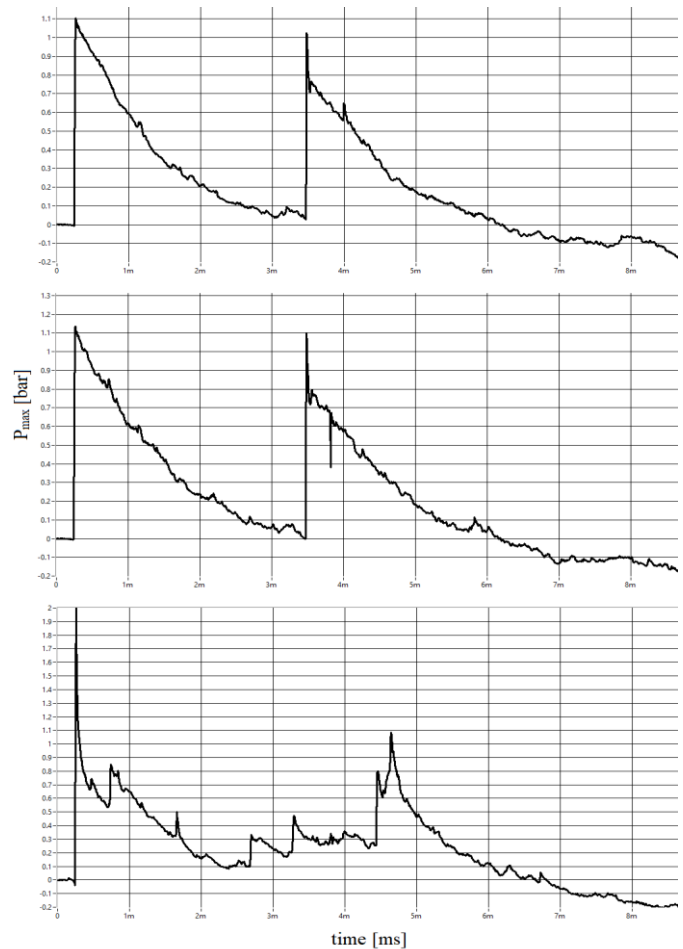
**Table 2.** Pressure impulse  $I_p \times 10^{-4}$ , [mbar·s]

Composition	Pressure impulse $I_p \times 10^{-4}$ , [mbar·s] at distance [m]				
	3 m	4 m	5 m	7 m	9 m
IPN	9.761	7.394	6.884	4.076	3.858
IPN/Al	19.148	16.173	19.468	13.433	12.949
IPN/Mg	19.670	16.875	20.453	14.229	13.841
TBE PBX	21.550	19.356	22.079	13.818	13.66

**Table 3.** Duration of the overpressure positive phase, t

Composition	Positive phase duration, t [ms] at distance [m]				
	3 m	4 m	5 m	7 m	9 m
IPN	1.725	2.155	2.585	5.195	4.965
IPN/Al	1.670	2.230	5.915	5.700	6.125
IPN/Mg	2.235	2.175	3.205	5.865	6.590
TBE PBX	1.915	2.715	6.405	7.40	8.770

The diagrams  $\Delta p = f(t)$  that were registered are similar – after a sharp peak at the beginning, the maximum overpressure decreases and then suddenly sharply rises due to the appearance of the reflected shock wave. As illustrative example,  $\Delta p = f(t)$  diagrams for the samples IPN/Al, IPN/Mg and TBE PBX are shown in Figure 1. Reflected shock waves for the sample of TBE PBX were registered somewhat later compared to IPN based charges. Thermobaric charge TBE PBX has the highest values of the overpressure at distances 4-7 m from the activation spot, as well as the longest durations of the positive phase of the pressure. This composition also has the highest impulse at distances 3-5 m. Composition with Mg has higher impulses at 7-9 m, as well as positive phase duration.

**Figure 1.** Diagrams  $\Delta p = f(t)$  for charges IPN/Al, IPN/Mg and TBE PBX (top to bottom)

### 3.2. Infrared imaging results

The obtained recordings from the IR camera were transformed into temperature-time diagrams providing an insight into the average values of the maximum recorded temperatures in the explosion surrounding and given in Figure 2, for the samples: IPN, IPN/Al, IPN/Mg.

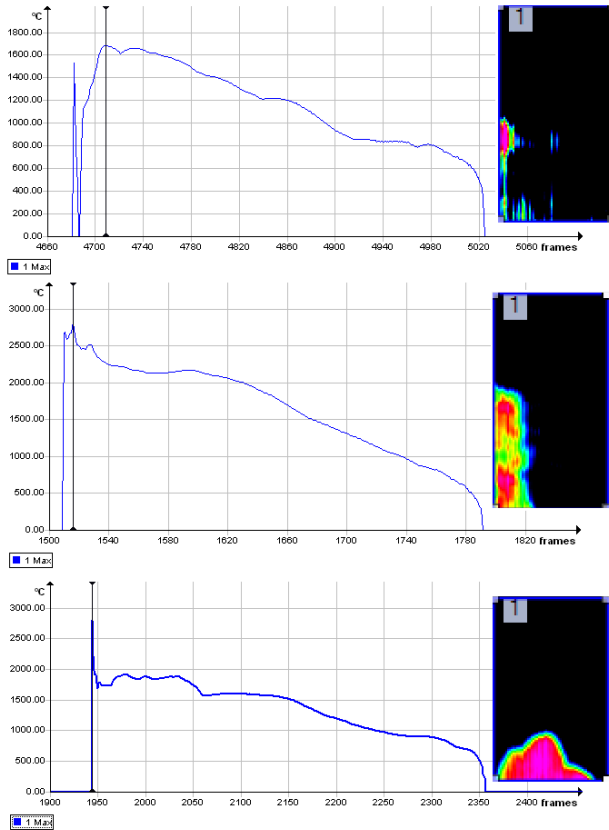


**Figure 4.** Temperature-time diagrams of the registered maximum temperatures with IR camera

The maximum registered temperatures are given in Table



**Figure 5.** Thermobaric fireball: TBE PBX (left) and IPN/Al (right)

Different shape of the fireballs is a consequence of the sample positioning, vertically, i.e. along the wooden

4. If we observe the curves and compare the time of holding the temperatures above some selected threshold, for example above 500 °C, it can be seen that among the three samples, the one containing Mg had the longest time of post-explosion combustion, or longest duration of the fireball. For the sample TBE PBX the IR recording was unsuccessful, due to operating error. However, earlier IR recordings for this type of TBE compositions have revealed that the registered temperature maximums reach up to 3460 °C, and that the approximate temperatures of post-detonation combustion are in range of 1800-2000 °C [5, 10].

**Table 4.** Thermal performance of FAE and TBE obtained by IR technique

Composition	Maximum registered temperature, °C	Post-explosion combustion temperature > 500°C duration, s
IPN	1687	2.589
IPN/Al	2822	2.086
IPN/Mg	2794	3.039

It is evident that spherical particles of fuel provide higher registered temperatures of the combustion compared to neat IPN. This is a consequence of different ease of ignition of the applied metal particles in air [8], as aluminium particles combust faster and releasing more heat rapidly, i.e. this composition had higher registered temperatures, while Mg provides longer duration of the fire-ball due to its slower burning.

The size of the thermobaric fireball was approximately the same for both types of the explosives, IPN based and TBE PBX, as can be seen in recordings made using a high speed camera, Figure 5.

stand. However, the width and height of the fireballs are similar in both cases.

#### 4. CONCLUSION

Large-scale field tests were performed on thermobaric explosive charges in order to compare gelled IPN-based compositions with TBE PBX. The experimental tests demonstrated that there is a significant difference in the performance of the prepared mixtures with Al and Mg regarding the blast and thermal output. The IPN-based compositions containing Al and Mg have significantly higher blast parameters and thermal output compared to non-metalized IPN, but TBE PBX have the highest blast parameters from 4 to 7 meters from the activation spot. These measurements provided crucial insights into the spatial distribution and intensity of the blast effects, which are essential for understanding the potential destructive capability of thermobaric explosives. Overall, the comparative study of FAE and TBE formulations not only contributes to advancing scientific knowledge in explosives research but also serves practical purposes in military and industrial applications. By elucidating the blast and thermal characteristics of these powerful explosives, researchers can better optimize their design and deployment strategies for various operational scenarios.

#### Acknowledgement

This work was supported by the Ministry of science, technological development and innovations (Serbia), Contract No. 451-03-66/2024-03/200325, and University of Defense, Military Academy, Proj. No. VA-TT/1/22-24.

#### References

- [1] Xing X.L., Zhao S.X., Wang Z.Y., Ge G.T. Discussions on thermobaric explosives (TBXs), *Propellants Explos. Pyrotech.*, 39 (1), 2014, pp. 14-17.
- [2] L. Türker, Thermobaric and enhanced blast explosives (TBX and EBX), *Defense Technology*, vol. 12(6), 2016, pp. 423-445.
- [3] Trzciński W.A., Maiz L., Thermobaric and Enhanced Blast Explosives – Properties and Testing Methods (Review), *Propellants Explos. Pyrotech.*, 2015, 40(4), 632-644.
- [4] Maiz L., Trzciński W.A., Szala M., Preparation and Testing of Thermobaric Composites, *New Trends Res. Energ. Mater., Proc. Semin.*, 18th, Pardubice, Czech Republic, 2015, 705-715.
- [5] D. Simić, Cast thermobaric PBX explosives- in Serbian (Liveni termobarični PBX eksplozivi), *Scientific technical information - monography series*, vol. 53(2), 2016. Military Technical Institute, Belgrade, ISSN 1820-3418.
- [6] D. Khavronichev, Weapons for the future- volumetric explosion bomb, <https://en.topwar.ru/2945-oruzhie-budushhego-bomby-obemnogo-vzryva.html>
- [7] D. Simić, R. Sirovatka, U. Andjelić, J. Bogdanov, S. Terzić: Thermobaric effect comparison of cast PBX and TNT in enclosure test, 19th Seminar on New Trends in Research of Energetic Materials NTREM 2016, Pardubice, Czech Republic, 20-22. april 2016, *Proceedings* p.947-953.
- [8] N. H. Yen, L. Y. Wang: Reactive Metals in Explosives, 37, 2012. *Propellants Explos. Pyrotech.*, pp. 143–155.
- [9] M. Krstović, D. Bajić, B. Fidanovski, M. Timotijević, S. Terzić, D. Knežević, Application of calorimetry to estimate the thermal performance of thermobaric explosives, 25th Seminar on New Trends in Research of Energetic Materials NTREM 2023, Pardubice, Czech Republic, 19-21. april 2023, *Proceedings*.
- [10] Simić, D., Andjelić, U., Knežević, D., Savić, K., Draganić, V., Sirovatka, R., Tomić, L. (2016) Thermobaric Effects of Cast Composite Explosives of Different Charge Masses and Dimensions. *Central European Journal of Energetic Materials*, 13(1): 161-182.
- [11] O. G. Iorga, T. V. Tigănescu, M. Sućeska, T. Rotariu, A. Marin, M. Munteanu, T. Zecheru, R. E. Ginghină, A method for estimation of blast performance of RDX-IPN-Al annular thermobaric charges, *Propellants Explos. Pyrotech.*, 46(7), 2021, pp. 1121-1135..



## UNSTEADY INTERNAL BALLISTIC CALCULATION OF ATYPICAL PROCESSES IN ROCKET MOTOR

SAŠA ŽIVKOVIĆ

Military technical institute, Belgrade, [sasavite@yahoo.com](mailto:sasavite@yahoo.com)

SAŠA ANTONOVIĆ

Military technical institute, Belgrade, [sale.antonovic82@gmail.com](mailto:sale.antonovic82@gmail.com)

MILOŠ FILIPOVIĆ

Military technical institute, Belgrade, [milos.filipovic.50@gmail.com](mailto:milos.filipovic.50@gmail.com)

MIRKO KARIĆ

Military technical institute, Belgrade, [karicmirko@gmail.com](mailto:karicmirko@gmail.com)

MARKO KARIĆ

Military technical institute, Belgrade, [karicmarko83@gmail.com](mailto:karicmarko83@gmail.com)

**Abstract:** In the case of an gyro-stabilized artillery rocket projectile, several atypical processes occur during the operation of a rocket motor with a free-standing propellant charge. A high rotation rate is required for the gyroscopic stabilization of the projectile, and consequently the elements of the rocket motor are exposed to significant centrifugal acceleration. Two effects arise as a consequence of rotation. The first effect is that the high centrifugal load in some cases leads to breakage of the propellant charge, and also to deviation from the predicted change of the burning area of the propellant charge. The second effect is the influence of centrifugal acceleration on the combustion process, and the increase in the burning rate of the propellant. Last effect which is considered is the nozzle erosion, which leads to a change in pressure in the combustion chamber. A non-stationary calculation of the pressure change in the combustion chamber was applied, which can successfully model the UB processes in the RM, which was adapted to successfully include the mentioned atypical processes.

**Keywords:** rocket motor; solid propellant, thrust, internal-ballistic calculation, burning area.

### 1. INTRODUCTION

The internal-ballistic (IB) calculation of a solid propellant rocket motor (RM) is reduced to the calculation of the effects of the combustion of the propellant charge in the combustion chamber [1]. The initial parameters that are taken into account are the characteristics of the propellant, materials and construction of the rocket motor itself [2]. In most cases, rocket motors have an approximately stationary or quasi-stationary mode of operation, operating time from a few tenths of a second to several minutes. Transient processes are only present at the beginning and at the end of motor operation [3]. In these cases, calculations with average values (stationary UB calculation) are traditionally applied. Quasi-stationary calculations [3] are also often used.

The importance of IB calculation is highlighted in the stages of designing a rocket motor, but it is also very important in the procedures of overhaul and other modifications of existing RM [4]. Quality IB calculation is also of great importance when identification of unexpected phenomena in RM, observed in experimental work, is required. The most common requirements for the design of missile systems is to predict the mass-functional

characteristics of the RM as accurately as possible, because these values are needed to determine the behaviour of the missile. These characteristics are RM total mass, mass of inert elements RM, thrust, operating pressure, dimensions, ignition time, etc [5].

The input data required for the calculation are the physico-chemical characteristics of the propellant, the geometrical characteristics of the rocket motor, the change of the burning area of the propellant grain  $Ab(x)$  (burn-back analyses), the function of the combustion rate change (the combustion law, e.g. in the form of Saint-Robert's law) [3]:

$$r = b \cdot p_o^n \quad (1)$$

The simplest form of IB RM calculation implies that the combustion surface and motor geometry are constant in time. The IB calculation [6] is reduced to analytical expressions that calculate the mean value of the operating pressure in the chamber, thrust, mass flow and motor operating time.

$$p_o = \left( \frac{\rho_p \cdot A_b \cdot b \cdot c_*}{A_t} \right)^{\frac{1}{1-n}} \quad (2)$$



The RM ignition and shutdown processes are considered separately, also mostly in analytical terms [3].

A somewhat more complex procedure is the quasi-stationary calculation in cases where there is a multi-phase (staged) or continuously variable operating mode [3]. The quasi-stationary procedure implies a time-discretized successive calculation, which gives time-dependent results, which accuracy depends on the time resolution. With this procedure, it is possible to predict the change in the operating regime of the RM mostly with satisfactory accuracy.

In certain cases, some atypical processes may occur in the RM, which complicate the IB calculation. Effects that are generally not covered by a typical IB calculation are:

- The function of burning rate is most often represented by Saint-Robert's law, which generally gives satisfactory accuracy. Using experimental methods, it is possible to determine the exact burning rate - pressure function, which can significantly deviate from this law (plateau and mesa effects);
- Spin-stabilized rocket projectiles are not frequently used in rocket technology, however there are a certain number of cases. In those conditions, the effect of centrifugal acceleration on the burning rate occurs, which complicates the IB calculation.
- In some cases, centrifugal or axial high intensity inertial force of can lead to the propellant fracture, changing the burning area, which additionally changes UB processes in RM;
- Erosion of the nozzle occurs due to insufficient thermal resistance, it also leads to the complex IB process, which complicates the calculation;
- The burning rate can be changed by erosive combustion, due to the occurrence of increased mass flux of the propellant products and heat transfer on the surface of the propellant charge;
- In the case of short work time or impulse RM, transient process becomes more influential in RM operation, because the duration of those processes and the working period are of the same order of magnitude.

All these processes are much more difficult to describe with the mentioned stationary or quasi-stationary UB calculations, so for their modeling the application of unsteady UB calculations is necessary.

## 2. UNSTEADY INTERNAL BALLISTIC CALCULATION

The basis of the unsteady IB calculation is the determination of the total pressure change in the combustion chamber, which can be calculated from the equation of continuity (Figure 1) [7].

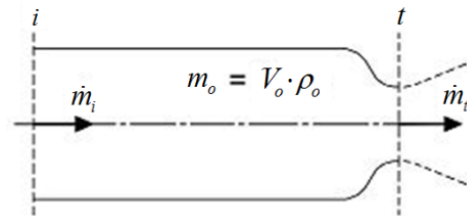


**Figure 1.** Mass balance of combustion products in the combustion chamber.

In transient flow of the propellant combustion products through the empty space of the rocket motor, the continuity equation has the following form:

$$\dot{m}_t(t) = \frac{d}{dt} m_o(t) + \dot{m}_i(t) \quad (3)$$

The mass flow rate of combustion products at the entrance of the calculation domain is determined by the amount of burned propellant per time:

$$\dot{m}_i(t) = A_b(t) \cdot r(t) \cdot \rho_p \quad (4)$$

The change in the mass of combustion products in the RM chamber free volume is:

$$\frac{d}{dt} m_o(t) = \frac{d}{dt} (V_o(t) \cdot \rho_o(t)) = V_o(t) \cdot \frac{d}{dt} \rho_o(t) + \rho_o(t) \cdot \frac{d}{dt} V_o(t) \quad (5)$$

Using the equation of state of an ideal gas:

$$\rho_o(t) = \frac{p_o(t)}{R \cdot T_o} \quad (6)$$

and the following relations:

$$\frac{d}{dt} V_o(t) = A_b(t) \cdot \frac{dx}{dt} = A_b(t) \cdot r(t) \quad (7)$$

$$V_o(t) = V_o(0) + \int_0^t A_b(t) \cdot r(t) dt$$

expression (5) takes the following form:

$$\dot{m}_o(t) = \frac{A_b(t) \cdot r(t) \cdot p_o(t)}{R \cdot T_o} + \frac{V_o(t)}{R \cdot T_o} \cdot \frac{d}{dt} p_o(t) \quad (8)$$

The mass flow rate of combustion products through the nozzle throat is:

$$\dot{m}_t(t) = \rho_t(t) \cdot A_t \cdot v_t \quad (9)$$

Based on gas dynamics relations for one-dimensional flows, it is possible to express critical values of flow parameters from eq. 8 as a function of total values (which these parameters have in the combustion chamber). These relations are valid for an ideal gas (single-phase and chemically inert), when the flow is isentropic, inviscid and one-dimensional. The mass flow rate through the nozzle throat takes the following form:

$$\dot{m}_t(t) = A_t \cdot \sqrt{\frac{\kappa}{R \cdot T_o} \cdot \left( \frac{2}{\kappa + 1} \right)^{\frac{\kappa+1}{\kappa-1}} \cdot p_o(t)} \quad (10)$$

When expressions 4 – 10 are combined with equation 3, it becomes a first-order differential equation, where combustion chamber total pressure is the dependent and time is the independent variable:

$$\frac{d}{dt} p_o(t) = \frac{R \cdot T_o \cdot A_b(t) \cdot r(t) \cdot \rho_p}{V_o(t)} - A_t \cdot \sqrt{\kappa \cdot R \cdot T_o} \cdot \left( \frac{2}{\kappa + 1} \right)^{\frac{\kappa + 1}{\kappa - 1}} \cdot p_o(t) - \frac{A_b(t) \cdot r(t) \cdot p_o(t)}{V_o(t)} \quad (11)$$

In this equation, the functions  $A_b(t)$ ,  $V_o(t)$  and  $r(t)$  are not explicitly defined, and they must be determined indirectly. The function  $A_b(x)$  is known, which is obtained by burn back analyses. In order to translate it into the time domain, the next substitution is used:

$$A_b[x(t)] = A_b \left[ \int_0^t r(t) dt \right] \quad (12)$$

Time change of the free volume of the RM can be calculated based on the change of the burning area:

$$V_o[x(t)] = V_o(0) + \int_0^x A_b[x(t)] dt \quad (13)$$

Similarly, the burning rate function  $r(p_o)$  is known, which, due to the dependence of pressure on time, also becomes time-dependent:

$$r(t) = r[p_o(t)] \quad (14)$$

The thrust coefficient can be determined theoretically [1] or experimentally [2]:

$$C_F = \frac{F_{real}}{p_o \cdot A_t} \quad (15)$$

And finally the thrust of a rocket motor as a function of time can be determined based on the following equation:

$$F(t) = C_F \cdot A_t \cdot p_o(t) \quad (16)$$

### 3. GYRO-STABILIZED ROCKET CHARACTERISTICS

The Plamen-D is 128 mm caliber rocket designated as spin stabilized artillery projectile; it is an old design and a mass-produced piece of ordnance. During its production, old technologies were used which resulted in low production costs, average material quality, but high construction reliability. The result of this concept is a cheap, reliable rocket with average performance. The construction of the rocket and the basic components of the rocket motor are given in figure 1.

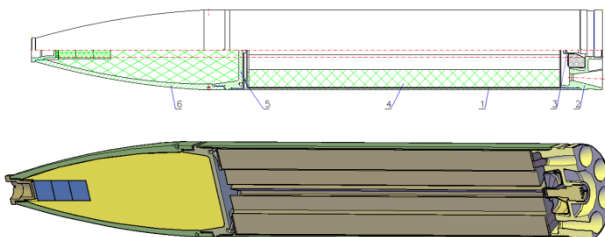


**Figure 2.** Cross-section of the PLAMEN-D rocket.

1 - Case, 2- Multi-nozzle block, 3 - Igniter,  
4 - Free standing grain, 5 - Forward closure, 6 - Warhead.

RM is with a free propellant charge of double base propellant. A star configuration is applied, inhibited on the outside and on both bases, which gives an approximately neutral motor operating regime. To ensure reliable RM assembly manufacturing tolerances resulting in gap between the grain and the chamber of about 0.5 mm.

The nozzle block of RM is made of steel and is realized in the form of a closure with eight nozzles. The nozzles are turned in the tangential direction in relation to the rocket axis, ensuring the circumferential component of the thrust force, i.e. the rotational moment. Thanks to this feature, the rocket achieves a high spin level, around  $27.000 \text{ min}^{-1}$ , i.e. gyroscopic stabilization.

The mentioned characteristics of RM cause the following atypical processes, which modeling is the subject of this work:

- erosion of the nozzle and change in the operation regime of the RM;
- fracture of the propellant grain due to centrifugal force;
- increase in burning rate due to the effect of centrifugal acceleration.

### 4. NOZZLE EROSION INFLUENCE ON ROCKET MOTOR OPERATION

The application of a steel nozzle block with multiple beveled nozzles is a practical and economical solution. On the other hand, the performance of this type of nozzle is relatively low, and erosion of the critical section also occurs, because the steel does not have sufficient thermal resistance to the RM combustion products. The operating time of the RM is relatively short, about one second, so a massive nozzle block can successfully perform the function, at the cost of moderate erosion.

RM nozzle erosion is not necessarily a negative phenomenon. Increase of the nozzle throat resulting the pressure decreasing, but thrust can remain constant or even increase. If the erosion is moderate, the nozzle can be designed so that the specific impulse and the thrust coefficient remain approximately constant. However, in most cases, this phenomenon is not reproducible, so there is a greater dispersion of the parameters of the RM operation, which can affect the accuracy of the rocket projectile. This is especially important with projectiles with a nozzle block. If there is a larger difference in the erosion of individual nozzles, an increase in the non-axiality of thrust will occur.

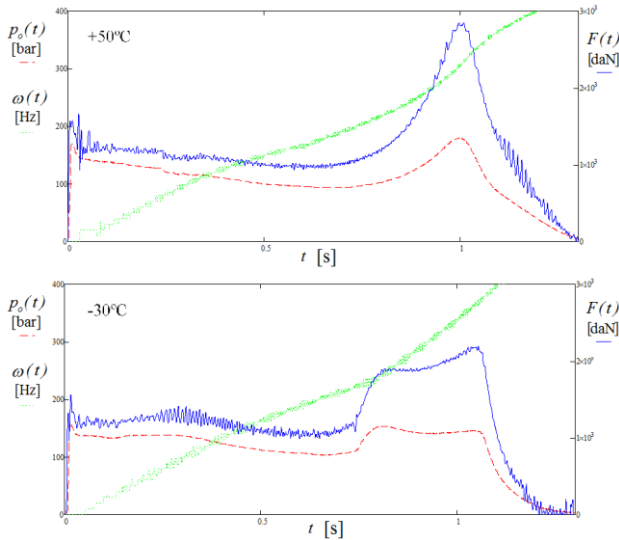


**Figure 3.** Pressure, thrust and spin - time curves at extreme temperatures of +50°C and -30°C.

The process of erosion is very complex, but it can be simulated in a relatively simply by empirical function of time. Typical results of pressure, thrust and spin - time curves measured at extreme temperatures -30°C and +50°C are shown in Figure 3.

The initial value of the diameter of the nozzle throat  $d_t^0$  is known before the RM firing, and also the initial value of the critical section area  $A_t^0$ .

If the motor operating regime is approximately neutral and there is no nozzle erosion, the thrust coefficient will be approximately constant. The thrust coefficient can be determined at the beginning of the motor operation when throat erosion is low.

$$C_F = \frac{F(0)}{p_o(0) \cdot A_t^0} \quad (17)$$

Based on this value, the critical section - time function, i.e. the average value for all nozzles of the throat diameter - time function can be calculated:

$$A_t(t) = \frac{F(t)}{p_o(t) \cdot C_F} \quad d_t(t) = \sqrt{\frac{A_t(t) \cdot 4}{8 \cdot \pi}} \quad (18)$$

The obtained time dependences can be approximated by linear functions. The following piecewise-linear functions are adopted for rocket motor operation at extreme temperatures:

$$d_t^i(t) = D_i + (D_{i+1} + D_i) \frac{t - T_i}{T_{i+1} - T_i} \quad (19)$$

Coefficients  $D$  and  $T$  for this function are given in table 1.

**Table 1.** Throat erosion equation coefficients

Temperature -30°C				Temperature +50°C			
$T_0$	0	$D_0$	0.01	$T_0$	0	$D_0$	0.01
$T_1$	0.5	$D_1$	0.011	$T_1$	0.5	$D_1$	0.011
$T_2$	1	$D_2$	0.012	$T_2$	1	$D_2$	0.013
$T_3$	5	$D_3$	0.012	$T_3$	5	$D_3$	0.013

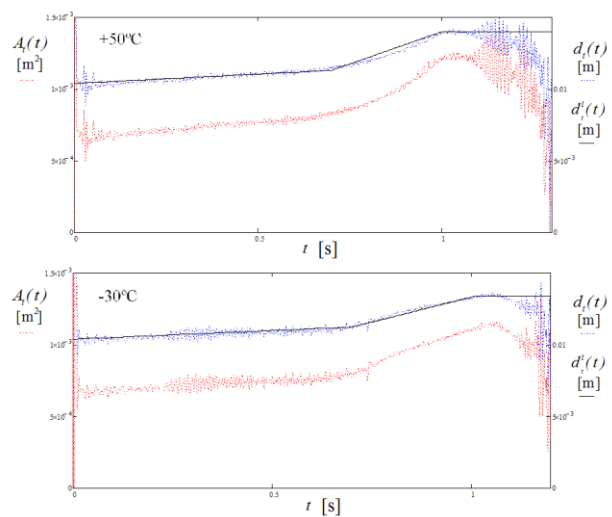


**Figure 4.** The average diameter and area of the nozzle throat, compared with linear approximation at extreme temperatures +50°C and -30°C.

After the RM test, the measured average values of the eroded critical sections approximately correspond to the final values of the calculated functions, 0.012 and 0.013 mm, respectively.

### 5. PROPELLANT GRAIN BREAKING DUE TO CENTRIFUGAL FORCE

The geometry of the propellant grain is shown in Figure 6. The configuration of the grain is a classic "star" profile. The burnback analysis of this type of grain is well known and can be performed using analytical methods [8].

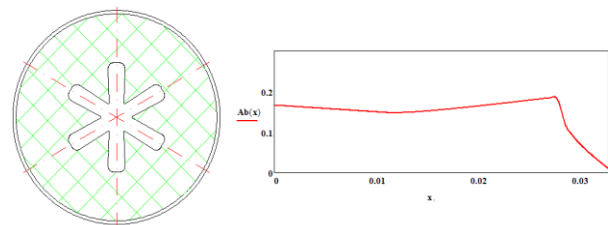


**Figure 5.** Cross-section of the propellant grain and the burning area curve.

The geometry, working conditions and characteristics of the propellant at -30°C are such, that in most cases the propellant cracks during the operation of the RM. This phenomenon was confirmed experimentally in a special RM. The test was carried out in static conditions on a special test stand, which enables free rotation simulating the rocket spin in the flight. In all experiments at low temperatures, a stepped pressure jump was observed at the end of RM operation (Figure 3).

In order to confirm the assumption that it is a fracture of the grain, an experiment was performed with special grains. They are prepared in such a way that their shape approximately corresponds to the grain geometry at the moment when the breaking occurs (Figure 6). When a grain was subjected to the appropriate rotation, it was determined that all propellant charges had breaking at the minimum web locations.

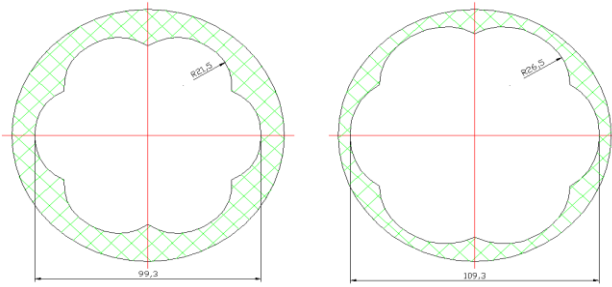


**Figure 6.** Cross-section of the propellant grain at two cracking moments.

The burn-back analysis including the grain breaking no longer fits the analytical model. In order to perform the calculation, a special numerical program for burn-back analysis SVOD [7] was applied. The calculation of the Burning area change was performed, taking into account the cracking of the PP at different web thickness. The calculation results are given in Figure 7.

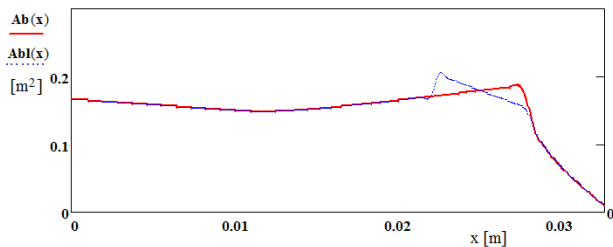


**Figure 7.** Burning area change without  $Ab(x)$ , and with grain breaking  $AbI(x)$ .

## 6. THE SPIN INFLUENCE ON THE BURNING RATE

The change in burning rate due to acceleration is a phenomenon in internal ballistics that has been known for a long time. The phenomenon is complex, it depends on a number of factors, such as: propellant type, geometry of the propellant grain, direction of the acceleration vector [9], etc. The applied gain in the periods near the end of the operation has surfaces that are almost perpendicular to the radial direction of the RM (Figure 6), so this effect is very pronounced.

The physicality of this process is reflected in the following phenomena:

1. Rotation reduces the mass flow rate at the nozzle throat, due to the redistribution of the flow field during rotation. This increases chamber pressure and consequently higher burning rate may result;
2. Viscous and boundary layer flow patterns are set up in the motor, increasing heat transfer to the propellant surface through greater mass transfer;
3. The radial acceleration forces can cause greater retention of the solid phase combustion products near the propellant surface.

All those phenomena are mostly complex and require thorough theoretical-experimental work [10]. Only the first phenomenon can be described by known relations from gas dynamics. Semi-empirical and experimental

methods [10] are mainly used for modeling these processes.

The burning rate law of the applied propellant was experimentally determined. At extreme temperatures, the burning rate was measured in a certain range of pressure. Due to the application of ballistic modifiers in propellant, the burning rate laws have a plateau effect and irregular shapes, shown in Figure 8.

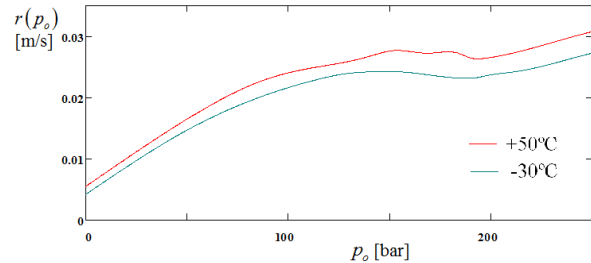


**Figure 8.** The burning rate curves at extreme temperatures of +50°C and -30°C.

The effects of rotation can be modeled using a semi-empirical methods [10]. The increase in the burning rate depends exponentially on the centrifugal acceleration, i.e. on the product of the square of the angular velocity and the radial distance of the burning surface from the axis of rotation:

$$r(p_o, x) = r(p_o) \left[ 1 + A \cdot e^{B \cdot r_s(x) \cdot \omega(x)^2} \right] \quad (20)$$

The burning surface radial distance can be approximated by a linear function. The influence of centrifugal acceleration comes to the fore in the second half of the RM operation, when the burning surface is approximately circular in shape (Figure 6):

$$r_s(x) = \begin{cases} r_s(0) + x, & x \leq x_k \\ r_s(x_k), & x \geq x_k \end{cases} \quad (21)$$

where  $x_k$  is the grain web thickness.

The angular velocity of the projectile is proportional to the thrust, and inversely proportional to the moment of inertia. Measurements show that the angular velocity of the projectile can be approximated by a linear function (Figure 3).

$$\omega(x) = \begin{cases} \omega_k \cdot \frac{x}{x_k}, & x \leq x_k \\ \omega_k, & x \geq x_k \end{cases} \quad (22)$$

The coefficients A and B in equation (22) can be determined based on the experimental results of the motor static test, until agreement with the calculated pressure curve is achieved.

## 7. SIMULATION OF RM OPERATION AND EXPERIMENTS COMPARISON

In addition to the described functions of the throat erosion, burn-back analysis and burning rate law, the input data for the unsteady IB calculation are the characteristics of the propellant, combustion products and RM (given in Table 2). Combustion products are obtained by thermo-chemical calculation [11].

**Table 2.** The RM characteristics

Characteristic	Value
Density [kg/m <sup>3</sup> ]	1617
Specific heat ratio	1.261
Temperature of combustion [K]	2381
Molar mass [kg/Kmol]	24.152
Nozzle throath diameter [m]	$10.4 \cdot 10^{-3}$
Start rocket motor free space [m <sup>3</sup> ]	$7.7 \cdot 10^{-4}$

After the calculation, the results were obtained in the form of a pressure - time curve. A comparison with the experimental results shows an extremely good agreement (Figure 9).

Applying the constant value of the thrust coefficient (17) in equation (16), the thrust-time curves are obtained (Figure 10).

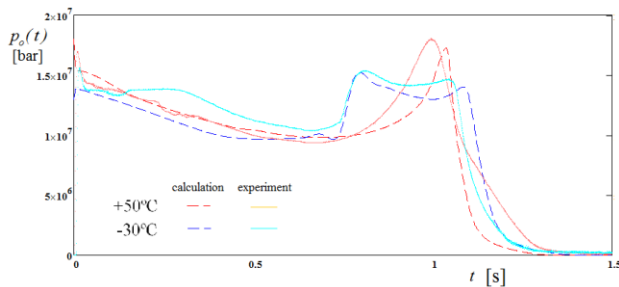


**Figure 9.** Comparison of calculated and experimental pressure-time curves, at extreme temperatures.

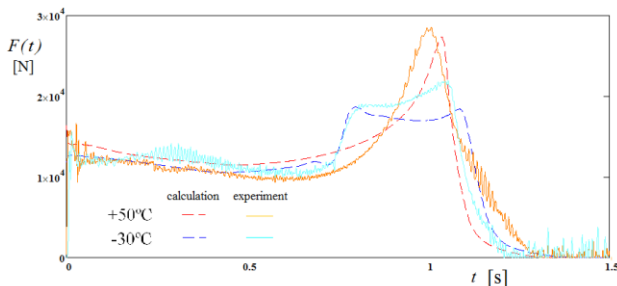


**Figure 10.** Comparison of calculated and experimental thrust-time curves, at extreme temperatures.

## 8. CONCLUSION

The described non-stationary internal-ballistic calculation can be successfully used to simulate the operation of a rocket motor with several atypical processes. An example of a spin-stabilized rocket is given, which design results with complex internal ballistic processes.

Nozzle erosion is not a rare phenomenon, but its modeling complicates the calculation. The method of identifying the function of the critical section change in time, based on measurements in a static experiment of a rocket motor is presented.

It was experimentally identified the occurrence of the fracture of the propellant charge due to the centrifugal load. Numerical burning surface analysis of the propellant charge was performed, which at a certain moment creates a multiple grain, when the burning area increase rapidly. Based on this analysis, a function of the burning area was formed depending on the burned web.

The interpolation method was applied to create the burning rate law, as dependence of the burning rate from the pressure in the motor chamber. This function is valid when the motor is running in static, without rotation. This function is extended to add dependency from centrifugal acceleration, using spin correction function. This dependency is based on an approximate linear function of the rocket spin and the burned web, and it is adjusted by two empirical coefficients until is achieve best agreement between calculation and experimental curves.

### Nomenclature

$A_b$	burning area
$A_t$	throat area
$b$	burn rate coefficient
$C_F$	thrust coefficient
$c^*$	characteristic velocity
$d_t$	nozzle throath diameter
$F$	thrust of a rocket motor
$F_{real}$	experimental measured thrust
$\dot{m}_i$	mass flow rate at inlet
$m_o$	mass of products in the RM chamber
$\dot{m}_t$	mass flow rate through the nozzle throath
$n$	pressure exponent
$p_o$	total pressure at chamber
$R$	gas constant of combustion products
$r$	burning rate
$T_o$	total temperature at chamber
$V_o$	free volume of the RM chamber
$v_t$	velocity at nozzle throath
$\rho_o$	density of combustion products in the chamber
$\rho_p$	density of propellant grain
$\rho_t$	density of combustion products at the nozzle throath
$\gamma$	specific heat ratio of combustion products

## Acknowledgements

This work was by Serbian Ministry of Defense and Serbian Ministry of Education, Science and Technological Development, Grant No 451-03-66/2024-03/200325.

## References

- [1] SUTTON,G.P., BIBLARZ,O.: *Rocket Propulsion Elements*, Wiley, New York, 2001.
- [2] ŽIVKOVIĆ,S., FILIPOVIĆ,M., ELEK,P.: *Experimental Determination Of Rocket Motor Internal Ballistic Coefficients And Performance Parameters*, Oteh, Belgrade, 2014.
- [3] GLIGORIJEVIĆ,N., DIVAC,S., LEMIĆ,D.: *Solid propellant rocket motors - selected topics*, Mti & Media center Odbrana, Belgrade, 2013.
- [4] MAKOTO,Y., SATOSHI,T., YOSHIHIRO,N., KENICHI,N.: *Development Status of Reusable Rocket Engine*, Transactions Jsass Space Technology Japan, 26(7) (2009) 13-18.
- [5] MARJANOVIĆ,G., KOZOMARA,S.: *State of the Propulsive-Group Development for Enhanced Anti – Armored Guided Missile*, Scientific Technical Review, 68(3) (2018) 56-63.
- [6] BARRERE,M., JAUMOTTE,A., VEUBEKE,B.F., VANDENKERCKHOVE,J.: *Rocket Propulsion*, Elsevier Publishing Company, Amsterdam-London-New York, 1960.
- [7] MARJANOVIĆ,G., ŽIVKOVIĆ,S., GLIGORIJEVIĆ,N.: *Program SVOD for solid propellant grain design*, Oteh, Belgrade, 2012.
- [8] SAVKOVIĆ,M., ŽIVKOVIĆ,C.: *Two Methods of rocket motor propellant grain Burn-back Analyses* (in Serbian), Oteh, Belgrade, 2009.
- [9] ANDERSON,J., B., REICHENBACH,R., E.: *An Investigation Of The Effect Of Acceleration On The Burning Rate Of Composite Propellants*, Naval Postgraduate School, Monterey, 1967.
- [10] CROWE,C., WILLOUGHBY,P.: *Effect of spin on the internal ballistics of a solid propellant motor*, AIAA Published Online, New York, 2012.
- [11] FILIPOVIĆ,M., KILIBARDA,N.: *The Calculation of Theoretical Energetic Performances of Composite Rocket Propellants*, J. Serb. Chem. Soc., 66(2) (2001) 107-11



# **OTEH 2024**

**11<sup>TH</sup> INTERNATIONAL SCIENTIFIC CONFERENCE  
ON DEFENSIVE TECHNOLOGIES**

*SECTION V*

**Integrated sensor systems and robotic systems - *ISSRS***



## IMPLEMENTATION OF AN ALGORITHM FOR AUTONOMOUS MOVEMENT ON A ROBOTIC PLATFORM

NINA MITRIČEVIĆ

Military Technical Institute, Ministry of Defence, Ratka Resanovića 1, Belgrade, [nina.mitricevic@mod.gov.rs](mailto:nina.mitricevic@mod.gov.rs)

RADE PAVLOVIĆ

Military Technical Institute, Ministry of Defence, Ratka Resanovića 1, Belgrade, [rade.pavlovic@mod.gov.rs](mailto:rade.pavlovic@mod.gov.rs)

**Abstract:** *The translation of unmanned systems into autonomous systems is increasingly prevalent in many researches. In this paper, the implementation of the existing algorithms on an unmanned ground platform was performed, as well as the validation of the obtained results in laboratory conditions. First, a simulation model was used to demonstrate the justification of the algorithms, and then the implementation was done on an unmanned platform. The results obtained by validation showed that the robotic platform can successfully perform tasks such as going to the desired location, returning to the initial position, as well as following the operator. In doing so, dynamic obstacles were used that the robotic platform successfully managed to overcome and reach the desired target.*

**Keywords:** UGV, robotics platform, autonomous, ROS.

### 1. INTRODUCTION

Unmanned ground vehicles (UGV) have become the focus of research in many countries because of their great potential in many applications including replacement of personnel in life-threatening situations. Upgrading the UGV to an autonomous vehicle additionally increases their reliability and efficiency. Some of the basic functions of the autonomous UGV are “Go to target”, “Return to home” and “Follow me”.

**Go to target** – The implementation of the functionality of going to the given location on the map implies the integration of the algorithm for simultaneous localization and mapping with the module for global path planning and local obstacle avoidance [1]. The central decision-making system that generates the actions of the autonomous unmanned vehicle is implemented in the form of a *Behavior tree*, which is a generalization of the *Finite State Machine* and provides greater flexibility and modularity in modeling the behavior of more complex agents. The behavior tree inherently takes into account the time required for the realization of actions in the physical world. The behavior tree mechanism is already integrated within the *Nav 2* library for mobile robot navigation in the ROS 2 environment. The **Return to home** functionality essentially boils down to the *Go to target* functionality, as the vehicle returns to the initial position along the same or optimal path.

**Target following** – Development of the target tracking functionality, which essentially boils down to the functionality of *go to target*, where the target location is not fixed but constantly updated based on the processed signal from the *UWB* sensor [2]. In other words, a continuous online path replanning is performed based on the update of the target using the tag.

**Manual Remote Control** – The development of the possibility of remote control of the robot by taking over the command from a human operator is based on communication through the *UWB* module [2]. The possibility of remotely controlling the movement of a mobile robot from a computer from the ROS application, via *Wi-Fi* communication, has been developed.

Navigation of an autonomous unmanned vehicle involves its simultaneous localization and terrain mapping (SLAM) as well as route planning on an existing map [1]. For vehicle navigation, odometry is also very important, a method that, based on sensors (most often encoders on wheels or motors), integrates the vehicle's distance traveled in order to determine its current location and position. Odometry, like other dead reckoning methods, is very sensitive to drift, primarily due to wheel slip, but can be combined with the SLAM algorithm for corrections.

### 2. ROBOTIC PLATFORM

The entire system is implemented on the *Rosbot 2 Pro* platform (figure 1), manufactured by *Husarion*. This is a mobile robotic platform with four wheels that comes equipped with several sensors, the most important of which are the encoders on the motors, used for odometric position measurement, and lidar, i.e. a laser sensor that scans the space in one plane around the robot [3]. The platform has a set of regular wheels and a set of omnidirectional „*mecanum*“ wheels, which enables the implementation of two different types of drives. The first is the so-called „*skid steer*“ drive, and this is characteristic of tracked vehicles, while the other is an omnidirectional drive that allows translation in all directions and turns the platform into a holonomic mechanical system. The „*skid steer*“ drive is modeled essentially the same as the differential drive, but the resulting odometry performance is worse due to wheel slippage. Instead of two drive



wheels and two passive support wheels, with differential drive, here we have four drive wheels, which implies that we have slippage during rotation. In other words, we now obtain the robot's kinematics from its dynamics, including contact forces and friction, resulting in a less accurate model.



**Figure 1** Mobile robotic platform ROSbot 2 Pro

The mobile platform contains an integrated computer *SBC UP board* with the following performance: processor Intel Atom x5-Z8350 1.44/1.92 GHz, 4 GB RAM, Intel® HD 400 GPU, 32GB eMMC. This development board supports a large number of operating systems, including *Ubuntu* which is required if we want to install the ROS package of libraries [4].

The model of the mobile robotic platform that will be used for laboratory validation of algorithms in the selected simulation environment is the so-called URDF (Unified Robotics Description Format) robot model that contains all the necessary kinematic and dynamic parameters of the robot in a text format, similar to the XML format. The URDF format describes the complete geometry of the robot in the form of a tree with a single starting node as the root. Essentially, this format contains a complete 3D model of the robot in mesh format along with additional information defining the type and position of the joints, the masses of the segments, as well as the positions of their centers of mass and the associated tensors of inertia. Also, the URDF model contains approximate models that can be used for collision detection, in order to reduce the computational load.

### 3. SYSTEM IMPLEMENTATION

A large number of different software packages and environments that support the physical simulation of mobile robotic systems are available for developing mathematical models and simulating the operation of sensors and different algorithms for localization, terrain mapping, local and global trajectory planning. Some of the physics simulators available are *Gazebo*, *Webots*, *PyBullet*, *Mujoco*, etc. In the final realization we used *Gazebo* simulator with integrated physics simulation module (*physics engine*). Although most of these simulators can work independently, we used the selected simulator in combination with a Robot Operating System (ROS), which facilitates the later implementation of the developed algorithms on a real hardware platform and the integration of the robot itself with the various sensors that are part of the system. At a later stage of work, after

implementation on real hardware, we used the *Rviz* library to visualize the movement of the robot on the map. The hardware connection of the robot to the network with the computer is shown in Figure 2.

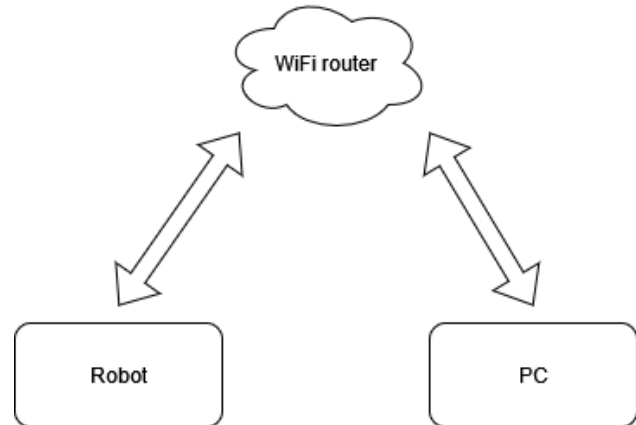


**Figure 2** Communication between the computer on the mobile robot platform and the control PC

A number of libraries for mapping, localization and motion planning of mobile robots in an unstructured dynamic environment were considered. The planner should consist of a global and a local planner and have an integrated dynamic obstacle avoidance algorithm. And the program package that was chosen for those needs is *Navigation 2* in the *ROS 2* environment, which supports all the necessary functionalities. Libraries such as *RTAB Map* and *SLAM Toolbox* are available for terrain mapping and robot localization. The *SLAM Toolbox* library was selected for implementation. The Robot Operating System - ROS - was chosen as the software base. This is not a real operating system in that sense, but a collection of software packages to facilitate the implementation of robotic systems and their integration with other hardware.

The first platform testing requires starting the robot in manual mode, using teleoperation. On the robot, it is necessary to run the manufacturer's launch script, which establishes communication with the motor drivers, loads the robot's physical parameters and starts the *diff\_drive\_controller* package, which calculates the position of the robot based on the encoder, and based on the commanded speed of the platform, recalculates the wheel speeds and sends that information to the motor drivers. After starting, the ROS topic */cmd\_vel* appears, to which we send the reference desired speed. The *teleop\_twist\_keyboard* package is launched on the personal computer, which enables intuitive control of the robot based on input from the keyboard. It publishes the set reference speed on the topic */cmd\_vel*, which due to distributed access via wireless network and router reaches the robot and it starts.

Due to odometric errors, especially due to wheel slippage during turning, we also included a lidar sensor using the *rplidar* package. It enables space scanning in one plane and 360 degrees around the robot. The integration of the entire system is facilitated by the popular and robust *navigation2* package. Inside it, using the *slam\_toolbox* package, we ran the space mapping algorithm. Using

odometric data from the encoder and lidar scanning, this package gradually builds a map of the space around the robot. The robot needs to be manually operated by teleoperation to explore the space and build a map. The entire process is monitored on a personal computer with the *Rviz* visualization tool. Within it, we can see the position of the robot, the map, the coordinate system, as well as the sensor readings of interest. After exploring the space with the robot, we saved the generated map to disk.

It is possible to constantly explore the space and use an algorithm to generate the map, but this puts a strain on the processor. Given that we have received a static map of the space, it is enough just to localize on it (dynamic obstacles will still be detected). Localization was performed by the *nav2\_amcl* package, which implements adaptive Monte-Carlo localization. This package loads a static map from disk and uses odometry and lidar sensor to localize the robot on the map.

The robot is localized, but for autonomous driving it is necessary to load planners. The global planner finds the path on the map to the target point and we tried the *A\** and *smac2d* algorithms. The local planner uses the *dynamic window approach* algorithm and enables dynamic obstacle avoidance. The block diagram of the software is given in figure 3.

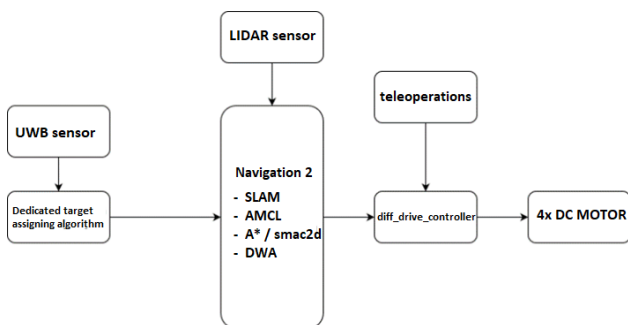


**Figure 3** Software architecture of the implemented system for navigation and tracking of a moving target

Using *Rviz* or *nav2\_simple\_commander* package, it is possible to assign a target to the robot. He moves to the target autonomously and avoids obstacles. The block diagram also shows the *UWB* sensor, the *NooploopLinktrack AOA* was selected, which provides a good price-quality ratio and has satisfactory performance [5]. A ROS node that communicates with the *UWB* sensor via USB and publishes the position of the tag (tracking object), which the field operator carries with him, as a coordinate system using the *tf* package for coordinate systems transformations, is written. In addition to this coordinate system, another one is published that has the same orientation but is closer to the robot by a predefined distance. This distance represents the desired offset from the target and is a control parameter that can be adjusted.

The human tracking algorithm has two basic modes. The first assigns a target to the robot, which guides it directly to the tag, by the shortest path, with periodic updates of the target position. More precisely, the target is not the tag itself, but an offset coordinate system so that the robot does not get too close to the person wearing the tag. The second mode follows the path (track) made by the operator with the tag. This is achieved by periodic memory storage of the read tag positions in the sheet, after which the memorized positions are sequentially passed to the robot as targets.

#### 4. ANALYSIS OF RESULTS

Adequate polygon with dummy obstacles was defined and modeled in a virtual simulation environment and a series of simulation scenarios in which all desired situations needed for adequate testing of algorithms was generated. The polygon is of appropriate complexity and with a sufficient number of objects, whose position, shape and dimensions can be varied, in order to test the *SLAM* algorithm for space mapping and robot localization. It was necessary to ensure a sufficient number of situations in which the robot encounters static or dynamic obstacles, in order to test the local planner and obstacle avoidance system. As well, a series of metrics for evaluating the performance of the developed algorithms had to be defined. For example, the iteratively generated map from *SLAM* was compared with the previously known *CAD* model of the map from the simulator, the accumulated error of the robot's position and orientation were measured, after traversing *N* circles along a closed path on the map, the accuracy and repeatability after sending the robot multiple times from one fixed initial position to one and the same target point were measured, etc.

After that, on the basis of the defined validation methodology and experiment setting, all foreseen scenarios were simulated and the necessary data for further analysis was logged.

The next step was the integration of the selected sensor systems on the existing mobile robotic platform with omnidirectional drive and transferring all functionalities from the simulation environment to the real system. Three appropriate tests were performed, ie. experimental protocols to test the robot's functionality in the real world. These are obstacle avoidance and navigation tests, target tracking, and movement accuracy and repeatability.

The obstacle avoidance and navigation test serves to validate the functionality of the robot's sensor system, implemented with the *SLAM* algorithm and the obstacle avoidance algorithm. The possibility of moving the robot in an unstructured environment, whose map is not fully known (contains immovable static obstacles) and which may contain dynamic obstacles, is tested.

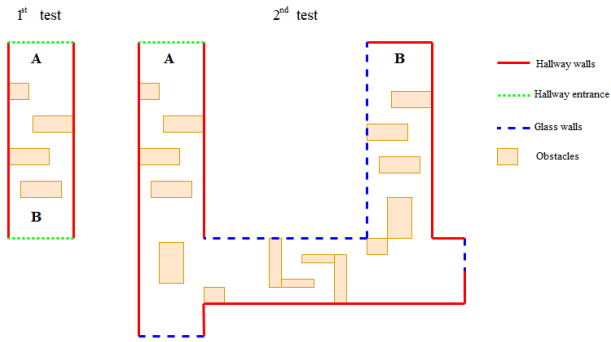


**Fig. 4** Illustration of the polygon that will be used to validate the obstacle avoidance system

Within a hallway shaped like the Cyrillic letter P, the robot needs to move from point A to point B while avoiding obstacles made up of cardboard boxes, furniture, walls and people. For the purposes of the test, points A and B will be assigned commands from the *ROS* environment. The first part of the test represents a movement where points A and B are seen within the air line, with a set of obstacles placed between them. The second part examines the movement of the robot between points A and B that are not visible within the air line, defining the starting position and the target at the ends of the hallway in the shape of the Cyrillic letter P. In this way, the walls themselves represent an obstacle to the robot's motion planning algorithm, which is a realistic scenario. The polygon is shown in Figure 4. The functionality of the *SLAM* algorithm, which performs simulated localization and terrain mapping, as well as the algorithm for global and local path planning, were tested on the same polygon, but with the additional introduction of dynamic obstacles, which were simulated by the movement of people in the scene, or by moving boxes. In this way, by successfully completing these tasks, the functionality of the robot for going to a predefined target point (*go to target*) and returning to the initial position (*return to home*) was validated.

The target tracking test validates the tracking functionality of the UWB tag carried by the operator in the field. A tape is glued on the floor as a predefined path that a person with a UWB tag will follow. The task of the robot is to follow the path made by the man, i.e. field operator. In doing so, it was observed whether the robot will follow each point through which the person has passed and thus it will also follow the glued tape or will make shortcuts along the air line. The presentation of this test is illustrated in Figure 5.

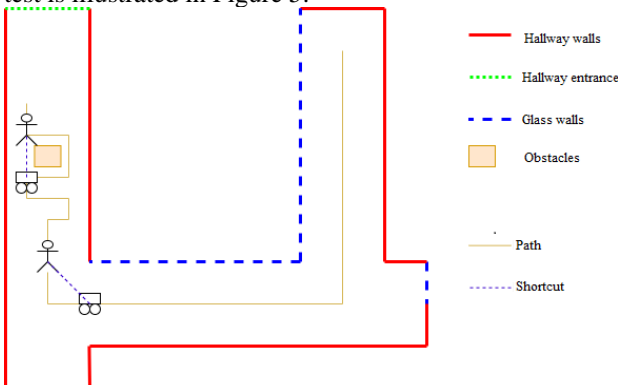


**Fig. 5** Illustration of a polygon that will be used to validate a moving target tracking system based on UWB sensor technology

In the second phase of this test, the robot's ability to return to its initial position after the mission was analyzed (*Return to Home*), whereby in this case the target is inverted, so the current position of the tag represents the starting point A, and the „home“ is point B. The robot successfully followed the operator, although it did not completely follow the same path, but made certain shortcuts. While, on the other hand, when checking the *Return to Home* function, the robot already had a map of the area and did not follow the same way, but estimated the shortest path back.

The test for checking the accuracy and repeatability of movement is used to validate the functionality of the *SLAM* algorithm based on a sensor system consisting of lidar sensor and encoder odometry. The robot should move along a programmed closed path, where the start and end points C coincide. In tests of this type, a square or figure eight path is used as a standard path. The initial point C represents the initial point C0. After one completed cycle along the path, the robot will be at point C1, and after one more at point C2, etc. After a predefined number of cycles, in this experiment it was 10, the accumulated error manifest itself in the fact that the point C10 is not coincide with the starting point C0, as illustrated in Figure 6. Also, in addition to the deviation in the position of the point C, a deviation in the final orientation of the robot also is observed compared to the initial one. Although the start and end points did not exactly match, the error is small enough to be discarded, and the task can be considered successfully completed. As a reference measurement system, the *VICON* movement recording system was used, that consists of a set of infrared cameras with a high image refresh rate ( $f > 600\text{Hz}$ ), which enables position measurement accuracy below 1mm. This system is based on the application of passive reflective markers that are placed on the object whose movement is recorded. By placing at least three markers that form a coordinate system, it was possible to determine the position and orientation of the object in space. It is necessary that at all times at least three cameras can see each marker.

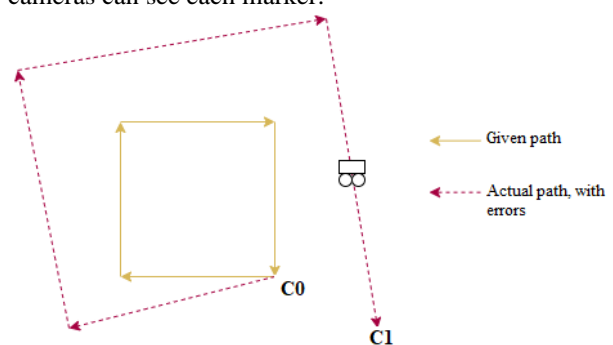


**Fig. 6** Illustration of the polygon that will be used to validate the accuracy and repeatability of the navigation system

## 5. CONCLUSION

Autonomous unmanned vehicles are increasingly used in both the civilian and military industries. In the civil industry, efforts are being made to introduce total autonomy in vehicles in order to reduce human error, which is a direct cause of traffic accidents. Also, the industry uses a large number of autonomous vehicles that successfully perform given tasks.

In the military industry, the main task of autonomous unmanned vehicles is to reduce human losses on the battlefield. In addition, autonomous vehicles can perform tasks that cannot be performed by existing systems (going to designated locations when communication with the operator is lost). As part of the research in this paper, the results obtained using standard algorithms for autonomous movement implemented on a real robotic platform are given. The algorithms have proven to be reliable for use in laboratory conditions with static and dynamic obstacles. The autonomous vehicle successfully managed to recognize and overcome all the obstacles it had on the way to the given location. In addition, the operator was successfully tracked along the path he was on.

All the mentioned results open the possibility to implement the same algorithms on robotic platforms that are intended for work in external conditions and perform

their testing.

## References

- [1] Corke, P. (2017). Navigation. In: Robotics, Vision and Control. Springer Tracts in Advanced Robotics, vol 118. Springer, Cham. [https://doi.org/10.1007/978-3-319-54413-7\\_5](https://doi.org/10.1007/978-3-319-54413-7_5)
- [2] Oh Seong Park, Jae Hoon Lee and Shingo Okamoto, "Position Estimation Method Using Multiple UWB Radio Communication Modules and Its Application to Mobile Robot"
- [3] Техничка документација сензора, [https://www.slamtec.ai/wp-content/uploads/2023/11/LD310\\_SLAMTEC\\_rplidar\\_datasheet\\_A2M12\\_v1.0\\_en.pdf](https://www.slamtec.ai/wp-content/uploads/2023/11/LD310_SLAMTEC_rplidar_datasheet_A2M12_v1.0_en.pdf), последње време приступа 11. 4. 2024.
- [4] Техничка документација мобилне роботске платформе Husarion ROSbot 2, <https://husarion.com/manuals/rosbot/#specification>, последње време приступа 16. 4. 2024.
- [5] Техничка документација UWB сензора Nooploop LinTrack AOA: [http://ftp.nooploop.com/software/products/uwb/doc/LinkTrack\\_AOA\\_Datasheet\\_V1.1\\_en.pdf](http://ftp.nooploop.com/software/products/uwb/doc/LinkTrack_AOA_Datasheet_V1.1_en.pdf), последње време приступа 16. 4. 2024.



# THE IMPORTANCE OF PINHOLE SIZE TARGET IN THERMOGRAPHIC AND RADIOMETRIC MEASUREMENT

KATARINA MIŠKOVIĆ

Military Technical Institute, Belgrade, [msc.katarina.miskovic@gmail.com](mailto:msc.katarina.miskovic@gmail.com)

**Abstract:** The paper describes how the pinhole size object influence radiometric and thermographic measurements (radiance and temperature). The measurements are done in laboratory conditions using MS 300 system with different pinhole sizes which represent spatial resolution of the object at known blackbody temperature. The measurement camera used for the experiment is calibrated scientific Flir SC7200 thermal camera. The pinhole effect can be used for better understanding and estimation of detection ranges of small targets on thermal imagers.

**Keywords:** thermography, pinhole size target, radiance, spatial resolution, blackbody.

## 1. INTRODUCTION

The thermal camera became an important element in vast number of industries recent years. There, it can be used for non-contact measurements or as an imager, to show the distribution of the radiation. The thermal cameras can be divided according spectral band where operate (1-3 $\mu$ m - short wave infrared SWIR, 3-6  $\mu$ m - mid-wave infrared MWIR, 6-15  $\mu$ m - long-wave infrared LWIR). As for the military applications of the thermal camera, it is usually used as an imager to help observer to see a scenery or for a gunner to enable him to spot and aim the target. There is no need for precise temperature measurement.

It is well known that the “4-bar” target is used to do the measurements according the STANAG 4347 to predict the ranges of thermal imager, but is there any correlation between small pinhole target and the ability of imagers to spot it even if the target is much smaller than a detector element. Is there any level of radiation reaching the detector/camera that enables the imager to spot the small pinhole target? The answer to these questions is aperiodic transfer function. Aperiodic transfer function (ATF) is defined as a normalized dependance of system response to a variable size square or circular target. It provides information on system ability to detect small targets.[1]

## 2. THE EXPERIMENTAL SETUP

The experiment is conducted in laboratory conditions at room temperature in the Laboratory for Optoelectronics of the Military Technical Institute. The background temperature was 24.66°C at the experiment beginning and at 25.19 °C at the end. The temperature deviation of 1°C can be neglected in this case because it has no significant impact on the target/object detection. The temperature reading was done by the blackbody temperature sensor. The blackbody at room temperature radiates mostly in infrared spectrum and it cannot be perceived by the human eye, so the special testing equipment is needed for

the experiment. The scientific thermal camera FLIR SC 7200 is used as the image sensor and placed in front of the collimator. The collimator's length is 2m. The purpose of the collimator is to simulate the object appearance from infinity. The rotary wheel with 8 pinhole size targets is placed on the top of the collimator, Picture 1. The targets radius dimensions are (40, 25.6, 6.4, 2, 0.8, 0.4, 0.2, 0.1) mm. The calibrated blackbody source is placed above the rotary wheel filled with targets with the purpose to radiate through the open part of the target - pinhole. The different amount of radiation is adjusted using the blackbody controller and passing through the target to be detected on the thermal camera. The generated blackbody radiation corresponds to (25,40,60,80) °C.

### 2.1. Results

The Table 1 represents temperature measurements of different amount of blackbody radiation passing through the various sizes of pinhole targets by SC7200. The calibrated thermal camera SC7200 detects infrared radiation which fall on the detector and generated signals are converted into temperature. So, the radiation readings are converted to the temperature unit of Celsius degree. When the blackbody temperature was set to 25°C the background temperature reading was 24.66 °C. It can be seen that the camera measured lower temperature than 25 °C, and one of the reasons is the losses of the collimator. Also, the temperature reading becomes difficult at the temperatures near the ambient temperature. Additionally, the temperature measurement accuracy of calibrated camera is  $\pm 1^\circ\text{C}$ . The similar accuracy error can be seen for blackbody temperature of 40°C, 60°C and 80°C for the largest pinhole target in the Table 1.

The calculated instantaneous field of view (IFOV) of SC7200 is 0.6mrad. The thermal camera can detect small targets of angular size smaller than the IFOV. The angular size can be understood as spatial resolution. The IFOV represents „the field of view” of the single pixel. For an ideal thermal camera, the gained signal is proportional to

the target area when the target area is smaller than IFOV, and the gained signal does not depend on the target area when the target area is bigger than IFOV [1].

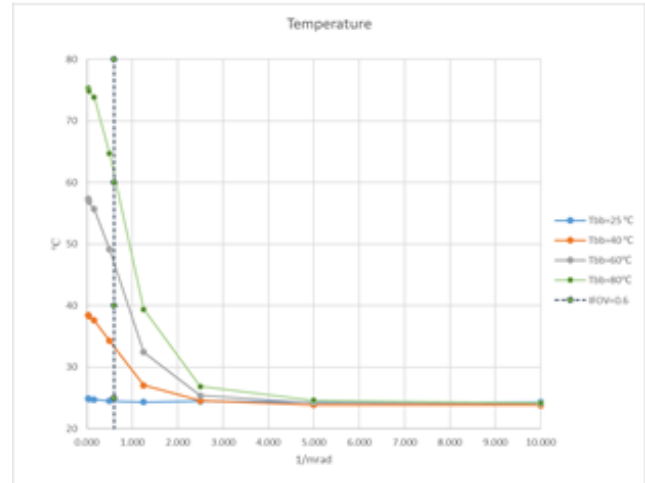


Picture 1 The measurement equipment

The Picture 2 shows the dependence of measured temperature for different blackbody radiance versus angular size of target dimension. When target area is bigger than IFOV, the measured temperature is almost equal to the temperature of the radiated radiation, but when it approaches to IFOV the measured temperature become lower than the radiated, which is well described with real ATF. The difference between the ideal and real ATF is caused by the image blur generated by the optical and electronic systems.

For the pinhole targets smaller than IFOV, the radiation passing through such a small size target depends not only on the target area but also on the blackbody radiation intensity. As it can be seen in the picture, the graph indicates that the SC7200 can detect targets smaller than

IFOV and the higher radiation the source is emitting the higher measured signal will be. In this example, the pinhole target is seen on spatial frequencies that are up to 8 times bigger that the IFOV. According to that, when it comes to the detection ranges of thermal imagers it can be concluded that the target smaller than IFOV can be detected and the range depends on its radiation level. The higher is the radiation of the target, the higher is spatial frequencies where the target can be spotted and the range of the thermal imager is longer. The conditions when the target area approaches zero is sometimes termed as blur efficiency or point visibility factor.



Picture 2 The dependence of measured temperature for different blackbody radiance versus angular size of target dimension

Table 1. The temperature measured by SC7200 for different target size and blackbody temperatures

Pinhole target size a[mm]	Inversed spatial size [1/mrad]	Blackbody absolute temperature [°C]				IFOV SC7200 0.6 mrad
		25	40	60	80	
40	0.025	24.9	38.5	57.37	75.36	Temperature [°C]
25.6	0.039	24.87	38.26	56.89	74.84	
6.4	0.156	24.74	37.61	55.7	73.9	
2	0.500	24.53	34.28	49.14	64.7	
0.8	1.250	24.33	<b>27.06</b>	32.46	39.4	
0.4	2.500	24.49	24.58	<b>25.4</b>	<b>26.9</b>	
0.2	5.000	24.33	23.88	24.24	24.6	
0.1	10.000	24.34	23.84	24.13	24.2	

### 3. CONCLUSION

The pinhole effect can be used for better understanding and estimation of detection ranges of small targets on thermal imagers. The paper describes how the pinhole

size object influence radiometric and thermographic measurements (radiance and temperature). Small target detection is also crucial for video surveillance systems in security, rescue and traffic monitoring as well as in aerial and maritime environments. The use of computational techniques for the detection of small target is an important

challenge for current artificial vision systems, and especially in thermal domain.

Due to the long distances between targets and infrared sensor, the target size can be smaller than one pixel, and still be detected. But the target can easily be confused with the background and sensor noise [3].

It can be concluded that the radiometric and thermographic analysis of small target can allow us unbiased assessment of the thermal imager performances in detection of small target on contrary to MDTD [4] which is subjective parameter that describes ability of the imager-human system for detection of small size targets. Accordingly, the analysis can be used as a parameter in advanced function in modern system for target detection which includes artificial intelligence.

## References

- [1] CHRZANOWSKI, K.: *Testing thermal imagers - Practical guide*, Military University of Technology, Warsaw, 2010.
- [2] FLIR, DC019U-L: SC7200 User manual.
- [3] Huang L. et al: *Infrared small target segmentation with multiscale feature representation*, Infrared Physics & Technology Vol 116, 2021.
- [4] ASTM standard E1311-99: *Standard test method for Minimum Detectable Temperature Difference for Thermal Imaging Systems*.



## IMPROVEMENT OF THE SIGNAL-TO-NOISE RATIO BY USING A STATISTICAL FILTER

MIODRAG VRAČAR

Belgrade, Serbia

[vracarmiodrag@mts.rs](mailto:vracarmiodrag@mts.rs)

STEVO VRAČAR

ITS INFORMATION TECHNOLOGY SCHOOL

Information Technology, New Belgrade, Serbia

[stevo5817@its.edu.rs](mailto:stevo5817@its.edu.rs)

**Abstract:** *The need to increase the signal-to-noise ratio is a significant task in almost all sensor applications that are exposed to a significant influence of ambient noise. The most common methods used to reduce ambient and/or measurement noise are based on the use of analog and digital filters or wavelet signal decomposition. The paper describes a new approach to signal filtering based on the application of the so-called a statistical filter that was realized by applying statistics of higher order, i.e. the fourth order cumulants. The statistical filter is successfully tested in analysis various types of sensor signals such as: acoustic, hydro acoustic, seismic, and other.*

**Keywords:** statistical filter, analog filter, digital filter, wavelet, signal analysis.

### 1. INTRODUCTION

Signals given by different sensors carry information of interest, almost always, they are compromised by noise, the nature of which can be different. It will almost never be possible to avoid the existence of the so-called ambient noise, which is a basic feature of the medium where the useful signal appears. Ambient noise is not the only component of signal interference. Namely, the noise of measuring system itself should be added to the ambient noise. In addition, to the unwanted components of the signal, one should add artificial noise that humans intentionally create in order to make the reception of the useful signal more difficult. This is especially emphasized in military applications.

Higher-order statistics (spectra) have begun to find wide applicability in many diverse fields, e.g.:

- sonar,
- radar,
- plasma physics,
- biomedicine
- seismic data processing,
- image reconstruction,
- harmonic analysis,
- harmonic retrieval,
- time-delay-estimation,
- adaptive filtering,
- array processing,
- blind equalization, and etc.

High-order statistics is one of the most effective tool in statistical pattern recognition approaches. The key basis

for such an attitude is in fact that cumulants can remove the influence of Gauss noise completely. In other words, higher-order statistics are applicable when we are dealing with non-Gaussian, or, in some cases possibly nonlinear processes, see [1,2].

The number of higher order statistics applications gave us an impulse to put into practice something that can be called statistical signal filtering by applying higher – order techniques. In the past few years, we have published several papers on this topic, see literature [3-5].

Until now, the usual procedure for removing the noise of signals, and improving Signal to Noise Ratio (SNR), involved the use of electronic filters. Electronic filters allow some parts of signal to pass, but stop others. Actually, electronic filters allow some signal frequencies applied at their input terminals to pass through their output terminals with little, or no reduction in signal level. In general, it can be said that there are two classes of electronic filters, analog and digital. Analog electronic filters are present in just about in every part of electronic equipment. Analog signal filtering can be based on the use of passive and/or active filters. Design of digital filters include infinite impulse response (IIR), or finite impulse response (FIR). FIR filter design is based on using digital signal processors, and IIR filters are based on analog filter design, see [6,7].

The function of digital FIR filters is realized by passing a digitized signal through a series of discrete delay elements and then multiplying the output of each delay element by a number, or coefficient, see [7].

Based on the above, a signal can be described in the time domain, or in the frequency domain. The time domain is



where an event, such as change of amplitude, is measured over time. The frequency domain is where the amplitude of signal is measured relative to the frequency. In many cases Fourier analysis of the signal is extremely useful because in many practical cases frequency content of the signal is important. By transforming signal into frequency domain the information about time is lost. That is not problem when we are dealing with stationary signals. But in non-stationary case that approach is not so good. In non-stationary case is used another approach which is based on so called short time Fourier analysis to correct these deiciency of classical Fourier approach.

Wavelet analysis makes next step in signal analysis which is based on windowing techniques with variable sized regions. The use of the time intervals of different size enable us to get more precise frequency informations of interest, shorten time intervals for high frequencies, and longer time intervals for low frequencies. In other words, a wavelet transform is able to measure the time-frequency variations of spectral components, but at the same time it has a different time-frequency resolution, see [8].

In this paper is introduced new domain for signal analysis – statistical domain. This domain enable to analyze how statistical properties of the signal change in time, that is, to what extent the statistical distribution of the signal deviates from the Gaussian distribution. This approach is justified by the fact that the events we want to analyze are usually caused by the release of some form of energy in a short time interval.

In this statistical approach, the fourth-order cumulants are used. If a random process is symmetrically distributed, then its third-order cumulant equals zero; hence, for such a process we have to use the fourth-order cumulants. The process, which is distributed with Laplace, Uniform, Gaussian, and Bernoulli – Gaussian distributions are symmetric, as it is known.

## 2. DEFINITIONS OF THE CUMULANTS

The starting point in defining of the cumulants are the moments of order  $n$ , where  $n$  is natural number. In a case of a stationary discrete time random process,  $X(k)$ , where  $k$  denotes discrete time, the moments of order  $n$  are given by Eq.(1), see [2].

$$m_n^x(\tau_1, \tau_2, \dots, \tau_{n-1}) = E\{X(k)X(k + \tau_1) \dots X(k + \tau_{n-1})\}, \quad (1)$$

where  $E\{\cdot\}$  denotes expectation operator, and  $(\tau_1, \tau_2, \dots, \tau_{n-1})$   $(n-1)$  cumulant lags. The cumulants of  $n$ -th order,  $c_n^x$ , up to 4-th order ( $n=1,2,3,4$ ), are given by following equations.

$$c_1^x = m_1^x = E\{X(k)\} \quad (2)$$

$$c_2^x(\tau_1) = m_2^x(\tau_1) - (m_1^x)^2 \quad (3)$$

$$c_3^x(\tau_1, \tau_2) = m_3^x(\tau_1, \tau_2) - (m_1^x)[m_2^x(\tau_1) + m_2^x(\tau_2) + m_2^x(\tau_2 - \tau_1)] + 2(m_1^x)^3$$

$$c_4^x(\tau_1, \tau_2, \tau_3) = m_4^x(\tau_1, \tau_2, \tau_3) - m_2^x(\tau_1)m_2^x(\tau_1)m_2^x(\tau_1 - \tau_2) - m_2^x(\tau_2)m_2^x(\tau_3 - \tau_1) - m_2^x(\tau_3)m_2^x(\tau_2 - \tau_1) - m_1^x[m_3^x(\tau_2 - \tau_1, \tau_3 - \tau_1) + m_3^x(\tau_2, \tau_3) + m_3^x(\tau_2, \tau_4) + m_3^x(\tau_1, \tau_2)] + (m_1^x)^2[m_2^x(\tau_1) + m_2^x(\tau_2) + m_2^x(\tau_3) + m_2^x(\tau_3 - \tau_1) + m_2^x(\tau_3 - \tau_2) + m_1^x(\tau_2 - \tau_1)] - 6(m_1^x)^4 \quad (4)$$

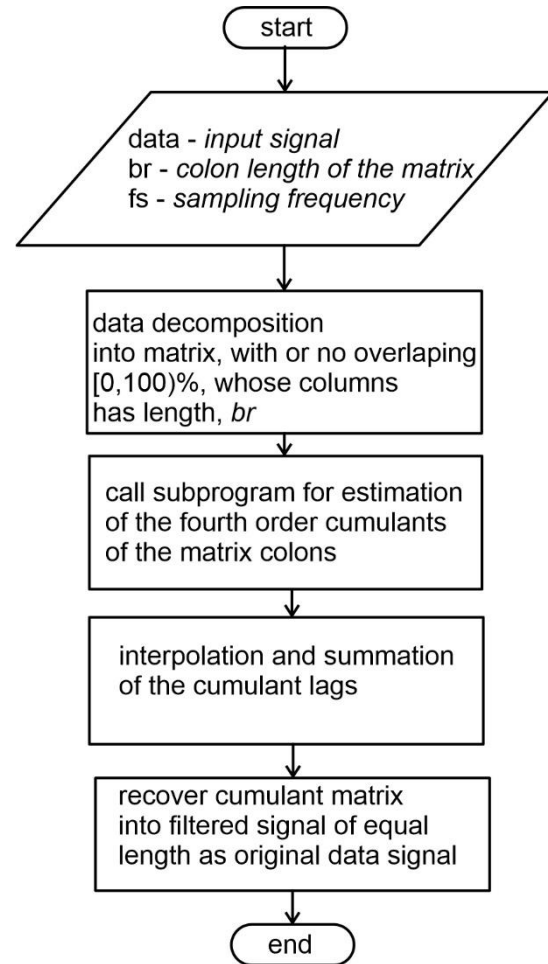


**Figure 1.** The flow chart of the algorithm of statistical filter, which is, based on the fourth order cumulants.

The analysis of the signal in so-called statistical domain is enabled by using of short-time the fourth-order cumulant estimation of the signal. The flow chart of the algorithm is shown in Fig.1. The approach is very similar to the short-time Fourier signal analysis in time-frequency domain where we track how the frequency content of the signal is changing in time, which is of particular interest in the case of non-stationar signals. The algorithm allows signal segmentation to be performed using rectangular windows of arbitrary duration, with or without overlapping. It should be noted that the application of this technique in signal analysis is a computationally very demanding process. Namely, it is necessary to calculate the fourth-order cumulant, see Eq. 5, of each time interval. Depending on the specific need, the number of time intervals can be relatively large, especially if the technique of overlapping time intervals is used.

The correctness of this concept in signal analysis has been demonstrated in many cases. Using this methodology, signals generated in various fields such as acoustics, hydroacoustics, seismics and others were analyzed. What's more, there are numerous situations when the application of this method is the only possible and effective one. With the introduction of the algorithm whose flow chart is shown in the Fig. 1, a practically new domain for signal analysis has been opened, the statistical domain, which is not behind the time and frequency domains.

### 3. EXAMLES OF STATISTICAL FILTER APPLICATION

The application of the method of statistical filtering of the signal using the filter described in previous section, which is based on the application of the fourth-order cumulants, has proven to be effective in removing ambient and measurement noise in many cases. If we assume that ambient and measurement noise have the Gaussian distribution, then by applying this method, these noises are completely removed from the signal. The Signal-to-Noise-Ratio (SNR) has become maximal. Such a result of maximizing the SNR is almost impossible to achieve by classic filtering of the signal in the time and frequency domain.

#### 3.1. Examples in acoustics

In the examples that follows, statistical filtering of a very noisy acoustic signals, originated firing from a 122 mm cannon at the test range, are shown, see Figs. 2-4.

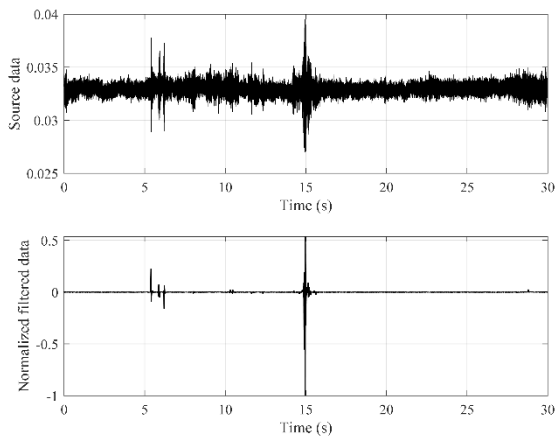


**Figure 2.** Source signal is acoustic, which originates from firing of a 122 mm cannon at a distance of about 3 km from measuring microphone.

By looking at the diagrams in the Fig.2, it can be concluded that ambient and measurement noise are completely suppressed. The same acoustic signal was also analyzed using the wavelet transform. After detailed checks, it was shown that the Debauchies coefficient of the seventh order,  $D_7$ , most closely describes the recorded acoustic signal, see Fig. 3.

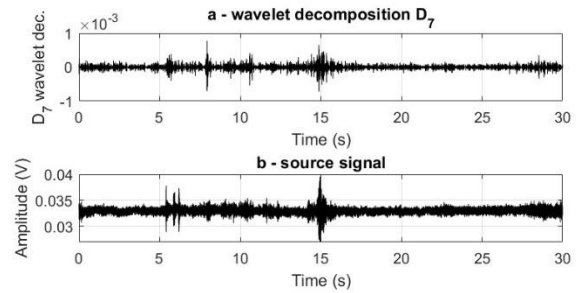


**Figure 3.** The Debauchies coefficient,  $D_7$ , of the same source signal from Fig. 2.

Based on the analysis of the results shown in Figs. 2 and 3, it can be concluded that the wavelet transformation did not significantly contribute to the noise reduction of initial acoustic signal.

In order to additionally illustrate the potential of the statistical filter in suppressing noise in acoustic signals, the results of noise suppression of a similar acoustic signal, but significantly more noisy than in the previous example is presented in Fig. 4.

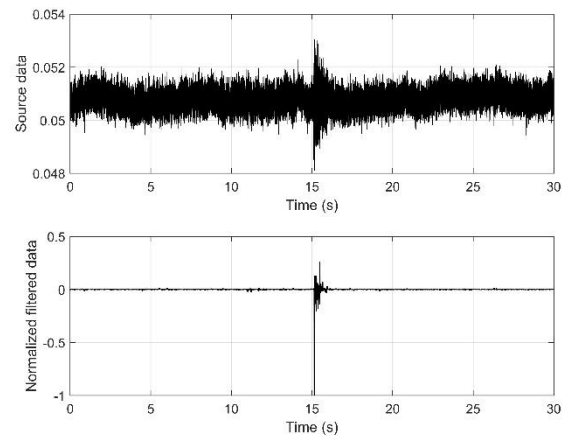


**Figure 4.** Very noisy acoustic signal produced by firing of a 122 mm cannon at the test range, diagram up, and statistically filtered signal, diagram down.

The diagrams in Fig. 4 perhaps best illustrate the power and potential of this method, bearing in mind that ambient and measurement noise are completely removed.

Finally, in Fig. 5, the source acoustic signal is shown, with good SNR even without additional filtering. But it is undoubtedly that the additional filtering of the signal made the SNR excellent – maximum.

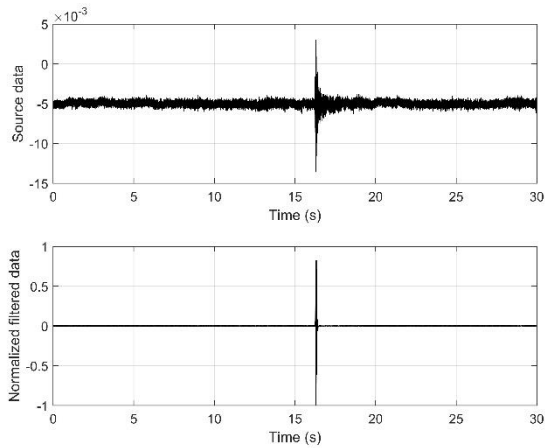


**Figure 5.** Relatively good acoustic source signal after filtration became excellent with maximum SNR.

The application of the statistical filtering method is confirmed in this case as well. Relatively good SNR of the source signal itself, became excellent, bearing in mind that all noise was completely suppressed, see Fig 5.

All acoustic signals were recorded using the microphones that were placed on the test range at the relatively large distances of several hundred meters from each other. The cannon, source of the acoustic signal, was located several kilometers from the measuring microphones.

### 3.2. Hydroacoustic data

Hydroacoustic data were downloaded from the internet [9], see Fig. 6. The launch of the torpedo was recorded using a hydrophone. The hydroacoustic signal that was recorded on that occasion was analyzed in two ways, the first, using the described statistical filtering method, and the second, method based on wavelet transformation.

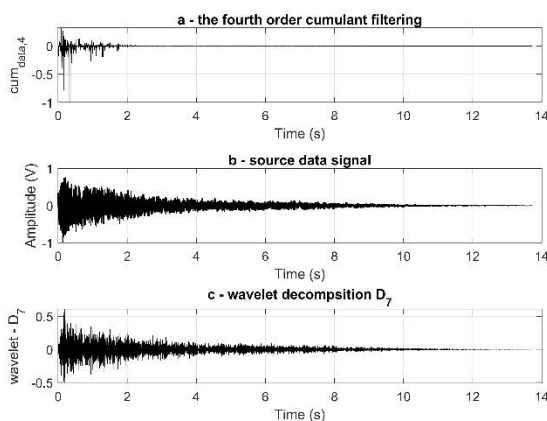


**Figure 6.** The noise of the torpedo during firing. a – filtered data, b – source signal, and c – wavelet decomposition,  $D_7$ .

By looking at the obtained result, see diagram a, it can be concluded that by applying the method of statistical filtering from the generated hydroacoustic noise, it is possible to significantly reduce the influence of reverberation, which is not possible with the application of wavelet transformation.

Results of the analysis, using a statistical filter, of the radiated hydroacoustic noise of the large ship, see Fig. 7.

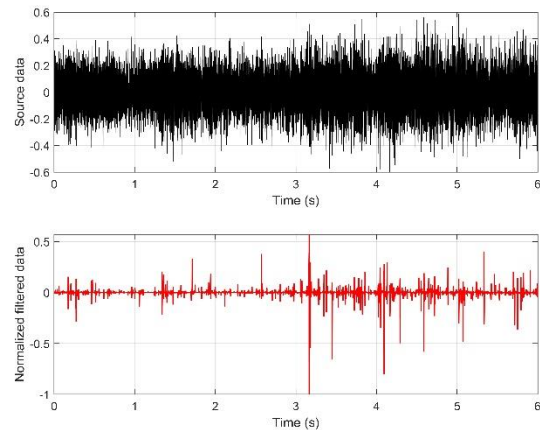


**Figure 7.** Radiated hydroacoustic noise of the large ship, speed 10 kn, and hydrophone, B&K 8104, was placed at 2 m under sea surface, and filtered data – diagram down.

Based on the conducted analysis, it can be concluded that the ship transfers a significant part of the propulsion energy into the water environment, creating significant underwater noise.

The next example, see the Fig. 8, refers to the movement of much quieter ship, with the same movement parameters: speed, trajectory and position of the measuring hydrophone.

Based on these two examples, it can be concluded that non-linear processes occur in the water environment as the result of the release of propulsion energy, and based on the amplitudes of the filter data, hypotheses can be derived about their size, propulsion system, and/or their class.

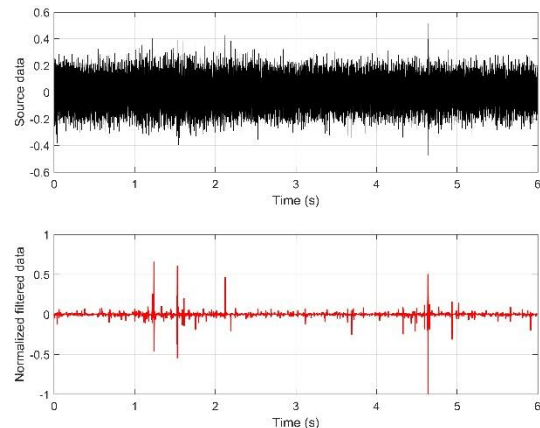


**Figure 8.** Radiated hydroacoustic noise of the small ship (diagram up), and filtered data (diagram down).

It should be pointed out that the noise recordings were not conducted in open sea conditions and far from human activities, but near the coast where human activities are very pronounced. This can explain the appearance of several very pronounced local maxima, especially in the case of a smaller and quieter ship, see Fig. 8.

### 3.3. Seismic data

Seismic data, with a lot of measurement noise, were taken by courtesy of the German company Sonicon GbR, Tübingen, in order to test the possibilities of the statistical filter.

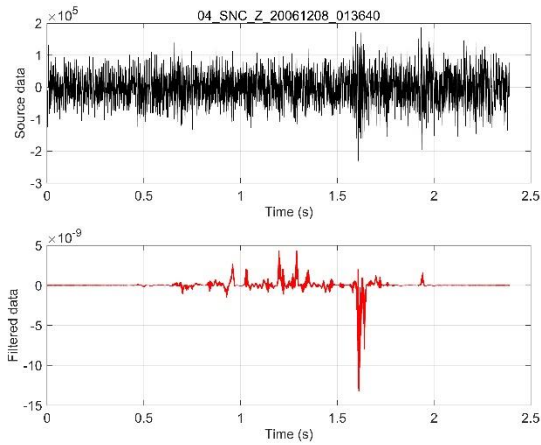


**Figure 9.** Statistical filtering of the very noisy seismic data, obtained by courtesy of Sonicon GbR, Tübingen. Source data diagram up, and filtered data diagram down.

The measurement noise is completely suppressed, which was confirmed by the representative of this German company.

## 4. CONCLUSION

The paper gives a detailed description of the working principle of the statistical filter, which is based on the application of the fourth-order cumulants. Its application has enabled the maximization of the SNR in numerous, or in all cases of the analyzed data. Characteristic signals were analyzed in numerous areas, starting with acoustics, hydroacoustics and seismic.

The proposed concept of a statistical filtering, allows introducing the statistical domain as an equal one in addition to the time and frequency domain in signal analysis, taking into account the obtained results.

In addition to the fact that the practical application of the statistical filter is computationally demanding, it can be said that its application is future, bearing in mind the

intensive development of computer technology.

Future work should provide an answer to the question of whether there is, and if so, what is the relationship between frequency and statistical domain.

## References

- [1] Jerry M. Mendel: *Tutorial on Higher Order Statistics (Spectra) in Signal Processing and System Theory: Theoretical Results and Some Applications*, PROCEEDINGS OF THE IEEE, VOL. 79, NO. 3, March 1991, pp 278-305.
- [2] Athina P. Petropulu: *Higher-Order Spectral Analysis*, Drexel University, @1999 by CRC Press LLC.
- [3] Miodrag Vračar and Stevo Vračar: *Detection of Direct Wave Front of Impulse Acoustic Events Using Higher-Order Statistical Methods*, 9<sup>th</sup> INTERNATIONALE SCIENTIFIC CONFERENCE ON DEFENSE TECHNOLOGIES OTEH 2020, Belgrade, Serbia, 15-16 October 2020, pp 227-226.
- [4] Miodrag Vračar and Stevo Vračar: *Optimization of the Algorithm for Estimating Time of Arrival of the Acoustic Wave Front by Choosing the Signal Filtering Method*, 10<sup>th</sup> INTERNATIONALE SCIENTIFIC CONFERENCE ON DEFENSE TECHNOLOGIES OTEH 2022, Belgrade, Serbia, 13-14 October 2022, pp 205-209.
- [5] Miodrag Vračar and Stevo Vračar: *On-Site Estimation of the Arrival Time of an Acoustic, Seismic or Hydroacoustic Strongly Distorted Signals*, SnT2023 CTBTO Scientific and technology conference, HOFBURG PALACE – Vienna and Online, 19-23 June, 2023, poster presentation P3.5-055.
- [6] Edited by Douglas F. Elliot: *Handbook of Digital Signal Processing Engineering Applications*, Academic Press Inc., Haricourt Brace Jovanovich, 1997.
- [7] Steve Winder: *Analog and Digital Filter Design*, Newnes, Second Edition, 2002.
- [8] Stéphane Mallat: *A WAVELET TOUR OF SIGNAL PROCESSING*, Academic Press, Second Edition, 1999.
- [9] <https://www.zapsplat/sound-effect-category/war-and-weapons>, 19. 05. 2021.



# DESIGN OF A SERVO MECHANISM FOR CONTROLLING MISSILE FINS IN PITCH AND YAW PLANES

NEBOJŠA JOVIČIĆ

Military Technical Institute, Belgrade, [nesapz@yahoo.com](mailto:nesapz@yahoo.com)

ALEKSANDAR STEFANOVIĆ

Military Technical Institute, Belgrade, [stefanovicva@outlook.com](mailto:stefanovicva@outlook.com)

MARIJANA STOJANOVIĆ

Military Technical Institute, Belgrade, [marijana552.17@gmail.com](mailto:marijana552.17@gmail.com)

MILOŠ PAVIĆ

Military Technical Institute, Belgrade, [meelos.pavic@gmail.com](mailto:meelos.pavic@gmail.com)

**Abstract:** This paper explores the design and implementation of a servo mechanism utilizing DC electromotors for control of missile fin position. This research is focused on the analysis and optimization of DC electromotors to enhance the performance of servo systems in terms of speed, torque, accuracy and efficiency. Combination of theoretical approaches and experimental test were performed to validate the proposed mechanical construction of a servo mechanism.

**Keywords:** mechanical design, servo mechanism, brushed DC motor, missile fin control surfaces.

## 1. INTRODUCTION

The missile control servo system plays a crucial role in the guidance, navigation, and stabilization of missiles. It is responsible for precisely directing the missile towards its target, compensating for external factors like wind, and ensuring the missile maintains its intended trajectory.

Missile control systems vary significantly depending on the type of missile (air-to-ground, ground-to-air, anti-ship, etc.) and the level of sophistication required for the mission. They integrate sensors, algorithms, actuators, and communication systems to ensure the missile reaches its target accurately and efficiently.

Air-to-ground missile control systems play a key role in ensuring precise delivery of the missile to its intended ground target. The choice of actuator technology within servo systems significantly impacts missile performance and overall efficiency.

The choice of actuator technology depends on factors such as missile size, intended mission, performance requirements, weight constraints, and cost. Advances in materials discovery and highly sophisticated engineering are increasingly influencing the development of new actuator technologies that provide improved performance characteristics for air-to-ground missile servo systems.

In summary, electromechanical actuators (EMA) are devices that convert electrical energy into mechanical movement. They play a significant role in various applications including aviation, robotics, automotive systems, and industrial mechanics. In the context of air-to-ground missile servo systems, EMAs are used to control missile flight surfaces such as ailerons or canards

to achieve precise maneuvering and guidance.

EMAs consist of an electric motor that generates torque, gearbox (if necessary), and a mechanical linkage system that may involve a combination of gears, levers, and other mechanical components in that way to translate the motor's rotational movement into linear or rotational movement of the control surface.

## 2. DC MOTOR SELECTION

For a successful selection of the motor, it is necessary to meet the technical requirements, which will be presented in the Tab. 1

Maximal angular velocity of canards	$\theta_{max} = 3 \text{ rad/s}$
Maximal torque	$M_{hmax} = 15 \text{ Nm}$
Maximal deflection angle	$\theta_{max} = \pm 25^\circ$

**Table 1.** Technical requirements

Following the above mentioned requirements and operating conditions in terms of supply voltage and nominal current, it is decided to use Maxon assembly with number 715337 where is included: 1) brushed dc motor (268214), 2) ball bearing screw drive (363970) with reduction 1:1, maximal feed force continuous 386 N, maximal feed velocity 133 mm/s and 3) Encoder MR, Type L, 256 CPT, 3 channels, with line driver.

Main characteristics of the dc motor (268214) are: Nominal voltage 24V, Nominal current 3.47 A, Nominal speed 8050 rpm, Nominal torque 0.856 Nm, Stall torque 1.02Nm.

Eq.1 and Eq.2 represent the gear ratios under the conditions of achieving maximum torque on the steering shaft and achieving maximum angular deflection speed, respectively.

$$i_{Mmax} \geq \frac{M_{hmax}}{\eta_G M_{mmax}} = \frac{15}{0.94 * 1.02} = 15.64 \quad (1)$$

$$i_{\omega max} \leq \frac{\omega_{mmax}}{\theta_{max}} = \frac{843}{3} = 281 \quad (2)$$

Demanded total load torque (including static and dynamic load) for our application is 15 Nm. Distance between axis of rotation and axis of motor in our case is 40 mm, so maximal axial force is 375 N, given in Eq. (3).

$$F = \frac{M}{r} = \frac{15}{0.04} = 375N \quad (3)$$

Eq.4 and Eq.5 represent the torque on the steering shaft and torque of the motor in arbitrary position, respectively

$$M_h = Fr \quad (4)$$

$$M_m = \frac{Fp\eta}{2\pi} \quad (5)$$

Torque ratio in arbitrary position is given by Eq.6.

$$i_M = \frac{M_h}{M_m} = \frac{2\pi Fr}{Fp\eta} = \frac{2\pi r}{p\eta} = 136 \quad (6)$$

where  $p = 2 \text{ mm}$  is thread pitch and  $\eta = 94\%$  is maximum efficiency of screw drive.

From Eq.6 can be concluded that condition (1) is satisfied.

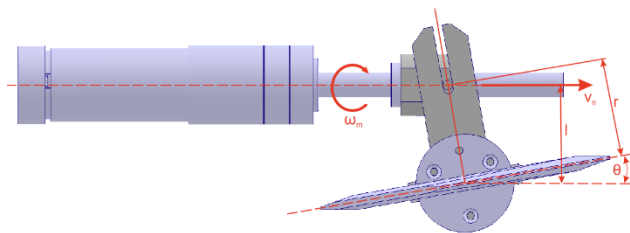


Figure 1. DC motor with its linkage system

Second demand is that system must satisfy angular velocity of 3rad/s.

Pitch thread is denoted as  $p$ , axial velocity of nut is  $V_n$ , mean thread diameter  $2r_n$ .

Therefore

$$\frac{V_n}{r_n \omega_m} = \tan\alpha = \frac{p}{2\pi r_n} \quad (7)$$

$$V_n = \frac{p\omega_m}{2\pi} \quad (8)$$

From Fig.1 it can be seen

$$V_n \cos\theta = r\dot{\theta} \quad (9)$$

$$\frac{p\omega_m}{2\pi} \cos\theta = r\dot{\theta} \quad (10)$$

$$\dot{\theta} = \frac{p\cos\theta}{2\pi r} \omega_m \quad (11)$$

$$\frac{\omega_{canard}}{\omega_m} = \frac{\dot{\theta}}{\omega_m} \quad (12)$$

$$i_{\omega} = \frac{\omega_{canard}}{\omega_m} = \frac{p\cos\theta}{2\pi r} = 125 \quad (13)$$

Eq.13 represents the angular velocity ratio in arbitrary position where can be seen that condition (2) is also satisfied.

### 3.SERVO SYSTEM DESIGN AND ANALYSIS

For the development of an air-to-ground guided missile, a servo system was developed for steering the missile along the pitch and yaw channels.

The simplified explanation of the servo mechanism's operation shown on Fig.1 involves a DC motor delivering torque through the rotation of a threaded spindle. This causes linear motion of the nut, which is transmitted through a system of levers to rotate the shaft to which the control surface, in our case the rudder, is attached. The Fig.2 to Fig.5 will illustrate the initial and final positions of the servo mechanism for a  $25^\circ$  angle in the positive direction.

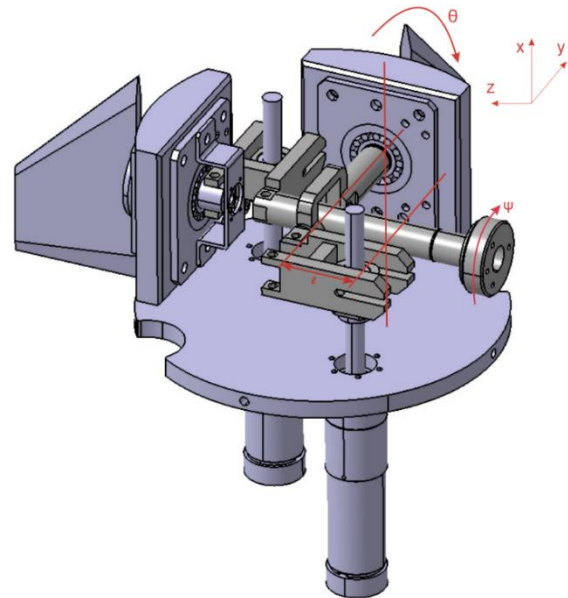


Figure 2. Air-to Surface missile Servo

For the displayed position of the servo mechanism in the image, we will adopt a coordinate system where the x-axis is along the direction of missile movement, the y-axis is the axis around which pitching occurs, and the z-axis is for yawing. Positive directions for rotations around these

axes will follow the right-hand rule convention. Both direct current motors with threaded spindles and nuts drive both axes and are positioned along the x-axis, corresponding to the missile's direction of travel. The initial or zero position of the servo mechanism is depicted in the image, where all angles and linear displacements are zero.

The servo analysis is divided into two parts for easier explanation.

## 1. Kinematics

Missile servo system kinematics involves the study of motion and geometry concerning the control surfaces of a missile. It analyzes how actuators, often driven by DC motors and threaded spindles, translate rotational motion into linear movement of control surfaces like fins or canards. By understanding this kinematics, engineers ensure precise adjustments of the missile's trajectory for accurate targeting and maneuverability during flight, enhancing overall operational effectiveness and mission success rates.

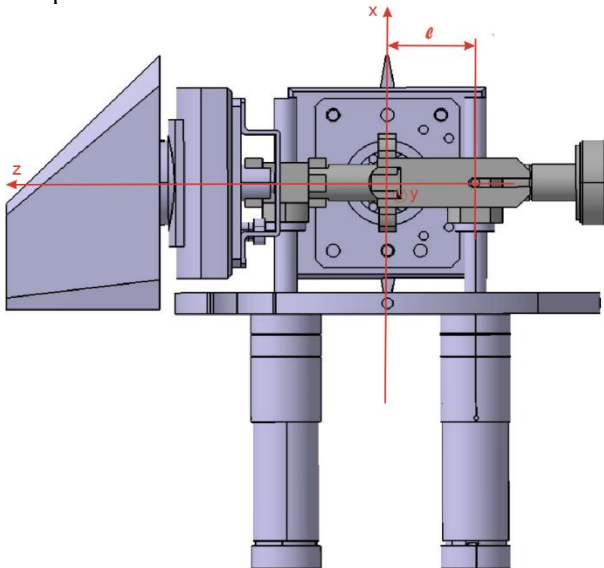


Figure 3. Servo initial position

The first fundamental kinematic equation of motion for a servo - mechanism shown on Fig.3 is:

$$x = l \tan \theta \quad (14)$$

The Eq.14 describes the relationship between the vertical linear displacement of the nut, marked in Fig.3 as x, and the rotational angle of the shaft with the fin, denoted as  $\theta$ .

$$x = l \tan \theta \quad \frac{d}{dt} \quad (15)$$

$$\frac{dx}{dt} = l \frac{d(\tan \theta)}{d\theta} \frac{d\theta}{dt} \quad (16)$$

$$x = l \frac{d(\tan \theta)}{d\theta} \frac{d\theta}{dt} \quad (17)$$

$$x = l \frac{1}{\cos^2 \theta} \dot{\theta} \quad (18)$$

$$\dot{\theta} = \frac{\cos^2 \theta}{l} \dot{x} \quad (19)$$

By finding the first derivative of the previous equation, it is obtained the expression that gives us the dependence of the angular velocity  $\dot{\theta}$  of the shaft on the linear velocity of the nut  $\dot{x}$ .

The dependence between the angular velocity  $\dot{\theta}$  and the linear velocity  $\dot{x}$  is indeed nonlinear. This nonlinearity arises because  $\dot{\theta}$  depends on the cosine squared of the angle  $\theta$ , which varies with the position of the nut  $x$ . As  $\theta$  changes, the relationship between  $\dot{\theta}$  and  $\dot{x}$  is not a simple linear proportionality but rather a function that involves trigonometric terms and the mechanical linkage geometry. In practical terms, this means that changes in the linear velocity  $\dot{x}$  do not result in directly proportional changes in the angular velocity  $\dot{\theta}$ . The exact relationship depends on the specific geometry and kinematics of the servo mechanism, including factors such as the length  $l$  and the angle  $\theta$  at any given time.

Using the equation, we obtained earlier:

$$\dot{\theta} = \frac{\cos^2 \theta \dot{x}}{l} \quad (20)$$

Where  $l = 40$  mm and  $\dot{x} = 133$  mm/s, for the given range from  $-25^\circ$  to  $+25^\circ$ , the angular velocity  $\dot{\theta}$  will be approximately 2.7 rad/s in both cases, with different signs due to the opposite direction of the angle  $\theta$ , and for 0 degree the value of angular velocity will be around 3.3 rad/s.

The second fundamental kinematic equation of motion is Eq.21, where  $r$  represents the shortest distance from the point where the force acts to the axis of rotation of the shaft. In this context,  $r$  represents the lever arm of the force.

$$r = \frac{l}{\cos \theta} \quad (21)$$

By taking the first derivative with respect to time, we obtain the following expression:

$$\frac{dr}{dt} = \frac{d}{dt} \left( \frac{l}{\cos \theta} \right) \quad (22)$$

$$\frac{dr}{dt} = l \frac{d}{dt} \left( \frac{1}{\cos \theta} \right) \quad (23)$$

$$\frac{dr}{dt} = l \left( \frac{0 * \cos \theta - 1 * (-\sin \theta)}{\cos^2 \theta} \right) \quad (24)$$

$$\frac{dr}{dt} = l \frac{\sin^2 \theta}{\cos^2 \theta} \frac{d\theta}{dt} \quad (25)$$

$$\dot{r} = l \frac{\sin \theta}{\cos^2 \theta} \dot{\theta} \quad (26)$$

which Eq.26 represents the relative velocity of the crankshaft along the fork groove.

$$\Delta r = l \frac{1 - \cos\theta}{\cos\theta} \tag{27}$$

Eq.27 represents distance of crankshaft from initial position to new position depended of angle  $\theta$  along the fork groove.

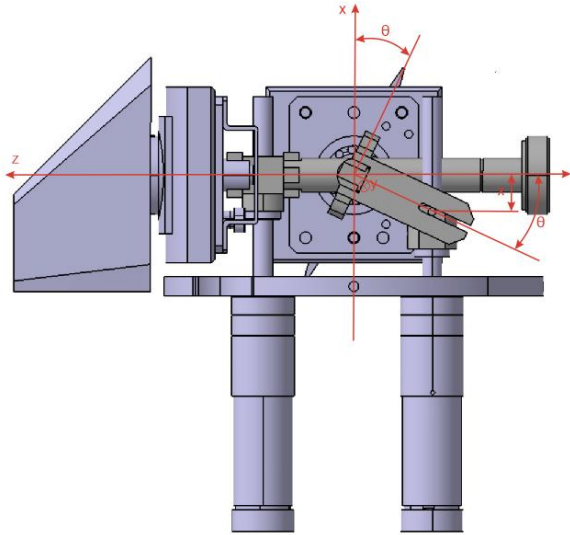


Figure 4. Angles and displacements on servo with aileron deflection of 25°

**2.Dynamics**

Missile servo system dynamics examines the complex interactions between forces, motion, and control inputs within the system. It focuses on how the servo actuators respond to external commands, environmental factors, and the missile's own aerodynamic forces during flight.

Engineers analyze these dynamics to optimize responsiveness, stability, and accuracy of the missile's control surfaces, ensuring effective navigation and targeting capabilities in varying operational conditions.

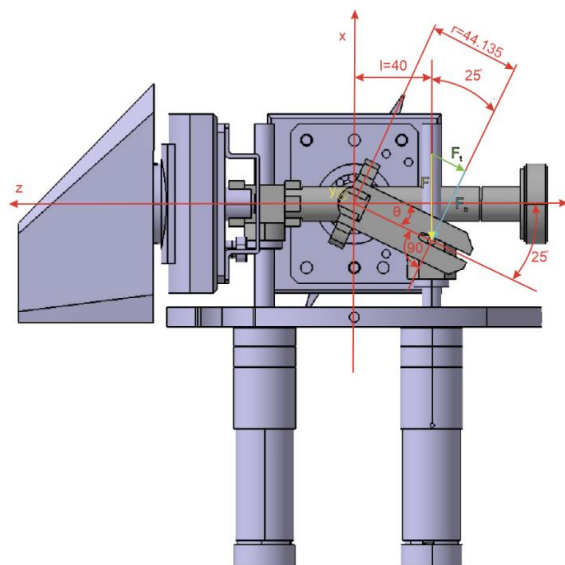


Figure 5. Forces applied on servo with aileron deflection of 25°

In the initial position, the torque equation can be written in the form of

$$M = Fl \tag{28}$$

It is interesting to notice that the torque remains the same regardless of the position of the mechanism, which is also expressed by the equation

$$M = F_N r = F \cos\theta \frac{l}{\cos\theta} = Fl \tag{29}$$

**4.CONCLUSION**

This study has investigated the design and implementation of a servo mechanism utilizing DC electromotors for the precise control of missile fin positions. Through a combination of theoretical analysis and experimental validation, we have demonstrated significant advancements in optimizing DC electromotors to achieve enhanced performance metrics such as speed, torque, accuracy, and efficiency. The findings underscore the effectiveness of our mechanical design in improving servo system capabilities, particularly in critical applications like missile fin control surfaces. Future research could explore further refinements in motor design and control algorithms to continually advance the performance and reliability of servo mechanisms in demanding operational environments.

**References**

- [1] Smith, J., Johnson, A., Brown, C., *Design and implementation of a servo system using DC motors for UAV control*, Proceedings of the IEEE International Conference on Robotics and Automation (ICRA)
- [2] Lee, S., Kim, H., Park, K., *Performance optimization of servo mechanisms using brushed DC motors*, Transactions of the Society of Mechanical Engineers, Series C
- [3] Chen, L., Wang, Q., Zhang, Y., *Design and control of a servo system using brushless DC motors for robotic manipulators*, IEEE Transactions on Robotics
- [4] Garcia, M., Martinez, P., *Modeling and control of a servo system with DC motors for precision positioning*, Control Engineering Practice
- [5] Wang, J., Li, S., Zhang, G., *Adaptive control of servo systems using DC motors in unmanned ground vehicles*, Journal of Intelligent & Robotic Systems





## TESTING THE ROLL STABILIZATION OF A SUPERSONIC SURFACE-TO-AIR GUIDED MISSILE

MARIJANA STOJANOVIĆ

Military Technical Institute, Belgrade, [marijana552.17@gmail.com](mailto:marijana552.17@gmail.com)

ALEKSANDAR STEFANOVIĆ

Military Technical Institute, Belgrade, [stefanovicva@outlook.com](mailto:stefanovicva@outlook.com)

NEBOJŠA JOVIČIĆ

Military Technical Institute, Belgrade, [nesapz@yahoo.com](mailto:nesapz@yahoo.com)

IVAN MARIĆ

Military Technical Institute, Belgrade, [ivanmaric094@gmail.com](mailto:ivanmaric094@gmail.com)

**Abstract:** This research examines the crucial role of roll stabilization in enhancing the performance of supersonic surface-to-air guided missiles, analyzing roll autopilot through variety of parameters in different phases of flight. Through systematic testing of missile models in wind tunnel tests, the optimal values are obtained. These values will be used in continuation of research project.

**Keywords:** missile, roll stabilization, supersonic, surface-to-air, parameters

### Nomenclature

$c$  - speed of sound

$C_i^\delta$  - The roll coefficient depending on the roll attitude

$C_i^p$  - The roll coefficient depending on the roll angular velocity

$G_r$  - velocity gyroscope

$K$  - error gain of roll angle

$K_\phi$  - gain of the roll transfer function

$l$  - missile length

$m$  - missile mass

$r_x$  - radius of inertia of the missile

$S_{ref}$  - referent surface

$T_\phi$  - time constant of the roll transfer function

$T_a$  - actuator time constant

$V$  - missile speed

$\rho$  - air density

$\omega_{n\phi d}$  - undamped natural frequency

$\zeta_{n\phi d}$  - damping ratio

$\phi$  - roll angle

$\phi_d$  - desired roll angle

### 1. INTRODUCTION

The development and deployment of supersonic surface-to-air guided missiles represent a significant advancement in modern defense capabilities. These missiles are designed to intercept and neutralize high-speed aerial threats, requiring exceptional precision and stability throughout their flight. One critical aspect of ensuring this

precision is the roll stabilization of the missile, which is essential for maintaining a stable and controlled trajectory.

Roll stabilization refers to the missile's ability to maintain its longitudinal axis alignment, preventing unwanted rotations around this axis that could destabilize its flight path. Achieving effective roll stabilization in a supersonic environment poses unique challenges due to the high speeds and dynamic aerodynamic forces involved. Therefore, rigorous testing of the missile model's roll stabilization is crucial to validate and refine the missile's design and control systems.

### 2. ROLL AUTOPILOT MODEL

The missile roll autopilot block diagram, Fig.1, represents the closed-loop control system employed to regulate the roll angle of a missile. The system integrates sensors for roll rate detection, a control algorithm for processing error signals, and actuators for applying corrective forces. A widely used roll attitude autopilot for missile roll angle control is a two-loop roll autopilot with the roll rate feedback in the inner loop and the roll angle feedback in the outer loop [1]. By dynamically adjusting the missile's control surfaces, the autopilot system ensures optimal roll stabilization and precise trajectory control, enhancing the missile's aerodynamic performance and accuracy [2].

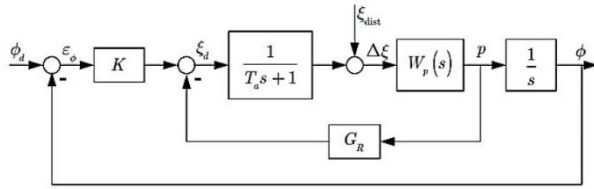


**Figure 1.** Block diagram of missile roll autopilot  
Missile transfer function:

$$W_p(s) = \frac{K_\phi}{T_\phi s + 1} \quad (2.1)$$

For the given (desired) values of undamped natural frequency  $\omega_{n\phi d}$  and autopilot damping ratio  $\zeta_{n\phi d}$ , the roll autopilot gains are [3]:

$$K = \frac{\omega_{n\phi d}^2 T_\phi}{K_\phi}; G_r = -\frac{1}{K_\phi} + \frac{2\zeta_{n\phi d} K}{\omega_{n\phi d}} \quad (2.2)$$

System transfer function:

$$\frac{\phi(s)}{\phi_d(s)} = \frac{KK_\phi}{T_a T_\phi s^3 + (T_a + T_\phi)s^2 + (1 + G_r K_\phi)s + KK_\phi} \quad (2.3)$$

Characteristic equation:

$$T_a T_\phi s^3 + (T_a + T_\phi)s^2 + (1 + G_r K_\phi)s + KK_\phi = 0 \quad (2.4)$$

The stability condition according to the Routh-Hurwitz criterion, for a third-order polynomial, is  $a_i > 0$  and  $a_2 a_1 > a_3 a_0$ . Since all coefficients of the polynomial are positive, we have:

$$K < \frac{(T_a + T_\phi)(1 + G_r K_\phi)}{K_\phi T_a T_\phi} = K_{lim} \quad (2.5)$$

The dynamics of the starter destabilize the roll autopilot, so it is necessary to perform stability verification according to the equation.

### 3. PARAMETER EVALUATION

Parameter evaluation for missile roll autopilot systems is crucial in ensuring optimal performance and stability during flight. This process involves rigorous analysis and testing to determine the most effective configuration of control parameters, thereby enhancing the system's ability to maintain desired trajectory and maneuverability under varying operational conditions.

Based on initial conditions in following table and equations (3.1) to (3.7)

$c = 340m/s$	$\rho = 1.225kgm^3$	$S_{ref} = 0.01287m^2$
$l = 0.128m$	$m = 26.75kg$	$I_x = 0.059kgm^2$
$C_l^{\delta} = -1.1420$	$C_l^p = -4.593$	$T_a = 0.1$

**Table 1.** Initial conditions

Moment of inertia with respect to x-axis

$$I_x = m * r_x^2 \quad (3.1)$$

Velocity of missile

$$V = c * M \quad (3.2)$$

Dynamic pressure

$$Q = \frac{1}{2} V^2 \rho \quad (3.3)$$

Rolling deviation coefficient

$$l_\xi = \frac{(Q * S_{ref} * C_l^{\delta})}{I_x} \quad (3.4)$$

Damping coefficient

$$l_p = \frac{(Q * S_{ref} * C_l^p)}{I_x * V} \quad (3.5)$$

Gain of the roll transfer function

$$K_\phi = -1 * \frac{l_\xi}{l_p} \quad (3.6)$$

Time constant of the roll transfer function

$$T_\phi = -\frac{1}{l_p} \quad (3.7)$$

the values of  $K$  and  $G_r$  for missile velocity at a speed of

$0.4Ma$  and at a speed of  $1.5Ma$  were obtained and are

shown in Tab.2.

0.4M, $\zeta=0.7$	$\omega$	$K_{lim}$	$K$	$G_r$
	6	0.2643	0.0997	0.0195
	10	0.4406	0.2768	0.0350
	14	0.6168	0.5426	0.0505
1.5M, $\zeta=0.7$	w	$K_{lim}$	$K$	$G_r$
	6	0.0250	0.0071	0.00064412
	10	0.0417	0.0197	0.0017
	14	0.0584	0.0386	0.0028

**Table 2.** The obtained values of the gain margin, gain  $K$  and  $G_r$  for  $\zeta = 0.7$  and different frequencies.

### 4. RESULT

In this section, we present the results of our research into the performance and effectiveness of the missile roll autopilot system under various operational scenarios. Through comprehensive analysis and experimentation, we aimed to provide insights into the system's ability to maintain stability, precision, and maneuverability during flight. Our findings encompass the evaluation of key parameters, their impact on performance metrics such as roll rate control and trajectory deviation, and comparisons between wind tunnel and field testing. These results are essential for advancing the understanding and optimization of missile autopilot systems, contributing to the enhancement of their reliability and operational effectiveness in aerospace applications.

The missile was tested in two phases in the trisonic T-38 wind tunnel, Fig.2, at a speed of  $0.4Ma$  and at a speed of  $1.5Ma$ . In both cases, the missile's roll angle, desired angle, and the angle error were observed for different autopilot parameters, specifically the values of the gains  $K$  and  $G_r$ . Regarding the test at a speed of  $0.4Ma$ , the parameters adopted for this test are given in Tab.3, and the results are shown in Fig.3 and Fig.4.



Figure 2. Missile in trisonic T38 wind tunnel

Table 3. Wind tunnel roll autopilot parameters of  $K$  and  $Gr$  for testing at  $0.4Ma$

$K$	$G_r$	$\alpha_{12} [^\circ]$
0.1	0.02	0
0.2	0.04	45
0.5	0.1	0

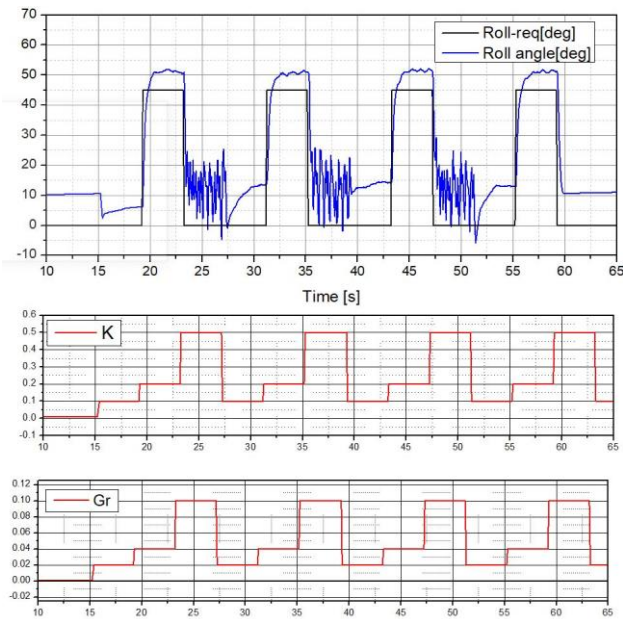


Figure 3. Desired and actual missile roll angle when testing at a speed of  $0.4Ma$

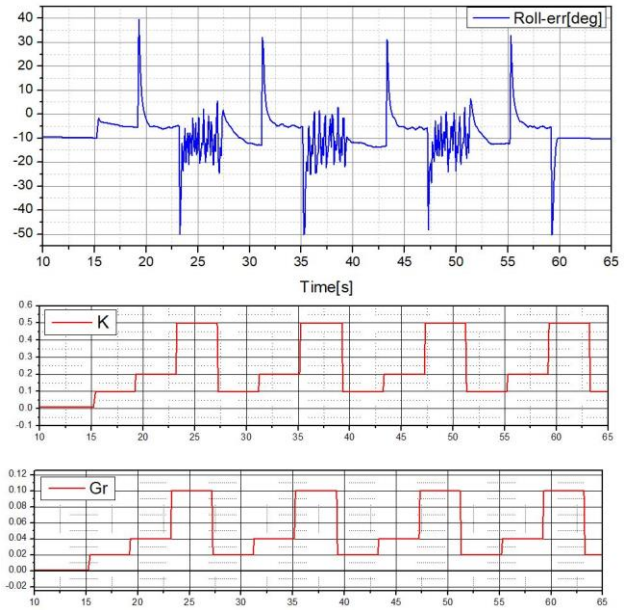


Figure 4. Roll error for different values of  $K$  and  $Gr$  when testing at a speed of  $0.4Ma$

From the Fig.3 and Fig.4 it can be seen for the gain values  $K = 0.5$  and  $Gr = 0.1$ , the system exhibits significant oscillations, whereas for  $K = 0.1$ ,  $Gr = 0.02$  and  $K = 0.2$ ,  $Gr=0.04$ , the rolling is stabilized. Additionally, in the case of these two gains, the roll error is smaller than 40, which is beneficial for the missile roll stabilization. Considering that it was necessary to change the motors, we repeated the tests on the missile with new motors, using the same coefficients. The testing was conducted twice to confirm the repeatability of the error.

During the rolling tests at a speed of  $1.5Ma$ , the following values of  $K$  and  $Gr$  were taken as shown in Tab.4. In both cases desired angle changes from  $0^\circ$  to  $45^\circ$  according to the appropriate table.

$K$	$G_r$	$\alpha_{12} [^\circ]$
0.04	0.004	0
0.04	0.004	45
0.02	0.002	0
0.02	0.002	45

Table 4. Wind tunnel autopilot parameters of  $K$  and  $Gr$  for testing at a speed of  $1.5Ma$

From the Fig.5 and Fig.6 it can be seen that the roll error is smaller than 40 for  $K = 0.04$  and  $Gr = 0.004$ , whether the rolling angle is  $0^\circ$  or  $45^\circ$ , which is good for roll stabilization. For  $K = 0.02$  and  $Gr = 0.002$ , the roll error is repeatable at a rolling angle of  $0^\circ$  and there are no oscillations as in the test at a speed of  $0.4Ma$ .

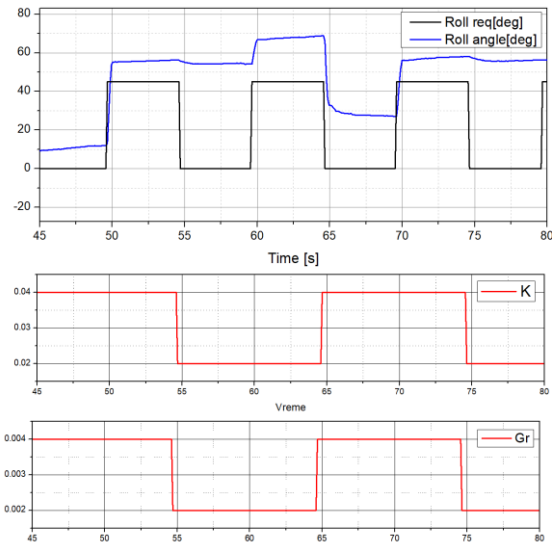


Figure 5. Desired and actual missile roll angle when testing at  $1.5Ma$

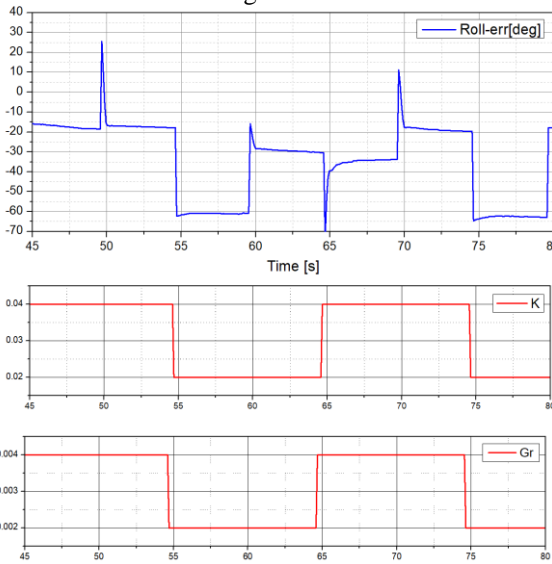


Figure 6. Roll error for different values of  $K$  and  $Gr$  when testing at a speed of  $1.5Ma$

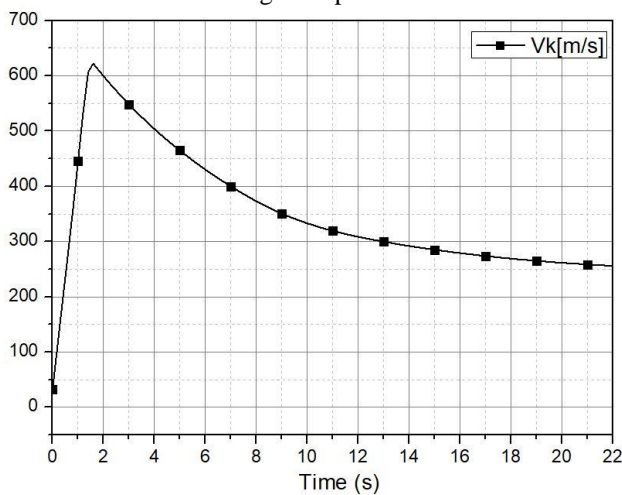


Figure 7. Flight velocity of the missile

After testing rolling at a speed of  $0.4Ma$ , corresponding to the subsonic field, and testing at a speed of  $1.5Ma$  in the supersonic field, parameters  $K$  and  $Gr$  were

determined for flight testing based on wind tunnel testing and according to the missile velocity graph, Fig.7.

Table 5. Flight test autopilot parameters of  $K$  and  $Gr$

Time [s]	$K$	$Gr$	$\alpha_{iz} [^\circ]$
0-10	0.02	0.002	0
10-15	0.04	0.004	0
15-20	0.2	0.04	0
20-25	0.2	0.04	45
25-	0.2	0.04	0

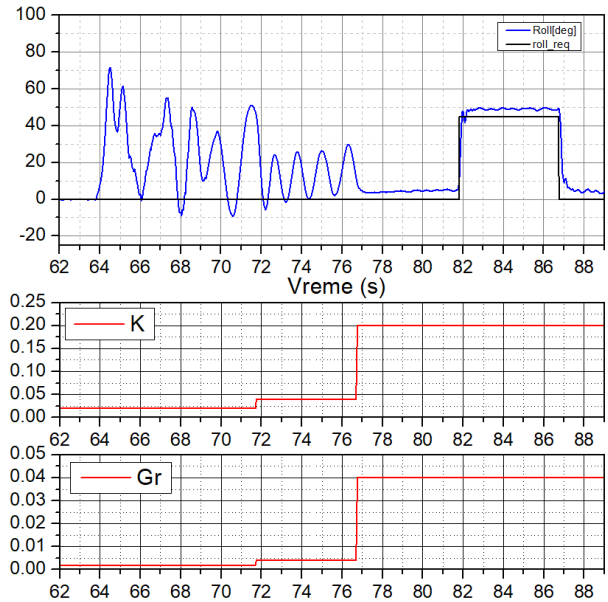


Figure 8. Desired and actual missile roll angle during flight test

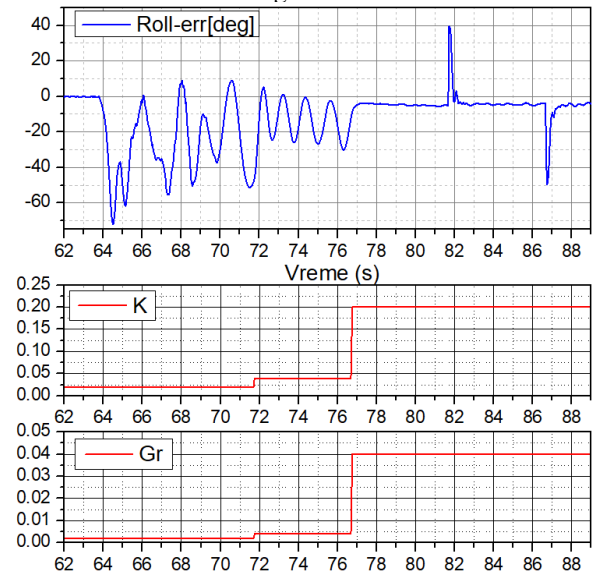


Figure 9. Roll error for different values of  $K$  and  $Gr$  during flight test

From the Fig.8 and Fig.9 it can be seen that after the flight testing, it was determined that during the period when the missile reaches its maximum speed, rolling occurs with a roll error reaching up to  $-60^\circ$ . After leaving the supersonic region, the error decreases and rolling stabilizes.

## 5. CONCLUSION

When the system reaches its maximum speed, it exhibits a static error of  $-60^\circ$  and experiences oscillations. This behavior indicates that the system struggles to maintain stability and accuracy at higher speeds. The oscillations suggest that the control mechanism is not adequately damping the deviations, leading to periodic fluctuations around the desired state.

Conversely, as the speed decreases, the system's performance improves significantly. The static error reduces to around zero, indicating a high level of accuracy and minimal deviation from the desired state. Additionally, the oscillations disappear, showcasing a

stable and well-damped response. This behavior highlights the system's capability to maintain control and accuracy at lower speeds, where the dynamics are less challenging to manage.

## References

- [1] NELSON, R.C.: *Flight Stability and Automatic Control*, Second Edition, McGraw-Hill, Boston, USA, 1998.
- [2] CUK, D., *Vodjenje i Upravljanje*, Masinski fakultet
- [3] MANDIĆ, S., PAVIĆ, M., PAVKOVIĆ, B., IGNJATOVIĆ, M., OCOKOLJIĆ, G.: *Aerodynamic Interceptors Efficiency for Subsonic Missiles Roll Attitude Control*, Military Technical Institute, Belgrade, SERBIA, 2017.

## AZIMUTH ANGLE ERROR DEPENDING OF THE INERTIAL NAVIGATION SYSTEM MOUNTING ERROR

VLADIMIR VUKMIRICA PHD

Military Technical Institute, Belgrade, [vukmiricavladimir@gmail.com](mailto:vukmiricavladimir@gmail.com)

IVANA TRAJKOVSKI MSC

Military Technical Institute, Belgrade, [trajivana@gmail.com](mailto:trajivana@gmail.com)

NADA ASANOVIĆ ENG

Military Technical Institute, Belgrade, [nadaasanovic@mts.rs](mailto:nadaasanovic@mts.rs)

ADRIJANA JOVANOVIĆ MSC

Military Technical Institute, Belgrade, [jovanovicadrijana@gmail.com](mailto:jovanovicadrijana@gmail.com)

**Abstract:** An artillery weapon that uses a precise Inertial Navigation System (INS) for orientation towards the North was considered. For this purpose, the axes of the INS must be aligned with the axes of the artillery weapons. If the axes of the INS are not well aligned with the axes of the weapon or if the axes of the barrel of the weapon is not perpendicular to the axis of elevation, then during the elevation of the axis of the weapon, an azimuth angle error may occur, which depends on the axis misalignments and the value of elevation angle. The result obtained by calculation based on spherical trigonometry and the results obtained by laboratory measurements are presented. The results obtained by calculation were confirmed by measurements. These results fully apply to rocket artillery. The obtained result shows that the minimization of the INS installation offset is needed to reduce the error at larger azimuth angles.

**Keywords:** artillery, azimuth error, rocket artillery, spherical trigonometry

### 1. DESCRIPTION OF THE METHOD

An artillery weapons with built-in Inertial Navigation System (INS) Fig. 1 are considered. The influence of the irregularity of the axis of the INS and the longitudinal axis of the weapon in relation to the axis of elevation on the azimuth values of the INS and weapon at elevation will be considered. The initial assumption is that the longitudinal axis of the INS is parallel to the plane formed by the elevation axis and longitudinal axis of the weapon. When the elevation axis and the longitudinal axis of the weapon are placed in the horizontal plane, the offset of the longitudinal axis of the INS in relation to the longitudinal axis of the weapon is determined.

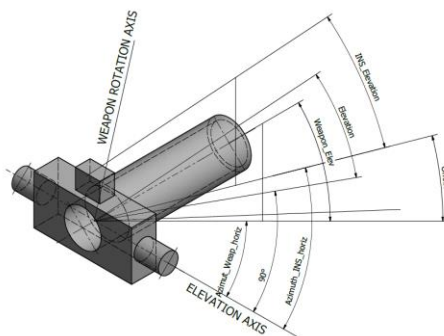


Figure 1 Artillery weapon with INS

The procedure for determining of the offset is as follows:

The rotation axis of the weapon is set to a known coordinate. At approximately the same height as the coordinate of the weapon, several points with known coordinates are determined, the distance from the weapon should be about 1 km and even more to the possibility of observation with rectification telescope. A rectification telescope is placed in the axis of the weapon barrel, which is used to guide the weapon barrel to known points. At each of known points the azimuth shown by the INS is read and the calculated azimuth between the weapon point and the observed point on the ground is noted. The procedure is repeated several times. The offset presents the difference between the azimuth readings of the INS and the azimuth of two known points. It is determined as the mean value of the readings of the measurement results.

If there is nonorthogonality of the longitudinal axis of the weapon or the longitudinal axis of the INS on the elevation axis, then when changing the angle about the elevation axis, the azimuth and elevation of the nonorthogonal axis will change. The equations of the basis which these changes are determined are obtained from spherical trigonometry Fig. 2.

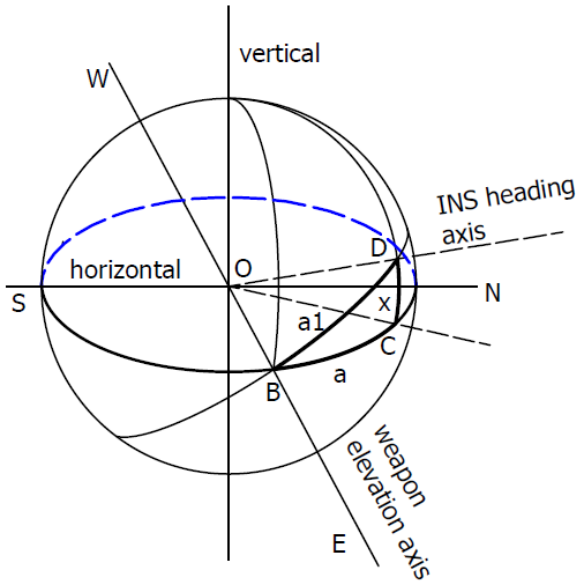


Figure 2 Spherical trigonometry model

On the Fig 2:

- B,C,D spherical angles at vertices B,C,D [1], [2]
- The E-W axis represents the weapon elevation axis
- The spherical angle B represents the angle of rotation about the elevation axis (elevation).
- The spherical angle  $x = \varphi_D$  represents the elevation at the angle a
- The angle  $a_1$  represents the rotation angle about the rotation axis of the weapon
- The angle a represent the horizontal projection of the angle  $a_1$

In the general case, if the coordinate of the points  $B(\lambda_B, \varphi_B)$  and  $D(\lambda_D, \varphi_D)$  are known, then the distance between these points is calculated according to the formula [1]:

$$\cos a_1 = \cos\left(\frac{\pi}{2} - \varphi_B\right) \cos\left(\frac{\pi}{2} - \varphi_D\right) - \sin\left(\frac{\pi}{2} - \varphi_B\right) \sin\left(\frac{\pi}{2} - \varphi_D\right) \cos(\lambda_B - \lambda_D) \tag{1}$$

$$\cos a_1 = \sin \varphi_B \sin \varphi_D - \cos \varphi_B \cos \varphi_D \cos(\lambda_B - \lambda_D) \tag{2}$$

In the special case when  $\varphi_B=0$ ,  $x = \varphi_D$  then:

$$\cos a_1 = \cos \varphi_D \cos(\lambda_B - \lambda_D) \tag{3}$$

For the right-angled spherical triangle ABC:

$$A = a = \lambda_B - \lambda_D \tag{4}$$

$$\cos a_1 = \cos \varphi_D \cos a \tag{3_1}$$

The sine theorem applies to the spherical triangle BCD [1], [2]:

$$\frac{\sin \varphi_D}{\sin B} = \frac{\sin a_1}{\sin C} = \sin a_1 \tag{5}$$

Based on equations (3), (4) and (5) the following calculations is carried out:

$$\sin \varphi_D = \sin a_1 \sin B \tag{6}$$

$$A = a = \arccos\left(\frac{\cos a_1}{\cos \varphi_D}\right) \tag{7}$$

Equation (7) determines the dependence of the azimuth angle on the angle of rotation about the axis of rotation of the weapon, which is the same angle of inclination in relation in relation to the vertical axis.

## 2. EXPERIMENTAL MEASUREMENTS

The INS GEONIX HP of the French manufacturer SAFRAN was used as reference for experimental measurements. The specified INS has declared azimuth determination accuracy of 1 mils ( $1\sigma$ ). Value 1 mils =  $360^\circ/64000$ .

The INS was mounted on a CARCO T-922 two-axis test table in the Inertial Sensors Laboratory of the Military Technical Institute. The longitudinal axis of the INS was set at  $90^\circ$  in relation to the external rotation axis of the test table, which represents the elevation axis of the weapon, and azimuth was measured at elevation  $0^\circ$  and  $\approx 70^\circ$ .

The next measurement was made when the angle of perpendicularity of the longitudinal axis of the INS was misaligned by  $0.62^\circ$  (wich is order of fielt test reults), and the measurement was made in the horizontal plane and at an elevation of  $\approx 70^\circ$ . After that the measurement was performed when the angle of perpendicularity of the longitudinal axis of the INS was misaligned by  $1.0^\circ$ , and the measurement was performed in horizontal plane and at an elevation of  $\approx 70^\circ$ . The obtained measurement results are sown in table 1.

Table 1. Resultsof measurement

Inner axis angle [°]	Outer axis angle [°]	Geonyx roll [°]	Geonyx heading [°]	Geonix pitch [°]	Note
110.86	0.03	0.01	359.99	0.0	Start
		-0.25	359.82	70.36	Outer axis $\approx 70^\circ$
110.78	70.33	-0.03	0.03	70.37	Adjust of axes
	0.03	0.02	0.06	-0.01	Outer axis $= 0^\circ$
110.22	0.03	0.02	0.62	-0.01	Misaligned $0.62^\circ$
	70.33	1.57	1.73	70.54	Outer axis $\approx 70^\circ$
109.85	0.03	0.02	1.00	-0.01	Misaligned $1.0^\circ$
	70.3	2.58	2.80	70.26	Outer axis $\approx 70^\circ$

### 3. ANALITICAL DETERMINATION

On the basis of the equation (7), the change in azimuth was calculated at misalignment of  $0.62^\circ$  and  $1.0^\circ$ . In doing so, it was assumed that the offset of the longitudinal axis of the INS in relation to the longitudinal axis of the weapon is  $0.1^\circ$ . In this way deviation of the longitudinal axis of the weapon from perpendicularity is simulated for the first case  $0.52^\circ$  ( $0.62^\circ - 0.1^\circ$ ) and for the second case  $0.9^\circ$  ( $1.0^\circ - 0.1^\circ$ ).

The results of the analytical determination shown are in Fig. 3 and Fig. 4.

Figure 3 Misalignment  $0.62^\circ$

Figure 4 Misalignment  $1.0^\circ$

### 4. ANALYSIS OF THE RESULTS OBTAINED

#### 4.1. Deviation at missalignment of $0.62^\circ$

Change in heading during experiment:

$$D \text{ heading } \_ex = 1.73^\circ - 0.62^\circ = 1.11^\circ$$

Change in azimuth analytically:

$$D \text{ heading } \_an = 89.38^\circ - 88.188^\circ = 1.192^\circ$$

Difference of results:

$$D \text{ heading } \_an - D \text{ heading } \_ex = 1.192^\circ - 1.11^\circ = 0.082^\circ$$

#### 4.2. Deviation at missalignment of $1.0^\circ$

Change in azimuth during experiment:

$$D \text{ heading } \_ex = 2.8^\circ - 1.0^\circ = 1.8^\circ$$

Change in azimuth analytically:

$$D \text{ heading } \_an = 89.0^\circ - 87.078^\circ = 1.922^\circ$$

Difference of results:

$$D \text{ heading } \_an - D \text{ heading } \_ex = 1.922^\circ - 1.8^\circ = 0.122^\circ$$

### 5. CONCLUSION

The experimental results were confirmed by spherical trigonometry results. The difference between experimental and analytical results is

- In the first case  $0.082^\circ = 1.46$  mils

- In the second case  $0.122^\circ = 2.17$  mils

These results show a good match considering declared accuracy of GEONYX 1 mils ( $1\sigma$ ), which means that an even better match would be obtained in a larger number of experimental measurements were performed.

The most important thing to note from these results is:

- The longitudinal axis of the INS must be adjusted to be parallel to the longitudinal axis of the weapon during installation. Only in that case, the INS will show the real elevation of the weapon's longitudinal axis in each elevation position, regardless of whether the weapon's longitudinal axis deviates from perpendicularity in relation to the elevation axis.
- If there is an offset of the installation of the longitudinal axis of the INS in relation to the longitudinal axis of the weapon, then when the elevation is changed, there is different of the azimuth of the INS and the azimuth of the weapon. The bigger the offset, the bigger the difference. The magnitude of difference increases as the elevation angle increases. The obtained result shows that the minimization of the INS installation offset is needed to reduce the error at larger azimuth angles.
- According to the elevation angle, the influence of installation offset is very small, it is practically negligible.

### References

- [1] Spherical Trigonometry: <https://www.gutenberg.org/files/19770/19770-pdf>
- [2] Spherical Trigonometry; <https://www.math.ucla.edu/~robjohn/math/spheretrig.pdf>
- [3] Land Inertial Navigation, Safran: <https://www.safran-group.com/sites/default/files/2022-06/Safran>





## UWB SENSOR PERFORMANCE IN UGV 'FOLLOW ME' APPLICATIONS WITH OBSTACLE INTERFERENCE

RADE PAVLOVIĆ

Military Technical Institute, Ministry of Defence, Ratka Resanovića 1, Belgrade, [rade.pavlovic@mod.gov.rs](mailto:rade.pavlovic@mod.gov.rs)

NINA MITRIČEVIĆ

Military Technical Institute, Ministry of Defence, Ratka Resanovića 1, Belgrade, [nmitricevic@gmail.com](mailto:nmitricevic@gmail.com)

SRĐAN SAVIĆ

Faculty of Technical Science, University of Novi Sad, Trg Dositeja Obradovića 1, Novi Sad, [savics@uns.ac.rs](mailto:savics@uns.ac.rs)

**Abstract:** Robots and autonomous systems are an evolving industry for the military. Although the military's interest in autonomous systems has been existed for decades, the use and application of such systems in experiments and in on the ground operations is relatively new and growing. One of the basic functions of the autonomous unmanned ground vehicle (UGV) is "Follow me", where the UGV follows a person or another vehicle (object). The basic sensor used to determine the position of the UGV in relation to the object is the ultra-wideband sensor (UWB). UWB wireless technology consists of tag which is worn by person and anchors on the UGV and has high precision and transmission rate. It is of fundamental interest that the UGV follows exactly the path followed by the person. At the same time, the UGV has to avoid static and dynamic obstacles that are on the way. This paper presents the impact of dynamic and static obstacles, which can be found in real situations, between the UGV and the person. The results of measuring the angle and distance between the tag and the anchor using obstacles of different dimensions and in different positions are given. Also, different distances between tag and anchor were considered, in order to find the optimal distance.

**Keywords:** UGV, robotics, autonomous, UWB sensor.

### 1. INTRODUCTION

During the recent years, the involvement of teleoperated, semi-autonomous and autonomous UGVs has seen a major increase both in case of civil and military applications. In both cases, the main motivator behind UGV application is the goal to exempt human workforce for dangerous tasks.

In the field of civil application, UGVs are mainly embodied in autonomous driving. High intelligent driver models can completely or partially replace the driver's active control [1]. Moreover, UGVs with sensors can easily act as "probe vehicles" and perform traffic sensing to achieve better information sharing with other agents in intelligent transport systems [2]. Thus, it has great potential in reducing traffic accidents and alleviating traffic congestion. In the field of military application, it is competent in tasks such as intelligence, monitoring and reconnaissance, transportation and logistics, demining and placement of improvised explosive devices, providing fire support, communication transfer, and medical transfer on the battlefield [3], which can effectively assist troops in combat operations.

UGV for military purposes must have a robust chassis which can give better results in all-terrain. The main objective in many applications is to carry the load consisting of first aids, necessary equipment required for soldiers. UGV includes some sensors which are used for

navigation and environment detection. Sensors can include compasses, odometers, gyroscopes, cameras for triangulation, laser, ultrasound range finders and infrared technology [4]. Unmanned ground vehicles are mostly Remote-Operated and Autonomous, although Supervisory Control is used to refer to situations in which a combination of decision-making by UGV systems and the remote human controller. UGV contains can be a small tank which can go through all types of terrains and continuously assist to the soldiers. UGV carries all types of loads or the extra ammunitions for soldiers and automatically follows them with the help of GPS communication. We can also use this kind of system for soldier tracking from base camp which is very useful in dangerous areas. UGV provides service in all terrains.

One of the most important functions of autonomous vehicles that have military applications is "Follow Me". To realize this functionality, a larger number of sensor fields can be used that can determine the relative position of the operator and the vehicle. UWB technology has also been introduced into the field of relative positioning in recent years because of its advantages of high precision and low cost UWB technology is not without limitations, UWB signals are very susceptible to interference due to their high frequency. When there are obstacles on the signal propagation path, such as non-line-of-sight (NLOS) conditions, UWB devices will cause incorrect measurements or data loss due to multipath effects. Obstacles that may appear are of static and dynamic nature. Static obstacles include obstacles that arise when

moving and visiting objects, where NLOS can occur. Dynamic obstacles are objects that are briefly encountered during movement. The paper provides an analysis of the results obtained in the case when there are obstacles between the antenna and the base station.

## 2. FOLLOW ME METHODS

Tracking of a moving target, specifically a human operator, can be based on different sensor technologies. A systematic overview of the situation in this area is given in [5].

The first approach is based on the application of different types of cameras and machine vision. Thermal cameras can help distinguish between living and non-living objects. Since the unmanned vehicle needs to follow a specific operator in the potential presence of other people, it is necessary to identify the target in some way. One possibility is the recognition of the operator's face, which can be problematic due to uncontrolled lighting in an open space, as well as occlusion due to operator movement among obstacles. Another option is to place a marker, such as a QR code or an ArUco tag on the target and visually recognize the tag. It is possible to combine front-view face recognition with marker recognition on the operator's back.

The second approach is suitable for tracking the target in open space and is based on the application of the global positioning system GPS, which allows tracking the target with an accuracy of approximately 10 m. There is a potential problem with signal loss in certain environments. For laboratory conditions and movement in a relatively small closed space, the efficiency is further degraded and the available precision is not sufficient.

The third approach is the localization of the moving target based on the IMU sensors that the subject wears. It performs localization based on a known initial state, integration of the travelled distance and drift estimation. One of the advanced technologies based on this approach is the Sensor Field Ops Remote Tracker (FORT) manufactured by PNI that uses a combination of magnetometer, gyroscope and accelerometer with advanced artificial intelligence algorithms, which largely eliminates sensor drift and magnetic interference where robustness is increased [6].

The fourth approach, which is probably the most reliable, is to mark the operator with some kind of active or passive tag that would allow the robot system to determine the distance and direction from which the tag signal comes, without the need for the tracking object to be directly visible to the robot. This approach is often based on the application of RFID tags, Bluetooth, WiFi or Ultra-Wide Band (UWB) technology [7-10]. The basic idea is illustrated in Figure 1. There are at least three base stations (anchor) that emit a signal and a tag located on the tracking object as a receiver. For indoor applications, such as warehouses or factories, anchors are fixed and prearranged to cover the entire area of interest. However, in our case when the robot needs to track a target in an open unknown terrain, all base stations must be fixed on

the robot. Object localization is most often based on triangulation or trilateration methods, as illustrated in Figure 2.

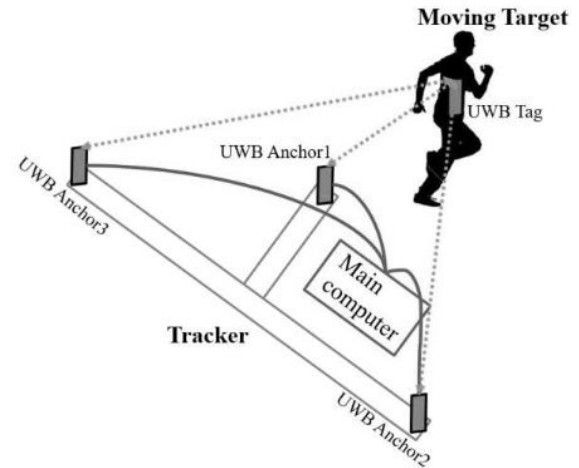


Figure 1. Basic setting of the moving target tracking system based on UWB technology.

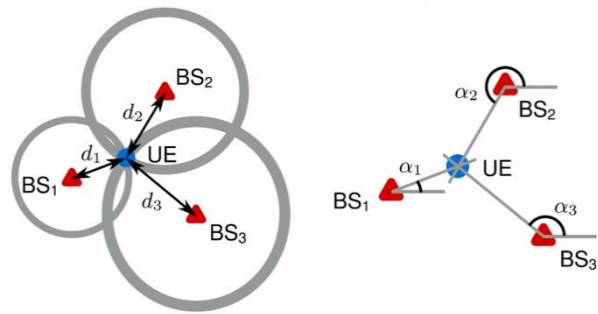


Figure 2. Illustration of the trilateration (left) and triangulation (right) methods.

The UWB modules use a two-way distance determination method which is called Two Way Ranging, and it is described schematically in 3.

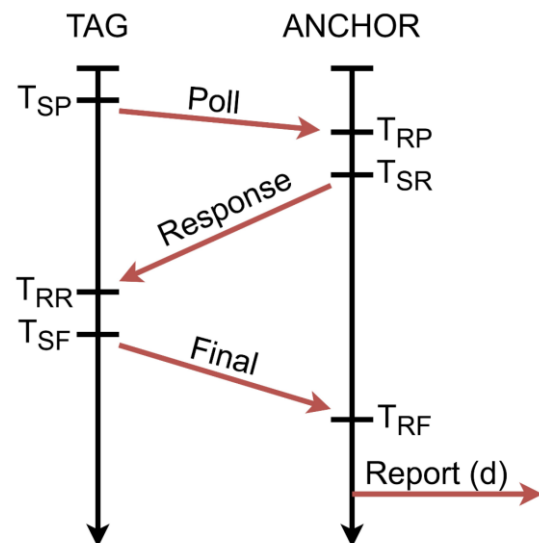


Figure 3. UWB Tag-Anchor communication diagram.

The anchor–tag distance (between the anchor to the tag) can be calculated using the following mathematical

formula:

$$d = c \left[ \frac{(T_{RR} - T_{SP}) - (T_{SR} - T_{RP}) + (T_{RF} - T_{SR}) - (T_{SF} - T_{RR})}{4} \right] \quad (1)$$

where  $c$  is the speed of light,  $T_{SP}$ ,  $T_{SR}$ , and  $T_{SF}$  are the times of sending the polls and the packet responses by the anchor and the tag; and  $T_{RP}$ ,  $T_{RR}$ , and  $T_{RF}$  are the times of receiving the polls and the packet responses by the anchor and the tag.

Compared to bluetooth technology, UWB is comparable in price and energy consumption, but it is significantly more accurate and has a much lower latency. Compared to WiFi technology, UWB is cheaper, uses less power, significantly more accurate and has lower latency. One of the realistic systems for following a person with an unmanned vehicle is given in Figure 4. In addition to this example, several unmanned vehicles can be connected to follow one object or create a series of unmanned vehicles so that each of them follows the vehicle in front of it.



Figure 4. Tracking the operator with an unmanned vehicle.

In this paper, the UWB sensor Nooploop LinTrack AOA was chosen for analysis and it is shown in Figure 5. This sensor consists of three units: tag, anchor (base station) and monitor. The typical repeatable precision of the sensor is  $\pm 5$ cm, and the angular precision of direction determination is  $\pm 5^\circ$ , with a refresh rate of 200Hz. The sensor allows determining the distance and the direction from which the signal from the tag is coming, which enables the tracking of the target marked with the tag. Determining the distance works on the principle of measuring the time it takes for an electromagnetic wave to travel from the tag to the base (time of flight) at the speed of light. An antenna array is integrated within the base station (anchor), with the help of which the relative angle between the tag and the base station can be determined based on the phase shift of the signal. This sensor has a ROS driver available.



Figure 5. Nooploop LinTrack AOA sensor. Base station (left) and tag (right).

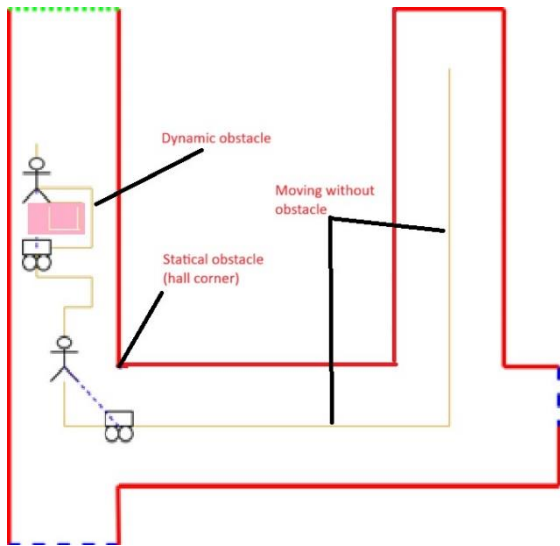
The entire system is implemented on the robotic platform Rosbot 2 Pro (Figure 6), manufactured by Husarion. This is a mobile robotic platform with four wheels and comes equipped with several sensors, the most important are the encoders on the motors, which are used for odometric position measurement and the LIDAR (laser sensor that scans the space in one plane around the robot). The platform has a set of ordinary wheels and a set of omnidirectional "mecanum" wheels, which allows the implementation of two different types of drive. The first is the so-called "skid steer" drive is characteristic of tracked vehicles, while the other is an omnidirectional drive that allows translation in all directions. The robotic operating system - ROS - was chosen as the software base. This is not a real operating system in that sense, but rather a collection of software packages to facilitate the implementation of robotic systems and their integration with other hardware.



Figure 6. Rosbot 2 Pro robotic platform.

### 3. ANALYSIS OF RESULTS

Checking the functionality of UWB tracking is performed using a tag that the field operator carries with him. A glued tape is placed on the floor as a predefined path along which a person with a UWB tag will move. The task of the robot is to follow the path followed by the man, i.e. field operator (Figure 7).



**Figure 7.** Illustration of the polygon that will be used to validate a moving target tracking system based on UWB sensor technology.

In doing so, it is observed whether the robot will follow each point through which the person has passed and thus it will also follow the glued tape or will make shortcuts along the air line.

Firstly, testing was performed in conditions where there are no obstacles between the operator with the tag and the vehicle with the base station. The distance between these two devices is 4.9m and it generally there are small changes, which are usually caused by noise in the system itself, as a result of external influences (figure 8). In the period of 200 samples for which the distance was measured, the standard deviation was 0,9 cm. This value confirms the high accuracy of the UWB sensor and can be used in real application.

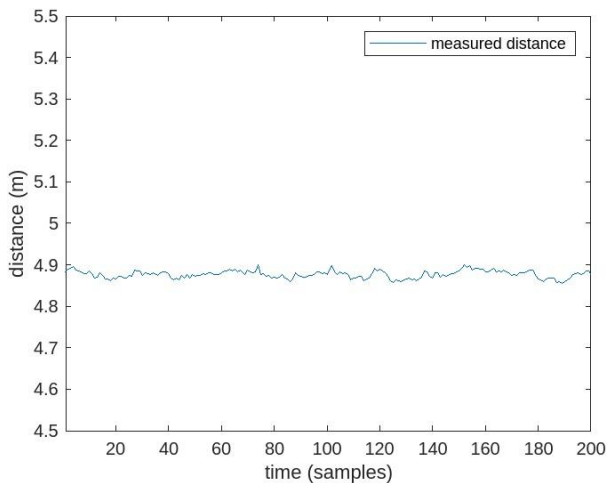


**Figure 8.** Measured values of the distance between the tag and the base station.

However, in addition to high accuracy, the obtained data can be filtered in order to reduce the probability that the vehicle makes some unwanted movements when the operator is moving or standing. In this work, a simple and computationally efficient low-frequency filter was used. The *movemean* filter performs data filtering by replacing

each data point  $m(i)$  with the mean value of neighbouring points defined within a specified filtering window:

$$s(i) = \frac{1}{2N+1} \sum_{i=-N}^N m(i) \tag{2}$$

where  $s(i)$  is the filtered value for the  $i$ -th data point,  $N$  is the number of adjacent data points on either side of  $s(i)$ , and  $2N+1$  is the total filtering range. The data obtained by filtering are shown in Figure 9. The figure shows that the deviations of the measured and true distance between the tag and the base station are significantly reduced and that in this case the movement of the vehicle is much more stable, which is confirmed by the standard deviation of the signal of 0,35 cm.

UWB devices also provide information about the angle between the base station and the tag. The results of the angle measurement for 200 samples are given in the figure 10. The results of the angle measurement are slightly noisier, but the accuracy is high and it is possible to use them in real systems. The standard deviation is 1.93 degrees.

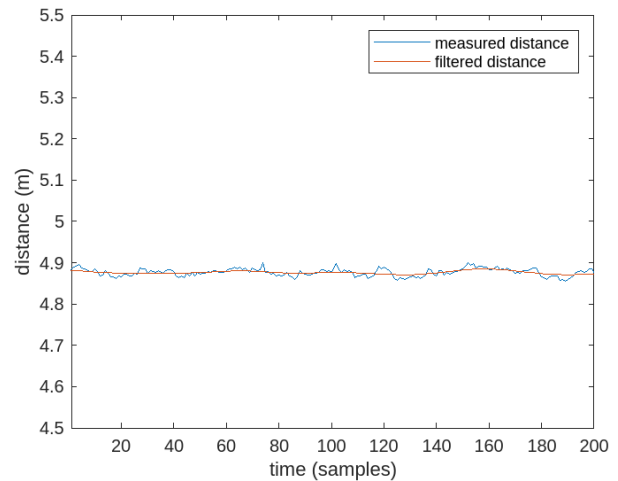


**Figure 9.** Measured and filtered values of the distance between the tag and the base station.

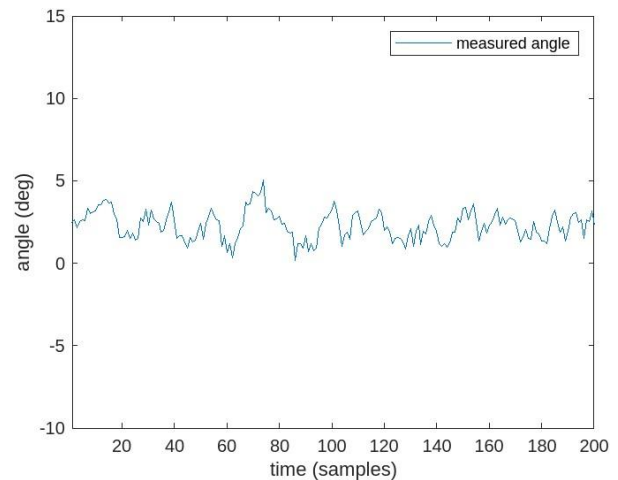


**Figure 10.** Measured values of the angle between the tag and the base station.

Similar to the distance data, filtering was done with the

*movemean* filter and the results were very good (figure 11), the standard deviation after filtering is 1.06 degrees.

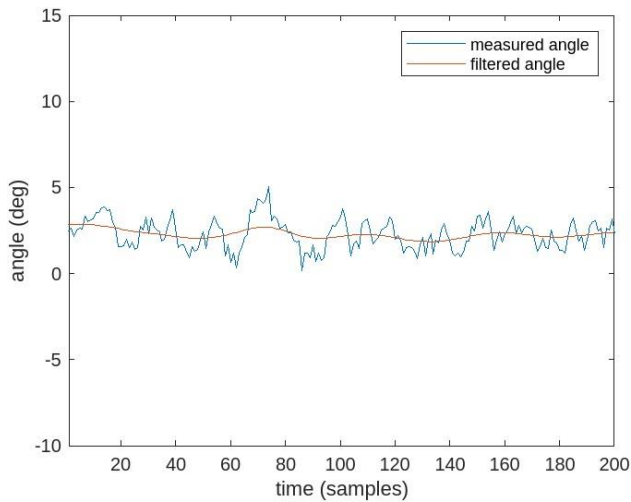


**Figure 11.** Measured and filtered values of the distance between the tag and the base station.

All previous results were obtained in ideal conditions, when there are no obstacles between the tag and the base station. In real situations, there may be various obstacles, such as obstacles encountered during movement (Figure 7) or some random dynamic obstacles during movement. During the test, the tag and the base station were at a constant distance, while a dynamic obstacle was used to see the effects. The results of the distance measurement are given, and it can be seen that when entering the obstacle, there is a change of 47 cm in peak. After that the data about the distance stabilizes (figure 12).

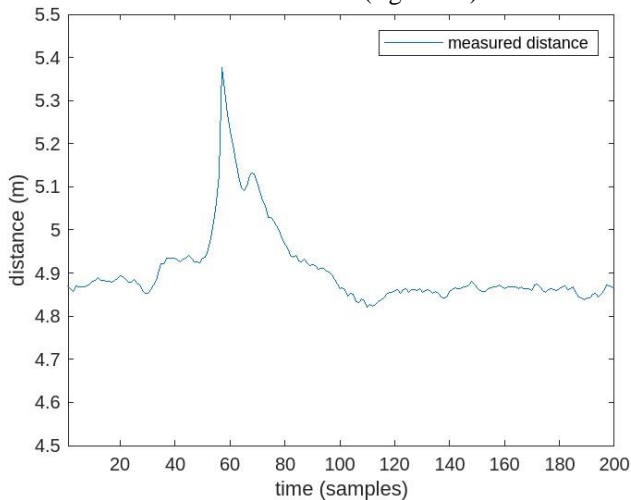


**Figure 12.** Measured values of the distance between the tag and the base station with obstacle.

Using the filter data are much smoother and a pick is smaller than in unfiltered data (figure 13), i.e. the deviation is 17cm. Although these values are not negligible, they do not affect the correct tracking of the operator.

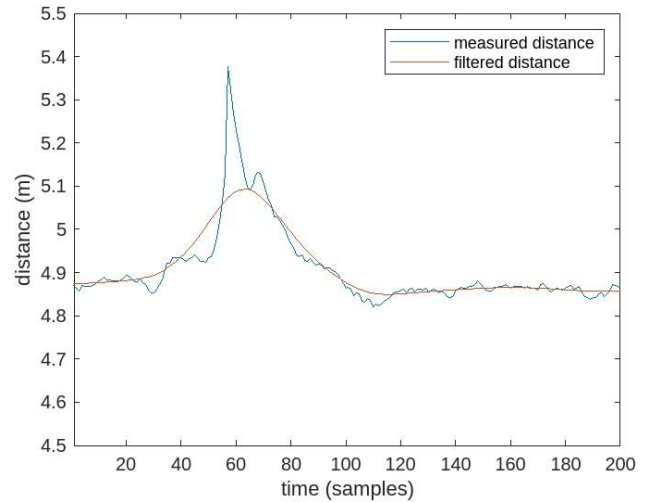


**Figure 13.** Measured and filtered values of the distance between the tag and the base station with obstacle.

A similar result is obtained when analyzing data on the angle between the tag and the base station (figure 14). There are also peaks when encountering an obstacle in the value of 7 degrees and after that the signal stabilizes.

Using the *movemen* filter (figure 15), the data obtained is significantly smoother, the error value does not exceed 2 degrees, where it is quite satisfactory for practical application.

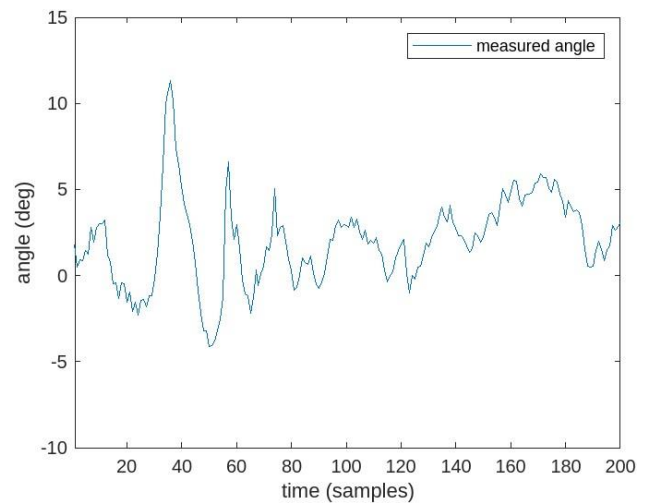


**Figure 14.** Measured values of the angle between the tag and the base station with obstacle.

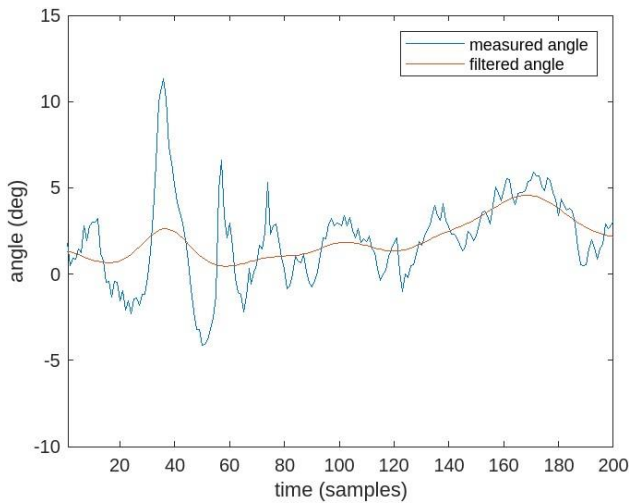


**Figure 15.** Measured and filtered values of the angle between the tag and the base station with obstacle.

#### 4. CONCLUSION

Unmanned ground vehicles are used in many applications, which is growing every day, both in the military and in the civilian industry. The autonomy of driverless vehicles reduces human influence in making a large number of decisions and increases safety and security. One of the essential functionalities of autonomous unmanned vehicles is the function of following the operator (human or another vehicle), more popularly called “follow me”. There are several possibilities for realizing this functionality, but it is most reliable to use sensors based on UWB technology. These sensors provide the distance and angle at all times between the operator wearing the tag and the vehicle on which the base station is located. In this way, a certain distance can be defined at which the vehicle will follow the operator. The data obtained with this sensor is quite reliable and accurate, but due to noise, it may deviate from the true value. A special problem is also the appearance of obstacles between the tag and the base stations, which leads to errors in determining the distance and angle.

Analysing the data, it was found that the error when obstacles appear is significantly greater when measuring the angle than the distance. Using the UWB sensor, the data obtained by measuring when obstacles appeared were in most cases slightly higher than the true value. When removing an obstacle or having LOS, the data stabilized and high accuracy was again obtained. There was no loss of data during the measurement, which confirms the reliability of this sensor.

Using simple filters such as the *movemean* filter yields data suitable for real-time operation on real systems. At the same time, deviations from the true value were reduced without losing significant data.

Further work will be based on the research of data fusion with other sensors in order to reduce the influence of obstacles between the tag and the base station on the accuracy of the obtained data.

#### References

- [1] Li, Z.; Gong, J.; Lu, C.; Xi, J. Importance Weighted Gaussian Process Regression for Transferable Driver Behaviour Learning in the Lane Change Scenario. *IEEE Trans. Veh. Technol.* 2020, 69, 12497–12509.
- [2] Rosique, F.; Lorente, P.N.; Fernandez, C.; Padilla, A. A Systematic Review of Perception System and Simulators for Autonomous Vehicles Research. *Sensors* 2019, 19, 648.
- [3] Chen, T.; Wang, R.; Dai, B.; Liu, D.; Song, J. Likelihood-Field-ModelBased Dynamic Vehicle Detection and Tracking for Self-Driving. *IEEE Trans. Intell. Transp. Syst.* 2016, 11, 3142–3158.
- [4] Patole, S.M.; Torlak, M.; Wang, D.; Ali, M. Automotive radars: A review of signal processing techniques. *IEEE Signal Process. Mag.* 2017, 34, 22–35.
- [5] Md Jahidul Islam, Jungseok Hong and Junaed Sattar, „Person Following by Autonomous Robots: A Categorical Overview“, To appear at the IJRR. Preprint (2019):1–32, Proceedings of the International Multi Conference of Engineers and Computer Scientists 2018 Vol IIMECS 2018, March 14-16, 2018, Hong Kong
- [6] <https://www.pnicorp.com/fort/>
- [7] Chen, Y.C.; Alexander, I.; Lai, C.; Wu, R.B. UWB-Assisted HighPrecision Positioning in a UTM Prototype. In Proceedings of the 2020 IEEE Topical Conference on Wireless Sensors and Sensor Networks (WiSNeT), San Antonio, TX, USA, 26–29 January 2020; pp. 42–45.
- [8] Raza, U.; Khan, A.; Kou, R.; Farnham, T.; Premalal, T.; Stanoev, A.;Thompson, W. Dataset: Indoor Localization with Narrow-band, UltraWideband, and Motion Capture Systems. In Proceedings of the 2nd Workshop on Data Acquisition to Analysis, New York, NY, USA, 10 November 2019; pp. 34–36.
- [9] Ghavami, M.; Michael, L.B.; Kohno, R. *Front Matter Ultra Wideband Signals and Systems in Communication Engineering*; John Wiley & Sons, Ltd.: Newark, NJ, USA, 2006; pp. 1–100.
- [10] Miller, L.E. Why UWB? A Review of Ultrawideband Technology. In Report to NETEX Project Office; DARPA National Institute of Standards and Technology: Gaithersburg, MD, USA, 2013; pp. 30–70.



# FRACTIONAL ORDER ITERATIVE LEARNING CONTROLLER WITH PSO-BASED PARAMETERS TUNING FOR ROBOTIC SYSTEMS

NIKOLA ŽIVKOVIĆ

Lola Institute Ltd., Kneza Višeslava 70a 11030 Belgrade, tel: (011) 25 46 423, [nikola.zivkovic@li.rs](mailto:nikola.zivkovic@li.rs)

MIHAILO LAZAREVIĆ

Faculty of Mechanical Engineering, Kraljice Marije 16 11060 Belgrade, tel: (011) 3302 338, [mlazarevic@mas.bg.ac.rs](mailto:mlazarevic@mas.bg.ac.rs)

JELENA VIDAKOVIĆ

Lola Institute Ltd., Kneza Višeslava 70a 11030 Belgrade, tel: (011) 25 46 423, [jelena.vidakovic@li.rs](mailto:jelena.vidakovic@li.rs)

STJEPKO PIŠL

Faculty of Mechanical Engineering, Kraljice Marije 16 11060 Belgrade, tel: (011) 3302 338 [stjepko.pisl@gmail.com](mailto:stjepko.pisl@gmail.com)

**Abstract:** *This research investigates the improvement of trajectory tracking in robotic systems by employing a model-based controller and a fractional-order iterative learning controller (FOILC). Robotic systems are subject to high uncertainty in the mathematical model, which directly impacts the quality of the model-based control strategy. This study focuses on parametric uncertainty in the robot model. The proposed solution capitalizes on the synergies between model-based control and fractional-order iterative learning strategy. FOILC controller's task is to mitigate the influence uncertainty has on trajectory tracking iteratively. Central to this investigation is the tuning of control parameters, a task undertaken by utilizing the Particle Swarm Optimization (PSO) algorithm. By leveraging PSO, the FOILC control parameters are optimized to maximize the system's performance by reducing the trajectory tracking error according to the chosen objective function. The efficiency of the proposed control algorithms is evaluated through extensive simulation on a three degree of freedom robot arm. The findings underscore the performance improvement of the tuned fractional-order iterative learning controller over its integer-order counterpart in trajectory tracking. These results not only validate the efficiency of the FOILC approach but also highlight the significance of fine parameter tuning methodologies in advancing the capabilities of robotic systems based on the dynamics model.*

**Keywords:** *Iterative learning control, robotics, fractional calculus, parameter tuning.*

## 1. INTRODUCTION

Trajectory tracking is one of the main problems in robotics, where the goal is to control a robot's motion to follow a desired trajectory. The desired trajectory is usually defined in operational space using Cartesian coordinates, representing the position and orientation of the robot's end-effector. Trajectory tracking can be a complex problem from the control design standpoint, especially when parametric uncertainties, unmodeled dynamics, or other uncertainties are present in the system. Uncertainty needs to be addressed to make the system's performance satisfactory. Robot manipulators are usually designated with repetitive tasks such as welding, assembly, sorting, etc. Iterative Learning Control (ILC) comes to mind as a solution to previously stated problems. One of the ILC's advantages is robustness to uncertainty without the precise knowledge of the process model [1], [2]. ILC is also suitable for repetitive tasks, where each repetition has the same initial conditions. ILC is a highly modular control strategy that can be incorporated into existing control systems without changing them [3].

Extending ILC with fractional calculus theory, one obtains Fractional Order Iterative Learning Control (FOILC) [4]. Fractional calculus is a generalization of integer order calculus [5]. The main advantage of fractional order controllers is that they possess more degrees of freedom compared to their integer-order counterparts, implying better performance [6]. An increased number of control system parameters requires tuning for better system response. There is a considerable number of research involving tuning fractional order PID controllers in literature, for example [7], [8], but the FOILC controllers lack the proper tuning procedure. The research in [9] deals with the problem of tuning FOILC control parameters on a linearized robot with no uncertainty. The main motivation for this research is to find an easy, computationally efficient, and performance-improving solution to tuning FOILC parameters. This research also aimed to determine the proposed controller robustness to various percentages of parametric uncertainties of the proposed tuned control system. The Particle Swarm Optimization (PSO) is our algorithm of choice for FOILC parameter tuning.

This paper consists of the following sections: Section II

describes the robot structure and the equations of motion are derived; Section III consists of the controller design description divided into subsections describing Inverse Dynamics, Fractional Order Iterative Learning Controller, and tuning procedure of the FOILC control parameters using PSO; Section IV showcases the simulation results of the previously presented controller.

## 2. ROBOT DYNAMICS DERIVATION

### 2.1. NeuroArm robot mechanical structure

The controller design presented in this paper is tested on the model of the NeuroArm robotic system with seven degrees of freedom (DOF) from the Laboratory of Applied Mechanics at the Faculty of Mechanical Engineering in Belgrade, Figure 1. The NeuroArm is a serial robot where the first three joints position the end-effector, while the following three joints orientate the end-effector. The 7th DOF is related to the gripper action. The mechanical structure of the NeuroArm robot is presented in Figure 2. In this contribution, we will only consider the 3-DOF positioning part of the NeuroArm kinematic chain.

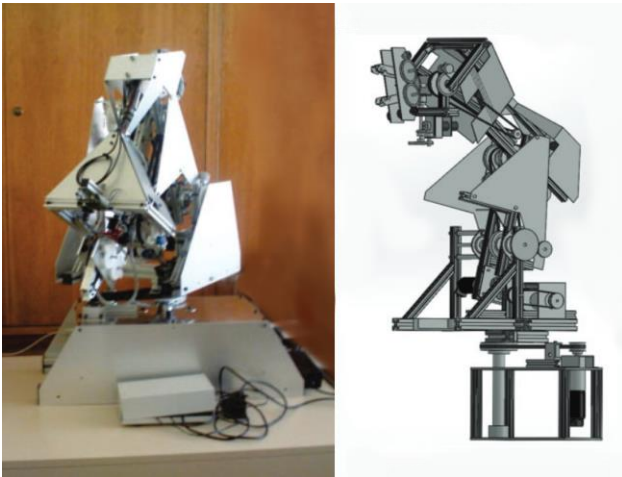


Figure 1. Robotic system NeuroArm

### 2.2. Equations of motion

The dynamic behavior of the robotic system is described with the equations of motion (1), which are herein derived using the Rodriguez approach [10]:

$$\mathbf{A}(\mathbf{q})\ddot{\mathbf{q}} + \mathbf{C}(\mathbf{q}, \dot{\mathbf{q}})\dot{\mathbf{q}} = \mathbf{Q}^a + \mathbf{Q}^g(\mathbf{q}), \quad (1)$$

where term  $\mathbf{A}(\mathbf{q})$  is  $n \times n$  inertia matrix, term  $\mathbf{C}(\mathbf{q}, \dot{\mathbf{q}})\dot{\mathbf{q}}$  is a  $n \times 1$  Coriolis and centrifugal forces vector, term  $\mathbf{Q}^g(\mathbf{q})$  is a  $n \times 1$  vector of generalized forces due to gravity, and terms  $\mathbf{q}, \dot{\mathbf{q}}$  are  $n \times 1$  vectors of generalized coordinates  $q_j, \dot{q}_j, j=1, \dots, n$  representing joint positions and speeds, respectively. Term  $\mathbf{Q}^a$  is  $m \times 1$  vector of joint actuation torques, where  $m$  is a number of actuated joints. In this case  $m=n=3$  since every joint of the robot has an independent source of actuation and only the first three DOFs of the NeuroArm are considered. The required data for deriving the equations of motion for the NeuroArm

presented in Figure 2. is listed in appendix in Table A.1.

Due to the complexity and inability to perfectly measure and estimate the parameters of the real-world robot, a level of uncertainty is present.

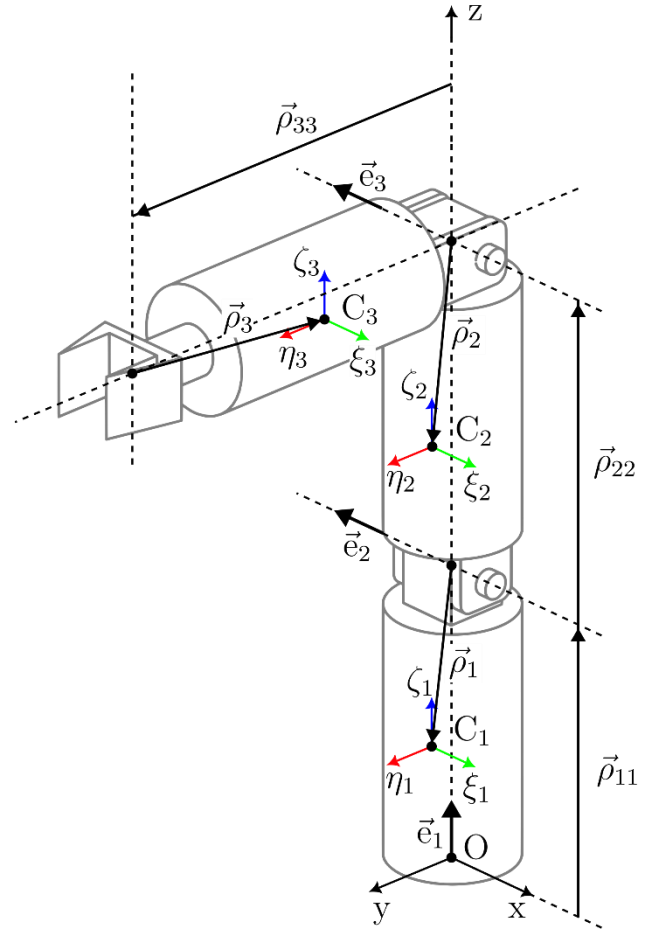


Figure 2. Mechanical structure of the NeuroArm

Hence, to better describe the impact of uncertainty on the behaviour of the robotic system and to test the proposed controller's performance, equations of motion (1) can be reformulated as:

$$(\mathbf{A}_N + \Delta\mathbf{A})\ddot{\mathbf{q}} + (\mathbf{C}_N + \Delta\mathbf{C})\dot{\mathbf{q}} - (\mathbf{Q}_N^g + \Delta\mathbf{Q}^g) = \mathbf{Q}^a, \quad (2)$$

where matrices  $\mathbf{A}(\mathbf{q})$ ,  $\mathbf{C}(\mathbf{q}, \dot{\mathbf{q}})$  and vector  $\mathbf{Q}^g(\mathbf{q})$  are split into nominal parts  $\mathbf{A}_N(\mathbf{q})$ ,  $\mathbf{C}_N(\mathbf{q}, \dot{\mathbf{q}})$  and  $\mathbf{Q}_N^g(\mathbf{q})$  and uncertain parts  $\Delta\mathbf{A}(\mathbf{q})$ ,  $\Delta\mathbf{C}(\mathbf{q})$  and  $\Delta\mathbf{Q}^g(\mathbf{q})$ . The dependence of matrices  $\mathbf{A}_N(\mathbf{q})$ ,  $\mathbf{C}_N(\mathbf{q}, \dot{\mathbf{q}})$ ,  $\Delta\mathbf{A}(\mathbf{q})$ ,  $\Delta\mathbf{C}(\mathbf{q})$  and vectors  $\mathbf{Q}_N^g(\mathbf{q})$ ,  $\Delta\mathbf{Q}^g(\mathbf{q})$  on generalized coordinates vectors  $\mathbf{q}$  and  $\dot{\mathbf{q}}$  will be omitted forward on.

## 3. CONTROL SYSTEM DESIGN

### 3.1. Solution to Inverse Dynamics problem

Robotic systems are coupled nonlinear, time-varying, Multiple Input Multiple Output (MIMO) systems, and as such, to successfully tackle the nonlinear dynamic coupling effects, a nonlinear control strategy is recommended. One of the most effective model-based nonlinear control strategies is Inverse Dynamics Control



(also known as Feedback linearization) [11], [12], [13]. Inverse Dynamics is a model-based control method. Inverse Dynamics, in theory, is the exact linearization of the system. Real-world robotic systems will always have some level of uncertainty, whether in mass or any other parameter, meaning that the exact linearization based on the derived model isn't achievable in practice. Considering the previous statement, the Inverse Dynamics accounts only for the nominal (known) part of the robot dynamics, and the vector of actuation torques  $\mathbf{Q}^a$  can be chosen such that it depends on those nominal parts:

$$\mathbf{Q}^a = \mathbf{A}_N \mathbf{u} + \mathbf{C}_N \dot{\mathbf{q}} - \mathbf{Q}_N^a, \quad (3)$$

where  $\mathbf{u}$  is a new input vector. Substituting (3) in (2), alternative form of the equations of motions is obtained:

$$\ddot{\mathbf{q}} = \mathbf{A}^{-1} \mathbf{A}_N \mathbf{u} - \mathbf{A}^{-1} (\Delta \mathbf{C} \dot{\mathbf{q}} - \Delta \mathbf{Q}^a). \quad (4)$$

### 3.2. Fractional order iterative learning controller

Continuing from (4), a new control input vector  $\mathbf{u}$  is to be chosen to stabilize the system and tackle the uncertain parts of the robot dynamics model. Iterative learning controllers have been proven successful in precise trajectory tracking and compensating for parametric uncertainties and deterministic disturbances [1]. Here, the FOILC PD $^\alpha$ -type controller is considered to improve trajectory tracking and ensure system robustness to uncertainties compared to integer order. The proposed linear control law  $\mathbf{u}$  is divided into the feedback and feedforward part, where the feedback part is a classical PD controller, and the feedforward part is previously mentioned FOILC. The control input vector  $\mathbf{u}$  is defined by the following equations:

$$\mathbf{u}_i = \mathbf{u}_i^{fb} + \mathbf{u}_i^{ff}, \quad (5)$$

$$\mathbf{u}_i^{fb} = \mathbf{K}_P \mathbf{e}_i + \mathbf{K}_D \dot{\mathbf{e}}_i, \quad (6)$$

$$\mathbf{u}_i^{ff} = \mathbf{Q}_f [\mathbf{u}_{i-1} + \mathbf{K}_P^{ff} \mathbf{e}_{i-1} + \mathbf{K}_D^{ff} D_{CL}^{\alpha_j} (\mathbf{e}_{i-1})], \quad (7)$$

where  $i$  is the iteration index,  $j$  is the joint index,  $\mathbf{e}_i = \mathbf{q}_d - \mathbf{q}_i$  is  $n \times 1$  vector of position errors,  $\dot{\mathbf{e}}_i = \dot{\mathbf{q}}_d - \dot{\mathbf{q}}_i$  is the  $n \times 1$  vector of velocity errors,  $\mathbf{K}_P$ ,  $\mathbf{K}_D$  are feedback gains,  $\mathbf{K}_P^{ff}$ ,  $\mathbf{K}_D^{ff}$  are feedforward learning gains,  $D_{CL}^{\alpha_j}$  is the fractional derivative operator of the order  $\alpha_j$  according to the Grunwald-Letnikov definition, and  $\mathbf{Q}_f$  is a zero-phase low-pass filter added to suppress learning of the undesired frequencies [14]. The overview of the proposed controller structure is displayed in Figure A.1 in appendix.

### 3.3. Tuning procedure using Particle Swarm Optimization

Introducing fractional derivative and integral operators in control laws gives more degrees of freedom to the controllers, implying that better performance can be

achieved. In [15], it is shown that increasing the fractional order  $\alpha$  value of the derivative operator leads to improved error convergence. Based on previous observations, it is only natural that the fractional order values are suitable for tuning after each iteration. Besides  $\alpha$ , there are learning gains  $\mathbf{K}_P^{ff}$  and  $\mathbf{K}_D^{ff}$  in the FOILC control law (7) that influence the system output and should be subject to the tuning procedure.

The PID-type ILC control laws like (7) don't have as well-established tuning procedures as classical PID controllers [16]. Hence, this research chooses the PSO algorithm as a simple solution to the FOILC control parameters tuning problem. Particle Swarm Optimization is a nature-inspired optimization algorithm that draws inspiration from the social behavior of organisms such as birds and fish. Introduced in [17], PSO has gained popularity as a powerful heuristic optimization technique for solving complex optimization problems. Since its beginnings, the PSO algorithm has undergone significant changes and improvements. The variation of the PSO algorithm used in this research can be found in [18], and PSO parameters are listed in Table 1. Most of the parameters in Table 1 are set by trial and error. The tuning procedure is carried out after each iteration  $i$ , and tuned variables  $\alpha$ ,  $\mathbf{K}_P^{ff}$  and  $\mathbf{K}_D^{ff}$  are used in the next iteration  $i+1$ . The objective function for the PSO algorithm to minimize is adopted in the following form:

$$J = P + \sum_{t=0}^T t e_i^T e_i T, \quad (8)$$

where  $T$  is the duration of one iteration,  $\mathbf{e}_i(t) = \mathbf{q}_d(t) - \mathbf{q}_i(t)$  is the position error and  $P$  is a penalty value that is added to the objective function according to the following cases:

$$P = \begin{cases} 0, & 0 < \alpha_j \leq 2 \wedge \mathbf{K}_P^{ff}, \mathbf{K}_D^{ff} > 0 \\ 1000, & \text{otherwise} \end{cases}, \quad (9)$$

The value  $P$  penalizes particles, which can cause unstable behavior, and such particles are eliminated from the search process by adding additional costs to them. The described control system with PSO tuning is given in appendix in Figure A.1.

**Table 1.** Parameters for the PSO algorithm.

Variable	Value
Population number	50
Iteration number	10
Initial value of the individual-best acceleration factor	2.5
Final value of the individual-best acceleration factor	0.5
Initial value of the global-best acceleration factor	0.5
Final value of the global-best acceleration factor	2.5
Initial value of the inertia factor	0.9

Final value of the inertia factor	0.4
-----------------------------------	-----

### 4. SIMULATION RESULTS

The simulation is carried out in Matlab 2022a (version 9.12) and Simulink (version 10.5) using the Runge-Kutta solver (ode4) for ordinary differential equations with fixed-step  $T_s = 0.001s$ . The desired trajectories are defined in joint space as cubic polynomials:

$$q_1^d = -0.25 t^3 + 0.75 t^2 \tag{10}$$

$$q_2^d = -0.15 t^3 + 0.45 t^2 \tag{11}$$

$$q_3^d = -0.075 t^3 + 0.225 t^2 \tag{12}$$

Due to the servo motors saturation limits, feedback gains KP and KD are limited to the following value ranges:

$$K_P \in (0,10], K_D \in (0,5]. \tag{13}$$

In this simulation, feedback gains are tuned by trial and error:

$$K_P = \text{diag}(10,10,10), K_D = (5,5,5). \tag{14}$$

The quality of the proposed fractional order iterative learning controller is measured using Maximum Absolute Error (MAE). For each joint, the MAE is calculated per iteration. The system performance is evaluated based on the convergence of the MAE over the iteration axis. Number of iterations is set to  $i_{max} = 10$ . Table 2., 3., and 4. shows optimized learning gains and fractional order values at the 10th iteration. The proposed controller is compared to the classical integer order ILC controller, and the performance improvement can be seen from Figure 3.

**Table 2.** Results of the tuning procedure for  $\Delta m = 0.1m_N$ .

Joint $j$	$\alpha_j$	$K_P^{\alpha_j}$	$K_D^{\alpha_j}$	J
1	1.05	5.17	0.61	1.3*10 <sup>-8</sup>
2	0.72	3.48	1.77	
3	1.47	7.18	1.33	

**Table 3.** Results of the tuning procedure for  $\Delta m = 0.2m_N$ .

Joint $j$	$\alpha_j$	$K_P^{\alpha_j}$	$K_D^{\alpha_j}$	J
1	1.36	0.96	0.04	9.4*10 <sup>-8</sup>
2	1.7	0.6	2.79	
3	0.06	5.05	1.9	

**Table 4.** Results of the tuning procedure for  $\Delta m = 0.3m_N$ .

Joint $j$	$\alpha_j$	$K_P^{\alpha_j}$	$K_D^{\alpha_j}$	J
1	1.8	7.28	1.17	3.9*10 <sup>-7</sup>
2	0.95	0.58	0.25	
3	2	2.35	0.36	

Figure 4. shows a comparison of MAE convergence for each joint for different levels of mass uncertainties. The proposed FOILC with PSO tuning shows improved convergence in comparison to integer order ILC, and PSO-FOILC achieves satisfactory MAE convergence for different percentages of mass and inertial uncertainties.

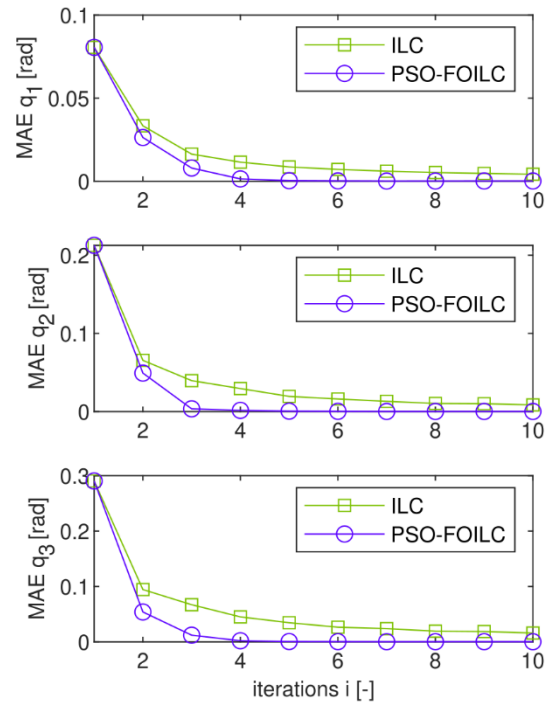


**Figure 3.** Comparison of maximum absolute error between integer order ILC and PSO tuned fractional order ILC for  $\Delta m = 0.1m_N$ .

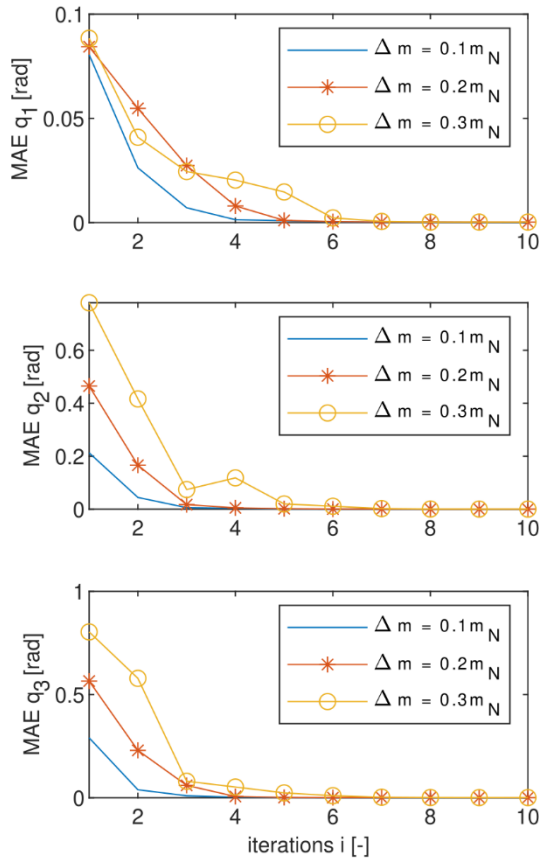


**Figure 4.** Maximum absolute error for different mass uncertainties per joint.

## 5. CONCLUSION

This paper investigated the performance of a PSO-tuned FOILC controller for a robotic system with parametric uncertainty. The key point is using a metaheuristic optimization algorithm PSO to tune FOILC parameters based on a defined objective function. Comparing PSO-FOILC with classical integer order ILC simulation results, it may be concluded that the former controller performed better. The tests with various percentages of mass uncertainty showed that PSO-FOILC successfully converges within ten iterations. The future prospect is to include feedback controller gains in the optimization process and friction in the robot model.

## Acknowledgment

This research has been supported by the research grants of the Serbian Ministry of Science, Technological Development and Innovations, grant No. 451-03-66/2024-03/ 200066 and grant No. 451-03-65/2024-03/200105 from 5.2.2024.

## References

[1] AHN, H.-S., CHEN, Y., MOORE, K. L.: *Iterative Learning Control: Robustness and Monotonic Convergence for Interval Systems*, in

Communications and Control Engineering, Springer, London, 2007.

[2] ARIMOTO, S.: *Iterative Learning Control*, Springer US, Boston, 1998.

[3] LONGMAN, R. W.: *Iterative learning control and repetitive control for engineering practice*, International Journal of Control, 73(10) (2000), 930–954.

[4] LI, Y., CHEN, Y., AHN, H.-S., TIAN, G.: *A Survey on Fractional-Order Iterative Learning Control*, J Optim Theory Appl, 156(1), (2013) 127–140.

[5] K. S. Miller and B. Ross, *An introduction to the fractional calculus and fractional differential equations*. New York: John-Wiley and Sons. Inc., 1993.

[6] SABATIER, J., LANUSSE, P., MELCHIOR, P., OUSTALOUP, A.: *Fractional Order Differentiation and Robust Control Design: CRONE, H-infinity and Motion Control*, Intelligent Systems, Control and Automation: Science and Engineering, 77, Springer Netherlands, Dordrecht, 2015.

[7] PRADHAN, R., MAJHI, S. K., PRADHAN, J. K., PATI, B. B.: *Optimal fractional order PID controller design using Ant Lion Optimizer*, Ain Shams Engineering Journal, 11(2) (2020), 281–291.

[8] VANCHINATHAN, K., SELVAGANESAN, N.: *Adaptive fractional order PID controller tuning for brushless DC motor using Artificial Bee Colony algorithm*, Results in Control and Optimization, 4 (2021), 100032.

[9] GHASEMI, I., RANJBAR NOEI, A., SADATI, J.: *Intelligent fractional order iterative learning control using feedback linearization for a single-link robot*, IIUMEJ, 18(1) (2017), 155–176.

[10] COVIC, V., LAZAREVIC, M.: *Mehanika robota*, Faculty of Mechanical Engineering, University of Belgrade, 2021.

[11] SPONG, M. W., HUTCHINSON, S., VIDYASAGAR, M.: *Robot Modeling and Control*, 2nd edition. Wiley, Hoboken, NJ, 2020.

[12] SLOTINE, J.-J. E., LI, W.: *Applied Nonlinear Control*, Prentice Hall, 1991.

[13] KELLY, R., DAVILA, V. S., LORÍA, A.: *Control of Robot Manipulators in Joint Space*, Advanced Textbooks in Control and Signal Processing, Springer, London, 2005.

[14] LONGMAN, R. W., HUANG, Y.-C.: *The Phenomenon of Apparent Convergence Followed by Divergence in Learning and Repetitive Control*, Intelligent Automation & Soft Computing, 8(2) (2002), 107–128.

[15] ŽIVKOVIĆ, N., LAZAREVIĆ, M., VIDA KOVIĆ, J.: *Assessment of fractional order impact on performance of fractional ILC controller for upper limb exoskeleton*, 16th International Conference On Accomplishments In Mechanical And Industrial Engineering, DEMI 2023, Banja Luka 1-2 June, pp. 333–337, 2023.

[16] BRISTOW, D. A., THARAYIL, M., ALLEYNE, A. G.: *A survey of iterative learning control*, IEEE Control Systems Magazine, 26(3) (2006), 96–114.

[17] EBERHART, R., KENNEDY, J.: *Particle swarm optimization*, Proceedings of the IEEE international conference on neural networks, (1995) 1942–1948.  
 [18] RAPAIC, M. R., KANOVIĆ, Ž.: *Time-varying PSO – convergence analysis, convergence-related*

*parameterization and new parameter adjustment schemes*, Information Processing Letters, 109(11) (2009), 548–552.

**APPENDIX A.**

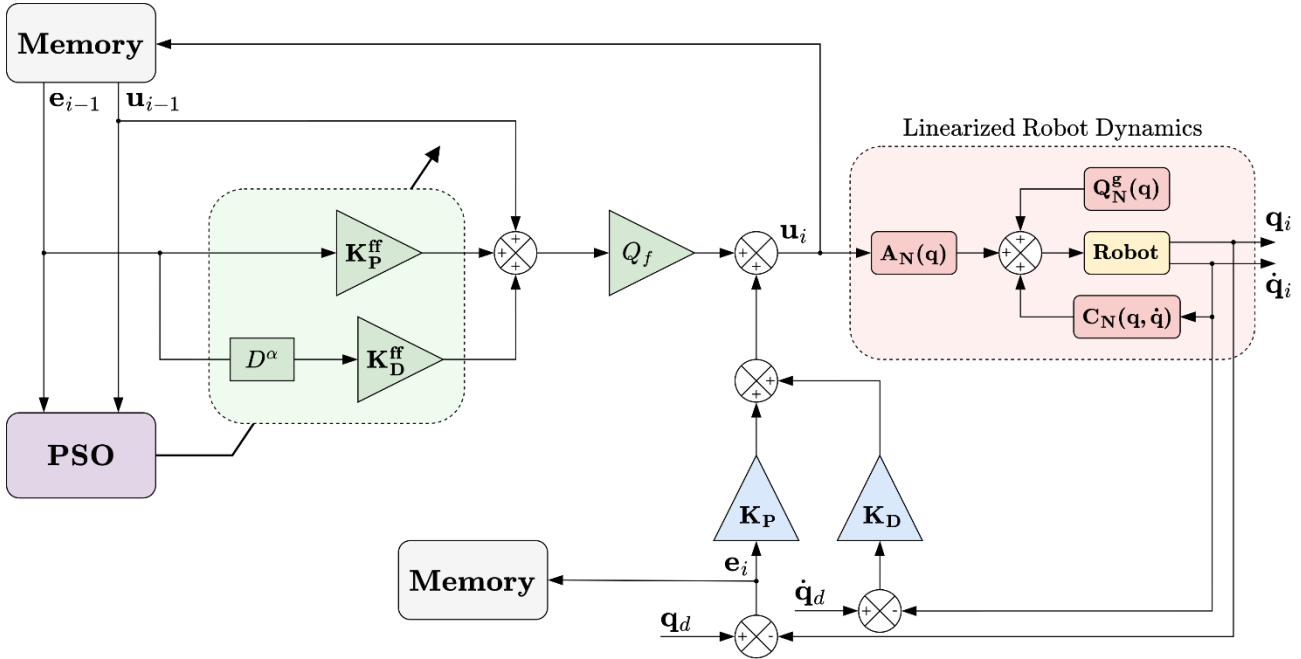


**Figure A.1.** Control system block diagram with PSO tuning.

**Table A.1.** Neuroarm robot manipulator parameters.

Joint $j$	1	2	3
$\mathbf{e}_j^\theta$	$[0 \ 0 \ 1]^T$	$[-1 \ 0 \ 0]^T$	$[-1 \ 0 \ 0]^T$
$\mathbf{p}_j^\theta$	$[0.023 \ -0.033 \ -0.17]^T$	$[0.051 \ -0.013 \ -0.223]^T$	$[0.029 \ -0.179 \ 0.047]^T$
$\mathbf{p}_{ff}^\theta$	$[0 \ 0 \ 0.47]^T$	$[0 \ 0 \ 0.235]^T$	$[0 \ 0.3 \ 0]^T$
$m_j$	3.36	2.25	1.67
$\mathbf{J}_c^\theta$	$\begin{bmatrix} 0.042 & 0.003 & 0.002 \\ 0.003 & 0.049 & 0.003 \\ 0.002 & -0.003 & 0.047 \end{bmatrix}$	$\begin{bmatrix} 0.034 & -0.002 & -0.009 \\ -0.002 & 0.045 & 0.003 \\ -0.009 & -0.046 & 0.016 \end{bmatrix}$	$\begin{bmatrix} 0.039 & -0.001 & -0.0002 \\ -0.001 & 0.01 & 0.002 \\ -0.0002 & 0.002 & 0.004 \end{bmatrix}$



## HIGH ACCURACY WEAPONS

DRAGAN KNEŽEVIĆ

Military Technical Institute, Belgrade, [dragan.knezevic@vti.vs.rs](mailto:dragan.knezevic@vti.vs.rs)

MILAN POPOVIĆ

SAF GeneralStaff, Belgrade, [popovicmilan184@gmail.com](mailto:popovicmilan184@gmail.com)

MILOŠ SIMIĆ

CNT, Belgrade, [cnt.beograd@gmail.com](mailto:cnt.beograd@gmail.com)

GORAN MARJANOVIĆ

Military Technical Institute, Belgrade, [gmarjanovic1961@gmail.com](mailto:gmarjanovic1961@gmail.com)

**Abstract:** Weapons and weapon systems of high accuracy, as well as the means to fight with them, represent the front and back of a new page in the development of military science and the construction of the armed forces. The mentioned weapons will define the character of the armed struggle in the near future. In this review paper, selected tube and missile systems were analyzed from the point of view of lethality, probability of destruction of targets and guidance systems.

**Keywords:** high-precision weapons, barrel system, missile system, lethal effects, target destruction probability, guidance system.

### 1. INTRODUCTION

With the development of the necessary technologies and techniques, that make it possible to approach of the ideal of "one grain for one goal", the human factor gains special importance in the outcome of armed combat, especially in frontal contact. Although the very term the high-accuracy weapons (HAW) is associated with the appearance of anti-tank submunitions, these weapons can to destroy targets of various types: mobile and stationary, large-sized and point-based, regardless of whether they are on land or water surface, in the air or under water. The high accuracy of hitting these assets is ensured by modern technical solutions and coupling with systems for: observation, guidance and destruction. The most common sensor systems for battlefield observation are television, thermal imaging, radar and laser sensors with high spatial resolution. They are mainly installed on satellites and/or platforms of aircraft, vessels and motor vehicles. Military geographic information and intelligence information of battlefield are also of great importance.

The representation of the HAW weapons and systems significantly contributes to changes in the form and methods of combat operations (c/o). Their application enables the destruction of objects of the interest (OI) both on the battlefield itself and in the areas of their concentration, in the depth of the territory. This combat technique becomes the main tool for the implementation of the deterrence strategy. This is due to the ability to respond quickly and precisely, directly to the elements of the enemy's development. The accuracy of hits is

achieved based on previously set elements for shooting, and on the basis of varying trajectories, time and direction of impact, types and characteristics of selected ammunition. These ordnance also have the capability for selective destruction.

By perfecting of lethality ordnance (LO) with a cumulative effect, penetration are increased, and this led to new armoring techniques, starting from steel with increased resistance of the breakthrough and ending with complex laminar armors based on ceramic and composite materials. This progress led to the improvement of the LO using a double cumulative head, increasing the caliber of the means, the use of grains with a kinetic effect, and therefore a different tactical application of these means. All of this were increased the probability of hits, and by introducing sensors into the target acquisition process, the effectiveness of conventional weapons were increased, too. With the introduction of microprocessors in the missile flight manage system, a new class of the LO, known as "smart ammunition", has emerged.

Strategic responses using HAW against aggressors are completely different from those that involve the use of weapons of great destructive power, primarily based on nuclear explosive dispositives, and/or weapons of mass destruction, which includes other chemical agents and biological agents, too. It is important to emphasize that the strategy, which implies the application of a different spectrum of HAW, does not exclude the possibility of protecting one's interests and rights by using weapons of great destructive power.

## 2. ANALYZED CRITERIA OF LO

### 2.1. Classification of LO

- 1) Unguided LO
- 2) precision-guided LO:
  - a) guided LO – correction of the projectile/missile's flight path is performed and a human is included in the control loop;
  - b) self-guided LO (smart) – correction of the projectile/missile's flight path is performed automatically based on target detection, its acquisition and determination of target and projectile/missile movement parameters using sensors on the missile/missile, and
  - c) fully automated self-guided LO (brilliant) - in addition to automatic detection, acquisition and definition of the necessary LO parameters for accurate hitting of the target, built-in algorithms define the way of activation and use of these weapons.

Self-guided LO (smart) can also be implemented as a submunition: with sensor igniter (MSU), with target detection (SMTD) and self-guided (SGM). Self-guided submunition with target detection can be implemented with a sensor igniter (SMSI) and with self-guidance in the final part of the trajectory (SMSGFPT).

### 2.2. Accuracy and precision of the LO

Achieving a high degree of accuracy and precision, from the various used weapons systems, it's of the utmost importance, if the aim is to transfer the effects of its LO to a specific target and hit nothing but the target. There are significant differences between indirect and direct fire weapon systems. In order to hit the target, it is necessary to know the exact positions of the target and the weapon. Also, before using any weapon system, it is necessary:

- for the selected weapon system to be configured, LO need to adapted to the size and type of the selected target,
- to adjust variables related to weather conditions, as well as
- to performe distancing and weapon alignment, among other factors.

In fig. 1, an illustration of the impact of systematic and random errors on precision and accuracy is given through the red circle, which represents the target area of action [1].

The accuracy of the hits indicates the degree of matching between the expected position of the mean value of the group of hits and the realized one. Accuracy, i.e. repeatability, represents the degree to which repeated hits under unchanged conditions show the same result. The illustration in Fig.1 also shows us that the elimination of systematic error improves the accuracy, but the precision does not change. If both accuracy and precision were achieved with the selected tool system and its LO, then we consider the applied weapon system with its LO as valid.

Weapon systems that use indirect fire (howitzers, mortars, unguided rockets, unguided aerial bombs, various cluster

munition dispersal systems) on targets are designed with a natural dispersion in relation to the mean point of impact (MPI) of the applied LO ( Fig. 1).

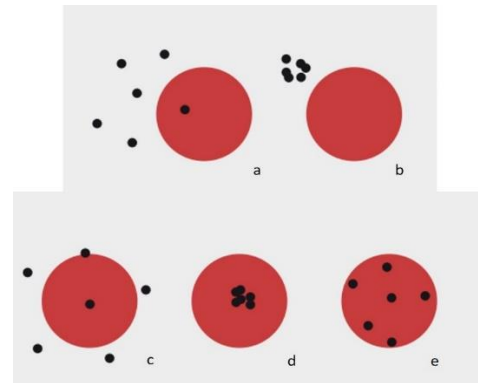


**Figure 1.** Illustration of the influence of systematic and random errors on the achieved precision and accuracy: a) low and accuracy and precision, b) low accuracy and high precision, c) high accuracy and low precision, d) high and accuracy and precision, e) high accuracy and optimal precision [1].

In these systems, accuracy refers to the weapon's ability to hit the desired MPI, while accuracy is a measure of the standard deviation from the MPI. For this purpose, the Circular Error Probable (CEP) was introduced to measure the accuracy of the weapon system. These calculations for determining the CEP of a weapon system are complex in terms of modeling, field testing, and statistical analysis of shot drop data under known conditions. A common approximation is the radius of the circle around the MPI, within which the impact points of 50% of the LO should be located. In practice, it is assumed that hits are achieved with an approximately normal distribution. In other words, this means that half of the ammunition fired, launched or thrown at the target would fall into the CEP of the weapon system, that is, 68% of the value is within the interval of plus-minus one standard deviation from the arithmetic mean; 93.7% will fall within twice the CEP radius, which corresponds to the case where 95% of the values lie within the interval of plus-minus two standard deviations; and 99.8% will fall within three times the CEP radius of the MPI, which corresponds to the case where about 99.7% of the values are within plus-minus 3 standard deviations (Fig.2). Clearly, a higher CEP indicates an increased uncertainty in the accuracy of the weapon system [1,2].

### 2.3. Lethality effect

Lethal effect will be considered as a criterion:

- estimated danger distance (RED, Risk-Estimate Distance) of suffering a lying soldier in winter clothes with a helmet during a 5-minute attack (physical incapacitation means that the soldier is physically unable to function in combat within a period of 5 minutes after the attack) at the value of the probability of incapacitation (PI, probability of incapacitation) less than 0.1%, i.e. less than 10%, and
- the degree of destruction of OI after the effect of LO is expressed in % [1,2]

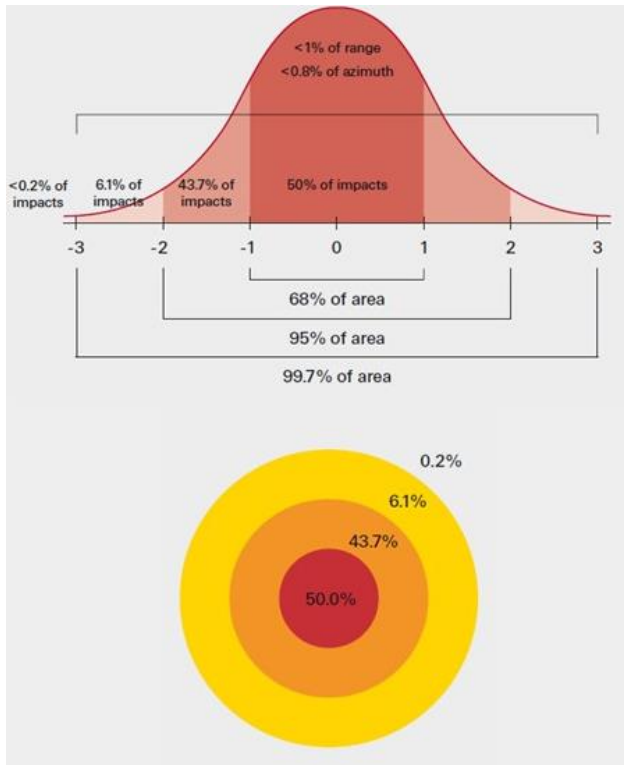


**Figure 2.** Error around MPI - Gaussian distribution and circular error probability (CEP) diagram [1].

## 2.4. HAW guidance systems

LO guidance refers to the various methods of guiding a missile/missile or guided bomb to a target. The accuracy of LO is a critical factor for its effectiveness. Guidance systems improve the accuracy of the LO by improving its guidance probability [2]. Guidance technologies can generally be divided into several categories: active, passive, preplanned and combined guidance. Projectiles, rockets and guided bombs generally use similar types of guidance systems, the difference between them being that projectiles follow a ballistic trajectory after being fired from the barrel of the weapon; rockets are propelled by an onboard motor, while guided bombs rely on the speed and altitude of the launcher aircraft for propulsion. They can also be categorized according to whether they are designed for static or dynamic purposes. With GOT (go onto target) the missile aims at both a moving and a fixed target, while with GOLIS (go onto location in space) the guidance system aims at a stationary (or almost stationary) target [3]. As a moving target can be an immediate threat to the missile launcher, its rapid elimination is necessary, while with the GOLIS system the problem is simpler due to the non-moving target.

The following ways of conducting LO are differenced:

*Command guidance*, when there is visual contact with the target, can be manual, semi-automatic or automatic. Semi-automatic guidance means that the tracking of the target is automatic, and the control and management of the missile is manual or vice versa. With the anti-aircraft defense system, we have command guidance beyond the visual field. In this case, the target seeker and the missile seeker can be oriented differently. The guidance system ensures

target interception.

*Proportional Navigation (PN)*, a guidance principle that dictates that the missile's velocity vector should rotate at a rate proportional to the line-of-sight rotation rate and in the same direction.

*Активно радарско навођење*, користи радарски систем на ракети да обезбеди сигнал за навођење.

*Semi-active guidance* uses a passive radar receiver on the missile and a radar target illuminator on the platform from which the projectile/missile is launched, or a laser receiver is used to guide the spot of the laser target illuminator.

*Passive guidance* uses either passive radar or detectors in the visible (VID) and infrared (IR) regions of the spectrum to detect the signature of the target being guided. Optoelectronic (OE) monitoring uses cameras in the appropriate part of the spectrum.

*Retransmission guidance (TVM, Track via missile)* is a hybrid command - semi-active - active radar guidance, in which the missile transmits the information of the reflected radar radiation of the target to the guidance station, which immediately transmits the corrected commands back to the missile.

We distinguish between self-directed LOs:

1. Fully autonomous systems, where the following stand out:
  - a) Pre-set guidance systems, before firing/launching, where based on information about the distance and direction of the target, the flight path is determined and programmed in the missile guidance system, which during the flight maneuvers the missile according to the defined trajectory without external information (uses its integrated accelerometers or gyroscopes), and
  - b) Inertial navigation systems (INS), which continuously receive incoming signals from sensors of translational motion, accelerometers, and rotational motion, gyroscopes, and based on them software calculates the necessary parameters of navigation in real time and compares the obtained results in relation to the reference or new spatial position ordnance in space.
2. Systems dependent on the nature of external sources (astronomical, astro-inertial, Earth's surface - topographical or photographic maps, magnetic), where the following stand out:
  - a) Astro-inertial navigation, which serves to correct small errors in determining position and speed resulting from the uncertainty of launch conditions in the submarine navigation system and errors accumulated during flight due to imperfect instrument calibration. It is used in submarine-launched ballistic missiles that do not have a stationary launch point, unlike silo-based intercontinental ballistic missiles.
  - b) Navigation according to the contour of the terrain, or topographically, (TERCOM, terrain contour) based on height maps of the country belt, or via a full 3D map, enables the management of the complex route of the missile from the launch site to the target. The correction of this data is done on the basis of assigned surveillance radar altimeters that track the missile during flight or by

using the Global Positioning System (GPS) or the Digital Scene Matching Area Correlator (DSMAC), photographically, which it uses a camera to monitor the terrain, digitize and compare the images with the stored scenes in the computer of the base station that guides the missile to the target.

3. Systems dependent on artificial sources in which we distinguish:

- Satellite navigation systems: GPS and GLONASS (Global navigation satellite system), and
- Long-range hyperbolic navigation systems, such as: Decca, LORAN, Omega, Chayka, Alpha.

### 3. ANALYZED SYSTEMS ACCORDING TO SELECTED CRITERIA LO

HAW of the weapons with the tube system caliber up to 30 mm are achieved by remotely controlled gyro-stabilized weapons systems, which, in addition to the basic armament, are also equipped with a suitable system for target acquisition and fire control. They are installed on ground combat vehicles or on combat platforms of vessels and aircraft. These systems use unguided LO and weapons elements for firing are picked out directly.

HAW of the weapons with the tube system caliber up to 125mm, which by direct fire achieve hits on the target with unguided ammunition (e.g. a tank, with an optoelectric day-night aiming device), have a  $CEP \leq 1.1m$ . The same CEP values are achieved with pipe systems whose projectiles are guided by the laser beam.

In the case of multi-barrel HAW systems, using the example of the 122mm Grad missile, the lethal surface is about  $700m^2$  for each high-explosive warhead that detonates upon impact with the ground, which corresponds to the surface of a circle with a radius of 15m. It should be taken into account that only the detonation of one missile warhead is considered here; when a beam of rockets hits one area, there is usually an overlapping of lethal areas. For the lethal area of the 122 MM 9M22 rocket, the probability of incapacitation at a distance of 15m from the detonation point is 36%. Modern multi-barrel high-accuracy rocket systems M270 (MLRS, Multiple Launch Rocket System) on tracks and M142 (HIMARS, High Mobility Artillery Rocket System) on wheels fire rockets: M57 with  $CEP \leq 9m$ , M30/M31 with  $CEP \leq 10m$  (GPS guidance  $CEP \leq 5m$ ). The M30/M31 rockets can be adjusted to operate above the ground from 3m and 10m. Modern multi-barrel HAW systems have the possibility of individual selection of the impact point of the system's effect zone [3,4,5].

A comparative view of the estimated distance of the danger of injury to a lying soldier from the effects of a mortar, tank and artillery projectile, a 122mm rocket, a classic MK 82 bomb and a cruise missile is shown in table 1.

**Table 1** Comparative view of the estimated distance of the danger of injury to a lying soldier [1,2,4]

Lethality Ordnance	RED 10	RED 0.1
80mm mortar projectile	80m	175m
120mm mortar projectile	100m	400m

120mm tank gun projectile	90m	250m
122mm artillery rocket	150m	500m
152/155mm art. gun projectile	125m	450m
MK 82 bomb 230 kg	250m	425m
Tomahawk cruise missile	80m	200m

The advantage of HAW on the example of the MK 82 bomb shows that with the unguided variant  $CEP \leq 94.5m$ , and with the guided variants:  $CEP \leq 1.1m$  with laser guidance,  $CEP \leq 5m$  with GPS and inertial guidance,  $CEP < 30m$  if the GPS guidance has jammed signal on trajectory and  $CEP \leq 1.1m$  when using the combined GPS-inertial-laser guidance method.

A comparative representation of circular fire deviation (CFD) accuracy is shown for several different air-to-ground HOWs in Table 2.

**Table 2.** Comparison of CFD accuracy [5]

Lethality Ordnance	CFD accuracy	SGH
AGM-65, Maverick,	2,5m	TI, TV, LR
Martel	3m	TV
AGM-84H/K SLAM-ER	2,5m	TI, GPS, 2wdt
ALARM	6-9m	-
SGH – self-guided head		LR - laser receiver
TI - thermal imaging		2wdt – two-way data connection
TV - television		

A comparative presentation of the probability of a hit for several different HAW air-ground is shown in Table 3.

**Table 3.** Comparison display of accuracy with hit probability [5]

Lethality Ordnance	hit probability	SGH
Панцирь-С1,	1 rocket, $p \geq 0,92$	I, radar
Roland	1 rocket, $p \geq 0,92$	radar
C-300B	2 rockets, $p \geq 0,96$	radar
MIM-104 Patriot	2 rockets, $p \geq 0,96$	radar

Mines with a sensor fuze are a specific the HAWs intended for anti-armor combat at short distances, with blocking narrow passages in the most likely directions of enemy armoured fighting vehicle. The sensor module of these devices uses several different sensors: IR, acoustic, seismic, active electromagnetic. The best results are obtained by using multiple sensors simultaneously. The average target detection range is about 100m. These sensors enable automatic observation of the area of effect and determination of movement parameters and target position during the programmed time of mine activity. Two secondary modules are also often used: a module for manually programming the mine's activity time and a module for protection against unwanted mine reuse.

### 4. LO WITH SMART SUBMUNITION

Submunition with target detection is a high-precision munition intended to destroy hard, point and armored targets at long distances with the aim of disorganizing, slowing down or breaking the concentration of armored vehicles in the depth of the combat deployment (II and III echelon) or in the waiting area (collection zone). It makes



it possible to carry out anti-armor combat at long distances with an effect on the upper surface of armored vehicles, which are the least protected by armor. These systems use a large number of different sensors at different levels and efficient systems for transmitting and processing information. Application of the "smart" system of submunitions in c/o implies the following:

- Detection and tracking of targets at the depth of the enemy's combat deployment (up to 100 km);
- Reliable and fast (in real time) transmission of intelligence data in sufficient volume to make a decision on the use of SMTD;
- Quick processing of intelligence data, decision-making for use;
- Launching of carrier missiles (dispensers) from HAW that ensures accurate delivery of dispensers to the target area;
- Distribution (discharge) of SMTD ensures sufficient coverage of the target area with a satisfactory density of action on it;
- Use of target detection sensors on submunitions for target selection, missile flight control and lethal effect of OI.

Submunitions are intended for impact on the upper surface of the target, which is usually the weakest protected by armor. The lethal effect on the target is achieved by cumulative jet (MSGFPT), kinetic grain (Mishay-Shardin effect) and destructive effect.

Focusing of the jet of combustion products during the combustion of the explosive charge, a primary cumulative jet with a temperature of about 3.000 °C is formed in the focal point, which spreads at a speed of about 10,000 m/s. After breaking through the armor due to melting by this jet, its effect on the living force inside the armor continues with increased pressure and causing explosive fire.

A kinetic grain is formed by an explosion behind a specially shaped disk, after which that disk is transformed into a projectile with an initial speed of more than 2000m/s. The mechanical destruction of the obstacle occurs due to the high speed (kinetic energy), shape and material of the projectile thus formed. For the optimal condition for the reshaping of the disk and the effect on the target, the activation of the warhead must be ensured at a distance of about 1000 caliber projectiles.

The destructive effect of submunitions is a backup variant of the lethal effect, if the conditions for the basic cumulative effect or kinetic grain effect are not met. Depending on the design of the warhead, this effect can disable armored vehicles by contacting through vehicle openings and acting on external sensor subsystems..

## 5. WEAPONS OF MASS DESTRUCTION AT THE BASE OF NED<sup>1</sup>

A *fission weapon* is a weapon whose explosive contribution is based solely on the fission reaction (often

referred to as an atomic bomb or A-bomb). In common types of such weapons, the explosion reaches a power of about 1kT to 500kT (the power of a nuclear explosion is measured by the equivalent of the classic TNT explosive and is expressed in kilotons - kT). This weapon can be employed using large caliber barrel systems.

A *thermonuclear weapon*, fusion weapon or hydrogen bomb (H bomb) consists of two main components: a primary nuclear fission stage (fueled by <sup>235</sup>U or <sup>239</sup>Pu) and a secondary nuclear fusion stage. Thermonuclear fuel is used for nuclear fusion: heavy isotopes of hydrogen (D, i.e. <sup>2</sup>H and T, i.e. <sup>3</sup>H) as a pure element or in modern weapons LiD (lithium deuteride). A fusion explosion begins with the detonation of the primary fission stage. The distance separating the primary and secondary assembly ensures that fragments of debris from the primary fission (which move much slower than X-ray photons) do not tear the secondary assembly apart before the explosive fusion process is fully completed. During the secondary stage of fusion, the nuclear effective cross section<sup>2</sup> increases. In modern weapons, lithium deuteride is used for fuel, so that the tritium component of the thermonuclear fuel is provided in collisions of free neutrons, emitted from the fissile plutonium explosive mixture, with lithium nuclei. The case of the thermonuclear weapon is also made of fissile material, in order to achieve a second fission with fast thermonuclear neutrons. Those bombs are classified as two-stage weapons (fission-fusion-fission). The rapid fission of the tamper case and radiation make the biggest contribution to obtaining radioactive fission products. The tamper is a layer of dense material surrounding the fissile material. It serves to reduce the critical mass of nuclear weapons and to delay the spread of the reacted material by keeping it longer in a supercritical state due to its inertia. This material also serves as a neutron reflector. In common types of such weapons, the explosion reaches a power of 50kT to 10MT.

A *neutron weapon* is a low "yield" thermonuclear weapon. It is projected that during the complex development of the thermonuclear phase of the reaction, the neutron effect in the area of the explosion will increase compared to the effect of the blast wave<sup>3</sup>. Projectiles with this tool are also used tactically with 155mm and 203mm tube systems, due to more effective armor penetration than conventional warheads (they pass through concrete, iron, earth, lead, human body). In common types of such weapons, the explosion reaches a power of 1kT to 20kT. When the power is greater than 10 kT, the radius of the lethal blast and thermal effect begins to exceed the radius of the lethal ionizing radiation. If a

<sup>2</sup> The concept of a " nuclear cross section" of the order of  $10^{-28}$   $m^2=10^{-24}$   $cm^2$  or 100 fm<sup>2</sup>, where a larger surface area indicates a higher probability of interaction. Total cross-sections refer to overall interaction processes, and for specific processes, such as elastic and inelastic scattering, in addition to neutron cross-sections, absorption cross-sections are of particular importance.

<sup>3</sup> Thus, it was achieved that the lethal radius of the neutron effect was greater than the radius of the explosion itself. Prompt neutrons created in this process quickly leave the further reaction, so that a large wave of prompt neutrons is obtained.

<sup>1</sup> NED, nuclear explosive dispositives

neutron weapon is designed for an anti-ballistic missile, the role of prompt neutrons after the explosion is to cause partial fission of nearby warheads and thus prevent the proper explosion process. The radius of the maximum distance from the dynamic target is about 100m.

A *cobalt bomb* is a nuclear weapon designed to radioactively contaminate a large area through radioactive fallout. Cobalt in the housing of this device, after the secondary phase of the thermonuclear reaction, interacts with prompt neutrons and changes to its isotope  $^{60}\text{Co}$ <sup>4</sup>, and then to its gas phase through atmospheric condensation. Contamination is achieved by extreme radioactive fallout, which falls to earth along with residual cobalt debris.

A *radiological bomb* (or dirty bomb) combines conventional explosives and radioactive material. These means are used for radioactive dispersal of NED and contamination of as large an area as possible. Contamination over a large area can also be achieved by using depleted uranium ammunition.

## 6. DEVELOPMENT TRENDS

For the purposes of analysis and development of the HAW systems, it is necessary to possess a powerful intellectual potential for the development of high-precision control systems and drives for weapon systems in the areas of: control systems, information technologies, precision mechanics, optics, electronics, hydraulics and computer technologies.

On the other hand, for the development, synthesis, integration and production of high-precision tools, it is necessary to master knowledge and dispose of technologies for the development or integration of the following subsystems and systems: inertial control systems and correlation-extreme guidance systems for aircraft, electric and electro hydraulic control and servo drives of different powers, optical-electronic systems, remote control systems, computer systems and their software, stationary and mobile automated complexes for receiving, interactive processing and transmission of video information, and multifunctional amplitude precise digital angle converters..

## 7. CONCLUSION

Compared to HAW, NED-based LO cover large areas and have a longer duration of action over them. From the point of view of the accuracy, NED-based weapons have significantly less limitations. If these assets are used as mines or as part of tactical LO, they can certainly be included in HAW.

In weapons with the tube system using unguided LO and bombs with sensor guidance achieve  $\text{CEP} \leq 1,1\text{m}$ .

Multiple rockets launchers of the HAW systems are characterized by the ability to adjust the effect above the ground up to 3m, as well as the selection of the point of impact of an individual projectile in the system's effect zone. Greater lethality is achieved with systems with a vertical or near-vertical attack path.

The high accuracy of missile systems was also achieved thanks to precise sensor systems for acquisition, software tools for precisely defined movement trajectory and flight control to the point of encounter with a dynamic target or the point of falling on a stationary target, as well as sensors for the most favorable assumption of LO activation in the close vicinity of the target.

Analyzing the LO effects on the target, the application of mines gives the highest accuracy, because they can always be placed in the selected position, and the corresponding LO effects can always be adjusted in relation to the preset time and space of the target's appearance in the waiting zone.

Analyzing the effects of lo on the target, the application of mines gives the highest accuracy, because they can always be placed in the selected position and the appropriate effects of LO can always be adjusted in relation to the time and spatial assumption of the appearance of the target in the waiting zone. The placement of mines makes it easier to achieve a horizontal effect, and their modular construction enables quick assembly and simple masking.

In ground systems, submunitions are used in shells of large-caliber tube systems (H155mm and H203mm).

For the development of the HAW system, in addition to intellectual potential, it is necessary to master knowledge and dispose of technologies for the development or integration of modern optoelectronic and inertial sensor systems, as well as other automated controllable systems for guiding and correcting the path for the LO.

## References

- [1] GICHD: *Explosive weapon effects – final report*, Geneva, February 2017
- [2] JAMES N. C.: *Fundamentals of Strategic Weapons: Offense and Defense Systems*, Volume 1, Martinus Nijhoff Publishers, HaGUE/Boston/London, 445 pages, 1981.
- [3] PAUL Z.: *Tactical and Strategic Missile Guidance*, Sixth Edition, Progress in Astronautics and Aeronautics, Vol 239, 2012.
- [4] PROJECT OF ALSA: *Multi-Service Tactics, Techniques, Procedures For The Joint Application Of Firepower*, USA, 2007
- [5] ГОЛОВИН С. А. И ДР: *Высокоточное оружие и борьба с ним*, Изд-во “Б.П.К.”, 1996

<sup>4</sup> This isotope is a strong emitter of gamma radiation with a half-life of 5.26 years. Comparing the gamma radiation of the fission products of the equivalent uranium bomb in the outer shell after one year, the radiation of  $^{60}\text{Co}$  is 8 times stronger than the fission products of uranium, and after five years 150 times stronger.



## MULTISENSOR IMAGE FUSION: DATASET, METHODS AND PERFORMANCE EVALUATION

MOHAMMED ZOUAOU LAIDOUNI

University of Defence Belgrade, Military Academy, [mohammedz.laidouni@gmail.com](mailto:mohammedz.laidouni@gmail.com)

BOBAN BONDŽULIĆ

University of Defence Belgrade, Military Academy, [bondzulici@yahoo.com](mailto:bondzulici@yahoo.com)

DIMITRIJE BUJAKOVIĆ

University of Defence Belgrade, Military Academy, [dimitrijebujakovic@gmail.com](mailto:dimitrijebujakovic@gmail.com)

TOUATI ADLI

University of Defence Belgrade, Military Academy, [adlitouati94@gmail.com](mailto:adlitouati94@gmail.com)

MILENKO ANDRIĆ

University of Defence Belgrade, Military Academy, [andricsmilenko@gmail.com](mailto:andricsmilenko@gmail.com)

**Abstract:** *Multisensor image fusion is a crucial research area aiming to enhance image clarity and comprehensibility by integrating information from multiple sensors. This paper presents a residual dense transformer (RDT) architecture for multisensor image fusion to address the challenges posed by the unique strengths and limitations of visual infrared (VIS), near-infrared (NIR), and long-wavelength infrared (LWIR) sensors. A comparative analysis is conducted with several state-of-the-art fusion methods using various objective evaluation indicators to assess the image fusion quality. We used a 313 triplet images collected from three datasets: TRICLOBS, MOFA, and MUDCAD, covering diverse environmental conditions such as foggy conditions and low illumination. Through the evaluation of the RDT and state-of-the-art fusion algorithms on this dataset, we observe that RDT achieve the best overall performance across multiple spectra image fusion. This work, thus, serves as a platform for developing and comparing new algorithms to deal with images from three sensors. which aids in the development of various applications such as object tracking, detection, and surveillance.*

**Keywords:** *Multisensor images; image fusion; multisensor dataset; residual dense transformer; deep leaning.*

### 1. INTRODUCTION

The development of image sensors and multisensor image fusion has been an important field of research for many years. By combining the complementary information from multiple image sensors about a same scene can produce a new single fused image with more clarity and understandability to be applied and enhance several applications such as object tracking, object detection, surveillance, military applications, facial analysis and recognition [1-4].

Sensor systems are categorized based on the wavelengths they capture and the three most used are visual infrared (VIS), near-infrared (NIR), and long-wavelength infrared (LWIR) [1]. To combine the strength of this sensors several algorithms have been proposed, including conventional algorithms and deep learning-based algorithms [5, 6]. Conventional algorithms according to their corresponding theories, can be classified into: multiscale transform-based algorithms, sparse representation-based algorithms, subspace-based methods, saliency-based algorithms, hybrid algorithms.

Considering the powerful feature representation capability of deep learning, researchers have proposed several algorithms such as CNN-, AE-, GAN-, and transformer-based algorithms. The basic components of CNN-, AE-, and GAN-based algorithms are convolutional layers which focus on local features and ignores some global information. To overcome this drawback, the transformer-based algorithms have been proposed to model the long-range dependency and capture the global context. However, these algorithms only stack transformer blocks without incorporating the global features of all previous blocks, which is essential for improving the fusion process by maximizing the use of all global information.

Furthermore, to evaluate the performance of image fusion algorithms across multiple spectra, many datasets have been used, including TNO [7], RoadScene [8], VIFB [9], KAIST [10], RGB-NIR [11]. However, current research on multisensor image fusion is suffering from several problems, such as the lack of a well-recognized multisensor image fusion dataset that can be used to compare image fusion performance across various spectral images of the same scene. As a result, it is common to observe that most of utilized dataset in

experiments in the literature usually contain only images from two different sensor (LWIR-VIS or NIR-VIS), which poses challenges in evaluating performance of fusion algorithms for multisensor image fusion.

To tackle the challenges mentioned above. In this work we use a residual dense transformer to maximize the use of the global features. Furthermore, we collect a multisensor image fusion dataset containing images from three sensors, including LWIR, NIR and VIS images. The images are collected from three available datasets TRICLOBS [12], MOFA [13] and MUDCAD [14] to facilitate the training and performance evaluation for multisensor image fusion. Thus, the main contributions of this work are summarized as follow:

- A residual dense transformer is used to maximize the use of the global features and produce a fused images with higher clarity and understandability.
- Training/testing dataset is created containing triplet images from LWIR, NIR and VIS spectra. These images are collected from three available datasets TRICLOBS, MOFA and MUDCAD, covering a wide range of environments, such as foggy condition and low illumination.
- Analysis and comparative evaluation of several state-of-art image fusion algorithms including traditional and advanced algorithms based on deep learning for the training/testing dataset.

The rest of the paper is organized as follows. Section 2 describes the databases used in this research. In Section 3, the framework of the residual dense transformer is presented, Next, the comparison performance of fusion methods is analyzed on the dataset. Finally, Section 4 concludes the paper.

## 2. DATABASES DESCRIPTION

In this research, three datasets are used, namely TRICLOBS, MOFA and MUDCAD. The general characteristics of these datasets are listed in Table 1.

**Table 1.** General characteristics of the datasets

Name	Image triplets	Image type	Resolution	Year
TRICLOBS	183	LWIR, NIR, VIS	480×640	2016
MOFA	84	LWIR, NIR, VIS	Various	2023
MUDCAD	46	LWIR, NIR, VIS	512×512	2023

TRICLOBS, MOFA and MUDCAD are multimodal image datasets contain images from the VIS, NIR and LWIR parts of the electromagnetic spectrum. TRICLOBS encompass outdoor scene representing various military and civilian surveillance scenarios at different locations [12]. MOFA dataset contain two main groups: indoor and outdoor scenery. The indoor scenery comprises of table top scenes and rooms with different objects category such as books, tools, electronics and toys. The outdoor scenery comprises of scenes from 8 different locations: university

campus buildings playground, crossroads, houses, garden, shore, grassland and pools [13]. MUDCAD dataset contain scene captured by an unmanned aerial vehicle in two different areas of the test site at the University of the Bundeswehr, Munich and under different environments, such as grassland, gravel and graveled soil, various bushes and trees, and both concrete and asphalt roads [14]. The representative images from TRICLOBS, MOFA and MUDCAD datasets are given in Figure 1.

**Table 2.** Train/test partition details of TRICLOBS, MOFA and MUDCAD datasets

Dataset	Train	Test
TRICLOBS	97	86
MOFA	65	19
MUDCAD	46	/

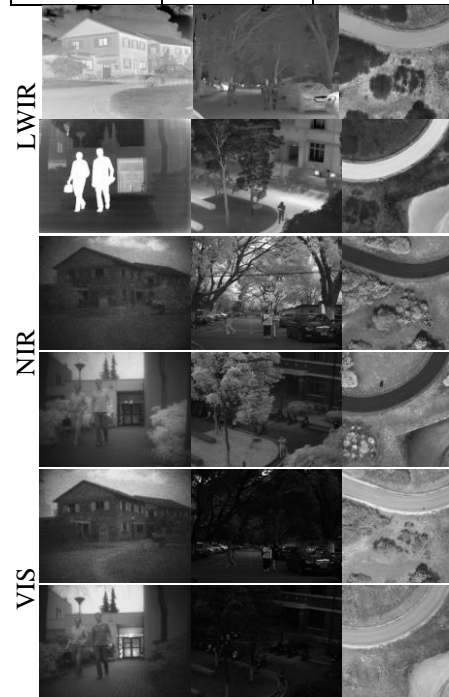


**Figure 1.** Representative images from TRICLOBS, MOFA and MUDCAD datasets

The dataset partition is provided in Table 2 including 208 triplets of LWIR, NIR and VIS images for training and 105 for testing. TRICLOBS, MOFA and MUDCAD are use in training set, while in testing set only TRICLOBS and MOFA are contributed. Each triplet of MOFA images has been registered to successful image fusion. As can be seen in Figure 1, the images cover a wide range of environments and conditions, such as indoor, outdoor, and remote sensing images which enrich the training and testing tasks.

## 3. METHOD

In this section, we first present the overall framework of the residual dense Transformer architecture and then we provide a detail about the loss function used for training.

### 3.1 Residual dense Transformer architecture

The overall framework of the RDT is shown in Figure 2 inspired by the work in RDN [15] and SDTFusion [16]. We design the RDT and it consists of three main modules: shallow feature extraction, global feature extraction, and reconstruction.

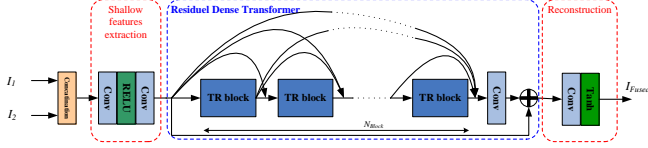


Figure 2. The general framework of the residual dense Transformer

At the beginning, the two-channel map is obtained by performing an element-wise concatenation on two inputs  $I_1$  and  $I_2$ , and then the two-channel map is fed to the first module to extract shallow features. After extracting the shallow features, they will be conducted through the RDT to extract the global features. The RDT consist of a multiple TR block densely connected and each TR block contain  $N_{TR}$  Swin Transformer. The Conv+RELU in the TR block is used to adapt the output channels of the previous TR block, while the Conv used in the RDT is used to fuse all the state of TR blocks. This architecture enables to retain more important information and improve the global feature extraction by incorporating the extracted features from all previous states. In the final module, convolutional and Tanh activation layers are used to integrate the channels information, and obtain the final fused image.

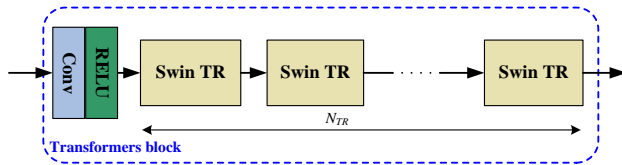


Figure 2. The structure of the TR block

### 3.2 Loss function

To unsupervised train the RDT for image fusion, a loss function composed of pixel sub-loss and gradient sub-loss are used, and is defined as:

$$L = \alpha \cdot L_P + \beta \cdot L_G \quad (1.1)$$

where  $\alpha$  and  $\beta$  are weighted parameters that control the balance between the sub-losses.  $L_P$  and  $L_G$  are the pixel and gradient sub-loss, respectively. They can be formulated as:

$$L_G = \|\nabla I_F - \max\{\nabla I_1, \nabla I_2\}\|_1 \quad (1.2)$$

$$L_P = \|\|I_F - \text{mean}(I_1, I_2)\|_1 \quad (1.3)$$

## 4. MULTISENSOR IMAGE FUSION

In this section, we firstly present the methods used in the comparative evaluation on collected dataset in section 4.1, and then quantitative evaluation metrics are provided in section 4.2. In Sections 4.3-4.5 are presented a qualitative and quantitative performance comparison of LWIR/VIS, LWIR/NIR and NIR/VIS image fusion.

### 4.1 Comparison algorithms

In this research, we incorporated 6 published fusion algorithms, including two traditional algorithms FPDE [9] and LatLRR [9] and four advanced algorithms based on deep learning, namely, RFN-Nest [17], U2Fusion [18], SwinFuse [19] and DataFuse [20].

These algorithms cover many algorithm types. FPDE is multi-sensor image fusion which is based on fourth order partial differential equations to get approximation and detail information from source images, and then the principal component analysis was applied to obtain the optimal weights to fuse the approximation and detail information. LatLRR algorithm is based on latent low-rank representation, which decompose the images into low-rank parts (global structure) and salient parts (local structure), and then, the low rank parts are fused by weighted-average strategy while the salient parts are simply fused by sum strategy. RFN-Nest is autoencoder-based algorithm that utilizes a residual fusion network learned via training using visible and infrared image pairs to perform feature fusion. In addition, they utilized multiscale features in the encoder and nest connection in the decoder to improve the fusion performance.

U2Fusion is CNN-based algorithm which use a densely connected fusion network. In the training phase, U2Fusion automatically estimates an adaptive similarity degrees of source images by using feature extraction and information measurement to preserve this similarity between the fusion result and source images.

SwinFuse is a transformer-based algorithm that use a transformer-based encoder to model the long-range dependency and capture a global context.

DataFuse is transformer-based algorithm, which use a dual-attention residual module to examine the significant regions of source images, and a Transformer module to preserve global complementary information.

**Table 3.** Quantitative performance comparison of LWIR/VIS image fusion on TRICLOBS and MOFA

	Method	information error-based		information features-based					structure similarity-based				human perception-inspired		information theory-based
		RMSE	PSNR	AG	$Q_{abf}$	SCD	$Q_P$	$Q_M$	MS-SSIM	$Q_C$	$Q_S$	CC	CV	CB	NMI
TRICLOBS	FPDE	0.086	58,800	2,561	0.437	1,443	0.462	0.688	0.897	0.639	0.778	0.619	980,792	0.418	0.471
	LatLRR	0.088	58,690	2,630	0.450	1,526	0.368	0.627	0.900	0.657	0.807	0.620	1018,591	0.420	0.416
	RFN-Nest	0.094	58,471	2,487	0.430	1,590	0.390	0.596	0.929	0.594	0.782	0.614	905,660	0.413	0.492
	U2Fusion	0.086	58,802	2,153	0.331	1,423	0.405	0.584	0.892	0.615	0.790	0.621	881,889	0.456	0.523
	SwinFuse	0.112	57,643	3,355	0.381	1,633	0.376	0.560	0.891	0.579	0.537	0.536	1098,377	0.561	0.552
	DataFuse	0.140	56,681	4,388	0.226	1,444	0.240	0.428	0.829	0.349	0.491	0.583	999,955	0.319	0.369
RDT	0.107	57,845	4,111	0.605	1,586	0.484	0.702	0.928	0.749	0.839	0.586	738,462	0.456	0.540	
MOFA	FPDE	0.079	59,196	3,370	0.464	1,072	0.395	0.502	0.882	0.576	0.708	0.729	556,295	0.419	0.407
	LatLRR	0.081	59,094	3,245	0.483	1,266	0.381	0.488	0.896	0.520	0.719	0.735	364,366	0.454	0.376
	RFN-Nest	0.088	58,755	3,414	0.484	1,674	0.387	0.434	0.940	0.560	0.718	0.735	554,969	0.414	0.426
	U2Fusion	0.079	59,208	2,431	0.334	1,054	0.416	0.406	0.870	0.512	0.706	0.736	504,359	0.456	0.451
	SwinFuse	0.098	58,245	3,406	0.334	1,180	0.358	0.460	0.769	0.336	0.466	0.673	500,019	0.533	0.429
	DataFuse	0.126	57,146	3,564	0.358	1,160	0.297	0.315	0.881	0.504	0.594	0.676	676,522	0.323	0.475
RDT	0.084	58,934	5,114	0.590	1,522	0.446	0.648	0.947	0.567	0.750	0.709	266,446	0.471	0.398	

The train parameters of the RDT are adapted by the Adam optimizer with learning rate of  $10^{-4}$ , and the epoch number is set to 30. The model parameter  $N_{TR}$  and  $N_{Block}$  are set to 2 and 3, respectively. The weighted parameter in the loss function  $\alpha$  and  $\beta$  are set to 20 and 10, respectively. All experiments were conducted using a computer equipped with an NVIDIA RTX3060 GPU and i7-11800H CPU. Default parameters reported by the corresponding authors of each algorithm were employed. To obtain sufficient training samples for deep learning-based algorithms, the training data were randomly cropped into  $64 \times 64$  patches, and then the models were retrained to perform the multisensor image fusion.

## 4.2. Evaluation metrics

To conduct a comprehensive quantitative evaluation, 14 frequently utilized objective evaluation indicators for image fusion are utilized, including, Root mean squared error (RMSE), Peak signal-to-noise ratio (PSNR) reveals the distortion during the fusion process at the pixel level, Average gradient (AG) measures the degree of clarity and sharpness, Objective gradient based image feature metric ( $Q_{abf}$ ) calculates the edge information, which is transferred from source images to the fused image, the sum of correlations of differences (SCD) measures the maximum information of the fused images containing each source image. phase congruency-based image feature metric ( $Q_P$ ) measures fusion performance by making comparisons within the local correlation between the feature maps of the fusion result and the source images. Multi-scale Scheme-Based image feature metric ( $Q_M$ ) calculate the edge preservation value of the fused image across multiple scale, structure similarity (MS-SSIM) evaluates the structural loss and distortion of fused images from the human visual system's perspective, Cvejie's Metric ( $Q_C$ ) use a local measurement of similarity between blocks of pixels in the input images and the fused images to estimate how well the important information in the source images is represented by the fused image. Piella's Metric ( $Q_S$ ) utilizes local measures to estimate how well the salient information from the inputs is present in the fused images. correlation coefficient (CC) measures the degree of linear correlation between the fused images and the source images., Chen-Varshney metric (CV) and Chen-Varshney metric (CB)

are tow metrics to evaluate the image quality of the fused images based on the human visual system perception, normalized mutual information (NMI) calculates the mutual information transformed from the input images to the fusion result.

## 4.3. LWIR and VIS image fusion

Figure 4 illustrates two groups of LWIR and VIS image pairs from the TRICLOBS and MOFA datasets and the fused images generated through different algorithms. As can be seen in Figure 4, FPDE, LatLRR, U2Fusion and SwinFusion suffer from low contrast and fail to present some scene detail. RFN-Nest, DataFuse and RDT display a good contrast.

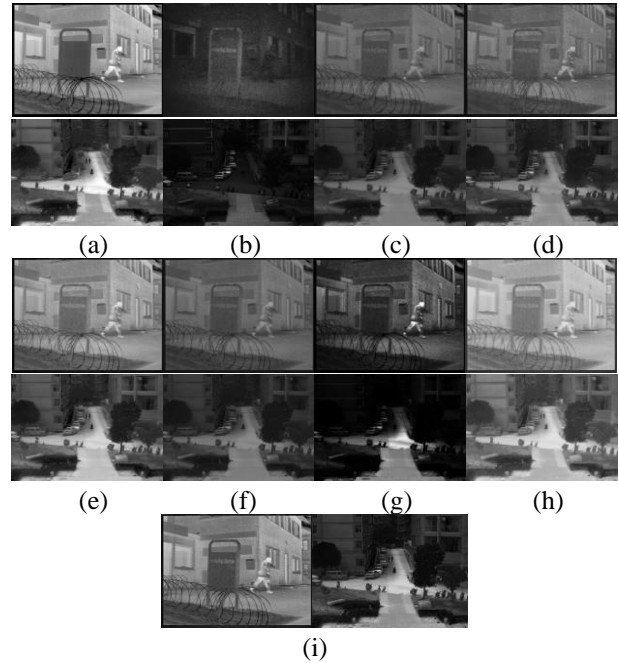


**Figure 4.** Qualitative performance comparison of LWIR/VIS image fusion on TRICLOBS and MOFA: (a) LWIR, (b) VIS, (c) FPDE, (d) LatLRR, (e) RFN-Nest, (f) U2Fusion, (g) SwinFusion, (h) DataFuse, (i) RDT

A quantitative comparison of RDT and several algorithms' performance on TRICLOBS and MOFA are shown in Table 3. The fused LWIR/VIS fused images are evaluated using 14 evaluation metrics, and for each metric, the best and the second-best methods are marked in red and green, respectively. RDT method shows the best overall performance in terms of information features, structure similarity and human perception. FPDE and U2Fusion show competitive performance in terms of information error, displaying the best and second-best performance in both RMSE and PSNR metrics.

#### 4.4. LWIR and NIR image fusion

In Figure 5, two groups of LWIR and NIR image pairs

from the TRICLOBS and MOFA datasets are provided along with fused images. FPDE, LatLRR, RFN-Nest, U2Fusion, and SwinFusion suffers from low contrast. RDT method displays a good performance in combining information from the both image modalities.

Table 4 presents the quantitative performance comparison of LWIR/NIR images fusion. As can be seen, RDT method show the best overall performance in term of information features, structure similarity, human perception and information theory in both MOFA and TRICLOBS datasets. The second-best overall results are shown by RFN-Nest method. Furthermore, FPDE obtains the best performance in term of information error.

**Table 4.** Quantitative performance comparison of LWIR/NIR image fusion on TRICLOBS and MOFA

	Method	information error-based		information features-based					structure similarity-based				human perception-inspired		information theory-based
		RMSE	PSNR	AG	Q <sub>abr</sub>	SCD	Q <sub>P</sub>	Q <sub>M</sub>	MS-SSIM	Q <sub>C</sub>	Q <sub>S</sub>	CC	CV	CB	NMI
TRICLOBS	FPDE	0.083	58,952	2,041	0.305	1,373	0.392	0.587	0.882	0.607	0.784	0.616	627,371	0.463	0.482
	LatLRR	0.105	57,949	2,923	0.418	1,418	0.392	0.633	0.900	0.664	0.759	0.548	388,914	0.369	0.546
	RFN-Nest	0.083	58,948	2,616	0.437	1,410	0.403	0.733	0.885	0.624	0.765	0.616	704,650	0.409	0.412
	U2Fusion	0.085	58,841	2,536	0.435	1,481	0.351	0.638	0.893	0.653	0.801	0.616	848,595	0.418	0.382
	SwinFuse	0.106	57,895	3,482	0.389	1,580	0.368	0.570	0.899	0.638	0.566	0.534	661,912	0.599	0.478
	DataFuse	0.093	58,519	2,824	0.492	1,605	0.412	0.645	0.938	0.653	0.790	0.596	499,178	0.406	0.473
	RDT	0.102	58,054	3,852	0.617	1,569	0.484	1.003	0.932	0.736	0.810	0.566	253,571	0.497	0.579
MOFA	FPDE	0.077	59,344	2,637	0.308	1,492	0.342	0.360	0.829	0.505	0.742	0.592	726,533	0.474	0.315
	LatLRR	0.103	58,047	3,472	0.397	1,499	0.336	0.337	0.838	0.569	0.678	0.507	928,844	0.391	0.425
	RFN-Nest	0.078	59,274	5,111	0.428	1,473	0.248	0.458	0.798	0.437	0.706	0.571	779,837	0.443	0.241
	U2Fusion	0.081	59,118	3,367	0.449	1,600	0.345	0.439	0.857	0.518	0.765	0.593	574,599	0.485	0.284
	SwinFuse	0.094	58,465	3,766	0.458	1,828	0.321	0.388	0.907	0.550	0.734	0.577	885,031	0.377	0.312
	DataFuse	0.101	58,123	3,874	0.347	1,726	0.303	0.402	0.821	0.429	0.583	0.573	801,136	0.541	0.296
	RDT	0.091	58,584	5,434	0.617	1,742	0.440	0.946	0.908	0.545	0.795	0.542	444,047	0.503	0.457

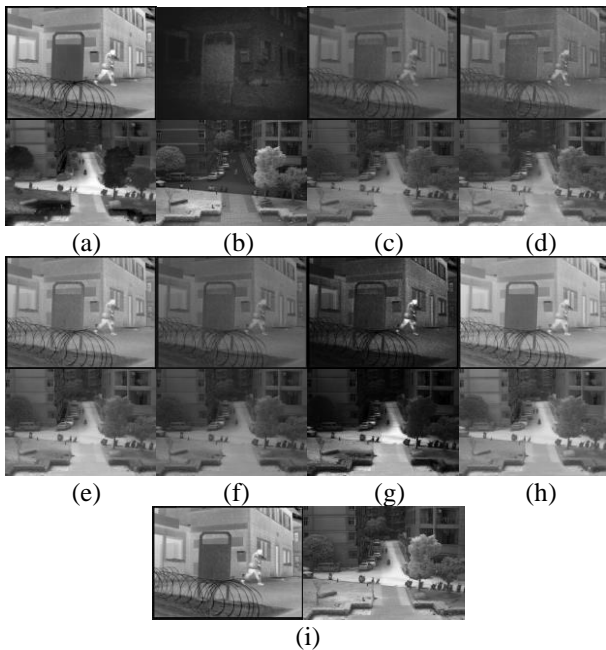


**Figure 5.** Qualitative performance comparison of LWIR/NIR image fusion on TRICLOBS and MOFA: (a) LWIR, (b) NIR, (c) FPDE, (d) LatLRR, (e) RFN-Nest, (f) U2Fusion, (g) SwinFusion, (h) DataFuse, (i) RDT

#### 4.5. NIR and VIS image fusion

Figure 6 provides qualitative comparison of several fusion algorithms on two groups NIR and VIS image pairs from the TRICLOBS and MOFA datasets. In the case of TRICLOBS image, all methods provide an unclear scene to a certain degree. In other hand, in MOFA image, DataFuse and RDT methods can describe the general details about the scene.

Table 5 shows the quantitative comparisons between RDT and the state-of-the-art algorithms. As one can see, RDT method shows the best overall performance in terms of information features, structure similarity, human perception and information theory in both MOFA and TRICLOBS datasets. RFN-Nest method shows the second overall performance, and displays the best results in terms of information error.

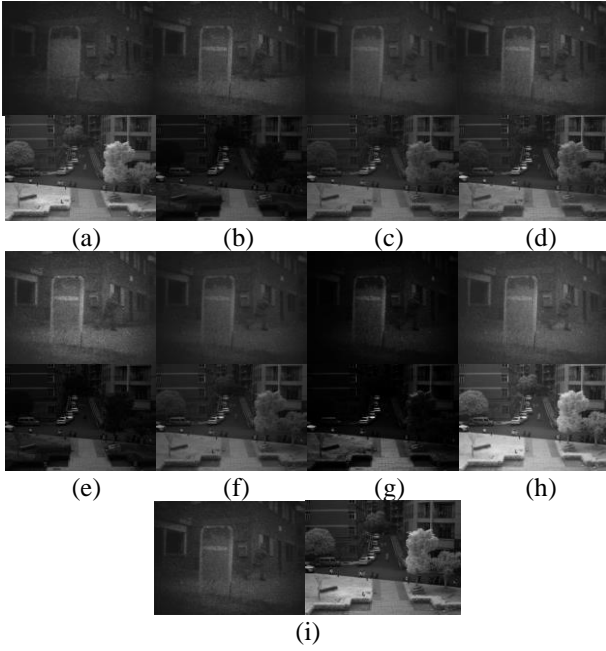


**Figure 6.** Qualitative performance comparison of NIR/VIS image fusion on TRICLOBS and MOFA: (a) NIR, (b) VIS, (c) FPDE, (d) LatLRR, (e) RFN-Nest, (f) U2Fusion, (g) SwinFusion, (h) DataFuse, (i) RDT

#### 4.6 Ablation study

In this section, ablation studies are performed to verify the effectiveness of RDT architecture, and the loss function design. The results of the ablation experiments on the LWIR+VIS image fusion is shown in Table 6. It is observed that removing the residual or the dense connection from the architecture degrade the overall performance which prove the importance of incorporating the features of the previous states. Furthermore, it is noticed that removing any term of the loss function change the global performance. Eliminating the gradient term allow the model to have better performance in information error-based metrics, in the other hand, without the intensity term the model can achieve better performance in some information features, structure similarity based-metrics. However, only the both terms allow the model to have a balance and achieve better overall performance.

**Table 5.** Quantitative performance comparison of NIR/VIS image fusion on TRICLOBS and MOFA

	Method	information error-based		information features-based					structure similarity-based				human perception-inspired		information theory-based
		RMSE	PSNR	AG	Q <sub>abr</sub>	SCD	Q <sub>P</sub>	Q <sub>M</sub>	MS-SSIM	Q <sub>C</sub>	Q <sub>S</sub>	CC	CV	CB	NMI
TRICLOBS	FPDE	0.027	63.957	1.746	0.425	0.728	0.435	0.735	0.968	0.691	0.919	0.932	116.863	0.585	0.558
	LatLRR	0.071	59.676	2.572	0.420	1.419	0.423	0.680	0.964	0.621	0.832	0.917	114.542	0.525	0.566
	RFN-Nest	0.027	63.960	1.904	0.452	0.685	0.433	0.756	0.966	0.721	0.918	0.932	122.073	0.564	0.556
	U2Fusion	0.032	63.140	2.130	0.422	1.021	0.387	0.734	0.959	0.691	0.909	0.926	127.170	0.540	0.508
	SwinFuse	0.137	56.859	3.482	0.170	0.540	0.109	0.517	0.616	0.443	0.452	0.143	2075.968	0.339	0.310
	DataFuse	0.043	61.904	2.527	0.505	1.300	0.500	0.764	0.920	0.541	0.844	0.871	94.497	0.635	0.782
	RDT	0.032	63.160	2.827	0.564	0.973	0.564	1.074	0.977	0.778	0.906	0.915	68.518	0.594	0.676
MOFA	FPDE	0.053	61.208	3.164	0.476	0.770	0.579	0.445	0.920	0.662	0.803	0.842	166.741	0.583	0.526
	LatLRR	0.087	58.903	5.664	0.555	1.198	0.547	0.264	0.940	0.473	0.556	0.759	152.950	0.479	0.363
	RFN-Nest	0.053	61.219	3.953	0.634	0.806	0.619	0.551	0.940	0.780	0.847	0.841	186.156	0.557	0.538
	U2Fusion	0.055	60.941	4.404	0.590	1.179	0.580	0.540	0.945	0.737	0.848	0.843	184.616	0.572	0.479
	SwinFuse	0.062	60.419	4.992	0.375	0.470	0.503	0.336	0.751	0.493	0.576	0.746	575.546	0.675	0.536
	DataFuse	0.089	58.712	3.874	0.304	0.278	0.218	0.391	0.627	0.556	0.579	0.476	1451.403	0.448	0.255
	RDT	0.055	61.005	5.543	0.719	1.276	0.675	1.189	0.983	0.745	0.890	0.784	86.608	0.599	0.703

**Table 6.** Ablation study on MOFA and TRICLOBS

Dataset	Method	information error-based		information features-based					structure similarity-based				human perception-inspired		information theory-based
		RMSE	PSNR	AG	Q <sub>abr</sub>	SCD	Q <sub>P</sub>	Q <sub>M</sub>	MS-SSIM	Q <sub>C</sub>	Q <sub>S</sub>	CC	CV	CB	NMI
Architecture	RDT	0.1030	58.0442	4.2940	0.6021	1.5743	0.4769	0.6921	0.9318	0.7158	0.8227	0.6086	652.2285	0.4587	0.5139
	w/o D	0.1043	57.9885	4.3190	0.5908	1.5867	0.4751	0.6205	0.9298	0.6998	0.8103	0.6062	668.8243	0.4556	0.5126
	w/o R	0.1032	58.0359	4.2702	0.5883	1.5723	0.4451	0.6990	0.9278	0.6999	0.8202	0.6007	624.0815	0.4601	0.5216
Loss	RDT	0.1030	58.0442	4.2940	0.6021	1.5743	0.4769	0.6921	0.9318	0.7158	0.8227	0.6086	652.2285	0.4587	0.5139
	w/o G	0.0949	58.3888	3.1802	0.3786	1.2577	0.2705	0.5660	0.7419	0.5417	0.7093	0.5250	1323.2103	0.4477	0.5239
	w/o P	0.1054	57.9486	4.5344	0.5799	1.6083	0.4356	0.4946	0.9396	0.6034	0.7835	0.6143	597.8346	0.4513	0.4579



## 4. CONCLUSION

In this paper, we present a RDT architecture for image fusion task. Furthermore, we collected set of 313 triplet images (LWIR, NIR and VIS) from 3 different datasets, TRICLOBS, MOFA and MUDCAD to build a novel training/testing dataset. This benchmark facilitates better understanding of the state-of-the-art image fusion approaches across 3 spectral bands, and can provide a platform for developing new algorithms which deal with multisensor images technology. An experiment is carried out to evaluate the performance of the RDT method compared to the state-of-the-art fusion algorithms on the collected dataset. The experiment is conducted through different image type fusion and illustrates that the RDT achieves the best overall performance.

Further research of this work, may include extending this dataset and implementing image fusion algorithms which deal with the three-sensor image fusion. Thus, it will help for selecting which algorithm is adequate for fusing specific sensors.

## References

- [1] Li, B., Xian, Y., Zhang, D., Su, J., Hu, X., Guo, W.: Multi-Sensor Image Fusion: A Survey of the State of the Art, *Journal of Computer and Communications* 100 (2021) 86–97.
- [2] Shopovska, I., Jovanov, L., Philips, W.: Deep visible and thermal image fusion for enhanced pedestrian visibility, *Sensors*, 19 (17) (2019) 3727–3746.
- [3] Zhang, J., Ding, Y., Yang, Y., Sun, J.: Real-time defog model based on visible and near-infrared information, 2016 IEEE International Conference on Multimedia & Expo Workshops (ICMEW), Seattle, WA, 2016.
- [4] Coffey, V.C.: Seeing in the dark: Defense applications of IR imaging, *Optics and Photonics News*, 22 (4) 2011 26–31.
- [5] Zhang, X., Demiris, Y.: Visible and Infrared Image Fusion Using Deep Learning. *IEEE Transactions on Pattern Analysis and Machine Intelligence*, 45 (8) (2023) 10535 - 10554.
- [6] Ma, J., Ma, Y., Li, C.: Infrared and Visible Image Fusion Methods and Applications: A Survey. *Information Fusion*, 45 (2018) 153-178.
- [7] TNO Image Fusion Dataset. Accessed: Oct. 10, 2022. [Online]. Available: [https://figshare.com/articles/dataset/TNO\\_Image\\_Fusion\\_Dataset/1008029](https://figshare.com/articles/dataset/TNO_Image_Fusion_Dataset/1008029)
- [8] Xu, H., Ma, J., Li, Z., Jiang, J.: FusionDN: A unified densely connected network for image fusion, *Proceedings of the AAAI Conference on Artificial Intelligence*, 2020
- [9] Zhang, X., Ye, P., Xiao, G.: VIFB: A visible and infrared image fusion benchmark, 2020 IEEE/CVF Conference on Computer Vision and Pattern Recognition Workshops (CVPRW), Seattle, WA, USA, 2020
- [10] Hwang, S., Park, J., Kim, N., Choi, Y., Kweon, I.S.: Multispectral pedestrian detection: Benchmark dataset and baseline. 2015 IEEE Conference on Computer Vision and Pattern Recognition (CVPR). Boston, MA, USA, 2015
- [11] Brown, M., Susstrunk, S.: Multispectral SIFT for scene category, *CVPR 2011*, Colorado Springs, CO, USA, 2011
- [12] Toet, A., Hogervorst, M.A., Pinkus, A.R.: The TRICLOBS dynamic multi-band image data set for the development and evaluation of image fusion methods. *PLoS One*. 11 (12) (2016) e0165016.
- [13] Xiao, K., Kang, X., Liu, H., Duan, P.: MOFA: A novel dataset for Multi-modal Image Fusion Applications. *Information Fusion* 96 2023 144-155.
- [14] Hupel, T., Stütz, P.: Measuring and Predicting Sensor Performance for Camouflage Detection in Multispectral Imagery, *Sensors*, 23(19) 2023 8025.
- [15] Zhang, Y., Kong, Y., Zhong, B., Tian, Y., Fu, Y.: Residual Dense Network for Image Super-Resolution. *Conference on Computer Vision and Pattern Recognition (CVPR)*. 2018
- [16] Pang, S., Huo, H., Liu, X., Zheng, B., Li, J.: SDTFusion: A split-head dense transformer based network for infrared and visible image. *Infrared Physics & Technology*, 128 (2024).
- [17] Li, H., Wu, X., Kittler, J.: RFN-Nest: An end-to-end residual fusion network for infrared and visible images, *Information Fusion*, 73 2021 72-86
- [18] Xu, H., Ma, J., Jiang, J., Guo, X., Ling, H.: U2Fusion: A unified unsupervised image fusion network. *IEEE Transactions on Pattern Analysis and Machine Intelligence*, 44 (1) 2020 502-518.
- [19] Wang, Z., Chen, Y., Shao, W., Li, H., Zhang, L.: SwinFuse: A Residual Swin Transformer Fusion Network for Infrared and Visible Images, *IEEE Transactions on Instrumentation and Measurement*, 71 2022 1-12
- [20] Tang, W., He, F., Liu, Y., Duan, Y., Si, T.: DATAFuse: Infrared and visible image fusion via dual attention transformer. *IEEE Transactions on Circuits and Systems for Video Technology*, 33 (7) 2023 3159–3172.



## COMPARATIVE ANALYSIS OF YOLO ALGORITHMS FOR AIRCRAFT DETECTION IN REMOTE SENSING IMAGES

TOUATI ADLI

University of Defence Belgrade, Military Academy, , [adlitouati94@gmail.com](mailto:adlitouati94@gmail.com)

DIMITRIJE BUJAKOVIĆ

University of Defence Belgrade, Military Academy, [dimitrijebukovic@gmail.com](mailto:dimitrijebukovic@gmail.com)

BOBAN BONDŽULIĆ

University of Defence Belgrade, Military Academy [bondzulici@yahoo.com](mailto:bondzulici@yahoo.com)

MOHAMMED ZOUAOU LAIDOUNI

University of Defence Belgrade, Military Academy, [mohammedz.laidouni@gmail.com](mailto:mohammedz.laidouni@gmail.com)

MILENKO ANDRIĆ

University of Defence Belgrade, Military Academy, [andricsmilenko@gmail.com](mailto:andricsmilenko@gmail.com)

---

**Abstract:** Accurate object detection in remote sensing images, particularly for military aircraft, is imperative for strategic decision-making. However, this task encounters numerous challenges, including diverse aircraft categories, their variable sizes and geometries, complex backgrounds, environmental factors (weather conditions, lighting variations, shadows) and sensor parameters. This paper presents a comparative study of three state-of-the-art detection algorithms, including YOLOv5, YOLOv7, and YOLOv8, and it aims to explore the strengths and limitations of each algorithm in addressing the above challenges. Considering the specific problem of military aircraft detection, the experimental results were conducted on the Military Aircraft Recognition dataset (MAR20). The obtained results demonstrate that YOLOv7 outperforms other algorithms in terms of detection performance, achieving a global mean average precision (mAP) and (mAP<sub>0.5</sub>) by 67.7%, and 90.3% respectively.

**Keywords:** Aircraft detection; remote sensing images; YOLO.

### 1. INTRODUCTION

Remote sensing target detection is a vital task in both civilian and military applications, including environmental monitoring, disaster management, urban planning, military surveillance, etc. [1]. The main objective of this task is to identify and categorize objects of interest in remote sensing images [2]. In the military field, aircraft pose significant strategic menaces, making their identification and localization critical factors that influence decision-making on the battlefield [2]. The aircraft targets detection remains a difficult task due to the several challenges it encounters [3-6], including, top-down view, aircraft types similarity, small and densely scattered objects, and target-background resemblance. Furthermore, a various external factor, including weather conditions, lighting, shadows, sensor parameters, etc., can significantly impact the accuracy of aircraft detection.

Object detection task in remote sensing image is carried out using traditional and deep learning techniques. Traditional approaches rely on handcrafted features and machine learning algorithms. In recent years, deep learning techniques have gained a significant attention,

and become the predominant methods for classification and target detection tasks [5]. Particularly, the appearance of convolutional neural networks (CNNs) [1]. The power of deep learning methods lies in automatically extracting and learning higher-level semantic features and providing a stronger feature representation capability unlike traditional machine learning methods that are based on handcrafted features [1].

Target detection algorithms can be divided into two main groups [1, 5, 7, 8]: single-stage target detection algorithms, and two-stage target detection algorithms. The single-stage algorithms, including You Look Only Once [9] (YOLO), Fully Convolutional One-Stage Object Detection (FCOS) [10], Single Shot MultiBox Detector (SSD) [11], Deconvolutional Single Shot Detector (DSSD) [12] and RetinaNet [13] are designed to detect a target within images by combining regression and classification tasks [5]. These models generally use a single feedforward step in order to create bounding boxes and class probabilities directly from entire image. The two stage target detection algorithms such as regions with convolutional neural networks (R-CNN) [14], Fast R-CNN [15], Faster R-CNN [16], Cascade R-CNN [17] and spatial pyramid pooling network (SPP-Net) [18] are based on generated collection of regions of interest (RoIs) from

image, to identify and classify the objects based on these regions [19]. Two-stage target detection algorithms show superior detection accuracy and slower detection speed [1, 5, 6]. In contrast, single-stage algorithms are generally faster and sacrifice detection accuracy, making them useful for applications where detection speed is critical.

This paper presents a comparative study for aircraft detection in remote sensing images of three state-of-the-art single-stage target detection algorithms, including YOLOv5 [20], YOLOv7 [21] and YOLOv8 [22]. The experimental results were conducted on the Military Aircraft Recognition (MAR20) [2] dataset, which the largest publicly available dataset for military aircraft recognition in remote sensing images. This paper is structured as follows: Section 2 provides an overview of YOLOv5, YOLOv7, and YOLOv8 algorithms. Following that, the obtained experimental results were presented and discussed in Sections 3 and 4, and in the last section is given study conclusion.

## 2. OVERVIEW OF THE YOLO ALGORITHMS

### 2.1. YOLOv5

YOLOv5 [20], introduced in 2020, is a real-time, one stage detection algorithm that prioritizes detection speed over accuracy through the utilization of a more compact network architecture. This strategy achieves a high efficiency in detection task [23, 24]. YOLOv5 encompasses five variants, namely, YOLOv5n, YOLOv5s, YOLOv5m, YOLOv5l and YOLOv5x. The YOLOv5 network architecture comprises four main components, which are: Input, Backbone, Neck and Prediction.

Before being fed into the network, the input image undergoes preprocessing to improve detection accuracy. The Backbone part extracts feature from input images, while the Neck component combines features from various detection layers of the Backbone using the PANet [25] strategy. The Prediction part employs a complete intersection over union (CIoU) loss function to improves the speed and accuracy of detection. Additionally, it utilizes non-maximum suppression (NMS) [26] to detect multiple and occluded objects in the input image.

### 2.2. YOLOv7

The YOLOv7 [21] represents a cutting-edge one-stage real-time object detection algorithm. It demonstrates a favorable compromise between detection speed and accuracy, surpassing the previous YOLO series in accuracy and speed. An outstanding novelty within YOLOv7 is the introduction of the E-ELAN methodology, which effectively guides computational blocks to capture a diverse range of features. This approach integrates convolutional layers followed by detection layers to predict bounding boxes and object classes, using methods like expansion and shuffling to improve learning dynamics while preserving gradient

flow integrity.

### 2.3. YOLOv8

YOLOv8 [22], is a real-time object detection algorithm, building upon the success of its predecessors, while integrating new features and improvements to make it faster, more accurate, and easier to use. YOLOv8 can be used in many tasks, including object detection, tracking, segmentation, image classification, and posture estimation. YOLOv8 comes in five variants, YOLOv8n, YOLOv8s, YOLOv8m, YOLOv8l and YOLOv8x.

## 3. EXPERIMENTS

In this section, we first present the dataset used in the experiments, called MAR20 dataset. Following this, it is provided an explanation of the used evaluation metrics and implementation details. The experiments primarily involve a comparative study of three detection algorithms, including YOLOv5m, YOLOv7 and YOLOv8m.

### 3.1. MAR20 Dataset

MAR20 [2] dataset is the largest public dataset for remote sensing image military aircraft recognition. It comprises 3842 high-resolution remote sensing images encompassing 22341 instances of 20 distinct aircraft types, labeled from A1 to A20 (refer to Fig. 1). These images were collected using Google Earth in 60 military airports. The majority of images in the dataset have a resolution of 800x800 pixels. Two annotation methods are given: horizontal bounding box and oriented bounding box for each target instance. Table 1 illustrates the distribution of instances for each aircraft type in the dataset.



**Figure 1.** The twenty aircraft types in MAR20 dataset.

In our experiments, the original training set, comprising 1331 images (7870 instances), was divided into training and validation subsets, encompassing 90% (1198 images) and 10% (133 images), respectively, and the whole test set was used for testing. The horizontal bounding box annotations were utilized throughout these experiments.

**Table 1.** Distribution of instances in train and test sets for each aircraft type.

Aircraft	Train	Test	All	Aircraft	Train	Test	All
A1	554	1092	1646	A11	151	356	507
A2	736	993	1729	A12	240	462	702
A3	316	860	1176	A13	561	1091	1652
A4	179	463	642	A14	659	1119	1778
A5	435	827	1262	A15	200	418	618
A6	107	334	441	A16	785	1847	2632
A7	191	489	680	A17	439	958	1397
A8	365	579	944	A18	160	148	308
A9	475	611	1086	A19	519	717	1236
A10	368	556	924	A20	430	551	981

### 3.2. Evaluation Metrics

For the evaluation of the object detection algorithms, we employ commonly used evaluation metrics, including mean average precision (mAP) averaged for intersection over union  $IoU \in \{0.5, 0.55, 0.6, \dots, 0.95\}$  (COCO's standard metric), mean average precision ( $mAP_{0.5}$ ) at  $IoU=0.5$  (PASCAL VOC's metric) [16], precision (P), and recall (R).

The IoU is computed by determining the overlapping area between the predicted region (A) and the actual ground truth (B):

$$IoU = \frac{A \cap B}{A \cup B} \quad (1)$$

where  $A \cap B$  indicate the intersection area of the predicted and ground truth bounding boxes and  $A \cup B$  is their union.

The expressions for P and R are defined as follows:

$$P = \frac{TP}{TP + FP}, R = \frac{TP}{TP + FN} \quad (2)$$

where,  $TP$  (true positives) refers to the number of positive samples correctly identified,  $FP$  (false positives) represents the number of negative samples erroneously identified as positive samples, and  $FN$  (false negatives) denotes the number of positive samples were incorrectly identified as negative samples.

The formulas of  $mAP_{0.5}$  and  $mAP$ , are given by:

$$mAP_{0.5} = \frac{1}{N} \sum_{i=1}^N AP_i, IoU = 0.5 \quad (3)$$

$$mAP = \frac{1}{N} \sum_{i=1}^N AP_i, IoU = 0.5 : 0.05 : 0.95 \quad (4)$$

where  $N$  is the number of categories, and  $AP_i$  is the average precision of each  $i$ -th category of objects. It represents the area under precision-recall curve and it can be calculated by:

$$AP = \int_0^1 P(R) dR \quad (5)$$

### 3.3. Implementation Details

The experimental platform runs on Windows 11, within an Intel® Core™ i7-12650H/16G @2.30GHz, equipped with an NVIDIA RTX 3050Ti/4GB. Python 3.9 and Pytorch framework (version 2.0.1) were used for implementation of algorithms, and CUDA 11.8 was utilized to accelerate the calculation.

In the training phase the Stochastic Gradient Descent (SGD) algorithm was utilized to optimize the loss function. Specifically, a momentum of 0.937 and a weight decay coefficient of 0.0005 were used. To enhance training stability, a warmup strategy was implemented. The initial learning rate was set at 0.01, with a batch size of 2 and the number of epochs was set at 300. The resolution of input image was maintained at 640x640 pixels.

### 3.4. Training results

Fig. 2 illustrates the variations of performance metrics, including  $mAP_{0.5}$  (Fig. 2 (a)),  $mAP$  (Fig. 2 (b)), recall (Fig. 2 (c)) and precision (Fig. 2 (d)) of YOLOv5m, YOLOv7 and YOLOv8m. These metrics measures the performance of object detection algorithms. The higher values indicative of improved accuracy in detection capabilities. YOLOv8m shows better training speed and efficiency compared to YOLOv5m and YOLOv7. However, YOLOv7 outperforms the others in terms of overall performance, particularly in  $mAP_{0.5}$  and recall.

## 4. EXPERIMENTAL RESULTS

A comparative evaluation was conducted between the YOLOv5m, YOLOv7, and YOLOv8m algorithms on the MAR20 dataset under the same configurations. Table 2 illustrates the comparative performance metrics for the three detection algorithms. These findings clearly demonstrate that YOLOv7 surpasses YOLOv5m and YOLOv8m across almost all metrics (precision, recall,  $mAP_{0.5}$ , and  $mAP$ ).

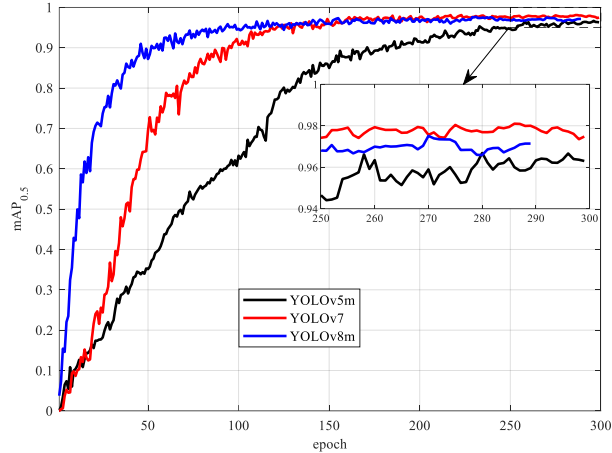
**Table 2.** Aircraft detection results

Algorithm	P (%)	R (%)	$mAP_{0.5}$ (%)	$mAP$ (%)	Inference time (ms)
YOLOv5m	82.2	82.2	86.9	64.5	<b>17.3</b>
YOLOv7	<b>85.6</b>	<b>84.2</b>	<b>90.3</b>	<b>67.7</b>	19.3
YOLOv8m	83.4	78.5	86.1	65.2	24.1

The YOLOv7 achieves  $mAP_{0.5}$  and  $mAP$  scores of 90.3% and 67.7% respectively, outperforming YOLOv5m by 3.4% and 3.2% respectively, and YOLOv8m by 4.2% and 2.5%.

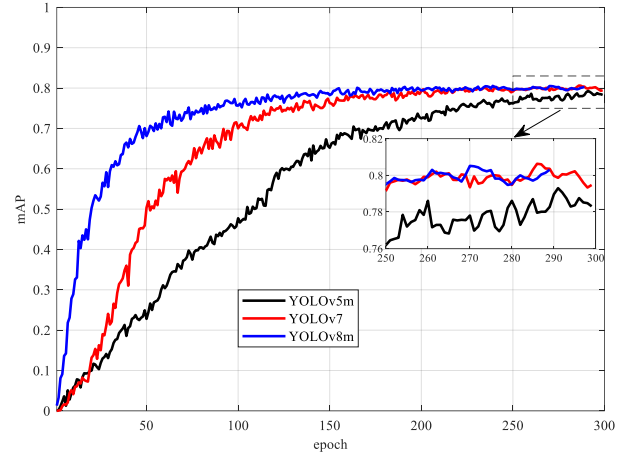
Furthermore, YOLOv7 exhibits exceptional precision in distinguishing aircraft features, reducing recognition errors, and attaining a recall rate of 84.2%, which is 2%

and 5.7% higher than YOLOv5m and YOLOv8m,

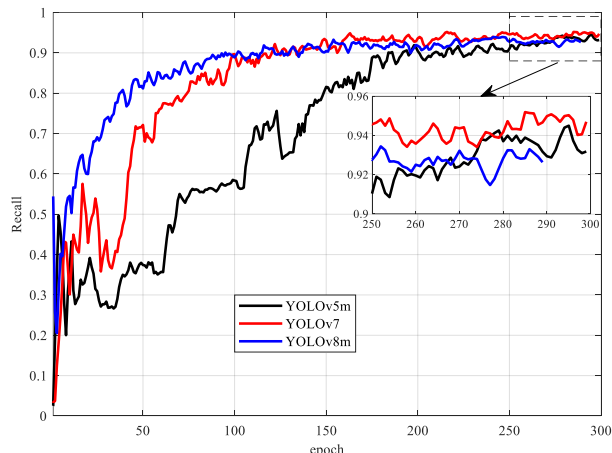


(a)

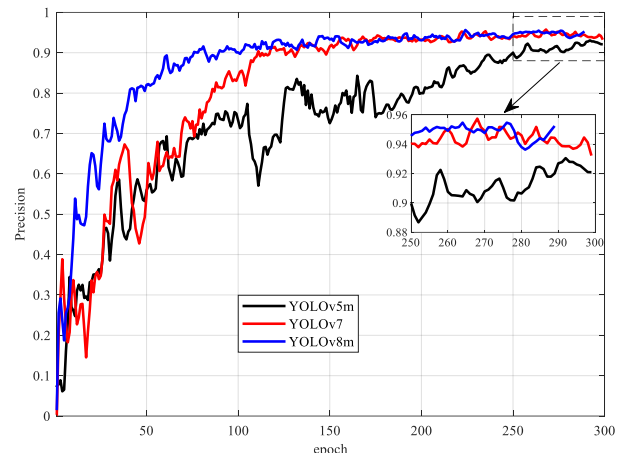
respectively.



(b)



(c)



(d)

**Figure 2.** Performance curve: (a)  $mAP_{0.5}$ , (b)  $mAP$ , (c) recall, and (d) precision.

While the YOLOv5m network architecture is comparatively smaller, resulting in a reduced inference time of 17.3 ms against 19.3 ms for YOLOv7 and 24.1 ms for YOLOv8m.

#### 4.1. Detection Results By-Class

For a more comprehensive comparative analysis, Table 3 presents the detection performance metrics, including  $mAP$ ,  $mAP_{0.5}$ , precision, and recall by classes, for the YOLOv5m, YOLOv7, and YOLOv8m detection algorithms. This detailed breakdown offers a clearer view of the strengths and limitations of each algorithm.

The analysis of the Table 3 shows that YOLOv7 algorithm demonstrates superior overall performance compared to YOLOv5m and YOLOv8m. It achieves the  $mAP$  exceeds or closely approaches 67%, except for aircraft types A5 (52.8%), A15 (40.8%), A13 (60.3.4%), A19 (62.1%) and A20 (62.7%), which exhibit lower detection rates. The observed low detection rate observed for aircraft types A15 and A13 across all algorithms can be attributed to their high similarity with other aircraft types (such as A5 and A16), as well as their relatively smaller size compared to other types. This similarity reduces the discriminative capacity of the features extracted by the network, making it challenging to

differentiate and detect these aircraft types.

Despite the lower instances number of aircraft A18 compared to other aircraft types, in addition the high inter-class similarity with aircraft A4, the YOLOv7 demonstrates high detection performance compared to other algorithms. It achieves a  $mAP$  of 64.8.5%,  $mAP_{0.5}$  of 80.4%, precision of 87%, and recall of 70.3%.

Fig. 3 presents detection results using YOLOv5m, YOLOv7 and YOLOv8m algorithms on the same images extracted from MAR20 test set, including four cases: successful detection, Fig. 3 (a), small object detection, Fig. 3 (b), false alarm, Fig. 3 (c), and target-background resemblance Fig. 3 (d).

In Fig. 3 (a) it is worth noting that all algorithms successfully detected and recognized correctly the aircraft type A5 instances, where YOLOv7 demonstrate the best overall confidence value.

Fig. 3 (b) shows the detection results of small objects. YOLOv5m and YOLOv8m misidentified the aircraft A5 instances and identified them as A15 (the images marked with red boxes contain misidentification), due to the high inter-class similarity between them. However, YOLOv7 successfully detects and identifies all instances with a high confidence value. In Fig. 3 (c) YOLOv7 successfully detect and identify all instances with better confidence

value. However, YOLOv5 and YOLOv8m algorithms show false alarm detection.

**Table 3.** Detection results of YOLOv5m, YOLOv7 and YOLOv8m algorithms on various classes of MAR20 dataset.

	YOLOv5m				YOLOv7				YOLOv8m			
	P (%)	R (%)	mAP <sub>0.5</sub> (%)	mAP (%)	P (%)	R (%)	mAP <sub>0.5</sub> (%)	mAP (%)	P (%)	R (%)	mAP <sub>0.5</sub> (%)	mAP (%)
A1	<b>75.1</b>	76.6	82.1	65.0	75.0	<b>84.1</b>	<b>85.5</b>	<b>68.7</b>	71.5	82.0	81.0	65.1
A2	98.6	84.8	95.5	69.1	<b>98.9</b>	<b>89.5</b>	<b>98.3</b>	<b>71.4</b>	98.3	77.6	92.4	67.9
A3	89.6	87.7	95.6	67.6	91.5	<b>91.7</b>	<b>97.2</b>	<b>70.0</b>	<b>93.4</b>	84.3	95.4	68.1
A4	76.2	<b>89.2</b>	87.4	65.8	83.4	83.6	<b>91.7</b>	<b>71.1</b>	<b>85.0</b>	84.4	89.7	67.0
A5	66.7	79.9	75.2	49.4	64.6	<b>83.1</b>	<b>80.8</b>	<b>52.8</b>	<b>66.9</b>	80.4	76.8	51.0
A6	93.7	<b>89.2</b>	94.9	71.7	96.2	86.2	<b>95.1</b>	<b>74.0</b>	<b>96.3</b>	84.1	94.3	72.6
A7	81.3	92.6	93.5	74.2	90.7	<b>94.9</b>	<b>97.6</b>	<b>78.7</b>	<b>90.8</b>	91.3	96.7	78.4
A8	86.1	94.6	94.4	73.6	85.8	<b>94.8</b>	<b>96.1</b>	<b>74.4</b>	<b>87.0</b>	91.4	94.1	73.5
A9	<b>89.5</b>	79.9	91.7	67.3	94.8	<b>85.8</b>	<b>94.2</b>	<b>69.6</b>	86.8	75.4	87.9	65.3
A10	<b>95.2</b>	93.9	98.1	70.4	93.0	<b>95.9</b>	<b>98.4</b>	<b>71.6</b>	92.8	91.2	96.3	70.4
A11	67.5	74.2	72.2	55.3	<b>72.9</b>	<b>85.2</b>	<b>85.7</b>	<b>67.3</b>	72.6	81.5	82.6	65.4
A12	83.9	85.7	92.6	70.9	<b>86.7</b>	<b>86.1</b>	<b>93.8</b>	<b>72.0</b>	83.7	78.0	89.4	69.1
A13	73.5	66.9	78.2	55.0	81.6	<b>74.6</b>	<b>85.6</b>	<b>60.3</b>	<b>84.4</b>	58.7	79.8	57.9
A14	92.9	83.8	93.6	71.5	<b>93.1</b>	<b>85.4</b>	<b>94.8</b>	<b>72.6</b>	92.2	79.3	93.1	71.4
A15	53.0	<b>59.1</b>	58.3	38.0	<b>59.9</b>	56.5	<b>63.5</b>	<b>40.8</b>	53.5	49.3	51.0	33.9
A16	<b>98.0</b>	<b>80.7</b>	<b>95.3</b>	71.6	97.2	78.1	95.1	72.0	97.3	71.9	94.4	<b>72.9</b>
A17	96.5	95.0	97.7	76.6	95.7	<b>95.1</b>	<b>97.9</b>	<b>77.9</b>	<b>97.2</b>	91.6	96.7	76.6
A18	72.3	<b>78.4</b>	76.2	59.5	<b>87.0</b>	70.3	<b>80.4</b>	<b>64.8</b>	63.5	69.3	66.5	54.7
A19	73.3	70.9	80.2	58.6	75.1	<b>79.1</b>	<b>84.7</b>	<b>62.1</b>	<b>76.6</b>	69.5	81.6	61.2
A20	81.5	80.9	84.8	59.5	<b>89.4</b>	<b>84.6</b>	<b>90.5</b>	<b>62.7</b>	78.0	78.8	82.2	61.2
All	82.2	82.2	86.9	64.5	<b>85.6</b>	<b>84.2</b>	<b>90.3</b>	<b>67.7</b>	83.4	78.5	86.1	65.2



**Figure 3.** Detection results of YOLOv5m, YOLOv7, YOLOv8m on the same images (a, b, c, and d) extracted from test set of MAR20 dataset.

Detection results in Fig. 3 (d) presents the case of target-background resemblance, YOLOv5m shows misidentification and cannot detect all instances, and YOLOv8 failed to detect all target instances within image. YOLOv7 demonstrate a high discrimination

performance and successfully detects almost all instances within image outperforming YOLOv5m and YOLOv8m.

### 5. CONCLUSION

A comparative study on aircraft detection in remote sensing images was conducted to evaluate three state-of-the-art detection algorithms, YOLOv5, YOLOv7, and YOLOv8, using MAR20 dataset. The experimental results demonstrate that YOLOv7 exhibits a superior overall detection performance compared to YOLOv5, and YOLOv8 algorithms. YOLOv7 achieves mAP<sub>0.5</sub> and mAP scores of 90.3% and 67.7% respectively, which are higher than YOLOv5m by 3.4% and 3.2% respectively, and higher than YOLOv8m by 4.2% and 2.5%. Moreover, YOLOv7 demonstrate better distinguishing between aircraft features, thus reducing recognition errors with a recall rate of 84.2%. Additionally shows a faster learning capacity compared to other algorithms in situation of lower aircraft instances number.

### References

- [1] Li Z, Yuan J, Li G, Wang H, Li X, Li D, Wang X. RSI-YOLO: object detection method for remote sensing images based on improved YOLO. *Sensors*. 2023; 23(14): 6414. <https://doi.org/10.3390/s23146414>.
- [2] Yu W, Cheng G, Wang M, Yao Y, Xie X, Yao X, Han J. MAR20: a benchmark for military aircraft recognition in remote sensing images. *Journal of Remote Sensing (Chinese)*. 2022. <https://doi.org/10.11834/jrs.20222139>.
- [3] Zuo J, Xu, G, Fu K, Sun X, Sun H. Aircraft type recognition based on segmentation with deep convolutional neural networks. *IEEE Geoscience*

- and Remote Sensing Letters. 2018; 15(2): 282-286. <https://doi.org/10.1109/LGRS.2017.2786232>.
- [4] Zhang L, Zhang Y. Airport detection and aircraft recognition based on two-layer saliency model in high spatial resolution remote-sensing images. *IEEE Journal of Selected Topics in Applied Earth Observations and Remote Sensing*. 2017; 10(4): 1511-1524. <https://doi.org/10.1109/JSTARS.2016.2620900>.
- [5] Zhou F, Deng H, Xu Q, Lan X. CNTR-YOLO: improved YOLOv5 based on ConvNext and transformer for aircraft detection in remote sensing images. *Electronics*. 2023; 12(12): 2671. <https://doi.org/10.3390/electronics12122671>.
- [6] Liu Z, Gao Y, Du Q, Chen M, Lv W. YOLO-Extract: improved YOLOv5 for aircraft object detection in remote sensing images. *IEEE Access*. 2023; 11: 1742-1751. <https://doi.org/10.1109/ACCESS.2023.3233964>.
- [7] Cao X, Zhang Y, Lang S, Gong Y. Swin-transformer-based YOLOv5 for small-object detection in remote sensing images. *Sensors*. 2023; 23(7): 3634. <https://doi.org/10.3390/s23073634>.
- [8] Ma J, Wang X, Xu C, Ling J. SF-YOLOv5: improved YOLOv5 with swin transformer and fusion-concat method for multi-uav detection. *Measurement and Control*. 2023; 56(7-8): 1436-1445. <https://doi.org/10.1177/00202940231164126>.
- [9] Redmon J, Divvala S, Girshick R, Farhadi A. You Only Look Once: unified, real-time object detection. *IEEE Conference on Computer Vision and Pattern Recognition (CVPR)*. 2016; Las Vegas, NV, USA; June 27-30, 2016. p. 779-788. <https://doi.org/10.1109/CVPR.2016.91>.
- [10] Tian Z, Shen C, Chen H, He T. FCOS: fully convolutional one-stage object detection. *IEEE/CVF International Conference on Computer Vision (ICCV)*. 2019; Seoul, Korea (South); October 27-02 November, 2019. p. 9626-9635. <https://doi.org/10.1109/ICCV.2019.00972>.
- [11] Liu W, Anguelov D, Erhan D, Szegedy C, Reed S, Fu CY, Berg AC. SSD: single shot multibox detector. *European Conference on Computer Vision (ECCV)*. 2016; 14th European Conference, Amsterdam, The Netherlands; October 11-14, 2016. p. 21-37. [https://doi.org/10.1007/978-3-319-46448-0\\_2](https://doi.org/10.1007/978-3-319-46448-0_2).
- [12] Fu CY, Liu W, Ranga A, Tyagi A, Berg AC. DSSD: deconvolutional single shot detector. *arXiv:1701.06659v1 [Preprint]*. 2017 [accessed 19 October 2023]: [11 p.]. Available from: <https://doi.org/10.48550/arXiv.1701.06659>.
- [13] Lin TY, Goyal P, Girshick R, He K, Dollár P. Focal loss for dense object detection. *IEEE International Conference on Computer Vision (ICCV)*. 2017; Venice, Italy; October 22-29 2017. p. 2999-3007. <https://doi.org/10.1109/ICCV.2017.324>.
- [14] Girshick R, Donahue J, Darrell T, Malik J. Rich feature hierarchies for accurate object detection and semantic segmentation. *IEEE Conference on Computer Vision and Pattern Recognition (CVPR)*. 2014; Columbus, OH, USA; June 23-28; 2014. p. 580-587. <https://doi.org/10.1109/CVPR.2014.81>.
- [15] Girshick R. Fast R-CNN. *IEEE International Conference on Computer Vision (ICCV)*. 2015; Santiago, Chile; December 07-13, 2015. p. 1440-1448. <https://doi.org/10.1109/ICCV.2015.169>.
- [16] Ren S, He K, Girshick R, Sun J. Faster R-CNN: towards real-time object detection with region proposal networks. *IEEE Transactions on Pattern Analysis and Machine Intelligence*. 2017; 39(6): 1137-1149. <https://doi.org/10.1109/TPAMI.2016.2577031>.
- [17] Cai Z, Vasconcelos N. Cascade R-CNN: delving into high quality object detection. *IEEE/CVF Conference on Computer Vision and Pattern Recognition*. 2018; Salt Lake City, UT, USA; 18-23 June, 2018. p. 6154-6162. <https://doi.org/10.1109/CVPR.2018.00644>.
- [18] Purkait P, Zhao C, Zach C. SPP-Net: deep absolute pose regression with synthetic views. *British Machine Vision Conference (BMVC)*. 2018. Available from: <https://doi.org/10.48550/arXiv.1712.03452>.
- [19] Zhao ZQ, Zheng P, Xu ST, Wu X. Object detection with deep learning: a review. *IEEE Trans. Neural Netw. Learn. Syst.* 2019; 30(11): 3212-3232. <https://doi.org/10.1109/TNNLS.2018.2876865>.
- [20] Jocher G. YOLOv5. Available online. 2023. <https://github.com/ultralytics/yolov5>. accessed 10 September 2023.
- [21] Wang CY, Bochkovskiy A, Liao HYM. YOLOv7: trainable bag-of-freebies sets new state-of-the-art for real-time object detectors. *IEEE Conference on Computer Vision and Pattern Recognition (CVPR)*. 2023; Vancouver, BC, Canada, June 17-24, 2023. p. 7464-7475. <https://doi.org/10.1109/CVPR52729.2023.00721>.
- [22] Jocher G, Chaurasia A, Qiu J. YOLOv8. Available online. 2023. <https://github.com/ultralytics/ultralytics>. accessed 25 September 2023.
- [23] Bai C, Bai X, Wu K. A review: remote sensing image object detection algorithm based on deep learning. *Electronics*. 2023; 12(24):4902. <https://doi.org/10.3390/electronics12244902>.
- [24] He K, Zhang X, Ren S, Sun J. Spatial pyramid pooling in deep convolutional networks for visual recognition. *IEEE Transactions on Pattern Analysis and Machine Intelligence*. 2015; 37(9): 1904-1916. <https://doi.org/10.1109/TPAMI.2015.2389824>.
- [25] Liu S, Qi L, Qin H, Shi J, Jia J. Path aggregation network for instance segmentation. *IEEE/CVF Conference on Computer Vision and Pattern Recognition*. 2018; Salt Lake City, UT, USA, June 18-23, 2018. p. 8759-8768. <https://doi.org/10.1109/CVPR.2018.00913>.
- [26] Neubeck A, Van Gool L. Efficient non-maximum suppression. *International Conference on Pattern Recognition (ICPR'06)*. 2006; Hong Kong, China; August 20-24, 2006; 3: p. 850-855. <https://doi.org/10.1109/ICPR.2006.479>.



## NOVEL INSTRUMENT FOR AERODYNAMIC PRESSURE MEASUREMENTS WITH EXCHANGEABLE MULTISENSOR MODULES

MILOŠ FRANTLOVIĆ

University of Belgrade – Institute of Chemistry, Technology and Metallurgy – National Institute of the Republic of Serbia, Njegoševa 12, 11000 Belgrade, Serbia, [frant@nanosys.ihtm.bg.ac.rs](mailto:frant@nanosys.ihtm.bg.ac.rs)

MILOŠ VORKAPIĆ

University of Belgrade – Institute of Chemistry, Technology and Metallurgy – National Institute of the Republic of Serbia, Njegoševa 12, 11000 Belgrade, Serbia, [worcky@nanosys.ihtm.bg.ac.rs](mailto:worcky@nanosys.ihtm.bg.ac.rs)

ŽARKO LAZIĆ

University of Belgrade – Institute of Chemistry, Technology and Metallurgy – National Institute of the Republic of Serbia, Njegoševa 12, 11000 Belgrade, Serbia, [zlazic@nanosys.ihtm.bg.ac.rs](mailto:zlazic@nanosys.ihtm.bg.ac.rs)

MILČE M. SMILJANIĆ

University of Belgrade – Institute of Chemistry, Technology and Metallurgy – National Institute of the Republic of Serbia, Njegoševa 12, 11000 Belgrade, Serbia, [smilce@nanosys.ihtm.bg.ac.rs](mailto:smilce@nanosys.ihtm.bg.ac.rs)

IVANA JOKIĆ

University of Belgrade – Institute of Chemistry, Technology and Metallurgy – National Institute of the Republic of Serbia, Njegoševa 12, 11000 Belgrade, Serbia, [ijokic@nanosys.ihtm.bg.ac.rs](mailto:ijokic@nanosys.ihtm.bg.ac.rs)

PREDRAG POLJAK

University of Belgrade – Institute of Chemistry, Technology and Metallurgy – National Institute of the Republic of Serbia, Njegoševa 12, 11000 Belgrade, Serbia, [predrag.poljak@nanosys.ihtm.bg.ac.rs](mailto:predrag.poljak@nanosys.ihtm.bg.ac.rs)

DUŠAN NEŠIĆ

University of Belgrade – Institute of Chemistry, Technology and Metallurgy – National Institute of the Republic of Serbia, Njegoševa 12, 11000 Belgrade, Serbia, [nesicad@nanosys.ihtm.bg.ac.rs](mailto:nesicad@nanosys.ihtm.bg.ac.rs)

DRAGAN TANASKOVIĆ

University of Belgrade – Institute of Chemistry, Technology and Metallurgy – National Institute of the Republic of Serbia, Njegoševa 12, 11000 Belgrade, Serbia, [dragant@nanosys.ihtm.bg.ac.rs](mailto:dragant@nanosys.ihtm.bg.ac.rs)

---

**Abstract:** Aerodynamic properties of objects such as aircraft, road and railway vehicles, wind turbines etc. are crucial for their operation, and must be tested during their development. In the case of large stationary objects such as bridges and buildings, aerodynamic effects are also important, and must be assessed. Key equipment for performing aerodynamic tests are multichannel pressure measurement instruments. In this work we present an innovative instrument intended for this purpose, and discuss some important aspects of its development. Main advantages of the instrument are its modularity, which is achieved by means of easily exchangeable multisensor modules, miniature dimensions, which are enabled by the development of specialized chips with multiple monolithically integrated sensing elements, novel hardware architecture capable of synchronous measurement on all pressure channels, and high measurement performance enabled by advanced signal processing. The design of multisensor modules, which consist of the developed chips and accompanying electronic circuitry in a compact sealed enclosure, will be described in more detail.

**Keywords:** multisensor, pressure measurement, instrument.

### 1. INTRODUCTION

Aerodynamic testing of road and railway vehicles, aircraft and wind turbines is a necessary step in their development. It is also performed on stationary objects

such as bridges, buildings and other architectural structures, in order to assess the influence of wind. Such tests can be performed in a controlled environment (wind tunnel) or in the open space, by using specialized multichannel pressure measuring instruments, which are commonly called pressure scanners. In this paper we



present the design of a novel instrument for aerodynamic pressure measurements, which offers several advantages over the existing ones, including modularity and miniature dimensions, high measurement performance, and the capability of synchronous measurements on all pressure channels. A unique MEMS multisensor chip with multiple monolithically integrated sensing elements enables high-performance pressure sensing and high channel density in a miniature package. Modularity is enabled by the development of compact multisensor modules exchangeable by the user, and also the specially designed miniature instrument housing. Synchronous measurements and high measurement throughput are achieved through the advanced hardware architecture that eliminates multiplexing of pressure sensor signals by having a separate signal path for each pressure channel. High measurement performance of the instrument is enabled by using advanced signal processing techniques.

In this paper, the main focus will be on the design of the multisensor module, which consists of four MEMS multisensor chips and accompanying electronic circuitry in a compact sealed enclosure.

## 2. MAIN CONCEPTS

In order to be suitable for applications that require placement in limited spaces (within structural parts of tested objects or inside of scale models), modern electronic pressure scanners must be of miniature dimensions. In addition to this requirement, a modular construction that enables a user to change the measurement range by exchanging sensor modules was also implemented in this work. This approach resulted in the instrument design shown in Figure 1. The main parts of the instrument are the signal processing unit and two exchangeable multisensor modules. The overall dimensions of the instrument are approximately 110 mm × 35 mm × 30 mm (excluding pressure ports and electrical connectors).

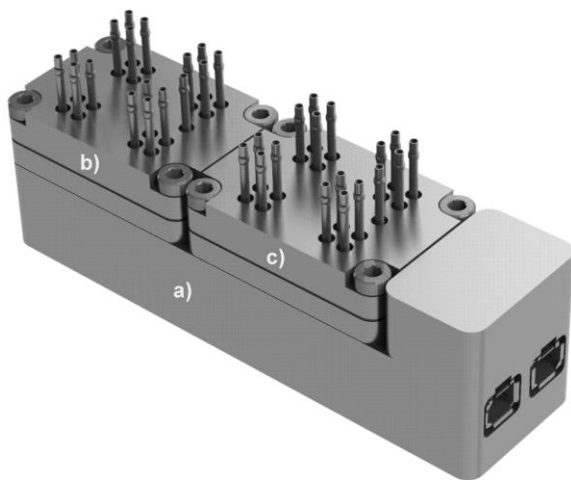


**Figure 1.** Visualization of the instrument for aerodynamic pressure measurements: a) signal processing unit, b) and c) multisensor modules

A key component for the realization of the instrument is the dedicated MEMS multisensor chip, developed and fabricated at the Institute of Chemistry, Technology and Metallurgy (ICTM), University of Belgrade. Apart from enabling the instrument's main functionality, it is crucial for achieving high pressure channel density without sacrificing the measurement performance. It contains four MEMS piezoresistive pressure sensing elements, two temperature sensing elements, and the accompanying electrical connections. Photographs of the fabricated chip are shown in Figure 2. Its pressure range is 100 kPa, but it can be made for other ranges, so to suit different measurement needs. A more detailed description of the multisensor chip is given in [1].

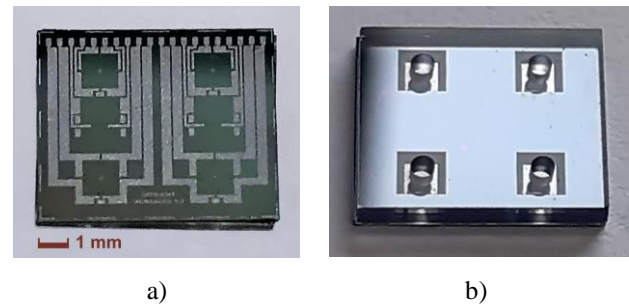


**Figure 2.** MEMS multisensor chip: a) top side, b) bottom side with anodically bonded glass plate

The hardware architecture of the multisensor instrument for aerodynamic pressure measurements represents an important next step in the development of such instruments, as it has a separate signal path for each of the pressure measurement channels. This is accomplished by using a separate signal conditioning circuit and analog-to-digital converter per channel. The absence of parasitic effects, which inevitably exist in conventional designs based on analog signal multiplexing, enables achieving higher sampling rates (up to the order of  $10^3$  samples per channel per second). Another significant advantage of this architecture is the capability of fully synchronous pressure measurement on all channels. This is important for performing aerodynamic experiments with unsteady flow fields and transient phenomena [2,3]. The instrument's hardware architecture is described in more detail in [4].

Digital signal processing is another important concept included in the instrument's design. After performing analog-to-digital conversion of the sensor signals, digital signal processing is applied on each pressure channel's measurement data in order to perform sensor correction. The correction is based on mathematical modeling and computer algorithms, and it greatly reduces the temperature dependence and non-linearity of the pressure sensing elements. In this way, the achievable measurement uncertainty can be significantly lower than 0.1 %FS in the temperature range of interest for the intended application (from 0°C to 50°C). Digital signal processing also enables the implementation of self-diagnostic features.

The communication between the instrument and the rest of the measurement system is via a high-speed digital

interface (Ethernet). There is also a connector for the power supply, with the synchronization input and some other optional signals. Thus, there are two miniature connectors on the signal processing unit, as illustrated in Figure 1.

### 3. MULTISENSOR MODULE

A simplified block diagram of the multisensor module is shown in Figure 3. Four MEMS multisensor chips (shown as violet rectangles) are placed in a sealed enclosure. Each of the pressure sensing elements (shown as blue squares with the letter P inside) has a pressure port through which the connection to an external pressure source is established. In this application, the measured pressure is differential, so it is measured as a difference between the pressure applied through the pressure port and a reference pressure. For that purpose, there is an additional pressure port (not shown in the diagram), that brings the reference pressure inside the module's enclosure. In this way, each pressure sensing element has the corresponding external pressure on one side of its diaphragm, and the common reference pressure on the other side, resulting in differential pressure measurement.

Apart from the pressure sensing elements, there are also temperature sensing elements on the multisensor chips (shown as yellow squares with the letter T inside), which are used for temperature compensation. This is necessary because semiconductor-based piezoresistive pressure sensors exhibit parasitic temperature dependence.

As all the mentioned sensing elements behave as resistive electrical networks, sensor excitation (here in the form of constant voltage) must be provided in order for them to generate the output signals. The signals from all the pressure sensing elements are brought directly to the multisensor module's connector. They are digitized and processed in the signal processing unit of the instrument.

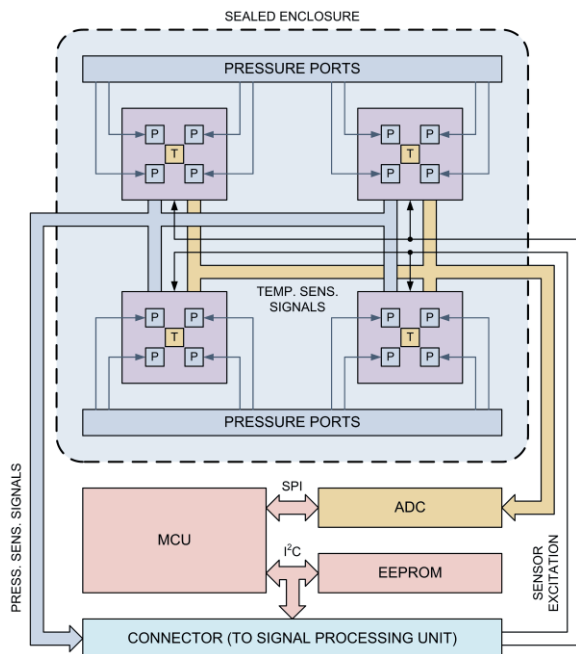


Figure 3. Simplified block diagram of the module

The signals from the temperature sensing elements are digitized and processed in the module, by using the analog-to-digital converter (ADC) and the microcontroller (MCU) [5], respectively. This yields the temperature values that correspond to the four multisensor chips. The built-in EEPROM contains calibration data, as well as other information necessary for module identification, operation and adjustments. These data are read-out and used by the signal processing unit. Both the EEPROM and the MCU are accessible through the multisensor module's connector, using the I<sup>2</sup>C interface.

A photograph of the main parts of the realized multisensor module prototype is shown in Figure 4. The mechanical assembly consists of the top and bottom part of the module's enclosure (both made of metal), and the rubber gasket for sealing of the enclosure. Shown in the top left corner of Figure 4 is the inside of the top part, with mounted multisensor chips and the circuit board for establishing electrical connections between the chips and the module's electronic circuitry. In the bottom left corner of Figure 4 is the bottom part of the enclosure with the gasket. The module's electronic circuitry (shown on the right) is realized in the form of a printed circuit board that consists of two 6-layer rigid parts and a 2-layer flexible part. The purpose of the flexible part is to avoid connector misalignment and mechanical stresses due to assembly and fabrication tolerances. The external appearance of the realized module prototype is shown in Figure 5.

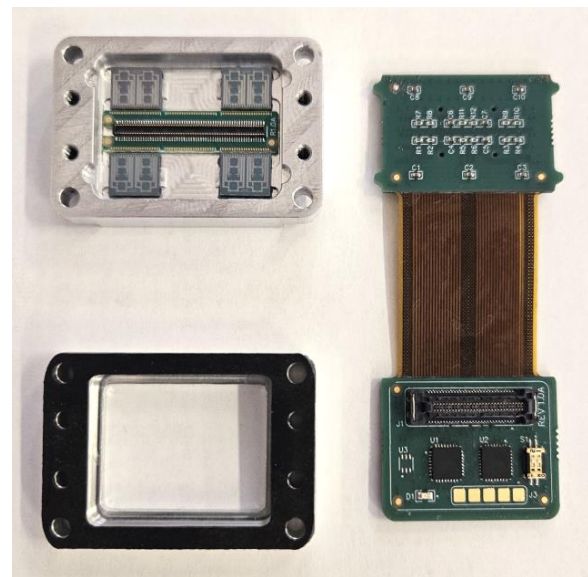


Figure 4. Photograph of the realized multisensor module prototype: main parts



**Figure 5.** Photograph of the realized multisensor module prototype: external appearance

#### 4. CONCLUSION

In this paper we presented the main features of the novel instrument for aerodynamic pressure measurements (pressure scanner). Compared to the existing instruments, it has several advantages, including modularity, miniature dimensions, and the capability of synchronous measurements on all channels. After the overview of the main concepts of the instrument's design, a description was given of the exchangeable multisensor module. The design of the module and the realization of the prototype were complex and multidisciplinary tasks, posing significant challenges in the fields of semiconductor sensor technology, component packaging, electrical and mechanical engineering. Similar can be said for the rest of the instrument's hardware, i.e. the signal processing unit, where a high level of functionality and performance must be achieved in a miniature package. The activities towards that goal are currently in the final stage. Apart from that, the software development, including advanced signal processing, communication and other functions, is also an important aspect of this work, and it is currently in progress.

#### Acknowledgments

This research was supported by the Science Fund of the Republic of Serbia, Grant No. 7754287, MEMS Multisensor Instrument for Aerodynamic Pressure Measurements – MEMSAERO. It was also supported by the Ministry of Science, Technological Development and Innovation of the Republic of Serbia, grant number 451-03-66/2024-03/200026.

The authors wish to express their gratitude to Marko Starčević, engineer from ICTM, Belgrade, for his valuable technical help and support.

#### References

- [1] Lazić, Ž., Smiljanić, M.M., Tanasković, D., Rašljčić Rafajilović, M., Cvetanović, K., Milinković, E., Bošković, M.V., Andrić, S., Poljak, P., Frantlović, M.: *Development of a MEMS multisensor chip for aerodynamic pressure measurements*, Eng. Proc. 58(52)(2023).
- [2] Wolff, T., Seume, J.R.: *Modeling the transient aerodynamic effects during the motion of a flexible trailing edge*, Journal of Physics: Conference Series, 753(8)(2016) 082038.
- [3] Nikoueeyan, P., Hind, M.D., Strike, A., Perry, M.C., Wimpenny, B., Mears, L.J., Shea, P.R., Collins, J.G., Walker, M.A., Pinier, J.T., Naughton, J.W.: *Evaluating the Utility of Pressure Scanners for Unsteady Pressure Measurements in Wind Tunnel Characterization of the Space Launch System*, AIAA AVIATION Forum, June 27-July 1, 2022, Chicago, IL & Virtual AIAA AVIATION 2022 Forum.
- [4] Frantlović, M., Lazić, Ž., Smiljanić, M., Jokić, I., Poljak, P., Nešić, D., Vorkapić, M., Tanasković, D.: *On the Design of a MEMS Multisensor Instrument for Aerodynamic Pressure Measurements*, Proc. 11<sup>th</sup> International Conference on Electrical, Electronics and Computer Engineering (IcETRAN), 3-6 June 2024, Niš, Serbia.
- [5] STMicroelectronics: *Arm® Cortex®-M0+ 32-bit MCU, up to 512KB Flash, 144KB RAM, 6x USART, timers, ADC, DAC, comm. I/Fs, 1.7-3.6V*, STM32G0B1xB/xC/xE datasheet - production data, December 2022.



## ANALYSING USAGE OF COMMERCIAL GRADE SINGLE ANTENNA INERTIAL NAVIGATION SYSTEM IN COMBAT UNMANNED GROUND VEHICLES FOR ESTIMATING ORIENTATION AND POSITION

GORAN DRAGOVIĆ

Military Technical Institute, Belgrade, [goran.dragovic@mod.gov.rs](mailto:goran.dragovic@mod.gov.rs)

NEDELJKO DUČIĆ

Faculty of Technical Sciences, Čačak, [nedeljko.ducic@ftn.kg.ac.rs](mailto:nedeljko.ducic@ftn.kg.ac.rs)

STEFAN JOVANOVIĆ

Military Technical Institute, Belgrade, [stefan.jovanovic@mod.gov.rs](mailto:stefan.jovanovic@mod.gov.rs)

MARKO SIMONOVIĆ

Military Technical Institute, Belgrade, [marko.simonovic@mod.gov.rs](mailto:marko.simonovic@mod.gov.rs)

DUŠAN BOŽIĆ

Military Technical Institute, Belgrade, [dusan.bozic@mod.gov.rs](mailto:dusan.bozic@mod.gov.rs)

**Abstract:** With increasing presence of combat Unmanned Ground Vehicles (UGV) in warzones throughout the world, in adverse and unknown terrain, their usage is limited without proper estimation of their orientation to true north and their position on world map. Until recently, Inertial Navigation System's (INS) were only cost effective in use with artillery, and their price was in range in tens of thousands of dollars. Recent development of commercial autonomous vehicles spawned a surge in developing cost effective Micro-Electromechanical System (MEMS) INS's, that are used in autonomous robots and vehicles. This paper analyzed sub - 3000 dollar MEMS INS with single antenna and integrated Real Time Kinematics (RTK) and examined if it's performance is suitable for usage in combat UGVs for tasks such as forward observing and guiding, artillery target acquisition and using its own armament for indirect fire. With the help of the MATLAB software package estimated orientation and position error from data that was acquired on test setup on combat UGV was analyzed, concluding there is certain potential in using mentioned types of INS's.

**Keywords:** MEMS, INS, UGV, GNSS, RTK.

### 1. INTRODUCTION

Knowing your position and orientation in an environment and acquiring your targets positions is one of the most important tasks in military operations. Militaries around the world are putting great effort in developing unmanned systems with before mentioned capabilities. Theaters in Ukraine (primarily), Palestine, Nagorno-Kharabakh region and many others have shown us usage of aerial scout drones for observing targets, acquiring targets position and relaying that information to First Person View (FPV) drone operators or artillery for precision strikes and effectively destroying the targets in mere minutes after acquisition has been made. One of the main aspects of combat UGVs is that they are controlled from a safe distance (more than a 1 km in between operator and UGV) usually via radio link. The sizes of present day combat UGVs and the type of camera used for navigating them limit their field of view (FOW), especially in urban

and open terrain with high obstacles (tall grass, valleys, trees, etc.). It is very easy for an operator to lose a sense of position and orientation of its system, especially if distance between them is large enough and terrain is unknown. The system needs to have a way of knowing or estimating its own position and orientation. Most common way (that doesn't rely on sensors) of estimating you position and orientation is back-calculation of three points for position and orienting to piquet, after you position is known, for determining orientation. These methods are time and work intensive, and do not always produce reliable outcomes. Integrating INS in a UGV greatly improves the combat efficiency of the system, as they can quickly acquire their position and orientation, and use the info for forward observing and guiding, target acquisition or to aim their own armament, and allow operator to navigate adverse and unknown terrain with relative ease.

### 2. Components of an INS

Components that MEMS INS's usually contain are following:

- Accelerometer
- Gyroscope
- GNSS receiver (GPS, GLONAS, BEIDOU...)
- Magnetometer
- Barometer
- Processing software (Sensor fusion)

Most important ones are accelerometer, gyroscope, GNSS receiver and internal software, while magnetometer and barometer are optional for most of the INS's on the market. Fusion of MEMS accelerometer and gyroscope is commonly known as Inertial Measurement Unit (IMU).

## 2.1 Accelerometer

Accelerometer are devices that are used to measure proper acceleration (rate of change of linear velocity) expressed in units of  $m/s^2$  or  $g$  ( $9.81 m/s^2$ ). Quality of the device is determined by the in-run bias stability (bias instability) expressed in units of  $\mu g$ , noise density expressed in units of  $\mu g/\sqrt{Hz}$ . Modern MEMS accelerometers have very low values for above-mentioned characteristics, and they are considered close to military standards and requirements [2].

## 2.2 Gyroscope

Gyroscopes are devices that are used to measure angular velocity. Same as accelerometers, in MEMS technology their quality is determined by the in-run bias stability (bias instability) expressed in units of  $^{\circ}/h$  and noise density expressed in units of  $^{\circ}/s/\sqrt{Hz}$ . Unlike accelerometers, values of these characteristics can be quite high and impactful on measurement of true angular velocity. Common values for in-run bias instability range from  $3600^{\circ}/h$  for low quality MEMS gyroscopes, to sub  $0.1^{\circ}$  for high quality ones, which are on par with lower quality fiber optic gyroscopes (FOG) and interferometric fiber optic gyroscopes (IFOG). Most of the MEMS gyroscopes are limited to low to medium tactical performance spectrum due to above-mentioned characteristics [3].

## 2.3 GNSS receiver

GNSS receivers are used to acquire signals from satellite constellation and determine position, altitude, time and speed. For proper functioning of the system, it needs to be able to get signals from at least four satellites. There are many things that can affect performance of GNSS receiver, as the number of available satellites, their geometry (represented as a value of Dilution of Precision), and noise introduced in different layers of atmosphere, refraction and reflection of signal, and many more [2]. Consensus is that GNSS receiver in optimal operation will provide position with sub 2 meters of circular error probability (CEP), while with the aid of (RTK), CEP can reach values as low as a few centimeters. One of the main downsides of using GNSS susceptibility to jamming and spoofing, but using more advanced signals acquisition and protections, their influences can be diminished [5]. INS's can have GNSS receiver with one

or two antennas, depending on the design. With two antennas, orientation can be determined in static, while with single antenna, orientation can be determined only in motion.

## 2.4 Magnetometer and Barometer

Magnetometer and Barometer can be part of the INS, but usually they are introduced as a backup or support to the before-mentioned devices. Magnetometer can quickly determine the orientation to the magnetic north, and therefore to the true north with not so good accuracy, which can aid in improvement of INS's determination of orientation, but its susceptibility to hard and soft iron disturbances can quickly lead INS astray. Calibration of the magnetometer is possible to negate hard and soft iron disturbances, but there is still question of local earth magnetic field anomalies and the model of the earth magnetic field can still cause poor performance of magnetometer. Barometer gives information about altitude with error ranging in no more than 2 meters, which is still by and order of magnitude bigger error, then the one acquired with GNSS in optimal conditions.

## 2.5 Processing software (Sensor fusion)

Having multiple devices that provide similar measurements is definitely good, as it provides redundancy to the system. Some devices will measure some values more accurate than the other, and determining which measurement to trust at which point is big part of the INS. This ambiguity is resolved using processing algorithms, most commonly Kalman filtering. In ready to use MEMS INS that are available on the market, there is no insight how this software functions. Characteristics of sensor fusion are declared most commonly with sensor fusion performance chart that states Yaw, Roll and Pitch determination accuracy based on the fixed reference plane (usually local earth reference plane) in values or degrees root mean square (RMS), and Position and Velocity error expressed as absolute value error. The values of Yaw, Pitch and Roll from sensor fusion algorithm are, most of the time, provided as Euler angle or quaternion values to the end user. Information from GNSS is usually provided in WGS84 format.

## 3. ANALYSIS OF TACTICAL ASSIGNMENTS AND TARGETS POSITION ESTIMATION REQUIREMENTS

As discussed in previous sections, INS will be used as a tool to easily get information of position and orientation of the UGV, and that information will further be used to conduct various tactical assignments. List of tactical assignments that require knowledge of orientation and position are following

- 1) Using UGVs armament for indirect fire upon known targets position (example, automatic grenade launcher (AGL) Mk19)

- 2) Determining target coordinates for guiding precision munitions (example, JDAM Mk80)
- 3) Determining target coordinates for unguided field artillery barrage (example, M114A1)
- 4) Determining target coordinates for unguided rocket artillery barrage (example, M270)
- 5) Determining target coordinates for guiding other drones or UGVs, and navigating own UGV

All of these tasks have different requirements and tolerances of error, for determining their targets coordinates or orientations. A Circular Error Probable (CEP) of aimed hits usually describes performance of artillery and guided munitions. We will use known CEP of listed weapons to get maximum allowed error of determining target position. For this purpose, we will assume that maximum allowed error in determining position for given tactical assignments is 25% of declared CEP of each weapon. For example, if we have a target with its own real location, and we want to engage it with a weapon that has a CEP of 40m, our requirement will be to estimate targets position, with a 10m circle of error around it. In the following figure, black dot represents real target position. Red circle shows error boundaries for estimated target position, whom radius is 25% of dark green circle. Dark green circle represents 1n CEP of weapon. Outer circles represent 2n CEP and 3n CEP, respectively.

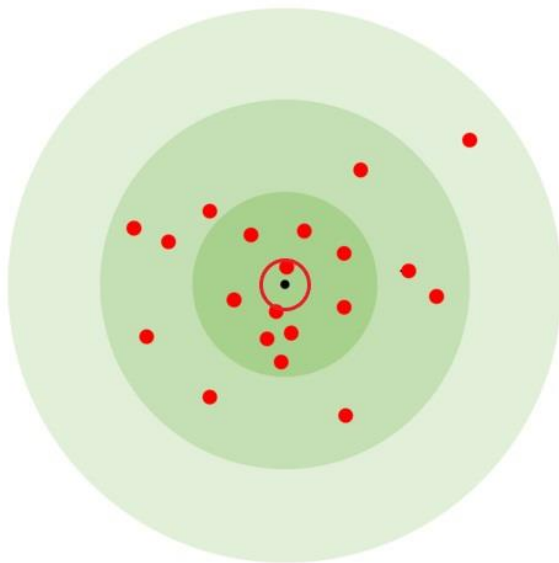


**Figure 1.** CEP of 20 hits, with 10 hits falling inside dark green circle with 1n radius

First tactical assignment (aiming) is different from the others, as we are not required to determine the target, but to orient towards a known target. Minimum requirement for it is to hit 2 out of 10 shells fired, at a group target with area 20m x 30m, distanced 600m ( $\pm 100m$ ) [9]. Optimal requirements are to hit 4 out of 10 shells. Recalculating these values, we get a CEP of 62m and 31m respectively. These values will later be used to calculate maximum allowed error in determining orientation. For second task, guiding the precision munition, the CEP for JDAM Mk80 can be in a range of 5 meters if the GNSS is

working correctly, and it will have CEP of no more than 30m for up to 100 seconds of free flight (no GNSS present) [10]. For our analysis, we will assume CEP of 15 meters. Third and fourth tasks have similar CEP of around 100 meters, but at different ranges.

CEP of 100m for M114A1 is declared at 15km[7], while for M270 it is declared at 10km [8]. We will assume same CEP for both systems. For last task in the list, there is no CEP, but we can arbitrarily declare, that a determined position with an error of  $\pm 15m$  for guiding others is more than enough, and that knowing its own position within a tolerance of declared GNSS CEP will be enough. All tasks with their requirements are listed in the table below, with calculated maximum allowed error for estimating position. These tasks require UGV to have integrated Geographical Information System (GIS) in its kit, or some other form of using battle map, for properly determining its own position and targets positions.

**Table 1.** Calculated values for maximum allowed error of estimating target position (n.d. – not defined)

Task	Range	CEP	Max. allowed error
Mk19 (min)	600m	62m	$\pm 7.75$
Mk19 (opt)	600m	31m	$\pm 3.875$
JDAM Mk80	n.d.	15m	$\pm 1.875$
M114A1	15km	100m	$\pm 12.5$
M270	10km	100m	$\pm 12.5$
Guiding	n.d.	n.d.	$\pm 15$

#### 4.MATHEMATICAL MODEL

After determining maximum allowed error for target position estimation, for each tactical assignment, we need to determine maximum errors for UGV positioning and orientation estimation. For simplicity, in this analysis, we will assume that UGV and a target are on a flat 2D plane (same elevation), to reduce the need for computation. Mathematical equation that represents the case is:

$$\dot{x} = (x + x') + (r + r') \cdot (\gamma + \gamma') \quad (1)$$

Where,  $\dot{x}$  represents estimated targets position,  $x$  UGVs real position,  $x'$  error from estimating UGVs position (GNSS induced),  $r$  real distance to the target,  $r'$  error of measuring distance,  $\gamma$  real UGVs orientation and  $\gamma'$  orientation error (INS induced, mechanical misalignment of axis, etc.). Assumption is that distance measurements error are negligible, which leaves us with influences solely that are GNSS/INS induced. As mentioned before, CEP of GNSS without RTK in optimal conditions is usually around 2m, meaning that 2n CEP (~94% of all GNSS acquired positions) will have a 4m ( $\pm 2m$ ) circle radius of possible position estimation around real position of UGV. For RTK aided GNSS, 2n CEP is usually can be in level of centimeters. We will assume value of 0.5m ( $\pm 0.25m$ ). This will give us maximum error in positioning in 2m and 0.25m respectively. Following figure represents the model of estimating targets position.

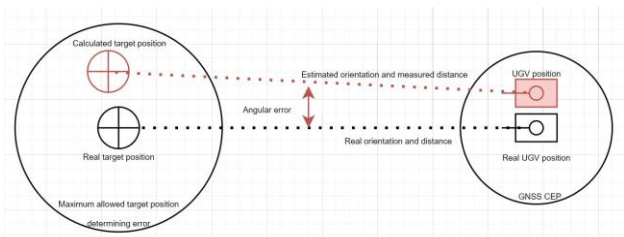


**Figure 2.** Graphical representation of estimating targets position with influence of various errors

In this analysis, worst-case scenario is processed. In that scenario, UGVs estimated position is on the outer edge of 2n CEP of GNSS, creating a right triangle with the real target position, and real UGV position. Estimated orientation is offset to the closer edge of the circle that represents error tolerance for target position estimation. With all this in mind, following tables contain calculated values of maximum error in orientation estimation of the UGV for tactical assignments, at various distances of 500m, 1500m and 3000m.

**Table 2.** Calculated values for maximum allowed error of estimating UGVs orientation without aid of RTK (o.o.b. – out of bounds)

Task (no RTK)	500m	1500m	3000m
JDAM Mk80	o.o.b.	o.o.b.	o.o.b.
M114A1	1.202°	0.4°	0.2°
M270	1.202°	0.4°	0.2°
Guiding	1.48°	0.496°	0.248°

**Table 3.** Calculated values for maximum allowed error of estimating UGVs orientation with aid of RTK

Task (RTK)	500m	1500m	3000m
JDAM Mk80	0.156°	0.053°	0.026°
M114A1	1.375°	0.457°	0.229°
M270	1.375°	0.457°	0.229°
Guiding	1.662°	0.554°	0.277°

**Table 4.** Calculated values for maximum allowed error of estimating UGVs orientation for

Task	Range	no RTK	RTK
Mk19(min)	600m	0.549°	0.691°
Mk19(opt)	600m	0.179°	0.321°

Guiding JDAM Mk80 without having precise location is not possible to be done reliably under these requirements and in this scenario. In scenario where precise enough location of UGV is known, allowed error for orientation requirement is very slim, even at very short range of 500m. Reducing the distance below 500m would increase the tolerances linearly, but with decrease in distance, there is increase in a chance that the UGV will be inside the blast radius of the JDAM. Same tight tolerances for estimated orientation are for aiming its own armament in an effort to achieve optimal performance (4 out of 10 shots in target). Other tasks have higher tolerances, which are in range from 1.662° to 0.457° for maximum error. It can be concluded, that expected tolerance for maximum error in orientation estimation should not exceed 0.5° for distances of up to 1500m. Distances beyond 1500m would require estimation of orientation that will most

likely be beyond capabilities of commercial INS, to provide them both regularly and reliably.

## 5. TEST SETUP

For testing, two INSs have been acquired. One sub-3000\$ commercial grade, single antenna with integrated RTK corrections. Other is military-grade in range of 100k\$ intended for orienting artillery, with ability to get orientation referenced to the true north, after 5 minute initialization time without a GNSS aid. Error produced by the military INS is in third decimal of measurement. These characteristics are tested and confirmed by the military of Serbia. Latter one will serve us as a reference for measuring the error in estimated orientation of the commercial grade one. For this purpose, a mount was made, that holds both INSs with their z (vertical) axis aligned. After mounting, the INSs mechanical offset in their axes is measured by a coordinate machine, with result of 0.084° of mechanical offset in CCW direction. Test rig was mounted on the drive surface of combat UGV and three test runs were conducted. Two without RTK, and one with the aid of RTK. RTK base station was located 16km away (not ideal), and their corrections were provided via RTK2GO website. Test runs were conducted with speeds below 10 km/h, with frequent turns, often being 90° to 180°.



**Figure 3.** Custom made mount housing both INSes

During test runs, after commercial INS reached steady state in referencing to the north, pauses in movement were made on random intervals and orientation of both INSs collected. One of the test runs can be seen in the following figure.



Figure 4. UGV pathing on one of test runs

For validation of GNSS, commercial INS was placed atop geolocation with known coordinates, which was provided by the Military Geographical Institute of Serbia. Two test runs were conducted, one without aid of RTK and other with the aid of RTK. In both cases acquisition lasted for 10 minutes ,after which their data was analyzed in order to estimate maximum absolute error of positioning.

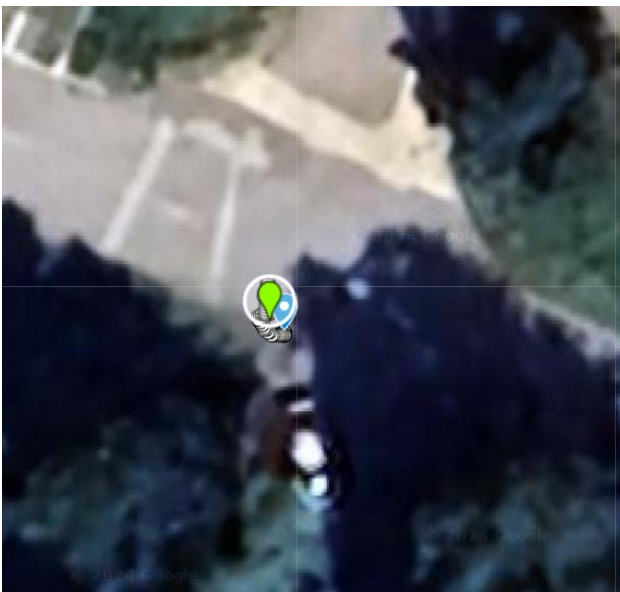


Figure 5. Test of acquiring positions via GNSS, atop known geolocation (light green marker)

6.DATA ANALYSIS

Collected data was processed and plotted with the help of software package MATLAB. In following figures, not all of the graphs are show, due to high number of them. In following figures, you can find few interesting examples. Their results will be given in a table.

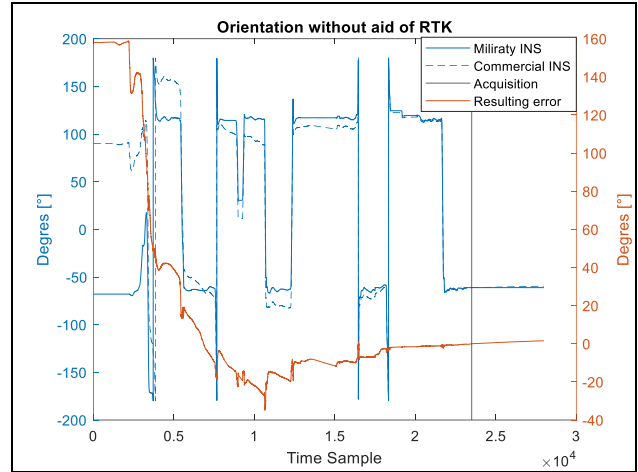


Figure 6. Graph showing absolute orientation values of both INSs and calculated error (no aid of RTK)

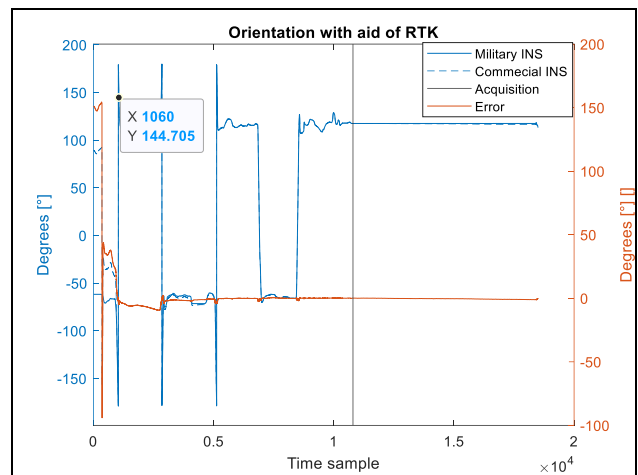


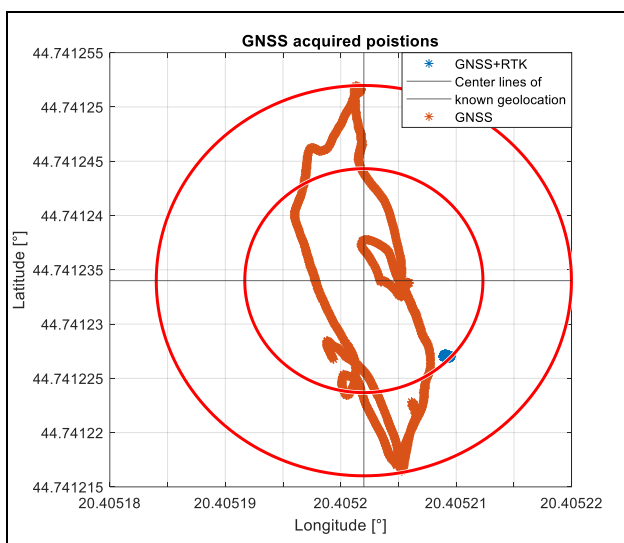
Figure 7. Graph showing absolute orientation values of both INSs and calculated error (with aid of RTK)

Table 5. Orientation error values from test runs

Test run	Absolute error value	RTK	0.5° Threshold
1.1.	0.034°	X	√
1.2.	2.087°	X	X
1.3.	0.387°	X	√
1.4.	10.063°	X	X
1.5.	6.896°	X	X
1.6.	0.136°	X	√
1.7.	0.252°	X	√
1.8.	0.669°	X	X
1.9.	0.486°	X	√
2.1.	1.085°	X	X
2.2.	1.053°	X	X
2.3.	0.244°	X	√
2.4.	0.051°	X	√
2.5.	1.673°	X	X
2.6.	0.462°	X	√
2.7.	0.127°	X	√
3.1.	0.767°	√	X
3.2.	0.073°	√	√
3.3.	0.087°	√	√
3.4.	0.112°	√	√



Looking at the table and given graphs, we can see wide range of values for orientation error. Most of them are in the range of  $0.05^\circ$  -  $2^\circ$ , with 1.4. and 1.5. notably deviating from the rest. These values can be attributed to the loss or poor acquisition of GNSS signal. What is even more interesting is that the orientation error on more than one occasion was below  $0.2^\circ$  for test runs without aid of RTK, while for test with RTK it was three times in a row below  $0.2^\circ$ . Testing for maximum amount of times that UGV has to move, and at what minimal speeds would greatly improve output of reliable orientation estimation. In these tests, movement speeds were random and not constant, as well as time of movement, as primary goal is testing for capabilities of commercial INS. It also has to be noted, with aid of RTK, orientation error was not exceeding  $0.4^\circ$  for most part of movement of the UGV.



**Figure 8.** Estimated positions acquired from GNSS and circles showing maximum deviation from known geolocation

In previous figure, acquisitions from GNSS, with and without aid of RTK are presented. Notable difference in dispersion of positions can be noticed, with RTK aided acquisition having very good grouping, while bare GNSS had substantial 'walk' around center point. RTK aided acquisitions have good grouping, but there is constant offset present, which drifted all position to southeast. Maximum distance of acquired location from bare GNSS was 2.0015m from known geolocation, giving us radius of circle (outer) 4.003m that is 0.003m higher than our prediction. GNSS+RTK produced maximum error of 0.9877m, giving us a circle (inner) with radius of 1.9754m, almost quadruple of what we predicted for this analysis. This can be attributed to the suboptimal conditions for using RTK, as RTK base station is 15km away, while optimal distance would be up to 5km, depending on the type of station itself. All acquisitions from GNSS+RTK fall inside circle with radius of 0.1172m, which is more than four times better than what we predicted, disregarding constants offset. High repeatability and absence of 'walk' are the reasons for low error produced during estimating orientation with aid

of RTK.

## 7.CONCLUSION

Taking in account all observations and measurements, it can be concluded that there is certain potential in using commercial grade INS in UGV for low to medium tactical assignments of guiding/navigating, forward observing and aiming its own armament. This can be extended to other systems that are intended in executing similar tasks. Ability to produce sub  $0.1^\circ$  orientation errors is present, but reliability and reproducibility has to be confirmed with further testing, which results would yield information about minimum speeds, times and types of movement that would produce reliable outcomes. GNSS testing, without aid of RTK yielded expected results, while RTK aided have not. As mentioned before, that can be attributed to the poor setup for testing RTK, and not to the system, but further test are required for confirmation. It has to be mentioned that additional testing of GNSS-denied performance is required that will yield times after which orientation would drift away beyond usage in static and dynamic motion conditions.

## Acknowledgment

This paper is a part of the research done within the project of the Univeriaity of Defence in Belgrade, No. VA-TT/1/24-26.

This work was supported by the Ministry of Science, Technological Development and Innovations of the Republic of Serbia (Contract No. 451-03-66/2024-03/200325).

## References

- [1] LACHAPELE, G. CANON, M. BIRD, J. : *Evaluation of GPS-Aided Artillery Positioning and Orientation Methods*, The University of Calgary, Department of National Defense, 1998
- [2] LACHAPELE, G. : *High Precision GNSS RTK navigation for Soldiers and Other Military Assets*, The University of Calgary, 2013
- [3] SCHMIDT, G. : *Navigation Sensors and Systems in GNSS Degraded and Denied environments*, IEEE Aerospace and Electronic Systems Society, Lexington, 2014
- [4] DUCKWORTH, G. BARANOSKI, E. : *Navigation in GNSS-Denied Environments: Signals of Opportunity and Beacons*, USA
- [5] VAN NIEKERK, A. COMBRINCK, L. : *The use of Civilian-type GPS Receivers by the Military and their Vulnerability to Jamming*, SANDF, 2011
- [6] RTO EDUCATIONAL NOTES : *MEMS Aerospace Applications*, Canada, USA, 2003
- [7] YEOW LIM, W. : *Predicting the Accuracy of Unguided Artillery Projectiles*, Naval Postgraduate School Monterey, 2016
- [8] GADIOT, G. : *Trajectory Simulation model for a Side Thruster Guided MLRS-type Vehicle*, TNO Prins Maurits Laboratory, Netherlands, 1998

[9] WEAPON HANDLING GUIDE: *MK19, 40-mm Grenade Machine Gun MOD3*, Department of Army, 2003

[10] Internet article: *Joint Direct Attack Munition*, link: [https://en.wikipedia.org/wiki/Joint\\_Direct\\_Attack\\_Munition](https://en.wikipedia.org/wiki/Joint_Direct_Attack_Munition)

[11] SEKULOVIĆ, D. ĐURKOVIĆ, V. MILOŠEVIĆ, M. : Pozicioniranje, orijentisanje i određivanje daljine do

cilja na smohodnom višecevnom raketnom lansirnom sistemu korišćenjem GPS i elektronskih karata, Vojnotehnički glasnik 3/10, 2010

[12] CVETKOVIĆ, N. OBRADOVIĆ, G. : *Accuracy analysis of gps-aided artillery positioning and orientation in main azimuth*, Military Technical Institute, Belgrade.



# APPLICATION OF SCREW THEORY AND ITS IMPLEMENTATION IN PYTHON FOR CONTROLLING A NIRYO ONE MANIPULATOR

VUK TODOROVIĆ

Faculty of Technical Sciences, University of Pristina in Kosovska Mitrovica, [vuk.todorovic01@gmail.com](mailto:vuk.todorovic01@gmail.com)

MILAN BLAGOJEVIĆ

Faculty of Technical Sciences, University of Pristina in Kosovska Mitrovica, [milan.blagojevic@pr.ac.rs](mailto:milan.blagojevic@pr.ac.rs)

NIKOLA NEŠIĆ

Faculty of Technical Sciences, University of Pristina in Kosovska Mitrovica, [nikola.nesic@pr.ac.rs](mailto:nikola.nesic@pr.ac.rs)

**Abstract:** *The representation of a robot's configuration can be diverse, each with its advantages and disadvantages. In this paper, we approach the problem using screw theory, which states that all rigid-body motion can be represented with a rotation and translation along a screw axis. Using this as a basis, we'll be tackling the inverse kinematic problem of robots, which lacks standardized ways of being determined, unlike the forward kinematics problem. With that in mind, here we will show a combined approach of the analytic and numerical way of solving the inverse kinematic problem on a Niryo One robotic manipulator. The analytic solution is derived by simplifying the robot's structure and then using those results as initial guesses for the Newton-Raphson numerical method which may produce up to 8 possible solutions. The theoretical foundation is then implemented using the Python programming language after which the solution is sent to the robot via a Niryo One ROS API – pyniryo.*

**Keywords:** *screw theory, inverse kinematics, Paden-Kahan subproblems, Newton-Raphson method, Python, Niryo One.*

## 1. INTRODUCTION

In the modern age, robotics is gaining an ever-increasing role in shaping modern life, hence why innovations are increasingly more directed towards this interdisciplinary scientific field. The structure of robots is complex and both individual and connected elements can significantly affect the whole structure and function of the mechanism. This is in favor of the fact that it is increasingly difficult to study one aspect of the robot's structure independently from the rest. Still, it is relatively easy to see how a dependent unit can affect the rest of the system and perform an analysis of its impact.

The essence of this paper lies in **screw theory** and its use for the analysis and synthesis of robot mechanics, as well as its application in controlling a **Niryo One manipulator** through the **Python** programming language and its publicly available libraries.

The work begins in the second chapter with some basic considerations that need to be taken into account, along with a theoretical movement model which we will follow and implement in an experiment.

In the third chapter, we get to the heart of this paper. After a brief overview of the task of determining a robot's inverse kinematics, we review the most important specifications of the Niryo One robot. In addition, the structure of the robot is displayed, the position of its joints, the type of communication and protocol, and **pyniryo** is specified as the Python library that allows us

to apply ROS (Robot Operating System) from a high level of abstraction for controlling the robot. At the end, the **Paden-Kahan subproblems** and **Newton-Raphson method** are explained as they will be implemented to solve the **inverse kinematics** of the robot at the end of the chapter.

An experiment showing the operation of the robot and the application of the previous theory is presented in the fourth chapter.

The mechanics presented have been compiled together in the Python library by Lynch and Park [4]. Based on that, the authors have also developed a more refined library along with the code from the experiment and a more extensive version of this paper [1].

## 2. NIRYO ONE MANIPULATOR

### 2.1. Basic Considerations

*Niryo Robotics* is a startup from France that designs and manufactures industrial robots, more precisely those robots are intended for personal and educational use purposes and the price is significantly lower than the average industrial robot whose price ranges between 20,000\$ and 200,000\$ [2]. The robot model used in this paper is from Niryo Robotics.

Apart from the open source software [7], the advantage of this robot is that the whole documentation can be found online for free at their website [6] and at GitHub [7].

## 2.2. Theoretical Movement Model

To showcase the proposed algorithm that this paper presents, in Table. 2.1 we have shown the planned sequential movements that the robot will perform.

**Table 2.1.** Niryo One theoretical movement model with coordinates in the robots space frame

Actuation	Transformation matrix
1. Starting position (calculated from pyniryo [7])	$\begin{bmatrix} 0,540 & 0 & 0,841 & 91,039 \cdot 10^{-3} \\ 0 & 1 & 0 & 0 \\ -0,841 & 0 & 0,540 & 190,529 \cdot 10^{-3} \\ 0 & 0 & 0 & 1 \end{bmatrix}$
2. Approach above the object	$\begin{bmatrix} 0 & 0 & 1 & 148 \cdot 10^{-3} \\ 0 & 1 & 0 & -148 \cdot 10^{-3} \\ -1 & 0 & 0 & 150 \cdot 10^{-3} \\ 0 & 0 & 0 & 1 \end{bmatrix}$
3. Descent to the object	$\begin{bmatrix} 0 & 0 & 1 & 148 \cdot 10^{-3} \\ 0 & 1 & 0 & -148 \cdot 10^{-3} \\ -1 & 0 & 0 & 88 \cdot 10^{-3} \\ 0 & 0 & 0 & 1 \end{bmatrix}$
4. Grip the object	N/A
5. Lift the object	Same as 2. Approach above the object
6. Approach above the objects destination	$\begin{bmatrix} 0 & 0 & 1 & 148 \cdot 10^{-3} \\ 0 & 1 & 0 & 148 \cdot 10^{-3} \\ -1 & 0 & 0 & 150 \cdot 10^{-3} \\ 0 & 0 & 0 & 1 \end{bmatrix}$
7. Descent to the objects destination	$\begin{bmatrix} 0 & 0 & 1 & 148 \cdot 10^{-3} \\ 0 & 1 & 0 & 148 \cdot 10^{-3} \\ -1 & 0 & 0 & 88 \cdot 10^{-3} \\ 0 & 0 & 0 & 1 \end{bmatrix}$
8. Release the object	N/A
9. Ascent from the object	Same as 6. Approach above the objects destination
10. Return to the start	Same as 1. Starting position

## 3. ROBOT MECHANICS

The approach with which we'll explore robot mechanics is based on **screw theory** which states that all rigid body motion can be interpreted as a rotation and a translation along a screw axis resulting in a helicoid trajectory.

For the interested reader, an extensive resource is available at [3, 5] for screw theory while in this paper we'll only be using the results from those sources.

The main issue we will be discussing here is the inverse robot kinematics problem for our 6 degrees of freedom (DOF) [2, 8] robot. That is to say, given a homogeneous transformation matrix  $\mathbf{T} \in SE(3)$  find the corresponding joint actuation angles  $\boldsymbol{\theta} \in \mathbb{R}^n$ ,

$$f(\mathbf{T}) = \boldsymbol{\theta}. \quad (1)$$

The inverse kinematics problem may not always have a closed-form analytical solution or the solution is not favorable for usage in practical situations. Typically for 6 DOF, there are a finite number of solutions while for robots with more than 6 DOF, there are usually infinitely many solutions.

On the other hand, there are numerical methods that, if the initial guess is sufficient, will always converge to a valid solution if it exists. The problem is, how do we ensure convergence? This can be achieved by:

- Starting the robot's motion from a known configuration and slowly changing the end-effector's goal configuration with the frequency of the calculation,
- Use an approximate analytical solution as the initial guess.

This paper tries to achieve exactly the second point, find an approximate analytical solution, and use that as an initial guess for the numerical method. This is represented as Algorithm 2.

### 3.1. Technical Specifications

The robot's technical characteristics are available in Table 3.1. The joints and their position are given in Fig. 3.1.

**Table 3.1.** Niryo One technical specifications where the range of rotation of the actuators are from the Niryo One ROS API – pyniryo and the rest from [2, 7, 8]

Specification	Value
<b>Mechanical specifications</b>	
Degrees of Freedom	6
Weight	3,3 kg
Max Reach	440 mm
Max Payload	0,5 kg
Repeatability	$\pm 0,5$ mm
Materials	Aluminium, PLA (3D printed)
Actuators	5 steppers and 2 servos
<b>End effector – Gripper 1</b>	
Weight	70 g
Length (gripper closed)	80 mm

Max opening width	27 mm
Picking distance from end-effector base	60 mm
Actuators range of rotation	
Joint 1	$-175,00000^\circ \div 175,00000^\circ$
Joint 2	$-109,44000^\circ \div 36,670000^\circ$
Joint 3	$-79,89000^\circ \div 89,960000^\circ$
Joint 4	$-174,76000^\circ \div 175,00000^\circ$
Joint 5	$-100,00000^\circ \div 110,01000^\circ$
Joint 6	$-144,96000^\circ \div 144,96000^\circ$
Electrical specifications	
Power Supply	11V $\div$ 6A
Power Consumption	$\sim$ 60W
Hardware	Arduino Mega, Raspberry Pi 3
Joint sensor	Magnetic sensor
Ports	4 USB, Ethernet
Software specifications	
Communication	Ethernet, Wi-Fi, Bluetooth, USB
User interface	Web app, Android app, iOS app, Gamepad
Programming interface	ROS, APIs, source code

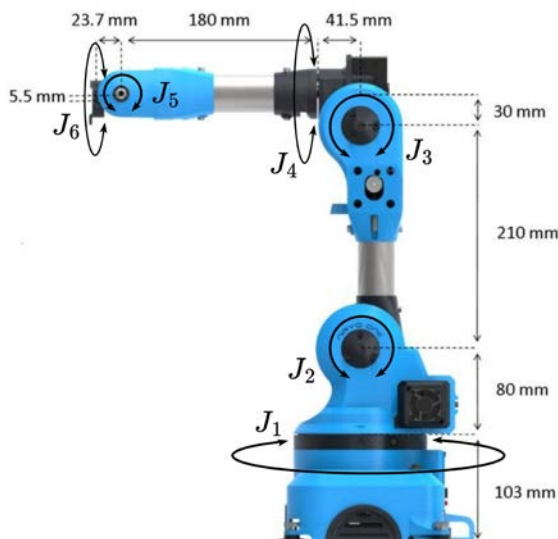


**Fig. 3.1.** Niryo Ones The position of the joints and their respective axis of rotation where  $J_i$  denotes the  $i$ -th joint

Because we can connect and manage our robot in several ways (see Table 3.1), we must explicitly state which way will be used for our application:

- Communication – Ethernet TCP/IP connection,
- Control interface – Niryo One ROS API, i.e. **pyniryo**.

Ethernet is a reliable and relatively fast way of communication that requires a wired connection (in our case wireless is unnecessary anyway), while pyniryo is the latest available Python ROS API for the Niryo One. We could also apply directly ROS but that would introduce additional complexity and is not the aim of this paper. The development environment used is *VS Code* while the Python version used is 3.12.5.

### 3.2. Paden-Kahan Subproblems

The **Paden-Kahan (PD) subproblems** are a set of subproblems, that depend on the geometry of the robot, and that may be systemically used for determining a closed-form analytical solution for the inverse kinematics of the manipulator.

Before examining the subproblems, one more thing to note is that for each solution related to a particular joint angle  $\theta_i$ , a valid solution is also

$$\theta = \theta_i \pm 2k\pi, \quad k \in \mathbb{N}. \quad (2)$$

This may turn out to be important in cases where a robot's joint has an asymmetric joint range limit, e.g, let's say we have a robot whose joint ranges are  $((-90^\circ, 90^\circ), (-225^\circ, 45^\circ), (-120^\circ, 90^\circ))$  but the solution vector  $\theta = (45^\circ, 150^\circ, -90^\circ)$  is out of range, meaning that we must change our solution and say that  $\theta = (45^\circ, -210^\circ, -90^\circ)$ .

With that in mind, we'll explore how the subproblems are formulated, their solution, and the conditions under which a solution exists.

#### Subproblem 1. Rotation about a single axis

**Problem.** Let  $\mathcal{S}$  be a zero-pitch screw axis  $h=0$  and  $\mathbf{p}, \mathbf{q} \in \mathbb{R}^3$  two points, find the corresponding rotation angle  $\theta$  such that

$$e^{[\mathcal{S}]\theta} \mathbf{p} = \mathbf{q}. \quad (3)$$

**Solution.** From the given subproblem it is evident that it corresponds to a rotation of the point  $\mathbf{p}$  to the point  $\mathbf{q}$  around the screw axis  $\mathcal{S}$  and we are looking for the angle  $\theta$  that satisfies this transformation.

The solution to this subproblem is given as

$$\theta = \text{atan2}(\omega_{\mathcal{S}} \cdot (\mathbf{u}' \times \mathbf{v}'), \mathbf{u}' \cdot \mathbf{v}') \quad (4)$$

where:

$$\mathbf{u}' = \mathbf{u} - \text{proj}_{\omega_{\mathcal{S}}} \mathbf{u}, \quad (5)$$

$$\mathbf{v}' = \mathbf{v} - \text{proj}_{\omega_{\mathcal{S}}} \mathbf{v}, \quad (6)$$

$$\mathbf{u} = \mathbf{p} - \mathbf{r}, \quad (7)$$

$$\mathbf{v} = \mathbf{q} - \mathbf{r}, \quad (8)$$

and  $\mathbf{r} \in \mathbb{R}^3$  is any point of the screw axis  $\mathcal{S}$ . To determine this point, we'll first examine the parametric definition of the screw axis

$$\mathcal{S} = \begin{bmatrix} \boldsymbol{\omega}_{\mathcal{S}} \\ \mathbf{v}_{\mathcal{S}} \end{bmatrix} = \begin{bmatrix} \hat{\boldsymbol{\omega}} \\ -\hat{\boldsymbol{\omega}} \times \mathbf{r} + h\hat{\boldsymbol{\omega}} \end{bmatrix}$$

and considering that our screw axis is zero-pitch, we may write

$$\mathbf{v}_{\mathcal{S}} = -[\boldsymbol{\omega}_{\mathcal{S}}]\mathbf{r} \quad (9)$$

and thus

$$\mathbf{r} = -[\boldsymbol{\omega}_{\mathcal{S}}]^\dagger \mathbf{v}_{\mathcal{S}}. \quad (10)$$

While we may be able to solve for  $\mathbf{r}$  analytically, it will always have an infinite amount of solutions (consider how the vector  $\mathbf{r}$  points to a line), which may pose a problem since we'll need an explicit solution to implement it programmatically.

The subproblem has a solution when the following relations are satisfied:

$$\begin{aligned} \boldsymbol{\omega}_{\mathcal{S}} \cdot \mathbf{u} &= \boldsymbol{\omega}_{\mathcal{S}} \cdot \mathbf{v} \\ \|\mathbf{u}'\| &= \|\mathbf{v}'\| \Leftrightarrow \|\mathbf{u}\| = \|\mathbf{v}\|. \end{aligned} \quad (11)$$

In the case when  $\mathbf{p} = \mathbf{q}$ , there are an infinite amount of solutions to this subproblem.

*Subproblem 2. Rotation about two subsequent axes*

**Problem.** Let  $\mathcal{S}_1$  and  $\mathcal{S}_2$  be zero-pitch screw axes  $h_1 = h_2 = 0$  that intersect and  $\mathbf{p}, \mathbf{q} \in \mathbb{R}^3$  two points, find the corresponding pair of rotation angles  $\theta_1$  and  $\theta_2$  such that

$$e^{[\mathcal{S}_1]\theta_1} e^{[\mathcal{S}_2]\theta_2} \mathbf{p} = \mathbf{q}. \quad (12)$$

**Solution.** This subproblem corresponds to two subsequent rotations of the point  $\mathbf{p}$  to the point  $\mathbf{q}$ , first around the screw axis  $\mathcal{S}_1$  for an angle of  $\theta_1$  and then around the screw axis  $\mathcal{S}_2$  for an angle of  $\theta_2$ .

In the case when the two screw axes overlap,

$$\mathcal{S}_1 = \pm \mathcal{S}_2 \Rightarrow \mathcal{S}_1 \cdot \mathcal{S}_2 = \pm \|\mathcal{S}_1\|^2 = \pm \|\mathcal{S}_2\|^2 \quad (13)$$

then we can rewrite (12) as

$$e^{[\mathcal{S}_1]\theta_1} e^{[\mathcal{S}_2]\theta_2} \mathbf{p} = e^{[\mathcal{S}_1]\theta_1} e^{-[\mathcal{S}_1]\theta_2} \mathbf{p} = e^{[\mathcal{S}_1](\theta_1 - \theta_2)} \mathbf{p} = \mathbf{q} \quad (14)$$

that lends itself to PD 1 if we say that

$$\theta = \theta_1 \pm \theta_2. \quad (15)$$

All combinations of the two angles  $\theta_1$  and  $\theta_2$  that satisfy (15) can be used, meaning that we may simplify this further by saying that one angle equals zero.

When the screw axes intersect at a point, (12) can be rewritten as a set of two equations

$$\begin{aligned} e^{[\mathcal{S}_1]\theta_1} \mathbf{p} &= \mathbf{c} \\ e^{-[\mathcal{S}_2]\theta_2} \mathbf{q} &= \mathbf{c} \end{aligned} \quad (16)$$

such that they may be solved as PD 1 if we say that

$$\mathbf{c} = \mathbf{z} + \mathbf{r} \quad (17)$$

and  $\mathbf{r} \in \mathbb{R}^3$  is the point of intersection between the two screw axes  $\mathcal{S}_1$  and  $\mathcal{S}_2$ . Since, in the general case, if we use (10), we'll get two different points  $\mathbf{r}_1 \neq \mathbf{r}_2$ , there is a need to use another method for determining  $\mathbf{r}$ . The property of the vector cross-product  $\mathbf{a} \times \alpha \mathbf{a} = \mathbf{0}$  allows us to write out (9) as a linear combination

$$-[\boldsymbol{\omega}_{\mathcal{S}_i}]\mathbf{r}_i = -[\boldsymbol{\omega}_{\mathcal{S}_i}](\mathbf{r} - \xi_i \boldsymbol{\omega}_{\mathcal{S}_i}) = \mathbf{v}_{\mathcal{S}_i}, \quad \xi_i \in \mathbb{R}, \quad i = 1, 2 \quad (18)$$

thus,

$$\mathbf{r} = \mathbf{r}_1 + \xi_1 \boldsymbol{\omega}_{\mathcal{S}_1} = \mathbf{r}_2 + \xi_2 \boldsymbol{\omega}_{\mathcal{S}_2} \quad (19)$$

and this can be solved as a linear system

$$\begin{bmatrix} \boldsymbol{\omega}_{\mathcal{S}_1} & -\boldsymbol{\omega}_{\mathcal{S}_2} \end{bmatrix} \begin{bmatrix} \xi_1 \\ \xi_2 \end{bmatrix} = \mathbf{r}_1 - \mathbf{r}_2. \quad (20)$$

If the system has a solution, then the screw axes intersect at the point defined by (19), otherwise the axes do not intersect and this subproblem has no solution.

The other variable from (17) is defined as:

$$\mathbf{z} = \alpha \boldsymbol{\omega}_{\mathcal{S}_1} + \beta \boldsymbol{\omega}_{\mathcal{S}_2} + \gamma (\boldsymbol{\omega}_{\mathcal{S}_1} \times \boldsymbol{\omega}_{\mathcal{S}_2}), \quad (21)$$

$$\alpha = \frac{(\boldsymbol{\omega}_{\mathcal{S}_1} \cdot \boldsymbol{\omega}_{\mathcal{S}_2})(\boldsymbol{\omega}_{\mathcal{S}_2} \cdot \mathbf{u}) - \boldsymbol{\omega}_{\mathcal{S}_1} \cdot \mathbf{v}}{(\boldsymbol{\omega}_{\mathcal{S}_1} \cdot \boldsymbol{\omega}_{\mathcal{S}_2})^2 - 1}, \quad (22)$$

$$\beta = \frac{(\boldsymbol{\omega}_{\mathcal{S}_1} \cdot \boldsymbol{\omega}_{\mathcal{S}_2})(\boldsymbol{\omega}_{\mathcal{S}_1} \cdot \mathbf{v}) - \boldsymbol{\omega}_{\mathcal{S}_2} \cdot \mathbf{u}}{(\boldsymbol{\omega}_{\mathcal{S}_1} \cdot \boldsymbol{\omega}_{\mathcal{S}_2})^2 - 1}, \quad (23)$$

$$\gamma = \pm \sqrt{\frac{\|\mathbf{u}\|^2 - \alpha^2 - \beta^2 - 2\alpha\beta(\boldsymbol{\omega}_{\mathcal{S}_1} \cdot \boldsymbol{\omega}_{\mathcal{S}_2})}{\|\boldsymbol{\omega}_{\mathcal{S}_1} \times \boldsymbol{\omega}_{\mathcal{S}_2}\|^2}}, \quad (24)$$

where  $\mathbf{u}$  and  $\mathbf{v}$  are defined by (7) and (8) respectively.

The subproblem can either have two pairs of solutions, one pair of solutions, or no solutions for the angles  $\theta_1$  and  $\theta_2$ . Two pairs of solutions are present when  $\gamma \neq 0$ , and one pair when (13) holds or  $\gamma = 0$ . No solutions exist when the square root from (24) is less than zero or certain conditions aren't met. The conditions for using this subproblem, in addition to the condition that the screw axes intersect, are (the implication of these conditions follows from (11) for (16)):

$$\begin{aligned} \boldsymbol{\omega}_{\mathcal{S}_2} \cdot \mathbf{u} &= \boldsymbol{\omega}_{\mathcal{S}_2} \cdot \mathbf{z}, \\ \boldsymbol{\omega}_{\mathcal{S}_1} \cdot \mathbf{v} &= \boldsymbol{\omega}_{\mathcal{S}_1} \cdot \mathbf{z}, \\ \|\mathbf{u}\|^2 &= \|\mathbf{z}\|^2 = \|\mathbf{v}\|^2. \end{aligned} \quad (25)$$

*Subproblem 3. Rotation to a given distance*

**Problem.** Let  $\mathcal{S}$  be a zero-pitch screw axis  $h = 0$ ,  $\mathbf{p}, \mathbf{q} \in \mathbb{R}^3$  two points, and  $\delta \geq 0 \in \mathbb{R}$  a real number, find the corresponding rotation angle  $\theta$  such that

$$\|\mathbf{q} - e^{[\mathcal{S}]\theta} \mathbf{p}\| = \delta. \quad (26)$$

**Solution.** From the given subproblem it is evident that it corresponds to rotating the point  $\mathbf{p}$  such that after the transformation, it is a distance of  $\delta$  from the point  $\mathbf{q}$ .

In the case that  $\delta = 0$ , (26) transforms into (3), i.e. PD 1

$$\|\mathbf{q} - e^{[S]\theta} \mathbf{p}\| = 0 \Rightarrow \mathbf{q} - e^{[S]\theta} \mathbf{p} = \mathbf{0} \Rightarrow e^{[S]\theta} \mathbf{p} = \mathbf{q}. \quad (27)$$

When  $\delta > 0$  then we have the usual case with the solution given as

$$\theta = \text{atan2}(\boldsymbol{\omega}_S \cdot (\mathbf{u}' \times \mathbf{v}'), \mathbf{u}' \cdot \mathbf{v}') \pm \arccos\left(\frac{\|\mathbf{u}'\|^2 + \|\mathbf{v}'\|^2 - \delta'^2}{2\|\mathbf{u}'\|\|\mathbf{v}'\|}\right) \quad (28)$$

where

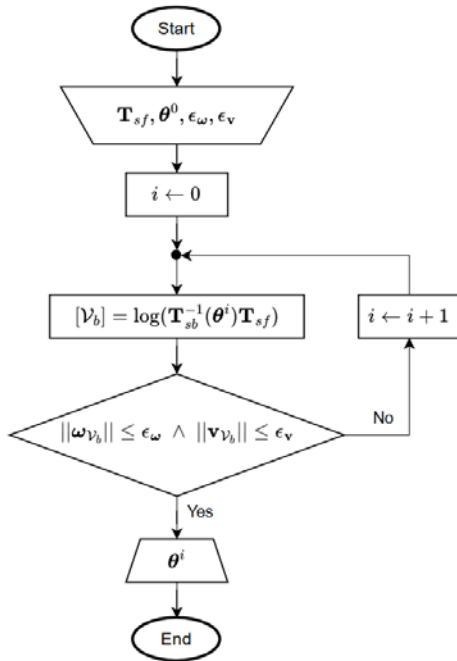
$$\delta'^2 = \delta^2 - |\boldsymbol{\omega}_S \cdot (\mathbf{p} - \mathbf{q})| \quad (29)$$

and the rest ( $\mathbf{u}'$ ,  $\mathbf{v}'$ ,  $\mathbf{u}$ ,  $\mathbf{v}$ ,  $\mathbf{r}$ ) are defined by (5)÷(10).

Based on (28) we notice that this subproblem may have two or one solution based on the angle defined by the arccos argument. It is also evident that we don't have a solution if the arccos argument is outside of the function's domain. There may also be no valid solutions even if (28) yields a proper value which occurs if (26) is not satisfied.

### 3.3. Newton-Raphson Numerical Method

The numerical method that we'll be analyzing here is the **Newton-Raphson** method used for nonlinear root-finding. The algorithm for the method, defined in the  $\{s\}$  frame, is stated in Algorithm 1.



**Algorithm 1.** Newton-Raphson numerical method in the robots space frame

### 3.4. Niryo One Mechanics

The manipulator can be simplified and graphically represented as shown in Fig. 3.2 where we have a space frame  $\{s\}$  and body frame  $\{b\}$  set to standard positions with our robot model (which is per the pyniryo interface).

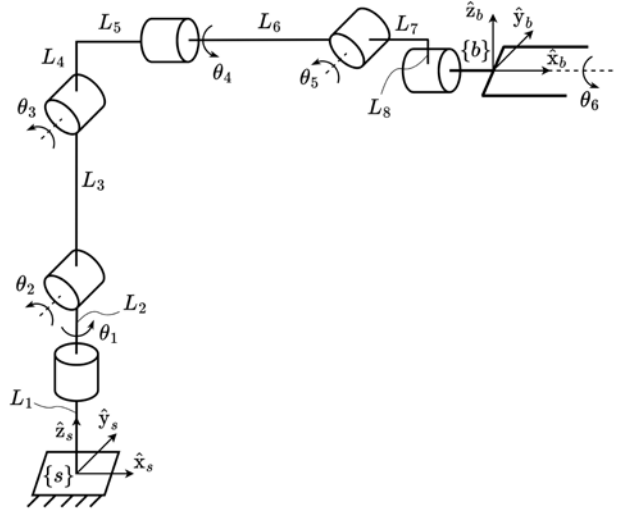


**Fig. 3.2.** Kinematic diagram of the Niryo One manipulator

The zero configuration of the Niryo One manipulator is therefore

$$\mathbf{M} = \begin{bmatrix} 1 & 0 & 0 & L_{S7} \\ 0 & 1 & 0 & 0 \\ 0 & 0 & 1 & L_{14} - L_8 \\ 0 & 0 & 0 & 1 \end{bmatrix}$$

where the values of the link lengths are given in Table 3.2. along with the definitions of the robots screw axes.

**Table 3.2.** Niryo One important kinematic values based on Fig. 3.1 and Fig. 3.2

Index number	Link length $L$ in mm	Screw axis in the $\{s\}$ frame – $\mathcal{S}$
1	103	$(0, 0, 1, 0, 0, 0)$
2	80	$(0, -1, 0, L_{12}, 0, 0)$
3	210	$(0, -1, 0, L_{13}, 0, 0)$
4	30	$(1, 0, 0, 0, L_{14}, 0)$
5	41.5	$(0, -1, 0, L_{14}, 0, -L_{56})$
6	180	$(1, 0, 0, 0, L_{14} - L_8, 0)$
7	23.7	/
8	5.5	/

As mentioned, we'll determine the inverse kinematics of the robot numerically, while using an approximate analytical solution as an initial guess analytically. Note that if we make an approximation and say that  $L_8 \approx 0$ , our manipulator closely resembles the structure of a PUMA robot for which the analytical solution is given in [5]. Therefore we will, by analogy, determine an approximate analytical solution to the PUMA robot.

We start from the expression of the direct kinematics in the  $\{s\}$  frame according to our robot model

$$\prod_{i=1}^6 e^{[S_i] \theta_i} \mathbf{M} = \mathbf{T}_{sf},$$

and multiply both sides by  $\mathbf{M}^{-1}$  to separate the unknowns from the known variables

$$\prod_{i=1}^6 e^{[S_i] \theta_i} = \mathbf{T}_{sf} \mathbf{M}^{-1} =: \mathbf{T}_1 \quad (30)$$

where

$$\mathbf{M}^{-1} = \begin{bmatrix} 1 & 0 & 0 & -L_{57} \\ 0 & 1 & 0 & 0 \\ 0 & 0 & 1 & L_8 - L_{14} \\ 0 & 0 & 0 & 1 \end{bmatrix}. \quad (31)$$

In four steps we will determine all of the joint angles.

*Step 1 (solve for  $\theta_3$ )*

Multiply both sides with a vector that points to the point of intersection of the axes  $S_1$ ,  $S_2$  and  $S_3$

$$\prod_{i=1}^3 e^{[S_i] \theta_i} \mathbf{q}_{456} = \mathbf{T}_1 \mathbf{q}_{456} \quad (32)$$

where the vector of intersection is defined as

$$\mathbf{q}_{456} = \begin{bmatrix} L_{56} \\ 0 \\ L_{14} \end{bmatrix}. \quad (33)$$

The previous relation (35) is a consequence of the fact that if a vector  $\mathbf{q}_S$  points to any point on a screw axis  $S$ , then the following holds true

$$e^{[S] \theta} \mathbf{q}_S = \mathbf{q}_S. \quad (34)$$

Next, we subtract both sides of (35) with the vector pointing to the intersection of the screw axes  $S_1$  and  $S_2$  to get

$$e^{[S_1] \theta_1} e^{[S_2] \theta_2} (e^{[S_3] \theta_3} \mathbf{q}_{456} - \mathbf{q}_{12}) = \mathbf{T}_1 \mathbf{q}_{456} - \mathbf{q}_{12} \quad (35)$$

where the vector  $\mathbf{q}_{12}$  is defined as

$$\mathbf{q}_{12} = \begin{bmatrix} 0 \\ 0 \\ L_{12} \end{bmatrix}. \quad (36)$$

Taking into account that homogeneous transformations preserve distances, norming both sides of (38) gives us

$$\|e^{[S_3] \theta_3} \mathbf{q}_{456} - \mathbf{q}_{12}\| = \|\mathbf{T}_1 \mathbf{q}_{456} - \mathbf{q}_{12}\| =: \delta \quad (37)$$

which can be solved using the results from PD 3.

*Step 2 (solve for  $\theta_1$  and  $\theta_2$ )*

Considering that, preceding this step, we have determined

$\theta_3$ , we come back to (35) and after manipulating the relation we get

$$e^{[S_1] \theta_1} e^{[S_2] \theta_2} (e^{[S_3] \theta_3} \mathbf{q}_{456}) = \mathbf{T}_1 \mathbf{q}_{456} \Rightarrow e^{[S_1] \theta_1} e^{[S_2] \theta_2} \mathbf{q}^{(1)} = \mathbf{p}^{(1)} \quad (38)$$

where

$$\mathbf{q}^{(1)} := e^{[S_3] \theta_3} \mathbf{q}_{456}, \quad (39)$$

$$\mathbf{p}^{(1)} := \mathbf{T}_1 \mathbf{q}_{456}, \quad (40)$$

which can be solved using PD 2.

*Step 3 (solve for  $\theta_4$  and  $\theta_5$ )*

After determining the first three angles which play a crucial role in the position of the robot's end-effector, we come back to (33) and separate the variables which are and aren't known

$$e^{[S_4] \theta_4} e^{[S_5] \theta_5} e^{[S_6] \theta_6} = e^{-[S_5] \theta_5} e^{-[S_2] \theta_2} e^{-[S_1] \theta_1} \mathbf{T}_1 \quad (41)$$

and multiplying both sides with the position vector  $\mathbf{q}_6$  of the screw axis  $S_6$  we get an equation that can be solved using PD 2

$$e^{[S_4] \theta_4} e^{[S_5] \theta_5} \mathbf{q}_6 = \mathbf{T}_2 \mathbf{q}_6 =: \mathbf{p}_6 \quad (42)$$

where the position vector, which mustn't be equal to  $\mathbf{q}_{456}$ , is defined as

$$\mathbf{q}_6 = \begin{bmatrix} q_6 \\ 0 \\ L_{14} \end{bmatrix}, \quad q_6 \in \mathbb{R} \setminus \{L_{56}\} \quad (43)$$

and the matrix  $\mathbf{T}_2$

$$\mathbf{T}_2 := e^{-[S_5] \theta_5} e^{-[S_2] \theta_2} e^{-[S_1] \theta_1} \mathbf{T}_1. \quad (44)$$

*Step 4 (solve for  $\theta_6$ )*

The last remaining angle can be calculated by separation in (33)

$$e^{[S_6] \theta_6} = \prod_{i=1}^5 \exp(-[S_{6-i}] \theta_{6-i}) \mathbf{T}_1 \quad (45)$$

and then multiply both sides by any vector  $\mathbf{q}^{(2)}$  which doesn't point to any point on the screw axis  $S_6$

$$e^{[S_6] \theta_6} \mathbf{q}^{(2)} = \prod_{i=1}^5 \exp(-[S_{6-i}] \theta_{6-i}) \mathbf{T}_1 \mathbf{q}^{(2)} =: \mathbf{p}^{(2)} \quad (46)$$

where

$$\mathbf{q}^{(2)} \in \mathbb{R}^3 \setminus \{\mathbf{q}_6\}. \quad (47)$$

At the end of our analysis, we emphasize that the maximum number of different angle coordinates which achieve the same desired configuration is 8 due to the multiplicity of solutions in the equations (40), (41), and (45). This can be represented by a graph as in Fig. 3.3.



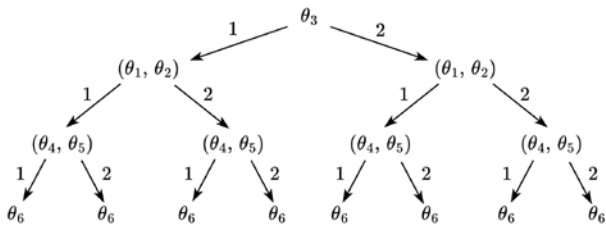


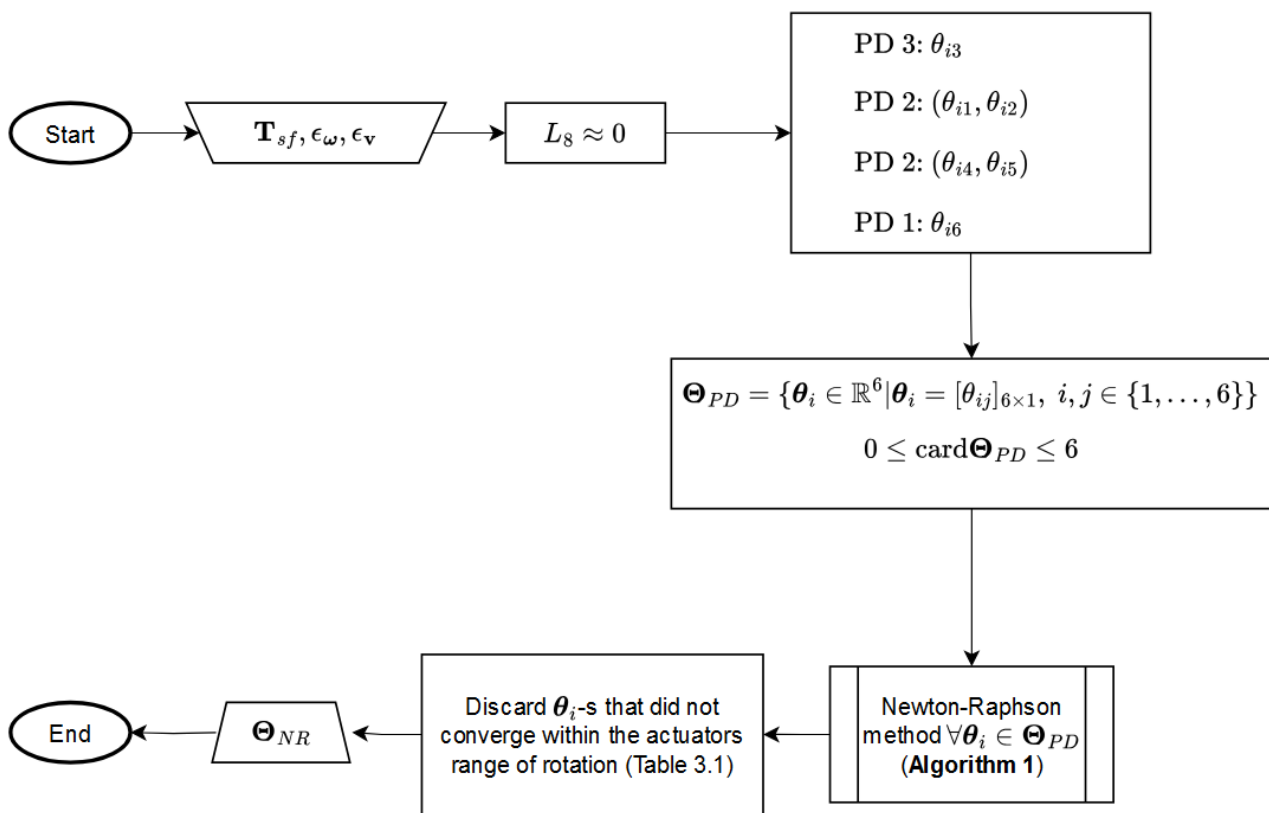
**Fig. 3.3.** Graf representing PD approximate solutions where the nodes represent the angle coordinates and the branches lead to different sets of solutions

The graf from Fig. 3.3 represents the most general case when all 8 solutions exist. Most often, there are less than 8 solutions. This is because either the robot cannot reach a certain end-effector position and orientation with all 8 robot configurations or the algorithm converges to a

certain configuration which would require the robot's actuators to move outside of their joint limit (see Table 3.1 for joint limits). If we have no PD solutions, then the desired configuration is outside the robot's workspace, otherwise it is inside.

Based on this chapter intended for determining Niryo One manipulator mechanics, an open-source Python library has been made and can be found on Github [1]. A larger portion of the library is related to general open-chain manipulators while only a single module is specialized for the Niryo One robot.

At the end, a graphical representation is shown on Algorithm 2.



**Algorithm 2.** Niryo One inverse kinematic algorithm. The sets  $\Theta_{PD}$  and  $\Theta_{NR}$  group the different valid solutions after applying the PD subproblems and Newton-Raphson method respectively

#### 4. EXPERIMENT

Using the aforementioned method of determining Niryo One's inverse kinematics, we'll conduct an experiment that will serve as some validity to the effectiveness of this approach.

**Problem.** Displace the provided object using the Niryo One manipulator. The starting and final location of the

object, measured in the robots  $\{s\}$  frame, are  $(148, -148, 0)$ mm and  $(148, 148, 0)$ mm respectively.

**Solution.** The code used is available on the same GitHub page as the code for the entire library [1]. The robot is displayed doing its task in Fig. 4.1.

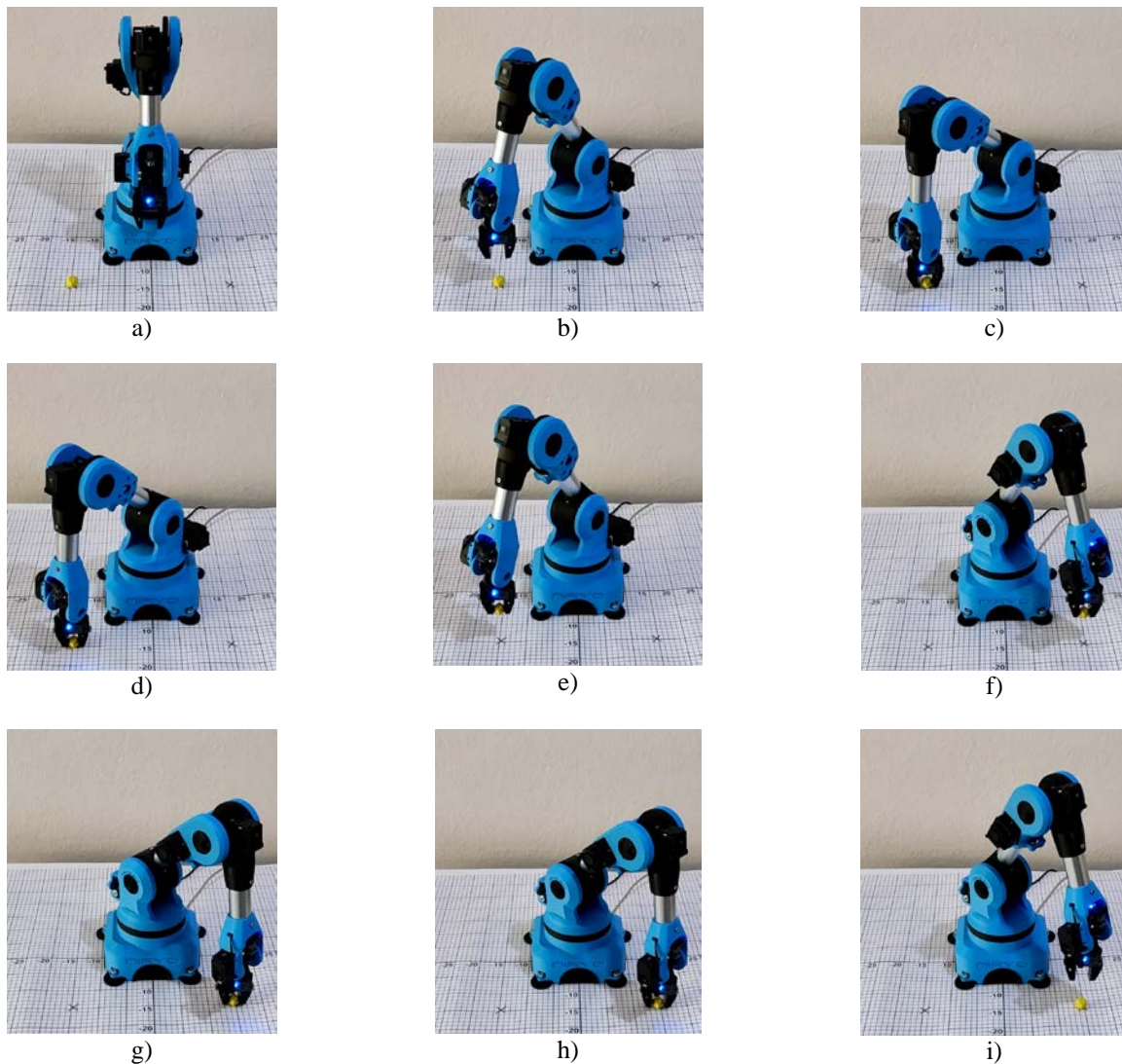


**Fig. 4.1.** Experiment: controlling the Niryo One manipulator. The experiment starts after the robot's calibration and ends when the robot returns to its starting position (which isn't shown here): a) Position 1 – starting position of the robot; b) Position 2 – approach above the object; c) Position 3 – descent to the object; d) Position 4 – gripping the object; e) Position 5 – lifting the object; f) Position 6 – approach above the objects destination; g) Position 7 – descent to the objects destination; h) Position 8 – release the object; i) Position 9 – ascent from the object.

## 5. CONCLUSION

Integration of various synergistic elements of robotic systems at a high theoretical and practical level can serve as a good example of engineering spirit, which was just performed in the work. Efficient calculation, clear formulation, easy implementation, lack of singularities, and the experiment on the Niryo One robot are evident indicators of the advantages of applying screw theory.

Another approach for determining a robot's inverse kinematics is based on the classic elimination theory from algebraic geometry, which is available at [5]. Python is a good choice for a fast and relatively simple implementation that can be refined at [1], to make the source code even more complete, robust, and efficient. In addition, the implementation in the C++ programming language would be ideal for a version of the source code that would be more suitable for the modern requirements

of practical robotics. Before that, of course, it is also possible to delve deeper into the possibilities of ROS to more fully exploit the potential of the Niryo One robot.

## Appendix: Mathematical Notation

The following notation is used:

- $\{s\}$  – space frame;
- $\{b\}$  – body frame;
- $L_{kn} = \sum_{i=k}^n L_i$  – sum of  $L_i$  link lengths;
- $\mathbf{x}_a = [x_{a1} \ x_{a2} \ x_{a3}]^T \in \mathbb{R}^3$  – vector. If a subscript is present, then it defines the coordinate frame (e.g. coordinate frame  $a$  in this case) of the vector;

- $\hat{\mathbf{a}}_a = \mathbf{a}_a / \|\mathbf{a}_a\| \in \mathbb{R}^3$  – unit vector of its bolded equivalent;
- $\mathbf{0} = [0 \ 0 \ 0]^T$  – the  $3 \times 1$  zero vector;
- $\mathbf{a} \cdot \mathbf{b}$ ,  $\mathbf{a}, \mathbf{b} \in \mathbb{R}^3$  – vector dot product;
- $\mathbf{a} \times \mathbf{b} = [\mathbf{a}]\mathbf{b}$ ,  $\mathbf{a}, \mathbf{b} \in \mathbb{R}^3$  – vector cross product (the  $[\ast]$  operator is explained below);
- $\text{proj}_{\mathbf{b}} \mathbf{a} = (\mathbf{a} \cdot \hat{\mathbf{b}})\hat{\mathbf{b}}$ ,  $\mathbf{a}, \mathbf{b} \in \mathbb{R}^3$  – vector projection of  $\mathbf{a}$  onto  $\mathbf{b}$ ;
- $\mathbf{A}^\dagger \in \mathbb{R}^{m \times n}$  – the Moore-Penrose pseudoinverse;
- $\mathbf{R}_{ab} \in SO(3)$  – Rotation matrix from the special orthogonal group. If a subscript is present, then it defines the orientation of the second letter frame in the first letter frame (e.g. orientation of the frame  $\{b\}$  in  $\{a\}$  in this case). Otherwise, the matrix represents an operator;
- $[\mathbf{x}] = \begin{bmatrix} 0 & -x_3 & x_2 \\ x_3 & 0 & -x_1 \\ -x_2 & x_1 & 0 \end{bmatrix} \in so(3)$ ,  $\mathbf{x} \in \mathbb{R}^3$  – vector skew-symmetric matrix representation;
- $\mathbf{T}_{ab} = (\mathbf{R}_{ab}, \mathbf{p}_{ab}) \in SE(3)$  – homogeneous transformation matrix from the special Euclidean group. If a subscript is present, then it defines the orientation and position of the second letter frame in the first letter frame (e.g. position and orientation of the frame  $\{b\}$  in  $\{a\}$  in this case). Otherwise, the matrix represents an operator;
- $\mathcal{S}_a = \begin{bmatrix} \boldsymbol{\omega}_{\mathcal{S}_a} \\ \mathbf{v}_{\mathcal{S}_a} \end{bmatrix} \in \mathbb{R}^6$ ,  $\boldsymbol{\omega}_{\mathcal{S}_a}, \mathbf{v}_{\mathcal{S}_a} \in \mathbb{R}^3$ , – screw axis. If a subscript is present, then it defines the coordinate frame (e.g. coordinate frame  $a$  in this case) of the screw axis;
- $[\mathcal{S}] = \begin{bmatrix} [\boldsymbol{\omega}_{\mathcal{S}}] & \mathbf{v}_{\mathcal{S}} \\ \mathbf{0}^T & 0 \end{bmatrix} \in se(3)$  – an  $se(3)$  representation of the screw axis, equivalent to  $[\mathbf{x}]$  explained before;
- $\mathcal{V}_a = \mathcal{S}_a \dot{\theta} = \begin{bmatrix} \boldsymbol{\omega}_{\mathcal{V}_a} \\ \mathbf{v}_{\mathcal{V}_a} \end{bmatrix}$  – twist. If a subscript is present, then it defines the coordinate frame (e.g. coordinate frame  $a$  in this case) of the twist;
- $[\mathcal{V}] = [\mathcal{S}]\dot{\theta} \in se(3)$  – an  $se(3)$  representation of the twist, equivalent to  $[\mathbf{x}]$  explained before;
- $\mathbf{M} \in SE(3)$  – zero/home configuration of an open chain manipulator in the  $\{s\}$  frame;

- $\mathbf{J}_b(\boldsymbol{\theta}) \in \mathbb{R}^{6 \times n}$  – the Jacobian of a manipulator defined in the  $\{b\}$  frame;
- $e^{[S]\theta} \mathbf{x} = \mathbf{T}\mathbf{x} = \mathbf{R}\mathbf{x} + \mathbf{p}$  – an abuse of notation where  $\mathbf{T}\mathbf{x}$  and  $e^{[S]\theta} \mathbf{x}$  are shorthand for  $\mathbf{R}\mathbf{x} + \mathbf{p}$ , and also  $e^{[S]\theta} = \mathbf{T}$ ,  $\mathbf{T} = (\mathbf{R}, \mathbf{p})$ ,  $\mathbf{x} \in \mathbb{R}^3$ ;

$$\bullet \text{atan2}(x, y) = \begin{cases} \arctan\left(\frac{y}{x}\right) & x > 0, \\ \arctan\left(\frac{y}{x}\right) + \pi & x < 0 \wedge y \geq 0, \\ \arctan\left(\frac{y}{x}\right) - \pi & x < 0 \wedge y < 0, \\ \frac{\pi}{2} & x = 0 \wedge y > 0, \\ -\frac{\pi}{2} & x = 0 \wedge y < 0, \\ \text{undefined} & x = 0 \wedge y = 0 \end{cases},$$

$x, y \in \mathbb{R}$

– a special function that is similar to the  $\arctan(y/x)$  function but with a larger domain of  $(-\pi, \pi]$ .

## References

- [1] Library containing the source code for robot mechanics. URL: [https://github.com/VuckoT/mehanika\\_robota](https://github.com/VuckoT/mehanika_robota).
- [2] Kickstarter Niryo One project. URL: <https://www.kickstarter.com/projects/niryo/niryo-one-an-open-source-6-axis-robotic-arm-just-f>.
- [3] Kevin M. Lynch and Frank C. Park. *Modern Robotics: Mechanics, Planning, and Control*. Cambridge University Press, 2017.
- [4] Modern Robotics Python library. URL: <https://github.com/NxrRLab/ModernRobotics/tree/master/packages/Python>.
- [5] Richard M. Murray, Zexiang Li, and S. Shankar Sastry. *A Mathematical Introduction to Robotic Manipulation*. CRC Press, 1994.
- [6] Niryo One website. url: <https://niryo.com/>.
- [7] Niryo Robotics on GitHub. URL: <https://github.com/NiryoRobotics>.
- [8] Niryo Robotics. *Niryo One Mechanical Specifications*. 2018.



**OTEH 2024**  
11<sup>TH</sup> INTERNATIONAL SCIENTIFIC CONFERENCE  
ON DEFENSIVE TECHNOLOGIES

*SECTION VI*

**Telecommunication and information systems - *TIS***



## EXAMINATION OF THE PROTECTION FACTOR WITH A LASER PHOTOMETER

MILJAN MILETIC

The Academy Of Applied Preschool Teaching And Health Studies section in Kruševac, Serbia,

[mmelektronik1@gmail.com](mailto:mmelektronik1@gmail.com)

MARINA ILIC

Military Technical Institute, Beograd, [marinailic1970@gmail.com](mailto:marinailic1970@gmail.com)

TATJANA MARKOVIC

Military Technical Institute, Beograd, [tanjin.mejl@gmail.com](mailto:tanjin.mejl@gmail.com)

**Abstract:** The work presented below deals with the modernization of the method for testing the protection factor of a protective mask against sodium chloride (NaCl) aerosols. The aim of the work is to show the possibility of modernizing the method which, unlike the existing method with a flame photometer (FP), uses a laser photometer (LP). The reason for this is the dependence of the accuracy of the method on the operation of the FP, which uses the combustion of hydrogen gas for its operation. Problems occur with changes in the hydrogen-oxygen concentration required for flame maintenance and FP operation, as well as the quality of hydrogen, which cannot be influenced. The main challenge in establishing the method is to find the ideal characteristics of the laser light source that enables the detection of aerosol NaCl particles and all other particles, especially carbon particles, whose number and concentration vary during the test, should be negligible, so filters for masking the photometer are not necessary for the operation of the new method. The function of the new method must meet the measurement of NaCl mass concentrations up to  $15\text{mg/m}^3$ , and the measurement sensitivity is  $5\text{ng/m}^3$ . The certified device FIELD MAX ii was used to adjust and detect the wavelengths of the laser photometer as well as to determine the required power of the laser light source.

**Keywords:** flame photometer(FP), laser photometer(LP), protective mask, mySql data base.

### 1. INTRODUCTION

As indicated in the abstract, the aim of the paper is to show the possibility of modernizing the method for testing NaCl aerosol particles behind a protective mask, that is, the method for checking efficiency. First, an adequate concentration of the test aerosol must be provided. From a 2% solution of sodium chloride reagent in distilled water, the aerosol generator produces an aerosol of sodium chloride. One large Collision atomizer is used, requiring an air flow of 100 l/min at a pressure of 7 bar. The atomizer and its housing are integrated into a channel that maintains a constant flow of air. To ensure complete drying of the aerosol particles, it may be necessary to heat or dehumidify the air. The mean indoor sodium chloride concentration should be  $(8 \pm 4)\text{mg/m}^3$ , with a variation not exceeding 10% throughout the effective working volume. The particle size distribution was determined as an equivalent aerodynamic diameter of  $0.02\text{ }\mu\text{m}$  to  $2\text{ }\mu\text{m}$ , with a mass mean diameter of  $0.6\text{ }\mu\text{m}$ .

In the following, the examination and checking of the concentration and size of the particles was carried out. When the reference values of the number and size of particles were obtained, a check was performed on a flame photometer with different mask samples.

A flame photometer serves as a valuable tool for accurately measuring the concentration of sodium chloride inside a face mask. To ensure the suitability of an instrument for this purpose, several key performance characteristics must be considered. First, the instrument should be specifically designed for the direct analysis of sodium chloride aerosols. Moreover, it should have the ability to measure NaCl aerosol concentrations ranging from  $15\text{ mg/m}^3$  to  $5\text{ ng/m}^3$ . In addition, the total aerosol sample required by the photometer should not exceed 15 l/min. Moreover, the response time of the photometer, excluding the sampling system, should not exceed 500 ms. Finally, it is necessary to minimize the response to other elements, especially carbon, since its concentration varies during the respiratory cycle. This can be achieved by ensuring that the bandwidth of the interference filter does not exceed 3 nm and by incorporating any necessary sideband filters. Figure 1 shows the used flame photometer that was used to collect data during this research.

It is important to note that a constant flow of air is maintained, which is filtered multiple times and without admixture of carbon and admixture of water or dirt in it. Air without condensate is delivered from the screw compressor, and after purification and dehumidification at a constant temperature of  $22^\circ\text{C}$ , it is delivered to the

flame photometer.

All measurement results were directly entered from the instrument or microcontroller into the MySQL database, from which, after processing and statistical processing, the graphs and tables presented in the paper were obtained.

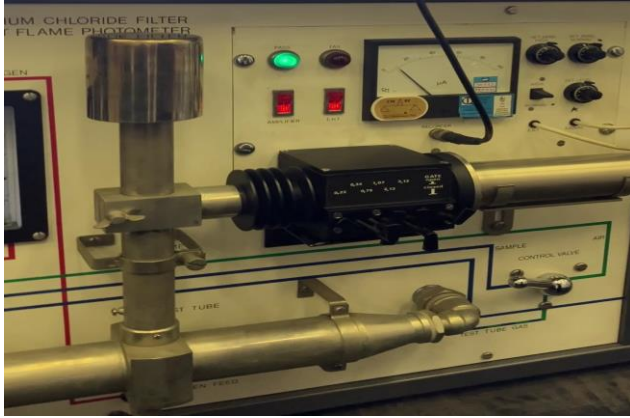


Figure 1. Flame photometer (FP)

## 2. FP MEASUREMENTS

After the fulfillment of the necessary conditions and calibration of the apparatus, the measurement of samples with the presence of NaCl particles and clean air for different filter levels was performed. Table 1 shows the values measured on the instrument (FIELD MAX ii.), for measuring the power and wavelength of light when burning clean air.

Table 1. Measurements power on a flame photometer during air combustion

Air					
N.o.	Filters	Average	STD	Min	Max
1	0	16.87n	235.7p	15.7n	17.4n
2	0.22	2.944n	152.1p	2.399n	3.399n
3	0.34	-645.5p	135.6p	-999.8p	-299.9p
4	0.75	-2.835n	102.2p	-3.099n	-2.599n
5	1.07	-5.075n	79.06p	-5.299n	-4.799n
6	2.13	-6.318n	115.2p	-6.698n	-5.899n
7	3.13	-6.774n	93.74p	-7.098n	-6.498n

The next step is to measure the value of the light level after burning the NaCl particles, when using different filters.

Table 2. Measurements power on a flame photometer during NaCl combustion

Sodium particles					
N.o.	Filter	Average	STD	Min	Max
1	0	21.97u	246.9n	21.09u	22.59u
2	0.22	6.334u	169n	5.799u	6.698u
3	0.34	1.569u	145.6n	1.1u	2u
4	0.75	-2.002u	102.4n	-2.299u	-1.7u

5	1.07	-4.519u	114.5n	-4.799u	-4.199u
6	2.13	-6.174u	123.8n	-6.498u	-5.899u
7	3.13	-6.746u	88.07n	-7.098u	-6.498u

Legend in tables 1 and 2 the following symbols have meaning:

u for micro, n is the symbol for nano, p for pico.

From the tables shown, the differences in measured values can be clearly seen when using clean air, that is, when burning particles of a mixture of air and NaCl. The difference in power ratio is several thousand times. This can also be seen with the naked eye when burning air without NaCl particles, the flame is imperceptible light blue, while when burning NaCl particles the flame is very yellow and very visible.

## 3. THE WORKING PRINCIPLE OF LP

The continuation of the research is related to the replacement of the flame photometer with a laser photometer: The plan is to place laser diodes in the vacuum tube on the front side, which will be the light source, then the light should be refracted through convex mirrors between which the sample with NaCl is brought. By passing the laser beam through the particles of air and NaCl, further detection is performed on a photo transistor that measures the level of particles in the sample. During the research, a large number of experiments were conducted with different wavelengths of the laser diode. The schematic view of the solution is presented in Figure 2.

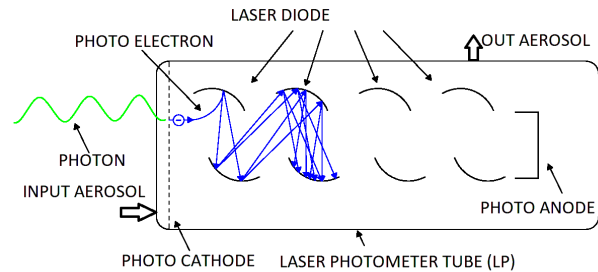


Figure 2. Laser photometer (LP)

In this research, the COHERENT OP-2 VIS photo probe element was used for signal collection



Figure 3. Photo detection probe

In addition to this probe, measurements were also made on various photo elements (photo transistors, photo

diodes, photo resistors), but the parameters were more or less within approximate limits, which depended more on the accuracy of the probe than on the particular type of element used.

#### 4. GRAPHS

In this chapter, graphs of measurement results obtained on the photo probe for different values of power and wavelength of the laser diode will be presented. All measurements were performed under the same conditions at the same concentration of NaCl aerosol and the same particle size as well as at the same humidity of the reagent entering the laser photometer. Figure 4 shows a graph for a laser diode with a wavelength of 200 nm and a power of 0.3 mW. We can see that only a very small part of the changes shown in the amplitudes in the 248 data points is registered on the graph.

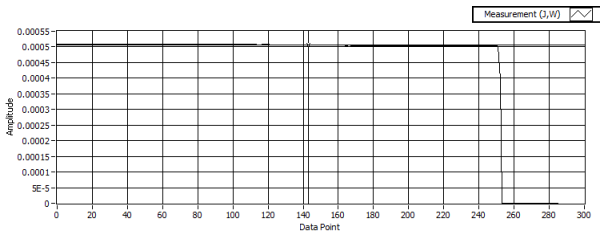


Figure 4. Graph for laser diode 200nm

Figure 5 shows a graph for a laser diode with a wavelength of 400 nm and a power of 0.3 mW. It can be seen that the change in amplitude between 90 and 120 data points is registered on the graph.

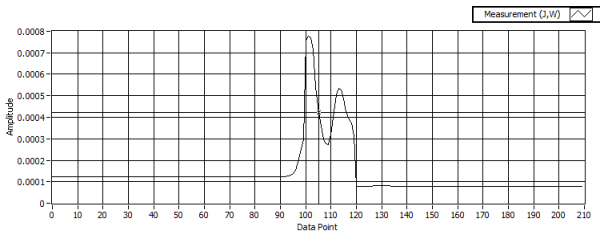


Figure 5. Graph for laser diode 400nm

Figure 6 shows a graph for a laser diode with a wavelength of 500 nm and a power of 0.3 mW. It can be seen that a large number of changes are registered on the graph through the entire scale of data points shown at amplitudes between 1 and 192 data points.

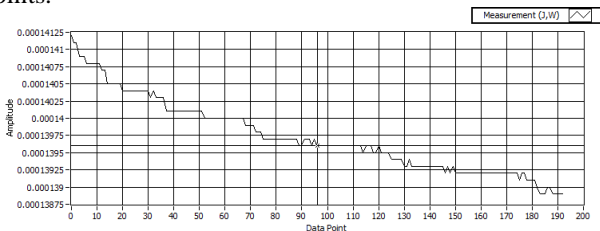


Figure 6. Graph for laser diode 500 nm

Figure 7 shows a graph for a 600nm laser diode with a power of 0.3mW. It can be seen that the change in amplitude between 130 and 210 data points is registered on the graph.

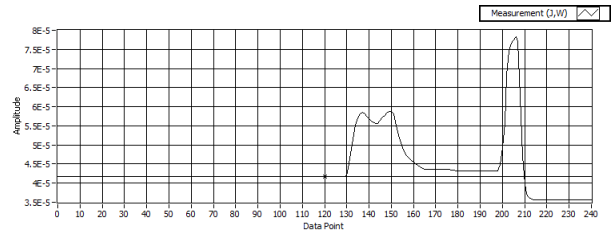


Figure 7. Graph for laser diode 600nm

Figure 8 shows a graph for a 700nm laser diode with a power of 0.3mW. It can be seen that the graph registers a large number of very frequent changes throughout the entire scale of data points displayed at amplitudes between 1 and 1, which last until the end of the measurement. On this graph, you can also see the highest power measured on the entire sensor range. This wavelength gives the best classification and the best reading for the presence of NaCl cells.

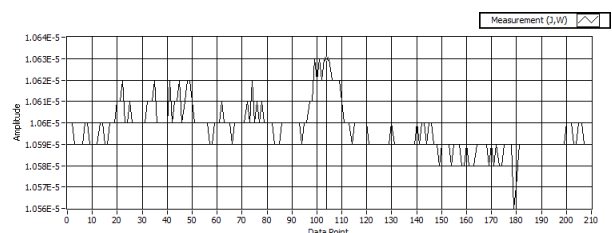


Figure 8. Graph for laser diode 700 nm

Figure 9 shows a graph for a laser diode with a wavelength of 800 nm and a power of 0.3 mW. It can be seen that changes in the range from 1 to 79 data points and amplitudes between 140 and 270 data points are registered on the graph.

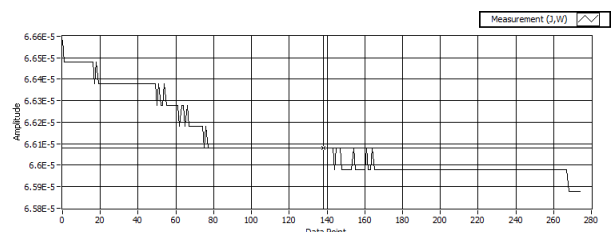


Figure 9. Graph for laser diode 800 nm

Figure 10 shows a graph for a laser diode with a wavelength of 900 nm and a power of 0.3 mW. It can be seen that the change in the range of 1-140 data points and the amplitude between 140 and 320 data points are registered on the graph. The displayed amplitudes are random with symbolic values in the reading, so when choosing this laser diode, one does not get a clear picture of the concentration change in relation to the power of the signal reading on the photometric sensor.

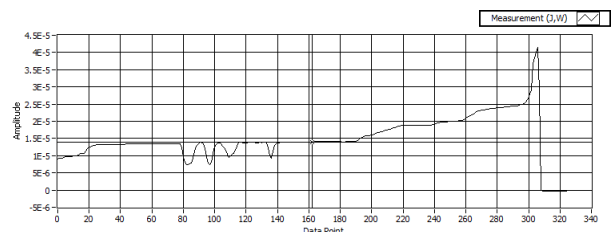


Figure 10. Graph for laser diode 900 nm

## 5. CONCLUSION

We hope that with this research we have made a contribution to the modernization of the method for measuring the effectiveness of protective masks in real conditions. The research showed the possibilities of using LF as a substitute for PF. The results obtained by measurement give the same or more precise data than using the previous system. Due to the simpler use of more precise results and resistance to external influences, it is recommended to use the LF application for efficiency measurement. The continuation of the research will refer to the possibility of replacing the testing reagent NaCl with Paraffin oil and finding the ideal values of power and wavelength of the laser diode for precise measurement. The possibility of using several laser diodes of different wavelengths and powers at the same time during the detection of these two types of reagents is being checked.

## References

- [1] Double Chooz collaboration, The Double Chooz antineutrino detectors, *Eur. Phys. J. C* 82 (2022) 804 [arXiv:2201.13285].
- [2] RENO collaboration, RENO: An Experiment for Neutrino Oscillation Parameter  $\theta_{13}$  Using Reactor Neutrinos at Yonggwang, arXiv:1003.1391.
- [3] IceCube collaboration, Calibration and Characterization of the IceCube Photomultiplier Tube, *Nucl. Instrum. Meth. A* 618 (2010) 139 [arXiv:1002.2442].
- [4] R. Dossi, A. Ianni, G. Ranucci and O.Y. Smirnov, Methods for precise photoelectron counting with photomultipliers, *Nucl. Instrum. Meth. A* 451 (2000) 623.
- [5] DarkSide collaboration, Light Yield in DarkSide-10: A Prototype Two-Phase Argon TPC for Dark Matter Searches, *Astropart. Phys.* 49 (2013) 44 [arXiv:1204.6218].
- [6] L.N. Kalousis, J.P.A.M. de André, E. Baussan and M. Dracos, A fast numerical method for photomultiplier tube calibration, 2020 JINST 15 P03023 [arXiv:1911.06220].
- [7] R. Brun and F. Rademakers, ROOT: An object oriented data analysis framework, *Nucl. Instrum. Meth. A* 389 (1997) 81.
- [8] M. Abramowitz and I.A. Stegun, *Handbook of Mathematical Functions: with Formulas, Graphs, and Mathematical Tables*, Dover Publications, 0009- Revised edition (June 1, 1965).
- [9] F. James and M. Winkler, C++ MINUIT User's Guide, <https://root.cern.ch/root/html/doc/guides/minuit2/Minuit2.html>.
- [10] L.N. Kalousis, Calibration of the Double Chooz detector and cosmic background studies, Ph.D. Thesis, University of Strasbourg (2012).
- [11] O.Y. Smirnov, Energy and spatial resolution of a large-volume liquid-scintillator detector, *Instrum. Exp. Tech.* 46 (2003) 327 [arXiv:1811.023





## CASE STUDY: IMPLEMENTATION PERSPECTIVES OF END-TO-END ENCRYPTION IN MILITARY IOT

KRISTINA ŽIVANOVIĆ

Center for Applied Mathematics and Electronics, Belgrade, [kristina.zivanovic@vs.rs](mailto:kristina.zivanovic@vs.rs)

DIMITRIJE KOLAŠINAC

Center for Applied Mathematics and Electronics, Belgrade, [dimitrije.kolasinac@vs.rs](mailto:dimitrije.kolasinac@vs.rs)

STEFAN IVANOVIĆ

Center for Applied Mathematics and Electronics, Belgrade, [stefan.ivanovic@vs.rs](mailto:stefan.ivanovic@vs.rs)

JOVANA MIHAILOV

Center for Applied Mathematics and Electronics, Belgrade, [jovana.mihailov@vs.rs](mailto:jovana.mihailov@vs.rs)

MARIJA ŠEKLER

Ministry of Defence, Belgrade, [marija.sekler@mod.gov.rs](mailto:marija.sekler@mod.gov.rs)

**Abstract:** In real-life IoT applications, data protection is a significant challenge, especially in military contexts where data can be hijacked or monitored. This paper focuses on implementing end-to-end security to safeguard data. System includes ArduinoUNO board with a GPS sensor, gathering coordinates of the monitored object, transferring them directly to a client Raspberry PI computer, which is in charge of encrypting the acquired data with a lightweight encryption algorithm, thus preparing it for transport through an unprotected network to the server. Server application receives data from the network, deciphers it and displays it on the map. The main idea is to provide the commander with a complete overview of the area of operation. The server application was developed using Qt Framework, while the client application was developed as a standard C++ console application. Another part of this research was also an Qt compatible C++ implementation of the elliptic curve algorithm suite in a separate library which was used both client and server-side. The system was tested and the coordinates data was successfully displayed on the server side. This system was correctly responding and deciphering data in real time causing negligible delay which does not impact practical usability of the system.

**Keywords:** Elliptic curves, Qt Framework, IoT systems, GIFT-COFB, Raspberry PI.

### 1. INTRODUCTION

In 2013. Global Standards Initiative on Internet of Things (IoT-GSI) has defined IoT (Internet Of Things) as global infrastructure of informatic society which provides advances services by physical and virtual cross-linking of things. [1]

Development of network infrastructure and mass incorporation of sensors in many portable devices, cars and vehicles, was the great base for developing this systems. Due to huge number of devices connected in network and large amount of data that are stored in them, there is a big risk of unauthorized access. [2] Security of data in IoT system must fulfill two demands: providing physical protection of devices, and providing integrity, secrecy, authenticity of data itself. [2]

Generally speaking, data protection comprises access control, user authentication, configuration of protective barriers, Intrusion prevention and intrusion detection

systems, secure boot etc. [3] All these methods leave risk of compromising end devices. The only way that guarantees data protection at the lowest level is encrypting those at the edge devices.

However, usually those devices have small processing power, limited memory and it is necessary to optimize existing cryptography algorithms which are usually very demanding in case of memory usage, and processing unit occupation. [4]

In this paper, the symmetric encryption algorithm that is used is the GIFT-COFB algorithm, which was one of the top 10 NIST (National Institute of Standards and Technology) finalists for the Lightweight Cryptography Standardization process, demonstrating its efficiency and security for constrained environments such as IoT devices and embedded systems. [4]

For digital signature and key exchange purposes, a dedicated library was developed encompassing all functionalities needed for implementing ECDSA (Elliptic curve Digital Signature Algorithm) and basic operations with elliptic curves. This library supports secure digital

signing using the ECDSA algorithm and facilitates key exchange operations. It ensures cryptographic operations are efficiently handled, making it suitable for applications requiring robust security measures in handling sensitive information.

## 2. SYSTEM ARCHITECTURE

The system designed and implemented for this research includes an Arduino UNO microcontroller, which, in combination with a GPS sensor, collects coordinate data of the tracked object. A Raspberry Pi 4 model B V1.2 acts as the gateway device, receiving data from the Arduino UNO microcontroller, encrypting it, and transmitting it over the network to a server application. The server application, hosted on a Linux operating system, decrypts the data and displays the locations on a map.

The infrastructure of system is shown on figure 1.

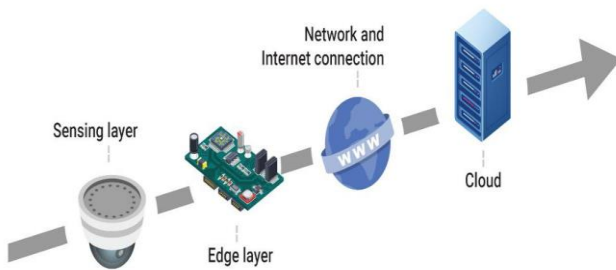


**Figure 1.** System infrastructure

The solution proposed in this paper precisely aligns with the structure depicted in Figure 1. In the future, the server application could be hosted on a remote server in the cloud. In that case, it would only be necessary to connect all the gateway devices (Raspberry Pi computers in this instance) to the network.

## 3. IMPLEMENTATION

The system designed and implemented in this work consists of a client and server application. The client application, hosted on a Raspberry Pi computer, is developed in C++. At this level, data from the Arduino microcontroller is collected via the port on the Raspberry Pi, continuously loaded into the program, encrypted, and sent over the TCP protocol to the "remote" server application. The server application is developed in C++ using the Qt framework.

Figure 2. shows the graphical interface of the server application. To access the database containing coordinate data, the QtQuick, QtLocation, and QtPositioning modules were required.

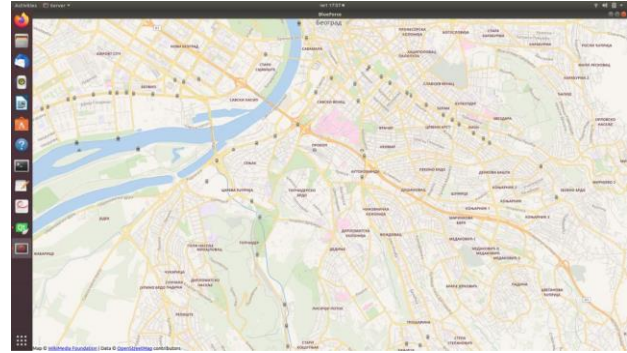


**Figure 2.** Server side application

QtQuick is a module in Qt that provides the language infrastructure and libraries for developing graphical applications. Instead of using QtWidgets, which is the foundation for creating graphical applications in the Qt environment, QtQuick objects and controls are used. Manipulation of these objects is achieved by writing code in QML (Qt Modeling Language). QML is a declarative language for designing graphical interfaces in Qt Quick applications. Additionally, this application can be extended with standard C++ code, facilitated by the C++ API, which allows calling QML functions from a C++ application and vice versa. QML is a declarative language, meaning it defines the application logic without specifying how it is achieved. QtQuick applications contain a main file, main.cpp (like all C++ applications), which loads the .qml file. [15]

The QtLocation module provides access to geolocation information of objects on the earth. It also enables searching for places and gathering information about them. Displaying the map itself cannot be done using C++ instead, QML must be used.

The system is designed to receive data from the network in a constantly active thread, verify the authenticity of the digital signature using the ECDSA algorithm, and decrypt the data using a symmetric algorithm GIFT-COFB. Verification of the digital signature also utilizes the SHA512 algorithm. Before receiving coordinates, the parties perform key exchange and session key generation. Once decrypted, the coordinates are signaled to the main user interface thread, which parses the received string, extracts the coordinates, and updates the map accordingly. Upon application startup, the map is loaded, an instance of the data-receiving class is created, the thread is started, and data reception begins.

The client application is a console-based program that involves receiving data from a GPS sensor, signing it, encrypting it, and sending it over the network to the server side. This application acts as the client in a TCP communication session. Messages are encrypted and sent in 64-bit sequences to the server.

## 4. RESULTS

The client application, operating in a console environment, gathers GPS data from a sensor via a USB

port (Arduino board), signs with ECDSA and encrypts it using the GIFT-COFB algorithm, and sends the encrypted messages over a TCP session to the server. On the server side, the application receives these encrypted data packets, decrypts them using a symmetric decryption, verify signature and subsequently processes and displays the extracted coordinates. The coordinates received on the server side, after decryption, are showcased in Figures 3 and 4. These results affirm the system's seamless operation in real-time, encompassing encryption, transmission, decryption upon reception, and the accurate display of sensor holder coordinates. This successful demonstration validates the system's capability to securely handle and present sensor data in a live environment.

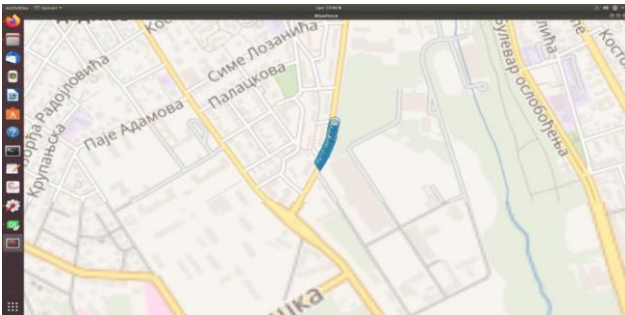


**Figure 3.** Received coordinates to server side application

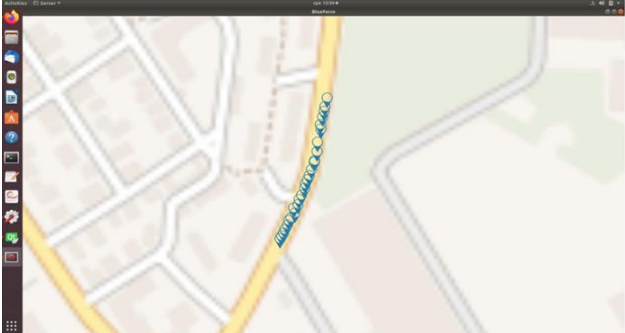


**Figure 4.** Received coordinates to server side application

Regarding time of execution of the encryption with GIFT-COFB, Table 1. presents measured time on Raspberry Pi 4B. With 4GB of RAM and Quad core Cortex-A72 (ARM v8) 64-bit 1.8GHz processor its been achieved 0,1178 ms per encryption. Encryption algorithm (GIFT-COFB) performed with 10 rounds.

**Table 1.** Time of execution

Algorithm	Time of execution [ms]
GIFT-COFB	0.1178

## 5. FUTURE APPLIENCES

This system could be applied effectively in scenarios such as vehicle tracking within a secure environment like a computer network supporting command operations.

To extend the system for tracking multiple objects simultaneously (such as people, vehicles, etc.) and displaying their consolidated positions, certain modifications would be necessary on both the client and server applications. Each client would need to be assigned a unique identifier so that upon reception on the server side, it can accurately associate incoming coordinates with the respective object.

Regarding the network infrastructure, no significant modifications would be required due to the use of the TCP protocol, which inherently supports multiple sessions with the server side. This capability allows for efficient handling of data from multiple clients simultaneously without the need for extensive network changes.

In summary, by implementing unique identifiers for clients and leveraging the existing TCP protocol, the system can effectively scale to track and display the positions of multiple objects in real-time within a secure network environment.

## 6. CONCLUSION

Thanks to their shorter keys, which require less memory and enable faster arithmetic operations compared to other cryptosystems, elliptic curves are the good choice for implementing public key cryptography in small devices with limited processing power and memory. [12]

Due to the specific requirements of an IoT system and the need for data encryption, the use of lightweight algorithms such as the GIFT COFB algorithm as symmetric algorithm has contributed significantly to the efficiency of the system.

Moving forward, it would be necessary to assess performance and potentially make modifications to meet the required efficiency in specific applications. The selection of algorithms, devices, and application architectures provides a solid foundation for further development in terms of performance optimization.

## References

- [1] K. Rose, S. Eldridge, L. Chapin, The Internet of Things: An Overview, The internet society (ISOC), 2015, 80.15: 1-53.
- [2] M. Nawir, A. Amir, N. Yaakob: Internet of Things (IOT): Taxonomy of security attacks, 3rd International Conference on Electronic Design (ICED), 2016, 11-12.
- [3] N. Abosata, S, Al. Rubaye: Internet of thing system of integrity: A comprehensive survey on security attacks countermeasures, Attacks and Countermeasures for Industrial Applications. Sensors 2021, 21, 3654.
- [4] M. El-hajj, H. Mousawi, A. Fadlallah: Analysis of Cryptographic Algorithms on IoT Hardware platforms, Future Internet, 2023.
- [5] S. Burton, Jr. Kaliski, Elliptic curves and Cryptography: A Pseudorandom Bit Generator and Other Tools, the Department of Electrical Engineering and Computer Science MIT, 1988.
- [6] S. Sridhar, S. Smys: Intelligent Security Framework for IoT Devices, Cryptography based End -To- End security Architecture, International Conference on Inventive Systems and Control, 2017.
- [7] W. Stallings, Cryptography and network security, Pearson, 2017.
- [8] Z. Musulin, Elipticke krivulje i kriptiranje, Prirodno-matematički fakultet, Zagreb, 2016.
- [9] B. Schneier: Primenjena kriptografija, Микрокњига, Београд, 2007.
- [10] B. S. Verkohovsky, Enhanced Euclid Algorithm for Modular Multiplicative Inverse and Its Application in Cryptographic Protocols, Scientific Research, 2010.
- [11] G. C. Kessler: An Overview of cryptography, Academia, 2015.
- [12] C. A. Lara-Nino, A. Diaz-Perez and M. Morales-Sandoval, "Elliptic Curve Lightweight Cryptography: A Survey," IEEE Access, vol. 6, pp. 72514-72550, 2018
- [13] A. Palve, H. Patel, Towards Securing Real time data in IoMT Environment, International Conference on Communication Systems and Network Technologies, 2018.
- [14] NMEA Generator, 03.08.2022.
- [15] L. Z. Eng, Hands-On GUI Programming with C++ and Qt5, Packt Publishing, Birmingham, 2018.



# OPTIMAL SOURCE LOCALIZATION IN A REAL RADIO CHANNEL BASED ON TDOA APPROACH USING THE HYBRID DIFFERENTIAL EVOLUTION ALGORITHM

MAJA ROSIĆ

Faculty of Mechanical Engineering, University of Belgrade, Belgrade, [mrosic@mas.bg.ac.rs](mailto:mrosic@mas.bg.ac.rs)

MILOŠ SEDAK

Faculty of Mechanical Engineering, University of Belgrade, Belgrade, [msedak@mas.bg.ac.rs](mailto:msedak@mas.bg.ac.rs)

**Abstract:** Accurate localization of sources in real radio channels is crucial for various applications ranging from military and civilian domains, notably in security, radar, and sonar systems. This paper presents a novel approach for source localization utilizing the Time Difference of Arrival (TDOA) method in a real radio channel environment. The localization problem is formulated as an optimization task, where the objective is to determine the optimal source location based on TDOA measurements obtained from multiple receivers with known positions, with the objective function derived using the least squares (LS) method. To address the complexity of the optimization problem, a hybrid approach that combines the Differential Evolution (DE) algorithm with conventional Nelder-Mead optimization algorithm has been proposed. The performance of the proposed hybrid algorithm is extensively evaluated and compared with traditional methods using numerical simulations. Results demonstrate the efficacy of the proposed approach in achieving superior localization accuracy in real radio channels, highlighting its potential for practical deployment in diverse applications.

**Keywords:** Localization, Optimization, Least Squares, Time Difference of Arrival, Wireless Sensor Networks.

## 1. INTRODUCTION

The problem of determining the unknown location of a source based on Time Difference of Arrival (TDOA) measurements from multiple receivers with known positions is critical in various applications, including military target tracking, environmental monitoring, telecommunications, security systems, and wireless sensor networks. TDOA-based source localization is intensively studied and applied in many fields due to its high ranging accuracy and relatively simple hardware requirements [1]. The core requirement in these applications is to accurately estimate the source location from a set of noisy measurements.

Localization algorithms typically employ various techniques such as Time of Arrival (TOA), TDOA, Received Signal Strength (RSS), or Angle of Arrival (AOA), depending on the available hardware. This paper focuses on source localization using TDOA measurements due to their high ranging accuracy and relatively simple hardware requirements [2].

The source location can be estimated using powerful methods like Least Squares (LS) and Maximum Likelihood (ML), which are effective in practical applications [3]. The TDOA measurement errors necessitate formulating the localization problem as an optimization task, specifically as a least-squares problem. The LS problem involves minimizing the sum of squared

errors between the estimated and measured distances. LS estimators are categorized into two types: Linear Least Squares (LLS), which provide closed-form solutions, and Nonlinear Least Squares (NLS). Weighted Least Squares (WLS) is an optimization technique where each data point is assigned a weight based on its variance, minimizing the sum of the weighted squared differences between observed and predicted values to improve estimation accuracy in the presence of heteroscedasticity. In this paper, the NLS estimator is used to accurately determine the source location from noisy TDOA measurements. The complexity of this problem makes the objective function of the NLS estimator highly nonlinear and multimodal [4]. Consequently, conventional optimization algorithms may struggle to find the global optimal solution due to their dependence on the initial solution.

To address this challenge, hybrid approach that combines the Differential Evolution (DE) [5] algorithm with the Nelder-Mead (NM) [6] method has been proposed. The DE algorithm is employed to explore the search space and identify promising regions, while the NM method is used to refine the solutions within these regions, thereby improving the convergence to the global optimal solution. This hybrid approach leverages the strengths of both algorithms: the global search capability of DE and the local optimization efficiency of NM. Hybrid optimization methods have shown superior performance in solving complex global optimization problems, as evidenced by numerous benchmark tests [7].

The paper is organized as follows: Section 2 presents the source localization problem based on TDOA measurements from multiple receivers with known positions. Section 3 describes the formulation of the localization problem as a least-squares estimation task, using both NLS and WLS approaches. Section 4 introduces the hybrid DE-NM method. Section 5 provides the Cramer-Rao Lower Bound (CRLB) for TDOA measurements, which serves as a benchmark for evaluating localization accuracy. Section 6 presents the simulation results of the proposed hybrid optimization algorithm compared to conventional methods. Finally, Section 7 concludes the paper and suggests directions for future research.

## 2. PROBLEM FORMULATION

In this section, the two-dimensional (2D) target localization problem using TDOA measurements under the line-of-sight (LOS) environment has been proposed. To determine the unknown position of a target, the considered localization problem requires measurements from at least four receivers with known positions, placed at coordinates  $(x_i, y_i), i = 1, 2, 3, 4$ , as illustrated in Fig. 1.

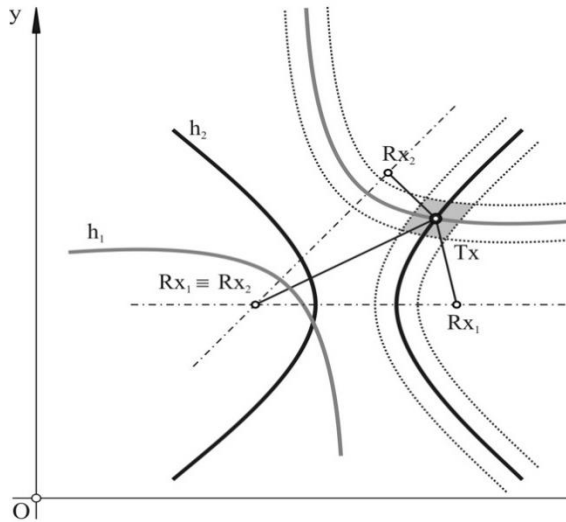


**Figure 1.** Geometrical model based on TDOA.

Assume that the range difference errors  $n_i$  can be modeled as independent Gaussian random variables with zero mean and variance  $\sigma^2$ , i.e.,  $\Delta d_{ij} \sim N(0, \sigma^2)$ . Without loss of generality, the first receiver is set at  $(x_1, y_1)$  as the reference receiver.

Using geometrical relationships between the target and the receivers, the target's unknown location  $(x, y, z)$  is determined. The unknown distances  $d_i$  from the target to the receivers are calculated by multiplying the measured times by the speed of light  $c$ . These distances can be calculated using the formula

$$d_i = c \cdot t_i \quad (1)$$

where  $t_i$  is the time taken for the signal to travel from the

target to the  $i$ -th receiver. The distances between the target and the receiver pairs  $i$  and  $j$  can be expressed as follows

$$d_i - d_j = c \cdot (t_i - t_j) \quad (2)$$

This equation can be rewritten in terms of the coordinates of the target and the receivers

$$\sqrt{(x-x_i)^2 + (y-y_i)^2} - \sqrt{(x-x_j)^2 + (y-y_j)^2} + n_i = \Delta d_{ij} \quad (3)$$

where  $\Delta d_{ij}$  represents the measured range difference between receivers  $i$  and  $j$ .

Without the noise, the TDOA measurements create hyperbolic equations that relate the target's position to the known receiver positions. For each pair of receivers, the hyperbola  $h_i$  (denoted on Figure 1) is defined by the property that the difference in distances from any point on the hyperbola to the two foci (receiver positions) is constant, specifically

$$\sqrt{(x-x_i)^2 + (y-y_i)^2} - \sqrt{(x-x_j)^2 + (y-y_j)^2} = \Delta d_{ij} \quad (4)$$

As shown in Fig. 1, the intersection of multiple 2D hyperbolas provides the geometric model for determining the target's unknown coordinates using TDOA data in the absence of noise.

In practical scenarios, noise is always present, causing the hyperbolas not to intersect at a single point. Therefore, it is necessary to use an appropriate optimization technique to minimize the localization error. The localization problem has been formulated as a NLS problem, aiming to minimize the sum of squared differences between the measured and calculated range differences.

## 3. LEAST SQUARE METHODS

This section presents the formulation of the LS method for the source localization model using the TDOA measurements described in the previous sections. Generally, the NLS problem formulation precedes the LS problem formulation. The objective function  $J_{NLS}(\mathbf{x})$  is defined as the sum of squared residuals between the estimated and measured TDOA values, expressed as

$$J_{NLS}(\mathbf{x}) = \sum_{i=1}^N (r_i(\mathbf{x}))^2 \quad (5)$$

where  $\mathbf{x}$  denotes the vector of decision variables, and the residual  $r_i(\mathbf{x})$  is calculated as

$$r_i(\mathbf{x}) = d_i - \hat{d}_i(\mathbf{x}) \quad (6)$$

Here,  $d_i$  represents the measured TDOA values, and  $\hat{d}_i(\mathbf{x})$  represents the estimated TDOA values. The minimization problem aims to find the optimal solution  $\mathbf{x}^*$  by solving

$$\mathbf{x}^* = \arg \min J_{NLS}(\mathbf{x}). \quad (7)$$

Since the TDOA problem results in nonlinear equations of hyperbolas, the following steps are necessary to transform these nonlinear equations into a suitable set of linear equations. First, squaring both sides of the hyperbola equations and introduce a new variable, resulting in

$$(x_i - x_1)(x - x_1) + (y_i - y_1)(y - y_1) + r_{i,1}R_1 = 0.5 \left[ (x_i - x_1)^2 + (y_i - y_1)^2 - r_{i,1}^2 \right] + d_i n_{i,1} + 0.5 n_{i,1}^2, \quad (8)$$

$i \in \{2, 3, \dots, N\}$ ,

where

$$R_1 = d_1 = \sqrt{(x - x_1)^2 + (y - y_1)^2}, \quad (9)$$

getting

$$(x_i - x_1)(x - x_1) + (y_i - y_1)(y - y_1) + r_{i,1}R_1 = 0.5 \left[ (x_i - x_1)^2 + (y_i - y_1)^2 - r_{i,1}^2 \right] + d_i n_{i,1} + 0.5 n_{i,1}^2, \quad (10)$$

$i \in \{2, 3, \dots, N\}$ ,

By neglecting second-order terms and linearizing the system of equations, the following is obtained

$$\mathbf{A}\boldsymbol{\theta} = \mathbf{b} + \mathbf{m}, \quad (11)$$

in which

$$\mathbf{A} = \begin{bmatrix} x_2 - x_1 & y_2 - y_1 & r_{2,1} \\ x_3 - x_1 & y_3 - y_1 & r_{3,1} \\ \vdots & \vdots & \vdots \\ x_N - x_1 & y_N - y_1 & r_{N,1} \end{bmatrix}, \quad (12)$$

$$\boldsymbol{\theta} = [x - x_1 \quad y - y_1 \quad R_1]^T, \quad (13)$$

$$\mathbf{b} = 0.5 \begin{bmatrix} (x_2 - x_1)^2 + (y_2 - y_1)^2 - r_{2,1}^2 \\ (x_3 - x_1)^2 + (y_3 - y_1)^2 - r_{3,1}^2 \\ \vdots \\ (x_N - x_1)^2 + (y_N - y_1)^2 - r_{N,1}^2 \end{bmatrix}, \quad (14)$$

$$\mathbf{m} = [m_{2,1} \quad m_{3,1} \quad \dots \quad m_{N,1}]^T. \quad (15)$$

where  $\mathbf{A}$  and  $\mathbf{b}$  are derived matrices from the linearized equations. Based on this linear matrix form, the WLS objective function is defined as:

$$J_{WLS}(\boldsymbol{\theta}) = (\mathbf{A}\boldsymbol{\theta} - \mathbf{b})^T \mathbf{W}(\mathbf{A}\boldsymbol{\theta} - \mathbf{b}) \quad (16)$$

where  $\mathbf{W}$  is the weighting matrix. The localization problem is then formulated as:

$$\mathbf{x}^* = \arg \min J_{WLS}(\boldsymbol{\theta}) \quad (17)$$

The linear LS problem formulated above provides an algebraic closed-form solution, which for the WLS

method is denoted as  $\mathbf{x}^*$ . This solution minimizes the linearized objective function  $J_{WLS}(\boldsymbol{\theta})$ . The optimal solution  $\mathbf{x}^*$  can be obtained using

$$\mathbf{x}_{WLS}^* = (\mathbf{A}^T \mathbf{W} \mathbf{A})^{-1} \mathbf{A}^T \mathbf{W} \mathbf{b} \quad (18)$$

The primary advantages of the WLS method are its simple implementation and computational efficiency. However, it may not achieve sufficient accuracy for highly nonlinear and complex problems.

#### 4. HYBRID DE-NM METHOD

The proposed hybrid DE and NM method is introduced in this section in the context of its application to the problem of locating emitting sources using TDOA measurements. The primary objective of hybridizing different optimization algorithms is to devise the most effective technique for solving the given optimization problem. By hybridizing the algorithms, it is possible to leverage the advantages of each algorithm while mitigating their respective disadvantages.

DE is a robust stochastic global optimization method that explores the search space by generating initial solutions randomly within defined boundary constraints, ultimately finding the global or near-global optimal solution. On the other hand, the NM method is a deterministic local search algorithm that refines the initial solution found by DE to locate the best global optimal solution for the problem at hand.

In this paper, the DE algorithm has been combined with the efficient NM local search method to create a hybrid DE-NM algorithm, enhancing both the efficiency and accuracy of the DE solution. Initially, the DE method explores the search space and identifies promising regions. Subsequently, the NM method is applied to these regions to fine-tune the solutions, thus achieving a more precise localization of the source.

This section provides a detailed overview of the DE and NM methods individually, followed by the description of the hybridization procedure that integrates these two techniques. The hybrid approach not only capitalizes on the global search capabilities of DE but also benefits from the local optimization strength of NM, resulting in a powerful and effective solution for the TDOA-based source localization problem in real radio channels.

##### 4.1 Differential evolution algorithm

The DE algorithm, developed by Storn and Price [6], is a stochastic population-based search method designed for global optimization in continuous search spaces. The DE algorithm is composed of four fundamental steps: initialization, mutation, crossover, and selection, each playing a crucial role in the evolutionary process aimed at finding the global optimal solution of the objective function.

#### 4.1.1 Initialization

The DE algorithm starts with an initial population of  $N_p$  individuals within the search space, where each individual represents a potential solution. The  $i$ -th individual in the population at generation  $G$  is denoted as  $\mathbf{x}_{i,G} = [x_{i,1,G}, x_{i,2,G}, \dots, x_{i,D,G}]$ , where  $D$  is the dimensionality of the problem. The  $j$ -th component of the  $i$ -th individual is initialized randomly within its bounds

$$x_{i,j,0} = x_{j,\min} + \text{rand}(0,1)(x_{j,\max} - x_{j,\min}) \quad (19)$$

where  $\text{rand}(0,1)$  is a uniformly distributed random number between 0 and 1.

#### 4.1.2 Mutation

In the mutation step, a new mutant vector  $\mathbf{v}_{i,G}$  is generated for each target vector  $\mathbf{x}_{i,G}$ . This is achieved by adding the weighted difference between two randomly selected vectors to a third vector. Common mutation strategies include DE/rand/1:

$$\mathbf{v}_{i,G} = \mathbf{x}_{r1,G} + F(\mathbf{x}_{r2,G} - \mathbf{x}_{r3,G}) \quad (20)$$

DE/rand/2:

$$\mathbf{v}_{i,G} = \mathbf{x}_{r1,G} + F(\mathbf{x}_{r2,G} - \mathbf{x}_{r3,G}) + F(\mathbf{x}_{r4,G} - \mathbf{x}_{r5,G}) \quad (21)$$

DE/best/1:

$$\mathbf{v}_{i,G} = \mathbf{x}_{\text{best},G} + F(\mathbf{x}_{r1,G} - \mathbf{x}_{r2,G}) \quad (22)$$

DE/best/2:

$$\mathbf{v}_{i,G} = \mathbf{x}_{\text{best},G} + F(\mathbf{x}_{r1,G} - \mathbf{x}_{r2,G}) + F(\mathbf{x}_{r3,G} - \mathbf{x}_{r4,G}) \quad (23)$$

Here,  $r_1, r_2, r_3$ , etc. are distinct integers randomly selected from the set  $\{1, 2, \dots, N_p\}$  and  $F$  is a scaling factor that controls the amplification of the differential variation.

#### 4.1.3 Crossover

The crossover step generates a trial vector  $\mathbf{u}_{i,G}$  by mixing the components of the mutant vector  $\mathbf{v}_{i,G}$  with the target vector  $\mathbf{x}_{i,G}$ . The binomial crossover method can be expressed as

$$u_{i,j,G} = \begin{cases} v_{i,j,G} & \text{if } \text{rand}(0,1) \leq C_r \text{ or } j = j_{\text{rand}} \\ x_{i,j,G} & \text{otherwise} \end{cases} \quad (24)$$

where  $C_r$  is the crossover rate, and  $j_{\text{rand}}$  is a randomly chosen index to ensure that  $\mathbf{u}_{i,G}$  gets at least one component from  $\mathbf{v}_{i,G}$ .

#### 4.1.4 Selection

Finally, in the selection step, the trial vector  $\mathbf{u}_{i,G}$  is compared with the target vector  $\mathbf{x}_{i,G}$ . For a minimization problem, the vector with the better objective function value is chosen for the next generation:

$$\mathbf{x}_{i,G+1} = \begin{cases} \mathbf{u}_{i,G} & \text{if } f(\mathbf{u}_{i,G}) \leq f(\mathbf{x}_{i,G}), \\ \mathbf{x}_{i,G} & \text{otherwise} \end{cases} \quad (25)$$

This process of mutation, crossover, and selection is repeated until a termination criterion, such as the maximum number of generations, is reached.

## 4.2 Nelder Mead Algorithm

The NM simplex method is a popular local search technique that does not require derivative information of the objective function [7]. It is primarily used for minimizing an objective function in an  $n$ -dimensional Euclidean space. The NM method begins with an initial simplex, a polyhedron with  $n+1$  vertices. The objective function is evaluated at each vertex, and the vertices are ranked based on their function values, with the best vertex denoted as  $\mathbf{x}_{\text{best}}$  and the worst vertex as  $\mathbf{x}_{\text{worst}}$ .

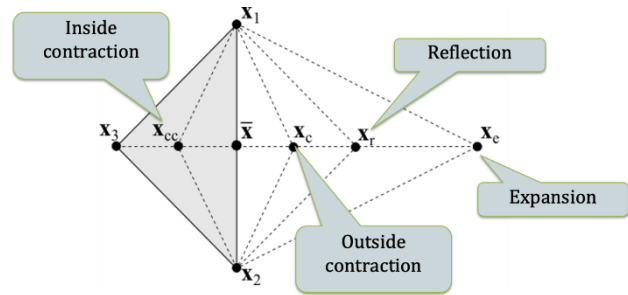


Figure 2. Operations of the NM algorithm

The NM method employs four geometric transformations: reflection, expansion, contraction, and shrinkage. These transformations iteratively improve the simplex's position, moving it closer to the optimal solution.

#### 4.2.1 Steps of the Nelder-Mead Method

##### Initialization

The initial simplex is generated using the initial vertex  $\mathbf{x}_0$  obtained from the DE algorithm. The remaining  $n$  vertices  $\mathbf{x}_i$  are generated as follows:

$$\mathbf{x}_i = \mathbf{x}_0 + \delta \mathbf{e}_i \quad \text{for } i = 1, 2, \dots, n \quad (26)$$

where  $\mathbf{e}_i$  is the unit vector along the  $i$ -th coordinate axis, and  $\delta$  is the initial step size.

##### Sorting

The vertices of the current simplex are evaluated and



ranked based on their objective function values:

$$f(\mathbf{x}_{\text{best}}) \leq f(\mathbf{x}_2) \leq \dots \leq f(\mathbf{x}_{\text{worst}}) \quad (27)$$

#### Reflection

A new vertex  $\mathbf{x}_r$  is generated by reflecting the worst vertex  $\mathbf{x}_{\text{worst}}$  about the centroid  $\mathbf{x}_c$  of the best  $n$  vertices:

$$\mathbf{x}_r = \mathbf{x}_c + \alpha(\mathbf{x}_c - \mathbf{x}_{\text{worst}}) \quad (28)$$

where  $\alpha$  is the reflection coefficient (typically  $\alpha = 1$ ). If  $f(\mathbf{x}_r) < f(\mathbf{x}_{\text{best}})$ , replace  $\mathbf{x}_{\text{worst}}$  with  $\mathbf{x}_r$  and terminate the iteration. Otherwise, proceed to expansion.

#### Expansion

If the reflection improves the solution, the algorithm tries to expand further in the same direction:

$$\mathbf{x}_e = \mathbf{x}_c + \gamma(\mathbf{x}_r - \mathbf{x}_c) \quad (29)$$

where  $\gamma$  is the expansion coefficient (typically  $\gamma = 2$ ). If  $f(\mathbf{x}_e) < f(\mathbf{x}_r)$ , replace  $\mathbf{x}_{\text{worst}}$  with  $\mathbf{x}_e$ . Otherwise, replace  $\mathbf{x}_{\text{worst}}$  with  $\mathbf{x}_r$ .

#### Contraction

If the reflection does not yield a better solution, the algorithm contracts the simplex:

#### Outside Contraction

If  $f(\mathbf{x}_r) < f(\mathbf{x}_{\text{worst}})$ :

$$\mathbf{x}_c = \mathbf{x}_c + \beta(\mathbf{x}_r - \mathbf{x}_c) \quad (30)$$

where  $\beta$  is the contraction coefficient (typically  $\beta = 0.5$ ). If  $f(\mathbf{x}_c) < f(\mathbf{x}_r)$ , replace  $\mathbf{x}_{\text{worst}}$  with  $\mathbf{x}_c$ . Otherwise, proceed to shrinkage.

#### Inside Contraction

If  $f(\mathbf{x}_r) \geq f(\mathbf{x}_{\text{worst}})$ :

$$\mathbf{x}_c = \mathbf{x}_c + \beta(\mathbf{x}_{\text{worst}} - \mathbf{x}_c) \quad (31)$$

If  $f(\mathbf{x}_c) < f(\mathbf{x}_{\text{worst}})$ , replace  $\mathbf{x}_{\text{worst}}$  with  $\mathbf{x}_c$ . Otherwise, proceed to shrinkage.

#### Shrinkage

If contraction fails to improve the solution, the simplex is shrunk towards the best vertex  $\mathbf{x}_{\text{best}}$ :

$$\mathbf{x}_i = \mathbf{x}_{\text{best}} + \sigma(\mathbf{x}_i - \mathbf{x}_{\text{best}}) \quad (32)$$

where  $\sigma$  is the shrinkage coefficient (typically  $\sigma = 0.5$ ).

These steps are repeated until a termination criterion, such

as the maximum number of iterations or a tolerance threshold, is met.

### 4.3 Proposed hybrid DE-NM method

The proposed hybrid Differential Evolution-Nelder-Mead (DE-NM) method for source localization effectively combines the global optimization strengths of the DE algorithm with the local refinement efficiency of the NM method. This hybrid approach operates in two main phases: the global search phase and the local refinement phase.

#### Initialization

An initial population of  $N_p$  candidate solutions is generated randomly within the search space boundaries. Each candidate solution represents a potential source location.

#### DE Phase

During the DE phase, iterations are performed to explore the search space by applying Mutation, Crossover and Selection operators. After  $N_{DE}$  iterations, the best solution  $\mathbf{x}_{DE}$  is selected from the DE population.

#### NM Phase

The best solution  $\mathbf{x}_{DE}$  from the DE phase is used as the initial solution for the NM method. The NM method then refines this solution through geometric transformations (reflection, expansion, contraction, and shrinkage) applied to the simplex formed by the current solution and neighboring points. This phase iteratively improves the solution to achieve higher accuracy.

The refined solution  $\mathbf{x}_{NM}$  is compared against a predefined accuracy threshold. If the solution meets the accuracy requirements, the algorithm terminates. If not, a new DE cycle is repeated.

This hybrid approach leverages the ability of DE algorithm to avoid local minima and the efficiency of NM in fine-tuning solutions. By alternating between global and local search phases, the DE-NM method enhances convergence rates and accuracy, making it suitable for precise source localization in noisy environments.

## 5. CRAMER-RAO LOWER BOUND

The Cramer-Rao Lower Bound (CRLB) is a theoretical lower bound on the variance of unbiased estimators [5]. It is an important concept in the field of statistical estimation theory, providing a benchmark for evaluating the efficiency of an estimator. The CRLB is derived from the inverse of the Fisher Information matrix (FIM), which quantifies the amount of information that an observable random variable carries about an unknown parameter upon which the likelihood depends. The relationship between CRLB and variance is

$$E\left[(\hat{\mathbf{x}} - \mathbf{x})(\hat{\mathbf{x}} - \mathbf{x})^T\right] \geq \text{CRLB}(\mathbf{x}) = \text{trace}\{\mathbf{I}(\mathbf{x})^{-1}\} \quad (33)$$

where  $E[\cdot]$  denoted the expectation operator and  $\mathbf{I}(\mathbf{x})$  is FIM given by

$$\mathbf{I}(\mathbf{x}) = -E\left[\frac{\partial^2 \ln(f(\mathbf{r}|\mathbf{x}))}{\partial \mathbf{x} \partial \mathbf{x}^T}\right], \quad (34)$$

The probability density function  $f(\mathbf{r}|\mathbf{x})$  can be defined as

$$f(\mathbf{r}|\mathbf{x}) = \frac{1}{(2\pi)^{(N-1)/2} |\mathbf{C}|^{1/2}} \cdot \exp\left(-\frac{1}{2}(\mathbf{r} - \mathbf{d}(\mathbf{x}))^T \mathbf{C}^{-1} \left(-\frac{1}{2}(\mathbf{r} - \mathbf{d}(\mathbf{x}))\right)\right), \quad (35)$$

where  $\mathbf{C}$  is covariance matrix is given as

$$\mathbf{C} = \begin{bmatrix} \sigma_1^2 + \sigma_2^2 & \sigma_1^2 & \cdots & \sigma_1^2 \\ \sigma_1^2 & \sigma_1^2 + \sigma_3^2 & \ddots & \sigma_1^2 \\ \vdots & \vdots & \ddots & \vdots \\ \sigma_1^2 & \sigma_1^2 & \cdots & \sigma_1^2 + \sigma_N^2 \end{bmatrix}. \quad (36)$$

After mathematical operations, the FIM can be obtained as

$$\mathbf{I}(\mathbf{x}) = \left[\frac{\partial \mathbf{d}(\mathbf{x})}{\partial \mathbf{x}}\right]^T \cdot \mathbf{C}^{-1} \cdot \left[\frac{\partial \mathbf{d}(\mathbf{x})}{\partial \mathbf{x}}\right]. \quad (37)$$

## 6. SIMULATION RESULTS

This section presents the results of numerical simulations performed to compare the localization performance of the proposed hybrid DE-NM method with the well-known WLS method and the derived CRLB. The simulation considers five receivers positioned at known coordinates:  $[150, 250]^T$  m,  $[1300, 200]^T$  m,  $[150, 1200]^T$  m,  $[1410, 1400]^T$  m and  $[600, 800]^T$  m.

For simulation purposes, the true position of the source is assumed to be at  $[250, 450]^T$ . To evaluate and compare the localization performance of the different algorithms, the Root Mean Square Error (RMSE) measure is employed, which is defined as:

$$RMSE = \sqrt{\frac{1}{N} \sum_{n=1}^N \|\hat{\mathbf{x}}(n) - \mathbf{x}\|_2^2}. \quad (38)$$

where  $\mathbf{x}$  and  $\hat{\mathbf{x}}(n)$  are the true and estimated positions of the source, respectively, and  $N$  is the number of Monte Carlo simulation runs.

Firstly, an illustration of the local search process of the proposed novel hybrid ADENM algorithm for the given passive target localization problem is depicted in Fig. 3.

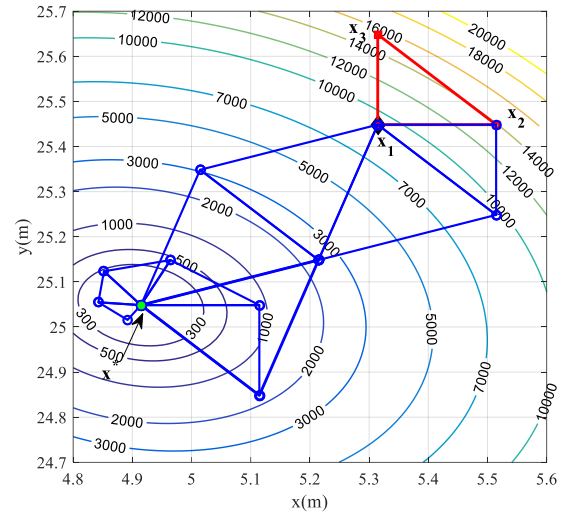


**Figure 3.** Illustration of the local search process of the proposed novel hybrid DE-NM algorithm

As can be observed from Fig. 3, the initial simplex is marked by a red triangle, in which the initial point  $\mathbf{x}_1$  for NM method is obtained as the global best solution found by DE algorithm, and the remaining vertices  $\mathbf{x}_2$  and  $\mathbf{x}_3$  are then generated. At each NM iteration, the vertices of the current simplex are ordered according to the objective function values. If a new vertex has a smaller objective function value than at least one of the existing vertices, it replaces the worst vertex, and by this way the new simplex is obtained. Thereafter, the new simplex moves through the search space in order to minimize an objective function by applying a series of geometric transformations such as reflection, expansion, contraction and shrinkage. As the evolution process proceeds the size of the simplexes are gradually reduced. This iterative process is repeated until the simplex are close enough to each other. Finally, the coordinates of the global optimum  $\mathbf{x}^*$  for a given objective function are found.

Next, the accuracy of the localization algorithms is evaluated based on different levels of TDOA measurement noise. In Figure 4 the RMSE of the DE-NM and WLS methods is plotted as a function of Signal-to-Noise Ratio (SNR), along with the calculated CRLB.

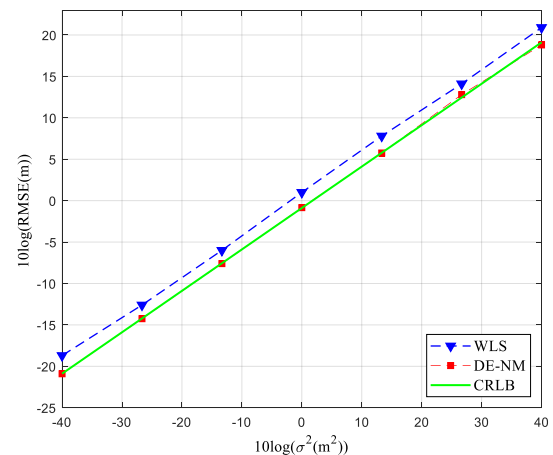


**Figure 4.** Comparison of RMSE versus SNR levels for different considered algorithms

The provided diagram illustrates a comparative analysis of two methods for source localization the WLS and DE-NM methods. The CRLB, depicted by a green solid line, serves as the benchmark for the best achievable performance. The DE-NM method, consistently aligns closely with the CRLB, indicating superior accuracy. In contrast, the WLS method, deviates more significantly from the CRLB, reflecting lower accuracy. The trends suggest that while both methods follow the general trajectory of the CRLB, the DE-NM method demonstrates a substantial accuracy advantage. This performance is underscored by the DE-NM method's ability to approach the theoretical lower bound more closely than the WLS method. In conclusion, the diagram validates that the proposed hybrid DE-NM method offers a more reliable and precise approach for source localization in noisy environments compared to the traditional WLS method, significantly enhancing localization accuracy.

Next, in with the aim to examine further the localization performance the cumulative distribution functions (CDFs) of the DE-NM and WLS localization methods are compared at SNR=20dB level.

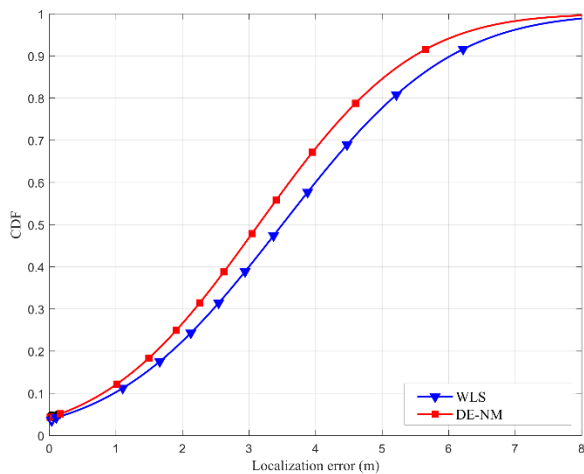


**Figure 5.** CDFs of the localization error of different localization algorithms for SNR = 20 dB.

The provided CDF diagram compares the localization error performance of the WLS method and the hybrid DE-NM method. The DE-NM method consistently exhibits higher CDF values than the WLS method across the error range, demonstrating that it achieves lower localization errors more frequently. Notably, at a localization error of approximately 2 meters, the DE-NM method achieves a CDF of around 0.4, surpassing the WLS method. This trend continues, with the DE-NM method maintaining a performance lead, especially at lower error thresholds. Overall, the CDF analysis underscores the superior accuracy and reliability of the hybrid DE-NM method in source localization tasks, confirming its robustness and effectiveness compared to the traditional WLS method.

In summary, the numerical simulations validate the effectiveness of the hybrid DE-NM method, showing significant improvements in localization accuracy over traditional methods under various noise conditions.

## 7. CONCLUSION

In this paper, a novel approach for source localization based on TDOA measurements has been proposed, utilizing a hybrid DE-NM method. The proposed method aims to improve the accuracy and reliability of source localization in real radio channel environments, addressing the inherent challenges posed by noisy measurements and complex optimization landscapes.

The hybrid DE-NM method combines the global search capability of the DE algorithm with the local refinement efficiency of the NM method. The DE algorithm is employed to explore the search space and identify promising regions. This phase ensures that the algorithm avoids local minima and covers a broad search area. Once the DE phase identifies a potentially optimal region, the NM method takes over to fine-tune the solution.

Our simulation results demonstrate the effectiveness of the proposed hybrid DE-NM method compared to traditional localization methods such as WLS. The DE-NM method consistently achieved lower RMSE values across various SNR levels, approaching the theoretical CRLB. This indicates that the DE-NM method not only outperforms the WLS method but also closely approaches the optimal performance achievable for unbiased estimators.

The CDF analysis further supports these findings, showing that the DE-NM method achieves higher cumulative probabilities for lower localization errors. This implies that the DE-NM method is more likely to achieve precise localization, making it a robust and reliable choice for practical applications requiring high accuracy.

In conclusion, the proposed hybrid DE-NM method offers a significant improvement over conventional localization techniques. Its superior accuracy, robustness, and efficiency make it well-suited for real-world applications where precise source localization is crucial. Future work may focus on further enhancing the algorithm's efficiency, exploring adaptive strategies for parameter tuning, and extending the approach to other types of localization problems.

## Aknowlegment

The research of M. Rosić was supported by the Serbian Ministry of Education and Science under Grant TR35029. The research of M. Sedak was supported by the Serbian Ministry of Education and Science under Grant No. TR35006.

## References

- [1] K. Lui, J. Zheng, and H. So, "Particle swarm optimization for time-difference-of-arrival based localization," in *Proc. 2007 15th European Signal Processing Conference*, 2007, pp. 414-417. doi: 10.5281/ZENODO.40289.

- [2] B. Xu, G. Sun, R. Yu, and Z. Yang, "High-Accuracy TDOA-Based Localization without Time Synchronization," *IEEE Trans. Parallel Distrib. Syst.*, vol. 24, pp. 1567-1576, 2013. doi: 10.1109/TPDS.2012.248.
- [3] Z.-F. Han, C. Leung, H. So, and A. Constantinides, "Augmented Lagrange Programming Neural Network for Localization Using Time-Difference-of-Arrival Measurements," *IEEE Trans. Neural Netw. Learn. Syst.*, vol. 29, pp. 3879-3884, 2018. doi: 10.1109/TNNLS.2017.2731325.
- [4] B. Huang, L. Xie, and Z. Yang, "TDOA-Based Source Localization With Distance-Dependent Noises," *IEEE Trans. Wireless Commun.*, vol. 14, pp. 468-480, 2015. doi: 10.1109/TWC.2014.2351798.
- [5] R. Storn and K. Price, "Differential Evolution – A Simple and Efficient Heuristic for Global Optimization over Continuous Spaces," *J. Glob. Optim.*, vol. 11, no. 4, pp. 341-359, 1997. doi: 10.1023/A:1008202821328.
- [6] J. A. Nelder and R. Mead, "A Simplex Method for Function Minimization," *Comput. J.*, vol. 7, no. 4, pp. 308-313, 1965. doi: 10.1093/comjnl/7.4.308.
- [7] M. B. Rosić, M. Sedak, M. Simić, and P. Pejovic, "An Improved Chaos Driven Hybrid Differential Evolution and Butterfly Optimization Algorithm for Passive Target Localization Using TDOA Measurements," *Appl. Sci.*, vol. 13, 2023. doi: 10.3390/app13020684.



## SIMPLE ENERGY DETECTOR FOR TWO-STAGE CLASSIFICATION FOR ANTIDRONE SYSTEMS

SNEŽANA ZUROVAC

Military Technical Institute, Belgrade, [zurovac@medianis.net](mailto:zurovac@medianis.net)

NIKOLA PETROVIĆ

Military Technical Institute, Belgrade, [npetrovicbrg@gmail.com](mailto:npetrovicbrg@gmail.com)

VASILIJAJOKSIMOVIĆ

Military Technical Institute, Belgrade, [vasilija.joksimovic@mod.gov.rs](mailto:vasilija.joksimovic@mod.gov.rs)

IVAN POKRAJAC

Military Technical Institute, Belgrade, [ivan.pokrajac@vs.rs](mailto:ivan.pokrajac@vs.rs)

DARKO MIKANOVIĆ

Military Technical Institute, Belgrade, [darko.mikanovic7@gmail.com](mailto:darko.mikanovic7@gmail.com)

BOBAN SAZDIĆ-JOTIĆ

Military Technical Institute, Belgrade, [boban.sazdic.jotic@vs.rs](mailto:boban.sazdic.jotic@vs.rs)

**Abstract:** Signal detection theory, a fundamental concept in various scientific disciplines, involves mandatory measuring of the signal features. This theory finds applications in telecommunications, radar technology, medical devices, automation and process control, geophysical research, biometric systems, and security systems, emphasizing its broad significance. Likewise, drone detection in the radio-frequency domain is necessary for signal detection and ensures efficient and reliable communication, surveillance, and security. The recent conflict between Russia and Ukraine has underscored the crucial role of drones in modern warfare. Our research can improve the detection of any malicious drones that pose a threat, thereby underlining the significance of the proposed methodology in modern electronic warfare. This is a specialized approach to drone signal detection based on two-stage classification with two key components: a method based on spectrogram energy detection and deep learning classification. Energy detection on the spectrograms is particularly effective when the signal's energy characteristics differ significantly from the surrounding noise. The practical applicability of our proposed method was evaluated using the publicly available VTI\_DroneSET dataset, which contains a diverse range of signals from three types of drones. Furthermore, we conducted tests with the VTI\_DroneUSRP dataset and signals from the NI-USRP-2954 receiver, demonstrating the effectiveness and practicality of the proposed method in real situations. The successful detection and identification of Wi-Fi, Bluetooth, and drone signals in both ISM frequency bands were performed, proving the method's reliability. The proposed approach improved execution times and energy savings, indicating that applying the energy detector on the spectrograms in a two-stage classification significantly enhances the performance of ADRO applications for real-time drone detection. Furthermore, we conducted a comparative analysis of different deep learning algorithms at the outset of two-stage classification, which is a potential basis for adopting this approach.

**Keywords:** artificial intelligence, deep learning, detection, drone, energy detector, receiver.

### 1. INTRODUCTION

Drones have emerged as a significant threat in contemporary military operations. Their small size, speed, and agility enable them to execute various combat maneuvers and cause substantial damage. Consequently, military entities heavily invest in developing effective antidrone (ADRO) systems and measures. The first step in any ADRO system involves a procedure that aims to detect all drones in the area of interest. The next step is the identification of detected drones, with the main task of separating malicious drones. Modern ADRO systems

might have a direction-finding or radar device to localize detected drones, which can help further analysis. These steps are essential to electronic warfare (EW) and are particularly challenging because they are realized in the complex and demanding battlefield domain.

Operating in an environment saturated with multiple signals from different users of the electromagnetic spectrum, an ADRO system faces a unique challenge in distinguishing between threats. It must effectively differentiate between commercial signals like Wi-Fi, Bluetooth, NFC, and LoRa and identify malicious drones amidst the noise of friendly ones. Distinguishing between different signals is crucial for ADRO systems that use

receivers as primary sensors. The goal is to detect signals quickly and with a high probability of accuracy, even if it means there might be some false alarms. One standard detection method is energy detection, also used in this paper. This method allows the ADRO system to quickly determine if a signal exists in the monitored frequency spectrum. By combining an energy detection method on spectrograms (EDS) with more advanced deep learning-based detectors, exceptional results can be achieved. Furthermore, using two-stage classifiers is also possible, as it can help reduce resources and speed up the detection and identification process. Considering the information provided, this research paper explores the potential of using the EDS method and deep learning (DL) algorithms to enable an ADRO system to detect and identify drones promptly.

This paper is structured as follows: Section 2 provides an overview of the literature on drone classification. Sections 3 and 4 present the methodology and discuss our experimental results, and the study conclusion is given in the last section.

## 2. LITERATURE REVIEW

According to existing studies, various classification techniques utilizing radio-frequency sensing systems are employed to achieve a common objective: identifying and accurately characterizing potential threats. As discussed in the Introduction section, enhancing input data accuracy can be achieved by applying multiple sensing modalities related to energy detection. Research in energy detection is predominantly associated with cognitive radio performance, explicitly focusing on estimating unused spectrum. In [1] and [2], the authors explore methods for identifying unused spectrum in the presence of signals from primary users, intending to perform spectrum reallocation without introducing harmful interference to existing users. This paper employs a similar methodology but with an inverted approach. In the detection process, spectrum sensing can be seen as a binary hypothetical testing problem with hypotheses  $H_0$  and  $H_1$  defined as nonexistent and existent signals of interest, which in binary form represents a state with no threat and a state with threat. In [3] the authors address the false alarm occurrence in the signal determination process. In this paper, the authors propose a preprocessing for detection to prescreen the false alarms by investigating the energy of the received signal. Whereas the conventional solutions to mitigate false alarms are in-decoder schemes, energy-based detection can be performed before the decoding trial. The false alarms described in the energy detection and classification process originate from ambient noise, including Bluetooth and Wi-Fi signals, and additional interference sources operating in the observed frequency ranges. Several approaches to extracting ambient noise have been applied in different studies. In [4] author proposed a solution for detecting and classifying radio-frequency signals from different UAV controllers in the presence of Bluetooth and Wi-Fi interference by developing multistage models supported by the a priori knowledge of Bluetooth and Wi-Fi signal specification that is well standardized. The first step in deciding

whether the detected signal is Wi-fi interference is performing bandwidth analysis. In [4], [5] are given detailed specifications on Bluetooth and Wi-Fi features. Following the bandwidth analysis, if a conclusive decision cannot be reached, the model proceeds to additional analysis, including modulation comparison and a detailed signal decomposition to identify the signal source accurately. Subsequent processing involves digital forensics analysis using a dataset of radio-frequency fingerprints for various drone types. Aside from selecting appropriate techniques, the primary challenge in classification processes is the limited access to drone signal datasets. In [6], the author reviews the existing literature on drone classification within the radio-frequency spectrum, focusing specifically on detection and identification. This review examines passive radio-frequency sensors, classification techniques, and datasets, shedding light on the associated challenges, presents a new categorization system, and comprehensively analyzes publicly available drone classification techniques. The results of this study demonstrate that DL algorithms are currently the most effective approach for addressing the challenge of drone classification within the radio-frequency domain. A major impediment is the need for a comprehensive, standardized framework for drone classification in this context, which should be tailored to end-user requirements. Additionally, findings from two ablative experiments underscore the importance of preprocessing raw I/Q radio signals as a critical step in the drone classification process. This paper applies machine learning and DL algorithms to input data obtained through energy detection and subsequent signal preprocessing.

## 3. METHODOLOGY

During our research, we followed a structured approach that involved multiple steps. Firstly, we accessed data from the datasets. Then, we utilized an EDS method and applied DL algorithms. For an in-depth understanding, refer to Figure 1, which provides a comprehensive overview of the methodology employed.

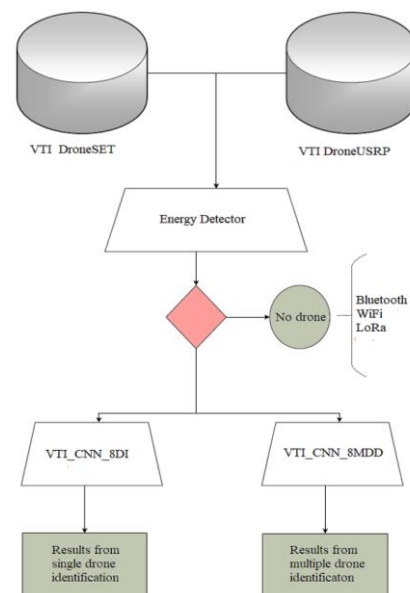
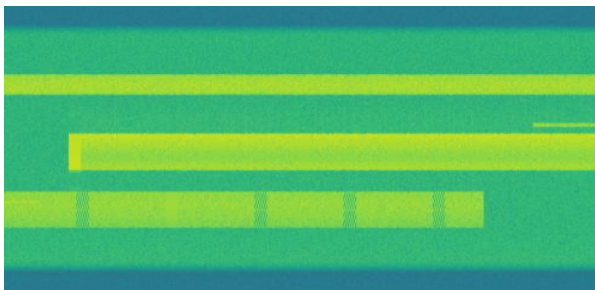


Figure 1. An overview of the methodology.

Figure 1 shows our research methodology, explaining the sequence of experiments realized with the EDS method and DL algorithms. Moreover, the input data consists of two datasets. The main idea of the EDS method is to reduce the number of spectrograms in the DL algorithms by jointly rejecting spectrograms with Wi-Fi and Bluetooth signals. Next, the methodology is presented by describing datasets, the EDS method, and DL algorithms.

### 3.1. Datasets

This research used two separate datasets: the VTI\_DroneSET introduced in [7] and VTI\_DroneUSRP. The VTI\_DroneSET is a radio-signal drone dataset created for research and development purposes for new ADRO systems. This dataset was verified through various research papers in [6], [8], [9], [10], [11], [12], [13] and will be used as a benchmark dataset. This dataset contains signals from drones and flight (operational) control. For the equipment under test (EUT), three different drones (DJI Phantom IV, DJI Mavic Zoom, and DJI Mavic 2 Enterprise) were used. Drones operated independently (one drone per experiment) and simultaneously (two and three per experiment). This dataset was obtained in laboratory conditions using Tektronix Real-Time Spectrum Analyzer, two receiving antennas (for two separate frequency bands) with corresponding cables and connectors. The Real-Time Spectrum Analyzer instantaneous records bandwidth of 110 MHz within 2.4 or 5.8 GHz ISM (Industrial, Scientific, and Medical) frequency bands and saves records directly in a \*.mat format suitable for loading and analyzing the MatLab application. Figure 2 shows the spectrogram of one example from the VTI\_DroneSET dataset.



**Figure 2.** The spectrogram of three drones operating simultaneously (source: VTI\_DroneSET dataset).

Figure 2 shows one example of a spectrogram of three drones operating simultaneously. It is essential to notice that the acquisition length of each signal was 450 ms, and the sampling frequency was 150 MSample/s for an instantaneous bandwidth of 110 MHz. All spectrograms were obtained using a short-time Fourier Transform (STFT) with 2048 frequency bins on zero mean (without DC component) segments of signals from the VTI\_DroneSET dataset. It is important to note that each recording from the dataset was segmented into 100,000 samples, identical to the time of acquisition of 0.67 ms.

The VTI\_DroneUSRP is a new dataset of frequency signals from drones and flight (operational) control recorded outdoors with the NI-USRP-2954 receiver [14]. The recording was made with 200 MHz bandwidth within the 433MHz, 880MHz, 2.4GHz, and 5.8GHz ISM

frequency bands. For the EUT, seven different drones (DJI Phantom IV, DJI Mavic 3T, DJI Mavic 2 Enterprise, DJI Mini 3, DJI Matrice 30T, DJI Matrice 300, and DJI Matrice 350RTK) were used. Drones operated independently (one drone per experiment) and simultaneously (up to four per experiment). The receiver has an FPGA module that processes the received signal with morphological operations to binarize the output and represent it in a spectrogram form with dimensions 2048x1000 pixels. The fast Fourier transformation length  $N=2048$  bins and the frame size  $F=1000$  are the output spectrograms' dimensions. This implies that the acquisition time is 10.24 ms for each spectrogram from the FPGA module. However, due to the necessary time for the signal processing, the FPGA module produces only four spectrograms per second. Figure 3 shows the spectrogram of one example from the VTI\_DroneUSRP dataset.

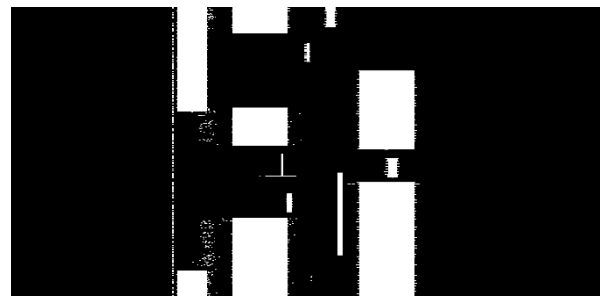


**Figure 3.** The spectrogram of three drones operating simultaneously (source: VTI\_DroneUSRP dataset).

Figure 3 shows one example of a spectrogram of three drones operating simultaneously. All spectrograms were obtained using a short-time Fourier Transform (STFT) with 2048 frequency bins on zero mean (without DC component) segments of signals from the FPGA module. It is important to note that Figure 2 represents the whole recording from the VTI\_DroneSET dataset (450 ms), while Figure 3 is a spectrogram of 1000 frames (10.24 ms). The spectrogram in Figure 3 is rotated 90 degrees for better user experience, waterfall effect, and visibility. Table 1 presents the summarized key dataset aspects for a better overall presentation.

**Table 1.** The dataset statistics.

Dataset name	VTI_DroneSET	VTI_DroneUSRP
Number of recordings	50	> 10,000
Length of recordings	450 ms	10.24 ms
Number of drones	3	7
Multiple drones	Yes (2 and 3)	Yes (2,3, and 4)
ISM bands	2.4/5.8	2.4/5.8
Environment	Laboratory	Outdoor
Type of data	Raw I/Q data	Spectrograms

### 3.2. Energy detection on spectrograms (EDS)

Energy detection strategies are primarily used for spectrum sensing. These strategies involve establishing a threshold based on the noise floor to differentiate and detect signals. Energy detection approaches are popular for spectrum sensing (detection of primary and secondary users of the radio frequency bands) because of their low computational complexity [15].

The proposed simple EDS method operates very simply. Its input data is an image generated by transforming the detected signal, a spectrogram from the receiver, into an array of numbers. Given numerical arrays are normalized to values within the range  $[0,1]$ . This step scales the image's pixel values to ensure consistency and comparability. After that, a binary array is created from the normalized array. The binary array is then summed up to calculate the signal's energy value. This sum represents the total number of pixels originally at maximum intensity in the image. The resulting sum provides the energy value of the detected signal, which can be used for further analysis or decision-making. The proposed EDS method was applied to the VTI\_DroneSET and the VTI\_DroneUSRP datasets to enhance the detection and identification. Another reason was to evaluate the resources (RAM, energy, and time) needed for the two-stage classification procedure. The maximum and minimum energy values of the signal of interest (drone signals) were obtained by applying the EDS method to the datasets. The main issue is correctly setting the threshold to separate signals of interest. The threshold is set empirically through measurements on both datasets for all samples of radio signals.

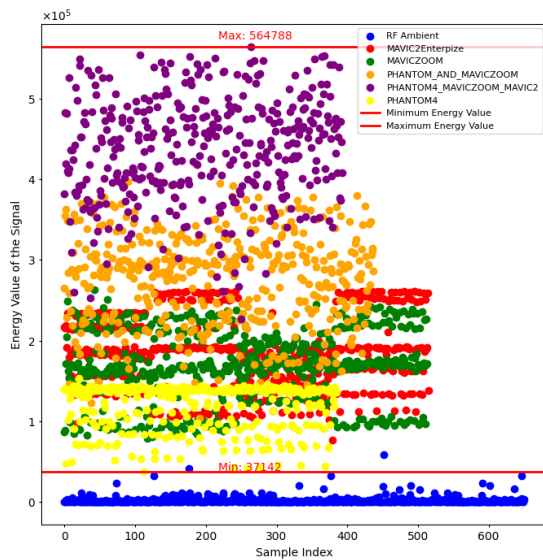


**Figure 4.** An example of a statistical analysis of the energy of the signals from VTI\_DroneSET.

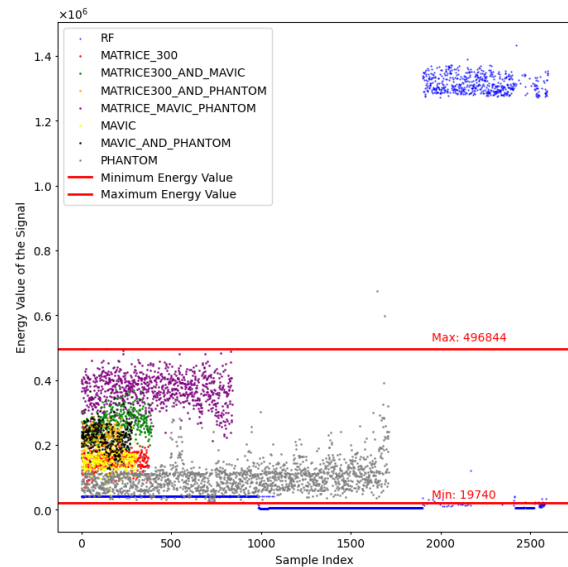


**Figure 5.** An example of a statistical analysis of the energy of the signals from VTI\_DroneUSRP.

Figures 4 and 5 show the results of applying the EDS method to the VTI\_DroneUSRP and the VTI\_DroneUSRP.

Figure 4 shows the results from the EDS method of the signals for seven distinct types of drones individually. The visualization of energy detection of spectrograms shown in Figure 4 provided a clear view that applying the EDS method makes it possible to separate the ambient noise from the signal of interest. In Figure 4, it can be seen that the energy value of the signal of interest ranges between 37,142 and 564,788. In Figure 5, it can be seen that the energy value of the signal of interest is between 19740 and 496,844. The EDS method was applied by setting the obtained threshold values. The EDS method first engages the signal spectrogram to determine its energy value. If the energy value falls within the predefined range of the signal of interest, the signal is sent to the model; otherwise, it is discarded.

It is essential to note that the proposed EDS method can effectively distinguish radio-frequency ambient (Bluetooth or Wi-Fi signals in the observed frequency ranges marked with blue color in Figures 4 and 5).

### 3.3. Deep learning models

The final stage involves engaging the two DL models to estimate the best practical implementation. However, both models consist of three convolutional blocks, fully connected layers, and a final softmax layer. The first three layers represent convolutional blocks with ReLU activation, batch normalization, and max pooling. These convolutional layers gradually increase the number of feature maps, starting with sixteen, thirty-two, and finally sixty-four output channels. After the final convolutional layer, the resulting feature maps are flattened and passed through three fully connected layers with ReLU activation and dropout regularization to reduce the likelihood of overfitting. The model concludes with a softmax layer providing either six or eight outputs, depending on the number of classes the network is designed to classify,



which is adapted to the specific cases of training data and the model's task.

The first DL model is the VTI\_CNN\_DI model trained for drone identification. This model is designed in one version with six output classes. The second model is the VTI\_CNN\_MDD model, which is trained to determine the number of drones and their identification. This model is designed in two versions, with six and eight output classes. The reason is that, within the VTI\_DroneSET dataset, there are at most six classes, so we must adopt this model to fit the presented problem. Both models were trained on both datasets for ten epochs using a batch size of thirty-two and the Adam optimizer. After the training, the DL models were used for inference to conduct experiments in real scenario applications.

#### 4. RESULTS

The objective of evaluating the impact of the EDS method and DL models is to minimize the time required to analyze incoming signals from the receiver and maximize the classification accuracy (identification of the type of drone) from the spectrogram. Additionally, the goal is to evaluate the usage of the proposed methodology on platforms where resources are limited. This adaptation was examined by measuring the energy consumption and average emission of CO<sub>2</sub>-equivalent (expressed in kg

emitted per kWh of electricity), which is a limiting factor in real-world applications.

The evaluation was conducted for two scenarios - using the EDS method with a threshold specific to the given dataset and without the EDS method - to demonstrate the effectiveness of this approach. Each model, combined with or without the EDS method, was assessed on two datasets with ambient samples (samples of radio-frequency ambient containing noise and Wi-Fi and Bluetooth). It is important to note that this is intentionally done because most received radio signals in real applications are from ambient). The samples of other classes are equally distributed, creating an unbiased problem. Table 2 presents duration, consumed energy, and average emissions to realize comprehensive analyses of the general performances of engaged two-stage classification.

Tables 3 to 5 show accuracies for both models with different scenarios in the inference process, using 782 spectrograms (the VTI\_DroneSET dataset) and 1140 spectrograms (the VTI\_DroneUSRP dataset). These results are used for a comparative analysis of accuracies for different classes.

**Table 2.** The overall performance of two-stage classifications during the inference process.

Model	EDS	Dataset	Number of spectrograms for prediction	Number of spectrograms for input in DL model	Average / Total execution time [s]	Execution time improvement [%]	Emissions of CO <sub>2</sub> -eq [kg]	Consumed energy [kWh]
VTI_CNN_6MDD 6 classes	No	VTI_DroneSET	782	/	0.017 / 13.02	65.8	0.0000077	0.00032
	Yes			624	0.007 / 4.45		0.0000007	0.00003
VTI_CNN_8DI 8 classes	No	VTI_DroneUSRP	1140	/	0.013 / 15.33	59.7	0.00014	0.00022
	Yes			828	0.007 / 6.18		0.00003	0.00005
VTI_CNN_8MDD 8 classes	No	VTI_DroneUSRP	1140	/	0.015 / 16.96	65.8	0.00017	0.00027
	Yes			855	0.007 / 5.79		0.00003	0.00005

**Table 3.** The accuracy [%] of two-stage classifications during inference for the eight classes from VTI\_DroneUSRP.

Model	EDS	Dataset	Ambient	One drone			Two drones			Three drones	Total
				Matrice 300	Mavic 2Ent	Phantom 4	Matrice 300 Mavic 2Ent	Matrice 300 Phantom 4	Mavic 2Ent Phantom 4	Matrice 300 Mavic 2Ent Phantom 4	
VTI_CNN_8MDD 8 classes	No	VTI_DroneUSRP	100	80	95	100	95	100	85	100	99.21
	Yes		100	80	95	100	95	100	85	100	99.21

**Table 4.** The accuracy [%] of two-stage classifications during inference for the eight classes from VTI\_DroneUSRP.

Model	EDS	Dataset	Ambient	One drone						Total	
				Matrice 30T	Matrice 350 RTK	Mavic 3T	Mini 3pro	Phantom 4	Matrice 300		Mavic 2Ent
VTI_CNN_8DI 8 classes	No	VTI_DroneUSRP	97	100	90	100	100	100	100	100	97.19
	Yes		97.5	100	90	100	100	100	100	100	97.63

**Table 5.** The accuracy [%] of two-stage classifications during inference for the eight classes from VTI\_DroneUSRP.

Model	EDS	Dataset	Ambient	One drone			Two drones		Three drones	Total
				Mavic 2Ent	Mavic Zoom	Phantom 4	Matrice 300 Mavic 2Ent	Matrice 300 Mavic 2Ent Phantom 4		
VTI_CNN_6MDD 6 classes	No	VTI_DroneSET	99.7	100	100	100	100	100	99.74	
	Yes		100	100	100	100	100	100	100	

Applying both models with and without the EDS method demonstrates the effect of energy detection. As previously mentioned, a much larger number of spectrograms obtained from receivers lack significant information. The EDS method effectively filters out many such spectrograms, thereby reducing the load on the DL model. In this case, the time required to process all incoming signals is significantly reduced - from 15 seconds for all inference data to 6 seconds, representing a 60% acceleration, while 73% of the total input data, i.e., 83% of the radio-frequency ambience, was discarded. In addition to reducing the time crucial for real-time drone detection, this approach significantly reduces carbon dioxide emissions into the atmosphere. The energy consumption is also substantially reduced, making this system applicable in real-scenario applications with limited power sources. If the proposed two-stage classification is used continuously for 24 hours, energy consumption without the EDS method, where four signal spectrograms are generated per second, amounting to 0.0667 kWh, while with the EDS method, it is 0.0152 kWh, which represents a significant saving. It is essential to note that this component is part of a more complex system, and every energy saving is necessary.

It is also important to note that the VTI\_CNN\_MDD model with the VTI\_DroneSET dataset has the best accuracy due to the quality of the drone signals when more drones are present in the image, making them more distinguishable by the EDS method. The VTI\_DroneSET dataset contains laboratory samples of drone signals, so a higher efficiency of this approach is expected compared to real-scenario applications for the other cases.

After the EDS method stage, spectrograms enter the DL model, which predicts the drone type and number. The EDS method indicates that the drone signal is possibly present in the spectrogram, while the model predicts classes. The model efficiently recognizes distinct types of drones in the images and provides information about the presence, number, and type of drones captured by the receiver in both time and space. All models deliver near state-of-the-art results, with the model being slightly more sensitive to specific drone types due to the lack of high-quality training data, as evidenced by the laboratory example of the VTI\_CNN\_MDD model with the VTI\_DroneSET dataset, where an accuracy of 100% was achieved in two-stage classification.

## 5. CONCLUSION

This study demonstrates the usefulness of the EDS method in aiding the DL models in improving their predictions. This approach minimizes resource consumption in terms of time and energy by reducing harmful gas emissions and enabling efficient drone detection based on recorded signals from the datasets. The proposed DL models were evaluated by applying two datasets (VTI\_DroneSET and VTI\_DroneUSRP) with and without the EDS method. The obtained results indicate a significant reduction in the execution time when the EDS method is engaged in the two-stage classification process - specifically, 65,8% for the VTI\_CNN\_MDD model and 59,7% for the VTI\_CNN\_DI model. By reducing the number of input spectrograms obtained from the USRP receiver for the proposed DL models, energy consumption and CO<sub>2</sub>-eq emissions have decreased. These execution times and energy savings suggest that applying the EDS method in a proposed two-stage classification effectively optimizes the performance of ADRO applications in real-time drone detection, where speed and accuracy of detection are of great importance. Further research should focus on expanding the VTI\_DroneUSRP dataset by collecting new data and improving the scope of two-stage or multistage classification.

## Acknowledgements

This work was by Serbian Ministry of Defense and Serbian Ministry of Education, Science and Technological Development, Grant No 451-03-66/2024-03/200325.

## References

- [1] J. Luo, G. Zhang, and C. Yan, "An Energy Detection-Based Spectrum-Sensing Method for Cognitive Radio," *Wirel Commun Mob Comput*, vol. 2022, no. 1, p. 3933336, Jan. 2022, doi: 10.1155/2022/3933336.
- [2] A. Nasrallah, A. Hamza, G. Baudoin, B. Toufik, and A. M. Zoubir, "Simple improved mean Energy Detection in spectrum sensing for cognitive radio," in *2017 5th International Conference on Electrical Engineering - Boumerdes, ICEE-B 2017*, Institute of Electrical and Electronics Engineers Inc., Dec. 2017, pp. 1–4. doi: 10.1109/ICEE-B.2017.8192177.
- [3] H. Ju, E. Cho, and S. H. Kim, "Energy-Detection based False Alarm Reduction in Polar-Coded Uplink Control Channel Transmission in 5G-NR," in *IEEE Vehicular Technology Conference*, Institute of Electrical and Electronics Engineers Inc., Apr. 2021. doi: 10.1109/VTC2021-Spring51267.2021.9448973.

- [4] M. Ezuma, F. Erden, C. K. Anjinappa, O. Ozdemir, and I. Guvenc, "Detection and classification of UAVs using RF Fingerprints in the Presence of Wi-Fi and bluetooth interference," *IEEE Open Journal of the Communications Society*, vol. 1, pp. 60–76, 2020, doi: 10.1109/OJCOMS.2019.2955889.
- [5] L. Ophir, Y. Bitran, and I. Sherman, "WI-FI (IEEE802.11) and bluetooth coexistence: Issues and solutions," in *IEEE International Symposium on Personal, Indoor and Mobile Radio Communications, PIMRC*, 2004, pp. 847–852. doi: 10.1109/pimrc.2004.1373819.
- [6] B. Sazdić-Jotić, I. Pokrajac, J. Bajčetić, and N. Stefanović, "Review of RF-based drone classification: Techniques, datasets, and challenges," *Vojnotehnicki glasnik*, vol. 72, no. 2, pp. 764–789, Apr. 2024, doi: 10.5937/vojtehg72-49286.
- [7] B. M. Sazdić-Jotić *et al.*, "VTI\_DroneSET," Mendeley Data. Accessed: Nov. 01, 2020. [Online]. Available: <https://data.mendeley.com/datasets/s6tggnp5n2/1>
- [8] T. Šević, V. Joksimović, I. Pokrajac, B. Radiana, B. Sazdić-Jotić, and D. Obradović, "Interception and detection of drones using RF-based dataset of drones," *Scientific Technical Review*, vol. 70, no. 2, pp. 29–34, 2020, doi: 10.5937/str2002029S.
- [9] M. Mokhtari, J. Bajčetić, B. Sazdić-Jotić, and B. Pavlović, "RF-based drone detection and classification system using convolutional neural network," in *29th Telecommunications Forum (TELFOR)*, IEEE, 2021, pp. 1–4. doi: 10.1109/TELFOR52709.2021.9653332.
- [10] B. Sazdić-Jotić, I. Pokrajac, J. Bajčetić, B. Bondžulić, and D. Obradović, "Single and multiple drones detection and identification using RF based deep learning algorithm," *Expert Syst Appl*, vol. 187, Jan. 2022, doi: 10.1016/j.eswa.2021.115928.
- [11] Y. Xue *et al.*, "UAV signal recognition of heterogeneous integrated KNN based on genetic algorithm," *Telecommun Syst*, vol. 85, no. 4, pp. 591–599, Apr. 2024, doi: 10.1007/s11235-023-01099-x.
- [12] S. Dafrallah and M. Akhloufi, "Malicious UAV detection using various modalities," Jan. 01, 2024, *Canadian Science Publishing*. doi: 10.1139/dsa-2023-0049.
- [13] A. Famili, A. Stavrou, H. Wang, J. M. Park, and R. Gerdes, "Securing Your Airspace: Detection of Drones Trespassing Protected Areas," Apr. 01, 2024, *Multidisciplinary Digital Publishing Institute (MDPI)*. doi: 10.3390/s24072028.
- [14] . Ettus Research, "USRP Software Defined Radio (SDR)," Ettus Research. Accessed: Sep. 05, 2024. [Online]. Available: <https://www.ettus.com/>
- [15] . N. Ibadik, A. F. Ashari, D. D. Ariananda, and W. Dewanto, "Frequency Domain Energy Detection for Multiband Spectrum Sensing in Cognitive Radio System," in *ICITEE 2022 - Proceedings of the 14th International Conference on Information Technology and Electrical Engineering*, Institute of Electrical and Electronics Engineers Inc., 2022, pp. 7–12. doi: 10.1109/ICITEE56407.2022.9954120.



## CONTEMPORARY CRYPTOGRAPHY: RECENT ACHIEVEMENT AND RESEARCH PERSPECTIVES

BORIŠA JOVANOVIĆ

University of Defence Belgrade, Military Academy and  
Applied Mathematics and Electronics Centre, Belgrade, [borisa.jovanovic@vs.rs](mailto:borisa.jovanovic@vs.rs)

IVAN TOT

University of Defence Belgrade, Military Academy, [ivan.tot@va.mod.gov.rs](mailto:ivan.tot@va.mod.gov.rs)

SILVANA ILIĆ

Applied Mathematics and Electronics Centre, Belgrade, [silvana.ilic@vs.rs](mailto:silvana.ilic@vs.rs)

**Abstract:** In modern times, cryptography has been considered as a branch of both mathematics and computer science, and is tightly related to information security. With the accelerated progress of the Internet and the increase of digital communication, the need for stronger and more effective methods of cryptographic protection has become more pronounced. With the rapid increase in computing power, the potential for breaking cryptographic algorithms also increases. This fact in modern cryptography creates a need for stronger and more advanced cryptographic algorithms. One development direction of modern cryptography is post-quantum cryptography, which can withstand the attacks of quantum computers. In addition to the potential threats to traditional cryptographic techniques, there is also the potential to integrate artificial intelligence tools with the process of developing and implementing cryptographic algorithms. For instance, advanced machine learning algorithms can be used to identify potential vulnerabilities in cryptographic systems and algorithms and improve their security. As technology continues to evolve, new techniques are being developed in the field of cryptography in order to stay one step ahead of new threats. In this paper, the current achievements of modern cryptography are explored and the research perspectives in this field are explained.

**Keywords:** post-quantum cryptography, algorithms, homomorphic encryption, quantum-resistant encryption, lightweight cryptographic algorithms.

### 1. INTRODUCTION

Cryptography is a science that studies techniques for converting information into an unreadable format in order to protect confidential messages from unauthorized access[1]. The earliest known cryptographic techniques date back to ancient civilizations, where methods such as simple transposition and substitution ciphers were used to conceal messages and prevent unauthorized people from reading and understanding messages. These techniques evolved over time to include more complex ciphers, such as the Caesar and Vigenere ciphers, which were used during the Middle Ages. The development of the typewriter and the subsequent increase in literacy rates led to the need for more secure encryption techniques, leading to the development of more complex ciphers such as the Playfair Cipher and Enigma.

Symmetric cryptographic algorithms are one of the oldest and most widely used types of encryption. Their work is based on the concept of using the same key to encrypt and decrypt a message. The history of symmetric cryptographic algorithms dates back to ancient times, where simple substitution ciphers were used to encrypt messages. Over time, more complex algorithms such as

the Hill cipher and the Data Encryption Standard (DES) were developed. The development of the Advanced Encryption Standard (AES) at the end of the twentieth century marked a significant improvement in the field of symmetric cryptographic algorithms as it provided stronger encryption and faster processing times.

An important component of modern cryptography are hash functions. A hash function is a mathematical function that takes an input (or message) and produces an output (or hash, or message fingerprint) of a fixed length [2]. Hash functions are primarily used to ensure data integrity because any change to the content of the original message will result in a different hash value.

Closely related to the application of the hash function is the digital signature technology. The goal of applying a digital signature is to provide a reliable method for user authentication and to ensure non-repudiation in digital communications. Digital signature technology is a mathematical scheme for demonstrating the authenticity of a digital message or electronic document. The development of digital signature technology dates back to the early 1980s, when the concept of asymmetric cryptographic algorithms was first introduced. Recently, various algorithms such as Digital Signature Algorithm (DSA) and Elliptic Curve Digital Signature Algorithm

(ECDSA) have been developed [3].

Major historical events and technological advances have driven the evolution of cryptographic algorithms. The emergence of the Internet and its development has resulted in an increase in digital communication, which further causes an increased need for strong, reliable and more efficient cryptographic algorithms. With the ever-increasing computing power, the potential for cracking encryption algorithms is ever-increasing. This has led to the need for stronger and more advanced cryptographic algorithms, such as post-quantum cryptography, that can withstand quantum computer attacks.

In addition to the potential threats to the security of cryptographic algorithms, there is also the potential for integrating artificial intelligence tools into the design and evaluation processes of cryptographic algorithms. For example, machine learning algorithms can be used to identify potential vulnerabilities in the design of a cryptographic algorithm and thus to define procedures for improving their security.

As digital communications continue to rapidly evolve, the importance of maintaining superiority in the application of cryptographic techniques cannot be overstated. This paper explores the future of cryptography, including developments in post-quantum cryptography, blockchain based cryptography, modern lightweight cryptographic algorithms, and other emerging technologies. The future of cryptography holds great promise as researchers work to develop new homomorphic and quantum-resistant encryption techniques, new methods for securing block chain technology, new generations of lightweight cryptographic algorithms, and modern multiparty computing systems.

The main contribution of this paper is its aspiration to help in understanding the basic principles and postulates of modern cryptography. If we properly understand the principles and applications of modern cryptography, we will be better able to preserve the privacy and security of our communications and to protect our digital assets.

## 2. MODERN CRYPTOGRAPHY – DIRECTIONS OF DEVELOPMENT

Modern cryptography develops in the environment of the comprehensive use of quantum computers and the increasing need to make the content of communication inaccessible to uninvited participants. This is where cryptography comes into play: it is a key tool for building quality solutions for cyber security. To that end, cryptographic algorithms are used in a large number of applications that surround us; examples range from social networks, smartphones and cloud servers to embedded systems such as medical implants, car keys and passports. New advanced technology systems such as autonomous cars and electronic voting will rely even more heavily on strong security mechanisms. Moreover, the number of applications for cryptography have increased dramatically, as new cryptographic techniques are invented and proven secure. For example, securely transacting with cryptocurrencies such as bitcoin requires

modern cryptography. As another example, hospitals may now share information about patients in a way that protects patient privacy while allowing the hospitals to apply statistical methods assessing the effectiveness of new treatments on the aggregate of the patients [4].

Such an environment influences the further development of cryptography, so the future of cryptography can be easily guessed. The most important research directions in modern cryptography are: research and development of new homomorphic and quantum-resistant encryption techniques; research and development of new methods for securing block chain technology; research and development of new generations of lightweight cryptographic algorithms and research and development of modern multiparty computer systems. In the following text of this paper, each of the mentioned directions of development of modern cryptography will be analyzed and explained in more detail.

### 2.1. Homomorphic encryption

Homomorphic encryption is a type of encryption that allows computation to be performed on ciphertext, meaning that data can be encrypted and manipulated without having to be decrypted first[5]. In other words, it allows performing various types of calculations on the data without revealing the data itself. This is a significant advance in modern cryptography as it enables secure computation and analysis over large data sets without compromising their confidentiality[6]. Homomorphic encryption technologies have numerous applications in a wide variety of fields such as healthcare, finance, and cloud computing[7]. For example, homomorphic encryption can be used to perform secure data analysis on sensitive data, such as medical records, without the need to disclose the data to unauthorized parties. It can also be used in cloud computing to protect data privacy while enabling secure cloud computing[8].

It is relatively easy to construct partially homomorphic encryption schemes, which are constructions that allow one mathematical operation to be performed on the ciphertext, typically multiplication or addition. Unfortunately, one mathematical operation is not sufficient for the majority of practical applications. For a long time finding a fully homomorphic encryption scheme that allows arbitrary operations was considered the holy grail of cryptography. The first such scheme was proposed by in [9] in 2009, which is based on lattices. This original system was quite impractical but since then numerous improvements have taken place. At the time of writing this paper, many competing schemes exist and use in practice is within reach[4].

In military applications, the homomorphic encryption technique can enable secure data processing in the cloud or other untrusted environments, preserving data confidentiality.

### 2.2. Quantum-resistant cryptography

The term post-quantum cryptography was coined to describe modern types of cryptosystems that are assumed

to be able to withstand attacks using large-scale quantum computers. Shor's algorithm[10] showed that cryptographic algorithms that are based on the hardness of factoring the product of two primes, or that are based on the hardness of computing discrete logarithms, are vulnerable to polynomial-time attacks using quantum computation. If and when quantum computers become available, cryptographic methods such as RSA or elliptic-curve cryptosystems will become vulnerable. While this seems to be a problem to be solved in the future, we already need to equip today's applications with cryptography that is resistant to quantum computer attacks in order to defend against "store now, decrypt later" adversaries[4].

In traditional cryptography (cryptography before the advent of quantum computers), the security of cryptographic systems relies on the complexity of mathematical algorithms, while in post-quantum cryptography, security relies on the laws of physics. Specifically, quantum cryptography uses the principle of quantum entanglement, which is based on the correlation of quantum states between two particles.

Today, post-quantum cryptography is an active field of research and several schemes have already been standardized. The National Institute of Standards and Technology has selected standardized, quantum-resistant digital signature algorithms including Crystals-Dilithium, Falcon, and Sphincs+. Also, the National Institute of Standards and Technology has chosen lattice-based KIBER as the key encapsulation mechanism for key establishment based on the encryption scheme. It was chosen as a result of a trade-off between assumed security and efficiency over conventional public-key schemes.

International standardization bodies have already compiled the first portfolio of standardized quantum-secure schemes for key encapsulation and digital signatures, which is currently still being expanded. In fact, with a large variety of standardized post-quantum cryptography schemes we will be ready to provide confidentiality and authentication services even in the era of powerful quantum computers[4].

From the available literature, it can be seen that quantum computing leads to both opportunities and risks for military communication systems. Quantum technologies such as post-quantum cryptography offer advanced methods for protecting military communications from potential quantum attacks. However, the same quantum capabilities can also be used to break traditional cryptographic methods, meaning that there is an urgent need for advances in quantum-resistant cryptographic solutions.

### 2.3. Block chain cryptography

Blockchain-based cryptography is a critical component of blockchain technology, which is widely used in various fields such as healthcare, finance, and supply chain management. It is a distributed ledger that records transactions in a secure and transparent manner. Cryptography is used in the blockchain to ensure the confidentiality, integrity and authenticity of the data stored in the blockchain network[11].

One of the basic cryptographic techniques used in blockchain is digital signature. A digital signature is a mathematical scheme that confirms the authenticity and integrity of a message or data. Digital signatures are used to verify transactions in the blockchain network, ensuring that the sender is the actual owner of the funds and preventing any unauthorized use of the data. Another critical cryptographic technique used in blockchain is cryptographic compression functions, better known as hash functions. Hash functions are used to create a unique digital fingerprint of the data stored in the blockchain network. This unique digital fingerprint, also known as a hash value, ensures that the data is protected from unauthorized access and cannot be changed without detection[11].

Blockchain-based cryptography plays a vital role in ensuring the security and transparency of data stored in the blockchain network. As blockchain technology continues to evolve, we can expect to see new cryptographic techniques and algorithms that will further enhance the security and efficiency of blockchain-based applications[12].

The development of blockchain technology brings with it increased data confidentiality and improved data availability that can help shape future military logistics and planning. Also, their development will make military communications more secure. In the long term, the application of blockchain technologies in the military will be a revolution if implemented well and many more military applications are found, in addition to being used wisely and affordably.

### 2.4. Lightweight cryptographic algorithm

Lightweight cryptography refers to a subset of cryptographic algorithms specifically designed to work efficiently on low-resource devices such as smart cards, RFID tags, and wireless sensor nodes. These devices often have limited processing power, memory and energy resources, making it a challenge to implement traditional cryptographic algorithms on them. Lightweight cryptography aims to address these challenges by developing cryptographic algorithms that have low computational and memory requirements while still providing a reasonable level of security.

The development of lightweight cryptography has become increasingly important with the proliferation of the Internet of Things (IoT) and other low-power, low-cost devices. These devices are becoming more and more present in our daily lives, and many of them require secure communication and authentication. Lightweight cryptography can provide a practical and effective solution for securing these devices, without sacrificing security. Some examples of lightweight cryptography algorithms include the SIMON and SPECK block ciphers, designed by the National Security Agency (NSA) for use in restricted environments. Another example is a lightweight version of the Advanced Encryption Standard (AES), known as AES-Lite. These algorithms have been adopted by various standardization bodies and are widely used in the industry to provide low-resource devices[13].

Embeddable cryptographic processors used for crypto modernization enable a range of new military communications applications, such as smartphones and rugged tablet computers for tactical use on the front lines, as well as secure tactical Wi-Fi, unmanned vehicle control and real-time targeting . Almost everyone has a feeling that embedded computing technology is constantly getting more powerful and efficient, while getting smaller and lighter. However, the need to preserve the power source while at the same time achieving satisfactory security of transmitted data opens the door to the application of light cryptographic algorithms in military communications.

### 2.5. Multiparty computation

Multiparty computation is a cryptographic technique that allows a group of parties to jointly compute a function on their private inputs, without revealing those inputs to each other or any third party. This technique allows parties to collaborate and calculate a result without sharing their individual data, which can be particularly useful in scenarios where data privacy is critical, such as financial transactions or medical research[14].

In multiparty computation, several parties provide input values and together compute a function from the input. Interestingly, when the protocol is completed, participants only know their input and response, but nothing about the input of other participants[15]. A standard example is a situation where three people want to know the highest salary in the group without revealing their individual salaries. Another application is determining the outcome of an election, i.e. electronic voting, or the highest bid at an auction based on encrypted data. Related to multiparty computation is secret sharing. The idea of (general) secret sharing is that out of  $n$  participants  $t$  must collaborate to compute a secret, e.g., a cryptographic key. A real-world scenario is that at least 2 out of 3 managers of a bank must get together to generate the secret code for opening a safe[4].

One possible application of the mentioned technologies in military communication systems is that, for example, to make a strategic decision in a specific situation, at least 5 out of 8 military decision-makers must gather to generate a secret code that is used to initiate special procedures.

## 3. CONCLUSION

Cryptography is a critical aspect of modern information security. It has evolved significantly over time, from basic substitution ciphers to sophisticated algorithms that ensure secure communication and transactions. Today, we have various types of cryptographic schemes, including symmetric and asymmetric encryption, hash functions, digital signatures, homomorphic encryption, post-quantum cryptographic algorithm, lightweight cryptography and multiparty computation. The development of lightweight cryptography has also enabled secure communication and transactions on low-power devices such as IoT devices. As technology continues to advance, the field of cryptography will play an increasingly important role in ensuring secure communication and transactions in an interconnected world. The future of cryptography is exciting and promising, and we can expect to see more innovations that will improve the security and privacy of military communication systems.

## References

- [1] BRUCE,S.: *Applied cryptography: protocols, algorithms, and source code in C. 2nd ed.* Hoboken, New Jersey: John Wiley & Sons; 1996
- [2] SOBTI,R., GEETHA,G.: *Cryptographic hash functions: A review.* International Journal of Computer Science Issues (IJCSI). 2012;9:461
- [3] MENEZES,A.J., VAN OORSCHOT,P.C., VANSTONE,S.A.: *Handbook of applied cryptography (202101 ed.)*. 2021;1:1-810
- [4] CRISTOF,P., JAN,P., TIM,G.: *Understanding cryptography From established symmetric and asymmetric ciphers to post-quantum cryptography*, Second Edition, Springer-Verlag GmbH DE, 2024
- [5] LAUTER,K.E., DAI,W., LAINE,K.: *Protecting privacy through homomorphic encryption*. Cham, Switzerland: Springer 2022
- [6] DOAN,T.V.T., MESSAI,M-L., GAVIN,G., DARMONT,J.: *A survey on implementations of homomorphic encryption schemes*. The Journal of Supercomputing. 2023 vol. 79 p. 15098-15139
- [7] CHATTERJEE,A., AUNG,K.M.M.: *Fully homomorphic encryption in real world applications*. Singapore: Springer; 2019
- [8] VIAND,A., KNABENHANS,C., HITHNAWI,A.: *Verifiable fully homomorphic encryption*. arXiv Preprint arXiv:2301.07041. 2023
- [9] CRAIG,G.: *Fully homomorphic encryption using ideal lattices*. In In Proc. STOC, pages 169–178, 2009
- [10] SHOR,W.P.: *Polynomial-time algorithms for prime factorization and discrete logarithms on a quantum computer*. SIAM Journal on Computing, 26(5):1484–1509, 1997.
- [11] BOLFIN,G.A.: *Cryptographic Primitives in Blockchain Technology: A Mathematical Introduction*. New York, USA: Oxford University

Press; 2020

- [12] ZHENG,Z., XIE,S., DAI,H., CHEN,X., WANG,H.: *An Overview of Blockchain Technology: Architecture, Consensus, and Future Trends*, 2017 IEEE International Congress on Big Data (BigData Congress), Honolulu, HI, USA, 2017, pp. 557-564,
- [13] DUTTA,I.K., GHOSH,B., BAYOUMI,M.: *Lightweight Cryptography for Internet of Insecure Things: A Survey*, 2019 IEEE 9th Annual Computing and Communication Workshop and Conference (CCWC), Las Vegas, NV, USA, 2019, pp. 0475-048
- [14] GOLDREICH,O.: *Secure multi-party computation. Manuscript. Preliminary version*. 1998 78 pages 1-78
- [15] RONALD,C., IVAN,D.: *Multiparty Computation, an Introduction*, Birkhauser Basel, Basel, 2005. pages 41-87





## AN EXAMPLE OF VHF RADAR SIGNAL PROCESSING

DARKO PIJEVIĆ

Military Technical Institute, Belgrade, [darko.pijevic@gmail.com](mailto:darko.pijevic@gmail.com)

ALEKSANDAR RISTIĆ

Military Technical Institute, Belgrade, [ristic1504@gmail.com](mailto:ristic1504@gmail.com)

DRAGAN NIKOLIĆ

Military Technical Institute, Belgrade, [dragan.a.nikolic@mod.gov.rs](mailto:dragan.a.nikolic@mod.gov.rs)

DEJAN IVKOVIĆ

Military Technical Institute, Belgrade, [divkovic555@gmail.com](mailto:divkovic555@gmail.com)

ZVONKO RADOSAVLJEVIĆ

Military Technical Institute, Belgrade, [zvonko.radosavljevic@gmail.com](mailto:zvonko.radosavljevic@gmail.com)

**Abstract:** Track While Scan (TWS) radars are generally used in defense systems, which supervise the positions of the target and generate the measurements, scan by scan. They measure a target's coordinates, determine its trajectory, and predict its next location. The selection and adaptation of the technical requirements of the optimal hardware for processing and displaying the radar image is related to several serious challenges, such as the availability and price of components on the market, the type of modulation, frequency agility, shielding from interference, computational complexity of processing, type and technology of the antenna system. In the paper, a complete example of coherent hardware processing (reception and transmission) of signals for VHF band radar is proposed. The proposed hardware generates trigger signals, modulates the transmit signal, transmits via a semiconductor HPA transmitter and then at the reception receives signals in the analog domain, converts them, processes them and displays the radar image on the monitor. The numerical experiments have shown the possibility of signal processing in real time on the selected platform showed the justification of the application.

**Keywords:** digital signal processing, doppler radar FPGA platform.

### 1. INTRODUCTION

Very High Frequency (VHF) radar techniques are easy to employ and commonly used in defense applications. Fast algorithms and powerful processors facilitate the development of several kinds of low power radars, but the reduction of the transmitted power has to be compensated by on-line processing of an encoded signal to maintain a favorable signal-to-noise ratio suitable for detection. Moreover, radars have to reconstruct return echoes with different travel times due to various origins (multi-path, adjacent objects, etc.) [1]. Such needs can be accomplished by means of signal phase coding and one of the most attractive is the reversal phase code. The composite echo signal must be processed to extract the physical information useful for the measurement considered. In this paper some algorithms used for on-line processing of phase-coded signals will be described, both in time and frequency domain. The trend in VHF radars is to simplify the system hardware, reduce transmitted power and develop more powerful techniques of signal processing. With the advent of powerful Digital Signal Processors (DSPs) and very fast PCs, the implementation

of these algorithms, that give to VHF radar systems the required performances, has become possible [2]. Although these algorithms can be implemented both in time and in frequency domain, working in frequency domain has given faster and more powerful results. The essential first step is the quadrature sampling and the Analog-to-Digital (A/D) conversion. The information is available in digital format, ready for the actual processing carried out in the second step. The quadrature sampling allows all the information included in the received signal to be captured for subsequent processing. These two passages are essential for the following detection process, to extract relevant information from the received echo (i.e. position, velocity, reflected energy, etc.). The third step is the operations on the processed signal, such as data display or data storage for further analysis (off-line), worked out by a PC. Nonetheless, in frequency domain new processing techniques are possible, so such an approach has become dominant [3].

The first step is usually implemented by a digital circuitry, which follows an analog receiver providing an amplification and filtering of the received echo (radio frequency). In some cases a good design of the receiver can limit the amount of noise entering the system: the

noise produced inside the receiver itself (thermal, due to images, etc.) and those coming from the environment that are not exactly inside the frequency band used by the radar system. In other cases it is difficult to discard such external noise, so different methods must be applied to increase the Signal-to-Noise ratio (S/N); they are implemented subsequently. The signal processing is usually done by a specific DSP, but, because of the calculation power of modern PCs, could be carried also on a general purpose computer [4].

Paper is organized as follows: at Section 2, a basic problem statement is given. Section 3 contains description of main radar processing. In Section 4 the results of experiments are given and in Section 5 the concluding remarks presented.

## 2. PROBLEM STATEMENT

The modern radar use pulse compression, that is to say we spread the transmitted pulse out in time and then process the received echo with a matched filter to de-spread it. The band-limit also return and demodulate radar signal to a complex base band. Also, we measure the echo power and the Doppler shift between successive echoes to obtain the desired measurements. The radar echo pulse demodulated and digitized into a number of complex samples. Each sample index corresponds to a specific time offset from the start of the radar pulse, so each sample represents the reflected energy at a specific range. The complex time series of samples at a given range gate can be processed with a Fourier transform to obtain the Doppler spectrum of the echo at that range, from which the mean velocity and variance can be obtained. For a pulsed radar, it can be shown that the pulse pair algorithm provides a reliable estimate of the mean Doppler frequency at each range gate:

$$R = \frac{1}{N} \sum_{k=0}^{N-1} S_{k+1} S_k^* \quad (1)$$

where  $S_k$  are successive samples at a range gate, \* indicates the complex conjugate and N is number of samples. We compute the average power along with the mean Doppler shift to provide a reference and for measuring the total area of the raindrops at a given altitude. The average power at each range is:

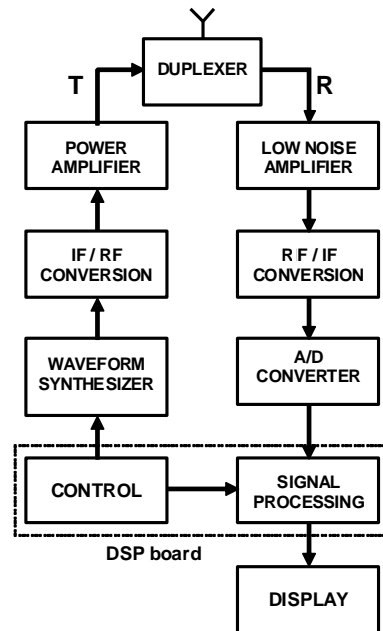
$$R = \frac{1}{N} \sum_{k=0}^{N-1} \text{Re}\{S_{k+1} S_k^*\} \quad (2)$$

We can transmit a long coded pulse, and then compress the echo into an impulse in the receiver using a matched filter. The idea is to spread the transmitted energy out over time to limit the peak transmitted power, then use correlation at the receiver to recover the range resolution. In our case, the coded transmit pulse is a linearly swept frequency 'chirp'. The transmitted pulse can be viewed as a convolution of an impulse and a filter with an impulse response equal to the desired transmitted waveform.

## 3. RADAR SIGNAL PROCESSING DESCRIPTION

### 3.1 Concept of Software Defined Radar

The scheme of software radar is shown in Pic.1. Each block consists of modular components, so it is possible to combine components, in order to achieve the desired function. The block waveform synthesizer generates an appropriate transmitted signal of a pulse or continuum nature that will modulate the hyper frequency carrier. He is flexible, which means that the transmitted signal shape can be changed during operation. For radars working with signals in an spread spectrum, the wavelength synthesizer generates a forward signal that is encoded by frequency or phase, which contributes to improved resolution at a distance. The IF/RF conversion block, the spectrum of the generated signal should be transmitted to the hyper-frequency range of the gigahertz level. On the basis of software radar concept we realized functional model of software radar receiver (SRR) from A/D converter to display [5]. After IQ demodulator follows A/D (Analog to Digital) converter and then follow blocks PXI platform.



Picture 1. Software defined radar system

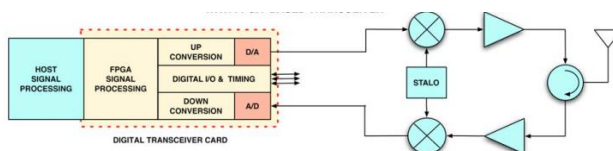
### 3.2. Design of Solid State VHF transceiver

Higher transmitted power was obtain by combining multiple amplifiers in parallel. In general power amplifier (PA) design theory, the method of using a conjugate match of the external networks connected to the input and output of the transistor devices, would seem to suffice. In practical situations this does not take into account the limitations of the devices. This paper aims to investigate the development of four separate VHF-Band radar HPA moduls using commonly available transistor. The moduls would be combined in paralel design in order to provide a high output power. In the investigation of these developments, certain aims need to be considered. Firstly, and most importantly for radar HPA design, is the available output power. It was decided that the designs

should, at least, meet the specified output power of the device being used. Secondly, the amplifiers should provide this output power over the specified bandwidth. Typical layout of a proposed cascaded power amplifier system has driver amplifiers, main power amplifiers as well as splitters, combiners, circulators and high power terminations. In our design there are no high power circulators and terminations. The input divider for four modules is standard Wilkins divider realized in microstrip. The output combiner is reflective four input type realized in the microstrip. It consists of  $25\Omega$  quarter of lambda transformer. The parallel work of two symmetrical transistors on the same device is allowed by the push pull configuration. There are two BALUNs: one at input and other at output. The BALUNs are original; in the technique of symmetrical microstrip. The BALUN is divider and the matching network at the same time. The RF switch is RSW-2-25P with the switch time of 10ns. During the receive time, the power amplifier must be turned off. In order to get fast switching on, the bias of MOSFET must be done prior to RF input signal.

### 3.3. Example of general purpose FPGA for Radar Controller and Signal Processor

The FPGA provides the computational foundation for a radar controller and signal processor, but it must be integrated with other hardware. A transceiver card is required which can provide receive, transmit and control signal functions. Commercial vendors provide products that provide this general-purpose functionality. The FPGA is typically combined with analog-to-digital and digital-to-analog converters, local memory, digital I/O lines and bus interfaces (Pic.2). The Pentek Model 7142 (Pic. 3) has compact card which is based on the Portable Mezzanine Card (PMC) format. A wide variety of carrier cards are available to host the PMC in common computer backplanes. The hardware vendor typically offers a board support package, which provides drivers and application libraries for the host system, and firmware source code for the FPGA. The first two provide facilities to access the card on various operating systems. The firmware package can be a version of VHDL code that will run on the FPGA and provide baseline functionality, so that the card can be used in some cases without any VHDL development. The end user can customize the supplied VHDL for their specific purposes.



Picture 2. Schematics of a radar system with FPGA transceiver.

The dashed line boxes denote functions that are performed by the FPGA firmware. The FPGA integrated circuit is enclosed within the heat sink.



Picture 3: The Pentek 7142 FPGA transceiver.

### 3.4. Matched filtering

The impulse response of a matched filter is defined by the particular signal to which the filter is matched. Matching will result in the maximum attainable SNR at the output of the filter when signal, to which filter it was matched, to which it was added white noise, are passed through it. In radar applications, SNR is of paramount importance, and matched filters are used extensively. The probability of detection is related to the SNR rather than to the exact waveform of the signal received. The input to the matched filter is the signal  $s(t)$  and additive white Gaussian noise with a two-sided power spectral density of  $N_0/2$ . Obtaining of the impulse response  $h(t)$  that will yield the maximum output SNR at a predetermined delay  $t_0$  was explained in [6]. We look for the response  $h(t)$  that will maximize SNR:

$$\left(\frac{S}{N}\right)_{out} = \frac{|s_0(t_0)|^2}{n_0^2(t)} \quad (3)$$

Let the Fourier transform of  $s(t)$  be  $S(\omega)$ , then the output signal at  $t_0$  is given by:

$$s_0(t_0) = \frac{1}{2\pi} \int_{-\infty}^{\infty} H(\omega) \cdot S(\omega) \exp(j\omega t_0) d\omega \quad (4)$$

The mean-squared value of the noise, which is independent of  $t$  is:

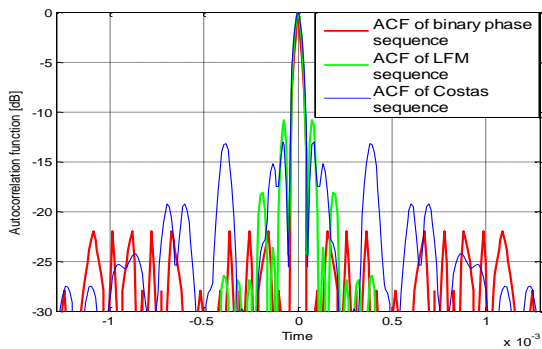
$$\overline{n_0^2(t)} = \frac{N_0}{4\pi} \int_{-\infty}^{\infty} |H(\omega)|^2 d\omega \quad (5)$$

After adding the values (3) in (2), and after the execution explained in [6], the maximum output SNR it was obtained when:

$$H(\omega) = K \cdot S^* \exp(-j\omega t_0) \quad (6)$$

In [6] it was derived that maximum SNR is  $2E/N_0$ . The impulse response is linearly related to the time-inverted complex-conjugate signal, which represents autocorrelation function (ACF). When the input to the matched filter is the correct signal plus white noise, the peak output response is related to the signal's energy.

In order to emphasize peak-side lobe ratio of sequences used in this paper, its ACF will be presented in decibels.



Picture 4. ACF of used radar sequences

Pic. 4 shows that the best peak-side lobe ratio is obtained using binary phase sequence with 25 elements, and amounts of 22 dB. Besides that it is important to note, that binary phase sequence has the same level of all side lobes, unlike other two sequences.

## 4. SIMULATION RESULTS

### 4.1. FPGA Zedboard

The FPGA ZedBoard, which was used in this paper, represents Zynq-7000 FPGA (Pic. 5) evaluation and development kit, and it is equipped with the reconfigurable devices. Zynq system on the chip (SoC) integrates a Xilinx 7-series FPGA and ARM Cortex-A9 dual core based processor system on same chip together. ZedBoard has coherent multiprocessor support, three watchdog timers, one global timer, and two triple-timer counters. In Zynq-7000 FPGA the parts containing intense computations are performed on FPGA. The control parts not containing computations can be done on the processor by using software.



Picture 5. The FPGA Zedboard

Hardware platform configuration for Zynq device consists of two parts: Processing System and Programmable Logic with 85000 cells. The intercommunication between two different portions of electronic circuits is described as Programmable Logic. The upper basic portion, called the processing system (PS), works like a traditional processor. It is mainly formed by the ARM Cortex-A9, DDR3 controller for external DDR3\_SDRAM memory and UART for serial communication. Programmable logic

part contains the structures of standard FPGA [5]. Because the FPGA Zedboard performs signal processing in digital form, it was necessary to perform digital to analog conversion for displaying of obtained signal [7]. For that operation the two-channel 12-bit D/A converter Pmod DA2 was applied, which was connected on six-pins PMOD connector JB. It is important that the sampling rate of this D/A converter is 16.5 Mega Sample, and that represents the limitation for displaying short signals with high sampling frequency, such as radar signals. In order to observe generating and processing of obtained signals, the instrument Analog Discovery in oscilloscope mode was used [8]. Using DIGILENT's software for this instrument it was possible to record results of matched filtering and compare it with results obtained in program MATLAB.

### 4.2. Development of a digital platform

As part of the continuation, it is necessary to define and test the effectiveness of suitable synchronization impulse waveforms as well as types of modulations for use in the test piece (TP) of the modernized radar. We perform the next required activities:

1. On the TP of the semiconductor transmitter, record the triggers on the Logic analyzer.
2. Put an artificial load of 50  $\Omega$  on the 1 MHz output.
3. Redirect triggers to FPGA (ZED board).
4. Generate our signal in the base band (1 MHz) with our sequence of 250 kHz, duration 4  $\mu$ S.
5. Perform signal processing in laboratory conditions and try to generate various types of modulation.
6. After completion, play sequences directly on the device measure output power.

The status of the solid-state radar transceiver in the meter range provides at its output a 1 MHz base band transmission pulse at carrier frequencies of 150-170 MHz. On the receiving side, a duplexer with PIN diodes is provided, behind which a low-noise amplifier is installed in the RF range. A module is missing that would lower the modulated signal to the intermediate frequency and/or base band. The shape and modulation of the transmission pulse, as well as the synchronization of the operation of all elements of the radar transceiver with trigger pulses is currently not under our control. In order to overcome the mentioned problems, it is necessary to (in the semiconductor transmitter part):

1. Generate your own trigger pulses - create a functional model on the microcontroller.
2. Generate a modulated signal in the basic range - create a functional model on the microcontroller and DDS signal generator.
3. Perform modulation of the transmission pulse in the basic range to the frequency of the carrier signal - not done.
4. Adjust the voltage and current levels of the generated signal in the RF range for further amplification on the semiconductor transmitter.

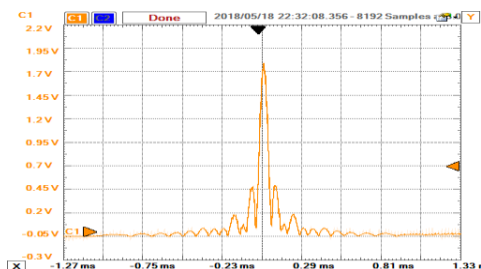
In the semiconductor receiver part, we create a stage of a super heterodyne receiver with an amplifier at intermediate frequency and/or base band in order to

provide the possibility for further digital signal processing and then connect the appropriate hardware assembly for the realization of a digital radar receiver and perform its programming [9].

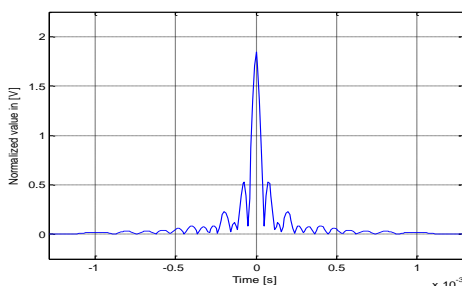
The problematic activities are realizing No.3 in the part of the transmitter and realizing No.1 in the part of the receiver. For the acquisition and digital processing of signals on the basic band of 250 kHz, we have the appropriate hardware components. This base band frequency can provide a resolution cell of at least 600m spatially, which is not by technical requirements, but can be used for testing in the selection of the required parameters. Considering that these are 16-bit A/D converters, as well as a combination of long and short pulse application, the installation of an analog block for Space Time Adaptive Processing (variable gain in reception time) is not necessary.

#### 4.3. Results of matched filtering of radar signals using the FPGA Zedboard

The performance analysis and confirmation of validity of the results obtained using FPGA Zedboard is presented. That will be realized performing comparison between results from the program Matlab, and results which were obtained using FPGA Zedboard, using instrument Analog Discovery in oscilloscope mode. On the output we expected a series of absolute values of autocorrelation peaks. In order to highlight the shape of autocorrelations on the output, it will be presented an enlarged picture of one autocorrelation. On the Pic. 6 and 7 it was displayed autocorrelations of LFM sequence with 25 elements.



**Picture 6.** The autocorrelation of LFM sequence obtained using FPGA Zedboard



**Picture 7.** The autocorrelation of LFM sequence obtained using program Matlab

## 5. CONCLUSION

In this paper, we present example of use the FPGA

technology in radar signal processing. Designing from a software architecture perspective, using tools such as integrated development environments, source code revision control and bug tracking, and creating embedded documentation will all greatly enhance project productivity. The FPGA is capable of very high signal processing performance, thus mitigating large data bandwidths and host CPU loads. The technology facilitates very flexible applications: the same hardware can be customized to meet quite different requirements simply by loading the application-specific firmware. Total system costs are reduced by leveraging the use of a single FPGA card among several systems, and by the consolidation of functions from many discrete hardware components onto a single card.

#### Acknowledgements

This work was by Serbian Ministry of Defense and Serbian Ministry of Education, Science and Technological Development, Grant No 451-03-66/2024-03/200325.

#### References

- [1] OPPENHEIM, V., A. SCHAFER, W. RONALD and J. R. BUCK, (1999): *Discrete-Time Signal Processing* (Englewood Cliffs, New Jersey, Prentice Hall), 2nd edition, pp. 870.
- [2] RABINER, L.R. and B. GOLD (1975): *Theory and Application of Digital Signal Processing* (Englewood Cliffs, New Jersey, Prentice Hall), pp. 762.
- [3] R. ANDRAKA, A. BERKUN, FPGAs Make a Radar Signal Processor on a Chip a Reality, Asilomar Conf., Feb.1999.DOI: 10.1109/ACSSC.1999.832392
- [4] SKOLNIK, M.I. (1980): *Introduction to Radar Systems* (Mc Graw-Hill, NY), 2nd edition, pp. 442.
- [5] B. R. Mahafza, *Radar Systems Analysis and Design Using MATLAB*, chapter 3, Chapman & Hall, New York 2000.
- [6] C. BIANCHI, S. UMBERTO, A. ZIRIZZOTTI, E. ZUCCHERETTI, Signal processing techniques for phase-coded HF-VHF radars, *Annals of geophysics*, January 2010, DOI: 10.4401/ag-4369.
- [7] N. Levanon, E. Mozeson, *Radar signals*, Chapter 7, John Wiley & Sons, New Jersey 2004.
- [8] *ZedBoard Booting and Configuration Guide*, Avnet, USA, April 2012.
- [9] *System Generator for DSP Getting Started Guide*, Xilinx, USA, UG639, December 2, 2009.
- [10] S. Brown, Z. Vranesić, *Fundamentals of Digital Logic with VHDL Design*, Third edition, Chapter 10, McGraw-Hill, New York, 2009
- [11] MARTIN. C. LOEW E. BURGHART C.,(2012) *A General Purpose FPGA Based Radar Controller and Signal Processor*, In procc. Of 92nd American Meteorological Society Annual Meeting (January 22-26, 2012).



## THE POWER CONSUMPTION OF EMBEDDED GPU COMPUTERS FOR DEEP LEARNING APPLICATIONS

BOBAN SAZDIĆ-JOTIĆ

Military Technical Institute, Belgrade, [boban.sazdic.jotic@vs.rs](mailto:boban.sazdic.jotic@vs.rs)

SNEŽANA ZUROVAC

Military Technical Institute, Belgrade, [zurovac@medianis.net](mailto:zurovac@medianis.net)

NIKOLA PETROVIĆ

Military Technical Institute, Belgrade, [npetrovicbrg@gmail.com](mailto:npetrovicbrg@gmail.com)

DRAGANA BOJIĆ

Military Technical Institute, Belgrade, [dragana.bojic@mod.gov.rs](mailto:dragana.bojic@mod.gov.rs)

**Abstract:** *The widespread use of GPU processors has significantly enhanced the usage of various artificial intelligence algorithms, especially machine and deep learning models. However, more capabilities introduced significant challenges in energy consumption, particularly on autonomous platforms with battery and autonomy constraints. Our research is crucial as it addresses the energy consumption issue on desktop and embedded GPU computers from a new angle, providing a practical and optimal measurement solution. We engaged various deep learning models to analyze and determine how different datasets for training and problems for inference affect energy consumption. Two separate platforms were used for the experiments: the NVIDIA Jetson NANO platform, a well-known type of embedded GPU computer widely used in deep learning applications, for the inference process just, and a desktop computer with two GeForce RTX 2060 for the training and inference processes. The image classification problem was involved during the training process on two separate datasets. In contrast, inference problems for object detection and drone classification were engaged on live videos and recorded RF signals during the inference process. Our methodology involved a systematic comparison of energy consumption across different models and datasets, ensuring the validity and reliability of our findings. Our findings underscore the potential to reduce energy consumption on embedded GPU computers by implementing a suitable deep learning model. This not only preserves the performance of the required process (drone radio frequency signal detection and identification and object detection in the video stream) but also paves the way for their effective use in real-life scenarios, thereby addressing a crucial need in deep learning. More importantly, we created an empirical methodology for measuring the energy consumption of embedded GPU computers for deep learning applications, directly impacting the development of energy-efficient deep learning systems.*

**Keywords:** *artificial intelligence, deep learning, drone, detection, embedded GPU computer, energy consumption.*

### 1. INTRODUCTION

Artificial intelligence (AI) algorithms are used in various fields, such as industry, medicine, agriculture, and defense, to automate processes and facilitate decision-making procedures. A prerequisite for such rapid development is, among other things, the development of computer science, primarily the upgrading of Graphics Processing Unit (GPU) processors and improvements in effective parallel processing of substantial amounts of data. Deep Neural Networks (DNN) have enabled state-of-the-art accuracy on many challenging artificial intelligence tasks, such as image classification and segmentation [1], [2], [3], object detection and tracking [4], [5], [6], [7], natural language processing [8], [9], [10], [11], [12], [13], and voice-based applications [14], [15].

However, this advanced technology is highly dependent

on high-performance computing (HPC) based on GPU processors and has an evident downside: it consumes significant energy. On the other hand, the authors in [16] have suggested putting a goal on the environmentally friendly deep learning (DL) models known as Green AI. To accomplish that, a huge problem arises when there is a demand to apply DL models to mobile applications where energy consumption is crucial for implementation [17], [18]. While most AI computation for training purposes currently resides online (cloud or local servers) or on desktop computers, using embedded GPU computers for inference locally near the sensor is desirable due to privacy, security, and latency concerns or limitations in communication bandwidth. Since mobile devices require batteries, reducing power consumption alleviates environmental problems and extends battery life, making low-power DL algorithms highly desirable for different use cases. In addition, a survey presented in [19] reveals that approximately 55% of respondents would leave a

negative review for a mobile application that drains a significant amount of battery. A similar prerequisite exists in functional applications, especially for military purposes where embedded and mobile systems must respond accordingly to responsive energy consumption. For example, military drones have limited batteries for flying operations and DL model inference. Accordingly, the research community has been increasingly interested in designing energy-efficient DL models, critical to realizing mobile AI applications. However, estimating energy consumption from the DL model is much more complicated than other metrics, such as storage cost (model size), throughput (number of operations), or latency (time of processing). This is because a huge portion of the energy is consumed by data movement, which is difficult to extract directly from the DL model.

Because of this, our research presents a study of energy consumption for DL models, especially methods that can be used for initial estimation. This paper explores how energy consumption is affected by using different GPU processors and DL models in two distinct stages of production (training or inference). This paper is structured as follows: Section 2 provides an overview of the methods for energy estimation. Sections 3 and 4 present the methodology and discuss our experimental results, and the study conclusion is given in the last section.

## 2. CURRENT ENERGY ESTIMATION METHODS

Energy consumption in embedded GPU computers is a prominent concern in computational research, and multiple studies have explored various optimization strategies. Based on our comprehension, current energy estimation methods can be classified into three groups.

The first group of papers incorporates an approach to reducing consumption by knowing computer operation processes and the lowest levels of computer computation to optimize calculations performed on the computer platform, primarily on the GPU processor. This group includes papers that predict the number of computational and memory access operations to predict energy consumption. The new energy monitoring and optimization capabilities as an autotuning tool for GPU processors were presented in [20]. Another approach called the SyNERGY was introduced in [21], which uses an energy measurement based on hardware performance counters such as SIMD (single instruction, multiple data) and bus access for the CPU obtained from actual execution runs of these models. The authors in [22] have proposed a methodology that can be used to evaluate the various DL models and energy-efficient techniques, with a guide for designing the energy-efficient DL models. They pointed out that the DL model's convolutional and fully connected layers dominated computation and energy consumption. An interesting method is introduced in [23] with the idea that it cannot optimize what cannot be measured and cannot optimize what is under-appreciated or neglected in the design. This is even important because most research tends to reduce inference latency and

enhance accuracy, often failing to consider the impact on energy efficiency.

The second group of papers includes empirical methods focusing on the results obtained through various experiments or comparing theoretical considerations and practical measurements. Authors in [24] presented measurements of the energy consumption on the Tier-2 HoreKa supercomputing system, presenting that model training and inference energy consumption should be considered separately. A comprehensive empirical method is given in [25] to profile the energetic consumption of inference tasks for some modern edge computers such as Asus Tinker Edge R [26], Raspberry Pi 4 [27], Google Coral Dev Board [28], Nvidia Jetson Nano [29], and one microcontroller Arduino Nano 33 BLE [30] with different DL models. The impact of the DNN architecture on the energy consumption and emissions produced, the trade-off between accuracy and energy efficiency, and the difference in the measurement method of the energy consumed using software-based and hardware-based tools were investigated in [31].

The third group of papers has focused on the development of separate AI models for predicting the level of energy consumption. It should be noted that this approach has also been used for other applications, such as prediction and reduction of energy consumption by the data centers. The authors in [32] have presented a practical framework based on the grid search to answer the above question. Additionally, authors in [33] have created BUTTER and BUTTER-E datasets to characterize the impact of hyperparameter choice on energy efficiency. Their research concludes that smaller networks sometimes consume less energy during training, and broad layers, particularly those with large input sizes, can be power consumers. Moreover, there are more benchmark datasets, such as NAS-Bench 101 [34]. This dataset evaluates various DL models and their associated loss and accuracy scores after training. Also, the authors in [35] estimated energy consumption and carbon emissions of DL models with the EC-NAS benchmark.

## 3. EXPERIMENTS

The methodology used in this study was designed to perform the following: hardware and software configuration (data and model loading), training or inference process, and analysis of the energy consumption results. Nine different models (AlexNet, InceptionV3, VGG16, VGG19, ResNet50, three various versions of YOLO models, and VTI\_CNN – our custom-made convolutional neural network) were initially configured with three different datasets (MINST [36], CIFAR-10 [37], and VTI\_DroneSET [38]). We measured CO<sub>2</sub> (carbon dioxide) total emission, energy consumption, FLOPS (floating-point operations per second), and accuracy for each model during training and inference processes.

**Hardware.** All measurements within this research were conducted on an embedded GPU computer, the Jetson Nano Developer Kit, and a desktop GPU computer with

two GeForce RTX 2060. NVIDIA leverages its GPU processors in the Jetson product line to deliver accelerated AI performance to edge platforms. The Jetson Nano's embedded GPU computer is developed based on the Maxwell architecture and incorporates a single streaming processor with 128 CUDA (compute unified device architecture) cores. Positioned as the lowest-end model in the product line, the Jetson Nano achieves a peak performance of 472 GigaFlops. [29]. We reviewed the 4GB model, while there are 2GB and 4GB RAM options with 5W and 10W power modes, respectively. The GeForce RTX 2060 is based on the Turing architecture GPU processor with 6 GB of GDDR6 RAM running at 14 Gbps and a GPU clock of 1.68 GHz. Moreover, it features 1,920 CUDA cores and 240 Tensor Cores that can deliver 52 TeraFlops of DL horsepower. The GeForce RTX 2060 has a total board power of 160W.

According to the authors in [39] the most effective method to measure accurate and fine-grained power consumption is to connect the device to an external power monitor (wattmeter) with a high sampling rate. Moreover, the same authors have set rules for measuring power to ensure consistency and reliability across different devices and testing conditions. Controlling environmental factors helps better understand power and energy consumption in DNN executions, so similar rules have been adopted for measurements:

- All wireless communication interfaces (Wi-Fi, Bluetooth, cellular network, and Near-Field Communication) and background applications and services were shut down to minimize interference with measurement accuracy.
- The Jetson Nano Developer Kit was used in headless mode (without monitor and peripherals) due to the more realistic conditions.
- Room temperature was set to be between 20 and 25°C, while the cooldown interval between individual experiments was set to be 5 minutes.

The external power meters used for the experiment are the Fluke 430-II Power Quality and Energy Analyzer and the Acuvim 3 Power Quality and Revenue Grade Energy Meter. However, due to the complicated setup and mandatory hardware adjustment, the experiments also used the CodeCarbon energy profiler [31], which is representative of internal power monitors (energy profilers). The study compares and cross-references their readings with those from an external.

**Software.** Two requests were considered within the experiments: Does the convolutional neural network (CNN) architecture impact energy consumption, and can general demands for embedded GPU computers be pointed out? We ground our experiments on publicly available models such as AlexNet [40], VGG [41], InceptionV3 (GoogLeNet) [42], ResNet50 [43] and YOLO models [44]. These models were selected as representative CNN models due to their various applications. We also evaluated our custom-made CNN model, specially designed for specific tasks (drone classification in the frequency domain).

In CNN models, the convolutional layer is crucial for extracting and refining features from input data. The energy consumption disparity between external memory access and computational (MAC) operations has led to integrating multiple levels of local memory within GPU processors, forming a memory hierarchy. This hierarchy reduces energy costs associated with external memory access but requires more energy than computation. As a result, the volume of weight movement may provide a more precise estimate of energy consumption. Therefore, current research in efficient CNN design primarily concentrates on creating empirical metrics for energy-efficient CNN models and leads to possibilities to reduce the number of filter weights and the number of multiplication and accumulation operations. It is important to note that these metrics do not necessarily correspond to energy consumption because energy consumption is influenced by data movement rather than computation, and the energy consumption of data movement is significantly impacted by the memory hierarchy and data flow.

The CNN models mentioned above were used to solve the two problems based on such prerequisites. The first is classifying objects on the video, and the second is classifying radio signals in the frequency domain. Even if we define such problems, it can be generalized that all results can be applied to the computer vision domain. All models and test procedures were built in Python. We used the CodeCarbon profiler, a Python package that enables us to track four numerical variables: 1) the emissions in carbon dioxide equivalent (CO<sub>2</sub>-eq) in kilograms, 2) the energy consumed by the infrastructure in kilowatt-hours, 3) the FLOPS required to train the model, and 4) the validation accuracy of the model obtained. The CodeCarbon energy profiler is based on software metrics and estimates the energy consumed during a model's training to estimate actual energy consumption reasonably [31].

The CO<sub>2</sub>-eq is a measure used to compare emissions from different greenhouse gases based on their global warming potential [45]. This value is calculated by multiplying the carbon intensity of the electricity used for computation (measured in kg of CO<sub>2</sub> emitted per kWh of electricity) by the net power supply consumed by the computational infrastructure (measured in kWh). Monitoring the power supply to the hardware occurs regularly and depends heavily on the type of hardware used.

Energy consumption is intricately linked to CO<sub>2</sub> emissions and is invariant concerning time and location. Monitoring the power supply to the hardware transpires frequently and is heavily contingent upon the type of hardware employed. The experiment was repeated three times, and the median energy consumption value, determined by both the wattmeter and the profiler, is being reported.

FLOPS epitomizes the number of floating-point operations per second necessary to execute a computational process. They estimate the process's workload based on a deterministic measure calculated by tabulating the costs of two fundamental operations:



addition and multiplication. FLOPS can be calculated using a model instance even before the commencement of training.

The overall CNN model score is finally calculated with the following equation:

$$CNN_{score} = \frac{CNN_{accuracy}}{Energy_{consumption}} \quad (1)$$

where  $CNN_{accuracy}$  is the accuracy of the used CNN model and  $Energy_{consumption}$  is measured energy consumption. The results from the training and inference process and external and profilers' energy measurements were analyzed concurrently to make a definitive conclusion.

#### 4. EXPERIMENTAL RESULTS

Every experiment (training or inference) was performed in three independent executions ( $K=3$ ) due to the statistical purposes and situation of hardware malfunctioning. Table 1 shows the average emissions produced.

**Table 1.** The average CO2-eq emissions.

CNN model	CO2-eq emissions [kg emitted per kWh of electricity]	
	CFAR10 dataset [32x32 / 60.000 images]	MNIST dataset [28x28 / 60.000 images]

**Table 2.** Scores of the CNN models for training process on the desktop with two GeForce RTX 2060.

Training process [ $K=3$ ] for image classification problem	Model	FLOPS [Gigaflops]	Datasets	Accuracy [%]	Internal power monitor		External power monitor	
					Energy consumption [kWh]	Score	Energy consumption [kWh]	Score
					AlexNet	39.1	CFAR10	75.16
			MNIST	96.71	0.01706	56.89079	0.016	60.61176
	VGG16	21.3	CFAR10	60.03	0.01090	55.52622	0.042	50.38429
			MNIST	93.55	0.01863	43.24232	0.047	59.95124
	VGG19	26.7	CFAR10	59.04	0.01256	47.11753	0.015	39.46621
			MNIST	93.23	0.01942	48.15551	0.016	57.42648
	ResNet50	6.6	CFAR10	20.40	0.01359	15.11031	0.015	13.31681
			MNIST	87.63	0.02235	39.32731	0.016	53.71520
	InceptionV3	14.5	CFAR10	65.01	0.02432	26.79580	0.021	30.61719
			MNIST	89.20	0.03052	29.27427	0.018	48.68782

**Table 3.** Scores of the CNN models for inference processes on the Jetson Nano Developer Kit for the object detection problem.

Inference process [ $K=3$ ]	Model	FLOPS [Gigaflops]	Problem	Model confidence [%]	Internal power monitor		External power monitor	
					Energy consumption [kWh]	Score	Energy consumption [kWh]	Score
					YOLOv5s	16.5	Object detection on live video	95.00
YOLOv7	36.9	0.13377	7.10175	0.149	6.37583			
YOLOv8s	28.6	0.03511	27.05781	0.031	30.64516			

**Table 4.** Scores of VTL\_CNN model for the drone classification problem on the different GPU processors.

Inference process [ $K=3$ ]	GPU Computer	CNN model	FLOPS [Gigaflops]	Problem	Accuracy [%]	Internal power monitor		External power monitor	
						Energy consumption [kWh]	Score	Energy consumption [kWh]	Score
						2 x GeForce RTX 2060	VTL_CNN	1.7	Drone classification on recorded RF signals
Jetson Nano Developer Kit	99.57	0.13066	7.62015	0.11588	8.59185				

Table 2 shows the average scores of the CNN models for the three ( $K=3$ ) training processes on the desktop with two GeForce RTX 2060 for solving classification problems with two datasets containing ten classes. The best result was obtained with the AlexNet model for the

AlexNet	0.000039373	0.000043659
VGG16	0.006836938	0.000047602
VGG19	0.007825523	0.000049091
ResNet50	0.001236008	0.000056854
InceptionV3	0.000061455	0.000074992

The VGG16, VGG19, and ResNet50 models have the worst results for used hardware configuration due to the highest CO2-eq emissions (CO2-eq or CO2 equivalent) expressed in kg emitted per kWh of electricity. However, the CO2-eq emission also depends on the dataset used for the training process. This is an expected outcome since external memory access in the case of the CFAR10 dataset requires more energy than the MNIST dataset. Interestingly, the CO2-eq emission results can fluctuate significantly for the CFAR10 dataset. The overfitting of these models can explain this phenomenon because they tend to learn details that are not important in the classification process. Moreover, this can be supported by the achieved accuracy of these models for CIFAR (see Table 2).

Tables 2 to 4 show the accuracy obtained from different CNN models, the two distinct stages of production (training or inference), the energy consumption measurements for internal or external power monitors, and the score corresponding to the ratio between the mentioned accuracy and power.

MNIST dataset and the VGG16 for the CIFAR-10 dataset. These results are consistent with findings from the literature, demonstrating that the proposed methodology can be utilized for further analysis. In [31], the authors compared three models and suggested that the VGG16 model outperformed the VGG19 and ResNet50.

Our research involved five models within the CIFAR-10 and MNIST datasets and indicated the same results, with the addition that the AlexNet model achieved the highest score compared with the models mentioned. Moreover, the results from internal and external power monitors are similar, which leads to the conclusion that internal monitors can be successfully used for general purposes because of their simplicity.

Table 3 shows the average scores of the YOLO models for the three ( $K=3$ ) training processes on the Jetson Nano Developer Kit for the object detection problem in the inference process within live video. The model's confidence in its prediction accuracy (indicating how confident it is that the predicted results correspond to its labeled class) for all measurements was 95%. The best results are obtained for the YOLO 8 model. Table 4 shows the average scores of the VTI\_CNN model for the drone classification problem on recorded RF signals. Better results are obtained with the desktop configuration because of the required external MAC operations necessary for the inference process. MAC operations in the Jetson Nano Developer Kit are more demanding because a dedicated pipeline for images streaming from the external memory to the model is needed during the inference process.

## 5. CONCLUSION

This study presents an empirical energy estimation methodology for CNN based on the architecture, dataset (MINST, CIFAR-10, and VTI\_DroneSET), and production problem (object detection on live videos or drone classification on recorded RF signals). We observed varying overall CNN model scores for the same dataset, demonstrating that the CNN architecture influences energy consumption. AlexNet and VGG16 yielded the best performance during training, while YOLO 8 excelled during inference. As a general observation, we established that internal energy profilers can effectively estimate energy consumption, offering crucial initial insights, especially in military mobile applications. Using this methodology and tool, researchers can quantify the energy consumption on the embedded GPU computers associated with various model choices during the initial design phase. This narrows the gap between CNN algorithm/hardware design and energy optimization. Further research lines can focus on experiments in different temperature conditions to find the relationship with this variable. Most embedded GPUs are intended for external applications, so detecting this impact is essential.

## References

- [1] H. Sun, X. Zheng, and X. Lu, "A Supervised Segmentation Network for Hyperspectral Image Classification," *IEEE Transactions on Image Processing*, vol. 30, pp. 2810–2825, 2021, doi: 10.1109/TIP.2021.3055613.
- [2] Y. Xiao, L. Daniel, and M. Gashinova, "Image Segmentation and Region Classification in Automotive High-Resolution Radar Imagery," *IEEE Sens J*, vol. 21, no. 5, pp. 6698–6711, Mar. 2021, doi: 10.1109/JSEN.2020.3043586.
- [3] J. Cheng *et al.*, "ResGANet: Residual group attention network for medical image classification and segmentation," *Med Image Anal*, vol. 76, p. 102313, Feb. 2022, doi: 10.1016/j.media.2021.102313.
- [4] T. Yin, X. Zhou, and P. Krähenbühl, "Center-based 3D Object Detection and Tracking," in *Proceedings of the IEEE Computer Society Conference on Computer Vision and Pattern Recognition*, 2021, pp. 11779–11788. doi: 10.1109/CVPR46437.2021.01161.
- [5] R. Ravindran, M. J. Santora, and M. M. Jamali, "Multi-Object Detection and Tracking, Based on DNN, for Autonomous Vehicles: A Review," Mar. 01, 2021, *Institute of Electrical and Electronics Engineers Inc.* doi: 10.1109/JSEN.2020.3041615.
- [6] L. Wen *et al.*, "UA-DETRAC: A new benchmark and protocol for multi-object detection and tracking," *Computer Vision and Image Understanding*, vol. 193, p. 102907, Apr. 2020, doi: 10.1016/j.cviu.2020.102907.
- [7] Y. Wang, V. Ilic, J. Li, B. Kisačanin, and V. Pavlovic, "ALWOD: Active Learning for Weakly-Supervised Object Detection," in *Proceedings of the IEEE International Conference on Computer Vision*, IEEE, Oct. 2023, pp. 6436–6446. doi: 10.1109/ICCV51070.2023.00594.
- [8] I. Popovic, D. Culibrk, M. Mirkovic, and S. Vukmirovic, "Automatic Speech Recognition and Natural Language Understanding for Emotion Detection in Multi-party Conversations," in *MuCAI 2020 - Proceedings of the 1st International Workshop on Multimodal Conversational AI*, Association for Computing Machinery, Inc, Oct. 2020, pp. 31–38. doi: 10.1145/3423325.3423737.
- [9] A. Galassi, M. Lippi, and P. Torroni, "Attention in Natural Language Processing," *IEEE Trans Neural Netw Learn Syst*, vol. 32, no. 10, pp. 4291–4308, Oct. 2021, doi: 10.1109/TNNLS.2020.3019893.
- [10] Y. Kang, Z. Cai, C. W. Tan, Q. Huang, and H. Liu, "Natural language processing (NLP) in management research: A literature review," Apr. 02, 2020, *Taylor & Francis*. doi: 10.1080/23270012.2020.1756939.
- [11] G. G. Chowdhury, "Natural language processing," *Annual Review of Information Science and Technology*, vol. 37, pp. 51–89, 2003, doi: 10.1002/aris.1440370103.
- [12] M. Zhou, N. Duan, S. Liu, and H. Y. Shum, "Progress in Neural NLP: Modeling, Learning, and Reasoning," Mar. 01, 2020, *Elsevier*. doi: 10.1016/j.eng.2019.12.014.
- [13] D. Ofer, N. Brandes, and M. Linal, "The language of proteins: NLP, machine learning & protein sequences," Jan. 01, 2021, *Elsevier*. doi: 10.1016/j.csbj.2021.03.022.
- [14] K. Chachadi and S. R. Nirmala, "Voice-Based Gender Recognition Using Neural Network," in *Lecture Notes in Networks and Systems*, vol. 191, Springer, Singapore, 2022, pp. 741–749. doi: 10.1007/978-981-16-0739-4\_70.
- [15] A. Ouhmida, O. Terrada, A. Raihani, B. Cherradi, and S. Hamida, "Voice-Based Deep Learning Medical Diagnosis System for Parkinson's Disease Prediction," in *2021 International Congress of Advanced Technology and Engineering, ICOTEN 2021*, Institute of Electrical and Electronics Engineers Inc., Jul. 2021. doi: 10.1109/ICOTEN52080.2021.9493456.
- [16] R. Schwartz, J. Dodge, N. A. Smith, and O. Etzioni, "Green AI," *Commun ACM*, vol. 63, no. 12, pp. 54–63, Nov. 2020, doi: 10.1145/3381831.
- [17] H. Wang, B. G. Kim, J. Xie, and Z. Han, "LEAF + AIO: Edge-Assisted Energy-Aware Object Detection for Mobile Augmented Reality," *IEEE Trans Mob Comput*, vol. 22, no. 10, pp. 5933–5948, Oct. 2023, doi: 10.1109/TMC.2022.3179943.
- [18] H. Wang and J. Xie, "User Preference Based Energy-Aware Mobile AR System with Edge Computing,"

- Proceedings - IEEE INFOCOM*, vol. 2020-July, pp. 1379–1388, Jul. 2020, doi: 10.1109/INFOCOM41043.2020.9155517.
- [19] Verizon Media, “Apigee Survey: Users Reveal Top Frustrations That Lead to Bad Mobile App Reviews.” Accessed: Jul. 15, 2024. [Online]. Available: <https://sg.finance.yahoo.com/news/apigee-survey-users-reveal-top>
- [20] R. Schoonhoven, B. Veenboer, B. Van Werkhoven, and K. J. Batenburg, “Going green: optimizing GPUs for energy efficiency through model-steered auto-tuning,” *Proceedings of PMBS 2022: Performance Modeling, Benchmarking and Simulation of High Performance Computer Systems, Held in conjunction with SC 2022: The International Conference for High Performance Computing, Networking, Storage and Analysis*, pp. 48–59, 2022, doi: 10.1109/PMBS56514.2022.00010.
- [21] C. Faviola Rodrigues, G. Riley, and M. Luján, “SyNERGY: An energy measurement and prediction framework for Convolutional Neural Networks on Jetson TX1,” *Proceedings of the International Conference on Parallel and Distributed Processing Techniques and Applications (PDPTA)*, pp. 375–382, 2018.
- [22] T. J. Yang, Y. H. Chen, J. Emer, and V. Sze, “A method to estimate the energy consumption of deep neural networks,” *Conference Record of 51st Asilomar Conference on Signals, Systems and Computers, ACSSC 2017*, vol. 2017-October, pp. 1916–1920, 2017, doi: 10.1109/ACSSC.2017.8335698.
- [23] X. Tu *et al.*, “Unveiling Energy Efficiency in Deep Learning: Measurement, Prediction, and Scoring Across Edge Devices,” *Proceedings - 2023 IEEE/ACM Symposium on Edge Computing, SEC 2023*, pp. 80–93, 2023, doi: 10.1145/3583740.3628442.
- [24] R. Caspart *et al.*, “Precise Energy Consumption Measurements of Heterogeneous Artificial Intelligence Workloads,” *Lecture Notes in Computer Science (including subseries Lecture Notes in Artificial Intelligence and Lecture Notes in Bioinformatics)*, vol. 13387 LNCS, pp. 108–121, 2022, doi: 10.1007/978-3-031-23220-6\_8.
- [25] S. P. Baller, A. Jindal, M. Chadha, and M. Gerndt, “DeepEdgeBench: Benchmarking Deep Neural Networks on Edge Devices,” *Proceedings - 2021 IEEE International Conference on Cloud Engineering, IC2E 2021*, pp. 20–30, 2021, doi: 10.1109/IC2E52221.2021.00016.
- [26] ASUS, “Tinker Edge R,” ASUS. Accessed: Jul. 15, 2024. [Online]. Available: <https://tinkerboard.asus.com/series/tinker-edge-r.html>
- [27] Raspberry, “Raspberry Pi 4 Model B,” Raspberry Pi. Accessed: Jul. 15, 2024. [Online]. Available: <https://www.raspberrypi.com/products/raspberrypi-4-model-b/>
- [28] Google, “Dev Board Coral,” Google. Accessed: Jul. 15, 2024. [Online]. Available: <https://coral.ai/products/dev-board/>
- [29] NVIDIA, “Jetson Nano,” NVIDIA. Accessed: Jul. 15, 2024. [Online]. Available: <https://www.nvidia.com/en-us/autonomous-machines/embedded-systems/jetson-nano/product-development/>
- [30] Arduino, “Arduino Nano 33 BLE,” 2020. Accessed: Jul. 15, 2024. [Online]. Available: <https://store.arduino.cc/products/arduino-nano-33-ble>
- [31] Y. Xu, S. Martínez-Fernández, M. Martínez, and X. Franch, “Energy Efficiency of Training Neural Network Architectures: An Empirical Study,” *Proceedings of the Annual Hawaii International Conference on System Sciences*, vol. 2023-Janua, pp. 781–790, Feb. 2023, [Online]. Available: <http://arxiv.org/abs/2302.00967>
- [32] M. Yan, H. Wang, and S. Venkataraman, “PolyThrottle: Energy-efficient Neural Network Inference on Edge Devices,” *ArXiv*, vol. abs/2310.1, Oct. 2023, [Online]. Available: <https://api.semanticscholar.org/CorpusID:264824281>
- [33] C. E. Tripp *et al.*, “Measuring the Energy Consumption and Efficiency of Deep Neural Networks: An Empirical Analysis and Design Recommendations,” *ArXiv*, vol. abs/2403.0, pp. 1–25, Mar. 2024, [Online]. Available: <http://arxiv.org/abs/2403.08151>
- [34] C. Ying, A. Klein, E. Real, E. Christiansen, K. Murphy, and F. Hutter, “NAS-Bench-101: Towards Reproducible Neural Architecture Search,” *36th International Conference on Machine Learning, ICML 2019*, vol. 2019-June, pp. 12334–12348, Feb. 2019, Accessed: Jul. 15, 2024. [Online]. Available: <https://proceedings.mlr.press/v97/ying19a.html>
- [35] P. Bakhtiarifard, C. Igel, and R. Selvan, “EC-NAS: Energy Consumption Aware Tabular Benchmarks for Neural Architecture Search,” in *ICASSP 2024 - 2024 IEEE International Conference on Acoustics, Speech and Signal Processing (ICASSP)*, IEEE, Apr. 2024, pp. 5660–5664. doi: 10.1109/ICASSP48485.2024.10448303.
- [36] L. Deng, “The MNIST database of handwritten digit images for machine learning research,” *IEEE Signal Process Mag*, vol. 29, no. 6, pp. 141–142, Nov. 2012, doi: 10.1109/MSP.2012.2211477.
- [37] A. Krizhevsky and G. Hinton, “Learning multiple layers of features from tiny images,” 2009. Accessed: Aug. 30, 2024. [Online]. Available: <http://www.cs.utoronto.ca/~kriz/learning-features-2009-TR.pdf>
- [38] B. M. Sazdić-Jotić *et al.*, “VTI\_DroneSET,” Mendeley Data. Accessed: Nov. 01, 2020. [Online]. Available: <https://data.mendeley.com/datasets/s6tggnp5n2/1>
- [39] A. Pathak, Y. C. Hu, and M. Zhang, “Where is the energy spent inside my app?: Fine grained energy accounting on smartphones with eprof,” *EuroSys’12 - Proceedings of the EuroSys 2012 Conference*, pp. 29–42, 2012, doi: 10.1145/2168836.2168841.
- [40] A. Krizhevsky, I. Sutskever, and G. E. Hinton, “ImageNet classification with deep convolutional neural networks,” *Commun ACM*, vol. 60, no. 6, pp. 84–90, 2017, doi: 10.1145/3065386.
- [41] K. Simonyan and A. Zisserman, “Very deep convolutional networks for large-scale image recognition,” in *3rd International Conference on Learning Representations, International Conference on Learning Representations, ICLR, 2014*, pp. 1–14. doi: 10.48550/arxiv.1409.1556.
- [42] C. Szegedy *et al.*, “Going deeper with convolutions,” in *2015 IEEE Conference on Computer Vision and Pattern Recognition (CVPR)*, IEEE, Jun. 2015, pp. 1–9. doi: 10.1109/CVPR.2015.7298594.
- [43] K. He, X. Zhang, S. Ren, and J. Sun, “Deep residual learning for image recognition,” in *2016 IEEE Conference on Computer Vision and Pattern Recognition (CVPR)*, IEEE, Jun. 2016, pp. 770–778. doi: 10.1109/CVPR.2016.90.
- [44] J. Redmon, S. Divvala, R. Girshick, and A. Farhadi, “You Only Look Once: Unified, Real-Time Object Detection,” in *2016 IEEE Conference on Computer Vision and Pattern Recognition (CVPR)*, IEEE, Jun. 2016, pp. 779–788. doi: 10.1109/CVPR.2016.91.
- [45] EuroStat, “European Environment Agency - Glossary.” Accessed: Sep. 16, 2024. [Online]. Available: <https://ec.europa.eu/eurostat/>



## PROPOSITION OF LABORATORY EQUIPMENT AND ITS UTILISATION FOR COMPLEX BATTLEFIELD IP NETWORK SIMULATION

DORĐE NEŠKOVIĆ

School of Electrical Engineering & Vlatacom Institute, Belgrade, [djordje.neskovic@vlatacom.com](mailto:djordje.neskovic@vlatacom.com)

MARKO MARKOVIĆ

School of Electrical Engineering & Vlatacom Institute, Belgrade, [marko.markovic@vlatacom.com](mailto:marko.markovic@vlatacom.com)

LARA KAŠČA

School of Electrical Engineering & Vlatacom Institute, Belgrade, [lara.kasca@vlatacom.com](mailto:lara.kasca@vlatacom.com)

STEFAN STANKOVIĆ

School of Electrical Engineering & Vlatacom Institute, Belgrade, [stefan.stankovic@vlatacom.com](mailto:stefan.stankovic@vlatacom.com)

MIROSLAV PERIĆ

Vlatacom Institute, Belgrade, [miroslav.peric@vlatacom.com](mailto:miroslav.peric@vlatacom.com)

MLADEN KOPRIVICA

School of Electrical Engineering, Belgrade, [kopra@etf.rs](mailto:kopra@etf.rs)

DEJAN DRAJIC

School of Electrical Engineering, Belgrade, [ddrajic@etf.rs](mailto:ddrajic@etf.rs)

**Abstract:** This paper gives a proposition for laboratory equipment and its use for simulation of effects of network topology and link state reconfiguration during battlefield operations. All equipment presented in this paper is based on open source software solutions and well-known hardware development platforms in order to minimize equipment cost as well as provide a simulation environment that is independent of any single manufacturer. Utilization of open source solutions gives us a level of security as it lessens a chance of traditional vendor abuse in more unfortunate circumstances. The core of the laboratory is based on a GNS3 simulator, which can be installed on all three major operating systems (Linux, Windows and Mac) and has the capability of simulating a network that can be added in between two physical end devices that we wish to test in various battlefield scenarios using highly available network adapters. In addition to that, we will focus on network intermediate devices (switches and routers) that are not dependent on any single manufacturer and are open source solutions that can be used for future development of secure and fully-known equipment. We present expected results for the transition of encrypted and unencrypted traffic.

**Keywords:** Network Simulation, Open Source Solutions, Battlefield Communication, GNS3 Simulator, Secure Network Solutions.

### 1. INTRODUCTION

Network simulation [1] plays a crucial role in testing and evaluating network performance, design, and security. It provides a controlled environment to model, analyze, and predict the behavior of real-world networks without the high costs and risks associated with live testing. In the modern world, where digital communication and data exchange form the backbone of various industries, ensuring the reliability, efficiency, and security of network infrastructures is paramount. Network simulation emerges as an indispensable tool for testing and evaluating network performance and behavior. It allows us to create virtual models of network environments. Setting up physical network infrastructures for testing purposes can be prohibitively expensive. Network simulation reduces the

need for physical hardware, allowing for comprehensive testing and experimentation without significant financial investment. Testing new configurations, protocols, or security measures on a live network carries inherent risks, including potential downtime or data breaches. Network simulations provide a safe environment to test and validate changes before deploying them in a live setting. Simulations can easily scale to model networks of various sizes, from small local area networks (LANs) to vast wide area networks (WANs). This flexibility allows for testing different scenarios and configurations, ensuring the network can handle future growth and diverse conditions. By simulating network traffic and user behavior, we can analyze the performance of a network under various loads and conditions. This helps in identifying bottlenecks, optimizing resource allocation, and enhancing overall network efficiency. New networking protocols can be rigorously tested in a simulated environment before being

rolled out. This ensures compatibility and performance standards are met, reducing the risk of deployment failures. Network simulations are invaluable for security testing, allowing for the assessment of network vulnerabilities and the effectiveness of security measures against potential threats. Simulated attacks and defenses help in building robust security protocols and incident response strategies. They facilitate learning and skill development in a risk-free setting. We can experiment with cutting-edge technologies and innovative network designs without the constraints of physical limitations. Simulations foster innovation by providing a sandbox environment for testing novel ideas and concepts. Network simulation is a powerful and versatile tool that enhances the capability to test, analyze, and optimize network performance, security, and scalability. It offers a risk-free, cost-effective, and flexible approach to network testing, ensuring that real-world deployments are reliable, efficient, and secure. This is all especially important in battlefield IP network simulations, which are the focus of this paper.

The focus of this paper is a proposal for network laboratory setup and its use for simulation of effects of network topology and link state for dynamic battlefield IP network simulation. The proposed solution allows network performance reconfiguration to simulate dynamic conditions and hard circumstances to simulate real-life problems in war. The laboratory proposed in this paper is based on free open source software and well-known and easily accessible hardware solutions.

The rest of the paper is organized as follows: The second section provides analysis of hardware and software needed for network simulation. The third will focus on open source hardware and software solutions for real-life network routers. The fourth section will focus on a simple laboratory proposition for battlefield IP network simulation. The fifth section concludes the paper and provides remarks on the expected performance of the proposed solution.

## 2. NETWORK SIMULATION SOLUTION

The core part of a network simulation laboratory is a network simulator itself. In this paper we will focus on GNS3 (Graphical Network Simulator-3) [2] [3], which is network simulation software that allows users to design, configure, and test complex network topologies. It provides a graphical interface where users can drag and drop various network devices, such as routers, switches, and firewalls, to create virtual network environments. One of the key features of GNS3 is its ability to integrate real network device images, enabling users to emulate real-world network hardware and software. This allows for highly realistic network simulations, making it an invaluable tool for learning, testing configurations, and troubleshooting network issues without the need for physical equipment. GNS3 supports a wide range of devices and can emulate Cisco IOS [4], Juniper [5], and other network vendors' operating systems. Additionally, it can integrate with other virtualization technologies [6] such as VMware [7] and VirtualBox [8], further expanding its utility and flexibility. Overall, GNS3 is a

powerful platform for network simulation, offering a practical, cost-effective way to gain hands-on experience with network design and troubleshooting. Its extensive features and realistic emulation capabilities make it an essential tool for both experimentation and professional development in the field of networking.

Integrating real equipment in GNS3 enhances its simulation capabilities by connecting virtual networks with physical devices. This setup allows users to test configurations and troubleshoot issues in a hybrid environment, combining virtual and real-world elements. By connecting GNS3 to actual routers, switches, and firewalls, users can validate configurations and network designs with greater accuracy. This integration is beneficial for advanced network training, real-world scenario testing, and bridging the gap between theoretical simulations and practical implementations.

GNS3 simulator can be installed on all three major operating systems (Linux, Windows and Mac); this offers complete flexibility for use with a computer that might already be available. The computer used for network simulation in the example given in this paper was a laptop with a Linux-based operating system, Ubuntu 22.04.4 LTS [9]. Within GNS3, Cisco router IOS images were used for router emulation. Connection between devices in an emulated environment could be either local with simulated Ethernet cables or serial for longer link simulation; on those links, various network conditions could be simulated, like delay for long-distance communication, packet loss, corruption, packet drop frequency, and custom filter options. This represents a great tool for complex battlefield network simulation of hard conditions and unstable networks.

GNS3 has within its emulated components a dedicated component for Cloud; this component is capable of connecting physical Ethernet interfaces. Since most personal computers have only one, or no, physical Ethernet port, use of Ethernet-to-USB adapters is an adequate solution (speed of 1 Gbps is recommended but not necessary). These adapters allow the connection of real hardware and end devices into a simulated environment. For example, two devices for secure communication could be connected to points in a simulated network and tested in various conditions and against attacks.

## 3. OPEN SOURCE ROUTERS

Open source software for network routers offers a cost-effective and flexible solution for managing network infrastructure. Open source router software is free to use, significantly reducing the cost compared to proprietary solutions. Utilization of open source solutions gives us a level of security as it lessens a chance of traditional vendor abuse in more unfortunate circumstances, as we are fully aware of its source code and each function. Users can modify the source code to meet specific requirements, offering unparalleled flexibility and control over network configurations. Open source projects benefit from active communities that contribute to software development, security updates, and troubleshooting, ensuring continuous improvement and

support. This allows for transparency, where code can be audited for security vulnerabilities, leading to more secure implementations. Many open-source router platforms offer advanced features and capabilities typically found in high-end commercial products, making them suitable for a wide range of applications, from home use to enterprise-level deployments. Overall, open-source software for network routers empowers users with cost-effective, customizable, and robust solutions for managing network infrastructure. Most of these solutions are Linux-based [10], like OpenWrt [11], which provides a fully writable file system with package management, allowing users to customize the firmware to their needs. OpenWrt supports a wide range of devices and offers features like advanced network monitoring, QoS (Quality of Service), and VPN capabilities. One other notable solution is DD-WRT [12], which is designed to replace the stock firmware on many commercial routers. It enhances router capabilities with features like increased range, improved signal strength, VPN support, and extensive networking tools. It's particularly favored for its user-friendly interface and stability.

But some Linux-based operating systems have the capability of adding router-like capabilities like Ubuntu, which supports IP forwarding. For the purpose of this research, two Kria [13] [14] robotics development kits with Ubuntu OS have been set up as routers. The archived port speed was 1 Gbps, which matches the specified port speed of the development kit. In the ever changing environment of battlefield simulations, probably the best routing algorithm is OSPF since it only needs to be aware of neighboring networks to set up, and it is supported by Ubuntu.

#### 4. LABORATORY FOR BATTLEFIELD IP NETWORK SIMULATIONS

The basic idea for the proposed laboratory is to have one PC with GNS3 installed on it with two Ethernet to USB adapters (preferably 1 Gbps), and within GNS3 installed images for routers that are most commonly used in real-life networks that we are trying to emulate; for example, in case of the environment used for this paper, Cisco IOS images were used, and for the sake of testing, both 100 Mbps and 1 Gbps were used. For link variable state testing, we propose a simple network with two routers, each one connected to one physical interface through a cloud feature, and a serial link between them (a serial link is used so link state changes such as delay work as they should). As seen in figure 1.

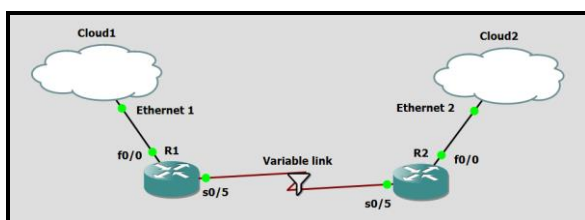


**Figure 1.** Simple emulated network for variable link state testing

The filtering feature allows for simulation of real-life link states like delay, packet corruption and packet loss. Adding those circumstances to the serial link allows us to test the behavior of devices or networks connected to physical interfaces in such conditions and to explore and develop necessary solutions on how to adapt devices and programs to overcome such situations. The proposition for what to connect to physical interfaces is to not connect just two end devices but to create networks that would be as close to the ones that would be used in real scenarios. For example, the first component behind the physical interface on each side should be a router, as it is most commonly the case in real life. Unlike an emulated one, a real hardware solution is the better option, since it is the only one that we have access to outside the laboratory environment. The router chosen for this research is the already mentioned Linux router based on Ubuntu with IP forwarding enabled and installed on a single-board computer development kit with two Ethernet ports. This allows us to be fully aware of router functionality and adapt it and configure it to specific needs. One port of the router is connected to a simulated network, which should, for experimentation purposes, be considered a public access network, while the other port should be connected to an Ethernet switch, so it would not limit us to just one device. The number of devices used for experimentation is limited by ports on the used switch; additionally, Wi-Fi access point could be used for testing wireless devices, but the best results are achieved when end devices are connected directly to the switch since this removes one more possible point of failure.

The other simple proposal that might be used for simulation of an environment with a lot of rerouting and circumstances when links are destroyed or down because of a power outage, might be simplified by emulating a slightly more complex network, as shown in figure 2. When testing the capabilities of our end devices and network devices, deleting links and connecting them again while communication is in progress would give a great idea of how a system of interest would function in such circumstances. These two simple network topologies give us a glimpse into the capability of such a laboratory solution. Furthermore, this could be expanded and combined to emulate complex networks weary close to the real-life scenario.

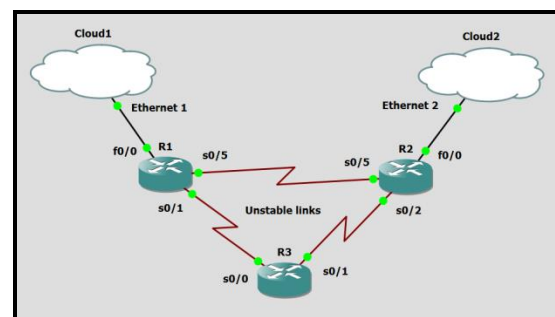


**Figure 2.** Simple emulated network for unstable link and rerouting testing

This is a simple and cheap solution for emulating complex and dynamic network environments. Also a great feature of GNS3 is that any link in a virtual

network can be analyzed separately via Wireshark [15], allowing for detailed traffic analysis. Also, for example, for testing of cryptography devices, this feature allows us to see what potential attacker that intercepted network traffic sees, and is helpful to figure out weaknesses in our systems.

One more notable feature that might be useful is the capability of GNS3 to connect to virtual machines hosted on the same device, which already has a virtual PC (VPC) as a component. This could be integrated into a simulated network to add traffic and take up resources to simulate a busy network. Example shown in figure 3.

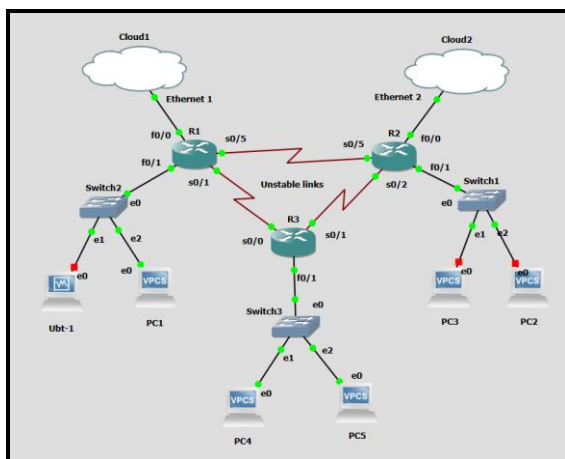


**Figure 3.** Example of virtual network with virtual PC to simulate realistic network conditions

This will allow us to add additional variability into simulated network conditions that reassemble real-life solutions more realistically. But users should keep in mind that the size of the simulated network is limited by the resources available to the device on which GNS3 is hosted. Each emulated device in a virtual network occupies resources, and the main limiter of network size is RAM memory. The utilization of RAM memory is defined by each component added to a network and GNS3 provides us with information on how much of it is occupied; it is not advisable for this value to pass 50%. Another important remark is that whenever a virtual network is connected to the real one, a significant loss of bandwidth will happen simply because the transition between networks is imperfect. Although all network equipment, real and emulated, is specified at 1 Gbps and works perfectly in normal conditions, the maximum network speed reached no more than 30 Mbps in a laboratory environment. Encryption of data between two end points was tested when implemented on real network hardware and emulated routers and gives expected results in limiting network speed. Also, there is a constant delay of approximately 10 ms for translation between a real and a virtual network per physical interface. These are serious limitations, but they themselves could be taken as part of wartime battlefield conditions and used as a baseline limitation of IP network.

## 5. CONCLUSION AND REMARKS

This paper highlights the critical role of network simulation in testing and evaluating network performance, design, and security, especially in the context of dynamic battlefield IP network simulations. By leveraging tools like GNS3, network simulations provide a cost-effective and risk-free environment for rigorous testing and validation of network configurations and protocols. The proposed laboratory setup, utilizing open-source software and accessible hardware, demonstrates a practical approach to simulating real-life network conditions, including the challenging scenarios encountered in warfare.

The use of GNS3 allows for realistic emulation of network hardware and the integration of physical devices, enhancing the simulation's accuracy and utility. By incorporating open-source router solutions like Linux-based routers, the laboratory setup remains flexible and customizable, supporting a wide range of testing scenarios. The proposed configurations for simulating network topology changes and link state variations offer valuable insights into the resilience and adaptability of network infrastructures under adverse conditions.

Despite some limitations, such as bandwidth reduction and latency when transitioning between virtual and real networks, these simulations provide a valuable baseline for understanding and improving network performance in critical environments. Overall, the methodology and tools discussed in this paper represent a significant advancement in network simulation, enabling robust testing and optimization of battlefield IP networks to ensure their reliability, efficiency, and security in real-world deployments.

The future work plan is to create a plug-and-play environment for testing complex network encryption devices to their limits with attack simulation along the simulation of network conditions.

## 6. ACKNOWLEDGEMENT

This paper was supported by Vlatacom Institute of High Technologies under the project P176.

## References

- [1] PETROVIĆ,R., SIMIĆ,D., STANKOVIĆ,S., PERIĆ,M.: Educational Platform for Examining the Influence of the Simulated Satellite Link on Overall Communication inside of Different IoT Systems, Proceedings of the 16th International Conference on Advanced Technologies, Systems and Services in Telecommunications (TELSIKS), 2023
- [2] <https://www.gns3.com/>
- [3] P. Gil, G. J. Garcia, A. Delgado, R. M. Medina, A. Calderón and P. Marti, "Computer networks virtualization with GNS3: Evaluating a solution to optimize resources and achieve a distance learning," *2014 IEEE Frontiers in Education Conference (FIE) Proceedings*, Madrid, Spain, 2014, pp. 1-4, doi: 10.1109/FIE.2014.7044343.
- [4] <https://www.cisco.com/>
- [5] <https://www.juniper.net>
- [6] G. Aryotejo, E. A. Sarwoko, A. Sugiharto and M. M. Hakim, "Performance of Virtual Machine Managers for Computer Network Learning," 2021 5th International Conference on Informatics and Computational Sciences (ICICoS), Semarang, Indonesia, 2021, pp. 155-159, doi: 10.1109/ICICoS53627.2021.9651899.
- [7] <https://www.vmware.com/>
- [8] <https://www.virtualbox.org/>
- [9] <https://releases.ubuntu.com/jammy/>
- [10] C. E. Palazzi, M. Brunati and M. Roccetti, "An OpenWRT solution for future wireless homes," 2010 IEEE International Conference on Multimedia and Expo, Singapore, 2010, pp. 1701-1706, doi: 10.1109/ICME.2010.5583223.
- [11] <https://openwrt.org/>
- [12] <https://dd-wrt.com/>
- [13] M. A. Aslam, S. Kumar and R. Holsmark, "An Efficient Router Architecture and Its FPGA Prototyping to Support Junction Based Routing in NoC Platforms," 2013 Euromicro Conference on Digital System Design, Los Alamitos, CA, USA, 2013, pp. 297-300, doi: 10.1109/DSD.2013.121.
- [14] <https://www.amd.com/en/products/system-on-modules/kria/k26/kr260-robotics-starter-kit.html>
- [15] <https://www.wireshark.org/>





# PERFORMANCE CHARACTERIZATION OF SECURE IP COMMUNICATION SYSTEMS FOR VARIOUS INTERACTIVITY LEVEL APPLICATIONS

LARA KAŠCA

School of Electrical Engineering & Vlatacom Institute, Belgrade, [lara.kasca@vlatacom.com](mailto:lara.kasca@vlatacom.com)

ĐORĐE NEŠKOVIĆ

School of Electrical Engineering & Vlatacom Institute, Belgrade, [djordje.neskovic@vlatacom.com](mailto:djordje.neskovic@vlatacom.com)

MARKO MARKOVIĆ

School of Electrical Engineering & Vlatacom Institute, Belgrade, [marko.markovic@vlatacom.com](mailto:marko.markovic@vlatacom.com)

STEFAN STANKOVIĆ

School of Electrical Engineering & Vlatacom Institute, Belgrade, [stefan.stankovic@vlatacom.com](mailto:stefan.stankovic@vlatacom.com)

MIROSLAV PERIĆ

Vlatacom Institute, Belgrade, [miroslav.peric@vlatacom.com](mailto:miroslav.peric@vlatacom.com)

**Abstract:** *This paper describes a measurement methodology for characterizing the performance of secure communication systems, with a particular focus on the third layer of the OSI model (Layer 3). Special emphasis is placed on analyzing the impact of network characteristics such as delay and packet error rate on Quality of Service (QoS). The network environment is simulated using multiple routers and links, incorporating the mentioned network parameters that will be varied. We have presented impact on various types of interactive communications, such as VoIP audio data and video streaming. Special care is also taken on differences when using encryption method.*

**Keywords:** *Secure communication systems, Quality of Service, VoIP intelligibility, Video streaming, Network simulation*

## 1. INTRODUCTION

In battlefield scenarios, communication networks face numerous challenges that can impact link reliability. The reliability of the link, aside from the drop of the link itself, can be reflected in, for example, among the others, the packet delay and the number of error packets. These factors are critical for the performance and effectiveness of military operations and should therefore be addressed. Additionally, encrypted communications are crucial in contexts where security and privacy are paramount, such as in military, governmental and corporate environments, for reasons like confidentiality, protection from eavesdropping, data integrity, handling of sensitive information etc.

In military contexts, the exchange of specifically audio and video data serves as a pivotal component for real-time communication, coordination and situational awareness. Encrypted radio transmissions facilitate rapid dissemination of commands and updates, crucial for prompt decision-making and synchronized actions. Meanwhile, live video feeds from aerial platforms such as cameras and drones provide surveillance, target identification and precise mission planning.

This study will focus on evaluating the audio and

video quality, specifically voice data and video streaming, by manipulating parameters in a hybrid network using GNS3 software. The network will include multiple routers configured with OSPF protocol inside GNS3 and two Linux PCs on the end sides of the network. By adjusting parameters of interest and varying input signal characteristics, we aim to assess the resulting audio and video quality.

Quality of Service (QoS) in VoIP and video streaming directly impacts user experience by managing key parameters such as latency, jitter and packet loss, which are crucial for maintaining clear voice communication and high-quality video playback. QoS ensures that network resources are efficiently utilized and prioritizes traffic to minimize delays and packet loss, thereby enhancing overall service reliability and user satisfaction.

This paper will also demonstrate how various softwares and applications can be used for networking purposes and for assessing the quality of audio/speech and video. Specifically, this paper utilized GNS3, Wireshark, VLC, FFmpeg, qTox, and the Linux Ubuntu 22.04 operating system. In this paper, an improvement on work [1] is introduced by simulating the desired network environment without the use of certain physical devices.

Chapter two provides an overall network configuration description and outlines the differences for two test scenarios: one used for evaluating audio quality and the

other for video streaming. Chapter three outlines the methodology for obtaining objective speech quality metrics, discusses relevant theoretical aspects and presents the resulting quantitative values, all adjusted for the serbian language. Analogously, chapter four details the setup for evaluating video streaming quality, followed by observational outcomes in form of subjective assessments and comments. Chapter five discusses the results and concludes the study.

## 2. NETWORK CONFIGURATION

As mentioned in introduction, a hybrid setup was used: GNS3 on Linux PC Eva (IP address: 192.168.2.13) on one side, in conjunction with a physical switch and another PC, Bob (IP address: 192.168.1.11), on the other side. The combination of the cloud and eno/eth interface enables 'exiting' the GNS3 environment as well as the host computer itself, providing connectivity with Bob's PC and thus creating a hybrid setup.

Routers R5 and R6 are connected to the networks of interest and the topology between them consists of four routers (R1-R4) connected in a square constellation with a cross-connection, simulating real life network, providing a backup path in case of a link drop. The topology of the entire network is shown in Figure 1 and the addresses of the routers' interfaces are listed in table 1. Routers are configured with the OSPF protocol.

Eva, although the GNS3 was launched on it, was used as an end device, accessing the Eva's terminal from the GNS3 environment using a later defined tap0 interface (192.168.2.25).

For each of the setups explained below, the same analysis was performed both with and without using IPsec, which was implemented within the GNS3 environment between routers R5 and R6. IPsec stands for Internet Protocol Security and is a secure network protocol suite that authenticates and encrypts packets of data to provide secure encrypted communication over IP. [2]

**Table 1.** Routers' interface names and addresses

Router	Interface	Interface address
1	f0/1	172.24.15.1
	s0/2	172.24.12.1
	s0/3	172.24.13.1
2	s0/1	172.24.12.2
	s0/3	172.24.23.1

	s0/4	172.24.24.1
3	s0/1	172.24.13.2
	s0/2	172.24.23.2
	s0/4	172.24.34.1
4	f0/1	172.24.46.1
	s0/2	172.24.24.2
	s0/3	172.24.34.2
5	f0/1	172.24.15.2
	f1/0	192.168.1.12
6	f0/1	172.24.46.2
	f2/0	192.168.2.22

### 2.1. Audio test setup

In the first part of the testing, when the focus was on audio data, communication was established between Bob and Eva using the qTox software. qTox is a completely free and open source, end-to-end encrypted messenger, focusing on user's privacy and security. [3] It supports messages, audio and video calls. Therefore, qTox has the ability to facilitate voice over IP (VoIP), enabling users to make voice and video calls using internet protocols for transmission which matches this study focus. Namely, the focus of the QoS testing was on speech intelligibility, as speech, unlike other audio data, is crucial in military applications.

Here and later during testing, the connection establishment was verified using ping. From there on, in qTox Bob's system sound was selected as the input sound source instead of microphone, while on Eva, the output sound was recorded in .wav format using FFmpeg. FFmpeg is a free and open-source software comprising a suite of libraries and programs for handling video, audio and other multimedia, with its core being a command-line tool. [4] Following call establishment, audio files (whose content will be explained in the next chapter) were played in the background on Bob using a preinstalled media player, thus being sent over the network and recorded on the other side of the topology.

Within GNS3, various filters were applied, including packet error rate (abbreviated in later text as PER) and link delay in combination with jitter effect. These filters were applied to the links through which the traffic passed (which can be seen, represented by a funnel icon, in Figure 1). The specific values used will be listed in the corresponding chapters.

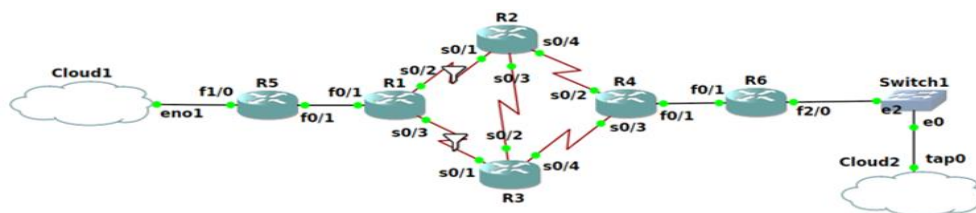


**Figure 1.** GNS3 network topology with interface labels and filtered links

### 2.2. Video streaming test setup

During testing of video stream behavior VLC media player ([5]) was used as a streaming platform, running as a server on Bob and as a client on Eva. VLC, widely known for playing movies, music and other media files, is also highly versatile and useful for various other purposes like streaming, allowing you to broadcast a media stream from one device or receive it on another via network or internet. UDP protocol and port 1234 were used. Similar to the VoIP testing, filters were applied to the links, with their specific values to be provided later. In Figure 2, it can be seen how video traffic appears in Wireshark before, during and after the establishment of IPsec. It can be noticed that the source and destination addresses, which initially show the real addresses of the end devices are changed afterward to the addresses of the routers between which the protocol is established.

### 3. VOIP AUDIO DATA

The quality of the audio signal regarding speech intelligibility in the various rooms/halls like classrooms, offices, concert halls, sports arenas etc. and on various channels (telecommunications systems, VoIP, etc.) can be determined using different objective measures, such as Speech Transmission Index (in further text: STI) factor, RASTI (stands for: rapid STI), STIPA etc. Methods of determining objective parameters are diverse and complex and they evolve over time. [6]

Before objective measures of speech intelligibility were developed, subjective methods were employed, requiring the participation of many individuals and extensive statistical analysis. In one widely cited publication, [7], it is shown that STI is correlated with subjective intelligibility scores from 167 different transmission channels obtained using pseudowords (also abbreviated as PB). Many research studies and papers have repeated and produced similar results. A graph from

tests are more time-consuming and obtained results can sometimes be difficult to compare with one another, e. g., due to the different participants, which however, in some situations, if chosen properly, can be an advantage because it introduces diversity of listeners and their auditory abilities ([9], [10]).

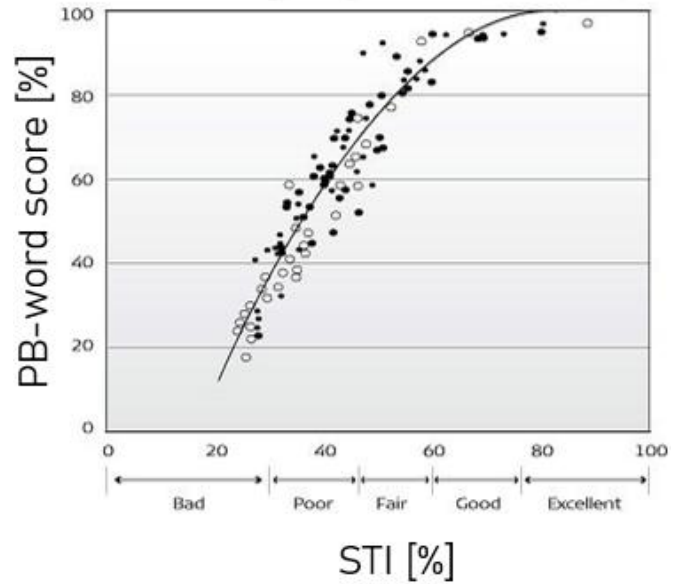


Figure 3. Relation between STI and PB-word score

One popular method (also used in [8], [9], [10], [11]) for assessing speech intelligibility involves using nonsense words or syllables in acoustic experiments known as logatomes or mentioned pseudowords. Logatomes are brief, meaningless words created by altering at least one letter in an existing word of specific language or combining various bigrams/trigrams. Speech contains multiple layers of information/redundancy that provide additional cues for understanding.

No.	Time	Source	Destination	Protocol	Length	Info
3349	22.807192	192.168.1.11	192.168.2.25	UDP	194	33445 → 33445 Len=152
3350	22.816598	192.168.2.25	192.168.1.11	UDP	274	33445 → 33445 Len=232
3351	22.817319	192.168.1.11	192.168.2.25	UDP	194	33445 → 33445 Len=152
3352	22.826844	192.168.2.25	192.168.1.11	UDP	274	33445 → 33445 Len=232

a)

7846	1804.212481	172.24.46.2	172.24.15.2	ISAKMP	150	Identity Protection (Main Mode)
7847	1804.253449	172.24.15.2	172.24.46.2	ISAKMP	346	Identity Protection (Main Mode)
7848	1804.273147	172.24.46.2	172.24.15.2	ISAKMP	346	Identity Protection (Main Mode)
7849	1804.314003	172.24.15.2	172.24.46.2	ISAKMP	150	Identity Protection (Main Mode)

b)

8025	2108.274415	172.24.15.2	172.24.46.2	ESP	166	ESP (SPI=0x673eaf9e)
8026	2108.284202	172.24.46.2	172.24.15.2	ESP	166	ESP (SPI=0xce272467)
8027	2108.284450	172.24.15.2	172.24.46.2	ESP	166	ESP (SPI=0x673eaf9e)
8028	2108.304535	172.24.46.2	172.24.15.2	ESP	166	ESP (SPI=0xce272467)

c)

Figure 2. Wireshark capture of video traffic before (a), during (b) and after (c) IPsec establishment

one of these ([8]) is shown in Figure 3. A literature review uncovers a wide array of subjective tests, primarily concerning the selection of test materials ([6]). Subjective

The redundancies that will be explained here are: acoustic, phonetic and lexical. Acoustic redundancy helps listeners through sound characteristics; phonetic is

achieved by reinforcing phonemes and lexical redundancy through contextual clues within the language. These forms of redundancy help ensure effective communication, even when the sound transmission medium, which affects the speech signal itself, is not ideal, whether it is a communication channel like VoIP or room acoustics.

Logatomes are convenient for measuring speech intelligibility because they lack contextual information found in real-life speech, enabling researchers to focus solely on phonetic processing and recognition without the influence of external factors. Logatomes differ across languages as they adhere to each language's phonotactic rules. Some examples of logatomes in Serbian language are: mumi, fase, rare, džudi, šizu... Due to gender-specific vocal characteristics, two distinct versions of logatomes are recorded—one tailored for female voices and another for male voices—reflecting the nuanced differences in speech patterns and phonetic traits between genders.

Experiments were conducted by playing on Bob's side five audio signals with different logatome sets consisting of fifty logatomes spoken by a female and fifty spoken by male and recording them using FFmpeg on Eva. Each set is phonetically and structurally balanced.

The network parameters that were varied during different audio playbacks, excluding the original one, were: 1) delay and jitter together, which were 10ms and 2ms, respectively; 2) PER, which was 15%; 3) PER which was 25% and 4) a combination of delay+jitter/PER of  $10\pm 2\text{ms}/20\%$ . The entire explained procedure was repeated without and with the use of IPsec.

Collected recordings were reproduced offline to listeners, on headphones and in quiet surroundings, who noted what they heard. By comparing with the correct responses, the quantity of correctly interpreted words for each scenario was obtained. Multiplying by 0.02 (or 2%) yields the value of the STI factor, which ranges from 0 to 1 (or 0% - 100%), determined for both female and male voice and graphically shown, expressed as a percentage, on Figure 4.

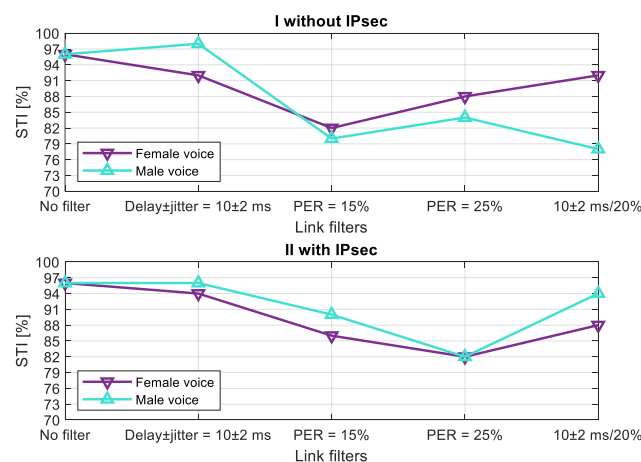


**Figure 4.** Comparison of female and male voice intelligibility without and with IPsec

For native language speakers, the relationship between STI and speech quality can be expressed using the following scale ([12]) with five bands:

- STI  $\in \{0, 0.3\}$  — bad quality,
- STI  $\in \{0.3, 0.45\}$  — poor quality,
- STI  $\in \{0.45, 0.6\}$  — fair quality,
- STI  $\in \{0.6, 0.75\}$  — good quality and
- STI  $\in \{0.75, 1\}$  — excellent quality.

Another measure, derived from STI, is CIS (stands for Common Intelligibility Scale) based on a mathematical relationship with STI ( $\text{CIS} = 1 + \log(\text{STI})$ ). [13] [14]

#### 4. VIDEO STREAMING

For testing quality of a video stream, Big Buck Bunny short movie was used. It is an animated film, made using Blender by Blender Institute. The video is freely available in multiple resolutions, including high ones like HD and 4K, making it suitable for testing different display qualities and resolutions. It is a widely recognized and standard piece of media. Different resolutions were downloaded from official source ([15]), in order from smallest to largest: 640x360 (360p), 853x480 (480p) and 1280x720 (720p). Tests, that is, streaming, were done, as mentioned earlier, using VLC Media Player.

The network parameters that were varied during different video playbacks, excluding the original one, were: 1) delay and jitter together, which were 10ms and 2ms, respectively; 2) PER, which was 2%; and 3) a combination of delay+jitter/PER of  $5\pm 1\text{ms}/1\%$ .

By simply observing the video quality on the receiving end, comments were derived from and listed in tables 2 and 3. It should be noted that all comments refer to the frames after the stream establishment and stabilization, during which image freezing is more likely to occur.

**Table 2.** Comments on video quality across resolutions and applied filters when not using encryption

Without IPsec			
Filter	360p	480p	720p
Original	Watchable, like on Tx side	Watchable, like on Tx side	Unwatchable, much worse, picture freezing
Delay±jitter 10±2 ms	Watchable, but sometimes choppy	Watchable, but sometimes choppy	Unwatchable, block artifacts, smearing, lagging and losing frames
PER = 2%	Unwatchable, rare occurrence of continuous scenes	Similar to 360p, more pronounced effect	Similar to 480p, even more pronounced effect
Delay±jitter 5±1 ms PER = 1%	Similar to PER = 2%	Similar to 360p, but worse	Completely unwatchable and unusable

**Table 3.** Comments on video quality across resolutions and applied filters when using encryption

With IPsec			
Filter	360p	480p	720p
Original	Watchable, like on Tx side	Watchable, little video stuttering	Unwatchable, more frequent stuttering, block artifacts
Delay±jitter 10±2 ms	Watchable, like on Tx side	Watchable, little video stuttering	Unwatchable, more frequent stuttering
PER = 2%	Unwatchable, rare occurrence of continuous scenes, mostly freezes rather than plays	Similar to 360p, more pronounced effect	Completely unwatchable and unusable
Delay±jitter 5±1 ms PER = 1%	Unwatchable, frequent video stuttering	Similar to 360p, block artifacts and smearing	Completely unwatchable and unusable

## 5. CONCLUSION

The speech intelligibility results show that when no filters were applied, the number of correctly interpreted words was the same without and with IPsec, for both male and female speech. On average, adding additional latency did not affect intelligibility, but increasing the packet error rate substantially degraded it. The combination of latency and PER highlighted that PER had a more significant impact. Male speech was generally understood as well as or better than female speech and IPsec did not considerably affect intelligibility. Any inconsistencies in conclusions could be due to different sets of logatoms used. Intelligibility did not drop below 75% in any scenario, indicating overall good quality.

For video quality, increasing resolution made the video more susceptible to degradation from filters. Even lower resolutions became unwatchable with more aggressive filters. Effects such as freezing, lagging, choppiness, block artifacts and smearing occurred more frequently with increasing degradation through filters. Also, video content could tolerate much lower PER levels compared to speech. Freezing, lagging and choppiness were unavoidable with higher resolutions. The observations and the data table show that IPsec did not impact video quality degradation.

Overall, this study explored the reliability of communication networks by evaluating audio and video quality under various network conditions. Using GNS3 software, a hybrid network was configured with multiple routers and Linux PCs, with a focus on voice data traffic and video streaming. The results showed that network parameters like delay, jitter and packet error rate noticeably affect speech intelligibility and especially video quality. Implementing IPsec provided secure communication and did not influence much in other ways except maybe introducing additional latency. The research highlighted the importance of Quality of Service (QoS) in managing network resources to maintain clear communication and high-quality video playback. The tools and methodologies demonstrated in this study offer valuable insights for optimizing communication networks.

## Acknowledgement

This paper was supported by Vlatacom Institute of High Technologies under the project P176.

## References

- [1] PETROVIĆ,R., SIMIĆ,D., STANKOVIĆ,S., PERIĆ,M.: *Educational Platform for Examining the Influence of the Simulated Satellite Link on Overall Communication inside of Different IoT Systems*, Proceedings of the 16th International Conference on Advanced Technologies, Systems and Services in Telecommunications (TELSIKS), 2023
- [2] <https://en.wikipedia.org/wiki/IPsec>
- [3] <https://www.linuxbabe.com/desktop-linux/install-qttox-messenger-on-linux>
- [4] <https://en.wikipedia.org/wiki/FFmpeg>
- [5] <https://www.videolan.org/vlc/download-ubuntu.html>
- [6] KUROWSKI,A., et al.: *A Novel Method for Intelligibility Assessment of Nonlinearly Processed Speech in Spaces Characterized by Long Reverberation Times*, Sensors, 2022, 22.4: 1641.
- [7] STEENEKEN,H.,J.,M., HOUTGAST,T.: *A physical method for measuring speech-transmission quality*, The Journal of the Acoustical Society of America, 1980, 67(1), 318–326. doi:10.1121/1.384464
- [8] <https://www.troldtekt.com/product-advantages/good-acoustics/advanced-acoustics/speech-intelligibility-and-speech-intelligibility-goals/>
- [9] KRUGER,K., GOUGH,K., HILL,P.: *A comparison of subjective speech intelligibility tests in reverberant environments*, Canadian Acoustics, 1991, 19.4: 23-24.
- [10] HODOSHIMA,N., ARAI,T.: *Effect of talker variability on speech perception by elderly people in reverberation*, Proceedings of the International Symposium on Auditory and Audiological Research. 2007. p. 383-388.
- [11] BRACHMAŃSKI, S.: *Automation of the logatom intelligibility measurements in rooms*, Archives of Acoustics, 2014, 32.4 (S): 159-164.
- [12] STEENEKEN,H.,J.,M.: *The measurement of speech intelligibility*, TNO Human Factors, Soesterberg, the Netherlands
- [13] BARNETT,P.,W., KNIGHT,R.,D.: *The Common Intelligibility Scale*, 1995, Proc. I.O.A. Vol 17, part 7.
- [14] BARNETT,P.,W.: *Overview of speech intelligibility*, 1999, Proc. I.O.A Vol 21 Part 5.
- [15] <https://peach.blender.org/download/>



# GRE TUNNEL UTILIZATION FOR MINIMIZING MULTI-VENDOR NETWORK EQUIPMENT ISSUES FOR VARIOUS TRANSMISSION CHANNELS

MARKO MARKOVIĆ

School of Electrical Engineering & Vlatacom Institute, Belgrade, [marko.markovic@vlatacom.com](mailto:marko.markovic@vlatacom.com)

LARA KAŠČA

School of Electrical Engineering & Vlatacom Institute, Belgrade, [lara.kasca@vlatacom.com](mailto:lara.kasca@vlatacom.com)

DORĐE NEŠKOVIĆ

School of Electrical Engineering & Vlatacom Institute, Belgrade, [djordje.neskovic@vlatacom.com](mailto:djordje.neskovic@vlatacom.com)

STEFAN STANKOVIĆ

School of Electrical Engineering & Vlatacom Institute, Belgrade, [stefan.stankovic@vlatacom.com](mailto:stefan.stankovic@vlatacom.com)

MIROSLAV PERIĆ

Vlatacom Institute, Belgrade, [miroslav.peric@vlatacom.com](mailto:miroslav.peric@vlatacom.com)

MLADEN KOPRIVICA

School of Electrical Engineering, Belgrade, [kopra@etf.rs](mailto:kopra@etf.rs)

GORAN MARKOVIĆ

School of Electrical Engineering, Belgrade, [gmarkovic@etf.rs](mailto:gmarkovic@etf.rs)

**Abstract:** In the realm of battlefield operations, where seamless communication is paramount, the utilization of all available networking equipment is indispensable. However, the diverse array of vendor equipment often poses compatibility challenges across different transmission channels. These issues are frequently rooted in the varying limitations of packet length among the equipment, leading to undesirable packet fragmentation and potential loss. To mitigate these challenges, we have explored the efficacy of GRE (Generic Routing Encapsulation) tunnel utilization. By employing GRE methodology, we can tailor packet length to optimize performance across specific transmission media and service types. Our focus lies particularly on high-interactivity applications crucial for battlefield environments, such as file transfer and video streaming, for both encrypted and unencrypted scenarios. We present the results of comprehensive experiments that have enabled us to identify optimal configurations for various scenarios, ensuring efficient communication.

**Keywords:** Multi-Vendor Network Equipment, GRE Tunneling, Battlefield Communication, Optimization.

## 1. INTRODUCTION

In the dynamic and high-stakes environment of battlefield operations, the importance of seamless and reliable communication cannot be overstated. Effective communication systems are the backbone of strategic coordination and operational success. However, the integration of networking equipment from various vendors often presents significant compatibility challenges, particularly across different transmission channels. One of the primary issues encountered is the disparity in packet length limitations among diverse equipment, which can lead to undesirable packet fragmentation and potential data loss. These fragmentation issues can critically impair the efficiency and reliability of communication, putting mission

outcomes at risk.

To address these challenges, our research has focused on the utilization of Generic Routing Encapsulation (GRE) tunnels. The principle of tunnels is to create a virtual network (overlay network) on top of a physical infrastructure (underlay network). This provides a logical interface that emulates a direct physical link connecting two sites, [1]. GRE tunnels allow for the encapsulation of a wide variety of network layer protocols, facilitating more flexible and efficient data transmission. By leveraging GRE methodology, we can customize packet lengths to align with the optimal performance parameters of specific transmission media and service types. Our investigation emphasizes high-interactivity applications that are essential in battlefield settings, such as file transfer and video streaming. These applications are

analyzed in both encrypted and unencrypted scenarios to ensure comprehensive understanding and applicability. In particular, the analysis focuses on the implementation of GRE over IPsec (Internet Protocol Security) to facilitate secure communication between multi-vendor environments. GRE over IPsec combines the flexibility of GRE tunneling with the robust security features of IPsec, providing a secure and versatile solution for network traffic encryption.

Our experimental approach involved using the File Transfer Protocol (FTP) to transfer a file while systematically varying the Maximum Transmission Unit (MTU) size to identify the fastest transfer rates. These tests were conducted under conditions with and without IPsec encryption to evaluate the impact of security protocols on performance. In parallel, we conducted video streaming experiments using VLC (VideoLAN Client), assessing video quality based on subjective user experiences to determine the optimal MTU settings for both encrypted and unencrypted scenarios.

The comprehensive data collected from these experiments has enabled us to pinpoint the most effective MTU settings for these applications, thereby enhancing the overall efficiency and reliability of communication systems in battlefield operations. These findings are crucial for ensuring that high-priority communications, such as confidential documents, orders in text form, and real-time video feeds, are transmitted with minimal delay and maximum fidelity. This is essential for supporting the success of military missions.

The remainder of this article is organized as follows: Section 2 provides an overview of the experimental setup and network and device configuration. This section details the hardware and software components used, the network topology, and the specific configurations applied to the devices involved in the experiments. Section 3 presents the results of our study, including performance metrics for file transfers over TCP and video streaming over UDP. The analysis covers both unencrypted and encrypted traffic, highlighting the differences in performance and any observed impacts on data integrity and transmission efficiency. Finally, Section 4 concludes the paper, summarizing the key findings and discussing their implications for future research and practical applications in network security and performance optimization.

## 2. EXPERIMENTAL SETUP AND NETWORK CONFIGURATION

In this section, we will provide a detailed overview of our work environment, covering network and device configurations. Operating in a multi-vendor setup, we use GRE tunnel to securely extend connectivity between different parts of our network. This configuration ensures dependable performance and secure communication across our infrastructure.

### 2.1. Experimental setup

Since we are discussing a multi-vendor environment and GRE tunnels, the main idea is to have two private Local Area Networks (LANs) communicating over a (secured) GRE tunnel, isolated from the rest of the network. Therefore, we require two endpoint routers (which are multi-vendor) whose interfaces connect their respective local private networks on one end, while their interfaces on the other end serve as the endpoints between which the GRE tunnel is established. On one side, we have a physical router in the form of a Linux device running Ubuntu, the Xilinx® Kria™ KR260 Robotics Starter Kit, further in the text, Kria. On the other side, there is a Cisco 3745 Router implemented in the GNS3 (Graphical Network Simulator-3) emulator environment, further in the text, RCisco.

GNS3 allows for the integration of virtual and physical devices to simulate complex networks. It utilizes Dynamips emulation software, originally designed to emulate Cisco routers, [2], to simulate Cisco IOS, [3]. This setup facilitates multi-vendor communication over GRE tunnel across a specific "complex" network topology between them. Figure 1. illustrates the experimental setup used for this purpose.

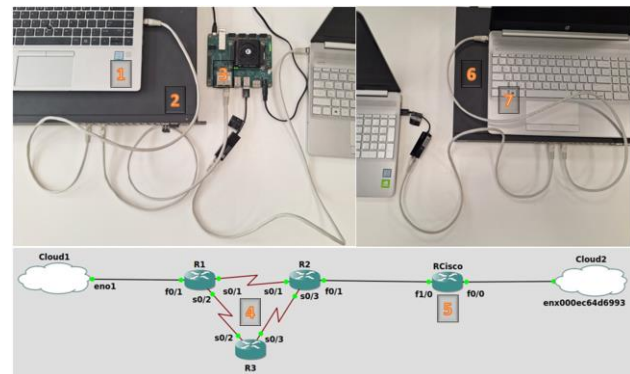


Figure 1. Experimental setup

On the figure above, the following are sequentially depicted:

- PC1 (1),
- DCN L3 Switch DCRS-5960; Switch1 (2),
- Kria (3),
- “Complex” Network (4),
- RCisco (5),
- DCN L3 Switch DCRS-5960; Switch2 (6),
- PC2 (7).

PC1 and Switch1 belong to the private network on the Kria side. The switch is included to demonstrate the expandability of the private network, though simplified for our case. Similarly, this applies to the private network on the RCisco side. Since these two PCs represent the communication endpoints, the GNS3 emulator runs on a third PC. The upper branch in the "complex" network between the GRE tunnel endpoints represents the current and main traffic path, while the lower branch serves as a backup path in case of main path failure, as a likely



scenario in military operations.

## 2.2. Network and device configuration

The following Table 1. displays the assigned IPv4 addresses for each of the devices/interfaces of interest. This is essential for network configuration, ensuring clarity in IP address allocation across key components.

**Table 1.** Assigned IPv4 addresses

Device/interface	IPv4 address with the prefix length
PC1	192.168.1.10/24
eth0 on Kria	192.168.1.1/24
USB on Kria	172.16.1.1/30
gre1 on Kria	10.0.0.1/30
f0/1 on R1	172.16.1.2/30
s0/1 on R1	172.16.3.1/30
s0/2 on R1	172.16.4.1/30
f0/1 on R2	172.16.2.2/30
s0/1 on R2	172.16.3.2/30
s0/3 on R2	172.16.5.1/30
s0/2 on R3	172.16.4.2/30
s0/3 on R3	172.16.5.2/30
f0/0 on RCisco	192.168.2.1/24
f1/0 on RCisco	172.16.2.1/30
tunnel0 on RCisco	10.0.0.2/30
PC2	192.168.2.20/24

To establish a GRE tunnel between the two multi-vendor routers, it is necessary to create a physical connection between them, i.e., between the USB interface on the Kria and the f1/0 interface on the RCisco. Initially, the OSPFv2 protocol is configured on R1, R2, and R3 (single area). OSPFv2 is a link-state routing protocol that employs a version of Dijkstra's shortest path first algorithm and is an open standard, [4]. In this way, traffic rerouting to the backup path is also enabled, in case of a main path failure. Currently, the Kria has only one static route defined to the network 172.16.2.0/30, via the USB interface as the outgoing interface, i.e., the next-hop IP address being the f0/1 interface of router R1. Similarly, the RCisco has only one static route defined to the network 172.16.1.0/30, via the f1/0 interface as the outgoing interface, i.e., the next-hop IP address being the f0/1 interface of router R2. After setting these static routes, the necessary physical connectivity is established. It is important to note that before establishing the GRE tunnel, the two private LANs must not be exposed to the rest of the network in any way to maintain the confidentiality of both private networks.

Now follows the configuration of the GRE tunnel. On the Kria side, the physical source of the tunnel will be the

USB interface (IP address 172.16.1.1), while the physical destination will be the f1/0 interface on the RCisco (IP address 172.16.2.1). Conversely, on the RCisco side, the physical source of the tunnel will be the f1/0 interface (IP address 172.16.2.1), while the physical destination will be the USB interface (IP address 172.16.1.1) on the Kria. The virtual interface gre1 on the Kria will be assigned the IP address 10.0.0.1/30, while the virtual interface tunnel0 on the RCisco will be assigned the IP address 10.0.0.2/30. Once the GRE tunnel is established, it is necessary to define one static route on each router. For the Kria, a static route to the network 192.168.2.0/24 (the private LAN on the RCisco side) needs to be defined via gre1 as the outgoing interface, i.e., 10.0.0.2 as the next-hop IP address. Similarly, on the RCisco, a static route to the network 192.168.1.0/24 (the private LAN on the Kria side) needs to be defined via tunnel0 as the outgoing interface, i.e., 10.0.0.1 as the next-hop IP address. This configuration enables communication between the LANs over the GRE tunnel. This brings us to our initial setup, where we will be able to examine the impact of changing the MTU on the traffic behavior of our applications.

The configuration on both the Kria and RCisco establishes a secure (GRE over) IPsec tunnel using IKEv1 (Internet Key Exchange version 1) for encryption and authentication, [5]. On the Kria router, StrongSwan is configured with AES-128 encryption, SHA-1 hashing, and MODP-1024 for Diffie-Hellman key exchange in Phase 1 (IKE). A pre-shared key is used for authentication between the local (172.16.1.1) and remote (172.16.2.1) endpoints. Phase 2 (IPsec) employs the same AES-128 encryption and SHA-1 hashing algorithms to protect traffic between the local subnet (192.168.1.0/24) and the remote subnet (192.168.2.0/24). Similarly, on the RCisco, IKEv1 Phase 1 is configured with AES-128 encryption, SHA-1 hashing, and Group 2 (MODP-1024) for key exchange, using the same pre-shared key for authentication. Phase 2 IPsec settings match those of the Kria – AES-128 for encryption and SHA-1 for hashing within a defined transform set. Next, we create a profile that utilizes this transform set. Finally, we apply the created profile to our tunnel0 (GRE) interface. Together, these configurations establish a robust and secure communication channel between the two networks. This brings us to our second setup, where we will be able to examine the impact of changing the MTU on the behavior of encrypted traffic in our applications.

The aforementioned encapsulations of the payload data, initially via a GRE tunnel and subsequently with IPsec, are illustrated in Figure 2. This figure also provides a comprehensive depiction of the packet structure at each stage of the process.

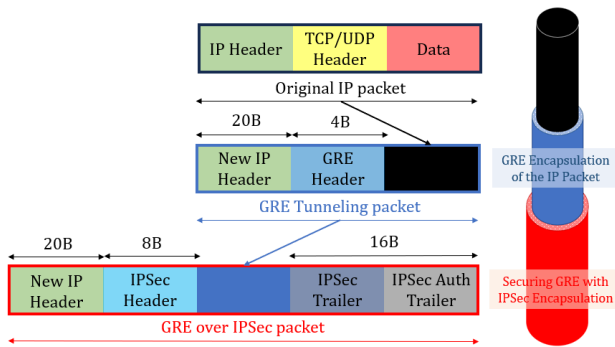


**Figure 2.** Detailed process of IP packet encapsulation using GRE tunnel and IPSec

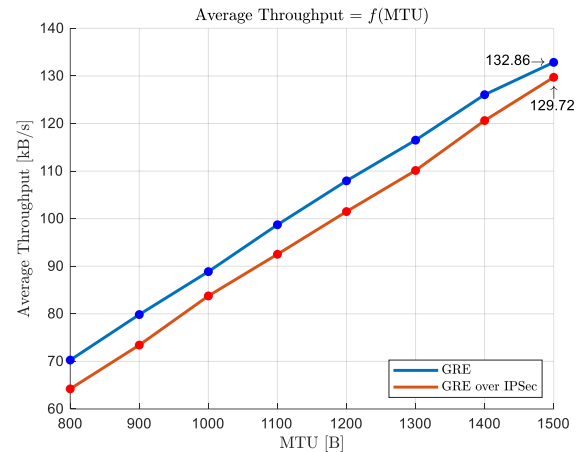


**Figure 3.** Average Throughput versus MTU

### 3. RESULTS AND DISCUSSION

The detailed results will now be presented, comparing encrypted and unencrypted traffic in parallel for each application.

#### 3.1. File transfer over TCP

Transmission Control Protocol (TCP) is a fundamental component of the TCP/IP suite, providing comprehensive transport layer services to applications. Positioned within the transport layer of the TCP/IP model, TCP ensures reliable communication by establishing, maintaining, and terminating connections between endpoints. Unlike User Datagram Protocol (UDP), TCP offers a more complex yet robust connection setup that ensures data integrity. TCP breaks down data streams into manageable units known as segments, which are reliably reassembled at the receiving end. This reliability is achieved through mechanisms that maintain the sequence of segments and allow for retransmission of any lost or corrupted data. TCP establishes a logical full duplex connection between application layer processes, ensuring bidirectional communication where data is transmitted in sequence and acknowledged upon receipt, [6].

As a file transfer protocol, FTP has been widely adopted for many years due to its robustness and simplicity in transferring files over networks. It provides a straightforward method for users to upload and download files between their local systems and remote servers, [7]. In our case, a 1MB file was used (generated as a random file of that size) to investigate the behavior of both encrypted and unencrypted traffic when changing the MTU size.

In Figure 3, a comparative scenario is depicted for both unencrypted and encrypted file transfers, showing achieved average throughput while varying the MTU size.

Smaller MTU means each packet can carry less data. This results in more packets needing to be sent to transmit the same amount of data compared to a larger MTU. This increased number of packets introduces additional overhead due to packet headers (e.g., IP, TCP/UDP headers) and protocol processing time, which reduce the overall throughput. Since the packet size exceeds the MTU of a network link, it needs to be fragmented into smaller packets that fit within the MTU. Fragmentation adds complexity to the transmission process as the source device has to break the packets down, and the receiving device has to reassemble them. This process can introduce delays and potentially increase the chance of packet loss or errors, further impacting throughput.

Traffic through a GRE tunnel is generally faster compared to GRE over IPSec due to the additional overhead and processing required by IPSec. IPSec provides encryption for the data traveling through the tunnel, which involves computationally intensive operations. Each packet must be encrypted on the sending end and decrypted on the receiving end, which adds processing time and can slow down the traffic. IPSec includes mechanisms for ensuring the authenticity and integrity of the data packets, such as hashing and verification processes. Also, IPSec adds extra headers to each packet for encryption and authentication purposes (see Figure 2). This adds further processing overhead compared to a plain GRE tunnel, which does not include such features.

#### 3.2. Video streaming over UDP

UDP is one of the core protocols in the TCP/IP suite, operating at the transport layer alongside TCP. Unlike TCP, UDP is connectionless and does not provide mechanisms for guaranteed delivery, sequencing, or error checking. Instead, UDP focuses on minimal overhead and high-speed transmission, making it suitable for applications where occasional packet loss is acceptable, such as real-time video streaming. UDP does not establish a connection before sending data. Each UDP packet (datagram) is independent and can be sent without prior communication, [8]. UDP does not guarantee delivery or order of packets. Overall, UDP is valuable in situations

where speed and low latency are critical, and where occasional packet loss can be tolerated without significant impact on application performance.

VLC is a free and open-source cross-platform multimedia player and framework that supports playback of most multimedia files, including DVDs, audio CDs, VCDs and a variety of streaming protocols, [9]. In our case, “BigBuckBunny\_320x180.mp4” video was used (it has become a popular example of open-source filmmaking and has been used in various educational and promotional contexts; it can be downloaded from [10]) to investigate the behavior of both encrypted and unencrypted traffic when changing the MTU size, by streaming it via VLC.

While this resolution may seem low by civilian standards, it offers several strategic advantages in military contexts. Firstly, in situations where covert surveillance is crucial, such as reconnaissance missions or movement monitoring, smaller, less conspicuous cameras with lower resolutions are easier to conceal and deploy discreetly. Secondly, lower resolution cameras consume less bandwidth and storage space, which is particularly important in remote or austere environments where resources like power and network connectivity are limited. Additionally, these cameras can operate efficiently in harsh conditions, such as extreme temperatures or rugged terrain, where robustness and reliability are paramount. Lastly, the reduced visual detail of 320x180 resolution may still provide sufficient information for situational awareness and decision-making, especially when coupled with advanced image processing and analytics technologies that enhance the interpretation of captured footage.

The following Table 2. presents the detailed subjective experience observed during video streaming on the client side, capturing insights from both unencrypted and encrypted traffic scenarios. The results show a remarkable similarity between the two cases, highlighting negligible perceptible differences in user experience despite the added encryption overhead.

**Table 2.** Descriptive subjective experience versus MTU

MTU [B]	Descriptive subjective experience
1500	Perfect viewing experience
1400	Watchable in a satisfactory manner
1300	Watchable, with slightly degraded graphics
1200 & 1100	Almost satisfactory viewing, occasional stuttering occurs
1000 & 900	Blurred scenes have started to appear
800	Significant stuttering during certain scenes
700 & 600	Less frequent appearances of scenes
500	Partially usable
≤ 400	Completely unusable

A larger MTU size allows for optimal data transmission without noticeable degradation, providing a seamless

viewing experience (MTU = 1500). Slight reduction in MTU starts to show minor impacts on video quality but remains generally acceptable for viewing (MTU = 1400). Further reduction in MTU leads to noticeable degradation in video quality, particularly in visual clarity and detail (MTU = 1300). Occasional interruptions or stutters begin to occur by further reducing the MTU, impacting the smoothness of video playback intermittently (MTU = {1200, 1100}). As MTU further decreases, video content becomes visibly blurry or pixelated, affecting overall viewing experience and clarity (MTU = {1000, 900}). Significant interruptions and delays in video playback become noticeable at MTU = 800. Video content may fail to load or display consistently at MTU = {700, 600}, leading to irregular viewing experiences with missing or delayed scenes. The last possible MTU value set for transmitting the video from which some useful data can be extracted is at a value of 500; video streaming becomes challenging with frequent interruptions or delays, making it difficult to follow content consistently. For the MTU ≤ 400, video content is severely disrupted or fails to load entirely, rendering it impossible to watch due to continuous buffering or playback issues.

#### 4. CONCLUSION

Based on the detailed setup and experimental findings, our study emphasizes the critical role of secure and efficient communication in military operations. The integration of GRE tunnels, particularly when combined with IPsec for encryption, offers a robust solution for maintaining confidentiality and reliability across multi-vendor environments. Our research highlights that while IPsec introduces additional overhead due to encryption and authentication processes, the performance impact is minimal under optimal MTU settings, ensuring that encrypted traffic remains viable for high-priority applications.

For file transfer protocols like FTP, our experiments demonstrate that varying MTU sizes significantly influence throughput, with larger MTUs generally yielding faster transfer rates. Even with IPsec encryption, the highest MTU setting (1500 bytes) proved to be the most efficient, underscoring the balance between security and performance in military communications. Similarly, in video streaming applications, MTU size plays a crucial role in maintaining high-quality transmission, where larger MTUs contribute to better user experiences, albeit with slight performance variations between encrypted and unencrypted scenarios.

In conclusion, configuration of GRE tunnel and GRE over IPsec in a multi-vendor environment, coupled with exploration of optimal MTU values, provides insights crucial for enhancing communication efficiency and reliability in military settings. These findings underscore the importance of adaptive network configurations that accommodate both security requirements and operational performance needs, ensuring mission-critical data is transmitted effectively and securely across dynamic battlefield environments.

## Acknowledgment

This paper was funded by Vlatacom Institute of High Technologies under the project P176.

## References

- [1] El Idrissi, D., Elkamoun, N., Lakrami, F., & Hilal, R. (2018). Study of the impact of routing and the profoundness of GRE tunnels on the performance of the transmission of real time applications in IP networks. *IJCSNS*, 18(7), 76.
- [2] <https://en.wikipedia.org/wiki/Dynamips> (last time accessed on 22.06.2024)
- [3] [https://en.wikipedia.org/wiki/Graphical\\_Network\\_Simulator-3](https://en.wikipedia.org/wiki/Graphical_Network_Simulator-3) (last time accessed on 22.06.2024)
- [4] W. V. Wollman and Y. Barsoum, "Overview of open shortest path first, version 2 (OSPF V2) routing in the tactical environment," *Proceedings of MILCOM '95*, San Diego, CA, USA, 1995, pp. 925-930 vol.3, doi: 10.1109/MILCOM.1995.483435.
- [5] <https://www.cisco.com/c/en/us/support/docs/security-vpn/ipsec-negotiation-ike-protocols/217432-understand-ipsec-ikev1-protocol.html> (last time accessed on 22.06.2024)
- [6] Orogun, A. O. Brief insight into transmission control protocol (TCP), 2017.
- [7] Liu Xia, Feng Chao-sheng, Yuan Ding and Wang Can, "Design of secure FTP system," *2010 International Conference on Communications, Circuits and Systems (ICCCAS)*, Chengdu, 2010, pp. 270-273, doi: 10.1109/ICCCAS.2010.5582002.
- [8] V. V. Belkhode and D. M. Dakhane, UDP-Based Multi-Stream Communication Protocol, *International Journal of Innovative Research in Electronics and Communications*, 2015, 2(7), pp. 11-15.
- [9] <https://www.videolan.org/> (last time accessed on 22.06.2024)
- [10] [https://download.blender.org/peach/bigbuckbunny\\_movies/](https://download.blender.org/peach/bigbuckbunny_movies/) (last time accessed on 22.06.2024)



## THE USE OF GEOGRAPHIC INFORMATION SYSTEMS (GIS) IN THE TEACHING OF MILITARY TOPOGRAPHY

MARKO STOJANOVIĆ

Military Geographical Institute - "General Stevan Bošković" and, University of Defence, Belgrade, Military Academy  
[stojanovicm80@yahoo.com](mailto:stojanovicm80@yahoo.com)

NENAD GALJAK

University of Defence, Belgrade, Military Academy, [galjaknenad@gmail.com](mailto:galjaknenad@gmail.com)

JASMINA M. JOVANOVIĆ

Faculty of Geography, University in Belgrade, Belgrade, [jasmina@gef.bg.ac.rs](mailto:jasmina@gef.bg.ac.rs)

MARKO SIMIĆ

Military Geographical Institute - "General Stevan Bošković", Belgrade, [marko.simic.rs@gmail.com](mailto:marko.simic.rs@gmail.com)

VLADIMIR VUČENOV

Air Force and Air Defence, Serbian Armed Forces, Belgrade, [vvucenov@gmail.com](mailto:vvucenov@gmail.com)

---

**Abstract:** *The introduction of digital technology in the process of creating topographic maps significantly changes the way spatial phenomena are used and presented. Geographic Information Systems (GIS) represent a modern tool that enables access to analysis, and interpretation of spatial data in digital form. In the context of military education, particularly in the teaching of Military Topography, GIS provides faster, more precise, and more detailed terrain visualization, which is essential for planning and conducting military operations. The paper compares the use of GIS technology with traditional methods of orientation and terrain analysis. It presents modern informational devices for geolocation and orientation in the field, used in the realization of thematic teaching content and special forms of teaching in the subject of Military Topography at the Military Academy. The impact of these devices on the quality and efficiency of military training was explored, and the use of these devices during extreme weather conditions was analyzed. Recommendations for further research and improvement of the teaching process in this subject are also given.*

**Keywords:** *GIS, Topographic map, Military topography.*

### 1. INTRODUCTION

Military Topography is a specialized scientific discipline that focuses on understanding the tactical properties of terrain, methods for land assessment, and the geographic, topographic, and tactical orientation necessary for combat operations. This field often involves conducting field measurements to support military operations and creating operational schemes, both in analog and digital formats.

The primary goal of Military Topography is to ensure that military personnel can effectively collect, interpret, and use terrain data for the efficient deployment of equipment and weapon systems. Topographic maps serve as a key resource for this purpose, and the ability to read and interpret these maps is crucial for decision-making in military contexts.

Modern military education incorporates technological innovations in all aspects of teaching. The integration of Geographic Information Systems (GIS) has brought new techniques and tools into the military topography

curriculum, enhancing the ability to analyze and visualize terrain data. By using GIS, cadets can more easily answer spatial questions and visualize their findings in real-time, improving their overall understanding of the subject matter [1].

### 2. TEACHING MILITARY TOPOGRAPHY

Military Topography is an essential part of military education, ensuring that future officers are well-prepared for field operations.

At the Military Academy in Belgrade, the subject is taught through a combination of lectures and practical exercises. Cadets learn to use traditional orienteering methods and modern geolocation tools to effectively assess terrain and plan military operations.

During classes, cadets learn to read and use topographic maps, understand scale, recognize topographical signs, and interpret relief representation with isohypses. This knowledge helps accurately determine the position of friendly and enemy units, identify natural obstacles, and

tactically utilize the terrain.

In addition to classroom sessions, practical exercises form a significant part of the training. These exercises are conducted in summer and winter at the Serbian Armed Forces' training centers.

Cadets learn to orient themselves in unfamiliar terrains using hand compasses, which is crucial during low visibility conditions, such as night operations or operations in dense fog or vegetation.



Figure 1. Orientation using a topographic map and compass

Military Topography education also involves modern technologies like satellite and aerial photogrammetry imagery, digital maps, Global Navigation Satellite Systems (GNSS), and GIS. These tools are increasingly vital in modern military planning and operations. Cadets learn how to use these tools to collect, analyze, and interpret geographic data.

Overall, these components of military topography training equip cadets to conduct operations under various conditions effectively. Soldiers well-versed in topography can quickly adapt to changing terrain conditions, contributing significantly to the success of any military mission.

### 3. TECHNOLOGICAL PROGRESS IN MILITARY TOPOGRAPHY

The integration of GIS and GNSS into military education represents a significant advancement in terrain analysis and visualization. These tools provide faster, more accurate assessments of terrain, aiding military personnel in planning and executing operations.

#### 3.1. The Serbian Army GIS software

The Serbian Army GIS software (SA GIS) is an application specifically designed to support operational planning through geospatial analysis and battlefield visualization. SA GIS primarily facilitates the creation of tools that analyze military aspects of terrain and their

subsequent effects on realizing planned operations.

Using this software offers both 2D and 3D terrain visualization, which significantly aids spatial analysis in planning and decision-making processes prior to the exercise conduction. With the use of certain tools, distances are easily calculated, land slopes determined, sightlines between points checked, fire zones displayed, and more.

SA GIS provides a comprehensive toolset, allowing users to establish the project, define the coordinate system, map workspace, and visual display. It also offers a broad range of terrain processing tools. The interface of this software and some of its capabilities are shown in Figures 2, 3 and 4.

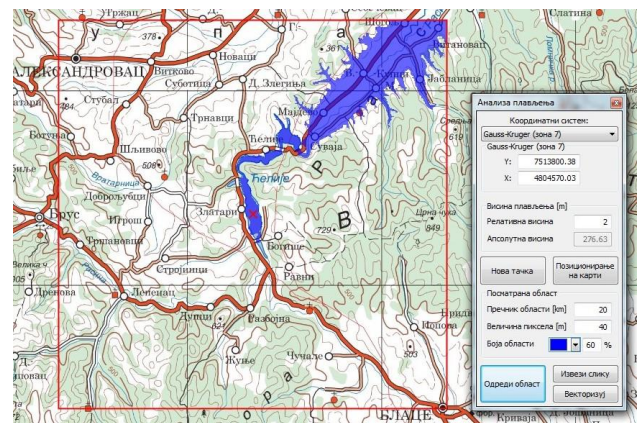


Figure 2. Analyzing flooding areas using SA GIS

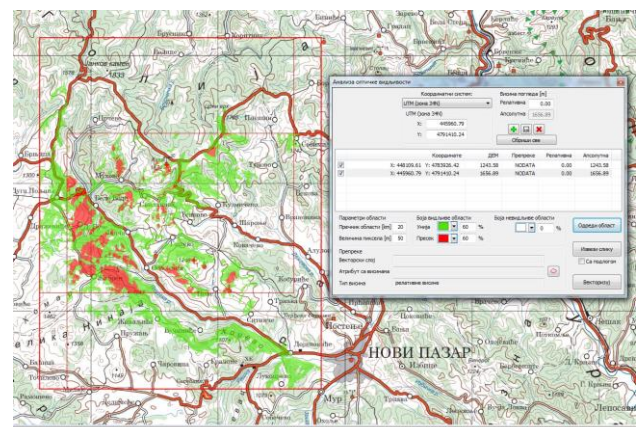
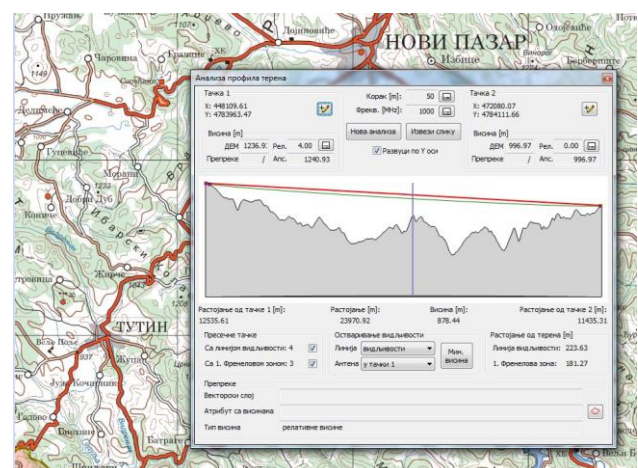


Figure 3. Analyzing optical visibility using SA GIS



**Figure 4.** Analyzing terrain profiles using SA GIS

SA GIS is used in the GIS cabinet at the Military Academy. This cabinet houses suitable desktop computers networked into a secure system. All spatial data for analysis and processing is sourced from a server-based database.



**Figure 5.** GIS cabinet [2]

### 3.2. Mobile GIS devices

Mobile GIS technology combines hardware, software, and information tools. It provides cartographic modeling, integrated representation of geographic and attribute data, as well as collection, storage, and analysis of geospatial information in the field [3]. Due to the technological advancements in handheld devices for GIS, they are both robust and easily portable. This versatility allows for their use in various conditions and terrains, making them ideal for military topographical training.



**Figure 6.** Mobile GIS devices

#### Tablets

In terms of mobile hardware, there are two tablets in active use, each boasting similar high-end characteristics. The first is the Dell Latitude 7230 Rugged Extreme Tablet. This piece of technology was specifically acquired for field reambulation of Topographic Maps at the Military Geographical Institute - "General Stevan Bošković". The second is a Trimble T100 tablet, which was purchased by the Military Academy to enhance the teachings of Military Topography.

The tablets are equipped with GIS software that allows users to visualize and analyze data immediately in the field. This possibility is of great importance for the decision-maker, because it enables a faster response to changes and optimization of resources.

Intended to withstand even the harshest conditions, these tablets are specifically designed for professional field use. Notable for their advanced performance capabilities, resilient housing, and extensive range of functionality, these tablets are armed with everything necessary for productive work in challenging field conditions. Their robustness is certified through resistance to falls, vibrations, dust, and extreme temperatures. Moreover, they are sealed against water and dust ingress, meeting the rigorous IP65 standard. Technologically, they are equipped with powerful processors that facilitate a broad spectrum of tasks, including advanced analytics and data processing. The tablets feature high-resolution screens with an anti-reflective coating, ensuring excellent visibility even under direct sunlight. The touch-sensitive screens can be used even with gloves, enhancing usability in various conditions. Their long-lasting batteries support hours of continuous work, and the Dell model even offers the option to replace the battery without the need to power down the device, thereby boosting productivity. Furthermore, they support a wide range of connectivity options, including Wi-Fi, Bluetooth, and 4G LTE, which ensures seamless connectivity with the database and other necessary devices. The specifications of these devices are given in Tables 1 and 2.

**Table 1.** Dell Latitude 7230 Rugged Extreme Tablet specifications [4]

Specification	Details
Processor	12th generation Intel Core i5-1240P
Memory (RAM)	16 GB LPDDR 2x
Storage	256 GB NVMe SSD
Operating system	Windows 11 Professional
Screen	12-inch FHD (1920 x 1080) anti-reflective, capacitive multi-touch
Graphics	Intel Iris Xe Graphics
GNSS	Integrated GNSS with support for GPS, QZSS, GLONASS, Galileo and BeiDou
Connection	Wi-Fi 6E, Bluetooth 5.2, optional 4G LTE and 5G
Ports	2 x USB 3.2 Gen 1 Type-A, 2 x Thunderbolt 4, HDMI, RJ-45, microSD
Battery	Double replacement battery, up to 25 hours of operation
Endurance	MIL-STD-810H, IP65
Dimensions	312 mm x 203 mm x 24 mm
Weight	1.35 kg

Both tablets were rigorously tested in harsh winter

conditions, at extremely low temperatures (below -20°C), where they proved to be exceptionally durable and functional. Additionally, they worked reliably and efficiently in hot summer conditions, even in environments with high humidity, intense sunlight, and heavy dust exposure.

**Table 2.** Trimble T100 tablet specifications [5]

Specification	Details
Processor	8th generation Intel Core i5
Memory (RAM)	16 GB LPDDR4
Storage	512 GB SSD
Operating system	Windows 10 Professional
Screen	10.1-inch WUXGA (1920 x 1200) capacitive multi-touch
Graphics	Intel HD Graphics 620
GNSS	Integrated GNSS with support for GPS, QZSS, GLONASS, Galileo and BeiDou
Connection	Wi-Fi 802.11, Bluetooth 5.1, 4G LTE
Ports	USB 3.0, microSD, SIM slot, audio jack
Battery	Lithium-ion, up to 10 hours of operation
Endurance	MIL-STD-810G, IP65
Dimensions	279 mm x 200 mm x 18.5 mm
Weight	1.65 kg

**TruPulse R360 rangefinder**

The TruPulse R360 is an advanced laser rangefinder designed for professionals who require the utmost precision and reliability in measuring distances and heights. This device is ideal for a wide range of applications, including surveying, engineering, forestry, environmental protection, and construction. The TruPulse combines high performance, ease of use, enabling users to perform measurements with high precision and efficiency.

**Table 3.** TruPulse R360 rangefinder specifications [6]

Specification	Details
Distance Accuracy to Typical / Weak Targets	± 0.2 m / ± 1 m
Inclination Accuracy	± 0.25° Typical
Max Range to Reflective / Nonreflective Targets	2000 m / 1000 m
Azimuth Accuracy	± 0.5°RMS; typical
Communication (COM Port / Bluetooth)	Windows and Android
Scope Magnification	7× / LCD
In-Scope Field of View	10 m on 91.5 m away
Environmental Rating	Waterproof IP56

Temperature Range	-20° to +60° C
Battery	Lithium-ion, up to 8 hours of continuous use
Dimensions	130 mm x 110 mm x 50 mm
Weight	385 g

The rangefinder has been tested in extreme weather conditions, where it provided extremely accurate measurements of non-reflective targets at a distance of up to 1000 meters. In addition to measuring distances, the TruPulse R360 can measure heights, slopes and horizontal distances, providing comprehensive data for a variety of applications. Equipped with Bluetooth technology, it offers easy data transfer to other devices and integration with GIS applications. It's designed to withstand tough off-road conditions, with a rugged construction that's dust and water-resistant, but it proved to be unreliable when measuring due to heavy precipitation (snow and rain) and in conditions of reduced visibility (fog and haze).

**Garmin Montana 700**

The Garmin Montana 700 is an advanced GPS device designed for diverse outdoor activities, including hiking, camping, fieldwork, and navigation. With its large screen, rugged design, and advanced navigation features, the Montana 700 provides users with a dependable tool for precise navigation and orientation.

The Garmin Montana 700 is equipped with a 5-inch touch-sensitive screen, which enables a clear and transparent display of maps and navigation information, even in direct sunlight. The device is built to withstand challenging conditions, with certification for resistance to water, shock, vibration, dust, and moisture. It supports multiple GNSS (GPS, GLONASS, and Galileo) for precise navigation in demanding environments. It also includes ABC sensors (altimeter, barometer, and compass) for added accuracy. The device comes pre-loaded with TopoActive maps for Europe. Furthermore, it supports Wi-Fi, Bluetooth, and ANT+ to connect with other devices. It allows users to load digital surfaces from other devices and download satellite images through the Garmin Explore application. A detailed specification is given in Table 4.

**Table 4.** Specifications Garmin Montana 700 [7]

Specification	Details
Storage	16 GB of internal memory, microSD slot for expansion
Screen	5-inch WVGA (800 x 480) touchscreen, sunlight readable
GNSS	GPS, GLONASS, Galileo
Connection	Wi-Fi, Bluetooth, ANT+
Ports	USB, microSD slot
Sensors	Altimeter, barometer, compass



Endurance	MIL-STD-810G, IPX7
Temperature Range	-20° to +60° C
Battery	Rechargeable lithium-ion, up to 18 hours in GPS mode
Dimensions	183 mm x 87.6 mm x 32.7 mm
Weight	397 g

The Garmin Montana 700 is a premium GPS device intended for dedicated enthusiasts and professionals who require reliable and precise navigation in all conditions. Its robust design, large screen, and advanced navigation features make it an ideal choice for outdoor activities and fieldwork.

### 3.3. Integration of modern devices

Technological progress witnessed through the implementation of GIS software and the use of

sophisticated mobile devices for orientation has significantly improved the capabilities of the Serbian Army. These tools enable precise planning, efficient execution of operations, and improved training, which are essential for the modern military. The integration of these modern technologies into military operations not only increases the efficiency and safety of military personnel but also contributes to better preparation for facing complex challenges in the field.

Using GNSS, locating the device itself is very simple and fast, but locating distant targets requires the interconnection of two devices. Figure 7 shows the integration of the rangefinder and the tablet using the ArcPad software, when determining the position of distant targets. The target is automatically positioned on the topographical surface, and all other measured parameters (coordinates, distance, azimuth and inclination) are displayed in an additional window. This integration eliminates the need for manual data entry, reduces the possibility of errors and speeds up the entire process.

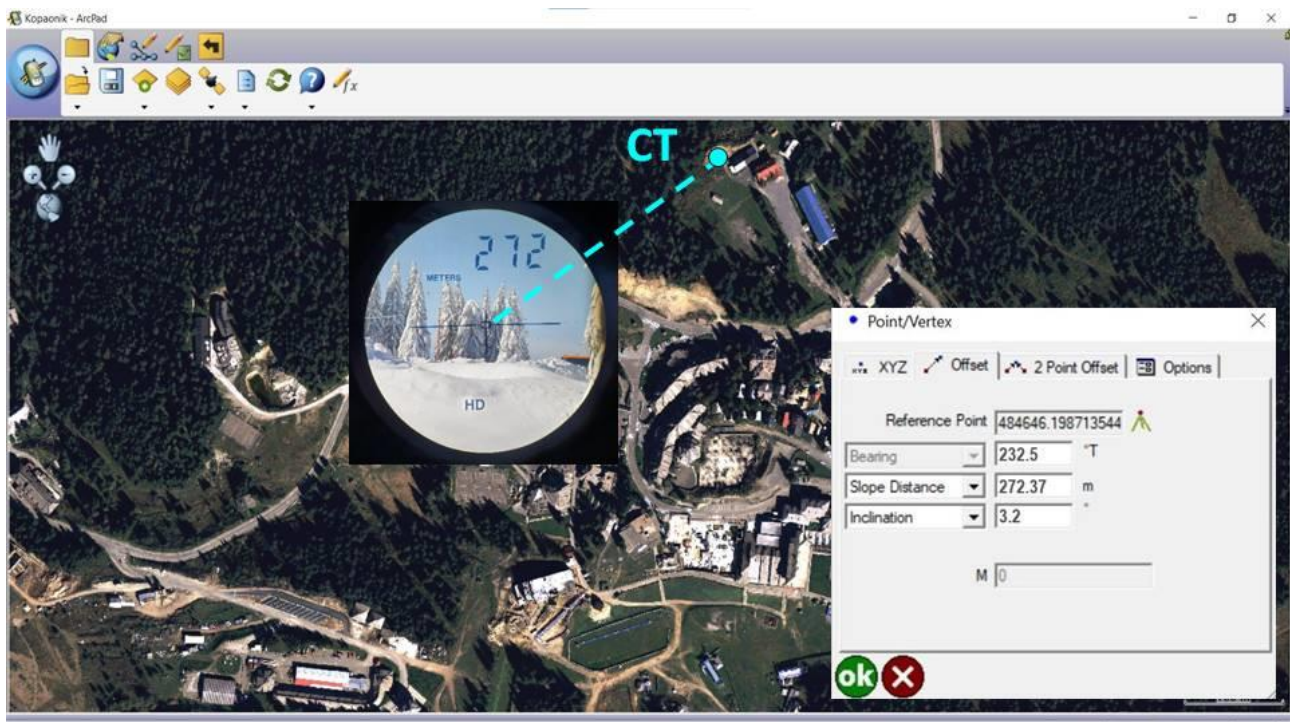


Figure 7. Locating a distant target by integrating mobile devices

## 4. COMPARISON OF TRADITIONAL AND MODERN METHODS

A significant challenge with traditional teaching methods in topography is promoting cadets' abstract thinking through three-dimensional visualization of two-dimensional topographical information. This visualization is crucial for learning how to make informed decisions in command. Without a solid grasp of basic topography concepts, conducting accurate spatial analysis becomes virtually impossible. Current GIS technologies can significantly enhance comprehension of these concepts and nurture abstract thinking. They do so by improving cadets' abilities to recognize, use, and analyze maps, and relate their content to real-world field examples.

By integrating modern GIS teaching methods, complex natural elements, spatial distribution of social phenomena, and abstract concepts can be presented in a dynamic, three-dimensional, intuitive manner. This approach enables efficient clarification of terrain information, improving the speed and accuracy of terrain element calculations. GIS technologies are already being used in topographic teaching, implementing interactive, autonomous, exploratory, and networked learning methods. These not only facilitate the acceptance of new information but also provide multisensory stimulation and combined visual-auditory perception. This results in cadets receiving more comprehensive and deeper information. A three-dimensional representation of the terrain, combined with various data of significance, besides enhancing teaching, facilitates on-the-spot

investigations at the battlefield rear, geographic evolution, development process, and distant space environment perception. Spatial analysis technology allows us to abstract battlefield environment problems into conceptual models, thereby solving specific terrain-related application problems [8].

While modern GIS technologies offer numerous advantages, traditional methods such as using printed maps and compasses remain vital. In cases where digital systems fail or are unavailable, military personnel must rely on these basic tools to continue their operations. Therefore, military education emphasizes a balance between traditional and modern methods.

The ability to navigate using traditional topographic methods ensures that soldiers are prepared for any situation, including those where technological tools are not available or reliable due to system failures or lack of satellite access.



**Figure 8.** Using traditional means combined with modern technologies in practical topography training

## 5. CONCLUSION AND RECOMMENDATIONS

Military topography teaching is a fundamental element of military education. It provides cadets with the necessary knowledge and skills to navigate the field effectively and plan military operations with precision. The combination of theoretical knowledge, practical training, and the use of modern technologies ensures that future officers are ready for the challenges that await them in their careers.

Through this comprehensive training, soldiers develop the ability to think critically, plan accurately, and execute tasks efficiently, which are critical to success in military operations.

The integration of traditional orientation methods with modern technological tools equips cadets with the comprehensive knowledge and skills needed to face complex challenges in the field. During classes, cadets are trained on how to use these technologies. However, the importance of mastering basic methods of orientation is also emphasized, equipping them to navigate even in situations where technology is not available or reliable.

In order to improve the teaching process of Military Topography, it is necessary to continue monitoring technological achievements. The idea is to create a realistic virtual environment in which different scenarios and terrains can be simulated. Using this simulator, cadets can practice the necessary skills required for precise movement in unfamiliar or complex conditions without going into the field. These simulations could offer a realistic and effective alternative for skill development in Military Topography.

## References

- [1] STOJANOVIĆ, M., MARKOVIĆ, V., KRIČKOVIĆ, Z., BANKOVIĆ, R.: *Potential usage of GIS in education*, International scientific conference on information technology and data related research - Sinteza, Belgrade, 2018, 255-260.
- [2] <https://www.va.mod.gov.rs/lat/225/laboratorije-225>
- [3] LIASHENKO, O., KYRYICHUK, D., RAIKO, H., DOROVSKA, I., CHEBUKIN, Y.: *Development of mobile GIS technology for monitoring spatially distributed emergencies*, In Proceedings of 20th International Multidisciplinary Scientific GeoConference SGEM 2020.
- [4] <https://www.dell.com/support/manuals/en-us/latitude-12-7230-rugged-laptop/lati-7230-rugged-setup-and-specifications/specifications-of-latitude-7230-rugged-extreme-tablet?guid=guid-7c9f07ce-626e-44ca-be3a-a1fb036413f9&lang=en-us>
- [5] [https://trl.trimble.com/docushare/dsweb/Get/Documnt-962385/022516-527A\\_Trimble\\_Geospatial\\_T100\\_DS\\_USL\\_0421\\_L\\_R\\_sec.pdf](https://trl.trimble.com/docushare/dsweb/Get/Documnt-962385/022516-527A_Trimble_Geospatial_T100_DS_USL_0421_L_R_sec.pdf)
- [6] <https://field-map.com/files/TruPulse%20360R.pdf>
- [7] [https://www.gpscentral.ca/wp-content/uploads/Garmin\\_Montana700\\_Specs.pdf](https://www.gpscentral.ca/wp-content/uploads/Garmin_Montana700_Specs.pdf)
- [8] JIN, F., WANG, C., ZHOU, X., WANG, C. *Application of ArcGIS Spatial Analysis Techniques on Topography teaching*, In Proceedings of the 2nd International Conference on Internet, Education and Information Technology, 2023, 413-418. [https://doi.org/10.2991/978-94-6463-058-9\\_67](https://doi.org/10.2991/978-94-6463-058-9_67)



# STANDARD CUMULANTS- BASED AUTOMATIC MODULATION CLASSIFICATION PERFORMANCE UNDER COLORED NOISE CHANNEL CONDITIONS

RADE R. BOŽOVIĆ

Faculty of Information Technologies, Alfa BK University, Belgrade, [rade.bozovic@alfa.edu.rs](mailto:rade.bozovic@alfa.edu.rs)

VLADIMIR D. ORLIĆ

Vlatacom Institute of High Technologies, Belgrade, [vladimir.orlic@vlatacom.com](mailto:vladimir.orlic@vlatacom.com)

**Abstract:** Automatic modulation classification (AMC) represents a wide used technique for signal processing whereas modulation format of received signal is not a priori known. It is of crucial importance for a variety of both military and commercial communications. Due to the low algorithm complexity, hardware requirements and the other relevant practical aspects, the algorithms based on fourth and sixth-order cumulant structures, and generally higher order statistics, remain competitive and interesting research topic. Signal degradation due to the presence of noise significantly deteriorates AMC performance. In this paper, performance of standard cumulants-based AMC algorithms is analysed in context of colored noise impact. This was done through Monte-Carlo simulations conducted in Matlab software in a propagation environment with colored noise channel.

**Keywords:** automatic modulation classification, colored noise, cumulants, feature based

## 1. INTRODUCTION

Automatic modulation classification (AMC) represents an important integral part for performance improvement of modern wireless communication systems and applications. It has adopted in both military (electronic warfare, spectrum surveillance) and commercial systems, such as cognitive radio (CR), software defined radio (SDR), spectrum management, Internet of Things (IoT), etc. AMC stands for technique for the process of modulation format recognition of unknown communication signals, without a priori knowledge about its transmission parameters. Thus logically AMC is placed between signal detection at receiver and its further demodulation, i.e. before the extraction of the very information carried by the signal itself [1-4].

Developed on the very beginning of AMC topic research process, feature - based (FB) methods with additional performance improvements, still remain quite competitive comparing to the other modern methods based on artificial intelligence, neural networks, machine learning, etc. It is mainly due to low algorithm complexity, hardware requirements, real-time applicability and the other relevant aspects for practical usage. Standard feature - based method consists of the two main steps. The first step represents determination and extraction of the feature of interest. The most popular features of interests are higher order statistics – moments and cumulants, whereas cumulants have some advantages due to their useful characteristics. Fourth-order cumulants and sixth-order cumulants structures are the most frequently considered for this purpose, although other

HOS-based solutions can be found in literature as well [5].

An insight into published research of these algorithms and their performances, shows that mostly additive white Gaussian noise (AWGN) was considered as the source of signal degradation. Unfortunately, wireless signals are corrupted not only due to wireless channels, but also due to imperfections of electronic subsystems of transmitters and receivers [6]. There are some other time-dependent noise components such as components or colored noise components which affect significantly the performance of the communication systems [7]. Thus, it is required to consider all these effects while processing the received radio signals. For real-time processing more accurate noise models and reconstruction of transmitted wireless signals is required and proposed in [8-11].

Colored noise represents significant source of signal degradation, quite present in practice, which to the best of our knowledge have not been addressed in AMC research so far. In this paper AMC performance is observed in context of colored noise impact, by using different standard cumulants-based AMC algorithms. The paper is organized as follows: considered fourth and sixth-order cumulants-based AMC algorithms are described and relevant formulas for cumulants' determination are shown in Section 2, colored noise is introduced and explained in Section 3, simulation environment and corresponding results are shown in Section 4, with the conclusions given in Section 5 of this paper.

## 2. AMC ALGORITHMS BASED ON HIGHER ORDER CUMULANTS

The received signal sequence  $y(n)$ , corrupted by noise during propagation, can be represented by:

$$y(n) = x(n) + g(n), \quad (1)$$

with  $x(n)$  standing for transmitted symbols (of an unknown modulation), and  $g(n)$  commonly representing zero-mean AWGN with variance of  $\sigma_g^2$ . For zero-mean random variable  $x$ , associated with transmitted data sequence  $x(n)$ , the second-order cumulant is:

$$C_{21,x} = E(|x|^2). \quad (2)$$

where  $E(\cdot)$  represents a mathematical expectation, realized as an average value over observed signal samples. The fourth-order cumulant and the normalized fourth-order cumulant of the same variable are given as:

$$C_{42,x} = E(|x^4|) - |E(x^2)|^2 - 2E^2(|x^2|), \quad (3)$$

$$\hat{C}_{42,x} = C_{42,x} / (C_{21,x})^2. \quad (4)$$

The standard (classical) sixth-order cumulant and its corresponding normalized value of the same random variable  $x$  are given as:

$$C_{63,x} = E(|x|^6) - 9E(|x|^4)E(|x|^2) + 12|E(x^2)|^2 E(|x|^2) + 12E^3(|x|^2), \quad (5)$$

$$\hat{C}_{63,x} = C_{63,x} / (C_{21,x})^3. \quad (6)$$

Apart from standard, the following formulas are used for general and unbiased sixth order cumulant [4], along with its corresponding normalized value:

$$C_{63,x\_UNB} = E(|x|^6) - 9E(|x|^4)E(|x|^2) + 18|E(x^2)|^2 E(|x|^2) - 6|E(x^2)| E(x^2 |x|^2), \quad (7)$$

$$\hat{C}_{63,x\_UNB} = C_{63,x\_UNB} / (C_{21,x})^3. \quad (8)$$

For random variable  $y$  associated with received sequence  $y(n)$ , normalized higher-order cumulants can be expressed in the following manner:

$$\hat{C}_{42,y} = \frac{C_{42,y}}{(C_{21,y} - \sigma_g^2)^2}, \quad (9)$$

$$\hat{C}_{63,y} = \frac{C_{63,y}}{(C_{21,y} - \sigma_g^2)^3}, \quad (10)$$

$$\hat{C}_{63,y\_UNB} = \frac{C_{63,y\_UNB}}{(C_{21,y} - \sigma_g^2)^3}. \quad (11)$$

Equations (9) - (11) describe the AMC execution within the receiver. While noise power is commonly considered to be known, it was shown that the same can be easily estimated also, without relevant loss in performance [12].

The decision-making process for modulation recognition

is based on a comparison of obtained values of normalized cumulant estimates with predefined thresholds, positioned at the middle of intervals between expected (theoretical) values corresponding with particular modulation formats [13]. Theoretical values for normalized cumulants' values, for considered BPSK, PAM and QPSK constellations, are shown in Table 1: in order to demonstrate comparison with results presented in work [4], these modulations formats are considered here as well. Many other modulation formats are presented in context of AMC in [14].

**Table 1.** Theoretical values of normalized cumulants

Constellation	$\hat{C}_{42}$	$\hat{C}_{63,x}$	$\hat{C}_{63,x\_UNB}$
BPSK	-2.0000	16.0000	16.0000
PAM-4	-1.3600	12.1600	8.3200
PAM-8	-1.2381	11.7600	7.1899
PAM-16	-1.2094	11.6817	6.9381
PAM-32	-1.2023	11.6632	6.8733
PAM-64	-1.2006	11.6587	6.8622
QPSK	-1.0000	4.0000	4.0000

## 3. COLORED NOISE

Additive white Gaussian noise (AWGN) is typically used to model practical noise process that affect wireless communications. However, real working conditions introduces some additional noise features which might be even non - Gaussian. This is mostly happening due to imperfections of electronic subsystems and components of both transmitter and receiver. There are some other time-dependent noise components such as components or colored noise components which affect significantly the performance of the communication systems. These various types of colored noises stand for important sources of signal degradations, consequently with a big impact on AMC performance as well. Therefore, some effective model that considers various practical noises, not only AWGN, is of interest for real-time signal processing and realization of AMC process and for its further considerations.

Generally, the term "noise signal" is referred to a signal produced by a stochastic process. Further, one considered the noise signal itself and not the underling process. The term "colored noise" is used to refer to any non-white noise signal whose Power Spectral Density (PSD) is not a constant, but is a function of the frequency [15].

AWGN is a Gaussian noise with equal intensities at different frequencies, it is due to thermal noise from transmitter and receiver antennas circuits. Random fading of propagation channel also contributes in it. Well known "flat" PSD of white noise is presented in Fig. 1. On the other side, colored noise may have different characteristics at different frequency bands. Violet, also called purple or differentiated white noise, is

characterised with power spectral density slope +6 dB/oct., +20 dB/dec. Blue noise spectral density is proportional to its frequency, i.e. power spectral density slope +3 dB/oct., +10 dB/dec. Its specific origin is not known. Pink, also called flicker or 1/f noise, is related to the flow of current due to slow fluctuations of properties of the material of electronic devices. It is characterised with power spectral density slope -3 dB/oct., -10 dB/dec. Also, there is red noise due to Brownian motion in the circuit and random walk behavior of received signals, also called brown or Brownian noise, with power spectral density slope -6 dB/oct., -20 dB/dec. Power Spectral Density (PSD) value of various colored noise, considered in this paper, is shown in Figures 2 - 5.

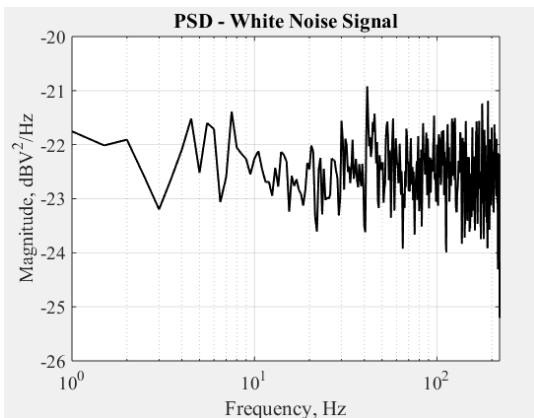


Figure 1. PSD – White noise signal.

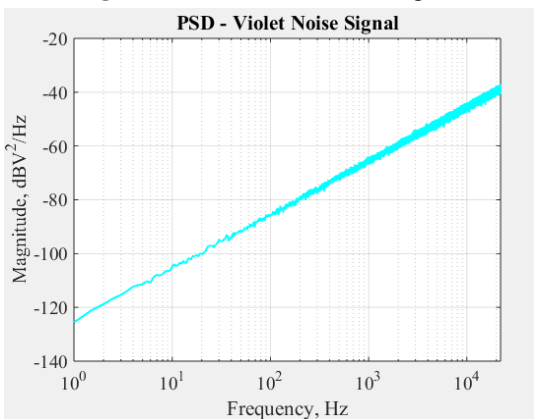


Figure 2. PSD – Violet noise signal

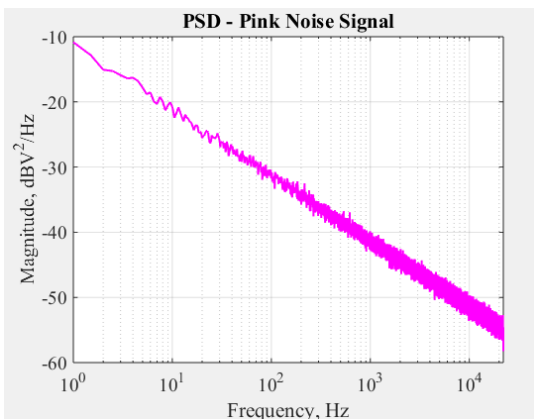


Figure 3. PSD – Pink Noise Signal

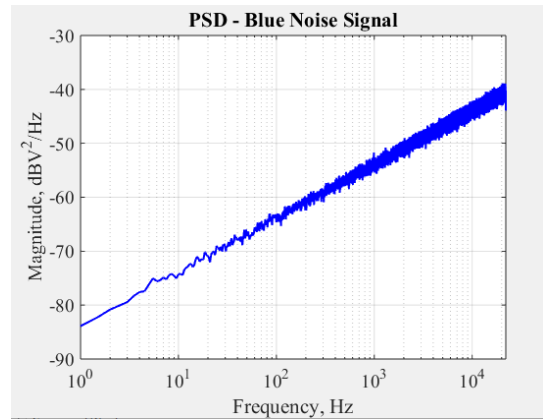


Figure 4. PSD – Blue noise signal

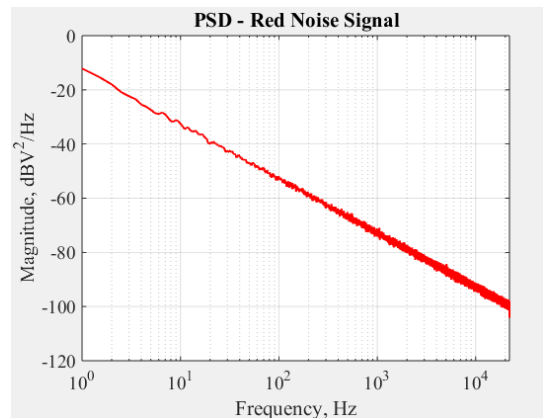


Figure 5. PSD – Red noise signal

Generation of the desired colored noise signal is in computer simulations obtained via spectral processing of a white noise signal: algorithm of the colored noise generation procedure, given in [16], [17], is shown in Figure 6.

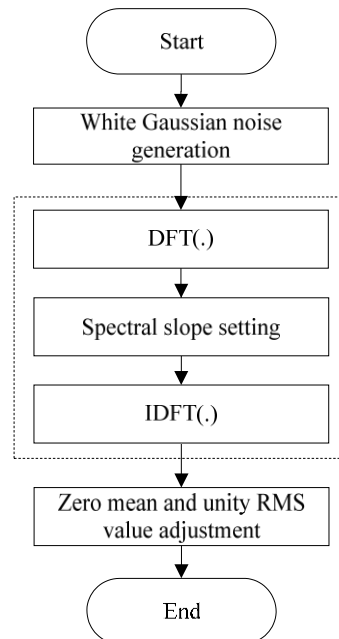


Figure 6. Algorithm for colored noise generation.

Analysis of performance for both standard cumulants of

sixth and fourth order and unbiased cumulants of sixth order is further done in following propagation scenarios: channel with AWGN, as well as colored noise channel. To the best of our knowledge, this is the first analysis of this kind for real and complex constellations.

#### 4. SIMULATIONS

To evaluate classification performance of cumulants-based AMC algorithms in the presence of colored noise and AWGN values of Probability of Correct Classification ( $P_{cc}$ ) parameter is calculated, through a series of carried out computer – based simulations. Simulations are conducted in MATLAB software package. The transmitted signal is modelled in form of complex (QPSK) and real (BPSK, PAM) constellation symbols, and corrupted by noise. As a reference, AMC performance reported under AWGN channel in [4], is presented in Figure 7.

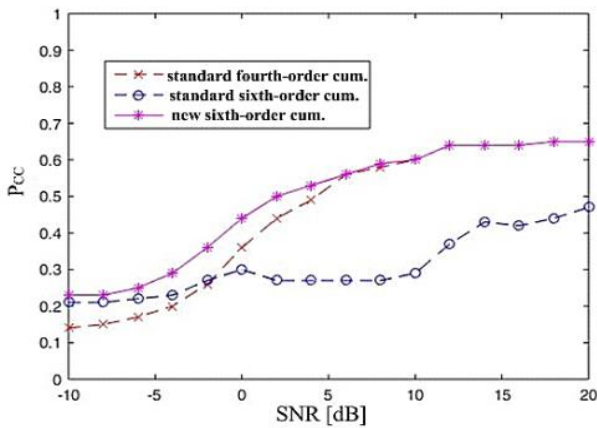


**Figure 7.** Correct classification probability, AWGN channel, [4].

For the conducted simulations overall sample size  $N$  was 2,000 symbols, with noise variance considered to be a priori known in every particular test. The colored noise was generated by algorithm shown in Figure 6, and it was generated as violet, pink, blue, and red noise, respectively. Novel AMC algorithm, based on unbiased sixth-order cumulants formula, was simulated along with standard AMC algorithm based on classical sixth and fourth-order cumulant formula, for the reasons of comparison. This was done by comparing obtained  $P_{cc}$  values, for the same real and complex constellations simultaneously, under the same considered channel environments. Presented performance evaluation was carried out through 2,000 Monte Carlo simulations, implemented in MATLAB software.

Probability of correct classification values for all considered AMC algorithms was calculated in a wide range of  $SNR$  values, from -10dB to 20dB. Different sets of modulation candidates were considered {BPSK; PAM-4; PAM-8; PAM-16; PAM-32; PAM-64; QPSK} under six different propagation scenarios - received signal was corrupted by: (i) violet noise, (ii) pink noise, (iii) blue noise, and (iv) red noise. Simulation results are shown in Figures 8 - 11, respectively.

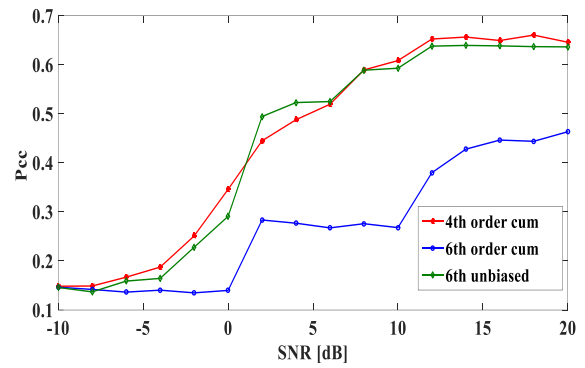


**Figure 8.** Correct classification probability, violet noise channel.

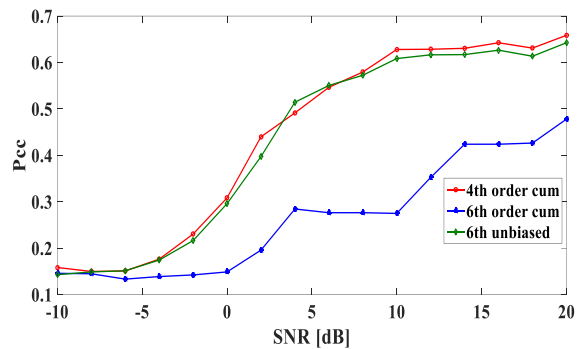


**Figure 9.** Correct classification probability, pink noise channel.

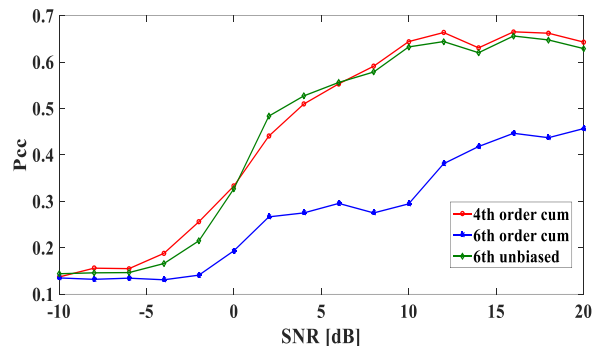


**Figure 10.** Correct classification probability, blue noise channel.

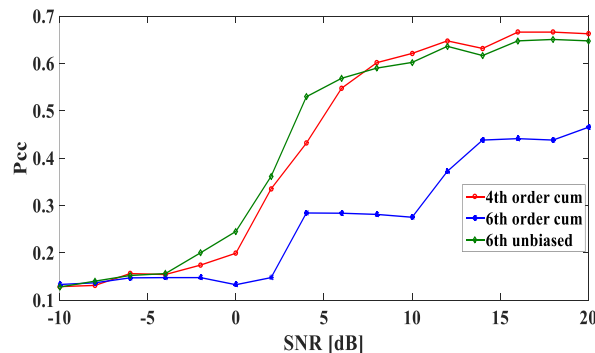


**Figure 11.** Correct classification probability, red noise channel.

According to the results, illustrated in figures above, it

can be noticed the following: for higher values of  $SNR$ , similar  $P_{cc}$  are achieved in the presence of colored noise and AWGN. But, for lower values of  $SNR$ , starting around 0dB, the presence of colored noise significantly degrades  $P_{cc}$ , for approximately 10% and more, depending of colored noise type, in comparison to AWGN. The biggest difference is noticed for AMC algorithm based on standard sixth-order cumulants. There is a difference among the colored noises (violet, pink, blue and red), with relatively highest degradation caused by red noise appearance.

Over the whole observed  $SNR$  range values,  $P_{cc}$  values for AMC algorithms based on standard fourth and novel unbiased sixth order cumulants are on higher level (for approximately 15-30%), comparing to standard sixth order cumulants. According to theoretical cumulants values from Table 1, that is expected behaviour due to decision thresholds for classification and unbiased feature which is improving classification of real signal constellations. Thus, these two algorithms are superior in AMC performance in comparison with standard sixth order cumulants based algorithm, for modulation classification of observed constellations in colored noise.

## 5. CONCLUSION

In this paper well known AMC algorithms based on higher-order cumulants are observed in context of signal degradation due to various colored noise types, and their performance was evaluated in intensive computer simulations through values of probability of correct classification,  $P_{cc}$ . The achieved results confirmed that presence of colored noise significantly deteriorates AMC performance, especially for lower  $SNR$  values. As working conditions due to electronic components and systems, both on transmitter and receiver side, often introduces colored noise and low  $SNR$  values, it is obviously of interest to consider its impact, as it will significantly degrade  $P_{cc}$  and consequently AMC performance. It was shown that algorithms based on fourth order standard and unbiased sixth-order cumulants have superior results in modulation classification in radio environment with real and complex signal constellations included.

## References

- [1] ELDERMERDASH, Y.A., DOBRE, O.A., ONER, M.: *Signal identification for multiple-antenna wireless systems: Achievements and challenges*, IEEE Commun. Surv. Tutor., 18(3) (2016) 1524–1551.
- [2] PAJIC, M.S., VEINOVIC, M., PERIC, M. et al.: *Modulation order reduction method for improving the performance of AMC algorithm based on sixth order cumulants*, IEEE Access, 8 (2020) 106386-106394.
- [3] SWAMI, A., SADLER, B.M.: *Hierarchical digital modulation classification using cumulants*, IEEE Trans. Commun., 48(3) (2000) 416-429.
- [4] SIMIC, M., STANKOVIC, M., ORLIC, V.D.: *Automatic modulation classification of real signals in AWGN channel based on sixth order cumulants*, Radioengineering, 30(1) (2021) 204-214.
- [5] HAZZA, A., SHOAI, M., ALSHEBELI, S.A. et al.: *An overview of feature-based methods for digital modulation classification*, 2013 International Conference on Communications, Signal Processing, and their Applications (ICCSPA), (2013), 1–6.
- [6] ORLIC, V.D., BOZOVIC, R.R.: *Signal constellation distortion and its impact on cumulant-based AMC performance*, In Proc. Int. Sci. Conf. Defensive Technol. OTEH, (2022), 333-339.
- [7] SONI, A., UPADHYAY, R., KUMAR, A.: *Analysis of colored noise and its effect on BER performance of wireless communication*, Journal of electrical and electronics engineering, 12(1) (2019), 45-50.
- [8] KHANDELWAL, A., CHARAN, C.: *Performance analysis of spectrum sensing under coloured noise*, 2017 2nd IEEE International Conference on Recent Trends in Electronics, Information & Communication Technology (RTEICT), (2017) 787-790.
- [9] LUO, C., CASASECA-DE-LA-HIGUERA, P., McCLEAN, S. et al.: *Characterisation of Received Signal Strength Perturbations using Allan Variance*, IEEE Trans. on Aerospace and Electronic Systems, (2018) 837-889.
- [10] LIN, X., JIAO, Y., ZHAO, D.: *An Improved Gaussian Filter for Dynamic Positioning Ships With Colored Noises and Random Measurements Loss*, in IEEE Access, 6, (2018), 6620-6629.
- [11] HOU, B., HE, Z., SUN, B. et al.: *Unscented particle filter for  $\alpha$ -Jerk model with colored noise*, Chinese Automation Congress (CAC), (2017) 6178-6183.
- [12] NERANDZIC, M., BOZOVIC, R.R., ORLIC, V.D.: *Impact of AWGN estimation on classification performance of AMC algorithms based on higher order cumulants*, 2021 29th Telecommunications Forum (TELFOR), (2021) 1-4.
- [13] ORLIC, V.D., DUKIC, M.L.: *Setting the optimal decision threshold and analysis of impact of sample size on automatic modulation classification based on sixth-order cumulants*. In Proc. Int. Sci. Conf. Defensive Technol. OTEH, (2012) 511-515.
- [14] PAJIC, M.S., VEINOVIC, M., ORLIC, V.D.: *Complex signal constellations in cumulants-based AMC: Statistics and performance*, Telfor Journal, 13(2) (2021) 63-68.
- [15] DOU, Z., SHI, C., LIN, Y. et al.: *Modeling of Non-Gaussian colored noise and application in CR multi-sensor networks*, Eurasip Journal on Wireless Communications and Networking (2017).
- [16] ZHIVOMIROV, H.: *A Method for Colored Noise Generation*, Romanian Journal of Acoustics and Vibration, 15 (1) (2018), 14-19.
- [17] ZHIVOMIROV, H.: *Pink, Red, Blue and Violet Noise Generation with Matlab*, MATLAB Central File Exchange, (2024).



# SENTINEL-1 SAR INTERFEROMETRY FOR TERRAIN MONITORING: A CASE STUDY OF MINE DYNAMICS

MILOŠ BASARIĆ

Military Geographical Institute - "General Stevan Bosković", Belgrade, [m-basaric@protonmail.com](mailto:m-basaric@protonmail.com)

DUŠAN JOVANOVIĆ

Faculty of Technical Sciences University of Novi Sad, Novi Sad, [dusanbuk@uns.ac.rs](mailto:dusanbuk@uns.ac.rs)

**Abstract:** The use of SAR (Synthetic Aperture Radar) and InSAR (Interferometric SAR) technology is very useful for monitoring changes in soil topography in industrial locations such as the Veliki Krivelj open pit mine near Bor. By analysing Sentinel-1 satellite data from January to May 2024, subcentimeter terrain changes were revealed, associated with exploitation activities and dynamic processes in the mine environment. This paper illustrates the effectiveness of InSAR methods in the detection of geodynamic changes, highlighting the potential for sustainable resource management and monitoring of topographic changes in industrial locations.

**Keywords:** Interferometric SAR (InSAR), Ground Deformation, Sentinel-1 Satellite Imagery, Open Pit Mines, Environmental Monitoring.

## 1. INTRODUCTION

In today's world, where industrial and natural processes are constantly shaping our planet, monitoring and understanding changes in soil topography is becoming crucial for sustainable resource management and environmental protection. Traditional methodological approaches are often limited in their ability to provide detailed and continuous information on the dynamics of terrain changes. On the other hand, the limitation of modern photogrammetric methods is their dependence on lighting and weather conditions, as well as logistical difficulties [1]. In this context, the use of SAR images (Synthetic Aperture Radar) and InSAR (Interferometric SAR) technology stands out as a powerful tool for precise and continuous measurement of vertical and horizontal changes in the Earth's surface, especially regarding the use of publicly available data such as e.g. from the Sentinel mission.

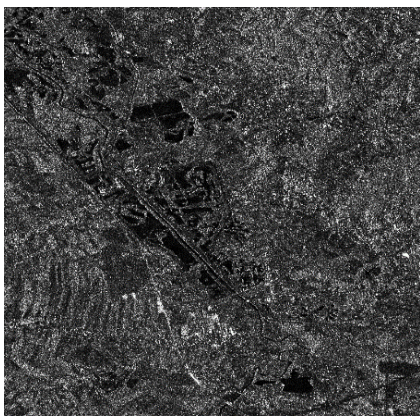
InSAR combines the capabilities of radar with the principles of interferometry to generate highly accurate digital terrain models. This technique relies on the analysis of phase differences between multiple radar images taken from the same orbit, enabling the detection of subcentimeter terrain changes. This means that InSAR can detect even the smallest deformations that can be caused by various geodynamic processes such as seismic

activity, landslides or resource exploitation. Accordingly, the application of InSAR technology for monitoring terrain topography changes in industrial locations such as mines has significant potential, and there is also a significant need for monitoring mining tailings [2]. Using the example of an open pit mine in Veliki Krivelj near Bor, this paper focuses on the demonstration of the effectiveness of InSAR methods in the detection and analysis of changes in the terrain, with the aim of showing how InSAR can be applied to monitor exploitation activities, identify potential geodynamic risks, optimize management natural resources and the method of waste disposal. Through the combination of theoretical foundations of InSAR technology, practical results obtained using Sentinel-1 mission images and analysis of the obtained results, this paper demonstrates the effectiveness of InSAR technology in monitoring changes in ground topography at industrial and other locations.

## 2. BASIC PRINCIPLES OF SAR

SAR is an imaging radar, which can produce high-resolution radar images of the Earth's surface from airborne and space-based platforms. By emitting microwave signals and collecting reflected waves, i.e. measured backscatter, SAR systems create a SAR image that represents a 2D representation of the measured backscatter signal [3] as shown in Figure 1.





**Figures 1.** Example of 2D representation of SAR image

Since SAR is an active sensor and uses the microwave range within the wide radio spectrum, it can record day and night, as well as the ability to penetrate clouds and, to some extent, rain [4]. One of the key advantages of SAR technology is its ability to synthesize a large effective radar aperture, even though the physical aperture may be relatively small. This is achieved by moving the platform (whether satellite or aircraft) and recording the reflected signals over time. By combining this data, SAR can produce high-resolution images, allowing detailed analysis of surface features. These characteristics of SAR technology make it particularly interesting and useful for monitoring topography for several technical reasons:

1. Continuous monitoring - The ability to record day and night enables continuous monitoring of changes in topography regardless of weather conditions, which is crucial for timely detection and response to terrain changes.
2. Penetration through clouds and rain - SAR can penetrate clouds and rain, enabling data collection even in adverse weather conditions, which is important for continuous monitoring and analysis throughout the year.
3. High resolution - SAR provides high-resolution images that allow detailed analysis and precise measurement of topographic changes, which is crucial for identifying and monitoring small ground movements, landslides or other geodynamic processes.
4. Wide coverage area - SAR systems can quickly and efficiently cover large areas, which is useful for monitoring topographic changes in large territories, such as mines or agricultural lands.

These advantages make SAR technology essential for accurate, reliable and continuous monitoring of topographic changes, enabling detailed analysis and quick reactions. Sentinel-1 stands out as one of the important sources of satellite SAR images due to its continuous global coverage, high image resolution and open data access. The Sentinel-1 mission, part of the European Copernicus program, consists of two satellites, Sentinel-1A (2014) and Sentinel-1B (2016-2021), which carry C-band SAR sensors, which means that the wavelength of the signal is about 5.6 cm, which is suitable for

topography monitoring because this wavelength enables good penetration through clouds and vegetation, which results in high reliability in obtaining data even in unfavourable atmospheric conditions. The C-SAR has four observation modes each with a different swath and resolution to suit their purpose: Stripmap (SM), Interferometric Wide swath (IW), Extra Wide swath (EW), and Wave (WV) mode. There are also 4 potential combinations of polarizations (one band VV or HH polarization, or two bands with VV+VH or HH+HV polarizations). Swath is depending on the mode, while the spatial resolution is 5m x 20m, while the height resolution is about 10 meters, which enables detailed mapping of surface features.

The mission is designed for global monitoring with a wide range of applications, including surface deformation monitoring, natural disaster management, monitoring of agricultural activities and monitoring of forest areas [5, 10]. Sentinel-1 data is open and freely available to users worldwide. The European Space Agency (ESA) provides access to this data through online platforms such as the Copernicus Open Access Hub. Users can download, analyze and use SAR data for research, scientific studies, as well as for practical applications in various industries. This open access policy encourages innovation, enhances global collaboration and enables a wide range of research and commercial activities.

### 3. SAR INTERFEROMETRY

Interferometry of SAR images (InSAR) is a method that uses the phase difference between two complex SAR observations taken from slightly different sensor positions to obtain information about the Earth's surface. The SAR signal contains amplitude and phase information. The amplitude represents the strength of the radar response (backscatter), while the phase is part of one complete cycle of the sinusoid (one SAR wavelength). The phase of the SAR image is determined mainly by the distance between the satellite dish and the target points on the ground.

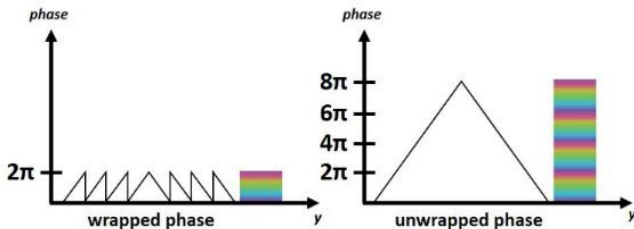
By combining the phase of these two images after co-registration, an interferogram whose phase is highly correlated with the topography of the terrain can be generated. In the case of differential interferometry (DInSAR), this topographical phase contribution is removed using a digital elevation model (DEM). The remaining variation in the interferogram can be attributed to surface changes that occurred between the two dates of image acquisition, as well as unwanted atmospheric effects [6]. The interferometric phase of each SAR image pixel is determined by the difference in the signal path from each of the two SAR sensors to the considered resolution cell. The generated interferogram contains the phase variation  $\phi$ , caused by several factors such as the Earth's phase curvature  $\phi_{flat}$ , topographic phase  $\phi_{DEM}$ , atmospheric conditions  $\phi_{atm}$ , noise  $\phi_{noise}$  (scatterers, different viewing angles, and volume scattering), and surface deformation  $\phi_{disp}$  between the two surveys (Equation 1).

$$\phi = \phi_{DEM} + \phi_{flat} + \phi_{disp} + \phi_{atm} + \phi_{noise} \quad (1)$$

Differential SAR interferometry (Equation 2) is used to estimate land surface contributions ( $\phi_{flat}$  and  $\phi_{DEM}$ ), removing them from the interferogram so that the remaining phase variation can be related to changes in surface elevation between the two surveys. This works best if atmospheric contributions and other noises are kept to a minimum as they are difficult to model. Therefore, it is advisable to anticipate this when selecting images. The coherence between the reference and secondary images serves as an indicator of the quality of phase information, evaluating the degree of similarity between the images for interferometric processing, while the loss of coherence can lead to poor results and is caused by temporal, geometric and volumetric decorrelation [7].

$$\phi - \phi_{DEM} - \phi_{flat} = \phi_{disp} + \phi_{atm} + \phi_{noise} \quad (2)$$

In an interferogram, the interferometric phase is ambiguous and is known only within a range of  $2\pi$ . In order to relate to the topographic height, the phase must be "unwrapped". The ambiguity height is defined as the height difference that causes an interferometric phase change of  $2\pi$  after smoothing the interferogram. The phase unwrapping process resolves this ambiguity by integrating the phase difference between adjacent pixels. After removing the integer height differences (corresponding to an integer number of phase cycles of  $2\pi$ ), the phase variation on the smoothed interferogram provides a measurement of the actual height change as shown in Figure 2. The unwrapping results should be interpreted as the relative height or displacement between the pixels in the two images.



Figures 2. Principle of phase unwrapping [6]

The quality and reliability of the unwrapping results depend on the initial coherence. For processing Sentinel-1 satellite images, which use radar technology (SAR), coherence between two images from different dates is a key indicator for analyzing changes on the ground. Coherence measures how similar or consistent two radar images are with each other. The coherence value ranges from 0 to 1, where 1 means complete similarity (high coherence), and 0 means complete lack of similarity (low coherence). For different applications, desired coherence values can vary. For monitoring terrain deformations, a high coherence value (usually above 0.6) is desirable to accurately detect small changes on the surface. Detection of changes in vegetation or urban areas requires medium coherence values (between 0.4 and 0.6). For erosion or landslide analysis, high coherence values are also

desirable, often above 0.6. In general, coherence above 0.5 is considered good for most applications, as it indicates significant similarity between two images, which can imply stability or minor changes. In this paper, a minimum coherence value of 0.3 was chosen to discard all images that are not similar. It is important to note that coherence can be low in areas with dense vegetation or changes in soil moisture, so it is crucial to contextualize the results according to the specific conditions of the terrain being analyzed..

The height resolution of 10 meters in Sentinel-1 SAR images enables detailed terrain mapping and precise detection of height differences at that level of precision. The combination of high horizontal resolution of about 5 meters and precise height resolution enables the identification of even the smallest changes in topography, which is useful for monitoring subcentimeter vertical displacements caused by geological, geotechnical or other changes in the terrain. This technology enables effective monitoring and analysis of terrain changes, which are key to understanding the dynamics and of geographic areas.

## 4. CASE STUDY OF MINE DYNAMICS

### 4.1. Geographic Context of the Mine

The subject of the analysis is the open pit of the Veliki Krivelj mine (located in the area of interest between coordinates: 44.163°N, 22.252°E and 44.049°N, 22.046°E). Veliki Krivelj is near the town of Bor in the eastern Serbia. The mine is located in an area geologically rich in copper and other minerals, which is the main reason for the development of mining operations in these locations. Its geographical position allows access to large reserves of mineral raw materials, which is key to its economic importance and continued exploitation.

This mine at national-level of Serbia is particularly significant to monitor due to the dynamic nature of their mining operations and their impact on the environment, and it goes through continuous changes in the exploitation of resources, which affects the topography and stability of the terrain. Monitoring these changes provides a deeper understanding of how mining activities affect the local ecosystem, water resources and surrounding communities. Also, the dynamics of exploitation can have long-term consequences on the local economy and social structure, which emphasizes the importance of systematic monitoring and management of this location.

### 4.2. Data

For the analysis of deformations in the territory of the mine, Sentinel-1 A images were used in pairs of adjacent acquisitions with the same swath shown in Figure 3. These are IW images, with a relative orbit number of 80 in the descending direction and VV&VH polarization, which is generally used in such analyses.



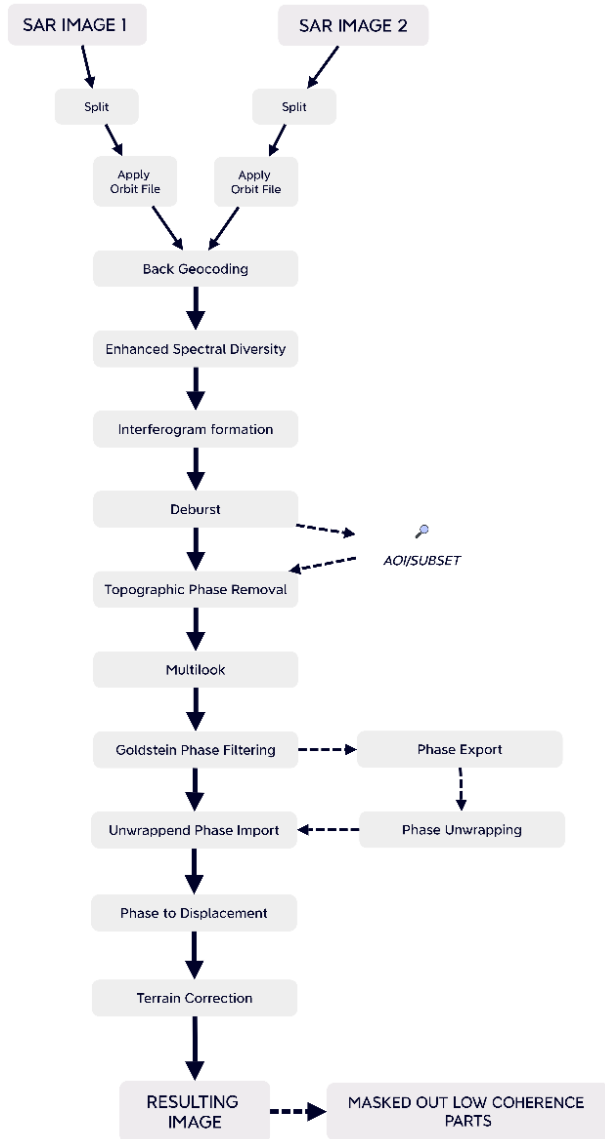
**Figure 3.** SAR Images footprint [8]

In this study, 12 images were used, in the period from 04.01.2024. to 15.05.2024. (the images in between are from 16.01, 28.01, 09.02, 21.02, 04.03, 16.03, 28.03, 09.04, 21.04. and 03.05.2024), which makes 11 interferometric analyses with a time window, i.e. a frequency of about 12 days. The selected period for SAR interferometric analysis enabled the use of fresh and recently available data from the Copernicus platform, which is crucial for the topicality of the research. Although seasonal changes may affect the coherence due to the growth of vegetation beginning in March and April, this period was chosen to make the most of the limited time for data collection and processing. IW types of images were used, which imply a wider observation zone and enable the coverage of a wider geographical area in one pass. The Sentinel-1 IW mode provides a wide coverage area in a single pass of the satellite, useful for observing large territories. The high spatial resolution of the images enables detailed mapping of the Earth's surface, crucial for the analysis of geological changes and urban development, as well as for monitoring the environment and disasters. The interferometric capabilities of IW mode support accurate measurement of ground displacement and deformation, making IW imagery a key tool for geoinformation studies. The images were processed in the open software SNAP, which is a free software developed by ESA.

### 4.3. Methodology

SAR data was processed using interferometric techniques to generate interferograms, a basic tool for terrain deformation analysis. Data processing includes differential interferometry - DInSAR (Differential

Interferometric Synthetic Aperture Radar), which enables the detection and quantification of vertical movements of the Earth's surface between two different moments in time. Data calibration was performed to eliminate atmospheric effects and other artifacts that may affect the accuracy of the results. The processing steps are shown as a flowchart in Figure 4. First, two adjacent SAR images from the same orbit from two temporally adjacent acquisitions were used. After downloading, they were "split" to extract the corresponding bursts from the images. Precise orbits were then applied to ensure maximum geolocation accuracy. The next step was "back geocoding", which enables correct alignment of SAR images in geographic space. Then the "enhanced spectral diversity" method was applied to improve the quality of spectral coherence. After that, an interferogram was formed that represents the phase difference between two SAR images, which enables the analysis of deformations in the field. The interferogram went through a "deburst" process to remove discontinuities. A "subset", i.e. an area of interest, was selected, in this case the Veliki Krivelj open pit territory, to reduce the amount of data for further processing. After that, topographic phase removal is applied, which could introduce errors in the analysis, in order to isolate and analyse only changes in phases that are caused by real surface deformations or other phenomena of interest, and not changes which are the result of differences in terrain height. Further, "multi-look filtering" is applied to reduce noise and increase the signal-to-noise ratio. "Goldstein phase filtering" was additionally used to remove remaining phase noises. After phase filtration, phases were exported ("Snaphu phase export") and then unwrapping was performed ("Snaphu phase unwrapping") to eliminate phase cycles. The unwrapped phases are then loaded and converted to displacements ("phase to displacement"), which enables the detection of metric displacements. Finally, "terrain correction" was performed to ensure the precise geolocation of the resulting data. Finally, the resulting image was masked, removing parts of the image with coherence less than 0.3 to ensure valid data. Together, these enable a detailed analysis of terrain deformations using the DInSAR (Differential Interferometric Synthetic Aperture Radar) method, providing valuable insights into changes in the mine area.



Figures 4. Processing workflow of SAR images

#### 4.4. Analysis Results

Analysis of DInSAR interferometry over the Veliki Krivelj open pit reveals significant changes in ground level during different time periods. Despite the lack of detailed information on geological and mining processes, as well as the dynamics of mine operation, it is possible to draw useful conclusions by analyzing the coherence of interferograms and identifying specific patterns in ground level changes. The open pit proved to be highly coherent

on the interferograms, which enables precise detection of changes. In some periods, activities were observed that indicate a decrease in the ground level, while in other periods, changes suggest an increase in the ground level. This analysis focuses on the identification and interpretation of these changes, using custom legends for each time window to highlight extreme displacement values. Based on the obtained results and visualizations for each time period, we can try to draw conclusions about the dynamic processes taking place in the open pit.

In DInSAR analysis, the phase difference conversion between two SAR images and the ground displacement value is crucial. The phase of the radar signal depends on the distance between the satellite and the ground surface, and the phase differences between two time-separated images detect the change in that distance.

Table 1. Extreme displacement values across interferograms

Dates of acquisition (Image 1 - Image 2)	Decreased Terrain Level [cm]	Increased Terrain Level [cm]
<b>04.01-16.01. (Pair 1)</b>	<b>-4.5</b>	<b>1.9</b>
16.01-28.01.	-3	4.2
28.01-09.02.	Not detected	3.2
09.02-21.02.	Not detected	3.9
21.02-04.03.	Not detected	6
03.04-03.16.	-3.2	1.3
16.03-28.03.	-2.4	3.8
<b>28.03-09.04. (Pair 2)</b>	<b>-4.3</b>	<b>2.6</b>
09.04-21.04.	Not detected	3
21.04-03.05.	-3	2.4
<b>03.05-15.05. (Pair 3)</b>	<b>-2.2</b>	<b>7.9</b>

The "phase to displacement" value represents the change in distance between the radar on the satellite and the ground surface between two SAR images, quantifying ground displacement in millimetres or centimetres. This value is relative, showing how much the distance between the satellite and a certain place on Earth has changed between two SAR images, depending on the position of the satellite and the geometry of the image. It does not give the absolute height or depth of a point on the ground, but only the change in height as an indication, which is useful for detecting ground movement dynamics. The phase differences are first converted to displacement and then used to create maps that show changes over time windows. Positive values indicate an uplift of the ground, while negative values indicate a lowering of the ground. The analysis of these values enables the detection and monitoring of changes due to mining activities or natural processes in the Veliki Krivelj mine, providing insight into relative ground movements during the analysed time periods.

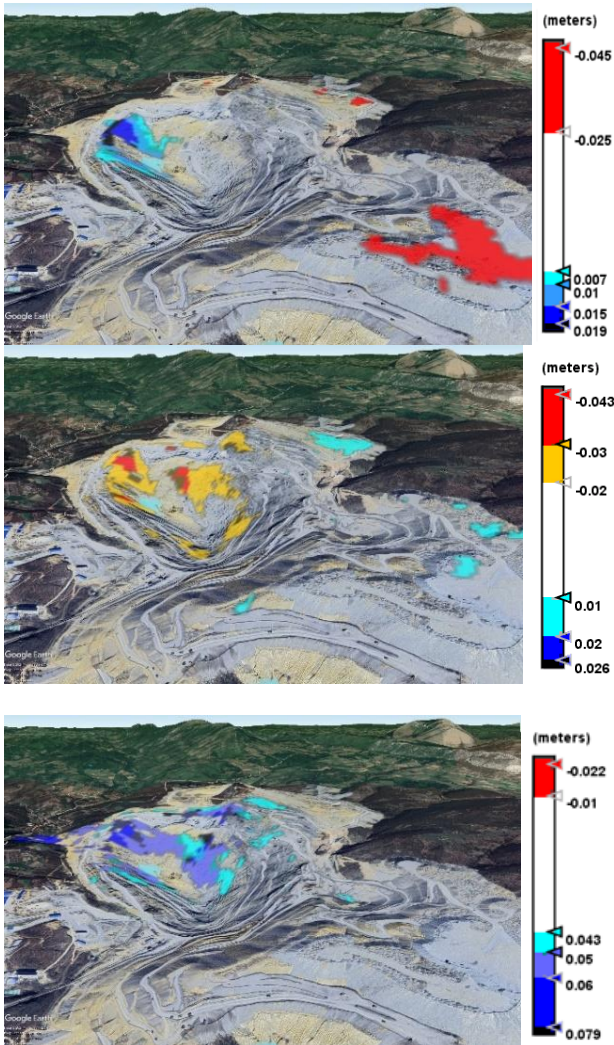


**Figure 5.** DinSAR Results: Pair 1 (top), Pair 2 (middle), Pair 3 (bottom)

Table 1 shows the results of interferometry with minimum and maximum values of the phase differences of the images converted to lengths (displacement). All extreme values are located in the open pit of the mine in all 11 interferograms. In order to ensure the accuracy and relevance of the results, values with a low level of coherence between images (less than 0.3) were neutralized. Only extreme displacement values are presented in the results, while small displacement values are not included in the visualization. This approach reduces the impact of possible noises caused by possible atmospheric effects and vegetation, enabling better identification and analysis of significant changes in the ground level. The visualization of the results was exported in KMZ format for display and verification on the digital terrain model in Google Earth. The results show significant changes in the ground level in the Veliki Krivelj open pit. Negative values of displacement (lowering of terrain or digging of material) vary up to -4.5 cm, while positive values (raising of terrain or accumulation of material) reach up to 7.5 cm. These changes indicate active geodynamic processes and mining activities. By neutralizing low coherence and focusing on

extreme values, the obtained data provide a clear insight into significant ground movements, useful for further analysis and monitoring of the mine's condition. In the table, the interferograms that have been specially selected are bolded, and the visualization for them is shown in Figure 5, providing a clearer insight into the extreme values for each time window. Orange and red colors represent areas where there is less material, i.e. where there is a noticeable decrease in the level of the ground (from higher to lower, respectively), while the shades of blue and black colors indicate the areas where material has been dumped, i.e. increase in ground level (from lower to higher values, respectively) in between two adjacent acquisitions of about 12 days. Such visualization helps to monitor natural processes, such as erosion or sedimentation, as well as mining activities, which may include tailings disposal or ore exploitation. For Pair 1, a decrease in the ground level of 2.5 to 4.5 cm is noticeable along the perimeter of the mining pit, while a slight increase of 0.7 to 1.9 cm is observed on the interior of the mine on the northwest side in a place that can be assumed to be a temporary dumped material. This may indicate processes such as sedimentation or redistribution of material due to mining activities or natural factors. The results for Pair 2 show more significant changes. An increase in the soil level of 1 to 2 cm was observed along the perimeter of the pit, while a decrease of 2 to 4.3 cm was detected inside the pit. This may suggest more complex geological processes or changes in the mining method during that period. Pair 3, as the last interferometer in the investigated period, shows the most pronounced changes. On the northern side of the interior and on the northern perimeter of the pit, a significant increase in the ground level from 4.3 to 7.9 cm was observed, while in other places there were no significant changes. These results indicate activities that may be related to mining processes or geological features, especially along the perimeter of the mine where consistent increases and decreases in ground level have been observed. Variations within a mine may be the result of local geological conditions or specific technological processes. Further research, with additional data on the dynamics of mining activities, geological features and weather conditions, is necessary to fully understand the causes of these changes in topography. This research provides the basis for further terrain analysis within the Veliki Krivelj mining area.

When analyzing the results that show maximum and minimum displacement values in the context of the DInSAR method, it is possible to point out that the interpretation of these changes as a consequence of mining activities has an intuitive logic, bearing in mind the known processes of depositing and removing materials in mines. However, since there are no additional sources available to support these findings, it is important to emphasize that the next phase of research should include more detailed verification and confirmation of the results. This need for further research may be a key aspect of the discussion, highlighting the importance of expanding the literature and additional studies that would confirm and deepen the understanding of the links between DInSAR results and specific mining processes.

The integration of this argument not only enhances the discussion, but also lays the foundation for future work aimed at improving the scientific validity and wider application of the results in practice.

## 5. CONCLUSION

In this research, which deals with the application of SAR technology for monitoring soil deformations in industrial locations such as open pit mines, the important role of Interferometric SAR (InSAR) in the analysis of these changes is highlighted. Using the example of Veliki Krivelj mine in Serbia, the research demonstrated the ability of Sentinel-1 satellite images to accurately detect vertical displacements of the terrain, which is essential for understanding the impact of mining activities on the environment. The analysis of the InSAR technique indicated the effectiveness of its use in the identification and quantification of soil deformations caused by exploitation, as well as in monitoring their long-term changes. This methodology enables detailed monitoring of areas of high coherence such as open pit mines, where complex processes such as subsidence, material accumulation or topographic changes often occur. The study highlights the importance of continuous monitoring of mining sites for sustainable resource management and environmental protection. By analyzing time series of interferograms, researchers were able to identify and characterize different phases of changes in soil deformations, which provides valuable insights into exploitation dynamics.

At the same time, despite challenges such as seismic activity or changes in vegetation that can affect the quality of the interferogram, SAR technology has shown indications of even subtle changes. This research highlights the need to integrate geologic, meteorological, and operational data to better understand the factors influencing soil change in mining environments. and additionally confirmed the results, which would be the subject of further research as well as application on examples of other open pits in Serbia to compare the results.

## References

- [1] LEŚNIAK, A., PORZYCKA-STRZELCZYK, S.: Environment monitoring using satellite radar interferometry technique (PSInSAR), 2008.
- [2] RAJKOVIĆ, R., BUGARIN, M., MARINKOVIĆ, V.: Analysis of the stability of the tailings disposal site 'Oštrejski planir' of the surface mine 'Bor' as a function of water content, *Mining and Metallurgy Engineering Bor*, no. 3, pp. 49-64, 2013, doi: 10.5937/mmeb1303049R.
- [3] "Introduction to Synthetic Aperture Radar," ArcGIS Pro, [Online]. Available: <https://pro.arcgis.com/en/proapp/latest/help/analysis/image-analyst/introduction-to-synthetic-aperture-radar.htm.s> [Accessed: 15.05.2024].
- [4] OUCHI, K.: Recent Trend and Advance of Synthetic Aperture Radar with Selected Topics, *Remote Sens.*, vol. 5, pp. 716-807, 2013. Available: <https://doi.org/10.3390/rs5020716>
- [5] "S1 Mission," SentiWiki, [Online]. Available: <https://sentiwiki.copernicus.eu/web/s1-mission>. [Accessed: 20.05.2024].
- [6] European Space Agency, "S1TBX TOPSAR Interferometry with Sentinel-1 Tutorial", ver. 2.0, Jun. 2018 [Online]. Available: [https://step.esa.int/docs/tutorials/S1TBX%20TOPSAR%20Interferometry%20with%20Sentinel-1%20Tutorial\\_v2.pdf](https://step.esa.int/docs/tutorials/S1TBX%20TOPSAR%20Interferometry%20with%20Sentinel-1%20Tutorial_v2.pdf)
- [7] "InSAR Principles: Guidelines for SAR Interferometry Processing and Interpretation," ESA TM 19, Pt. A, [Online]. Available: [https://www.esa.int/esapub/tm/tm19/TM-19\\_ptA.pdf](https://www.esa.int/esapub/tm/tm19/TM-19_ptA.pdf). [Accessed: 10.06.2024].
- [8] Copernicus Sentinel Data, "Sentinel-1A SAR Footprint Image, Orbit 80, Slice 21," Copernicus European Space Agency, "ESA Sentinel Application Platform (SNAP)," [Online]. Available: <https://step.esa.int/main/toolboxes/snap/>. [Accessed: 10.05.2024].
- [9] JOVANOVIĆ, D., GAVRILOVIĆ, M., BORISOV, M., GOVEDARICA, M.: Deforestation monitoring with Sentinel 1 and Sentinel 2 images – the case study of Fruska gora (Serbia), *Šumarski list* 145, br. 3-4 (2021): 127-134., <https://doi.org/10.31298/sl.145.3-4.2>



## ANALYSIS OF TRAFFIC ACCIDENTS IN NOVI SAD USING GIS TECHNOLOGY

DEJAN DJORDJEVIĆ

Military Geographical Institute - "General Stevan Bosković", Belgrade, [dejanjordjevic.vgi@gmail.com](mailto:dejanjordjevic.vgi@gmail.com)

MILOŠ BASARIĆ

Military Geographical Institute - "General Stevan Bosković", Belgrade, [m-basaric@protonmail.com](mailto:m-basaric@protonmail.com)

IVAN GARIĆ

Military Geographical Institute - "General Stevan Bosković", Belgrade, [ivan.garic@yahoo.com](mailto:ivan.garic@yahoo.com)

**Abstract:** This paper investigates the spatial and spatio-temporal distribution of traffic accidents in Novi Sad using GIS technology, analyzing open data from 2015 to 2023. Thematic maps, KDE method and k-means cluster analysis were used to identify high-risk areas. The Space-Time Cube tool enabled spatio-temporal analysis, while the Emerging Hot Spot Analysis revealed trends and anomalies in the concentration of accidents. The results contribute to a better understanding of accident dynamics, enabling more efficient planning of safety measures and directing resources to high-risk areas. The findings highlight critical areas and suggest measures to improve traffic safety.

**Keywords:** Traffic accidents, GIS, spatial analysis, high-risk areas, preventive measures.

### 1. INTRODUCTION

Traffic accidents (TA) represent one of the most significant problems of modern urban environments, causing serious economic, health and social consequences. In a city like Novi Sad, with a growing population and an increasing number of vehicles, the frequency of traffic accidents is becoming alarming. These accidents result not only in material damage, but also in serious injuries and loss of life, which further burdens the health system and affects the quality of life of residents. Effective traffic management and reducing the number of accidents requires a deep understanding of the spatial patterns of traffic accidents and the factors that influence them. In this context, Geographic Information Systems (GIS) represent a powerful tool for analyzing and visualizing traffic accident data. GIS enables the identification of high-risk areas and the analysis of various factors such as traffic infrastructure, weather conditions, and the behavior of road users.

The aim of this study is the application of GIS technology for the analysis of traffic accidents in Novi Sad, with a special focus on identifying critical points and understanding the key causal factors. The collected data on traffic accidents over a period of eight years (2015-2023) includes information on the location of accidents, type of accident, road conditions and other relevant parameters. This data was analyzed using advanced GIS software, which enabled the creation of thematic maps that visualize the spatial patterns of accidents. In addition to spatial analysis, various statistical methods were used in the study in order to identify the key factors that

influence the frequency of traffic accidents. The results of this study provide valuable insights that can be useful for decision makers, urban planners and traffic planners. The identification of high-risk areas enables directing resources to the most critical points, while the analysis of causal factors provides the basis for the development of targeted preventive measures. Recommendations arising from this study include the improvement of traffic infrastructure, installation of additional signage, implementation of educational campaigns and improvement of traffic regulation. In conclusion, this study emphasizes the importance of using GIS technology in the analysis of traffic accidents and provides concrete guidelines for improving traffic safety in Novi Sad. Through accurate mapping and detailed data analysis, it is possible to identify key areas and risk factors, which contributes to the development of more effective strategies to reduce the number of traffic accidents and improve overall traffic safety.

### 2. TRAFFIC ACCIDENTS AND THEIR ANALYSIS

Traffic accidents represent a significant social problem with a wide range of consequences for safety, economy and health. Analysis of these accidents has a key role in developing strategies to reduce and prevent them. Various methodologies are used in traffic accident research in order to identify the causes, risk factors and forms of their prevention. Descriptive analysis is the basic methodology used to study the characteristics of traffic accidents such as location, time, participants, vehicle types, and traffic conditions. This approach provides basic insights into accident patterns and trends [1].

By using GIS technologies, researchers can identify geographical zones with increased risk, as well as analyze the impact of various factors on traffic safety [2]. Statistical analysis is applied to investigate the relationship between different variables and traffic accidents, which includes correlation analyses, regression models and classification analyses [3]. Qualitative analysis includes detailed analysis of qualitative data such as witness reports, participant testimonies, and police reports. This approach provides additional insights into the causes and circumstances that lead to traffic accidents. Factors that can affect the likelihood and severity of traffic accidents include speed, alcohol and other opiates, bad roads, improper use of mobile devices while driving, lack of safety measures and infrastructure deficiencies. A complex analysis of these factors enables the identification of potential strategies and interventions to reduce the risk and consequences of traffic accidents [4].

In the context of traffic accidents, GIS enables the integration of different types of data in order to better understand the spatial distribution of accidents and identify critical points in traffic flows [5]. The use of GIS technologies allows analysts to visualize the distribution of traffic accidents on maps, which helps identify geographic patterns and locations of increased risk. These analyzes are of essential importance for the development of effective strategies for traffic safety, the planning of infrastructure investments and the application of specific traffic measures at critical locations. The application of GIS technologies represents an important aspect in traffic accident research, providing advanced analytical tools for understanding spatial patterns and the impact of factors on traffic safety. The continuation of the development and application of GIS opens up new opportunities for the improvement of traffic accident prevention strategies and more efficient management of traffic flows.

The use of Geographic Information Systems (GIS) extends beyond civilian applications, as it is also critical in military operations, especially in urban environments where the movement of military vehicles and personnel requires careful planning. In military contexts, traffic accident data, such as the one analyzed in this study, can provide valuable insights into the safest and most efficient routes for troop and equipment transportation. By identifying high-risk areas where accidents are frequent, GIS analysis enables military planners to avoid potential hazards, ensuring that military convoys can move through urban areas with minimal disruption and reduced risk. The same GIS tools that analyze civilian traffic accidents can be applied to simulate the movement of military vehicles, enhancing logistical efficiency and operational safety.

### 3. DATA AND METHODOLOGY

#### 3.1. Data

Data on traffic accidents were taken from the National Open Data Portal [6], where numerous open data sets in the possession of state authorities of the Republic of Serbia, including state administration authorities,

autonomous provinces and local governments, are published. The open data portal is not only a repository but also a platform for interaction with users, allowing them to add supplementary data and examples of data usage. Data on traffic accidents, published by the Ministry of the Interior, includes information by Police Departments and Municipalities, including the unique ID number of the accident, police department, municipality, date and time of the accident, geolocation of the place, type of accident, vehicle number, participant status and detailed description [7].

These data do not include accidents on the territory of Kosovo and Metohija. They are available in the form of tables by year for the period from 2015 to 2024, with an updated situation for the current year 2024. The downloaded Excel spreadsheets were customized by adding a row with column names and a new column showing the time of the accident in a format suitable for later processing, then saved in .csv format for loading into GIS software. All tables are consistent in form, structure and content. Each accident in the tables is marked with geographic coordinates in the WGS 84 projection, which is widely used in GIS applications. The tables were loaded into ArcGIS Pro, where the accidents were visualized according to the coordinates, which resulted in spatial data of point geometry in .shp format. Each accident on the map corresponds to one point that contains all the additional data from the initial table.

A subset of data was used for the territory of the Novi Sad Police Department for the period from 2015 to 2023.

#### 3.2. GIS Methodology

For a deeper understanding of patterns for understanding the occurrence of traffic accidents, various statistical methods were used, including: descriptive statistics and spatial statistical analysis. In this study, ArcGIS Pro software [8], one of the most powerful tools for GIS analysis, was used.

Descriptive statistics provide basic information about the data, such as the number of traffic accidents, the average number of accidents by time period, and variations in the frequency and severity of accidents. This step is crucial because it allows us to identify the underlying characteristics of the data and to determine if there are significant anomalies or patterns that require further investigation. Before embarking on a more detailed spatial and temporal analysis, the presentation of descriptive statistics will provide us with the necessary context and enable a better understanding of the complexity and dynamics of traffic accidents. The Summary Statistics tool generated tables with different summarized data based on individual categories of data in the attribute table. This tool provides a number of statistical measures such as sum, average, minimum, maximum and standard deviation for given categories.

Geographic Information System (GIS) is the key tool used in this study to analyze and visualize traffic accident data. GIS enables the integration and analysis of spatially referenced data, which is essential for identifying patterns



and trends.

The first step in the GIS analysis was the creation of a spatial database with information on all accidents. Each accident is represented as a point on the map, with associated attributes (date, time, type of accident, etc.). After that, various GIS functions were used to analyze the spatial distribution of accidents. Spatial analysis included the following steps:

1. *Data visualization* - Thematic maps were created that show the spatial distribution of accidents by year, types of accidents, and other relevant criteria. These maps provide a visual insight into accident concentrations and help identify high-risk areas.
2. *Density analysis* - The kernel density estimation (KDE) method was used to estimate the density of traffic accidents in space. KDE enables the identification of "hot spots" where the concentration of accidents is the highest, which is crucial for directing preventive measures and resources.
3. *Cluster analysis* - K-means cluster analysis was used to group accidents into clusters based on their spatial and attribute characteristics. This enabled the identification of similar groups of accidents and a better understanding of their common characteristics.
4. *Spatio-temporal analysis* - Spatio-temporal analysis of traffic accidents using the tool identifies trends and anomalies over time, discovering new hot spots and changes in the concentration of accidents.

The results of GIS and statistical analysis were integrated in order to obtain a comprehensive picture of the spatial and causal factors of traffic accidents in Novi Sad. The spatial patterns identified through the GIS analysis were correlated with the results of the statistical analysis in order to better understand the factors that contribute to the occurrence of accidents.

## 4. RESULTS AND DISCUSSION

### 4.1. Display of descriptive statistics

The display of descriptive traffic accident statistics provides basic information on data such as the number of traffic accidents, the average number of accidents by time period, as well as variations in the frequency and severity of accidents. In this way, we gain insight into the basic characteristics of the data and identify significant patterns that require further analysis.

The results shown in Table 1 show significant variations in the number of traffic accidents by year. The highest number of accidents was recorded in 2019 (4728), while the lowest number was recorded in 2015 (904). Most of the accidents resulted in material damage (52.5%), while accidents with injured persons made up a significant part (46.7%), and accidents with dead persons were relatively rare (0.8%).

**Table 1.** Number of TAs according to the outcomes by years

Year	Outcome	Number of TAs	
		by outcome	by year
2015	damage material	282 (31.2%)	904
	fatalities	6 (0.7%)	
	injuries	616 (68.1%)	
2016	damage material	2414 (54.3%)	4448
	fatalities	32 (0.7%)	
	injuries	2002 (45%)	
2017	damage material	2426 (52.1%)	4656
	fatalities	16 (0.3%)	
	injuries	2214 (47.6%)	
2018	damage material	2304 (53.7%)	4292
	fatalities	42 (1%)	
	injuries	1946 (45.3%)	
2019	damage material	2432 (51.4%)	4728
	fatalities	42 (0.9%)	
	injuries	2254 (47.7%)	
2020	damage material	2148 (52.4%)	4096
	fatalities	42 (1%)	
	injuries	1906 (46.5%)	
2021	damage material	2360 (53.8%)	4390
	fatalities	42 (1%)	
	injuries	1988 (45.3%)	
2022	damage material	1164 (54.1%)	2150
	fatalities	14 (0.7%)	
	injuries	972 (45.2%)	
2023	damage material	2322 (53.7%)	4326
	fatalities	24 (0.6%)	
	injuries	1980 (45.8%)	

The distribution of traffic accidents by time periods of the day shows that most accidents occur between 08:00 and 20:00, with the peak between 12:00 and 16:00. The results are shown in Table 2.

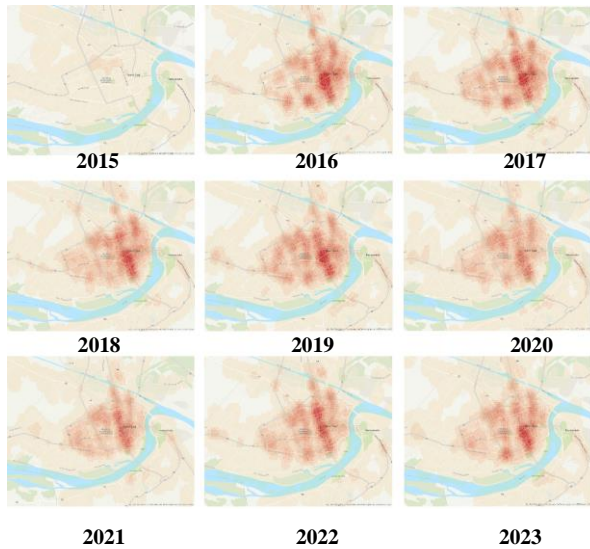
**Table 2.** Distribution of TAs according to time windows by years

Year	Time window						Mean time
	00-04	04-08	08-12	12-16	16-20	20-24	
2015	54	92	186	224	236	112	13:33
2016	260	408	990	1204	1020	566	13:31
2017	200	430	996	1278	1114	638	13:53
2018	254	424	934	1188	962	530	13:24
2019	302	398	968	1322	1124	614	13:38
2020	202	352	850	1186	1012	494	13:47
2021	258	392	890	1206	1068	576	13:45
2022	129	200	425	589	509	298	13:02
2023	206	356	948	1180	1030	606	13:53

### 4.2. Spatial analyzes and distribution of accidents

Spatial data visualization is crucial when dealing with large datasets. Vector point representation is not an effective approach for thousands of traffic accidents per year, so it is necessary to use raster data forms. Heatmaps, generated by the Kernel Density method, allow easy identification of patterns and clusters through color gradation, which facilitates the interpretation of density and concentration of events.

Figure 1 shows the results of the analysis of the density of traffic accidents in Novi Sad, where the dark red areas indicated the highest density of accidents. This enables quick identification of critical areas that require additional attention and analysis.



Figures 1. Heatmaps of TAs by years

The analysis showed that certain parts of the city are more prone to more accidents, which may be related to traffic junctions, intensive traffic or specific infrastructural characteristics. To identify the geographic center or center of concentration of traffic accidents, the Mean Center tool was applied. This tool calculates the average X and Y coordinates of all crash points, placing a new point on the map that represents the midpoint for the given data set. This analysis can be performed in an alternative way by focusing on specific cases within the attribute table (Case Field), which enables the identification of central points related to certain phenomena. Figure 2 shows the central points over the years in relation to the outcomes of traffic accidents.



Figures 2. Mean center points by outcomes and years

It is noticeable that the center points are grouped when it comes to outcomes with material damage and injuries, except for 2015, when the mean center point deviated significantly from the others. In contrast, the central points related to fatal traffic accidents vary spatially. This indicates a lack of consistent spatial pattern for these accidents, meaning they may occur in different locations each year. The lack of clearly defined "hot spots" for fatal accidents can make predictive analysis and application of preventive measures difficult.

After that, the Cluster and Outlier Analysis (Anselin Local Moran's I) statistical method was applied, which identifies spatial clusters of high and low values, as well as isolated locations in the data [9]. Figure 3 shows the results of this analysis for the year 2023, which showed that high values are clustered in the city core, while low values are identified along the periphery, especially along the road infrastructure.

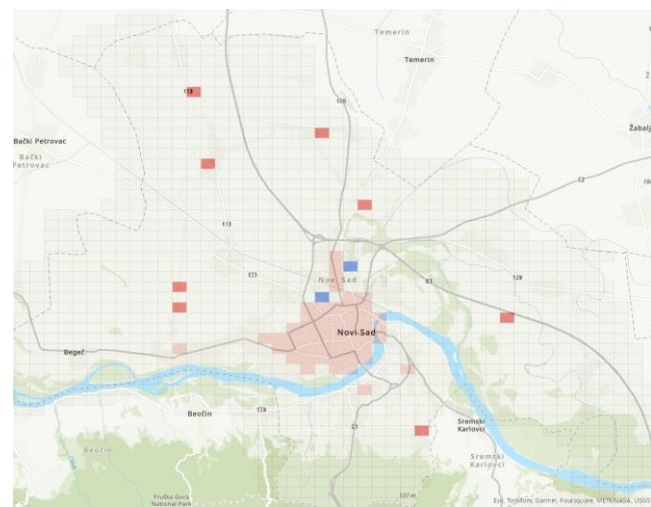


Figure 3. Cluster analysis for 2023

Figure 4 shows a legend for understanding the results shown in Figure 3. Cluster analyzes indicate the sporadic occurrence of fatal traffic accidents in the peripheral parts of the city, while clearly defined hotspots are not observed.

Symbol	Clusters type	Description
	High-High (HH) cluster	High values surrounded by high values.
	High-Low (HL) outlier	High value surrounded by low values (isolated high value).
	Low-High (LH) outlier	Low value surrounded by high values (isolated low value).
	Low-Low (LL) cluster	Low values surrounded by low values.
	Not Significant	These characteristics are not statistically significant.

Figures 4. Cluster analysis legend

These results suggest that traffic density in the city center is associated with a higher number of traffic accidents, while in the periphery the number of traffic accidents is relatively smaller and evenly distributed. This analysis provides important insights for local planners and decision makers in understanding the distribution of traffic incidents in the city.

### 4.3. Spatio-temporal analysis of traffic accidents

Spatio-temporal analysis of traffic accidents represents an integrative approach that enables a detailed examination and understanding of how traffic accidents are distributed and changed in space and time. This analysis uses geographic information along with weather data to identify patterns and trends that may be invisible in simpler analyses.

Space-Time Cube (STC) is an advanced analytical format that enables the integration and analysis of spatial and temporal data. Data on events that occur at specific time intervals and at specific locations are converted into a three-dimensional cube where two dimensions are spatial (x and y coordinates), and the third dimension represents time. This approach enables the identification of trends in the occurrence of traffic accidents over time [10].

Emerging Hot Spot Analysis is a spatio-temporal analysis based on STC. It is used to identify trends in geographic data, focusing on changes in the spatial and temporal patterns of traffic accident hotspots. This analysis detects new and unexpected areas with a significant increase or decrease in accident concentration over time. STC divides the data into time bins or increments (a period of 3 months was used in this paper), enabling a detailed analysis of trends and anomalies. Figure 5 shows the summarized result of this analysis, identifying the key hot spots in Novi Sad in the period from 2015 to 2023.

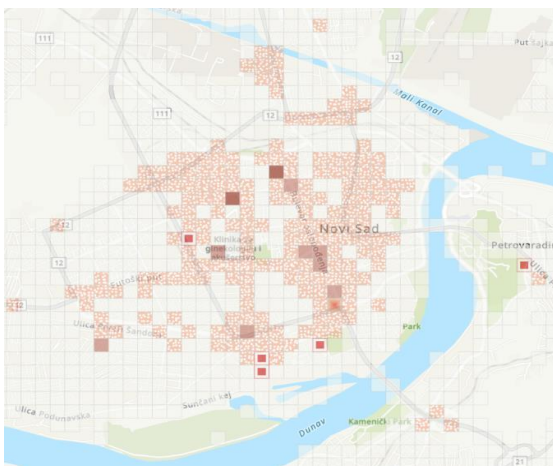


Figure 5. Emerging hot spot analysis results

Figure 6 shows part of the legend that is represented when displaying the results in this analysis with additional descriptions.

Symbol	Name	Description
	New Hot Spot	Statistically significant hot spot only for the most recent time step.
	Consecutive Hot Spot	Series of statistically significant hot spots in the most recent time steps.
	Intensifying Hot Spot	Location that is consistently hot and becoming hotter.
	Persistent Hot Spot	Location that is consistently hot (90% of bins are statistically significant hot spots).
	Diminishing Hot Spot	Location that is consistently hot but cooling down.
	Sporadic Hot Spot	Location that is intermittently hot and not hot.

Figure 6. Emerging hot spot analysis legend

What can be noticed is the appearance of new hot spots in certain parts of the city, with an accent on the group of these hot spots at Liman 4 area, as well as intensifying hot spots at the intersection of Bulevar Oslobođenja and Bulevar Cara Lazar streets. Also, we see that most of the city center is characterized by sporadic hot spots, while persistent hot spots and consecutive hot spots are visible in places that were previously identified as places with the highest incidence of traffic accidents (Bulevar Oslobođenja street, Sajmište area, Detelinara area, corner of Bulevar Europa street and Bulevar Cara Lazar street).

### 4.4. Discussion

The results of the analysis of traffic accidents in Novi Sad in the period from 2015 to 2023 provide a comprehensive insight into the temporal and spatial patterns of these events. Through descriptive statistics, spatial analysis and the use of advanced GIS tools, significant insights have been obtained that can help improve traffic safety and infrastructure planning.

Analysis of the number of traffic accidents by year shows significant variations. The number of accidents increased sharply between 2015 and 2016, after which it remained relatively stable until 2023. The highest number of accidents was recorded in 2019 (4728), while the lowest number was in 2015 (904). The average time of accidents is around 13:30, which indicates a high frequency of accidents in the early afternoon. These data are crucial for planning traffic controls and interventions during the most critical periods of the day.

Spatial distribution of traffic accidents is shown using raster maps and the Kernel method. The results indicate a high concentration of accidents along the main roads. These areas have been identified as critical zones that require special attention and interventions. Application of the Mean Center tool provided additional insights into changes in the spatial distribution of accidents over the

years. Mean Center analysis showed that the mean points of traffic accidents were consistent for accidents with material damage and injured persons, while the mean points for accidents with fatal outcome varied, which indicates the unpredictability of these events.

Cluster and Outlier Analysis (Anselin Local Moran's I) identified spatial clusters and extreme values. The results for 2023 showed that clusters of high accident values are concentrated in the city core, while clusters of low values are located on the outskirts of the city. These findings indicate a higher density of traffic accidents in the central parts of the city, which is expected due to the higher traffic density.

The analysis of traffic accidents in Novi Sad shows significant spatial and temporal variability in the frequency and severity of accidents. The high concentration of accidents along the main roads and in urban centers indicates the need for targeted interventions. It is recommended to improve infrastructure, increase traffic controls in critical periods and at designated places where a large number of TAs are connected, driver education and continuous analysis of data on traffic accidents in order to identify new trends and causes of changes.

The findings from the GIS analysis of traffic accidents in Novi Sad can have broader implications, particularly in military applications. The identification of high-density accident zones and spatial clusters is not only useful for improving civilian traffic safety but also for optimizing military convoy routes and logistics planning. In military operations, the ability to avoid accident-prone areas and to predict traffic patterns can be crucial for the success of missions, especially in urban environments. GIS tools allow military planners to simulate various scenarios, ensuring that routes are both safe and efficient. Additionally, the integration of spatial and temporal data through GIS can improve decision-making processes in emergency situations, enabling faster and more secure deployment of military resources.

## 5. CONCLUSION

This paper focuses on the analysis of traffic accidents in Novi Sad using GIS technologies and geostatistical methods. The aim of the research is to identify the spatio-temporal patterns of accidents and the factors that influence their occurrence. The application of GIS technologies enables the visualization and analysis of spatial data in a new way, which is of great importance for understanding the causes and dynamics of traffic accidents.

The research results confirmed the existence of defined accident patterns that suggest different influences such as infrastructure, road conditions and traffic density. The analysis of public data from the National Open Data Portal proved their usefulness and usability for various spatio-temporal analyses.

The research applied specific methods for geostatistical analysis and spatial modeling, which led to the identification of the main hotspots with a high number of

accidents. This significantly improved the understanding of the causes of traffic accidents at the local level and highlighted the importance of applying GIS technologies for traffic safety management.

This research represents significant progress in the analysis and management of traffic safety, demonstrating that GIS technologies and geostatistical methods can be successfully applied in other locations in Serbia and beyond.

In addition to civilian traffic safety applications, GIS technology plays a crucial role in military logistics and operations, providing critical insights for route optimization and risk management. The findings from this study could be applied to enhance military transport strategies, ensuring safer and more efficient movement of troops and equipment through urban environments by avoiding high-risk areas identified in the analysis.

## References

- [1] Munasinghe, D. (2023). Spatial Analysis of Urban Road Traffic Accidents Using GIS. *British Journal of Multidisciplinary and Advanced Studies*, 4(6), 70–83.
- [2] Afolayan, A., Easa, SM, Abiola, OS, Alayaki, FM, & Folorunso, O. (2022). GIS-based spatial analysis of accident hotspots: A Nigerian case study. *Infrastructures*, 7(8), 103.
- [3] Aghasi, N. (2018) Spatio-Temporal Analysis on Urban Traffic Accidents: A Case Study of Tehran City, Iran. *Journal of Geographic Information Systems*, 10, 603-642.
- [4] Malczewski, J. (2006). GIS-based multicriteria decision analysis: A survey of the literature. *International Journal of Geographical Information Science*, 20(7), 703-726.
- [5] Pleerux, N. (2020). Geographic information system-based analysis to identify the spatiotemporal patterns of road accidents in Sri Racha, Chon Buri. *Current Applied Science and Technology*, 20(1), 59-70.
- [6] Open Data Portal of the Republic of Serbia, "Open Data Portal", Accessed on May 27, 2024, available at:<https://data.gov.rs/sr/discover/>
- [7] Data on traffic accidents by police administrations and municipalities, "Portal of open data", Accessed on May 27, 2024, available at:<https://data.gov.rs/sr/datasets/podatsi-osaobratshajnim-nezgodama-po-politsijskim-upravama-i-opshtinama/>
- [8] Esri. (2023). ArcGIS Pro (Version 3.01) [Software]. Redlands, CA: Environmental Systems Research Institute. Accessed on 28 May 2024, available at:<https://www.esri.com/en-us/arcgis/products/arcgis-pro/overview>
- [9] Esri. Cluster and Outlier Analysis (Anselin Local Moran's I) (Spatial Statistics). Retrieved June 4, 2024, available at:<https://pro.arcgis.com/en/pro-app/3.0/tool-reference/spatial-statistics/cluster-and-outlier-analysis-anselin-local-moran-s.htm>
- [10] Esri. How Create Space Time Cube works. Retrieved June 11, 2024, available at:<https://pro.arcgis.com/en/pro-app/latest/tool-reference/space-time-pattern-mining/learnmorecreatecube.htm>



## DETERMINATION OF ELECTROMAGNETIC FIELD STRENGTH IN AREAS OF INCREASED SENSITIVITY AROUND RADIO TRANSMITTERS

ANA MATOVIĆ

Military Quality Control, Belgrade, [ana.matovic4@gmail.com](mailto:ana.matovic4@gmail.com)

ELMEDIN BIBEROVIĆ

Telecom Serbia, Novi Pazar, [Elmedin@telekom.rs](mailto:Elmedin@telekom.rs)

MILAN GLIGORIJEVIĆ

Alfa Bk University, Belgrade, [milan.gligorijevic@alfa.edu](mailto:milan.gligorijevic@alfa.edu)

**Abstract:** *In the modern world, electromagnetic radiation has become very intense, so there is no space on the planet that it does not reach. Thus, the living world and people are continuously exposed to these radiations of different frequencies and wavelengths. In the last thirty years, numerous tests have been carried out in the world's most reputable laboratories, but so far no direct evidence has been found that these radiations are harmful to the human body, unless it is about radiation at small distances from the radiation source. The rapid development of electronic devices and equipment leads to the fact that people live and technical devices function in an environment where electromagnetic interference (EMI - Electromagnetic Interference) is increasingly pronounced. The presence and influence of electromagnetic fields is very harmful to human health. That's why the paper discussed tests to reduce the presence and influence of electromagnetic fields on the human body.*

**Keywords:** *electromagnetic radiation, non-ionizing radiation, ionizing radiation, test point, electric field.*

### 1. INTRODUCTION

Knowledge of radiation existed far in the past. Normally, at that time only the influence of natural radiation was taken into account. Although the people of that time were probably not even aware of what kind of radiation they were, and even gave them some supernatural properties and called them various names, such as "demon door", "devil's field" and the like, they were still aware of their negative impact on human life. health. They tried to protect themselves from the aforementioned radiations by avoiding places where there was a large amount of natural radiations, observing the relationship between animals and plants in selected places, trusting various fortune tellers, seers and talisman records. Unfortunately, part of this tradition, due to the low technical culture, has been retained by certain layers of the citizenry to this day. "When man is unable to understand natural phenomena, he tends to give them supernatural properties" Albert Einstein. Radiation is the transfer of energy via a particle or wave. Radiation transmitted by particles (neutrons, protons, mesons, etc.) is called corpuscular radiation, and that transmitted in the form of waves is called electromagnetic radiation. Electromagnetic radiation represents a change in the electromagnetic field as a function of time. This radiation is the carrier of electromagnetic interaction (force) and can be interpreted as a wave or as a particle, depending on the case. Particles that quantify electromagnetic radiation are photons. Each charge generates an electromagnetic field by changing the speed of movement. This information spreads through space at the speed of light and the properties of the corresponding electromagnetic wave are directly related to the dynamics of the change in charge movement. Alternatively, if we look at electromagnetic radiation as

the emission of particles (photons), the energy they carry is directly related to the wavelength, that is, the frequency of the waves. The higher the frequency, the higher the energy of the photon. The exact relationship is described by Planck's relation  $E = h\nu$  where  $E$  is the energy of the photon,  $h$  is Planck's constant, and  $\nu$  is the frequency of the wave. The properties of electromagnetic radiation depend on its wavelength and as such are divided into electric, radio and microwaves, then infrared, visible and ultraviolet light, X-rays and gamma rays. The entire range of wavelengths of electromagnetic radiation is called the electromagnetic spectrum.

The presence and influence of electromagnetic fields is very harmful to human health. With the intention of controlling and reducing electromagnetic interference to the smallest possible extent, a large number of standards have been adopted in the world to regulate this area. The European Committee for Electrotechnical Standardization (CENELEC - European Committee for Electrotechnical Standardization) issued a document entitled "Human exposure to electromagnetic fields - High frequency (10 kHz to 300 GHz)" (ENV 50166-2) on November 30, 1994.

In addition to this document, there are other internationally adopted standards in this area (IRPA - International Committee for Non-Ionizing Radiation, IEC - International Electrotechnical Commission, IEEE - Institute of Electrical and Electronics Engineers, CISPR - Comité International Spécial des Perturbations Radioélectrique).

JUS N.NO.205 - in the range from 30 MHz to 300 GHz, the norm for the general human population is 2 W/m<sup>2</sup>, i.e. 27.45 V/m.

The GSM system operates in the 900 MHz band (UHF

band). The increased concentration of electromagnetic energy in this range causes effects on people that can be roughly classified into two basic categories:

- Thermal effects
- Stimulant effects

The intensity of the mentioned effects increases with the increase in the concentration of electromagnetic energy. As the distance from the radiation source increases, the impact of electromagnetic emission on the human body decreases. The influence of electromagnetic waves on the human body has a cumulative character. Their impact is directly proportional to the length of the exposure.

## 2. TERMS AND DEFINITIONS

**Electric field strength** - a vector quantity (E) that corresponds to the force exerted on a charged particle regardless of its movement in space, expressed in volts per meter (V/m).

**Reference limit levels** - levels of exposure of the population to electric, magnetic and electromagnetic fields that serve for practical assessment of exposure, in order to determine whether there is a probability that the basic limits will be exceeded. Reference limit levels are defined in the Rulebook on limits of exposure to non-ionizing radiation (Official Gazette RS No. 104/09).

**Reference (limit) value (V/m)** – Reference limit level of electric field strength for a certain frequency in accordance with Tab. 2 of the Rulebook on limits of exposure to non-ionizing radiation (Official Gazette of the RS No. 104/09).

**Test location** – Physical space where the test was performed. Most often, it is the location of the radio transmitter / radio base station, with its immediate surroundings (typically from 0 to 150m distance).

**Test point** - The position, typically in the vicinity of the radio transmitter, where the measuring antenna is placed and where the level of the electromagnetic field is measured.

**Measured electric field strength** – Electric field strength measured at the test point using measuring equipment. It is expressed in volts per meter (V/m).

**Maximum (extrapolated) electric field strength** – The maximum electric field strength that the source can generate in real operation, calculated based on the measured value and source parameters (N- number of channels (GSM), i.e., N-power coefficient (UMTS, CDMA, LTE) It is presented primarily for GSM, UMTS and CDMA sources, whose field strength depends on the current traffic (number of users).

$$E_{max} = E\sqrt{N} \tag{1}$$

In the case of LTE sources (in accordance with SRPS EN 50492, Annex L.), the maximum electric field strength is:

$$E_{max} = \sqrt{\frac{Nrs}{BF} \sqrt{Ers_{PORT1}^2 + Ers_{PORT2}^2}} \tag{2}$$

*Ers\_PORT1* – measured electric field strength value for antenna port 1 (RS – Reference Signal)

*Ers\_PORT2* - measured value of electric field strength for antenna port 2 (RS - Reference Signal)

BF - Power Boosting Factor

*Nrs* – the ratio of the maximum total output power of the base station to the reference signal power of the base stations.

**Total electric field strength** - Total electric field strength (measured or maximum) at a certain point calculated on the basis of all measured / maximum values at individual frequencies:

$$E_{sum} = \sqrt{E^2_1 + E^2_2 + \dots + E^2_n} \tag{3}$$

**Exposure factor** - The estimated human exposure parameter at a specified location for each operating frequency of a radio source, expressed in relation to the corresponding limit value. If the electric field strength is measured, the exposure factor is equal to the ratio of the square of the electric field strength and the square of the reference value:

$$\text{Exposure factor} = \frac{E^2}{E^2_{ref}} \tag{4}$$

*E* – electric field strength at a certain frequency

*E<sub>ref</sub>* – limit value of electric field strength at a certain frequency

**Total exposure factor** - The maximum value of the sum of the exposure factors of the equipment under test and all relevant sources in the frequency range 100kHz - 40GHz.

## 3. TEST METHODS

The examination method is based on the following standards:

- SRPS EN 50400:2008/A1:2013, - SRPS EN 50492:2010
- SRPS EN 50492:2010/A1:2014, - SRPS EN 50413:2010
- SRPS EN 50413:2010/A1:2014, - SRPS EN 50383:2012
- SRPS EN 50383:2012/AC:2013, - SRPS EN 5042:2008
- SRPS EN 61566:2009

In order to ensure the maximum relevance of the results, the determination of the zones that are most exposed to the electromagnetic field is carried out using:

-Calculation:

a. the area at ground level where the maximum field is expected is determined

b. the most exposed floors of the building are determined

- On-site measurements:

c. the spatial distribution of the field is determined

d. the most exposed zones are determined (the most exposed apartments, terraces or outdoor location)

e. points of maximum field are determined

The calculated exposure factor refers to the peak field values at the maximum field point, which the source can generate in the worst case within its operating conditions, in accordance with SRPS EN 50400 and SRPS EN 50383.

In the case of the need for a detailed examination of the level of exposure to high-frequency non-ionizing radiation within a certain space, a six-minute spatial averaging procedure is applied to assess the exposure of the whole body in accordance with SRPS EN 50492, which is described in detail in the internal document "TU-IEM-VF Methodology of testing high-frequency EM fields".

### 4. MEASURING EQUIPMENT

In accordance with the requirements of the SRPS EN 61566 t6.2.3 and SRPS EN 50492 t8.2 standards, when measuring in complex field conditions (there are signals from multiple sources of different/unknown directions and polarizations), it is mandatory to use an isotropic measuring probe. The applied measuring instruments meet the technical conditions prescribed by these standards.

The frequency range (27MHz - 3GHz) of the equipment for frequency selective measurement enables the measurement of all relevant high-frequency signals and the precise determination of total exposure:

**Table 1.** Frequency range

Radio FM	TV VHF DVB-T2	CDMA	TV UHF DVB-T2	LTE 800	GSM/UMTS 900	GSM/LTE 1800	UMTS 2100
87 - 109	174-230	420 - 430	470 - 790	791-821	935-960	1805-1880	2110-2170 MHz

Broadband measurement (100kHz - 8GHz) and Frequency selective measurement (27 MHz - 3GHz) is carried out using the following measuring equipment:



**Figure 1.** Broadband instrument for measuring electric field strength and spectrum analyzer

#### 4.1 Location description

The radio base station "NP37/NPU37 Sjenica 2", of the mobile operator Tekekom Srbija, is located within a business building, at Milorad Jovanovića bb, in Sjenica. The Ericsson RBS2116 radio base station is used for coverage in the GSM900 range, and the NSN Flexi base station in the UMTS2100 range. The RBS cabinet is located in a room in the attic of the building in question. The transceiver configuration is 2+2+4 for the GSM900 system and 2+2+2 for the UMTS2100 system. The antenna system is three-sector with azimuths 10°/120°/260°, respectively by sector. It consists of a total of 3 panel antennas, manufactured by Kathrein, in each of the sectors, one type 80010485, (which works in the bands of 880 - 960 MHz and 1920 - 2180 MHz). The height of the antenna bases from the ground level is 16.0m, for all sectors. The antennas are located on the support, on the roof of the building in question. Electrical tilts, respectively by sector, amount to 6°/6°/6° for the GSM900 system and 4°/4°/4° for the UMTS2100 system. Mechanical tilts, respectively by sectors 0°/0°/0° for both systems. The location also houses the equipment of the mobile operator Telenor.

**Table 2.** Equipment data

GSM900			
Sector designation	NP37D1	NP37D2	NP37D3
Cabinet	Ericsson 2116		
Carrier configuration <sup>1</sup>	2	2	4
Transmitter output power <sup>2</sup> [W]	40	40	18
Transmitter serial number <sup>3</sup>	/	/	/
Antenna type	K 800 10485	K 800 10485	K 800 10485
Antenna heigh [m]	16.0	16.0	16.0
Azimuth (°)	10	120	260
Tilt	Electric tilt(°)	6	6
	Mechanical tilt(°)	0	0
Feeder type	½"	½"	½"
Feeder length [m]	15	15	15

UMTS2100			
Sector designation	NPU37A <sub>L</sub>	NPU37B <sub>J</sub>	NPU37C <sub>K</sub>
Cabinet	NSN Flexi		
Carrier configuration <sup>4</sup>	2	2	2
Transmitter output power <sup>5</sup> [W]	20	20	20
Transmitter serial number <sup>6</sup>	/	/	/
Antenna type	K 800 10485	K 800 10485	K 800 10485
Antenna heigh [m]	16.0	16.0	16.0
Azimuth (°)	10	120	260
Tilt	Electric tilt(°)	4	4
	Mechanical tilt(°)	0	0
Feeder type	½"	½"	½"
Feeder length [m]	15	15	15

**Table 3.** Environmental conditions

Examination time	Temperature (°C)	Air humidity (%)	Weather conditions
15:00 - 19:30 (28.09.2016)	18.9	51	sunny
09:00 - 09:30 (29.09.2016)	18	40	sunny

In order to minimize the influence of the environment on the results, when measuring, the measuring antenna is at least 1m away from reflective surfaces (if there are sources below 300MHz), or 0.5m (if all sources are above 300MHz).

During the detailed test, the operator is not present near the measuring antenna.

#### 4.2 Identification of sources of electromagnetic radiation

Based on data from the RATEL (Republic Agency for Electronic Communications) database, the following sources of electromagnetic radiation were registered in the immediate vicinity of the test location (up to 150m away):

**Table 4.** Registered sources of EM radiation

Operator	Frequency	Location
Telekom Srbija	939.5000 MHz - 949.1000 MHz	SIENICA, M. JOVANOVIĆA <a href="#">op.</a> , KP 754
	2125.0000 MHz - 2140.0000 MHz	SIENICA, MILORADA JOVANOVIĆA <a href="#">nn.</a>
	23331.0000 MHz	MIL. JOVANOVIĆA NN., KP 754, NP37
Telenor	1805.1000 MHz - 1815.1000 MHz	SIENICA, M. JOVANOVIĆA <a href="#">op.</a>
	949.3000 MHz - 958.9000 MHz	SIENICA, M. JOVANOVIĆA <a href="#">op.</a>
	2110.0000 MHz - 2125.0000 MHz	SIENICA, MILORADA JOVANOVIĆA <a href="#">op.</a>
	949.3000 MHz - 958.9000 MHz	MILORADA JOVANOVIĆA <a href="#">op.</a>
	23142.0000 MHz	MILORADA JOVANOVIĆA <a href="#">op.</a>
Radio AMARO	2110.0000 MHz - 2125.0000 MHz	MILORADA JOVANOVIĆA <a href="#">op.</a>
Radio AMARO	94.5000 MHz	SIENICA

By checking the RATEL database, it was determined that there are no sources in the 100kHz - 30MHz and 3GHz - 6GHz bands in the vicinity of the test site.

In the vicinity of the location, there are directed radio links of the mobile operator Telekom Srbija (23GHz) and Telenor (23GHz).

### 4.2 Visual inspection

A visual inspection identified the registered sources of electromagnetic radiation from the RATEL database:



Figure 2. Registered sources of EM radiation

## 5. DETERMINATION OF THE DOMAIN OF EXAMINATION

The relevant testing domains include zones of increased sensitivity (In accordance with the definition from the "Regulations on limits of exposure to non-ionizing radiation" Official Gazette RS 104/09) located in the directions of radiation and in the immediate vicinity of the antennas of the tested radio transmitter. For tall objects (buildings) the range of the most exposed heights / floors is determined. These are the parts of the building that are in the direction of the antenna's direct radiation beam or closest to it. The following objects / zones of importance for the investigation were observed at the location:

Table 5. Objects of importance for testing

No.	Description of the residential building / residential zone	Distance from the transmitter (m)
D1	Objects and surroundings of the site at ground level, in the direction of the third sector of the azimuth 260°	Up to 150m
D2	Objects and surroundings of the site at ground level, in the direction of the third sector of the azimuth 120°	Up to 150m
D3	Objects and surroundings of the site at ground level, in the direction of the third sector of the azimuth 10°	Up to 150m
D4	Elementary school „12. Decembar“ (Nova nn)	od 50-200m
D5	Object SPO (Milorada Jovanovića nn)	/

All results of the preliminary scan represent current measured field values and refer exclusively to the period in which the measurement was made.

### 5.1 Preliminary scan indoors-exposed objects

In each exposed object, a preliminary scan of the electric field strength is performed in the rooms, in order to determine the distribution of the field and to determine the zone-room in which the field is maximum. The results of this scan are given in the table:

Table 6. preliminary scan of closed space

Mark	Date	Description of the test zone	E <sub>mean</sub> value (V/m) <sup>11</sup>	E <sub>max</sub> (V/m) <sup>12</sup>
D1-1	28.09.2016	Building under construction SPO2, III floor, planned terrace of the apartment	2.59	2.92
D1-2		Building under construction SPO2, III floor, planned living room	1.80	2.42
D2-1		Object S17 (Milorada Jovanovića No. 14), III floor, apartment 14, terrace	3.47	4.37
D2-2		Object S17 (Milorada Jovanovića No.14), III floor, apartment 14, living room	0.57	2.37
D3-1		Object S02 (Ahmeta Abdagića No. 52), IV floor, apartment 22, terrace	2.26	2.87
D3-2		Object S02 (Ahmeta Abdagića No. 52), IV sprat, stan22, living room	1.02	1.16
D4-1		Elementary school „12.decembar“ (Nova nn), II floor, chemistry classroom	0.55	0.68
D4-2		Elementary school „12.decembar“ (Nova nn), I floor, classroom 14.	0.45	1.90
D4-3		Elementary school „12.decembar“ (Nova nn), II floor, corridor	1.16	2.43
D4-4		Elementary school „12.decembar“ (Nova nn), II floor, classroom 10	0.08	1.41
D4-5	Elementary school „12.decembar“ (Nova nn), ground floor, TIO classroom	0.71	0.90	
D4-6	Elementary school „12.decembar“ (Nova nn), ground floor, sports hall	0.23	0.50	
D4-7	Elementary school „12.decembar“ (Nova nn), ground floor, classroom 5	0.75	1.21	
D4-8	Elementary school „12.decembar“ (Nova nn), ground floor, classroom 3	0.60	1.26	
D4-9	Elementary school „12.decembar“ (Nova nn), ground floor, classroom 1	0.47	0.88	
D4-10	Elementary school „12.decembar“ (Nova nn), ground floor, Serbian language classroom.	1.78	2.14	
D5-1	29.09.2016	Object SPO (Milorada Jovanovića nn), IV floor, office 11	1.41	1.69
D5-2		Object SPO (Milorada Jovanovića nn), IV floor, Office 10	1.67	1.77
D5-3		Object SPO (Milorada Jovanovića nn), IV floor, corridor	1.06	1.40

<sup>11</sup> Mean measured strength of el. fields in the range 100kHz - 8GHz

<sup>12</sup> Maximum measured strength of el. fields in the range 100kHz – 8GHz

### 5.2 Preliminary scanning in an open area-suburban residential zone, surroundings of the transmitter

The distribution of the electric field in the vicinity of the location is determined by scanning the space with a broadband instrument for measuring the strength of electricity. fields (in the range 100kHz - 8GHz). The results of the preliminary broadband test in an open space are shown in the following picture:



Figure 3. Spatial distribution of the field in the vicinity of the antenna system



## 6. TEST RESULTS AT MAXIMUM FIELD POINTS

Based on the results of the preliminary scan, the most exposed zones were determined. In the general case, a precise location of the point of the maximum field was additionally carried out within each selected test zone in a closed space. At the selected position in the open space, a broadband measurement is performed at three heights and the most exposed height is determined at which frequency selective measurement is performed in order to determine the field level from individual sources in detail, as well as to estimate the total exposure.



Figure 4. Positions of test points

Test point T1										
Measurement start time:	15:51 (28.09.2016)	GPS Lat:	/	GPS Lon:	/					
Position of the test point:	Building under construction SP02, III floor planned terrace of the apartment									
Distance from reflective objects			Local environmental conditions							
wall	ceiling	Metal fence	vehicles	Other	Leaves	Moist soil	People	other		
1.2m	2.5m	-	-	-	ne	ne	ne	-		
Local electromagnetic field sources present:			Fluo bulbs	WiFi	Phone	Microwave	TV/comp.			
Is there?			no	no	no	no	no			
Active during measurement?			no	no	no	no	no			
Broadband measurement 100kHz – 8GHz:		The most exposed height (m)		1.5	Esr (V/m)	2.59				

Test point T2										
Measurement start time:	16:07 (28.09.2016)	GPS Lat:	/	GPS Lon:	/					
Position of the test point:	object S17 (Milorada Jovanovića No. 14), III floor, apartment 14, terrace									
Distance from reflective objects			Local environmental conditions							
wall	ceiling	Metal fence	vehicles	Other	Leaves	Moist soil	people	other		
1m	1m	1m	-	-	no	no	no	-		
Local electromagnetic field sources present:			Fluo bulbs	WiFi	phone	microwave	TV/comp.			
Is there?			no	no	no	no	no			
Active during measurement?			no	no	no	np	no			
Broadband measurement 100kHz – 8GHz:		The most exposed height (m)		1.5	Esr (V/m)	3.47				

Test point T3										
Measurement start time:	16:31 (28.09.2016)	GPS Lat:	-	GPS Lon:	-					
Position of the test point:	Object S02 (Ahmeta Abdagića 52), IV floor, apartment 22, terrace									
Distance from reflective objects			Local environmental conditions							
wall	ceiling	Metal fence	vehicles	Other	Leaves	Moist soil	people	other		
1m	1m	1m	-	-	no	no	no	-		
Local electromagnetic field sources present:			Fluo bulbs	WiFi	phone	microwave	TV/comp.			
Is there?			no	no	no	no	no			
Active during measurement?			no	no	no	no	no			
Broadband measurement 100kHz – 8GHz:		The most exposed height (m)		1.5	Esr (V/m)	2.26				

Test point T4										
Measurement start time:	17:47 (28.09.2016)	GPS Lat:	/	GPS Lon:	/					
Position of the test point:	Elementary school „12.decembar“ (Nova nn), II floor, corridor									
Distance from reflective objects			Local environmental conditions							
wall	ceiling	Metal fence	vehicles	Other	Leaves	Moist soil	people	other		
1m	1.5m	-	-	-	no	no	no	-		
Local electromagnetic field sources present:			Fluo bulbs	WiFi	phone	microwave	TV/comp.			
Is there?			no	no	no	no	no			
Active during measurement?			no	no	no	no	no			
Broadband measurement 100kHz – 8GHz:		The most exposed height (m)		1.5	Esr (V/m)	1.16				

Test point T5										
Measurement start time:	18:01 (28.09.2016)	GPS Lat:	/	GPS Lon:	/					
Position of the test point:	Elementary school „12.decembar“ (Nova nn), ground floor, Serbian language classroom									
Distance from reflective objects			Lokalni uslovi okruženja							
wall	ceiling	Metal fence	vehicles	Other	Leaves	Moist soil	people	other		
1m	1.5m	-	-	-	no	no	no	-		
Local electromagnetic field sources present:			Fluo bulbs	WiFi	phone	microwave	TV/comp.			
Is there?			no	no	no	no	no			
Active during measurement?			no	no	no	no	no			
Širokopojasno merenje 100kHz – 8GHz:		Najizloženija visina (m)		1.5	Esr (V/m)	1.78				

TEST POINT T6										
Measurement start time:	18:31 (28.09.2016)	GPS Lat:	43°16'21.0" N	GPS Lon:	20°0'13.2" E					
Position of the test point:	Path in the park, next to playground, in the III sector, 50m from the location									
Distance from reflective objects			Local environmental conditions							
wall	ceiling	Metal fence	vehicles	Other	Leaves	Moist soil	people	other		
-	-	2m	-	-	no	no	no	-		
Local electromagnetic field sources present:			Fluo bulbs	WiFi	phone	microwave	TV/comp.			
Is there?			no	no	no	e	no			
Active during measurement?			no	no	no	no	no			
Broadband measurement 100kHz – 8GHz:		The most exposed height (m)		1.5	Esr (V/m)	2.36				

Test point T7											
Measurement start time:		09:22 (29.09.2016)		GPS Lat:		/		GPS Lon:		/	
Position of the test point:				object SPD (Milorada Jovanovića nn), IV floor, office 10							
Distance from reflective objects				Local environmental conditions							
wall	ceiling	Metal fence	vehicle	other	Leaves	Moist soil	people	other			
2m	1.5m	-	-	-	no	no	no	no			
Local electromagnetic field sources present:				Fluo bulbs	WiFi	phone	microwave	TV/comp.			
is there?				no	no	no	no	no			
Active during measurement?				no	no	no	no	no			
				The most exposed height (m)		1.5		Esr (V/m)		1.67	
Droadband measurement 100kHz – 8GHz:											

Figure 5. Tested points

### 6.1 Assessment of compliance of the investigated source with reference values

Based on the "Regulations on sources of non-ionizing radiation of special interest, types of sources, method and period of their examination", Sl. Gazette 104/09, sources of special interest are considered sources of electromagnetic radiation whose electromagnetic field in the zone of increased sensitivity reaches at least 10% of the amount of the reference limit value prescribed for that frequency.

Table 7. The electric field strength of the Telekom GSM900 base station

Telekom GSM900			
TEST POINT	Electric field strength (V/m)	Reference value (V/m)	percentage (%)
T1	2.30	16.86	13.7
T2	2.87	16.86	17.0
T3	1.46	16.86	8.7
T4	0.51	16.86	3.0
T5	0.83	16.86	4.9
T6	0.99	16.86	5.9
T7	1.11	16.86	6.6

The test results show that the electric field strength of the Telekom GSM900 base station in the test points T1 and T2 is higher than 10% of the reference limit value for the given range.

Table 8. The electric field strength of the Telekom UMTS2100 base station

Telekom UMTS2100			
TEST POINT	Electric field strength (V/m)	Reference value (V/m)	Percentage (%)
T1	1.66	24.40	6.8
T2	1.07	24.40	4.4
T3	1.19	24.40	4.9
T4	0.98	24.40	4.0
T5	0.44	24.40	1.8
T6	0.38	24.40	1.5
T7	0.30	24.40	1.2

The test results show that the electric field strength of the Telekom UMTS2100 base station in all test points is lower than 10% of the reference limit value for the given bands.

## 7. CONCLUSION

The test results show that the total maximum electric field strength in the GSM900 range, in all test points, is lower than the reference value for the GSM900 range (16.8 V/m prescribed by the Rulebook on limits of exposure to non-ionizing radiation).

The test results show that the total maximum electric field strength in the UMTS2100 range, in all test points, is lower than the reference value for the UMTS2100 range (24.4 V/m prescribed by the Rulebook on limits of exposure to non-ionizing radiation).

Based on the obtained results, it can be concluded that the examined source meets the requirements of the Rulebook on limits of exposure to non-ionizing radiation, in terms of total exposure.

### References:

- [1] Telekom Srbija a.d: Izveštaj o ispitivanju elektromagnetnog zračenja, EM-2016-339,2016
- [2] Elmedin Biberović, Milan Plazinić: Planning and Designing of Mobile Telephony in Order to Preserve and Protect the Environment. IMPEDE 2019, Academy of Engineering Sciences of Serbia, Beograd. ISBN: 978-86-901238-0-3
- [3] Ana Matovic, and Marija Matovic “Sensitivity optimization of direct form realization of active – RC allpole filters, Facta Universitatis, Ser.:Electronics and Energetic, vol.Vol.16; no.2, pp 259-271, Aug 2003.
- [4] UEU 137:Studija o proceni uticaja na životnu sredinu bazne stanice mobilne telefonije,2017
- [5] Stefanovic Mihajlo, Sekulovic Nikola, Gligorijević Milan, Bandjur Milos, Spalevic Petar, Popovic Zoran (2011) Statistics of signal envelope in composite multipath fading/shadowing microcellular environment,technics technologies education management-ttem, 6(4) 1147-1151
- [6] Mirjana S.,Aleksandar N.,Đorđe E, Elektromagnetno zračenje u okolini radio predajnika Telfor Beograd 20204



## DIGITAL RADIO SYSTEM FOR REMOTE MONITORING AND CONTROL ON THE MEDIUM VOLTAGE DISTRIBUTION NETWORK USING THE PDR 300 RADIO DEVICE AS A TRANSMITTER

MARIJA MATOVIĆ

Electrodistribution, Kraljevo, [marija.matovic@es.rs](mailto:marija.matovic@es.rs)

ANA MATOVIĆ

Military Quality Control, Belgrade, [ana.matovic4@gmail.com](mailto:ana.matovic4@gmail.com)

IVICA MARJANOVIĆ

Military Quality Control, Belgrade, [ivicabeogrd@gmail.com](mailto:ivicabeogrd@gmail.com)

**Abstract:** *As part of the expansion of the medium-voltage distribution network of the system for remote monitoring and control, the communication connection of the end locations with the control center will be made. For many years, remote monitoring and control systems of the medium-voltage electric distribution network based on digital packet radio communication have been used, using the open protocol DNP3 between remote stations and data concentrators, as well as between data concentrators and SCADA applications. The systems work according to the event, that is, the end stations initiate communication in the event of an event, while the end stations are periodically polled from the concentrator to determine whether the remote station is in communication. Implementation of the DNP3 protocol throughout the system enabled an event logger with time created at remote stations with millisecond resolution. Due to the location expansion of the medium voltage distribution network into a system for remote monitoring and control, the communication connection of the end locations with the control center will be made. The purpose is that all end locations can be managed from the control center, so that from the control center it will be possible to read measurements and signals on the switchgear and issue commands. The remote monitoring and control system consists of a SCADA server, data concentrator, repeater and PDR 300 radio end devices.*

**Keywords:** *radio device PDR 300, remote monitoring and control, communication protocols.*

### 1. INTRODUCTION

For the modernization of the existing system of remote monitoring and management of the medium voltage distribution network, for the operation of the monitoring system, the radio device PDR 300 is used, which is a transceiver, which enables the transmission of telemetry data, necessary for the operation of the monitoring and control system over long distances [12]. The field of application of data transmission networks with PDR 300 radio devices is in water/wastewater treatment plants, electricity distribution, gas distribution, oil distribution, wind turbines, industrial process management, remote traffic control, railway communication systems, remote control with assistance PLC elements.

PDR 300 radio PDR 300 supports operation with a wide range of existing communication protocols widely used in remote monitoring and control systems, including DNP3, IEC870, RP570, COMLI, Modbus, Cooper/PG&E 2179, L&G Telegyr 8979, Twacs by DCSI, Turtle by Hunt, Exoline, Cactus, PRIP and Aquacom by ITT Flygt. It also supports the User Defined Protocol option, which provides the ability to use any communication protocol that you define yourself the user [7]. In many modern systems for data transmission, as well as in the system of

remote monitoring and management of the medium voltage distribution network, high security is insisted upon. That's why the PDR 300 enables extremely secure encryption of radio messages, namely the 128 bit key XTEA cipher.

This radio device for data transmission is suitable for remote monitoring and management of medium voltage distribution network, which works on the roll call principle, as well as in systems with event-triggered communication. In systems with event-triggered communication, the functionality of the PDR 300 device called Collision Avoidance is used, which prevents the "collision" of radio messages, thereby significantly speeding up communication between devices in the system. The device also supports Peer-To-Peer communication mode.

The PDR 300 radio device system consists of one master device and a maximum of 120 slave devices. Each slave device can work as a signal repeater, an independent device or can be connected to one or more RTU devices (Remote Terminal Unit) or IED devices (Intelligent Electronic Device).

The message can be transmitted to the end radio device via up to six devices, ie. in seven jumps. In this way, the message in the PDR 300 radio device system can be

transmitted over a distance of over 300 km (190 miles), depending on the specific topography of the terrain of the remote monitoring and control system of the medium voltage distribution network [8]. The data transfer rate can be 4800, 9600 or 19200 bps. Forward Error Correction is a standard function that enables the correction of a very large number of errors in signal transmission, which occur due to the appearance of noise, thereby increasing the sensitivity of the radio device.

The RTU/IED/SCADA system for remote monitoring and control connects to the PDR 300 radio device via a standard RS-232 serial interface. The baud rate of the serial interface is adjustable between 600 and 19200 bps. The configuration of the PDR 300 radio device involves setting a minimum number of parameters, which are easily accessed using a handheld terminal or a personal computer, using a standard terminal program in Windows.

The PDR 300 radio provides non-invasive diagnostics, remote parameter modification and has built-in test and verification functions, easily accessed via a handheld terminal or personal computer, which is achieved using the PDR 300 radio. This radio has two Ethernet ports that use standard RJ45 connector and communication speed from 10Mbps to 100Mbps. It is used for software support and updates. Also, it is intended for future TCP/IP protocols.

The remote monitoring and control system of the medium voltage distribution network uses a data collection device, or the data concentrator GW 502 is a central and communication unit, which provides excellent protocol conversion functions. Available master protocols: IEC60870-5-101, IEC60870-5-103, IEC60870-5-104, IEC61850, DNP3, SPA, (Netcon 8830, 8810), Modbus, Tecoma, ANSI, NPA, Procol, ADLP80, ADLP180, RP570, RP571, (Felek 400, 4000), etc. As the product is in constant development, the number of supported protocols is constantly increasing.

**2. AREA OF APPLICATION**

Reasons for using wireless technologies:

- Avoid laying cables in places where it is difficult, expensive or impossible.
- No leased dial-up connections are used, thus reducing costs. Independence from communication service providers is achieved.

Areas of application:

- Water/wastewater treatment plants
- Distribution of electric energy
- Gas distribution
- Oil distribution
- Wind generators
- Management of industrial processes
- Remote traffic control
- Communication systems on railways
- Remote control with the help of PLC elements



**Figure 1.** Examples of typical data network configurations with PDR 300 radios

**Point – to – point**

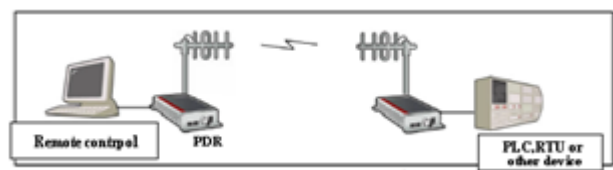


**Figure 2.** Point-to-point

**Point – to – multipoint**

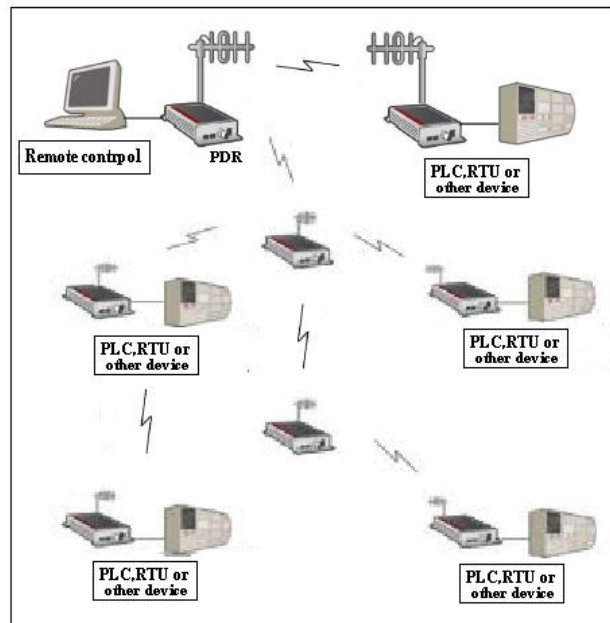


**Figure 3.** Point-to-multipoint

**Distribution of electricity**

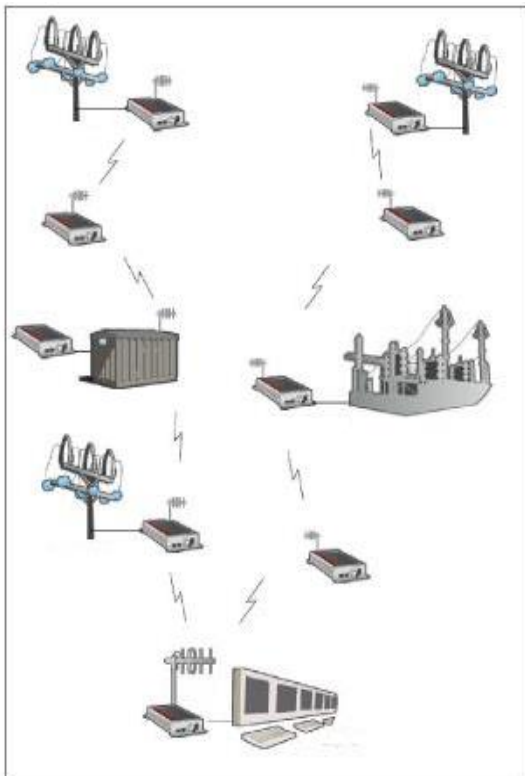


**Figure 4.** PDR radios in the power distribution network management system

**3. FUNCTIONALITY OF THE PDR 300 RADIO DEVICE**

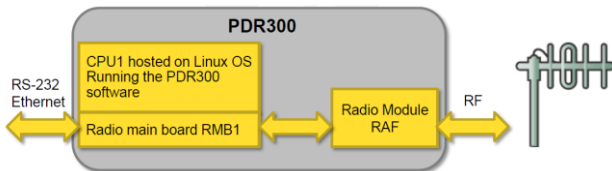


**Figure 5.** Functional block diagram of the PDR 300 radio device

**RS-232 to RF**

Serial data comes to the serial port. The MCU (Micro Controller Unit) analyzes the data and frames it, then sends it to the modulation unit. The entire message is temporarily stored in the processor's memory before being forwarded to the modulation unit. The modulation unit converts the sequence of bits into a 4-level baseband signal that is modulated in the radio transmitter.

**RF to RS-232**

The modulation unit decodes the 4-level baseband signal and forwards it to the MCU. The MCU analyzes the message and sends it to the serial port or forwards it via radio, if the device is working as a repeater in the case of that particular message.

**FEC - Forward Error Correction**

When sending data, FEC (Forward Error Correction) bits are added to the data being transmitted, before it is converted to a 4-level baseband signal. When receiving data, based on the information from the FEC bits, the FEC algorithm is applied, which corrects errors in signal transmission. A large part of such errors can be corrected using the FEC functionality.

**CRC – Cyclic Redundancy Checksum**

When sending a signal, at the end of the message, i.e. data string, a CRC byte or bytes is appended. The CRC byte is calculated based on the content of the message. The receiver checks the CRC byte according to the received data and thus detects errors in signal transmission. Corrupted messages are eliminated. If the CRC byte is incorrect, the radio receiving the message does not send back a Non-acknowledgement message (NACK). Any retransmission of the signal should be initiated by the connected IED. This is triggered using a response delay.

**Communication**

The radio device PDR 300, in the data transmission system, can work as a master or slave/repeater. In each radio device in the system, information about the path for signal transmission, addresses of remote end stations (RTU - Remote Terminal Unit), identification of radio devices and repeaters is configured.

When the control system sends a message to the master device, the master recognizes the address of the message, i.e. its destination. The master checks whether there is a slave device with an identification corresponding to the address from the message in the table of radio devices in the system. If there is, the master checks whether the message should be forwarded through one of the repeaters in the system. Finally, the master transmits the message to the slave device. The response of the slave device is transmitted in the same way.

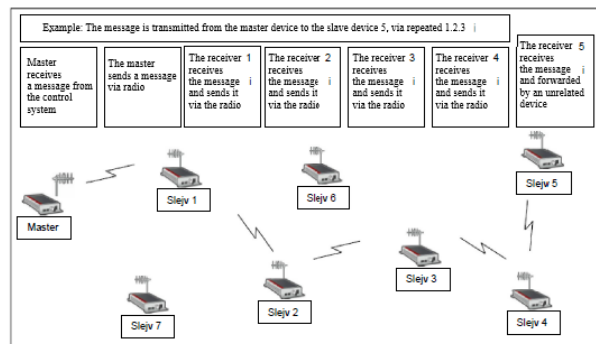


**Figure 6.** Example of message transmission in the PDR system

### Protocols supported by the PDR 300 radio

The radio device PDR 300 currently supports the following protocols for SCADA system communication with the RTU:

- DNP3
- IEC870 (IEC 870-5-1) RP570
- COMLI
- Modbus RTU
- Aquacom
- DCSI
- Hunt 1
- Telegyr 8979
- Cooper/PG&E 2179
- Exoline
- Cactus
- ADJ

These protocols are available as factory settings in the configuration menu of the PDR 300 radio. Protocols not listed can be used using the User Defined Protocol option, which is available in the same configuration menu.

In normal cases, it is only necessary to select the desired protocol in the master radio device. The Direct Routing option is selected in the slave radio, if the message is always forwarded to the same master radio.

#### User Defined Protocol

The User Defined Protocol option can be applied to any protocol that contains a destination address. The destination address can consist of one or two bytes of data and must always be in the same position in each type of message.

Normally, the User Defined Protocol option is configured only in the master radio. The Direct Routing option is selected in slave radios, if messages are always forwarded to the same master radio.

#### Direct Routing

The Direct Routing option can be applied in all slave devices of the PDR 300 radio device network, if their messages are always forwarded to the same master devices or to the SCADA system. This eliminates the need to enter addresses of SCADA systems or RTU devices into slave radios. It is only necessary to configure the communication path from the slave device to the master device.

### 4. ENCRYPTIO – CODING, ENCRYPTION

The radio device PDR 300 has the option of encoding (encrypting) messages. A 128-bit encryption key, called XTEA, is used. The user can define a code key, as a hexadecimal numerical value of 32 characters in length, in each radio device in the network.

XTEA's digital encryption makes the radio network as secure as any other encrypted system or encrypted IP network.

### 5. SENSITIVITY OF THE PDR 300 RADIO RECEIVER

The sensitivity of the receiver depends on the frequency used, the distance between the channels (12.5 / 25 kHz) and the bit rate (4800, 9600 or 19200 bps). The sensitivity of the receiver is measured by introducing an attenuation to a signal consisting of a known sequence of bits, until a bit error occurs. This is an example of a common way of representing receiver sensitivity:

$$-110\text{dBm @ BER (Bit Error Rate)} < 1 \times 10^{-6}$$

The value of the sensitivity of the receiver in many cases depends on the known sequence of bits used in its measurement. A series of random bits is used when determining the sensitivity of the receiver, which includes all possible variations in the arrangement of bits in the series and represents the most difficult possible case, which is why it gives very reliable measured values of the sensitivity of the receiver.

Insufficiently good sensitivity of the receiver can be compensated by using antennas with amplification or increasing the power of the output signal. The application of antennas with amplification is the solution most often used in such cases.

It should be noted that the effects of improper antenna installation cannot be compensated by the use of a highly sensitive radio device.

Sensitivity can be used in signal propagation analyzes in radio network planning.

**Table 1.** PDR 300 radio receiver sensitivity

Model	Frequency range [MHz]	Channel width [kHz]	Data transe rate [bps]	Sensivity BER < 1x10 <sup>-6</sup>
PDR 300	UHF 440 - 470	12.5	4800 / 9600	-116 dBm / - 110 dBm
PDR 300	UHF 440 - 470	25	9600 / 19200	-113 dBm / - 105dBm

### 6. STRENGTH OF THE TRANSMITTER

Power ranges of radio transmitters are from 0.001 to 5.0 W.

Radios can be set by the user to a certain range of output signal strength. This is achieved by using a suitable configuration interface, and there is also an option for remote control.

### 7. TRANSMITTER STRENGTH RSSI – RECEIVED SIGNAL STRENGTH INDICATION - INDICATION OF THE POWER OF THE RECEIVED SIGNAL

The value of the RSSI magnitude is used to determine the quality of the radio link. RSSI values can be obtained by running the Radio Link Test from the configuration menu.

The PDR 300 radio device measures RSSI values with the help of an A/D converter. The strength of the received signal is obtained by measuring the voltage and is

expressed in volts and translated into a value expressed in dBm.

The following graph shows typical RSSI voltage values given as a function of signal level.

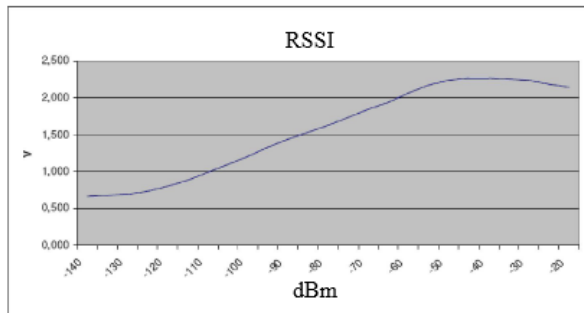


Figure 7. RSSI

## 7. CONCLUSION

For the implementation of the system for remote monitoring and control, he suggests the radio device PDR 300 due to its good technical characteristics. The main advantage of this device is that it enables the transmission of telemetry data, necessary for the operation of the monitoring and management system, over long distances. The device is intended to work in specific environments that require point-to-multipoint data transmission, which are found in water treatment plants, waste water, industrial plants, power systems, gas extraction plants, oil extraction plants, wind turbine plants, plants for managing industrial processes, plants for remote traffic control, for railway communication systems, plants for remote control with the help of PLC elements.

One of the essential features of the PDR 300 radio device is that it supports work with a wide range of existing communication protocols of wide use, which are used in remote monitoring and control systems, which provides the possibility of using any communication protocol, determined by the user himself.

A very important feature is the reliability of the PDR 300 radio device when transmitting messages in the system, where messages can be transmitted over a distance of over 300 km (190 miles), depending on the specific topography of the terrain. Also, an important application of this radio device is in systems that work on the roll call principle, as well as in systems with event-triggered communication. In systems with event-triggered communication, the functionality of the PDR 300 device called Collision Avoidance is used, which prevents "collision" of radio messages, which significantly speeds up communication between devices in the system.

Simplicity of access using a handheld terminal or personal computer enables non-invasive diagnostics, remote parameter modification and has built-in functions for testing and verification, are the main advantage of this radio device, as well as Forward Error Correction, a standard function that enables the correction of a very

large number of errors in signal transmission, which occur due to the appearance of noise, which increases the sensitivity of the radio device.

## Literature

- [1] S. Stankovski, N. Đukić, S. Tegeltija, R. Kovač and I. Baranovski, "Wireless Parking Access Control," 15. International Scientific Conference on Industrial Systems, pp. 136-139, 2011.
- [2] E. Ferro and F. Potorti, "Bluetooth and Wi-Fi Wireless protocols: a survey and a comparison," Wireless Communications, pp. 12 – 26, 2005.
- [3] R. Kovač, S. Horvat, I. Šenk, L. Tarjan and V. Jovanović, "Wi-Fi system for monitoring the student attendance at university lectures," 15. International Scientific Conference on Industrial Systems, pp. 160-164, 2011.
- [4] Z. Rongbo and Y. Yuhang, "Model-based admission control for IEEE 802.11e enhanced distributed channel access," AEU - International Journal of Electronics and Communications, vol. 61, no. 6, pp. 388–397, June 2007.
- [5] G. Ostojic, S. Stankovski, M. Lazarevic and V. Jovanovic, "Implementation of RFID technology in parking lot access control system," Proceedings of the 1st RFID Eurasia Conference in Istanbul, Turkey, pp. 49-53, 2007.
- [6] L. Tarjan, I. Šenk, R. Kovač, S. Horvat and G. Ostojic, "Automatic identification based on 2D barcodes," 15. International Scientific Conference on Industrial Systems, pp. 130-135, 2011.
- [7] Akbar A., et al., 2013, Session Initiation Protocol, International Journal of Scientific and Engineering Research Volume 4, ISSN 2229-5518, str. 5.
- [8] <http://mreze.layer-x.com/>, Septembar, 2014., Eldis Mujarić, dipl. ing., Računalne mreže,
- [9] TelecomSpace, Signaling Connection Control Part (SCCP), available at <http://telecomspace.com/ss7-sccp.html>, 15.7.2014.
- [10] A. S. Tanenbaum, Računarske mreže, Микро књига, Београд, 2005.
- [11] Комутациони системи, available at <http://telekomunikacije.etf.rs/predmeti/te4ks/docs/KS/KS10.docx>
- [12] D. Mitić, „SYSTEM FOR REMOTE SUPERVISION AND CONTROL OF POWER ELECTRONICS DEVICES”, 32. Međunarodni skup MIPRO 2009, Zbornik Radova Telekomunikacije i informacije, Vol. II. CTI, ISBN 978-953-233-043-4, Opatija, Hrvatska, Maj 25-29. 2009. god.
- [13] Časlav Stefanović, Marija Matović, Danijel Đošić, Srđan Maričić, Ana Matović, "Level crossing rate of the random variables", INFOTEH-JAHORINA, Vol. 10, Ref. B-I-4, ISBN 978-99938-624-6-8, Mart 20-23, 2013.



## THE LEVEL CROSSING RATE OF THE NAKAGAMI-M RANDOM PROCESS

IVICA MARJANOVIĆ

Military Quality Control, Belgrade, [ivicabeogrd@gmail.com](mailto:ivicabeogrd@gmail.com)

ANA MATOVIĆ

Military Quality Control, Belgrade, [ana.matovic4@gmail.com](mailto:ana.matovic4@gmail.com)

MARIJA MATOVIĆ

Electrodistribution, Kraljevo, [marija.matovic@es.rs](mailto:marija.matovic@es.rs)

**Abstract:** In this paper, the level crossing rate of the Nakagami-m random process will be determined. To calculate the level crossing rate we will determine the mean value of the first derivative of the Nakagami-m random variable. This mean value is determined using the joint probability density of the Nakagami-m random variable and its first derivative. The level crossing rate of the Nakagami-m random process is one of the statistical characteristics of another type of telecommunication system performance analysis.

**Keywords:** Nakagami-m random variable, first derivative of Nakagami-m random variable, the level crossing rate of the nakagami-m random process

### 1. INTRODUCTION

The level crossing rate of the Nakagami-m random process is used in telecommunication system performance analysis, by which we determine the mean failure duration at the output of the wireless system and the joint probability density of the signal envelope at the output of the wireless system and its first derivative. The Nakagami-m distribution is a general distribution, and Rayleigh distributions and one-sided Gaussian distributions can be derived from this distribution as special cases. The Nakagami-m distribution can be used to describe the rapidly changing signal envelope in a linear medium without a dominant multi-cluster component [4,5].

The Nakagami-m random variable has two parameters. The parameter  $r$  represents the mean power Nakagami-m random variable. The parameter  $m$  is the sharpness of the Nakagami-m fading and has a large change. For small values of the parameter  $m$ , the fading is deeper and sharper and the performance of the system is worse. For smaller values of the parameter, the probability of failure and the probability of system error increases. For higher values of the parameter  $m$ , the fading depth decreases [8]. In this case, the failure probability decreases, the error probability increases and the channel capacity increases. When the parameter  $m$  tends to infinity, the fading disappears. The Rayleigh distribution and the one-sided Gaussian distribution can be obtained from the Nakagami-m distribution. For the parameter  $m=1$  the Nakagami-m distribution changes to the Rayleigh

distribution, and for  $m=0.5$  the Nakagami-m distribution changes to the one-sided Gaussian distribution. A squared Nakagami-m random variable can be represented as a sum of  $\tau m$  squared Gaussian random variables. These Gaussian random variables have a mean of zero and a variance of  $\tau^2$ .

In this paper, the level crossing rate of the Nakagami-m random process will be determined. This mean number is determined as the mean of the first derivative of the Nakagami-m random variable. This mean value is determined using the joint probability density of the Nakagami-m random variable and its first derivative. The first derivative of the Nakagami-m random variable is the Gaussian random variable. Nakagami-m random variable and its first derivative are mutually independent. Based on this, the joint probability density function probability density of the Nakagami-m random variable and the first derivative of the Nakagami-m random variable is equal to the product of the probability density of the Nakagami-m random variable and the probability density of the first derivative of the Nakagami-m random variable. The expression for the level crossing rate Nakagami-m random variables turns into the expression for the level crossing rate Rayleigh random variables for values of the parameter  $m=1$ . Using the expression for the probability density of the Nakagami-m random variable, expressions for calculating the moments of the Nakagami-m random variable can be obtained. Nakagami-m random variable can be obtained.



## 2. SQUARED NAKAGAMI-M RANDOM VARIABLE

The squared Nakagami-m random variable  $y$  can be written as the sum of  $2m$  squared  $2m$  Gaussian random variables:

$$y^2 = y_1^2 + y_2^2 + \dots + y_{2m}^2 \tag{1}$$

Where  $y_i$  are Gaussian random variables:

$$P_{y_i}(y_i) = \frac{1}{\sqrt{2\pi}\sigma} e^{-\frac{y_i^2}{2\sigma^2}}, \quad i = 1, 2, \dots, 2m \tag{2}$$

The first derivative of the squared Nakagami-m random variable  $y$  is:

$$\dot{y} = \frac{1}{y}(y_1 \dot{y}_1 + y_2 \dot{y}_2) \tag{3}$$

The random variables  $\dot{y}_1, \dot{y}_2, \dots, \dot{y}_{2m}$  are Gaussian random variables. Based on this is the linear transformation of Gaussian random variables. The probability density of  $\dot{y}$  is Gaussian.

The mean value of the first derivative of the squared Nakagami-m random variable  $\dot{y}$  is:

$$\overline{\dot{y}} = \frac{1}{y}(y_1 \overline{\dot{y}_1} + y_2 \overline{\dot{y}_2} + \dots + y_{2m} \overline{\dot{y}_{2m}}) = 0 \tag{4}$$

Since:

$$\overline{\dot{y}_1} = \overline{\dot{y}_2} = \dots = \overline{\dot{y}_{2m}} = 0 \tag{5}$$

The variance from the first derivative of the squared Nakagami-m random variable  $\dot{y}$  is:

$$\sigma_{\dot{y}}^2 = \frac{1}{y^2} (y_1^2 \sigma_{\dot{y}_1}^2 + y_2^2 \sigma_{\dot{y}_2}^2 + \dots + y_{2m}^2 \sigma_{\dot{y}_{2m}}^2) \tag{6}$$

Where in:

$$\sigma_{\dot{y}_1}^2 = \sigma_{\dot{y}_2}^2 = \dots = \sigma_{\dot{y}_{2m}}^2 = \pi^2 f_m^2 \frac{r}{m} = \beta^2 \tag{7}$$

After substituting (7) into (6) is getting:

$$\sigma_{\dot{y}}^2 = \frac{1}{y^2} \beta^2 (y_1^2 + y_2^2 + \dots + y_{2m}^2) = \beta^2 \tag{8}$$

## 3. JOINT PROBABILITY DENSITY OF THE SQUARED NAKAGAMI-M RANDOM VARIABLE AND THE FIRST DERIVATIVE OF THE SQUARED NAKAGAMI-M RANDOM VARIABLE

The joint probability density of the squared Nakagami-m random variable and the first derivative of the squared Nakagami-m random variable  $y$  and  $\dot{y}$  is:

$$P_{y,\dot{y}}(y,\dot{y}) = P_y(y) P_{\dot{y}}(\dot{y}) = \frac{2}{\Gamma(m)} \left(\frac{m}{r}\right)^m y^{2m-1} \frac{1}{\sqrt{2\pi}\beta} e^{-\frac{y^2}{2\beta^2}} \tag{9}$$

## 4. LEVEL CROSSING RATE OF THE SQUARED NAKAGAMI-M RANDOM VARIABLES

The level crossing rate of the squared Nakagami-m random variables  $y$  is:

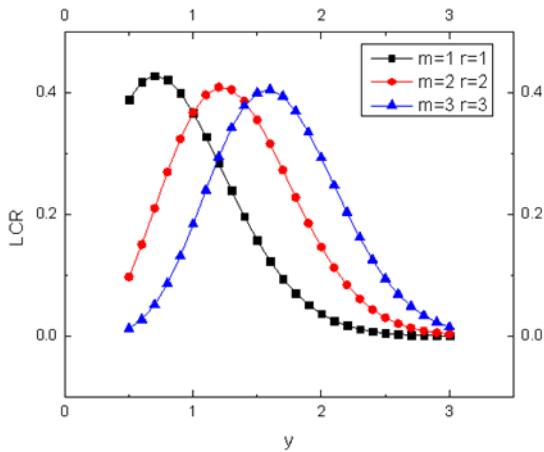
$$N_y = \int_0^{\infty} d_y \dot{y} P_{y,\dot{y}}(y,\dot{y}) = \frac{2}{\Gamma(m)} \left(\frac{m}{r}\right)^m y^{2m-1} \frac{1}{\sqrt{2\pi}} e^{-\frac{m}{r}y^2} \pi f_m \left(\frac{r}{m}\right)^{1/2} \tag{10}$$

The normalized value of the level crossing rate squared Nakagami-m random variable  $y$  is:

$$\frac{N_y}{\sqrt{2\pi} f_m} = \left(\frac{m}{r}\right)^{m-1/2} y^{2m-1} e^{-\frac{m}{r}y^2} \tag{11}$$

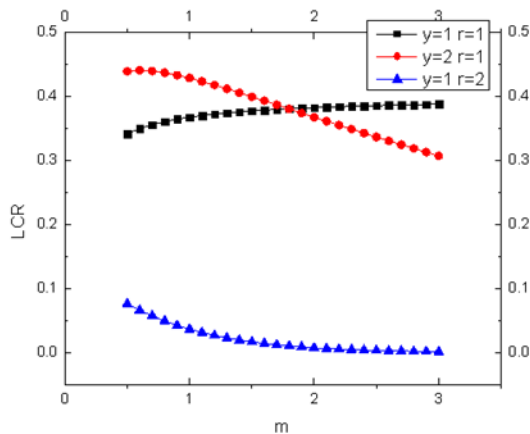
## 5. NUMERICAL RESULTS

Figure (1) shows the level crossing rate of the Nakagami-m random variable depending on the envelope  $y$  for various values of the fading sharpness  $m$  and the mean power of the Nakagami-m random variable  $r$ . Depending on envelope  $y$ , the level crossing rate increases for smaller values of envelope, then the curve reaches a maximum and then the curve decreases. For higher values of the parameters  $m$  and  $r$ , the maximum of the curve overflows into the area of large values of the parameter  $y$ . Mean values of envelope  $y$  have the greatest influence on the level crossing rate of the Nakagami-m random process. The shape of the level crossing rate curve does not depend much on the fading sharpness  $m$  and the mean power  $r$ . The influence of parameters  $m$  and  $r$  on level crossing rate decreases for higher values of fading sharpness  $m$  and mean power  $r$ . With an increase in level crossing rate, the quality of transmission decreases, that is, the probability of failure and the probability of error increase, while the channel capacity decreases.



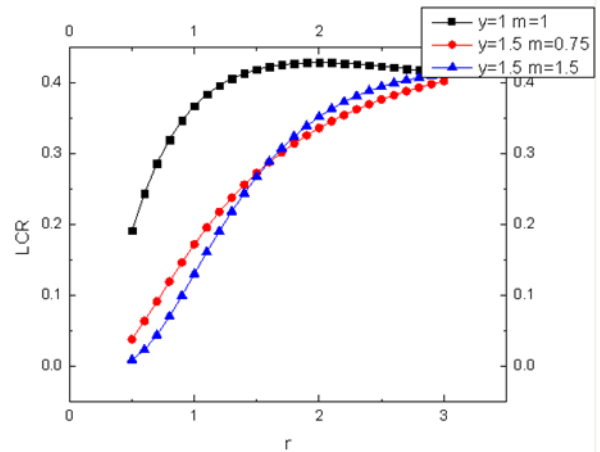
**Figure 1.** Level crossing rate of Nakagami-m random variable depending on envelope  $y$  for various values of fading sharpness  $m$  and mean power of Nakagami-m random variable  $r$ .

Figure (2) shows the level crossing rate of the Nakagami-m random variable depending on the fading sharpness  $m$  for various values of envelope  $y$  and mean power  $r$ . For parameter values  $y=1$  and  $r=1$ , the curve of the level crossing rate increases depending on the parameter  $m$ . The slope of this curve is not significant. For smaller values of the parameter  $m$ , the influence of the parameter  $m$  on the level crossing rate is somewhat greater. For the parameter  $y=1$  and  $r=1$ , the level crossing rate curve decreases. The slope of this curve is slightly higher than in the previous case. The level crossing rate curve for  $y=1$  and  $r=2$  decreases with the increase in the sharpness of fading  $m$ . The level crossing rate curves for  $y=1, r=2$  and  $y=2, r=1$  intersect. The slope of the curve for  $y=1$  and  $r=2$  is not significant. The curve tends to zero.



**Figure 2.** Level crossing rate of Nakagami-m random variable depending on the sharpness of fading  $m$  for various values of envelope  $y$  and mean power  $r$

Figure (3) shows the curve of the level crossing rate Nakagami-m random variable depending on the mean power for various values of envelope  $y$  and sharpness fading  $m$ . For parameter values  $y=1$  and  $m=1$ , the level crossing rate curve has a slight maximum. The curve rises sharply, reaches a maximum, and then declines slightly. For  $y=1.5$  and  $m=0.75$ , the level crossing rate curve increases with the increase in mean power  $y$ . The steepest slope of this curve occurs for the mean values of mean power  $r$ . The level crossing rate curve  $y=1.5$  and  $m=1.5$  does not differ much from the previous curve.



**Figure 3.** Level crossing rate of the Nakagami-m random variable depending on the average power for various values of envelope  $y$  and fading sharpness  $m$

## 6. CONCLUSION

Fast and slow fading have an impact on system performance and limit channel capacity. It is very important how fading degrades the performance of the system and therefore it is necessary to determine the second-order performance of the telecommunication system such level crossing rate of the envelope signal, the mean duration of the system failure and the joint probability density of the envelope signal and the first derivative of the envelope signal. In this paper, we determined the level crossing rate of the Nakagami-m random process signal, which is applied in the performance analysis of the telecommunications system, by means of which we determine the mean failure duration at the output of the wireless system of the system and the joint probability density of the envelope of the signal at the output of the wireless system and its of the first extract. The results obtained in this way can be used to calculate the average failure time of telecommunication systems in the presence of Nakagami-m fast fading. The mean time of failure of the system can be determined as the quotient of the probability of failure and the level crossing rate. The joint probability density of the signal envelope and the first derivative of the signal envelope is determined by the transformation of the random variables. Using analytical expressions, which are presented in the paper, the system can be simulated, which allows designers to create rational systematic solutions for the desired performance of the system.

**Literature**

- [1] G. L. Stuber, "Mobile communication", Kluwer; USA, 2003, 2nd edn ; USA, 2003, 2nd edn
- [2] Yao, Y., and SHEIKH, A.: 'Outage probability for microcell mobile radio systems with co- channel interferers in Rician/Rayleigh environment', Electron. Lett., 1990, 26, pp. 864-866.
- [3] W.C.Y. Lee, "Mobile communications engineering", Mc-Graw-Hill New York, USA, 2001.
- [4] LIN, J., KAO, W., and LEE, T.: ' Outage and coverage considerations for microcell mobile radio systems in shadowed- Rician/ shadowed-Nakagami environment', IEEE Trans. Veh. Technol., 1999, 48, (1).
- [5] KARAGIANNIDIS, G., GEORGOPOULOS, C., and KOTSPOULOS, S.: ' Outage probability analysis for a Rician signal in L Nakagami interferers with arbitrary parameters', KICS J. Commun.Networks, 1999, 1, (1), pp.26-31.
- [6] M.A. Blanco, Diversity receiver performance in Nakagami fading in Proc. IEEE Southeastern Conf. Orlando, 1983, pp. 529-532.
- [7] Dragana Krstić, Petar Nikolić, Marija Matović, Ana Matović, Mihajlo Stefanović "The Satellite Telecommunication System Performances in the Presence of Nakagami Fading on Satellite and Earth Station" , ICWMC 2010, The Sixth International Conference on Wireless and Mobile Communications, September 20-25, 2010 - Valencia, Spain.
- [8] F.Lazarakis, G.S. Tombras, and K. Dangakis, "Average channel capacity in a mobile radio environment with Rician statistics," IEICE Trans. Commun., vol.E77-B, no. 7, pp. 971-977, July 1994.



**OTEH 2024**  
11<sup>TH</sup> INTERNATIONAL SCIENTIFIC CONFERENCE  
ON DEFENSIVE TECHNOLOGIES

*SECTION VII*

**Materials and technologies - *MT***



## PORTABLE RAMAN SPECTROSCOPY FOR DETECTION OF AMMONIUM NITRATE–FUEL OIL EXPLOSIVE PRECURSORS

DENIS DINIĆ

CBRN Defense Centre, Kruševac, University of Defense Belgrade, Military Academy, [denis.dinic@yahoo.com](mailto:denis.dinic@yahoo.com)

BRANISLAV STOJKOVIĆ

CBRN Defense Centre, Kruševac, University of Defense Belgrade, Military Academy, [banestojkovic3@gmail.com](mailto:banestojkovic3@gmail.com)

DIJANA AKSENTIJEVIĆ

CBRN Defense Centre, Kruševac, [dijanasaric88@gmail.com](mailto:dijanasaric88@gmail.com)

MILAN TANIĆ

University of Defense Belgrade, Military Academy [milantanic@yahoo.com](mailto:milantanic@yahoo.com)

NEGOVAN IVANKOVIĆ

University of Defense Belgrade, Military Academy

NEMANJA JOVANOVIĆ

Technical Faculty in Bor, University of Belgrade, Bor [nemanjanikjov77@gmail.com](mailto:nemanjanikjov77@gmail.com)

MARKO ANĐELKOVIĆ

CBRN Defense Centre, Kruševac, [markoandjelk@gmail.com](mailto:markoandjelk@gmail.com)

**Abstract:** A handheld Raman spectrometer was used as a sensor for the detection of ammonium nitrate ( $\text{NH}_4\text{NO}_3$ , AN), fuel oil (FO), AN-water solutions, and AN-soil mixtures deposited on materials such as glass and tape to simulate the field conditions of explosive detection. AN is an inorganic oxidizing salt that is commonly used in mining explosives. A significant explosive mixture is Ammonium nitrate–fuel oil (ANFO). However, owing to its widespread accessibility, AN-based explosives are also utilized for the manufacture of improvised explosive devices (IEDs). The portable Raman system with a laser operating at 785 nm wavelength is used to analyze simulated sites manipulated with IEDs. Characteristic Raman bands from AN were found at  $710\text{ cm}^{-1}$  and  $1050\text{ cm}^{-1}$ , and  $1440\text{--}1470\text{ cm}^{-1}$  for FO. The relative limit of detection of AN in water was less than 0.1%.

**Keywords:** Raman spectroscopy, Ammonium nitrate, fuel oil, explosive, IEDs.

### 1. INTRODUCTION

Global security risks and the threat of terrorism have been growing rapidly in recent decades. Improvised explosive devices (IEDs) are commonly used for this purpose. These devices are not fueled by traditional familiar explosive materials such as 3-Nitrotoluene (TNT) but can be produced from homemade explosives and unexploded military ordinances [1].

Ammonium nitrate–fuel oil (ANFO) is a widely used explosive mixture. This type of explosive is used in coal and metal mining. Since the 1995 ANFO attack on a federal building in Oklahoma City, improvised explosive devices (IEDs) have attracted enormous attention because of concerns regarding their widespread use in terrorism [2]. ANFO explosives are popular among terrorists because of their simplicity of preparation. It can be prepared industrially, or it can also be made at home very

easily. From a chemical-technological point of view, it is possible to differentiate three different versions of ANFO explosives: ammonium nitrate and fuel; ammonium nitrate, fuel, and powder metal (usually aluminum or magnesium); and ammonium nitrate, fuel, and wooden powder. They are explosive and decompose via detonation. The main disadvantages of this material are its low water resistance and problems related to non-ideal detonation, which generally requires a booster [3,4].

Rapid and precise identification of explosives is a crucial task for public security and safety, particularly with the recent proliferation of IEDs. Explosives ordnance disposal (EOD) specialists, bomb technicians, forensic scientists, hazardous material (HazMat) technicians, Chemical, Biological, Radiological, and Nuclear Specialist (CBRN) specialists, and first responders meet a broad set of challenges in the course of their missions and consequently require a broad set of tools to assist them in the completion of their duties [5].

A wide range of instruments can be used in the field to identify various explosives and their precursors rapidly and accurately. One particularly useful technology in the battle against IEDs is Raman spectroscopy. Raman spectroscopy is a technique that measures the frequency shift of inelastically scattered light from the sample when the photon from incident light strikes a molecule and produces a scattered photon. A Raman spectrometer comprises a light source, a monochromator, a sample holder, and a detector. Raman spectroscopy has been used for the analysis of explosives based on ammonium nitrate [6,7].

This study aimed to evaluate a handheld Raman spectrometer for the analysis of ammonia nitrate and fuel oil in combination with several types of substrates to simulate the detection of explosive precursors at high interferences from different materials. The effect of the integration time on the Raman figures of merit is also detailed.

## 2. EXPERIMENTAL

### 2.1. Materials and chemicals

Ammonium nitrate (AN,  $\text{NH}_4\text{NO}_3$ ) was obtained from Centrohem (Serbia). Pure AN crystals were ground to powder size. Fuel oil (FO, CAS: 68553-00-4) was obtained from NIS (Serbia). Silver Duct tape was obtained from Würth (Germany). To mix the AN and soil, a soil sample was taken from a local site. Soil sample was collected from the upper layer of the soil to a depth of 10 cm. Before mixing AN with soil, the soil sample was cleaned from vegetation and stones and brought to a constant mass by drying in an oven at 105 °C. After that, the sample was homogenized by mechanical mixing and brought to a uniform distribution by sieving through a 0.25 mm sieve.

### 2.2. Instrumentation and software

The characteristics of the obtained samples were investigated using a handheld Raman spectrometer (Serstech ARX, Sweden) in the optical range 2300–400  $\text{cm}^{-1}$  with a resolution of 8  $\text{cm}^{-1}$ . The portable Raman system used in this research included a laser operating at 785 nm wavelength. The obtained results were processed using the program software, ChemDash Pro, Excel, and Origin Pro 9.

## 3. RESULTS AND DISCUSSION

The field conditions are being simulated in this research to identify IEDs. We used a Handheld Raman spectrometer for measurement of the explosive precursors (AN and FO), some substrates commonly present in field and clutter materials (soil, glass, water, and tape), and their mixtures.

The Raman spectra of each explosive precursor and tape are shown in Figure 1. The Raman spectra of soil and glass samples are not shown because there was no useful

information on spectra due to the high-intensity fluorescence detected.

Characteristic Raman bands from AN were found at 710  $\text{cm}^{-1}$  and 1050  $\text{cm}^{-1}$  which are associated with the  $\text{NO}_3^-$  in-plane deformation and  $\text{NO}_3^-$  symmetric stretch. Comparison of these spectra with the reference spectra [8] of the AN showed that the AN could be easily identified by Raman spectra. FO, a minor component of ANFO, is readily detected and identified. FO showed several wide bands, with bands at 1440–1470  $\text{cm}^{-1}$  detected as CH stretching. The tape shows Raman spectra rich in sharp bands coinciding with the bands of PVC (650  $\text{cm}^{-1}$ –CCl stretch, 1300  $\text{cm}^{-1}$ –CH rocking, 1450  $\text{cm}^{-1}$ – $\text{CH}_2$  bending, and 1620  $\text{cm}^{-1}$ –aromatic ring stretch).

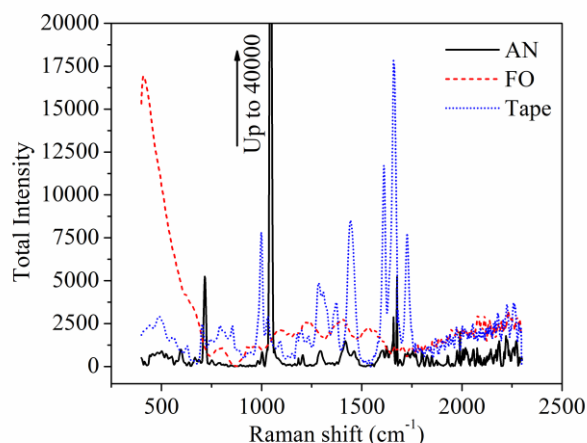


**Figure 1.** Spectra of explosive precursors (AN and FO) and tape. Integration time: 30 s

Figure 2 shows spectra of a mixture of AN-water which can be found in the area where was manipulated with IEDs. Small amounts of AN could be scattered in the surrounding ponds or leak from the surface of the container due to wet weather conditions.

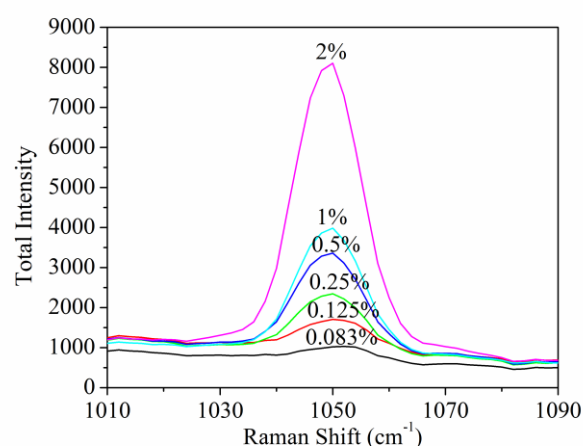


**Figure 2.** Effect of AN percentage on AN-water solutions. AN Raman band 1050  $\text{cm}^{-1}$ . The percentage value represents AN. Integration time: 30 s

With these techniques, we can detect AN in water

mixtures in less than 1%. The useable band was at 1050  $\text{cm}^{-1}$  and the band at 710  $\text{cm}^{-1}$  was not visible for lower concentrations of AN in water.

Figure 2 shows that the intensity of the band at 1050  $\text{cm}^{-1}$  decreased as the AN concentration in water decreased. This result is in full agreement with the results obtained by Diaz et al., who used a laser with different characteristics [6].

Soil mixtures with the explosive precursors (AN and FO) were also tested. The useable spectra were obtained only for AN-soil mixtures because these spectra had no characteristic band of the FO due to the high fluorescence emission of the soil [9]. The spectra of the AN, soil, and AN-soil mixtures are shown in Figure 3.

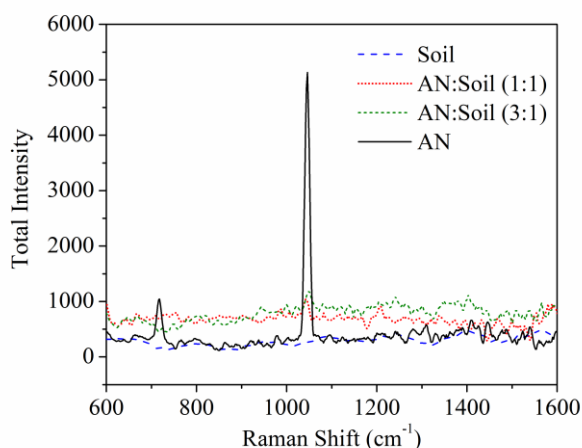


**Figure 3.** Effect of the relationship between AN and soil. AN Raman band at 710  $\text{cm}^{-1}$  and 1050  $\text{cm}^{-1}$ . Integration time: 30 s

The characteristic band of AN at 1050  $\text{cm}^{-1}$  can be seen for the AN and all investigated AN-soil mixtures and the band at 710  $\text{cm}^{-1}$  is visible for the concentrations higher than 90% of AN in the mixture. We detected AN in the 1:1 AN-soil mixture which is also the lowest detectable concentration. The concentration lower than 50% AN in the mixtures cannot be detected due to the high fluorescence emission of the soil. The identification of AN in soil would likely require considerable effort for sample homogenization. Similar allegations were reported by Diaz et al. [6].

#### 4. CONCLUSION

This study shows Raman's capability for the detection and identification of IEDs in field conditions through the investigated potential of the explosive precursors (AN and FO), some substrates commonly present in field and clutter materials (soil, glass, water, and tape) and its mixtures. The portable Raman spectrometer with

optimization of device parameters could be a good tool for fast response in real situations in field conditions. In addition to pure substances, this technique can also be used to identify their mixtures with water (a concentration of AN less than 0.1%) and soil (a concentration of AN up to 50%), which can be found in the field in real situations.

#### References

- [1] GLACKIN, J.M.E., GILLANDERS, R.N., ERIKSSON, F., FJÄLLGREN, M., ENGBLOM, J., MOHAMMED, S., SAMUEL, I.D.W., TURNBULL, G.A.: *Explosives detection by swabbing for improvised explosive devices*, Analyst, 145 (2020) 7956-7963.
- [2] CHUNG, S.T., YOON, Y., PARK, H.J.: *Screening and prioritizing the precursors of improvised explosive devices from commodity chemicals being controlled under Korean regulations*, Journal of Loss Prevention in the Process Industries, 26(6) (2013) 1679-1684.
- [3] FIGULI, L., KAVICKY, V., JANGL, S.: *ZVAKOVA, Z.: Comparison of the Efficacy of Homemade and Industrially Made ANFO Explosives as an Improvised Explosive Device Charge*, Communications – Scientific Letters of the University of Zilina, 20(2) (2018) 23-27.
- [4] FABIN, M., JAROSZ, T.: *Improving ANFO: Effect of Additives and Ammonium Nitrate Morphology on Detonation Parameters*, Materials, 14(19) (2021) 5745.
- [5] ALBRIGHT, R.: *Cleanup of Chemical and Explosive Munitions*, Elsevier, 2012.
- [6] DIAZ, D., HAHN, D.W.: *Raman spectroscopy for detection of ammonium nitrate as an explosive precursor used in improvised explosive devices*, Spectrochimica Acta, Part A: Molecular and Biomolecular Spectroscopy, 233 (2020) 118204.
- [7] STOKES, R.J., FOULGER, B., BLANCO-RODRIGUEZ, A.M., TANG, L., WHITAKER, K., POPE, T.: *Explosive and precursor identification using a portable spatially offset Raman spectroscopy (SORS) device*, Artificial Intelligence for Security and Defence Applications, 12742 (2023) 1274209.
- [8] ALI, E.M.A., EDWARDS, H.G.M., SCOWEN, I.J.: *Raman spectroscopy and security applications: the detection of explosives and precursors on clothing*, Journal of Raman Spectroscopy, 40(12) (2009) 2009-2014.
- [9] XING, Z., DU, C., ZENG, Y., MA, F., ZHOU, J.: *Characterizing typical farmland soils in China using Raman spectroscopy*, Geoderma, 268 (2016) 147-155.



## INFLUENCE OF TEMPERING TEMPERATURE ON MECHANICAL PROPERTIES OF G42CrMo4 CAST STEEL

DORĐE IVKOVIĆ

Faculty of engineering, University in Kragujevac, Sestre Janjić 6, 34000, Kragujevac, Serbia, [djordje.ivkovic@fink.rs](mailto:djordje.ivkovic@fink.rs)

DUŠAN ARSIĆ

Faculty of engineering, University in Kragujevac, Sestre Janjić 6, 34000, Kragujevac, Serbia, [dusan.arsic@fink.rs](mailto:dusan.arsic@fink.rs)

ANĐELA MITROVIĆ

Faculty of engineering, University in Kragujevac, Sestre Janjić 6, 34000, Kragujevac, Serbia, [andjamt99@gmail.com](mailto:andjamt99@gmail.com)

VLADIMIR MILOVANOVIĆ

Faculty of engineering, University in Kragujevac, Sestre Janjić 6, 34000, Kragujevac, Serbia, [vladicka@kg.ac.rs](mailto:vladicka@kg.ac.rs)

DRAGAN ADAMOVIĆ

Faculty of engineering, University in Kragujevac, Sestre Janjić 6, 34000, Kragujevac, Serbia, [adam@kg.ac.rs](mailto:adam@kg.ac.rs)

VESNA MANDIĆ

Faculty of engineering, University in Kragujevac, Sestre Janjić 6, 34000, Kragujevac, Serbia, [mandic@kg.ac.rs](mailto:mandic@kg.ac.rs)

MARKO DELIĆ

Faculty of engineering, University in Kragujevac, Sestre Janjić 6, 34000, Kragujevac, Serbia, [marko.delic@kg.ac.rs](mailto:marko.delic@kg.ac.rs)

**Abstract:** This paper explores the effects of tempering temperatures on the mechanical properties of G42CrMo4 cast steel, a versatile alloy commonly used in automotive and construction industries. Tempering, a critical step in the heat treatment process, aims to reduce residual stresses and enhance material reliability. The study investigates the influence of tempering temperatures (450°C and 600°C) on the steel's strength, ductility, and hardness through a series of experimental investigations, including heat treatment, machining, and tensile testing. Results indicate that while normalization treatment offers moderate strength and good ductility, quenching and tempering at 450°C significantly increase strength at the expense of ductility. Conversely, tempering at 600°C strikes a balance between strength and ductility.

**Keywords:** G42CrMo4, quenching, tempering, tensile test

### 1. INTRODUCTION

Aim of this paper is to demonstrate, the effect of various tempering temperatures on mechanical properties of alloyed cast steel G42CrMo4. This particular cast steel, known for its high strength, impact toughness, and hardness, is frequently used in the automotive, construction, and various other industries. The chemical composition of G42CrMo4 cast steel in combination with suitable heat treatment, contributes to its mechanical properties such as high strength, impact toughness, and hardness, making it suitable for applications in automotive, construction and many other industries [1].

In some earlier researches it was also proved that tempering could be successfully used for lowering both amount of residual stress as well as deformation on hard-faced parts [2, 3].

J. Wang et. al in the paper entitled "Effect of rapid tempering at high temperature on microstructure, mechanical properties and stability of retained austenite of medium carbon ultrafine bainitic steel" investigated the

influence of rapid tempering on various properties of ultrafine bainitic steels, providing a good support for developing tempering process for this steel type. [4]

K. Gupta et al. in the paper "CO<sub>2</sub> corrosion resistance of low-alloy steel tempered at different temperatures" investigates the influence of tempering temperatures on the corrosion resistance of materials, therefore giving good foundation when choosing tempering temperatures for materials exposed to CO<sub>2</sub>. [5]

S. Henschel in his research [6], investigates the influence of non-metallic inclusions on fracture toughness of material at various temperatures, thus giving information on material behaviour in such conditions.

D. Kreweth et al. [7] presented a research related to fracture behaviour of G42CrMo4 steel under high-cycle fatigue regime. Fractural behaviour was monitored using thermal camera, thus time needed for crack to form and to grow up to part failure is determined. The mentioned studies did not directly investigate the tensile properties of castings in different conditions, but they helped compare



the results in the improved (heat-treated) state. Apart from steel standards, we have not found similar research in the literature.

**2. MATERIALS AND METHODS**

G42CrMo4 cast steel belongs to the group of alloyed cast steels. Its chemical composition is shown in Table 1.

This cast steel often undergoes different heat treatments to adjust mechanical properties for a certain purpose.

**Table 1.** Chemical composition of G42CrMo4 cast steel [8]

Chemical element	C	Si	Mn	Cr	Mo	P	S
Amount, %	0.38-0.45	max 0.4	0.6-0.9	0.9-1.2	0.15-0.30	0.025	0.035

**Table 2.** Mechanical properties of G42CrMo4 cast steel [8]

State	R <sub>m</sub> , MPa	R <sub>p0.2</sub> , MPa	A, %	Z, %	Impact energy, J
Normalized	670	435	25.2	60	87
Q+T	1100-1300	900	10	40	30

G42CrMo4 cast steel due to its favourable properties is widely used in industry. Despite the long presence of G42CrMo4 cast steel in industry application, research of this material is still ongoing.

Primary goal of tempering is to reduce residual stresses in the material caused by previous thermal processes, such as quenching or welding. This helps to improve the overall stability and reliability of the material. Temperatures for tempering typically range from 300°C to 600°C [9]. The specific temperature chosen depends on the desired outcome and the material being treated.

Experimental investigation involved preparing initial pieces, their heat-treating, machining specimens on a CNC lathe, and conducting tensile tests. The heat treatment process included quenching the material followed by tempering at different temperatures. By examining the mechanical properties such as yield strength, tensile strength, and elongation of G42CrMo4 cast steel in its normalized state and after quenching and tempering at moderate (450°C) and high (600°C) temperatures, aim is to provide a comprehensive understanding of how tempering temperature affects the performance of this alloyed cast steel.

The selection of the most favourable thermal treatment regime for the examined steel was performed based on the TTT diagram (Fig. 1) for the considered steel, and the aim of the heat treatment was to achieve the most favourable values of strength and ductility [1].

Typical heat treatment for this cast steel consists of quenching and tempering (Q+T). Therefore, this cast steel was chosen for experimental investigations. Mechanical properties of cast steel in both normalized and quenched heat-treated states found in literature are shown in Table 2.

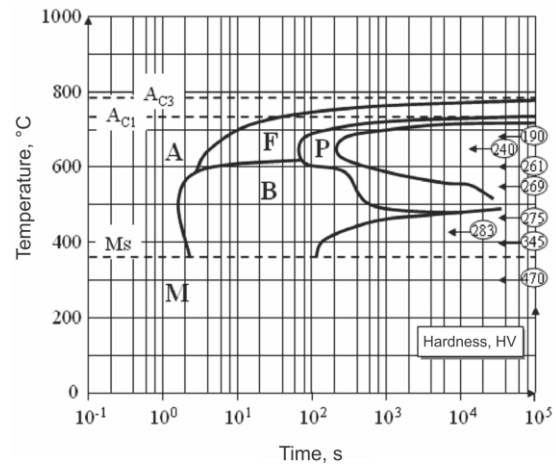


**Figure 1.** TTT diagram for 42CrMo4 steel [1]

In both cases, tempering was conducted after the quenching. For quenching, the material was heated in an electric furnace up to 860°C, held at that temperature for 1 hour, and cooled down to room temperature in an oil bath. After cooling down in oil, the material was once again heated. In the case of moderate tempering, the material was heated up to 450°C, held for 45 minutes, and then cooled down in free air. In the case of high tempering, the material was reheated up to 600°C after quenching, held at that temperature for 45 minutes, and afterward cooled down in free air, as in the case of moderate tempering. Thermal cycles for both heat treatments are given in Figures 2 and 3 [1].

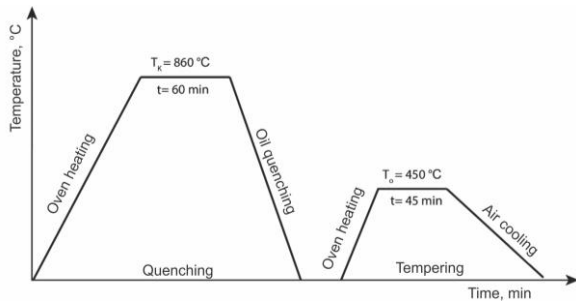


**Figure 2.** Heat-treatment regime for mid-tempered specimens [1]

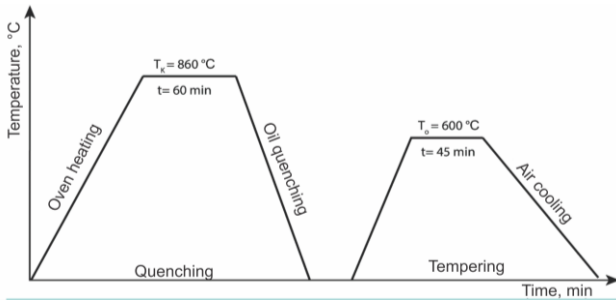


**Figure 3** Heat-treatment regime for high-tempered specimens [1]

After the heat treatment was successfully conducted, specimens for tensile tests were machined from heat-

treated material on a CNC lathe. For tensile testing, specimens with an initial diameter ( $d_0$ ) of 9 mm and a gauge length of 90 mm were used. The appearance of the prepared specimens after machining is given in Fig. 4.



**Figure 4.** Geometry of specimens prepared for tensile tests [1]

After machining of specimens, tests were conducted. Tensile tests of specimens were conducted on a universal testing machine ZWICK/ROELL Z100. The tensile test was conducted with a loading rate of 10 mm/min at room temperature.

### 3. RESULTS AND DISCUSSION

After the conducted test on prepared specimens (normalized, mid-tempered, and high-tempered), the following results were obtained and displayed in Table 3. Stress-strain curves are displayed in Figures 5-7.

**Table 3.** Results obtained by tensile testing [1, 8]

Heat-treatment	Specimen number	Rp0.2, MPa	Rm, MPa	A, %
Normalized	1	360	760	18
	2	360	746	15.33
	3	346	755	16.67
Q+T (at 450°C)	1	1531	1616	2.01
	2	1649	1673	5.2
	3	1628	1628	2.51
Q+T (at 600°C)	1	801	966	6.66
	2	809	963	6.01
	3	831	973	6.33

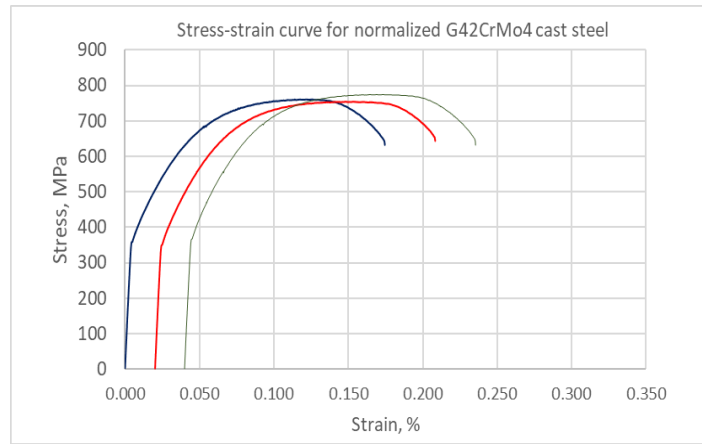


**Figure 5.** Stress-strain curves for normalized samples of G42CrMo4 cast steel [3]

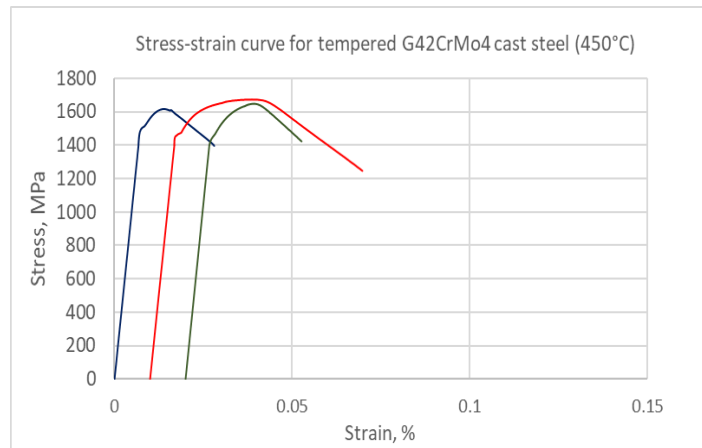


**Figure 6.** Stress-strain curves for the quenched and mid-tempered samples of G42CrMo4 cast steel [1]

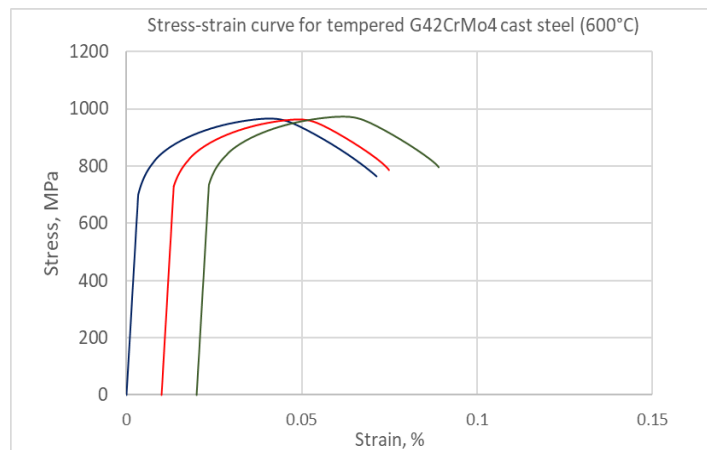


**Figure 7.** Stress-strain curves for quenched and high-tempered samples of G42CrMo4 cast steel [1]

Tempering temperatures closer to 300°C generally result in higher hardness and strength, while higher temperatures lead to increased ductility and toughness. This is achieved through the redistribution of carbon atoms in the material, which affects its microstructure and mechanical properties. One can conclude that tempering is a critical step in the heat treatment process, allowing for the adjustment of mechanical properties to meet specific performance requirements while ensuring the stability and integrity of the material [2].

By analysis of the results given in section 4, one can conclude that specimens which were subjected to the

normalization treatment achieve moderate yield stress values (346-360 MPa), with slight variation among the test specimens. Moderate tensile strength ranging from 746 to 760 MPa is measured. Elongation values range from 15.33% to 18%, showing acceptable ductility for this treatment. Overall, this heat treatment allows for G42CrMo4 cast steel to achieve a good compromise between strength and ductility.

Specimens that were quenched and tempered at 450°C showed greater values of yield stress and tensile strength. Yield stress value for this material state ranges between 1531 and 1649 MPa, which is far greater than values for

normalized specimens. Tensile strength ranges from 1616 to 1673 MPa, exceeding double the value of tensile strength for normalized specimens. That results were expected since the lower tempering temperature provides greater mechanical properties [10].

Values of elongation for this state of material are significantly lower than values in the normalized state. For this state, elongation ranges from 2.01% to 5.20% compared to the range from 15.33% to 18% of normalized specimens. This indicates reduced ductility which is caused by applied heat-treatment.

Specimens tempered at 600°C achieve mechanical properties which are intermediate compared to the previous two states. Yield stress values range from 801 to 831 MPa and tensile strength values from 966 to 973 MPa. Values for both properties are higher than values for the normalized state but lower when compared to values achieved with specimens tempered at 450°C. Elongation values range from 6.01% to 6.66%, suggesting that ductility is still reduced when compared with normalized specimens. When comparing with values achieved for specimens tempered at 450°C, ductility is improved.

#### 4. CONCLUSION

In this paper, on specimens prepared from alloyed cast steel G42CrMo4, effect of various tempering temperatures on mechanical properties was demonstrated. Three batches of tensile specimens were prepared. One batch was machined from normalized G42CrMo4, the second was quenched and tempered at 450°C, and the third was also quenched and tempered at 600°C.

Following conclusions could be drawn:

- Normalizing treatment provides moderate strength and good ductility,
- Quenching and tempering at 450°C result in high strength but reduced ductility and
- Quenching and tempering at 600°C offer a balance between strength and ductility.

In conclusion, the results of the mechanical testing highlight the versatility of G42CrMo4 cast steel and emphasize the importance of thoughtful material selection and heat treatment optimization in engineering design and manufacturing processes.

#### References

- [1] DIMITRIJEVIĆ, F., *Selection of most favorable heat-treatment for 42CrMo4 steel and G42CrMo4 cast steel*, Master thesis, Faculty of Engineering, University of Kragujevac, Kragujevac, Serbia, 2020.
- [2] ARSIĆ, D., LAZIĆ, V., NIKOLIĆ, R., ALEKSANDROVIĆ, S., DJORDJEVIĆ, M., HADZIMA, B., VIČAN, J., Influence of tempering on the deformation level of the multi-layer hard faced samples, *Procedia Engineering*, 111 (2015) 49-56.
- [3] LAZIĆ, V., ARSIĆ, D., NIKOLIĆ, R., HADZIMA, B., Experimental determination of residual stresses in the hard-faced layers after hard-facing and tempering of hot work steels, *Procedia Engineering*, 153 (2016) 392-399.
- [4] WANG, J., LI, H., WANG, Q., LIANG, Z., GAO, S., SUN, L. GAO, YANG, X., LI, Z., Y. ZHANG, F. Effect of rapid tempering at high temperature on microstructure, mechanical properties and stability of retained austenite of medium carbon ultrafine bainitic steel, *Journal of Materials Research and Technology*, 28 (2024) 3144-3154,.
- [5] GUPTA, K., HARATIAN, S., MISHIN, O., AMBAT, R., CO2 corrosion resistance of low-alloy steel tempered at different temperatures, *Corrosion Science*, 232 (2024) 112027.
- [6] HENSCHER, S., KRÜGER, L., Modelling of crack initiation in a G42CrMo4 steel with non-metallic inclusions. *Steel research international*, 87(1) (2016) 29-36.
- [7] KREWERTH, D., LIPPOMANN, T., WEIDNER, A., BIERMANN, H. Application of full-surface view in situ thermography measurements during ultrasonic fatigue of cast steel G42CrMo4, *International Journal of Fatigue*, 80 (2015) 459-467
- [8] IVKOVIĆ Dj.: Influence of heat-treatment on production process for responsible welded structures made from G42CrMo4 cast steel, Master thesis, Faculty of Engineering, University of Kragujevac, Kragujevac, Serbia, 2022.
- [9] JOVANOVIĆ M., LAZIĆ V., ARSIĆ D., 2017. *Material Science*, Faculty of Engineering, University of Kragujevac, Kragujevac, Serbia, ISBN 978-86-6335-042-7. (in Serbian).
- [10] *Steel Heat Treatment Handbook*, 2nd Edition; Routledge, Taylor & Francis Group, 2002.



**THE INFLUENCE OF THE PHASE TRANSFORMATION:  
Fhyd → FE<sub>3</sub>O<sub>4</sub>, OCCURS DURING THE ANNEALING  
TREATMENT OF SOL-GEL SYNTHESIS, ON THE  
ABSORPTION PROPERTIES OF THE FINAL SYNTHESIS  
PRODUCT (Fe<sub>3</sub>O<sub>4</sub>/C HOLLOW-SPHERE NANOPARTICLES)**

VIOLETA NIKOLIĆ

Vinča Institute of Nuclear Sciences, University of Belgrade, Mike Petrovića Alasa 12-14, P.O. Box 522, 11001  
Belgrade, [violeta@vinca.rs](mailto:violeta@vinca.rs)

ZORAN IVIĆ

Vinča Institute of Nuclear Sciences, University of Belgrade, Mike Petrovića Alasa 12-14, P.O. Box 522, 11001  
Belgrade, [zivic@vinca.rs](mailto:zivic@vinca.rs)

JOSE F. M. L. MARIANO

Universidade do Algarve, FCT, Campus de Gambelas, 8005-139 Faro, Portugal  
Center of Physics and Engineering of Advanced Materials (CeFEMA), IST, Universidade de Lisboa, Av. Rovisco Pais,  
1096-001 Lisboa, Portugal  
[jmariano@ualgt.pt](mailto:jmariano@ualgt.pt)

**Abstract:** *In this paper, we perform a theoretical study of the possible improvement of the absorption properties (> 8 GHz) of the sample consisting of Fe<sub>3</sub>O<sub>4</sub>/C hollow sphere nanoparticles, prepared by sol-gel method. In order to achieve proposed goal, we examine the impact of the phase transformation of the sample, occurred during the annealing treatment. It was found that the presence of the Fhyd → Fe<sub>3</sub>O<sub>4</sub> phase transformation, occurred during the thermal treatment process, decreases the absorption power of the final synthesis product. Accordingly, we considered ways to mitigate the effects of phase transformation as a mean of improving absorption efficiency. For this purpose, we propose a theoretical framework that relies on a simple quantum mechanical Hamiltonian. We suggest that the absence of the Fhyd → Fe<sub>3</sub>O<sub>4</sub> phase transformation, could improve the absorption properties of the final sample (Fe<sub>3</sub>O<sub>4</sub>/C).*

**Keywords:** *sol-gel, Hamiltonian, quantum entanglement.*

## 1. INTRODUCTION

Sol-gel synthesis method enables production of high-quality nanoparticles, which could be used for a numerous different applications.

Magnetic nanoparticles, prepared by the sol-gel method (mostly magnetite (Fe<sub>3</sub>O<sub>4</sub>)), can be used for various military purposes, among others, as adsorbing agents. Accordingly, one of the promising applications of use of material, containing Fe<sub>3</sub>O<sub>4</sub> nanoparticles, prepared by sol-gel method, is the absorption of electromagnetic (EM) waves [1]. Based on the chemical composition, it is desirable that the magnetic absorbents are nanocomposite compounds, because single-phase absorbents do not show strong absorption, due to weak magnetic losses [1]. Various coated magnetic nanoparticles can participate in the process of radar absorption in the X-band area, or in the electromagnetic camouflage of submarines [2] (ferrites [1], magnetite, and Ni-ferrite nanoparticles coated by titanium dioxide [3], nanoparticle systems containing silicon nanoparticles [4], composites

containing gadolinium and iron nanoparticles [5], etc.). Literature has shown that radar-absorbing applications (important in the construction of stealth materials) could be improved by using nanoparticle systems, which change color in the presence of a magnetic field [6]. Note that the nanocomposite, consisting of Fe<sub>3</sub>O<sub>4</sub> core-shell nanoparticles and mesoporous carbon hollow spheres (Fe<sub>3</sub>O<sub>4</sub>/C), synthesized by sol-gel method, are capable to achieve an ultra-wide absorption band of 8 GHz [7].

On the other hand, sol-gel synthesis procedure is thoroughly investigated with the aim of improving properties of the final synthesis product. For example, in the case of mentioned army application, it is of importance to improve materials absorbing properties. Accordingly, in this article will be discussed theoretical suggestions of the possible modifications of a mentioned synthesis, with the aim of improvement of the absorbing properties of the synthesized samples. Annealing process is step in a synthesis procedure, which determines size of the magnetic nanoparticles and matrix pores, diffusion of gases through the matrix, final structural properties of the

sample, etc. One of the aspects that affects growth of the silica matrix pores (as well as the nanoparticles within the pores), is the phase transformation of the different phases, of which are consisted annealed sample. Noteworthy, the role of phase transformation in sol-gel synthesis has not yet been unambiguously established. It is not known whether the presence of the phase transformations of the sample improves or hinders its final properties.

*On the other hand, phase transformations occurs in a different stages of sol-gel synthesis, but in this article, accent will be on the phase transformations, triggered by annealing process. Brief overview on the annealing treatment confirms that annealing treatment represents essential part of sol-gel synthesis, during which nanoparticles growth in the matrix pores. Also, final structure and size of the pores is achieved via heating process. Since literature showed that annealing treatment presents part of sol-gel, which is of the highest importance for defining of absorption properties of the final synthesis product [7], here will be discussed presence/absence of phase transformation during annealing treatment, and its impact on the absorption properties of the final sample.*

In order to better understand the role of phase transformations during annealing treatment, this article will discuss whether it is more energetically advantageous to anneal a sample with or without the presence of its phase transformation.

Let us recall that the changes, resulting in phase transformations, are very sophisticated, and that the energy imbalance at the quantum level leads to the appearance of phase transformation. Accordingly, the discussed question will be examined at the quantum level, taking into account the change of the Hamiltonian (H) of the system model. Given Hamiltonian will be introduced to describe the samples, formed in the furnace, with and without the presence of their phase transformation, respectively.

## 2. RESULTS AND DISCUSSION

### 2.1. Comments on the synthesis

In a Ref. [7], sol-gel synthesis was performed, in order to synthesize 9 – 10 nm Fe<sub>3</sub>O<sub>4</sub> nanoparticles, by using iron nitrate precursor (Fe(NO<sub>3</sub>)<sub>3</sub>). The solid phase of iron nitrate is unstable in air, and oxidizes very easily, so it is not convenient starting precursor. Iron nitrate in the liquid phase is not so easy to prepare reproducible, due to the difficulty in determining the exact concentration of iron cations, which varies, depending on how much nitric acid is evaporated, which is most often quite arbitrary. Noteworthy, literature has shown that an excess of nitrate anions slower the matrix crystallization (affects the diffusion of gases, and therefore the formation of pores) [8].

Another issue, characteristic for using iron nitrate precursor, is obtaining the final product through phase transformations, occurred during the annealing treatment. Before the annealing treatment, the sample consists of Fhyd nuclei, which is a common name for different types

of oxyhydroxide species. Fhyd formula is determined variously: 5Fe<sub>2</sub>O<sub>3</sub>·9H<sub>2</sub>O, 2FeOOH·2.6H<sub>2</sub>O, Fe<sub>3</sub>HO<sub>8</sub>·4H<sub>2</sub>O, Fe<sub>3</sub>O<sub>3</sub>(OH)<sub>9</sub> or Fe<sub>4</sub>O<sub>5</sub>(OH)<sub>2</sub>·2.6H<sub>2</sub>O [9]. Although, from a practical point of view, all the given formulas are essentially equivalent (and for this reason are often reduced to the formula of hydrated iron oxyhydroxide, FeOOH·0.4H<sub>2</sub>O), from a quantum point of view, the difference is significant. For simplicity, here will be assumed that only one phase transformation occurred, from Fhyd to Fe<sub>3</sub>O<sub>4</sub> nuclei formation.

From the energetic point of view, question of phase transformations is not negligible. Taking into account quantum aspect, phase transformations, started from different formulas, will be characterized by different energy losses. Having on mind that, usually, the exact formula of Fhyd (of which the non-annealed sample consists) is not known, it is very difficult to get a precise insight into the path of the presented phase transformations, and therefore into the exact magnetostructural properties of the prepared magnetite nanoparticle. To avoid the use of iron nitrate precursors, and to improve the reproducibility of the synthesis, the use of other iron precursors, such as iron sulfate, could be suggested.

On the other hand, in order to improve the absorption properties of the samples, this study proposes a modification of the given synthesis. The proposed modification of the synthesis would be based on the application of the seeding method, as part of the sol-gel synthesis, which would enable the growth of magnetite nanoparticles, during the annealing process, without phase transformation (seeding would replace the growth of magnetite nanoparticles via the Fhyd → Fe<sub>3</sub>O<sub>4</sub> phase transformation). So, the use of already prepared Fe<sub>3</sub>O<sub>4</sub> of smaller size, and their consequent homogeneous dispersion in the alkoxide solution is recommended here, which allows avoiding the mentioned phase transformation during the annealing treatment. As a potential seeds, already prepared Fe<sub>3</sub>O<sub>4</sub> nanoparticles, coated with oleic acid (which acts as a stabilizing agent), and synthesized by the solvothermal synthesis method, starting from the FeSO<sub>4</sub>·7H<sub>2</sub>O precursor [10], could be used. Once when the particles are prepared, the oleic acid layer can be removed by washing the nanoparticles with methanol [11]. Proposed nanoparticles have a regular, spherical shape, characterized by high monodispersity and a narrow particle size distribution of (4.8 ± 1.3) nm. During the annealing treatment, the given nanoparticles can be expected to grow to 9 – 10 nm, which was the size of the particles used in a discussed synthesis [7].

In order to investigate whether the proposed modification of the synthesis method (use of already prepared Fe<sub>3</sub>O<sub>4</sub> nanoparticles) can improve the absorption properties of the sample prepared in [7], the influence of phase transformations during the annealing treatment will be considered from a quantum point of view. Recall, Ref. [7] showed that annealing is the most important step to control the absorption properties of the absorber material (a sample annealed at 400°C absorbed in the bandwidth of 5.7 GHz, while annealing the sample, taken from the same bench, at 500°C, extended that bandwidth to 8

GHz). Accordingly, in this study, the sample prepared by annealing at  $500^\circ C$ , during which the phase transformation  $F_{hyd} \rightarrow Fe_3O_4$  [7] occurs, will be designated as S1, and the theoretical sample, synthesized without phase transformation of iron species (which could be prepared by seeding  $Fe_3O_4$  nanoparticles), will be labeled as S2.

## 2.2. Theoretical model

Heat is the main characteristic of the annealing process. It interacts with the sample (crystal lattice of a solid body) at the quantum level, through the vibrational energy of atoms. During the annealing treatment, heat transfer (via conduction, convection and radiation) occurs through the sample.

Note that this phenomenon is related to the electromagnetic (EM) radiation. During heating a sample, atoms vibrate, and a large number of electrons and other excitations are transported within the crystal lattice, inducing, in that way, changes at the quantum level. As a result of vibration, EM radiation is emitted. In the opposite case, during absorption of EM radiation, absorbed part of the EM wave is turned into heat, which consequently brings to the increased vibration of the atoms, of which is sample consisted of. The sample's temperature rises, with the aim to equalize emission and absorption, in order to achieve thermal equilibrium between the sample and its surroundings. These processes occur simultaneously, which additionally complicates examination of the impact of the phase transformations, induced by annealing treatment, on the energy changes at quantum level. Here is proposed that thermal treatment impacts sample through disturbing quantum entanglement (QE) of the system, which results in its phase transformation.

To get deeper insight in this issue, simplified theoretical model will be postulated.

### 2.2.1. The form of the model Hamiltonian

Recall here that different forms of Hamiltonian, postulated in literature, are proposed for the interaction between EM and atom. Despite, in the context of considered case (annealing process, as a part of sol-gel synthesis method, and formation of  $Fe_3O_4/C$  nanoparticles), a satisfactory theoretical model to describe the Hamiltonian for interaction of heat radiation and atom, has not yet been postulated. In this study, mentioned model will be proposed.

Afterwards, with the aim to comment absorption properties of the investigated samples, it will be discussed Hamiltonian of the interaction of EM radiation and samples, considering contribution of their Hamiltonian, defined during annealing treatment. In order to simplify, it will be used the same form of Hamiltonian for description of interaction between different forms of radiation (heat and EM) with the discussed samples. Such Hamiltonians are consisted of a three terms, describing field, atom, and interaction between atom and field, respectively (in other words, Hamiltonian is defined as:

$$\hat{H} = \hat{H}_{field} + \hat{H}_{atom} + \hat{H}_{int}.$$

To chose appropriate form of model Hamiltonian, recall that temperature difference (i.e., entropy) is related to the quantum entanglement, which depicts to importance of the annealing process for the absorption properties of the samples. In 2021 was experimentally shown that temperature differences in superconductor can be used to entangle pairs of electrons [12], which confirmed that it is possible to entangle electrons with heat. Although it is much complicated to experimentally observe this in the case of high temperatures, it could be assumed that temperature difference (a main characteristic of an annealing treatment), affects quantum entanglement.

The entropy of entanglement is characterized by von Neumann entropy, which presents the Gibbs entropy in the quantum statistical mechanics [13]. On the other hand, as the lowest-order approximation to the von Neumann entropy, which would quantify the degree of coherence losses (in the case of the interaction of the atom, with EM radiation), the degree of entanglement between the subsystems can be quantified by linear entropy [14]. In the literature, coherence loss is understood as the purity loss [14]. Since the purity describes how much a state is mixed, this magnitude is related to the linear entropy, but also, to the phase transformations.

One of the first models, suitable to describe phenomena, appeared in a quantum system as a consequence of the interaction between a two-level atom and an EM field within a cavity, is Tavis-Cummings model. Such a model could be extended to the application in a various solid state systems, and it is used in literature to discuss the interacting Heisenberg spin chain [15]. If a given Hamiltonian is modified, in order to be applicable for N-level atoms (with the constant coupling parameters), Hamiltonian takes a form [14]:

$$\hat{H} = \hbar\eta\hat{\sigma}_z + \hbar\mu\hat{j}_z + \lambda_1\hbar(\hat{\sigma}_- + \hat{\sigma}_+)(\hat{j}_+ - \hat{j}_-) + \lambda_2\hbar(\hat{j}_+ - \hat{j}_-) + \lambda_3\hbar(\hat{\sigma}_- + \hat{\sigma}_+) \quad (2.2.1.1)$$

Here,  $\lambda_{1-3}$  are coupling parameters,  $\hat{\sigma}_+$  and  $\hat{\sigma}_z$  are two-level atom Pauli operators. In a given expression, third term is given as (2.2.1.2):

$$\hat{H}_{int} = \lambda_1\hbar(\hat{\sigma}_- + \hat{\sigma}_+)(\hat{j}_+ - \hat{j}_-) + \lambda_2\hbar(\hat{j}_+ - \hat{j}_-) + \lambda_3\hbar(\hat{\sigma}_- + \hat{\sigma}_+) \quad (2.2.1.2)$$

In this case, linear entropy could be recognized as a suitable criterion to monitor the purity loss of the investigated quantum system [14], and it is defined by expression [16]:

$$P(t) = Tr[\hat{\rho}_a(t)(1 - \hat{\rho}_a(t))] \quad (2.2.1.3)$$

where is  $\hat{\rho}_a(t)$  - atomic density operator.

After discussion of the wave function, and calculations of the expectation values of the Pauli operators, equation for the linear entropy for the atomic state is expressed in the form of eq. (2.2.1.4) [14]:

$$P(t) = \frac{1}{2} \left( 1 - (\sigma_x^2(t) + \sigma_y^2(t) + \sigma_z^2(t)) \right) \quad (2.2.1.4)$$

This equation clearly indicates importance of a linear entropy (through the impact of Pauli operators) for the total Hamiltonian of a modeled quantum system. Having on mind that linear entropy can be understand as a Shannon entropy, which is directly analogous to the entropy in statistical thermodynamics [17], it is

understandable that it presents important parameter of a closed thermodynamic system in the annealing furnace, which impacts the absorption power of the annealed samples.

### 2.2.2. The form of the model Hamiltonian, applied in a discussed case

Theoretical model proposed within this study will be discussed relying on second quantization, which enables postulation of the Hamiltonian for solid state body. To discuss impact of the quantum effects on the investigated samples (in this case, nanocomposite absorber, containing  $Fe_3O_4$  nanoparticles), it should be performed formal quantization of the excitation, and quantum corrections will be introduced into the defined form of the Hamiltonian. In other words, instead of position and momentum operators, interacting part of the samples will be described by creation and annihilation operators.

Although heat interacts with the atom through the vibrations of its crystal lattice, and contributes more to the second Hamiltonian term ( $\hat{H}_{atom}$ ), the emphasis of the postulation of the model Hamiltonian will be on the third term, since it is the term of the Hamiltonian, which describes the interaction between radiation and atoms in the case of heat, as well as in the case of EM radiation. In other words, it is the term of Hamiltonian, whose variation impacts absorption power of the annealed samples. Another reason for devoting special attention to this term of Hamiltonian is a fact, that variation of a synthesis parameters impacts absorption properties of the final sample, while absorption occurs as a result of interaction between atom and radiation. Accordingly, it will be postulated that modification of a third term of a model Hamiltonian ( $\hat{H}_{int}$ ) is affected due to phase transformation, which occurs as a result of the radiating of a sample with the heat, during annealing treatment. Consequently, in the case of all Hamiltonian investigated in this study, the term describing interaction between radiation and atom, will be considered.

In the postulated model, as part of the sample that interacts with radiation, the excitation (in the form of exciton, created during the annealing treatment, as a result of the interaction of radiation and atoms) of a two-level atom, will be considered. Exciton Hamiltonian will be described as  $H(S1)$ , in the case of a model system, where a given model atom was subjected to the phase transformation under the impact of the annealing treatment. It will be postulated that the form of  $H(S1)$  defines the absorption capability of a sample S1 (literature sample, capable to absorb in a wave range of 8 GHz [7]). Exciton of a model atom, described as  $H(S2)$ , will refer to the theoretical sample in the system of the furnace, whose formation is not characterized by the presence of phase transformation during annealing treatment.

At atomic level, phase transformation represents re-arrangement of the atoms within crystal lattice, and consequently, re-arrangement of the crystal lattice structure. It is important to note that, at quantum level, phase transformation could be considered only as the energy contribution, appeared due incorporation of the atom in a different position within the crystal lattice.

To simplify model, it will be neglected: changes in the crystal lattice structure (structural transformation of the crystal lattice, due rearrangement of the atoms during phase transformation), exciton-vibron interaction [18], heat quantum nature and interpretation (it will be considered only as radiation), and temporal dimension of the problem (exact time-dependent dynamical operators are still not defined, and due to the simplicity of the problem, time component of the problem will be neglected). Consequently, presence/absence of a phase transformation, occurred during annealing treatment within the sample, will be considered as the only difference between the samples. Model Hamiltonian will be defined with reference on phase transformation. In order to simplify, all discussed Hamiltonian will have the same form.

The form of Hamiltonian of interaction between atom and radiation, described by eq. (2.2.1.2) and applied on the case of interaction between exciton and radiation, will be used to describe  $H(S1)$  and  $H(S2)$ . Formation of exciton triggers re-arrangement of the atoms, atoms positions in crystal lattice, and structure of crystal lattice. Having on mind that energy contribution of the phase transformation appears under the impact of the heat radiation, it contributed to the 3<sup>rd</sup> term of Hamiltonian, which describes interaction between radiation and atom.

Accordingly, model will discuss energy contribution of appearance of phase transformation, on the Hamiltonian of the excitation. Because of the presence of phase transformation, energy dissipation occurs on the node of the crystal lattice, which reflects on the energy of the atom system, and on the transfer of excitation. Recall that dissipated energy presents a difference between kinetic and potential energy, and describes how much potential energy was irreversible converted into heat. Accordingly, dissipation energy presents energy loss, appeared via phase transformation of the sample S1, during annealing treatment, which is not presented in the case of the S2. This, mathematically, reflects on the Hamiltonian of the samples, during annealing treatment ( $H(S1)^{ann}$  and  $H(S2)^{ann}$ ), and  $H(S1)^{ann}$  will be characterized by modified  $\hat{H}_{int}$  term, describing energy losses due to the appearance of phase transformation in the system:

$$H(S1)^{ann} = \hbar\eta\hat{\sigma}_z + \hbar\mu\hat{j}_z + \lambda_1\hbar(\hat{\sigma}_- + \hat{\sigma}_+)(\hat{j}_+ - \hat{j}_-) + [\lambda_2\hbar(\hat{j}_+ - \hat{j}_-) + \lambda_3\hbar(\hat{\sigma}_- + \hat{\sigma}_+) + \hat{H}_{phase\ tr.}] \quad (2.2.2.1)$$

$$H(S2)^{ann} = \hbar\eta\hat{\sigma}_z + \hbar\mu\hat{j}_z + \lambda_1\hbar(\hat{\sigma}_- + \hat{\sigma}_+)(\hat{j}_+ - \hat{j}_-) + [\lambda_2\hbar(\hat{j}_+ - \hat{j}_-) + \lambda_3\hbar(\hat{\sigma}_- + \hat{\sigma}_+)] \quad (2.2.2.2)$$

Modification of the expression for Hamiltonian, by considering the energy changes, induced by phase transformation  $F_{hyd} \rightarrow Fe_3O_4$ , requires considering of the dissipation energy, which is estimated by eq. (2.2.2.3):

$$\hat{H}_{phase\ tr.} = \hat{T} - \hat{V} \quad (2.2.2.3)$$

Where is  $\hat{T}$  - operator of the exciton kinetic energy, and  $\hat{V}$  - operator of exciton potential energy. Described dissipation energy represents energy loss, for which reason is  $\hat{H}_{int}^{modif} < \hat{H}_{int}$ . Accordingly,  $H(S2)^{ann} > H(S1)^{ann}$ . Post-annealed atoms (modeled samples) already contains defined energy



content in the form of Hamiltonians, formed during annealing, and its value is further modified by the same amount of modifications for both atoms, so interaction with EM radiation, reflecting in the form of absorption capability, involves only further modification of the third term.

$$H(S1) = \frac{H(S1)^{ann}}{\hat{H}_{int}^{modif}} + \hat{H}_{radiation\ of\ the\ field}^{modif} + \hat{H}_{atom}^{modif} + \hat{H}_{int}^{modif} \quad (2.2.2.4)$$

$$H(S2) = \frac{H(S2)^{ann}}{\hat{H}_{int}^{modif}} + \hat{H}_{radiation\ of\ the\ field}^{modif} + \hat{H}_{atom}^{modif} + \hat{H}_{int}^{modif} \quad (2.2.2.5)$$

Since the further modified terms of the discussed Hamiltonians are changed for the same amounts, it depicts to the fact that  $H(S2) > H(S1)$ . In other words,  $\hat{H}_{int}(S2) > \hat{H}_{int}(S1)$ , which depicts to the stronger interaction between atom S2 and radiation at quantum level. Having on mind that the same form of Hamiltonian is applied for description of the post-annealed atoms, it could be proposed that the higher value of  $H(S2)$ , initiated by the higher value of  $\hat{H}_{int}(S2)$  term, should reflect in the improved absorption properties of the atom S2. In classical Newton mechanics, S2 represents absorber, synthesized by the same synthesis method as sample S1, but during the annealing process, the preparation of sample S2 did not involve its phase transformation.

Here could be considered mechanism, proposing explanation of the QE impact on absorption properties of the sample. It is proposed that the disturbance of QE, and consequent changes in the purity losses, could be described by variations in linear entropy, which contributes to the 3<sup>rd</sup> term of Hamiltonian, also [15]. On the other hand, 3<sup>rd</sup> term is a term of Hamiltonian, which describes interaction between atom and radiation. Since disturbance in QE is triggered by heat treatment, which induces, at the atomic level, occurrence of phase transformation, and, in the same time, contributes to the term of Hamiltonian which describes interaction between atom and radiation, it means that QE disturbance impacts absorption properties of the annealed sample.

Recall that linear entropy is related to the entire value of Hamiltonian through Pauli operators (eq. (2.2.1.4), characteristic for 3<sup>rd</sup> term of Hamiltonian), which means that variations in Hamiltonian value (induced by rearrangement of the atoms, during phase transformation), impacts linear entropy value. Changes in linear entropy, in the same time, reflects changes in the purity losses, induced by variation of QE. Heat in the furnace induces growth of the nanoparticles, and arranges the atoms in various positions, in different crystal lattices (observed as phase transformation). Accordingly, it could be proposed that changes in QE at quantum level (reflected in the variations of a purity losses, and, consequently, linear entropy of the quantum system) impacts absorption properties of the sample.

In other words, in this study is postulated that the improvement of the absorption properties of the samples

prepared by the sol-gel method could be achieved, if the annealing process took place without the phase transformation of the annealed samples. It is proposed that presence of phase transformation affects QE of the samples at the quantum level, which impacts linear entropy. Note that phase transformation and linear entropy are described by the third term of Hamiltonian, which describes interaction between excitation and radiation. Consequently, interaction between heat radiation and excitation induces changes in the linear entropy value, which contributes to the value of the macroscopic entropy magnitude, describing the investigated thermodynamic system of the annealed samples. Impact of presence/absence of phase transformation, on the QE of the investigated samples, is transmitted via entropy value, which further affects final absorption ability of the examined samples (mathematically described, again, via a third term of Hamiltonian).

### 3. CONCLUSION

This theoretical research was done in order to get deeper insight in the impact of the annealing treatment on the final properties of the annealed samples. It was investigated impact of the presence/absence of phase transformation of samples, prepared by the sol-gel method, on their quantum properties (quantum entanglement), as well as on their macroscopic properties (absorption power of the final samples). The study revealed that quantum entanglement affects the absorption properties of the finite sample, via linear entropy and through the contribution of the third term of the Hamiltonian.

A modification of the sol-gel method, in which the seed method would be used, instead of the synthesis of magnetic nanoparticles from iron precursors, is proposed. This approach would ensure the absence of phase transformation of Fe<sub>3</sub>O<sub>4</sub> nanoparticles during the annealing treatment, which has been shown to be energetically more favorable for improving absorption properties of the sample (> 8 GHz).

### Acknowledgements

The research was funded by the Ministry of Education, Science and Technological Development of the Republic of Serbia (451-03-66/2024-03/ 200017). Z. I. acknowledges support by the "Vinča" Institute, special grant No. 23-DMS0-0172/2 dated 21.12.2023. Research received no external funding.

### References

- [1] Zhao, Y., & Ji, G. (2022). Multi-spectrum bands compatibility: New trends in stealth materials research. *Science China Materials*, 65(11), 2936-2941.
- [2] Abed, M. S., & Jawad, Z. A. (2022). Nanotechnology for defence applications. In *Nanotechnology for electronic applications* (pp. 187-205). Singapore: Springer Nature Singapore.
- [3] Das, S., Nayak, G. C., Sahu, S. K., Routray, P. C., Roy, A. K., & Baskey, H. (2015). Titania-Coated

- magnetite and Ni-Ferrite nanocomposite-based RADAR absorbing materials for camouflaging application. *Polymer-Plastics Technology and Engineering*, 54(14), 1483-1493.
- [4] Kuznetsov, A. I., Miroshnichenko, A. E., Fu, Y. H., Zhang, J., & Luk'Yanchuk, B. (2012). Magnetic light. *Scientific reports*, 2(1), 492.
- [5] Stanciu, C. D., Hansteen, F., Kimel, A. V., Kirilyuk, A., Tsukamoto, A., Itoh, A., & Rasing, T. (2007). All-optical magnetic recording with circularly polarized light. *Physical review letters*, 99(4), 047601.
- [6] Vilusz, E. (Ed.). (2008). Military textiles. Elsevier.
- [7] Cheng Y, Cao J, Li Y, et al. (2017). The outside-in approach to construct Fe<sub>3</sub>O<sub>4</sub> nanocrystals/mesoporous carbon hollow spheres core-shell hybrids toward microwave absorption. *ACS Sustainable Chemistry & Engineering*, 6(1), 1427–1435.
- [8] Nikolić, V. N., Spectroscopic investigation of the influence of NO<sub>3</sub><sup>-</sup> anions on the crystallization of SiO<sub>2</sub> matrix, SPIG 2022, 5-9 October, Belgrade, Serbia, ISBN: 978-86-82296-02-7, 2022, pp. 80.
- [9] Nikolić, V. N., Vasić, M. M., Kisić, D. (2019). Observation of c-CuFe<sub>2</sub>O<sub>4</sub> nanoparticles of the same crystallite size in different nanocomposite materials: The influence of Fe<sup>3+</sup> cations. *Journal of Solid State Chemistry*, 275(1), 187-196.
- [10] Nikolić, V. N., Tadić, M., Jovanović, S., & Spasojević, V. (2019). Tracking of the electronic re-ordering in Fe<sub>3</sub>O<sub>4</sub>/OA nanoparticles using magnetometry. *Ceramics International*, 45(14), 17429-17437.
- [11] Hoerr, C. W., Harwood, H. J. (1952). The solubilities of oleic and linoleic acids in common organic solvents. *The Journal of Physical Chemistry*, 56(9), 1068-1073.
- [12] Tan, Z. B., Laitinen, A., Kirsanov, N. S., Galda, A., Vinokur, V. M., Haque, M., ... & Hakonen, P. J. (2021). Thermoelectric current in a graphene Cooper pair splitter. *Nature Communications*, 12(1), 138.
- [13] Longo, R., Xu, F. (2021). Von Neumann entropy in QFT. *Communications in Mathematical Physics*, 381(2), 1031-1054.
- [14] Abdalla, M. S., Ahmed, M. M. A., Khalil, E. M., Obada, A. F. (2016). The interaction between a single two-level atom coupled to an N-level quantum system through three couplings. *Annals of Physics*, 364(1), 168-181.
- [15] Loss, D., DiVincenzo, D. P. (1998). Quantum computation with quantum dots. *Physical Review A*, 57(1), 120.
- [16] Angelo, R. M., Furuya, K., Nemes, M. C., Pellegrino, G. Q. (2001). Recoherence in the entanglement dynamics and classical orbits in the N-atom Jaynes-Cummings model. *Physical Review A*, 64(4), 043801.
- [17] Shannon, C. E. (1948). A mathematical theory of communication. *The Bell system technical journal*, 27(3), 379-423.
- [18] Zhang, Z., Wang, J. (2016). Origin of long-lived quantum coherence and excitation dynamics in pigment-protein complexes. *Scientific Reports*, 6(1), 37629.



## THE DESIGN AND PREPARATION OF CERIUM-DIOXIDE AND ZIRCONIUM(IV)HYDROXIDE-INCORPORATED NANOFIBERS FOR THE DEGRADATION OF CHEMICAL WARFARE AGENTS

MAJA VITOROVIĆ-TODOROVIĆ

Military-Technical Institute, Belgrade, [majavitod@gmail.com](mailto:majavitod@gmail.com)

TAMARA VUJATOVIĆ-VELIMIROV

Military-Technical Institute, Belgrade, [tamara.vujatovic@gmail.com](mailto:tamara.vujatovic@gmail.com)

STEVAN STUPAR

Military-Technical Institute, Belgrade, [stevan.stupar13@gmail.com](mailto:stevan.stupar13@gmail.com)

DANICA BAJIĆ

Military-Technical Institute, Belgrade, [simic\\_danica@yahoo.com](mailto:simic_danica@yahoo.com)

**Abstract:** Specifically designed nanofibers enriched with chemically active nanoparticles, capable of destruction of chemical warfare agents (CWA's) and other toxic chemicals are highly desirable for the incorporation in personal protective equipment and decontamination items. In this work, we prepared six types of nanofibrous materials, based on the two types of polymers, polyvinylchloride (PVC) and polyvinylbutyral (PVB). As carriers of active chemistry, nanoparticles of cerium-dioxide ( $\text{CeO}_2$ ) and zirconium(IV)hydroxide ( $\text{Zr}(\text{OH})_4$ ) were used. The morphology of the samples obtained and their qualitative chemical composition was investigated by scanning electron microscopy (SEM). The degradation ability of the nanofibrous mats was firstly investigated in an aqueous environment, over wide range of buffered pH conditions, using spectrophotometric method and paraoxon-ethyl as a model compound. A rather slow, but significant degradation of paraoxon-ethyl was observed on nanofibers which contained  $\text{CeO}_2$  nanoparticles in neutral conditions. The sulphur mustard (HD) adsorption was investigated in non-aqueous environment using GC-MS method. The samples made of PVC exerted strong adsorption of HD with almost six fold reduction in HD concentration but without any degradation of the test compound. In conclusion, nanofibers obtained showed strong adsorption ability in non-polar solvents, but further modification of  $\text{CeO}_2$  and  $\text{Zr}(\text{OH})_4$  nanoparticles are necessary to enhance their CWA degradation ability.

**Keywords:** protective materials, nanofibers, nanoparticles, degradation, chemical warfare agents.

### 1. INTRODUCTION

Engineered materials capable of capture and removal of chemical warfare agents (CWA), toxic industrial chemicals (TICs) and biological agents (bacteria, fungi and viruses) are highly desirable for protective textile applications. The very recent events regarding the highest air pollution in Europe in the past ten years and unprecedented Covid-19 pandemics, more than ever increased the need for the enhancement and/or development and implementation of the new types of the efficient protective materials which can be incorporated in the protective overgarments and masks that serve to maintain the exposure to these agents as low as possible. Therefore, one of the main objectives of our current research activities are design of the lightweight protective composite fabrics, based on the nano-scaled supramolecular entities (particles and fibers) which will meet the following performance requirements:

1. Lightweight and breathability – the resulting material should maintain or increase the overall comfort comparing to materials which are used in the current protective overgarments and masks;
2. Incorporation of active chemistry – the material should incorporate the possibility not only to retain CBW agents but also to destruct (decontaminate and disinfect) the agents in efficient manner and on the reasonable time-scale. This will provide additional protection for the users, reduce the possibility of the cross-contamination and resolve the problems of the secondary waste storage and post-use decontamination and disinfection procedures.
3. Reusability and durability – the resulting nano-engineered material should enable multiple usage and should possess optimal physical and mechanical properties to ensure its durability.

4. The material should be eco-friendly *i.e.* biodegradable and/or recyclable.

Several research groups described nanofibers made of different kinds of polymers decorated with chemically active nanoparticles including titanium-dioxide ( $\text{TiO}_2$ ), cerium-dioxide ( $\text{CeO}_2$ ) and zirconium(IV)-hydroxide ( $\text{Zr}(\text{OH})_4$ ) [1-4]. In this work, we prepared six types of nanofibrous materials, based on the two types of polymers, polyvinylchloride (PVC) and polyvinylbutyral (PVB). As carriers of active chemistry, nanoparticles of cerium-dioxide ( $\text{CeO}_2$ ) and zirconium(IV)-hydroxide ( $\text{Zr}(\text{OH})_4$ ) were used. The morphology of the samples obtained and their qualitative chemical composition was investigated by scanning electron microscopy (SEM). The degradation ability of the nanofibrous mats was firstly investigated in an aqueous environment, over wide range of buffered pH conditions, using spectrophotometric method and paraoxon-ethyl as model compounds. The sulphur mustard (HD) degradation was investigated in non-aqueous environment using GC-MS methods.

## 2. MATERIALS AND METHODS

All chemicals were purchased from Sigma Aldrich or Merck, and were used as received.

### 2.1. Electrospinning

Electrospinning was performed on Linari Starter Kit apparatus, with stationary collector. The 5 mL syringe was used with 0.8 mm needle diameter. The distance between needle tip and collector plate was set to 15 cm, and the feed rate of the syringe was set to 1 mL/h, in all experiments. The voltage applied between needle tip and collector plate was 25 kV.

To obtain PVC nanofibers without nanoparticles (sample 1, **S1**), the 10% PVC solution in dimethylformamide (DMF) /tetrahydrofuran (THF) 3:2 mixture was used. Briefly, 1.5 g of PVC was dissolved in 8.58 mL of DMF and 6.08 mL of THF. The solution was left to stir over night, approximately for 12 h, using magnetic stirrer. The 3 mL of the solution were transferred into syringe. The ambient conditions during electrospinning were 21,1 °C and relative humidity of 44%.

To obtain the PVC nanofibers with  $\text{CeO}_2$  nanoparticles (sample 2, **S2**) or  $\text{ZrO}_2$  nanoparticles (sample 3, **S3**), the 10 wt% of the nanoparticles was used, calculated in regard to polymer weight. Briefly, 0.3 g of nanoparticles were suspended in 17.6 mL of DMF and 12.16 mL of THF. To de-agglomerate nanoparticles, the suspension was sonicated using Bandelin Sonopuls homogenizer, set to 30 W, and pulse regimen for 2s of ultrasound and pause for 1 s, during 30 minutes. After that, 3 g of polymer was added; the mixture was stirred for 30 minutes and sonicated for 30 minutes under the same conditions. The ambient conditions during electrospinning were 23.2 °C and relative humidity of 46%.

To obtain PVB nanofibers without nanoparticles (sample 4, **S4**), the 10wt% of the polymer was used and ethanol as a solvent. Briefly, 3 g of PVB was dissolved in 34.61 mL EtOH, and mixture was stirred using magnetic stirrer for 1 hour. The ambient conditions during electrospinning were 20.2 °C and relative humidity of 43%.

To obtain the PVB nanofibers with  $\text{CeO}_2$  nanoparticles (sample 5, **S5**) or  $\text{ZrO}_2$  nanoparticles (sample 6, **S6**), the 10 wt% of the nanoparticles was used, calculated in regard to polymer weight. The samples were prepared according to the same procedure as described for the S2 and S3, and ambient conditions during electrospinning were 22.0 °C and relative humidity of 43%.

### 2.2. Characterisation of the nanofibers

The quality, morphology and diameter of nanofibers as well as dispersion of the nanoparticles on their surface were investigated by scanning electron microscopy using JEOL JSM-660 LV microscope. The surface of the samples was covered with layer of gold to assure conductivity. The EDS analysis was done by energy-dispersive spectrometer EDS OXFORDX-Max with Aztec software.

### 2.3. Degradation of paraoxone

Degradation ability of the samples was investigated in both aqueous media and organic solvent. Series of aqueous buffers were used, including: 0.1 M phosphate buffer pH=7.0, 0.1 M phosphate buffer pH=8.0, 0.1 M Tris.HCl pH 8.5, 0.05 M Glycinate buffer pH 10.5. As a model compound for monitoring the degradation reaction, paraoxon was used. The 1.5 mg/mL paraoxon stock solution was prepared by dissolution of 11.7  $\mu\text{L}$  of the compound in 10 mL of the corresponding media, except for the deionized water and phosphate buffer pH 7.0, where due to low solubility of paraoxon, 2 mL of acetone and 8 mL of water of buffer were used. In all other aqueous media solubility of paraoxon was good.

To investigate degradation ability of the nanofibers toward paraoxon, in polypropylene eppendorf microcuvette around 0.05 g of nanofibers was placed and 1 mL of paraoxon stock solution was added. In specified time intervals an aliquot of 20  $\mu\text{L}$  was drawn from the mixture, and 980  $\mu\text{L}$  deionized water was added. The remaining concentration of paraoxon was determined by measuring absorbance of the solution at 280 nm, by using Cary UV/Vis 50 spectrophotometer.

### 2.4. Adsorption of the sulfur mustard on the nanofibers

HD stock solutions for the calibration of the GC-MS instrument were made by dissolution of 1  $\mu\text{L}$  of HD in 2 mL of *n*-hexane in the screw-top vial. The series of final calibration standards were made directly into GC-MS vials according to the data given in the Table 1.

**Table 1.** Concentrations of the HD calibration standards

No.	Vstock [ $\mu$ L]	Vsol [ $\mu$ L]	Cppm	C [ $\mu$ g/mL]	C [ $\mu$ M]
1	5	995	2.5	3.175	20
2	10	990	5	6.35	40
3	12	988	6	7.62	48
4	16	984	8	10.16	64
5	20	980	10	12.7	80

Calibration standards were analyzed on Shimadzu GC-MSQP2020 instrument, and the peak area in the chromatogram and the creation of the calibration curve (peak area vs. concentration) was done in Shimadzu LabSolution software. For the quantification of HD the characteristic and the most intensive mass ion  $m/z$  109 was used. The condition in the chromatograph and mass detector are given in the Table 2.

**Table 2.** GC-MS conditions

GC Conditions	
Parameter	Value
Starting column temperature	40 °C, 3 min
Temperature program	40-150°C, 10°C/min, 150-280 °C, 25°C/min, 280 °C, 10,8 min
Injector temperature	250 °C
Injection type	Grob type. Splitless t 0,75 min
Column type	DB-5 ili RTX-5
Column dimensions	30 m x 0,25 mm ID x 0,25 $\mu$ m
Carrier gas	Helium, 32 cm/sec
MS Conditions	
Parameter	Value
Temperature transfer line	280 °C
Temperature ion source	230 °C
Temperature detector	150 °C
Electron energy	70 eV
Mass range	35-500 $m/z$
Scanning rate	3,15 scan/sec
Library	NIST 05 Mass Spectral Data Base

For the monitoring absorption of HD on the nanofibers, approximately 50 mg of the nanofiber samples cut into smallest possible pieces was placed in the 5 mL screw-top vial, and 1  $\mu$ L of HD and 2 mL of *n*-hexane was added. At the beginning of the experiment, and afterwards in specified time intervals 20  $\mu$ L aliquots of the solution were drawn and diluted to 1 mL with acetonitrile directly into GC-MS vial and analyzed under the same conditions as standard HD solutions. The concentration of the unadsorbed HD remaining in the solution is determined from the calibration curve. If the adsorption process is very fast and intensive, so that remaining amount of HD is out of calibration range, than additional specified amount of HD is added in the solution which contain nanofibers, and adsorption is monitored accordingly.

The possible HD degradation products were determined by direct analysis of the solutions above nanofibers

without any dilution, and by the silylation of the samples using BSTFA agent.

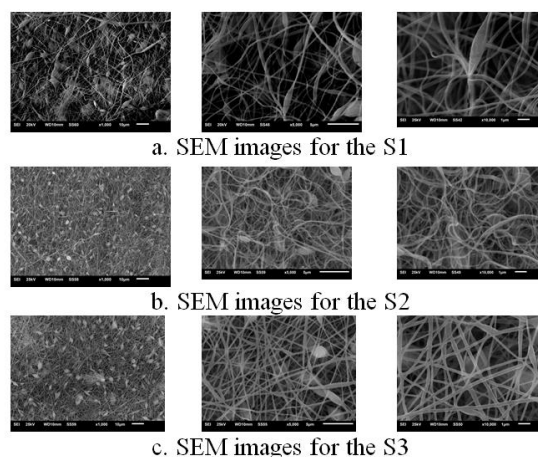
### 3. RESULTS AND DISCUSSION

#### 3.1. Electrospinning and morphological characterization of nanofibers

Electrospinning of the PVC solution without (S1) and with nanoparticles (S2 and S3) was performed at expected manner, with formation of evenly distributed nanofibers in Taylor cone, without visible twisting or breaking, indicating that optimal viscosity of the PVC solution was used as well as optimal syringe feeding rate. Therefore, very homogenous membranes or mats were obtained, given on Figure 1. Electrospinning of the PVB solutions was also satisfactory although viscosity of the solution was slightly lower comparing to PVC, which caused leaking of the solution from the syringe.

**Figure 1.** Nanofiber membranes obtained by electrospinning.

Morphological characterization of nanofibers was performed by scanning electron microscopy, and semi-quantitative elemental analysis was done by energy-dispersive X-ray analysis. In Figure 2, the images of the samples 1-3 obtained under 1000, 5000 and 10000x magnifications are given.



c. SEM images for the S3

**Figure 2.** The images of the samples 1-3 obtained under 1000, 5000 and 10000x magnifications.

In all three samples it is visible that nanofibers had uneven diameter and morphology, and formation of bead-like structures of micrometer dimensions, indicating that viscosity of the polymer solution was low, and probably the fracture of nanofibers during electrospinning occurred

resulting in the formation of these bead-like structures, although we stated previously that this process was not visible during electrospinning process. Sample S2 had the highest density of nanofibers and significantly lower fiber diameter than other two samples. In order to avoid the formation of beads and to obtain more evenly distributed nanofibers in relation to their diameter in the future studies, it is necessary to increase viscosity of the solution somehow, probably by using different solvent or polymer with higher Mw.

On Figure 3, the images of the samples 4-6 obtained under 1000, 5000 and 10000x magnifications are given.

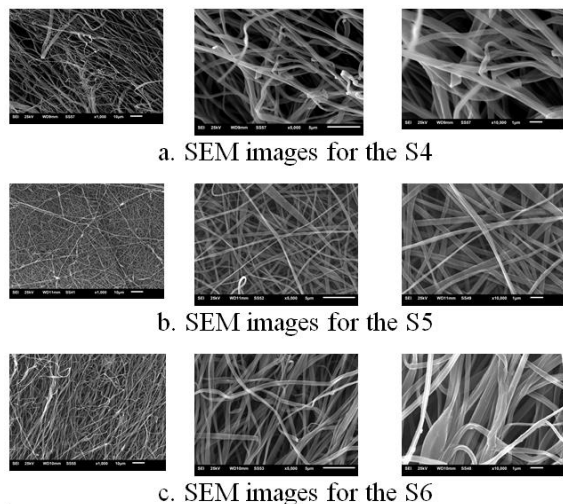


**Figure 3.** The images of the samples 4-6 obtained under 1000, 5000 and 10000x magnifications.

The three samples S4-S6, exhibited uneven morphology and fiber diameter without beads formation, indicating an optimal viscosity of the PVB solution. This is in accordance with findings of Yener and coauthors [5] which stated that ethanol is the best solvent for PVB solutions electrospinning. Similarly with the results obtained for the samples S1-S2, it seems that presence of the CeO<sub>2</sub> and Zr(OH)<sub>4</sub> nanoparticles reduces average fiber diameter, and this effect is especially evident in case of CeO<sub>2</sub> nanoparticles.

The average fiber diameter was estimated by the measurement in as many fiber points as possible in SEM software and calculation of the average value and standard deviation (Figure 4). Sample 1 had the average fiber diameter of  $0.385 \pm 0.197$  nm and sample 5 had  $0.349 \pm 0.108$  nm.

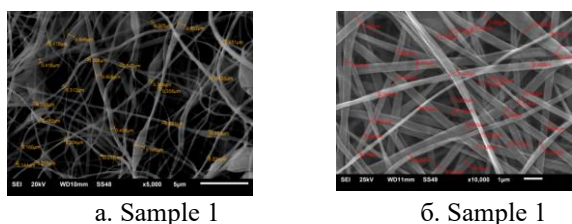


**Figure 4.** Estimation of the average fiber diameter for the samples 1 and 5.

Semiquantitative elemental analysis by EDS was performed for the samples 5 and 6 and the results are

given in the Table 3. A rather homogeneous and even distribution of cerium or zirconium atoms was observed in both of these samples.

**Table 3.** EDS analysis for the samples 5 and 6.

Sample	Analysis spot	EDS spectrum	Wt % element
S5			C=70,25%, O=24,09%, Ce=5,63%
S5			C=73,82%, O=20,26%, Ce=5,92%
S5			
S6			C=66,73%, O=27,98%, Zr=5,28%
S6			
S6			

### 3.2. Degradation ability of the nanofibers toward paraoxone

Paraoxone is used as a model compound for the nerve agents, primarily due to its lower toxicity, but another convenience is that it gives yellow *p*-nitrophenoxy anion as hydrolysis and decomposition product, with absorption maximum at 407-412 nm, which may be determined by spectrophotometry. It is also possible to determine paraoxon concentration directly since it has absorption maximum in the UV area around 278 nm.

Various methods for the determination of the decomposition ability of various nanomaterials toward paraoxone can be found and the basic difference between these methods is the type of medium used in the experiment and relative mass ratio of the nanomaterial and the model compound. Some of the studies used aqueous media of different pH and buffer type, while other studies used organic protic solvents (methanol, ethanol and isopropanol) or nonpolar solvents such as heptane. For instance, Zhan and coworkers [6] investigated degradation of paraoxone in the presence of various CeO<sub>2</sub> nanoparticles in different buffers including: ammonia buffer NH<sub>3</sub>/NH<sub>4</sub>Cl, *N*-methylmorpholine buffer, Tris buffer, 4-(2-hydroxyethyl)-piperazine-1-ethanesulfonic acid, and sodium-phosphate buffer. Authors did not specified the pH values of the each single buffer, but

stated that the pH range was from 6.0 to 12.0. The mass ratio of nanomaterial and analyte was 100:1. Wang and coauthors [7] investigated degradation of methyl-paraoxone in aqueous environment in 0.45 ethyl-morpholine buffer (pH 10.0) using mass ratio of nanofibers and model compound of 3:1. Another studies monitored degradation of paraoxone in polar organic solvents, and for example the study of Ramashehan et al. [8] which followed degradation of paraoxone in acetone under different starting concentrations of paraoxone (10, 25 and 50 mM), but they did not specified the mass of the nanofibers used in experiments. Another studies used heptane as a solvent.

Taking into account that nanofibers obtained aim to be used for the development of the novel protective materials with self-decontaminating properties, it would be realistic to examine materials obtained with challenge of the real chemical warfare agent in the vapor or aerosol form. However, the experimental setup of this kind would be complicated, expensive and extremely unsafe, so we decided that the degradation ability of the nanoparticles used and nanofibers obtained should be examined in aqueous environment in the following media: mixture of deionized water and acetone (vol. ratio 8:2, pH 5.5), 0.1 M phosphate buffer pH 7.0, 0.1 M phosphate buffer pH 8.0, 0.1 Tris buffer pH 8.5 and 0.05 Glycinate buffer pH 10.5. Preliminary experiments comprised determination of the paraoxone stability in buffers used, taking into account its fast degradation under high pH values. A very fast degradation of paraoxone was observed in almost all buffers with and without  $\text{CeO}_2$  and  $\text{Zr}(\text{OH})_4$  nanoparticles. It was concluded that all buffers with basic pH conditions are unsuitable for monitoring of the rate of decomposition reaction, due to very fast reaction both in the presence and in the absence of the nanofibers. However, paraoxon was very stable in the mixture of acetone and deionized water in slightly acidic environment pH 5.5, so the degradation ability of the sample 2 was investigated under these conditions. A rather slow but statistically significant degradation of paraoxone was observed, as showed in Figure 4.

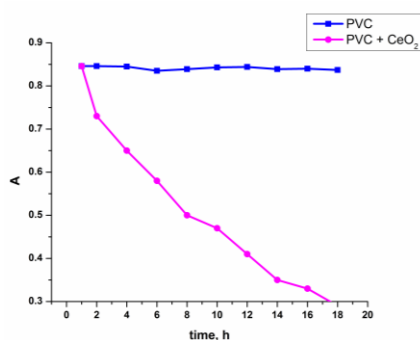


**Figure 4.** Degradation of paraoxone in the presene of sample 2, in of water/acetone mixture.

### 3.3. Adsorption of the HD on the nanofibers

Calibration of the instrument for HD was done using series of standard HD solutions and GCMSLabSolution software. The calibration curve and the corresponding HD

peak are given on the Figure 5. Calibration curve had a satisfactory correlation coefficient,  $R^2=0.98$ . The peak areas of the calibration standard solutions are given in the Table 4.

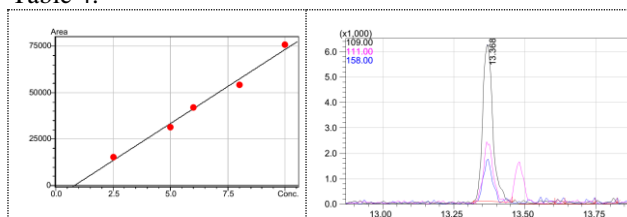


**Figure 5.** HD calibration curve (left) and characteristic ions in HD chromatogram.

**Table 4.** HD peak areas for the standard solutions

C, ppm	Peak hight
2,5	631043
5	1291002
6	1763935
8	2135618
10	3249810

In the first set of experiments adsorption of HD was determined on samples **S1**, **S2** and **S3**. In screw-top vials 64 mg of S1, 57 mg of S2 and 62 mg of S3 was placed and HD and *n*-hexane was added. In specified time intervals aliquots of the solution above nanofibers were drawn and the remaining quantity of HD was determined. The areas of HD peaks as well as its estimated concentration are given in the Table 5. It is evident that after 1h of reaction time the HD concentration was extremely low, so additional 2  $\mu\text{L}$  of HD were added which gives the total HD concentration of 30 ppm. After that, the remaining HD concentration was determined in 1h intervals and those samples were designated as N1-N4 in the Table 5.

**Table 5.** HD concentration in solution treated with nanofiber samples S1-S3

Sample	Peak	C, ppm
S1 0h	186445	0.8
S1 1h	189934	0.8
S1 N1	1556584	6.0
S1 N2	1771252	5.9
S1 N3	1639314	5.9
S1 N4	1492626	5.5
S2 0h	250839	1.25
S2 1h	301276	1.00
S2 N1	1874424	7
S2 N2	1430416	5.7
S2 N3	1591757	5.5
S2 N4	1597607	5.5
S3 0h	282945	1.4

S3 1h	374752	1.2
S3 N1	1454896	5.9
S3N2	1587533	5.7
S3 N3	1400440	5.5
S3 N4	1620532	5.5

It is evident in the Table 5 that samples of nanofiber treated with the first, lower HD concentration (10 ppm), rapidly adsorb HD from the *n*-hexane, resulting in the final concentration which is out of the range of calibration curve. This means that almost 10-fold reduction in the HD concentration was achieved. After addition of another aliquot (2  $\mu$ L) of HD, the very fast adsorption still occurred resulting in the 6-fold reduction of HD concentration, yielding the final concentration of HD around 5 ppm. It is evident that further reduction in concentration in the last two hours of monitoring did not occur which is indication that equilibrium was achieved between adsorption/desorption processes, and that probably pure physisorption without HD decomposition took place. This was confirmed by additional GC/MS analysis, since no HD degradation products were found.

#### 4. CONCLUSION

In this work, we described preparation and morphological characterization of different nanofibers made of the two types of polymers, PVC and PVB and without or with chemically active nanoparticles CeO<sub>2</sub> and Zr(OH)<sub>4</sub>. Six types of samples **S1-S6** were obtained and morphological characterization of nanofibers was performed by scanning electron microscopy. The samples made of PVC had more uneven morphology and showed pearl-like structure formation. Degradation ability was firstly investigated in aqueous environment, over wide range of pH values. In all basic buffers, paraoxon was unstable, so it was difficult to discern which part of paraoxone was degraded due to basic environment only and which was degraded due to catalyst present. However, paraoxon was stable in acidic environment (pH 5.5) and a rather slow, but statistically significant decomposition was observed in the presence of the **S1** in the mixture of water and acetone. Samples **S1-S3** showed very fast adsorption of HD in nonpolar organic solvent, as determined by GC-MS methods. In conclusion, the obtained nanofibers showed good adsorption capacity toward HD, but future studies should include or modify nanoparticles with enhanced degradation properties.

#### Acknowledgements

This work was by Serbian Ministry of Defense and Serbian Ministry of Education, Science and Technological Development, Grant No 451-03-66/2024-03/200325.

#### References

- [1] SENIĆ, Ž., BAUK, S., SIMIĆ, D., VITOROVIĆ-TODOROVIĆ, M., MARKOVIĆ, T., RAJIĆ, D.: *The preliminary comparative analysis of different routes for TiO<sub>2</sub> nanoparticles synthesis and their deposition on textiles. The methyl-orange degradation and VX detoxication study*, Digest Journal of Nanomaterials and Biostructures, 8 (2013) 711-719.
- [2] SUNDARRAJAN, S., and RAMAKRISHNA, S.: *Fabrication of nanocomposite membranes from nanofibers and nanoparticles for protection against chemical warfare stimulants*, J Mater Sci 42 (2007) 8400–8407.
- [3] JANOŠ, P., KURAN, P., KORMUNDA, M., STENGL, V., GRYGAR, T. M., DOSEK, M., STASTNY, M., EDERER, J., PILAROVA, V., VRTOCH, L.: *Cerium dioxide as a new reactive sorbent for fast degradation of parathion methyl and some other organophosphates*, J. Rare Earths, 32, (4), 2014, 360-366.
- [4] KIM, S., YING, W. B., JUNG, H., RYU, S. G., LEE, B., and LEE, K. J.: *Zirconium Hydroxide-coated Nanofiber Mats for Nerve Gas Decontamination*, Chemistry – an Asian Journal, 12(6), 2017, 698-705.
- [5] YENER, F., and YALCINKAYA, B.: *Electrospinning of polyvinylbutyral in different solvents*, e-Polymers 2013, No 021.
- [6] ZHAN, S.-W., TSENG, W.-B., TSENG, W.-L.: *Impact of Nanoceria Shape on Degradation of Diethyl Paraoxon: Synthesis, Catalytic Mechanism, and Water Remediation Application*, Environmental Research, 188 (2020) 109653.
- [7] WANG, S., POMERANTZ, N.L., DAI, Z., XIE, W., ANDERSON, E.E., MILLER, T., KHAN, S.A., PARSONS, G.N.: *Polymer of intrinsic microporosity (PIM) based fibrous mat: combining particle filtration and rapid catalytic hydrolysis of chemical warfare agent simulants into a highly sorptive, breathable, and mechanically robust fiber matrix*, Materials Today Advances, 8 (2020) 100085.
- [8] RAMASESHAN, R., SUNDARRAJAN, S., LIU, Y., BARHATE, R.: *Functionalized polymer nanofibre membranes for protection from chemical warfare stimulants*, Nanotechnology 17 (2006) 2947–2953.





## THE INFLUENCE OF DESIGN CONDITIONS ON THE FAILURE OF THE UNIVERSAL CROSS JOINT (UCJ) OF THE CARDAN COUPLING

SAŠA SPASENIĆ

Kontrol Inspekt D.O.O., Belgrade, [spasenic\\_sale@yahoo.com](mailto:spasenic_sale@yahoo.com)

MILETA RISTIVOJEVIĆ

Kontrol Inspekt D.O.O., Belgrade, [miletaristivojevic@gmail.com](mailto:miletaristivojevic@gmail.com)

VLADIMIR MILOVANOVIĆ

Faculty of Engineering University of Kragujevac, Kragujevac, [vladiccka@kg.ac.rs](mailto:vladiccka@kg.ac.rs)

ALEKSANDAR DIMIĆ

University of Belgrade Faculty of Mechanical Engineering, Belgrade, [adimic@mas.bg.ac.rs](mailto:adimic@mas.bg.ac.rs)

STEFAN DIKIĆ

University of Belgrade Faculty of Technology and Metallurgy, Belgrade, [sdikic@tmf.bg.ac.rs](mailto:sdikic@tmf.bg.ac.rs)

SRETEN SPASENIĆ

Kontrol Cert D.O.O., Belgrade, [sreten.spasenic@yahoo.com](mailto:sreten.spasenic@yahoo.com)

**Abstract:** In the system of power transmission from the driving to the operating machine, cardan couplings are components of vital importance. Due to the ability to transmit power over long distances, as well as insensitivity to the coaxiality of the connecting shafts, they have found wide application in all branches of mechanical engineering. In the plant for the production of profiled semi-finished steel products, a volumetric failure of the sleeve on the universal cross joint (UCJ) of the cardan coupling occurred. This type of failure occurs very rarely with cardan couplings. In order to understand the real reason for the failure of the sleeve, analytical and numerical models were formed, and tests of materials and fracture surfaces were carried out. The influence of the line load distribution at the mating surfaces and the geometric stress concentration on the load capacity of the UCJ was analyzed using the developed models. With the increase in the unevenness of the line load distribution, the influence of tangential stresses on the stress state in the critical cross-section significantly increases. It is concluded that the simultaneous influence of the uneven line load distribution and the geometric stress concentration led to the failure of the UCJ sleeve.

**Keywords:** Universal cross joint, cardan coupling, sleeve failure, stress concentration, load distribution.

### 1. INTRODUCTION

In mechanical systems, the power from the driving machine to the working machine is delivered through a gearbox, which transforms that power - adapts it to the needs of the working machine in terms of the number of revolutions and torque. Couplings play a very important role in this power transmission process. They connect driving and working machines and gearboxes into one functional unit. Their failure interrupts the chain of transmission of power from the driving machine to the working machine, which also means the interruption of the functioning of the machine system. That is why it is very important that the couplings perform their function reliably and safely.

According to the working conditions regarding the required co-axiality of the connected shafts and the mutual distance of the driving and working machine from

the gearbox, a large number of different types of couplings have been developed. Couplings that are not sensitive to the coaxiality of the connected shafts and can connect shafts at greater distances are cardan couplings. They are widely used in agricultural machinery, rail, cargo and combat vehicles, as well as in heavy industry [1-3]. In the vehicle industry, the universal joint is one of the most critical parts of both the engine and the transmission system of a vehicle [4].

In a rolling mill for the production of rod profiles, the power from the driving machine (electric motor) to the working machine is transmitted and transformed by means of a multi-stage gearbox. The gearbox has one input and two output shafts. The output shafts of the power transmission are connected to the roller shafts by a telescopic shaft by means of cardan couplings.

On one sleeve of the universal cross joint (UCJ) of the cardan coupling, which connects the telescopic shaft and the roller shaft, there was a volumetric destruction - breakage of the driven sleeve. The load from the sleeve to the coupling fork is transferred by means of two needle bearings, placed on the sleeve. By inspecting the contact surfaces of the sleeve, a markedly uneven load distribution was observed in the needle bearings, that is, the bearing located on the upper half of the sleeve had a negligibly small part in transmitting the working load. The conducted analysis showed that this was one of the main reasons for the breakage of the shaft sleeve. It is an important aspect of these bearings that while in action they never go through complete cycles. In other words, each of these bearings revolves only a few degrees around its axis before returning to its original position. Therefore, there are only a group of rolling bodies in these bearings that take the bearing load [5].

Bearings are very important machine elements because they have a significant influence on the correct functioning of the components of the machine assemblies. At the same time, they can be very sensitive if the installation and maintenance conditions deviate from the prescribed ones. There are a large number of accidents, serious and less serious, caused by the failure of rolling bearings. One failure is described in the paper [6]. In the gearbox, at one support of the intermediate shaft, the outer ring of the conical roller bearing, is installed in the housing with a loose fit. As a result, the outer ring rotated and thus generated thermal energy, which eventually led to the volumetric destruction of the gear teeth and parts of the bearing. By the analysis of information and data obtained in many researches related to this area referred the fact that exploitation reliability of Cardan shaft in working machines are directly determined primary by reliability of needle bearing and cross shafts [2].

In this paper, the generated damage to the UCJ is reviewed in detail. An ultrasonic and magnetic method was applied in order to see possible defects in the material. In addition, an analytical and numerical analysis of the stress state was performed. On the basis of the conducted analyses, it was concluded that the uneven engagement of the needle bearings in load transmission and the design conditions of the UCJ generated large local stresses that led to the formation of the initial crack. It spread over time and led to the volumetric destruction, i.e. breakage of the sleeve of the UCJ.

## 2. DAMAGE ANALYSIS OF THE UCJ SLEEVE OF THE CARDAN COUPLING

Surface and volumetric damage were generated on the sleeve of the UCJ of the cardan coupling which connects the shaft of the working machine and the telescopic shaft. Destruction in the form of local plastic deformations appeared on the contact surface of the sleeve in question, Figure 2.1a. It is common that after long-term usage, unilateral wear occurs at a joint's shaft journal; this eventually leads to grooves forming on the contact surface of the universal joint, which in turn causes looseness and

noise [7]. In addition to the surface destructions, volumetric destruction in the form of breakage were also generated on the sleeve, Figure 2.1b. The surface damage is located in the load zone of the needle bearing, i.e. in the zone where the load is transferred between the sleeve and the bearing.



**Figure 2.1.** a) Surface damage of the sleeve in the form of local plastic deformations, b) volumetric damage of the sleeve in the form of breakage

Formed damage is manifested by the appearance of grooves due to plastic deformation of the surface layers of the contacting surfaces of the sleeve and rolling elements -- needles. The direction of the grooves coincides with the direction of the longitudinal axis of the sleeve. Grooves are not present along the entire length of the sleeve's contact surface. They extend from the beginning of the contact surface, which is located near the root of the sleeve, to approximately the middle of the length of the sleeve, Figure 2.1a.

On the basis of the generated surface damage on the sleeve, Figure 2.1a, it can be concluded that the depth of the formed grooves changes along the sleeve. It is the largest at the beginning of the contact surface, which is located near the root of the sleeve. Then it gradually decreases, and in the middle of the length of the sleeve it is negligibly small. On the basis of these damages, it can be concluded that the load distribution along the length of the contact of the contacting parts, the sleeve and the rolling bodies (needles), was uneven. Due to such distribution of the line load, the contact surface on the upper part of the sleeve's length participated minimally in the transmission of the working load.



**Figure 2.2.** Fracture of the sleeve of the UCJ

In the case of the considered UCJ of the cardan coupling, which connects the telescopic intermediate shaft and the shaft of the working machine (rollers of the rolling mill),

there was a volumetric destruction of the sleeve, Figure 2.2a and 2.2b. The fracture occurred on the sleeve of the UCJ, which is connected to the fork of the intermediate shaft. On the surface of the fracture, two zones are clearly visible, the zone of dynamic and the zone of static destruction, Figure 2.1b. The size of the fatigue failure zone is approximately 30% of the static failure zone. On the basis of this fact, it can be concluded that the process of dynamic destruction gradually expanded and progressed. The fracture surface does not lie in one plane, but in two planes that form an angle of  $90^\circ$ . This means that, in addition to normal stresses, tangential stresses also had a strong influence on the destruction process.

### 3. LOAD DISTRIBUTION AND STRESS STATE OF THE UCJ SLEEVE

#### 3.1. The influence of the geometric characteristics of the UCJ on the load distribution

The nominal load in the form of tangential force caused by torque is not evenly distributed along the line of contact of the meshed parts of the universal joint. The highest intensity of the nominal load is in the points belonging to the root of the sleeve, diagram in Figure 3.1. The lowest intensity of the nominal load is in the points belonging to the top of the sleeve. The difference between these limit values of the nominal loads depends on the geometric dimensions of the sleeve. In order to analyze the influence of the geometric dimensions of the sleeve on the uniformity of the distribution of the nominal load along the sleeve, a corresponding analytical expression was formed.

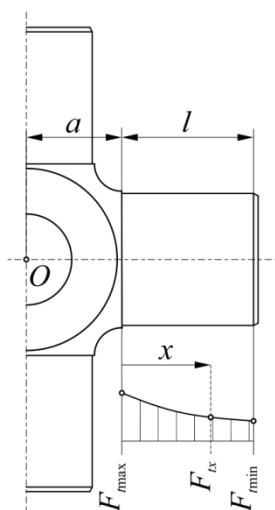


**Figure 3.1.** Distribution of the nominal load along the sleeve of the UCJ

The ratio of the nominal load in the form of a tangential force at an arbitrary point ( $x$ ) on the slant height of the sleeve, to its maximum value, was observed:

$$\psi = \frac{F_{tx}}{F_{tx\max}} = \frac{1}{1 + k \cdot \frac{l}{a}}, \quad (1)$$

wherein:

$$k = x / l,$$

$l$  – sleeve length,

$a$  – the distance of the root of the sleeve from the axis of rotation of the cross.

The correlation between the nominal load and the geometric characteristics of the sleeve is shown by the diagram in Figure 3.2. Higher values of the geometric parameter  $k$  and ratio  $l/a$  correspond to higher unevenness of the nominal load distribution. Small values of the ratio  $l/a$  correspond to a smaller gradient of change in the nominal load from the root to the top of the sleeve of the UCJ. This means that the degree of uneven distribution of the nominal load on the sleeve will be smaller if the sleeve is further away from the axis of rotation.

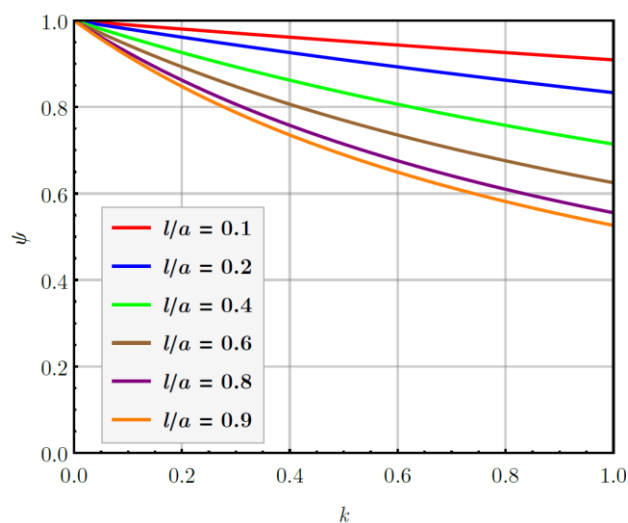


**Figure 3.2.** The influence of the geometry of the UCJ on the distribution of the nominal load along the sleeve

## 4. EXPERIMENTAL ANALYSIS

### 4.1. Ultrasonic testing

Ultrasonic testing (UT) was performed in order to examine subsurface and internal defects in material. The method is based on sending a high frequency sound through the metallic product and analyzing its reflections. Examination was performed in accordance with standard SRPS EN ISO 16810, using both longitudinal and transversal waves. The impulse-echo, ultrasonic method, was performed.

Testing with longitudinal waves was performed by dual crystal straight probes as well as with single crystal probes, while testing with transversal waves was performed only by single crystal probes.

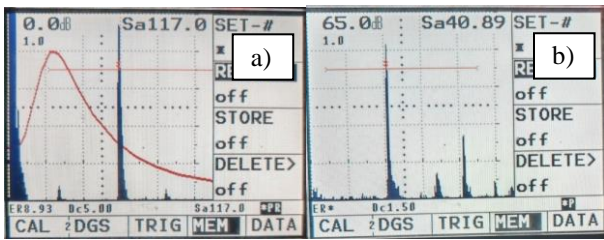


**Figure 4.1.** Diagrams of material testing using the ultrasonic method

Figures 4.1a and 4.1b show diagrams of material testing using the ultrasonic method. On the basis of these diagrams, it is clearly seen that there are no defects in the material of the sleeve of the universal joint cross.

#### 4.2. Chemical composition

In order to determine the type of material of the cardan cross, tests of the chemical composition were carried out. The chemical composition of the material was determined by two different methods. The first method is Optical Emission Spectrometry, and the second method used is X-ray fluorescence (XRF). The test conditions are given in the Table 4.1.

**Table 4.1.** Test conditions for determining chemical composition

Standard-method:	Optical Emission Spectrometry (SRPS C.A1.011:2004)
Equipment used:	Belec Compact Port
Type of probe:	Argon probe (Belec)
Surface condition:	60 grit sandpaper
Test instruction:	Manufacturer's instructions
Calibration blocks:	Belec 101, 102, 108, 110
Temperature of the object:	20°C
Testing according to:	KT KI - UP 002/14

Individual results of testing according to the mentioned method are given in Table 4.2.

**Table 4.2.** Chemical composition in mass % – OES method

<b>C</b>	<b>Si</b>	<b>Mn</b>	<b>Cu</b>	<b>Al</b>
0,297	0,234	0,86	0,012	0,031
<b>Cr</b>	<b>Mo</b>	<b>Ni</b>	<b>V</b>	<b>Ti</b>
1,026	0,004	0,009	0,015	0,053
<b>Nb</b>	<b>Co</b>	<b>W</b>	<b>Sn</b>	<b>Pb</b>
0,008	<0,01	<0,01	0,021	<0,003

Based on the obtained chemical composition, it was determined that the material of the UCJ corresponds to the material 34Cr4 (1.7033) according to Belec database. Grade 34Cr4 belongs to quenched and tempered steels.

## 5. ANALYSIS OF LOAD CAPACITY OF THE SLEEVE

In the considered sleeve of the UCJ, there is a pronounced uneven distribution of the line load on the contact surface of the joint and the rolling elements - needles, Figure 2.1. It has a great influence on the stress state in the critical cross-section of the sleeve. In order to analyze the influence of the distribution of the line load on the load carrying capacity of the critical cross-section of the sleeve, appropriate analytical models were formed.

The influence of line load distribution on the stress state and safety factor in the critical cross-section of the sleeve was analyzed. In the case of uniform-theoretical distribution of the line load, each point on the contact line of the contacting surfaces equally participates in the transmission of the working load, Figure 5.1a. The actual distribution of the line load in real working conditions is uneven. With this distribution, each point on the contact line participates differently in the load transfer, figure 5.1b. One characteristic case occurs when only one point does not participate in load transfer, Figure 5.1c. Another characteristic case occurs when one part of the contact line does not participate in load transfer, Figure 5.1d.

In the considered UCJ, two needle bearings are placed between the sleeves of the cross and the fork. After dismantling the coupling, an uneven distribution of the line load was registered by visual control. Figure 2.1.a, that is, one needle bearing, placed closer to the root of the sleeve, was significantly more involved in transferring the load. The engagement of the second bearing, placed closer to the top of the sleeve, is less than the first bearing.

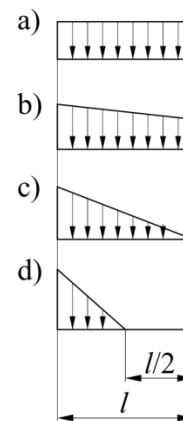


**Figure 5.1.** Line load distribution along the line of contact between the sleeve and the needle bearing

The mechanical model of the UCJ sleeve represents a cantilever that is loaded with a transverse force. Due to the action of this force, normal stresses due to bending and tangential stress due to shearing are generated in the critical cross-section of the cantilever-sleeve. By observing the ratio of tangential and normal stress, an analytical model was formed for the analysis of the influence of the line load distribution on the stress state at the root of the sleeve:

$$\varphi = \frac{\tau}{\sigma} = \frac{5}{18} \cdot \frac{1}{\frac{1}{6} + \left(1 - \frac{x}{l}\right)} \quad (1)$$

For the analysis of the influence of the distribution of the line load on the load capacity of the sleeve root, the ratio of the safety factor against volume destruction due to tangential stresses - shearing and due to normal stresses - bending was observed:

$$\lambda = \frac{S_{\tau}}{S_{\sigma}} = \frac{3}{10} + \frac{9}{5} \left(1 - \frac{x}{l}\right) \quad (2)$$

Based on the analytical expressions (1) and (2), the corresponding dependencies shown in Figure 5.2 were formed.

Based on the dependencies shown in Figure 5.2, the following conclusions can be drawn:

- In case of uniform distribution of line load, Figure 5.1a, when  $x/l = 0.5$  the normal stress is 2.5 times higher than the tangential stress. At the same time, the safety factor against failure due to the effect of tangential stresses is 20% higher than the safety factor due to the effect of normal stresses.
- In the case of uneven load distribution, when all points on the contact line do not participate equally in the load transfer, Figure 5.1b, and when  $x/l = 0.6$ , the normal stress is 2.0 times higher than the tangential stress. At the same time, the safety factors against failure due to the action of tangential and normal stresses are mutually equal.
- In the case of uneven load distribution, when one part of the contact line does not participate in the load transfer, Figure 5.1d, and when  $x/l = 0.8$ , the normal stress is 25% higher than the tangential stress. At the same time, the safety factor against failure due to the effects of normal stress is 40% higher than the safety factor due to the effects of tangential stress.

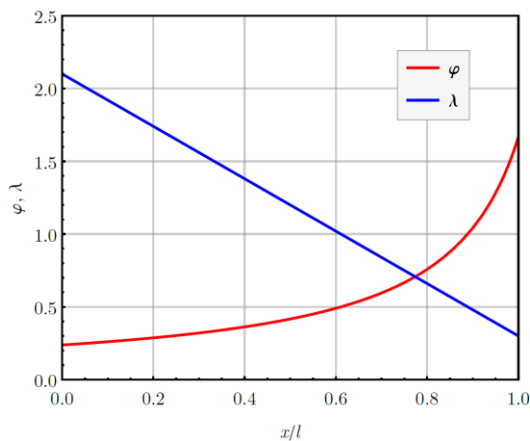


**Figure 5.2.** The influence of line load distribution on the stress state and load capacity of the UCJ sleeve root

A numerical model was created for the analysis of the stress state at the root of the sleeve, at the source of the stress concentration of the UCJ. The stress concentration is caused by the geometrical characteristic of the section, i.e. the transition from a large to a small sleeve diameter. In addition to this stress concentration, there is an untreated surface step on the UCJ sleeve root which is a consequence of the manufacturing technology. It is marked with a white arrows in Figure 2.2a. In the [1], stress concentration at the point of support due to inadequate finishing, caused the occurrence of an initial crack. In the [8], it was shown that by optimizing the geometrical shape of the cardan joint cross, operating stress can be reduced by up to 40%. The optimization mainly related to the cross-section with stress concentration in the form of a transition radius at the root of the sleeve. In [9] the results of numerical simulation of stress-strain state at critical zones of Cardan joint elements implicate that small modification of design solution can result in significant reduction of maximal stress levels. However, one should be careful with this type of optimization, because the increase of fillet, to some limit, induced reduction of stress concentration level. The further increase of fillet over the limit induced increase of maximal stresses [4].

In the case of uniform load distribution, Figure 5.1a, the stress state is shown in Figure 5.3.

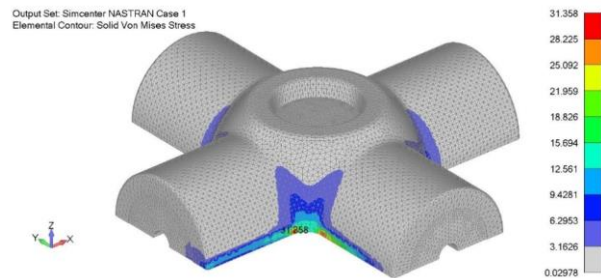


**Figure 5.3.** Stress state of UCJ in MPa

Figure 5.4 shows the stress state at the root of the sleeve for the case of uneven load distribution, Figure 5.1c and Figure 5.1b.

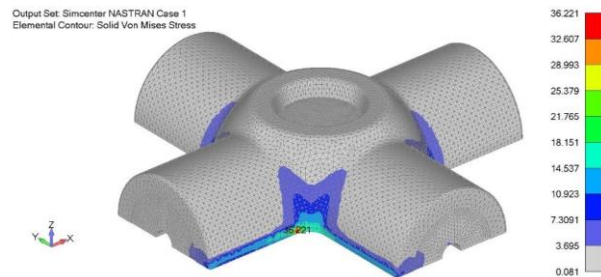


**Figure 5.4.** Stress state of UCJ in MPa

The stress state at the root of the sleeve in the case of extremely uneven load distribution, when one part of the contact line does not participate in load transmission, Figure 5.1d, is shown in Figure 5.5.

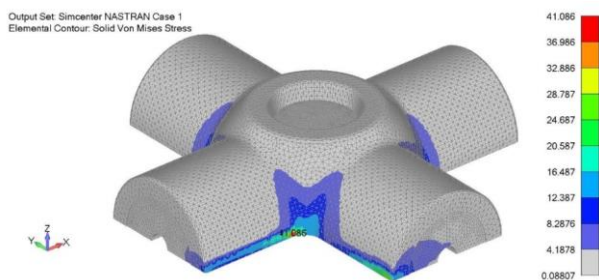


Figure 5.5. Stress state of UCJ in MPa

The stress at the root of the sleeve, at the source of the stress concentration in case of extremely uneven load distribution (Fig. 5.5) is 32% higher than the stress generated in the case of uniform load distribution (Fig. 5.3). Compared to uneven load distribution (Fig. 5.4), the stress is 14% higher with extremely uneven load distribution.

Based on the conducted analysis, it follows that with an increase in the unevenness of the load distribution, the influence of the tangential stress on the volume load capacity of the sleeve increases. It is known that the dynamic strength due to bending is significantly higher than the dynamic strength due to tangential shear stresses. This means that the sleeve of the UCJ in the critical cross-section has a significantly lower ability to resist volumetric destruction due to the effect of tangential stresses compared to normal stresses due to bending. Accordingly, the fracture surface of the UCJ does not lie in a plane that is perpendicular to the longitudinal axis of the sleeve, but in planes that form an angle of  $45^\circ$  with this axis, Figure 2.2b. Large tangential stresses in combination with geometric stress concentration participated in the formation of the initial crack and its propagation until the final destruction - dynamic fracture of the sleeve.

## 6. CONCLUSIONS

Conducted theoretical and experimental research showed that volumetric destruction - dynamic fracture of the joint of the UCJ of the cardan coupling did not occur due to the existence of defects in the material of the joint, the quality (chemical composition) of the material of the joint and/or the occurrence of an overload - heavy workload. Large stresses at the root of the sleeve in the cross section of the stress concentration are generated due to the extremely uneven distribution of the load along the line of contact of the sleeve and the bearing needles. The geometric stress concentration is present at the root of the sleeve and at the rounding radius of the holes formed on the front surfaces of the UCJ. Tangential stresses in combination with geometric stress concentration led to the fracture of the UCJ. Based on the large zone of fatigue destruction,

which is approximately 30% of the static destruction zone, it can be stated that the process of dynamic destruction gradually expanded and progressed under the influence of the workload.

## Acknowledgment

The presented paper is a result of the research supported by MPNTR RS according to the Contract No. 451-03-65/2024-03/200105 and Contract No. 451-03-65/2024-03/200135. The authors wish to acknowledge and thank the company Kontrol Inspekt D.O.O. in Belgrade for support and for encouragement in the research realization.

## References

- [1] SAVKOVIĆ M., GAŠIĆ M., PETROVIĆ D., ZDRAVKOVIĆ N., PLJAKIĆ R.: *Analysis of the drive shaft fracture of the bucket wheel excavator*, Engineering Failure Analysis 20 (2012) 105–117.
- [2] IVANOVIĆ L., JOSIFOVIĆ D., RAKIĆ B., STOJANOVIĆ B., ILIĆ A.: *The influence of variation in position of output shaft to load on the cardan joint cross shaft*, International Congress Motor Vehicles & Motors 2012, MVM2012-045.
- [3] STRUZ J., HRUZIK L., HAVLIK J.: *Cardan Shaft Load and Its Variation with Length*, ICMD 2020, AHE 17, pp. 343–355, 2023.
- [4] IVANOVIĆ L., JOSIFOVIĆ D., RAKIĆ B., STOJANOVIĆ B., ILIĆ A.: *Shape variations influence on load capacity of cardan joint cross shaft*, The 7<sup>th</sup> International Symposium KOD 2012, 24-26 May, Balatonfured, Hungary.
- [5] VESALI F., REZVANI M. A., KASHFI M.: *Dynamics of universal joints, its failures and some propositions for practically improving its performance and life expectancy*, Journal of Mechanical Science and Technology 26 (8) (2012) 2439~2449
- [6] RISTIVOJEVIĆ M., LUČANIN V., DIMIĆ A., MIŠKOVIĆ Ž., BURZIĆ Z., STAMENIĆ Z., RACKOV M.: *Investigation of the heavy duty truck gear drive failure*, Engineering Failure Analysis 144 (2023) 106995.
- [7] AN K., WANG W.: *Transmission performance and fault analysis of a vehicle universal joint*, Advances in Mechanical Engineering 2017, Vol. 9(5) 1–10.
- [8] IVANOVIĆ L., JOSIFOVIĆ D., ŽIVKOVIĆ K., STOJANOVIĆ B.: *Cross Shaft Design From the Aspect of Capacity*, Scientific Technical Review, 2011, Vol.61, No.1.
- [9] IVANOVIĆ L., JOSIFOVIĆ D., ILIĆ A., STOJANOVIĆ B., ŽIVKOVIĆ K.: *Optimization of cardan joint design from load capacity aspect*, International Congress Motor Vehicles & Motors 2014, MVM2014-011.



## ADSORPTION OF ORGANOPHOSPHATE PESTICIDES ON NITROGEN-DOPED CARBON CRYOGELS AND THE ASSESSMENT OF THEIR NEUROTOXIC EFFECTS

VLADAN J. ANIĆIJEVIĆ

University of Defence Belgrade, Military Academy, [anicijevic.v@gmail.com](mailto:anicijevic.v@gmail.com),

TAMARA TASIĆ

VINČA Institute of Nuclear Sciences - National Institute of the Republic of Serbia, University of Belgrade, Belgrade, [tamara.tasic@vin.bg.ac.rs](mailto:tamara.tasic@vin.bg.ac.rs)

VEDRAN MILANKOVIĆ

VINČA Institute of Nuclear Sciences - National Institute of the Republic of Serbia, University of Belgrade, Belgrade, [vedran.milankovic@vin.bg.ac.rs](mailto:vedran.milankovic@vin.bg.ac.rs)

DALIBOR B. JOVANOVIĆ

Organization for the Prohibition of Chemical Weapons, Hague, The Netherlands, [jovcadach@hotmail.com](mailto:jovcadach@hotmail.com)

RADOVAN M. KARKALIĆ

University of Defence Belgrade, Military Academy, [rkarkalic@yahoo.com](mailto:rkarkalic@yahoo.com)

MILOŠ BALJOZOVIĆ

Surface Science and Coating Technologies, Empa, Swiss Federal Laboratories for Materials Science and Technology, Dübendorf, Switzerland, [milos.baljozovic@psi.ch](mailto:milos.baljozovic@psi.ch)

BILJANA M. BABIĆ

Institute of Physics, University of Belgrade, Belgrade, [biljana.babic@ipb.bg.ac.rs](mailto:biljana.babic@ipb.bg.ac.rs);

IGOR A. PAŠTI

Faculty of Physical Chemistry, University of Belgrade, Belgrade, [igor@ffh.bg.ac.rs](mailto:igor@ffh.bg.ac.rs)

TAMARA D. LAZAREVIĆ-PAŠTI

VINČA Institute of Nuclear Sciences - National Institute of the Republic of Serbia, University of Belgrade, Belgrade, [tamara@vin.bg.ac.rs](mailto:tamara@vin.bg.ac.rs)

---

**Abstract:** Efficient removal of different pollutants from the environment has become one of the most important challenges of modern society. The nitrogen-doped carbon cryogels were synthesized and characterized using XPS. All investigated materials have similar composition and structural disorder. By analyzing XPS spectra, the content of carbon, oxygen, and nitrogen can be obtained, and the existence of functional groups containing these elements can be detected. Dimethoate, malathion, and chlorpyrifos removal were investigated under stationary and dynamic conditions. Stationary conditions demonstrated successful removal of aliphatic dimethoate and malathion by all investigated materials. Conversely, the materials with the lowest and highest nitrogen content proved ineffective with aromatic chlorpyrifos. Under dynamic conditions, all materials effectively removed malathion and chlorpyrifos while exhibiting suboptimal performance for dimethoate adsorption. The demonstrated efficacy suggests the potential application of these materials in water treatment. The toxicity of these pesticide solutions decreases over time, indicating that more toxic products were not formed.

**Keywords:** carbon cryogel; organophosphate pesticides; water remediation; adsorption.

### 1. INTRODUCTION

Unfortunately, organophosphate pesticides (OPs) pose a significant hazard to both humans and the majority of animals, primarily ascribed to their ability to inhibit the

crucial enzyme acetylcholinesterase (AChE) [1].

An interesting class of carbonaceous materials nowadays is carbon cryogels (CC). They are especially attractive due to their developed and controllable mesoporosity [2]. Nitrogen-doped carbon cryogels (CCN) were synthesized by a sol-gel polycondensation process, employing

precursors such as resorcinol and formaldehyde. Subsequently, the hydrogels obtained were dried and subjected to carbonization in an inert atmosphere [3, 4]. The procedure is described in detail in our paper [5]. The characterization and assessment of nitrogen-doped carbon cryogels as adsorbents was done using XPS to elucidate their structural properties and surface functionalities. Additionally, the investigation under both stationary and dynamic conditions provides valuable insights into the adsorption behavior of these materials, particularly their effectiveness towards different pesticide classes. Furthermore, the toxicity reduction assessment of treated samples offers a novel contribution, demonstrating the potential of nitrogen-doped carbon cryogels not only for efficient pesticide removal but also for mitigating the toxicity of contaminated water. Motivated by the significant threat posed by pesticides to non-targeted organisms and the challenges associated with their widespread use, this study addresses the pressing need for efficient pesticide remediation strategies.

## 2. EXPERIMENTAL

### 2.1. XPS analysis

XPS analysis was done using SPECS Analyzer Phoibos 150. As an X-ray source, monochromatic Al K $\alpha$  (400 W) was used. Data were acquired using SpecsLab2 software and processed using Unifit2013 with its internal database of sensitivity factors.

### 2.2. Adsorption studies

We conducted two sets of experiments to investigate the efficiency of adsorption of investigated OPs on CC. The first set was done in a batch system, while the second was done in a cryogel-modified nylon membrane filter.

Investigated carbon cryogels were dispersed in double-distilled water, and the desired amount of dimethoate (2-dimethoxyphosphinothiolsulfanyl-N-methylacetamide), malathion (diethyl 2-dimethoxyphosphinothiolsulfanylbutanedioate), and chlorpyrifos (diethoxy-sulfanylidene-(3,5,6-trichloropyridin-2-yl)oxy- $\lambda^5$ -phosphane) stock solutions (Pestanal, Sigma Aldrich, Denmark) was added to provide the targeted concentration of adsorbent (10 mg cm $^{-3}$ ) and OP (5 $\times$ 10 $^{-4}$  mol dm $^{-3}$ ). The performance of each adsorbent was quantified as the OP uptake (the percentage of adsorbed OP from the solution), defined as:

$$AD / \% = \frac{C_0 - C}{C_0} \times 100 \quad (1)$$

where  $C_0$  and  $C$  stand for the OP concentration before and after the adsorption experiment, respectively [6].

### 2.3. UPLC analysis

The Waters ACQUITY Ultra Performance Liquid Chromatography (UPLC) system, coupled with a tunable UV detector controlled by the Empower software, was employed for the study. Chromatographic separations

were conducted using an ACQUITY UPLC<sup>TM</sup> BEH C18 column with dimensions of 1.7  $\mu$ m, 100 mm  $\times$  2.1 mm (Waters). PDA spectra of dimethoate, malathion, and chlorpyrifos concentration 1 $\times$ 10 $^{-4}$  mol dm $^{-3}$  are shown in Figure 1.

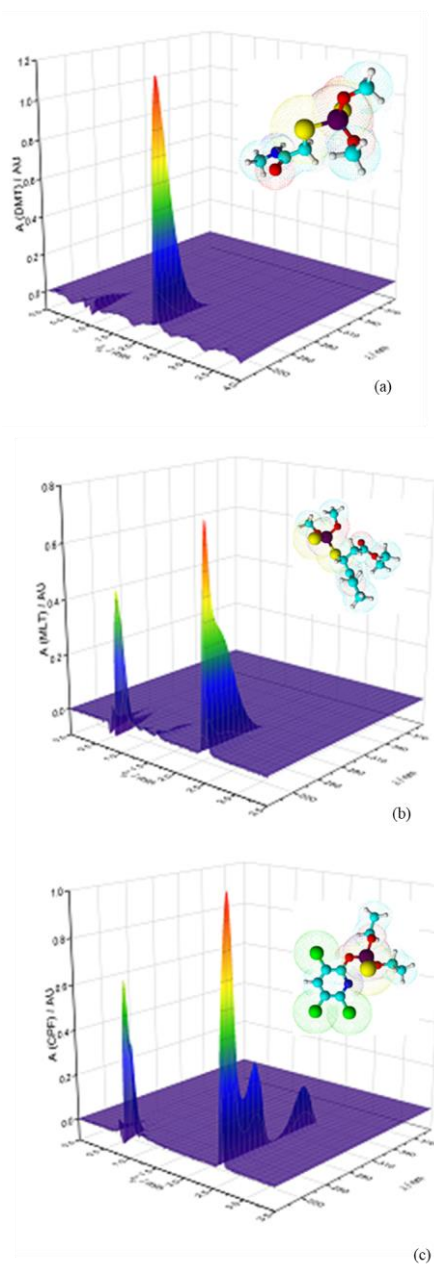


**Figure 1.** PDA spectra of dimethoate (a), malathion (b), and chlorpyrifos (c) concentration 1 $\times$ 10 $^{-4}$  mol dm $^{-3}$

### 2.4. Neurotoxicity assessment

Toxicity assessment of the samples before and after adsorption experiments was done *via* measurements of AChE inhibition. Besides performing AChE inhibition measurements to quantify the toxicity of the investigated OPs, these tests also provide information about potential transformations of OPs into more toxic forms due to the contact with adsorbents. It particularly relates to the formation of oxo-forms of OPs, which are much more toxic than corresponding thio-forms [7]. These oxidation



products can exert toxic effects at concentrations below the detection limits of UPLC. Hence, it is important to estimate the toxicity of the final samples *via* bioanalytical assay since their limit of detection is lower. AChE activity was assayed according to modified Ellman's procedure. It should be noted that in these measurements, the enzyme concentration was chosen to give an optimal spectrophotometric signal. Physiological effects were quantified as AChE inhibition given as AChE:

$$I / \% = \frac{A_0 - A}{A_0} \times 100 \quad (2)$$

where  $A_0$  is the AChE activity in the absence of OP and  $A$  is the AChE activity measured after exposure to a given OP [6].

### 3. RESULTS AND DISCUSSION

#### 3.1. XPS analysis

The X-ray photoelectron spectra of the examined materials were recorded to determine their structure and chemical composition. The spectra of C1s, O1s, and N1s are shown in Figure 2.

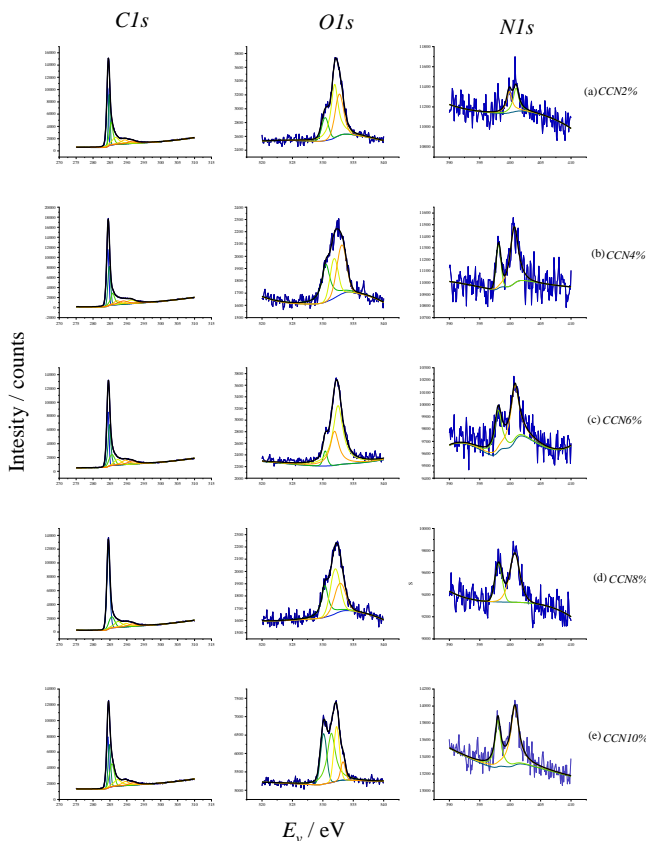


**Figure 2.** C1s (left), O1s (in middle), and N1s (right) XPS spectra of the CCN sample with (a) 2%, (b) 4%, (c) 6%, (d) 8% and (e) 10% N.

In the case of C1s spectra (Figure 2), deconvolution was performed for all the examined materials. Bands with different intensity maximum positions depending on the binding energy were obtained and can be assigned to

different groups. The band with the highest intensity, which has a maximum at 284.5 eV, can be attributed to the C=C  $sp^2$  bond, while other bands are also present: C-C at 285.1 eV, which is attributed to the  $sp^3$  bond, C-O<sub>x</sub> at 285.9 eV attributed to the epoxy and hydroxyl groups, C=O and N-C=O band at 287.5 eV and finally a weak intensity band at 290.0 eV attributed to  $\pi \rightarrow \pi^*$ . The component at 292.5 eV is ascribed to the same transition in N-containing carbons and carbons rich in carboxylic groups. O1s spectra (Figure 2) have a broad band in the region from about 530 to about 535 eV, which was deconvolved into several components. This band originates from various types of C-O bonds. Bands with maxima at 530.3 eV and 531.8 eV attributed to the C=O bond, at 532.5 eV attributed to the C-O-C bond, and at 533.7 eV belonging to C-OH and H-OH  $sp^3$  bonds. N1s spectra (Figure 2) showed the presence of two main types of nitrogen moieties in the carbon structure: pyrrolic/pyridonic and quaternary nitrogen.

**Table 1.** Assignment of chemical groups in studied cryogels, as determined using XPS analysis

Element	$E_b$ / eV	Assignment
C	284.5	C=C ( $sp^2$ )
	285.1	C-C ( $sp^3$ )
	285.9	C-O <sub>x</sub>
	287.5	C=O
	290.0	$\pi \rightarrow \pi^*$
	292.5	$\pi \rightarrow \pi^*$ (N-containing C)
O	530.3	C=O
	531.8	C=O
	532.5	C-O-C
	533.7	C-OH, H-OH
N	398.8	Pyrrolic/Pyridonic N
	400.8	Quaternary N

All tested cryogels have bands with the same maximum position, but their intensities differ, as shown in Table 1. Band intensities are directly proportional to the content of certain groups in the material, and these data can be used for quantitative composition determination.

**Table 2.** Chemical composition of investigated carbon cryogels

Sample	C at. %	N at. %	O at. %
CCN2%	97.06	0.24	2.70
CCN4%	98.19	0.39	1.42
CCN6%	97.55	0.59	1.85
CCN8%	96.74	0.73	2.53
CCN10%	93.90	1.00	5.08

The chemical composition of the tested materials is

shown in [Table 2](#). From [Table 2](#), it is evident that the amount of nitrogen incorporated into the material during the synthesis is about 10% of the added amount. By analyzing the displayed spectra, the content of carbon, oxygen, and nitrogen can be obtained, and the existence of functional groups containing these elements can be detected.

### 3.2. OP adsorption on carbon cryogels

From the data presented in [Figure 3](#), it can be seen that aliphatic organophosphates, dimethoate, and malathion are very successfully adsorbed on all tested cryogels under static conditions in batch studies. Dimethoate could not be detected in the supernatant decanted after adsorption. It means that the dimethoate concentration dropped below  $1 \times 10^{-8} \text{ mol dm}^{-3}$ , which is the detection limit of the instrument used for this analysis (UPLC) under the given experimental conditions. These results suggested that all dimethoate from the solution is adsorbed on all tested materials. In the case of malathion, it was possible to detect low concentrations of pesticides in the decanted supernatants, in concentrations ranging from  $10^{-7}$  to  $10^{-8} \text{ mol dm}^{-3}$ , which is practically negligible considering that the initial malathion concentration was  $5 \times 10^{-4} \text{ mol dm}^{-3}$ .

On the other hand, with aromatic chlorpyrifos, the situation is different. The material with the highest nitrogen content, CCN10, turned out to be completely inefficient in this case. In contrast, the CCN8 proved to be the most suitable adsorbent, which adsorbed 43% of the available chlorpyrifos. Materials CCN2, CCN4, and CCN6 adsorbed about 20% of the available pesticide.

The adsorption of  $5 \times 10^{-4} \text{ mol dm}^{-3}$  malathion, chlorpyrifos, and dimethoate on  $10 \text{ mg cm}^{-3}$  carbon cryogels doped with nitrogen was also examined under the dynamic conditions in filter studies.  $10 \text{ mg}$  of each of the tested adsorbents was injected into nylon filters. Next,  $1 \text{ cm}^3$  of  $5 \times 10^{-4} \text{ mol dm}^{-3}$  solution of each tested organophosphate is filtered through the modified nylon filter within 1 min. In the filtrate, the concentration of the remaining pesticides was determined chromatographically. The results are presented in [Figure 3](#).

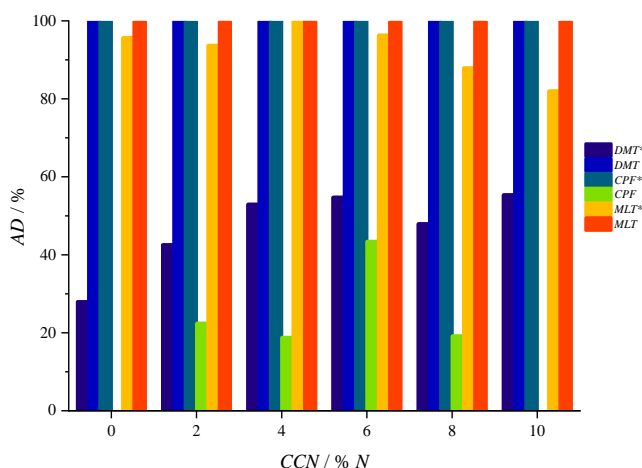


**Figure 3.** OPs removal using N-doped carbon cryogels under stationary and dynamic conditions (marked by \*).

Adsorption using filters under dynamic conditions showed a different trend of results compared to the experiment in batch. From the results given in [Figure 3](#), it can be seen that aromatic chlorpyrifos is the one that is completely adsorbed to all tested materials. The remaining traces of pesticides in the filtrates could not be detected since their concentration was below the instrument's detection limit ( $1 \times 10^{-8} \text{ mol dm}^{-3}$ ). It is also obvious that under dynamic conditions, aliphatic malathion is adsorbed in a high percentage on all investigated cryogels. Material CCN4 showed the best result and almost completely adsorbed the initial amount of pesticides (99%). Material CCN8 adsorbed 96% malathion and material CCN4 94% under the given experimental conditions. CCN6 and CCN10, with 88% and 82% of adsorbed malathion, respectively, showed slightly lower performance. Even though the percentage of adsorbed pesticides varies from 82 to 99, we can say that all investigated materials under dynamic conditions are effective adsorbents for the remediation of malathion due to the fact that amounts that could be found in real samples are significantly lower than investigated.

Unlike chlorpyrifos and malathion, the investigated materials yielded significantly inferior results in terms of dimethoate adsorption under dynamic conditions. The adsorption percentages range from 43% to 56% of the initial concentration. The uptake increased with the increase of nitrogen content in the adsorbent structure. It is evident that nitrogen addition has a favorable effect on dimethoate adsorption efficiency under dynamic conditions, but nitrogen content does not play a significant role in the given framework. Although the adsorption efficiency under these conditions is about 50%, this result, although significantly poorer than the adsorption of the other two pesticides, is by no means negligible, considering the already discussed situation in the environment. Moreover, there are cases when the adsorption rate is critical (e.g., adsorption of chemical warfare with the structure of organophosphate) and plays a more significant role than adsorption efficiency. Under those circumstances, materials that adsorb many potential pollutants under dynamic conditions have the advantage, even if adsorption efficiency is not 100%.

### 3.3. Physiological effects

As shown in [Figure 4](#), AChE inhibition is induced for the initial concentration of OPs used in the adsorption experiments, which is connected to the neurotoxic effects of OPs. Also, it is noticeable that AChE inhibition for the samples without the adsorbent for batch studies decreases in comparison to those in filter studies. This discrepancy is attributed to the previously discussed instability of OPs at room temperature, where batch samples are exposed for 24 hours, whereas filter studies involve only a brief exposure of a few minutes. Chlorpyrifos showed complete inhibition of AChE activity under the given experimental conditions for both initial and apparent initial concentrations since it is highly toxic in both amounts.

However, after the adsorption of OPs on carbon cryogels, purified water samples in the cases of malathion and

dimethoate in batch studies and chlorpyrifos and dimethoate in filter studies induced no AChE inhibition. Other samples induced lower AChE inhibition compared to non-purified samples, suggesting a decrease in solution toxicity after incubation with all investigated carbon cryogels. This observation also confirms the absence of oxidation and the formation of more toxic byproducts during the interaction between OPs and cryogels.

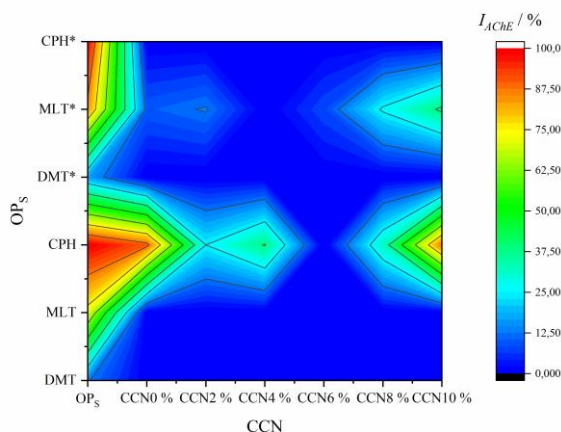


**Figure 5.** Inhibition of AChE activity in the presence of chlorpyrifos, malathion, and dimethoate before (without adsorbent added) and after the adsorption on investigated carbon cryogels in batch and filter\*

#### 4. CONCLUSION

In conclusion, our study elucidates the complex relationship between the properties of nitrogen-doped carbon cryogels and their adsorption performance towards organophosphate pesticides. Despite minimal alterations in carbon morphology, nitrogen incorporation induces significant changes in textural properties and subtle variations in chemical composition, shaping adsorption behavior. Overall, our findings highlight the complexity of OP adsorption onto nitrogen-doped carbon cryogels, emphasizing the need for a comprehensive understanding of material properties and OP characteristics for effective pesticide remediation strategies. By shedding light on the complicated interplay between chemical structure, surface properties, and adsorption mechanisms, our study contributes to the advancement of adsorbent materials for environmental applications, making way for innovative and sustainable water treatment technologies.

#### Acknowledgment

This work was partially supported by the Ministry for Science, Technological Development and Innovation of the Republic of Serbia (451-03-66/2024-03/200017 and 451-03-65/2024-03/200146), and Ministry of defence Republic of Serbia (VA-TT/1/22-24).

#### References

- [1] ANIĆIJEVIĆ, V., TASIĆ, T., MILANKOVIĆ, V., BREITENBACH, S., UNTERWEGER, C., FÜRST, C., BAJUK-BOGDANOVIĆ, D., PAŠTI, I. A. and LAZAREVIĆ-PAŠTI, T., *How Well Do Our Adsorbents Actually Perform? - The Case of Dimethoate Removal Using Viscose Fiber-Derived Carbons*, International Journal of Environmental Research and Public Health, 2023.
- [2] MINOVIĆ, T. Z., GULICOVSKI, J. J., STOILJKOVIĆ, M. M., JOKIĆ, B. M., ŽIVKOVIĆ, L. S., MATOVIĆ, B. Z. and BABIĆ, B. M., *Surface characterization of mesoporous carbon cryogel and its application in arsenic (III) adsorption from aqueous solutions*, Microporous and Mesoporous Materials 201 (2015) 271-276.
- [3] BABIĆ, B., KALUĐEROVIĆ, B., VRAČAR, L. and KRSTAJIĆ, N., *Characterization of carbon cryogel synthesized by sol-gel polycondensation and freeze-drying*, Carbon 42 (2004) 2617-2624.
- [4] BABIĆ, B. M., VRAČAR, L. M., RADMILOVIĆ, V. and KRSTAJIĆ, N. V., *Carbon cryogel as support of platinum nano-sized electrocatalyst for the hydrogen oxidation reaction*, Electrochimica Acta 51 (2006) 3820-3826.
- [5] LAZAREVIĆ-PAŠTI, T., ANIĆIJEVIĆ, V., KARKALIĆ, R., BALJOZOVIĆ, M., BABIĆ, B. and PAŠTI, I. A., *Nitrogen-Doped Carbon Cryogels as Adsorbents: Efficient Removal of Organophosphate Pesticides from Water and Assessment of Toxicity Reduction*, C 10 (2024) 56.
- [6] TASIĆ, T., MILANKOVIĆ, V., BATALOVIĆ, K., BREITENBACH, S., UNTERWEGER, C., FÜRST, C., PAŠTI, I. A. and LAZAREVIĆ-PAŠTI, T., *Application of Viscose-Based Porous Carbon Fibers in Food Processing—Malathion and Chlorpyrifos Removal*, Foods 12 (2023) 2362.
- [7] LAZAREVIĆ-PAŠTI, T., ANIĆIJEVIĆ, V., BALJOZOVIĆ, M., ANIĆIJEVIĆ, D. V., GUTIĆ, S., VASIĆ, V., SKORODUMOVA, N. V. and PAŠTI, I. A., *The impact of the structure of graphene-based materials on the removal of organophosphorus pesticides from water*, Environmental Science: Nano 5 (2018) 1482-1494.



## PRELIMINARY INVESTIGATION OF BAMBOO FIBRE METALLIZATION VIA CHEMICAL/ELECTROCHEMICAL METHODS

IVANA MLADENVIĆ

Institute of Chemistry, Technology and Metallurgy, University of Belgrade, Njegoševa 12, 11 000 Belgrade, Serbia,  
[ivana.mladenovic@ihtm.bg.ac.rs](mailto:ivana.mladenovic@ihtm.bg.ac.rs)

DUŠAN NEŠIĆ

Institute of Chemistry, Technology and Metallurgy, University of Belgrade, Njegoševa 12, 11000 Belgrade, Serbia,  
[dnesic@nanosys.ihtm.bg.ac.rs](mailto:dnesic@nanosys.ihtm.bg.ac.rs)

MARKO OBRADOV

Institute of Chemistry, Technology and Metallurgy, University of Belgrade, Njegoševa 12, 11000 Belgrade, Serbia,  
[marko.obradov@ihtm.bg.ac.rs](mailto:marko.obradov@ihtm.bg.ac.rs)

MILOŠ VORKAPIĆ

Institute of Chemistry, Technology and Metallurgy, University of Belgrade, Njegoševa 12, 11000 Belgrade, Serbia,  
[worcky@nanosys.ihtm.bg.ac.rs](mailto:worcky@nanosys.ihtm.bg.ac.rs)

MARIJA VUKSANOVIĆ

University of Belgrade, Department of Chemical Dynamics, and Permanent Education, „VINČA” Institute of Nuclear Sciences - National Institute of the Republic of Serbia, Mike Petrovića Alasa, 11 000 Belgrade, Serbia,  
[marija.vuksanovic@vin.bg.ac.rs](mailto:marija.vuksanovic@vin.bg.ac.rs)

NEBOJŠA NIKOLIĆ

Institute of Chemistry, Technology and Metallurgy, University of Belgrade, Njegoševa 12, 11000 Belgrade, Serbia,  
[nnikolic@ihtm.bg.ac.rs](mailto:nnikolic@ihtm.bg.ac.rs)

DANA VASILJEVIĆ RADOVIĆ

Institute of Chemistry, Technology and Metallurgy, University of Belgrade, Njegoševa 12, 11000 Belgrade, Serbia,  
[dana@nanosys.ihtm.bg.ac.rs](mailto:dana@nanosys.ihtm.bg.ac.rs)

**Abstract:** In this study, the multifunctional potential of conductive textile fibres based on natural bamboo metalized with chemical/electrochemical deposits and copper particles/layers was investigated. The synthesis was done in three steps: pre-treatment of nonconductive textiles; chemical deposition of Cu particles by the cyclic dipping method; and obtaining conductive bamboo fibres using the electroplating method. The Cu layer was electrodeposited galvanostatically on bamboo from the sulphate electrolytes without wetting agents. To tighten the textile bamboo cloth, a frame designed using 3D printing was used because immersing the textile in the electrolyte and during drying causes wrinkles and creases, which affect the non-uniform distribution of both conductive particles and the thickness of the copper metallization layer. Characterized by SEM and optical microscopy, the chemical and electrochemical depositions of Cu around the bamboo fibres were confirmed. The particles filled the micro spaces between the bamboo fibres and on the surface of the fibres and made the network. This network between nonconductive fibre-conductive nano particles and a conductive Cu layer contributes to increasing the electrical conductivity of the synthesized multifunctional composite. The electroplating of Cu in the form of a compact layer as shells contributed to the trapping of Cu particles on the bamboo fibres themselves, so they are not removed after washing.

**Keywords:** copper, natural bamboo fibres, electroplating, flexible conductive textile, additive technology, microstructure.

### 1. INTRODUCTION

One of the eco-friendly building materials that have been used for various engineering fields around for millennia is bamboo. Bamboo will acquire new properties when

combined with metal elements, including conductivity, weather resistance, anti-corrosion, and electromagnetic shielding [1]. Bamboo fibres and metal coatings are separated by a natural barrier. This research suggests employing an effective and sustainable electrodeposition technology with chemical activation of non-conductive natural bamboo fibres to fabricate new bamboo-based

metal composites (BMC), which are made of copper coating and bamboo substrate without the need for adhesive. Using a low-temperature process, the copper coatings is synthesized via electrochemically way on the activated bamboo fibres after chemical reaction and then characterized.

One of the plants that grow very fast is bamboo three, which may reach a maximum growth rate of 100 cm per day and can be exploited and cut every 5-6 years, unlike standard trees like oak, pine or hybrid varieties where you must wait several decades for yield [2]. From a material point of view, this natural source of fibres has environmental advantages such as moisture resistance, climate tolerance, and structural rigidity. Modern material technologies enable raw bamboo to be transformed into a variety of industrial goods that are seen to be perfect replacements for lumber in the construction sector.

The latest research points to a responsible and environmentally conscious use of natural resources. So, bamboo as a material becomes interesting in the textile industry as well [3]. The textile industry used more advantages of these kind natural fibres, such as: environmentally friendly characteristics, softness, breathability, antibacterial features, but textile engineering deals with solving a few disadvantages of this class of materials such as: very low capacity to absorb dyes, limits of various pre-treatment methods, ability to absorb liquids (sweat), eliminate unsuitable compounds like lignin and hemicellulose.

Zhang at all used chemical and non-electric technique, named electroless plating, in the metallization of natural materials (bamboo fibres) to investigate the effects of electroless process on the thermal stability, electrical and magnetic conductivity, and moisture absorption of bamboo fibres with variation the metal type deposits [4].

Wang at all described a hierarchically porous hybrid filter membrane based on FeOOH (iron(hydr)oxides) / bamboo fibre composite for very effective As(III)-ions removal [5]. The authors applied electrodeposition technique for synthesized nano sheets of FeOOH, directly on carbonized bamboo substrate. This paper illustrates highly applicable research of the hybrid membrane composite in treating arsenic-contaminated water.

Textiles like as bamboo or cotton can be employed in military applications that require electromagnetic shielding and medical sanitary if military members are injured, as well as in environmentally friendly applications like as electrodes for machines [6].

The chemical composition of bamboo fibre varies depending on the age of the plant, the location, i.e. the natural habitat and the type of bamboo. According to research conducted by a group of authors, bamboo fibre consists of the following compounds: 73.83% of cellulose, 12.49% of hemicellulose, 10.15% lignin, 3.16% an aqueous extract and 0.37% pectin [7].

Metallization process or surfaces-metal coating is produced by electrochemically depositing technique (old name "electroplating") a thin layer of reduced metal ions

using electric current on electrically conductive substrates [8]. In order to ensure that the metal particles adhere to the surface effectively, the substrate needs to be cleaned before electroplating. Numerous factors, including the interface between the coating and substrate, the coating and environment, and the coating material itself, have an impact on the process [9]. Galvanostatically electrodeposition technique generally involves three primary steps on cathode: (i) ion migration, (ii) electron transfer, and (iii) intercalation of adsorbed metal ions [10].

The electrochemical deposition (ED) technique of the thin metallic films or coatings on a flexible non-conductive fibre-substrate has several advantages and disadvantages over other techniques. The advantages are as follows: 1. easy controlling the morphology, deposition rate and thickness; 2. technique that is reasonably priced; 3. simple and eco-friendly process with a high deposition rate, 4. industrially scalable technique, 5. compatible technique with other metallization techniques such as chemical – electroless and spray deposition techniques, and 6. large selection of materials or alloys that can be deposited in this way. The biggest disadvantage of this technique is that it requires a conductive substrate for the current to flow between the electrodes through the electrolyte and that during deposition there may be contamination of the electrolyte and incorporation of impurities from the cathode material.

When it comes to textile materials or polymers, they are generally natural insulators and it is necessary to make the surfaces conductive, before electroplating process.

## 2. EXPERIMENTAL

### 2.1. Chemical pre-treatment of bamboo fibre textile

A piece of bamboo cloths is pre-treated with citric acid to increase the functional groups over the cellulose structure before the metal particles are deposited on the bamboo substrate. First, 0.5 l of distilled water was used to dissolve 7.5 g of citric acid, and the mixture was well-stirred. For 2h, the bamboo substrates were submerged in the solution at 100 °C. After that, the submerged fibres were dried for 30 minutes at 90 °C and rinsed with distilled water.

### 2.2. Chemical deposition of Cu particles on bamboo fibre textile by the cyclic dipping and reduction methods

The process of chemical reduction method was used to deposit the copper particles to achieve the conductivity of the bamboo fibres for the further electrodeposition process. Textile samples were immersed in solution of dissolved copper-sulphate (5 g) in deionized water (0.5 l) for approximately 15-20 minutes and dried in the oven at 90 °C for 10 minutes [6]. The procedure of dipping bamboo samples and drying in oven were continuously carried out up to 10 cycles.

The modified bamboo substrate was then added to the sodium hydrosulfite ( $\text{Na}_2\text{S}_2\text{O}_4$ ) solution (10 g/l) [6]. Among all reducing agents, sodium hydrosulfite is the most consistent and produces the tiniest particles, which is its advantage. For almost 40-50 minutes, the reduction process was carried out. During the reduction, the colour of the bamboo fabric changes from light yellow to brown, which is proof that the reduction has been done successfully. In this way, the activation of non-conductive fibres and reduction of copper were successfully performed, and an excellent foundation was created for the further step of electrochemical deposition of copper.

### 2.3. Electrodeposition method of copper films on bamboo fibre textile

Galvanostatic regime – DC (direct current) with electrolyte magnetic mixing (DC/MS regime) applied and used to generate copper films on modified bamboo substrate at constant current density ( $j = 100 \text{ mA}\cdot\text{cm}^{-2}$ ). The following electrolyte was utilized in the electrodeposition processes: 240 g/l  $\text{CuSO}_4 \cdot 5 \text{ H}_2\text{O} + 60 \text{ g/l H}_2\text{SO}_4 + 1 \text{ l H}_2\text{O}$ . Copper particle-coated activated bamboo cloth served as the cathode of the source, and copper metal bars served as the anode. The electroplating bath solution was constantly agitated (100 rpm). The temperature and pH-values were maintained at  $25 \pm 0.5 \text{ }^\circ\text{C}$  and 0.30, respectively. The copper thickness is controlled by an optical microscope. The surface of the deposition is  $1 \text{ cm} \times 1 \text{ cm}$ , and the surface of the entire frame on which the bamboo fabric was stretched was  $4 \text{ cm} \times 4 \text{ cm}$ . The design of the frame using the 3D printing method for fabric tensioning will be shown in the results section.

### 2.4. Characterization of bamboo fibres

#### 2.4.1. Optical microscopy

An optical microscope with the lowest magnification was used to observe pure bamboo fibres, then bamboo fibres with deposited copper particles, and to observe the thickness of the copper films deposited by the electrodeposition method with variations deposition times (30, 60, 90, and 120 minutes).

#### 2.4.2. Field Emission Scanning Electron Microscope

The microstructure of the raw bamboo fibres; activated bamboo fibres with copper particles, and electrodeposited copper films on textile were investigated using a 20 kV emission scanning electron microscope (FE-SEM Mira3 Tescan XMU). This FE-SEM was also utilised to investigate the structural characteristics of pure copper coatings electrodeposited on modified bamboo fibres. Sample of raw bamboo fibres have been sputtered with a thin layer of Au prior to imaging to achieving conductivity. The other samples (bamboo + Cu particles and bamboo + Cu particles + Cu films) did not require sputtered with a conductive Au layer.

The image analysis software named Image Pro Plus [11] was applied in order to processing FE-SEM pictures. This

program is very suitable for determining copper particle size, fibre's diameter and distribution of individual particles on bamboo fibre.

#### 2.4.3. Water absorption test

Before water absorption test, all the bamboo-fibres samples were placed in an oven for at least 12 h to reduce the moisture. Then, raw bamboo sample, bamboo + Cu particles, and bamboo + Cu particles + Cu film ( $4 \text{ cm} \times 4 \text{ cm}$ ) were immersed in deionized water. To evaluate the effect of absorption water during the experiment, the content of water absorbed in the bamboo-materials were calculated by the weight difference. The mass of dry samples and samples after immersion in water was measured. Weights of samples were measured with an analytical balance. The amount of absorbed water ( $Q$ ) at the time ( $t$ ) was defined as [12]:

$$Q = \frac{m - m_0}{m_0} \cdot 100 \quad (1)$$

where  $m$  (g) was the bamboo-based samples mass after immersion in water at the time  $t$  (min), and  $m_0$  was the dry specimen mass (g). The amount of absorbed water -  $Q$  values, was plotted vs. time to give the water absorption curve. Before weight detection (wet samples), the samples were first centrifuged.

## 3. RESULTS

### 3.1. 3D-printing-PLA frame design

The production of the bamboo textile tensioning frame was carried out using additive technology. An acid-resistant and environmentally friendly filament was chosen. In the enclosure realization, polylactic acid (PLA) thermoplastic and biodegradable polymer [13] with a diameter of 1.75 mm was used.

The diameter of the nozzle of 3D printer was 0.4 mm. The nozzle's maximum temperature is usually defined by software, and according to the material characteristics. Also, PLA is environmentally acceptable and is a non-toxic thermoplastic material. It is known to be derived from renewable sources such as cornstarch. The following parameters should be considered in printing process: infill density, wall line contours, infill orientation, and number of shells.

The selected printing parameters are shown in Table 1. The realized PLA filament frame with woven bamboo fabric is shown in Figure 1.

The production of auxiliary tools facilitates the work in the deposition of copper particles and the uniform deposition of the copper film. On the other hand, it allows us to fix the textile electrode in the solution and adjust the height as well as the distance from the copper electrode. An opening is left in the middle of the holder, which allows connecting the contacts without them getting wet, which is another advantage of the holder designed in this way.

**Table 1.** Printing parameters

Printing parameters	Values
Layer Height	0.15
Wall Line Contour	2
Top Layers	2
Bottom Layers	2
Printing Temperature	210°C
Build Plate Temperature	65°C
Printing Speed	50 mm/s
Travel Speed	80 mm/s
Infill Density	100%
Infill Orientation	-45°/+45°

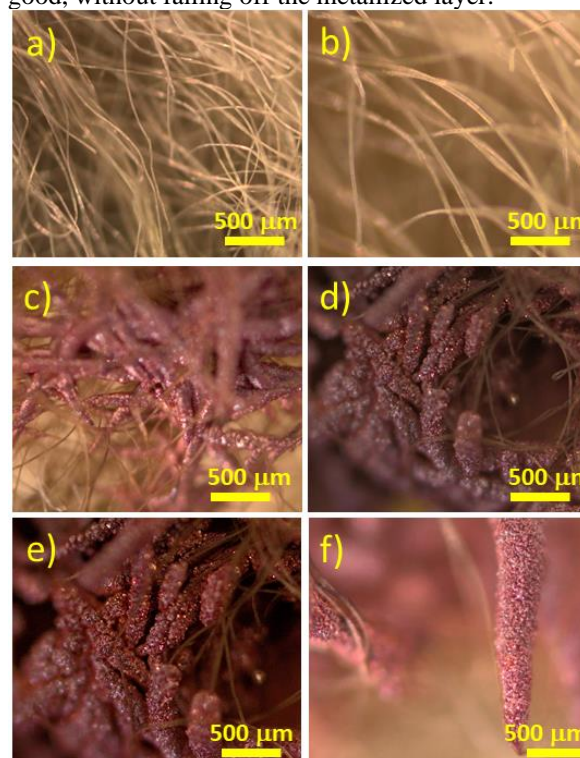
**Figure 1.** Designed holder with a frame made of PLA filaments for the needs of tensioning bamboo textiles during metallization process.

### 3.2. Optical microscopy of bamboo samples, before and after metallization

The photographs taken on the optical microscope are shown in Figure 2. Figure 2a shows bamboo fibres in their original form before modification and reduction. Figure 2b shows bamboo fibres after deposition of copper particles, while Figures 2c-f represent photographs after an electroplating of copper film with variation of plating times. In Figure 2b, the fine deposited copper particles cannot be observed, but will be confirmed using FE-SEM microscopy.

The diameter of the metallized fibres ranges from 60 to 300  $\mu\text{m}$  (depending on the deposition time), indicating that the deposition rate is 2  $\mu\text{m} / \text{min}$ , approximately. The extension of the deposition time affects the joining of the metallized fibres and the bending of the fibres inward (Figures 2d and 2e), due to the increase in the mass of the metal layer. Further extension of the deposition time (120 min) leads to the formation of a copper powder structure, see Figure 2f. It is interesting that the adhesion strength of the copper film to the modified bamboo fibres is very

good, without falling off the metallized layer.

**Figure 2.** The photos from optical microscope of a) raw bamboo fibres (non-treated), b) bamboo fibres with Cu particles (chemically activated). The electrodeposited copper films with variation deposition times on activated bamboo fibres were given, also: c)  $t = 30$  min, d)  $t = 60$  min, e)  $t = 90$  min, and f)  $t = 120$  min. The galvanostatically mode was used and constant current density ( $j = 100 \text{ mA} \cdot \text{cm}^{-2}$ ).

### 3.3. Water absorption test

In Figure 3 the water absorption curves for three samples: raw bamboo fibres, bamboo + Cu particles (after 10 cycles of dipping method), and bamboo + Cu particles + copper film (electrodeposited sample obtained using current density  $-j = 100 \text{ mA} \cdot \text{cm}^{-2}$  and deposition time  $t = 30$  min) are presented. Comparing metalized and non-metalized bamboo fibres, the improvement of water hostility can be recorded.

The maximum amount of absorbed water,  $Q$ , (Figure 3) is 225 % (for raw bamboo), 161 % (for bamboo + deposited Cu particles) and 155 % for bamboo coated with Cu films. From the apparent absorbed water curves, bamboo fibres with Cu particles and Cu films show comparable weaker wetting properties than raw bamboo fibres.

The copper particles deposited on the bamboo fabric have the function of hindering the penetration of water into the bamboo fabric and cellulose chain [14, 12]. As such, they act as a super moisture barrier and increase the hydrophobicity of the fabric. The high concentration of lignin on surface of bamboo fibres and specific microstructure of these natural fibres seems to be responsible for their water absorbed properties.

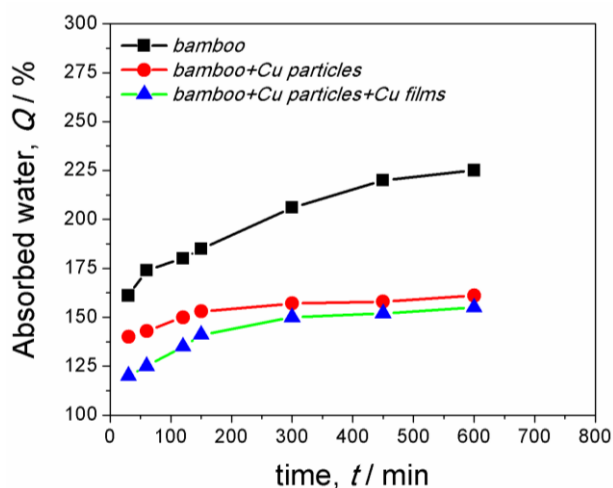


**Figure 3.** Water absorption curves for bamboo (black line), bamboo with Cu particles deposited chemically (red line), and bamboo fibres with Cu particles and electrodeposited Cu films (green line).

### 3.4. Microstructural analysis of uncoated/coated bamboo fibres

The FE-SEM micrographs with different magnifications of uncoated (Figures 4a and 4c), and copper coated bamboo fibres with Cu particles before reduction process (Figures 4b and 4d) are presented. The structure with well-developed micro-bubbles and the striped structure are confirmed by FE-SEM analysis.

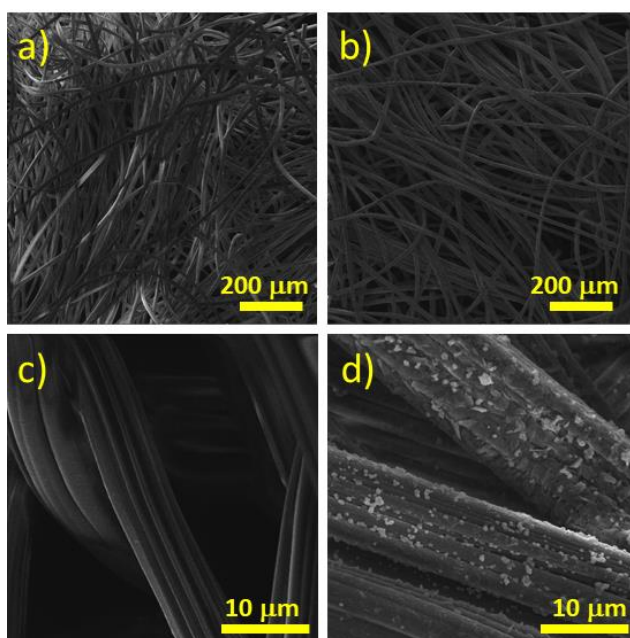


**Figure 4.** The FE-SEM micrographs of a) raw bamboo fibres (uncoated sample), and b) bamboo fibres with Cu particles activated on chemically ways. The magnifications were:  $\times 200$  (a, b), and  $\times 5\,000$  (c, d).

The uncoated bamboo fibres have a very smooth and compact surface (Figure 4c), and some vertical holes are observable. These vertical grooves are very suitable places for copper crystallites after metallization, because

these grooves prevent the precipitation of nano particles from falling off (Figure 4d). The bamboo + Cu particles sample is uniformly covered with Cu nano particles and very well dispersed on bamboo surface (Figure 4d). We can see that the surface of bamboo + Cu particles sample is rougher than that of raw bamboo sample if compared Figures 4c and 4d.

The average diameter of the measured bamboo fibres is 11  $\mu\text{m}$ , and the distribution of diameters are from 5.5 for smaller fibres to 16.5  $\mu\text{m}$  for larger ones (Figure 5a). The formation of different shapes of Cu particles can be seen with variations of particle's diameters in the range of 155 to 550 nm (see Figure 5b). The average diameter of the deposited copper nanoparticles on the bamboo fibres is 325 nm.

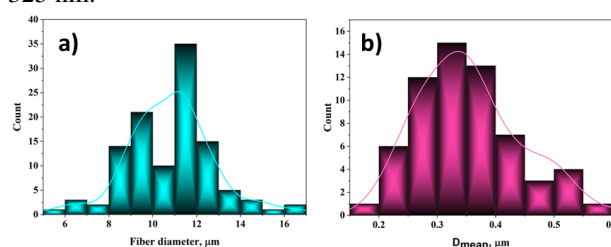


**Figure 5.** The distribution of a) bamboo fibre diameter and b) copper particles size deposited on bamboo fibre before reduction process.

The FE-SEM micrographs of copper films electrodeposited on activated bamboo fibres with Cu particles (Figures 6a and 6b) are presented.

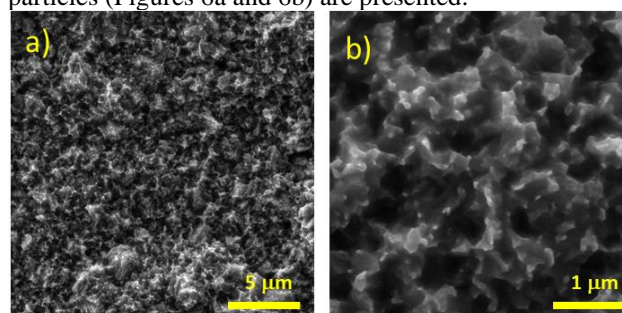


**Figure 6.** The FE-SEM micrographs of electrodeposited copper films on activated bamboo fibres after 30 minutes of electroplating process: a) magnification is  $\times 5000$ , and b)  $\times 50\,000$ .

Two different magnifications were applied:  $\times 5000$  and  $\times 50\,000$ . The electroplating time was fixed at 30 minutes. As seen from these figures, the fine-grained Cu films were formed at the modified bamboo fibres. The honeycomb-like structure that turns into a copper powder form is noted at higher magnification (Figure 6b). Copper nano sized grains tend to form micro agglomerates and holes between them. There is a possibility that these cavities retain air, and by their very nature represent a gaseous barrier for the penetration of water during absorption measurements [14]. The reduction of water penetration into Cu films such as obtained nanostructured films can also be explained by the increase in surface roughness [15].



## 4. CONCLUSION

Copper film was deposited on modified bamboo-fibre substrate by dipping/reduction processes to prepare bamboo + Cu particles + Cu film composite. The copper particles were distributed on the bamboo fibre very good, with diameter size about 325 nm. By chemical reduction of copper particles on bamboo fibres, it is obtained a conductive substrate for further electrochemical deposition of copper films.

Using additive technology, a fabric tensioning frame was designed. An environmentally friendly material (PLA) was used.

The water absorption curves showed a higher resistance to water penetration in the composite than in pure bamboo fibres. The water resistance of the textile was achieved by simple metallization, and thus the electrical conductivity is expected to increase of the textile. Further research will be focused on characterization electrical properties of the composite.

Similarly, the conductive bamboo-based textiles composites showed washing stability, and without observed loss of copper film after intense washing in the washing machine.

## Acknowledgments

This work was funded by Ministry of Education, Science and Technological Development of Serbia (Grants No. 451-03-66/2024-03/200026 and 451-03-66/2024-03/200017).

## References

- [1] Chen, J., Wang, L., Zhou, H.: *Novel bamboo-based metal composites prepared with a high-efficiency thermal spraying method: a preliminary study*, Wood Science and Technology, 58 (2) (2024) 487–502.
- [2] Li, Z., Chen, C., Mi, R., Gan, W., Dai, J., Jiao, M., Xie, H., Yao, Y., Xiao, S., Hu, L.: *A Strong, Tough, and Scalable Structural Material from Fast-Growing Bamboo*, Advanced materials, 32 (10) (2020) 1906308.
- [3] Hasan, M., Islam, R.: *Advancements in chemical pretreatment techniques for enhancing bamboo fibre quality in textile applications: a critical review*, Journal of Fashion Technology & Textile Engineering, 10 (1) (2024) 55–63.
- [4] Zhang, Q., Wang, K., Chen, Y., Tang, X., Zhao, Q., Fu, Q.: *Improving the Thermal Stability and Functionality of Bamboo Fibers by Electroless Plating*, ACS Sustainable Chemistry & Engineering, 10 (50) (2022) 16935–16947.
- [5] Wang, Y., Gu, Y., Li, H., Ye, M., Qin, W., Zhang, H., Wang, G., Zhang, Y., Zhao, H.: *Electrodeposition of hierarchically amorphous FeOOH nanosheets on carbonized bamboo as an efficient filter membrane for As(III) removal*, Chemical Engineering Journal, 392 (1) (2020) 123773.
- [6] Ali, A., Hussain, F., Kalsoom, A., Riaz, T., Zaman Khan, M., Zubair, Z., Shaker, K., Militky, J., Noman, M.T., Ashraf, M.: *Multifunctional Electrically Conductive Copper Electroplated Fabrics Sensitized by In-Situ Deposition of Copper and Silver Nanoparticles*, Nanomaterials, 11 (11) (2021) 3097.
- [7] Nurul Fazita, M.R., Jayaraman, K., Bhattacharyya, D., Mohamad Haafiz, M.K., Saurabh, C.K., Hussin, M.H., H.P.S., A.K.: *Green Composites Made of Bamboo Fabric and Poly (Lactic) Acid for Packaging Applications—A Review*, Materials, 9 (6) (2016) 435.
- [8] Tseghai, G.B., Malengier, B., Fante, K.A., Nigusse, A.B., Van Langenhove, L.: *Integration of Conductive Materials with Textile Structures, an Overview*, Sensors, 20 (23) (2020) 6910.
- [9] Ojstršek, A., Plohl, O., Gorgieva, S., Kurečič, M., Jančič, U., Hribernik, S., Fakin, D.: *Metallisation of Textiles and Protection of Conductive Layers: An Overview of Application Techniques*, Sensors, 21 (10) (2021) 3508.
- [10] Bari, D., George, A.: *Electrodeposition of nickel*, Modern electroplating, 5 (1) (2000) 79-114.
- [11] <https://Mediacy.Com/Image-Pro/>
- [12] Lu, Y., Xue, L.: *Electromagnetic interference shielding, mechanical properties and water absorption of copper/bamboo fabric (Cu/BF) composites*, Composites Science and Technology, 72 (7) (2012) 828-834.
- [13] Kristiawan, R.B., Imaduddin, F., Ariawan, D., Arifin, Z.: *A review on the fused deposition modelling (FDM) 3D printing: Filament processing, materials, and printing parameters*, Open Engineering, 11 (1) (2021) 639-649.
- [14] Fuentes, C.A., Tran, L.Q.N., Dupont-Gillain, C., Vanderlinden, De Feyter, W.S., Van Vuure, A.W. Verpoest, I.: *Wetting behaviour and surface properties of technical bamboo fibres*, Colloids and Surfaces A: Physicochemical and Engineering Aspects, 380 (1) (2021) 89-99.
- [15] Ye, Z., Lou, M., Jia, X., Shen, J., Lu, P., Huang, H., Ye, G., Yan, B.: *Reduction of the water wettability of Cu films deposited on liquid surfaces by thermal evaporation*, Colloids and Surfaces A: Physicochemical and Engineering Aspects, 650 (1) (2022) 129569.



# THE DESIGN AND SYNTHESIS OF THE FOUR NOVEL DUAL REVERSIBLE INHIBITORS OF ACETYLCHOLINESTERASE BASED ON THE TACRINE AND AROYLACRYLIC ACID PHENYLAMIDE SUBSTRUCTURES

TAMARA B. VUJATOVIĆ-VELIMIROV

Military Technical Institute, Belgrade, [tamara.vujatovic@gmail.com](mailto:tamara.vujatovic@gmail.com)

MILAN R. NIKOLIĆ

Faculty of Chemistry, University of Belgrade, [mnikolic.chem@gmail.com](mailto:mnikolic.chem@gmail.com)

MAJA D. VITOROVIĆ-TODOROVIĆ

Military Technical Institute, Belgrade, [mvitod@chem.bg.ac.rs](mailto:mvitod@chem.bg.ac.rs)

**Abstract:** Organophosphorous chemical warfare agents (i.e., nerve agents) exhibit toxic effects mainly through covalent, irreversible inhibition of acetylcholinesterase (EC 3.1.1.7), an enzyme that terminates cholinergic neurotransmission, by hydrolyzing acetylcholine at nerve and nerve-muscle junctions. Use of nerve agents is strictly limited to research purposes only and it is under control of Organisation for the Prohibition of Chemical Weapons, OPCW. Despite all efforts to limit the use of nerve agents, unfortunately the danger of nerve agents being used in war aggression and terrorist attacks is still present. The reversible inhibition of AChE was suggested as the pre-treatment option against nerve agents' intoxications. Aiming to investigate novel pre-treatment options, we designed and synthesized the four novel compounds of tacrine and aroylacrylic acid phenylamide moieties, connected via a long methylene chain to target two distinct topologically separated anionic areas on the AChE. The inhibitory activity of the compounds toward the Electric eel AChE's as well as the horse serum BChE was determined by Ellman assay. The designed compounds may represent a new class of promising leads for developing more effective pre-treatment options.

**Keywords:** Cholinesterase, dual-binding inhibitors, nerve agents, pre-treatment, tacrine, aroylacrylic acid derivatives.

## 1. INTRODUCTION

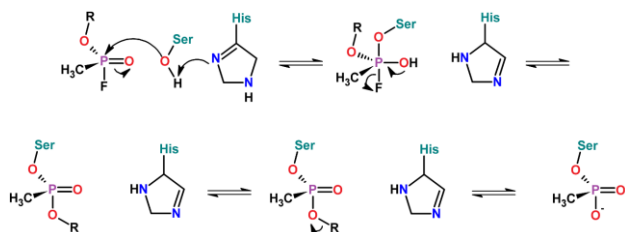
The use of chemical and biological weapons in war was firstly prohibited by Geneva Protocol in 1925 as a part of Geneva Conventions. Geneva Conventions are international humanitarian laws that establish international legal standards for humanitarian treatment in war and each country that has signed it is obligated, among other, to prevent employment of chemical weapons in war. Today, the use of organophosphorous chemical warfare agents (i. e. nerve agents, OP) is restricted to research purposes only and it is monitored by Organization for the Prohibition of Chemical Weapons, OPCW. Despite all efforts, cases of use of nerve agents are still recorded in terroristic attacks and military aggressions.

Cholinergic nerve system is the target of nerve agents. They exert their toxic effects by covalent binding to the catalytic Ser203 of acetylcholinesterase (AChE, EC 3.1.1.7.), enzyme responsible for cease of neurotransmission in cholinergic nervous system. AChE is a carboxylesterase which terminates cholinergic neurotransmission by hydrolyzing the neurotransmitter acetylcholine (ACh) in a synaptic cleft of nerve- and

nerve-muscle junctions [1]. In the peripheral nervous system, acetylcholine accumulation leads to persistent muscarinic receptor overstimulation that triggers various symptoms, including miosis, profuse secretions, bradycardia, bronchoconstriction, hypotension, and diarrhea. It also leads to overstimulation of nicotinic receptors, causing severe skeletal muscle fasciculation and subsequent weakness. Central nervous system-related effects include anxiety, restlessness, confusion, ataxia, tremors, seizures, cardiorespiratory paralysis, and coma.

Mechanism of nerve agent binding to catalytic Ser203 residue of AChE is presented in Scheme1. Covalent complex that is formed between AChE and nerve agent is similar to the acetylated enzyme which is formed during hydrolysis of the ACh. Hydrolysis of the OP-AChE complex is an extremely slow process. In some instances, depending on the structure of the nerve agent bound to AChE, dealkylation, i.e., leaving of alkoxy group from AChE-nerve agent phosphate occurs, resulting in a negatively charged dealkylated AChE-OP complex [2]. This process is called aging and therapeutic intervention by an oxime (pralidoxime or obidoxime) is only possible before the onset of this process [3]. Also, oximes are permanently positively charged which prevents them to cross blood-brain barrier, which means if applied on time,

they can only reactivate AChE in peripheral nervous system, while central nervous system AChE still remains inhibited.



Scheme 1. Mechanism of AChE phosphorylation by nerve agents.

Depending of the bulkiness of alkoxy group of nerve agent, aging process occurs in different time interval. In case of soman this interval is very short and AChE is irreversibly inhibited in just a few minutes [4]. Because of time sensitive application of standard treatment, which is not possible in battlefield conditions, and lack of the ability of oximes to reactivate AChE in central nerve system, new approach was suggested. The so called pre-treatment consists of application of pseudo-irreversible or reversible inhibitors of AChE to healthy individuals when there is a reasonable suspicion of increased danger of nerve agent poisoning. Reversible inhibitor would occupy active site of AChE during the exposure to nerve agents. In this way, part of AChE would be protected against irreversible inhibition by nerve agent which would enable easier recovery and greater chances of survival of affected individuals.

In the past several decades, protective effects toward nerve agent poisoning of many reversible inhibitors AChE were examined [5]. Initially, the emphasis of these tests was on already available anticholinergic drugs. One of the first compounds investigated as a pre-treatment option was pyridostigmine bromide, which is used for treatment of *Myasthenia gravis*. Protective effects of Huperzine A, natural product of plant *Huperzia Serrata*, was thoroughly examined against nerve agent poisoning [6]. The advantage of Huperzine A is reflected in its ability to pass through a blood-brain barrier, which means that AChE in central nerve system can be reached and protected during nerve agent poisoning. [7] Protective effects of FDA-approved drugs for the treatment of Alzheimer's disease, donepezil and galantamine, were also investigated [8-12]. [8]-[12]

In this work we present the design, synthesis, NMR characterization, and anticholinesterase activity of four novel nanomolar dual-binding reversible inhibitors of cholinesterases.

## 2. MATERIALS AND METHODS

### 2.1. Chemistry

All chemicals were purchased from Sigma Aldrich or Merck, and were used as received. The  $^1\text{H}$  and  $^{13}\text{C}$  NMR spectra were recorded in  $\text{CDCl}_3$  or  $d_6$ -DMSO on Bruker AVANCE400/101 MHz instrument. Chemical shifts are

reported in parts per million (*ppm*) relative to solvent shift. Spin multiplicities are given as follows: *s* (singlet), *d* (doublet), *t* (triplet), *m* (multiplet). Synthetic procedures for aroylacrylic acid amides and 9-chloro-1,2,3,4-tetrahydroacridine were previously described in the literature [13-14].

Synthetic procedure for **N1-(1,2,3,4-Tetrahydro-9-acridinyl)-heptane-1,7-diamine(4)**: 1,7-diamino octane (0.89 g, 6.9 mmol), 9-chloro-1,2,3,4-tetrahydroacridine (0.5 g, 2.3 mmol) and 2 mL of 1-pentanol were added to the stainless-steel reactor. Reactor was sealed and heated to 160-165 °C for 8<sup>h</sup>. After that, reaction mixture was transferred into separation funnel, diluted with ethyl acetate and washed with 10% aqueous solution of sodium hydroxide, deionized water and saturated aqueous solution of sodium chloride. Organic layer was dried over anhydrous magnesium sulphate and filtered. Solvents were removed under reduced pressure. Crude compound was purified using *dry-flash* column chromatography on silica gel that was previously thermally treated at 100 °C for 30 min and cooled at room temperature before use. Solvent system used for purification was  $\text{CHCl}_3/\text{MeOH}/\text{Et}_3\text{N}=7/3/0.07$ . Pure compound was obtained as yellow semi-solid with reaction yield of 42%.  $^1\text{H}$  NMR (400 MHz,  $\text{CDCl}_3$ )  $\delta$  7.94 (*d*,  $J = 8.4$  Hz, 1H, tacrine-CH), 7.89 (*d*,  $J = 8.4$  Hz, 1H, tacrine-CH), 7.54 (*t*,  $J = 7.6$  Hz, 1H, tacrine-CH), 7.33 (*t*,  $J = 7.6$  Hz, 1H, tacrine-CH), 3.47 (*t*,  $J = 7.2$  Hz, 2H, linker-NH-CH<sub>2</sub>-), 3.05 (*s*, 2H, tacrine-CH<sub>2</sub>), 2.74 – 2.62 (*overlapped m*,  $J = 14.9, 7.9$  Hz, 4H, linker-NH-CH<sub>2</sub>- and tacrine-CH<sub>2</sub>), 1.96 – 1.85 (*overlapped m*, 6H, tacrine-CH<sub>2</sub>, linker-NH- and linker-NH<sub>2</sub>), 1.65 (*quin*,  $J = 14.4, 7.2$  Hz, 2H, linker-NH-CH<sub>2</sub>-CH<sub>2</sub>-), 1.46 – 1.26 (*m*, 8H, linker-CH<sub>2</sub>-).  $^{13}\text{C}$  NMR (101 MHz,  $\text{CDCl}_3$ )  $\delta$  158.55, 150.90, 147.58, 128.82, 128.37, 123.68, 122.94, 120.36, 115.99, 49.60, 42.18, 34.12, 33.64, 31.84, 29.32, 27.02, 26.88, 24.91, 23.18, 22.90.

General synthetic procedure for compounds **9-12**: N1-(1,2,3,4-Tetrahydro-9-acridinyl)-octane-1,7-diamine was dissolved in DCM, catalytic amount of  $\text{Et}_3\text{N}$  (15%) was added and reaction mixture was stirred for 15 min. Then the chosen aroylacrylic acid phenylamide was added to reaction mixture in molar ratio of N1-(1,2,3,4-Tetrahydroacridin-9-yl)-octane-1,7-diamine /aroylacrylic acid phenylamide=1/1. The reaction mixture was stirred at room temperature for 24<sup>h</sup>. Reaction progress was monitored by TLC (solvent system  $\text{Tol}/\text{EA}/\text{MeOH}/\text{Et}_3\text{N}=2/2/1/0.05$ ). Crude compounds were obtained by solvent evaporation on rotary vacuum evaporator and purified by gradient *dry-flash* column chromatography on Florisil using the solvent systems hexane/ethyl acetate/  $\text{NH}_4\text{OH}=1/1/0.02$ , hexane/ethyl acetate/methanol/ $\text{NH}_4\text{OH}=6/2/1/0.18$ , hexane/ethyl acetate/methanol/ $\text{NH}_4\text{OH}=1/1/1/0.03$ .

Synthetic procedure for **N-(phenyl)-4-(3,4-methylphenyl)-4-oxo-2-[7-(1,2,3,4-tetrahydro-9-acridinylamino)-heptylamino]-butyramide (9)**:

In addition to general procedure, the white solid was formed and filtered from reaction mixture before solvent

evaporation. Compound was obtained as yellow semi-solid with the reaction yield of 61%.  $^1\text{H}$  NMR (400 MHz,  $\text{CDCl}_3$ )  $\delta$  9.58 (s, 1H, amido-NH-), 7.95 (d,  $J = 8.5$  Hz, 1H, tacrine-CH), 7.92 (d,  $J = 8.5$  Hz, 1H, tacrine-CH), 7.74 (s, 1H, aroyl-*o*-CH), 7.71 (d,  $J = 7.8$  Hz, 1H, aroyl-*o*-CH), 7.59 (d,  $J = 7.8$  Hz, 2H, phenyl-*o*-CH), 7.57 – 7.51 (m, 1H, tacrine-CH), 7.36 – 7.29 (overlapped m, 3H, tacrin-CH and phenyl-*m*-CH), 7.21 (d,  $J = 7.8$  Hz, 1H, aroyl-*m*-CH), 7.09 (t,  $J = 7.4$  Hz, 1H, phenyl-*p*-CH), 3.68 (dd,  $J = 8.7, 3.1$  Hz, 1H, ABX), 3.62 (dd,  $J = 17.4, 3.1$  Hz, 1H, ABX), 3.47 (t,  $J = 7.1$  Hz, 2H, linker-NH-CH<sub>2</sub>-), 3.26 (dd,  $J = 17.4, 8.7$  Hz, 1H, ABX), 3.06 (s, 2H, tacrine-CH<sub>2</sub>-), 2.75 – 2.66 (overlapped m, 3H, tacrine-CH<sub>2</sub> and linker-NH-CH<sub>2</sub>-), 2.57 (dt,  $J = 11.5, 7.1$  Hz, 1H, linker-NH-CH<sub>2</sub>-), 2.34 – 2.27 (overlapped m, 6H, aroyl-CH<sub>3</sub>), 1.96 – 1.87 (m, 4H, tacrine-CH<sub>2</sub>-), 1.64 (quin,  $J = 14.1, 7.2$  Hz, 2H, linker-NH-CH<sub>2</sub>-CH<sub>2</sub>-), 1.54 – 1.46 (m, 2H, linker-NH-CH<sub>2</sub>-CH<sub>2</sub>-), 1.43 – 1.30 (m, 6H, linker-CH<sub>2</sub>-).  $^{13}\text{C}$  NMR (101 MHz,  $\text{CDCl}_3$ )  $\delta$  198.58, 172.10, 150.99, 143.46, 137.92, 137.24, 134.35, 130.10, 129.43, 129.13, 128.70, 128.49, 128.34, 126.06, 124.22, 123.76, 122.98, 120.27, 119.40, 115.90, 77.16, 59.69, 49.59, 48.54, 40.32, 34.04, 31.85, 30.28, 29.33, 27.26, 27.02, 24.89, 23.16, 22.87, 20.18, 19.89.

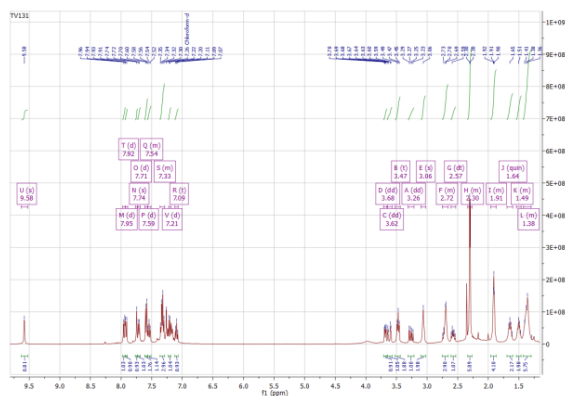


**Figure 1.**  $^1\text{H}$  NMR spectrum of *N*-(phenyl)-4-(3,4-methyl-phenyl)-4-oxo-2-[7-(1,2,3,4-tetrahydro-9-acridinylamino)-heptylamino]-butyramide (9).

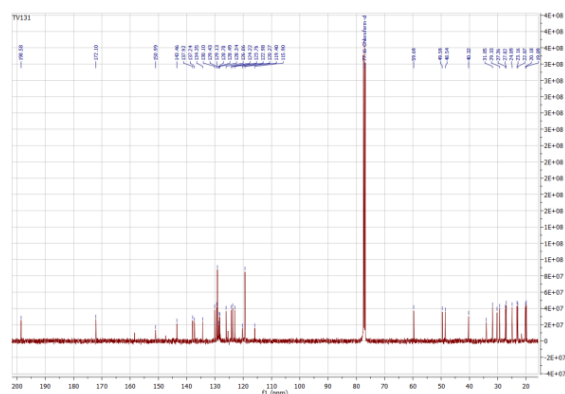


**Figure 2.**  $^{13}\text{C}$  NMR spectrum of *N*-(phenyl)-4-(3,4-methyl-phenyl)-4-oxo-2-[7-(1,2,3,4-tetrahydro-9-acridinylamino)-heptylamino]-butyramide (9).

Synthetic procedure for *N*-[4-(propan-2-yl)-phenyl]-4-(3,4-methyl-phenyl)-4-oxo-2-[7-(1,2,3,4-tetrahydro-9-acridinylamino)-heptylamino]-butyramide (10):

Following the general procedure compound was obtained as yellow semi-solid with the reaction yield of 63%.  $^1\text{H}$  NMR (400 MHz,  $\text{CDCl}_3$ )  $\delta$  9.46 (s, 1H, amido-NH), 7.95 (d,  $J = 8.5$  Hz, 1H, tacrine-CH), 7.91 (d,  $J = 8.5$  Hz, 1H, tacrine-CH), 7.58 – 7.47 (overlapped m, 4H, tacrine-CH, aroyl-*o*-CH), 7.34 (t,  $J = 7.6$  Hz, 1H, tacrine-CH), 7.28 – 7.22 (overlapped m, 2H, phenyl-*o*-CH and solvent), 7.21 – 7.15 (m, 2H, phenyl-*m*-CH), 7.12 (d,  $J = 7.8$  Hz, 1H, aroyl-*m*-CH), 3.67 (dd,  $J = 8.6, 3.2$  Hz, 1H, ABX), 3.54 (dd,  $J = 17.5, 3.2$  Hz, 1H, ABX), 3.48 (t,  $J = 7.2$  Hz, 2H, linker-NH-CH<sub>2</sub>-), 3.22 (dd,  $J = 17.5, 8.6$  Hz, 1H, ABX), 3.06 (s, 2H, tacrine-CH<sub>2</sub>-), 2.87 (sept,  $J = 6.9$  Hz, 1H, phenyl-*p*-CH(CH<sub>3</sub>)<sub>2</sub>), 2.77 – 2.66 (overlapped m, 3H, linker-NH-CH<sub>2</sub>- and tacrine-CH<sub>2</sub>-), 2.58 (dt,  $J = 11.5, 7.1$  Hz, 1H, linker-NH-CH<sub>2</sub>-), 2.35 (overlapped m, 4H, aroyl-*m*-CH<sub>3</sub> and aroyl-*p*-CH<sub>3</sub>), 1.96 – 1.88 (m, 4H, tacrine-CH<sub>2</sub>-), 1.66 (dt,  $J = 14.4, 7.1$  Hz, 2H, linker-NH-CH<sub>2</sub>-CH<sub>2</sub>-), 1.56 – 1.47 (m, 2H, linker-NH-CH<sub>2</sub>-CH<sub>2</sub>-), 1.45 – 1.33 (m, 6H, linker-CH<sub>2</sub>-), 1.22 (d,  $J = 6.9$  Hz, 6H, phenyl-*p*-CH(CH<sub>3</sub>)<sub>2</sub>).  $^{13}\text{C}$  NMR (101 MHz,  $\text{CDCl}_3$ )  $\delta$  202.54, 171.83, 158.47, 150.98, 145.00, 136.89, 135.63, 135.57, 135.52, 132.78, 132.19, 129.74, 129.17, 128.75, 128.49, 128.36, 127.01, 125.43, 123.77, 122.98, 120.31, 119.54, 115.94, 59.82, 49.61, 48.51, 42.98, 34.07, 33.74, 31.87, 30.34, 29.37, 27.31, 27.05, 24.91, 24.17, 23.18, 22.90, 21.58, 21.21, 21.01.

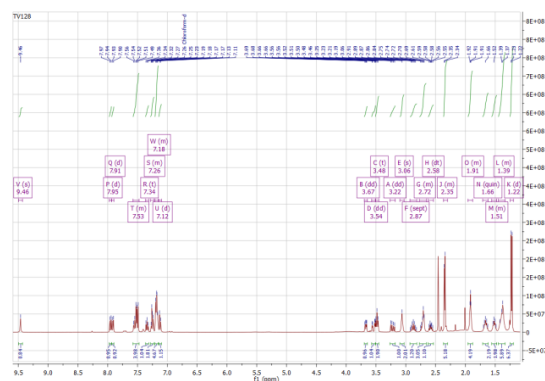


**Figure 3.**  $^1\text{H}$  NMR spectrum of *N*-[4-(propan-2-yl)-phenyl]-4-(3,4-methyl-phenyl)-4-oxo-2-[7-(1,2,3,4-tetrahydro-9-acridinylamino)-heptylamino]-butyramide (10).

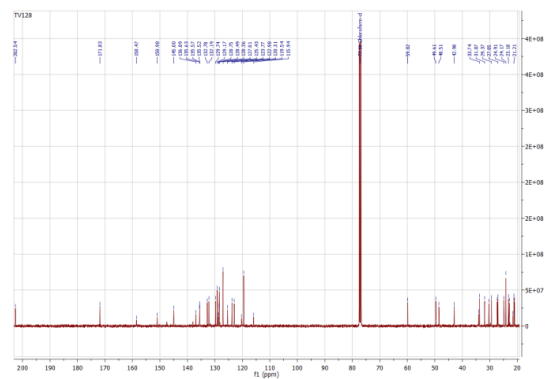


**Figure 4.**  $^{13}\text{C}$  NMR spectrum of *N*-[4-(propan-2-yl)-phenyl]-4-(3,4-methyl-phenyl)-4-oxo-2-[7-(1,2,3,4-tetrahydro-9-acridinylamino)-heptylamino]-butyramide (10).

Synthetic procedure for *N*-(3,5-methoxy-phenyl)-4-(3,4-methyl-phenyl)-4-oxo-2-[7-(1,2,3,4-tetrahydro-9-acridinylamino)-heptylamino]-butyramide (11):

Following the general procedure compound was obtained as yellow semi-solid with the reaction yield of 16%. <sup>1</sup>H NMR (400 MHz, CDCl<sub>3</sub>) δ 9.57 (s, 1H, amido-NH), 7.99 – 7.92 (overlapped m, 2H, tacrine-*o*-CH), 7.74 (s, 1H, aroyl-*o*-CH), 7.71 (d, *J* = 7.8 Hz, 1H, aroyl-*o*-CH), 7.55 (t, *J* = 7.5 Hz, 1H, tacrine-*m*-CH), 7.34 (t, *J* = 7.5 Hz, 1H, tacrine-*m*-CH), 7.21 (d, *J* = 7.8 Hz, 1H, aroyl-*m*-CH), 6.84 (d, *J* = 2.1 Hz, 2H, phenyl-*o*-CH), 6.23 (t, *J* = 2.1 Hz, phenyl-*m*-CH 1H), 3.77 (s, 6H, phenyl-OCH<sub>3</sub>), 3.68 – 3.64 (m, 1H, ABX), 3.63 – 3.56 (m, 1H, ABX), 3.50 (t, *J* = 7.1 Hz, 2H, linker -NH-CH<sub>2</sub>-), 3.25 (dd, *J* = 17.3, 8.7 Hz, 1H, ABX), 3.07 (s, 2H, tacrine -CH<sub>2</sub>), 2.73 – 2.65 (overlapped m, 3H, tacrine -CH<sub>2</sub> and linker NH<sub>2</sub>-CH<sub>2</sub>), 2.59 – 2.51 (m, 1H, linker NH<sub>2</sub>-CH<sub>2</sub>), 2.34 – 2.25 (m, 6H, aroyl-*m*-CH<sub>3</sub> and aroyl-*p*-CH<sub>3</sub>), 1.91 (s, 4H, tacrine -CH<sub>3</sub>), 1.65 (quin, *J* = 14.2, 7.3 Hz, 2H, linker -NH-CH<sub>2</sub>-CH<sub>2</sub>-), 1.56 – 1.46 (m, 2H, linker -NH-CH<sub>2</sub>-CH<sub>2</sub>-), 1.42 – 1.28 (m, 6H, linker -CH<sub>2</sub>-). <sup>13</sup>C NMR (101 MHz, CDCl<sub>3</sub>) δ 198.52, 172.19, 161.27, 143.52, 139.68, 137.27, 134.31, 130.12, 129.45, 128.74, 128.36, 126.07, 123.86, 123.06, 97.69, 96.68, 77.16, 59.72, 55.53, 49.55, 48.48, 40.24, 31.83, 30.26, 29.32, 27.27, 27.03, 24.82, 23.10, 22.76, 20.19, 19.89.

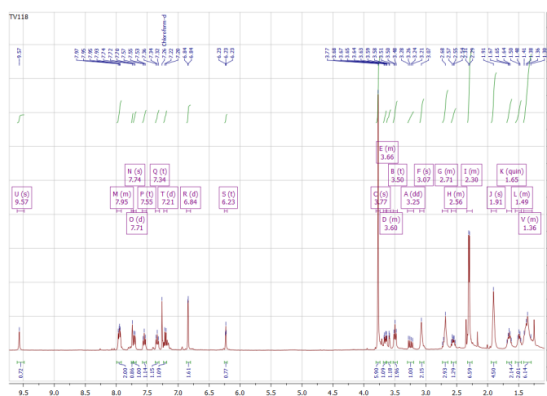


**Figure 5.** <sup>1</sup>H NMR spectrum of *N*-(3,5-methoxy-phenyl)-4-(3,4-methyl-phenyl)-4-oxo-2-[7-(1,2,3,4-tetrahydro-9-acridinylamino)-heptylamino]-butyramide (11).

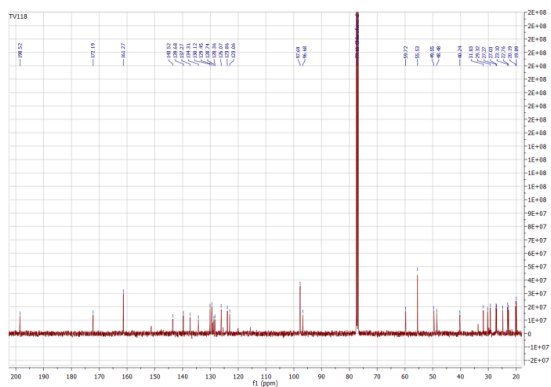


**Figure 6.** <sup>13</sup>C NMR spectrum of *N*-(3,5-methoxy-phenyl)-4-(3,4-methyl-phenyl)-4-oxo-2-[7-(1,2,3,4-tetrahydro-9-acridinylamino)-heptylamino]-butyramide (11).

Synthetic procedure for *N*-(3,5-methoxy-phenyl)-4-(2,5-methyl-phenyl)-4-oxo-2-[7-(1,2,3,4-tetrahydro-9-acridinylamino)-heptylamino]-butyramide (12):

In addition to general procedure, the white solid formed and filtered from reaction mixture before solvent evaporation. Compound was obtained as yellow semi-solid with the reaction yield of 79%. <sup>1</sup>H NMR (400 MHz, CDCl<sub>3</sub>) δ 9.54 (s, 1H, amido-NH-), 7.95 (d, *J* = 8.5 Hz, 1H, tacrine-CH-), 7.90 (d, *J* = 8.5 Hz, 1H, tacrine-CH-), 7.57 – 7.50 (m, 2H, tacrine-CH- and aroyl-*o*-CH), 7.33 (t, *J* = 7.6 Hz, 1H, tacrine-CH-), 7.28 – 7.10 (m, 2H, aroyl-*m*-CH and aroyl-*p*-CH), 6.84 (d, *J* = 2.0 Hz, 2H, phenyl-*o*-CH), 6.23 (s, 1H, phenyl-*p*-CH), 3.77 (s, 6H, phenyl-3,5-diOCH<sub>3</sub>), 3.66 (dd, *J* = 8.5, 3.2 Hz, 1H, ABX), 3.53 (dd, *J* = 17.6, 3.2 Hz, 1H, ABX), 3.48 (t, *J* = 7.2 Hz, 2H, linker-NH-CH<sub>2</sub>-), 3.24 (dd, *J* = 17.6, 8.5 Hz, 1H, ABX), 3.06 (s, 2H, tacrine-CH<sub>2</sub>-), 2.75 – 2.65 (overlapped m, 3H, linker-NH-CH<sub>2</sub>- and tacrine-CH<sub>2</sub>-), 2.61 – 2.52 (m, 1H, linker-NH-CH<sub>2</sub>-), 2.46 (s, 3H, aroyl-*o*-CH<sub>3</sub>), 2.34 (s, 3H, aroyl-*m*-CH<sub>3</sub>), 1.95 – 1.87 (m, 4H, tacrine-CH<sub>2</sub>-), 1.70 – 1.60 (m, 2H, linker-NH-CH<sub>2</sub>-CH<sub>2</sub>-), 1.56 – 1.46 (m, 2H, linker-NH-CH<sub>2</sub>-CH<sub>2</sub>-), 1.44 – 1.30 (m, 6H, linker-CH<sub>2</sub>-). <sup>13</sup>C NMR (101 MHz, CDCl<sub>3</sub>) δ 202.38, 172.10, 161.26, 158.48, 150.97, 139.66, 136.78, 135.59, 135.57, 132.84, 132.22, 129.75, 129.16, 128.71, 128.47, 128.35, 125.42, 123.75, 122.98, 120.32, 115.95, 97.70, 96.65, 59.83, 55.52, 49.60, 48.43, 42.72, 34.05, 31.88, 30.30, 29.35, 27.31, 27.07, 24.90, 23.17, 22.89, 21.57, 21.23, 21.01.

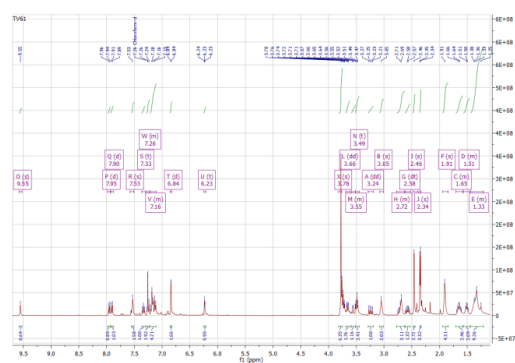


**Figure 7.** <sup>1</sup>H NMR spectrum of *N*-(3,5-methoxy-phenyl)-4-(2,5-methyl-phenyl)-4-oxo-2-[7-(1,2,3,4-tetrahydro-9-acridinylamino)-heptylamino]-butyramide (12).

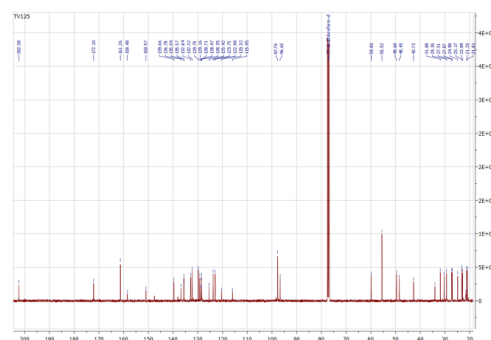


**Figure 8.** <sup>13</sup>C NMR spectrum of *N*-(3,5-methoxy-phenyl)-4-(2,5-methyl-phenyl)-4-oxo-2-[7-(1,2,3,4-tetrahydro-9-acridinylamino)-heptylamino]-butyramide (12).

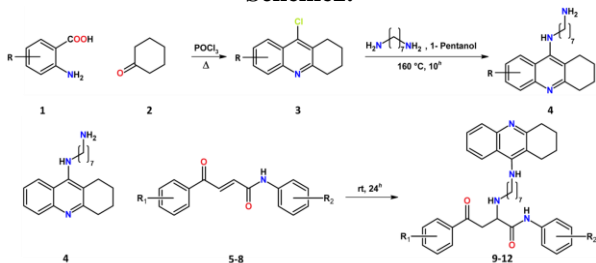
## 2.2. Biology

The inhibition potency of the compounds **9–12** toward E. Eel AChE and horse serum BChE (*Eq*BChE) was evaluated by Ellman assay, using the type VI-S enzyme (Sigma) and acetylthiocholine iodide (in final concentration 0.28 mM) as a substrate. The measurements were done on Epoch Microplate Spectrophotometer (Biotek Instruments, USA). A broad range of concentrations, which produce 20–80% of enzyme activity inhibition, were used for each compound. The reaction took place in the final volume of 0.2 mL of 0.1 M potassium phosphate buffer, pH 8.0, containing 0.02 U/mL of AChE and 0.3 mM of 5,5-dithio-bis(2-nitrobenzoic)acid (DTNB), used to produce yellow anion of 5-thio-2-nitrobenzoic acid in reaction with thiocholine released by AChE. The tested compound (5  $\mu$ L) was added to the enzyme solution (95  $\mu$ L), followed by the addition of DTNB (95  $\mu$ L) and substrate (5  $\mu$ L). The reaction was monitored for 3 min (absorbance was measured every 30 s), and the color production was measured at 412 nm. Determination of inhibition curves was performed at least in triplicate. One triplicate sample without a test compound was always present to yield 100% of AChE activity.

## 3. RESULTS AND DISCUSSION

### 3.1. Chemistry

The synthetic path for compounds **9–12** is given in **Scheme 2**.



**Scheme 2.** Synthetic path for compounds 9-12.

The Niementowski reaction between 2-aminobenzoic acid **1** and cyclohexanone **2** proceeded smoothly to give **3**. Compound **4** was obtained in the nucleophilic aromatic substitution ( $S_NAr$ ) reaction of compounds **3** and 1,8-diaminooctane (linker). The reaction took place in a sealed stainless steel reactor. Although a triple amount of linker was used, a considerable amount of tacrine homodimer<sup>1</sup> was formed as a by-product, and it was separated from the targeted compound **4** as described in synthetic procedure. Michael's addition of **4** and substituted acryloyl phenylamides **5–8** was used to obtain the final products, compounds **9–12**. Procedures for the synthesis of acryloyl phenylamides are described in the previous work [16]. General structure of synthesized compounds was given on **Figure 9**, while substitution (R1, R2) and corresponding reaction yields are

presented in **Table 1**.

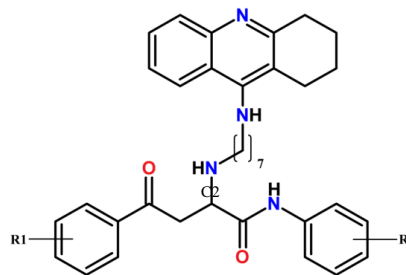


**Figure 9.** General structure of compounds 9-12. R1 is representing substitution of aroyl- and R2 substitution of phenylamide segment.

**Table 1.** Reaction yield for compounds **9–12**.

No.	R1	R2	Yield (%)
9	3,4-CH <sub>3</sub>	-H	61
10	3,4-CH <sub>3</sub>	4-CH(CH <sub>3</sub> ) <sub>2</sub>	63
11	3,4-CH <sub>3</sub>	3,4-OCH <sub>3</sub>	16
12	2,5-CH <sub>3</sub>	3,4-OCH <sub>3</sub>	79

The final synthetic step for all presented compounds went smoothly with adequate reaction yield. In case of compound **11**, reaction yield is notably lower than that of the other three compounds. Comparing the reaction yields of compounds **9** and **10**, it can be observed that R2 substitution does not have any significant influence on reaction yield since **10** has a very bulky isopropyl group, and **9** lacks R2 substitution, but reaction yields of these compounds are very similar. The reaction yields of compounds **11** and **12** drastically differ. This may suggest that substitution pattern at aroyl ring (R1) has greater impact on the overall reaction yield than substitution at phenylamide ring (R2).

This can be ascribed to the greater influence of R1 substituents on the overall conformation of the acryloyl phenylamide and its subsequent influence on the electrophilic properties of C2-carbon which may be, depending on the conformation, more or less susceptible to nucleophilic attack of the Michael's donor. Further study is needed in order to accurately determine the way in which R1 has the influence on reaction yield.

### 3.2. Biology

Inhibition potency of compounds **9–12** was determined toward *Ee*AChE and *Eq*BChE. The results are shown in **Table 2**. All compounds are highly potent nanomolar inhibitors of *Ee*AChE and *Eq*BChE.

**Table 2.** IC<sub>50</sub> values of compounds 9-12.

No.	R1	R2	IC <sub>50</sub> (nM±SD)	
			<i>Ee</i> AChE	<i>Eq</i> BChE
9	3,4-CH <sub>3</sub>	-H	33.56±1.24	2.11±0.27
10	3,4-CH <sub>3</sub>	4-CH(CH <sub>3</sub> ) <sub>2</sub>	64.91±1.75	2.32±0.12
11	3,4-CH <sub>3</sub>	3,4-OCH <sub>3</sub>	42.71±1.39	2.13±0.46
12	2,5-CH <sub>3</sub>	3,4-OCH <sub>3</sub>	45.03±0.61	1.97±0.09

All compounds exhibited low nanomolar activity toward *Eq*BChE. Having in mind that all IC<sub>50</sub> values are very similar and about 2 nM, it is evident that a great variety of acryloyl fragment substituents may be accommodated

<sup>1</sup> *N,N'*-Bis-(1,2,3,4-tetrahydro-acridin-9-yl)-octane-1,8-diamine.

in the upper part of *EqBChE* active site gorge.

The variation in AChE inhibition potency may be ascribed to the variation in the nature, position and bulkiness of substituents at phenylamide moiety of molecules. The lowest activity of **10** can be ascribed to the bulky isopropyl substituent in *p*-position of phenylamide fragment (R2), indicating possible steric hindrance between this moiety of **10** and PAS amino acid residues of AChE. Somewhat higher potency have derivatives **11** and **12**, with less bulky dimethoxy substituents, and finally, the most active derivative **9**, lacks any substituents at phenylamide ring. All this indicates that any kind of phenylamide substitution has negative effects on AChE inhibition potency. Also, the position of -CH<sub>3</sub> group at aroyl fragment (R1) is not the determining factor for compounds inhibition potency toward *EeAChE*.

Comparing the results of our previous work [14] with inhibition potency of compounds **11** and **12**, the greatest impact on activity toward *EeAChE* has the linker length. Briefly, in previous work compounds similar in structure to **11** and **12** were synthesized. The only difference was the length of linker: 1,8-diaminooctane was used in previous work, while here we used 1,7-diaminoseptane-linker, shorter for one methylene group. The compounds with longer linker showed greater activity toward *EeAChE*. The possible explanation for this effect can be ascribed to the inability of compounds with shorter linker to properly accommodate in the AChE gorge and subsequently the interaction in PAS may not be optimal or are weaker than those of compounds with longer linker. To confirm this theory, further study of AChE-compound interactions is needed.

The greater inhibition potency of **9-12** toward *EqBChE* is expected since the anchoring moiety of the derivatives, i.e. tacrine fragment, has a greater potency toward BChE than AChE.

## 5. CONCLUSION

Four new reversible, dual-binding AChE inhibitors were synthesized and their inhibitory activity toward *EeAChE* and *EqBChE* was examined. Path for synthesis consisted of five reaction, including reaction of Niementowski, nucleophilic aromatic substitution, and Michael's addition as last step. Compound **9**, **10** and **12** gave adequate reaction yields, while reaction of compound **11** resulted in lower reaction yield. Compound **9** exhibited lowest IC<sub>50</sub> toward *EeAChE* and the least active was compound **10**. All compounds exhibited similar activity toward *EqBChE*. All compounds exhibited low nanomolar activity toward both cholinesterase and are considered good leads for further research.

## References

[1] Tôugu, V.: *Acetylcholinesterase: Mechanism of Catalysis and Inhibition*, *Curr. Med. Chem. – Central Nervous System Agents*, 1 (2) (2001) 155-170.

[2] Kovach, I. M.: *Structure and dynamics of serine hydrolase-organophosphate adducts*, *J Enzyme Inhib*, 2 (3) (1988) 199-208.

[3] Michel, H. O., Hackley, B. E., Berkowitz, L., List, G., Hackley, E. B., Gillilan, W., Pankau, M., *Ageing and dealkylation of soman (pinacolylmethylphosphonofluoridate)-inactivated eel cholinesterase*, *Archives of Biochem and Biophys*, 121(1), (1967) 29-34.

[4] Levy, A., G. Cohen, E. Gilat, R. Duvdevani, N. Allon, S. Shapira, S. Dachir, E. Grauer, Y. Meshulam, I. Rabinovitz, *Therapeutic versus prophylactic treatment strategies against nerve-agent induced brain injuries*, *Proc. Med. Def. Biosci. Rev.* (2000) 280–290.

[5] Vitorović-Todorović M. D., Vujatović-Velimirov T. B., *The reversible inhibitors of acetylcholinesterase as pretreatment options against nerve agents' intoxications*, U 1st (Ur.), *Sensing of Deadly Toxic Chemical Warfare Agents, Nerve Agent Simulants, and their Toxicological Aspects* (2022) 503-528, Elsevier, Radarweg 29, PO Box 211, 1000 AE Amsterdam, Netherlands.

[6] Grunwald, J., Raveh, L., Doctor, B. P., Ashani, Y., *Huperzine A as a pretreatment candidate drug against nerve agent toxicity*, *Life Sci*, 54(14), (1994) 991-997.

[7] Laganière, S., Corey, J., Tang, X. C., Wülfert, E., Hanin, I., *Acute and chronic studies with the anticholinesterase huperzine a: Effect on central nervous system cholinergic parameters*, *Neuropharmacology*, 30(7), (1991) 763-768.

[8] Janowsky, D. S., Davis, J. M., & Overstreet, D. H., *Antagonism of anticholinesterase (DFP) toxicity by donepezil plus scopolamine: A preliminary study*, *Pharmac, Biochem and Behavior*, 77(2), (2004) 337-343.

[9] Janowsky, D. S., Davis, J. M., Overstreet, D. H., *Anticholinesterase (DFP) toxicity antagonism by chronic donepezil: A potential nerve agent treatment*, *Pharmac. Biochem, and Behavior*, 81(4), (2005) 917-922.

[10] Haug, K. H., Myhrer, T., Fonnum, F., *The combination of donepezil and procyclidine protects against soman-induced seizures in rats*, *Toxicol and App Pharmacol*, 220(2), (2007) 156-163.

[11] Albuquerque, E. X., Pereira, E. F. R., Aracava, Y., Fawcett, W. P., Oliveira, M., Randall, W. R., Hamilton, T. A., Kan, R. K., Romano, J. A., & Adler, M., *Effective countermeasure against poisoning by organophosphorus insecticides and nerve agents*, *Proceedings of the National Academy of Sciences of the United States of America*, 103(35) (2006) 13220-13225.

[12] Alexandrova, E. A., Alkondon, M., Aracava, Y., Pereira, E. F. R., & Albuquerque, E. X.: *Galantamine prevents long-lasting suppression of excitatory synaptic transmission in CA1 pyramidal neurons of soman-challenged guinea pigs*, *Neurotoxicolog*, 44, (2014) 270-278.

[13] Vitorović-Todorović M. D., Erić Nikolić A., Kolundžija B., Hamel E., Ristić S., Juranić I. O., Drakulić B. J.: *(E)-4-aryl-4-oxo-2-butenic acid amides, chalcone-aroilacrylic acid chimeras: design, antiproliferative activity and inhibition of tubulin polymerization*, *Eur J Med Chem*, 62 (2013) 40-50.

- [14] Vujatović T. B., Nikolić M. R., Vitorović-Todorović M. D., *The design and synthesis of three novel dual reversible inhibitors of acetylcholinesterase based on the tacrine substructures*, (2022) 10<sup>th</sup> International Scientific Conference on Defensive Technologies, 380-386, Belgrade: The Military Technical Institute.





## SIGNIFICANT CHARACTERISTICS OF LEAD AND ALLOYS WITH ANTIMONY IN THE PRODUCTION OF SMALL ARMS AMMUNITION

MIROSLAV PAPOVIĆ

Prvi partizan a.d., Užice, [mpapovic@prvipartizan.com](mailto:mpapovic@prvipartizan.com)

**Summary:** *The use of lead and its alloys is significant for military purposes (the production of revolver, handgun, rifle and other bullets). Bullets for small arms ammunition are mostly made of a two component alloy of lead and antimony. Bullets can be made only of lead/antimony alloy (lead bullets) or with a jacket (usually made of CuZn alloy) in which lead and antimony core is placed. Due to the specific purpose, the quality of lead and alloys with antimony must be high in order to provide the required ammunition characteristics: bullet velocity, accuracy (chemical composition and homogeneity of alloys), effects on the target (mass, shape, hardness), bullet weight (chemical components, type of alloys, density), pressure of powder gases (bullet hardness), the reduction of barrel lead process (chemical composition, hardness) ... This paper will present the results of the chemical composition (Optical emission spectrometry), hardness according to Vickers HV1 method and densities for two deliveries of refined lead and seven lead/antimony alloys. The obtained results present the characteristics of refined lead and lead/antimony alloys used for production of bullets for small arms ammunition, and are a good basis for designers of bullets for designing products and obtaining defined requirements.*

**Key words:** *lead, lead/antimony alloy, bullets for small arms ammunition, chemical composition, hardness according to Vickers HV1, density*

### 1. INTRODUCTION

The use of lead and its alloys with antimony is significant for the production of sheets, tapes, pipes, wires, batteries, plates for protection against radioactive radiation, chemical apparatus, lead paints, military purposes (production of rifle and other bullets)...

A two component alloy of lead and antimony is used for the production of small arms ammunition. Bullets can be made only from the lead/antimony alloy (lead bullets), or bullets with jacket (mostly of CuZn alloy), in which lead and antimony core is placed.

Lead is quite soft, ductile metal and can be cut with a knife.[1] Hardness according to Brinell is only 4 kp/mm<sup>2</sup>, according to Vickers 5 N/mm<sup>2</sup> [3] and according to Mohs scale 1,5, yield strength is from 0,5 to 0,8 kp/mm<sup>2</sup>, tensile strength from 1,1 to 1,9 kp/mm<sup>2</sup>, contraction 100% and elongation up to 50%. It belongs to heavy metals, its density is 11,34 g/cm<sup>3</sup>. The structure, as with other metals with a cubic face-centered crystal lattice, consists of polygonal grains with twins. The melting point is low, 327°C, so recrystallization after the deformation occurs already at room temperature. Therefore, hardening of lead by cold deformation is not possible. In the case of electrolytic lead, the grains growth occurs already at 100°C.

Antimony occurs in four allotropic modifications: a stable metallic form and three metastable forms (explosive, gray amorphous and yellow) [2]. Metallic antimony is a brittle, silvery, shiny-gray metal, of Brinell hardness 30-58 kp/mm<sup>2</sup>, Vickers 30-60 N/mm<sup>2</sup> [3], according to Mohs

scale its hardness is 3, tensile strength 11,4 MPa, density 6,68 g/cm<sup>3</sup> and a melting point of 630,5°C (at the same time, its volume decreases and when it solidifies, it increases). Elemental antimony has got a layered structure whose layers are consisted of joined, wrinkled, six-membered rings. Nearest and next-nearest neighbors form an irregular octahedral complex, where the three atoms in the same double layer are slightly closer than the three atoms in the next. This relatively dense packing is the cause of the high density (6,68 g/cm<sup>3</sup>), but the poor connection between layers leads to the low hardness and brittleness of antimony. [4]

Significant characteristics of alloys from which lead bullets and cores for small arms ammunition are made are chemical composition, hardness and density.

According to the recommendations, lead bullets and lead cores are made of refined lead and antimony.

The chemical composition of refined lead by grades is given in the Table 1. [5]

The chemical composition of refined antimony by grades is given in the Table 2. [6]

Lead and antimony alloys are denoted PbSbX, where the X refers to percentage content of antimony in the alloy in mass fractions, while the content of permitted impurities is conditioned by the basic standards for refined lead and antimony.

Lead-antimony alloys form a simple eutectic system (Figure 1.). The eutectic point is at 88,9% Pb + 11,1% Sb and 252°C. An  $\alpha$  -solid solution rich in lead dissolves

3,5% Sb at the eutectic temperature, and only 0,44% Sb at 100°C. The  $\beta$ -solid solution, rich in antimony, dissolves about 5% Pb at the eutectic temperature. The melting point of lead is lowered by the addition of antimony, and

the melting point of antimony by the addition of lead. Since  $\alpha$ - and  $\beta$ -solid solutions are separated primarily from the melt during cooling, and not pure metals, from Raoult's law does not apply.

**Table 1.** Composition of lead grades SRPS EN 12659 : in % (percentage mass concentration)

Designation	Lead content min.	ELEMENTS									
		Ag max.	As max.	Bi max.	Cd max.	Cu max.	Ni max.	Sb max.	Sn max.	Zn max.	Totally
PB990R	99,990	0,0015	0,0005	0,0100	0,0002	0,0005	0,0002	0,0005	0,0005	0,0002	0,010
PB985R	99,985	0,0025	0,0005	0,0150	0,0002	0,0010	0,0005	0,0005	0,0005	0,0002	0,015
PB970R	99,970	0,0050	0,0010	0,030	0,0010	0,0030	0,0010	0,0010	0,0010	0,0005	0,030
PB940R	99,940	0,0080	0,0010	0,060	0,0020	0,0050	0,0020	0,0010	0,0010	0,0005	0,060

**Table 2.** SRPS C.E1.200 :1988 Refined antimony in block – Technical conditions

Type	Designation	Sb min.	As max.	Pb max.	Fe max.	S max.	Totally remaining
1	Sb 99,60	99,60	0,08	0,20	0,05	0,04	0,03
2	Sb 99,50	99,50	0,10	0,27	0,05	0,04	0,04
3	Sb 99,5	99,5	0,16	0,30	0,06	0,04	0,04

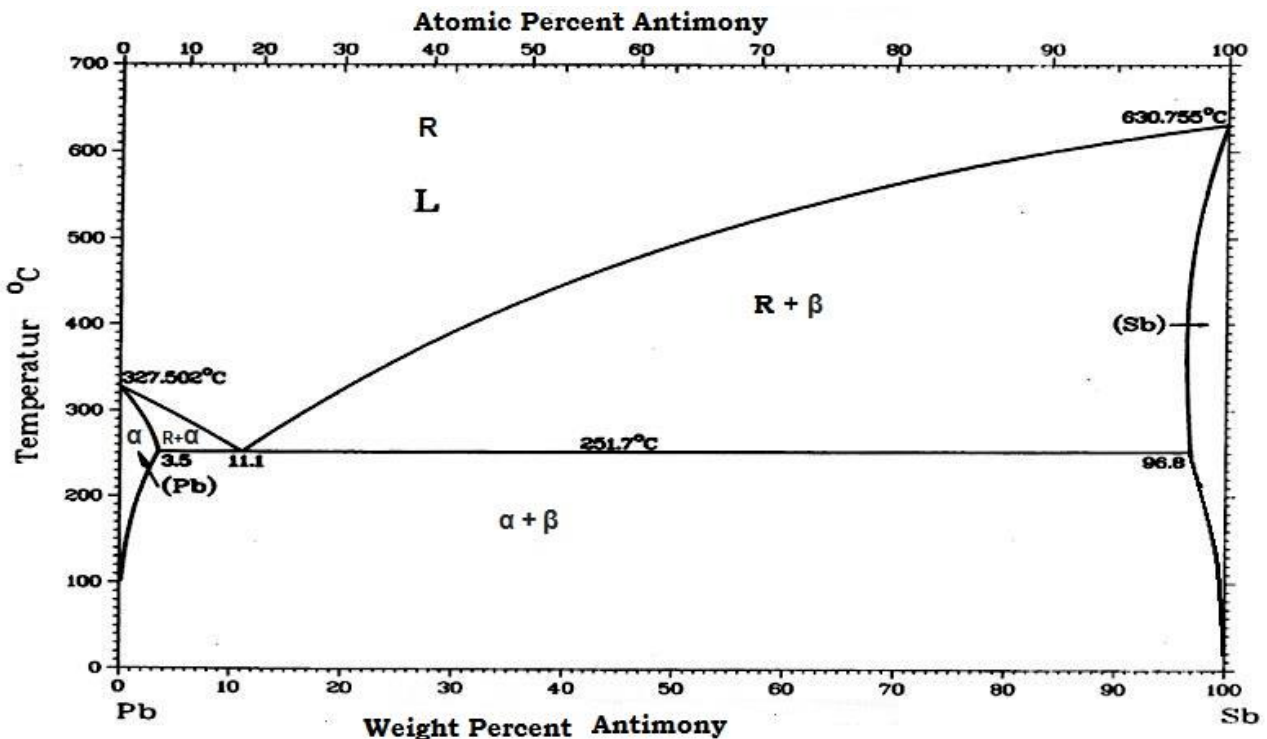


**Figure 1.** State diagram Lead - Antimony

On the state diagram of the lead-antimony, it should be understood that the left from 3,5% Sb is the  $\alpha$ -solid solution with a separated  $\beta$ -precipitate, from 3,5 to 11,1% Sb primary  $\alpha$ -solid solution and eutecticum ( $\alpha + \beta$ ), at 11,1 % Sb only eutecticum ( $\alpha + \beta$ ), from 11,1 to 95% Sb  $\beta$ -solid solution and eutecticum ( $\alpha + \beta$ ) and from 95 to 100% Sb  $\beta$ -solid solution with a separate  $\alpha$ -precipitate. In the phase field, the designation " $\alpha + \beta$ " refers only to type of crystals actually present. Nothing is said about their distribution and size i.e. whether it is a primary crystal, eutecticum or and the absolute amount. The alloy

structure must be derived based on the course of crystallization.

The structural rectangle in Figure 2. provides data on the type and the amount of the structural components in an eutectic system. It shows that, in the case of equilibrium, the alloy with 50% Pb + 50% Sb contains 54% of eutecticum, 44% of primary  $\beta$ -solid solution and 2% of  $\alpha$ -precipitate.

On the cooling curves, separation of primary crystals gives an inflection point, and solidification of the eutectic melt, i.e. the rest of the melt, occurs at constant temperature

gives which is presented as a plate on cooling curve. Figure 3. shows a selection of various colling curves of the lead-antimony system. While pure lead (curve 1) and pure antimony (curve 5) show stoppage at a melting temperature of 327°C and 630°C, respectively, all hypoeutectic alloys have an inflection point, which shows the primary separation of  $\alpha$ - solid solution (curve 2), and all hypereutectic alloys have an inflection point that shows the primary separation of  $\beta$  –solid solution (curve 4). All Pb-Sb alloys which contain Sb between 3,5 and 95% show stoppage at eutectic temperature of 252°C, caused by the solidification of the eutecticum (curves 2,3,4). The cooling curve for eutectic alloy shows change in cooling rate only during eutectic reaction which is illustrated as a plate. (curve 3). The length of the eutectic stoppage, assuming the same weight of the melt, is proportional to the amount of solidified eutecticum, so it is the largest in the eutectic alloy. [1]

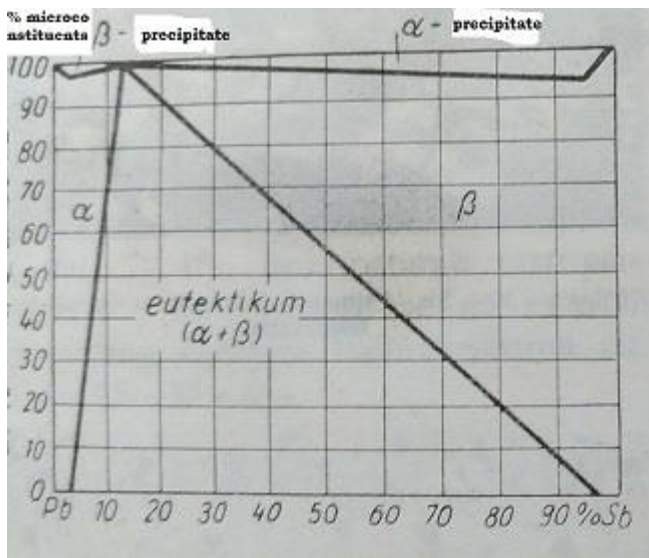


Figure 2. Structural rectangle of lead - antimony alloy

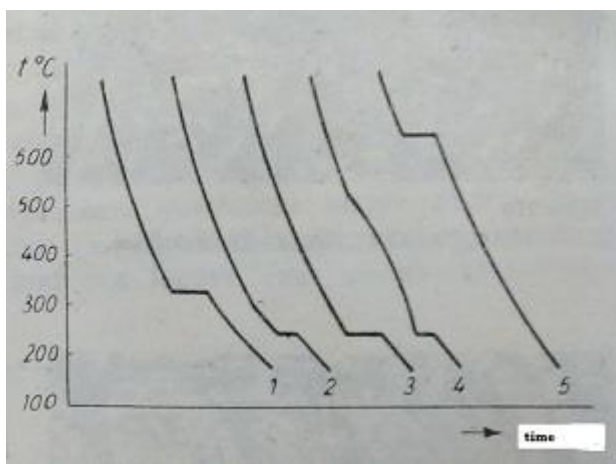


Figure 3. Cooling curves of lead-antimony alloys:  
1 : 100% Pb, 2: PbSb5, 3: PbSb11, 4: PbSb60, 5: 100%Sb

## 2. EXPERIMENTAL PART

Determination of characteristics is performed on delivered samples (1,2,7,8,9), as well as on samples produced in our production (3,4,6) from refined lead and antimony

(composition stated in Table 3.).

**Table 3.** Refined antimony for sample alloying 3,4,6  
In % (percentage mass concentration)

Grades des.	Sb	As	Pb	Fe	S
<b>Sb 99,60</b>	99,67	0,002	0,109	-	-

Chemical composition of refined lead and PbSbX alloys is determine by the Optical emission spectrometry (OES) by spark excitation according to Standard SRPS ENV 12908 Lead and lead alloys – Analysis with optical emission spectrometry (OES) by spark excitation [7] on device *Spectro Maxx F LMX 06* .

For each sample, five to ten analyses have been performed, based on the quantity delivered, and on different samples.

Determination of hardness of refined lead and antimony, as well as their alloys, was performed in accordance with Standard SRPS EN ISO 6507-1:2018 – Metal materials – Vickers hardness test method - Part 1: The testing method [8] with HV1 load on device *Falcon 500 Inova Test*. The hardness is tested on five separate samples, two places for each sample, meaning that there were ten measurements for each sample with a known chemical composition. Determination of density of the samples was performed according to the Standard ISO 2781 : 2018 – Rubber, vulcanized or thermoplastic [9], by the method A: sample weight and the mass of water equal to the volume of the sample is determined using a balance with a spring (the accuracy 0,0001 g). The apparent mass of tested sample once immersed in water is less than the sample weight in air by the mass of water displaced, where the volume of displaced mass of water is equal to sample volume for testing. The test sample was free of cracks and dust, and weighed at least 2,5 grams. For all samples of refined lead, antimony and alloys, the measurement was performed on three different pieces.

## 3. RESULTS AND DISCUSSION

The results of chemical composition of refined lead and PbSbX alloys are given in the Table 4. The table shows the results of the mean content values with the corresponding standard deviation. From the obtained results, it can be concluded that the quality of refined lead is in accordance with requirements of the Standard, and that it corresponds to grade PB970R. PbSbX alloys in its chemical composition contain impurities in accordance with allowed content of impurities, which is determined by the impurities content of refined lead and antimony. In further analysis, it can be claimed that it's a binary PbSbX alloy, and that the influence of impurities can be disregarded. A very small standard deviation for all elements shows that all samples are homogeneous, i.e. the chemical composition is uniform.

The hardness results according to the Vickers method with HV1 load of refined lead and PbSbX alloys are given in the Table 5. The table shows results of mean hardness values with the corresponding standard deviation. The hardness of refined lead conform to theory according ( to Vickers method – 5 N/mm<sup>2</sup> [3]). The obtained hardnesses

**Table 4.** Chemical composition of samples of refined lead and PbSbX alloys: Composition in % (percent mass concentration) / Standard deviation

Designation of sample	Designation of material	Lead composition	Elements									
			Ag	As	Bi	Cd	Cu	Ni	Sb	Sn	Zn	S
Sample 1	PB970R	99,979	0,0017	0,001	0,0111	<0,00005	0,00054	0,00013	0,001	0,00028	0,00013	<0,0010
		0,0026	0,00001	0,00012	0,00006	0,000	0,00014	0,00001	0,00008	0,0001	0,00003	0,000
Sample 2	PB970R	99,977	0,00058	0,001	0,0153	<0,00005	0,00077	0,00013	0,001	0,00033	0,00047	<0,0010
		0,0019	0,00001	0,0014	0,00006	0,000	0,00041	0,00002	0,00007	0,0001	0,00017	0,000
Sample 3	PbSb1,26	98,717	0,0016	0,0029	0,0105	<0,00010	0,0021	0,00021	1,26	<0,00030	0,00051	0,002
		0,0172	0,00005	0,00021	0,00013	0,000	0,0026	0,0001	0,0172	0,00001	0,0008	0,00038
Sample 4	PbSb2,43	97,55	0,0016	0,0048	0,0104	<0,00010	0,0010	0,00027	2,43	<0,00030	0,00021	0,0024
		0,0412	0,00007	0,00017	0,0001	0,000	0,00015	0,00005	0,041	0,000	0,00005	0,00046
Sample 5	PbSb4,48	95,50	0,0019	0,0011	0,0115	<0,00010	0,00041	0,00042	4,48	<0,00030	0,00019	0,0019
		0,028	0,00003	0,00028	0,00008	0,000	0,00004	0,00007	0,0028	0,000	0,00001	0,00016
Sample 6	PbSb6,57	93,39	0,0018	0,0137	0,0102	<0,00010	0,00077	0,0002	6,57	<0,00030	0,00024	0,0028
		0,10	0,00003	0,00018	0,00012	0,000	0,00002	0,00009	0,10	0,000	0,00001	0,00022
Sample 7	PbSb9,1	90,84	0,0014	0,0012	0,0054	0,00048	0,0391	0,0032	9,1	<0,00030	0,00029	0,0019
		0,0385	0,00001	0,00015	0,00004	0,00003	0,00021	0,00009	0,0381	0,000	0,000	0,0004
Sample 8	PbSb11,06	88,92	0,0022	0,0014	0,0131	<0,00010	0,00076	0,00043	11,06	<0,00030	0,00029	<0,0010
		0,182	0,00052	0,00023	0,0019	0,000	0,00046	0,00009	0,185	0,000	0,00002	0,00007
Sample 9	PbSb12,45	87,52	0,0026	0,0079	0,0052	0,00019	0,0046	0,0016	12,45	<0,00030	0,00029	<0,0010
		0,795	0,00019	0,0014	0,00025	0,000	0,0001	0,0001	0,794	0,000	0,00002	0,000

**Table 5.** Hardness HV1 and density (g/cm<sup>3</sup>) of samples

Designation of sample / Designation of material	HV1 / $\delta$	$\rho$ (g/cm <sup>3</sup> ) / $\delta$
Sample 1 PB970R	4,67 / 0,07	11,354 / 0,014
Sample 2 PB970R	3,32 / 0,18	11,3337 / 0,022
Sample 3 PbSb1,26	8,60 / 0,48	11,1978 / 0,065
Sample 4 PbSb2,43	10,38 / 0,42	11,145 / 0,030
Sample 5 PbSb4,48	14,08 / 0,53	10,983 / 0,029
Sample 6 PbSb6,57	14,41 / 0,66	10,9515 / 0,179
Sample 7 PbSb9,1	15,10 / 0,43	10,7714 / 0,156
Sample 8 PbSb11,06	13,1 / 0,57	10,503 / 0,0377
Sample 9 PbSb12,45	16,77 / 1,0	9,954 / 0,122
Refined antimony Sb 99,60	68,8/4,71	6,65/0,038

for tested samples of 3,32 and 4,67 N/mm<sup>2</sup> confirm this. Although by chemical composition they belong to the same 970R group, differences in hardness values were obtained for different deliveries.. These differences may be the result of the chemical composition (different content of impurities affect the course of crystallization in microvolumes), the origin of the refined lead (whether it's obtained from ores or recycling process), technological production process (cooling speed and other conditions of lead crystallization)...

In order to answer the question about differences in hardness of two tested samples of refined lead, it would be necessary to know all information about lead production. Since no complete information is available it is only possible to speculate .

Therefore, this information must be kept in mind in the process of designing and manufacturing of bullets for small arms ammunition. In the production process of bullets for small arms ammunition, the chemical composition of refined lead and antimony is controlled, and based on it, the criteria for the raw materials acceptance for alloy production is carried out, in order to obtain alloys with the required characteristics.

The hardness of PbSbX alloys increases by increasing antimony content (Figure 4. curve 1), until at the eutectic point (11,1 % Sb) occurs decrease in hardness, and after that, the hardness continues to increase. The hardness of the alloy depends on the type and quantity of structural components of the alloy, their distribution and size, i.e. whether it is a primary crystal, eutectic or precipitate. The structure of the alloy must be derived based on the course of crystallization. The structural rectangle in Figure 2. provides data on the type and quantity of structural components in a eutectic system.

The increase in hardness with an antimony content of up to 3,5% ( $\alpha$ -solid solution with separated  $\beta$ -precipitate) is significant and the hardness increases from about 5 N/mm<sup>2</sup> to about 12 N/mm<sup>2</sup>. The increase in hardness with antimony content from 3,5 to 11,1 % (primary  $\alpha$  - solid solution and eutectic ( $\alpha + \beta$ )) is insignificant and increases from 14,08 HV1 (Sb content 4,48 %) to 15,10 HV1 for an antimony content of 9.1%.

Hence, when added twice the amount of antimony, the hardness increases by only one HV1 hardness unit.

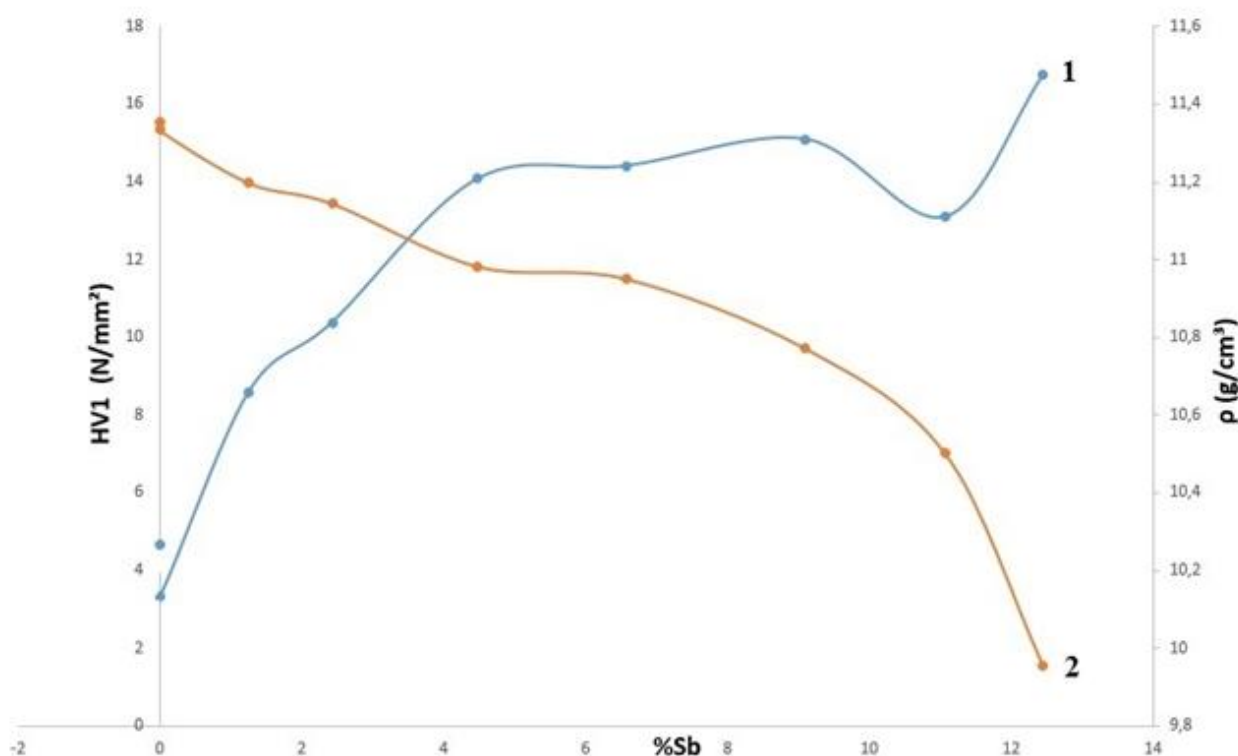


**Figure 4.** Dependence of Vickers hardness HV1 (curve 1) and density (curve 2) on antimony content obtained in this research

If the hardness of the alloy is an important characteristic for the product, it is recommended that no more than 5% antimony be added to the alloy, as this will result in twice as much antimony being consumed and very little influence on hardness.

To achieve the highest optimum hardness, it is recommended to provide an alloy with 4 to 5% antimony. At the eutectic point (only eutectic ( $\alpha + \beta$ )), there is a drop in hardness, due to the structure of the alloy that is being produced, that is the reason why is not recommended to make alloys that are in the zone around the eutectic point (10,5 to 11,5 % Sb). After the eutectic point, with the antimony content increase, the hardness of the alloy increases (12,45% Sb – hardness 16,77 HV1). Due to the high price of refined antimony (five to seven times more expensive than lead), there is a stand that it is not economically viable to produce alloys with antimony contents higher than 11,5% since it produces small increase in hardness.

The results of the densities of refined lead and PbSbX alloys are shown in Table 5., and the average density values with related standard deviation are provided. The obtained results for the density of refined lead match the literature value 11,34 g/cm<sup>3</sup> [1] (11,3337 and 11,354 g/cm<sup>3</sup>). Small differences (in the second decimal place) probably come from the presence of impurities that are within the limits prescribed for refined lead. The obtained results for the density of refined antimony coincide with the literature value of

6,68 g/cm<sup>3</sup> [2] (6,65 g/cm<sup>3</sup>).

With an increase in the antimony content in the alloy, the density of the alloy decreases due to the addition of alloying antimony with a lower density than the base metal, which is shown in Figure 4. - curve 2. As the bullet mass or core of small arms ammunition are directly dependent on the density of the alloy, also taking into account other requested requirements for the product, alloys can be selected during the product design phase and later during manufacturing in accordance with the previously determined alloy characteristics.

## CONCLUSIONS

In this research are determined chemical composition, hardness according to the Vickers HV1 method and density for two shipments of refined lead and seven lead/antimony alloys. Based on the obtained results, the conclusions are as follows:

1. The quality of refined lead is in accordance with the requirements of Standard SRPS EN 12659 and corresponds to type PB970R. The quality of the refined lead corresponds to the recommendations for the bullet production and bullet core for small arms ammunition.
2. PbSbX alloys in their chemical composition have an impurity content in accordance with the permitted impurity content, which is determined by the impurity content of refined lead and antimony. The influence of

impurities can be ignored, and all other analysis were performed with assertion that it is a binary alloy PbSbX.

3. The hardness of refined lead is in accordance with the theory (according to Vickers 5 N/mm<sup>2</sup>).

The obtained results for hardness of tested samples of 3,32 and 4,67 N/mm<sup>2</sup> confirm this, but also indicate that there are differences for different deliveries even though they belong to the same PB970R group according to their chemical composition. In the process of bullet production of small arms ammunition, the chemical composition of refined lead and antimony is controlled and based on it the acceptance of raw materials for alloy production is carried out. The hardness of the initial raw materials also affects the characteristics of the alloys and should be defined and determined in the raw material verification process, in order to obtain alloys with the required characteristics..

4. The hardness of PbSbX alloys increases with the increase in antimony content (Figure 4.), until in the eutectic point (11,1% Sb) occurs decrease, and after that, the hardness continues to increase. The increase in hardness with an antimony content of up to 3,5% ( $\alpha$ -solid solution with a separated  $\beta$ -precipitate) is significant and the hardness increases from about 5 N/mm<sup>2</sup> to about 12 N/mm<sup>2</sup>.

The increase in hardness with antimony content from 3,5 to 11,1 % (primary  $\alpha$ -solid solution and eutectic ( $\alpha + \beta$ )) is insignificant and increases from 14,08 HV1 (Sb 4,48 %) to 15,10 HV1 (Sb 9,1%). Meaning, when added twice the amount of antimony, the hardness increases by only one HV1 hardness unit.

At the eutectic point (only eutectic ( $\alpha + \beta$ )), there is a drop in hardness due to the structure of the alloy that is being produced. After the eutectic point (11.1% Sb), by increasing the antimony content in the alloy ( $\beta$ -solid solution and eutectic ( $\alpha + \beta$ )), the hardness of the alloy increases (16,77 HV1 – 12,45% Sb).

5. The obtained results for the density of refined lead match the literature value of 11,34 g/cm<sup>3</sup> (11,3337 and 11,354 g/cm<sup>3</sup>).

6. Obtained results for the density of refined antimony match the literature value of 6,68 g/cm<sup>3</sup> (6,65 g/cm<sup>3</sup>).

7. By increasing antimony content in the alloy, the density of the alloy decreases (Figure 4.) due to the addition of alloying antimony with a lower density (6,68 g/cm<sup>3</sup>) from the base metal. As the bullet mass or core of small arms ammunition is directly dependent on the density of the alloy, alloys can be selected in the product design phase based on the determined density dependence of the antimony content in the alloy.

### Acknowledgements:

I would like to thank my colleagues from the Laboratory of Prvi Partizan Uzice for their help while working on the experimental part of this research: Vesna Mirković, Snežana Jovičić and Mileša Filipović.

### References

- [1] H. Suman: Metallography, Serbian Institute for Publishing, Belgrade 1965, 151-157; 503-504; 509.
- [2] S. Arsenijevic: General and inorganic chemistry, Science book, Belgrade 1990, 394
- [3] [www.matweb.com](http://www.matweb.com)
- [4] [www.sr.wikipedia.org](http://www.sr.wikipedia.org)
- [5] SRPS EN 12659: Lead and lead alloys-Lead, Institute for Standardization of Serbia 2013.
- [6] SRPS C.E1.200:1988: Refined antimony in block - Technical conditions, Institute for Standardization of Serbia 1988.
- [7] SRPS ENV 12908: Lead and lead alloys - Analysis by optical emission spectrometry (OES) with spark excitation, Institute for Standardization of Serbia 2013.
- [8] SRPS EN ISO 6507-1:2018 – Metallic materials – Vickers hardness test – Part 1: Test method, Institute for Standardization of Serbia 2018.
- [9] ISO 2781:2018: Rubber, vulcanized or thermoplastic — Determination of density, International Organization for Standardization 2018.



## ADSORBING DANGER: CARBON MATERIAL COMBATting ORGANOPHOSPHATE

TAMARA TASIĆ

University of Belgrade, "VINČA" Institute of Nuclear Sciences - National Institute of the Republic of Serbia, Mike Petrovica Alasa 12-14, 11000 Belgrade, Serbia, [tamara.tasic@vin.bg.ac.rs](mailto:tamara.tasic@vin.bg.ac.rs)

VEDRAN MILANKOVIĆ

University of Belgrade, "VINČA" Institute of Nuclear Sciences - National Institute of the Republic of Serbia, Mike Petrovica Alasa 12-14, 11000 Belgrade, Serbia, [vedran.milankovic@vin.bg.ac.rs](mailto:vedran.milankovic@vin.bg.ac.rs)

VLADAN ANIĆIJEVIĆ

University of Defence Belgrade, Military Academy, Generala Pavla Jurišića Šturma 33, 11000 Belgrade, Serbia, [anicijevic.v@gmail.com](mailto:anicijevic.v@gmail.com)

IGOR PAŠTI

University of Belgrade, Faculty of Physical Chemistry, Studentski Trg 12, 11000 Belgrade, Serbia, [igor@ffh.bg.ac.rs](mailto:igor@ffh.bg.ac.rs)

TAMARA LAZAREVIĆ-PAŠTI

University of Belgrade, "VINČA" Institute of Nuclear Sciences - National Institute of the Republic of Serbia, Mike Petrovica Alasa 12-14, 11000 Belgrade, Serbia, [tamara@vin.bg.ac.rs](mailto:tamara@vin.bg.ac.rs)

**Abstract:** Organophosphates are a class of compounds known for their use as chemical warfare agents. These agents have been utilized in military contexts due to their ability to act as nerve agents, disrupting the nervous system's function. However, beyond their military application, organophosphates pose significant risks to human health and the environment. Exposure to these compounds can lead to severe neurological effects and even death in high concentrations. Moreover, organophosphates can persist in the environment, contaminating soil, water, and air, posing long-term risks to ecosystems and public health. Therefore, developing effective strategies for removing organophosphates is crucial. This study investigates the efficacy of carbon material in removing organophosphate malathion from aqueous systems. Carbon material was characterized using SEM and EDX. Experimental results were analyzed using four nonlinear isotherm models: Freundlich, Langmuir, Temkin, and Dubinin-Raduskevich model. The study revealed that 1 g of the examined material could adsorb 18.92 mg of malathion at 25°C. Furthermore, neurotoxicity was assessed, and it was found that treatment with the adsorbent led to a reduction in toxicity. The findings underscore the promising role of carbon material as an effective adsorbent for removing malathion.

**Keywords:** malathion, adsorption, neurotoxicity.

### 1. INTRODUCTION

Organophosphate compounds, such as malathion (**Figure 1**), are used as chemical warfare agents because they disrupt the nervous system by inhibiting acetylcholinesterase (AChE), an essential enzyme for nerve function [1]. This inhibition leads to the accumulation of acetylcholine, causing continuous nerve signal transmission, resulting in muscle spasms, respiratory failure, and potentially death [2].

Malathion is an organophosphate insecticide commonly used to control insects in agricultural and residential areas [3]. Though malathion has relatively low toxicity to humans and mammals, it can transform into a more toxic compound, malaaxon, through oxidation by environmental factors such as air and sunlight or through metabolic processes in organisms [4]. This transformation

involves replacing malathion's sulfur atom with an oxygen atom, significantly increasing its potency as an acetylcholinesterase inhibitor and, thereby, its toxicity [5]. Environmental conditions, like high temperatures and certain microbes, can accelerate this conversion, raising concerns about potential health risks. Therefore, while malathion is generally safe when used correctly, the possibility of malaaxon formation necessitates careful monitoring and management to prevent harmful effects on humans and non-target organisms [6].

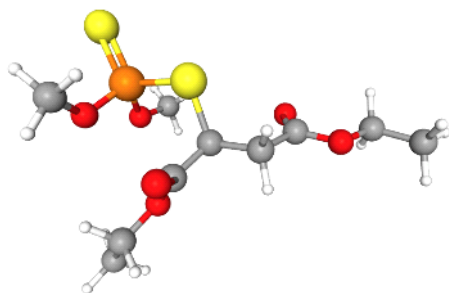


**Figure 1.** Structure of malathion

Removing these compounds from the environment is crucial because their high toxicity poses severe risks to human health and ecological systems. Persistent soil, water, and air contamination can lead to long-term exposure, affecting populations and wildlife and disrupting ecosystems. Therefore, effective removal strategies are essential to mitigate these hazards and ensure public and environmental safety [7, 8].

Various methods have been investigated for eliminating organophosphates, including biodegradation, photocatalysis, electrochemical treatment, membrane separation, and oxidation. Among these, adsorption has gained attention for its simplicity and cost-effectiveness [7].

Different types of materials can be used to remove organophosphate from the environment. Activated carbon, in particular, has proven highly effective due to its large specific surface area, porosity, thermal stability, and low reactivity with acids and bases. Carbon materials produced from agricultural, industrial, or biomass waste carbonization also present a sustainable and efficient option for organophosphate removal [9, 10].

The study aims to investigate the efficacy of carbon material in removing the organophosphate malathion from aqueous systems. This includes determining the carbon material's adsorption capacity for malathion and evaluating its potential for reducing toxicity.

## 2. MATERIALS AND METHODS

### 2.1. Material synthesis

Viscose fibers were used as the precursor. These fibers were thoroughly washed with distilled water before use. Post-washing, they were centrifuged using a spin dryer for 15 minutes and then dried at 90 °C for 24 hours in a drying cabinet.

The carbonization process involved loading 100 – 400 g of the precursor into a chamber furnace (HTK 8 W, Carbolite Gero GmbH, Germany). After evacuating the chamber, a nitrogen flow of 250 L h<sup>-1</sup> was introduced. The sample was heated to 850 °C at a rate of 1.0 °C min<sup>-1</sup> and held at that temperature for 30 minutes. Cooling to room temperature was conducted under a nitrogen atmosphere.

Following carbonization, the activation process occurred in a rotary kiln (RSR-B 120/500/11, Nabertherm GmbH, Lilienthal, Germany). For this, 10 g of the carbonized material was placed in the center of a quartz glass reactor. Initially, the setup was purged of air using N<sub>2</sub> at a flow rate of 100 L h<sup>-1</sup>. The sample was then heated from room temperature to 770 °C under an N<sub>2</sub> flow rate of 50 L h<sup>-1</sup> and maintained at this temperature for 30 minutes to ensure uniform heating throughout the reactor. Afterwards, the N<sub>2</sub> flow was stopped, and CO<sub>2</sub> was introduced at a flow rate of 45 L h<sup>-1</sup> for 180 minutes. The activation process was completed by the termination of the CO<sub>2</sub> flow and restarting of the N<sub>2</sub> flow (50 L h<sup>-1</sup>) until the kiln was cooled to room temperature.

### 2.2. Material characterization

The assessment of the structure and elemental composition of the samples was conducted using the PhenomProX Scanning Electron Microscope (SEM) from Thermo Fisher Scientific (Waltham, MA, USA), in combination with Energy Dispersive X-ray Analysis (EDX). Nicolet iS20 FT-IR spectrophotometer (Thermo Fisher Scientific, Waltham, MA, USA) was used for the FTIR spectra recording. The applied wavenumber range was from 4000 to 500 cm<sup>-1</sup> with 64 scans and 4 cm<sup>-1</sup> resolution.

### 2.3. Adsorption experiments

Adsorption experiments were conducted in stationary conditions, where adsorbent was initially dispersed in double-distilled water and then combined with organophosphate stock solution to achieve desired concentrations. The mixture underwent shaking and incubation at 25 °C, followed by centrifugation and filtration of the supernatant through a nylon filter. Ultra-performance liquid chromatography (UPLC) was then used to analyze the malathion concentration post-adsorption. Uptake efficiency was calculated as follows:

$$\text{Uptake} = 100\% \times (C_0 - C_{eq})/C_0 \quad (1)$$

, where  $C_0$  is the initial concentration of organophosphate, and  $C_{eq}$  is the concentration after adsorption. Control experiments were conducted without adsorbent. Malathion analysis utilized the Waters ACQUITY UPLC system with a photodiode array (PDA) detector, employing a mobile phase of 40% acetonitrile in water (v/v) and 60% pure acetonitrile.

### 2.4. Neurotoxicity of malathion

Measurements of AChE inhibition were conducted to monitor and quantify changes in the toxicity of malathion solutions pre- and post-adsorption. This assessment also aimed to explore any potential conversion of malathion into more toxic forms during hydrolysis, which could induce adverse effects even at concentrations below the detection threshold of UPLC. AChE activity was evaluated using a modified Ellman's procedure, wherein 1 U/mL AChE was exposed to malathion solutions before and after adsorption experiments at 37 °C in 50 mmol



dm<sup>-3</sup> PB pH 8.0 (final volume 0.650 cm<sup>3</sup>). The enzymatic reaction was initiated by adding acetylcholine-iodide along with DTNB as a chromogenic reagent and allowed to proceed for 8 min before termination with 10% sodium dodecyl sulfate (SDS). Thiocholine, the enzymatic reaction product, reacted with DTNB, forming 5-thio-2-nitrobenzoate, the optical absorption of which was measured at 412 nm. Physiological effects were quantified through AChE inhibition, calculated as follows:

$$\text{AChE inhibition (\%)} = 100 \times (A_0 - A) / A_0 \quad (2)$$

, where A<sub>0</sub> and A represent AChE activity in the absence of malathion and after exposure to malathion, respectively.

### 3. RESULTS AND DISCUSSION

#### 3.1. Materials characterization

To investigate the morphology of the material, we used SEM. From **Figure 2**, it can be seen that the morphology of the sample is the same and reflects the morphology of precursor viscose fibers.

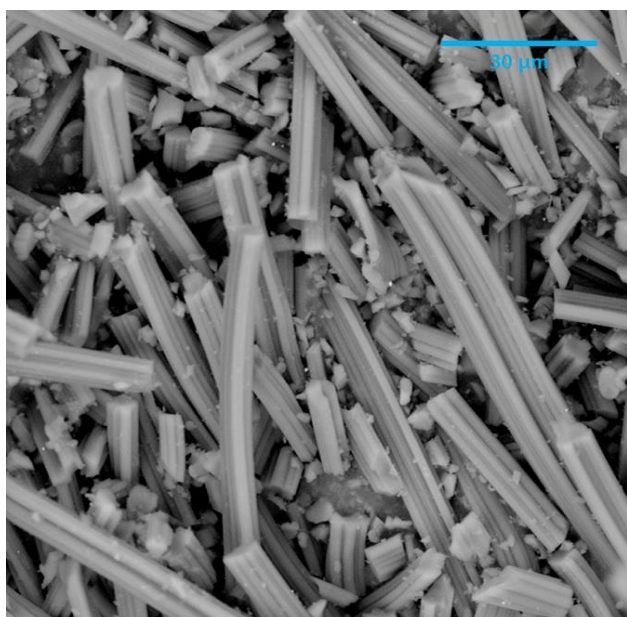


**Figure 2.** SEM micrograph of the carbon material

Also, the chemical composition of the material was investigated using EDX analysis. The material was found to have 91.83% carbon, 7.91% oxygen, 0.22% sodium and 0.05% sulfur.

From the FTIR spectra presented in **Figure 3**, it can be seen that two bands stand out. The first band at 1613 cm<sup>-1</sup> represents the in-plane vibrations of sp<sup>2</sup> hybridized C=C bonds, while the second band at 1242 cm<sup>-1</sup> is attributed to C-OH vibrations [11].

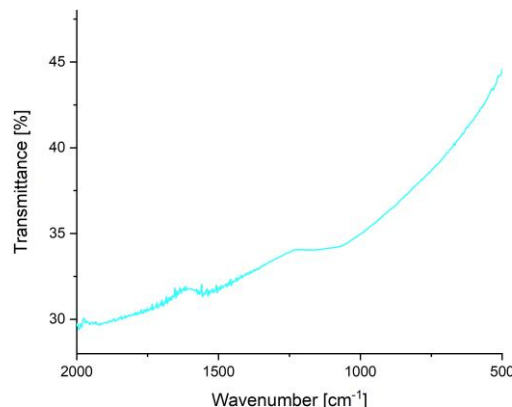


**Figure 3.** FTIR spectra of investigated carbon material

#### 3.2. Adsorption isotherms

The thermodynamic aspects of the adsorption process for malathion were investigated by constructing adsorption isotherms and fitting experimental data to various adsorption isotherm models, each offering unique insights into the process. Freundlich (3), Langmuir (4), Temkin (5), and Dubinin-Radushkevich (6) models were employed for this analysis. **Figure 4** illustrates the experimental data points alongside the corresponding fits, while the fitted parameters are presented in **Table 1**.

$$q_e = K_F C_e^{1/n} \quad (3)$$

$$q_e = \frac{q_{max} K_L C_e}{1 + K_L C_e} \quad (4)$$

$$q_e = \frac{RT}{b_T} \ln K_T C_e \quad (5)$$

$$q_e = q_{DR} e^{-K_{DR} \epsilon^2} \quad (6)$$

where q<sub>e</sub> (mg g<sup>-1</sup>) represents equilibrium adsorption capacity, C<sub>e</sub> (mg dm<sup>-3</sup>) equilibrium adsorbate concentration, K<sub>F</sub> (mg g<sup>-1</sup> (mg dm<sup>-3</sup>)<sup>1/n</sup>) and n Freundlich constants, K<sub>L</sub> (dm<sup>3</sup> mg<sup>-1</sup>) and q<sub>max</sub> (mg g<sup>-1</sup>) Langmuir constant and theoretical maximum adsorption capacity of the monolayer, b<sub>T</sub> (J g mol<sup>-1</sup> mg<sup>-1</sup>) and K<sub>T</sub> (dm<sup>3</sup> mg<sup>-1</sup>) Temkin isotherm constant, q<sub>DR</sub> maximum adsorption capacity, K<sub>DR</sub> (mol<sup>2</sup> J<sup>-2</sup>) constant associated with the mean free adsorption energy per mole of adsorbent, ε = RT × ln(1 + 1/C<sub>e</sub>).

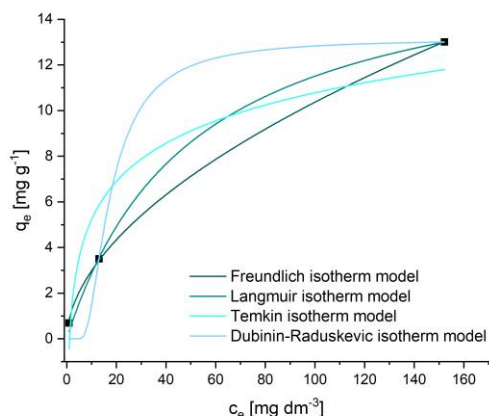


**Figure 4.** Adsorption isotherms for malathion removal at 25°C

**Table 1.** Parameters for the adsorption of malathion onto carbon material using Freundlich, Langmuir, Temkin, and Dubinin-Radushkevich isotherm at 25°C

Parameters	
Freundlich isotherm	
n	1.81
$K_F ((dm^3 mg^{-1})^{1/n})$	0.81
$\chi^2$	0.026
$R^2$	0.999
Langmuir isotherm	
$K_L (dm^3 mg^{-1})$	0.01
$q_{max} (mg g^{-1})$	18.92
$\chi^2$	0.334
$R^2$	0.988
Temkin isotherm	
$K_T (dm^3 mg^{-1})$	0.74
$b_T (J g mol^{-1} mg^{-1})$	1082.67
$\chi^2$	6.825
$R^2$	0.755
Dubinin-Raduskevich isotherm	
$q_{DR} (mg g^{-1})$	13.02
$K_{DR} (mol^2 J^{-2})$	$1.05 \times 10^{-4}$
$E (J mol^{-1})$	69.13
$\chi^2$	5.602
$R^2$	0.799

From the parameters presented in **Table 1**, it can be concluded that the Freundlich isotherm model best fits the experimental data, indicating predominantly physisorption on the heterogeneous surface of carbon material. The n value in the Freundlich isotherm model is 1.81, indicating the adsorption process's favorable nature. Additionally, analysis based on the Dubinin-Radushkevich model, specifically the calculated adsorption free energy per mole of adsorbent ( $E < 8 kJ mol^{-1}$ ), verifies that the adsorption process of malathion is predominantly physisorption, indicating the absence of chemical bond formation between malathion and the investigated activated carbon material.

### 3.3. Neurotoxicity of malathion solutions

The toxicity of the malathion solution was evaluated using the AChE inhibition assay described in Section 2.4., with results presented in **Figure 5** and **Table 2**. Data from toxicity assessments indicated a consistent reduction in the toxicity of malathion solutions following adsorption treatment under the specified experimental conditions. Importantly, this process did not generate more toxic byproducts that would lead to stronger inhibition of AChE.

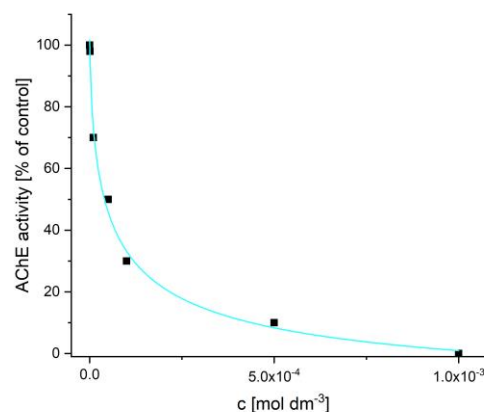


**Figure 5.** The dependence of AChE activity inhibition from malathion concentration

**Table 2.** AChE inhibition of malathion solution

C (mol dm <sup>-3</sup> )	AChE inhibition (% of control)
$2.5 \times 10^{-6}$	5.00
$2.5 \times 10^{-5}$	22.39
$5 \times 10^{-5}$	26.64
$1.25 \times 10^{-4}$	47.63
$2.5 \times 10^{-4}$	63.41

## 4. CONCLUSION

Activated carbon material derived from viscose fibers was employed to remove malathion from water, demonstrating promising results. Specifically, 1 gram of the investigated material exhibited the capability to adsorb 18.92 mg of malathion. Moreover, the adsorption process followed the Freundlich isotherm model under the given conditions, indicating that the adsorption process is most likely physisorption onto the heterogenous surface of carbon material. Additionally, toxicological analysis of aqueous malathion solutions post-treatment with the adsorbent revealed a declining trend in toxicity, indicating the absence of more toxic byproducts formed during the process. Thus, the removal of malathion utilizing the tested adsorbent proved to be successful.

### Acknowledgments

The researchers acknowledge the support provided by the Serbian Ministry of Education, Science and Technological Development (contract number: 451-03-66/2024-03/200017 and 451-03-65/2024-03/200146).

**References**

- [1] MUKHERJEE, S., GUPTA, R.D., *Organophosphorus Nerve Agents: Types, Toxicity, and Treatments*, J Toxicol, 2020 3007984.
- [2] CLOVIĆ, M.B., KRSTIĆ, D.Z., LAZAREVIĆ-PAŠTI, T.D., BONDŽIĆ, A.M., VASIĆ, V.M., *Acetylcholinesterase inhibitors: pharmacology and toxicology*, Curr Neuropharmacol, 11 (2023) 315-335.
- [3] REED, N.R., RUBIN, A.L., *Malathion*, in *Encyclopedia of Toxicology (Third Edition)*, P. Wexler, Academic Press, Oxford, 2014.
- [4] TCHOUNWOU, P., PATOLLA, A., YEDJOU, C., MOORE, P., *Environmental Exposure and Health Effects Associated with Malathion Toxicity*, InTech, 2015.
- [5] JEDNSEN, I.M., WHATLING, P., *Chapter 71 - Malathion: A Review of Toxicology*, in *Hayes' Handbook of Pesticide Toxicology (Third Edition)*, Academic Press, New York, 2010 1527-1542.
- [6] DAR, M.A., KAUCHIK, G., *Optimizing the malathion degrading potential of a newly isolated Bacillus sp. AGM5 based on Taguchi design of experiment and elucidation of degradation pathway*, Biodegradation, 33 2022 419-439.
- [7] ORE, O.T., ADEOLA, A.O., BAYODE, A.A., ADEDIPE, D.T. NOMNGONGO, P.N., *Organophosphate pesticide residues in environmental and biological matrices: Occurrence, distribution and potential remedial approaches*, Environmental Chemistry and Ecotoxicology, 5 2023 9-23.
- [8] MALI, H., SHAH, C., RAGHUNANDAN, B.H., PRAJAPATI, A.S., PATEL, D.H., TRIVEDI, U., SUBRAMANIAN, R.B., *Organophosphate pesticides an emerging environmental contaminant: Pollution, toxicity, bioremediation progress, and remaining challenges*, Journal of Environmental Sciences, 127 2023 234-250.
- [9] ANICIJEVIC, V., LAZAREVIĆ-PAŠTI, T., VASIC ANICIJEVIC, D., KARKALIC, R., *Esters of Organophosphorus Acids - Toxicity, Application and Removal from the Environment*, Scientific Technical Review, 2019.
- [10] BOSE, S., SENTHIL KUMAR, P., RANGASAMY, G., PRASANMEDHA, G., KANMANI, S., *A review on the applicability of adsorption techniques for remediation of recalcitrant pesticides*, Chemosphere, 313 2023 137481.
- [11] DUN, W., GUIJIAN, L., RUOYU, S., XIANG, F., *Investigation of Structural Characteristics of Thermally Metamorphosed Coal by FTIR Spectroscopy and X-ray Diffraction*, Energy & Fuels, 27 2013 5823-5830.



## ORGANOPHOSPHORUS NEUROTOXINS REMEDIATION IN DYNAMIC CONDITIONS

VEDRAN MILANKOVIĆ

University of Belgrade, “VINČA” Institute of Nuclear Sciences - National Institute of the Republic of Serbia, Mike Petrovica Alasa 12-14, 11000 Belgrade, Serbia, [vedran.milankovic@vin.bg.ac.rs](mailto:vedran.milankovic@vin.bg.ac.rs)

TAMARA TASIĆ

University of Belgrade, “VINČA” Institute of Nuclear Sciences - National Institute of the Republic of Serbia, Mike Petrovica Alasa 12-14, 11000 Belgrade, Serbia, [tamara.tasic@vin.bg.ac.rs](mailto:tamara.tasic@vin.bg.ac.rs)

VLADAN ANIĆIJEVIĆ

University of Defence Belgrade, Military Academy, [anicijevicj.v@gmail.com](mailto:anicijevicj.v@gmail.com)

IGOR PAŠTI

University of Belgrade, Faculty of Physical Chemistry, Studentski Trg 12, 11000 Belgrade, Serbia, [igor@ffh.bg.ac.rs](mailto:igor@ffh.bg.ac.rs)

TAMARA LAZAREVIĆ-PAŠTI

University of Belgrade, “VINČA” Institute of Nuclear Sciences - National Institute of the Republic of Serbia, Mike Petrovica Alasa 12-14, 11000 Belgrade, Serbia, [tamara@vin.bg.ac.rs](mailto:tamara@vin.bg.ac.rs)

**Abstract:** Organophosphorus neurotoxins (OPNs) are a class of chemical compounds widely known for their potent neurotoxic effects. OPNs work by inhibiting the enzyme acetylcholinesterase (AChE), which breaks down the neurotransmitter acetylcholine in the nervous system. This research investigates using spent coffee grounds carbonized at 900°C and subsequently activated with H<sub>3</sub>PO<sub>4</sub> and KOH to remove chlorpyrifos (CHP) and malathion (MLT) from aqueous solutions. The activated carbon material is integrated into a filtration system designed to rapidly and efficiently remove these neurotoxins. In the initial cycle, the adsorption capacities for CHP and MLT were found to be 67% (11.7 mg g<sup>-1</sup>) and 78% (12.8 mg g<sup>-1</sup>), respectively, demonstrating high effectiveness in decontamination efforts. The filter was washed using 5 mL of 50% ethanol and reused for 10 cycles. It is shown that it exhibits durability, as it can be successfully regenerated and reused without significant loss in adsorption efficiency. As the material has high surface areas and shows no specific adsorption of the neurotoxins, it can be concluded that it can successfully be used to resolve chemical threats in water sources during military operations.

**Keywords:** filters, malathion, chlorpyrifos, spent coffee grounds, adsorption

### 1. INTRODUCTION

Organophosphorus neurotoxins (OPNs) are a prominent class of chemical compounds recognized for their significant neurotoxic effects. Among these, malathion (MLT) and chlorpyrifos (CHP) are widely used pesticides that pose substantial risks to human health and the environment. Malathion and chlorpyrifos exert their toxic effects primarily by inhibiting acetylcholinesterase (AChE), a crucial enzyme responsible for the breakdown of the neurotransmitter acetylcholine in the nervous system. Inhibition of AChE results in the accumulation of acetylcholine at synaptic junctions, leading to continuous stimulation of muscles, glands, and central nervous system receptors. This can cause a range of symptoms from mild, such as headaches and dizziness, to severe, including respiratory paralysis and death [1, 2].

Though considered less toxic to humans than other organophosphates, MLT can cause serious health effects

upon exposure. Acute exposure can result in symptoms like nausea, vomiting, abdominal cramps, diarrhea, excessive sweating, salivation, and muscle twitching. Chronic exposure has been linked to more severe consequences, including respiratory issues, cognitive impairments, and even cancer [3].

CHP is another potent organophosphorus compound extensively utilized in agricultural practices. Exposure to CHP has been associated with various adverse health effects. Acute exposure can lead to symptoms such as blurred vision, muscle weakness, convulsions, and, in extreme cases, death. Long-term exposure has been implicated in developmental and behavioral disorders, particularly in children, due to its profound impact on the developing nervous system [4].

Given the significant health risks posed by MLT and CHP, effective remediation techniques are essential to minimize their impact on public health and the environment. This research explores the use of spent coffee grounds (SCG) carbonized at 900°C and

subsequently activated with  $\text{H}_3\text{PO}_4$  and KOH for the remediation of these neurotoxins from aqueous solutions. Military operations demand the highest quality standards. These standards include material selection and performance requirements that would protect from air and water threats. Developing a filtration system incorporating this activated carbon material offers a promising solution for rapidly and efficiently removing MLT and CHP, thereby addressing chemical threats in water sources and ensuring safety during military operations and other critical scenarios.

## 2. MATERIAL AND METHODS

### 2.1. Material synthesis and characterization

The adsorbent 900PC was prepared from SCG. After brewing a mixture of coffee obtained from the local market (80% Arabica and 20% Robusta) with boiling water, the mixture was allowed to cool to room temperature over 2 hours. SCG was then separated by filtration and left to dry at room temperature for 24 hours. The carbonization process was conducted in a tube furnace (Protherm Electrical Tube Furnace, Protherm Furnaces, Turkey) under a nitrogen flow of  $100 \text{ L h}^{-1}$ . The sample was heated to  $900^\circ\text{C}$  at a rate of  $5^\circ\text{C}$  per minute and maintained at this temperature for 60 minutes. Afterward, it was cooled to room temperature under a nitrogen atmosphere. The carbonized sample was then treated with  $\text{H}_3\text{PO}_4$  (Centrochem, Stara Pazova, Srbija) at a mass ratio 1:2 (material:  $\text{H}_3\text{PO}_4$ ) and returned to the furnace. It was heated again to  $900^\circ\text{C}$  at a rate of  $5^\circ\text{C}$  per minute under a nitrogen flow and maintained at this temperature for 60 minutes under a  $\text{CO}_2$  flow of  $100 \text{ L h}^{-1}$ . Finally, the sample was cooled to room temperature under a nitrogen atmosphere. To prepare a stock suspension, 100 mg of the material was weighed and washed sequentially with 50 mL of  $0.1 \text{ mol dm}^{-3}$  NaOH, 50 mL of  $0.1 \text{ mol dm}^{-3}$  HCl, and 50 mL of deionized water, then suspended in 50 mL of 50% ethanol (J.T. Baker, Phillipsburg, NJ, USA), resulting in a final concentration of  $2 \text{ mg mL}^{-1}$ .

Synthesized material was characterized using SEM, EDX, FTIR, and Zeta potential measurements to determine the material's morphology, chemical composition, functional groups, and isoelectric point (IEP).

### 2.2. Adsorption experiments under dynamic conditions

To investigate adsorption under dynamic conditions, a commercial nylon membrane filter (pore size  $0.22 \mu\text{m}$ , diameter 13 mm, KX Syringe Filter, Kinesis) was modified to contain a layer of adsorbent. This modification involved injecting 0.5 mL of the materials stock suspension into the commercial filter. The solvent was then removed from the filter using compressed air. The pesticide solution was injected through the modified filter at 1 mL per minute. The filtrate was subjected to UPLC analysis to determine the pesticide concentration. A control experiment was conducted using an unmodified filter.

To investigate the adsorbent regeneration and reuse, the filter was washed using 5 mL of 50% ethanol solution and reused as the adsorbent for the same pesticide.

The concentration of OPNs was determined using UPLC. A Waters ACQUITY UPLC with a PDA detector was used to determine the pesticide concentration. BEH C18 column was used under isocratic conditions: mobile phase A - 10% acetonitrile in water and B - pure acetonitrile. The injected volume was  $5 \mu\text{L}$ , while the flow rate was  $0.2 \text{ mL min}^{-1}$  in all cases. The mobile phase in the case of the MLT consisted of 40%A and 60%B, while in the case of CHP, it consisted of 20%A and 80%B for individual detection. The retention time for MLT under these conditions was 2.5 min, while it was 2.7 min for chlorpyrifos. Both pesticides were detected at a wavelength of 200 nm. Control experiments were performed identically but without the presence of the material.

### 2.3. Neurotoxicity assessment

The physiological effects of the treated solutions were analyzed through AChE inhibition measurements using a modified Ellman's procedure. 2.5 IU of commercially purified AChE from an electric eel was exposed to the organophosphate solutions in a  $50 \text{ mmol dm}^{-3}$  phosphate buffer at pH 8.0 and  $37^\circ\text{C}$  in a final volume of 0.650 mL. The enzymatic reaction was initiated by combining AChI with DTNB as the chromogenic reagent. The reaction was allowed to proceed for 8 minutes before being stopped with 10% sodium dodecyl sulfate (SDS). Thiocholine, the reaction product, reacts with DTNB to form 5-thio-2-nitrobenzoate, whose optical absorption was measured at 412 nm using UV-VIS Perkin Elmer, Lambda 35 spectrophotometer. The enzyme concentration was maintained at a level that produced an optimal spectrophotometric signal. The physiological effects were quantified as AChE inhibition, calculated as follows:

$$I = 100 \times \frac{A_0 - A}{A_0} \quad (1)$$

where  $A_0$  and  $A$  stand for the AChE activity in the absence of OP and the one measured after exposure to a given OP.

## 3. RESULTS

### 3.1. Physicochemical properties of the material

SEM micrography and EDX analysis were performed to examine the materials' morphology and elemental composition. The SEM micrograph and EDX spectrum are given in **Figure 1**. The SEM micrograph shows that the material has a granular, heterogeneous, and highly porous structure, resembling the previously reported morphology of the precursor, SCG [5]. EDX analysis revealed a high percentage of C, O, and P, 46.27, 36.76, and 6.97 at.%, respectively. Besides mentioned, N, K, Ca, Mg, Na, and Si are also present in the sample as the chemical footprint of the precursor.

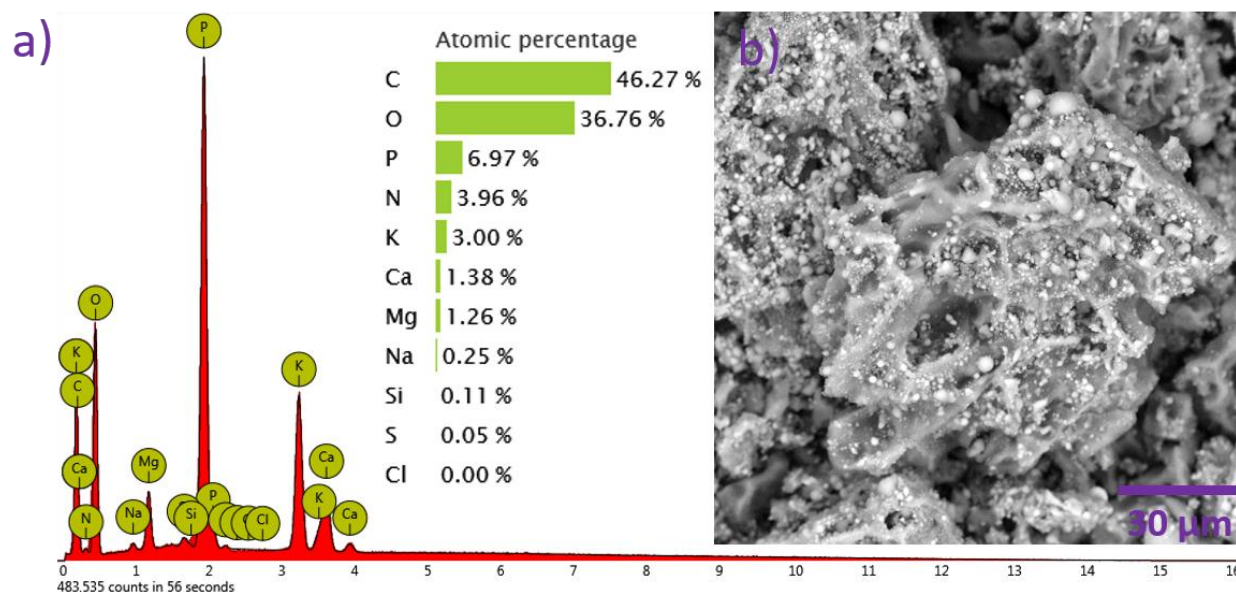


**Figure 1.** a) EDX spectrum and elemental composition in at.% of 900PC; b) SEM micrograph of 900PC (magnification 2000×)

The FTIR spectrum of 900PC is given in **Figure 2**. The observed bands in the spectrum correspond to specific vibrations. The band at  $1554\text{ cm}^{-1}$  indicates the presence of condensed aromatic rings, signifying aromatic carbon-carbon double bonds (C=C) within the carbon structure. These aromatic rings enhance the material's  $\pi$ -electron system, improving its adsorption properties through  $\pi$ - $\pi$  interactions with adsorbates. The band at  $1227\text{ cm}^{-1}$  is assigned to the stretching vibration of phosphorus-oxygen double bonds (P=O), suggesting the presence of phosphorus-containing functional groups. These groups may stem from phosphorus compounds in the precursor material or be introduced during the carbonization and activation processes, potentially enhancing the material's adsorption affinity for certain contaminants. The band at  $1079\text{ cm}^{-1}$  is linked to the coupling of aromatic carbon-hydrogen (C-H) in-plane deformation vibrations and carbon-oxygen (C-O) stretch vibrations in primary alcohols, indicating the presence of aromatic C-H bonds and hydroxyl (OH) functional groups, likely derived from phenolic compounds in the precursor material. These functional groups contribute to the material's hydrophilicity and surface reactivity, affecting its adsorption behavior towards polar contaminants [6]. The band at  $877\text{ cm}^{-1}$  corresponds to vibrations from 3-4 condensed aromatic rings, pointing to carbonaceous structures with multiple fused aromatic rings. These condensed aromatic structures enhance the material's graphitic nature and provide additional adsorption sites for contaminants through  $\pi$ - $\pi$  interactions [7].

By examining the dependence of the zeta potential of the materials' suspension on pH (**Figure 3**), it can be seen that the isoelectric point of 900PC is at  $\text{pH}=4.87$ . As the suspension's initial pH value used in adsorption experiments was 6, it can be concluded that 900PC has a slightly negatively charged surface.

The specific surface area of 900PC, determined by  $\text{N}_2$  adsorption, is  $846\text{ m}^2\text{ g}^{-1}$ , while the total pore volume is

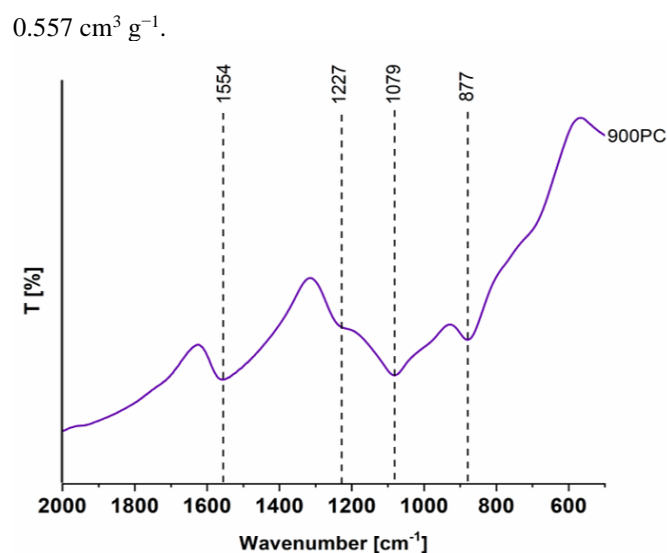


**Figure 2.** FTIR spectrum of 900PC

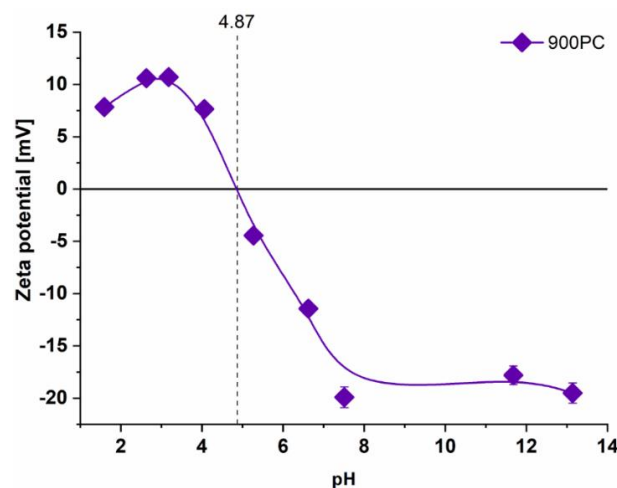


**Figure 3.** Dependence of zeta potential of pH with

indicated IEP for 900PC

### 3.2. Adsorption of OPNs onto 900PC under dynamic conditions. Regeneration and reuse.

The obtained results are shown in **Figure 4**. By observing the presented results, it can be concluded that the material can successfully remediate 98% of MLT and 97% of CHP under dynamic conditions. It can be regenerated using 5 mL of 50% ethanol solution and reused for at least 10 cycles without significantly impacting the adsorption capacity, as it loses around 10% of its efficiency after the 10<sup>th</sup> cycle. These results indicate that 900PC is not a selective adsorbent, making it suitable for application in the remediation of various chemical threats from water sources.

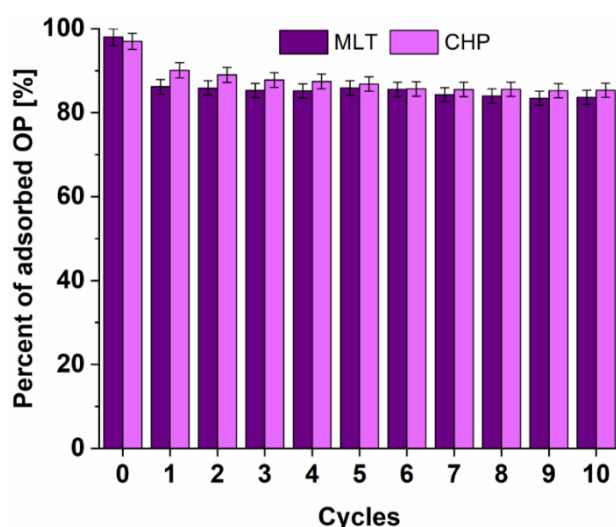


**Figure 4.** Histogram representing the percent of adsorbed OP through 10 cycles of regeneration and reuse

### 3.3. Assessment of AChE activity inhibition after MLT and CHP remediation using 900PC

The neurotoxicological assessment was performed as described in Section 2.3, and the histogram showing the difference in the activity inhibition of AChE before and after the adsorption of MLT and CHP is shown in **Figure 5**. It can be seen that the AChE inhibition due to the contact with samples was highly reduced after the adsorption in all cases, indicating that no more toxic products, such as OPNs' oxo-forms, were formed during this process. The reduction in AChE activity inhibition is crucial for the intended application, as if more toxic

Neurotoxicological assessments indicate that the 900PC material significantly reduces AChE inhibition after the adsorption of MLT and CHP, suggesting that the adsorption process does not produce harmful by-products. This finding underscores the safety and reliability of using 900PC in filtration systems designed to remove chemical threats in water sources.

The study highlights the potential application of 900PC material in developing filtration systems for military operations and other critical scenarios where stringent quality standards for material selection and performance

products are forming during the process, the interaction of OPNs with the material could lead to more severe neurotoxic effects.

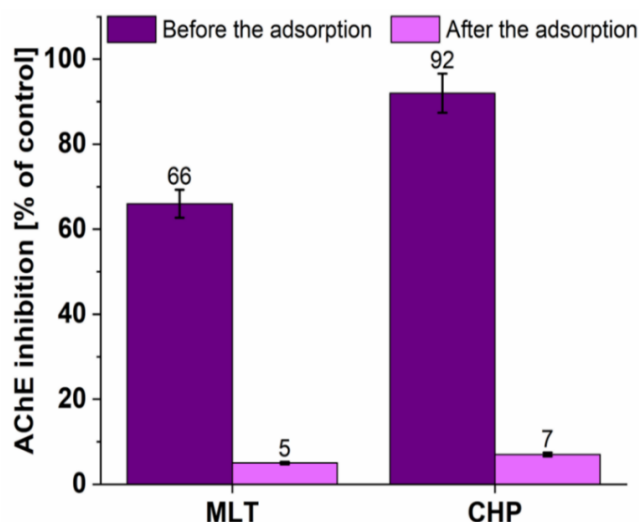


**Figure 5.** Histogram of AChE activity inhibition before and after the adsorption of MLT and CHP using AC-SCG

## 4. CONCLUSION

In conclusion, this research demonstrates that the 900PC material, produced from SCG carbonized at 900°C and activated with H<sub>3</sub>PO<sub>4</sub> and KOH, is highly effective in remediating OPNs, MLT, and CHP from aqueous solutions. The material exhibits excellent adsorption capacities, successfully removing 98% of MLT and 97% of CHP. This high level of performance is attributed to the material's highly porous structure, which enables efficient adsorption of these toxic compounds. As this material did not exhibit significant differences in the percent of adsorbed OPN, it is concluded that it is non-selective and that its application is not limited just to OPNs.

Furthermore, the 900PC material shows impressive durability and reusability. It retains its high adsorption efficiency over at least 10 regeneration cycles, losing only about 10% of its capacity. This reusability is achieved by regenerating the material with a 50% ethanol solution, demonstrating a practical and cost-effective approach for maintaining its performance.

are required. By providing protection against neurotoxins in water, the 900PC material contributes to enhanced safety and protection during operations.

### Acknowledgment

The researchers acknowledge the support provided by the Serbian Ministry of Education, Science and Technological Development (contract number: 451-03-66/2024-03/200017 and 451-03-65/2024-03/200146).

## References

- [1] JOKANOVIĆ, M.: *Neurotoxic effects of organophosphorus pesticides and possible association with neurodegenerative diseases in man: A review*, *Toxicology*, 410 (2018) 125-131
- [2] ČOLOVIĆ M., KRSTIĆ D., LAZAREVIĆ-PAŠTI T., BONDŽIĆ A., VASIĆ V., *Acetylcholinesterase inhibitors: pharmacology and toxicology*, 11 (2013) 315-335
- [3] ELMORSY E., AL-GHAFARI A., AL DOGHAITHER H., SALAMA M., CARTER W.G., *An Investigation of the Neurotoxic Effects of Malathion, Chlorpyrifos, and Paraquat to Different Brain Regions*, 11 (2013) 315-335
- [4] LAZAREVIĆ-PAŠTI T., VASIĆ V., *Toxicity of Chlorpyrifos and Its Removal from the Environment*, *Advances in environmental research*, (2019) 1-48,
- [5] MILANKOVIĆ V., TASIĆ T., PEJČIĆ M., PAŠTI I., LAZAREVIĆ-PAŠTI T., *Spent Coffee Grounds as an Adsorbent for Malathion and Chlorpyrifos—Kinetics, Thermodynamics, and Eco-Neurotoxicity*, *Foods*, 12 (2023) 2397
- [6] NAUSHAD M., ALQADAMI A., ALOTHMAN Z., ALSOHAIMI I., ALGAMDI M., ALDAWSARI A., *Adsorption kinetics, isotherm and reusability studies for the removal of cationic dye from aqueous medium using arginine modified activated carbon*, *Journal of Molecular Liquids*, 293 (2019) 111442
- [7] NAIR R., MONDALM., WEICHGREBE D., *Biochar from co-pyrolysis of urban organic wastes—investigation of carbon sink potential using ATR-FTIR and TGA*, *Biomass Conversion and Biorefinery*, 12 (2022) 4729-4743





# INVESTIGATION OF THE DEPENDENCE OF PRESSURE DROP AND PARTICLES FLOW RATE ON THE PARTICLE DIAMETER IN SPOUT-FLUIDIZED BED

TEODORA STANČIĆ

Military Technical Institute, Belgrade, [teodorastancic@gmail.com](mailto:teodorastancic@gmail.com)

MIHAL ĐURIŠ

Institute of Chemistry, Technology and Metallurgy – National Institute of the Republic of Serbia, University of Belgrade, Belgrade, [mdjuris@tmf.bg.ac.rs](mailto:mdjuris@tmf.bg.ac.rs)

TATJANA KALUĐEROVIĆ RADOIČIĆ

Faculty of Technology and Metallurgy, University of Belgrade, Belgrade, [tanjak@tmf.bg.ac.rs](mailto:tanjak@tmf.bg.ac.rs)

**Abstract:** *The spouted and spout-fluidized bed systems have been designed to overcome the limitations of fluidized systems, particularly where there is a need to utilize large particles in the process. These beds have great significance and are applied for various processes in industry. They are formed by introducing fluid into a column with a packed bed, establishing the vertical transport of particles upwards through the center of the column. The entire packed bed in the annular area slides down as the particles are transported upwards from the bottom of the bed. Sometimes, a central pipe is installed in the axis of the spouted bed column, through which transport occurs, significantly reducing the pressure drop in column and increasing operational efficiency. The aim of the presented paper is the measurement of fluid flowrate, particle flowrate, and pressure drops in spout-fluidized bed with a central pipe, at a certain distance from the bottom of the bed. Glass particles were used for these measurements, and their characterization was performed initially. Fluid flow was varied in the annulus and central pipe, followed by measurements of pressure drops.*

**Keywords:** *fluidization, glass particles, pressure drop, spouted bed*

## 1. INTRODUCTION

The terms "fluidization" and "fluidized bed" were initially employed in the 1940s to describe the use of a fluidized bed for the drying of peas, lentils, and flax seeds. With the development of fluid catalytic cracking, a process for converting heavy hydrocarbons in petroleum refineries, fluidization became a mature process operation with a growing number of practical applications and occupies a significant place in the industry today. [1]

One of the most significant characteristics of a fluidized system is the effective mixing within the fluidized bed, enabling efficient heat transfer between solid particles and gas. It is primarily used for physical processes such as drying, mixing, granulation, cooling, and heating, but it is also utilized for chemical operation involving interactions between solids and gases. Such processes are fast, achieve excellent homogeneity, and offer the possibility of continuous operation in devices for continuous production. [2]

The properties of a fluidized bed depend on the type of material, particle size, shape and qualities. The behavior of one material during fluidization cannot be extrapolated to the behavior of another material. [3]

Pressure drop in a fluidized bed is given by Eq. (1):

$$-\frac{\Delta P}{H} = (\rho_p - \rho_f) g (1 - \varepsilon) \quad (1)$$

where: ( $\Delta P$ )- the pressure drop in the bed;  $H$ - the column height;  $g$ - the gravity constant;  $\rho_p$  – the density of the bed;  $\rho_f$  – the density of the fluid;  $\varepsilon$ - the porosity of the bed [4]

Fluidization is a well-studied concept. It occurs when the frictional force between the fluid and particles becomes equal to the effective weight of the bed per unit surface area of the column. In that moment, particles redistribute, causing the bed to expand, while its porosity increases. As fluid velocity increases the distance between particles expands, leading to an increase in porosity. However, the pressure drop remains constant. The fundamental fluidization equation states that the pressure gradient in the bed is proportional to the particle concentration. [4]

Research has shown that in multiphase flow systems, two-phase moving fluid-particles beds occur in forms such as packed bed, spouted bed, spout-fluidized bed, spout-fluidized bed with a central pipe and spout-fluidized bed with a central pipe and conical base. These systems can be implemented within a cylindrical column by installing a nozzle at its flat or conical base and using an annular fluid distributor. [4,5]

The spouted bed represents a moving bed of particles that occurs in such fluid flow through a nozzle, providing vertical particle transport upwards in the form of a fountain. Consequently, particle movement downwards occurs in the annular space, forming a packed bed. In addition to the described particle movements, there is also their radial movement from the annular part to the central part of the bed (fountain), most pronounced at the top of the bed. At the top of the fountain, particles lose kinetic energy and fall onto the top of the annular space. The primary benefit of this system is the possibility of gas-particle contact for particles that cannot be fluidized. [6]

The establishment of the fountain bed is illustrated in Figure 1, where (a) presents a packed bed with particles in a quiescent state. Subsequently, with the introduction of fluid into the system, the fountain bed forms at the point of minimal fluidization velocity (b). As the fluid flow rate increases, a more pronounced fountain forms, as shown in Figure 1 (c). Following this stage, the bed transforms and becomes filled with large bubbles. (d) [7]

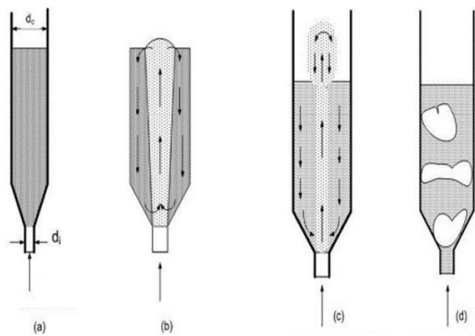


Figure 1. Establishment of the fountain bed [7]

The spout-fluidized bed is formed by simultaneously introducing fluid into the particle bed through a nozzle and an annular distributor. This allows for the combination of spout bed characteristics with those of the spout-fluidized bed, with the latter exhibiting significantly lower pressure drop compared to the spouted bed. [8] In comparison to the spouted bed, better gas-particle contact and better mixing within the annulus are facilitated. [7]

Some deficiencies of the spout and spout-fluidized beds have led to their development, resulting in the draft-tube insert placed within the bed axis at a certain distance from the nozzle or column base. The utilization of such a draft-tube insert enables a reduction in pressure drop within the bed. Such a bed is physically divided into two zones: vertical particle transport within the draft-tube and moving packed/fluidized bed particles within the annular space (Fig. 2).

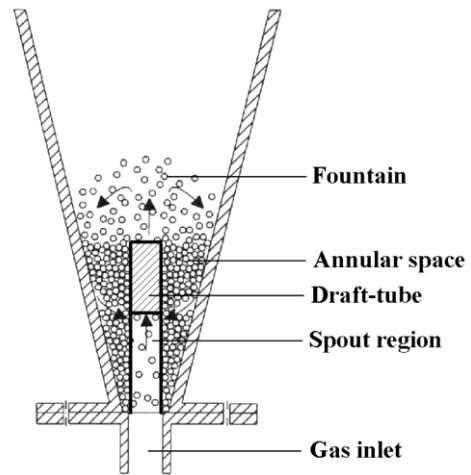


Figure 2. Spout-fluidized bed with a central pipe [4]

The aim of this paper is to experimentally investigate the pressure gradient and particle flow rate through a modified spout-fluidized bed with a draft tube, using spherical glass particles.

## 2. EXPERIMENTAL DETAILS

The apparatus used in the experiment consists of: a fluidization column with a central pipe and a bypass, six sensors measuring pressure in the central pipe, and three sensors measuring pressure in the annulus, at a known height from the bottom of the column, valves, two rotameters, a compressor, and a blower. Air was used for fluidization, with the blower providing air flow through the annulus, while the compressor provided air flow through the draft-tube. Rotameters were used to determine the required air flow necessary for the experiment: one rotameter measured the air flow through the pipe and the other measured the flow through the annulus. Valves were used to adjust the air flow through the pipe. The fluidization column is shown in Figure 3.

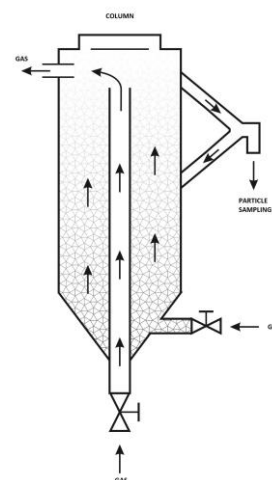


Figure 3. Schematic representation of the fluidization column

The column contains particles, and experiments were conducted using glass particles, referred to as Glass Particles 1. Using the bypass, the particles circulate and return to the column, with a portion of the particles being captured in a collection vessel. The mass of the captured particles is measured over a precisely defined time interval.

**2.1. Characterization of particles**

The appearance of Glass Particles 1 used in the experiments is shown in Figure 4. The total mass of glass particles used was 5790g.



**Figure 4.** The appearance of Glass Particles 1

*Determining the average particle diameter*

Before the experiments began, the particles were characterized by measuring their diameter and density. The diameter was determined by measuring 50 randomly selected glass particles using a digital micrometer. For each particle, the diameter was measured, and based on the number of samples taken, the average particle diameter was calculated.

$$ds = \frac{\sum di}{n} \tag{2}$$

Where *ds* is the calculated average diameter,  $\sum di$  is the sum of all measured diameters, and *n* is the number of measured diameters. The obtained average particle diameter was 1.07mm.

*Determining the density of particles*

The density of the particles was measured using a pycnometer. Using a digital scale, the mass of the empty pycnometer (*m<sub>pik</sub>*), the mass of the pycnometer with particles (*m<sub>pikc</sub>*), the mass of the pycnometer with water (*m<sub>pikv</sub>*), and the mass of the pycnometer with particles and water (*m<sub>pikc,v</sub>*) were measured. Based on the known formula for determining density and the obtained masses, the density of the particles was calculated. The density of the glass particles used in the experiments was 2796 kg/m<sup>3</sup>.

$$\rho = \frac{(m_{pikc} - m_{pikv})}{((m_{pikc} - m_{pik}) + m_{pikv}) - m_{pikc,v}} \tag{3}$$

**2.2. Experiments in spout-fluidized bed**

In the described experimental setup, 81 measurements were taken with Glass Particles 1. During each experiment, the air flow rate through the central pipe and the air flow rate through the annulus were varied. The air flow rate through the central pipe for Glass Particles 1 ranged from 160 to 260 l/min. The air flow rate through the annulus for Glass Particles 1 was varied from 8 to 12 m<sup>3</sup>/h. The maximum air flow rate through the central pipe for Glass Particles 1 was limited to 260 l/min because pressure sensors exceeded their range at higher flow rates, making such measurements impractical. The lower limit of the range where measurements were conducted represents the minimum flow rate at which a spout-fluidized bed is established in the tested system. The conditions of the experiment are shown in Table 1.

For each experiment, both air flow rates through the central pipe and the annulus were set. A known mass of glass particles, measured before the experiment began, was introduced into the fluidization column, which was then sealed. Airflow was subsequently enabled. At a specified airflow rate, the time taken for the particles to exit the system via the bypass, once it was opened, was measured. The particles were collected in a collection vessel, their mass was measured, and then they were reintroduced into the column to continue the experiment.

**Table 1.** Conditions of the experiment

type of particles	flow through	
	annulus, m <sup>3</sup> /h	central pipe, l/min
Glass Particles 1	8	160
		210
		170
		220
		180
		230
		190
		240
		200
		250
	12	260

### 3. RESULTS AND DISCUSSION

For glass particles 1, the pressure profiles through the central pipe and the annulus were determined, as well as the impact of fluid flow rate in the central pipe and in the annulus on the pressure gradient. Based on the measured mass of particles at different fluid flows through the central pipe and annulus, the particle flows and the dependence of particle flow on fluid flow were determined. All the obtained results are graphically presented in the continuation of the paper.

#### 3.1. PRESSURE PROFILE

For glass particles, the pressure profile in the system along the height of the column in the central pipe and in the annulus is shown. The results of experimental measurements are that higher fluid flows through the system will result in higher pressure.

*The pressure profile along the central pipe*

The pressure profile in the central pipe is shown in Figures 5 and 6. The sensors were positioned to measure the pressure at a point relative to atmospheric pressure. The minimum flows in the central pipe and in the annulus at which a spouted-fluidized bed is formed for glass particles 1 are 160 l/min and 8 m<sup>3</sup>/h.

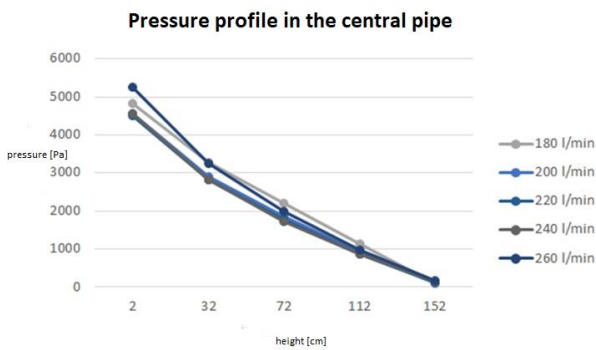


**Figure 5.** The pressure profile along the central pipe for different flows through the pipe for Glass Particles 1 at constant flow in the annulus of 8 m<sup>3</sup>/h

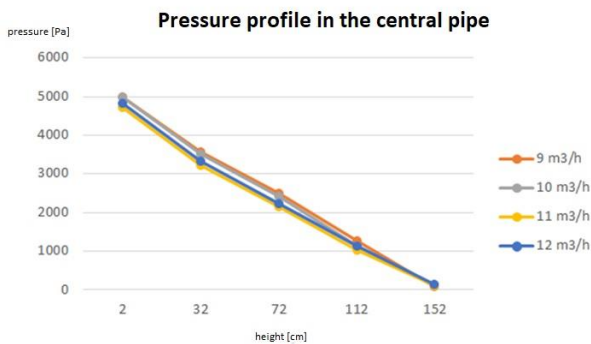


**Figure 6.** The pressure profile along the central pipe for different flows through the annulus for Glass Particles 1 at constant flow in the central pipe of 160 l/min.

Figures 5 and 6 illustrate the pressure profile along the central pipe for Glass Particles 1. The x-axis represents the height where sensors were positioned to measure pressure, with their values shown on the y-axis. The sensors are located within the central pipe. From these figures, it can be concluded that increasing the fluid flow through both the central pipe and the annulus leads to an increase in pressure within the system. Additionally, a clear observation is the decrease of the pressure from bottom to top of the column (with the highest pressure at the bottom). The results obtained for the lowest flow rate through the central pipe of 160 l/min at constant flow rate through the annulus of 8 m<sup>3</sup>/h were not considered valid because the bed remained unstable throughout the experiment. Similar considerations apply to the results obtained for the flow rate through the annulus of 8 m<sup>3</sup>/h at constant flow rate through the central pipe of 160 l/min.

#### 3.2. THE INFLUENCE OF FLUID FLOW ON PRESSURE GRADIENT

For each experimental pressure measurement in the central pipe and annulus, the pressure gradient was determined at characteristic points. The dependence of the pressure gradient in the central pipe on the flow rate in the central pipe was established, assuming constant flow in the annulus. Similarly, the dependence of the pressure gradient in the central pipe on the flow rate in the annulus was determined, assuming constant flow in the central pipe. Results were obtained and graphically presented for glass particles. The x-axis shows fluid flow values, and the y-axis shows pressure drop.

*The influence of flow on the pressure gradient in the central pipe*

Figures 7 and 8 illustrate the impact of flow rate on the pressure gradient in the central pipe for Glass Particles 1. In Figure 7, the pressure gradient in the central pipe (y-axis) is plotted against the fluid flow rate in the annulus (x-axis), varied from 8 to 12 m<sup>3</sup>/h, with flow rates through the central pipe ranging from 160 to 260 l/min.

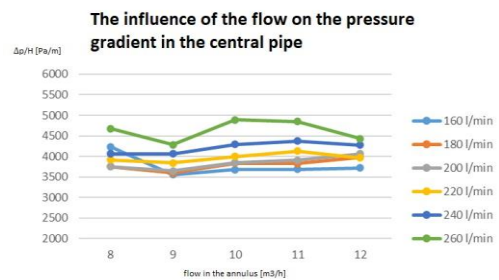


**Figure 7.** Pressure gradient in the central pipe as a function of fluid flow in the annulus for different flows through the pipe for Glass Particles 1

**Figure 8** shows the pressure gradient in the central pipe (x-axis) plotted against the fluid flow rate through the central pipe (y-axis), varied from 160 to 260 l/min, with flow rates through the annulus ranging from 9 to 12 m<sup>3</sup>/h. According to the expected trend, increasing the fluid flow

leads to a greater pressure drop in the central pipe.

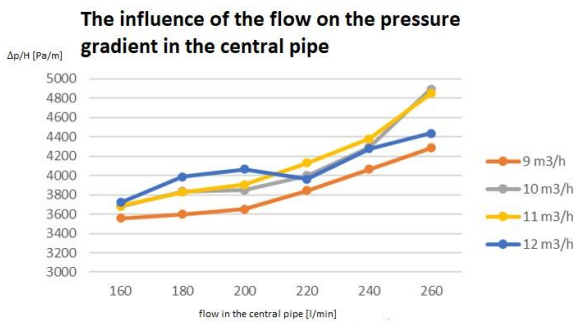


**Figure 8.** Dependence of the pressure gradient in the central pipe on the fluid flow through the central pipe for different flows through the annulus for Glass Particles 1

The influence of fluid flow on the pressure gradient in the annulus

Figure 9 shows the influence of flow on the pressure gradient in the annulus, with fluid flow through the annulus (x-axis) varied from 8 to 12 m³/h, while fluid flow through the central pipe (y-axis) varied from 160 to 260 l/min. From this figure, it can be concluded that increasing the fluid flow through both the central pipe and the annulus leads to an increase in the pressure gradient in the annulus. Additionally, it can be observed that the flow rate through the annulus has a greater impact on the pressure gradient in the annulus compared to the flow rate through the central pipe.

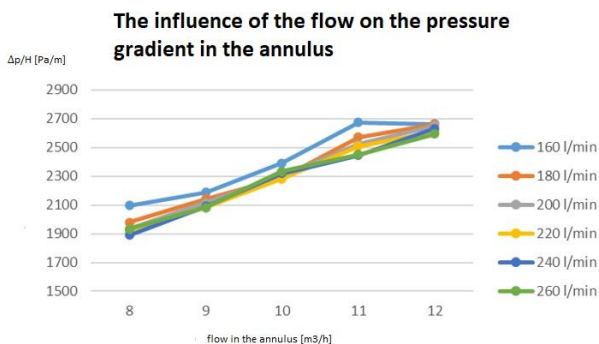


**Figure 9.** Pressure gradient in the annulus as a function of fluid flow in the annulus for different flows through the pipe for Glass Particles 1

### 3.3 THE INFLUENCE OF FLUID FLOW ON PARTICLE FLOW

For each experimental fluid flow measurement, the mass flow of the particles through the system was determined. Using the mass of particles, the mass flow rate and volumetric flow rate of particles of known density, previously determined in the system, were calculated. Fluid flows in both the annulus and central pipe were varied to establish the dependency of particle flow rates on fluid flow rates, which is further detailed in the study.

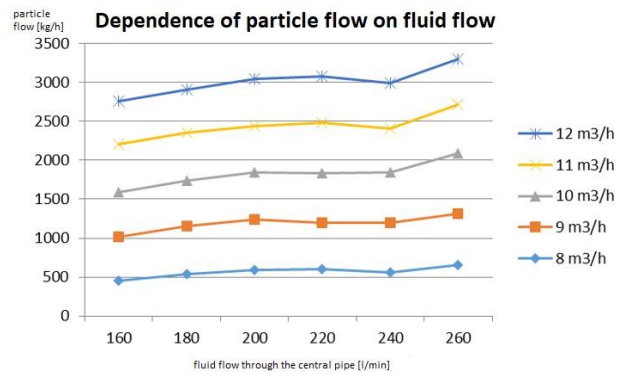


**Figure 10.** Dependence of particle flow on fluid flow through the central pipe for different flows through the annulus for Glass Particle 1

It can be seen that increasing the fluid flow through both the central pipe and the annulus results in an increase in the flow of Glass Particle 1 through the system. The increase is approximately linear.

### 4. CONCLUSIONS

From the obtained results of the pressure profiles along the central pipe for Glass 1, it can be concluded that the minimum flows at which a spouted-fluidized bed forms are 160 l/min through the central pipe and 8 m³/h through the annulus. The lowest pressure in the spouted-fluidized system containing Glass Particles 1 is at the top of the column. Increasing the fluid flow through both the central pipe and the annulus leads to an increase in pressure within the system.

The influence of flow on the pressure gradient in the central pipe for Glass 1 can be determined with minimum flows of 8 m³/h through the annulus and 160 l/min through the central pipe. Flows were varied up to 12 m³/h and 260 l/min. Increasing the fluid flow results in a greater pressure drop in the central pipe. Additionally, increasing the fluid flow through both the central pipe and the annulus leads to an increase in the pressure gradient in the annulus. The flow rate through the annulus has a greater impact on the pressure gradient in the annulus than the flow rate through the central pipe.

Experimental profiles and pressure drops were investigated in a spouted-fluidized bed with a draft tube, using glass particles for the experiments. Pressure profiles along the central pipe and the annulus, pressure gradients in the central pipe and the annulus, as well as particle circulation flows within the system, were determined.

The conclusion drawn from the analysis of the results is that higher fluid flows through both the central pipe and the annulus lead to higher pressure within the spout-fluidized bed. Increasing both flows results in an increase in the pressure gradient. As for pressure drops, they also increase with higher fluid flows.. Based on the results, it was also determined that increasing the gas flow rate through the central pipe and the annulus leads to increased particle flow through the system.

**References**

- [1] MATHUR, K., EPSTEIN, N., *Spouted Beds*, Academic Press, New York, 1974.
- [2] MILANOVIĆ, A., *Optimizacija postupka oblaganja topljenjem u uređaju tipa fluidizirajućeg sistema: izrada i karakterizacija granula sa modifikovanim oslobađanjem paracetamola*, doktorska disertacija, Farmaceutski fakultet, Beograd, 2021.
- [3] GRACE, J. R. (2020). *Introduction, History, and Applications. Essentials of Fluidization Technology*, Wiley, online library, 1–9
- [4] STANČIĆ, T., *Eksperimentalno ispitivanje padova pritisaka i protoka čestica u fontansko-fluidizovanom sloju*, završni rad, TMF, Beograd, 2022.
- [5] POPOVIĆ, A., MILIĆEVIĆ, S., MILOŠEVIĆ, V., IVOŠEVIĆ, B., ČARAPIĆ, J., JOVANOVIĆ, V., POVRENOVIĆ D., *Fenton proces za tretman industrijskih otpadnih voda u disperznim sistemima*, stručni rad, TMF, Beograd, 2019.
- [6] KALUĐEROVIĆ-RADOIČIĆ, T., *Skripta višefazni sistemi*, TMF, Beograd
- [7] TRIPALO, B., JEŽEK, D., BRNČIĆ, M., BOSILJKOV, T., KARLOVIĆ, S., *Fontanski sloj, teorija i primjena*, pregledni rad Zagreb, Hrvatska, 2009., 5-9
- [8] ARSENIJEVIĆ, Z., *Sušenje rastvora i suspenzija u pokretnom sloju inertnih čestica*, doktorska disertacija, TMF, Beograd, 2006.



## MICROSTRIP DC-BLOCK ON TEXTILES USING ONLY SELF-ADHESIVE COPPER TAPE

DUŠAN NEŠIĆ

Centre of Microelectronic Technologies, Institute of Chemistry, Technology and Metallurgy, University of Belgrade  
[nesicad@nanosys.ihtm.bg.ac.rs](mailto:nesicad@nanosys.ihtm.bg.ac.rs)

DRAGAN TANASKOVIĆ

Centre of Microelectronic Technologies, Institute of Chemistry, Technology and Metallurgy, University of Belgrade  
[dragant@nanosys.ihtm.bg.ac.rs](mailto:dragant@nanosys.ihtm.bg.ac.rs)

MILOŠ VORKAPIĆ

Centre of Microelectronic Technologies, Institute of Chemistry, Technology and Metallurgy, University of Belgrade  
[worcky@nanosys.ihtm.bg.ac.rs](mailto:worcky@nanosys.ihtm.bg.ac.rs)

**Abstract:** Self-adhesive copper tape with non-conductive glue is used for DC-block on textiles. As capacitance, overlapping of copper strips was used, and the dielectric is the non-conductive glue of the strips. Two overlapping lengths were realized and measured. Due to the specificity of the textile, especially when worn, the cases of flat structure and when it is in S-shape were measured. The structure is easy to put on and take off and does not damage the textile. By easily correcting the length of the overlap, the range of impervious lower frequencies can be changed.

**Keywords:** Microwave on textiles, DC-Block, Self-Adhesive Copper Tape

### 1. INTRODUCTION

The application of microwave structures on textiles is becoming more and more common [1-4]. In this case, the technique must be adapted to both the textile substrate and the applicable metallization.

Textile as a substrate is soft, flexible, somewhat anisotropic and rough. There is no precisely determined dielectric constant and no precisely determined thickness [3,4].

Conductive thread (embroidery), direct application of a conductive layer (paste, ink, etc.) and conductive self-adhesive tapes are the basic techniques of metallization on textiles. Conductive self-adhesive tapes have several advantages [4-6]. The most important are [4]: easy to put on and take off without damaging the textile, metallization similar to printed circuit boards (well-defined conductive layer) and easy formation of multi-layered (overlapped) structures.

DC-blockers in microstrip are important structures in microwaves. They are predominantly constructed on the basis of lateral coupling [7-9], which occupies more surface area and requires a narrow lateral gap for capacity. The solution can be also vertical coupling [10], which includes a multi-layered structure but without a narrow lateral gap.

The vertical coupling is more suitable for metallization on textiles. It is easier and more precise processing with easier formation of a multi-layered structure with avoided lateral coupling. DC-block on textile substrate using

vertical coupling is given in [11]. The capacity is formed by screen printing of silver on commercially-available polyurethane (PU) film 50  $\mu\text{m}$  thick as the interface layer on textile (felt). An additional thermal treatment was done to fix the PU dielectric on the textile which complicates the process.

A simpler structure can be formed just using direct overlap of two Cu tapes with non-conductive glue (around 15  $\mu\text{m}$  thick and around  $\epsilon_r = 1.3$ ) as a dielectric layer [12]. This makes direct use of the possibility of easy formation of overlapped layers using Cu tapes. Substrate is felt about  $h=0.9$  mm, dielectric constant around  $\epsilon_r = 1.3$ .

### 2. REALIZATION AND MEASUREMENT

An example of the structure is given in Fig. 1 [12] where the overlap area on the microstrip line represents the DC-block. The overlap area is between the black vertical lines in Fig.1. Overlapping was first realized on adequately cut 4 mm wide strips for 50  $\Omega$  microstrip. One strip is glued to the appropriate length over the other and then they are glued together to the textile. A special self-adhesive tape was used to transfer the formed structure [4]. Simulations for low frequencies depending on the capacitance between two microstrip structures are given in Fig. 2.

The structures were measured flat and S-shaped, Fig. 3. The S-shape was chosen as the most complicated shape in clothing textiles. Two overlaps are fabricated: 11 mm and 5 mm. Both are measured flat and S-shaped.

First, a structure with an overlap of 11 mm was made and measured, Fig.4. The measured attenuation value of 1 dB

at 0.1 GHz corresponds to a capacitance of about 30 pF in low frequency simulation. The results are good up to about 5 GHz for the flat structure, while for the S-shape it is about 4.5 GHz, and that is because of the  $S_{11}$ .

The overlap part was then trimmed to 5 mm and the new structure was also measured, Fig.5. The measured attenuation value of 3 dB at 0.1 GHz corresponds to a capacitance of about 15 pF in low frequency simulation. The results are good up to near 5.5 GHz for the both flat and the S-shape structure.



**Figure 1.** DC-block construction using Cu adhesive tape on felt substrate [12]. The overlap area on the microstrip line is between the black vertical lines.

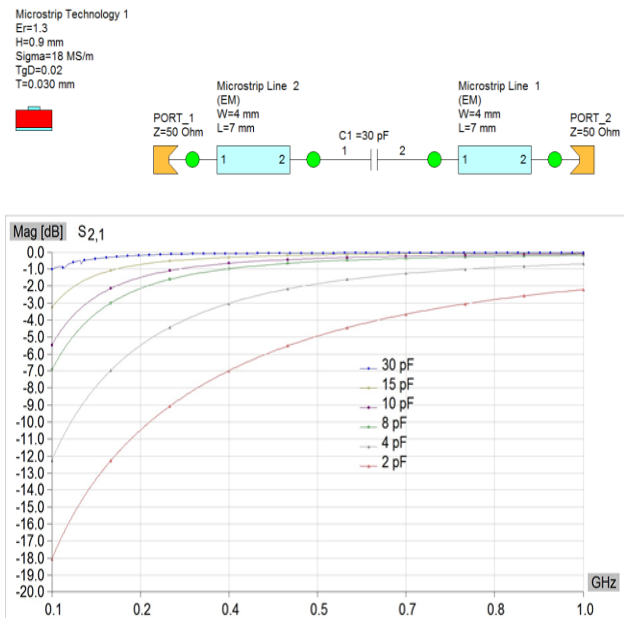


**Figure 2.** Simulations for low frequencies depending on capacity: simple model and results. Lower  $S_{21}$  corresponds to lower capacity [12]



**Figure 3.** S-shape structure

### 3. CONCLUSION

The paper presents microstrip DC-block on textile with use only self-adhesive copper tape. Implementation is

simple; easy to put on and easy to take off, which supports the sustainability of textiles. The dielectric is just a non-conductive glue between the overlap of two copper strips.

The folds are realized as 11 mm and 5 mm, with the second realized as trimming of the first. The S-shape measurement in addition to the flat state measurement perturbed the S-parameters very little. Logically, an 11 mm overlap has a lower DC-block than a 5 mm overlap. The latter has a slightly higher acceptable higher frequency. Good for lower microwave frequencies in communications, up to 6 GHz.

This type of DC-block structure is easy to apply and occupies a small area due to vertical coupling. This especially applies to textile structures, especially clothing. As it is easy to put on, it is also easy to take off without damaging the textile. It is suitable for suppressing low frequencies and DC in military application without complicated technological process such as printing and embroidery.

Disadvantage can be the imperfection of textiles as a substrate for microwaves. Also, it depends on the fineness of the workmanship.

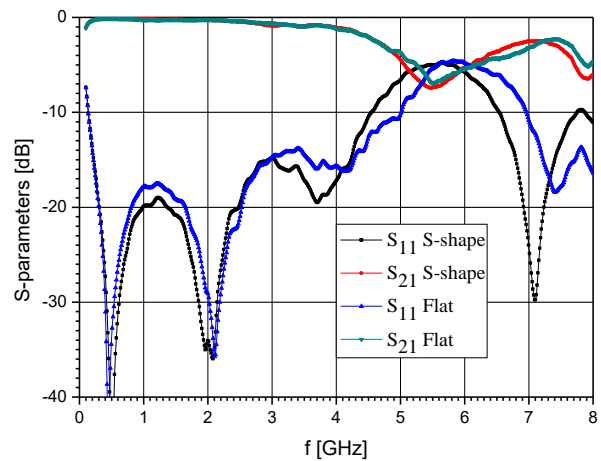


**Figure 4.** Overlap 11 mm: The measured S-parameters, flat and S-shape, 0.1 GHz to 8 GHz

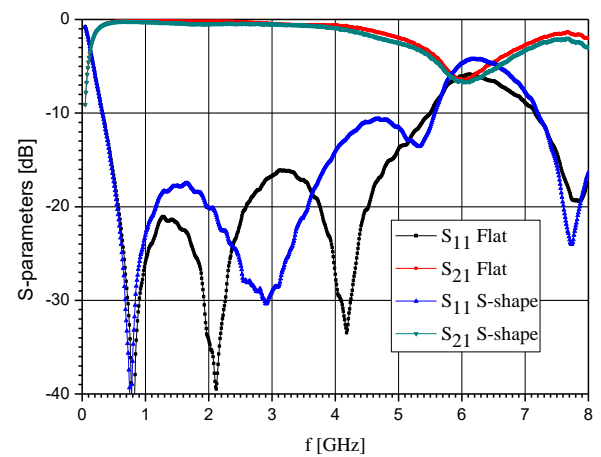


**Figure 5.** Overlap 5 mm: The measured S-parameters, flat and S-shape, 0.1 GHz to 8 GHz



## Acknowledgement

The authors thank to V. Milosević (Institute of Physics, Belgrade), M. Potrebić and M. Tasić (School of Electrical Engineering, University of Belgrade) for help in measuring.

This work was financially supported by the Minister of Science, Technological Development and Innovation of the Republic of Serbia (Grant No. 451-03-47/2023-01/200026).

## References

- [1] WAGIH,M.: *Microwave-Enabled Wearables: Underpinning Technologies, Integration Platforms, and Next-Generation Roadmap*, IEEE Journal of Microwaves, Vol. 3, Iss. 1, pp 193 – 226, 2023
- [2] TSOLIS,A., BAKOGIANNIS,S., ANGELAKI,C., ALEXANDRIDIS,A.A.: *Review of Clothing Components in the Development of Wearable Textile Antennas: Design and Experimental Procedure*, Sensors 2023, 23, 3289.
- [3] CUPAL,M., RAIDA,Z.: *Frequency Limits of Textile-Integrated Components*, 2020, 23rd International Microwave and Radar Conference (MIKON)
- [4] NEŠIĆ,D.: *Application of conductive tapes and foils in textile electronics*, 2023 10th International Conference on Electrical, Electronic and Computing Engineering (IcETRAN), East Sarajevo, Bosnia and Herzegovina, 2023, pp. 1-11
- [5] ALIMENTI,F., MEZZANOTTE,P, DIONIGI,M., VIRILI,M., ROSELLI,M.: *Microwave Circuits in Paper Substrates Exploiting Conductive Adhesive Tapes*, IEEE Microwave and Wireless Components Letters, Vol. 22, Iss. 12, 2012
- [6] NEŠIĆ,D., TANASKOVIĆ,D., VORKAPIĆ,M.: *Application of Self-Adhesive Conductive Material on Textiles*, TEKSTILNA INDUSTRIJA, Vol. 70, No 4, 2022.
- [7] KAUR,A., MALHOTRA,J.: *An Efficient Design of a DC-Block Band Pass Filter for the L Band*, Transactions on Electrical and Electronic Materials, vol. 18, no. 2, pp. 62–65, Apr. 2017.
- [8] WU,F., LIU,X., LIU,Y.A., YANG,Y.: *Analysis and Design of Dual-Band Micro strip DC-Block*, J. of Electromagn. Waves and Appl., Vol. 25, 1763–1772, 2011
- [9] JUN,S., CHANG,K.: *Compact Square DC-Block Bandpass Filter with Slots*, Progress in Electromagnetics Research Letters, Vol. 38, 17–23, 2013
- [10] TAO,Z., ZHU,J., ZUO,T., PAN,L., YU,Y.: *Broadband Microstrip-to-Microstrip Vertical Transition Design*, IEEE Microwave and Wireless Components Letters, Vol. 26, No. 9, pp. 660-662, 2016
- [11] WAGIH,W., KOMOLAFE,A., HILLIER,N.: *Screen-Printable Flexible Textile-Based Ultra-Broadband Millimeter-Wave DC-Blocking Transmission Lines Based on Microstrip-Embedded Printed Capacitors*, IEEE Journal of Microwaves, Vol. 2, no. 1, 2022
- [12] NEŠIĆ,D., TANASKOVIĆ,D., VORKAPIĆ,M.: *Microstrip DC-Block on Textiles Using Self-Adhesive Copper Tape*, 2023 16th International Conference on Advanced Technologies, Systems and Services in Telecommunications (TELSIKS-2023), 34-36.



# DETERMINATION OF NATURAL BACKGROUND RADIATION IN AN URBAN AREA AS AN ASPECT OF NUCLEAR SECURITY DETECTION ARCHITECTURE: AN EXAMPLE FROM THE CITY OF KRUŠEVAC, SERBIA

MILAN TANIĆ

Serbian Radiation and Nuclear Safety and Security Directorate, Belgrade, [milantanic@yahoo.com](mailto:milantanic@yahoo.com)

DENIS DINIĆ

University of Defense Belgrade, Military Academy, [denis.dinic@yahoo.com](mailto:denis.dinic@yahoo.com)

STEVAN STUPAR

Military Technical Institute, Belgrade, [stevan.stupar13@gmail.com](mailto:stevan.stupar13@gmail.com)

**Abstract:** *The potential consequences of a nuclear security event could be catastrophic; therefore, all appropriate measures should be taken to prevent them. Detection, as one of nuclear security's functions, involves recognizing criminal or unauthorized acts with nuclear security implications, or measurements indicating the unauthorized presence of nuclear or other radioactive material at associated facilities, activities, or strategic locations. Determining natural background radiation in advance for such locations can certainly enhance the effectiveness of nuclear security detection architecture. In this research, measurements of natural background radiation were conducted at 324 points evenly distributed throughout the City of Kruševac, Serbia, including locations and objects most vulnerable to exploitation by potential adversaries. The ambient dose equivalent rate was determined using a handheld radioisotope identification device based on scintillation gamma spectroscopy and mapped using geostatistical software. The measured dose rates fell within the expected ranges for Serbia, as well as for the broader region and worldwide. No orphan sources were detected. Statistical tests indicated a significant difference in dose rate values between paved and unpaved urban surfaces. Furthermore, the most common false positives in radioisotope identification were ascertained. It is concluded that utilizing the methodology applied in this work for collecting readings and spectra on natural background radiation proved to be a cost-efficient means of facilitating the assessment of alarms or alerts, as well as detecting the presence of suspicious or unauthorized nuclear or radioactive material in the environment.*

**Keywords:** *Nuclear security, material out of regulatory control, radioisotope identification device, gamma-ray spectroscopy, alarm.*

## 1. INTRODUCTION

The properties of nuclear and other radioactive materials have many legitimate, useful, and beneficial applications in medicine, energy production, research, industry, agriculture, etc. These materials are highly regulated and strictly controlled. However, due to their widespread use, nuclear and radioactive materials are also susceptible to being exploited for security violations. Nuclear security is defined as the prevention of, detection of, and response to, criminal or intentional unauthorized acts involving or directed at nuclear material, other radioactive material, associated facilities, or associated activities where those substances are used [1]. A nuclear security event is an event that may potentially or actually have an impact on nuclear security. Such events encompass a broad spectrum of activities, including unauthorized removal (illegal taking), illicit trafficking, unauthorized sale or transfer of nuclear or other radioactive material, sabotage of nuclear or other radioactive material or associated

equipment, or other malicious use of nuclear or other radioactive material, including cyber-attacks. Therefore, they must be addressed from a security standpoint [1].

While a regulatory framework related to nuclear security exists in the Republic of Serbia and all relevant stakeholders, i.e. competent authorities, have been identified, there is a lack of knowledge and awareness regarding nuclear security issues. Therefore, certain terms need to be further elaborated.

Regarding nuclear security issues, the key points involve malicious acts and materials outside regulatory control (MORC). MORC refers to the absence of direct control over material by an authorized person as mandated by regulatory requirements. This occurs in situations where nuclear or other radioactive material is present without appropriate authorization or in quantities that should be under regulatory oversight, but such control is absent due to failure or non-existence of regulatory measures [2]. Real-life examples of MORC include incidents such as lost in transit, illicit trafficking, theft, and orphan sources.

A malicious act is defined as an act or attempted unauthorized removal of nuclear material or radioactive material [3, 4] or sabotage, with the intent to cause death or physical injury to any person, material damage to any property, or damage to the environment [4]. An individual performing or attempting to perform a malicious act is an adversary [5].

A significant risk in nuclear security is the potential for adversaries to use nuclear or other radioactive material to create devices that expose people to radiation (RED, radiation exposure device), disperse radioactive material into the environment (RDD, radiation dispersion device), or even create a nuclear explosion (IND, improvised nuclear device) [6]. The potential consequences of a nuclear security event, particularly those involving RED, RDD, and IND, could be catastrophic. These events typically result in four main types of consequences: health, economic, environmental, and societal [1].

Prevention, detection, and response are the main nuclear security functions that must be in place to counter potential malicious acts. Prevention measures aim to deter adversaries from attempting or committing malicious acts, detection measures aim to discover such attempts or acts, and response measures are designed to address malicious acts that have already occurred or in progress. Considering MORC, detection measures rely on use of radiation detection instruments (technical detection capabilities), operation information, and medical surveillance for suspicious radiation injuries or illnesses (non-technical detection capabilities) [7].

The Nuclear Security Detection Architecture (NSDA) refers to the comprehensive network of nuclear security systems and measures, established within a suitable legal and regulatory framework, essential for executing a national strategy to detect nuclear and other radioactive MORC. The NSDA plays a crucial role in safeguarding individuals, property, society, and the environment from the adverse effects of nuclear security events by improving a state's ability to monitor and regulate the movement of nuclear and other radioactive materials [8]. However, given that states have limited resources, they should employ methods to identify which nuclear security measures will be most effective in reducing risk. The effectiveness of specific detection measure is evaluated and prioritized using a risk-informed approach [6]. Determining the natural background radiation in the area of identified targets of potential exploitation should certainly be included by competent authorities in a risk-informed approach, since one of the very first signs of a nuclear security event involving the dispersion of nuclear or radioactive material would be dose rate values above the natural background level in the affected area.

Target within a nuclear security event implies nuclear material, other radioactive substances, associated facilities, activities, or other locations and objects vulnerable to exploitation by nuclear security threats, including major public events, strategic locations, sensitive information, and assets [1]. Urban areas, due to their concentration of numerous locations that may be

targeted by nuclear security threats and the potential consequences for people, property, and the environment, are identified as having the highest probability of experiencing a nuclear security event. These targets include buildings, monuments, and places of symbolic importance such as government buildings, private institutions, palaces, museums, religious sites, and locations of cultural or political significance. Additionally, urban targets encompass transport infrastructure, critical infrastructure like power generation facilities, water treatment plants, bridges, and information systems that serve large populations, as well as dense population areas and major public events.

Since the initial assessment of an alarm or alert is the most crucial detection step, having information on the radiation levels in and around potential targets beforehand is essential for the successful and timely indication of a nuclear security event. This becomes even more important considering that natural background radiation exists due to cosmic rays, cosmogenic and terrestrial radionuclides, making it difficult to identify specific radiation signals in an environment with many benign radiation sources. Moreover, background radiation levels often vary throughout the day, typically slightly increasing during daylight hours and decreasing in the evening.

Instruments detect elevated radiation levels by comparing the ambient radiation against known background levels. A significant spike in radiation triggers an alarm. Radiation detection instruments used for nuclear security purposes generally measure gamma and neutron radiation. Nuclear and other radioactive materials emit radiation as a consequence of radioactive decay. However, different materials vary in the amount and type of ionizing radiation they emit, resulting in differences in the shape and strength of the instrument's signal.

Radiation detection instruments vary in size, mobility, capabilities, and features. For nuclear security purposes, they can be roughly divided into several categories: personal radiation detectors (PRD), portable radiation scanners (PRS), fixed radiation portal monitors (RPM), and hand-held instruments. Hand-held instruments are further classified into specific groups: gamma search devices, neutron search devices, and radioisotope identification devices (RID) [1, 7, 9]. RIDs locate and identify radionuclides present in the examined media. They are typically handheld but can also be worn as backpacks or mounted on vehicles. These instruments are capable of collecting and analyzing energy spectra to identify isotopes. Additionally, they can be used as dose rate meters, survey instruments, and to locate nuclear and other radioactive materials. Consequently, RIDs are widely used by nuclear security officers after an alarm from a PRD or RPM to confirm the alarm and identify the source. Due to their versatility, characteristics, and wide availability, RID devices are ideal for measuring natural background radiation for nuclear security purposes.

The literature review revealed that the consideration of natural background radiation in urban areas as part of NSDA for cities in Serbia has not yet been undertaken so

far. Therefore, the objectives of this study were: 1) to determine natural background radiation by collecting gamma-ray spectra and measurement of ambient dose equivalent rates in the area of the City of Kruševac, Serbia, using a proven RID; 2) to spatially map the collected data; and 3) to identify the most common challenges associated with radiation detection using instruments, in order to understand the limitations of the selected detection device when integrating these measurements into NSDA.

## 2. MATERIALS AND METHODS

Kruševac is a midsized city in central Serbia, serving as the administrative center of the Rasina District. With a population of 53,746 according to the 2022 Census and covering a total area of approximately 11.3 square kilometers, it represents an average Serbian city. Kruševac is a vital hub for local industries and commerce, significantly contributing to regional economic development. Its strategic location ensures easy access to major cities in Serbia, making it a key transit point and regional center, including the possible transport of radioactive sources. Kruševac was the medieval Serbian capital and holds great historical importance and heritage. Given these factors, the city contains numerous potential targets that could be exploited by adversaries in the context of nuclear security. There are no nuclear or associated facilities within the city's borders. Among authorized radiation practices, medical ones are predominant. One of the measuring stations equipped with instrument that continuously monitors air radioactivity, as part of the national early warning system for nuclear or radiological emergencies, is located in Kruševac. This station is also integrated into the European Radiological Data Exchange Platform (EURDEP).

All measurement were carried on using a hand-held RID ThermoScientific RIIDEye M-GN, equipped with a 2" × 2" NaI(Tl) crystal scintillation detector. The intrinsic efficiency for the  $^{137}\text{Cs}$  662 keV photo-peak was 26.5 %. The resolution for the same photopeak was experimentally determined to be 8.31 %. This radiation spectrometer was calibrated to identify gamma-rays and radionuclides between 0.25 keV and 3 MeV. Operating voltage of integral high voltage supply was 400 V. The settings for the amplifier were as follows: coarse gain 1, fine gain 1.29, shaping time 1.28  $\mu\text{s}$ , and negative polarity. The lower and upper level discriminators (LLD and ULD) were set 0.80 % and 100 %, respectively, expressed as a percentage of the full spectrum below/above spectral information was not captured. The zero offset was 0.1445 % of the spectrum. High voltage, gain and zero offset were adjusted by coarse calibration using an unshielded 37 kBq  $^{137}\text{Cs}$  source, performed daily when sampling was carried on. Fine energy calibration was factory set up. Conversion gain (total number of channels) was 256. RID used in this research are specifically designed for search missions and the identification of radionuclides and nuclear materials. The isotope identification algorithm employs quadratic compression conversion (QCC), which addresses

challenging peaks by increasing the number of channels and concurrently compressing high-energy peaks to enhance the signal-to-noise ratio. The system is constructed in accordance with ANSI 42.34 standards, and the data is provided in the ANSI 42.42 spectral report format, which is compatible with any PC-based software for review

All measurements of the ambient dose equivalent rate in the air  $\dot{H}^*(10)$ , were taken at a height of 1 m from the ground. The sampling time was 300 s. Sampling time was calculated based on a desired 1 % uncertainty of the gamma count rate at a 95 % confidence level. An initial assessment of the gamma count rate at ten random locations showed that an average value of 134 cps (counts per second) could be expected. Measurements were carried on from March to May 2024, during daylight. The similar methodology was utilized in the research with similar design [10].

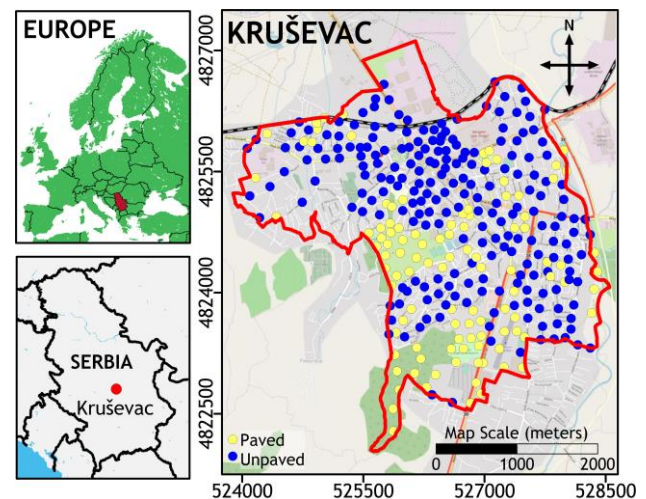


**Figure 1.** Map of the study area with denoted measurement points

A total of 324 measurement points were randomly selected to evenly cover the entire territory of the City of Kruševac, with sampling density of approximately one point per 40,000  $\text{m}^2$ . This included all locations critical from a nuclear security perspective, such as the City Hall, headquarters of governmental and self-governmental institutions, green markets, sports centers, schools, main squares, most visited parks, churches, and the most occupied parking places. One-third of all measurement points were unpaved. All measurement points were freely and easily accessible to the public. Areas with restricted access, such as military facilities and industrial complexes, were excluded from the research. The coordinates for each measurement point were determined by a GPS device with a precision of  $\pm 3$  m, and using GeoSrbija, a portal of the Serbian Geodetic Authority. A map of the study area including the locations of all measurement points is presented in Figure 1.

Statistical analyses were performed using the IBM SPSS Statistics v.20 software package. The spatial presentation of the results was done using Surfer Golden Software 12, with inverse distance weighting (IDW) used as the

interpolation method. This method assumes that the influence of the variable decreases with the increase in distance from the point where the value of the variable is known.

### 3. RESULTS AND DISCUSSION

Descriptive statistics of ambient dose equivalent rate (hereinafter: dose rate) determined at all measurement points in this work are listed in Table 1. The dose rate values ranged from 10.09 to 103.68 nSv h<sup>-1</sup> with an average of 55.52 nSv h<sup>-1</sup>. The mean dose rate obtained in this study was considerably lower than the mean annual dose rates in the Republic of Serbia in 2022, which varied from 105 to 137 nSv h<sup>-1</sup> [11].

Background radiation under normal conditions originates from cosmic radiation, as well as natural and anthropogenic radionuclides in the soil, air, and ground surface. Radiation emitted from primordial terrestrial radionuclides represents the main component [12]. NaI scintillator detectors, based on their features, measure terrestrial radiation very well (103 % response) but only 30 % of secondary cosmic radiation [13]. Therefore, the obtained mean dose rate value is in good accordance with the worldwide average outdoor absorbed dose rate of 56 nGy h<sup>-1</sup>, which corresponds to 41 nGy h<sup>-1</sup> when taking into account a conversion coefficient of 0.7 Sv Gy<sup>-1</sup> [12].

**Table 1.** Descriptive statistic of the ambient dose equivalent rate  $\dot{H}^*(10)$  (in nSv h<sup>-1</sup>, unless otherwise indicated)

Parameter	$\dot{H}^*(10)$	Parameter	Value
Mean	55.52	St. deviation	21.05
Median	48.50	CV/%	37.91
Minimum	10.09	Skewness	0.52
Maximum	103.68	Kurtosis	-0.80

The dataset distribution was tested using the Shapiro–Wilk test, and it showed no normal distribution ( $p = 0$ ), which is expected given the nature of environmental measurements and the large sample size. Data were tested for outliers according to Grubbs’ criteria, and no outliers were detected.

Dose rates may strongly vary over short distances, and it is important to detect these local changes as clearly as possible. The measured doses varied according to the cover of the particular location, as well as the geological background, soil types, and the types of building materials used in buildings or other constructions in close proximity to the particular measurement point (hereinafter: MP).

There were two groups of MPs based on their cover: 1) paved and 2) unpaved. The unpaved MPs had no pavement, tiles, or other types of artificial cover and often featured vegetation on the surfaces. The type of MP at a certain location in the study area was chosen based on the most dominant type of cover and the authors’ judgment of where residents would have the highest occupancy time

outdoor. The spatial distribution of paved and unpaved MPs is shown in Figure 1. For the 106 unpaved MPs, the dose rate values ranged from 10.09 to 102.59 nSv h<sup>-1</sup> with a mean of 79.32 nSv h<sup>-1</sup>. In contrast, for the 218 paved MPs, the dose rate values ranged from 12.79 to 103.68 nSv h<sup>-1</sup>, but the average value was notably lower at 43.95 nSv h<sup>-1</sup>. A Box-Whisker plot of the dose rate values for the total number of MPs, as well as for the two groups of MPs separately, is provided in Figure 2.

The dose rate values obtained for unpaved MPs are in good agreement with the values obtained at the automatic measuring station in Kruševac in the sampling period (approximately 80 nSv h<sup>-1</sup>), which is also installed at locations with unpaved grassy surface. Results of continuous monitoring can be accessed via the EURDEP platform (<https://remap.jrc.ec.europa.eu/Advanced.aspx>, measuring station RS31156).

The coefficient of variation (CV) is the most obvious statistical parameter for describing data variability. This factor taken into account all MPs was 37.91 %, indicating uneven distribution of dose rate values across the study area, which may suggest anthropogenic influence on radionuclide specific activity contributing to radiation levels. However, further examination of the two datasets showed that their standard deviations were quite low, resulting in low CV values of 17.60 % and 18.02 % for unpaved and paved MPs, respectively. These findings clearly indicate no anthropogenic influence on dose rate values in the study area.

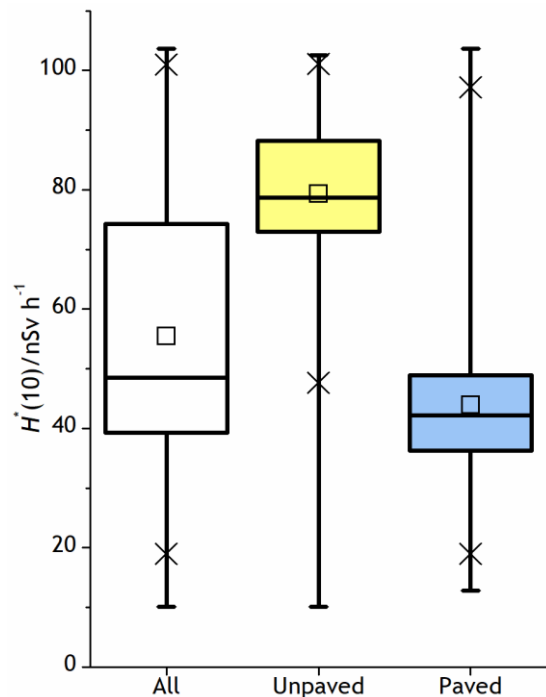


**Figure 2.** Box (25<sup>th</sup>-75<sup>th</sup> quartile) and Whisker (min-max) plot of the ambient dose equivalent rate (square represents mean values, and crosses 1<sup>st</sup> and 99<sup>th</sup> percentile)

Bearing in mind that dataset was not normally distributed, but the sample size was large enough ( $n = 324$ ), an independent samples  $t$ -test was conducted to compare the

means of the ambient dose equivalent rate between two groups of measurement points, those with paved surfaces and those with unpaved surfaces. Levene's test for equality of variances indicated that variances of the two groups were assumed equal ( $p = 0.372$ ). The t-test revealed significant differences between the two groups ( $t = 23.097$ ,  $p = 0$ ), with a mean difference of  $35.37 \text{ nSv h}^{-1}$ . The 95 % confidence interval for the mean difference ranged from  $32.36$  to  $38.38 \text{ nSv h}^{-1}$ . Based on eta square value ( $\eta^2 = 0.55$ ), the effect of ground cover on the ambient dose equivalent rate was considered large.

An isodose map was produced to represent the spatial variability of the dose rates due to natural background radiation and is presented in Figure 3.

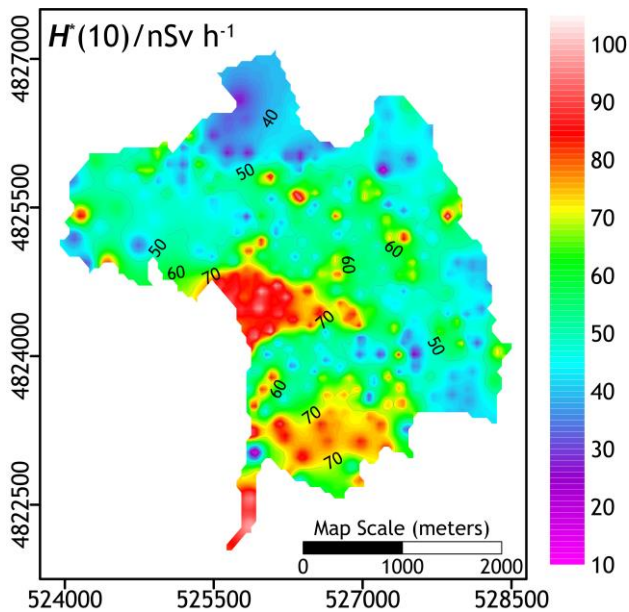


**Figure 3.** Spatial distribution of ambient dose equivalent rate depicted using IDW to a power as the gridding interpolation method

As can be noticed, depending on the color and its intensity, which is proportional to the dose rate value, two regions can be clearly delineated. The first region is located in the south of the study area, where the lowest dose rates were measured and interpolated. This is an industrial zone with no vegetation and virtually no unpaved surfaces. The second region, which spreads to the south and southwest of the study area, is where the highest dose rates were measured. This region includes the largest city park (Memorial Park "Slobodište") and a dense deciduous forest. Moreover, this is the least urbanized part of the city.

Primordial natural radionuclide  $^{40}\text{K}$ , along with radionuclides belonging to the  $^{238}\text{U}$  ( $^{226}\text{Ra}$ ) and  $^{232}\text{Th}$  radioactive families, are the most dominant radionuclides in soil. Potassium-40 was identified at 77% of MPs, while  $^{226}\text{Ra}$  and  $^{232}\text{Th}$  were identified at 11 % and 5 % of MPs, respectively. The MPs where the last two radioisotopes were identified were those where the highest dose rates were determined. The majority of  $^{40}\text{K}$  and  $^{232}\text{Th}$  positive identifications were recorded at unpaved MPs.

Conversely,  $^{226}\text{Ra}$  was recorded above paved MPs with granite tiles or in the close vicinity of buildings. Therefore, one can conclude that the  $^{226}\text{Ra}$  identification is mostly a consequence of higher  $^{238}\text{U}$  content in building materials.

False positive (hereinafter: FP) is defined as the situation when the instrument identified one or more radionuclides that were not present as being present without making any correct identification other than  $^{40}\text{K}$  [14].

The existence of FPs was verified by additional spectrum acquisition at measurement points (MPs) where unexpected radionuclides were identified. That measurement was taken using a  $2'' \times 2''$  NaI(Tl) scintillation detector (ORTEC 905-3) with the ScintiPack Photomultiplier Base (Model 296) coupled with a digiDART portable multichannel analyzer. Spectra were collected with a 512 conversion gain. The obtained spectra were later processed and inspected using ScintiVision 32 software. Each measurement (spectrum acquisition) lasted 600 seconds.

The most frequent radionuclides other than natural ones, that were identified were:  $^{133}\text{Xe}$  and  $^{109}\text{Cd}$  (26),  $^{103}\text{Pd}$  (6),  $^{192}\text{Ir}$  and  $^{88}\text{Y}$  (5),  $^{238}\text{Pu}$  and  $^{239}\text{Pu}$  (3),  $^{233}\text{U}$  (2),  $^{54}\text{Mn}$  and  $^{57}\text{Co}$  (1). The number of MPs where each particular radionuclide was identified is given in parentheses. It is worth mentioning that all of them were identified with a low level of confidence, and measured dose rates were not high. Further verification of the mentioned isotopes confirmed that they were not present in the environment, so their identifications were FPs. Therefore, it can be concluded that neither MORC nor orphan sources were detected in the study area. Given that some of listed radionuclide appeared in the same spectrum, the overall FP rate was 19 %. Similar FP rates were found in other research evaluating the features of hand-held RIDs [14].

All of the FPs are artificial radionuclides. Since there were no authorized radiation practices in Kruševac involving these radionuclides, their presence was considered unexpected. The most probable reasons for such an FP rate were short counting time, a limited radionuclide library, and the QCC spectrum analysis algorithm specifically designed for nuclear security purposes, especially for the identification of special nuclear material. Moreover, all of them, except  $^{192}\text{I}$ ,  $^{88}\text{Y}$ , and  $^{54}\text{Mn}$ , emit low-energy gamma rays with low intensity. Further discussion of FPs is beyond the scope of this paper.

#### 4. CONCLUSION

This research is the first of its kind in the study area. The level of natural background radiation was determined for the entire territory of the City of Kruševac. The authors concluded, based on the average values of the dose rate, that these values are below the background levels for Serbia. Paving of public roads, sidewalks, and other urban areas was identified as a major contributor to the reduction of dose rates at various points in the study area. Although the range of the dose rates was similar in the

two groups of MPs, their mean values differed by a factor of 1.80. Nevertheless, the values of the ambient dose equivalent rate for unpaved surfaces were in good agreement with background levels for Serbia.

The knowledge of natural background radiation and particularly the availability of maps of dose rates due to background radiation are important in order to detect artificial radioactive contamination after a nuclear security event and to evaluate its impact on the population.

Determination of natural background radiation in advance for urban environments is one of the activities that certainly can enhance the effectiveness of NSDA by contributing to capacities to monitor and control the movement of nuclear and other radioactive material. This is particularly important because if nuclear security event had occurred, most measurements would have been taken by responders who are non-technical personnel and will need some kind of "standard" to compare and interpret the obtained results. Therefore, this process may serve as an auxiliary component of technical support for detection within the framework of NSDA.

This research was conducted as a preliminary study. Further investigation will focus on increasing the measurement point density to cover the entire city, up to one point per 20,000 m<sup>2</sup>, employing additional radiation equipment relevant to nuclear security (e.g. PRDs), measuring additional quantities (gross count rate, gamma, and neutron count rate), conducting indoor measurements (in dwellings, schools, and other buildings), performing those measurements in different seasons to assess temporal variability of the natural background, conducting geostatistical analysis of the obtained results, and assessing the radiation risk for the population under normal circumstances.

## Acknowledgements

This work was by Serbian Ministry of Defense and Serbian Ministry of Education, Science and Technological Development, Grant No 451-03-66/2024-03/200325.

## References

- [1] INTERNATIONAL ATOMIC ENERGY AGENCY, *Objective and Essential Elements of a State's Nuclear Security Regime*, Nuclear Security Series No. 20, IAEA, Vienna, 2013.
- [2] INTERNATIONAL ATOMIC ENERGY AGENCY, *Nuclear Security Recommendations on Nuclear and Other Radioactive Material Out of Regulatory Control*, Nuclear Security Series No. 15, IAEA, Vienna, 2011.
- [3] INTERNATIONAL ATOMIC ENERGY AGENCY, *Nuclear Security Recommendations on Radioactive Material and Associated Facilities*, Nuclear Security Series No. 14, IAEA, Vienna, 2011.
- [4] INTERNATIONAL ATOMIC ENERGY AGENCY, *Security of Radioactive Material in Use and Storage and of Associated Facilities*, Nuclear Security Series No. 11-G, IAEA, Vienna, 2019.
- [5] INTERNATIONAL ATOMIC ENERGY AGENCY, *Security of Radioactive Material in Use and Storage and of Associated Facilities*, Nuclear Security Series No. 8-G (Rev. 1), IAEA, Vienna, 2020.
- [6] INTERNATIONAL ATOMIC ENERGY AGENCY, *Risk Informed Approach for Nuclear Security Measures for Nuclear and Other Radioactive Material out of Regulatory Control*, Nuclear Security Series No. 24-G, IAEA, Vienna, 2015.
- [7] INTERNATIONAL ATOMIC ENERGY AGENCY, *Detection in a State's Interior of Nuclear and Other Radioactive Material out of Regulatory Control*, Nuclear Security Series No. 47-T, IAEA, Vienna, 2024.
- [8] INTERNATIONAL ATOMIC ENERGY AGENCY, *Nuclear Security Systems and Measures for the Detection of Nuclear and Other Radioactive Material out of Regulatory Control*, Nuclear Security Series No. 21, IAEA, Vienna, 2013.
- [9] INTERNATIONAL ATOMIC ENERGY AGENCY, *Nuclear Security Systems and Measures for Major Public Events*, Nuclear Security Series No. 18, IAEA, Vienna, 2012.
- [10] AMARAL, R.D.S., et al.: *Environmental Ionizing Radiation Dose Outdoor in an Inhabited Area with a High Concentration of Urano-Phosphate in Northeast of Brazil*, Radiation Protection Dosimetry, 181(3) (2018) 181-189.
- [11] SERBIAN RADIATION AND NUCLEAR SAFETY AND SECURITY DIRECTORATE: *The Annual Report on Public Exposure to Ionizing Radiation in the Republic of Serbia in 2022*, SRBATOM, Belgrade, 2023.
- [12] UNITED NATION SCIENTIFIC COMMITTEE ON THE EFFECT ON IONIZING RADIATION, *Sources and Effect on Ionizing Radiation, UNSCEAR 2008, Report to the General Assembly with Scientific Annexes, Volume I, Annex B*, United Nations, New York, 2010.
- [13] VULETIĆ, V., et al.: *Comparison of Gamma Dose Rate Values in Air Measured by GM Counters, Ionization Chambers, and Thermoluminescence Dosimeters*, in Proceedings of the XXV Symposium of the Radiation Protection Society of Serbia and Montenegro, Kopaonik, pp. 289-292, 2009.
- [14] PIBIDA, L., UNTERWEGER, M., KARAM, R.: *Evaluation of Handheld Radionuclide Identifiers*, Journal of Research of the National Institute of Standards and Technology, 109(4) (2004),



## INVESTIGATION OF THE POSSIBILITY OF APPLICATION OF BIOINDICATORS IN REDUCTION LEVEL CONCENTRATIONS OF RADIOLOGICAL CONTAMINANTS

NATAŠA PAJIĆ

Military Technical Institute, Belgrade, [natasa.pajic969@gmail.com](mailto:natasa.pajic969@gmail.com)

ŽELJKO SENIĆ\*

Military Technical Institute, Belgrade, Belgrade, [zsenic1@gmail.com](mailto:zsenic1@gmail.com)

SONJA BAUK

Military Technical Institute, Belgrade, Belgrade, [bauk.sonja@gmail.com](mailto:bauk.sonja@gmail.com)

**Abstract:** Bioindication and biomonitoring imply the use of biological parameters to monitor the state and quality of environment. The main task of biomonitoring program is to define appropriate indicators, whose presence and specific behavior will indicate effects of environmental and ecosystem disturbances. Biological indicators are unique indicators of state of environment, which give a signal about the ecological status of ecosystem. Using bioindicators as an early warning sign of radiological accident can help in conservation environment. The presented results indicate that lichens are good bioindicators of environmental pollution with radioactive isotope ( $^{137}\text{Cs}$ ). Higher level of ( $^{137}\text{Cs}$ ) on our territory was indicated on Chernobyl accident, what is shown by measurement of activities of samples in this study.

**Key words:** biomonitoring, indicators, cesium, ecosystem

### 1. INTRODUCTION

The appearance of radioactivity dates back to the beginning of the world. The world we live in has been radioactive since its inception. Radioactive elements can be found in soil, air, water, food, and therefore in all living beings. According to the method of origin, they are divided into those that are present on Earth, and those that arise as a result of cosmic radiation, as well as those that arise as a result of human influence. Natural radioactivity is the result of decay of naturally unstable nuclides. All these radionuclides have a long half-life. An exception is radon gas, which has a half-life of 3.8 days. They are divided into three series: uranium  $^{238}\text{U}$ , neptunium  $^{237}\text{Np}$  and thorium  $^{232}\text{Th}$ . Primary radioactive elements in nature are uranium, thorium and potassium. Potassium-40 is a beta-gamma emitter, with a physical half-life of  $T_{1/2} = 1.28 \times 10^9$  years [1].

Radioactive radiation changes the structure and properties of the material it passes through. The most significant effect is ionization. The earliest and most common use of ionizing radiation is to diagnose injuries and diseases. However, ionizing radiation has enough energy to ionize some atoms in the body. Such ions disrupt biochemical processes in cells, which can lead to various disorders in the functioning of cells in their division, which causes serious diseases. For the safety of the human population, it is necessary to monitor the level of radionuclides in the environment.

Systematic measurement of natural radionuclides in soil,

food, animal feed, air and water can determine the radionuclides that enter the human body through food. Some bioindicator species can also be used for monitoring; such as mosses, lichens, ferns and mushrooms.

Mosses accumulate a high dose of radioactivity. They are one of the most important collectors of radionuclides from the air and as such represent a bioindicator of radioactive fallout. They have the ability to retain a large part of radioactive fallout. Given the prevalence and simplicity of sampling, mosses provide a complete insight into the state of contamination of a certain area.

### 2. MOSSES AND LICHES AS BIOMONITORS

Biomonitoring of the environment represents a series of methods that monitor the impact of contamination on biological processes in organisms. Given the frequent distribution of organisms in a certain area, this allows biomonitoring to have great advantages over other methods. Some species are very sensitive to pollution, while others are very tolerant of air pollution and are used as a kind of indicator. Mosses grow in groups, forming a cluster, small "cushions" or carpet like forms. [2]





**Figure 1.** Moss colony

Mosses are perennial plants of slow growth, they are extremely sensitive biological organisms from the point of view of radioactivity monitoring. They can be used to collect reliable information about air and environmental pollution with radioactive substances, especially in the conditions of radiological accidents. The main content of radionuclides is in the upper green parts of the plant and it is estimated that the accumulation of radionuclides is concentrated in the upper parts of the plant. Direct deposition of radionuclides on that type of plants is the most important way of their contamination. From the point of biomonitoring, it is necessary to pay attention to the following properties of bioindicators

- (a) the absence of a root system prevents the reception of ions from the soil or some other substrate,
- (b) an underdeveloped cell membrane allows the absorption of metal ions along the entire surface of the cell,
- (c) the specific composition of the partition wall contributes to rapid ion exchange,
- (d) the ability to accumulate and tolerate a high concentration of metals, radioactive contamination of an area after a nuclear,

Mosses have several advantages over settling tanks used for pollution detection. Mosses are very widespread, and their sampling is very simple and inexpensive. Likewise, some types of mosses are capable of accumulating heavy metals to high concentrations, significantly higher than those obtained in samples from settling collectors. Thus, various analytical techniques can be used to obtain more precise results, because the concentrations of radionuclides in mosses are generally well above the detection limit. [3]

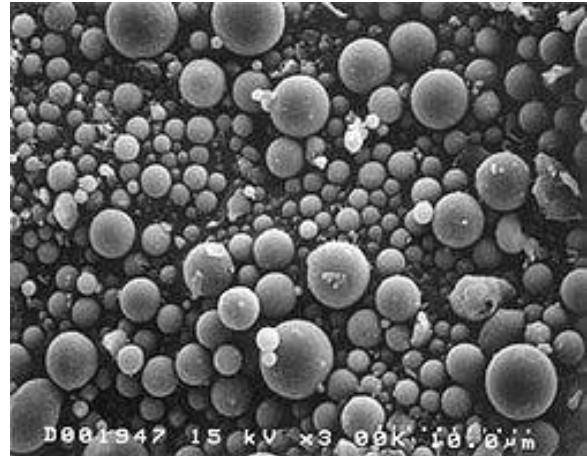


**Figure 2.** Scanning electron microscope (SEM) images of aerosol particles detected on the surface of mosses

In areas where mosses occur in their natural habitats, air pollution can be assessed by means of active biomonitoring, using moss bags. Samples are collected from uncontaminated areas in bags that are transported to the region that is in the process of monitoring. The measurement procedure is performed before and after exposure of the sample to radiological contamination.

Radioactive elements can accumulate in mosses to very high concentrations, so they represent an effective biological indicator of radionuclides.

### 2.1. Lichens as biomonitors

Lichens are organisms adapted to survive in extreme conditions. They survive in areas of high humidity and drought, large light and temperature changes, high levels of radioactivity and high concentrations of polluting substances.

Information on the spatial and temporal distribution of radionuclide pollution is obtained by exposure to the emission of fission products.



**Figure 3.** Lichens colony

Lichens are specific organisms in the body of which lichen acid compounds are formed. the acid that is formed is usnic acid, which has found great use in medicine, the

perfume industry, and the cosmetic industry. In addition to lichen acids, lichens contain and build compounds such as antioxidants, which have found application in pharmacology.

Lichens are considered accumulators of radionuclides, heavy metals and pesticides from the environment, which is most likely a consequence of the reaction of organic acids created by lichens. [4]

Due to the ability of lichens to absorb  $^{137}\text{Cs}$  from the environment and to concentrate it in their body, lichens are an important element of radioecological studies of ecosystems, and environmental monitoring using lichens is important for assessing the radiation load of organisms living in that area.

### 3. MATERIAL AND METHODS

Samples of bioindicators (moss and lichen) were collected in the area of Belgrade parks and forests (Kosutnjak, Makis, Zvezdara forest, Avala, Topcider park).

The activity was determined by the gamma spectrometric method (HPGe detector with an efficiency of 56% and a resolution of 1.72 keV for  $^{60}\text{Co}$  at 1.3 MeV).

The samples are delivered to the laboratory, cleaned of visible impurities (soil, grass), dried and measured in Marinelli bowl with a volume of 1l.

Spectrum processing was performed using the software package GammaVision 32. The relative measurement uncertainty of sample preparation and measurement is up to 10%. The activity of  $^{134}\text{Cs}$  was determined via the  $\gamma$ -lines at energies of 604 KeV, 796 KeV and 802 KeV,  $^{137}\text{Cs}$  via the  $\gamma$ -line at the energy of 661.6 KeV, and  $^{40}\text{K}$  via the  $\gamma$ -line at energy of 1460 KeV.

The measured activity was converted into a dose assuming that all emitted particles (gamma and beta) were absorbed in the tissue that accumulated  $^{137}\text{Cs}$ .

#### 3.1. Equipment and calibration

Calibration of the detector for measuring plant samples was done with a reference radioactive material, a matrix of silicone resin in Marinelli geometry. As a calibration source, a 1000ml mix standard of the MBSS 2 type in Marinelli geometry of the Inspectorate for ionizing radiation Czech metrological institute (Inspectorate for ionizing radiation Czech metrological institute) was used - certificate number: Cert.No: 9031-OL-159/08 total activities 41, 48 KBq on August 31, 2023 ( $^{241}\text{Am}$ ,  $^{109}\text{Cd}$ ,  $^{139}\text{Ce}$ ,  $^{57}\text{Co}$ ,  $^{60}\text{Co}$ ,  $^{203}\text{Hg}$ ,  $^{88}\text{Y}$ ,  $^{113}\text{Sn}$ ,  $^{85}\text{Sr}$ ,  $^{137}\text{Cs}$ ). The time of measuring the samples is 60000 s.

#### 3.2. Examination of radioactivity by gamma spectrometry

Gamma spectrometry is today a highly developed and applicable method for monitoring and measuring the activity of samples from the environment. Gamma spectrometry makes it possible to identify radionuclides

present in the sample and determine their concentration by detecting the emission of gamma photons from a specific sample. All detector systems used in  $\gamma$  radiation spectrometry consist of a detector and associated electronics. The conversion of photon energy into the kinetic energy of electrons and positrons occurs through some of the previously mentioned interactions. The result of each individual interaction is the creation of a certain amount of charge carriers, which can be detected and measured. The generated charge carriers are collected on the detector electrodes with the help of an electric field, and the collection time itself depends on the type and geometry of the detector. In the case of gas detectors, the collection time is a few milliseconds, while with semiconductor detectors it is only a few nanoseconds.

The main characteristics of the detector come from the density, volume and atomic number of the material from which it is made. It is these quantities that are related to the probability of interaction of x radiation with the detector material and the probability that the entire energy of the gamma radiation photon will be deposited in the detector volume. [5]

Semiconductor detectors, as the most widely used detectors, can be viewed as ionization chambers in the solid state, which differ according to the density and dimension of their detector volume. Unlike the previously used gas detectors, the use of semiconductors provides an advantage, first of all, in the amount of energy used to create an electron-positron pair.

Semiconductor detectors, as the most widely used detectors, can be viewed as ionization chambers in the solid state, which differ according to the density and dimension of their detector volume. Unlike the previously used gas detectors, the use of semiconductors provides an advantage, first of all, in the amount of energy used to create an electron-positron pair.

In semiconductor detectors, this energy is about ten times less than the energy required to create an electron-ion pair in gas detectors. The advantage is also reflected in their quick response and small size.

The working principle is based on the passage of radiation through the depletion region, during which electron-hole pairs are created, which are quickly ejected from this region due to the effect of the existing electric field. The resolution depends on the energy deposited in the detector, that is, at higher energies, the resolution is better.

The first semiconductor material used for the detection of gamma radiation was silicon (Si), and later germanium (Ge) was used, which had an exceptional energy resolution, which is why it was widely used in spectrometry of photon radiation. In order to improve the performance of germanium detectors, a new material known as high-purity germanium with an active volume about 1 cm wide was obtained. Due to germanium detectors, gamma spectrometry is a widely used measurement technique for determining the concentration

of radionuclide activity in various samples.

### 3.3. Determination of radionuclide activity

The specific activity of radionuclides is determined based on the expression

$$A = \frac{N}{\varepsilon \cdot \gamma \cdot ts \cdot V(m)}$$

Equation means:

$N = N_s - \frac{ts}{tb} \cdot N_b$  – corrected total area under a given photopeak of the corresponding gamma energy in the spectrum

$N_s$  – the total area of the photo peak in the spectrum

$N_b$  – the corresponding total area of the photo peak in the basic radiation spectrum

$tb(s)$  – total time of basic radiation spectrum recording

$ts(s)$  – total time of recording the spectrum of the sample

$\varepsilon$  – efficiency on the gamma energy of the photo tip

### 3.4. Sample preparation and gamma emitter spectrometry methods

The preparation of plant culture samples consists of drying at room temperature, concentration, i.e. mineralization at a temperature of 450°C and closing with parafilm in order to establish a radioactive balance.

Mineralization is carried out for the purpose of concentrating plant cultures and water in order to reduce the overall measurement uncertainty of measurement and minimal detection of specific activity, but also to increase the efficiency of detection.

The sample preparation procedure was based on the recommendations of IAEA 25. [6]

The measurement geometry was determined depending on the type of samples and for that purpose a plastic Marinelli geometry of 1000 ml was used for non-mineralized plant, soil and sediment samples.

### 3.5. Sample preparation and gamma emitter spectrometry methods

Since the distribution of radionuclides in the soil is not uniform, the radium equivalent index  $R_{aeq}$  was determined. This index compares the specific activity of materials containing different amounts of  $^{226}\text{Ra}$ ,  $^{232}\text{Th}$  and  $^{40}\text{K}$ .  $R_{aeq}$  was calculated using the following formula and expressed in Bqkg-1

$$R_{aeq} = CRa + 1,43CTh + 0,07CK$$

The definition of  $R_{aeq}$  is based on the assumption that a specific activity of 370 Bqkg-1 originating from  $^{226}\text{Ra}$ , or a specific activity of 259 Bqkg-1 originating from  $^{232}\text{Th}$ , or a specific activity of 4 810 Bqkg-1 originating from  $^{40}\text{K}$ , produces the same gamma dose rate.

External absorbed dose

Based on the results of measuring the activity of radionuclides in the soil, the strength of the external absorbed dose of gamma radiation 1 m above the ground, which originates from the detected radionuclides  $^{226}\text{Ra}$ ,  $^{232}\text{Th}$  and  $^{40}\text{K}$  in Bqkg-1, was determined using the following formula:

$$D(nGyh^{-1}) = 0.462C_{Ra} + 0.604C_{Th} + 0.0417C_{K},$$

Equation means:

$C_{Ra}$ ,  $C_{Th}$ ,  $C_{K}$  represent specific activities of  $^{226}\text{Ra}$ ,  $^{232}\text{Th}$  and  $^{40}\text{K}$  in soil

Calculation of the annual effective dose ( $DE$ )

The annual effective dose is determined using the formula:

$$DE (mSv) = 0.7(SvGy^{-1}) \cdot 365 (days) \cdot 24 (h) \cdot D(nGyh^{-1}) \cdot 0.2$$

The formula for estimating the annual effective dose includes a coefficient of 0.7  $SvGy^{-1}$ , which represents the conversion of the absorbed dose in the air into an effective dose, as well as the external factor K (0.2), i.e. the time a person spends in the external environment, i.e. 20% [ 7]

### 3.6. Soil-plant transfer factor (TF)

The external hazard index  $Hex$  was calculated using the formula:

$$Hex = CU 370 + CTh 259 + CK 4810 \leq 1,$$

Equation means:

$CU$ ,  $CTh$ ,  $CK$  represent the specific activity of  $^{226}\text{U}$ ,  $^{232}\text{Th}$  and  $^{40}\text{K}$  in Bqkg-1

The maximum value of  $Hex$  equal to unity corresponds to the upper recommended limit  $R_{aeq}$  of 370 Bqkg-1 [8]

The value of this index must be less than unity in order for the impact of radionuclides on the environment to be considered negligible.

### 3.6. Soil-plant transfer factor (TF)

**Table 1.** Average values of soil-plant transfer factors of individual elements in the soil of the wider area of Belgrade area:

Element	Plant community	Parts of plant	Mean and standard deviation
Be	Meadow	Halm	4,2±1,3
Cs	Grass	Halm	4,2±1,3
	Meadow	Halm	6,3±2,4
	Moss	Halm	7,5±1,8
K	Meadow	Halm	3,1±1.8

Pb	Grass	Halm	9,2±4,8
	Meadow	Halm	1,3±4
Ra	Grass	Halm	3,1±1.11
	Meadow	Halm	7,1±2,6
	Moss	Halm	6,9±4,5
Th	Lichen	Halm	4,2±3,1
	Meadow	Halm	9,9±5,5
U	Moss	Halm	1,7±9,4
	Grass	Halm	4,6±5,3
	Meadow	Halm	3,6±5,9

The International Atomic Energy Agency (1994) defined the transfer factor as the ratio of the specific activity of radionuclides in dry plant mass to the specific activity of radionuclides in soil. The soil-plant transfer factor was calculated for  $^{226}\text{Ra}$ ,  $^{232}\text{Th}$ ,  $^{40}\text{K}$ ,  $^{238}\text{U}$ ,  $^{235}\text{U}$ ,  $^{137}\text{Cs}$  and  $^{210}\text{Pb}$  using the formula:

$$TF = \frac{\text{radionuclide activity per unit of dry mass (Bqkg}^{-1}\text{)}}{\text{radionuclide activity per unit of dry soil (Bqkg}^{-1}\text{)}}$$

The quantification of radionuclide uptake by plants was monitored through the "soil-plant" transfer factor for all radionuclides, and the results are presented in Table 1. The transfer factor research results for  $^{40}\text{K}$  are higher than for  $^{226}\text{Ra}$  and  $^{232}\text{Th}$ , which is in accordance with literature values. The maximum value of TF- $^{40}\text{K}$  was found in the samples from the control area "Makis", TF- $^{226}\text{Ra}$  in the samples of Zvezdara forest. In the case of  $^{210}\text{Pb}$ , higher values of the transfer factor were obtained, which is in accordance with the fact that the plant, in addition to absorbing this radionuclide from the soil, can also absorb it through the leaves.

The transfer factor for lead in the moss samples from Avala of 1.75 is similar to the values obtained from other localities, while in the twigs it is 1.38. A lower value of TF- $^{137}\text{Cs}$  was found in *Cetraria islandica* in this test compared to *Pseudevenia furfuracea*, which determined that the mean value of Tf in the leaves is 0.019, and in the soil 0.036. Lichens from the area of Kosutnjak show different transfer factor values, and also in a large number of samples due to very low specific activity, Tf could not be determined. Potassium, as one of the most widespread elements in nature, is part of the method of monitoring radionuclides and other indicators of the state of the environment in order to optimally manage areas covered by forest vegetation.

## 4. RESULTS AND DISCUSSION

### 4.1 Determination of activity correlation

Table 2 presents the results of the activity level of natural and artificial radionuclides in moss samples collected in the area of Belgrade parks and forests (Kosutnjak, Makiš, Zvezdara forest, Avala, Topcider park). Correlations of activity levels of radiocesium-137 and potassium-40, as well as some natural radionuclides, are graphically presented. Analyzing the data shown in table 2, it is obvious that most moss samples are most contaminated with radiocesium-137, compared to natural radionuclides, whose values are uniform. Of the natural radionuclides,  $^{40}\text{K}$  is the most abundant in the moss samples from all the examined localities

**Table 2.** Radionuclide activity levels in moss samples (Bq/kg)

Sample	Location	Radionuclide					
		$^{137}\text{Cs}$	$^{134}\text{Cs}$	$^{40}\text{K}$	$^{226}\text{Ra}$	$^{238}\text{U}$	$^{232}\text{Th}$
<i>H. splendens</i>	Kosutnjak	117	< 0,5	229	15,6	8,2	14,6
<i>H. cupressiforme</i>	Kosutnjak	42,2	0,2	119	7,1	4,6	7,3
<i>H. cupressiforme</i>	Z. forest	105	0,5	277	26,6	8,6	22,4
<i>S. calcicola</i>	Kosutnjak	61,1	0,2	414	31,5	28,2	34,0
<i>H. cupressiforme</i>	Avala	24,6	< 0,8	319	17,7	<15,4	14,5
<i>H. splendens</i>	T. park	177	< 1,0	173	17,0	<19,0	15
<i>S. purum</i>	Z. forest	43,6	< 0,7	50,2	<13,4	<12,2	2,4
<i>N. crispa</i>	Makis	190	0,2	68,2	9,4	6,0	2,7
<i>H. cupressiforme</i>	Makis	326	1,9	120	10,3	12,8	2,1
<i>H. splendens</i>	Z. forest	109	< 0,7	78,2	<11,5	< 9,1	2,9

As cesium and potassium are metabolically similar elements, it should be expected that higher levels of  $^{40}\text{K}$  activity imply lower levels of  $^{137}\text{Cs}$  activity. The ratio of activity levels of these radionuclides in the tested samples is not such that any correlation can be established, especially in moss samples that are more contaminated with radiocesium. The same radionuclides were examined in soil samples and no dependence was found between the activity concentration of  $^{137}\text{Cs}$  and  $^{40}\text{K}$  [9].

Cesium came into the soil after the huge amount of precipitation and became more concentration, so its varied from place to place. The obtained results indicate the great capacity of mosses and lichens to absorb radiocesium. In addition, the examined ecosystems represent almost closed biological communities, in which the level of radioactive contamination is kept relatively stable for a long period of time.

229	117
119	42.2
277	105
414	61.1
319	24.6
173	177
50.2	43.6
68.2	190
120	1116
132	1257

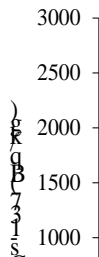


**Figure 4.** Dependence of <sup>137</sup>Cs activity level on <sup>40</sup>K

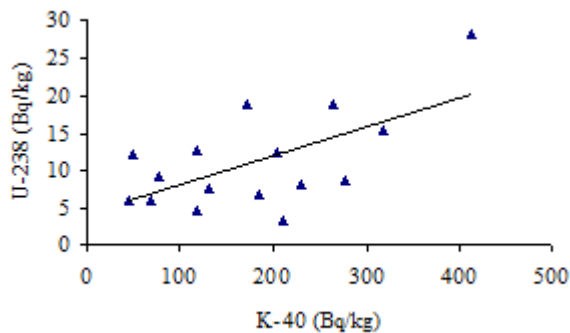


**Figure 5** Dependence of <sup>238</sup>U activity level on <sup>40</sup>K

Considering the data for natural radionuclides <sup>238</sup>U, <sup>226</sup>Ra and <sup>232</sup>Th and their correlations with the activity levels of <sup>40</sup>K, a straight-line dependence of the activity levels of these radionuclides with <sup>40</sup>K is evident.

The linear dependence of <sup>238</sup>U and <sup>232</sup>Th activity levels on <sup>40</sup>K has already been investigated and confirmed in soil samples [10], and our research points to the conclusion that these regularities are also shown in bioindicator samples, such as mosses.

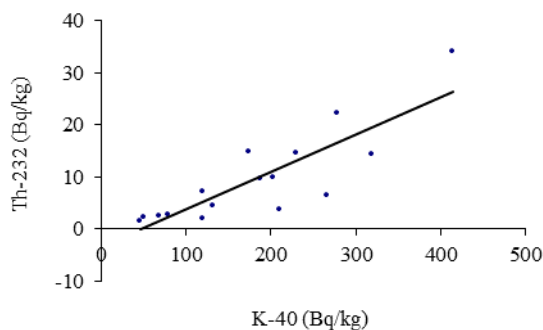


**Figure 6.** Dependence of <sup>232</sup>Th activity level on <sup>40</sup>K

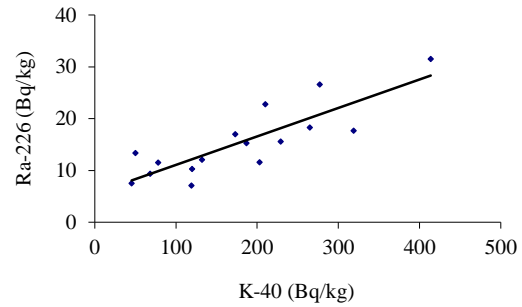


**Figure 7 .** Dependence of <sup>226</sup>Ra activity level on <sup>40</sup>K

By comparing the values of the strength of the absorbed doses in the bioindicators on all five ecosystems, a higher radiation load of mosses compared to lichens is observed. The difference in the degree of <sup>137</sup>Cs accumulation in mosses and lichens is caused by the difference in the morphological structure and physiological characteristics of these plant species. Mosses are characterized by a large surface-to-mass ratio (almost 10 times greater than this ratio for grass), which explains the high capacity of these species to absorb radionuclides.

Although the examined bioindicator species accumulate high activities of <sup>137</sup>Cs, the radiation load (up to 14.13 mSv/year) is below the level at which changes occur in the reproductive cycle of plants. This indicates the suitability of using mosses and lichens as bioindicator species.

When assessing the state of the ecosystem, a number of factors should be taken into account: sampling method, spatial and temporal variations for all samples and age indices of organisms. Apart from altitude, other influences are also present here. It is especially important to take into account the processes of vertical migration of radiocesium, as well as the influence of specific characteristics of the studied ecosystems associated with these processes.

Given that mosses and lichens are characterized by a wide geographical and ecological distribution of species, availability throughout the year, long life and a high degree of tolerance to pollutants, data on the radiation load caused by internal irradiation of these species can serve as a basis for evaluating different ecosystems from the aspect of radioactive contamination

All the results presented in this paper indicate that lichens are good bioindicators of environmental pollution with radiocaesium and that the activity levels of this radioactive isotope have significantly decreased since the accident in Chernobyl. Also, the results indicate that there was no new contamination with this isotope.

## 5. CONCLUSION

All the results presented in this paper indicate that lichens and mosses are good bioindicators of environmental pollution with radiocesium.

The activity levels of  $^{137+134}\text{Cs}$  in lichens and mosses collected in the territory of Belgrade are at the level of recommended values for the territory of Serbia.

Investigations of the basic indicators of the state of the environment in the examined locations on the territory of the city of Belgrade indicate the quality of the environment, the possible degree of changes that can potentially affect humans and the entire living world.

## References

- [1] M. Krmar, D. Radnović and M. V. Frontasyeva, Moss Biomonitoring Technique Used to Study the Spatial and Temporal Atmospheric Deposition of Heavy Metals and Airborne Radionuclides, In D.T. Mihailović Ed., *Essays of Fundamental and Applied Environmental Topics*, Nova Publishers Inc., pp. 159-192, ISBN: 978-1-61942-522-4. (2012)
- [2] S. Stanković, A. Stanković, G. Pantelić: Zagađenost lišaja i mahovina Istočne Srbije prirodnim i veštačkim radionuklidima, plenarno predavanje, *Ekološka istina, Zbornik radova, Zaječar*, 1999, 16-19
- [3] H.G. Zechmeister, K. Grodzińska, G. Szarek-Łukaszewska, Bryophytes. In: B.A. Markert, A.M. Breure, H.G. Zechmeister (Eds.), *Bioindicators and Biomonitors*, Elsevier, London, 2003,
- [4] Marović G. The role of bioindicators in assessing radioactive contamination. *Arh hig rada toksikol* 1990;41:371-378.
- [5] Debertin, K., Helmer, R. G., 1988. *Gamma- and X-ray Spectrometry with Semiconductor Detectors*, Elsevier, New York.
- [6] Review of Probabilistic Safety Assessments by Regulatory Bodies, Safety Reports Series No.25, International Atomic Energy Agency Vienna 2002.
- [7] United Nations, Scientific Committee on the Effects of Atomic radiation, UNSCEAR, 2000. RAPPORT VOLUME I
- [8] Mitrović, B., Ajtić, J., Lazić, M., Andrić, V., Krstić, N., Vranješ, B., & Vićentijević, M. (2016). Natural and anthropogenic radioactivity in the environment of Kopaonik mountain, Serbia. *Environmental Pollution*, 215, 273–279. <http://doi.org/10.1016/j.envpol.2016.05.031>
- [9] S. Dragović, G. Bačić, S. Stanković: Radiation body burden of some bioindicator species, II Regional Symposium "Chemistry and the Environment", 18-21. June, Kruševac, 345-346.
- [10] M. Krmar et. al.: Međusobni odnosi radionuklida u zemljištu, *Zbornik radova XX Simpozijuma Jugoslovenskog društva za zaštitu od zračenja*, Tara 99, 87-90.



# DETERMINATION OF THE TEMPERATURE PROFILE OF SELECTED MOBILE PHONE CHARGERS AS A SAFETY FACTOR IN TERMS OF THERMAL RADIATION

LJUBIŠA TOMIĆ

Technical Test Center, Vojvode Stepe 445, 11000, Belgrade, [ljubisa.tomic@gmail.com](mailto:ljubisa.tomic@gmail.com)

SAŠA VESELINOVIĆ

Technical Test Center, Vojvode Stepe 445, 11000, Belgrade, [sasa.veselinovic@mod.gov.rs](mailto:sasa.veselinovic@mod.gov.rs)

MARINA SIMOVIĆ PAVLOVIĆ

Teleoptik Žiroskopi, Filipa Višnjića 31, Belgrade, [simovicmarina99@gmail.com](mailto:simovicmarina99@gmail.com)

KATARINA NESTOROVIĆ

Military Technical Institute, Belgrade, [katarina.nestorovic993@gmail.com](mailto:katarina.nestorovic993@gmail.com)

DARKO JANKOVIĆ

University of Defence Belgrade, Military Academy, Veljka Lukića Kurjaka 33, Belgrade, [darkoojanko@gmail.com](mailto:darkoojanko@gmail.com)

DARKO VASILJEVIĆ

Institute of Physics, University of Belgrade, Pregrevica 118, 11000, Belgrade, [darko@ipb.ac.rs](mailto:darko@ipb.ac.rs)

**Abstract:** *The surface temperatures of several commercial chargers for contemporary mobile phones with nominal power outputs from 10 W to 120 W were compared in this paper. Using a thermal imaging camera, the charger's surface temperature was recorded while it was connected to the main power source. To determine how the temperature on the charger's surface depended on the phone's charge level, an analysis of the thermograms that were captured was done. In this manner, the impact of the phone's charging speed on the charger's heating and, consequently, the safety factor concerning the charger's overheating, are ascertained. The battery charge range that was observed was 10% to 90%.*

**Keywords:** *mobile phone chargers, thermal radiation, thermal camera, temperature profile*

## 1. INTRODUCTION

The presented research dealt with the temperature profile of different mobile phone chargers. The surface temperatures of modern commercial devices were monitored. The idea was to find a relationship between the heating of the charger and the battery charge level. This type of analysis is of great importance for assessing the safety of using different mobile phone chargers.

Such measurements can also help to find optimal solutions in terms of sizing these devices. As modern times are looking for devices of smaller dimensions, the problem of temperature dissipation in small volumes arises. [1] It is precisely these kinds of tests that find safe and satisfactory solutions.

Seen from the perspective of new technologies, the most promising is the possibility of converting thermal energy into electricity sufficient to charge a mobile phone. [2] This kind of analysis can additionally serve for this type of research. Therefore, it is a practical, safe and innovative solution.

## 2. EXPERIMENTAL

The tested chargers for mobile phones are with nominal power outputs from 10 W to 120 W. The battery charge range that was observed was 10% to 90%. The phone used for measurements was VIVO Y21S with battery of 5000 mAh. The VIVO Y21S was developed in 2021.

The Lepton 2.0 thermal camera core for Android was first released by renowned manufacturer FLIR Systems [3]. The central component of the system is an 80 × 60 pixel FPA uncooled microbolometer, covering the 8 μm to 14 μm long-wavelength infrared (LWIR) spectrum. The temperature sensitivity of the pixels is less than 50 mK, and their size is 12 μm. Figure 1 represents a photography and the thermal image of the phone charger taken during the charging.

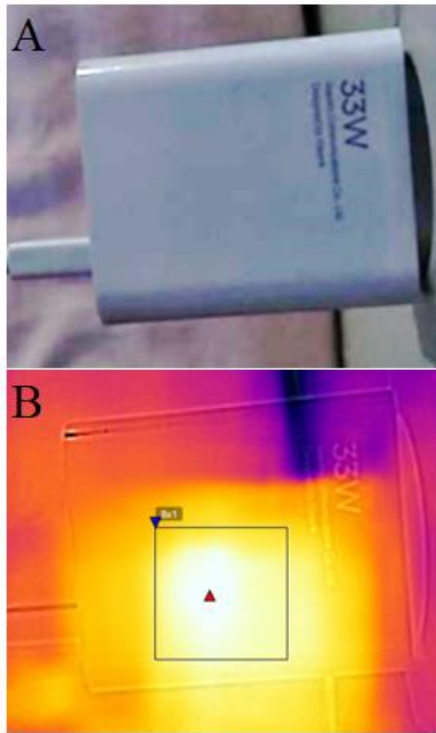


**Figure 1.** Charger VIVO 33 W: photography (A) and the thermal image (B)

Testing was conducted using this kind of thermal camera along with a CAT S60 mobile phone. A JPEG format is the end outcome. [4]

### 3. RESULTS AND DISCUSSION

The first observed combination is the VIVO Y21S phone and the VIVO Mobile Communication Co, Ltd 10W charger. Figure 2 shows the graph of charger heating depending on the percentage of the phone's charge, while the figure 3 shows the graph of charger heating depending on the time of charging. In this way, the influence of the charging time on heating can be independently observed, as well as the influence of the battery charge percentage on heating.

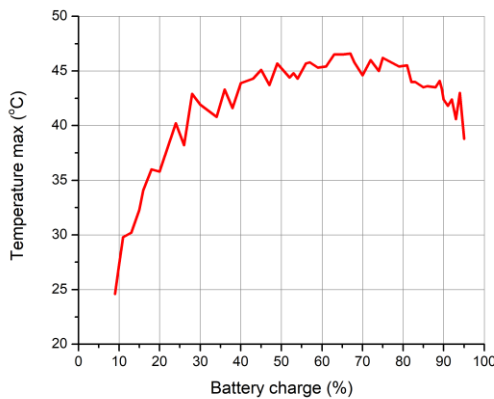


**Figure 2.** Temperature change diagram for VIVO-VIVO 10 W combination depending on the charging percentage

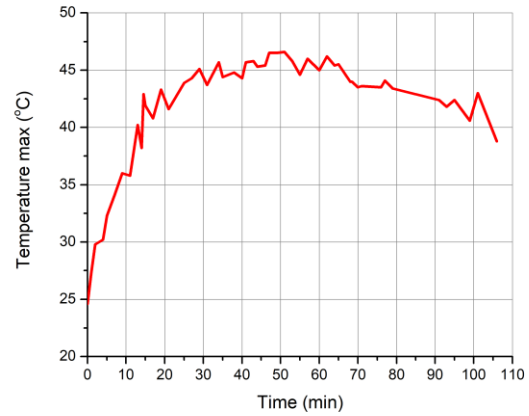


**Figure 3.** Temperature change diagram for VIVO-VIVO 10 W combination depending on time of charging

The same phone charged with a 33 W charger was observed and the graph of heating as a function of charge percentage is shown in Figure 4.

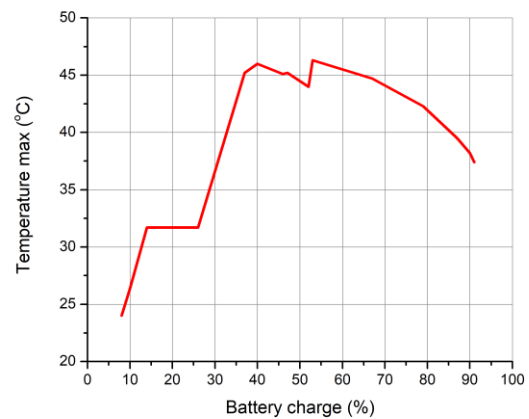


**Figure 4.** Temperature change diagram for VIVO-VIVO 33 W combination depending on the charging percentage

The same heating profile is observed for both above mentioned combinations. The maximum temperature for the combination with the 33 W charger reaches a value of 46.3°C at 53% charge. Almost the same temperature maximum of 46.5°C was measured for the combination with the 10 W charger, except that the maximum was observed at 63% charge. This maximum indicates a total warming of 23°C.

The time dependence of the heating of the charger is also shown on the diagram on the figure 5.



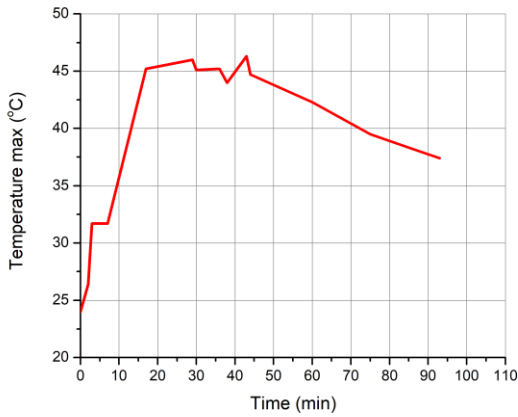


**Figure 5.** Temperature change diagram for VIVO-VIVO 33 W combination depending on the time of charging

The next observed combination is again the VIVO phone, with the Xiaomi Communication Co., Ltd 120W charger, where much less heating is observed, more precisely 16°C (Figure 6).

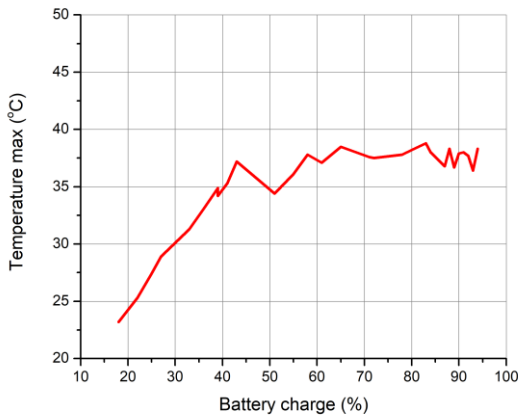


**Figure 6.** Temperature change diagram for VIVO-Xiaomi 120 W combination

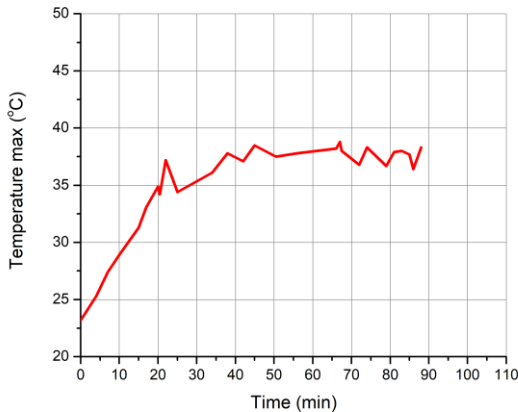


**Figure 7.** Temperature change diagram for VIVO-Xiaomi 120 W combination (time dependence)

The diagram above represents the dependence of the heating of the charger on the time of charging (Figure 7).

Based on the obtained results, it is possible to analyze different circumstances. Some initial conclusions have been drawn which will serve as postulates for further investigation:

- Although the same temperature rise is observed for the 33W and 10W chargers, it is evident that the 33W charger heats up faster.

When the diagrams from Figures 2, 4 and 6 are combined into one diagram (Figure 8), it can be noticed that the higher the power of the charger, the lower the heating of the charger.

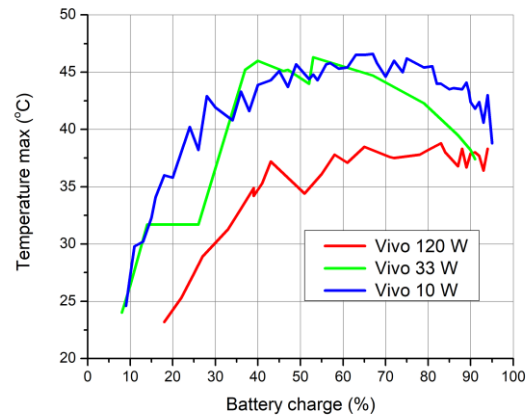


**Figure 8.** Temperature change diagram for VIVO phone charged with three types of charger depending in the charging percentage

The diagram on the Figure 9 is the combination of the diagrams from Figures 3, 5 and 7 in one.

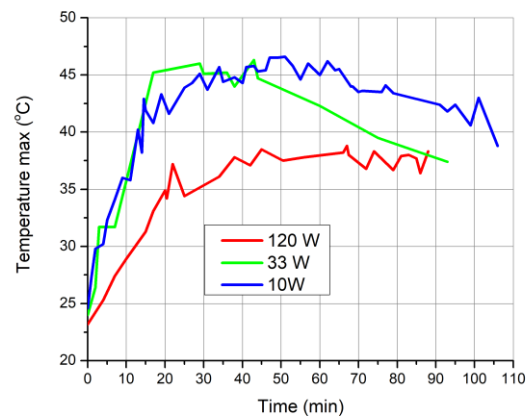


**Figure 9.** Temperature change diagram for VIVO phone charged with three types of charger in time dependence

By looking at the graphs in Figures 2 to 7, you can see uneven heating, more precisely charging periods when the charger heats up more, completely irregularly distributed during charging. This data is interesting for further examination of key charging moments in terms of

efficiency and safety.

#### 4. CONCLUSION

The paper presents the examination of mobile phone chargers in terms of safety during use as well as charging efficiency. Different types of chargers have been tested in combination with VIVO phone. The temperature profile of charger heating was analyzed as a function of battery charge percentage and battery charging time. Some interesting relations have been observed that are used in further, more extensive research in the field of safety of using chargers and improving their capabilities.

#### Acknowledgements

M.S.P. and D.V. acknowledge the support of the EU: the EIC Pathfinder Challenges 2022 call through the Research Grant 101115149 (project ARTEMIS). M.S.P., and D.V. acknowledge the support of the Office of Naval Research Global through the Research Grant N62902-22-1-2024.

#### References

- [1] SLUIJS,F.: *Thermal Modeling to Optimize Design in Mobile Charging Applications*, 23rd International Workshop on Thermal Investigations of ICs and Systems (THERMINIC) , IEEE, 2017.
- [2] DALWADI,D., AGARWAL,M., PRIYA,S., GORADIYA,B.: *Performance Evaluation of Mobile Charger Using Heating Technology*, Kalpa Publications in Engineering 1, 412-417, 2017.
- [3] <https://lepton.flir.com/>
- [4] TOMIC,LJ., DAMNJANOVIC,V., MISKOVIC,K., VASILJEVIC,D., PAVLOVIC,D., BONDZULIC,B., MUNIC,N.: *Combustion Heat Release Estimation by Means of Thermal Imaging*, 8<sup>th</sup> International Scientific Conference on Defensive Technologies OTEH 2018, Belgrade,2018.



## INFLUENCE OF SMALL ARMS AMMUNITION ON TARGETS MADE OF GRANULAR MATTER

MARINA SIMOVIĆ PAVLOVIĆ

Teleoptik Žiroskopi, Filipa Višnjića 31, Belgrade, [simovicmarina99@gmail.com](mailto:simovicmarina99@gmail.com)

VLADIMIR OBRADOVIĆ

Teleoptik Žiroskopi, Filipa Višnjića 31, Belgrade, [vladimir.obradovic@ziroskopi.rs](mailto:vladimir.obradovic@ziroskopi.rs)

DARKO JANKOVIĆ

University of Defence Belgrade, Military Academy, Veljka Lukića Kurjaka 33, Belgrade, [darkoojanko@gmail.com](mailto:darkoojanko@gmail.com)

MAJA PAGNACCO

University of Belgrade, Institute of Chemistry, Technology and Metallurgy, Department for Catalysis, NJegoševa 12, Belgrade, [maja.milenkovic@ymail.com](mailto:maja.milenkovic@ymail.com)

LJUBIŠA TOMIĆ

Technical Test Center, Vojvode Stepe 445, 11000, Belgrade, [ljubisa.tomic@gmail.com](mailto:ljubisa.tomic@gmail.com)

DARKO VASILJEVIĆ

Nanophotonics Lab, Photonics Center, Institute of Physics, University of Belgrade, Pregrevica 118, Belgrade, [darko@ipb.ac.rs](mailto:darko@ipb.ac.rs)

**Abstract:** *The behavior of granular matter under the impact of projectiles with varying calibers is examined in this work. Different granulations were used to make the samples - targets, which were then assembled differently. The samples were created using a variety of sand kinds with varying moisture contents and densities. Two cameras were used to investigate the behavior of the tested substrate following the projectile impact: a thermal camera and a high-speed camera. The state of the samples after the action was also reviewed. When it comes to evaluating the effects of a projectile striking a granular substrate as a target, these experiments may be of ballistic significance. Examining the granular materials' physical characteristics and their importance for use in the development of materials for the manufacture of military-grade protective materials is the main goal of the test.*

**Keywords:** *granular matter, new military materials, projectile's impact*

### 1. INTRODUCTION

This paper presents a thorough analysis of the impact of projectiles on granular matter [1] with many possible applications. It is an experiment to see how ammunition affects a particular target or surface in an open space. This influence is determined in different ways that will be described in the text of the paper, but additional types of analysis can also be included. As this is a very fast or short process, an ultra-fast and thermal camera were used for observation. In this specific case, a sandy substrate of different granulations was examined as well as some solid materials. As for the ammunition, the most typical calibers were used in real shooting conditions. The benefits of utilizing this kind of material for a military protective material were discussed with keeping on mind the significance of this kind of test in the broader ballistic context.

### 2. EXPERIMENTAL

A new, very similar experiment with rifle ammo was carried out, based on the air rifle experiment previously reported elsewhere [2]. Calibers 7.62 mm and 5.56 mm were used. The 7.62 mm caliber [3] is very widespread and is used by famous rifles such as the AK-47 and the SKS Carbine. It is also predominantly used in weapons of the Serbian Zastava brand and many others. An alternative to this caliber is the 5.56 mm bullet [4], which was developed in the USA. This refers to the standard NATO caliber that is utilized, for instance, in M16 rifles. The characteristics of the described calibers is shown in table 1.

**Table 1.** Bulet characteristics

Bullet characteristics			
Bullet	Mass	Length	Diameter
7.62	7,9 g	24 mm	7,62 mm
5.56	4,0 g	23 mm	5,56 mm

During shooting, speeds of approximately 700 m/s were measured for caliber 7.62 mm, while for caliber 5.56 mm, a speed of approximately 895 m/s was measured.

Three types of sand of different granulations and densities were used as the first test substrate. The first type of sand is coarse sand with a density of 1770 kg/m<sup>3</sup>, the second is fine sand with a density of 1700 kg/m<sup>3</sup> and the third is absorbing sand with a density of 1340 kg/m<sup>3</sup>. In the main experiment, all three kinds of sand were mixed with water and placed on the base according to a predetermined scheme. The base is constructed as a box on the bottom of which there is an armor plate.

Second type of material for target was a construction cement. This is a solid target and is investigated in the same way as the sandy target on the same base. It is made with same types of sand mixed with a cement to get greater strength. As a reference, the testing was additionally done on the box with an armor plate with no extra substrate.

In the experiment, no weapon was used during the actual firing. Instead, a stationary block for experimental investigations was used. The block measures 900 mm in height by itself, and 1100 mm when the barrel is added.

The FLIR SC620 24° Package thermal imaging camera and the Phantom v9.1 ultra-fast camera were the two types of cameras used in the experiment. Data processing is performed in the program FLIR ResearchIR Max ver 4.40.12.38.

### 3. RESULTS AND DISCUSSION

The temperature profile of the granular substrate as well as the target made of construction cement and armor plate were observed during and after the impact of the projectile. Temperatures at characteristic moments were measured and compared. It was also easier to observe the splattering of granular matter on the thermal images, as well as some additional analysis in that direction.

Figure 1 shows the thermograph of the moment of penetration of the projectile into the sandy substrate. The point of impact, i.e. impact area, is easy to see, as well as trajectories of granulation particles. The trajectories show the end points where the particles are at the moment the image is taken, while the paths of those particles are seen as slightly brighter, more precisely slightly cooler lines. As a whole, the entire area within which the energy transfer occurred, that is, the area within which the movement of granulation particles occurred due to the impact of the projectile, is singled out.

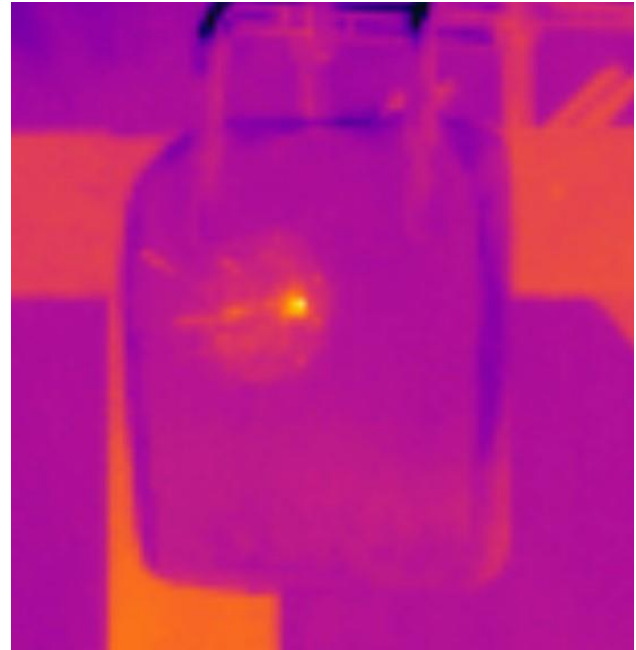
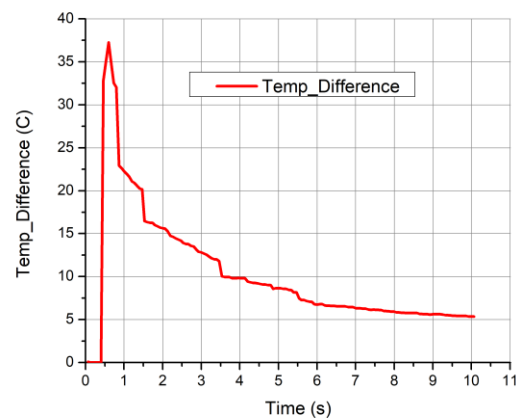


**Figure 1.** Thermograph of the moment of penetration of the projectile into the sandy substrate

Thermal analysis showed an increase in temperature in the area of impact and scattering of the grains.

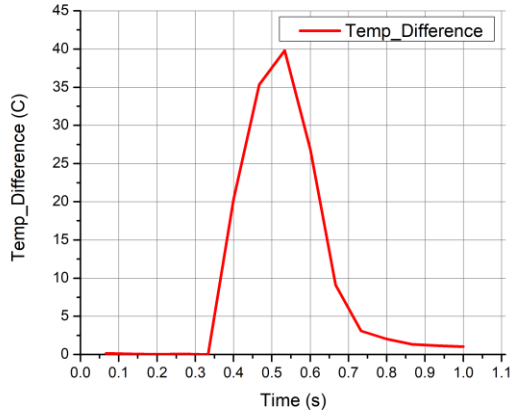
Below are the results of the thermal analysis, i.e. temperature change diagrams. Shots of the impact of the 7.62 mm x 39 projectile with an initial velocity of 740 m/s and a velocity measured at the target of 700 m/s were selected. An area of 20 pixels where the impact of the projectile was registered was observed. The diagrams show the maximum temperature in the given area.

The first diagram (Figure 2) shows the change in temperature at the moment of hitting the armor plate. An increase in temperature of about 37 degrees is observed.



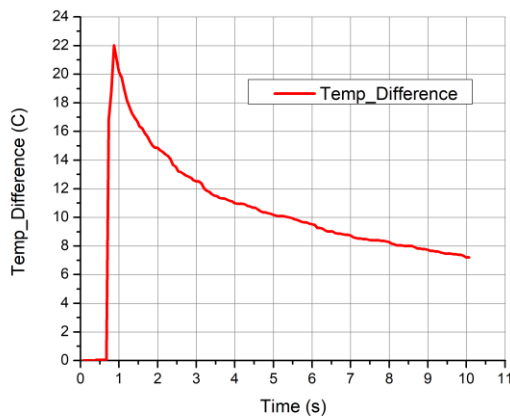
**Figure 2.** Temperature change diagram for armour plate hitting

Figure 3 represents the moment of hitting the sandy substrate which measures a bit higher temperature change than for armour plate, the increase of 40 degrees.



**Figure 3.** Temperature change diagram for sand substrate hitting

The last diagram (Figure 4) is for a target made of construction cement. In this case, a much smaller temperature change was recorded. The increase was about 22 degrees.



**Figure 4.** Temperature change diagram for construction cement hitting

From the diagrams obtained, it is evident that the temperature increased for all three cases. In the diagrams shown (Figures 2-4), only the curves of temperature changes of the specific substrate are isolated.

Figure 5 shows a diagram of the temperature change during the entire experiment with a sandy substrate. Here, the temperature is measured not only during the interaction of the projectile with the sand substrate, but also the next moment when the projectile hits the bottom of the base, that is, the armor plate. In this case, it can be observed that after a huge increase in temperature, there is an extremely fast cooling of the substrate, and then reheating when it hits the plate at the back. Such rapid cooling of the granular substrate is a very interesting feature and can represent a great advantage for use when constructing protective materials.

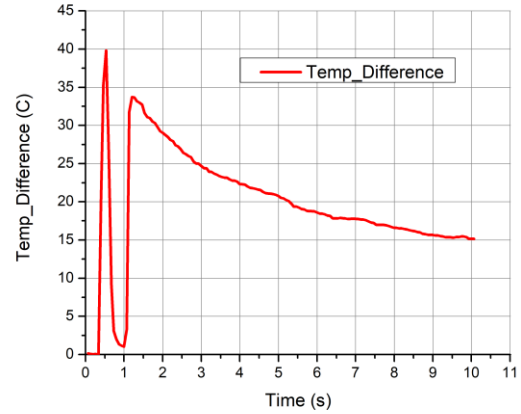


**Figure 5.** Temperature change diagram for both the sand substrate and armor plate hitting

The analysis of the solid substrate shows heating in a smaller range, which is favorable when viewed as a single material. For a combination of materials in which a significant temperature jump measured with sand could be a signal for some behavior of another material from the combination, this profile is already much more interesting. Looking at it this way, the first advantage for using granulates in protective materials is precisely this big jump in temperature. Especially important is the moment of cooling at a high speed, which is not observed with a solid surface. In this way, the overall material does not overheat. The third advantage refers precisely to the phenomenon observed when comparing the diagram in Figure 2 and the diagram in Figure 5. It can be seen that when shooting only the armor plate, there was a noticeably higher heating of the plate than in the case when the bullet first hit the sandy substrate. This is explained by the loss of kinetic energy during the transfer of heat to the sand, and therefore less heat energy is transferred to the plate itself (which then heats the cooled sand again). This is important because sand, as a very loose material, although it has no stopping power, definitely reduces the kinetic energy. Therefore, granular materials can be used in the construction of protective ballistic materials to create a redistribution of energy that ultimately leads to stopping the projectile in combination with other hard or more resilient materials.

#### 4. CONCLUSION

Bearing in mind that granular substrates that have no stopping power were investigated, this research was based on the examination of impact energy transfer through the granular substrate. The obtained results firstly suggest that granular matter is an excellent structure for use in protective ballistic materials in combination with other materials. This research also showed that it is very important to apply optical methods to examine the effect of projectile on the substrate, more precisely the target. The possibility of obtaining the temperature profile, the impact energy distribution profile, but also the very distribution of the grains of the substrate is of great importance for ballistics and many other applications.

## Acknowledgements

M.S.P., M.P. and D.V. acknowledge the support of the EU: the EIC Pathfinder Challenges 2022 call through the Research Grant 101115149 (project ARTEMIS). M.S.P., M.P. and D.V. acknowledge the support of the Office of Naval Research Global through the Research Grant N62902-22-1-2024.

## References

- [1] JANKOVIC,D., SIMOVIC PAVLOVIC,M., OCHSENHOFER,M., RADISAVLJEVIC,I., VASILJEVIC,D.: *Analysis of Projectile Effects on Different Types of Materials*, Conference on Advances in Science and Technology, Herceg Novi, 2024.
- [2] JANKOVIC,D., SIMOVIC PAVLOVIC,M., PAGNACCO,M., NESTOROVIC,K., RANDJELOVIC,A., VASILJEVIC,D.: *Is the Threat Posed by Air Weapons Underrated? – Analysis of the Impact of a Projectile Fired From an Air Rifle on a Sandy Substrate*, Archibald Reiss Days, Belgrade, 2023.
- [3] FLORES-JOHNSON,E.A., SALEH,M., EDWARDS,L.: *Ballistic Performance of Multi-layered Metallic Plates Impacted by a 7.62-mm APM2 Projectile*, International Journal of Impact Engineering, 38(12), 1022-1032, 2011.
- [4] SCEPANOVIC,D., ALBREHT,M., ERDELJAN,D., MILIVOJEVIC,V., PETROVIC,M., CUK,V., DJUKNIC,M.: *Evaluation of the New Type of Military Bullet and Rifiling*, Journal of Trauma and Acute Care Surgery, 28(1), S68-S72,1988.



## CATALYTIC PROPERTIES OF PAPER-IMMOBILIZED HORSE SERUM BUTYRYLCHOLINESTERASE

SONJA BAUK

Military Technical Institute, Belgrade, [bauk.sonja@gmail.com](mailto:bauk.sonja@gmail.com)

NATAŠA PAJIĆ

Military Technical Institute, Belgrade, [natasa.pajic969@gmail.com](mailto:natasa.pajic969@gmail.com)

**Abstract:** Fast and reliable detection of toxic organophosphates (OPs) is an important safety issue due to their widespread application, extreme toxicity and potential use as chemical warfare agents. Recently, paper has attracted considerable attention as inexpensive, biodegradable, biocompatible and hydrophilic material, which is owing to its unique features very suitable matrix for fabrication of fast-responding and low-cost analytical tools in health and environmental applications. Bioactive paper sensors with immobilized enzymes that enable colorimetric readout are used for naked-eye detection and able to operate without sophisticated equipment. Cholinesterases (ChEs) are enzymes susceptible to inhibition by OPs with high sensitivity and this property enabled the invention of simple detectors and disposable analytical devices for OPs assay. This work reports simple and cost-effective immobilization of commercial horse serum butyrylcholinesterase (BChE) on paper-based matrix and describes the catalytic properties of the immobilized enzyme relevant from some practical aspects related to storage and operating conditions.

**Keywords:** butyrylcholinesterase, organophosphates, immobilization, cellulose, detection.

### 1. INTRODUCTION

The immobilization of enzymes from the cholinesterase (ChE) family is the most important step in the design and fabrication of various bioanalytical tools that are widely used in many areas, including life science research, drug discovery, clinical diagnostics, environmental monitoring, food safety control, forensics and military defense [1]. Their function is based on enzyme inhibition, since their output signals, according to a measurable property, correspond to the activity of the immobilized enzyme, which decreases after exposure to the target analyte.

The application of immobilized ChEs in such a large number of different fields is due to the wide variety of species exerting the anti-ChE effect. ChE inhibitors, as target analytes of ChE-based analytical tools, comprise a diverse group of compounds such as glycoalkaloids, aflatoxins, anatoxins, organophosphate and carbamate pesticides, nerve agents, anti-Alzheimer drugs, heavy metals and several others [2]. Among others, one of the main and most widespread applications of immobilized ChEs is aimed at the determination of toxic organophosphates (OPs). Although these compounds are very harmful for wildlife and human health and the most toxic of them belong to the group of chemical warfare agents (CWAs), they are still intensively used for agricultural, industrial, household and medical purposes. The health risks and threats to life associated with their use trigger the need for reliable, fast and inexpensive analytical systems that can enable the early detection of this type of environmental contaminants [3].

So far, a large number of different biosensing platforms have been proposed for a range of ChE inhibitors, as this topic has been the subject of many research and development activities over several decades. In addition to electrochemical, photoelectrochemical, optical and piezoelectric biosensors with signal acquisition that mainly relies on instruments, considerable efforts in this field are directed towards inventing simple detectors and disposable analytical devices, which are particularly suitable for military, environmental and agricultural purposes [4][5]. They are often designed in the form of various tubes, dipsticks and strips and able to operate without any instrumental device, since their work relies on the colorimetric readout method. This method provides a visual color change as an analytical signal that is observable by the naked eye or can be evaluated using smartphones and available applications and software to convert captured images into corresponding data [6][7].

Regardless of whether it is a very simple device or a more complex one, the selection and effectiveness of the enzyme immobilization method are crucial for its performances and determine its storage and operating conditions. Over the past decades, various techniques have been applied for immobilization of ChEs from different sources on supports made of different materials, but there is no immobilization strategy without certain limitations and drawbacks [8]. Some of the most common disadvantages are related to process reproducibility, enzyme stability, desorption or leakage, loss of enzyme activity and product cost-effectiveness, but there are also many other issues whose resolution would contribute to certain improvements in this field. Enzyme

immobilization techniques can generally be divided into covalent and physical methods, according to the molecular forces between the enzyme and the support matrix, but combination of different techniques can often be found in the literature. Physical methods include adsorption and entrapment. They are simple, cost-effective and widely used due to the least effect on enzyme activity, which is the result of weak interaction with the carrier and the absence of chemical bonds.

The selection of a suitable immobilization technique in the fabrication of ChE-based analytical device depends on many different factors, taking into account its intended mode of operation, as well as the characteristics of the materials to be used for enzyme attachment. Considering the irreversible nature of ChEs inhibition by OPs and aforementioned trends towards simple testing devices, paper substrates have emerged as an attractive alternative to more sophisticated analytical platforms for this type of application. Paper is the most abundant and inexpensive cellulosic product that has recently attracted considerable attention as a matrix for fabrication of low-cost analytical tools. The immobilization of ChEs on paper surface led to the invention of various fast-responding tools for rapid screening and early diagnosis in health and environmental applications [9][10]. Paper-based biosensors provide rapid detection of OPs with minimal equipment requirements and with advantages of cost effectiveness, simple fabrication, disposability and stability.

Recently, we studied the application of a simple and cost-effective method for the immobilization of horse serum butyrylcholinesterase (BChE) on Whatman filter paper. In this work, two immobilizates obtained by the same technique were additionally examined, in order to gain a better insight into their properties relevant to some aspects related to their practical application.

## 2. MATERIAL AND METHODS

### 2.1. Material

Lyophilized horse plasma butyrylcholinesterase (BChE, with the activity of  $\geq 10$  U/mg protein according to manufacturer's declaration), bovine serum albumin (BSA) and gelatin from porcine skin (high gel strength) were purchased from Sigma-Aldrich, as well as butyrylthiocholine iodide (BSChI,  $\geq 99.0\%$ ) and 5,5'-dithiobis (2-nitrobenzoic acid) (DTNB,  $\geq 98\%$ ). All other reagents were of analytical grade.

Filter paper Whatman No. 1 manufactured as circular disks with a diameter of 15 mm (paper circles) was used as a support matrix for enzyme immobilization.

Two different solutions containing BChE ( $\sim 10$  U/mL) and BSA (1%) or gelatin (0.5%) in phosphate buffer (PB, 50 mM, pH 7.4) were used to obtain two types of immobilizates (paper circles with immobilized enzyme), designated as ImA and ImG, respectively. The immobilization procedure consisted of applying the prepared enzyme solutions in aliquots of 20  $\mu$ L to the surfaces of the paper circles, which after drying at laboratory temperature (25 °C) were stored in closed glass

vessels and kept in the refrigerator until use.

### 2.2. Activity assay

The BChE activity measurements were performed essentially according to the method of Ellman [11][11], using BSChI (2 mM) as the substrate and DTNB (0.32 mM) as the indicator (Ellman's reagent). Free enzyme (20  $\mu$ L) was added to a cuvette containing PB (2.64 mL) preincubated at 25 °C, followed by addition of DTNB (0.24 mL) and substrate (100  $\mu$ L). The formation of the yellow anion obtained from the reaction between Ellman's reagent and the thiocholine generated by enzymatic hydrolysis of the substrate was monitored by measuring the linear increase in absorbance at 412 nm. The measurement of the immobilized enzyme activity was carried out as described above, except that one paper circle with immobilized BChE was taken instead of free enzyme and placed in a dry cuvette before all others reagents. All results were obtained by measurements performed in triplicate and measured values are presented as mean  $\pm$  SD. One unit of enzymatic activity was defined as the amount of enzyme that catalyzes the hydrolysis of 1  $\mu$ mol of butyrylthiocholine per minute.

### 2.3. Temperature effects on activity and stability

Bioactive papers with immobilized BChE were exposed to a temperature of 55 °C for 2 hours in two different conditions: a) in an oven, where each sample was placed in a dry closed vessel, and b) in a water bath, where each sample was immersed in PB (2.64 mL) in a sealed cuvette. After the heat treatment, the samples were left at room temperature to cool slowly for the next 2 hours before each was transferred to a clean cuvette for the residual activity measurement by the standard assay method. The activity of PB remaining in the thermostated cuvette after sample removal was also determined, as well as the total activity in the cuvette containing the immersed sample in PB. The percentage of the residual activity was calculated considering the initial activity of the tested immobilizate before heat treatment as 100%.

### 2.4. The visual response's dependency on substrate concentration

The immobilized BChE activity was visualized with five test solutions (S1 – S5) containing DTNB (4 mM) and BSChI at concentrations of 1.5 mM (S1), 3 mM (S2), 6 mM (S3), 9 mM (S4) or 12 mM (S5).

An aliquot of 20  $\mu$ L of test solution was applied to the surface of ImA or ImG. The yellow color development was monitored up to 5 minutes from the start of reaction. Color changes were captured every 30 second by smartphone camera, with an LED light as the only light source and at a constant distance between the sample and the camera.

### 2.5. The effect of washing

The one paper circle was immersed in 3 mL of PB for 2 minutes at 25 °C. After that, it was withdrawn and



transferred to a clean cuvette for the residual activity measurement, or it was subjected to a next washing cycle with new portion of 3 mL PB. The washing PB solutions from all washing cycles performed on one immobilizate (up to 4 cycles) were also collected for subsequent activity determination. The percentage of the residual activity was calculated considering the activity of the unwashed sample as 100%.

## 2.6. The effect of sample matrix on visual response

An aliquot of 20  $\mu$ L of PB was applied to the surface of ImA or ImG and allowed to spread and absorb for defined time. Subsequently, the visual response of the immobilizate was monitored using a test solution with DTNB (4 mM) and BSChI (6 mM), as described in the Section 2.4.

## 3. RESULTS AND DISCUSSION

### 3.1. Temperature effects on activity and stability

In the immobilization process, the aliquots of enzyme solution with 1 % BSA ( $217 \pm 6$  mU) or 0.5 % gelatin ( $213 \pm 7$  mU) were used to obtain immobilizates ImA and ImG. Under the conditions defined by the assay method, ImA and ImG showed activities of  $95 \pm 5$  mU and  $53 \pm 4$  mU, so activity yields of 44% and 25% were achieved, respectively.

Temperature-induced changes in the properties of the obtained immobilizates were studied in two different scenarios. In the first, bioactive paper was in a dry state, surrounded by ambient air in a closed vessel that was placed in an oven. In the second, it was immersed in a cuvette filled with PB and placed in a water bath.

In an attempt to assess the influence of a similar temperature oscillation during storage conditions, after heat treatment at 55 °C for 2 hours the vessels and cuvettes with the tested samples were left for an additional 2 hours at room temperature to slowly cool down.

The activity measurements were performed on a dry sample taken from a vessel treated in an oven, on a sample removed from a cuvette treated in a water bath and on PB remaining after sample removal. Also, additional samples were subjected to treatment in a water bath to measure the activity of the total contents of the cuvette (sample immersed in PB) (Table 1).

The results showed that none of the stabilizers protected the immobilizates from activity decline under the tested conditions. However, the thermal effects on dry samples were more severe on ImG, and the presence of BSA in ImA samples appears to be more beneficial for retaining the BChE activity at high temperatures.

**Table 1.** The residual activities of the samples and PB after heat treatment (starting activities of ImA and ImG are shown at the first row)

Sample	ImA		ImG	
	mU	%	mU	%
before heat treatment	$95 \pm 5$	100	$53 \pm 4$	100
from a vessel after oven	$59 \pm 3$	62	$11 \pm 3$	20
from a cuvette after water bath	< 1	< 1	< 1	1
PB only after water bath	$79 \pm 2$	83	$66 \pm 1$	123
paper and PB after water bath	$75 \pm 2$	79	$64 \pm 2$	120

The activities of all samples treated in the water bath and withdrawn from PB were negligible, and the results on the activities remaining in PB after samples removal confirmed the enzyme leakage from the support to an almost the same extent with both ImA and ImG. That is visually more noticeable at Figure 1, where all activities are presented in normalized form, with a value of 100% assigned to the initial activity of free enzyme in the starting enzyme solution used for immobilization.

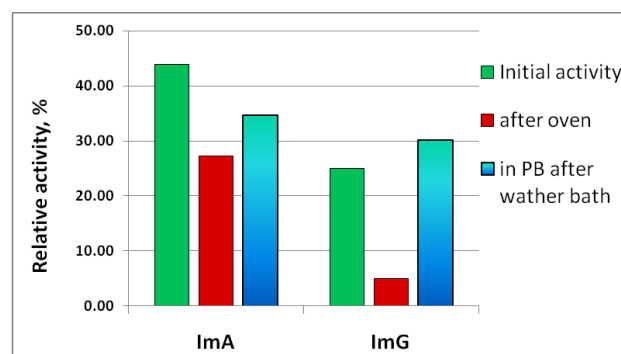


**Figure 1.** The influence of temperature on ImA, ImG and their incubation PB after different incubating conditions, relative to the initial activity of the free enzyme

An additional experiment was performed to test the stability of samples immersed in PB without heat treatment. Cuvettes with ImA and ImG immersed in PB were left at room temperature for 4 hours. The activities remaining in PB after removal of ImA and ImG were  $163 \pm 8$  mU and  $113 \pm 2$  mU, while activities remaining at papers were less than 2 mU and 4 mU, respectively. The obtained results imply that the presence of gelatin contributes more to the enzyme stability from the aspect of leakage, but also that the enzyme leakage, regardless of the temperature conditions, is a characteristic property of the immobilizates resulted from the applied immobilization procedure.

### 3.2. The visual response's dependency on substrate concentration

The activity of paper-immobilized BChE can be visually evaluated in different reaction systems, and one of the most used is based on the yellow color produced by the enzymatic reaction according to Ellman's method. The analytical performances of the obtained bioactive papers were examined at five different substrate concentrations with test solutions S1- S5. The visual responses of ImA and ImG upon addition of test solutions were digitally recorded, and their images up to 5 minutes from the start of the reaction are shown in **Figure 2**. The resulting color on the samples surfaces changed from colorless to yellow at a rate that was higher with increasing BSChI concentration and the most noticeable differences in color intensity were achieved during the first two minutes. Increasing the concentration of BSChI above 6 mM (S3) had a minor visual effect that was only visible with ImA.

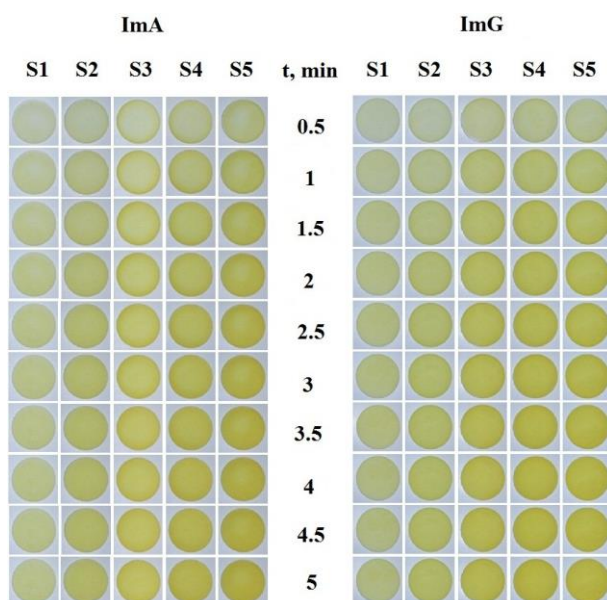


**Figure 2.** Comparative display of color development on ImA and ImG depending on reaction time at different substrate concentrations in test solutions S1 – S5

Considering the dependence of the yellow color intensity on the enzyme loading on paper and the fact that the visual responses of ImA and ImG were practically the same, it is conclusive that lower activity yield of ImG is a consequence of some limitations that are relevant under the assay conditions, but not when the substrate is applied directly to ImG surface. Among other reasons, this could originate from the differences between liquid transport mechanism in a porous substrate immersed in a liquid medium and the process of droplet absorption from the porous substrate surface.

### 3.3. The effect of washing

The samples of ImA and ImG were washed by repeated immersion in 3 mL of PB for 2 minutes and the residual activities on the paper circles were monitored for up to four washing cycles. **Table 2** summarizes the measured activities of ImA and ImG.

**Table 2.** The residual activities of ImA and ImG after washing cycles

No. of washing cycles	ImA		ImG	
	mU	%	mU	%
-	95 ± 5	100	53 ± 4	100
1	28 ± 1	29	19 ± 2	36
2	17 ± 2	18	20 ± 1	37
3	12 ± 1	13	11 ± 2	20
4	9 ± 1	9	10 ± 2	19

The results confirmed that most of the enzyme molecules on the surfaces of ImA and ImG samples were only loosely bound or unbound and therefore released rapidly upon immersion in the PB. Most of the enzyme activity was lost during the first washing cycle, after which both samples retained approximately 30 % of their initial activity. With subsequent washing steps, the activity of ImA gradually decreased, remaining at less than 10 % after the fourth washing cycle, while the activity of ImG decreased in a stepwise manner to approximately 20 %. After the second washing cycle, both ImA and ImG had a similar number of enzyme units measured in conditions defined by the assay method, and the same trend was maintained until the fourth washing cycle. The effects of enzyme loss by washing ImA and ImG samples shown in **Figure 3** reveal the dominance of weakly bound enzyme on the immobilizate prepared in the presence of BSA.

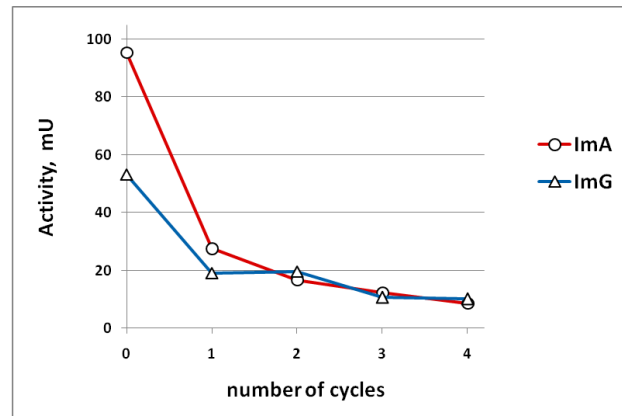


**Figure 3.** The activity of ImA and ImG samples depending on the number of washing cycles performed

The activities of the buffer solutions collected during washing steps are shown in **Table 3**. The total amount of enzyme units released from ImA after four consecutive washing cycles was twice the number of enzyme units released from ImG, providing further support for the observation that BChE is better retained when immobilized in the presence of gelatin.

To study the effects of washing on ImA and ImG performances related to their visual responses, the immobilizates obtained after one washing cycle were subjected to color reaction by addition of test solution with 6 mM BSChI (S3) and color development was monitored as described in the Section 2.4. **Figure 4**

compares the visual effects of unwashed ImA and ImG samples versus the samples obtained after one cycle of washing.

**Table 3.** The total activities of washing PB after washing cycles performed on ImA and ImG samples

No. of washing cycles	washing PB of ImA		washing PB of ImG	
	mU	%	mU	%
1	64 ± 5	67	11 ± 6	21
2	105 ± 13	110	34 ± 2	64
3	99 ± 8	104	41 ± 8	76
4	116 ± 7	122	55 ± 7	103

Upon one cycle of washing, the color on ImA sample developed slowly and had a low intensity and uneven distribution until the end of the fifth minute from the start of the reaction, which led to the conclusion that this immobilizate is not suitable for the application by immersion into the testing liquid.

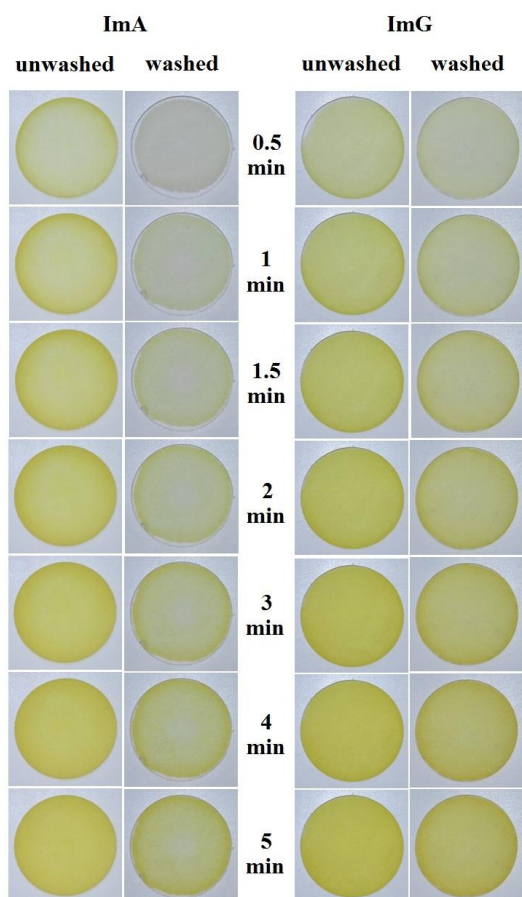


**Figure 4.** Comparison of color development on unwashed and washed ImA and ImG samples

Unlike washed ImA sample, ImG after washing still provided observable color changes that occurred at a slower rate than in unwashed sample, but with uniform color distribution and intensity that developed to an appropriate level during reaction monitoring.

### 3.4. The effect of sample matrix on visual response

The simple devices for visual detection of ChEs inhibitors are mostly intended to be used by applying a certain volume of the testing liquid sample directly to the surface of the detector’s sensing zone and allowing the eventual inhibition reaction to occur for some time. For a reliable analysis of the results, it is important to know all the possible influences that the sample matrix can have on the obtained visual responses. Among the various physico-chemical changes that can arise from samples of different composition, the effects of the PB on visual responses of ImA and ImG, if any, should be the least pronounced. But when applied on the surfaces of ImA and ImG, PB affected the visual responses of immobilizates and its influence was dependent on the time elapsed until the addition of the test solution with DTNB and BSChI. The effects of the incubation with PB for 2 minutes and 15 minutes before the onset of the visual reaction are shown in **Figure 5**.

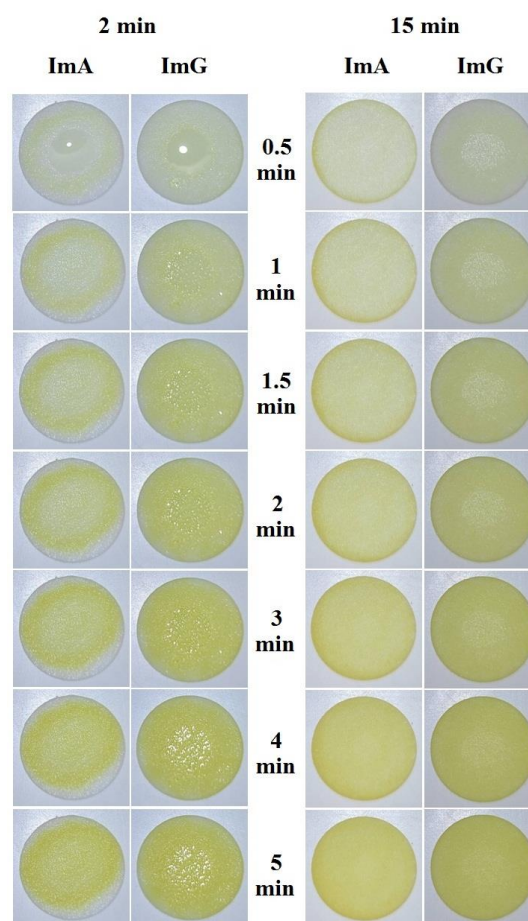


**Figure 5.** Visual responses of ImA and ImG when the test solution S3 was applied after 2 minutes or 15 minutes incubation with PB

Images taken when the reaction started after 2 minutes of incubation with PB showed slow absorption of the liquid droplet, partial coloring of ImA and reflection from the wetted surface of ImG, all of which made them unsuitable for further data processing using appropriate image analysis software, therefore unusable for the objective

evaluation of the obtained results. These effects disappeared with increasing incubation time, as can be seen in the images taken when the visual responses were initiated after 15 minutes of incubation with PB.

#### 4. CONCLUSION

The immobilization of BChE was carried out by simple deposition method using enzyme solutions with BSA or gelatin as stabilizers and Whatman No. 1 paper as support. The properties of the resulting immobilizates (ImA or ImG, respectively) were examined from a few aspects relevant for biodetection applications.

The immobilized BChE was characterized by a fast and visible color change that was most noticeable during the first two minutes after contact with the solution containing the indicator (4 mM) and the substrate in concentrations of 6 mM or higher, and also by practically the same yellow color intensity on the surfaces of ImA and ImG. Both immobilizates were prone to enzyme desorption and leakage owing to abundance of loosely bound and unbound enzyme molecules, which was expected for the applied immobilization procedure. According to visual responses of samples subjected to one washing cycle of 2 minutes in PB, ImA was found to be unsuitable for visual detection purposes by immersion in the sample due to inhomogeneous and weak color intensity, while after the same treatment ImG still provided adequate visual readouts with uniform color distribution. Tests with the application of PB as a sample matrix expected to have the least adverse effect, confirmed that the use of ImA and ImG in detection by the sample deposition method is highly dependent on the incubation time, which is essential for the uniform liquid distribution and thus for obtaining useful visual responses that can be further processed. The temperature-induced activity decrease was less pronounced in ImA when the samples were stored in dry form.

The application of physical immobilization techniques in the fabrication of simple analytical devices for visual screening and monitoring of ChEs target analytes is favorable due to their low-cost and simplicity, but the drawbacks, which are mainly caused by weak bonds between the enzyme and the support, usually affect the performances of the resulting analytical tools. The characterization of the immobilized ChE as their biorecognition element is a necessary step for establishing the direction of further improvements, since the immobilized enzymes properties are crucial for defining the possibilities and limitations of their use.

#### References

- [1] ŠTĚPÁNKOVÁ, Š., VORČÁKOVÁ, K.: *Cholinesterase-based biosensors*, Journal of Enzyme Inhibition and Medicinal Chemistry, 31 (2016) 180–193.
- [2] SOLDATKIN, O. O. et al.: *Application of butyrylcholinesterase-based biosensor for simultaneous determination of different toxicants using inhibition and reactivation steps*, Electroanalysis, 36 (6) (2024) e202300400.
- [3] AYAZ, S. et al.: *A novel acetylcholinesterase inhibition based colorimetric biosensor for the detection of paraoxon ethyl using CUPRAC reagent as chromogenic oxidant*, Talanta, 266 (2024) 124962.
- [4] TSOUNIDI, D. et al.: *AChE-based electrochemical biosensor for pesticide detection in vegetable oils: matrix effects and synergistic inhibition of the immobilized enzyme*, Analytical and Bioanalytical Chemistry, 415 (4) (2023) 615-625.
- [5] ISSAKA, E. et al.: *Advanced visual sensing techniques for on-site detection of pesticide residue in water environments*, Heliyon, 9 (3) (2023) e13986.
- [6] BŘÍZOVÁ, A., PITSCHMANN, V.: *Simple Chemical and Cholinesterase Methods for the Detection of Nerve Agents Using Optical Evaluation*, Biosensors, 13 (12) (2023) 995.
- [7] XUE, J. et al.: *Portable sensors equipped with smartphones for organophosphorus pesticides detection*, Food Chemistry, 434 (2024) 137456.
- [8] VINOETHA ALEX, A., MUKHERJEE, A.: *Review of recent developments (2018-2020) on acetylcholinesterase inhibition based biosensors for organophosphorus pesticides detection*, Microchemical Journal, 161 (2021) 105779.
- [9] WU, Y. et al.: *Sensitive inkjet printing paper-based colorimetric strips for acetylcholinesterase inhibitors with indoxyl acetate substrate*, Talanta, 162 (2017) 174-179.
- [10] TSAGKARIS, A.S. et al.: *A microfluidic paper-based analytical device ( $\mu$ PAD) with smartphone readout for chlorpyrifos-oxon screening in human serum*, Talanta, 222 (2021) 121535.
- [11] ELLMAN, G. L., COURTNEY, K. D., ANDERS, V., FEATHERSTONE, R. M.: *A new and rapid colorimetric determination of acetylcholinesterase activity*, Biochemical Pharmacology, 7 (2) (1961) 88–95.



## MAGNETOIMPEDANCE EFFECT OF NANOCRYSTALLINE FeNiSiB and FeCuVSiB RIBBONS

RADOSLAV SURLA

Military Technical Institute, Belgrade, Serbia, [ekorade@gmail.com](mailto:ekorade@gmail.com)

MILICA M. VASIĆ

Faculty of Physical Chemistry, University of Belgrade, Belgrade, Serbia, [mvasic@ffh.bg.ac.rs](mailto:mvasic@ffh.bg.ac.rs)

DRAGICA M. MINIĆ

Faculty of Physical Chemistry, University of Belgrade, Belgrade, Serbia, [dminic@ffh.bg.ac.rs](mailto:dminic@ffh.bg.ac.rs)

LJUBICA RADOVIĆ

Military Technical Institute, Belgrade, Serbia, [ljubica.radovic@mod.gov.rs](mailto:ljubica.radovic@mod.gov.rs)

NEBOJŠA MITROVIĆ,

Faculty of Technical Sciences, University of Kragujevac, Serbia, [nebojsa.mitrovic@ftn.kg.ac.rs](mailto:nebojsa.mitrovic@ftn.kg.ac.rs)

PAVEL CRNOMARKOVIĆ,

Military Technical Institute, Belgrade, Serbia, [pavel@ptt.rs](mailto:pavel@ptt.rs)

**Abstract:** The Magnetoimpedance (MI) effect of Fe-based nanostructured alloy ribbons  $Fe_{72}Ni_8Si_{10}B_{10}$  (A) and  $Fe_{72}Cu_1V_4Si_{15}B_8$  (B) was studied, compared for the two ribbons, and finally correlated with their composition and microstructure. The nanostructured ribbons were prepared by melt-spinning on a cold rotating disk. Basic characterization of the studied ribbons was performed by XRD and SEM-EDX techniques. It was found that the MI ratio of ribbon A is significantly lower than that of ribbon B, but the effects were observed at different frequencies. The maximal MI ratio of ribbon A was detected at 57.57 MHz, while in the case of ribbon B, that was the frequency of about 13 MHz. The structure of both ribbons consists of a certain amount of nanocrystals,  $\alpha$ -(Fe, Ni) for the ribbon A and  $\alpha$ -Fe(Si) for the ribbon B, which are embedded in an amorphous matrix. The MI effect and the frequency of its maximum are determined by the mobility of the magnetic domains in the samples, which is correlated with the microstructural specificities of individual ribbons.

**Keywords:** Magnetoimpedance effect, nanostructure, melt-spinning,  $\alpha$ -Fe(Si),  $\alpha$ -(Fe, Ni)

### 1. INTRODUCTION

Magnetoimpedance (MI) effect is defined as the influence of external DC field on the change in impedance of ferromagnetic sample. It was discovered at the beginning of the last decade of the twentieth century, and nowadays, it is applied in magnetic field sensors with high sensitivity [1-5]. Some ferromagnetic amorphous / nanocrystalline alloys were found to exhibit the MI effect.

The impedance of ferromagnetic material declines with an increase in magnetic field, but on the other hand, it grows with an increase in the frequency of the current flowing through the sample.

Most commonly, the MI ratio is expressed using the following equation:

$$\Delta Z/Z(\%) = 100\% \cdot (Z(H) - Z(H_{max})) / Z(H_{max}), \quad (1)$$

where  $Z(H_{max})$  is impedance at the maximum value of external magnetic field. Depending on the material

considered, at  $H=0$ , the remanent magnetization can affect the impedance, and further, with increase in magnetic field, such magnetization become annulled, resulting in asymmetry of MI-diagram for different magnetic field directions ( $-H$  and  $+H$ ).

The dependence of magnetoimpedance on frequency is related to the skin effect. This effect is characterized by penetration depth, which grows with an increase in magnetic field (due to decrease in magnetic permeability), and decline with increase in frequency. Alternating current causes the occurrence of eddy currents, which include the grouping of charges that transmit the electrical energy to the peripheral parts of the conductor. The skin depth can be defined as:

$$\delta_m = (\rho / (\pi \cdot \mu \cdot f))^{-1/2}, \quad (2)$$

where  $\rho$  is specific electrical resistivity,  $\mu$  is magnetic permeability, and  $f$  is frequency.

Beside the aforementioned, the MI ratio depends on the

domain structure of magnetic material, which is determined by the material composition and microstructure, and is closely related to the preparation technology.

The maximal MI ratio occurs at specific values of external magnetic field and frequency of the current flowing through the sample. It can be determined experimentally, and it is tightly related to the microstructure of the material.

## 2. EXPERIMENTAL PROCEDURE

In this work, the  $\text{Fe}_{72}\text{Ni}_8\text{Si}_{10}\text{B}_{10}$  ribbon-shaped alloy (A) was subjected to experimental measurements of magnetoimpedance, and then compared with our previous MI research [4, 6] of the  $\text{Fe}_{72}\text{Cu}_1\text{V}_4\text{Si}_{15}\text{B}_8$  ribbon (B). The ribbon-shaped alloys, 1.5 mm wide, were prepared by melt-quenching, which included rapid cooling of the melt on a cold wheel rotating at 2000 rpm. The average thickness of the alloys A and B is around 55  $\mu\text{m}$  [7].

Microstructure of the studied alloys was examined by means of X-ray diffraction analysis (XRD). For this purpose, a Rigaku SmartLab diffractometer equipped with a Cu  $K\alpha$  radiation source was used. Rietveld refinement was conducted to estimate the contents and microstructural parameters of individual phases in the samples. Scanning electron microscopy (SEM), with a SEM JEOL JSM-6610-LV microscope, was carried out to examine the surface morphology of the samples (shiny side).

In order to study the magnetoimpedance effect of the ribbons, measurements of the impedance were performed in homogeneous magnetic field of 15 kA/m, generated using the pair of Helmholtz coils, with an instrument Vector Network Analyser Agilent 8753ES. The sample holder was specially designed to allow measurements on the ribbon-shaped samples, 1 cm in length.

## 3. RESULTS AND DISCUSSION

### 3.1 XRD analysis

XRD analysis of the as-cast alloy ribbons reveals the composite structure, including the presence of crystalline phases in the samples, beside the amorphous matrix, Figures 1 and 2.

The abundance of crystalline grains inside the ribbon is not homogeneous due to differences in cooling rates occurring during the ribbon preparation. Namely, the wheel-side of the ribbon (matte side) is cooled faster and thus solidifies faster than the opposite (shiny side), resulting in larger crystalline fraction at the shiny side of the ribbon, Table 1.

Figures 1 and 2 represents the XRD patterns of the A and B alloy ribbons, respectively, indicating the alloy structure consisted of bcc iron ( $\alpha$ ) crystals embedded in amorphous matrix. The bcc iron phase is denoted as  $\alpha$ -Fe(Ni) and  $\alpha$ -Fe(Si) in the case of A and B, respectively,

Figures 1 and 2, considering the solubility of Si and Ni elements in the bcc iron structure.

The average crystallite size of the bcc iron phase was estimated from the XRD patterns for both ribbons, amounting to 53 and 40 nm for A and B, respectively.

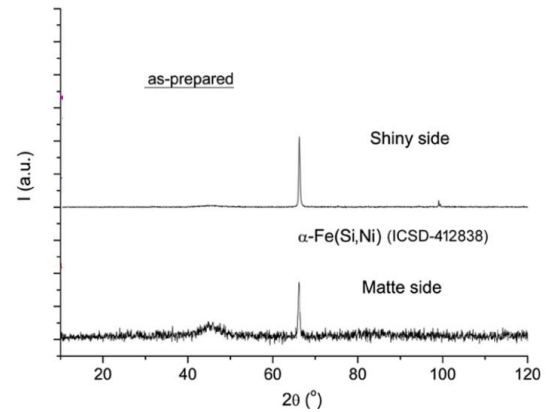


**Figure 1.** XRD patterns of the  $\text{Fe}_{72}\text{Ni}_8\text{Si}_{10}\text{B}_{10}$  (A) alloy ribbon.

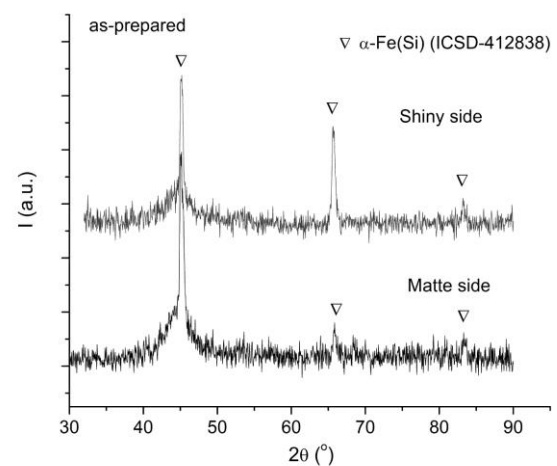


**Figure 2.** XRD patterns of the  $\text{Fe}_{72}\text{Cu}_1\text{V}_4\text{Si}_{15}\text{B}_8$  (B) alloy ribbon.

**Table 1.** Weight fraction of the bcc iron crystalline structure at matte and shiny sides of the studied ribbons.

Ribbon	Matte side	Shiny side
$\text{Fe}_{72}\text{Ni}_8\text{Si}_{10}\text{B}_{10}$ (A)	5 wt.%	14 wt.%
$\text{Fe}_{72}\text{Cu}_1\text{V}_4\text{Si}_{15}\text{B}_8$ (B)	18 wt.%	20 wt.%

### 3.2 SEM analysis

Relatively uniform surface morphology of both ribbons, A and B, can be observed in the SEM micrographs presented in Figures 3 and 4. Some dents at the surface of the ribbons resulted from the preparation procedure, including melt quenching.

EDX analysis, performed in the regions marked on the micrographs, confirmed the presence of the elements

specified in the alloy designation, at the ribbon surface, Table 2.

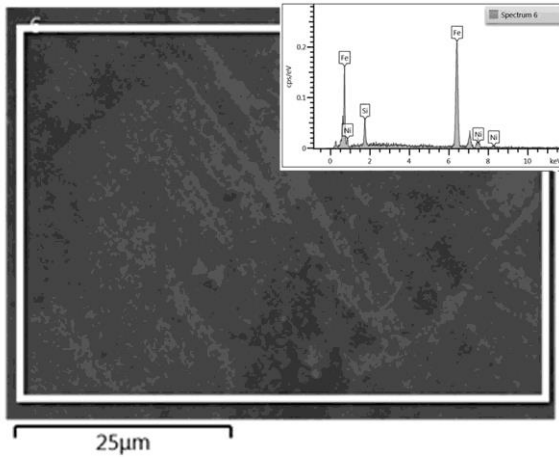


**Figure 3.** SEM micrograph (with EDX spectrum) of the as-cast Fe<sub>72</sub>Ni<sub>8</sub>Si<sub>10</sub>B<sub>10</sub> (A) alloy ribbon.

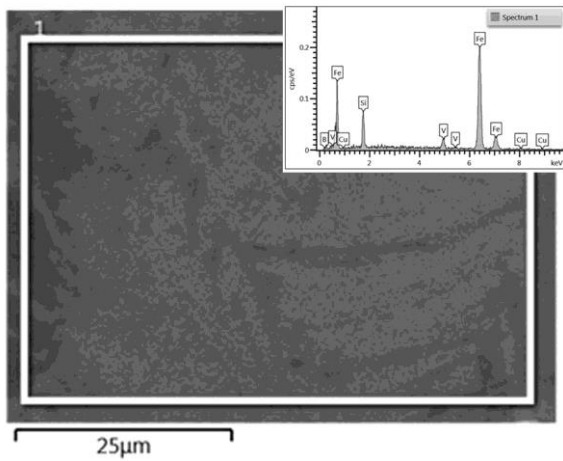


**Figure 4.** SEM micrograph (with EDX spectrum) of the as-cast Fe<sub>72</sub>Cu<sub>1</sub>V<sub>4</sub>Si<sub>15</sub>B<sub>8</sub> (B) alloy ribbon.

**Table 2.** Results of the EDX analyses (at. %) performed for the alloy ribbons studied in the work.

	Fe	Ni	Si	
Fe <sub>72</sub> Ni <sub>8</sub> Si <sub>10</sub> B <sub>10</sub>	79.3	9.6	11.1	
	Fe	Cu	V	Si
Fe <sub>72</sub> Cu <sub>1</sub> V <sub>4</sub> Si <sub>15</sub> B <sub>8</sub>	79.1	1.1	4.5	15.3

### 3.3. Magnetoimpedance measurements

The MI ratio of the Fe<sub>72</sub>Ni<sub>8</sub>Si<sub>10</sub>B<sub>10</sub> (A) alloy ribbon at various frequencies and magnetic fields was studied, and the obtained results are presented in Figures 5-8. The maximal MI ratio, 26%, is observed for frequencies 57-58 MHz (MI<sub>max</sub>= 26% for f= 57.57 MHz and H= 847.2 A/m, while H<sub>max</sub>=15kA/m).The dependence of MI ratio of A on frequency for various magnetic field values is presented in Figures 5 and 6. The effect grows with increase in magnetic field up to 847.2A/m (Figure 5), while further increase in magnetic field leads to decline in the MI ratio (Figure 6).

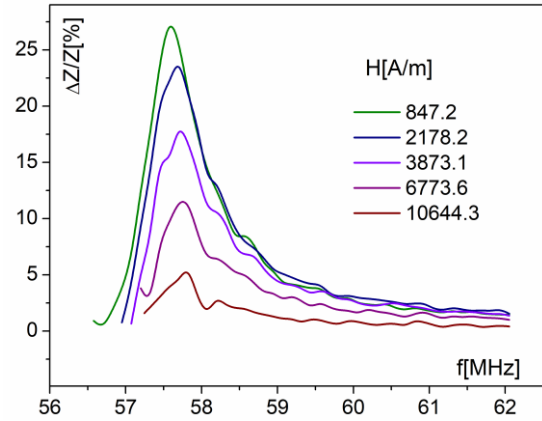


**Figure 5.** Dependence of MI ratio of Fe<sub>72</sub>Ni<sub>8</sub>Si<sub>10</sub>B<sub>10</sub> (A) alloy ribbon on frequency for magnetic field ranging 0-847.2 A/m; H<sub>max</sub>=15 kA/m.

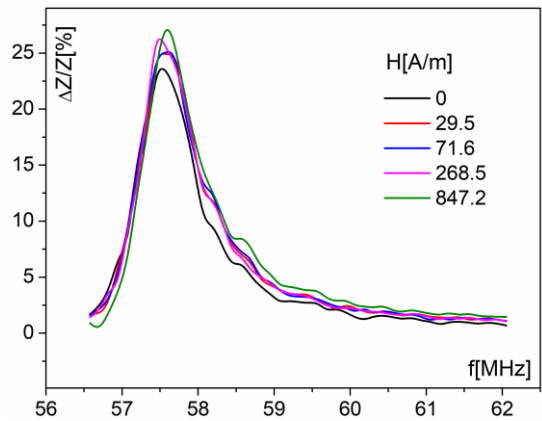


**Figure 6.** Dependence of MI ratio of Fe<sub>72</sub>Ni<sub>8</sub>Si<sub>10</sub>B<sub>10</sub> (A) alloy ribbon on frequency for magnetic field ranging 847.2-10644 A/m; H<sub>max</sub>=15 kA/m.

Figures 7 and 8 show the dependence of MI ratio of A on magnetic field for characteristic frequencies. The growth of the MI ratio with frequency up to f= 57.57 MHz, Figure 7, and decline of the MI ratio with further increase in frequency (f > 57.57 Hz, Figure 8) can be observed.

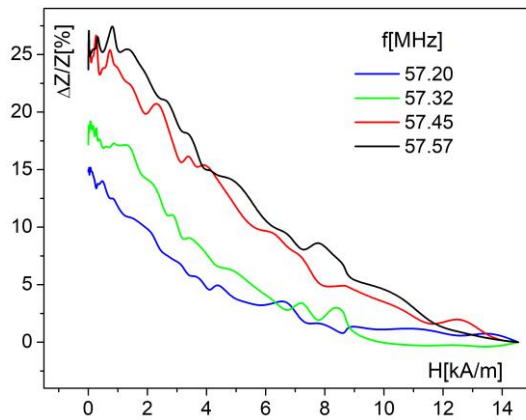


**Figure 7.** Dependence of MI ratio of Fe<sub>72</sub>Ni<sub>8</sub>Si<sub>10</sub>B<sub>10</sub> (A) alloy ribbon on magnetic field for frequency ranging 57.2-57.57 MHz; H<sub>max</sub>=15 kA/m.

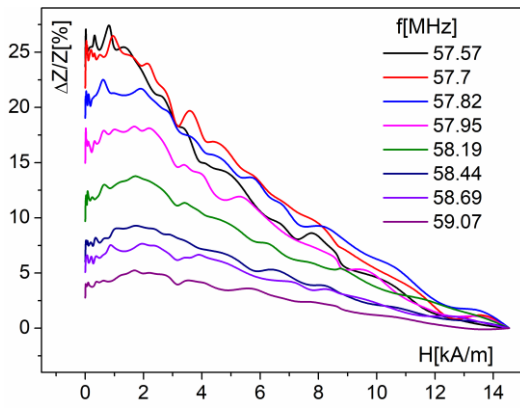


**Figure 8.** Dependence of MI ratio of  $\text{Fe}_{72}\text{Ni}_8\text{Si}_{10}\text{B}_{10}$  (A) alloy ribbon on magnetic field for frequency ranging 57.57-59.07 MHz;  $H_{\text{max}}=15$  kA/m.

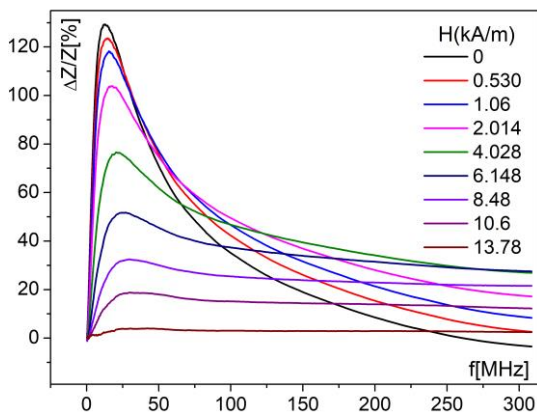


**Figure 9.** Dependence of MI ratio of  $\text{Fe}_{72}\text{Cu}_1\text{V}_4\text{Si}_{15}\text{B}_8$  (B) alloy ribbon on frequency for positive magnetic field ranging 0-13.8 kA/m;  $H_{\text{max}}=14.8$  kA/m.

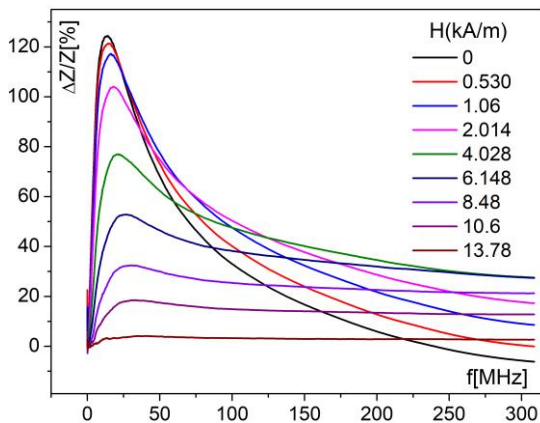


**Figure 10.** Dependence of MI ratio of  $\text{Fe}_{72}\text{Cu}_1\text{V}_4\text{Si}_{15}\text{B}_8$  (B) alloy ribbon on frequency for negative magnetic field ranging 0-13.8 kA/m;  $H_{\text{max}}=14.8$  kA/m.

The maximal MI ratio of the  $\text{Fe}_{72}\text{Cu}_1\text{V}_4\text{Si}_{15}\text{B}_8$  (B) alloy ribbon, obtained for  $H_{\text{max}}$  of around 15 kA/m, amounts to 125-129% (129% for  $f=13$  MHz,  $H=0$  and + direction, and 125% for  $f=12.5$  MHz,  $H=106$  A/m and - direction), Figures 9-12, and it is several times larger than that of the ribbon A. By the way, our previous research of the ribbon B [4] revealed  $MI_{\text{max}}=153\%$ , but for  $H_{\text{max}}=21.2$  kA/m ( $f=18.55$  MHz and  $H=0$  A/m).

Better MI ratio of the ribbon B than that of the ribbon A can be attributed to better mobility of magnetic domains in the case of B, which is related to the microstructure and composition of the material. Crystal size is very important microstructural parameter, where it is thought that the nanocrystal size lower than the magnetic exchange length considerably reduces the contribution of magnetocrystalline anisotropy of the nanocrystals to the overall magnetic anisotropy of the material [8, 9], affecting its overall magnetic behavior. For Fe-based alloys, the ferromagnetic exchange length is 20-40 nm [10]. For the studied alloy ribbons, A and B, certain difference in the crystallite size of the bcc iron phase is observed (53 nm for A, and 40 nm for B), which has an effect on the average anisotropy, considering its proportionality to the sixth power of the crystal size [10]. For the crystals formed in the as-cast ribbons, the crystallite size is connected with the chemical composition of the alloy. In the B ribbon, Cu and V elements are present, where Cu makes the nucleation process faster and V decreases the crystal growth rate, thus yielding lower crystallite size than that of the Fe-based alloys without such additives, while similar components are not present in the ribbon A.

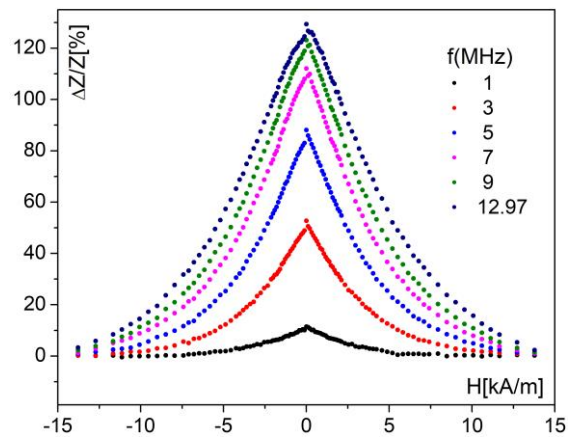


**Figure 11.** Dependence of MI ratio of  $\text{Fe}_{72}\text{Cu}_1\text{V}_4\text{Si}_{15}\text{B}_8$  (B) alloy ribbon on magnetic field for frequency ranging 1-13 MHz;  $H_{\text{max}}= \pm 14.8$  kA/m.

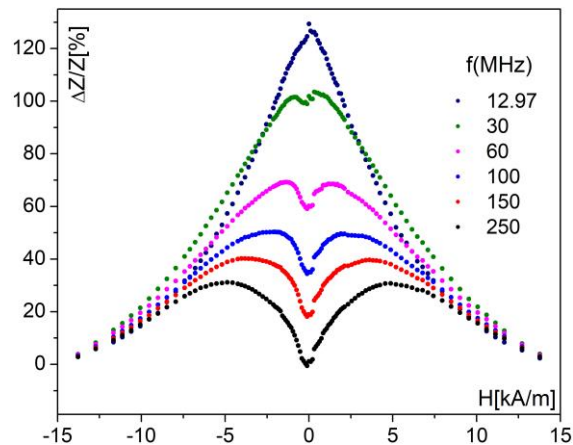


**Figure 12.** Dependence of MI ratio of  $\text{Fe}_{72}\text{Cu}_1\text{V}_4\text{Si}_{15}\text{B}_8$  (B) alloy ribbon on magnetic field for frequency ranging 13-250 MHz;  $H_{\text{max}}= \pm 14.8$  kA/m.



## 5. CONCLUSION

The magnetoimpedance effect is observed for both alloys studied in this work, suggesting their potential application in MI sensors. The effect is more pronounced for the  $\text{Fe}_{72}\text{Cu}_1\text{V}_4\text{Si}_{15}\text{B}_8$  (B) alloy, and thus its magnetoimpedance sensitivity to an external magnetic field is larger. The MI effect of the  $\text{Fe}_{72}\text{Ni}_8\text{Si}_{10}\text{B}_{10}$  (A) is weaker and occurs at higher frequencies. The MI effect is significantly dependent on the microstructure of the materials. The microstructure consisted of the bcc iron ( $\alpha$ ) crystals embedded in amorphous matrix is crucial for the magnetic behavior of both alloys. Appropriate choice of chemical composition of the material and preparation conditions allow the production of alloy ribbons with desired microstructure, and thus the design of materials with targeted properties, in this case potentially applicable in the MI elements.

## Acknowledgments

This work was supported in part by the Ministry of Science, Technological Development and Innovation of the Republic of Serbia, Faculty of Technical Sciences Čačak, University of Kragujevac under Grant 451-03-66/2024-03/200132, Faculty of Physical Chemistry, University of Belgrade, under Grant 451-03-66/2024-03/200146, and Military Technical Institute under grant 451-03-66/2024-03/200325.

## References

- [1] Panina, L.V., Mohri, K.: *Magneto-impedance Effect in Amorphous Wires*, Applied Physics Letters, 65(9), (1994), 1189 – 1191.
- [2] Kraus, L.: *Theory of Giant Magneto-impedance in the Planar Conductor with Uniaxial Magnetic Anisotropy*, Journal of Magnetism and Magnetic Materials, 195(3), (1999), 764 – 778.
- [3] Surla, R., Mitrović, N., Đukić, S., Ibrahimović, V.: *Amorphous  $\text{Fe}_{72}\text{Cu}_1\text{V}_4\text{Si}_{15}\text{B}_8$  Ribbon as Magneto-Impedance Sensing Element*, Serbian Journal of Electrical Engineering, 13(3), (2016), 381-394.
- [4] Surla, R., M., Vasić, Mitrović, N., Radović, Lj., Minić, D.: *Magnetic properties of  $\text{Fe}_{72}\text{Cu}_1\text{V}_4\text{Si}_{15}\text{B}_8$  alloy with a composite amorphous/ nanocrystalline structure*, Journal of Magnetism and Magnetic Materials, 564 (2022) 170141
- [5] SURLA, R.: Doktorska disertacija: *Uticao odgrevanja na strukturne transformacije i magnetna svojstva legure  $\text{Fe}_{72}\text{Cu}_1\text{V}_4\text{Si}_{15}\text{B}_8$* , FTN Čačak, Univerzitet u Kragujevcu, 2021.
- [6] Vasić M., Surla R., Mitrović N., Minić Dragica., Mitrović N., Maričić A., Minić Dušan: *Thermally induced microstructural transformations of  $\text{Fe}_{72}\text{Cu}_1\text{V}_4\text{Si}_{15}\text{B}_8$  alloy*, Metal. Mater. Trans. A 48 (2017) 4393–4402.
- [7] Surla, R., M., Vasić, Mitrović, N., Minić, D.: *Synthesis and characterization of  $\text{Fe}_{72}\text{Cu}_1\text{V}_4\text{Si}_{15}\text{B}_8$  metallic glass ribbons prepared by melt spinning casting*, 9<sup>th</sup> International Scientific Conference on Defensive Technologies, Belgrade, 8-9, October 2020.
- [8] Herzer, G.: *Grain structure and magnetism of nanocrystalline ferromagnets*, IEEE Transactions on Magnetics, 25 (1989) 3327-3329.
- [9] Kulik, T.: *Nanocrystallization of metallic glasses*, Journal of Non-crystalline Solids, 287 (2001) 145-161.
- [10] Herzer, G.: *Anisotropies in soft magnetic nanocrystalline alloys*, Journal of Magnetism and Magnetic Materials, 294 (2005) 99-106.



## ALTERNATIVES TO CADMIUM PROTECTION IN DEFENSE AND AEROSPACE INDUSTRY

KONSTANTIN KOMATINA

Vlatacom Institute, Belgrade, [konstantin.komatina@vlatacom.com](mailto:konstantin.komatina@vlatacom.com)

MILAN IGNJATOVIĆ

Vlatacom Institute, Belgrade, [milan.ignjatovic@vlatacom.com](mailto:milan.ignjatovic@vlatacom.com)

STEFAN TOMIĆ

Vlatacom Institute, Belgrade, [stefan.tomic@vlatacom.com](mailto:stefan.tomic@vlatacom.com)

DUNJA CRNOGORAC

Vlatacom Institute, Belgrade, [dunja.crnogorac@vlatacom.com](mailto:dunja.crnogorac@vlatacom.com)

**Abstract:** This paper presents results that were achieved during salt fog testing in order to determine the possibility of replacing cadmium surface protection treatment with plasma or ion nitriding. Additional oxidation processes were implemented. Salt fog tests were conducted in accordance with relevant MIL-STD 810 test standard. Paper will focus on the experimental procedure and results, theoretical background will be mentioned in short terms. There is no numerical analysis, or complex interpretation of the test results. Conclusion will describe next course of action.

**Keywords:** plasma nitriding, cadmium, defence industry

### 1. INTRODUCTION

Domestic defence and aerospace industry has long relied on cadmium surface treatments to achieve high degree of surface protection. Additional passivation processes were usually required after main cadmium protection. Such processes were reserved for highly stressed parts and components that were expected to reliably operate in most aggressive of environments. Technological parameters of cadmium protection processes are defined by domestic defence standards

According to regulations<sup>1</sup> that were set by EU governing bodies, cadmium surface coating is banned. Cadmium coatings present a health and safety hazard due to toxicity and carcinogenic properties, thus, it is necessary to produce a protection treatment that will be safe for its operators, but also be effective as or nearly as cadmium.

### 2. TEST PARAMETERS

There is a wide array of scientific papers[1] and studies available[2], however, rarely are stringent military test procedures applied or referenced. Usually authors will reference commercial applications in both automotive or aerospace industry.

Throughout the duration of the test, following conditions inside the chamber were met and maintained[3].

- a) Spray duration : 48 hours
- b) Test chamber temperature between 32 and 36 degrees C
- c) Relative air humidity 84 %
- d) Solution NaCl 5%, pH value around 6,5
- e) Salt fog concentration 138 cm<sup>3</sup>/48 h
- f) Dry temperature from 43 °C to 49 °C in duration of 24 hours

It bears mentioning that between the „wet“ phase and the drying phase, no additional cleaning processes were performed. Main goal is to allow the salt build up to remain on the surface. Such salt deposits, on poorly protected components and parts, will inevitably lead to base material corrosion and in case of systems that have moving parts, will clog or disable the operation of such parts. MIL-STD 810 also envisions electrical tests to determine adverse effects on electrical properties after the salt fog, however, this is beyond the scope of this paper.

<sup>1</sup>REACH regulations

<sup>2</sup>Domestic designation is Č 5432, VP additional

<sup>3</sup>Data retrieved from sij group web site “steelselector.sij.si”  
“SIQUAL 6580 Steel”

### 3. MATERIAL CONSIDERATIONS

In order to perform a salt fog test, three test samples were prepared. Samples were made from 1.6580 steel bars.

30CrNiMo8<sup>2</sup> steel is widely used in aerospace and defence, as it combines excellent mechanical properties with good machinability. This steel belongs to group of steels intended for heat treatment and can be easily heat treated to achieve high surface hardness, making it ideal for highly stressed shafts, cranks, bolts etc.

Major drawback however is its tendency to easily corrode, even with the main alloying element being chrome. Steel components made from 1.6580 will show signs of surface corrosion even at room temperature conditions, especially if they are kept in humid environments.

**Table 1:** Mechanical properties<sup>3</sup>

Bar diameter	0,2% proof stress	Tensile strength	Elongation
[mm]	[N/mm <sup>2</sup> ]	N/mm <sup>2</sup>	%
40 to 100	900	1100 -1300	10

Chemical composition is stated in table bellow

**Table 2:** Chemical composition

C	Si	Mn	Cr	Mo	Ni
[%]	[%]	[%]	[%]	[%]	[%]
0,30	0,40 max	0,45	2,0	0,40	1,9

### 4. TEST SAMPLES

As mentioned previously, test samples are three steel cylinders measuring as 60mm in diameter and 120mm in length. They are marked numerically from 1 to 3.

On all three cylinders, holes are drilled in order to provide mounting points for installation inside the chamber.

Test samples are oriented in three distinct positions:

- 1) Vertical
- 2) Horizontal
- 3) Slanted at 45 degrees



**Figure 1:** Test sample 1



**Figure 2:** Test sample 1 side position



**Figure 3:** Test sample 3 – side position

### 5. SURFACE PROTECTION PARAMETERS

Three samples in question were subjected to following conditions in order to create a hard nitriding surface layer. Thickness of said layer is of several micrometers. Table bellow gives the overview of protection parameters.

**Table 3:** Process parameters

Sample no.	Protection process	Duration [h]	Coating thickness [μm]
1	Nitriding	15	5
2	Nitriding + Oxidation	20	5
3	Nitriding	20	5

All three test samples were nitrated, in varying duration of the process itself. However, sample number two is the only one that was subjected to oxidization process. Thus we have varied only two parameters, duration of the process and post process itself.

## 6. RESULTS AND DISCUSSIONS

After the aforementioned salt fog process was completed, test samples were taken for evaluation.

Photos of the samples are given bellow



**Figure 5:** Test sample number two



**Figure 6:** Test sample number 1



**Figure 7:** Test sample number 3

As can be seen from the supplied photographs, all three samples have base material corrosion and thus have failed

the test.

However, sample number two has by far performed the best. Reason as to why lies in the added oxidization process. On two sides of sample number two there are observable spilages of salt corrosion that affected the sample, on the other two sides there are not.

## 7. FUTURE WORK AND ADDITIONAL INFORMATION

On the previous page, a peculiar phenomom regarding the sample number two was mentioned. One possible solution is to continue with the nitriding and oxidization processes and to optimize the process in order to achieve a sufficient protection.

This avenue lends itself to continuos study of effects nitriding layers in domain of surface protection. Possible downside of course is that no degree of optimization can solve for adverse conditions perscribed in MIL-STD-810 509.5

In recent years, in the automotive industry there has been a discussion about the possible use of a zinc- nickel galvanizing method that could effectively replace cadmium.

This potential solution should be explored and future work will focus on zinc-nickel treatments.

## References

- [1] : J.C Diaz-Guillen; J.S Zamarripa-Pina; E.E Granda Gutierrez; M.A Gonzales-Albarran; J.A Diaz-Guillen; S.I Perez-Aguilar; J.Candeles-Ramirez, "Increase of Salt Fog Corrosion Resistance of Plasma Nitrided Steel by Pulsed Plasma Post Oxidation", 2013
- [2] : P Wach; J Michalski; K Burdynski; A Ciski, Anticorrosion nitrided layers on unalloyed and alloyed steels, 2017
- [3] : Department of Defense, "Environmental engineering considerations and laboratory tests, 2008"



## Cu -DECORATED TiO<sub>2</sub> NANOPARTICLES AS THE PHOTOCATALYTIC MATERIAL FOR CIPROFLOXACIN DEGRADATION

MARIJA KOVAČEVIĆ

Department of Physical Chemistry, VINČA Institute of Nuclear Sciences-National Institute of the Republic of Serbia, University of Belgrade, Mike Alasa 12-14, Belgrade, Serbia, e-mail: [marija.kovacevic@vin.bg.ac.rs](mailto:marija.kovacevic@vin.bg.ac.rs)

SANJA ŽIVKOVIĆ

Department of Physical Chemistry, VINČA Institute of Nuclear Sciences-National Institute of the Republic of Serbia, University of Belgrade, Mike Alasa 12-14, Belgrade, Serbia, e-mail: [sanjaz@vin.bg.ac.rs](mailto:sanjaz@vin.bg.ac.rs)

MILOŠ D. MILOVIĆ

Institute of Technical Sciences of SASA, Knez Mihajlova 35/IV, 11000, Belgrade, Serbia, e-mail: [milos.milovic@itn.sanu.ac.rs](mailto:milos.milovic@itn.sanu.ac.rs)

DRAGANA VASIĆ ANIĆIJEVIĆ

Department of Physical Chemistry, VINČA Institute of Nuclear Sciences-National Institute of the Republic of Serbia, University of Belgrade, Mike Alasa 12-14, Belgrade, Serbia, e-mail: [draganav@vin.bg.ac.rs](mailto:draganav@vin.bg.ac.rs)

**Abstract:** Efficient removal of antibiotic residues from the water using environmentally friendly and zero-waste technologies represents an emerging challenge. The increasing development of photocatalytic materials needs a comprehensive and systematic approach to understand the principles behind their performance. In this contribution, the Cu-decorated TiO<sub>2</sub> nanoparticles were prepared using various input amounts of Cu (0.5 – 2%), employed for photocatalytic degradation of ciprofloxacin solution (30 mg photocatalyst per 50 mL of solution), and compared to bare TiO<sub>2</sub> at the same concentration. The observed performance improvement of investigated photocatalytic material compared to bare TiO<sub>2</sub> upon decoration with Cu was discussed from various aspects. Some of them include: morpho-structural changes (increase of active surface for photocatalysis upon reduced agglomeration), chemical effects (the improved generation and reactivity of active oxygen species upon modification of their adsorption properties), and modification of photochemical properties of the semiconductor material itself (impact of metal decoration on the band gap structure).

**Keywords:** Rutile TiO<sub>2</sub>; Photocatalysts; Degradation.

### 1. INTRODUCTION

Environmental water pollution by antibiotics from households, farms, and hospitals represents an emerging concern worldwide. Ciprofloxacin (CIP), a synthetic fluoroquinolone derivative, is among the most frequently used medication for human treatment, which is stable, difficult to decompose and resistant to common water treatments [1,2]. There are many articles that include oxidation of ciprofloxacin by ozonation, electrochemical oxidation, Fenton reagent, and photocatalytic degradation with UV light using a different semiconducting- and nanomaterials [3,4]. Main disadvantages of current photocatalytic degradation include: limitations to laboratory-size use fast charge recombination, limited ability of photo-generated electrons and holes to migrate, and potential toxicity of byproducts [5]. On the other hand, the rapid progress in developing novel materials is expected to help overcoming these difficulties.

The correlation between fundamental material properties

and its catalytic performance has been of persisting interests in investigation of the photocatalyzed processes. The simultaneous use of experimental and theoretical approach contributes to the multi-level understanding of the materials performance, from the chemical and electronic properties to the application level and the possibility to predict catalytic performance of the materials that are not synthesized yet.

This contribution deals with TiO<sub>2</sub> decorated by Cu deposition onto its surface, which was applied to degrade ciprofloxacin photocatalytically in an aqueous solution. The prepared photocatalysts was characterized by XRPD and SEM analysis, and the ciprofloxacin degradation was monitored by UV-Vis spectrometry. The DFT analysis of OH radical binding on photocatalyst model surfaces has revealed the correlation between catalytic improvement and the chemical properties of the photocatalyst materials.

## 2. METHODS

### 2.1. TiO<sub>2</sub> nanoparticles preparation

Titanium (IV)-isopropoxide (Sigma-Aldrich, St. Louis, MO, USA, 97%) was dissolved in isopropanol and stirred on a magnetic stirrer at room temperature, after 10 minutes deionized water (pH = 6) was added dropwise during 3h. The molar ratio of titanium (IV)-isopropoxide: isopropanol:water was fixed at 5:3:10. The as-prepared precipitate was filtrated and washed using ethanol, dried overnight in the drying oven at 100 °C, then it was calcined at 700 °C for 5 hours and left in the oven to cool down.

### 2.2. Structural and morphological characterisation of the TiO<sub>2</sub> nanoparticles

The X-ray powder diffraction (XRPD) measurements were conducted on Philips PW 1050 X-ray diffractometer using Ni-filtered Cu radiation and Bragg-Brentano focusing geometry. The diffraction intensities have been recorded in the 5–70° 2θ range with a step size of 0.02° and accounting time of 6 s per step. Scanning electron microscopy (SEM) was performed with a PhenomProX electron microscope (Phenom, Thermo Fisher Scientific, Waltham, MA, USA).

### 2.3. Photodegradation experiments

The procedure of photodegradation was carried out with 30 mg of catalyst for the ciprofloxacin commercial solution for infusion, diluted by distilled water up to the concentration  $4.75 \times 10^{-4}$  M. The reaction mixture was stirred for 30 minutes in the dark, alongside blank (solution ciprofloxacin without catalyst). Next, the blank and the reaction mixture were irradiated under UV light (Philips TUV 15W UVC Disinfection, Poland) for 4 hours. The photodegradation process was monitored by recording the UV-Vis spectra (LLG Labware, Detroit, MI, USA) in the wavelength range from 190 to 500 nm. The 3 mL aliquots were drawn in time interval 25 min and filtrated prior to the recording of UV-Vis spectra.

### 2.4. Theoretical calculations

For DFT calculations, a *pwscf* code of the Quantum ESPRESSO package (version 7.2) was used [6]. Ultrasoft pseudopotentials based on GGA-PBE approximation with a plane wave kinetic energy cutoff of 50 eV were implemented. Optimized rutile bulk parameters were  $a = 4.639$  Å and  $c = 2.968$  Å. The TiO<sub>2</sub> surface was modelled as a (110) slab in a 4-layer 1×1 (17-atom) cell. There was at least a 25 Å vacuum between slabs, and the dipole correction was employed to avoid interaction between periodic images. All calculations were spin polarized. Hubbard correction (GGA+U) was used in a simplified version of Cococcioni and de Gironcoli's work [7]. An effective U value of 3.0 eV for the Ti-d states was used. The k-point grid was sampled through a Monkhorst–Pack scheme, using 4×4×1 k-points. Electronic and ionic force convergence criteria were  $10^{-6}$  Ry and  $10^{-4}$

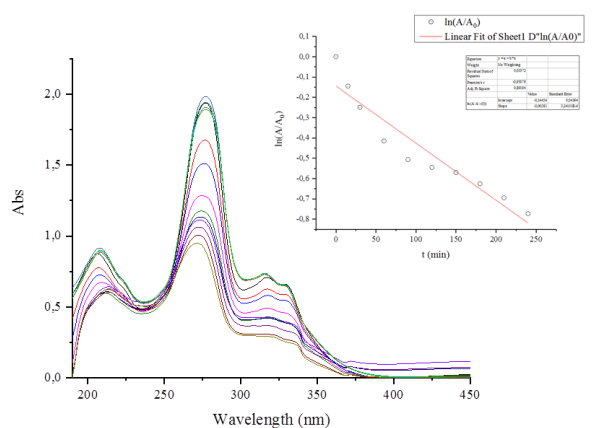
Ry/Bohr, respectively.

## 3. RESULTS AND DISCUSSION

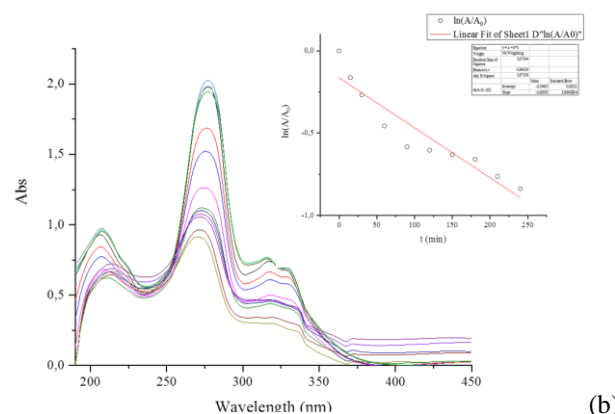
Ciprofloxacin degradation efficiency was measured as the relative depletion of absorbance of the characteristic peak at 277 nm. Degradation rate constants were calculated from the decrease in absorbance at 277 nm, assuming the pseudo-first-order kinetics (Equation (1)):

$$A = A_0 e^{-kt} \quad (1)$$

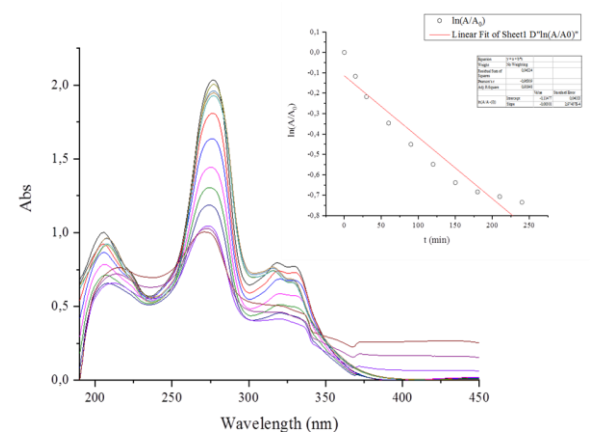
where  $A_0$  is the absorbance at time at zero minute, and  $k$  ( $\text{min}^{-1}$ ) is a pseudo-first-order rate constant.



(a)



(b)



(c)

**Figure 1.** UV-Vis spectra of the ciprofloxacin solution of the initial concentration  $4.75 \times 10^{-4}$  M during 240 min of photodegradation with 30 mg 0.5% TiO<sub>2</sub>(Cu) (a), 1% TiO<sub>2</sub>(Cu) (b) and 2% TiO<sub>2</sub>(Cu) (c). Corresponding linear forms used to calculate rate constants are given as inserts

The linearization of Equation (1) was applied to obtain the rate constant  $k$  from the slope of the graph (Equation (2)):

$$\ln \frac{A}{A_0} = -kt \quad (2)$$

The UV-Vis spectra of ciprofloxacin degradation using TiO<sub>2</sub> with Cu input concentrations 0.5%, 1%, and 2% are represented in Figure 1, and the corresponding linearized forms (2) are given as insert.

Calculated pseudo-first order rate constants are represented in Table 1. The pseudo-first order rate constants exhibit similar values in all three Cu input concentrations. The efficiency of CIP degradation achieves 51% within 240 minutes. However, the degradation efficiency is in average increased compared to bare TiO<sub>2</sub>, which achieves no more than 44% at the same experimental conditions [8].

**Table 1.** Pseudo-first order rate constants and efficiencies of CIP degradation for different Cu input concentrations

Catalyst material	$k$ (min <sup>-1</sup> )	Degradation of CIP (%)
0.5% TiO <sub>2</sub> (Cu)	0.0028	48
1% TiO <sub>2</sub> (Cu)	0.0030	46
2% TiO <sub>2</sub> (Cu)	0.0030	51

XRD patterns of TiO<sub>2</sub> with input Cu amounts 0.5-2% are represented in Figure 2. Regarding the phase composition of the TiO<sub>2</sub>(Cu) samples, it is the same as the bare TiO<sub>2</sub> powder. However, the absolute intensities of the peaks decrease over the entire range upon increase of input Cu amount. Possibly, metal deposition changes the relative intensity of individual planes due to a change in surface energy.

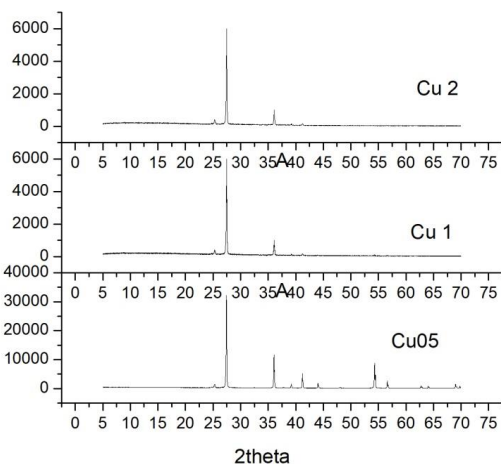


**Figure 2.** XRD patterns of TiO<sub>2</sub> with at three input

concentrations of Cu (2%, 1% and 0,5%)

SEM images comparing bare TiO<sub>2</sub> and TiO<sub>2</sub>(Cu) with 0.5% input Cu are represented in Figure 3.

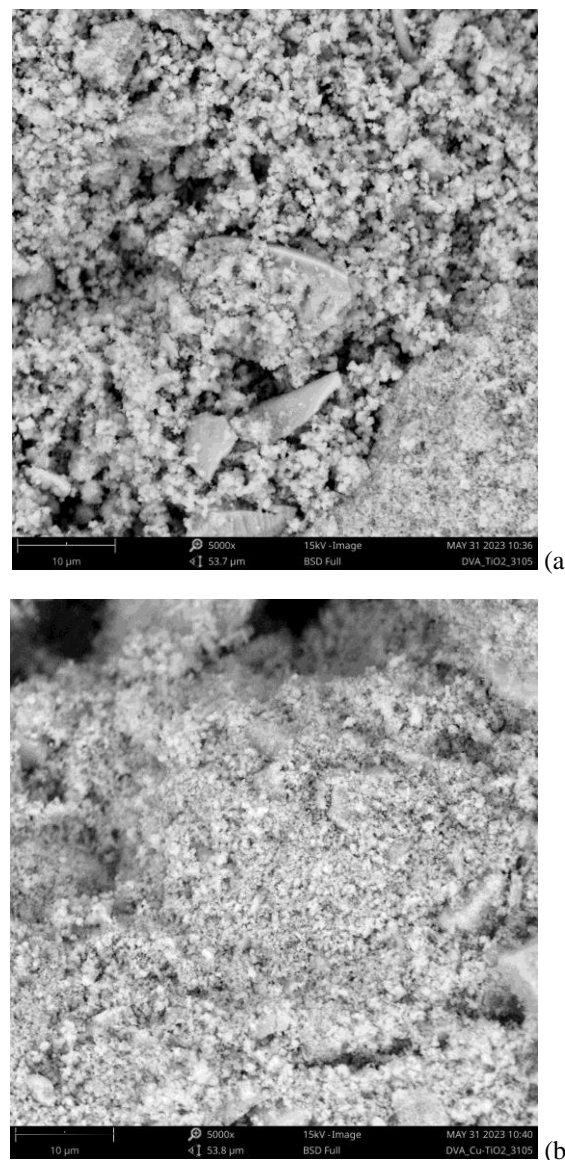


**Figure 3.** SEM images of bare TiO<sub>2</sub> (a), and TiO<sub>2</sub>(Cu) (b) at magnification 5000.

As obvious from Figure 3, addition of Cu results in a remarkable reduction of average particle size of TiO<sub>2</sub>, possibly due to the significant reduction of agglomeration of smaller 20-30 nm TiO<sub>2</sub> particles upon deposition of Cu onto the TiO<sub>2</sub> surface.

Chemical effect of deposited Cu at coverage 0.25 ML on the photocatalytic performance is evaluated through DFT calculations of OH binding energy on metal top site of TiO<sub>2</sub>(110) surface model (Table 2). Decrease of OH-radical binding energy in TiO<sub>2</sub>(Cu) compared to bare TiO<sub>2</sub> potentially implies that the OH-radical is more reactive towards organic compounds because it is more efficiently desorbed.

**Table 2.** DFT calculated binding energies of OH radical on selected sites of model surfaces TiO<sub>2</sub>, and TiO<sub>2</sub>(Cu)

Surface model	Binding site	E <sub>ads</sub> , OH
Bare TiO <sub>2</sub>	Ti-top	-3.95 eV
TiO <sub>2</sub> (Cu)	Cu-top	-3.39 eV

Corresponding PDOS for TiO<sub>2</sub>(110) surface with deposited Cu is represented in Figure 4. The PDOS features originating from Cu d-orbitals appear in the bandgap suggesting the modification of semiconductor properties of TiO<sub>2</sub> surface upon Cu deposition.

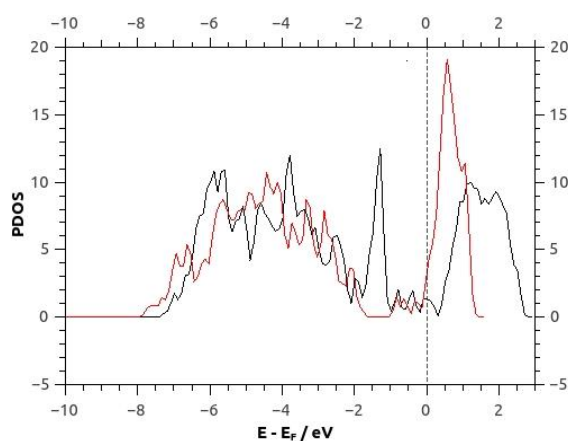


**Figure 4.** PDOS structure of TiO<sub>2</sub>(Cu) (coverage 0.25 ML) vs bare TiO<sub>2</sub>

## 4. CONCLUSION

The provided approach in investigation of TiO<sub>2</sub>(Cu) systems for photocatalytic degradation of ciprofloxacin contributes to the understanding of performance on experimental and theoretical level. Variations of input Cu concentration do not have significant impact on the degradation kinetics and efficiency. However, the degradation reaction is in average more efficient on TiO<sub>2</sub>(Cu) compared to bare TiO<sub>2</sub>. Morphological changes upon Cu deposition on TiO<sub>2</sub> result in the change of surface energy and the decrease of particle size upon reduced agglomeration. DFT calculations of OH binding energy predict that the photogenerated OH-radicals bound on Cu-top site could be more reactive towards organic compounds compared to these on bare TiO<sub>2</sub>, while PDOS confirm appearance of Cu d-states in the TiO<sub>2</sub> bandgap.

## Acknowledgements

The authors would like to thank the Ministry of Science, Technological Development, and Innovation of the

Republic of Serbia [grant number 451-03-66/2024-03/200017 and 451-03-66/2024-03/200175].

## References

- [1] KUTUZOVA, A., DONTSOVA, T., KWAPINSKI, W.: *Application of TiO<sub>2</sub>-Based Photocatalysts to Antibiotics Degradation: Cases of Sulfamethoxazole, Trimethoprim and Ciprofloxacin*, *Catalysts*, 11, (2021). <https://doi.org/10.3390/catal11060728>
- [2] LIU, Y., CAI, D., LI, X., WU, Q., DING, P., SHEN, L., YANG, J., HU, G., WU, J., ZHANG, L.: *Occurrence, fate, and risk assessment of antibiotics in typical pharmaceutical manufactories and receiving water bodies from different regions*, *PLoS One*. 18, e0270945- (2023).
- [3] ABDULRAHMAN, S., SHNAIN, Z., IBRAHIM, S., MAJDI, H., *Photocatalytic Degradation of Ciprofloxacin by UV Light Using N-Doped TiO<sub>2</sub> in Suspension and Coated Forms*, *Catalysts* 2022, 12(12), 1663. <https://doi.org/10.3390/catal12121663>
- [4] YAKAMERCAN, E., AYGÜN, A., SIMSEK, H.: *Antibiotic ciprofloxacin removal from aqueous solutions by electrochemically activated persulfate process: Optimization, degradation pathways, and toxicology assessment*, *Journal of Environmental Sciences*. 143, 85–98 (2024). <https://doi.org/10.1016/j.jes.2023.08.013>
- [5] KOE, W. S., LEE, W., CHONG, W. C., PANG, Y. L., SIM, L. C.: *An overview of photocatalytic degradation: photocatalysts, mechanisms, and development of photocatalytic membrane*, (2020)
- [6] GIANNOZZI, P., BARONI, S., BONINI, N., CALANDRA, M., CAR, R., et al: *QUANTUM ESPRESSO: a modular and open-source software project for quantum simulations of materials*, *Journal of Physics: Condensed Matter*. 21, 395502 (2009). <https://doi.org/10.1088/0953-8984/21/39/395502>
- [7] COCOCCIONI, M., and GIRONCOLI, S. *Linear response approach to the calculation of the effective interaction parameters in the LDA+U method* *Phys. Rev. B* 71, 035105 (2005) <https://doi.org/10.1103/PhysRevB.71.035105>
- [8] KOVAČEVIĆ, M., SIMIĆ, M., ŽIVKOVIĆ, S., MILOVIĆ, M., TOLIĆ STOJADINOVIĆ Lj., RELIĆ, D., and VASIĆ ANIČIJEVIĆ, D: *Ciprofloxacin degradation with metal-decorated TiO<sub>2</sub> photocatalysts – a systematic experimental and DFT study*, In preparation





## SELECTIVE ELECTRODEPOSITION TO EXTRACT COBALT AND NICKEL FROM LEACHING SOLUTION

JONAS MITTERECKER

Process Metallurgy and Metal Recycling, RWTH Aachen University, Intzestraße 3, D 52072 Aachen, Germany;  
[jonas.mitterecker@rwth-aachen.de](mailto:jonas.mitterecker@rwth-aachen.de)

MILICA KOŠEVIĆ, MARIJA MIHAILOVIĆ\*

University of Belgrade - Institute of Chemistry, Technology and Metallurgy - National Institute of the Republic of Serbia, Department of Electrochemistry, Njegoševa 12, 11 000 Belgrade, Serbia; [milica.kosevic@ihm.bg.ac.rs](mailto:milica.kosevic@ihm.bg.ac.rs),  
[marija.mihailovic@ihm.bg.ac.rs](mailto:marija.mihailovic@ihm.bg.ac.rs)

**Abstract:** Leaching solutions of complex ore concentrates are rich in different elements, some hindering the extraction of others. Chemically similar elements are difficult to extract using conventional separation methods. Electrochemical techniques are employed for Co and Ni selective extraction out of so-called pregnant leaching solution (PLS). Selective electrodeposition using chronoamperometry (CA) as a tool was used to extract cobalt and/or nickel from the solution. Besides different ions depositing at applied cathodic potential, hydrogen evolution reaction also occurs, which can impede deposition of the desired metals. Previous Linear sweep voltammetry (LSV) analysis of prepared model solutions at different pH values, and upon H<sub>2</sub>O<sub>2</sub> addition, was conducted. The removal of metal ions from the solution, can be performed with adjusting the pH and applied potential (E), so their combination in electrochemical hydro-extraction for Ni and Co is investigated. It has been demonstrated that Fe can be separated from Ni and Co through Fe precipitation in the pH range of 3–6, followed by the electrochemical extraction of Ni/Co.

**Keywords:** metal ions extraction; leaching selectivity.

\*corresponding author [marija.mihailovic@ihm.bg.ac.rs](mailto:marija.mihailovic@ihm.bg.ac.rs)

### 1. INTRODUCTION

Cobalt and nickel are now considered critical raw materials. Cobalt plays a vital role in various electrical applications, especially in the fast-growing market of electric vehicles [1]. The demand for nickel is expected to increase significantly in the coming decades, primarily due to the rising need for fast-working and high-tech steels, which have broad industrial applications [2].

The primary source of these metals is lateritic ores [3]. These ores are in an oxidized state and contain high amounts of iron, which is undesirable for the extraction processes of cobalt and nickel. Due to the low content of cobalt and nickel in the ores, a meticulous processing route is essential. The development of new technologies, including advanced precipitation methods, makes processing such ores economically and technically viable.

Generally, iron precipitation occurs at a lower pH, where cobalt and nickel remain stable in the solution. Iron removal is typically achieved by adding bases to adjust the pH of the pregnant leach solution. Precipitation has been challenging due to the overlapping behavior of iron, nickel, and cobalt. This paper aims to delve deeper into this ternary system. It also partially presents a new approach using electrochemical methods for extraction experiments.

### 2. EXPERIMENTAL

Lateritic ore concentrate leaching was performed in a standard glass cell, employing stirring unit and temperature control. The reaction flask was placed inside of a temperature controlled heating unit (SAF Wärmetechnik GmbH, Germany) and temperature was kept constant at 70 °C for 2 h. The lateritic ore concentrate was leached with 1M H<sub>2</sub>SO<sub>4</sub> at a stirring speed of 300 rpm. Liquid to solid ratio upon the leaching was 5:1. The ore solid residue was filtered off using a centrifuge, and the resulting clear solution was then utilized for further electrochemical investigations.

Electrochemical measurements were performed in a standard three electrode system using potentiostat/galvanostat, model SP-200 (Bio-Logic SAS, France). Glassy carbon electrode served as working electrode, Pt wire as counter electrode and saturated calomel electrode (SCE) as a reference electrode. All measurements were conducted in the as prepared filtered solution (pH 0.5) and in the NaOH-treated filtered solution (pH 3.7). Addition of NaOH was performed under constant stirring at 500 rpm in a separated beaker. Cyclic voltammetry advanced (CVA) was performed with a sweep rate of 10 mV s<sup>-1</sup>, according to Open circuit potential; -1200 mV to 1200 mV; Cathodic holding time was 2 minutes. Chronoamperometry (CA) was employed

for the electrodeposition of ions from the solution on the GC electrode.

### 3. ELECTROCHEMICAL LEACHING APPROACH

Selective electrodeposition using chronoamperometry (CA), by applying a constant potential to the PLS, as a tool was used to extract cobalt and /or nickel from the solution. This leads to the reduction of the cobalt and nickel ions from the solution and their deposition on the working electrode. The value of deposition potential was determined using the Nernst equation (1). This potential then was adjusted to the concentration of the obtained leachate (pH = 0.5).

$$E(\text{Co}/\text{Co}^{2+}) = E_0(\text{Co}/\text{Co}^{2+}) + \frac{R * T}{z * F} * \ln(c(\text{Co}^{2+})) \quad (1)$$

Where:  $z$  - number of exchanged electrons,  $F$  - Faraday constant,  $R$  - ideal gas constant,  $T$  - Temperature in K,  $c$  - concentration of ion in the solution. Standard potentials were given versus SHE, having in mind that:  $E$  (vs SCE) =  $E$  (vs SHE) – 0.244 V.

Immersing GC working electrode in the filtered solution applying potential required for Co deposition, can lead to deposition of some other ions from solution, meaning that electrodeposition is not selective. Fe ions present in this solution (5,97g/L) should be in the  $\text{Fe}^{3+}$  form, according to the Pourbaix diagram. In this case  $\text{Fe}^{3+}/\text{Fe}^{2+}$  reaction could have occurred as well. This transition would have been registered as current peaks, so it would be difficult to differentiate which peak corresponded to which process.

Out of this reason, the only metals that could be deposited at the used potentials are nickel, cobalt and iron. Fe deposition, though, should only take place at lower potentials, according to the calculations. Deposition of other metals should not be possible, since their potential of reduction is more negative to the electrodeposition potentials. Chromium is unlikely to deposit as well, hindered by lower hydrogen overpotential and therefore main reaction is hydrogen evolution (HER), instead of deposition of chromium.

Besides different ions depositing at applied cathodic potential, hydrogen evolution reaction also occurred. This reaction can impede deposition of the desired metals, so applied potential was negative enough for the metal deposition to happen, but not too negative to have hydrogen evolution. The addition of oxidizing agent  $\text{H}_2\text{O}_2$  enables the onset of  $\text{Fe}^{3+}/\text{Fe}^{2+}$  reaction at altered potentials, what benefits the selectivity of extraction process. In order to reach maximum selectivity and minimum hydrogen evolution, potentials of -680 mV and -900 mV were chosen for the electrodeposition using CA in these experiments.

#### 3.1. Linear Sweep Voltammetry analysis

Linear sweep analysis of prepared solution at different pH and upon treatment with  $\text{H}_2\text{O}_2$  are shown, but for

comparison the LSV curves of non- $\text{H}_2\text{O}_2$ -treated solution are presented as well. The removal of metal ions from the solution, especially iron, chromium and aluminum, can be performed with adjusting the pH. The LSV curves focus on anodic dissolution of the deposit from leachate with addition of hydrogen peroxide into the leachate and different potential applied in for preceding electrodeposition.

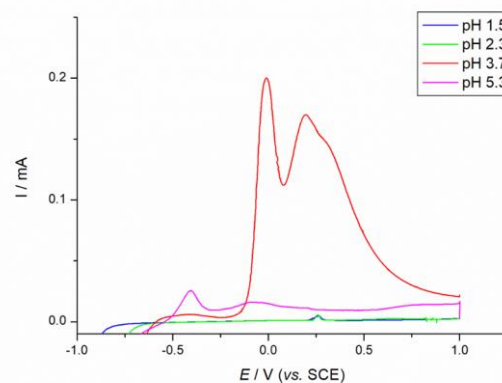


**Figure 1.** LSV curves, potential of -900 mV, without  $\text{H}_2\text{O}_2$ , varying pH,  $v = 10 \text{ mV s}^{-1}$

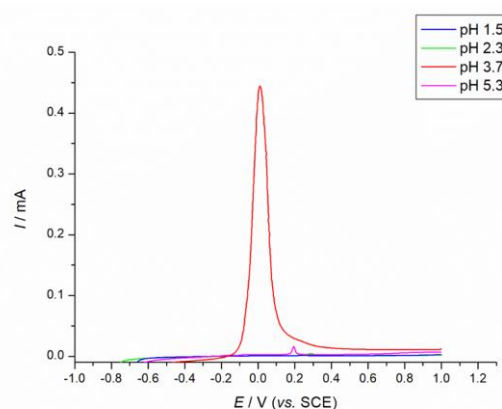


**Figure 2.** LSV curves, potential of -680 mV, without  $\text{H}_2\text{O}_2$ , varying pH,  $v = 10 \text{ mV s}^{-1}$

Figures 1 and 2 show the same LSV at different pH, but with different electrodeposition potential, Fig. 1 presents results with potential of -900 mV, while Fig.2 presents LSV with -680 mV, which is preferable for Fe deposition. At pH 1.5 and 2.3 only one peak can be found at the potential of 0.2 V. Intensity of the peaks are considerably lower with respect to pH 3.7, reaching a maximum of 0.01 mA. At pH 3.7 one major peak can be found at the anodic potential of 0 V. The intensity reaches a maximum of 0.45 mA. At pH 5.3, one anodic peak is visible at the potential of 0.2 V.

Figure 3 shows a comparison of the hydrogen-peroxide treated solution at different pH; while potential of electrodeposition for both trials is -680 mV. Anodic peaks at both pH are at similar positions, indicating the deposition of similar phases. Peaks are registered at -0.4 V (only for pH 1.5), 0 V, 0.2 V and 0.3 V. The current of

the maximum, though, is higher for the solution with higher pH, being around 0.3 mA at most. The similarity of the LSV curves for both pH at the same potential of -680 mV indicate the same metal deposition on the electrode surface.

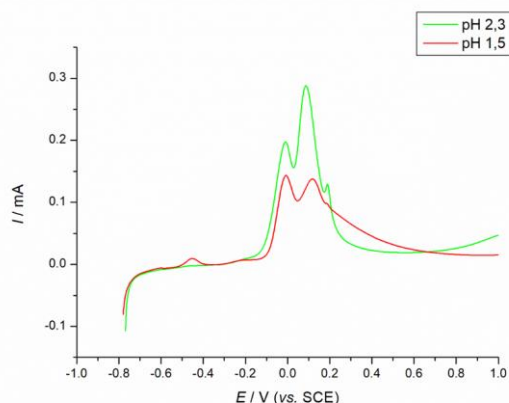


**Figure 3.** Comparison of LSV, potential of -680 mV, with 10 ml H<sub>2</sub>O<sub>2</sub>, pH 1.5 and 2.3,  $v=10 \text{ mV s}^{-1}$

Main difference of both pH is the amount of metallic compound on the surface, resulting in higher peaks for pH 2.3 and different resolution of the peaks. Reason for this is the suppressed initial evolution of hydrogen as a side reaction during electrodeposition at higher pH. The activity of H<sup>+</sup> ions appear to play a major role for the presence of different phases, indicating improved formation of Ni and Co with increasing pH.

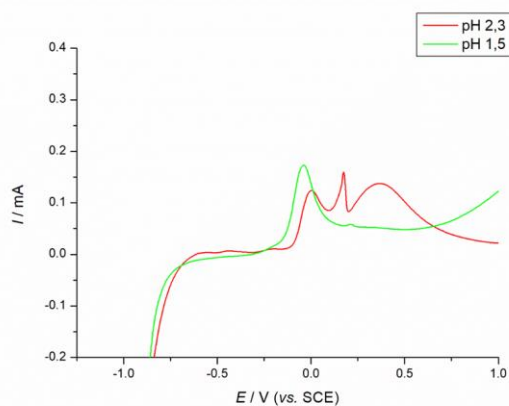


**Figure 4.** Comparison LSV, potential of -900 mV, with 10 ml H<sub>2</sub>O<sub>2</sub>, pH 1.5 and 2.3,  $v=10 \text{ mV s}^{-1}$

When the solutions treated with H<sub>2</sub>O<sub>2</sub> at different pH (1.5 and 2.3), but at higher deposition potential of -900 mV, a complex variation of anodic peaks is observed. The comparing curves are shown in Figure 4. The major peak is present around 0 V for both curves, indicating the same phase is present at both pH. The anodic peaks of 0.2 V and 0.4 V for the solution of pH 2.3 indicate the presence of a more complex deposition at the electrode. Especially the anodic peak at 0.4 V shows the presence of Fe at the electrode surface, since it is unique for all LSV curves for the investigated H<sub>2</sub>O<sub>2</sub> treated solutions. The higher pH of 2.3 enhance the formation of iron during electrodeposition. At lower pH of 1.5, the formation of iron is hindered by hydrogen evolution.

### 3.2 Chronoamperometry

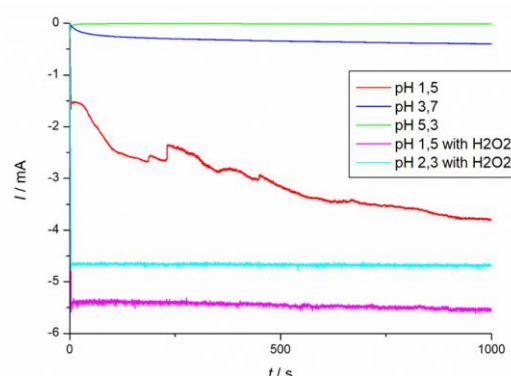


**Figure 5.** CA diagram registered during electrodeposition of different leachates, with and without H<sub>2</sub>O<sub>2</sub>, potential of -900 mV, N<sub>2</sub> saturated, 1000 rpm.

CA curves for the leaching solutions at different pH, with and without addition of H<sub>2</sub>O<sub>2</sub> are presented in Fig.5. It can be seen that with pH increasing, the currents are lower and more stable, indicating metal deposition on the surface of the working electrode competing with HER that dominates at lower pH of 1.5. On the other hand, LSV curves show only minor peaks for low pH values due to onset of HER.

### 4. CONCLUSION

It is demonstrated that selective removal of undesired metal ions from a PLS of lateritic ore can be achieved. Nevertheless, the precipitation behavior in the lateritic ore system deviates from the Pourbaix diagrams of the particular metals. Further studies should be conducted using measurements of redox potential to gain more parameters of this complex system, such as PLS.

### References

- [1] Deetman, S.; Pauliuk, S.; van Vuuren, D. P.; van der Voet, E.; Tukker, A.: Scenarios for demand growth of metals in electricity generation technologies, cars, and electronic appliances, *Environmental science & technology* 52 (2018), no. 8, pp 4950–4959
- [2] Davis, J. R. (ed.): *Nickel, cobalt, and their alloys*, 1. ed., Materials Park, Ohio: ASM International, 2000. (ASM specialty handbook)
- [3] Slack, J. F.; Kimball, B. E.; Shedd, K. B.; Schulz, K. J.; DeYoung, J. H.; Seal, R. R.; Bradley, D. C.: *Critical Mineral Resources of the United States—Economic and Environmental Geology and Prospects for Future Supply*, 2017.

This research has been financially supported by the Ministry of Science, Technological Development and Innovation of Republic of Serbia (Contract No: 451-03-66/2024-03/200026).

This research is the result of the CAPTAIN project funded by the Science Fund of the Republic of Serbia, grant No.6463002.



## INFLUENCE OF PROCESS PARAMETERS IN ADDITIVE MANUFACTURING ON THE QUALITY OF PRODUCED METAL PARTS

MAJA MLADENOVIĆ

Independent researcher, Belgrade, [mmaja011@gmail.com](mailto:mmaja011@gmail.com)

JOVANA MANDIĆ

Military Technical Institute, Belgrade, [jmandic96@gmail.com](mailto:jmandic96@gmail.com)

ALEKSANDAR ČITIĆ

Military Technical Institute, Belgrade, [woteusrb@gmail.com](mailto:woteusrb@gmail.com)

VESNA PEJOVIĆ

Military Technical Institute, Belgrade, [vesna3393@gmail.com](mailto:vesna3393@gmail.com)

ALEKSA GRUBIĆ

Military Technical Institute, Belgrade, [aleksa.grubic@mod.gov.rs](mailto:aleksa.grubic@mod.gov.rs)

SRĐAN ŽIVKOVIĆ

Military Technical Institute, Belgrade, [srdjan.zivkovic@mod.gov.rs](mailto:srdjan.zivkovic@mod.gov.rs)

**Abstract:** The paper presents the results of investigating the influence of different additive manufacturing parameters on the microstructural and mechanical properties of the produced metal specimens. Metal specimens were obtained by additive manufacturing (AM) on the PBF-LB machine in steel quality of X2CrNiMo17-12-2 (steel 316L). Visual examination, microscopic analysis, hardness tests and tensile tests were performed. Significant porosity as well as reduced elongation of tensile specimens was observed in specimens manufactured before parameter correction. After adjusting the process parameters i.e. reducing the laser power, scanning speed and hatch spacing, no porosity was observed. Moreover, improved mechanical properties were obtained, which meet the criteria for conventionally produced steel X2CrNiMo17-12-2 as defined by the standard SRPS EN 10088-3. This shows that the material properties of AM metal parts strongly depend on process parameters. In order to ensure a high quality of AM metal parts, it is necessary to perform material characterization (structural and mechanical testing of specimens) after every parameter adjustment.

**Keywords:** powder bed fusion - laser beam, additive manufacturing process parameters, material characterization, 316L steel, porosity

### 1. INTRODUCTION

Additive manufacturing (AM) enables the creation of complex geometries that are often unattainable through traditional manufacturing methods, offering benefits such as reduced part numbers, lightweight structures, and advanced performance characteristics [1, 2]. The market for AM has grown remarkably in the last years, with projections suggesting an increase from approximately \$4 billion in 2014 to over \$23 billion by 2026 [2].

One of the most prominent AM techniques for producing metal parts is Powder Bed Fusion - Laser Beam (PBF-LB), also referred to as Laser Powder Bed Fusion (LPBF) and Selective Laser Melting (SLM). This process uses a high-power laser to melt and fuse metallic powders layer by layer, facilitating the creation of intricate and high-precision components [3, 4]. Industries such as

aerospace have already adopted PBF-LB for serial production due to its ability to produce parts with high efficiency and material conservation [1, 3].

The process parameters in PBF-LB, including but not limited to laser power, scanning speed, layer thickness, and hatch distance, have a strong influence on the quality of the final product [3, 4, 5]. The mechanical properties of parts manufactured through PBF-LB are highly influenced by these process parameters. Studies have shown that variations in parameters such as laser energy density and scanning strategies can significantly affect the porosity and hardness of the produced parts [3, 4]. For instance, Shin et al. [4] found that optimizing laser energy density is essential to minimize porosity and enhance the mechanical properties of stainless steel 316L parts.

Despite the advancements in PBF-LB, metallurgical defects such as porosity, lack of fusion, spatters and partially melted particles on the parts' surface, cracks,

balling, loss of alloying elements and residual stress remain challenges that can compromise the integrity of the manufactured parts. These defects arise due to the rapid melting and cooling cycles inherent in the PBF-LB process. [3, 4, 5].

As it was previously shown by Röttger et al. [6], the process parameters optimized and provided by different machine manufacturers can greatly vary from each other, leading to statistically significant variability in mechanical properties and the extent of metallurgical defects in the parts processed by different PBF-LB machines. Effective quality control measures, including process monitoring and thorough material quality investigation after manufacturing, are essential to mitigate these issues and ensure consistent part quality.

## 2. EXPERIMENTAL WORK

### 2.1 Material and methods

A commercially available PBF-LB machine was used to produce two identical sets of samples made of stainless steel 316L. For this, two different sets of process parameters were applied – parameter set I and parameter set II – with the respective default scanning strategies. Both parameter sets were as defined by the machine manufacturer and are proprietary information. The adjustments applied to the parameter set II in comparison to the values in the parameter set I were as following: hatch distance was reduced by ~30%, and laser power as well as scanning velocity was reduced by ~10%. Nitrogen was used as the shielding gas in both manufacturing processes, and both processes were performed using the powder from the same metal powder batch. The manufacture process in both trials was conducted as any commercial AM supplier would operate, i.e., according to the user manual instructions of the PBF-LB machine.

For parameter set I, three vertically oriented square bars were manufactured in order to investigate the tensile properties. A smaller sample was also manufactured for microstructure analysis and hardness measurement.

The manufactured parts using parameter set II was expanded in comparison to the set I parts by adding three horizontally oriented square bars to the build, in order to investigate the anisotropy of mechanical properties. A schematic of the sample orientation on the base plate is shown in Fig. 1.

Visual examination of the manufactured parts was performed after wire-cutting the bars from the base plate by naked eye and magnifying glass as well as by Leica stereo microscope equipped with DFC 245 camera, and was documented with photographs.

In order to verify compliance with the material designation of stainless steel X2CrNiMo17-12-2 / SRPS EN 10088-1 (equivalent to steel designation AISI 316L) [7], the chemical composition of the manufactured parts was analyzed by Optical Energy Spectrometer (OES) Belec Compact Port.

Hardness was measured by Brinell method (HB 2,5/187,5), according to SRPS EN ISO 6506-1 [8].

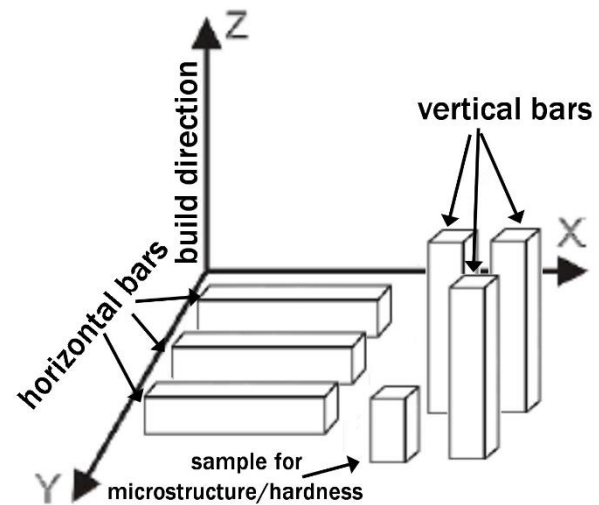


**Figure 1.** Schematic of the orientation of parts manufactured using parameter set II.

The manufactured square bars were machined to produce cylindrical tensile test specimens. Tensile tests were performed in accordance with SRPS EN ISO 6892-1 [9]. The  $L_0$  length of the short proportional cylindrical tensile specimen was 25 mm at a specimen diameter of 6 mm. The tensile test was performed using a constant speed of 5 mm/min.

In order to examine the microstructure, the appropriate samples were prepared by grinding, polishing and etching using a solution of 65% HCl and 35% HNO<sub>3</sub>. The polished and etched surfaces were examined using light microscopy. Microstructure was examined both on surfaces parallel and perpendicular to the build direction.

## 3. RESULTS

### 3.1 Visual examination

The lateral surface of the bars manufactured using the parameter set I were visibly rougher than those made applying the parameter set II. Upon looking at the lateral surfaces under the stereo microscope, it was observed that the surface of parameter set I specimens was less uniform, with zones of coarse spherical particles, Fig. 2a. Such coarse zones were not observed at parameter set II specimens, Fig. 2b.

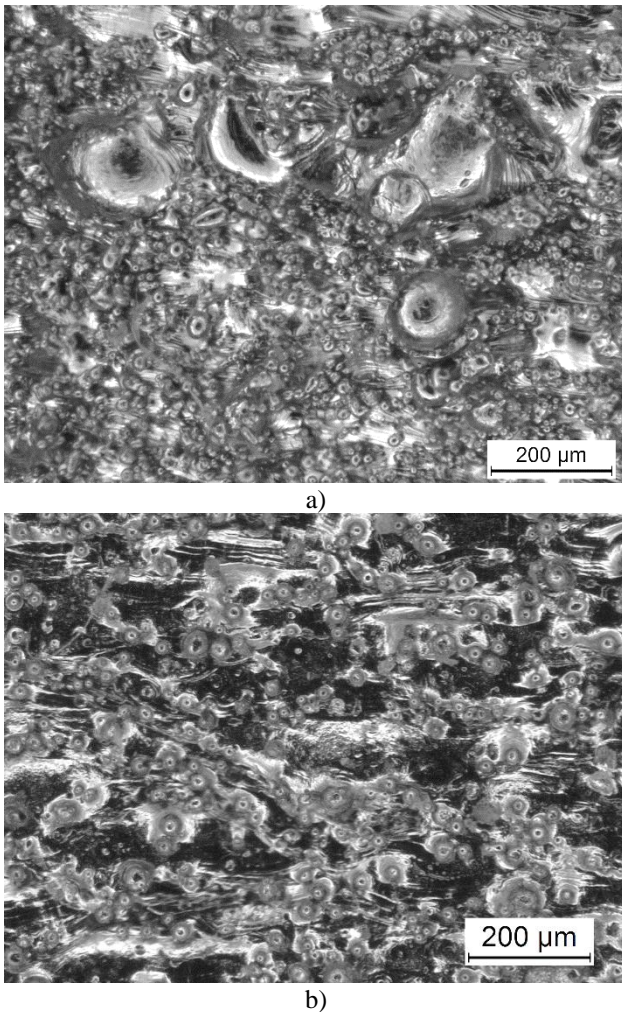


**Figure 2.** Lateral surfaces of manufactured bars using (a) parameter set I and (b) parameter set II.

### 3.2 Chemical composition

The chemical composition of the additively manufactured parts is given in Table 1.

**Table 1.** Chemical composition of the manufactured parts.

Element	Set I, mass. %	Set II, mass. %
C	0.02	0.02
Si	0.52	0.51
Mn	0.65	0.80
P	0.033	0.044
S	0.004	0.008
Cu	0.21	0.19
Cr	16.73	17.51
Mo	2.44	2.38
Ni	11.20	10.69
V	0.04	0.08
Co	0.07	0.12

Results showed that chemical composition of the additively manufactured parts is in accordance with the chemical composition of stainless steel X2CrNiMo17-12-2 as required by the standard SRPS EN 10088-1 [7].

### 3.3 Hardness

Results of hardness measurements of the manufactured samples are given in Table 2.

**Table 2.** Hardness of the manufactured samples, HB

specimen	Hardness, HB 2.5/187.5			average
set I	216	216	220	218
set II	224	221	226	224

### 3.4 Tensile properties

The average values of the modulus of elasticity (E), yield strength (YS), ultimate tensile strength (UTS) and elongation ( $A_5$ ) observed during tensile testing of specimens are shown in Table 3. Characteristic stress-strain diagrams are shown in Fig. 3. The diagrams indicate that the fracture of parameter set I specimens occurs immediately after reaching the maximum force, with almost no post-uniform elongation observed. The values of tensile properties are lower for parameter set I specimens when comparing to the specimens made using parameter set II in the same orientation.

**Table 3.** Results of tensile tests.

specimen	E [GPa]	YS [MPa]	UTS [MPa]	$A_5$ [%]
set I vert.	172	410	571	28.3
set II vert.	221	508	628	52.6
set II horiz.	247	585	694	44.4

### 3.5 Microstructure

Upon polishing the samples, pores within the material visible to the naked eye were observed on the specimens made using parameter set I, Fig. 4a. Fig. 4b-c shows the microstructure of the specimens made using parameter set I as polished. Large pores, some of which were up to 500  $\mu\text{m}$  in length were observed, as well as many smaller pores with a length up to 50  $\mu\text{m}$ . Large pores were not observed on polished samples made using parameter set II, instead a small number of fine spherical gas pores was spotted, Fig. 5a.

Fig. 4d-f and Fig. 5b-e show the microstructure of samples made using parameter set I and II, respectively, as etched. On all samples it was observed that the structure on the macro-scale consists of clear solidification tracks, Fig. 4d-e and Fig. 5b-d. On the micro-scale, a fine cellular substructure was revealed, Fig. 4f, and 5e. Instances of grains crossing solidification track boundaries are also noticeable on all analyzed samples, Fig. 4d, and 5d.

On the parameter set I samples it was observed that porosity mostly occurs between solidification tracks in the material. Crack formation starting from porosity and following the solidification track boundary between layers was also observed, Fig. 4d.

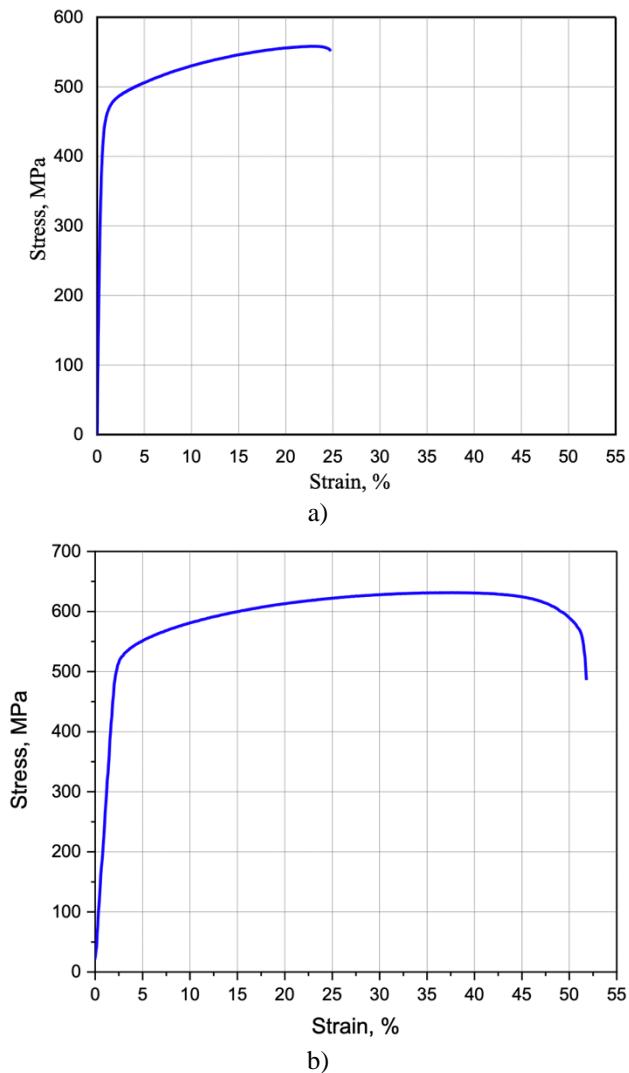


**Figure 3.** Characteristic stress-strain curves of vertical tensile specimens made using (a) parameter set I, (b) parameter set II.

#### 4. DISCUSSION

The appearance of spherical particles embedded on the lateral surfaces of the set I samples has been attributed to the balling phenomenon. The balling defect arises due to the interplay between surface tension and wettability, which significantly influence the molten melt pool's formation [3]. When individual melt tracks fail to properly coalesce with the substrate, the surface tension causes the molten material to contract into spherical shapes, leading to balling. Additionally, inadequate wetting of remaining solid particles and the underlying substrate, often due to surface impurities, exacerbates this defect. The balling defect is considered as a severe process defect in PBF-LB manufacturing, and often leads to formation of pores, high surface roughness and reduced density of manufactured parts.

Results of chemical composition analysis showed that the composition of the manufactured parts is in accordance with the chemical composition of stainless steel X2CrNiMo17-12-2 as required by the standard SRPS EN 10088-1 [7], which is equivalent to stainless steel AISI

316L. This result shows that the metal powder retained its material designation after the manufacturing processes, indicating that no significant loss of alloying elements because of possible vaporization due to extremely high temperatures right underneath the laser beam occurred.

The hardness of both examined samples is in the range typical for 316L grade steel manufactured by PBF-LB process and is comparable to the hardness specified by the standard for semi-finished products made of this material in annealed condition [10].

Tensile tests showed that the specimens made using parameter set I have poorer mechanical properties than those made using parameter set II. This difference is the highest for elongation (28.3% in comparison to 52.6% for vertical orientation). The values of mechanical properties are significantly reduced in the presence of metallurgical defects, namely pores, cracks or lack of fusion [4, 5, 6]. Therefore, the lower values of the modulus of elasticity, strength, and elongation, as well as the lack of post-uniform elongation of set I specimens, have been attributed to the extensive presence of macroscopic and microscopic defects throughout the material.

The results of the tensile testing also showed that the set II specimens prepared from vertical bars have a lower strength, modulus of elasticity and elongation than the horizontal bars specimens. It has been previously established that parts produced by layer-by-layer manufacturing can exhibit an anisotropy of mechanical properties [5]. Defects such as inclusions, oxidations, melting defects and pores are more prevalent at the interface between layers, and act as stress concentrators. In vertically built tensile specimens, these layer boundaries are perpendicular to the loading direction, which causes earlier yielding and lower strength and elongation values in comparison to horizontally built specimens. Nonetheless, it is worth noting that the mechanical properties of both vertically and horizontally oriented set II specimens meet the criteria for conventionally manufactured semi-finished products made of steel X2CrNiMo17-12-2, as defined by the standard SRPS EN 10088-3 [10].

Microstructural analysis revealed significant porosity in the parts manufactured using parameter set I. The irregular shape and large size of these defects indicates that their cause is insufficient fusion, which occurs when the liquid metal does not adequately penetrate the previously solidified layer and results in poor metallurgical bonding [3].

The solidification tracks revealed after etching represent melt pools that were generated by the scanning laser beam during manufacturing. The appearance of grains crossing melt pool boundaries can be explained by formation of new grains by epitaxial growth: the previously solidified layer experiences partial remelting during the melting of a newly coated powder layer; this in turn makes it possible that the new layer solidifies by maintaining the same crystallographic orientation of the nearby grains [5].

The observed formation of a cellular substructure in all examined samples is characteristic for PBF-LB process

and is primarily driven by rapid solidification rates and high thermal gradients. These conditions promote the development of cellular dendrites within the microstructure, characterized by fine, columnar grains.

This cellular substructure enhances the mechanical properties of the steel by refining the microstructure [3, 5, 6].

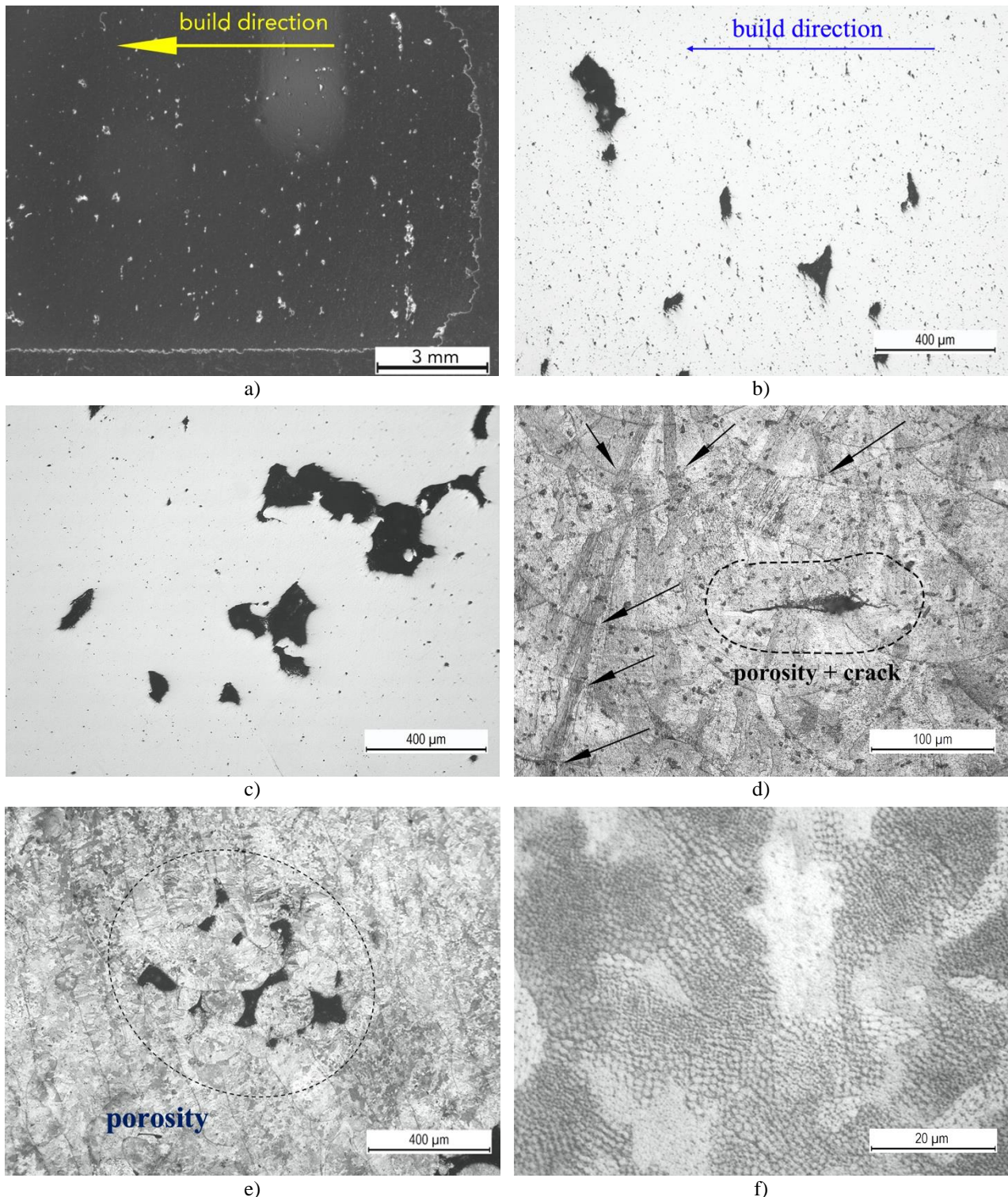


**Figure 4.** (a) Polished set I sample, as observed under stereo microscope. White areas represent macroscopic pores within the material. (b-c) Microstructure of the set I sample as polished. Observed are surfaces (b) parallel and (c) perpendicular to the build direction. Large and small pores are visible as dark spots. (d-f) Microstructure of the set I samples as etched. Observed are surfaces (d) parallel and (e) perpendicular to the build direction. Epitaxial grain growth is marked with arrows. (f) Cellular substructure revealed at higher magnifications.



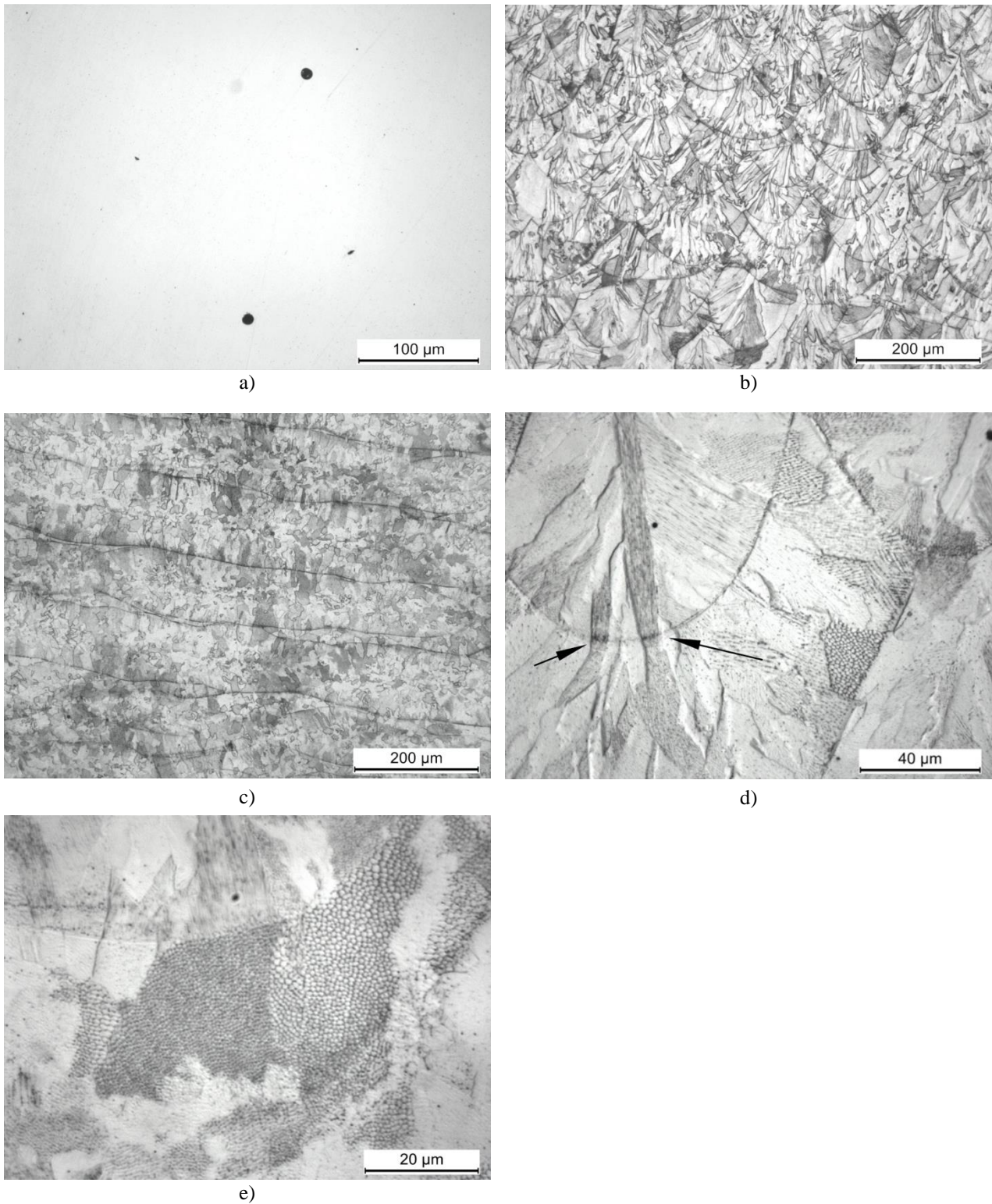


**Figure 5.** (a) Microstructure of the set II samples as polished, observed on a surface parallel to the build direction. The dark spots represent small gas pores. (b-e) Microstructure of the set II samples as etched. Observed are surfaces (b, d, e) parallel and (c) perpendicular to the build direction. Epitaxial grain growth is marked with arrows. (e) Cellular substructure revealed at higher magnifications.

It was observed that the porosity in set I samples mostly occurs between solidification track layers, which as discussed previously is intrinsic to the layer-by-layer manufacturing process. In the set II samples, no insufficient fusion defects and only a very small amount of gas pores were detected, and their presence is considered to not have a significant impact on the material quality.

## 5. CONCLUSION

This study highlights the significant impact of process parameters on the quality of stainless steel X2CrNiMo17-12-2 (AISI 316L) parts fabricated using Powder Bed Fusion – Laser Beam (PBF-LB). Key findings include:

1. The balling defect, considered a severe defect in the PBF-LB process, is observed in samples produced using parameter set I. This defect contributes to high surface roughness and possibly to porosity.
2. Chemical composition analysis confirmed the retention of alloying elements in the manufactured parts, ensuring compliance with the required material designation of stainless steel X2CrNiMo17-12-2.
3. Samples made using parameter set I exhibited poorer mechanical properties, particularly elongation, compared to those made using parameter set II. This reduction is due to the presence of metallurgical defects such as pores, cracks, and lack of fusion defects.
4. Anisotropy of mechanical properties was observed, with vertically built specimens showing lower strength, modulus of elasticity, and elongation than horizontally built specimens.
5. Significant porosity due to insufficient fusion was found in parts manufactured with parameter set I, while set II samples showed minimal defects, indicating better overall quality.

In conclusion, parameter set II demonstrated a significant improvement in mechanical properties and reduced defect prevalence compared to set I. It was shown that additive manufacturing of metal components using process parameters provided by the machine manufacturer does not guarantee defect-free parts. Material characterization (including microstructural examination and mechanical testing of specimens) must be conducted after setting up the AM machine and after each parameter optimization in order to ensure high-quality AM metal parts. Optimizing PBF-LB process parameters is crucial for minimizing defects, ensuring material integrity, and achieving desired mechanical properties in metal components. Future research should focus on further refining these parameters and exploring advanced post-processing techniques to

enhance the performance and reliability of PBF-LB-manufactured parts.

## References

- [1] J. Reijonen, R. Björkstrand, T. Riipinen, Z. Que, S. Metsä-Kortelainen and M. Salmi, "Cross-testing laser powder bed fusion production machines and powders: Variability in mechanical properties of heat-treated 316L stainless steel," *Materials & Design*, vol. 204, 2021.
- [2] S. Malbašić, S. Živković, B. Nedić, A. Đorđević and A. Grubić, "Process Planning and Optimization Techniques in Additive Manufacturing," *Scientific Technical Review*, vol. 73, no. 2, pp. 33-41, 2023.
- [3] S. R. Narasimharaju, W. Zeng, T. L. See, Z. Zhu, P. Scott, X. Jiang and S. Lou, "A comprehensive review on laser powder bed fusion of steels: Processing, microstructure, defects and control methods, mechanical properties, current challenges and future trends," *Journal of Manufacturing Processes*, vol. 75, pp. 375-414, 2022.
- [4] W.-S. Shin, B. Son, W. Song, H. Sohn, H. Jang, Y.-J. Kim and C. Park, "Heat treatment effect on the microstructure, mechanical properties, and wear behaviors of stainless steel 316L prepared via selective laser melting," *Materials Science & Engineering A*, vol. 806, 2021.
- [5] R. Casati, J. Lemke and M. Vedani, "Microstructure and Fracture Behavior of 316L Austenitic Stainless Steel Produced by Selective Laser Melting," *Journal of Materials Science & Technology*, vol. 32, pp. 738-744, 2016.
- [6] A. Röttger, J. Boes, W. Theisen, M. Thiele, C. Esen, A. Edelmann and R. Hellmann, "Microstructure and mechanical properties of 316L austenitic stainless steel processed by different SLM devices," *The International Journal of Advanced Manufacturing Technology*, vol. 108, pp. 769-783, 2020.
- [7] *SRPS EN 10088-1 – Stainless steels – Part 1: List of stainless steels.*
- [8] *SRPS EN ISO 6506-1 – Metallic Materials – Brinell Hardness Test – Part 1: Test Method.*
- [9] *SRPS EN ISO 6892-1 – Metallic Materials – Tensile Testing – Part 1: Method of Test at Room Temperature.*
- [10] *SRPS EN 10088-3 – Stainless steels – Part 3: Technical delivery conditions for semi-finished products, bars, rods, wire, sections and bright products of corrosion resisting steels for general purposes.*

## Acknowledgement

This work was supported by the Ministry of Science, Technological Development and Innovations (Serbia), Contract No. 451-03-66/2024-03/200325.



## FAILURE ANALYSIS OF WELDED JOINT BETWEEN ROCKET MOTOR CASE AND FINS

ALEKSANDAR ČITIĆ

Military Technical Institute, Belgrade, [woteusrb@gmail.com](mailto:woteusrb@gmail.com)

NADA ILIĆ

Military Technical Institute, Belgrade

MAJA MLADENOVIĆ

Military Technical Institute, Belgrade

VESNA PEJOVIĆ

Military Technical Institute, Belgrade

**Abstract:** In this paper a fractured welded joint between rocket motor case and fins was examined. The goal of this study was to determine the cause of fracture which occurred during high pressure probe. Specimens taken from the fractured surface were examined using scanning electron microscope. In order to determine material properties and welded joint quality, chemical analysis, microstructural examination, and microhardness measurements were performed. Macroscopic examination showed that initialization of fracture was on outer surface of the case. Observations of fracture surface using SEM revealed mixed mode of failure, lamellar cleavage, and ductile rupture, without visible plastic deformation. Spherical particles based on Fe and O were also seen on fracture surface. Microhardness measurements showed high difference in microhardness value between base material and heat affected zone (HAZ). Detailed analysis showed that inadequate preparation and welding procedure resulted with unsatisfactory microhardness distribution which led to fracture.

**Keywords:** welded joint, fracture, microhardness

### 1. INTRODUCTION

Welding is a technological process of joining two or more metal pieces using heat or pressure. Currently, welding is fast replacing other joining processes and is extensively used for fabrication of many differently components and structures such as missile and rocket parts, ships, bridge structures, pressure vessels, storage tanks etc. Since there is heat input during welding, consequently there are changes in metals microstructure around weld joint. This nonuniform microstructure across welded joint leads to nonuniform mechanical characteristics that can affect joint behavior during exploitation. Welding can also introduce defects in material such as pores, slag inclusions, etc. which all have negative effects on quality of welded joint. Failures of welded joint can have profound consequences on the safety of people and can produce financial losses. Thus, finding the cause of failure can help in avoiding such scenarios in futures and lead to improving welding practices (1-2).

Research presented in this paper deals with a failure of welded joint between rocket case motor and fins, which failed during high pressure probe.

### 2. EXPERIMENTAL PROCEDURE

The chemical composition of base material of rocket case meets the requirements for 42CrMo4 steel according to standard SRPS EN 10083-3 (3). The chemical composition of rocket case material is presented in table 1. Samples for microstructural analysis were prepared using standardized preparation process, wet grinding up to P1200 grinding paper and fine polishing up to 1µm diamond paste. After etching with 3% Nital solution, samples were observed under Leica optical microscope. Microhardness was measured by Vickers method (HV1) and is performed on samples taken from the fractured and non-fractured regions. Leica stereo microscope was used to observe the major features of the fracture surface and was documented by photographs. Scanning electron microscope (JEOL 6010LV) was used to detect the fracture morphology while energy dispersive spectrometer (Oxford instrument X-Max) was used for elemental analysis of fracture. It should be noted that EDS is semi-quantitative analysis. Heat treatment of sample taken from welded joint was performed in laboratory Heraeus furnace on 500°C for 45 minutes after which sample were cooled on still air to room temperature. Used welding technique, welding parameters and filler material are not known.

**Table 1.** Chemical composition of rocket case material

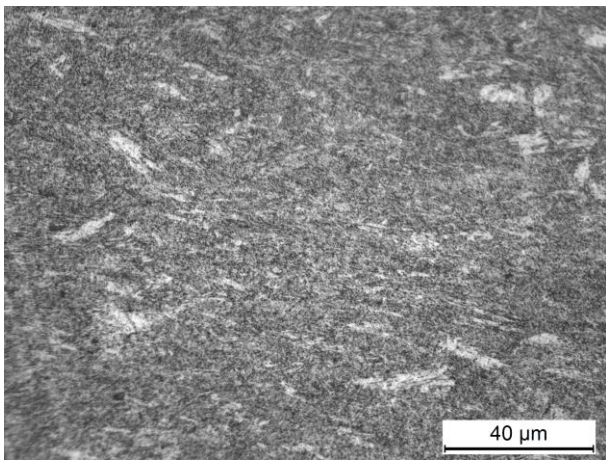
Element	Rocket case material mass%.	Standard requirements
C	0,43	0,38-0,45
Si	0,27	max 0,40
Mn	0,76	0,60-0,90
Cr	1,1	0,90-1,20
Mo	0,18	0,15-0,30
P	0,011	max 0,025
S	0,014	max 0,035
Fe	Balance	Balance

### 3. RESULTS

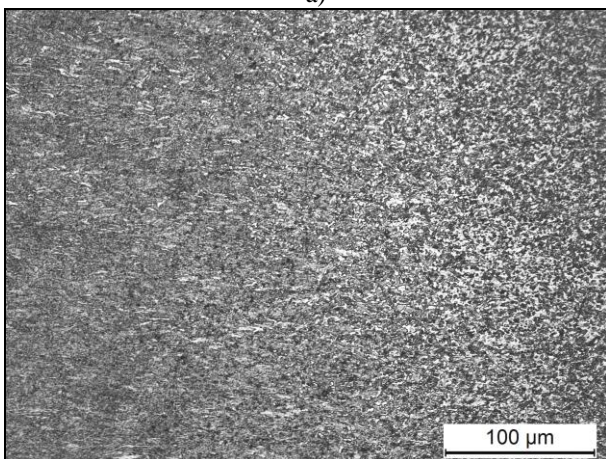
#### 3.1. Microstructure analysis

Microstructure analysis was performed on the sample taken near the fracture initiation site. Microstructure of sample is shown on figure 1.

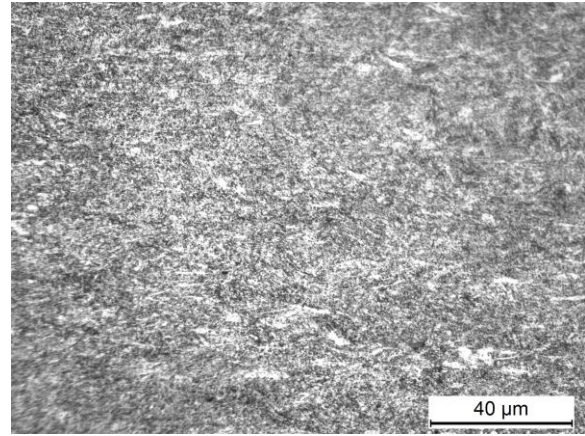
HAZ microstructure, consists of martensite. Microstructure of base material of motor case is fine grained tempered martensite.



a)



b)



c)

**Figure 1.** Microstructure of a) HAZ near fracture initiation site, b) at HAZ/BM border and c) base material of rocket case

#### 3.2. Microhardness measurements

Microhardness measurements were performed on the sample taken from the fractured welded joint.

In table 2 are shown values of microhardness measured on sample taken from fractured welded joint, while figure 2 presents microhardness distribution diagram.

**Table 2.** Microhardness values of sample 1, taken from fractured welded joint.

Sample 1	HV1	Mean
HAZ	692; 675	684
HAZ/BM	564; 581; 572	572
BM	312; 339; 340; 357; 348; 355; 371; 358; 351; 332; 356	367

BM-base material of rocket case; HAZ-heat affected zone.

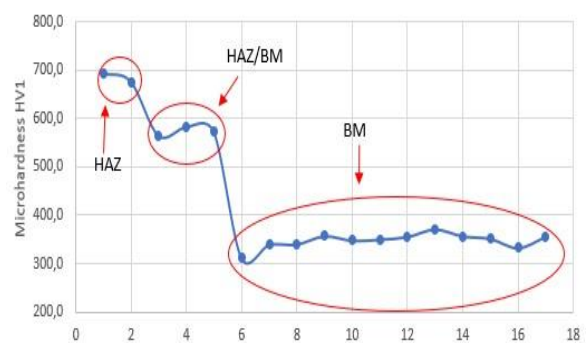


**Figure 2.** Microhardness distribution diagram of sample 1, taken from fractured surface.

From the results presented in table 2, there is significant difference in microhardness values between heat affected zone (HAZ) and base material (BM) of rocket case, more than 300HV1.

To try to reduce difference in microhardness between HAZ and BM, heat treatment of welded joint was performed on 500°C for 45 minutes. Heat treatment was performed on sample taken from the non-fractured welded joint.

Measured microhardness values after heat treatment are shown in table 3, and microhardness distribution diagram is shown on figure 3.

Based on measured values of microhardness, it is clear that heat treatment reduced difference in microhardness between HAZ and BM of rocket case motor, from more than 300HV1 to around 70HV1.

**Table 3.** Microhardness values of welded joint, after heat treatment

Sample 2	HV1	Mean
BM 1	309; 311; 302; 303	306
HAZ 1	363; 378; 377	373
FL1	346	346
WM	353; 354; 346; 340; 335; 345; 344	345
FL 2	302	302
HAZ 2	237; 259; 289	262
BM 2	241; 241; 248; 247	244

BM1-base material of rocket case; HAZ-heat affected zone; FL-fusion line; WM-weld metal; BM2-base material of fins holder.

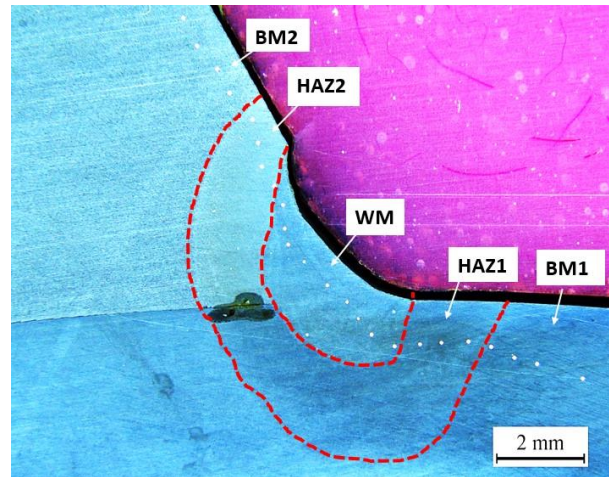
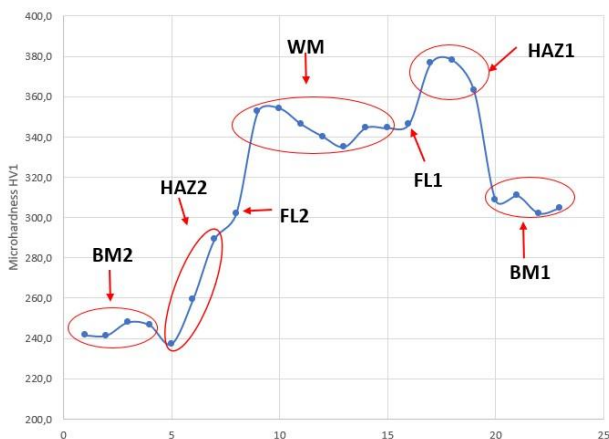


**Figure 3.** Microhardness distribution diagram of welded joint, after heat treatment.

### 3.3. Macroscopic and fractographic analysis

On figure 4 is shown picture of fractured rocket case, as well as position of samples taken for microstructure analysis (Sample 1) and hardness measurements (Sample 1 and 2), while on figure 5 is shown fractured surface.

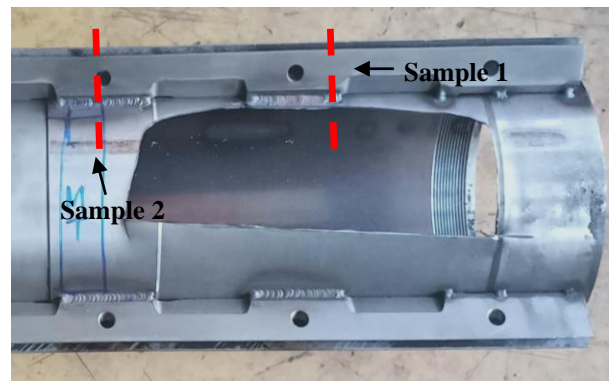


**Figure 4.** Part of rocket case with fractured surface.

Fracture initiation site (FIS) is on the outer surface of the rocket case, and no visible deformation was observed. However, arrow like pattern on fracture surface was observed which can provide insight on how crack propagated through material.

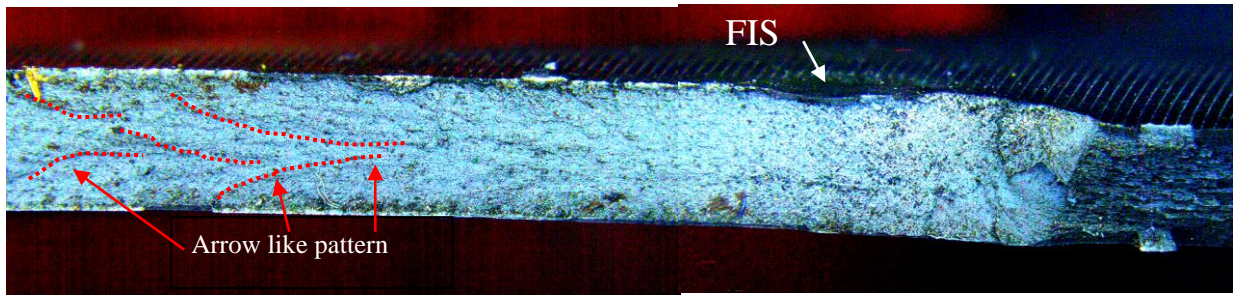


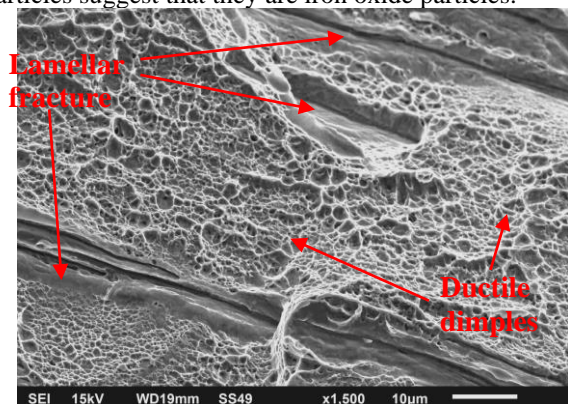
**Figure 5.** Macroscopic morphology of fractured surface with fracture initiation site (FIS)

To determine micromechanism of fracture, fractured surface was analyzed in more details with scanning electron microscope. SEM analysis showed two types of fracture, figure 6a:

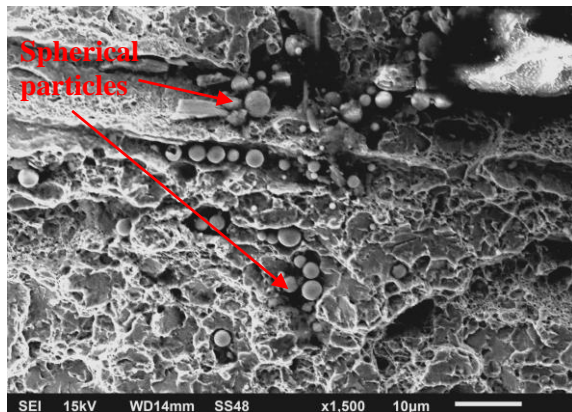
- Ductile fracture, with shallow and polygonal ductile dimples and
- Lamellar fracture in heat affected zone (HAZ) which is caused by stresses normal to surface of rocket case.

SEM investigation also showed high number of globular particles present in root of welded joint, figure 6b.

Semiquantitative EDS analysis, figure 7, of spherical particles showed that they contain iron, oxygen, and carbon. High concentration of iron and oxygen in these particles suggest that they are iron oxide particles.



a)



b)

**Figure 6.** a) Characteristic morphology of fractured surface, b) Spherical particles at root of welded joint

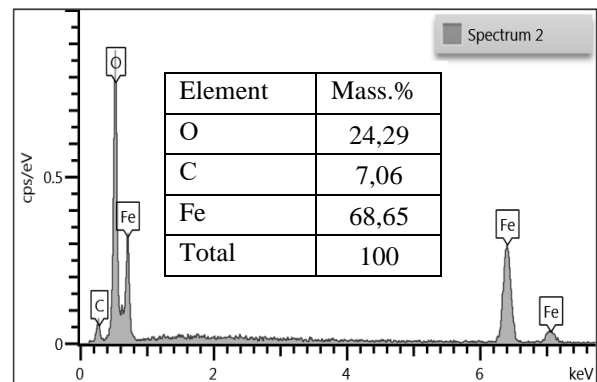
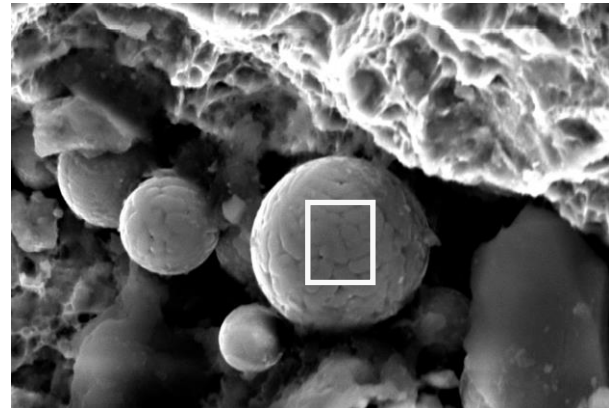


**Figure 7.** EDS analysis of spherical particles.

#### 4. DISCUSSION

The chemical composition of the base material of the chamber corresponds to the chemical composition of steel 42CrMo4 according to SRPS EN 10083-3 (3).

A macroscopic examination of the fracture showed that the initiation site of fracture is on the outer wall of the chamber, in the zone of the welded joint. The crack, in the initial phase of growth, extended at an angle of  $45^\circ$  to the outer surface of the rocket case. At a further stage of propagation, the crack changes direction and extends at an angle of  $90^\circ$  to the outer surface of the rocket case. No deformation of the material was observed in the vicinity of the fracture. On the fracture surface, arrow-shaped patterns were observed, which indicate the place of fracture and the direction of spread of the crack.

Fractographic examination of the fracture surface on the SEM revealed two fracture mechanisms: lamellar

cleavage, i.e., stratification of the material in the direction of the thickness of the rocket case wall as well as ductile fracture with shallow low-energy pits. In the root of the welded joint, spherical inclusions based on iron and oxygen are seen. These inclusions were seen along the entire length of the root pass. Fact that these particles were found only in the root of welded joint suggest that welding process during root pass was not properly performed, aka weld metal was not shielded good enough. Nonproper shielding led to absorption of oxygen from atmosphere and formation of oxide particles.

By measuring the microhardness of the welded joint at the point of fracture and outside the fracture site, it was determined that there is a difference between the hardness of the base metal and the heat affected zone and amounts to  $\approx 300$  HV1. A major difference in microhardness is undesirable because it contributes to the brittleness of the welded joint. Such significant difference in microhardness can be attributed to observed microstructure. Microstructure in HAZ is martensite which have high hardness values. The microstructure of the base metal is fine grained tempered martensite.

Due to the enormous difference in hardness between the base metal and the heat affected zone, heat treatment of the sample was performed. Heat treatment resulted in a reduction in the difference in microhardness values to  $\approx 70$  HV1. This is attributed to decrease in residual stresses in the welded area (5).

Based on obtained results, the cause of failure of welded joint can be attributed to microstructural and microhardness variations across welded joint. Furthermore, observed oxide spherical particles in root pass indicate apparent lack of proper standard welding process.

Overall, the failure of welded joint can be attributed to all the after mentioned causes. The formation of martensite microstructure, which have high hardness, is dependent on the heat input during welding. At lower heat inputs, due to faster cooling, the formation of martensite is more expected. On the other hand, in high heat input conditions (lower cooling rates) the formation of martensite becomes less preferred, instead polygonal and ferrite structures become more dominant. Therefore, controlling the welding temperature as well as cooling rates can significantly affect the formation of different microstructures (6).

#### 4. CONCLUSIONS

This study investigates failure of welded joint between

rocket case and fins holder. Key findings include:

1. Fractographic investigation revealed mixed mode of fracture: ductile and lamellar fracture,
2. High number of oxide-based particles is seen in root pass indicating lack of proper welding procedure,
3. Microhardness distribution across welded joint showed significant difference between HAZ and BM ( $\approx 300$  HV1) which increases brittleness of welded joint,
4. Applied heat treatment reduced difference in microhardness values between HAZ and BM,
5. Microstructure of HAZ is martensite, which is in direct correlation with heat input during welding.

#### Acknowledgement

This work was supported by the Ministry of Science, Technological Development and Innovations (Serbia), Contract No. 451-03-66/2024-03/200325.

#### References

- [1] G. Vukelic, G. Vizentin, R Bakhtiari, Failure analysis of a steel pressure vessel with a composite wrap repair proposal, *International journal of pressure vessels and piping*, 193 (2021) 104476
- [2] R. Sehgal, S Angra, V. Sharma, Failure cause analysis of welded joints, *Indian journal of engineering and material sciences*, 14 (2007) 24-30
- [3] SRPS EN 10083-3 – Steels for quenching and tempering – Part 3: Technical delivery conditions for alloy steels
- [4] SRPS EN ISO 6507-1 – Metallic materials – Vickers hardness test – Part 1: Test method
- [5] A.S. Aloraier, S. Joshi, J.W.H. Price, K. Alawadhi, Material properties characterization of low carbon steel using TBW and PWHT techniques in smooth-contoured and U-shaped geometries, *International journal of pressure vessels and piping*, 111-112 (2013) 269-278
- [6] M. Taghipour, A. Bahrami, H Mohammadi, V Esmaeili, Root cause analysis of a failure in a flange-pipe welded joint in a steam line in an ammonia plant: Experimental investigation and simulation assessment, *Engineering Failure Analysis*, 192 (2021) 105730



## EFFECTS OF DIFFERENT SURFACE PREPARATIONS ON BONDING PROPERTIES OF ALUMINIUM ALLOY EN AW-5754

NATAŠA ZDRAVKOVIĆ

Faculty of Mechanical Engineering, University of Niš, Niš, Serbia, [natasa.zdravkovic@masfak.ni.ac.rs](mailto:natasa.zdravkovic@masfak.ni.ac.rs)

DAMJAN KLOBČAR

Faculty of Mechanical Engineering, University of Ljubljana, Ljubljana, Slovenia, [damjan.klobcar@fs.uni-lj.si](mailto:damjan.klobcar@fs.uni-lj.si)

DRAGAN MILČIĆ

Faculty of Mechanical Engineering, University of Niš, Niš, Serbia, [dragan.milcic@masfak.ni.ac.rs](mailto:dragan.milcic@masfak.ni.ac.rs)

MIODRAG MILČIĆ

Faculty of Mechanical Engineering, University of Niš, Niš, Serbia, [miodrag.milcic@masfak.ni.ac.rs](mailto:miodrag.milcic@masfak.ni.ac.rs)

VUKAŠIN PAVLOVIĆ

Faculty of Mechanical Engineering, University of Niš, Niš, Serbia, [vukasin.pavlovic@masfak.ni.ac.rs](mailto:vukasin.pavlovic@masfak.ni.ac.rs)

ALEKSIJA ĐURIĆ

Faculty of Mechanical Engineering, University of East Sarajevo, East Sarajevo, Bosnia and Herzegovina;  
[aleksija.djuric@ues.rs.ba](mailto:aleksija.djuric@ues.rs.ba)

**Abstract:** Adhesive bonding is a well-established technique for joining materials. This article deals with the challenges of bonding metals, such as aluminium alloy EN AW-5754. To improve the strength of bonded joints, suitable surface preparation prior to bonding is essential. In this work, the surface of the aluminium alloy using three different epoxy adhesives was subjected to two different methods of surface preparation, such as laser cleaning and sanding by hand with sandpaper. The adhesion properties of the bonded surface were determined by measuring the surface roughness parameters ( $R_a$  and  $R_z$ ) for different surface preparations as well as the mechanical property (tensile lap-shear strength). It was found that the bond strength of the aluminium alloy changed depending on the surface preparation and adhesive used, indicating that using the same adhesive and material with different preparation methods can lead to significant variations in bond strength. Therefore, choosing an appropriate surface preparation method that is suitable for the parts to be bonded and their surface roughness is crucial as it increases the strength of the bonded joints.

**Keywords:** adhesive bonding; surface preparation; aluminium alloy EN AW-5754; epoxy adhesives.

### 1. INTRODUCTION

Bonding aluminium alloy materials is a contemporary method of joining, increasingly favored for its numerous advantages over welded, riveted, and bolted connections. These benefits include reduced stress concentration, lighter weight, and simpler manufacturing processes [1,2]. The strength of a bonded joint is influenced by many technical and mechanical factors [3,4]. These include the environmental conditions, the design of the joint, the type of adhesive, the type of load applied to the joint and the methods of surface preparation prior to bonding [4,5]. Proper surface preparation prior to bonding is of great importance and should result in adequate adhesion or bond strength between the adhesive and the bonding surfaces. All impurities must be removed from the bonding surfaces to eliminate contamination or weak interfaces, but also to improve the strength of the bonded joints [6,7]. This is achieved by a variety of chemical,

mechanical and other preparation methods.

In terms of surface preparation to achieve better bonding properties, a number of researchers [8-10] have suggested using mechanical removal methods prior to bonding to remove contaminants and create geometric patterns on the bonding surfaces. Arenas [11], Mirski [3] and da Silva et al. [12] investigated the surface preparation of aluminium alloys for bonding. It was found that sanding as a surface preparation plays an important role in bonding, since increasing the surface roughness of the bonding surfaces improves the surface contact between the adhesive and the bonding surface, allowing proper functionality of the joints with high strength of the bond under shear conditions. Sanding preparation with sandpaper of different grits is widely used and is of greater importance in production as it is incredibly cost-effective, requires less training time and costs less than other preparations.

Another surface preparation that is fast becoming increasingly important to improve surface roughness and



therefore the strength of bonded joints is laser surface preparation. Many recent scientific studies have focused on understanding the nature of bonded joints formed after laser treatment of aluminium materials. Feng et al. [13] used the laser for texturing and to create surface patterns with improved bond performance and aging resistance. Rechner et al. [14] pointed out increased bond strength and durability after laser ablation and how the laser treatment improved surface cleaning while altering the oxide layer. Mandolino et al. [15] analyzed laser cleaning at different power ratios and pulse frequencies and obtained the best results: up to twice the reference, where surface preparation was only cleaned with acetone. It is evident that laser surface preparation provides a combination of increased surface area, mechanical interlocking and a change in surface chemistry, all at once. However, to the author's knowledge, the effect of laser cleaning on the strength of bonded joints and the properties of the aluminium alloy EN AW-5754 is still insufficiently researched.

Research on the impact of surface preparation on the mechanical properties of bonded joints was conducted using the aluminium alloy EN AW 5754, chosen for its extensive use in various industries, including automotive body and frame manufacturing, railways, shipbuilding, aviation, transport tank production, and the food industry.

The role of surface preparation on bond strength has not yet been thoroughly investigated in the literature, although it has a major influence on the properties of adhesive joints. The comparison of the maximum strength of joints made of EN AW-5754 aluminium alloy prepared with P180 sandpaper and laser cleaning has hardly been considered so far, although both preparations have been shown to give good results. The present study focused on investigating the effect of different surface preparation methods on the formation of strong aluminium bonded joints, which were evaluated using the single-lap shear test with three different epoxy adhesives. The effects of surface roughness and failure mode on the experimental shear strength properties of two different surface preparations were investigated.

## 2. EXPERIMENTAL WORK

Aluminium alloy EN AW-5754 was used for this investigation. It is suitable for a wide range of industrial applications due to its favourable strength-to-weight ratio, excellent ductility and machinability, and remarkable resistance to corrosion and thermal effects. The chemical composition of the aluminium alloy EN AW-5754 is presented in Table 1 and its mechanical properties are given in Table 2 [16].

**Table 1.** Chemical composition of EN AW-5754 (weight %)

Si	Fe	Cu	Mn	Mg	Cr	Zn	Ti
0.26	0.26	0.04	0.25	2.81	0.04	0.03	0.01

**Table 2.** Mechanical properties of EN AW-5754

Yield Strength (MPa)	Tensile Strength (MPa)	Elongation to Break (%)	Module of Elasticity (GPa)
180	236	16.5	70

The specimens are prepared as 2.0 mm-thick sheets, cut into pieces 100 mm × 25 mm by waterjet, according to the EN 1465 standard [17]. The specimens are used to produce joints with an overlap of 12.5 mm, bonded with adhesive, and then subjected to static shear tests. The standard mould was used to ensure correct placement and overlap during bonding. The adhesive layer thickness was maintained at 0.3 mm using glass beads embedded in the selected adhesives. The geometry of the mould and the dimensions of the test specimens are shown in Figure 1.

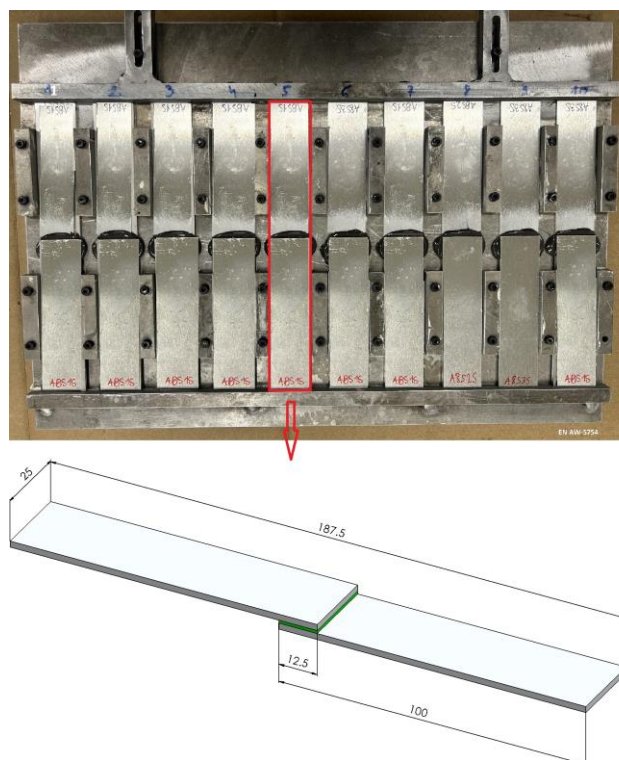


**Figure 1.** Mould for bonding and dimensions of the test specimens for the single lap-shear test [17]

To conduct a comparative study on the effects of different surface preparations on the bonding properties of aluminium joints, two surface preparation methods were used:

**Mechanical abrasion:** Each specimen was cleaned with SIKA Remover-208, a solvent-based cleaning agent for heavily soiled, which is used to clean and degrease the surface before bonding. The bonded surface was sand uniformly by hand with 180-grit sandpaper for approximately 30 seconds in one axial direction at medium pressure, followed by cleaning with SIKA Remover-208 before bonding.

**Laser cleaning:** The surface was cleaned with a Jetlaser M100 laser without prior preparation. The pulse energy was set to 1.25 mJ, the pulse overlapped to 8%, and the power to 45 W. The laser beam's energy is highly

powerful and focussed, which allows for the formation of microscopic shells or grooved structures on the material in the processing zone.

Three types of epoxy adhesives were selected for this study, namely, the two-component (2C) acrylic/epoxy hybrid adhesive SikaFast®-580 [18], epoxy adhesive SikaPower®-880 (2C) [19] and epoxy hybrid adhesive SikaPower®-492 G a one-component (1C) [20]. The epoxy adhesive was applied to the cleaned surfaces and then cured in a drying and heating chamber (ED 56 Binder GmbH). Selected mechanical properties of the adhesives are described in Table 3. After the curing period was complete, the joints were taken out of the chamber. The dimensions of the bonded joints were checked with a digital caliper and the strength of the bonded joints was tested.

**Table 3.** Mechanical properties of the adhesives [18-20]

Adhesive	SikaFast®-580	SikaPower®-880	SikaPower®-492G
Tensile strength (MPa)	12	22	29
Elongation at break (%)	15	3.3	8
Module of elasticity (MPa)	900	2220	2190
Viscosity (Pa·s)	150	100	230

The adhesion was determined by the tensile lap-shear test according to the ISO 4587 standard [21]. The lap shear tests of the lap joints were performed at room temperature using an INSTRON 8802 250 kN testing machine under displacement control at a test speed of 1 mm/min.

The selection of surface preparation and adhesive bonding properties should ensure that the weakest point in a bonded joint occurs within the adhesive layer, rather than at the interface of the parts being bonded. Cohesion failure is the ideal failure mode to accurately demonstrate the performance of bonded joints. The basic failure modes are shown in Figure 2 [22].

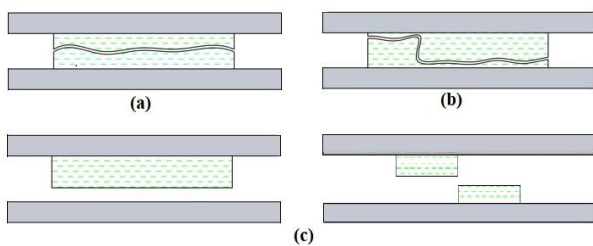


**Figure 2.** Failure modes of adhesive bonded joints (a) Cohesion Failure (CF); (b) Special Cohesion Failure (SCF); (c) Adhesion Failure (AF) [22]

After the tension lap-shear test, the fracture surfaces were analyzed. The specimens were photographed with a high-resolution digital camera and processed with ImageJ image processing software 1.8.0. (NIH, Bethesda, USA) (Figure 3).

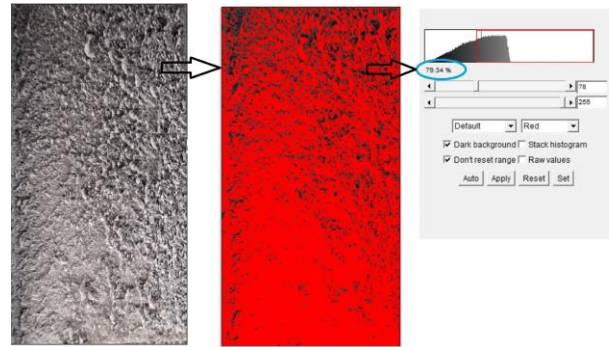


**Figure 3.** The method for deriving fracture mode percentages. (a) Photograph of the examined fracture surface. (b) Processing of the photo with ImageJ software. (c) Color scale-based determination of the failure mode percentage.

In the example of the fracture surface in Figure 3, the areas of the fracture surface that have a thick layer of adhesive on the fracture surface are colored red. This percentage corresponds to 79.34% in the example in Figure 3 - b, as shown in Figure 3 - c. Based on this simple procedure, the percentages of the failure modes were derived and are shown for all specimens.

### 3. RESULTS AND DISCUSSION

The surface roughness of the samples prepared with P180 sandpaper and with laser was measured at three points (central, edge and random) for each sample. The measurement results of two surface roughness parameters, Ra and Rz, in relation to the different surface preparations are shown in Figure 4 (a,b).

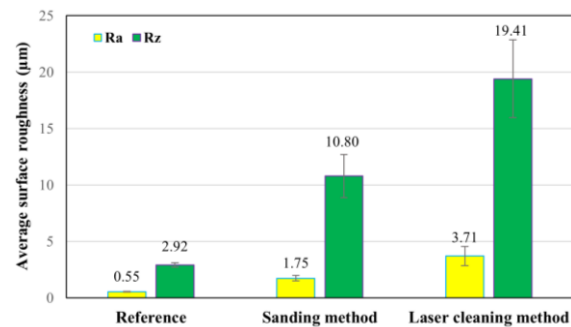


**Figure 4.** Average surface roughness of the aluminium alloy EN AW-5754 depending on the surface preparation

It was observed that surface preparation with sandpaper is characterized by lower surface roughness compared to laser cleaning method. The average Ra and Rz values for the sandpaper were  $\pm 1.75 \mu\text{m}$  ( $1.46 - 1.91 \mu\text{m}$ ) and  $\pm 10.8 \mu\text{m}$  ( $8.65 - 12.33 \mu\text{m}$ ). After the laser cleaning method, the increased average roughness values for Ra and Rz were  $\pm 3.71 \mu\text{m}$  ( $3.1 - 4.51 \mu\text{m}$ ) and  $\pm 19.41 \mu\text{m}$  ( $15.65 - 23.46 \mu\text{m}$ ), respectively.

The static tensile lap-shear test results of the single-lap bonded aluminium joints in relation to two different surface preparations and adhesive types are displayed in the form of a graph in Figure 5.

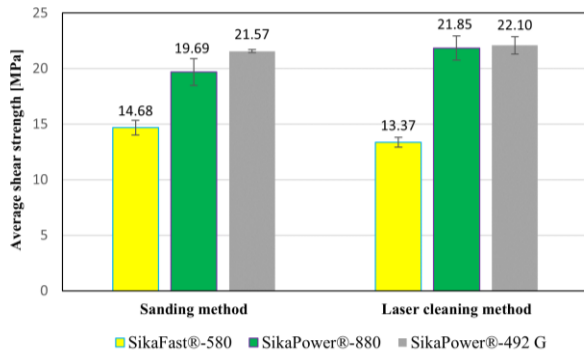


**Figure 5.** Average tensile lap-shear strength of adhesive bonded joints in relation to the method of surface preparation. The first bar shows bonded parts prepared with P180 sandpaper; the second bar shows a laser cleaning preparation

Adhesive SikaFast®-580 exhibited lower strength compared to other adhesives. However, samples prepared using sanding method demonstrated higher strength than those prepared with laser cleaning. Laser cleaning enhanced the mechanical strength of bonded joints using adhesive SikaPower®-880 by up to 2 MPa compared to other preparation methods, indicating that this adhesive responds well to different surface preparation methods.

The maximum strength of the SikaPower®-492 G adhesive after application of the laser cleaning method was comparable to that obtained with the sanding method. This indicates that the adhesive performs consistently well regardless of whether the surface preparation is done by laser cleaning or sanding. The results show that both surface preparation methods, sanding and laser cleaning, influenced the generation of sufficient surface roughness and increased tensile lap-shear strength. Analysis of the static tensile lap-shear test results revealed correlations between the surface preparation methods, the adhesives used, and the strength of the bonded joints.

Figure 6, Figure 7 and Figure 8 present examples of fractures in bonded joints made with adhesives SikaFast®-580, SikaPower®-880, and SikaPower®-492 G.

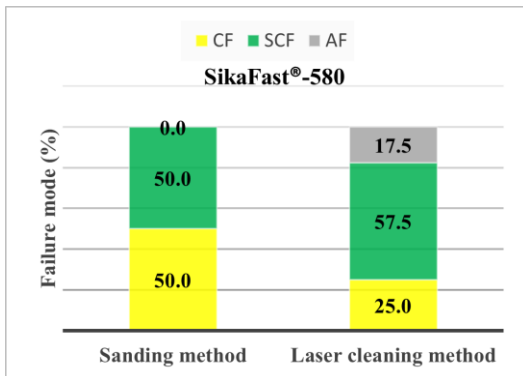


**Figure 6.** Percentage of failure mode distribution of the adhesive SikaFast®-580 for the aluminium alloy EN AW-5754 depending on the surface preparation. CF—cohesion failure; SCF—special cohesion failure; AF—adhesion failure

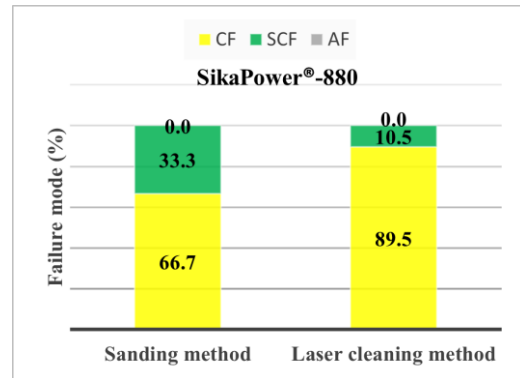


**Figure 7.** Percentage of failure mode distribution of the adhesive SikaPower®-880 for the aluminium alloy EN AW-5754 depending on the surface preparation. CF—cohesion failure; SCF—special cohesion failure; AF—adhesion failure

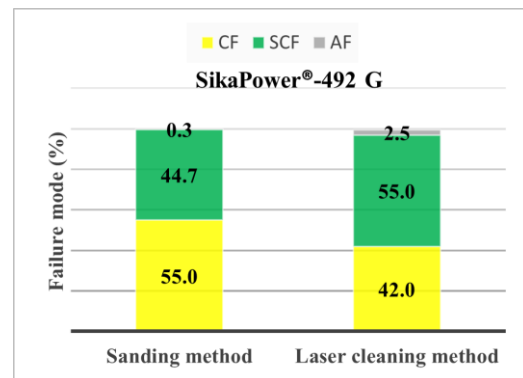


**Figure 8.** Percentage of failure mode distribution of the adhesive SikaPower®-492 G for the aluminium alloy EN AW-5754 depending on the surface preparation. CF—cohesion failure; SCF—special cohesion failure; AF—adhesion failure

Adhesive SikaFast®-580 showed an adhesion failure of 17.5% after laser cleaning, which is certainly related to the fact that the results of the static tensile lap-shear test showed low strength in these surface preparations, in contrast to the preparation with P180 sandpaper, where cohesive failure dominated and increased the shear strength value.

Adhesive SikaPower®-880 gave very consistent results, mostly cohesive failure. This confirms the assertion that this adhesive is much more sensitive to surface preparation and that the tensile lap-shear strength was variable, proving that this adhesive leads to cohesive failure in all preparations.

Cohesive failure or special cohesive failure dominated with adhesive SikaPower®-492 G, which showed the highest tensile lap-shear strength value after both preparations.

#### 4. CONCLUSION

This study investigated the effects of two different methods of surface preparation sanding by hand with P180 sandpaper and laser cleaning on the tensile lap-shear strength of single-lap joints of EN AW-5754 aluminium

alloy with three different epoxy adhesives, SikaFast®-580, SikaPower®-880 and SikaPower®-492 G. The effects of surface roughness and tensile lap-shear strength were investigated and a significant failure analysis was performed. Based on the investigations carried out and the evaluation of the knowledge gained, the following conclusions were drawn:

Proper surface preparation is essential for the production of strong bonded joints. Surface contaminants were removed and the bonding surface was developed uniformly, resulting in increased bond strength and adsorption. Laser cleaning can alter the original milled surface and significantly increase the Ra value.

- Laser cleaning as surface preparation for bonding resulted in the maximum tensile lap-shear strength of the bonded joints with adhesives SikaPower®-880 and SikaPower®-492 G. In contrast, surface preparation with sandpaper in combination with adhesive SikaFast®-580 resulted in higher tensile lap-shear strength and improved failure properties compared to laser cleaning. This shows that in addition to surface preparation, the correct choice of adhesive also has a major influence on strength and bonding properties.
- The application of SikaPower®-880 epoxy adhesive for bonding materials showed optimal results for all preparations and cohesive failure for all preparations, indicating that this adhesive responds well to different surface preparation methods.
- The bonding strength varies depending on the surface preparation method. Consequently, using the same adhesive and material with different preparation methods can result in significant variations in bond strength. Choosing an appropriate surface preparation method that is suitable for the parts to be bonded and their surface roughness is crucial as it increases the strength of the bonded joints.

## Acknowledgments

This work was supported by the Ministry of Science, Technological Development and Innovation of the Republic of Serbia (Contract No. 451-03-65/2024-03). The authors would like to thank mr. Robert Zimšek, mr. Marko Živaljić and mr. Toni Đorđević for their contributions.

## References

- [1] FERNANDES, T. A. B., CAMPILHO, R. D. S. G., BANEJA, M. D., da SILVA, L. F. M.: *Adhesive Selection for Single Lap Bonded Joints: Experimentation and Advanced Techniques for Strength Prediction*, The Journal of Adhesion, (2015) 91:841–862.
- [2] MARQUES, C.A., MOCANU, A., TOMIĆ, Z.N., BALOS, S., STAMMEN, E., LUNDEVALL, A., ABRAHAMI, S.T., GÜNTHER, R., DE KOK, J.M.M., DE FREITAS, S.T.: *Review on Adhesives and Surface Treatments for Structural Applications: Recent Developments on Sustainability and Implementation for Metal and Composite Substrates*. Materials (2020), 13, 5590.
- [3] MIRSKI, Z., WOJDAT, T., ZIMNIAK, Z., ŁACKA, I., PAWEŁKO, A.: *Effect of the Preparation of Aluminium, Magnesium and Titanium Alloys Surface on Properties of Adhesive Bonded Joints*, Bulletin of the Institute of Welding in Gliwice, (2017), 61(5) pp. 81-90.
- [4] PIZZI, A., MITTAL, K.L.: *Handbook of Adhesive Technology*; CRC Press: Boca Raton, FL, USA, 2017.
- [5] EBNESAJJAD, S., EBNESAJJAD, C.: *Surface Treatment of Materials for Adhesive Bonding*, 2nd ed.; William Andrew Inc.: Norwich, NY, USA, 2013.
- [6] YUDHANTO, A., ALFANO, M., LUBINEAU, G.: *Surface preparation strategies in secondary bonded thermoset-based composite materials: A review*, Compos Pt A-Appl Sci Manuf (2021), 147:106443.
- [7] RUDAWSKA, A.: *Surface Treatment in Bonding Technology*, Academic Press: an imprint of Elsevier, London, UK, 2019.
- [8] ŁYCZKOWSKA, K., MIARA, D., RAMS, B., ADAMIEC, J., BALUCH, K.: *The Influence of MSR-B Mg Alloy Surface Preparation on Bonding Properties*, Materials, 16, (2023), 3887.
- [9] BOUTAR, Y., NAÏMI, S., MEZLINI, S., SIK ALI, M. B.: *Effect of surface treatment on the shear strength of aluminium adhesive single-lap joints for automotive applications*, Int. J. Adhes. Adhes. 67 (4), (2016), 38-43.
- [10] BROCKMANN, W.: Steel adherends. In *Durability of Structural Adhesives*, A.J. Kinloch (ed.), Elsevier Applied Science, London, (1983) Chapter 7, 306.
- [11] ARENAS, J. M., ALÍA, C., NARBÓN, J.J., OCAÑA, R., GONZÁLEZ, C.: *Considerations for the industrial application of structural adhesive joints in the aluminium–composite material bonding*, Composites: Part B 44, (2013), 417–423.
- [12] DA SILVA, L.F.M., FERREIRA, N.M.A.J., RICHTER-TRUMMER, V., MARQUES, E.A.S.: *Effect of grooves on the strength of adhesively bonded joints*, (2010), Int. J. Adh. Adhes. 30 (8), 735-743.
- [13] FENG, Z., ZHAO, H., TAN, C., ZHU, B., XIA, F., WANG, Q., CHEN, B., SONG, X.: *Effect of laser texturing on the surface characteristics and bonding property of 30CrMnSiA steel adhesive joints*, Journal of Manufacturing Processes 47, (2019), 219–228.
- [14] RECHNER, R., JANSEN, I., BEYER, E.: *Influence on the strength and aging resistance of aluminium joints by laser pre-treatment and surface modification*, Int. J. Adhes. Adhes. 30 (7), (2010), 595–601.
- [15] MANDOLFINO, C., LERTORA, E., GENNA, S., LEONE, C., GAMBARO, C.: *Effect of laser and plasma surface cleaning on mechanical properties of adhesive bonded joints*, Procedia CIRP 33, (2015), 458 – 463.

- [16] Thyssenkrupp Materials Services GmbH, Material Data Sheet EN AW-5754 (EN AW-AlMg3) Essen, Germany, 2017.
- [17] EN 1465; Adhesives—Determination of Tensile Lap-Shear Strength of Bonded Assemblies, 2009. European Standard: Brussels, Belgium.
- [18] Provisional Product Data Sheet-SikaFast®-580, (2022). Sika Services AG: Zurich, Switzerland.
- [19] API-SikaPower®-880, Material Card, 2022. Sika Services AG: Zurich, Switzerland.
- [20] API-SikaPower®-492 G, 2022. Material Card; Sika Services AG: Zurich, Switzerland.
- [21] ISO 4587; Adhesive Lap—Shear Strength of Rigid-to-Rigid Bonded Assemblies, (2003). ISO: Geneva, Switzerland.
- [22] ISO 10365; Adhesives—Designation of main failure patterns (2022). ISO: Geneva, Switzerland.



## CAVITATION EROSION MONITORING OF 42CrMo4 STEEL SAMPLES USING THE IMAGE AND MORPHOLOGICAL ANALYSIS

ANA ALIL

University of Belgrade, Institute of Chemistry, Technology and Metallurgy- National Institute of the Republic of Serbia, Belgrade, Serbia, [ana.alil@ihtm.bg.ac.rs](mailto:ana.alil@ihtm.bg.ac.rs)

STANICA NEDOVIĆ

University of Montenegro, Maritime Faculty, Kotor, Montenegro, [snedovic335@gmail.com](mailto:snedovic335@gmail.com)

SANJA MARTINOVIĆ

University of Belgrade, Institute of Chemistry, Technology and Metallurgy- National Institute of the Republic of Serbia, Belgrade, Serbia, [s.martinovic@ihtm.bg.ac.rs](mailto:s.martinovic@ihtm.bg.ac.rs)

TATJANA VOLKOV HUSOVIĆ

University of Belgrade, Faculty of Technology and Metallurgy, Belgrade, Serbia, [tatjana@tmf.bg.ac.rs](mailto:tatjana@tmf.bg.ac.rs)

**Abstract:** *The choice of steel depends on environmental factors like temperature, pressure, and chemical exposure. Steel components in machinery often face varying conditions that can lead to damage, such as cavitation erosion. In this study, steel 42CrMo4 samples were chosen to represent a common and widely used steel. Application of this type of steel is often related to the statically and dynamically stressed components for vehicles, engines, and machines, where corrosion or cavitation can occur. The behavior of steel samples under conditions of cavitation erosion in distilled water was the focus of this paper. Testing was performed using a standard cavitation vibratory setup using a stationary specimen, according to the ASTM G-32 procedure. Image and morphological analyses were implemented to quantify the level of sample degradation caused by cavitation. The observed changes in the monitored parameters during testing are linked to the degradation mechanism of cavitation erosion. The results showed that pits began forming within 60 minutes, and afterward, the growth and merging of these pits significantly impacted the degradation process.*

**Keywords:** *Cavitation erosion, Image analysis, Degradation level, Morphology analysis.*

### 1. INTRODUCTION

A thorough understanding of the material's behavior during cavitation is essential for engineers and researchers to evaluate its performance and durability. The objective of this approach is to provide the development of more reliable and long-lasting steel components for industrial use. Steel 42CrMo4 is selected because of its exceptional mechanical properties, such as strength, toughness, and wear resistance. It is commonly used in applications where durability and resistance are crucial, including the automotive, aerospace, and hydraulic sectors [1]. Steel 42CrMo4 is essential in marine engineering, hydraulic systems, and power generation [2]. In marine equipment parts, it is used for producing propellers and other underwater components that are constantly exposed to cavitation and corrosion. In hydraulic systems, it is essential for components like pumps and valves that experience high-pressure fluctuations. In power generation, it is crucial for turbine blades and other parts that are subjected to intense cavitation forces [1-3]. However, the marine equipment parts made of 42CrMo4 steels are very susceptible not only to corrosion but also to cavitation erosion due to their synergistic effect. The subject of some investigations was based on the synergistic effect of cavitation erosion-corrosion, but

mainly focusing on non-ferrous metals [4,5]. Thus, the purpose of this study was to examine the effects of cavitation and corrosion on steel 42CrMo4 first separately, and then in simultaneous action.

The term "cavity" originates from the Latin word 'cavus', meaning hollow [6]. Cavitation refers to the dynamic process involving the formation, growth, and collapse (implosion) of bubbles within a liquid. The beginning of cavitation is closely related to liquid pressure [7-15]. When implosion happens in close vicinity of a solid surface, material can detach from a surface inducing surface erosion and resulting in cavitation damage. This damage is observed in various hydraulic constructions including ship propellers, hydrofoils, dam overflows, valves, tunnels, hydraulic pumps, and turbines [7,12,15-18]. Numerous studies have been extensively conducted by researchers like Hofmann et al. (2022) [19] relating the cavitation erosion of martensitic stainless steel X3CrNiMo13-4 QT780. Gao et al. (2019) [20] conducted cavitation erosion tests on stainless steels 316L and 420 to predict damage. Raami et al. (2023) [21] improved the cavitation erosion resistance of AISI 420 stainless steel through quenching and partitioning heat treatment. Building on the work of Lloyds Register, Basumatary (2017) [6] investigated the cavitation erosion of various materials including duplex stainless steel (DSS) and as-cast nickel aluminium bronze (NAB), 13/4 martensitic

stainless steel, 42CrMo4 low alloy steel, carbon fibre reinforced composites, and LRAH32 low carbon steel. Basumatary et al. observed the response of these materials to cavitation erosion in laboratory prepared ASTM standard seawater in a NaCl solution (3.5%) and found that DSS and NAB exhibit superior resistance [22] thus focusing their subsequent research on these materials.

Additionally, Bărbulescu et al. (2023) [23] investigated brass corrosion under cavitation conditions in seawater, while Vuksanović et al. (2021) [24] examined the cavitation resistance of aluminum-zirconium composites. These studies provide valuable insights into materials' behavior under cavitation, however, there is a lack of research specifically focused on the cavitation resistance of 42CrMo4 steel. To assess cavitation resistance in annealed 42CrMo4 steel, Bordeas et al. (2017) [25] proposed utilising the roughness parameter Rz, which would complement the findings of Dojčinović's (2013) [26] study on quenched and tempered 42CrMo4 steel.

The main aim of this study is to analyze cavitation erosion in 42CrMo4 steel samples using image and morphological analysis.

## 2. EXPERIMENTAL

The samples for cavitation testing were prepared by cutting in the form of rectangular prisms with dimensions of width and length of 20 mm × 20 mm. To obtain standardized samples, a 10 mm thick plate was processed on a milling machine and reduced to a thickness of 4 mm. The prepared samples were subjected to a cavitation erosion test using the ultrasonic vibration method (with a stationary sample), following ASTM G32-16 standard. An ultrasonic generator with a frequency of  $20 \pm 0.2$  kHz created cavitation bubbles. The ultrasonic horn had a 16 mm diameter, and the working distance between the horn tip and the specimen was set to 0.5 mm. Test samples were placed on a platform in a beaker of distilled water at  $22 \pm 1^\circ\text{C}$ . The specimens were weighed before and after each cavitation exposure period. An optical microscope monitored surface damage morphology. Mass measurements were taken using an analytical balance with 0.1 mg accuracy.

To evaluate surface erosion, the samples were inspected with a trinocular metallurgical microscope (EUME, EU Instruments, Gramma Libero, Belgrade) at different magnifications. Additionally, SEM images were captured using a JEOL JSM-5800 to observe changes during cavitation erosion. Defects from cavitation erosion can be described using morphological descriptors and quantified with image analysis tools in the Image Pro Plus 6.0 software (IPP) package (Media Cybernetics, 2006, Rockville, MD). The sample surface was scanned at 1200 dpi resolution after each cavitation erosion period and processed with IPP. Morphological features that best characterize the surface defects (pits) were selected after segmenting the defects.

## 3. RESULTS AND DISCUSSION

The results that are most commonly used for degradation monitoring represent the mass loss during testing and are presented in Figure 1. Different periods of cavitation were marked. The Incubation period (I) is very short, indicating that the sample is most sensitive to pit formation, and the energy for pit formation is rather low. The accumulation period (II) lasted for 30 min (10-40 min), followed by an attenuation period lasting 20 min (40-60 min). The steady-state period began after 60 min. As the exposure time was 120 min, further experiments will provide the results for the duration after this period.

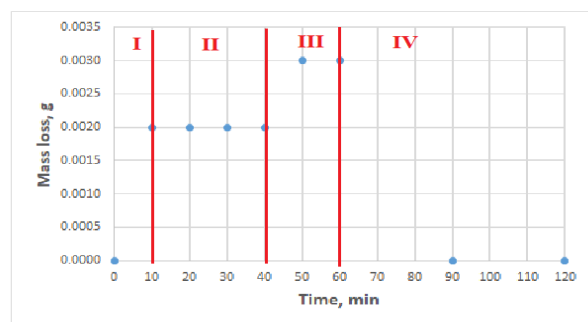


**Figure 1.** Mass loss during cavitation testing

Samples images using optical (OM) and scanning electron (SEM) microscopy before and after testing for 120 minutes are presented in Figure 2.

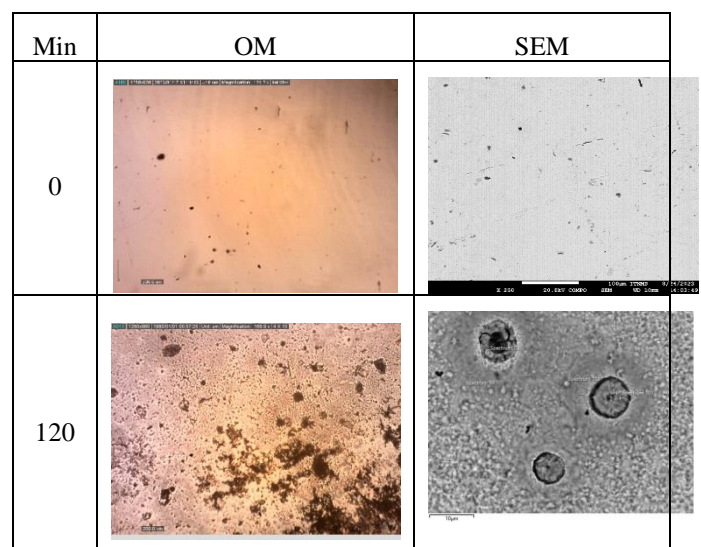


**Figure 2.** Image of the samples using OM and SEM before and after 120 minutes of testing

Morphological analysis was performed using Image-Pro Plus software, which enables the quantitative analysis of selected morphological parameters. The parameters that were selected and monitored were the average pit area, total pit area, and the number of formed pits. The results are shown in Figure 3.

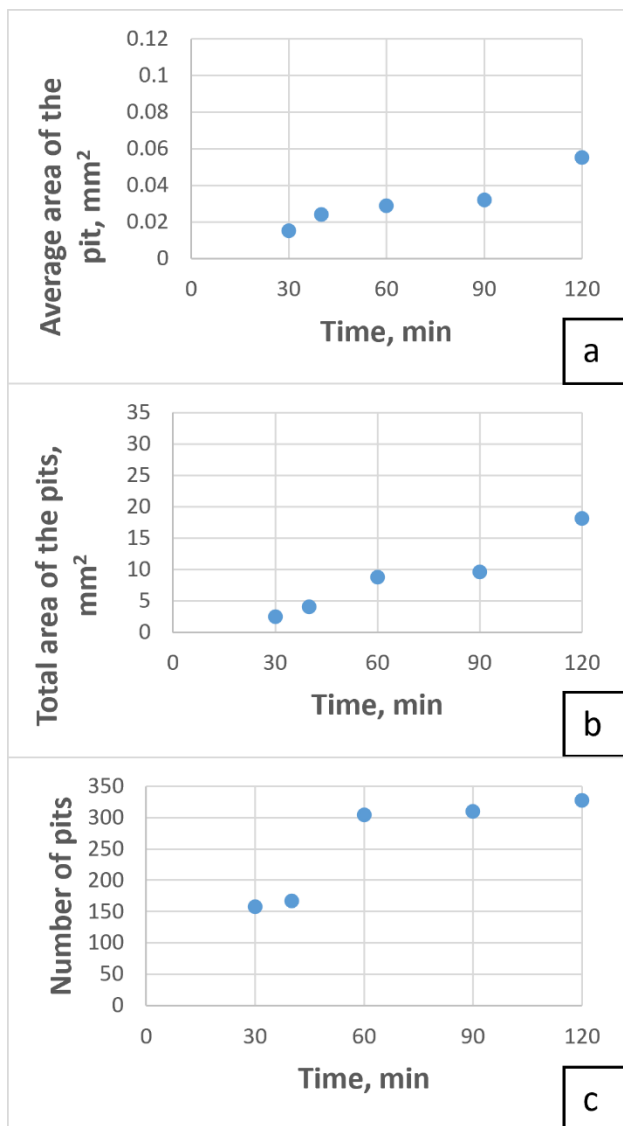


**Figure 3.** Monitoring of morphological parameters during testing (average values): a) single pit area, b) total pit area, and c) number of formed pits

The total area of the formed pits and the average area of the formed single pit increased during the experiment, as expected (Figure 3a and 3b). These results are in correlation with the increasing number of pits (Figure 3c), thus leading to the conclusion that forming pits is the dominant mechanism during cavitation testing. After 60 min, this increase slowed, which suggests that pit growth and merging of the smaller single pits also have a significant influence on the degradation mechanism.

#### 4. CONCLUSION

The cavitation erosion of 42CrMo steel sample was monitored using mass loss and morphological analysis. Mass loss results were used to divide the cavitation erosion into four periods as well as the duration of each period. Quantitative morphological analysis was performed using selected parameters such as the average area of the single pit, the total area of the pits, and the number of formed pits. These changes in the monitored parameters during testing could be related to the

degradation mechanism during cavitation erosion. The results indicated that pit formation occurred over 60 min, after which pit growth and merging of the formed pits had a significant influence on the degradation mechanism.

#### Acknowledgements

This work was supported by the Ministry of Science, Technological Development and Innovation of the Republic of Serbia (Contract No. 451-03-65/2024-03/200135 and 451-03-66/2024-03/200026.).

#### References

- [1] XU,Q., YANG,X., LIU,J., JIANG,D., QIU,Z.: *Improved corrosion resistance of 42CrMo4 steel by reconstructing surface integrity using ultrasonic surface rolling process*, Materials Today Communications, 35 (2023) 105932.
- [2] ZHU,Z., LU,Y., XIE,Q., LI,D., GAO,N.: *Mechanical properties and dynamic constitutive model of 42CrMo steel*, Materials & Design, 119 (2017) 171-179.
- [3] BARTOŠÁK,M., HORVÁTH,J., ŠPANIEL,M.: *Isothermal low-cycle fatigue and fatigue-creep of a 42CrMo4 steel*, International Journal of Fatigue, 135 (2020) 105538.
- [4] SONG,Q.N., TONG,Y., XU,N., SUN,S.Y., LI,H.L., BAO,Y.F., JUANG,Y.F., WANG,Z.B., QIAO,Y.X.: *Synergistic effect between cavitation erosion and corrosion for various copper alloys in sulphide-containing 3.5% NaCl solutions*, Wear, 450-451 (2020) 203258.
- [5] QIN,Z., CAO,L., DENG,Y., ZHONG,C., HU,W., WU,Z.: *Effect of oxide film on the cavitation erosion-corrosion behavior of nickel-aluminium bronze alloy*, Corrosion, 76(12) (2020) 1136-1146.
- [6] BASUMATARY,J.: *Cavitation erosion-corrosion in marine propeller materials*, PhD thesis, Faculty of Engineering and Environment, University of Southampton (2017).
- [7] DOJČINOVIĆ,M.: *Uticaj strukture na mehanizam razaranja čelika pod dejstvom kavitacije*, PhD thesis, Faculty of Technology and Metallurgy, University of Belgrade (2007).
- [8] DOJČINOVIĆ,M., VOLKOV HUSOVIĆ,T.: *Cavitation damage of the medium carbon steel: Implementation of image analysis*, Materials Letters, 62 (2008) 953-956.
- [9] HATTORI,S., MORI,H., OKADA,T.: *Quantitative evaluation of cavitation erosion*, Journal of Fluid Engineering, 120 (1) (1998) 179-182.
- [10] OKADA,T., HATTORI,S.: *Proceeding of the international symposium on aerospace and fluid science*, Sendai, Japan (1993) 347-350.
- [11] STELLER,K.: *Proceeding of the 6<sup>th</sup> international conference on erosion by liquid and soil impact*, Cambridge, UK (1983) 121-125.
- [12] DOJČINOVIĆ,M., MAROVIĆ,S.: *The morphology of cavitation damage of heat-treated medium carbon steel*, Journal of Serbian Chemical Society, 71(8-9) (2006) 977-984.
- [13] KONDOH,K., UMEDA,J., WATANABE,R.: *Cavitation resistance of powder metallurgy aluminium*



- matrix composite with AlN dispersoids, *Materials Science and Engineering A*, 499 (2009) 440-444.
- [14] KARIMI,A., MARTIN,J.L.: *Corrosion erosion of materials*, *International metals reviews*, 31(1) (1986) 1-26.
- [15] BREGLIOZZI,G., SCHINO,A.D., AHMED,S.I.-U J.M.KENNY, HAEFKE,H.: *Cavitation wear behavior of austenitic stainless steels with different grain sizes*, *Wear*, 258(1-4) (2005) 503-510
- [16] HAMMIT,F.G.: *Cavitation and multiphase flow phenomenon*, McGraw-Hill, New York, 1980.
- [17] KNAPP,R.T., DAILY,J.W., HAMMIT,F.G.: *Cavitation*, McGraw-Hill, New York, 1970.
- [18] OKADA,T., IWAI,Y., HATTORIS., TANIMURA,N.: *Relation between impact load and the damage produced by cavitation bubble collapse*, *Wear*, 184 (1995) 231-239.
- [19] HOFMANN,J., THIÉBAUT,C., RIONDET,M., LHUISSIER,P., GAUDION,S., FIVEL,M.: *Comparison of acoustic and hydrodynamic cavitation: material point of view*, *Physics of Fluids*, 35 (1) (2023) 017112.
- [20] GAO,G., ZHANG,Z., CAI,C., ZHANG,J., NIE,B.: *Cavitation damage prediction of stainless steels using an artificial neural network approach*, *Metals*, 506 (9) (2019) 1-11.
- [21] RAAMIL., VARIS,T., VOLTONEN,K., WENDLER,M., VOLKOVA,O., PEURA,P.: *Enhancing the cavitation erosion resistance of AISI 420-type stainless steel with quenching and partitioning*, *Wear*, 527-527 (2023) 204897.
- [22] BASUMATARY,J., NIE,M., WOOD,R.J.K.: *The synergistic effects of cavitation erosion–corrosion in ship propeller materials*, *Journal of Bio- and Tribo-corrosion*, 1(12) (2015) 1-12.
- [23] BĂRBULESCU,A., DIMITRIU,C.S.: *Fractal characterization of brass corrosion in cavitation field in seawate*, *Sustainability*, 3816 (15) (2023) 1-14.
- [24] VUKSANOVIĆ,M., GAJIĆ-KVAŠČEV,M., VOLKOV-HUSOVIĆ,T., JANČIĆ-HEINEMANN,R.: *Advanced damage resistance monitoring procedure on the composite materials surface exposed to cavitation testing*, *Wear*, 474-475 (2021) 203877.
- [25] BORDEASU,I., POPOVICIU,M.O., GHERA,C., MICU,L.M., PIRVULESCU,L.D., BENA,T.: *The use of  $R_z$  roughness parameter for evaluation of materials behavior to cavitation erosion*, *IACS 2018 IOP Conference on Applied Sciences, Materials Science and Engineering* 294(1) (2018) 012010.
- [26] DOJČINOVIĆ,M.: *Measurement of roughness as an alternative method in the assessment of cavitation resistance of steel*, *Hemijaska industrija*, 67(2) (2013) 323-330.



## CAVITATION EROSION MONITORING OF MULLITE CERAMIC SAMPLE USING IMAGE ANALYSIS

SANJA MARTINOVIĆ

University of Belgrade, Institute of Chemistry, Technology and Metallurgy- National Institute of the Republic of Serbia, Belgrade, Serbia, [s.martinovic@ihm.bg.ac.rs](mailto:s.martinovic@ihm.bg.ac.rs)

ANA ALIL

University of Belgrade, Institute of Chemistry, Technology and Metallurgy- National Institute of the Republic of Serbia, Belgrade, Serbia, [ana.alil@ihm.bg.ac.rs](mailto:ana.alil@ihm.bg.ac.rs)

TATJANA VOLKOV HUSOVIĆ

University of Belgrade, Faculty of Technology and Metallurgy, Belgrade, Serbia, [tatjana@tmf.bg.ac.rs](mailto:tatjana@tmf.bg.ac.rs)

**Abstract:** Numerous industrial equipment are designed to withstand harsh operating conditions that among others include cavitation erosion. This study examined the cavitation erosion behavior of mullite, a common material used in furnace linings and casting processes such as Lost Foam which is a novel way to produce castings offering both high quality and reasonably priced. The ultrasonic vibratory method with a stationary sample was employed to achieve cavitation erosion, while image analysis was used to measure the degree of surface deterioration. This study aimed to assess the lifetime of mullite under cavitation exposure by quantifying the morphological parameters of the defects through image analysis and by monitoring material behavior. The obtained results were discussed and analyzed in order to understand degradation mechanisms and sample resistance to cavitation erosion. The results demonstrate that mullite is highly resistant to cavitation, as the volume loss is minimal and the surface degradation is below 6% after 180 minutes of exposure.

**Keywords:** Mullite, Cavitation erosion, Non-destructive evaluation, Image analysis.

### 1. INTRODUCTION

Cavitation is a phenomenon in which vapor bubbles form in a rapidly flowing liquid when it suddenly enters a region of low pressure. While some bubbles already exist in the fluid, others are formed and expand under these conditions. The formation of low-pressure regions can be influenced by factors such as high fluid velocity, sharp edges or corners, and turbulent flow conditions, which can result in conditions where the pressure drops significantly and lead to the formation of cavitation bubbles. If fluid flow enters a region of high pressure afterward, bubbles may rapidly collapse or implode which often results in the generation of a micro-jet and shock wave. Various factors, including liquid temperature, chemical activity, flow rate, pressure drop, and the presence of dissolved or steam gas influence the implosion of bubbles. If the bubble collapse occurs close to a solid component, it can cause significant damage to the surface, resulting in erosion and a reduction in the material's overall lifespan and performance. Hardened stainless steels, titanium alloys, and high-performance ceramics are among the materials resistant to cavitation because they are designed to endure the erosive effects of cavitation and maintain their integrity even under high fluid velocities and turbulent flow conditions. The cavitation phenomenon affects various industries and equipment, such as automotive engines, marine

propellers, pumps, hydraulic turbines, and fuel injectors. Therefore, it is crucial to select cavitation-resistant materials and explore all possibilities for extending the lifespan and improving the performances of these components [1-5].

Mullite, a ceramic material, was selected for this study due to its unique composition and structure offering a high melting point, low thermal expansion, and excellent mechanical properties. Specifically, its exceptional hardness gives it excellent wear resistance and allows it to endure repetitive impact and abrasion. In addition to its high hardness, mullite also possesses excellent fracture toughness and strength, making it highly resistant to cracking and deformation under the erosive forces of cavitation. Mullite's resistance to cavitation makes it a desirable material for various applications such as components for pump impellers, marine propellers, and hydraulic machinery. This property enables the material to endure high-velocity fluid flow and the erosive impact of cavitation, ensuring its durability and longevity. Furthermore, mullite is resistant to corrosion and extreme temperatures, making it an ideal choice for applications that require resistance to harsh environments, and also to a combination of all mentioned environment conditions. Additionally, mullite is lightweight, making it suitable for applications where weight is an important factor. Mullite is a well-known ceramic and refractory material often used for linings, coatings, or fillers of linings in furnace

walls. The extreme conditions in industrial furnaces, including high temperatures and erosion effects caused by solid particles from loading and the flow of molten slag and metal, are somewhat comparable to the harsh conditions experienced during cavitation. Specifically, parts of furnaces and devices are exposed to solid materials and high-speed fluid flow [6-10]. Therefore, it is very important to conduct various tests to examine the installed material, in this study the mullite, for cavitation resistance.

## 2. EXPERIMENTAL

Mullite ceramic samples were prepared using pure mullite powders with granulation of 40  $\mu\text{m}$ , which were initially processed by micronizing grinding in a vibrating mill with agate balls to achieve a grain size of 15-25  $\mu\text{m}$ . The goal was to obtain powders with specific grain sizes and shapes that would exhibit improved properties, better grain packing, and greater densification during pressing. This process aimed to provide a homogeneous sintered structure that would have good resistance to cavitation. Such finely ground powders were then pressed in a mold under a pressure of 1 MPa to form cylindrical samples with a diameter of 30 mm and thickness of 3 mm. The sintering process was carried out at a temperature of 1200 °C according to the following regime: raising the temperature to 1000 °C at a rate of 5 °C/min for 200 min; 1000-1200°C with a heating rate of 2°C/min for 100 min; at 1200°C, the samples were dwelled for 1 hour.

The resistance of mullite samples to cavitation erosion was assessed using the ultrasonic vibration method with a stationary sample, following the ASTM G-32 standard. The purpose of this method is to simulate cavitation erosion conditions to predict the material's behavior within a short period, typically 2-10 hours. The advantages of this approach include its small testing device, sample size, and low energy input. The method involves creating and imploding cavitation bubbles on the sample's surface and then measuring the sample's mass loss during exposure to cavitation, thus providing a quantitative measure of material resistance. The ASTM G-32 standard defines testing conditions, sample preparation, and procedures for result interpretation. The stationary sample method is an indirect cavitation testing technique, which involves placing the sample in a water bath under a mechanical vibrations concentrator at a specified distance. This method is particularly useful for testing hard and brittle materials like mullite. Cavitation erosion tests were conducted in distilled water at a temperature of  $22 \pm 2$  °C, using a vibration frequency of  $20 \pm 0.2$  kHz, and an amplitude of mechanical vibrations at the top of the ultrasonic probe of  $50 \pm 2$   $\mu\text{m}$ . The distance between the test sample and the ultrasonic probe was 0.5 mm. During the cavitation test, the samples were dried to constant mass, weighed with an analytical balance with an accuracy of  $\pm 0.1$  mg to calculate the mass loss, and photographed in digital form for further image analysis after each certain testing period. The monitoring of cavitation erosion was 180 minutes.

The Image Pro Plus 6.0 software program (IPP) was used

to quantify surface defects caused by cavitation erosion (Media Cybernetics, 2006, Rockville, MD). This process involves the recognition of differently colored damaged and undamaged areas on the sample surface thus extracting defects and providing valuable information about the objects. The IPP analyzes photographs in various formats and automatically counts, measures, and classifies data about the extracted objects. The IPP allows the direct export of all measured data into Microsoft Excel thus enabling the enormous datasets of measured values to be processed.

## 3. RESULTS

According to the standard that establishes criteria for the interpretation of the results, after measuring the sample weight, mass loss of material was calculated. Subsequently, knowing the value of tested material density, the volume loss of material was calculated and the results are shown in Figure 1.

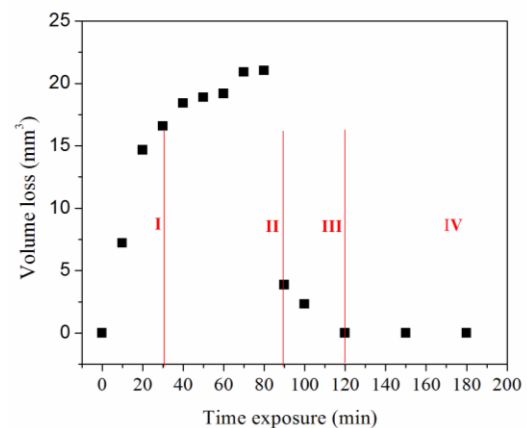


**Figure 1.** Volume loss of eroded material during cavitation.

Besides the proposed way of analyzing results, a non-destructive method of image analysis was applied to monitor the surface changes that occurred during the testing.

After each period of cavitation exposure, surface samples were scanned with a resolution of 1200 dpi, Figure 2. The obtained images were then processed using the Image Pro Plus software program. Using IPP tools, the total area of the surface defects was measured so the level of degradation could be calculated according to Equation 1. The level of surface degradation is defined as the ratio of the damaged surface area and the original surface area.

$$\text{Level of degradation (\%)} = P/P_0 \cdot 100$$

where P is the total degraded area ( $\text{mm}^2$ ) and  $P_0$  is the area of the sample surface ( $\text{mm}^2$ ). The diagram in Figure 3 shows the calculated values of degradation level during the testing. This method provides a reliable and objective assessment of the extent of degradation caused by cavitation exposure.

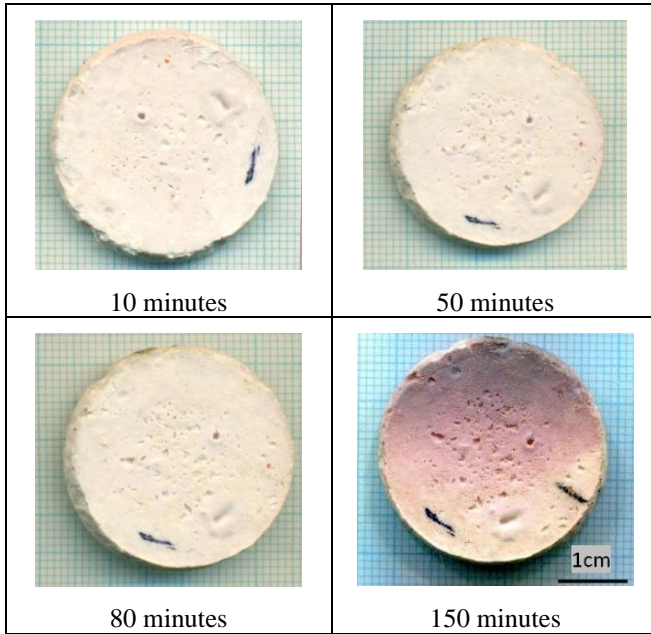


**Figure 2.** Scanned images of the specimens' surface during the cavitation testing.

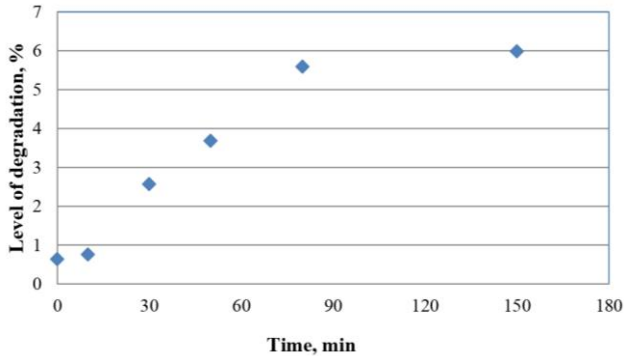


**Figure 3.** Level of degraded area during the cavitation testing.

## 4. DISCUSSION

Material volume loss is a consequence of material erosion during the cavitation experiment, as shown in Figure 1. It is evident that there is a continuous increase in volume loss during the first 80 minutes of treatment, firstly very rapid up to 30 minutes and then getting quite slower reaching a maximum. It can be assumed that the number of defects and pits, along with their dimensions (area and depth) increased throughout the experiment. The results also indicate that initial surface imperfections were present at the beginning of the experiment.

A visual inspection of the mullite samples, shown in Figure 2, indicates that the surface of the reference sample was not ideal and that there were already some damages present even before the sample was tested. Additionally, it is evident that with the exposure to cavitation, the number, shape, and size of surface defects will increase and will change over time as they are exposed to cavitation.

The graph in Figure 1 shows the results of volume loss over time exposure to the cavitation. The diagram

distinctly identifies the four typical stages of the cavitation process, as marked in Figure 1. The first is known as the incubation period, which lasts for the initial 30 minutes of cavitation exposure. As shown in Figure 3, during this period, a slight degradation occurs amounting to less than 3% of the sample's surface area. This period is characterized by the appearance of small and shallow surface flaws and pits. In the second stage, known as the acceleration period, there is significant mass and volume loss as well as surface degradation. This stage lasts until 80 minutes of cavitation exposure, as shown in Figs 1 and 3. The results indicate that this period is characterized by the appearance and growth of defects and pits equally on the surface and in the depth. During the third stage, which occurs after 80 minutes and lasts until 120 minutes of cavitation testing, new defects rarely form on the sample surface. Instead, the prevailing degradation mechanism involves the growth of defects that have already formed. The last period is known as the steady state during which there is no substantial material loss and the surface degradation level is nearly negligible as well.

Obtained results show that mullite is a very resistant material under exposure to cavitation since values of volume loss are quite small and the surface degradation level is below 6 % after 180 minutes of cavitation exposure.

## 5. CONCLUSION

The cavitation erosion of the mullite sample was studied by measuring and calculating the material volume loss and assessing the level of surface degradation using image analysis.

In summary, the applied approach is useful for determining the extent of degradation caused by cavitation exposure reliably and objectively.

The volume loss results showed the existence of four distinct periods of cavitation erosion and the duration of each period. The obtained results demonstrate that mullite exhibits high resistance to cavitation. The volume loss is minimal, and the surface degradation is below 6% after 180 minutes of exposure.

The level of surface degradation was quantitatively determined by measuring the total area of the formed pits using image analysis software tools. Image analysis showed a slight degradation of less than 3% occurs initially, with minor surface flaws appearing. In the acceleration period, which lasts until 80 minutes of cavitation, significant mass loss, volume reduction, and surface damage occur. Defects and pits grow during this stage. In the final stage, from 80 to 120 minutes, new surface defects rarely form.

Changes observed in material volume loss and the level of degradation during testing can be related to the degradation mechanism, which is essential for optimizing material selection and designing the material production process.

## Acknowledgments

This work was supported by the Ministry of Science, Technological Development and Innovation of the Republic of Serbia (Contract No. 451-03-65/2024-03/200135 and 451-03-66/2024-03/200026.).

## References

- [1] REEDHAR, B.K., ALBERT, S.K., PANDIT, A.B.: *Cavitation damage: Theory and measurements—A review*, *Wear* 372-373 (2017) 177–196.
- [2] QIU, N., WANG, L., WU, S., LIKHACHEV, D.: *Research on cavitation erosion and wear resistance performance of coatings*, *Engineering Failure Analysis*, 55 (2015) 208-223.
- [3] OKADA, T., IWAI, Y., HATTORI, S., TANIMURA, N.: *Relation between impact load and the damage produced by cavitation bubble collapse*, *Wear* 184 (2) (1995) 231-239.
- [4] BRENNEN, Ch.E.: *Cavitation and bubble dynamics*, Oxford University Press, New York, 1995.
- [5] KRELLA, A.K., Zakrzewska, D.E.: *Cavitation erosion-Phenomenon and test rigs*, *Advances in Materials Science*, 18 (2018) 2, 15-26.
- [6] BENGISU, M.: *Engineering Ceramics*, Springer, 2001.
- [7] MEDVEDOVSKI, E.: *Wear-resistant engineering ceramics*, *Wear*, 249 (2001) 821-828.
- [8] SCHNEIDER, H., SCHREUER, J., HILDMANN, B.: *Structure and properties of mullite—A review*, *Journal of the European Ceramic Society*, 28 (2) (2008) 329-344.
- [9] CAO, X.Q., VASSEN, R., STOEVER, D.: *Ceramic materials for thermal barrier coatings*, *Journal of the European Ceramic Society* 24 (1) (2004) 1–10.
- [10] PRSTIC, A., AĆIMOVIĆ-PAVLOVIĆ, Z., TERZIĆ, A., PAVLOVIĆ, LJ.: *Synthesis and characterization of new refractory coatings based on talc, cordierite, zircon and mullite fillers for lost foam casting process*, *Archives of Metallurgy and Materials*, 59 (1) (2014) 89-95.



## CORROSION OF 42CrMo4 STEEL IN MARINE ENVIRONMENT USING SEM/EDS ANALYSIS

STANICA NEDOVIĆ

1 University of Montenegro, Maritime Faculty, Kotor, Montenegro, [snedovic335@gmail.com](mailto:snedovic335@gmail.com)

ANA ALIL, SANJA MARTINOVIĆ

<sup>2</sup>University of Belgrade, Institute of Chemistry, Technology and Metallurgy- National Institute of the Republic of Serbia, Belgrade, Serbia, [ana.alil@ihm.bg.ac.rs](mailto:ana.alil@ihm.bg.ac.rs), [smartinovic@tmf.bg.ac.rs](mailto:smartinovic@tmf.bg.ac.rs)

TATJANA VOLKOV-HUSOVIĆ

<sup>3</sup>University of Belgrade, Faculty of Technology and Metallurgy, Belgrade, Serbia, [tatjana@tmf.bg.ac.rs](mailto:tatjana@tmf.bg.ac.rs)

### Abstract:

Many steels are used in specific environments, while one of these is maritime applications. High-strength 42CrMo4 steel finds numerous applications in the marine industry, including shaft parts, crankshafts, connecting rods, drilling joints, pump parts, steam turbines, and salvage equipment. In order to provide performance reliability in the marine environment, it is essential to study the corrosion resistance of surfaces of 42CrMo4 steel components and parts. The steel's behavior is typically evaluated in a synthetic NaCl solution, which is prepared as a standard substitute for seawater. This paper is focused on the behavior of the steel samples under corrosion conditions in NaCl solution. The level of sample surface degradation which is caused by the corrosion over a 4-month exposure period was evaluated using SEM/EDS analysis. The mass loss increased during the testing period, following an almost linear model in all time periods.

**Keywords:** corrosion, NaCl solution, mass loss, SEM/EDS analysis, degradation level

## 1. INTRODUCTION

Corrosion is defined as the gradual degradation of metal properties caused by a chemical reaction or an electrochemical reaction with the surrounding atmosphere. The physical breakdown of metals is classified as damage, wear, and erosion. Metals decompose in contact with moisture/water (H<sub>2</sub>O), bases (NaOH, CaCO<sub>3</sub>, NaHCO<sub>3</sub>, etc.), acids (HCl, H<sub>2</sub>SO<sub>4</sub>, HNO<sub>3</sub>, etc.), salts (NaCl), liquid chemicals, aggressive metal varnishes and gases (formaldehyde, gases containing sulfur and ammonia) [1].

Seawater is a complex mixture of inorganic salts (mainly sodium chloride), dissolved gases (especially oxygen), suspended solids, organic matter, and organisms [2]. Seawater is a 3.5 to 4 percent solution of various salts, of which 86% is sodium chloride [3]. In addition to sodium and chloride ions, there are also magnesium, calcium and potassium ions forming strong alkalis, as well as sulfates and bicarbonates that create weak acids, which is why the pH is basic, around 8 [4]. Corrosion rate in seawater depends on several factors: salt concentration, seawater flow, biofilm on the metal surface in the sea, dissolved oxygen concentration, and temperature [5].

Corrosion processes in seawater can be divided into four basic corrosion zones: atmospheric corrosion zone, tidal zone, underwater corrosion zone, and corrosion present in the mud zone [5]. The main factors affecting metal

corrosion in seawater medium are chemical, physical, and biological factors [6]. Doubling the amount of oxygen doubles the rate of the corrosion process [5]. In this paper corrosion will be monitored using mass loss and SEM/EDS analysis.

## 2. EXPERIMENTAL

The following is a description of the materials to be used, their production and chemical composition, sample preparation that includes mechanical processing of the sampled material, and sample characterization showing characteristic sizes and their contribution to corrosion testing.

### 2.1 Material

The material used in this research is low alloy steel 42CrMo4, which was processed by classical casting – as cast. The chemical composition of the mentioned material was done at the Institute of black metallurgy in Nikšić is shown in Table 1.

**Table 1.** Chemical composition 42CrMo4 low alloy steel

42CrMo4					
Element (wt. %)	C	Cr	Mo	Mn	Si
	0.40	0.93	0.20	0.65	0.29
	Ni	Cu	Al	S	P
	0.03	0.04	0.044	0.003	0.009

\*Fe-balanced

The steel was delivered by Kovintrade international trade d.d. Celje as hot rolled plates with dimensions of 10 mm × 1000 mm × 2000 mm according to the following procedure. After casting, the material in the form of billets was processed by hot rolling, the billets were heated to a temperature equal to 2/3 of the melting temperature of iron before hot rolling. After heating at 1024°C, the material passes through four flat rollers, and then the bars are straightened. Samples for corrosion testing were cut in the form of rectangles with dimensions of width and length of 20 mm × 20 mm. To obtain standardized samples, a 10-millimeter thick plate was processed on a milling machine and reduced to a thickness of 4 millimeters.

## 2.2. Corrosion testing

The corrosion behavior of structural steel 42CrMo4 was investigated by immersion, whose samples were immersed in a 3.5% NaCl solution according to ISO 11130 (E). The mass loss and SEM analysis were monitored at the beginning, after 30, 60, 90, and 120 days. Control of the metal surface consisted of examining the surface with a scanning electron microscope (SEM) at a magnification of 1000x. The elemental composition of samples was analyzed by the EDS method. The results of the mentioned tests gave an insight into the corrosion behavior of metals.

## 2.3. Mass loss

One of the criteria used to evaluate the results of the corrosion test, in which the samples were immersed in a salt solution, is mass loss. By weighing the specimen before and after cleaning (specimen should be weighed to three decimal places), the amount of metal loss can be determined. The mass of the samples was measured before and after each testing interval using an analytical balance with an accuracy of ± 0.1 mg, in accordance with the standard ISO 8407.

The degree or level of corrosion was measured as the mass loss of the steel samples before and after the corrosion tests. The samples were weighed and the mass loss was calculated using Equation (1) [7].

$$\text{Mass loss} = \frac{M_i - M_f}{M_i} \cdot 100 \quad (1)$$

Where  $M_i$  and  $M_f$  are the masses (in grams) of the sample before and after corrosion experiments, respectively.

## 3. RESULTS AND DISCUSSION

### 3.1. Mass loss

The relationship between the mass loss and the corrosion duration is shown in Figure 1. The mass loss increased during the testing period, following an almost linear dependence from 0 g for an uncorroded sample to 1.6 % after 120 days of immersion in a 3.5% NaCl solution.

The obtained mass loss results indicate that as the time

spent in saltwater increases, more corrosion occurs. This suggests that there is a corresponding increase in corrosion with an increase in the time spent in saltwater.

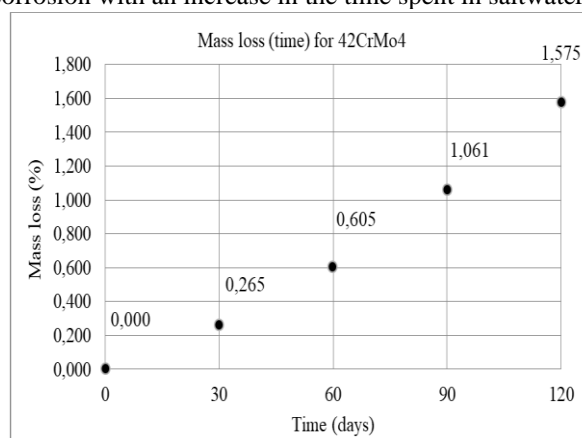


Figure 1. Mass loss for 42CrMo4 before and during testing

### 3.2. SEM/EDS analysis

SEM/EDS analysis was applied to monitor corrosion behavior of the samples. In Tables 2 and 3 results for samples after 30 and 120 days will be given, respectively.

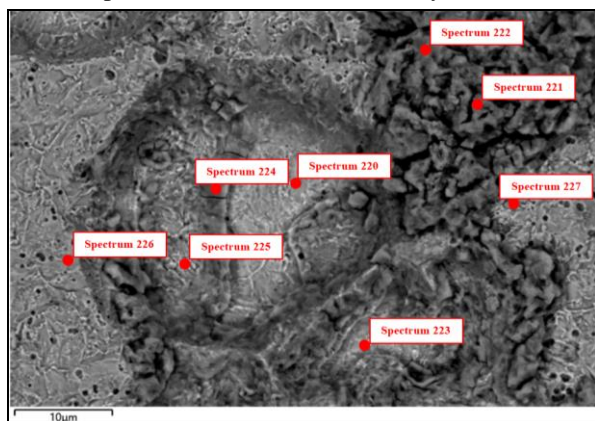
Table 2. SEM images and elemental composition (on marked spots) of 42CrMo4 after 30 days

Element	Spectrum					
	25	26	27	28	29	30
	Wt. (%)					
Fe	94.95	84.13	66.75	79.63	65.28	92.45
O	2.84	12.07	30.62	15.72	33.07	2.74
Cr	0.95	2.33	0.69	3.10	0.31	2.12
Cl	/	0.08	0.65	0.14	0.69	1.52
Mn	0.70	0.57	0.45	0.56	0.52	0.82
Cu	/	/	/	/	/	0.19
Al	0.14	0.16	/	0.24	/	/
S	0.06	0.29	0.63	0.32	/	0.09
Si	0.36	0.24	0.11	0.20	0.13	0.06
Ni	/	0.13	/	0.11	/	/
Ca	/	/	0.09	/	/	/

Since the corrosion behavior is investigated, the presence of elements that could be a consequence of sample contamination are omitted, for example, the elements that make up the composition of seawater, namely Na, Cl, K, Mg, Ca, Sr, Br, and F because they do not exist in steel.

Table 2 shows SEM images and elemental composition (on marked spots) of 42CrMo4 after 30 days in 3.5% NaCl solution. Considering the chemical composition (Table 1), the EDS analysis gives almost the same elemental composition, with the omission of molybdenum, but increased content of oxygen (spectra 26-29) and Cr, are evident (spectra 26, 28 and 30).

**Table 3.** SEM images and elemental composition (on marked spots) of 42CrMo4 after 120 days.



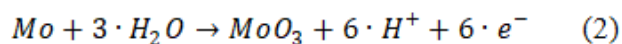
Element	Spectrum							
	220	221	222	223	224	225	226	227
	Wt. (%)							
Fe	96.16	65.90	66.81	95.43	70.96	94.86	95.90	89.29
O	1.09	27.55	26.42	2.11	26.15	2.71	1.78	7.58
Cr	1.31	3.93	5.00	1.08	0.93	1.12	1.15	1.89
Cl	/	0.80	0.26	/	0.76	/	/	0.05
Mn	0.80	1.10	0.57	0.79	0.66	0.74	0.71	0.71
Al	/	0.19	0.23	/	/	/	/	0.10
Si	0.37	0.31	0.37	0.36	0.27	0.34	0.33	0.20
Mo	0.26	0.23	0.32	0.21	0.27	0.23	0.13	0.19

After 120 days of corrosion, content of oxygen is increasing, and specific corrosion zones rich with oxygen are formed (spectra 221, 222, and 224).

At the other zones, oxygen content is higher than after 30 days of corrosion testing. At the same spots Cr is detected with higher level compared to average. Some slightly increased level of Mo is also evident. These results indicate the cooperative influence of Cr and Mo, the corrosion, with whose oxides a passive layer is formed on the surface of the steel.

The morphology of the samples at the beginning and the changes that occurred later during the time period of the test were monitored. SEM analysis revealed that more corroded areas will appear on the surface of the samples after 120 days compared to 30 days exposure.

Studies of the cooperative effect of Cr and Mo on the corrosion resistance of superaustenitic stainless steels by Bingbing Li et al point to Pourbaix's graph showing that Fe, Cr, and Mo form stabilized complexes  $\text{CrO}_4^{2-}$ ,  $\text{Fe}_2\text{O}_3$ , and  $\text{MoO}_4^{2-}$  under neutral conditions at 0.3 V [8]. While describing the electrochemical behavior of molybdenum by Klocke et al. of 42CrMo4 steel, the existence of models with different oxidation states in sodium nitrate and sodium chloride solutions was also taken into account. In this case, the molybdenum passivates as follows (Equation 2) [9]:



This means that if Cr oxides as the oxides of the first alloying element do not provide sufficient corrosion resistance, molybdenum oxides are the ones that are passivated and thus protect the material.

#### 4. CONCLUSION

Corrosion behavior in the marine environment of the selected steel (42CrMo4) sample was performed using NaCl solution.

Corrosion behavior was monitored using mass loss and EDS analysis. The time of exposure was selected to be 120 days.

Mass loss was almost linear dependent versus time of exposure, which indicates nearly the same rate of degradation.

SEM photographs could be used for morphology analysis of the level of degradation, and EDS results could be used to monitor the changes in chemical composition due to different oxides formation during the corrosion of the sample. The results of the EDS analysis of steel 42CrMo4 indicate the cooperative influence of Cr and Mo, with whose oxides a passive layer is formed on the surface of the steel.

#### References

- [1] RAJA,P.B., ISMAIL,M., GHOREISHIAMIRI,S., MIRZA,J., ISMAIL,M. C., KAKOOE,S. RAHIM,A. A.: *Reviews on corrosion inhibitors – a short view*, Chemical engineering communications, (2016) 1-4.
- [2] PETER S. LISS, MARTIN T. JOHNSON, Editors, *Ocean-Atmosphere Interactions of Gases and Particles*, SBN 978-3-642-25642-4 ISBN 978-3-642-25643-1 (eBook) DOI 10.1007/978-3-642-25643-1 Springer Heidelberg New York Dordrecht London
- [3] AKID,R.: *Corrosion of engineering materials*, Sheffield, Materials research institute, Sheffield Hallam university, 532-535 (2004) 503-508.
- [4] ROBERGE,P. R.: *Handbook of corrosion engineering*, McGraw-Hill Inc, (2000) 136- 201.
- [5] DANTAS,A., DANTAS,R., GONÇALO CIPRIANO, P.G., JESUS,A., LESIUK,G., FONSECA,C., MOREIRAA,P., A.F.O. CORREIA,P., *A methodology to evaluate seawater corrosion on quasi-static tensile properties of a structural steel*, Engineering Failure Analysis 164 (2024) 108613
- [6] HOU,X., GAO,L., CUI,Z., YIN,J.: *Corrosion and protection of metal in the seawater desalination*, IOP Conference series: Earth and environmental science, 108 (2018) 2-3.
- [7] APOSTOLOPOULOS, C. A., MICHALOPOULOS, D.: *Effect of corrosion on mass loss, and high and low cycle fatigue of reinforcing steel*, Journal of materials engineering and performance, 15 (6), (2006) 742-749.
- [8] LI, B., LANG, Y., CHEN, H., QU, H., FENG, H., SUN, X., TIAN, Z.: *Studies on the cooperative influence of Cr and Mo on the pitting corrosion*



*resistance of super austenitic stainless steels,*  
Materials, 16 (2023) 13-15.

- [9] KLOCKE, F., HARST, S., ZEIS, M., KLINK, A.:  
*Energetic analysis of the anodic double layer during*

*electrochemical machining of 42CrMo4 steel,*  
Procedia CIRP 42 (2016) 398-399.



## ADHESIVE JOINING OF 3D PRINTED PARTS

ALEKSIJA ĐURIĆ

University of East Sarajevo, Faculty of Mechanical Engineering, Vuka Karadžića 30, East Sarajevo, RS, Bosnia and Herzegovina, [aleksija.djuric@ues.rs.ba](mailto:aleksija.djuric@ues.rs.ba)

BILJANA MARKOVIĆ

University of East Sarajevo, Faculty of Mechanical Engineering, Vuka Karadžića 30, East Sarajevo, RS, Bosnia and Herzegovina, [biljana.markovic@ues.rs.ba](mailto:biljana.markovic@ues.rs.ba)

DRAGAN MILČIĆ

University of Niš, Faculty of Mechanical Engineering, Aleksandra Medvedeva 14, Niš, Serbia, [dragan.milcic@masfak.ni.ac.rs](mailto:dragan.milcic@masfak.ni.ac.rs)

SRĐAN SAMARDŽIĆ

University of East Sarajevo, Faculty of Mechanical Engineering, Vuka Karadžića 30, East Sarajevo, RS, Bosnia and Herzegovina, [srdjan.samardzic@ues.rs.ba](mailto:srdjan.samardzic@ues.rs.ba)

MIODRAG MILČIĆ

University of Niš, Faculty of Mechanical Engineering, Aleksandra Medvedeva 14, Niš, Serbia, [miodrag.milcic@masfak.ni.ac.rs](mailto:miodrag.milcic@masfak.ni.ac.rs)

NATAŠA ZDRAVKOVIĆ

University of Niš, Faculty of Mechanical Engineering, Aleksandra Medvedeva 14, Niš, Serbia, [natasa.zdravkovic@masfak.ni.ac.rs](mailto:natasa.zdravkovic@masfak.ni.ac.rs)

---

**Abstract:** *The additive technologies such as 3D printing are an important part of all branches of industry, primarily due to the possibility of production parts with complex geometries. The aim of the research presented in this paper is the analyze of joining 3D printed polymer parts with adhesive. Furthermore, the aim of this research is to analyze the strength of lap adhesive joints under different loads. FDM technology, PLA materials and two-component epoxy adhesive were used to fabricate the testing specimens.*

**Keywords:** *FDM technology, PLA materials, two-component epoxy adhesive*

### 1. INTRODUCTION

The application of additive technologies, such as 3D printing, today is not only focused on the rapid prototyping, but also on the production of functional parts and tools for the needs of various branches of industry [1, 2]. The number of patent applications related to 3D printing grew at an average annual rate of 36% from 2015 to 2018, more than ten times the average annual growth of all applications filed with the European Patent Office in the same period combined [3]. One of the most common additive manufacturing technology is Fused Deposition Modelling (FDM) and Polylactic acid (PLA) is the one of most used raw material [4-6]. One of the biggest disadvantages of the commercial use of 3D printers with FDM technology is the limited build volume for the production of parts, and therefore there is often a need to apply joining technologies to produce functional parts of larger dimensions [7]. A review of the literature in the field of joining polymeric materials was provided by Silva

et al. [8]. It was concluded that the most commonly used technologies are adhesive joining, mechanical joining and welding. Generally, adhesive bonding has the advantage for application to other technologies due to avoiding stress concentrations, high strength-to-weight ratio, and ease of fabrication [9, 10]. Furthermore, the research presented in this paper will analyze the joining of 3D printed polymer parts with two-component epoxy adhesive.

Adhesive bonding is a constantly growing research field due to the increasing interest it receives from industries such as the automotive, aerospace, marine, and military industry [11-15]. The research activity in this field can be divided into several sub-disciplines, such as adhesive materials, design and manufacturing concepts, and modelling approaches. Two-component polyurethanes have been developed as an alternative to the conventional one-component materials, being used in structural applications, with high ductility and fracture toughness [16]. Phases in the adhesive bonding process are shown in Figure 1. One of the important parts of the adhesive

joining process is surface preparation. The method of surface preparation prior to bonding is crucial for optimum joint performance and has a significant impact on the quality of the adhesively bonded joint [9].

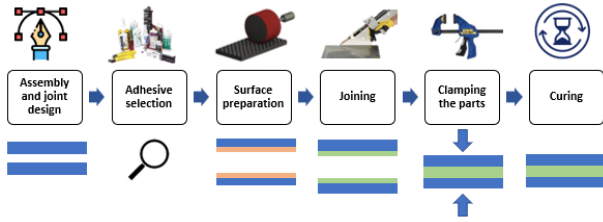


**Figure 1.** Phases in the adhesive bonding process [17]

Depending on the position of the parts to be joined, the following various types of adhesive joints are distinguished: single lap joint, double lap joint, tapered lap joint, scarf joint, butt joint, strap joint, double strap joint, tapered double strap joint, and stepped lap joint [17]. The commonly used adhesive joint configuration in load carrying structures is the single lap joint (SLJ). Despite its apparent simplicity, the stress and strain states and the failure mechanisms in SLJs are complex [18].

Adhesive lap-shear bond strength is determined by stressing a single-overlap joint between rigid adherends in shear by the application of a tensile force parallel to the bond area and to the major axis of the specimen. For testing single-lap joints reference is standard ISO 4587 [19]. During the tensile-shear testing, the adhesive is going to fail only in shear. The shear stress value is equal to the average shear stress on the adhesive layer. The peak shear stress occurs at the ends of the bonded area [20]. On the other hand, the failure mode of adhesive joints can be different, and it's an important quality characteristic of adhesive joints. As the reference for failure mode analysis is normally used standard ISO 10365 [21]. But, generally there are four main failure modes in the adhesive single lap joints during the tensile-shear test: (a) Adhesive fracture (AF); (b) Adhesive-cohesive fracture (ACF); (c) Cohesive fracture (CF); (d) Subtractive fracture (SF) [22].

## 2. ADHESIVE JOINTS OF PLA POLYMER 3D PRINTED PARTS - STATE OF THE ART

Mohammad Reza Khosravani et al. [10] investigated mechanical performance, structural integrity and failure behaviors of single lap joints with 3D printed PLA adherends. It was concluded that using the standard tensile test, the cohesive failure mode is the dominant failure mode on single-lap joints, regardless of the printing parameters of the PLA adherends and the adhesive thickness.

The results of tensile-shear tests of the single-lap adhesive joints of PLA adherends produced with additive manufacturing are presented in the study by Atahan M. G. et al. It showed almost linear load-displacement variations and a sudden failure. The load capability was increased slightly with an increasing loading rate due to the strain-hardening property of both PLA and adhesive materials.

The failure initiated at the free edge of the top adherend-adhesive interface propagated a small distance along this interface. The top adherend failed suddenly through the adherend (cross-section) thickness.

Franziska Bürenhaus et al. [24] investigated, inter alia, the influence of the adhesive type on the bond strength. The parts to be investigated were made of ULTEM 9085. Six different adhesives (acrylate resin, polyurethane adhesive, and epoxy resins) and their compatibility with the ULTEM 9085 parts are investigated. The results show that the maximum lap-shear strength can be achieved by using two-component epoxy resins.

The research of Uğur Kemiklioğlu et al. [25] uses three-dimensional 3D printed materials, polyethylene terephthalate glycol and polylactic acid, and two adhesive types with ductile and brittle properties for single lap joints, analyzing their mechanical performance through tensile-shear testing. Adhesively bonded joints were produced with 0.2, 0.3 and 0.4 mm bonding thickness. Results reveal that auxetic adherends exhibit higher strength compared to flat surfaces. Interestingly, the strength of ductile adhesives in auxetic bonded joints increases with adhesive thickness, while brittle adhesive strength decreases with thicker auxetic bonds.

Many studies [26-29] in recent years have dealt with analyzing factors influencing the strength of the adhesive joint of parts 3D printed made of PLA and other polymer. Common to all studies is that the load capacity is significantly influenced by the quality of the surface of the 3D printed parts, as well as the thickness of the adhesive, the type of adhesive.

Based on the analyzed state of the art, it was decided that the subject of this study will be the analysis of the influence of the surface quality of 3D printed parts made of PLA on the load capacity of the adhesive joint. The contribution of this study is reflected in the application of the type of adhesive that contains beads that control the constancy of the thickness of the adhesive layer over the entire bonded surface.

## 3. EXPERIMENTAL PROGRAM

### 3.1. Experimental set-up

To achieve the aim of the paper, it is necessary to test the single-lap adhesive joints of 3D printed specimens by the recommendations of the standard ISO 4587:2003 [30]. A 3D printer Creator 3 Pro (FlashForge, China) was used for printing the test adherends with dimensions shown in Figure 2. The Creator 3 Pro is a professional and industrial IDEX (Independent Dual Extrusion) 3D printer. Usage of this printed it is possible to print two objects at the same time, either a copy or a mirrored version. For 3D printing of adherends was used mirrored mode. The layout of adherends for 3D printing, as well as the setting of parameters, was arranged in the FlashPrint (FlashForge, China) software. Figure 3 shows the layout of the samples (adherends) for printing, while Table 1 shows the parameters used for 3D printing.

PolyLite™ PLA material (Polymaker, China) is used for the 3D printing of adherends. The properties of PolyLite™ PLA 3D printing material are given in Table 2.

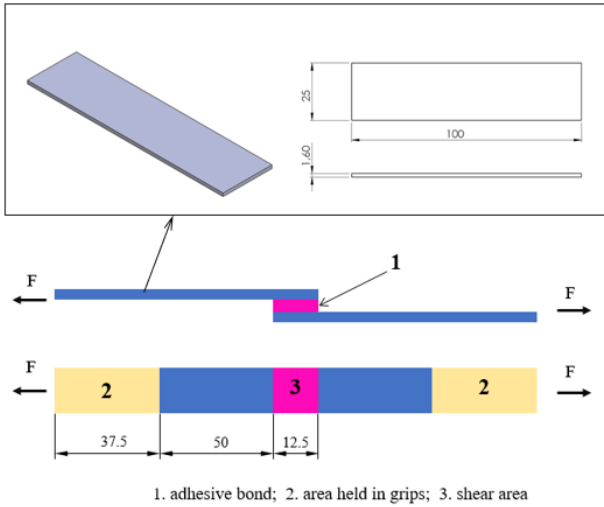


**Figure 2.** Dimensions of the specimens according to the recommendations of the standard ISO 4587:2003

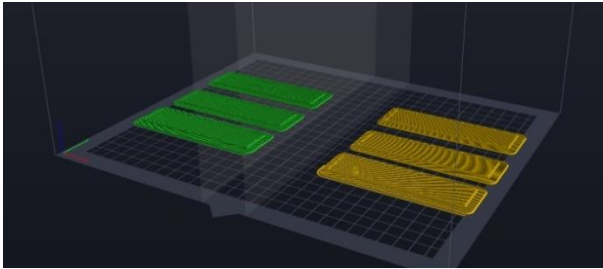


**Figure 3.** Layout of the adherends (mirror mode)

**Table 1.** 3D printing parameters

Parameters	Typical value
Technology	FDM
Nozzle quantity	2
Nozzle temperature	200 °C
Bed temperature	55 °C
Printing speed	50 mm/s
Infill	100 %
Layer thickness	0.18 mm
Starting angle	45°
Crossing angle	90°

**Table 2.** The properties of PolyLite™ PLA material

Property	Typical value
Density	1.17 - 1.24 (g/cm <sup>3</sup> at 21.5 °C)
Young's modulus (X-Y)	2636 ± 330 (MPa)
Tensile strength (X-Y)	46.6 ± 0.9 (MPa)
Elongation at break (X-Y)	1.9 ± 0.2 (%)
Charpy impact strength	2.7 ± 0.2 (kJ/m <sup>2</sup> )

The appearance of the adherends after 3D printing is shown in Figure 4. The side of the sample that was on the platform is called the back side, and the opposite side is the front side.

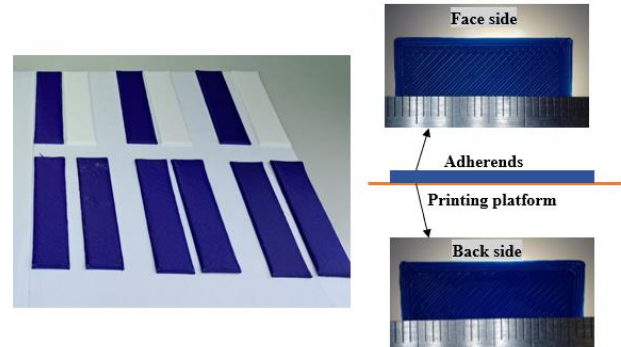


**Figure 4.** The appearance of the adherends after 3D printing

To determine the possible influence of surface quality on the load capacity of the adhesive joint of 3D printed adherends, two adherends were bonded face to face side, two adherends were bonded face to back side, and two adherends were bonded back to back side.

The test specimens are marked as follows:

- A1 and A2 - adhesion between back and back side;
- B1 and B2 - adhesion between face and face side;
- C1 and C2 - adhesion between face and back side.

The adhesive that was used in this study is a structural two-component epoxy adhesive SikaPower®-1277 (Sika, Switzerland). SikaPower®-1277 cures at room temperature has good non-sag properties, and contains glass beads of 0.3 mm to ensure an optimal bonding thickness. The characteristics of adhesive are given in the Product data sheet [31].

Before adhesion, the adherends were sanded with P120 grit sandpaper and cleaned with Sika Cleaner P. The bonding was done at room temperature (around 23 °C), and a thin layer of adhesive was applied (the thickness is controlled by glass beads of 0.3 mm). To apply the adhesive, the gun HDM 500 manufactured by HILTI was used with a nozzle for mixing the components in a ratio of 2:1. The nozzle recommended by the adhesive manufacturer was used. After joining the two materials, additional plastic clamps were set in order to avoid movement during curing. Curing lasted 72 hours at room temperature. The complete adhesive procedure is shown in Figure 5.

The tensile-shear tests were done on SHIMADZU AGS-X 20 kN (SHIMADZU, Kyōto, Japan) test machine. The speed of the cross-head was 2 mm/min. Aim of the test was to determine the failure load and failure mode of the adhesive joint.



**Figure 5.** Adhesive joining procedure of 3D printed adherends

### 3.2. Results and discussion

Fig. 6 shows the force-displacement curve for three adhesive joints of 3D printed adherends. The failure load value achieved during the test is given in Table 3. The failure load for all specimens ranged from approximately 1000 N to 1350 N and a clear conclusion can be drawn that the adhesion process in this case did not influence the load capacity of the joint.

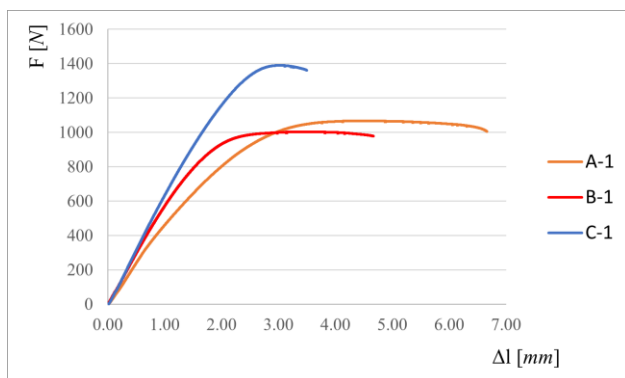


**Figure 6.** Force-displacement curve for three 3D printed adherends.

**Table 2.** The properties of PolyLite™ PLA material

Mark	The failure load (N)	The average failure load (N)
A-1	1066.93	1135.855
A-2	1204.78	
B-1	1003.38	998.772
B-2	994.164	
C-1	1389.84	1359.67
C-2	1323.50	

The previous claim was additionally confirmed by the fact that all specimens fail in SF (Subtractive fracture) mode (Fig. 7). This type of joint failure shows that the strength of the adhesive is greater than the strength of parts made by 3D printing from PLA material. These results show that with high-quality adhesives, the quality of the surface of the parts obtained by 3D printing from PLA material the load capacity of the joint is not influenced.

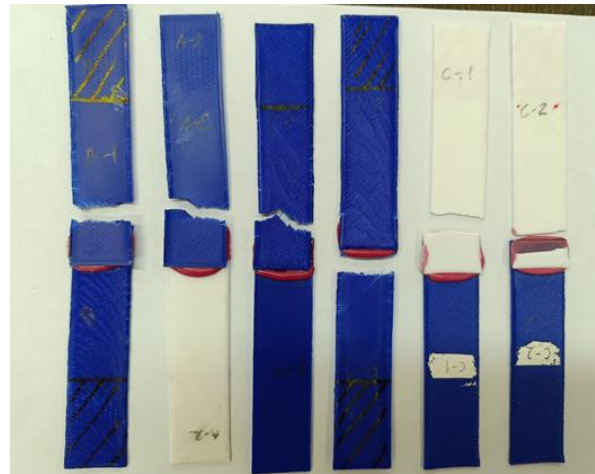


**Figure 7.** The specimens after the tensile-shear test - Subtractive fracture

## 5. CONCLUSION

This research presents the possibility of joining 3D printed parts with adhesion. After the research, the following conclusions were reached:

- 3D printed parts can be very successfully joined using two-component epoxy adhesives;
- SikaPower®-1277 adhesive with glass beads of 0.3 mm was used for joining 3D printed parts, which has a high tensile strength, so all the tested specimens fail in the SF mode. According to previously the quality of the surface of the parts obtained by 3D printing from PLA material does not influence the load capacity of the joint. The failure load for all specimens ranged from 1000 N to 1350 N.
- Proper choice of adhesives for joining parts obtained by 3D printing can significantly facilitate the joining process. Future research directions should be focused on 3D printing materials that have better mechanical properties than PLA materials and application in civil and military industry.

## References

- [1] SHAHRUBUDINA, N., LEEA, T.C., RAMLAN, R.: *An Overview on 3D Printing Technology: Technological, Materials, and Applications*, 2nd International Conference on Sustainable Materials Processing and Manufacturing (SMPM 2019), 2019.
- [2] JANDYAL, A., CHATURVEDI, I., WAZIR, I., RAINA, A., & HAQ, M. I. U.: *3D printing—A review of processes, materials and applications in industry 4.0.*, Sustainable Operations and Computers, 3, (2022) 33-42.
- [3] <https://www.tctmagazine.com/additive-manufacturing-3d-printing-news/european-countries-47-per-cent-3d-printing-patents/> 10.07.2024.
- [4] TÜMER, E. H., ERBİL, H. Y.: *Extrusion-based 3D printing applications of PLA composites: a review*, Coatings, 11(4), 2021.
- [5] MAZURCHEVICI, A. D., NEDELCO, D., POPA, R.: *Additive manufacturing of composite materials by FDM technology: A review*, IJEMS 27(2) (2020) 179-192.
- [6] SUBRAMANIAM, S. R., SAMYKANO, M., SELVAMANI, S. K., NGUI, W. K., KADIRGAMA, K., SUDHAKAR, K., IDRIS, M. S.: *3D printing: overview of PLA progress*, In AIP conference proceedings 2059 (1) (2019).
- [7] TIWARY, V. K., P, A., MALIK, V. R.: *An overview on joining/welding as post-processing technique to circumvent the build volume limitation of an FDM-3D printer*, Rapid prototyping journal, 27(4) (2021), 808-821.
- [8] SILVA, L. R. R., MARQUES, E. A. S., DA SILVA, L. F.: *Polymer joining techniques state of the art review*, Welding in the World, 65(10) (2021), 2023-2045.
- [9] ZDRAVKOVIĆ N, KLOBČAR D, MILČIĆ D, ZUPANČIĆ M, ŽUŽEK B, MILČIĆ M, ĐURIĆ A.: *Influence of Surface Preparation of Aluminum Alloy AW-5754 and Stainless Steel X5CRNI18-10 on the Properties of Bonded Joints*, Materials, 17(11) (2024) 2561.
- [10] KHOSRAVANI, M. R., SOLTANI, P., WEINBERG, K., REINICKE, T.: *Structural integrity of adhesively bonded 3D-printed joints*, Polymer Testing, 100 (2021) 107262.
- [11] CAVEZZA, F., BOEHM, M., TERRY, H., & HAUFFMAN, T.: *A review on adhesively bonded aluminium joints in the automotive industry*, Metals, 10(6) (2020) 730.
- [12] HART-SMITH, J. *Aerospace industry applications of adhesive bonding*. In *Adhesive bonding*, Woodhead Publishing, (2021) 763-800.
- [13] DELZENDEHROOY, F., AKHAVAN-SAFAR, A., BARBOSA, A. Q., BEYGI, R., CARDOSO, D., CARBAS, R. J. C., DA SILVA, L. F. M. *A comprehensive review on structural joining techniques in the marine industry*, Composite Structures, 289 (2022) 115490.
- [14] BAUTISTA, A., CASAS-RODRIGUEZ, J. P., SILVA, M., PORRAS, A.: *A dynamic response analysis of adhesive-Bonded single lap joints used in military aircrafts made of glass fiber composite material under cyclic impact loading*, International Journal of Adhesion and Adhesives, 102 (2020) 102644.
- [15] DESCHEPPER, D., GRAY, D., MOY, P., WALTER, T., JENSEN, R., POLLUM, M., REARICK, B. (2024). *Testing Military-Grade Adhesive in Extreme Loading Conditions*, Distribution statement, (2024).
- [16] BORGES, C. S., AKHAVAN-SAFAR, A., TSOKANAS, P., CARBAS, R. J., MARQUES, E. A., DA SILVA, L. F.: *From fundamental concepts to recent developments in the adhesive bonding technology: a general view*, Discover Mechanical Engineering, 2(1) (2023) 8.
- [17] ĐURIĆ, A., KLOBČAR, D., MILČIĆ, D., MARKOVIĆ, B., SAMRADŽIĆ, S., ZDRAVKOVIĆ, N., MILČIĆ, M.: *Analysis of the possibility of joining DP steel and CFRP with epoxy adhesive and hybrid joining technology*, The 12th International Conference on Machine and Industrial Design in Mechanical Engineering (KOD 2024), Balatonfüred, Hungary, 2024.
- [18] NATU, A. V., ANKIT, R. S., NITINKUMAR, R. A.: *Variation of Adhesive Strength in Single Lap Joint (SLJ) with Surface Irregularities*, American Journal of Mechanical Engineering, 7 (2) (2019), 61-67.
- [19] ISO 4587:2003 - Adhesives — Determination of tensile lap-shear strength of rigid-to-rigid bonded assemblies.
- [20] SHAIKH, S., ANEKAR, N., KANASE, P., PATIL, A., TARATE, S.: *Single lap adhesive joint (SLAJ): a study*. Int. J. Eng. Technol, 7 (2) (2017) ,64-70.
- [21] ISO 10365:2022 - Adhesives — Designation of main failure patterns.
- [22] MARKOVIĆ, B., ĐURIĆ, A., & PERENDIJA, M.: *Research of adhesive Al-sheet joints in the development of lightweight structures*, Acta Technica Corviniensis-Bulletin of Engineering, 16(2) (2023), 1-6.
- [23] ATAHAN, M. G., APALAK, M. K.: *Loading-rate effect on tensile and bending strength of 3D-printed polylactic acid adhesively bonded joints*, Journal of Adhesion Science and Technology, 36(3) (2022), 317-344.
- [24] BÜRENHAUS, F., MORITZER, E., HIRSCH, A.: *Adhesive bonding of FDM-manufactured parts made of ULTEM 9085 considering surface treatment, surface structure, and joint design*, Welding in the World, 63 (2019), 1819-1832.
- [25] KEMIKLIOĞLU, U., DEMIR, S., & YÜKSEL, C.: *Mechanical behavior investigation of fused deposition modeling joints by using different bonding geometry with variable adhesive thickness*, Rapid Prototyping Journal, 30(3) (2024), 547-554.
- [26] TIWARY, V. K., PADMAKUMAR, A., & MALIK,

- V.: *Adhesive bonding of similar/dissimilar three-dimensional printed parts (ABS/PLA) considering joint design, surface treatments, and adhesive types*, Proceedings of the Institution of Mechanical Engineers, Part C: Journal of Mechanical Engineering Science, 236(16) (2022), 8991-9002.
- [27] BRANCEWICZ-STEINMETZ, E., VALVERDE VERGARA, R., BUZALSKI, V. H., SAWICKI, J.: *Study of the adhesion between TPU and PLA in multi-material 3D printing*, Journal of Achievements in Materials and Manufacturing Engineering, 115(2) (2022).
- [28] ANAÇ, N.: *Assessment of adhesively bonded joints of similar and dissimilar materials: industrial case study*, Processes, 11(5) (2023), 1312.
- [29] BRANCEWICZ-STEINMETZ, E., SAWICKI, J., & BYCZKOWSKA, P.: *The influence of 3D printing parameters on adhesion between polylactic acid (PLA) and thermoplastic polyurethane (TPU)*, Materials, 14(21) (2021), 6464.
- [30] ISO 4587:2003 - Adhesives — Determination of tensile lap-shear strength of rigid-to-rigid bonded assemblies
- [31] PRODUCT DATA SHEET - SikaPower®-1277 Version 04.01 (04 - 2022).



## CORROSION PROPERTIES OF LOW-CARBON STEEL WELDED JOINT IN SYNTHETIC SEA WATER ENVIRONMENT

MIHAEL BUČKO

University of Defense Belgrade, Military Academy, [mbucko@tmf.bg.ac.rs](mailto:mbucko@tmf.bg.ac.rs)

MILAN JOVANOVIĆ

Military Technical Institute, 11000 Belgrade

SRETEN PERIĆ

University of Defense Belgrade, Military Academy, 11000 Belgrade

DRAGANA LAZIĆ

Military Technical Institute, 11000 Belgrade

JELENA MARINKOVIĆ

Military Technical Institute, 11000 Belgrade

RADOVAN RADOVANOVIĆ

The Academy of Criminalistic and Police Studies, 196 Cara Dusana Street, 11080 Belgrade

**Abstract:** In this study corrosion properties of welded joint of low carbon steel were tested. The welded joint was made using S355JR steel by the metal inert gas technique (MIG welding process). Corrosion properties of used base metal (BM) and welded joint were investigated by the electrochemical techniques including open circuit potential, electrochemical impedance spectroscopy and potentiodynamic polarization. All tests were conducted in 3.5 wt.% NaCl solution. The obtained results show that the lowest corrosion rate is present on the welded joint surface. This interesting result may be explained by the difference in the chemical composition of welded joint and base metals. Namely, the carbon content is the lowest in the welded joint, and consequently, the density of cathodic sites is the lowest in this area, as compared to the base metal parts.

**Keywords:** welded joints; corrosion behavior; polarization; EIS

### 1. INTRODUCTION

Low-carbon steels, containing less than 0.25% C, are widely used in structural applications due to their excellent mechanical properties, good formability and weldability. Their vast application is recognized in various industries such as automotive, civil engineering, and oil industry, for structural parts (beams, turbine blades, pipes, etc). [1,2]. Their strength and ductility make it suitable for the demanding conditions of semi-trailer structures, providing durability and reliability in transport applications [3,4]. Generally, carbon steel has been the popular choice of structural material as it is abundantly available, inexpensive with the adequate mechanical properties, but it has a good general corrosion rate [5].

When a welded structure is exposed to water containing corrosion-aggressive ions such as chloride ions, corrosion becomes severe, even in a short period of exposure [5]. Corrosion of low-carbon MIG-welded joint can be influenced by several factors, including chemical composition of the base metal, the quality of the welded

joint and environmental conditions. The weld metal may exhibit different corrosion resistance compared to the base metal due to change in microstructure and chemical composition. Differences in carbon content, as well as welding parameters lead to different microstructural morphologies formed in weld metal compared to base metal. With increase of carbon content, the corrosion rate increases too. Content of the ferrite phase decreases as carbon content increases, which leads to the increase of the cathode – anode area ratio of a galvanic couple. This is because corrosion forms on ferrite phase (anode) prior to cementite (cathode). Consequently, the corrosion is accelerated with the increase of carbon content [6]. The corrosion rate is the rate at which each metal deteriorates in a particular environment [7].

In this research, corrosion behavior of the MIG welded low-carbon steel joint was monitored through the change of electrochemical parameters of the weld metal and the base metal. Corrosion test was performed by electrochemical methods for all specimens in environment of 3.5% NaCl solution.



## 2. EXPERIMENTAL WORK

### 2.1 Materials

Low carbon steel was used for fabrication of the welded joint using MIG welding method.

Corrosion tests were carried out on a sample taken from cross section of the welded joint. Sample, for further electrochemical testing, was prepared by using grinding and polishing techniques. Revealing the macroscopic appearance of welded joint was done by etching in 3% Nital reagent and recording on stereomicroscope „Leica“.

### 2.2 The chemical composition of the samples

The chemical composition of the base materials (BM) and the weld metal (WM) was determined by optical emission spectrometry on BELEC Compact Port HLC device. The determination of steel quality was carried out in accordance with the SRPS EN 10025-2 standard [8].

### 2.3 Electrochemical Methods

The instrument Gamry Interface 1010E Potentiostat/Galvanostat/ZRA was used for electrochemical measurements. The 3.5 wt.% aqueous NaCl solution, open to the air at room temperature, was regarded as electrochemical corrosion medium simulating sea environment. The corrosion tests were performed in an electrochemical cell with three electrodes: saturated calomel (SCE) as a reference, platinum as a counter electrode, and the steel part as the working electrode. The base metal and the weld metal were working electrodes with an exposed area of 1.0 cm<sup>2</sup>. To establish a stationary state, i.e., a stable open circuit potential, the steel plate was immersed in the test solution for 1h prior to all electrochemical measurements. Impedance measurements were performed at open circuit potential in the frequency range from 0.01 Hz to 100 kHz with 10 points per decade using a 10 mV amplitude of sinusoidal voltage, and polarization measurements were performed in the potential range from -250 mV to +250 mV vs.  $E_{corr}$ . All electrochemical tests were performed at 298 K. The obtained data were analyzed using the Gamry E-Chem Analyst software package.

## 3. RESULTS AND DISCUSSION

### 3.1 Material

Macroscopic appearance of the cross section of the welded joint is shown in Figure 1.

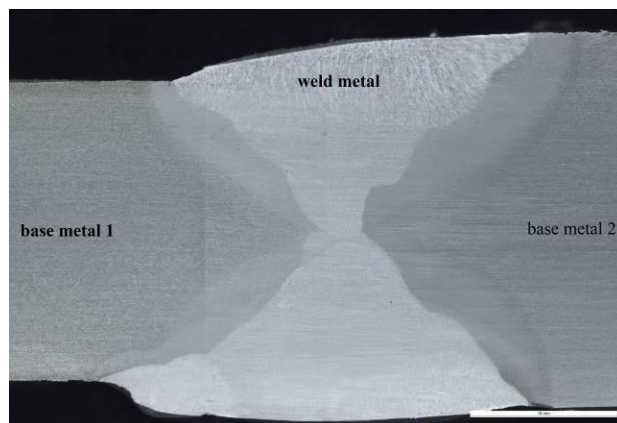


Figure 1. Macroscopic appearance of welded joint.

### 3.2 Chemical composition

The chemical composition of the base metal and welded metal are given in Table 1.

Table 1. Chemical composition, wt. %

	C	Si	Mn	P	S	N	Cu	Fe
BM 1	0.135	0.212	1.315	0.024	0.017	0.005	0.367	Bal.
BM 2	0.224	0.458	1.222	0.016	0.012	0.005	0.178	Bal.
WM	0.099	0.714	1.294	0.012	0.014	0.004	0.105	Bal.

The results of chemical analysis show that both base metals of weldment were made of a low-carbon steel grade S355JR. The carbon content of the three samples differs significantly. The lowest C content is observed at the surface of the weld joint. Although BM1 and BM2 are made of the same metal, their C content differs because the chemical composition analysis at the BM1 has been performed at the spot closer to the welding zone, as compared to the BM2. To conclude, the carbon content in the base metal increases with the distance from the welding zone.

### 3.3 Electrochemical Impedance Spectroscopy Test

Impedance spectra were recorded 1 hour after the application of the corrosion agent, following the establishment of a stable open circuit potential. Experimental data shown in Figure 2 were fitted using the equivalent electrical circuit (Figure 3). The values of polarization resistance of BM1 and BM2, as well as the WM are 1393, 727.7 and 1737 ohm, respectively.

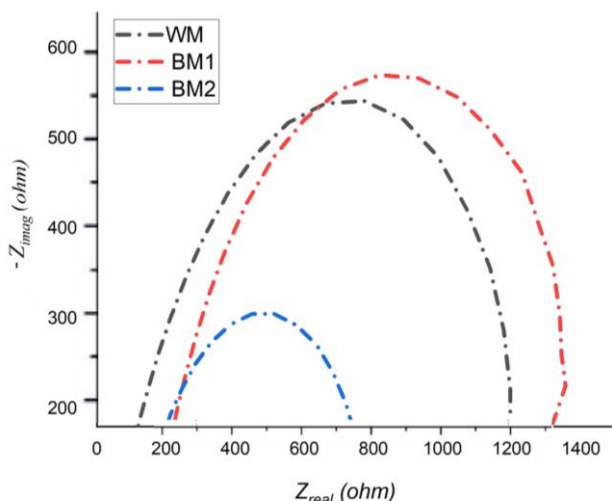


**Figure 2.** Nyquist diagram of BM1, BM2 and WM in 3.5 wt% NaCl solution.

The elements of the equivalent circuit are the electrolyte resistance ( $R_s$ ), the resistance of the charge transfer ( $R_p$ ), and an element with a constant phase angle ( $CPE$ ). The  $CPE$  directly depends on frequency and is often used instead of the capacitance of the passive layer for non-homogeneous surfaces [9,10]. The base metal 1 and welded joint show significantly higher semicircle of the Nyquist loop, in comparison to the base metal 2, showing their increased corrosion resistance. This difference may be explained by the difference in the carbon content. As Table 1 depicts, BM2 possesses the highest carbon content, which produces more cathodic sites on the metal surface.

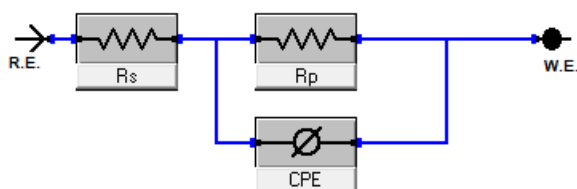


**Figure 3.** Model of the electrical equivalent circuit used to fit EIS data.

### 3.4 Potentiodynamic Polarization Test

The polarization curves for all samples have typical characteristics of active dissolution in 3.5% NaCl aqueous solution [11].

The welded joint shows the most negative corrosion potential in chloride solution. Base materials have more positive corrosion potentials, which differ slightly and are -691 mV and -684 mV, respectively. The test results showed that the WM has the lowest corrosion current density, and therefore the lowest corrosion rate, which means that WM is more corrosion resistant compared to the base material [9]. As mentioned in the impedance analysis, the lowest corrosion rate of the weldment is probably the result of the lowest carbon content, i.e., the lowest number of cathodic sites on the corroding surface.

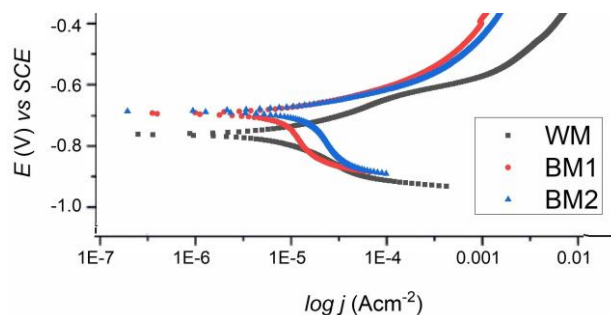


**Figure 4.** Polarization Tafel curves of BM1, BM2 and WM samples.

**Table 2.** Electrochemical parameters of BM1, BM2 and WM obtained from polarization curves in 3.5 wt% NaCl solution.

Sample	$-E_{corr}/mV$	$j_{corr}/\mu A cm^{-2}$	Corrosion rate / $mm y^{-1}$
BM1	691	49	$563 \times 10^{-3}$
BM2	684	70	$805 \times 10^{-3}$
WM	761	11	$129 \times 10^{-3}$

## 5. CONCLUSION

The results obtained from the chemical analysis showed that both base metals and the welded joint are made of a low-carbon steel quality S355JR and that the weldment has the lowest carbon content. Electrochemical methods have shown that the weld metal has the lowest corrosion current density, and therefore the lowest corrosion rate. The lowest corrosion rate of the weldment is probably the result of the lowest carbon content, i.e., the lowest number of cathodic sites on the corroding surface.

## Acknowledgement

This work was supported by the Ministry of Science, Technological Development and Innovations (Serbia), Contract No. 451-03-66/2024-03/200325.

## References

- [1] MAMAT,M.F., HAMZAH,E., Corrosion behavior of low carbon steel welded joint in NaCl solution, *Advanced Materials Research*, 845 (2014) 173-177.
- [2] URADE, V.P., AMBADE, S.P., An overview of welded low nickel chrome-manganese austenitic and ferritic stainless steel, *Journal of Material Science and Engineering*, 5 (2016) 231-237.
- [3] POPOVYCH,P., SHEVCHUK,O., POBEREZHNA,L., KOVAL,Y., POBEREZHNY,L., MUROVANYI,I., HRYTSANCHUK,A., Corrosion-fatigue failure of tractor trailers metal materials in aggressive environments, *KOM – Corrosion and Material Protection Journal*, 64(2) (2020) 45-51.
- [4] MOHAMMAD, HM., Effect of current-welding on the corrosion behavior of low-carbon steel (1020) TIG welding joints, *Journal of Engineering and Sustainable Development*, 24 (2020) 1-8.

- [5] RAZAK,NAA., SHING,SN., Investigation of effects of MIG welding on corrosion behavior of AISI 1010 carbon steel, *Journal of Mechanical Engineering and Sciences (JMES)*, 7 (2014) 1168-1178.
- [6] SUN,F., LI,X., CHENG,X., Effects of carbon content and microstructure on corrosion property of new developed steels in acidic salt solution, *Acta Metallurgica Sinica (English Letters)*, 27(1) (2014) 115-123.
- [7] GRGUR,B., *Korozija i zaštita, Tehnološko-metalurški fakultet, Beograd, 2020.*
- [8] SRPS EN 10025-2 - Toplovaljani proizvodi od konstrukcionih čelika - Deo 2: Tehnički zahtevi za isporuku nelegiranih konstrukcionih čelika
- [9] PAUNOVIC,M., Završni master rad: Koroziona stabilnost i mehanička svojstva zavarenog spoja legure aluminijuma AA6082, TMF, Beograd, 2021.
- [10] WANG,YY., JIANXING,Y., ZHANGD,Y., YAN,Z., QIWEI,Y., Microstructure evolution and corrosion behavior of dissimilar 304/430 stainless steel welded joints, *Journal of Manufacturing Processes*, 50 (2020) 183-191.
- [11] HUANG,BS., YANG,J., LU,DH., BIN,WJ., Study on the microstructure, mechanical properties and corrosion behavior of S355JR/316L dissimilar welded joint prepared by gas tungsten arc welding multi-pass welding process, *Science and Technology of Welding and Joining*, 21 (2016) 1-8.



## ENHANCED METHOD FOR MEASURING MATERIAL RESISTANCE TO BURNING NAPALM MIXTURE

TATJANA MARKOVIC

Military Technical Institute, Beograd,  
[tanjin.mejl@gmail.com](mailto:tanjin.mejl@gmail.com)

MARINA ILIC

Military Technical Institute, Beograd,  
[marinailic1970@gmail.com](mailto:marinailic1970@gmail.com)

ZELJKO SENIC

Military Technical Institute, Beograd,  
[zsenic1@gmail.com](mailto:zsenic1@gmail.com)

SONJA BAUK

Military Technical Institute, Beograd,  
[bauk.sonja@gmail.com](mailto:bauk.sonja@gmail.com)

MILJAN MILETIC

The Academy of Applied Preschool Teaching And Health Studies section in Kruševac, Serbia,  
[mmelektronik1@gmail.com](mailto:mmelektronik1@gmail.com)

**Abstract:** This paper introduces an advanced method for evaluating the resistance of materials to the effects of a burning napalm mixture. This enhanced method integrates more accurate and rapid temperature measurement and control of experimental conditions, advanced thermo graphic and quantitative analysis. The study involves a comparative analysis of thermal resistance results for various protective materials obtained using the new method. The enhanced measurement approach demonstrates significant improvements in data accuracy and processing speed, offering valuable insights into material performance under extreme thermal stress. This advancement is crucial for developing and accessing materials designed for high-temperature resistance applications.

**Keywords:** thermal resistance, material testing, napalm, high-temperature measurement, protective materials, temperature sensors, data accuracy, comparative analysis..

### 1. INTRODUCTION

The method for testing material resistance to burning napalm mixtures was developed to examine the characteristics of military uniforms and protective gear under extreme thermal conditions. Fires and burnings are often a consequence of conventional weapons use, occurring frequently in various types of accidents. Extreme thermal effects are seen during nuclear explosions and when projectiles filled with napalm explode, dispersing the incendiary napalm mixture as drops of varying sizes. Despite international conventions banning the use of napalm and nuclear weapons, these weapons remain in many military arsenals, meaning their use cannot be entirely ruled out [1].

Napalm, a weaponized chemical mixture designed to produce a highly flammable gel-like substance, has garnered attention and concern for its destructive power and inherent toxicity. Its composition, which includes aluminum salts, polystyrene, and benzene, leads to

explosive ignition and devastating effects in military operations. The harmful impacts of napalm exposure and the risk of severe burn injuries from explosive delivery devices are considerable [2].

The original thickening agent in napalm was a blend of naphthenic and palmitic acids, giving rise to the trade name "napalm," though it was more commonly referred to as a firebomb fuel-gel mixture. Numerous variations of the chemicals used in napalm have been developed. The most common modern formulation includes aluminum salts, polystyrene, and benzene. Detonation is achieved through various explosive compounds that ignite phosphorus, which burns at a temperature sufficient to ignite the fuel mixture.

Due to its consistency, napalm adheres to exposed surfaces, increasing its lethality and destructive power. Additionally, its increased viscosity allows the ignited liquid to maintain a directed stream when dispersed under pressure, making it suitable for use in military flamethrowers. Napalm burns at the same temperature as the flammable liquids in its composition, typically

gasoline, kerosene, diesel fuel, or benzene. Direct contact with burning napalm causes full-thickness burns. Extensive contact can lead to a rapid drop in blood pressure, loss of consciousness, and death.

Military uniforms are crafted from high-quality fabrics integrated with flame retardants. These flame retardant textiles are primarily designed to lower ignition susceptibility and slow down flame propagation. Conventional textiles can be made flame retardant through chemical after-treatments, incorporating comonomers into their structures, or by adding flame retardant additives during the extrusion process. High-performance fibers, which possess inherently high levels of flame and heat resistance, require the synthesis of entirely aromatic structures. However, these fibers are expensive and are utilized only when the performance requirements warrant the cost [3, 4].

When exposed to the effects of burning napalm mixture the soldier's clothing, intended to protect the body, is subjected to intense thermal effects that cause it to burn through, resulting in severe burns to the skin. The extent of skin damage depends on several factors, including the intensity of the heat source, duration of heat exposure, the area of skin affected, the mode of heat transfer, the age and health condition of the injured person, and the anatomical structures of the skin exposed to heat. Generally, first-degree burns can be expected in temperature ranges of 40 to 45°C, second-degree burns between 45 and 60°C, and third-degree burns above 60°C.

The following section will describe an advanced method for measuring the resistance of materials to the effects of burning napalm mixture. Additionally, twelve types of materials used in CBRN protection for various protective equipment will be tested [5].

## 2. METHODS AND MATERIALS

### 2.1. Methods

The method for measuring the resistance of materials to the effects of burning napalm mixture consists of a measuring head with seven temperature sensors (Figure 1), a control box, and a display screen for real-time observation of temperature changes (Figure 2). The data is collected by a computer, which provides the results in the form of tables and graphs, showing the temperature change over time during exposure to the napalm mixture (current temperature, average temperature, maximum temperature, and minimum temperature) [6, 7].

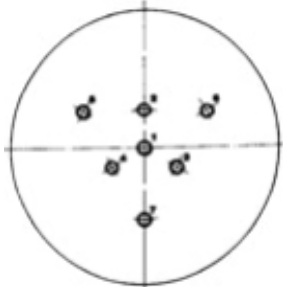


Figure 1. Position of the sensors on the measuring head

The measuring head is first placed on the sample holder, followed by the test material sample on the measuring head. A drop of the prepared napalm mixture with a volume of 2 cm<sup>3</sup> is then dispensed onto the outer surface of the material sample using a syringe and ignited. At the moment the napalm mixture is ignited, temperature measurement and software data processing are initiated. The measurement is conducted over a 60-second interval because the napalm mixture naturally extinguishes itself after 45 to 50 seconds. Materials that do not contain flame retardants burn for a longer duration.

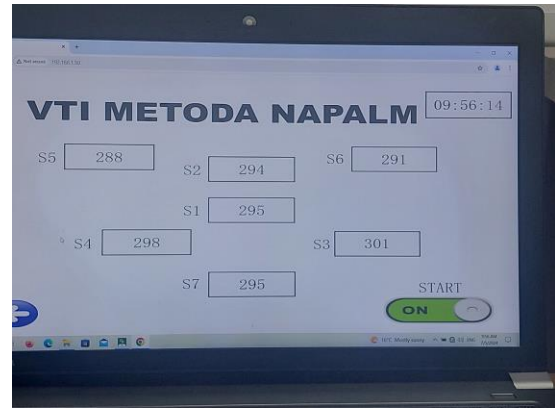


Figure 2. Display screen for real-time observation of temperature changes

Figure 3 illustrates an example of a graph displayed on the device's screen. In this case, the graph shows of the average temperature as a function of the burning time of the napalm mixture. Table 1 provides an example of a table shown on the device's screen after measurements have been taken and shows temperature measurements on temperature sensors S1 to S7, under the Protective coverall M5.

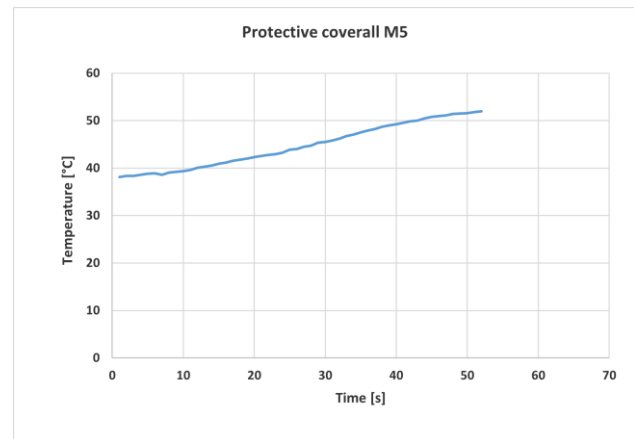


Figure 3. Graph for Protective coverall M5.

Table 1. Temperature measurements on sensors S1 to S7 under the M5 Protective coverall

Protective coverall M5						
N.o.	T <sub>S1</sub> [°C]	...	T <sub>S7</sub> [°C]	Average T [°C]	Min [°C]	Max [°C]
1	40.00		39.90	39.60	36.70	40.70
2	40.40		40.50	40.03	37.10	41.20
3	40.70		40.80	40.29	37.30	41.50
4	41.00		41.10	40.56	37.50	41.90

5	41.30		41.30	40.89	37.90	42.30
6	41.60		41.50	41.11	38.10	42.70
7	42.10		41.90	41.51	38.50	43.20
8	42.40		42.10	41.73	38.70	43.50
9	42.70		42.40	42.00	39.00	43.70

Unlike the old method, which consisted of three procedures based on the visual abilities of the observer, which includes: measuring the burn-through time of the material sample, measuring the temperature on the opposite side of the material exposed to the effects of napalm, and visually assessing the material's behavior, the method provides a more accurate picture by measuring temperature in real-time (measurements per second), utilizing more sensitive temperature sensors capable of detecting changes as small as 0.05 °C. It also collects data and presents the measurements both graphically and in tabular form.

**2.2. Materials**

Various types of materials (insulating and filtering) used for the production of CBRN equipment were tested. These include rubberized materials for the production of protective gloves (Protective gloves M3, M4 in Serbian army and chemical resistant gloves Shown Best 879-09 used by inspector of OPCW), protective overshoes (Protective overshoes M1 in Serbian army and Exoskin B1 CBRN protective boots used by inspector of OPCW), Protective mask M3 and material for decontamination tents, as well as textile materials which consists in an outer layer of nylon/cotton with a water-repellent coating and an inner layer with activated carbon to adsorb a wide library of toxic agents (protective suits OFZ, protective coverall M3, M5 and textile material for Ballistic protective vest).

**3. THE EXPERIMENTAL RESULTS AND DISSCUSION**

Observing various materials burning under a napalm mixture, it can be seen that some materials do not burn through for the entire duration of the napalm mixture's combustion, while others burn through in a very short time (Table 2).

**Table 2.** Burn-through time and maximal temperature

Name of protective gear	Burn-through time [s]	Max temperature [°C]
Protective coverall M3	35 s	85.5
Protective coverall M5	/	56.3
New material M5 PC	/	56
Protective suit OFZ	upper layer 25 s	57
Protective mask M3	/	28.7
Textile material for Ballistic protective vest	8 s	74
Protective gloves M3	15 s	81.2

Protective gloves M4	/	37.8
Material for decontamination tent	/	44.5
Protective overshoes M1 upper part	35 s	64
Protective overshoes M1 sole	/	46.3
Protective gloves OPCW	10 s	69.6
Protective boots OPCW	15 s	50.2

When discussing burns, second and third-degree burns incapacitate soldiers from continuing combat and other activities and necessitate medical treatment. In Figure 4, the maximum temperatures beneath different materials during the burning of the napalm mixture are shown. It is shown that only the materials intended for the M3 mask and the M4 gloves provide adequate protection against burning napalm mixtures and cannot cause first-degree burns.

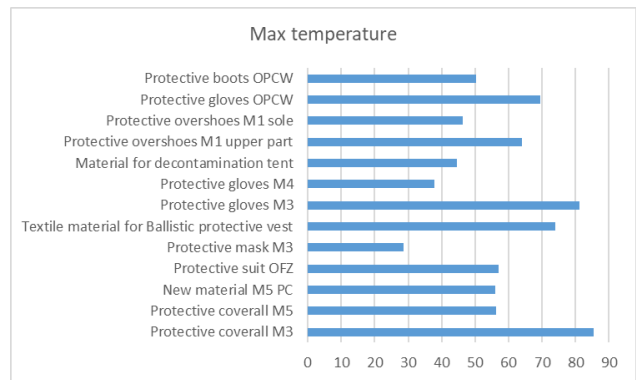


**Figure 4.** The maximum temperatures beneath the material with burning napalm mixture.

During the development phase, protective garments and gear must satisfy a range of tactical and technical requirements before they can be approved for use in armaments and military equipment. Regarding the thermal protective properties of body protection means, they must shield the user from burning napalm mixture for a minimum of 15 seconds.

It is obvious that materials that burn through in a short time may not show high temperatures on the sensors, as they are in brief contact with them, but they certainly do not provide the necessary time protection sufficient to allow a soldier to neutralize the effects of napalm. In this case, the M3 protective gloves, OPCW gloves Shown Best 879-09, and OPCW protective boots Exoskin B1 CBRN do not meet the required standards of thermal protection.

On the other hand, equipment such as the protective coverall M5, protective mask M3, and protective gloves M4, fully meet the thermal protection requirements. They are made from insulating materials such as as elastomers (butyl rubber) and thermoplastics (polyethylene). Insulating gear possess good protective properties but poor thermoregulatory characteristic. Their function is to shield the body, legs, and arms from CBR contamination.

They are used in scenarios involving CBR weapons, decontamination processes, reconnaissance missions, and stays on contaminated grounds, where protection for just a few hours is necessary. Also, the fire resistance of material are improved with additives or coatings. While the specific mechanisms may vary, the goal is to either prevent combustion or increase the thermal energy needed to initiate it. These mechanisms might involve creating an oxygen barrier, stabilizing intermediate pyrolysis products, and forming a char to inhibit the formation of flammable, volatile substances.

The material used for the floor and lower edges of the decontamination tent also falls under insulating materials and provides satisfactory thermal protection. It could be considered to make the roof of the tent from the same insulating material for complete thermal protection.

The textile material for the ballistic protective vest is only a part of the materials used in the vest's construction and does not provide an adequate picture of thermal protection. A ballistic vest is an item of body armor that helps absorb the impact and reduce or stop penetration to the torso by firearm fired projectiles and fragmentation from explosions and is made from aramid, an aromatic polyamide fiber. It is a class of synthetic fibers known for its exceptional strength, heat resistance, and chemical stability. Heat resistance strongly depends on the thickness of the material. Aramid fibers are used in various high-tech applications, including ballistic protection, fire-resistant clothing, composite materials for the aerospace and automotive industries, as well as in high-strength cables and ropes. The most well-known examples of aramid fibers are Kevlar and Nomex, both products of DuPont.

Garments made from filtration materials, such as protective suit OFZ, are superior to those made from isolating materials. They allow for extended stays in contaminated zones and the performance of higher physical and mental tasks. Additionally, these garments provide excellent protection against RCB agents. For personal body protection during prolonged exposure to contaminated environments and while performing strenuous tasks in warm conditions, the filtering protective suit is unrivaled. The materials used in OFZ, unlike those in isolating garments, are permeable to air and water vapor, making them more physiologically suitable and reducing the risk of heat stress during task execution. The protective suit OFZ consists in an outer layer of nylon/cotton with a water-repellent coating and an inner layer with activated carbon to adsorb a wide library of toxic agents. This filtering material demonstrated good protection against burning napalm mixtures as it did not completely burn through during exposure to the burning napalm mixture.

In Figure 5, it can be seen that the OFZ material reaches a temperature of 40-45°C in 35 seconds, which provides sufficient time for the development of procedures and timeframes that a soldier can use to mitigate the effects of napalm.

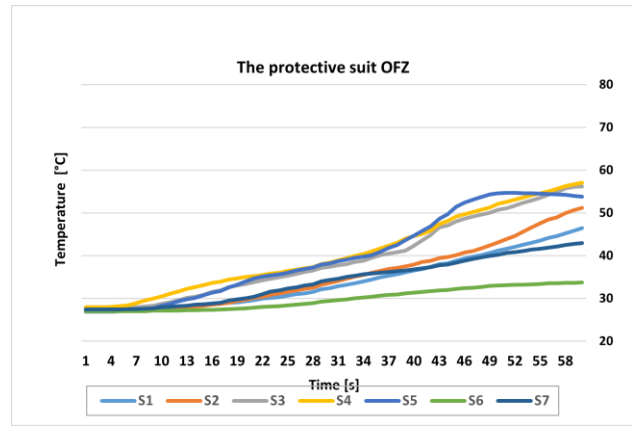


Figure 5. The temperatures beneath the OFZ material with burning napalm mixture (S1 to S7 are temperature measurements on seven sensors).

Additionally, the graph shows that the material does not transfer heat evenly, so areas not affected by the napalm mixture will not cause burns.

Similarly, the following conclusions can be drawn for the other materials: protective suits M5 and M3 do not adequately protect against burns. M5 barely covers a period of 15 seconds, while M3 cannot provide protection for less than 12 seconds (Figure 6 and 7).

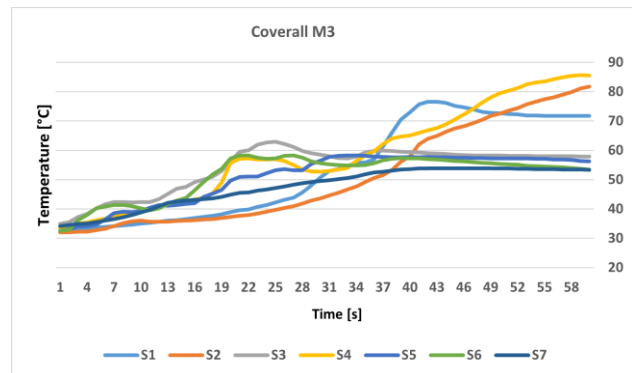


Figure 6. The temperatures beneath the material M5 coverall with burning napalm mixture (S1 to S7 are temperature measurements on seven sensors).

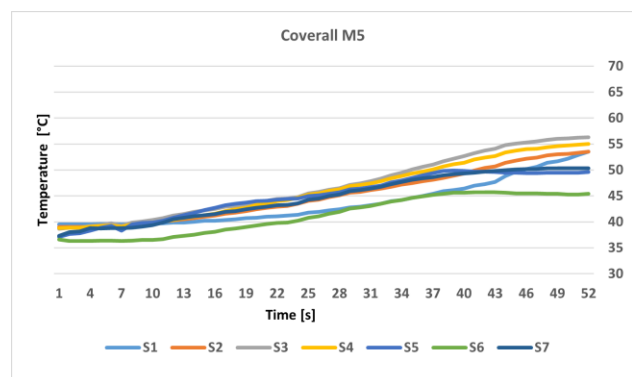


Figure 7. The temperatures beneath the material M3 coverall with burning napalm mixture (S1 to S7 are temperature measurements on seven sensors).

## 4. CONCLUSION

From the above, it can be inferred that this method incorporates more precise and faster temperature measurement and control of experimental conditions, along with advanced thermographic and quantitative analysis compares to the old method based on measuring the burn-through time of the material sample and the temperature on the opposite side of the material exposed to the effects of napalm. This enhanced approach significantly improves data accuracy and processing speed, providing valuable insights into material performance under extreme thermal stress. This progress is essential for developing and evaluating materials intended for high-temperature resistance applications.

The tested materials exhibited varying levels of resistance to burning napalm mixtures, with OFZ showing the best thermal resistance among textile materials, and M4 gloves and M3 mask demonstrating superior insulating properties due to the added flame retardants. These findings underscore the importance of enhancing thermal resistance to ensure adequate protection in extreme conditions.

## References

- [1] .D. McLean, Burns and Military Clothing, J. R. Army Med. Corps 147 (2001) 97–106.
- [2] Gregory T. Guldner; Richard J. Chen; Curtis Knigh, Napalm Toxicity, National Library for Medicine, January 2024.
- [3] F. Hull, J. Gambill, A. Hansche, G. Agni, J. Evangelista, C. Powell, M. Auerbach, J. Dillon, Ö. Arnas, Engineering an undergarment for flash/flame protection, Proceedings, ASME-IMECE 2011-63888, Denver, CO, 2011
- [4] Nelly Couzon a, Jérémy Dhainaut a, Christine Campagne b, Sébastien Royer a, Thierry Loiseau a, Christophe Volkringer, Porous textile composites (PTCs) for the removal and the decomposition of chemical warfare agents (CWAs) – A review, Coordination Chemistry Reviews Volume 467, 15 September 2022, 214598.
- [5] Dusan S. Rajic, Zeljko J. Kamberovic, Radovan M. Karkalic, Negovan D. Ivankovic, Zeljko B. Senic, Thermal resistance testing of standard and protective filtering military, Hem. Ind. 67 (6) 941–950 (2013)
- [6] Z. Senic, M. Jevremovic, R. Karkalic, Determination of the resistance of soldiers garment means to the he effect of burning napalm mixture, OTEH, 2007.
- [7] SORS 6704:1988, RCB body protection – Test method for resistance of materials to the effects of napalm mixture, Direction for Standardization, Codification and Metrology, Ministry of Defense, Republic of Serbia.





## STRUCTURAL AND MAGNETIC PROPERTIES OF CoFeSiB AMORPHOUS WIRE GMI ELEMENT

NEBOJŠA MITROVIĆ

Faculty of Technical Sciences Čačak, University of Kragujevac, Serbia, [nebojsa.mitrovic@ftn.kg.ac.rs](mailto:nebojsa.mitrovic@ftn.kg.ac.rs)

JELENA ORELJ

Faculty of Technical Sciences Čačak, University of Kragujevac, Serbia, [jelena.orelj@ftn.kg.ac.rs](mailto:jelena.orelj@ftn.kg.ac.rs)

BORIVOJE NEDELJKOVIĆ

Faculty of Technical Sciences Čačak, University of Kragujevac, Serbia, [borivoje.nedeljkovic@ftn.kg.ac.rs](mailto:borivoje.nedeljkovic@ftn.kg.ac.rs)

RADOSLAV SURLA

Military Technical Institute, Belgrade, Serbia, [ekorade@gmail.com](mailto:ekorade@gmail.com)

VLADIMIR PAVLOVIĆ

Faculty of Agriculture, University of Belgrade, Serbia, [vlaver@agrif.bg.ac.rs](mailto:vlaver@agrif.bg.ac.rs)

**Abstract:** In this study, the amorphous soft magnetic  $Co_{68.15}Fe_{4.35}Si_{12.5}B_{15}$  wires prepared by the conventional in-rotating water melt-spinning technique were investigated. The XRD pattern of the as-cast wire sample exhibits a very weak diffusive peak that reveals the amorphous structure. The DTA thermogram shows one exothermic process, which results from crystallization with a peak temperature of 566 °C. The XRD pattern of the sample annealed at 700 °C shows the presence of two diffraction peaks: the first could be ascribed to the crystal phase  $\epsilon$ -CoSi (structure of P2 order), and the second could belong to crystal phases  $Co_2B$  and  $\epsilon$ -CoSi (P2 order).

The giant magnetoimpedance (GMI) frequency behavior (ranging from 50 Hz to 5 MHz) was monitored as a function of an external dc magnetic field applied parallel to the wire sample. The critical frequency of about 5 kHz - 7 kHz was observed with the initial increase of MI. In the medium frequency range (which usually starts at about 1 MHz) the skin effect and the magnetization vector rotation mechanism are dominant in the process of circular magnetization (the movement of the magnetic domain walls is blocked). Therefore, the shape of dependence of the MI-ratio on the external DC magnetic field changes significantly and the appearance of a peak is recorded. The attained peak value of the impedance modulus of about 35  $\Omega$  was registered at the highest frequency of 5 MHz. The maximum GMI ratio of 334% was recorded at a frequency of 0.95 MHz (@ 7.72 kA/m).

**Keywords:** Co-rich amorphous wires, in-rotating water melt spinning, ac Joule-annealing, GMI element

### 1. INTRODUCTION

The magnetoimpedance (MI) effect observed in soft magnetic wires or ribbons or thin films is one of the most interesting phenomena that can be exploited for magnetic sensors and related devices [1-3]. The impedance of ferromagnetic amorphous wires is a function of a few parameters: the operating frequency  $f$ , the intensity and orientation of the external dc magnetic field  $H_{ex}$ , and the amplitude of the alternating current  $I_{cc}$  flowing through the sample, i.e.  $Z(H_{ex}, f, I_{cc})$  [4, 5]. The MI-effect is the result of the interactions of an external dc magnetic field with magnetic domains whose structure depends on the internal stresses evolved during the rapidly quenching process of the alloy melt in-rotating water melt-spinning technique used to produce amorphous wires. In amorphous ferromagnetic wires with a negative magnetostriction coefficient (cobalt-based alloys  $Co_{68.15}Fe_{4.35}Si_{12.5}B_{15}$ ), the domain structure consists of the

internal magnetic domain, surrounded by circular domains alternately distributed along the direction of the wire [6, 7].

In order to analyze the influence of operating frequencies on the MI-effect, two frequency ranges were examined:

(a) the low-frequency range (from about 10 kHz to about 1 MHz) in which the domain wall displacement effect is dominant [8]; and

(b) the beginning of medium frequencies (from 1 MHz to 5 MHz) in which the main influences are the skin effect and the rotation of the magnetization vector as a mechanism of the circular magnetization process (the movement of the domain walls is blocked) [9].

This paper presents structural and magnetic properties of  $Co_{68.15}Fe_{4.35}Si_{12.5}B_{15}$  amorphous wires, which exhibit giant magnetoimpedance effect (GMI), i.e. they have a value of a few hundred percent of a MI ratio ( $\Delta Z/Z (\%) = 100 \% \cdot [|Z(H)| - |Z(H_{max})|] / |Z(H_{max})|$ ) in a relative low dc magnetic fields (with maximum value  $H_{max}$ ). This enables numerous applications of GMI-

elements as: magnetic field, rotation, pressure, and current sensors, for electronic compasses, navigation/GPS, biomagnetic measurements, magnetic memories, security systems, traffic control and industrial process, cosmic research, sports equipment, ... [10, 11].

## 2. EXPERIMENTAL PROCEDURE

The amorphous soft magnetic  $\text{Co}_{68.15}\text{Fe}_{4.35}\text{Si}_{12.5}\text{B}_{15}$  wires with diameters of 100  $\mu\text{m}$  and 120  $\mu\text{m}$  were prepared by conventional in-rotating water melt-spinning technique [12, 13]. The morphology of the surface of the amorphous wires was examined by optical microscopy (OM) and scanning electron microscopy (SEM). The structural investigation was performed by the XRD experiments (Philips PW 1050 diffractometer using  $\text{Cu-K}\alpha$  radiation  $\lambda = 0.154 \text{ nm}$ ).

Thermal properties were investigated by differential thermal analysis (DTA) using TA Instruments DTA SDT 2960 at a constant heating rate of 20  $^{\circ}\text{C}/\text{min}$ ., in a helium atmosphere. Chemical analysis of the constituent elements of the alloy was performed by scanning electron microscopy (SEM JEOL JSM-6390 LV) equipped with EDS Oxford Instruments X-MaxN device.

The giant magnetoimpedance (GMI) frequency behavior was monitored as a function of an external dc magnetic field applied parallel to the wire sample. The impedance of the samples of amorphous wires with a length of about 17 mm was measured by the four-point method using the LCR Hi-TESTER HIOKI 3532-50, in the frequency range from 50 Hz to 5 MHz. During the experiments performed in 1-D Helmholtz coils ( $H_{\text{max}} = 7.72 \text{ kA/m}$ ) the constant amplitude  $I_{\text{cc}}$  of the alternating current in wire samples was fixed at 7 mA.

## 3. RESULTS AND DISCUSSION

Figure 1.a shows the surface of the investigated amorphous wires recorded by optical microscopy (OM). Areas of increased roughness can be observed on the surface, created during the process of rapid quenching of the melt. During the wire magnetization process, these areas appear as pinning centers on the magnetic domain walls [14], which deteriorates the magnetically soft properties of alloys (low coercivity and high permeability) [15].

SEM micrographs of amorphous wires enable to determination of the diameter of the examined samples with large precision. The image in Figure 1.b shows slight deviations from the mean value of the wire diameter of 120  $\mu\text{m}$ , thus confirming the high reliability of the technology of obtaining amorphous wires by quenching the melt of metal alloys by in-rotating water melt-spinning technique.

EDS experiments confirmed the presence and homogeneous distribution of all constituent elements in the alloy (see Figure 1.c). The DTA thermogram of the as-cast wire presented in Figure 2. shows the single exothermic process, which results from the crystallization event with a peak temperature of 566  $^{\circ}\text{C}$ .

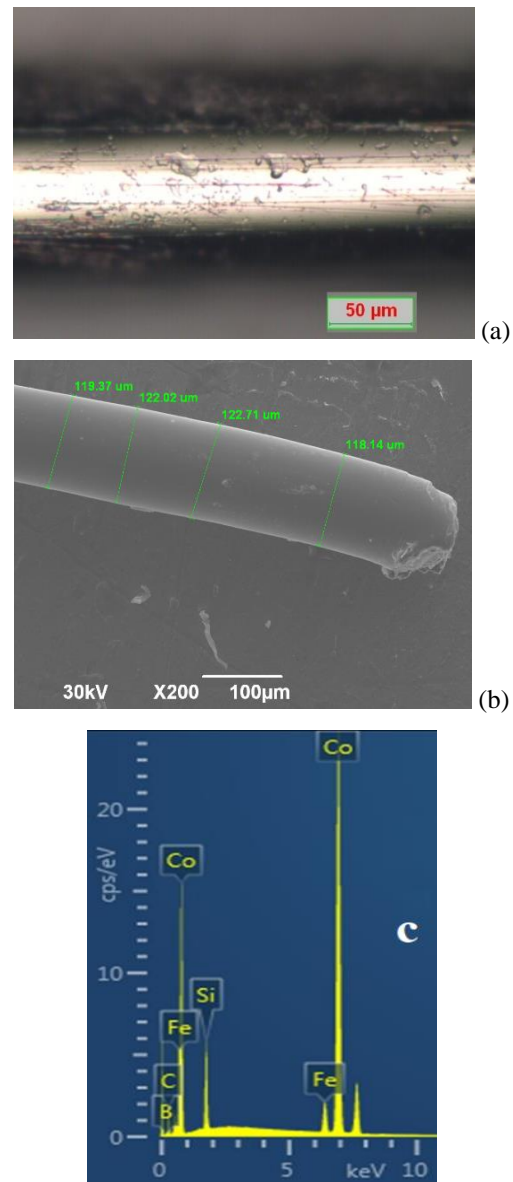


**Figure 1.** The surface (a), SEM micrograph (b), and elemental EDS microanalysis (c) of the  $\text{Co}_{68.15}\text{Fe}_{4.35}\text{Si}_{12.5}\text{B}_{15}$  amorphous wire.

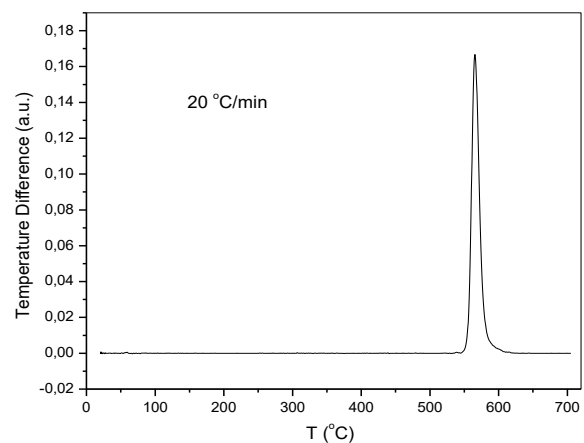


**Figure 2.** DTA thermogram of  $\text{Co}_{68.15}\text{Fe}_{4.35}\text{Si}_{12.5}\text{B}_{15}$  as-cast 120  $\mu\text{m}$  thick wire (heating rate 20  $^{\circ}\text{C}/\text{min}$ .).

The XRD pattern of the as-cast wire sample exhibits a very weak diffusive peak that reveals the amorphous

structure (Figure 3.a). The XRD pattern of the sample annealed at 700 °C shows the development of two diffraction peaks: the first one that could belong to the crystal phase  $\epsilon$ -CoSi (structure of P2 order), while the second one could be ascribed to crystal phases Co<sub>2</sub>B and  $\epsilon$ -CoSi (P2 order) (Figure 3.b).

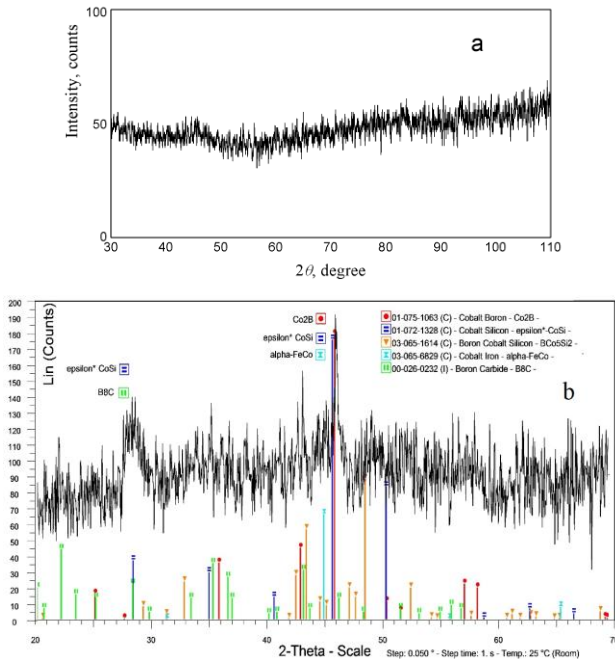


**Figure 3.** XRD pattern of as-cast (a) and sample annealed at 700 °C (b) of the Co<sub>68.15</sub>Fe<sub>4.35</sub>Si<sub>12.5</sub>B<sub>15</sub> wire.

The as-cast wires were Joule heated with alternating current amplitude of 100 mA (@ 50 Hz) for 60 s in air, followed by slow-cooling performed on ramping down the annealing current at a rate of 5 mA/s [16]. The electrical resistivity of the 17 mm long sample remains at the constant value of 133  $\mu\Omega\cdot\text{cm}$  and confirms the still amorphous and stress relief state. Figure 4. shows the frequency response of the GMI ratio in zero fields and a field  $H_{\text{ex}}$ , for different external dc magnetic fields. The critical frequency of about 5-7 kHz was observed as the point with an initial increase in the MI-effect.

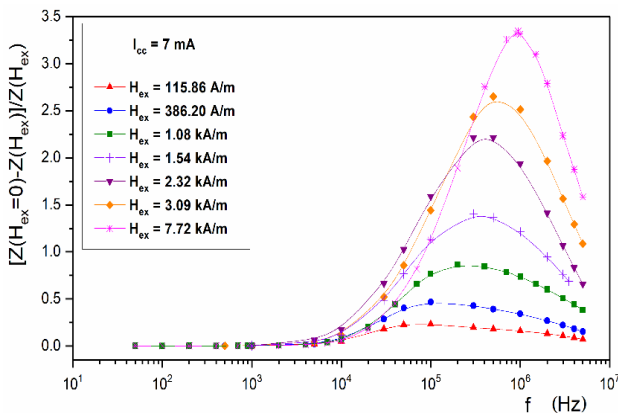


**Figure 4.** Frequency response of the GMI ratio in zero fields and a field  $H_{\text{ex}}$ , for different external dc magnetic fields in the range  $H_{\text{ex}} \in [116 \text{ A/m}, 7.72 \text{ kA/m}]$ .

The GMI ratio of 334% was recorded at a frequency of

950 kHz at the maximum magnetic field experiments ( $H_{\text{max}} = 7.72 \text{ kA/m}$ ).

Magnetic field dependence of the modulus of the impedance in the medium field range ( $H_{\text{ex}} < H_{\text{max}} \approx 463 \text{ A/m}$ ) is given in Figure 5.

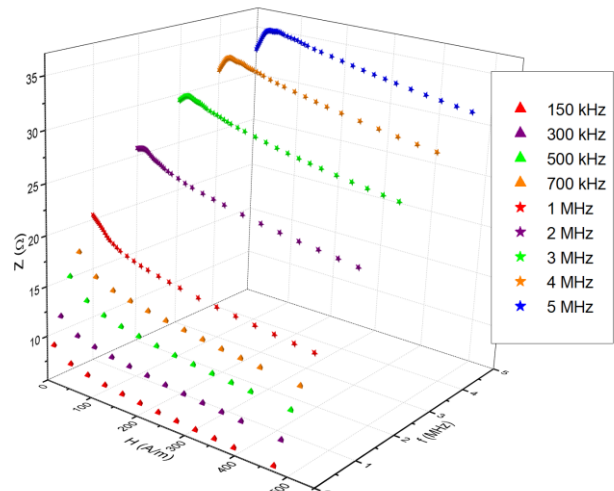


**Figure 5.** Magnetic field dependence of the modulus of the impedance in Co<sub>68.15</sub>Fe<sub>4.35</sub>Si<sub>12.5</sub>B<sub>15</sub> wire (medium field range  $H_{\text{ex}} < H_{\text{max}} \approx 463 \text{ A/m}$ ) and in the investigated frequency range  $f \in [150 \text{ kHz}, 5 \text{ MHz}]$ .

In the range of low operating frequencies ( $f < 1 \text{ MHz}$ ), the magnetic permeability  $\mu$  decreases with the increase of the direct magnetic field  $H_{\text{ex}}$  (at a constant frequency  $f$  and a constant amplitude of the current through the sample  $I_{\text{cc}}$ ). An increase in the magnetic penetration depth  $\delta_m(H_{\text{ex}})$  results in a decrease in the impedance modulus of the wire sample. Experiments show that the curves are characterized by a constant decrease with an increase in the magnetic field, as well as a constant increase in the impedance modulus with an increase in the operating frequency. The attained peak value of the impedance modulus of about 35  $\Omega$  was registered at the highest frequency of 5 MHz. In the medium operating frequency range (which usually starts at about 1 MHz) the skin effect and the magnetization vector rotation mechanism are dominant in the process of circular magnetization (the movement of the magnetic domain walls is blocked). The shape of dependence of the MI on the external dc magnetic field changes significantly and the appearance of a peak positioned at the anisotropy field  $H_k$  for all frequencies  $f \geq 2 \text{ MHz}$  is recorded.

Figure 6. shows the MI-ratio of the tested MI-element with operating frequency as a parameter in the range  $f \in [1 \text{ MHz}, 5 \text{ MHz}]$  (at magnetic field  $H_{\text{max}} \approx 0.463 \text{ kA/m}$ ). The highest value  $\Delta Z/Z$  was registered at 1 MHz, while with a further increase in frequency, a constant decrease was recorded, as a consequence of a decrease in circular permeability. The insert in Figure 6. shows a linear increase in the magnetic anisotropy field  $H_k(f)$  with increasing frequency. Magnetic field GMI sensor operates in the region of linear increasing the impedance modulus (i.e.  $H_{\text{ex}} < H_k$ ) [17], and therefore, the increase in the magnetic anisotropy field  $H_k$  enlarges the application region when the operating frequency increases from 2

MHz to 5 MHz.

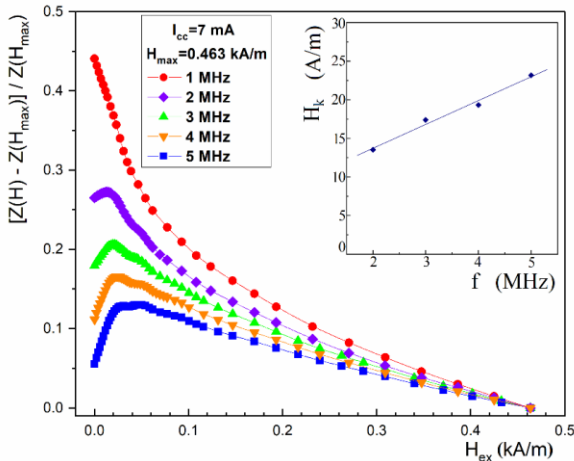


**Figure 6.** MI-ratio with frequency as a parameter in the range  $f \in [1 \text{ MHz}, 5 \text{ MHz}]$  ( $H_{\max} \approx 0.463 \text{ kA/m}$ ).

#### 4. CONCLUSION

The investigation of the wire GMI-element of  $\text{Co}_{68.15}\text{Fe}_{4.35}\text{Si}_{12.5}\text{B}_{15}$  alloy at frequencies of the order of megahertz led to the generalized conclusion that the optimal operating frequencies are defined by the need to avoid the dominant influence of longitudinal anisotropy, i.e. the dynamics of domain magnetization inside the wire, which significantly reduces the sensitivity of the micromagnetic sensor. The attained peak value of the impedance modulus of about  $35 \Omega$  was registered at the highest frequency of 5 MHz. The dominant influence of circular magnetic anisotropy through the mechanism of rotation of the magnetization vector in the domains distributed around the circumference of the cylindrical wire leads to significant changes in the skin depth  $\delta_m$  ( $H_{\text{ex}}$ ,  $f$ ) under the influence of a dc magnetic field and enables a significant increase in the skin depth as well as a decrease in magnetoimpedance  $Z$ . The maximum GMI ratio of 334% was recorded at a frequency of 0.95 MHz (@ 7.72 kA/m).

#### Acknowledgement

This research is supported in part by the Ministry of Science, Technological Development and Innovation of the Republic of Serbia, Faculty of Technical Sciences Čačak-University of Kragujevac, under Grant No. 451-03-66/2024-03/200132.

#### References

- [1] PANINA,L.,V., MOHRI,K.: *Magneto-impedance effect in amorphous wires*, Applied Physics Letters, 65(9) (1994) 1189–91.
- [2] PHAN,M.,H., PENG,H.,X.: *Giant magnetoimpedance materials: fundamentals and applications*, Progress in Materials Science, 53(2) (2008) 323–420.
- [3] MITROVIĆ,N.,S., KANE,S.,N., TYAGI,P.,V., ROTH,S.: *Effect of dc-Joule-heating thermal*

*processing on magnetoimpedance of  $\text{Fe}_{72}\text{Al}_5\text{Ga}_2\text{P}_{11}\text{C}_6\text{B}_4$  amorphous alloy*, Journal of Magnetism and Magnetic Materials 320(20) (2008) e792-96.

- [4] DAS,T.,K., MITRA,A., MANDAL,S.,K., ROY,R.,K., BANERJI,P., PANDA,A.,K.: *Parametric controls on giant magnetoimpedance (GMI) behaviour of CoFeSiBCr amorphous wires for prospective sensor applications*, Sensors and Actuators, A 220 (2014) 382-87.
- [5] SURLA,R., VASIĆ,M., MITROVIĆ,N., RADOVIĆ,Lj., MINIĆ,D.: *Magnetic properties of  $\text{Fe}_{72}\text{Cu}_1\text{V}_4\text{Si}_{15}\text{B}_8$  alloy with a composite amorphous/nanocrystalline structure*, Journal of Magnetism and Magnetic Materials, 564(2) (2022) 170141.
- [6] JIANG,S., WANG,H., ESTEVEZ,D., HUANG,Y., ZHANG,L., SHEN,H., NING,Z., QIN,F., SUN,J.: *Surface microstructural design to improve mechanical and giant magneto-impedance properties of melt-extracted CoFe-based amorphous wires*, Materials & Design, 204 (2012) 109642.
- [7] LIU,J., QIN,F., CHEN,D., SHEN,H., WANG,H., XING,D., PHAN,M.,H., SUN, J.: *Combined current-modulation annealing induced enhancement of giant magnetoimpedance effect of Co-rich amorphous microwires*, Journal of Applied Physics, 115 (2014) 17A326.
- [8] KNOBEL,M., VÁZQUEZ,M., KRAUS,L.: *Giant magnetoimpedance*, Handbook of Magnetic Materials, vol. 15, 1<sup>st</sup> ed. BUSCHOW,K.,H.,J. Ed., Elsevier, Amsterdam, 2003.
- [9] LACHOWICZ,H.,K., GARCIA,K.,L., KUZMINSKI,M., ZHUKOV,A., VAZQUEZ,M.: *Skin-effect and circumferential permeability in micro-wires utilized in GMI-sensors*, Sensors and Actuators, A, 119(2) (2005) 384–89.
- [10] MOHRI,K., YAMAMOTO,M., UCHIYAMA,T.: *Application topics of amorphous wire CMOS IC magneto-impedance micromagnetic sensors for IoT smart society*, Journal of Sensors, 2019 (2019) 8285240.
- [11] KARNAUSHENKO,D., KARNAUSHENKO,D.,D., MAKAROV,D., BAUNACK,S., SCHÄFER,R., SCHMIDT,G.,O., *Self-assembled on-chip-integrated giant magneto-impedance sensorics*, Advanced Materials, 27(42) (2015) 6582-89.
- [12] MASUMOTO,T., OHNAKA,I., INOUE,A., HAGIWARA,M., *Production of Pd-Cu-Si amorphous wires by melt spinning method using rotating water*, Scripta Metallurgica, 15(3) (1981) 293-96.
- [13] <http://www.phys-iasi.ro/en/equipment-conventional-wires-preparation>, Accessed on: July. 03, 2024.
- [14] BUSCHOW,K.,H.,J., DE BOER,F.,R.: *Physics of Magnetism and Magnetic Materials*, Kluwer Academic/Plenum Publishers, New York, 2003.
- [15] GONZÁLEZ-LEGARRETA,L., PRIDA,V.,M., HERNANDO,B., TALAAT,A., IPATOV,M., ZHUKOVA,V., GONZÁLEZ, J., ZHUKOV,A.:

- Tailoring of soft magnetic properties and high frequency giant magnetoimpedance in amorphous ribbons*, High Performance Soft Magnetic Materials, ed. ZHUKOV, A. Springer Series in Materials Science, Springer Cham, 2017.
- [16] ORELJ, J.,M., MITROVIĆ,N.,S., PAVLOVIĆ,V.,B.: *MI-sensor element features and estimation of penetration depth and magnetic permeability by magnetoresistance and magnetoreactance of CoFeSiB amorphous wires*, IEEE Sensors Journal, 23(13) (2023) 14017-24.
- [17] NABIAS,J., ASFOUR,A., YONNET,JP.: *Temperature dependence of giant magnetoimpedance in amorphous microwires for sensor application*, IEEE Transaction on Magnetic, 53(4) (2017) 4001005.



## EXAMINING FATIGUE OF FIBER REINFORCED POLYMER: A COMPREHENSIVE REVIEW

AMER. ALSAMMARRAIE

Mechanical Department/ Engineering College/Tikrit University, Tikrit-Iraq, [amircraft@tu.edu.iq](mailto:amircraft@tu.edu.iq)

MURAJA S. SLMAN

Mechanical Department/ Engineering College/Tikrit University, Tikrit-Iraq, [muraja.s.salman@st.tu.edu.iq](mailto:muraja.s.salman@st.tu.edu.iq)

**Abstract:** Since their introduction in the 1950s, composite materials have been extensively studied for their fatigue performance across various engineering fields. Numerous publications have documented experimental investigations into how these materials perform under different loading and environmental conditions. Fiber-reinforced polymer (FRP) composites are increasingly replacing metals due to their high strength and stiffness. These composites face various static and fatigue loads in service, necessitating fatigue tests to assess cyclic behavior. Unlike metals, where a single crack propagates to failure, composites exhibit complex fatigue damage with multiple micro-cracks forming early in the process. FRP composites serve as pivotal structural materials across diverse industries. Yet, before their incorporation into structures, meticulous testing of both test coupons and structurally representative samples is essential to evaluate their physical attributes, particularly their fatigue properties. Regrettably, the considerable expense entailed in fabricating coupons for these evaluations poses a notable hindrance to the extensive integration of fibre-reinforced polymer (FRP) into end products. The objective of this study is to forecast and simulate the fatigue lifespan of FRP composites. Extensive research in this domain will be outlined within this paper, encompassing diverse prediction methodologies employed to ascertain the fatigue endurance of these materials.

**Keywords:** Fatigue life, fiber-reinforced polymer, (FRP), fatigue test, carbon fiber

### 1. INTRODUCTION

The rapid development in industries has created a need for materials with enhanced strength, hardness, and density, while also reducing costs and improving sustainability. Composite materials have emerged as a solution that meets these requirements and are widely used in various applications. These materials consist of a combination of two or more components, with one serving as a matrix and the other in the form of particles or fibers as reinforcement. Research studies have shown that composite materials can effectively replace many traditional materials, offering significant improvements in structural, mechanical, and frictional properties, particularly when reinforced with fibers[1],[2],[3]. FRP are composite materials typically consisting of fibers embedded in a matrix material. Due to their outstanding properties such as low weight, high specific strength, rigidity, and excellent resistance to corrosion and fatigue[4],[5]. FRP composites are extensively employed in the construction of automotive structures, and aerospace, marine and aircraft applications [6]. In military defence systems, reinforced polymers are widely used to manufacture components such as helmets, body armour, and ballistic protection panels for light vehicles, boats, and helicopters. These materials are characterized by excellent mechanical properties, such as high strength, stiffness, and a great capacity for energy absorption. They

also contribute to reducing weight compared to traditional materials, which improves vehicle mobility and fuel efficiency while maintaining a high level of protection[7]. FRP composites face cyclic loading in various applications, leading to fatigue failure, a common issue. Understanding and addressing this failure mode is crucial for ensuring the reliability and longevity of FRP structures[4],[8]. Carbon fiber reinforced polymers (CFRPC) are considered one of the best and most famous types of reinforced polymers. These composites are witnessing increased usage across various advanced technology industries, including aerospace, defence, marine, and sporting goods. This trend is attributed to the unique combination of high specific strength and stiffness[9]. These materials excel in enduring both constant and cyclic loads, serving as effective alternatives to traditional metal alloys. CFRP exhibit robust fatigue resistance along the fiber direction due to their exceptional stiffness, preventing local damage initiation. However, their anisotropic nature and varying stiffness coupling can induce notable strains perpendicular to the fibers or at the fiber/resin interface, potentially leading to fatigue damage due to mismatches in elastic properties [10]. the replacement of metallic components with CFRP-based alternatives leads to significant weight savings [11]. despite extensive studies, understanding the fatigue behavior of fiber-reinforced composites remains complex due to differences from metal fatigue. Composites experience multiple simultaneous cracks, complicating

fatigue assessment. Damage mechanisms like fiber breakage, matrix cracking, delamination, and debonding degrade mechanical properties such as strength and stiffness. Therefore, research often focuses on the degradation of residual strength and stiffness during fatigue[12]. This study aims to explore modern methods for predicting material fatigue life, particularly focusing on reinforced composites. It provides an overview of their significance across engineering fields, emphasizing their unique fatigue behavior compared to metals. Previous research on fatigue life determination in composites is reviewed, highlighting both progress and gaps. The study also examines fatigue behavior and failure patterns, including micro-crack initiation and propagation. Strategies for improving composite fatigue performance are summarized, with practical implications and future research recommendations provided.

## 2. FATIGUE FAILURE

Fatigue has long been a major industrial concern. The increased use of composite materials highlights their complex fatigue behavior compared to metals. Unlike metals, where fatigue damage typically appears as a single crack, composites exhibit various forms of damage such as delamination, matrix cracking, fiber failure, debonding, and void growth, influenced by testing conditions and material composition[13]. In composites, failure criteria like the hashing criterion have been adapted from static to fatigue conditions by replacing static strength with fatigue or residual strength. This adaptation is supported by the presence of Characteristic Damage States (CDS) in composites under fatigue loading. Fatigue induces cracks parallel to the fiber direction in multidirectional laminates, creating a degraded but integrated material state. Each fatigue cycle is akin to a quasi-static loading process, enabling failure prediction with each cycle[14]

### 3. Composites of Fiber Reinforced Polymer (FRP)

Today, composite materials are gaining an edge over conventional materials due to their superior specific strength, and excellent stiffness and fatigue properties, although they have lower fire resistance. In recent decades, polymer composites have been widely adopted as alternatives to traditional materials across various applications. Their ability to fulfill diverse design requirements, coupled with their robust mechanical and physical properties, makes them ideal for meeting specific application demands[15]. Composite materials can be tailored to specific service conditions, much like natural composites such as wood and bone, which have evolved to meet specific mechanical needs. This adaptability makes them attractive for industrial applications[16]. Composite materials are categorized by their components: the base material (matrix or binder) and the filler material. The matrix holds the filler, which can be sheets, particles, fibers, or whiskers from natural or synthetic sources as reinforcement. As shown in Figure 1, composites are classified into three main categories based on their structure[1].

(FRP) composites, known for their heterogeneous and anisotropic properties and lack of plastic deformation, are

widely used in many applications. (CFRP) and glass fiber-reinforced polymers are preferred over traditional materials due to their excellent strength-to-weight ratios, customizable strength, high fatigue resistance, toughness, and resilience to high temperatures and oxidation, making them ideal for various engineering applications [17].

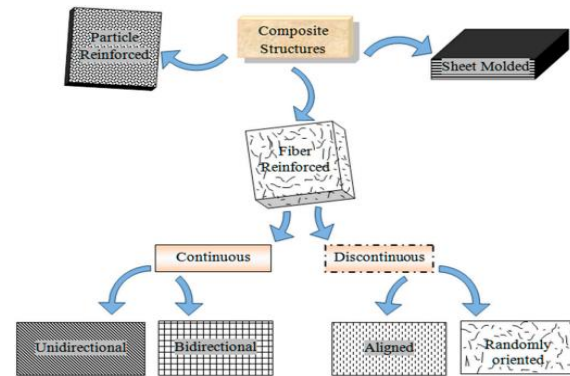


Figure 1. Types of Composite Materials.

### 3.1. Carbon fiber reinforced polymer (CFRP)

Carbon, a vital element for life, forms the basis of numerous compounds, totalling approximately 1.7 million. Derived from sources like coal, oil, and diamonds, carbon fibers possess exceptional properties including high strength, stiffness, and resistance to heat, moisture, and chemicals. When combined with polymer matrices to create CFRP composites, they offer advantages such as high strength-to-weight ratios and fatigue resistance. Despite drawbacks like high costs and low impact resistance, CFRP find extensive use in aerospace, automotive, electronics, medical, and sports equipment industries due to their superior strength and lightweight properties compared to steel and aluminium [18]. Table 1 provides a summary of the most important properties of carbon fibres [19].

Table 1: properties of carbon fibres.

Property	Young's modulus (GPa)	Ultimate tensile strength (MPa)	Percent of elongation	Density ( $g/cm^3$ )	Specific strength (Mpa/g. $cm^3$ )
value	220-350	2300-3700	0.7-1.7	1.8-2	1300-1900

## 4. FATIGUE OF CFRP

In their investigation into the fatigue life of CFRP composites. Lu Ke and colleagues examined the fatigue performance of steel plates that have been reinforced with CFRP for enhanced strength and durability emphasizing the role of adhesive properties. They tested 20 various specimens to evaluate fatigue life, analyze failure modes, and observe crack propagation patterns. The study revealed that epoxy resin-based structural adhesives, notably Araldite 420 and J133C, provided superior

bonding with CFRP. This significantly improved the fatigue life of the CFRP-reinforced steel plates[20]. Selim Mrzljak et al. studied the effect of oriented carbon nanofibers on the mechanical properties of bidirectional polymer-reinforced carbon fibers was studied. They produced carbon nanofiber-reinforced polymer with and without orientation using a press hot. Their results showed that the orientation of carbon nanofibers has a significant effect on the mechanical and fatigue properties with guidance, it was observed that it increases the force, reduces the resulting damage, and slows it down[21]. J.-D. Wacker and his team investigated the computational prediction of fatigue life for CFRP adherents in hybrid adhesive joints. They examined two fatigue life models based on multiaxial stress and strain energy density related to various failure modes. Using finite shell and volume elements for stress analysis, they predicted the fatigue lifespan of hybrid steel-CFRP single-lap joints, considering geometric nonlinearity. The models showed reasonable accuracy compared to experimental data until initial ply failure, but further refinement is needed to improve predictive precision[22]. Jianxiong Gao et al. studied how stiffness degradation affects the fatigue life and reliability of FRP composites. They developed a probability model accounting for the randomness in initial and critical stiffness, finding that stiffness degradation follows a distinct pattern: rapid decline, slower phase, and then another rapid decline before failure. Their model accurately fit experimental data and outperformed existing models, enhancing the understanding and prediction of stiffness degradation to improve the reliability and longevity of FRP composites[4]. Slavko Mijatov and his team developed a novel composite material for rocket propulsion liner insulation, using hydroxyl-terminated polybutadiene (HTPB) with carbon fibers (CF) and inorganic filler powders (IFPs). They introduced an elastomeric adhesive to enhance mechanical properties and heat resistance. Various formulations with different CF and IFP loadings and NCO/OH ratios were rigorously tested for viscosity, rheological and mechanical properties, and geometric compatibility. Dynamic mechanical analysis (DMA) and small-scale ablation tests confirmed that these new materials provide excellent thermal insulation and ablation characteristics, making them ideal for rocket propulsion applications [23]. Li Bowen et al. they studied utilized molecular dynamics (MD) simulations to investigate the mechanical behavior of epoxy resin reinforced with multilayer graphene during fatigue. They examined the degradation of performance under axial and transversal fatigue, respectively. Despite significant differences in loading rates between atomic and macroscopic scales, the MD method proved feasible, as evidenced by a noticeable drop in mean stress during simulation. Performance degradation was observed to be most rapid in the initial cycles, with degradation occurring faster in the transversal direction compared to the axial[24]. Mithil Kamble and colleagues conducted research aimed at enhancing the fatigue resistance of CFRP by incorporating nano-silica, thereby producing nano-modified carbon fibers. Their study showcased a significant enhancement in fatigue life, with the addition

of nano-silica resulting in fatigue life improvements of 6-7 times under high cycle fatigue conditions. Through their investigation, they elucidated the mechanism behind this performance enhancement, attributing it to the ability of nano-silica to interrupt and prolong the initial crack propagation phase. This, in turn, delays the ultimate failure of the carbon fiber-reinforced polymer, leading to an augmentation in fatigue life[25]. Md Sarower Tareq et al. investigated the flexural stress behavior and fracture toughness of CFRP composites enhanced with graphene nanosheets. Through bending stress tests, they analyzed the primary mode of plate fracture. Employing the two-parameter Weibull distribution function, they made estimations regarding both the likelihood of failure and the fracture toughness. The results highlighted a significant enhancement upon incorporating graphene nanosheets, with an average fatigue life increase ranging from 155% to 190%, along with improved fracture toughness. In essence, these composite materials exhibited prolonged fatigue life and delayed crack formation within the matrix attributed to the presence of nanoparticles[9]. Xiang-FaWu et al. They experimentally studied the fatigue residual tensile strength and its probability distribution on PMC sheets made of unidirectional CF. The statistical analysis of the experimental data revealed that the residual tensile strength of the samples conformed to the two-parameter Weibull model with a reliability of 95.2%. As the cycles increased, the value of the residual fatigue strength decreased, while its deflection increased. They emphasized that the experimental study they used is valuable for understanding fatigue strength in addition to reliable design and prediction of the performance of composite structures[26]. Aida Cameselle-Molares and her team investigated the delamination behavior of GFRP/balsa sandwich panels featuring circular disbonds subjected to out-of-plane fatigue loading. Two configurations of face sheets were examined: SPA (comprising solely woven plies) and SPB (consisting of woven plies combined with continuous filament mat). The study revealed that 2D crack propagation led to stable advancement and slower crack growth rates under load control conditions. The SPB configuration exhibited inferior performance under fatigue with an R ratio of 0.1, yet displayed a prolonged lifespan and arrested crack propagation at higher R ratios. Furthermore, they noted an elevation in cyclic stiffness attributed to the in-plane stretching stresses in the debonded face sheets[27]. They investigated the augmentation of fatigue strength in sugarcane fiber-reinforced epoxy composites (SFRPC) through a novel treatment method. This treatment resulted in a significant improvement in cyclic fatigue strength CF and extended fatigue life by up to 40%. Evaluation of fatigue performance involved bending cyclic fatigue tests, and comparing treated and untreated SFRPCs with CFRPC. Finite element models and statistical analysis were utilized to assess the treatment's impact and load ratios. Enhanced fatigue behavior was observed, supported by SEM imaging. The stress-strain-life relationship suggested that the increased CFS in treated SFRPCs stemmed from shear yielding due to the fracture of the glass layer on the fibers[28]. Hemanth Kumar and



colleagues delved into the fatigue behavior of glass fiber-reinforced epoxy composites subjected to cyclic bending loads, employing neural networks for predictive analysis. Through rotating bending stress tests with reversed load cycles, they observed a decrease in the fatigue life of the glass fiber composites with rising stress levels. The efficacy of neural networks was validated by juxtaposing their predictions with experimental outcomes. Notable observations encompassed matrix cracking and fiber interfacial debonding. Furthermore, the utilization of backpropagation algorithms enabled neural networks to proficiently classify failure modes[6]. mitigates the impact of weak interfaces on the structural reliability of FRP laminates, S.S.R. Kolor and colleagues devised a cyclic cohesive zone model (CCZM). This model aptly characterizes interlaminar fatigue failure by incorporating fatigue-induced degradation of strength, stiffness, and critical energy release rate. Utilizing experimental data and finite element analysis, they applied the model to unidirectional CFRP specimens. At key interfaces, shear stress exhibited variation ( $\tau_{max} = 30$  MPa,  $R = 0.1$ ), revealing a sigmoidal damage pattern. Crack initiation occurred after 301,750 cycles, exhibiting a consistent crack front progression.[29]. Xin Wang et al. examined how salt solution exposure affects the fatigue behavior of basalt fiber-reinforced polymer (BFRP) composites at stress ratios of  $R = 0.1$  and  $0.8$ . They found that while static strength was stable, fatigue strength decreased due to saltwater. SEM revealed early interface debonding and deterioration over time in aged samples, leading to varied fatigue lives and degradation. The study concluded that saltwater significantly impacts BFRP's fatigue strength, crucial for long-term performance[30]. Shoutan Song et al. delved into the fatigue characteristics of CFRP. Their study employed an innovative wedge-type anchorage system during fatigue testing of CFRP tendons. The adoption of this novel fixation system demonstrated exceptional fatigue resistance, as evidenced by the absence of tendon slippage or failure upon fixation. Predictions generated using Whitney's method provided a confidence level of 95%[31]. Ayoub Yari Boroujeni et al. investigated a novel technology, Graphitic Structure by Design (GSD), aimed at growing uniform, multi-walled carbon nanotubes. They explored two different configurations: one with a uniform patterned covering and the other with a checkerboard-like coating on woven carbon fiber. Tensile tests were conducted on the carbon fiber to determine properties such as modulus of elasticity, failure stress, and tensile strength. Additionally, fatigue life was tested at three stress levels. Their findings revealed a significant 150% improvement in the fatigue life of carbon fibers with both uniform and patterned multi-walled carbon nanotubes. Fractography analysis highlighted the role of MWCNTs in shielding the fiber yarn from matrix cracks, leading to substantial enhancements in fatigue life[10]. Priscilla Rocha Vieira et al. They studied focused on the fatigue behavior of pultruded Glass-fiber Reinforced Polymer composites. Static tests measured the material's strength and elasticity. Fatigue tests ( $R=0.1$ , 4Hz) were performed to establish the S-N curve and analyze damage progression and failure modes. Typically, fatigue damage started with matrix

cracks, potentially leading to delamination, fiber failure, and ultimately, specimen rupture. Tomography revealed misaligned fiber layers and numerous voids, contributing to material heterogeneity and variability in experimental results[32]. Mondher Haggui and his team investigated the mechanical characteristics and damage mechanisms of flax fiber-reinforced thermoplastic composites under both static and fatigue loading conditions. Static tensile tests were conducted to discern mechanical properties and elucidate damage mechanisms, whereas fatigue tests were employed to assess material stiffness. The findings unveiled four distinct acoustic event categories during failure: matrix cracking, fiber debonding, fiber pull-out, and fiber breakage. It was noted that the composite structure played a pivotal role in influencing damage density and behavior under both static and cyclic loading. [33]. Moustafa Mahmoud and his team explored the effects of incorporating cellulose nanocrystals into polymers to develop nanocomposites with continuous glass fibers, thereby merging the advantages of both traditional and nanomaterials. They produced four types of samples: Unreinforced polyester (UR), Glass fiber-reinforced polyester, Nano polyester composites (NP), and Nano glass fiber-reinforced composites (NGFRP). Their innovative material combinations revealed that NGFRP can significantly enhance the fatigue life of composite structures while also lowering manufacturing costs. This material design shows great potential for applications in the biomedical, energy, and electronics industries[34]. Pritam V. Kulkarni and his team conducted a study utilizing a conditional test aimed at extending the fatigue life of carbon fiber reinforced plastic sheets. They fabricated composite sheets with carbon fibers oriented in multiple directions. The study demonstrated that the proposed test is an effective, non-destructive method for estimating the fatigue life of composite plates. From the experimental results, they derived empirical equations that establish a relationship between fatigue life and natural repeatability[12]. CFRP is highly valued by gas turbine engine manufacturers for its exceptional properties and lightweight nature. M. Nikhamkin et al. developed a fatigue testing method for CFRP that reduces the number of samples needed to determine fatigue properties. Using the "Standard Test Method for Tension-Tension Fatigue of Polymer Matrix Composite Materials," their approach reduced test specimen use by 83.3% and structural specimens by 62.5%. This method effectively determined the acceptable fatigue limit, showing potential for significant sample reduction[35]. S. Backe et al. conducted a study with the goal of saving time and materials in the analysis of the fatigue behavior of carbon fiber reinforced polymer composites. They developed a novel, short-time procedure for calculating the fatigue life of these composites, focusing on a series of tests to increase the cyclic load for all plates. The advanced overload test was performed at a frequency of 5 Hz with a stress ratio of  $R=0.1$ . This method proved effective in calculating fatigue life. Utilizing accumulated irreversible deformation energy as a metric for estimating fatigue life represents a completely new approach, offering significant potential for efficient and accurate fatigue life

estimation[11]. K. Tanaka et al. conducted an in-depth study on how fiber orientation affects crack propagation behavior, using single-edge specimens taken from an injection-molded sheet. By employing Fracture Mechanics parameters determined through Finite Element Method (FEM) based on anisotropic elasticity, they established correlations between the crack propagation rate and various factors. The key findings are as follows: fiber reinforcement significantly enhanced crack propagation resistance, particularly when examining the relationship between crack propagation rate and stress range. Fatigue cracks were found to propagate under mixed mode loading conditions, and the crack propagation rate data correlated with the range of the total energy release rate[36]. Fabio Baschnagel et al. studied the fatigue behavior of CFRP tapes loaded with pins under tensile stress. These tapes are used in various applications, such as sailing yacht rigging systems, crane suspension cables, and bridge suspenders. They conducted extensive tensile and fatigue tests on the tapes, subjecting them to millions of loading cycles. The tests revealed that the pin-reinforced CFRP tapes have a significant stress limit, approximately half of their ultimate tensile strength, and identified a fatigue limit when the tape withstands a substantial number of load cycles. Their findings were used to develop an S-N curve for the material[37].

## 6. CONCLUSION

For the past seven and a half decades, the scientific and engineering communities have been deeply engrossed in unravelling the mysteries surrounding the fatigue behavior of composite materials, with a particular focus on FRP composites. These materials have garnered widespread interest since their inception in various industrial applications. As researchers delved deeper into their fatigue characteristics, it became increasingly evident that the fundamental principles governing fatigue phenomena are applicable across a broad spectrum of materials and structural configurations. The complex interplay of continuous and cyclic loading, coupled with fluctuations in temperature, stress concentrations, and environmental factors, plays a pivotal role in dictating the degradation and eventual failure of composite materials[5]. These multifaceted factors contribute to the intricate fatigue behavior observed in FRP composites and other similar materials. While significant strides have been made in understanding and predicting the fatigue life of FRP composites, the field remains vast and ripe for further exploration. Specialized research papers have documented substantial advancements in fatigue life prediction techniques. However, the quest for a comprehensive understanding of fatigue behavior continues unabated. The objective of this research was to delve into sophisticated methodologies, state-of-the-art forecasting techniques, and empirically validated strategies to delve into the complexities of fatigue behavior in composite materials. Despite considerable progress, the pursuit of a comprehensive grasp of fatigue life in composites persists, highlighting an ongoing commitment to innovation and enhancement in the critical realm

## References

- [1] “Polymers | Free Full-Text | Fiber-Reinforced Polymer Composites: Manufacturing, Properties, and Applications.” Accessed: May 26, 2024. [Online]. Available: <https://www.mdpi.com/2073-4360/11/10/1667>
- [2] D. Chukov, S. Nematulloev, V. Torokhov, A. Stepashkin, G. Sherif, and V. Tcherdyntsev, “Effect of carbon fiber surface modification on their interfacial interaction with polysulfone,” *Results Phys.*, vol. 15, p. 102634, Dec. 2019, doi 10.1016/j.rinp.2019.102634.
- [3] G. Sherif, D. Chukov, V. Tcherdyntsev, and V. Torokhov, “Effect of Formation Route on the Mechanical Properties of the Polyethersulfone Composites Reinforced with Glass Fibers,” *Polymers*, vol. 11, no. 8, p. 1364, Aug. 2019, doi: 10.3390/polym11081364.
- [4] “Probabilistic modelling of stiffness degradation for fiber reinforced polymer under fatigue loading - ScienceDirect.” Accessed: May 26, 2024. [Online]. Available: <https://www.sciencedirect.com/science/article/abs/pii/S1350630720306087>
- [5] A. P. Vassilopoulos, “The history of fiber-reinforced polymer composite laminate fatigue,” *Int. J. Fatigue*, vol. 134, p. 105512, May 2020, doi: 10.1016/j.ijfatigue.2020.105512.
- [6] H. Kumar C and R. P. Swamy, “Fatigue life prediction of glass fiber reinforced epoxy composites using artificial neural networks,” *Compos. Commun.*, vol. 26, p. 100812, Aug. 2021, doi: 10.1016/j.coco.2021.100812.
- [7] K. Czech et al., “Hybrid Polymer Composites Used in the Arms Industry: A Review,” *Materials*, vol. 14, no. 11, p. 3047, Jun. 2021, doi: 10.3390/ma14113047.
- [8] S.-P. Zhu, D. Liao, Q. Liu, J. A. F. O. Correia, and A. M. P. De Jesus, “Nonlinear fatigue damage accumulation: Isodamage curve-based model and life prediction aspects,” *Int. J. Fatigue*, vol. 128, p. 105185, Nov. 2019, doi: 10.1016/j.ijfatigue.2019.105185.
- [9] M. S. Tareq, B. Jony, S. Zainuddin, M. Al Ahsan, and M. V. Hosur, “Fatigue analysis and fracture toughness of graphene reinforced carbon fibre polymer composites,” *Fatigue Fract. Eng. Mater. Struct.*, vol. 44, no. 2, pp. 461–474, Feb. 2021, doi: 10.1111/ffe.13371.
- [10] A. Y. Boroujeni and M. Al-Haik, “Carbon nanotube – Carbon fiber reinforced polymer composites with extended fatigue life,” *Compos. Part B Eng.*, vol. 164, pp. 537–545, May 2019, doi: 10.1016/j.compositesb.2018.11.056.
- [11] S. Backe and F. Balle, “A novel short-time concept for fatigue life estimation of carbon (CFRP) and metal/carbon fiber reinforced polymer (MCFRP),” *Int. J. Fatigue*, vol. 116, pp. 317–322, Nov. 2018, doi: 10.1016/j.ijfatigue.2018.06.044.
- [12] P. V. Kulkarni, P. J. Sawant, and V. V. Kulkarni, “Fatigue life prediction and modal analysis of carbon fiber reinforced composites,” *Adv. Mater. Process. Technol.*, vol. 4, no. 4, pp. 651–659, Oct. 2018, doi: 10.1080/2374068X.2018.1488799.
- [13] R. J. Huston, “Fatigue life prediction in composites,” *Int. J. Press. Vessels Pip.*, vol. 59, no. 1–3, pp. 131–140, Jan. 1994, doi: 10.1016/0308-0161(94)90148-1.

- [14] W. Lian and W. Yao, "Fatigue life prediction of composite laminates by FEA simulation method," *Int. J. Fatigue*, vol. 32, no. 1, pp. 123–133, Jan. 2010, doi: 10.1016/j.ijfatigue.2009.01.015.
- [15] "Natural fiber reinforced polymer composites: history, types, advantages and applications | Materials Engineering Research." Accessed: May 26, 2024. [Online]. Available: <https://www.syncsci.com/journal/MER/article/view/267>
- [16] T. W. Clyne and D. Hull, *An Introduction to Composite Materials*. Cambridge University Press, 2019.
- [17] M. Altin Karataş and H. Gökkaya, "A review on machinability of carbon fiber reinforced polymer (CFRP) and glass fiber reinforced polymer (GFRP) composite materials," *Def. Technol.*, vol. 14, no. 4, pp. 318–326, Aug. 2018, doi: 10.1016/j.dt.2018.02.001.
- [18] D. Ozkan, M. S. Gok, and A. C. Karaoglanli, "Carbon Fiber Reinforced Polymer (CFRP) Composite Materials, Their Characteristic Properties, Industrial Application Areas and Their Machinability," in *Engineering Design Applications III*, vol. 124, A. Öchsner and H. Altenbach, Eds., in *Advanced Structured Materials*, vol. 124, Cham: Springer International Publishing, 2020, pp. 235–253. doi: 10.1007/978-3-030-39062-4\_20.
- [19] H. A. Hashim, J. K. Oleiwi, and Q. A. Hamad, "Investigation of Mechanical and physical properties of polymeric composites for a prosthetic socket," University of Technology, Baghdad, Iraq, 2022.
- [20] L. Ke, A. Chen, Z. Feng, C. Li, and Y. Li, "Fatigue performance of CARBON FIBER-REINFORCED POLYMER strengthened single-edge cracked steel plates: Effects of adhesive property and CFRP arrangement," *Polym. Compos.*, p. pc.28172, Jan. 2024, doi: 10.1002/pc.28172.
- [21] S. Mrzljak *et al.*, "Effect of carbon nanofibre orientation on fatigue properties of carbon fibre-reinforced polymers," *J. Compos. Mater.*, vol. 57, no. 6, pp. 1149–1164, Mar. 2023, doi: 10.1177/00219983221150496.
- [22] J. -D. Wacker, K. Tittmann, I. Koch, D. Laveuve, and M. Gude, "Fatigue life analysis of carbon fiber reinforced polymer (CFRP) components in hybrid adhesive joints," *Mater. Werkst.*, vol. 52, no. 11, pp. 1230–1247, Nov. 2021, doi: 10.1002/mawe.202100046.
- [23] S. Mijatov, "DEVELOPMENT OF POLYMER COMPOSITE LINER AS INSULATION MATERIAL: RHEOLOGICAL, MECHANICAL AND THERMAL PROPERTIES," 2022.
- [24] L. Bowen, L. Yong, C. Jianzhong, H. Li, and Z. Xiaoyu, "Fatigue performance of carbon fiber reinforced epoxy resin: A molecular simulation," *Polym. Adv. Technol.*, vol. 32, no. 4, pp. 1518–1530, Apr. 2021, doi: 10.1002/pat.5188.
- [25] M. Kamble, A. S. Lakhnot, S. F. Bartolucci, A. G. Littlefield, C. R. Picu, and N. Koratkar, "Improvement in fatigue life of carbon fibre reinforced polymer composites via a Nano-Silica Modified Matrix," *Carbon*, vol. 170, pp. 220–224, Dec. 2020, doi: 10.1016/j.carbon.2020.08.029.
- [26] X.-F. Wu and O. Zholobko, "Experimental Study of the Probabilistic Fatigue Residual Strength of a Carbon Fiber-Reinforced Polymer Matrix Composite," 2020.
- [27] A. Cameselle-Molares, A. P. Vassilopoulos, and T. Keller, "Two-dimensional fatigue debonding in GFRP/balsa sandwich panels," *Int. J. Fatigue*, vol. 125, pp. 72–84, Aug. 2019, doi: 10.1016/j.ijfatigue.2019.03.032.
- [28] A. Vedrtnam and D. Gunwant, "Modeling improved fatigue behavior of sugarcane fiber reinforced epoxy composite using novel treatment method," *Compos. Part B Eng.*, vol. 175, p. 107089, Oct. 2019, doi: 10.1016/j.compositesb.2019.107089.
- [29] S. S. R. Koor, M. A. Abdullah, M. N. Tamin, and M. R. Ayatollahi, "Fatigue damage of cohesive interfaces in fiber-reinforced polymer composite laminates," *Compos. Sci. Technol.*, vol. 183, p. 107779, Oct. 2019, doi: 10.1016/j.compscitech.2019.107779.
- [30] X. Wang, X. Zhao, and Z. Wu, "Fatigue degradation and life prediction of basalt fiber-reinforced polymer composites after saltwater corrosion," *Mater. Des.*, vol. 163, p. 107529, Feb. 2019, doi: 10.1016/j.matdes.2018.12.001.
- [31] "Materials | Free Full-Text | Experimental Research and Analysis on Fatigue Life of Carbon Fiber Reinforced Polymer (CFRP) Tendons." Accessed: Apr. 23, 2024. [Online]. Available: <https://www.mdpi.com/1996-1944/12/20/3383>
- [32] P. R. Vieira, E. M. L. Carvalho, J. D. Vieira, and R. D. Toledo Filho, "Experimental fatigue behavior of pultruded glass fibre reinforced polymer composite materials," *Compos. Part B Eng.*, vol. 146, pp. 69–75, Aug. 2018, doi: 10.1016/j.compositesb.2018.03.040.
- [33] M. Haggui, A. El Mahi, Z. Jendli, A. Akrouf, and M. Haddar, "Static and fatigue characterization of flax fiber reinforced thermoplastic composites by acoustic emission," *Appl. Acoust.*, vol. 147, pp. 100–110, Apr. 2019, doi: 10.1016/j.apacoust.2018.03.011.
- [34] "Fatigue and tensile behaviors of fiber-reinforced thermosetting composites embedded with nanoparticles - Moustafa Mahmoud Yousry Zaghloul, Yasser S Mohamed, Hassan El-Gamal, 2019." Accessed: May 31, 2024. [Online]. Available: <https://journals.sagepub.com/doi/abs/10.1177/0021998318790093>
- [35] M. Sh. Nikhamkin, N. A. Sazhenkov, and D. Samodurov, "Fatigue Testing Method of Test Coupon and Structurally Equivalent Samples of Carbon Fiber Reinforced Polymer for Gas Turbine Engine Parts and Assemblies," *Solid State Phenom.*, vol. 284, pp. 43–47, Oct. 2018, doi: 10.4028/www.scientific.net/SSP.284.43.
- [36] K. Tanaka, K. Oharada, D. Yamada, and K. Shimizu, "Fatigue crack propagation in short-carbon-fiber reinforced plastics evaluated based on anisotropic fracture mechanics," *Int. J. Fatigue*, vol. 92, pp. 415–425, Nov. 2016, doi: 10.1016/j.ijfatigue.2016.01.015.
- [37] F. Baschnagel, V. Rohr, and G. P. Terrasi, "Fretting Fatigue Behaviour of Pin-Loaded Thermoset Carbon-Fibre-Reinforced Polymer (CFRP) Straps," *Polymers*, vol. 8, no. 4, Art. no. 4, Apr. 2016, doi: 10.3390/polym8040124.



## REVIEW ON GRAPHITE PLUGGED BRONZE BUSHINGS

<sup>A</sup>AMIR ALSAMMARRAIE, <sup>B</sup>MAKI H. ZAIDAN, <sup>C</sup>ALI K. A. ALJBOURY  
Mechanical Department/ Engineering College/Tikrit University, Tikrit-Iraq,

<sup>A</sup>[amircraft@tu.edu.iq](mailto:amircraft@tu.edu.iq)

<sup>B</sup>[makihajzaidan@tu.edu.iq](mailto:makihajzaidan@tu.edu.iq)

<sup>C</sup>[eng.alikhalaf1982@gmail.com](mailto:eng.alikhalaf1982@gmail.com)

**Abstract:** The purpose of lubricating contacting surfaces is to lower wear and friction by adding a layer of low shear strength or separating the surfaces with a fluid coating. While adhering a lubricating solid to a worn surface can be done in a variety of ways, the end effect is always the same: in practically dry conditions, a low friction medium is deposited to minimize wear and friction between two relatively moving surfaces. Graphite is mechanically pressed under extreme pressure into a bearing's grooves to form graphite filled bearings. High loads may be handled by this material, and the graphite acts as self-lubricant. This kind of bearing offers a self-lubricating, maintenance-free bearing solution and operates well in high temperatures. This study seeks to present an extensive review of the mechanisms, performance, drawbacks, and possibilities for productivity and environmental sustainability of graphite-plugged bronze bushings used in machining.

**Keywords:** Graphite, bronze, solid lubricant, friction, wear

### 1. INTRODUCTION

Self-lubricating materials have been increasingly popular for bearing applications for several years, due to economic, environmental, and even technological grounds. This allows for the exclusion of external lubricants like oil or grease and simplifies the design [1]. With increasing shortages of materials and energy, there will be an increasing demand for longer product lifespans, more wear resistance, and lower friction through lubrication. From the standpoint of performance and reliability, the latter is an undesired phenomenon. The term "tribological materials" refers to materials that are intended to reduce wear and friction. In addition, these materials need to meet requirements for damping, thermal expansion, strength, stiffness, and fatigue life. Achieving a balance between these conflicting objectives and minimizing friction from bulk materials used to build tribological components becomes practically impossible from a practical design perspective [2]. To achieve the self-lubricating characteristic, the wear resistance metal back combined with solid lubricants can continually offer a lubricating source during the bearing operation. This material is suitable for a range of operating circumstances due to its low friction factor and the metal's ability to withstand large loads and impacts. This review paper aims to provide an overview of graphite plugged bronze bushings and the graphite that is used as a solid lubricant and their applications in extreme conditions.

### 2. SOLID LUBRICANT

In these and many more conditions, solid lubricants—defined as any solid material intended to reduce friction

and wear between two moving surfaces—are utilized. Solid lubricants are divided into various categories. The two most prevalent kinds are inorganic (which includes MoS<sub>2</sub> and graphite, soft metals, metal oxides, nitrides, and hBN-based lubricants) and organic (which includes polymer-based materials like polyimide and polytetrafluoroethylene). Lubricants that are inorganic and organic can be classified according to their operating temperatures. Liquid lubricants or greases are not suitable for lubricating bearings used in vacuum, extremely high temperatures, or high radiation environments [3]. To put it simply, the specific lubricating needs of extreme operating environments, like corrosive atmospheres and temperatures ranging from -200 to 850C, require a substantial amount of solid substance [3]. Because of their low shear strength and ease of adhesion to the friction surface, solid lubricants can coat the surface of the friction pairs with a steady, continuous lubricant. As a result, friction and wear on the friction pairs are decreased [4]. Like solid lubricants, self-lubricating materials are essential for bearing applications. High temperature performance is achieved due to their self-lubricating characteristics, which reduce the requirement for grease or other lubricants. Graphically (graphite/metal) alloys leverage graphite's unique characteristics, resembling a set of cards having layers that are simple to remove. The crystal system of graphite is hexagonal (Fig.1). Strong bonds hold the carbon atoms in sheets together. The weak connections between the sheets cause graphite to have a decreased shearing strength under friction stress. This helps create a lubricating covering and makes smearing graphite easier. So it can be used as a solid lubricant and become one of the foundations of solid lubrication [6]. Self-lubricating composites can be made using a variety of processes, including machining [7], powder metallurgy [8 - 10] and semi-solid casting [11]. The self-lubricating

qualities and dry sliding characteristics of composites made of metal have been the subject of many investigations to now. The solid lubricant and backing metal are equally as crucial to the creation of composites as the manufacturing method.

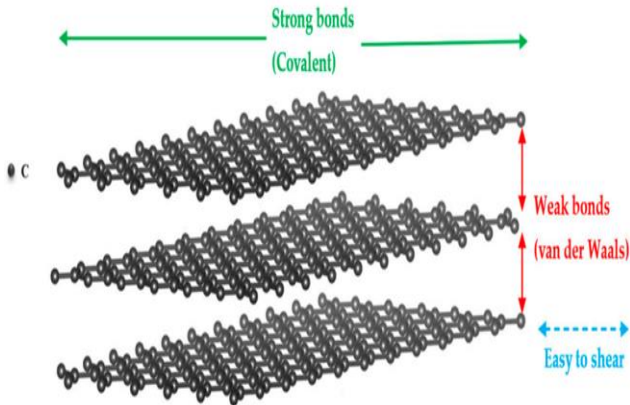


**Fig. 1:** Crystalline Structure of Graphite [5].

Though numerous recent research concentrate on utilizing nickel (Ni) [9, 12], aluminium alloys [6], steel [7, 13], and molybdenum disulfide [9] as backing metals (matrix), the other studies are more interested in solid lubricants, such as polytetrafluoroethylene [7, 13], graphite [12, 6, 10, 8], and aluminium dioxide plus silver [14]. However, very few scientific investigations were published on self-lubricating composites; these studies focused mostly on the use of solid lubricants made of graphite and bronze as backing metals [8, 15]. The dry sliding behavior of graphite composites based on bronze in the case of Fe-based contacts is not well understood. As previously mentioned, traditional casting and powder metallurgy methods can be used to create composites based on bronze. By using traditional casting, a nonhomogeneous structure is created because of huge variances in the densities of Cu and graphite (about 8.96 and 2.25 gr/cm<sup>3</sup>, respectively) and solidification temperatures (1083°C and 3,550°C, respectively) [16]. Nonetheless, other variables need to be managed, including high temperature sintering, mixing, and powder manufacture and this approach waste excessive amounts of energy [15]. Another method for creating bronze-graphite composites is to mechanically drill holes in the bronze and then insert graphite mass into the holes which is an oilless bearing. The types of oilless bearings:

1. Graphite plugged bronze plates
2. Graphite plugged bronze washers.
3. Graphite plugged bronze bushings.



(a)



(b)

**Fig. 2:** oilless bearings: (a): graphite plugged bronze bushings. (b): graphite plugged bronze plates

## 2.1. Lubricants Based on Carbon (Graphite)

Graphite is a solid laminar lubricant that is only made of carbon atoms. These atoms arrange themselves into a hexagonal lattice, with covalent bonds tying the layers together loosely. Graphite's remarkable lubricating properties are attributed to its hexagonal structure, which arranges parallel basal planes that are slightly out of alignment. Because basal planes glide over one another so easily, lubrication relies on this property, which makes solid lubricants with low friction coefficients useful [5]. Figure 1 illustrates a schematic picture of graphite's atomic structure. Graphite absorbs air, oxygen, moisture, and hydrocarbon vapours to achieve low-shear strength as a solid lubricant. However, this need restricts its application in vacuum settings or at high altitudes [17]. Graphite's coefficient of friction (CoF) has been tested several times. One study found that graphite has a CoF of approximately 0.1 at temperatures below 100 °C [18]. In the range of 100 °C to 425 °C, the coefficient increases to approximately 0.4. In a second investigation, it was discovered by Peace et al. [19] that graphite maintains lubricity up to 600 °C, even in oxidizing conditions. It can also function as a lubricant at temperatures as high as 1100 °C to 1200 °C.

## 3. GRAPHITE PLUGGED BRONZE BUSHINGS

One kind of bearing composed of graphite and bronze is the bronze bushing with a graphite plug. Graphite plugged bronze bushings are manufactured with machined holes and/or grooves into which graphite is inserted. They are frequently employed in many applications due to their desirable feature of providing continuous lubrication in harsh environments where oil or grease is difficult to reach [20]. The graphite plugs act as solid lubricants, and the bronze material gives the bushing strength and durability. Under extreme pressure, graphite is mechanically pressed into the grooves and holes. When the bronze bushing is moving relative to one another, the graphite plugs that are embedded within it release lubricating particles which form a film of lubricant between the shaft and bushing. By decreasing friction between the bushing and the shaft or other moving elements, this self-lubricating feature minimizes wear and increases the bushing's lifespan. This eliminates the need for manual lubrication, making these bushings ideal for applications where regular maintenance is difficult or where traditional lubrication methods are impractical. Bronze bushings with plugs made of graphite are available in various alloys and can be specially made to meet specific industrial requirements. They are known for having superior friction, wear, and seizure resistance. These bushings are used in many different sectors and applications, including agricultural machinery, industrial mixers, oil and gas, and even applications involving seawater.

### 3.1 Reasons for choosing graphite-plugged bronze bushings.

#### 3.1.1 Total self-lubricating: No oil or grease is necessary:

Bushings can be used in cases where oiling is difficult, costly, or not possible due to the self-lubricating characteristics. Even at low speeds and with high loads, excellent lubrication is accomplished.

#### 3.1.2. Excellent Wear Resistance:

When oil film development is challenging, such as in high load, low velocity, reciprocating, oscillating, and intermittent motions, excellent wear resistance is achieved.

#### 3.1.3. Low Friction Coefficient: Typically 0.04 to 0.2:

Friction is reduced by self-lubrication using solid lubricants that are carefully placed in.

#### 3.1.4. Extended Operational Temperature Range: -415°F to 1,100°F:

Excellent performance is demonstrated in both hot and cold temperatures.

#### 3.1.5. Corrosion and Chemical Resistance:

Water and caustic chemicals have little effect on performance.

#### 3.1.6. Cost Competitive:

When compared to similar self-lubricating goods, the superior service life results in lower maintenance, replacement, and end-item downtime costs.

## 4. PREVIOUS STUDIES RELATED TO SELF-LUBRICATING BUSHINGS.

It is evident from reading the literature that significant research has been done on estimating the wear and friction of the bronze matrix combined with graphite in the form of whiskers and particles [21–24]. Frictional elements composed entirely of bronze often experience severe adhesive and abrasive wear under high stress situations [25]. On the other hand, the addition of graphite particles into the metallic matrix greatly aids in lubricating the sliding contact and mitigating wear [21 – 24]. The wear graphite debris was found to be able to be preserved by an experiment with texture creation on the copper-graphite composite surface, which further allowed for lowering friction because the transfer layer was simple to produce [26]. The mechanism of mechanical damage in graphite filled bronze composite is rarely studied due to its extreme conditions, which makes it a special instance. This type of solid bronze body minimizes wear and friction because it is drilled readily and filled with solid graphite plugs. In 1999 (J. A. Jones et al) [27] who worked in the US Army Corps of Engineers presented

actual use cases for self-lubricating bushings. According to the Corps' experience, the majority of bearings with lubrication plugs exhibit poor performance in small-movement applications, which nearly exclusively comprise the intended hydropower applications. A poor experience with 30 upgraded machines from 1992 onward was also recorded by J. C. Jones [28] in 2001. He claimed that swelling of lubricant plugs reduced bearing clearance and increased friction and that increased friction with lubricant-plugged bronze bearings and delaminated lining in polymer-lined bearings resulted in a loss of servomotor capacity. The methods for lubricating with grease were put back in place in some instances. Jan Ukonsaari et al. have reported on the performance of numerous bearing types in dry conditions when exposed to different oscillating motion patterns [29]. Eight bearing types in all were tested using a specialized test rig under two distinct motion patterns. Among the eight varieties of bearings were:

Oiles JM3: Oiles 500 JM3 SL4: tin Bronze, Graphite and lead lubricating plugs.

Oiles JM7: Oiles 500 JM7 SL4: aluminum Bronze, lubricant plugs with graphite and lead.

Surface characteristics related to friction and wear are found to be suitable for wicket gate guide vane applications. Only four types were thoroughly investigated in this study, and two of those types are thought to be more appropriate.

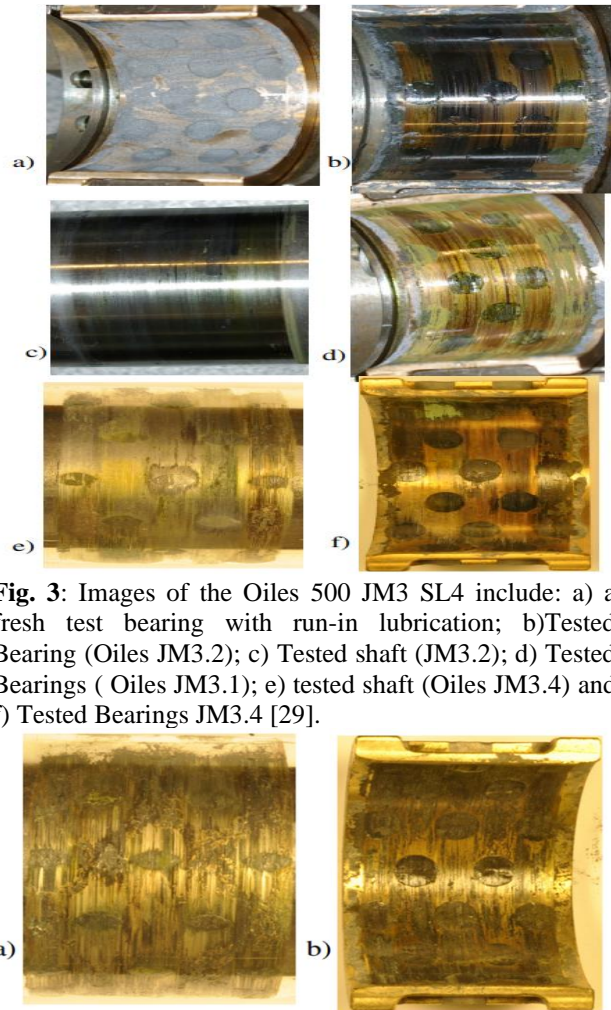


**Fig. 3:** Images of the Oiles 500 JM3 SL4 include: a) a fresh test bearing with run-in lubrication; b) Tested Bearing (Oiles JM3.2); c) Tested shaft (JM3.2); d) Tested Bearings ( Oiles JM3.1); e) tested shaft (Oiles JM3.4) and f) Tested Bearings JM3.4 [29].

**Fig. 4:** Photographs of tested Oiles JM7.4 a) shaft, and b) bearing [29].

(Jun Jiang et al.)[20] used numerous topographic characterizations and computational analysis to study the wear characteristics and contacting stress of graphite filled bronze sliding plates from the field experiment. The findings showed that localized fatigue and erosion were present together with abrasive and adhesive wear, which dominated the contacting surface of the graphite-plugged bronze plate. (Zhao et al.)[30] used aluminium bronze, aluminium bronze-based inlay solid self-lubricating bearing (ISSLB), tin bronze, and tin bronze-based ISSLB materials to perform friction and wear experiments on 45# carbon steel under varying loads (Fig. 5). Under the same load, the wear and friction characteristics of the new self-lubricating bearing material and the old copper alloy were contrasted. The study looked at the effects of wear parameters and friction caused by C-MoS2 composite solid lubricant. While bronze-based ISSLB materials perform better than aluminium bronze-based ISSLB materials in terms of wear and friction, copper-based ISSLB materials show exceptional wear resistance.

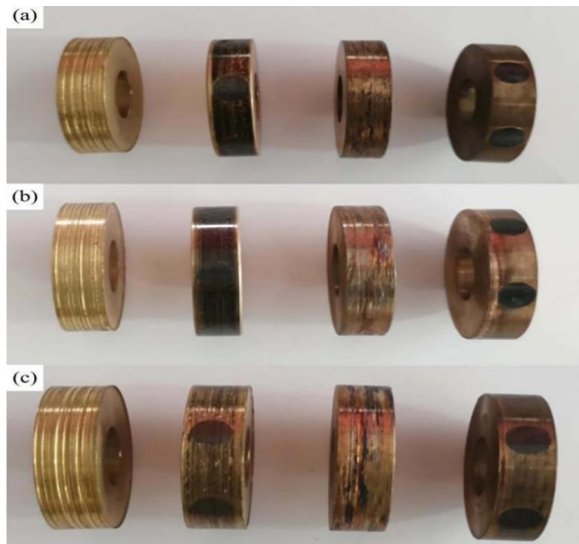
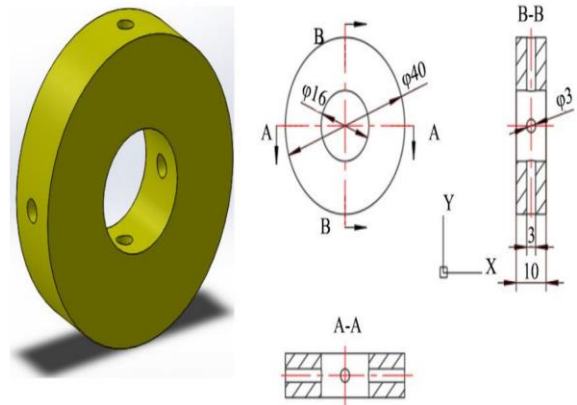


**Fig. 5:** Sample images taken at three different loads: 100 N, 300 N, and 500 N [30].

The effect of graphite-MoS2 composite solid lubricant on the tribological characteristics of copper-based bearing materials in dry conditions was examined by (Chen et al.)[31]. The graphite-MoS2 combination has been incorporated in the matrix of ZQA19-4 aluminium bronze and ZQSn6-3 tin bronze, respectively (figure 6). The results demonstrate that self-lubricating bearing materials with integrated copper have lower friction coefficients and wear rates than conventional copper-based bearing materials. In addition, the wear performance of tin bronze inlaid self-lubricating bearing material is better than that of aluminium bronze inlaid self-lubricating bearing material.



(a) Three-dimensional diagram (b) Two-dimensional diagram

**Fig. 6:** The diagram of sample geometry [31].

Graphite is used as a solid lubricant to study the tribological characteristics of tin bronze and 45 steel with varying filled pore structure sizes [4]. Using an orthogonal equivalent test on a grease-filled MMW-1A tester, the effects of filling pore diameter, depth, and area distribution rate on wear characteristics and friction were examined. Three factors were discovered to have the biggest effects on test results: filling pore diameter > area distribution rate > and filling pore depth. The optimal filling pore size under working conditions is 3 mm, 12%, and 0.5 mm.

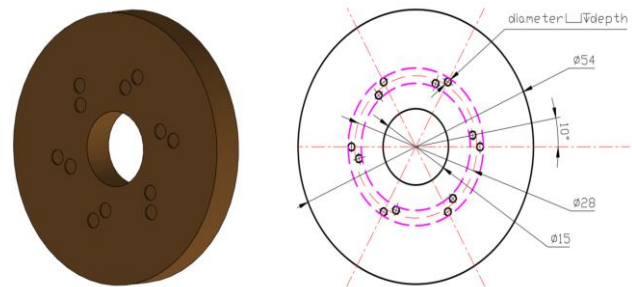


**Fig. 7:** Filling pore structure: (a) 3D diagram, (b) 2D diagram [4]

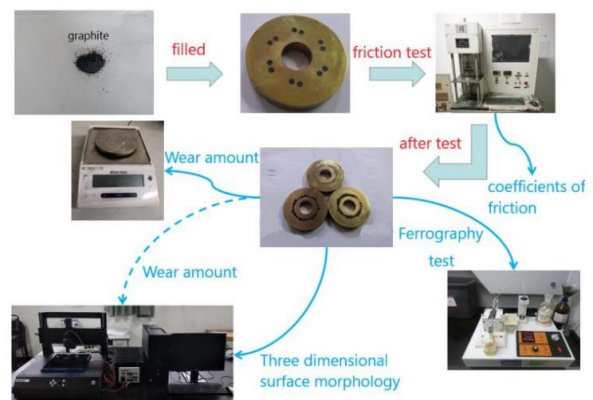


**Fig. 8:** Friction and wear test scheme [4].

Moreover, because graphite is present, the solid bronze is resistant to extreme marine conditions like acid raid and distilled or seawater [32]. Surface texture is one of the primary methods of surface engineering for achieving the desired tribological properties. The goal of surface texturing technology is to create microstructure arrays on a surface with a desired size, shape, and arrangement without altering the material to obtain special characteristics. Square, round, triangular, and elliptical structures are examples of common texture types [33]. Several studies have examined the impact of surface texture type. A study found that adding texture to the surface of a copper-graphite composite reduced friction by preserving worn graphite debris and making the transfer layer easier to create [34]. The surface texture of journal bearings is seen in Figure (9). The following are typical texture attributes: convex body height, texture spacing, pit diameter, depth, depth-to-diameter ratio, groove width, and substrate surface roughness.



Fig. 9: Surface textures of plain bearings [35].

The mechanical and tribological performance is determined by the strength of the interface between the surrounding metal and the graphite plug. Graphite, however, has a relatively weak chemical affinity for copper. Graphite can separate from the matrix under highly stressed shearing conditions, leading to worsened wear of the bronze matrix [36]. Regarding the mechanical characteristics at the interface between bronze plugs and graphite, stress is commonly believed to build up at this point between the heterogeneous phases, which negatively impacts the material's resistance to fatigue and wear [20]. Therefore, one of the primary fields of concern should be the stress situation between the bronze matrix and graphite plug, which is closely related to the interfacial shearing and compressive stresses during the friction process [37].

### 5. DESIGN OF GRAPHITE PLUGGED BRONZE BUSHINGS.

Between 30 and 35% of the surface area should be covered by the generally accepted standard solid lubricant. The proportion may differ depending on the application. To help with the design of bronze bushings with filled graphite, the National Bronze Manufacture in Michigan has created a quick reference guide as shown in Table (1).

Table 1. Calculation of lubrication coverage and plug size


**Calculation of Lubricant Coverage and Plug Size**  
Percentage of Graphite or Solid Lube Coverage


Drill Size	10 %	15%	20%	25%	30%	35%	40%	45%	50%
3/16	8.95	13.43	17.9	22.38	26.85	31.33	36.81	40.28	44.5
1/4	3.03	7.54	10.05	12.57	15.08	17.6	20.11	22.63	25
5/16	3.22	4.83	6.44	8.05	9.66	11.27	12.88	14.49	16.1
3/8	3.23	3.35	4.47	5.59	6.7	7.82	8.94	10.06	11.1
7/16	1.64	2.46	3.28	4.1	4.92	5.75	6.57	7.39	8.2
1/2	1.28	1.89	2.51	3.14	3.77	4.4	5.03	5.66	6.28

1. Choose the appropriate drill or plug size.
2. Locate the desired solid lubricant coverage. Use factor number opposite drill or plug size.
3. Multiply bushing ID x bushing length. Multiply factor number to obtain the number of holes or plugs.

Example: 2" ID x 2-1/2 OD x 2" Length

1. 1/4 plug diameter
2. 35% coverage from chart 17.6
3. 2 x 2" length x 17.6 + 70 drilled holes or plugs.





**Quality Bronze Products Since 1911**  
28070 Hayes Road, Roseville, MI 48066  
Phone: 586-791-2000 Toll Free: 800-875-3558  
Fax: 586-791-9044 Email: sales@nationalbronze.com  
[www.nationalbronze.com](http://www.nationalbronze.com)

### 6. CONCLUSION

Based on experimental results and applications of graphite plugged bronze bushing, we conclude that the following factors should be taken into account when constructing a self-lubricating graphite bronze bushing:

- **Wear and friction:** The bushing needs to be made with as little wear and friction as possible. Although self-lubrication is provided by the graphite in the bushing, the mating surface and operating circumstances should also be considered in the design.
- **Load capacity:** The bushing needs to be able to support the loads applied to it without breaking down or deforming. This is dependent upon the bushing's geometry and material qualities.
- **Temperature and surroundings:** The bushing must be able to function in the specified temperature range and surrounding circumstances without degrading or breaking. Temperature-related effects on the graphite in the bushing should be taken into account in the design, along with other environmental considerations.

### References

[1] Xiang D., Shan K., "Friction and wear behavior of self-lubricating and heavily loaded metal-PTFE composites", *Wear* 260, 1112-1118, 2006.

[2] Thomas W. Scharf, S. V. Prasad, "Solid lubricants: a review". *Journal of Material Science*, 48:511-531, 2013.

[3] Sunil T., Sandeep M., Kumaraswamy R., Shravan A., "A Critical Review on Solid Lubricants". *International Journal of Mechanical Engineering and Technology*, 7(5), 193-199, 2016.

[4] Xu X., Feng Z., Xiao N., Liu B., Zhao X., "Effect of Graphite Filling Pore Structure Size on the Tribology



- Behaviors of Tin Bronze/45 Steel Pairs With Grease Under Low-Speed and Heavy Load Conditions". *Tribology in Industry*, Vol. 45, No. 2, 351-366, 2023.
- [5] Hedayati, H., Mofidi, A., Al-Fadhli, A., Aramesh, M., "Solid Lubricants Used in Extreme Conditions Experienced in Machining: A Comprehensive Review of Recent Developments and Applications". *Lubricants*, 12, 69, 2024.
- [6] Rajaram, G., Kumaran, S. and Srinisava Rao, T., "Sliding wear behavior of Al-Si/graphite composite", *Tribology Transactions*, Vol. 54 No. 1, pp. 115-121, 2011.
- [7] Xiang, D., Shan, K., "Friction and wear behavior of self-lubricating and heavily loaded metal-PTFE composites", *Wear*, Vol. 260, pp. 1112-1118, 2006.
- [8] Jia, J., Chen, J., Zhou, H., Wang, J. and Zhou, H., "Friction and wear properties of bronze-graphite composite under water lubrication", *Tribology International*, Vol. 37 No. 5, pp. 423-429, 2004.
- [9] Parucker, M.L., Klein, A.N., Binder, C., Junior, W.R. and Binder, R. (2014), "Development of self-lubricating composite materials of nickel with molybdenum disulfide, graphite and hexagonal boron nitride processed by powder metallurgy", *Journal of Materials Research*, Vol. 17 No. 1, pp. 180-185, 2014.
- [10] Cui, G., Niu, M., Zhu, S., Yang, J. and Bi, Q., "Dry-sliding tribological properties of bronze-graphite composites", *Tribology Letters*, Vol. 48 No. 2, pp. 111-122, 2012.
- [11] Kulusa, J., Malec, W., Juszczak, B., Malara, S. and Cwolek, B., "Microstructure and tribological properties of tin bronze-graphite composites made by stir casting", *Metalurgija*, Vol. 55, pp. 19-21(2016).
- [12] Zhao, H., Lie, L., Hu, W. and Shen, B., "Friction and wear behavior of Ni-graphite composites prepared by electroforming", *Materials & Design*, Vol. 28 No. 4, pp. 1374-1378 (2007).
- [13] Xiang, D., Shu, W. and Li, K., "Friction and wear behavior of a new 40Cr steel-PTFE fabric composite under heavy loads", *Materials Science and Engineering: A*, Vol. 483/484, pp. 365-368, 2008.
- [14] Cui, G., Li, J. and Wu, G., "Friction and wear behavior of bronze matrix composites for seal in antiwear hydraulic oil", *Tribology Transactions*, Vol. 58 No. 1, pp. 51-58, 2015.
- [15] Zhang, P., Du, Y. and Zeng, D., "Preparation QT13.5-3.5 graphite lubricant material with semi-solid casting technology", *Journal of Materials Science and Technology*, Vol. 17 No. 1, pp. 155-158, 2001.
- [16] Toktas G., Yilmaz I., "Tribological properties of self-lubricating bronze-graphite composite against Fe-based alloys", *Industrial Lubrication and Tribology*, 68/6, 665-670, 2016.
- [17] Allam, I.M. "Solid Lubricants for Applications at Elevated Temperatures: A Review". *J Mater. Sci.*, 26, 3977-3984, 1991.
- [18] Sliney, H.E., "Solid Lubricants"; Lewis Research Center: Cleveland, OH, USA, 1991.
- [19] Blau, P.J., "Friction Science and Technology: From Concepts to Applications", 2nd ed.; CRC Press: Boca Raton, FL, USA, 2008.
- [20] Jiang J, Wan SH, Yi G, Wang J, Chang J, Jin W, Lei J, Lu B, Qu F, "A case study on the wear mechanism and stress evolution of graphite plugged bronze wear plate from the field trial", *Engineering Failure Analysis* 131, 2022.
- [21] Ma WL, Lu JJ. "Effect of sliding speed on surface modification and tribological behavior of copper-graphite composite". *Tribol Lett*; 41: 363-370, 2011.
- [22] Rohatgi PK, Ray S, Liu Y. Tribological properties of metal matrix-graphite particle composites. *Int. Mater. Rev.*; 37: 129-149, 1992.
- [23] Auechalitanukul C., McCuiston R.C., Bunlangsup B., Naikorn C., Tapanan S., "Properties of sintered bronze-graphite containing natural anhydrite", *Key Eng. Mater.* 751, 19-24, 2017.
- [24] Ahmad H., Stelzer R., Nestler D., Nendel W., Kroll L., Wagner G., "The development of lead-free sliding contacts based on bronze-graphite composites through powder injection moulding, *Key Eng. Mater.* 742, 205-212, 2017.
- [25] Cui G., Bi Q., Yang J., Liu W., Effect of normal loads on tribological properties of bronze-graphite composite under seawater condition, *Tribol. Trans.* 57 (2), 308-316, 2014.
- [26] Hashemi M., "Microstructure and wear behavior of a manganese bronze bearing material under unlubricated conditions", *Tribol. Trans.* 58 (4), 750-757, 2015.
- [27] Jiang X.F., Song J.J., Su Y.F., Zhang Y.S., Hu L.T., "Novel design of copper-graphite self-lubricating composites for reliability improvement based on 3D network structures of the copper matrix", *Tribology Letters*. 66:143, 2018.
- [28] Jones J.A., Palylyk R.A., Willis P., Weber R.A., "Greaseless Bushings for Hydropower Applications: Program, Testing, and Results", CERL Technical Report 99/104, 1999.
- [29] Jones J. C., "Wicket Gate Bushings - Grease vs. Greaseless", USBR - 2001 Power O&M Workshop, April 10-12, Reno, Nevada, 2001.
- [30] Jan Ukonsaari J., Prakash B., "Paper Title: Performance and surface characteristics of slow oscillating journal bearing types subjected to various motion pattern", *Engineering, Environmental Science*, 2014.
- [31] Zhao L., Li J., Yang Q., Wang Y., Zhang, X., Li H., Yang Z., Xu D., Liu J., "Study on Friction and Wear Properties of New Self-Lubricating Bearing Materials", *Crystals*, 12, 834, 2022.
- [32] Chen, Cuicui, Qi Y., Qi Ch., Wang Ya., Xu Do., Li He., Zhang Xi., Harvey Ch., and Liu Ji., "Tribological Properties of Copper-embedded Self-lubricating Bearing Materials". Loughborough University, 2022.
- [33] Cui G. J., Bi Q. L., Niu M. Y., Yang J., Liu W. M., "The tribological properties of Bronze-SiC-Graphite composites under seawater condition". *Tribology International*, 60, 25-35, 2013.
- [34] Du F., Li D., Sa X., Li C., Yu Y., Li C., Wang J., Wang W., "Overview of Friction and Wear Performance of Sliding Bearings", *Coatings*, 12, 1303, 2022.
- [35] Jiang X.F., Song J.J., Su Y.F., Zhang Y.S., Hu L.T., "Novel design of copper-graphite self-lubricating composites for reliability improvement based on 3D network structures of the copper matrix", *Tribol. Lett.* 66:143, 2018.
- [36] Lu, X.; Khonsari, M.M. "An experimental investigation of dimple effect on the stribeck curve of journal bearings". *Tribol. Lett.*, 27: 169-176, 2007.
- [37] Gheorghie S., Sontea S., in: "Proceedings of Powder Metallurgy World Congress and Exhibition", Granada, Spain, 1998.
- [38] Deshpande P.K., Lin R.Y., "Wear resistance of WC particle reinforced copper matrix composites and the effect of porosity", *Material Science and Engineering A* 418 (1-2)137-145, 2006.



## IMPACT OF ACTIVE FILLER COMPOSITION MODIFICATION ON THE SORPTION CHARACTERISTICS OF FILTERS

BILJANA MIHAJLOVIĆ

TRAYAL Corporation, Kruševac, [aktivni.ugljevi@gmail.com](mailto:aktivni.ugljevi@gmail.com)

MARINA ILIĆ

Military Technical Institute, Belgrade, [marinailic1970@gmail.com](mailto:marinailic1970@gmail.com)

TATJANA MARKOVIĆ

Military Technical Institute, Belgrade, [tanjin.mejl@gmail.com](mailto:tanjin.mejl@gmail.com)

VUKICA GRKOVIĆ

TRAYAL Corporation, Kruševac, [vukica.g30@gmail.com](mailto:vukica.g30@gmail.com)

**Abstract:** To expand the protection range of filters against industrial chemical agents, with a focus on carbon monoxide, beyond the protection offered by the existing M3 and CBRN filters, a new alternative filter, named CO CBRN ESC Filter, was developed with a modified active filler composition. In accordance with defined requirements and existing equipment, the laboratory testing was conducted to evaluate the effect of the modified active filler composition in the CO CBRN ESC Filter on the sorption characteristics, specifically regarding protection against NBC agents and industrial toxic chemicals. The CO CBRN ESC Filter contains a dual-component active filler, consisting of a layer of activated carbon impregnated with calcium chloride salts and a layer of hopcalite, which is a mixture of copper and manganese oxides.

**Keywords:** alternative CO CBRN ESC Filter, dual-component active filler, physical-mechanical testing, sorption characteristics of filters.

### 1. INTRODUCTION

The onset of the 21st century, marked by terrorist attacks and other forms of threats, has highlighted the need for the protection of both civilian populations and defense personnel. The impact of toxic chemical agents in the form of gases, vapors, and liquid and solid aerosols, which may be employed in such situations but are not classified as warfare agents, often leads to systemic paralysis and unintended consequences. These toxic chemical agents are typically easily accessible and simple to deploy<sup>[1], [2]</sup>

The need for respiratory protection devices, particularly filters, imposes new and additional requirements for their development. In response to emerging global trends, TRAYAL Corporation, in collaboration with experts from the Military Technical Institute, developed an alternative filter to expand the protection range against various industrial toxic chemicals, with a focus on carbon monoxide. The results of the testing of this alternative filter, referred to as the CO CBRN ESC (hereinafter referred to as the alternative filter), provided a basis for its justified application in various situations. The test gases used to examine the alternative filter included representatives of NBC toxic agents (phosgene, chloropicrin, and hydrogen cyanide), supplemented by

gases representative of industrial toxic chemicals (sulfur dioxide, cyclohexane, ammonia, and carbon monoxide). The filters were tested in a laboratory under precisely defined and controlled parameters, including the input concentration and flow rate of the test gas, as well as the humidity and temperature of the air and test gas mixture, which partly correspond to conditions in accidental situations. Accidental conditions imply the potential presence of unforeseen toxic chemical agents, as well as faster movement of the user and accelerated breathing due to fear and panic. Therefore, it is necessary to conduct comparative tests of the alternative filters by modifying one testing parameter, such as only the airflow, to gain a clearer understanding of the filter's applicability in emergency situations.

Previous studies have presented the impact of changing the impregnation of activated carbon as the active filler in M3 Filters, as well as the effect of the height of the active filler on the sorption characteristics of M3 and CBRN Filters under defined testing parameters. The results obtained from these studies provided a good starting point for establishing new protection requirements for the alternative filter against carbon monoxide, to which the tested M3 and CBRN Filters did not respond, alongside the spectrum of other test gases for which the M3 and CBRN Filters met the established criteria. Additionally, the alternative filter can be used with a protective mask

(both half and full-face masks) as well as with an evacuation hood employed in emergency situations (e.g., fires).<sup>[2]</sup>

Given the decades-long tradition of producing carbon monoxide (CO) filters at TRAYAL Corporation, the challenge of developing this alternative filter was well-founded. The alternative filter analyzed in this study shares similarities with previous generations of filters, where a dual-component filler (impregnated activated carbon and hopcalite)<sup>[4]</sup> was used as the active filler. The alternative filter must also meet requirements concerning filter weight limitation (up to 330 g) and inhalation resistance, making it easily applicable for potential users, such as when wearing an evacuation hood or as a filter for children's masks and other masks and half masks.

The CO CBRN ESC Filter contains a dual-component active filler, comprising a layer of activated carbon impregnated with calcium chloride salts<sup>[3]</sup> and a layer of hopcalite, which is a mixture of copper and manganese oxides<sup>[4]</sup>. The activated carbon in the alternative filter is produced using TRAYAL Corporation's manufacturing technology, with granulation corresponding to that of the M3 filter's active filler. The activated carbon has an activity level, defined by an iodine number, of no less than 1250 mg/g of activated carbon. Hopcalite, the second component of the alternative filter's active filler, is a material already used at TRAYAL Corporation and consists of a mixture of copper and manganese oxides. The hopcalite is sourced from a long-standing supplier, with the homologation of the mixture performed at TRAYAL Corporation.

The alternative filters used for sorption testing with the test gases were filled with the aforementioned dual-component filler and manufactured according to the standard technology used for M3 Filters. Besides modifications in the active filler, these filters also feature a modified anti-aerosol insert to more effectively utilize the designed space for the active filler.

## 2. EXPERIMENTAL PART

The examination of sorption properties of the CO CBRN ESC filter was conducted in accordance with the SORS 8748 and SRPS EN 14387 standards.

### 2.1. Methods for Testing Sorption Characteristics of the CO CBRN ESC Filter against NBC Test Gases (Phosgene, Chloropicrin, and Hydrogen Cyanide)

The methods for testing involve monitoring and recording the protection time as an indicator of the filter's sorption properties when exposed to test gases (phosgene, chloropicrin, and hydrogen cyanide) under defined conditions and testing parameters. These methods include maintaining constant input concentrations of test gases and the relative humidity of the test gas-air mixture while varying the flow rate of the incoming gas mixture. The testing method for sorption characteristics of the CO CBRN ESC filter against NBC test gases phosgene, chloropicrin, and hydrogen cyanide is conducted in accordance with the SORS 8748 standard.

The flow rate of the air and test gas mixture (phosgene, chloropicrin, and hydrogen cyanide) is adjusted until the

defined input concentration for the specific test gas and the relative humidity of the gas mixture are achieved. This process is repeated when varying the flow rate of the incoming gas mixture for a specific test gas. The time is measured from the moment the air and test gas mixture enter the filter until the indicator paper changes color. The measured time indicates the protection time of the filter against the specific test gas.<sup>[5]</sup>

### 2.2. Methods for Testing Sorption Characteristics against the Effects of Industrial Toxic Test Gases (Sulfur Dioxide, Cyclohexane, Ammonia, and Carbon Monoxide)

The testing methods involve monitoring and recording the protection time as an indicator of the filter's sorption properties when exposed to test gases (sulfur dioxide, cyclohexane, ammonia, and carbon monoxide) under defined testing conditions and parameters. This includes maintaining constant input concentrations of test gases and the relative humidity of the gas-air mixture while varying the flow rate of the incoming gas mixture.

The method for testing sorption characteristics against the effects of sulfur dioxide and ammonia is conducted in accordance with the SRPS EN 14387 standard, while the testing of sorption characteristics against the effects of cyclohexane and carbon monoxide is carried out according to the manufacturer's internal method.<sup>[6]</sup>

#### 2.2.1. Procedure for testing sorption characteristics method against the effects of sulfur dioxide and ammonia

The flow rate of the air and test gas mixture (sulfur dioxide, cyclohexane, and ammonia) is adjusted until the defined input concentration for the specific test gas and the relative humidity of the gas mixture are achieved. This process is repeated when varying the flow rate of the incoming gas mixture for the specific test gas. The time is measured from the moment the air and test gas mixture enters the filter until the indicator paper changes color. The measured time indicates the protection time of the filter against the specific test gas.

#### 2.2.2. Procedure of the Testing Method for Sorption Characteristics of the CO CBRN ESC Filter against Carbon Monoxide

The gas analyzer and artificial lungs are activated, and the flow rate of the air and carbon monoxide gas mixture is adjusted until the defined input concentration, relative humidity and temperature of the gas mixture in the detection system are achieved. The time is measured from the moment the gas mixture is introduced into the test filter until the gas analyzer detects an output concentration of carbon monoxide test gas in the system at 200 ppm

#### 2.2.3. Procedure of the Testing Method for Sorption Time Characteristics of the CO CBRN ESC Filter against Cyclohexane

The flow rate of the air and cyclohexane gas mixture is adjusted until the required input concentration of the test gas and the relative humidity of the gas mixture in the detection system are achieved. The time is measured from

the moment the cyclohexane and air gas mixture is introduced into the test filter until an output concentration of cyclohexane at 10 ppm is detected in the system.

### 3. RESULTS AND DISCUSSION

The CO CBRN ESC filter contains a dual-component active filling, consisting of a layer of activated carbon impregnated with calcium chloride salts, as well as a layer of hopcalite, which is a mixture of copper and manganese oxides ( $\text{Cu}^{2+}$  and  $\text{Mn}^{+}$ ). The activated carbon in the alternative filter is produced using the technology developed by TRAYAL Corporation, while the hopcalite is purchased from a long-term supplier and homologated immediately before filling the filter.

#### 3.1. Testing Results of the Physical-Mechanical Characteristics for Both Layers of Active Filling and the Filter

To gain a more comprehensive understanding of the potential broader application and enhanced functionality of the alternative filter, it is necessary to test the following physical-mechanical characteristics for both layers of active filling, in accordance with the SORS 8830/05 standard: moisture content, bulk density, mechanical strength, and granulometric composition. [8] The testing results of the characteristics of the active fillings are presented in Table 1.

**Table 1.** Physical-mechanical characteristics for both layers of active filling in the CO CBRN ESC filter

ACTIVE FILLINGS	Activated Impregnated $\text{CaCl}_2$	Hopcalite
<b>MOISTURE CONTENT [%]</b>	1.1	0.48
Bulk Density [G/L]	520.9	785.0
<b>MECHANICAL STRENGTH [%]</b>	78	63
<b>GRANULOMETRIC COMPOSITION (%)</b>		
>1.8 MM	0.00%	3.16%
> 1.6 MM	0.41%	21.19%
>1.4 MM	6.03%	20.04%
0.7-1.4 MM	92.66%	54.91%
	0.89%	0.61%
	0.01%	0.09%

Furthermore, for the alternative filter to be easily applicable when wearing a mask or evacuation hood, it must meet defined requirements regarding the filter's mass (up to 330 g) and inhalation resistance. For these reasons, before testing the filter's sorption characteristics, it is necessary to examine the following physical-mechanical characteristics of the CO CBRN ESC filter in accordance with SORS 8829 and SRPS EN 14387 standards: mass, inhalation resistance, and filtration efficiency using paraffin aerosol mist. The testing results of the CO CBRN ESC filter's characteristics are presented

in Table 2.

**Table 2.** Physical-mechanical characteristics for both layers of active filling in the CO CBRN ESC filter

Filter Type	Mass [g]	Отпор филтера (Pa)	Ефикасност филтрирања (%)
CO CBRN ESC	315	110	$1 \times 10^{-3}$
CO CBRN ESC	330	120	$1 \times 10^3$
CO CBRN ESC	327	113	$1 \times 10^3$

The obtained test results presented in Table 1 meet all the requirements related to the physical-mechanical characteristics of the active layers in the filter, while the results in Table 2 satisfy all the requirements for the physical-mechanical characteristics of the CO CBRN ESC filter. This fact is significant not only because it fulfills the necessary requirements but also as confirmation that the manufacturing technology for the alternative filter is justified in terms of functionality and protection, providing a solid basis for the potential application of this filter. Additionally, these preliminary tests are a prerequisite for evaluating the possibility of expanding the protection range of the alternative filter, particularly its use in emergency situations, by testing the filter's sorption characteristics against NBC toxic gases, as well as industrial toxic gases, with a focus on carbon monoxide.

#### 3.2. Testing Results of the Sorption Characteristics of the CO CBRN ESC Filter against NBC Test Gases (Phosgene, Chloropicrin, and Hydrogen Cyanide)

The testing of the sorption characteristics of the CO CBRN ESC filter against NBC test gases (phosgene, hydrogen cyanide, and chloropicrin), expressed as protection time (minutes), was conducted under the following conditions:

- Input concentration of the test gas (phosgene and hydrogen cyanide): 1000 ppm,
- Input concentration of the test gas (chloropicrin): 2200 ppm,
- Relative humidity of the air-gas mixture (phosgene, hydrogen cyanide, and chloropicrin): 80%, and
- flow rate of the air-gas mixture (phosgene, hydrogen cyanide, and chloropicrin): 30 l/min and 64 l/min.

The values of the tested input concentrations of the test gases (phosgene, hydrogen cyanide, and chloropicrin), as well as the humidity of the input test gas-air mixture, were kept constant for all the tested filters. To simulate conditions closer to those encountered during the use of filters in accidental situations, we tested the sorption characteristics of the filters at different gas mixture flow

rates of 30 l/min and 64 l/min. [7],[6], [9]

The obtained testing results of the sorption characteristics of the CO CBRN ESC filter against NBC test gases (phosgene, hydrogen cyanide, and chloropicrin), expressed as protection time (minutes), are presented in Table 3 (relative humidity of the gas-air mixture is 80 %).

**Table3.** Sorption Characteristics of the Filter Against NBC Test Gases (Phosgene, Hydrogen Cyanide, and Chloropicrin)

Test gas	Input concentration [ppm]	Protection time [min] 30 l/min	Protection time [min] 64 l/min
Phosgene	1000	25	11
		23	10
		24	9
Chloropicrin	2200	36	29
		37	30
		34	28
		29	14
Hydrogen cyanide	1000	27	12
		30	12

### 3.3. Testing Results of the Sorption Characteristics of the CO CBRN ESC Filter against Industrial Toxic Test Gases (Sulfur Dioxide, Cyclohexane, Ammonia and Carbon Monoxide)

The testing of the sorption characteristics of the CO CBRN ESC filter against industrial toxic test gases (sulfur dioxide, cyclohexane, ammonia), expressed as protection time (minutes), was conducted under the following conditions:

- Input concentration of the test gas (sulfur dioxide, cyclohexane, ammonia): 1000 ppm
- Relative humidity of the air-gas mixture (sulfur dioxide, cyclohexane, ammonia): 70% until breakthrough,
- Flow rate of the air-gas mixture (sulfur dioxide, cyclohexane, ammonia): 30 l/min and 64 l/min.

The testing of the sorption characteristics of the CO CBRN ESC filter against the industrial toxic test gas (carbon monoxide), expressed as protection time (minutes), was conducted under the following conditions:

- Input concentration of the test gas (carbon monoxide): 2500 ppm,
- Relative humidity of the air-gas mixture (carbon monoxide): 80% until the breakthrough concentration of 200 ppm, temperature 50 °C, and
- Flow rate of the air-gas mixture (carbon monoxide): 30 l/min and 45 l/min.

Due to the characteristics of the testing apparatus for evaluating the sorption characteristics of the filter against carbon monoxide, it was not possible to set a flow rate of 64 l/min. The apparatus uses artificial lungs with a working rate of 20 cycles per minute (1.5 l per cycle). The maximum setting allowed by the apparatus is 30 cycles per minute (1.5 l per cycle), or 45 l/min.

The obtained testing results of the sorption characteristics of the CO CBRN ESC filter against these gases (sulfur dioxide, cyclohexane, ammonia and carbon monoxide),

expressed as protection time (minutes), are presented in Table 4.

**Table4.** Sorption characteristics of the filter against industrial test gases (sulfur dioxide, cyclohexane, ammonia and carbon monoxide)

Test gas / Input concentration [ppm]	Relative humidity [%]	Protection time [min] 30 l/min	Protection time [min] 64/ 45* l/min
Sulfur dioxide 1000	70	28	10
		30	9
		24	10
Ammonia 1000	70	108	38
		107	39
		112	39
Cyclohexane 1000	70	68	34.6
		67	29.1
		66	30
Carbon monoxide* 2500	80	36	7
		35	8
		39	8.3

Given that the tests revealed that the new filter does not meet the protection time requirements (15 minutes) for higher flow rates of test gases, specifically against certain NBC gases (phosgene and hydrogen cyanide) and industrial gases (carbon monoxide and sulfur dioxide), filters with a new ratio of activated carbon to hopcalite layers (favoring hopcalite) were produced. Additional testing of the sorption characteristics of the new filters against industrial gases was conducted, and the results are presented in Table 5.

**Table 5.** Sorption characteristics of the filter (from a new batch) against industrial test gases (sulfur dioxide, cyclohexane, ammonia and carbon monoxide)

Test gas / Input concentration [ppm]	Relative humidity [%]	Protection time [min] 30 l/min	Protection time [min] 64/ 45* l/min
Sulfur dioxide 1000	70	46	14
		51	12
		45	
Ammonia 1000	70	110	38
		109	39
		113	
Cyclohexane 1000	70	48	20
		51.4	20.4
		49	21
Carbon monoxide* 2500	80	43	8
		39	10
		46	9.3

## 4. CONCLUSION

The aim of this study is to extend the protection range of the filter to include both NBC agents and industrial toxic gases, as prescribed by the SRPS EN 403 standard. TRAYAL Corporation has developed a filter under the working name CO CBRN ESC, which differs from the M3 and CBRN standard filters in the composition of its active filling. The active filling consists of two distinct components: a layer of activated carbon impregnated with calcium chloride and a layer of hopcalite, with a standard filling height. Accordingly, the influence of the active

filling composition on the sorption characteristics of the filter against NBC agents and industrial toxic gases was examined. To simulate conditions similar to those in accidental situations, the flow rate of the gas mixture was varied, while parameters such as the relative humidity of the gas mixture and the input concentration of the test gas remained constant and were defined by the standard.

Additionally, to meet the functional requirements of this filter and its application as a component of military masks, half-masks, children's protective masks, and evacuation hoods, the testing results for the overall mass of the filter and inhalation resistance have shown that the filter meets the specified requirements.

The testing results indicated that the alternative filter did not meet the required protection time (15 minutes) for higher gas mixture flow rates against the following test gases: phosgene, hydrogen cyanide, and acidic gases such as sulfur dioxide and carbon monoxide. For this reason, additional tests were conducted on filters with an adjusted ratio of activated carbon to hopcalite layers, favoring hopcalite. The results of these sorption characteristic tests on the new filter showed an improvement in protection time against sulfur dioxide, while the protection time against cyclohexane decreased.

These new tests have opened up the possibility for a more detailed researching into the impact of changing the ratio of active filling layers, specifically the homologation of these layers, on the filter's sorption characteristics against all toxic agents. This could serve as a foundational basis for future articles and research in this field.

## References

- [1] Impact of the altered texture of the active filling of the filter on the sorptive characteristics with the special reference to the efficiency of filtering, by Ilic M, SenicŽ, Petrović V Mihajlović B, Grković V
- [2] Impact of the different active filling height of the filter on the sportive characteristics of filtering, by M. Ilić, T. Marković, B. Mihajlović, V. Grković, S. Bauk
- [3] Adapted from Smisek, M. and Cerny, S., in Active Carbon, Elsevier Publ. Co., Amsterdam, 1970; and Jankowska H., Swiatkowski A., and Choma, J., in Active Carbon, Ellis Howard, England, 1991. With permission
- [4] Letał Mists, Eric. R. Taylor, An Introduction to the natural and Militar Sciences of Chemical, Biological Warfare and Terorism
- [5] SORS 8748:2004, Personal CBRN protect device, Requirements and methods testing
- [6] SRPS EN 14387:2013, Respiratory protective devices- Gas filter(s) and combined filter(s)- Requirements, testing, marking, Institute for Standardization of Serbia.
- [7] SORS 8829:2005, Filter, Combined filter M3, Requirements and methods testing
- [8] SORS 8830:2005, Personal CBRN protect device, Active carbon KI M3 for combined filter, Requirements and methods testing;
- [9] NIOSH Standard, Attachment A, Statement of Standard for Chemical, Biological, Radiological, and Nuclear (CBRN) For Air-Purifying Escape Respirator, September 30<sup>th</sup> 2003 year.



## EFFECT OF TEMPERING PARAMETERS ON MICROSTRUCTURE AND HARDNESS OF A LOW ALLOY ARMOR STEEL

GVOZDEN JOVANOVIĆ

Institute for Technology of Nuclear and Other Mineral Raw Materials, Belgrade, Serbia, [g.jovanovic@itnms.ac.rs](mailto:g.jovanovic@itnms.ac.rs)

DRAGOMIR GLIŠIĆ

University of Belgrade, Faculty of Technology and Metallurgy, Belgrade, Serbia, [gile@tmf.bg.ac.rs](mailto:gile@tmf.bg.ac.rs)

STEFAN DIKIĆ

University of Belgrade, Faculty of Technology and Metallurgy, Belgrade, Serbia, [sdikic@tmf.bg.ac.rs](mailto:sdikic@tmf.bg.ac.rs)

ESMAIL ALI SALEM AHMED

College of Civil Aviation and Meteorology, Tripoli, Libya,

University of Belgrade, Faculty of Technology and Metallurgy, Serbia, Belgrade [esmail\\_682005@yahoo.com](mailto:esmail_682005@yahoo.com)

NENAD RADOVIĆ

University of Belgrade, Faculty of Technology and Metallurgy, Serbia, Belgrade, [nenrad@tmf.bg.ac.rs](mailto:nenrad@tmf.bg.ac.rs)

**Abstract:** The final stage of heat treatment that gives high hardness to armor steels its final structure and characteristics is tempering after quenching. The precipitation of carbides from the supersaturated solution is influenced by the tempering regime selected. The steel used in this work was a low alloy quenched and tempered steel (commercial name "PROTAC"), with following chemical composition: 0.32 wt.% C, 0.44 wt.% Mn, 0.98 wt.% Cr, 3.09 wt.% Ni, 0.43 wt.% Mo, 0.019 wt.% Nb, 0.003 wt.% Ti, 0.035 wt.% V. The samples were tempered at various temperatures between 200 and 500°C for varying periods of time after being quenched in oil at 925°C. The samples were examined using hardness testing, scanning electron microscopy, and light microscopy. The highest value of hardness of 430 HV was obtained after tempering at 300°C for 15 min. Due to the comparatively short tempering duration, this result was attributed to the precipitation of coherent and semi-coherent ferrous carbide particles rather than alloying element carbides. After reaching the maximum value of 430 HV hardness drops with further increase of temperature. The increase of hardness by prolonged tempering time was higher at 300°C than at 200°C.

**Keywords:** Armor Steel, Quenching and Tempering, Kinetics of Tempering, Hardness

### 1. INTRODUCTION

Due to the great diversity in alloyed steels and the inevitable overlap in chemical composition, there was a need to classify steels according to their heat treatment. Therefore, quenched and tempered steels (Q+T steels) are those that undergo these last steps in thermal processing after which they obtain final microstructure and properties [1,2]. When it comes to the best ratio of strength and toughness, microstructurally it comes to thermomechanically rolled fine-grain structural steels and quenched and tempered steels [3,4]. The choice of tempering regime determines the process of precipitation of carbides from the supersaturated solution. The long duration and high temperatures of tempering (200-700°C) can provide huge variations in morphology of tempered martensite and mechanical properties [5]. Despite the fact that tempering increases strength at the expense of toughness Q+T steel are still unmatched when it comes to having increased toughness among high strength steels.

Heat treatment regime controls the size and distribution of carbide particles in steels. This is of crucial importance for the dominant strengthening mechanism in quenched and tempered steels is precipitation hardening, followed by grain refinement [5].

The aim of this work was to examine different tempering regimes of quenched steel under commercial conditions and to determine the influence of heat treatment process parameters on microstructural changes and mechanical properties in terms of hardness.

### 2. MATERIALS AND METHODS

Low alloy high hardness armor steel (HHA) produced by Acroni d.o.o. Jesenice, Slovenia under commercial name Protac 500 was used in this investigation. Chemical composition of the steel is given in Table 1. As received 8 mm thick plates in quenched condition were soft annealed at 700°C for 4 hours in a protective argon atmosphere and furnace cooled, in order to prepare them for cutting and

machining. In order to remove previous structure and prepare for further thermal treatment samples cut from the plates were homogenized at 1050°C for 5 min in a protective argon atmosphere and cooled in still air. Samples were afterwards austenitized at 925 °C for 5 min in a protective argon atmosphere and quenched in oil. Quenched samples were tempered at temperatures of 200, 300, 400 and 500 °C, at different times, as given in Table 2.

**Table 1.** Chemical composition of the Protac 500 steel.

Chemical Composition (%)						
C	Si	Mn	P	S	Cr	Ni
0,32	0,76	0,44	0,008	<0,001	0,98	3,09
Mo	B	Cu	Al	V	Ti	Nb
0,43	0,0009	0,16	0,033	0,035	0,003	0,019

**Table 2.** Tempering temperature and time.

200 °C	300 °C	400 °C	500 °C
15 min	5 min	15 min	15 min
30 min	15 min		
60 min			

Metallographic specimens of quenched and tempered samples were prepared by grinding, mechanical polishing and etching in 2% solution of HNO<sub>3</sub> in ethanol (2% nital). Microstructures were examined by light microscopy using Reichart-Jung MeF3 (Vienna, Austria) metallographic microscope, and by scanning electron microscopy JEOL JEOL JSM 6610LV equipped with EDS. Strength of the samples were evaluated by Vickers hardness test with a load of 30 kgf.

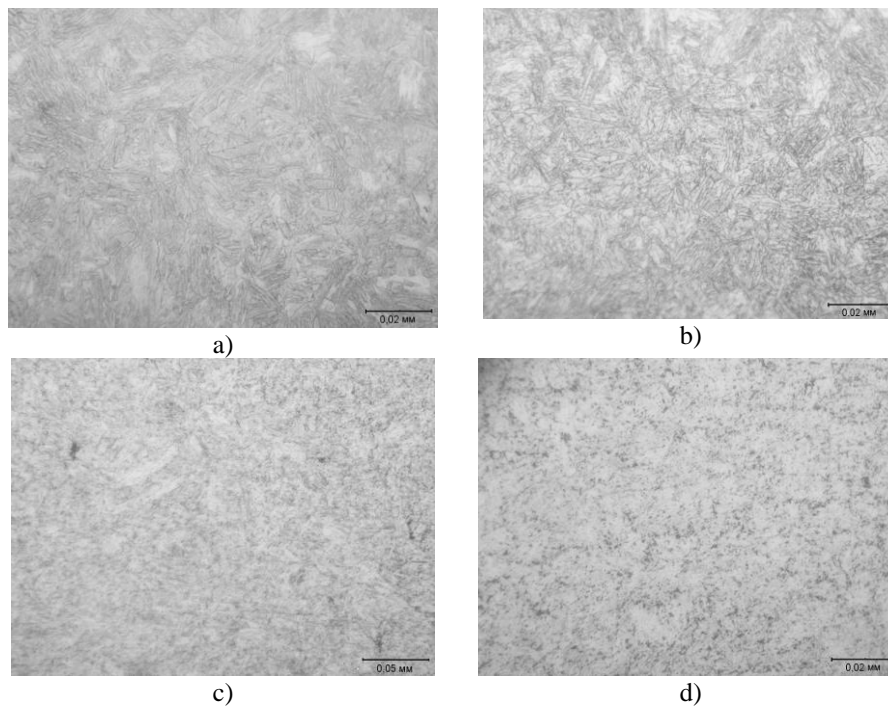


**Figure 1.** Optical micrographs of the quenched and tempered samples microstructure at different temperatures: a) 200 °C/15 min, b) 300 °C/15 min, c) 400 °C/15 min, d) 500 °C/15 min.

### 3. RESULTS AND DISCUSSION

The quenched microstructure is characterized by martensitic needles in the entire volume of the sample. The martensitic needles are of random orientation and it can be assumed that the previous austenite grain size is less than 20 µm. The impact of tempering temperature after 15 min is shown with light microscopy in Figure 1 and with SEM in Figure 2.

After tempering of 15 min at 200°C microstructural changes are evident with light microscopy and with the increase of tempering time the previous austenite grain boundary becomes more pronounced. At the SEM level for tempering at 200°C there are noticeable morphology in microstructure that do not correspond to martensite, which decrease with longer tempering times. At 300°C after tempering for 15 min, the martensitic needles are much sharper and pronounced than after 5 min. Moreover, at the SEM the cementite plate can be noticed after 15 min at this temperature. For tempering temperature of 400°C at the light microscopy level it is noticeable that the martensitic needles are blurry, unclear and dissolved, while at the SEM level the microstructure is interspersed with cementite plates. Finally for tempering at 500 °C complete coarsening of the carbide can be observed at the light microscopy level, while at the SEM level the martensitic morphology is completely absent.



The general tempering of carbon steels is divided into four stages [6]: First stage (up to 250°C), deposition of transitional  $\epsilon$ -iron carbide, partial loss of tetragonality of the martensitic lattice; Second stage (200°C - 300°C), decomposition of residual austenite into ferrite and

cementite; Third stage (200°C - 350°C), replacement of  $\epsilon$ -iron carbide with cementite and complete loss of tetragonality of the martensitic lattice; Fourth stage (above 350°C), coarsening and spheroidization of cementite, recrystallization of ferrite.

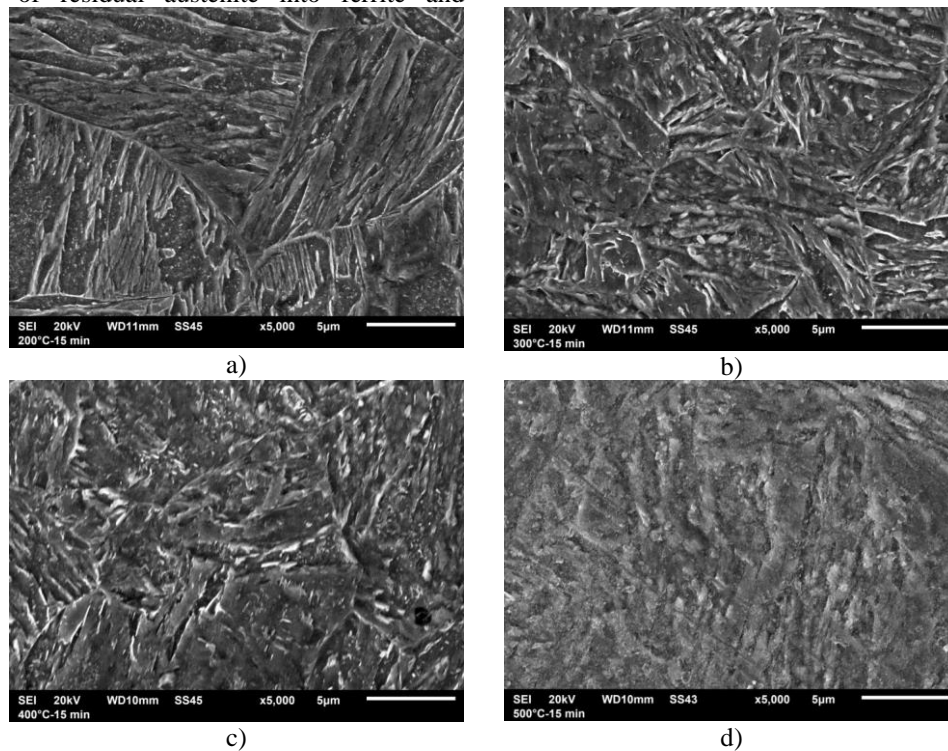


**Figure 2.** SEM micrographs of the quenched and tempered samples microstructure at different temperatures: a) 200 °C/15 min, b) 300 °C/15 min, c) 400 °C/15 min, d) 500 °C/15 min.

At low temperature tempering at 200°C it is expected to see the effects of the first and second stage of tempering. This is reflected in fine carbide particles after noticed after 15 min, that loose the visibility as tempering time increases. This lose in visibility can be attributed to the second interval and the retained austenite dissolution [6-7]. The end of the second stage of tempering and the beginning of the third is noticed at 300 °C.

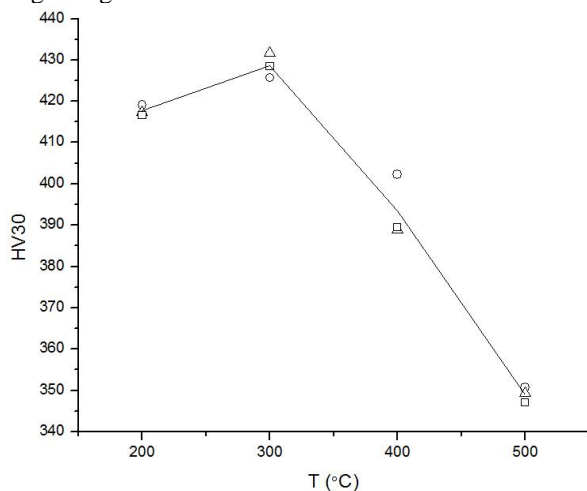


**Figure 3.** Vickers Hardness (HV30) dependence on tempering temperature (tempering time 15 min).

Additionally, some cementite plates can be seen after 60 min for tempering at 200°C so that can also mark the start of the third stage of tempering. The third interval is observed at 400°C, the martensite matrix completely loses its tetragonality but retains a needle-like morphology permeated with cementite plates, while at 500°C carbide coarsening is noticeable and ferrite (formerly martensite) takes the form of bainite. Figure 3 demonstrates the dependence hardness on tempering temperature after 15 minutes. As the temperature increases, the hardness increases, reaches a maximum value of 430 HV, and then decreases. Maximum hardness was obtained for firing at 300°C.

At high tempering temperature at 500°C the loss of hardness is contributed to the absence of alloying element carbides due to their low content and an insufficient time for their formation. Therefore, during the fourth tempering stage there was no participation hardening and only the effect of present carbide coarsening is noticed both in microstructure and hardness.

Figure 4 shows how measured hardness changes over time for tempering at temperatures of 200°C and 300°C. It was found that at 300°C, the increase in hardness with increasing tempering time is more intense than during tempering at 200°C.

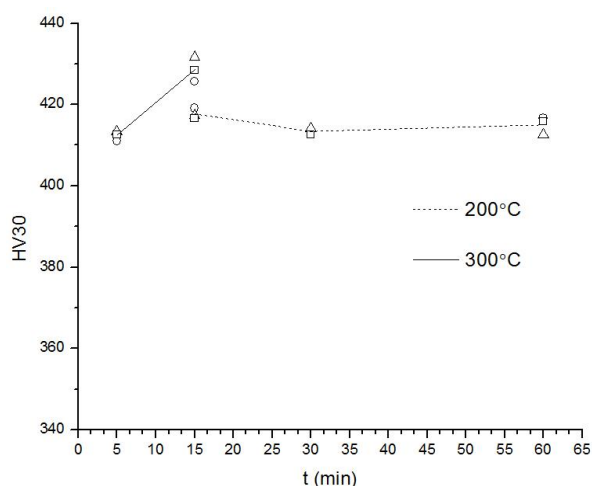


**Figure 4.** Vickers Hardness (HV30) dependence on tempering time (at 200 °C and 300 °C).

In terms of hardness as it does in microstructure tempering for 5 min at 300°C shows similar effects as after 30 min at 200°. Since release is a diffusion-controlled process, at higher temperatures it takes a shorter time for certain changes to occur.

The highest hardness value for the sample tempered for 15 min at 300°C can be attributed to the beginning of the third stage of tempering, the implementation of cementite plates inside the matrix that has not completely lost the tetragonality of the martensitic base. More precisely, diffusion in this stage enabled the kinetic conditions for the formation of finely dispersed coherent or semi-coherent particles, which in the mechanical sense have the strongest effect of increasing the hardness of the material [6-7].

#### 4. CONCLUSION

According to the microstructural analysis and hardness measurements of a quenched and tempered low alloy high hardness armor steel the following conclusions are made:

- With increasing temperature, the hardness increases, reaching a maximum value of 430 HV, and then decreases with increasing temperature.
- The highest hardness is achieved after tempering at 300°C/15 min. The reason for this is the deposition of coherent and semi-coherent iron carbide particles and not

carbides of alloying elements due to the short release time.

- The increase in hardness with increasing tempering time is more intense at 300°C than during tempering at 200°C.
- It is assumed that this behavior is due to kinetics of carbide precipitation and coarsening. Process seems to be most productive at 300°C.

#### Acknowledgement

This work was supported by the Ministry of Science, Technological Development and Innovation of the Republic of Serbia (Contract No. 451-03-66/2024-03/200023 and 451-03-65/2024-03/200135)

#### References

- [1] *Properties and Selection: Irons, Steels, and High-Performance Alloys*, ASM Metals Handbook Volume 1, 10th Edition, ASM International, Metals Park, Ohio, 1991.
- [2] MARDER, A.,R., KRAUSS, G.: *The Morphology of Martensite in Iron- Carbon Alloys*, Transactions ASM, 60 (1967) 651–660.
- [3] BALLIETT, T.,A., KRAUSS, G.: *The Effect of the First and Second Stages of Tempering on Microcracking in Martensite of an Fe-1.22% C Alloy*, Metallurgical and Materials Transactions A, 7 (1976) 81–86
- [4] SWARR, T., KRAUSS, G.: *The Effect of Structure on the Deformation of As-Quenched and Tempered Martensite in an Fe-0.2% C Alloy*, Metallurgical and Materials Transactions A, 7 (1976) 41–48
- [5] CARON, R.,W., KRAUSS, G.: *The Tempering of Fe-C Lath Martensite*, Metallurgical and Materials Transactions, 3 (1972) 2381–2389
- [6] HONEYCOMBE, R., BHADSHIA, H., *Steels: Microstructure and Properties, Chapter 9 –THE TEMPERING OF MARTENSITE*, Butterworth-Heinemann, (2017) 183-207
- [7] KRAUSS, G.: *Steels: Processing, Structure, and Performance - Chapter 17 – Tempering of Steel*, ASM International, (2005) 327-352



# OTEH 2024

11<sup>TH</sup> INTERNATIONAL SCIENTIFIC CONFERENCE  
ON DEFENSIVE TECHNOLOGIES

## *SECTION VIII*

**Quality, standardization, metrology,  
maintenance and exploitation - *QSMME***



## ANALYSIS OF RESULTS OBTAINED DURING CALIBRATION OF FORCE TRANSDUCERS

IGOR GORŠIĆ

Military technical institute, Belgrade, [gorsic@gmail.com](mailto:gorsic@gmail.com)

SAŠA ANTONOVIĆ

Military technical institute, Belgrade, [sale.antonovic82@gmail.com](mailto:sale.antonovic82@gmail.com)

VIOLETA BRNIN

Military technical institute, Belgrade, [violetabrnin79@gmail.com](mailto:violetabrnin79@gmail.com)

SAŠA GUNDELJ

Military technical institute, Belgrade, [gundelj@yahoo.com](mailto:gundelj@yahoo.com)

**Abstract:** This paper demonstrates difference between results obtained during calibration of force transducers using standard method, which includes “warm up” of transducer before starting calibration, according to ISO 376 and calibration which does not include “warm up”. Transducers were calibrated with dead weight machines Schenck Df-0.2 and DF-1.0. Paper will show is there significant difference between these two methods.

**Keywords:** force transducer, static calibration, method.

### 1. INTRODUCTION

For the purpose of measuring, transducers with different ranges are used. Transducers that measure both compression and tension are in use. Transducers are regularly calibrated every two years, and more frequently if there is suspicion of damage to the transducer. For calibration Schenck machines Df-0.2 and Df-1.0 for applying force (in kN), with defined steps which are depending of mass of weights, and HBM DMP41 machine for obtaining results that transducers show (mV/V), this unit also gives power supply to transducer.

Results of calibration are given in [mV/V] and they are used to calculate percentage of hysteresis and linear equation of right, percentage of deviation from right which is presented in coordinated system where on X-axis are values of force applied to transducer and on Y-axis are values that are measured from transducers, hysteresis and deviation show is transducer working properly.

In equation constant is less important than coefficient because the constant represents a distance of point where right intersect Y-axis and that is corrected when taring and zeroing range on indicator HBM DMP41 and when measuring system is set to zero. Coefficient represents angle that right make with axis. Coefficient is used in acquisition software during measurement to calculate voltage [mV/V] to force [N].

### 2. CALIBRATION

#### 2.1 Procedure

Transducers are calibrated according to ISO 376:2011 standard.

This standard defines conditions for calibration, temperature should be between 18 to 28°C, with deviation of  $\pm 1^\circ\text{C}$  during calibration, reference temperature for transducers is 23°C (Temperature range from  $-10^\circ\text{C}$  to  $+45^\circ\text{C}$ ).

All calibrations were done at 20°C to 25°C, so temperature deviation wasn't calculated (Temperature coefficient is 0.015% per 10K)<sup>[2]</sup>.

The transducer should be in the same room (with the same conditions) as the calibration machine for at least 12 hours before calibration. The cables should be approximately the same length as the one used during measurement.

Warm up is defined as a series of applying maximum force and realizing load to prepare the transducer for calibration.

The first three applied forces increase to their maximum without stopping at any value during the increase of force, and then they are reduced to zero without stopping. Next two passes are rising force and stopping at values that will be used during calibration, and then reducing force without stopping.

Then once more, without pausing either up or down.

The last four sets are two sets: one that involves applying and realizing with stopping, and one that involves no stopping.

After every realizing of force transducer is rotated approximately 120 degrees, value depends of connections on transducer<sup>[1]</sup>.

The scheme for warming up is shown in Figure 1. The values of steps in force for calibration should be distributed evenly for full load and are depending of steps defined by machine (mass of weights).

The compression was used to calibrate all Transducers we considered in this paper. Transducers that measure tension force should be calibrated with a tension.

All transducers considered in this paper are class 1, meaning that the minimum force required is at least 1000 times the resolution of the indicator.

Resolution of both, force applying machine (Schenk machines) and indicator (DMP41) is  $10^{-5}$ .

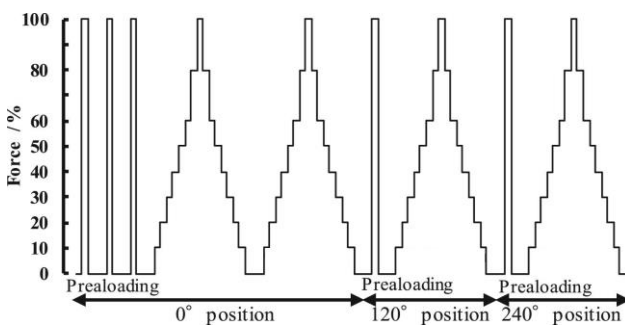


Figure 1. Scheme of warming up.

## 2.2. Transducers

All transducers used for this paper were calibrated at the end of two-year period. For purpose of measuring without worm up all other conditions are followed (temperature, time spent on same temperature with machine...), every transducer is first measured without worm up and then, at least one day later, according to ISO 376 with warm up, except two of them that have two channels, they were first calibrated with warm up and then were "on shelf" for 30 days, then measured first day channel A, then another day channel B.

For the purpose of this paper, we tested and calibrated six transducers of different ranges, producers, types, and channels, as shown in Table 1.

Transducers are of different production years. One was not used for this calibration (new), while for another it was the second calibration (almost new), and others have been used for a couple of years.

Newer transducers (number I and VI) are produced by HBM and are model U10M (number I) and Z4A (Number VI), others are produced by BLH and are C3P1 (Number II), U3G2 (Number III, IV) and U3G1 (Number V), all transducers showed in this paper are compression used and calibrated.

Transducers are considered working properly when percentage of hysteresis and deviation from right are less than 0.3%.

Capacity of Transducer are given as they are in their properties, new transducers are given in [kN], old in [lbs] and calculated to [kN].

Two new transducers have larger capacity then capacity of Df-1.0 Schenk machine, so they were calibrated up to maximum force of machine, with is 80% for one and 50% of capacity for another. It is considered to be enough, according to ISO 376<sup>[1]</sup>, if transducer is accurate in half of range it can be extrapolated to be accurate in full range.

Calibrations were done by stopping at the same values as once used during 'warm up', and at every stop, the transducer was given enough time to stop changing the value of the voltage.

Table 1. List of transducers

No.	Capacity	Channels	Age
I	125kN	2	<i>Almost New</i>
II	200lbs/0.9kN	1	<i>Old</i>
III	500lbs/2,2kN	2	<i>Old</i>
IV	20000lbs/90kN	1	<i>Old</i>
V	10000lbs/45kN	1	<i>Old</i>
VI	200kN	1	<i>New</i>

## 3. RESULTS

Results of calibration without worms are given in Table 2. The results of calibration with worms are given in Table 3.

In tables with yellow, marks values that are out of limits for valid transducers.

In tables, letters A and B indicate the channels of the transducer. When there are two channels, as here, number 1 indicates that the transducer has only one channel.

**Table 2.** Results of calibration without „warm up“

No.	Channels	Deviation from right	Hysteresis	Constant [N/(mV/V)]
I	A	0,42	0,72	-61.061,87
	B	0,15	0,21	-59.771,87
II	1	0,10	0,11	-297,3
III	A	0,08	0,15	-745,27
	B	0,06	0,11	-745,99
IV	B	4,19	2,51	-29.704,68
V	1	6,83	1,14	-13.601,10
VI	1	0	0	100.170,84

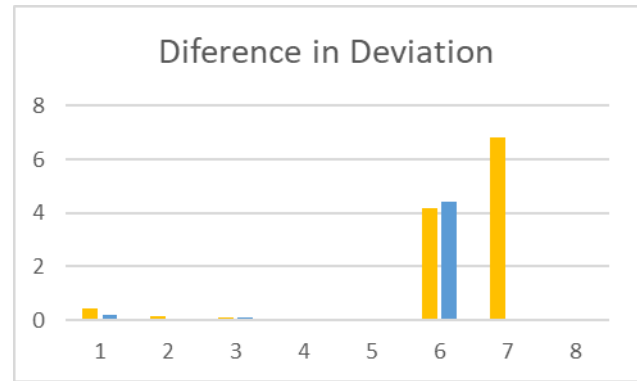
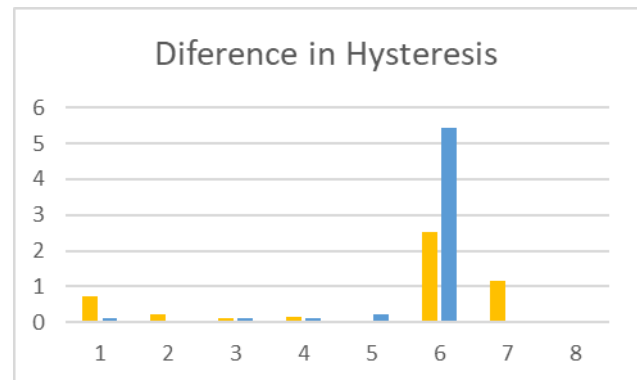
**Table 3.** Results of calibration with „warm up“

No.	Channels	Deviation from right	Hysteresis	Constant [N/(mV/V)]
I	A	0,22	0,11	-61.215,58
	B	0,06	0,02	-60.251,84
II	1	0,10	0,11	-297,3
III	A	0,06	0,12	-745,16
	B	0,07	0,21	-745,74
IV	1	4,41	5,44	-28.935,03
V	1	0,03	0,01	-14.808,19
VI	1	0	0	100.202,89

Transducer number IV was in an accident where it was overloaded few years ago, back then channel A was destroyed, but channel B showed correct values and now its deviation and hysteresis are our limits, so it is considered not working properly, and it can't be used for measuring any more.

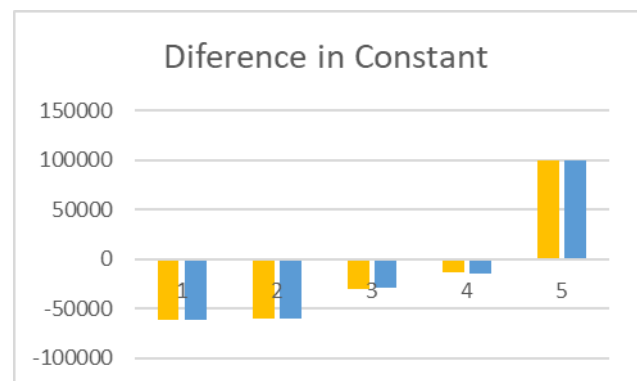
Differences in deviation from the right and hysteresis are shown in Figures 2 and 3. Yellow collar in the figures shows data from tests without 'warm up', and blue shows data from tests in accordance with ISO 376.

Data shows that transducer which is not working properly shows too big deviation and hysteresis in both tests. Another two transducers (channel A on transducer I and transducer V) are under limit for both criteria and are working properly, but when testing without "warm up" test showed too big deviation and hysteresis.

**Figure 2.** Diference in Devioation from right**Figure 3.** Diference in Hysteresis

Figures 4 and 5 show difference in constant of right (angle between right and axis). They are shown in two diagrams because of big difference in values.

In Figure 4 Transducers I, IV, V and VI are shown and first two columns are channels A and B for transducer I. In Figure 5 Transducers II and III are shown where first column are transducer II and second and third are channels A and B for transducer III.

**Figure 4.** Diference in Constant for bigger values

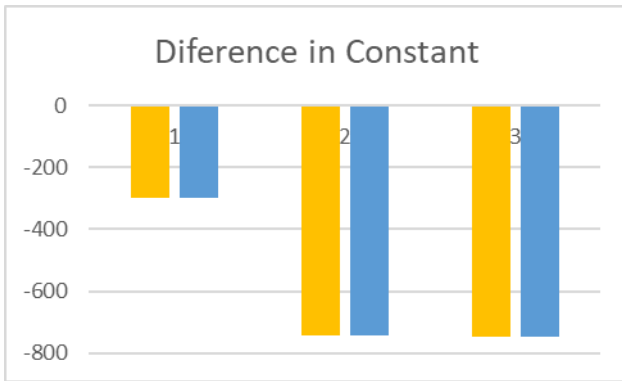


**Figure 5.** Diference in Constant for smaller values

In Figures and Tables, it is shown that there is no significant difference between constants when testing with and without “warm up”.

#### 4. CONCLUSION

Results show that there is no significant difference in constants when calibrating transducer without “warm up” and calibrating in accordance with ISO 376, this characteristic allow transducers to be used without “worming up” for measuring. Difference is becoming more obvious when calculating hysteresis and deviation from right, calibration without “warm up” even showed

some transducers (I-A and V) not working properly, and they are showing working properly when calibration is done in accordance with standard.

All this show that calibration of transducer demands worm up. It shows can it be avoid in case we are certain transducer is working properly and we need only to calculate constant, for example for new transducer (Transducer VI – hysteresis and deviation in both cases are close enough to zero – they have value on fifth or sixed position after decimal point), but every regular calibration after few years or when suspecting on damage of transducer must be done according to ISO 376 standard.

#### References

- [1] ISO 376:2011 *Metallic materials – Calibration of force-proving instruments used for the verification of uniaxial testing machines*, 2011, last reviewed 2023, no changes
- [2] *Mounting instructions for transducers* (HBM U10M and Z4A and BLH C2P1, U3G1 and U3G2). *Operating manual* Digital precision measuring device DMP41



## COORDINATE METROLOGY DATA MANAGEMENT OF MACHINE PARTS MADE BY METAL ADDITIVE MANUFACTURING

SRDJAN ŽIVKOVIĆ,

Military Technical Institute Belgrade, [srdjan.zivkovic@mod.gov.rs](mailto:srdjan.zivkovic@mod.gov.rs)

SLOBODAN MALBAŠIĆ

Ministry of defence Republic of Serbia, Material Resources Sector, Defence Technologies Department,  
[slobodan.malbasic@mod.gov.rs](mailto:slobodan.malbasic@mod.gov.rs)

MILOŠ STEPANOVIĆ

Military Technical Institute Belgrade, [hunter.milos@gmail.com](mailto:hunter.milos@gmail.com)

**Abstract:** The rapid development of Additive Manufacturing (AM) technologies has further highlighted the importance of coordinate metrology in the entire production process. AM often equivalent with reverse engineering (RE) and rapid prototyping (RP) in which the role of coordinate metrology is crucial. All AM technologies require (more or less) machine finishing operations, so coordinate metrology play key-role to production quality management. The paper will present two cases from practice: The first example is RE of the individual machine part that requires a higher scope of machining after production on 3D\_Print machines. The results of coordinate metrology are a key starting point of machining of complex spatial shape. Another example is the fast processing of the results of the optical (contactless) coordinate metrology of points cloud of mass production of turbine blades. The mathematical model was tested on the optical measurement results of the turbine blades produced by PBF-LB/M (Powder Bed Fusion - Laser Beam/Metal). The developed mathematical method is easily applicable to the serial production of aircraft turbine blades made with precise casting or forging.

**Keywords:** coordinate metrology, additive manufacturing, complex spatial forms, production quality.

### 1. INTRODUCTION

The place and role of metrology, including coordinate metrology, is best illustrated by the words of William Thomson, better known as Lord Kelvin, spoken at the end of the 19<sup>th</sup> century: „I often say that when you can measure what you are speaking about, and express it in numbers, you know something about it; but when you cannot measure it, when you cannot express it in numbers, your knowledge is of a meagre and unsatisfactory kind.“[1]

The increasingly frequent application of additive manufacturing technologies in combination with classical machining technologies has put coordinate metrology in the foreground. In reverse engineering cases this is quite obvious but also in engineering "forward" coordinate metrology is a key factor in managing the quality of production.

The increasing use of contact and contactless measuring systems in production processes has greatly shortened the time delays between machining operations. If we add to this that complex spatial forms cannot be measured by linear measuring instruments (Vernier instruments), coordinate metrology has been given a role in the production process just as Lord Kelvin defined it.

In this paper, two case studies from the practice of applied coordinate metrology on machine parts made by AM

(Additive Manufacturing) laser fusion of metal powder in the build chamber (PBF-LB/M) will be presented.

Both machine parts are defined by complex spatial shapes; the first is an example is a rounded cycle of reverse engineering of the impeller (diffuser), after production on 3D\_Print in metal, must be finalized by milling machining.

Another example is the turbine blade of an aircraft engine, made 3D\_print in metal, for which it is necessary to quickly answer the question of whether it is in the required tolerances or not taking into account the mass production of these blades.

### 2. DESIGN FOR AM

The last decade has led to the full maturation of additive manufacturing. AM has experienced serious improvements and has become equal to classical technological procedures. This is the reason why it is increasingly being used in a diverse range of industries such as automotive, consumer goods, medical devices, aerospace, defense, etc.

Generally speaking, each machine part can be produced by applying different technological procedures, subtracting or adding materials. This is absolutely true if we ignore the time and cost of production. The role and task of the production mechanical engineer is to manufacture the machine part in the required quality in



the shortest possible time and at the minimum price. In the phase of designing mechanical parts, it is necessary to consider the planned technological process. It is clear that the design of sand cast parts is different from that of mechanical parts that are made by forging. This feature is called Manufacturability.

When we talk about the methods of adding and subtracting materials, different design features present completely different challenges in both production methods [2]. There are several factors that need to be considered in the design phase to efficiently produce parts using additive manufacturing. The basic characteristics of designing for classic manufacturing technologies in contrast to designing for additive manufacturing are shown in Table 1.

**Table 1.** DfMA vs DfAM [3]

DfMA (Design for Manufacture & Assembly)	DfAM (Design for Additive Manufacturing)
Focus on keeping the geometry as simple as possible	The complexity of the geometry increases the demand for AM
Segmentation of parts for easier production and assembly	Consolidation of the total number of parts / functions, increases the demand for AM
Designing within production constraints	The design goal is functionality, not limitation (bionic shapes and honeycomb/lattice structures are encouraged)

**2.1. Designing Rules for AM**

Although many scientific papers [2][3][4] and specialized journals articles have been written on the topic of design rules for AM, not a small number of engineers still do not understand the essence and reasons for these rules. This clearly indicates that the key is the education.

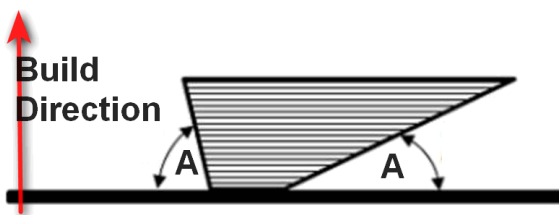


**Figure 1.** Faces requiring support

The rule that stands out everywhere as the first is illustrated in Figure 2: faces with an angle greater than 45 degrees in relation to the build direction must have support, Figure 1. The consequence of this rule is that machining (mainly milling) of the faces with the support is necessary. Additional machining increases the total manufacturing time and thus the total price of the final product [5].

Another important rule is shown in Figure 2. The minimum faces distances are generally constrained by the additive manufacturing method.

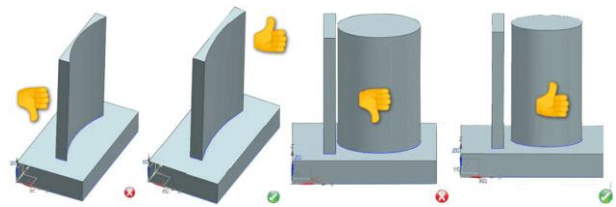


**Figure 2.** Minimum distance btw Faces [2]

The minimum thickness or minimum distance of faces directly depends on the AM method and the resolution of the machine itself. If it is not possible to avoid it, for various reasons, it is quite possible that post processing is necessary. Specifically speaking, any AM production requires post-processing, more or less. Minimally, it is necessary to treat it with sand or pellet and removing the auxiliary supports [7].

If at the design stage the geometry had to be thickened or widened due to AM technological limitations, the scope of additional machining will not be so small. In a case study, one such example will be explained in detail here.

The third follows from the previous two rules: minimum feature size (Pocket/Island/Text) or minimum hole diameter [2]. It should not be forgotten that during AM production, a large amount of heat is introduced, which can lead to unwanted deformations of the work piece. It follows from the previous that the relationship between the diameter and the height of the boss has its own limitations, which are an integral part of the AM design rules [6].

If we know AM is just another production technology, how an average designer can know all the design rules for AM but also for all classic technologies (turning, milling, casting, forging, bending, punching, molding...)?

How to apply all these rules quickly and immediately to a truck assembly with 10,000 components? Large ships, of course, have a million components! The solution of this task is the automation of the entire process. It is necessary for the designer to have at his disposal a service that, after activation, immediately gives an answer to the applying appropriate manufacturing technology of the all parts in the assembly.

**2.1. Automation of DfMA & DfAM Principles**

'Design for Manufacturability' or 'Design for Manufacturing' (DfM) is a methodology involves designing with intent to minimize the cost of production and time-to-market, without compromising on the quality of the product. In 1958 ASME (American Society of Mechanical Engineers) published a book it is explains the principles of DfM, although not used this term.

Manufacturability is not a new term, but automation of the application of this principle is necessary in the 21<sup>st</sup> century. DfM is a tool for designers, added to CAD, that facilitates upstream manufacturability validation and identification of areas of a design that are difficult, expensive or otherwise impossible to manufacture.

Rule Manager allows to manufacturing engineer to specify the rules which designer must to use. Rules are

saved by category which allows manufacturing engineer to customize the type of rules that are used for analysis.

*DfM* is CAD/CAM add-in, is shipped with the rule modules for Milling, Turning, Sheet Metal fabrication, Injection molding, Casting, Die casting, Welding, Additive Manufacturing and Assembly, Figure 3.

This add-on is available for all well-known *CAD/CAM* systems: CATIA V5, SOLIDWORKS, PTC Creo Parametric, Siemens PLM NX, SolidEdge, Autodesk Inventor. This add-in is applicable in very wide areas of mechanical engineering: Medical device, Aerospace and defense, Automotive, High-Tech Industry (smart devices) & Industrial Manufacturing.

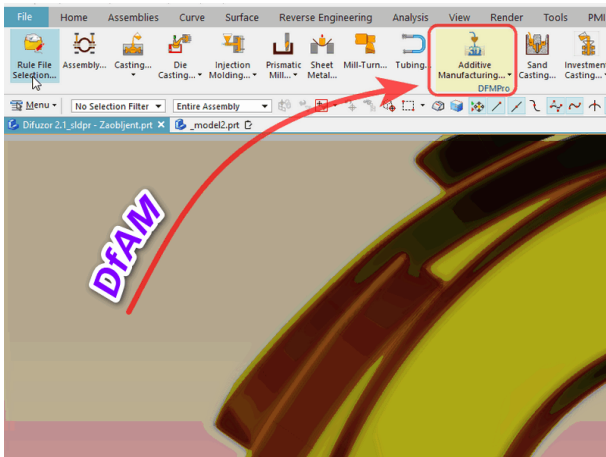


**Figure 3.** *DfAM* Add-In for CAD/CAM [3]

The rules manager allows you to set the rules and parameters for a very wide range of different 3D printing technologies: Fused Deposition Modeling (FDM), Stereolithography (SLA), Poly-Jet (3DP), Selective Laser Sintering (SLS), Direct Metal Laser Sintering (DMLS), Metal Powder Bed Fusion (MPBF). Similar to conventional machine tools, AM machines with different resolution and accuracy exist for the same technology.

Rule Manager allows to manufacturing engineer to specify the rules which designer have to use. Rules are saved by category which allows manufacturing engineer to customize the type of rules that are used for analysis [8]. Importance of the Rules are noted with following letters:

- {I} = Insignificant
- {L} = Low
- {M} = Medium
- {H} = High
- {C} = Critical

From all of the above, it is obvious that each production plant has its own rules that are specific and different from similar production plants. These differences may refer to the accuracy class, the size of the working space of machine tools, the number of degrees of freedom of simultaneous control, conventional and unconventional machining methods. These differences can be very large in cases where a factory does not have a technological process, e.g., sand casting. All this does not have to be known to the designer; the production facility can be

dislocated, in another city or even a continent.

The importance of designing for manufacturing is underlined by the fact that about 70% of manufacturing costs of a product (cost of materials, processing, and assembly) are determined by design decisions, with production decisions (such as process planning or machine tool selection) responsible for only 20% [8].

### 3. CASE STUDY – DIFFUSER

The first example is the manufacture of four diffusers, different geometries but very similar complexity. It is a classic example of *RE*; it has not any documentation, neither electronic nor paper. Diffusers are spare parts because they wear out during exploitation. Originally these parts made by sand casting and post processed by turning and milling.



**Figure 4.** Diffuser N°3 on the CMM & touch trigger probe measuring path

The contracting authority requested a geometry redesign based on the submitted (damaged) sample and its manufacture from stainless steel. Considering that the working space of the AM machine in MTI is the largest in Serbia and amounts to 450x450x500 [mm], the maximum diameter of the diffuser (472mm) required building of parts inclined in the working space of the AM machine. This means that the build vector is not coincident with the axis of rotation of the diffuser. This required additional analysis after the redesign, Figure 3. Such an analysis cannot be carried out without a specialized *DfAM* module.

In the first step, CMM was used to generate the initial CAD model based on the sample. After, remodeling and customizing the design for AM making in metal powder was started. The submitted sample was designed for casting in sand and therefore had inclined faces for easier removal from the mold. The AM process has different

technological requirements and remodeling has been carried out so that the part does not lose its functionality.

After AM building of diffuser, before separating from the building plate, the diffuser is measured at CMM. Figure 5. shows the measurement of diffuser geometry N°2. on CMM; measurement results are shown in the same figure. All diffusers are made inclined, auxiliary supports are added to basic geometry. In Figure 4, auxiliary supports are highlighted. The same figure shows the trajectory of the measuring probe during the measurement of the primary datum plane.

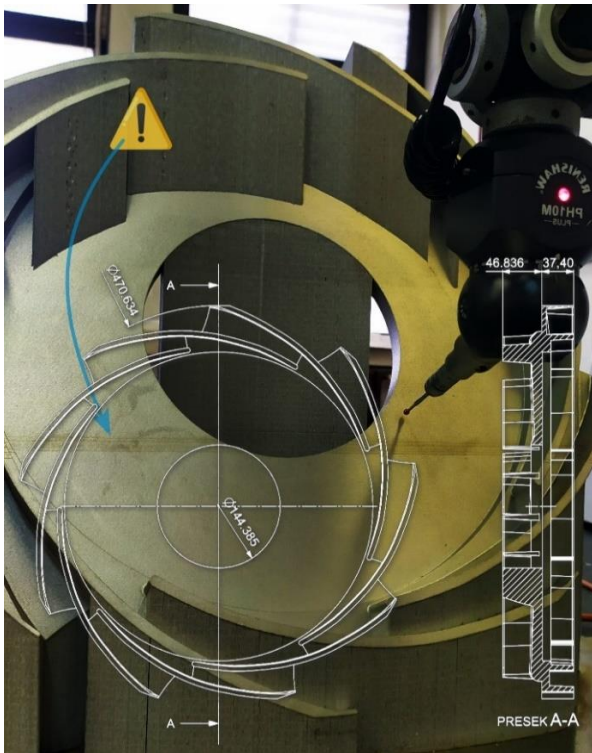


**Figure 5.** Diffuser N°2 on the CMM & measured results

The task of measuring on the CMM is double: the first is to check if the designed geometry is in the required tolerances; Second, to precisely and accurately determine the datum features for the positioning on the milling machine for necessary post processing. Figure 4 shows the measurement path for determining the datum plane for the purpose of placing on the working table of the milling machine. The diffuser has no rectangular elements, and therefore angular positioning is critical and very tricky. The data obtained on the CMM must be clearly and unambiguously transferred to the operator on the milling machine.

In Figure 5, an arrow and an exclamation mark {! →} pointed an anomaly on the built diffuser. In one zone (strip) it can be observed that the color of the built diffuser is different. During the building of the diffuser, there was a disruption-interruption in the power supply. It is known for MPBF technology that interruptions in work due to very different reasons, are undesirable because it requires re-preparation of the working chamber as well as reheating of the working part. It was suspected that there were unwanted hollows inside the built diffuser, and for this reason the machine part was recorded with X-rays.

All the X-rays photographs showed that the unwanted hollows did not include the internal structure of the diffuser.

#### 4. CASE STUDY – TURBINE BLADE

Another case study is an aircraft engine turbine blade, shown in Figure 6. The blade is small, much smaller than the diffuser from the first case study. It is built in metal powder by PBF-LB/M technology.

Aircraft engine turbine blades are made by precision casting or forging. The blades root is subsequently finished by grinding with a profiled grinder. The whole process is expensive because it requires using of complicated and very expensive molds. This is acceptable for serial and mass manufacturing processes. For the development phase as well as for small series, using the PBF-LB/M manufacturing process is cost-effective.



**Figure 6.** Turbine Blade built on an AM machine

All cases, single, small-series or large-series manufacturing necessarily require geometric inspection of the definition airfoils. A typical geometric inspection report of the airfoil of a selected section of a turbine blade is shown in Figure 7. The theoretical airfoil is shown undeformed, everything else is shown enlarged to make it easier to see: measured airfoil, upper tolerance limit and lower tolerance limit. The direction of deviation is shown by arrows. Deviations out of tolerance limits are marked with red arrows. The turbine blade was measured in 8 sections, shown on the left side of Figure 9. Each section was measured in 60 points (30 upper side + 30 lower side); that amount is a total of 480 measurement points.

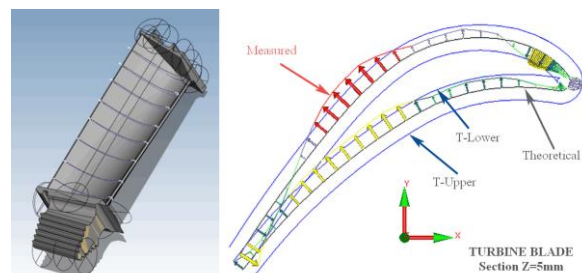


**Figure 7.** Turbine Blade: geometric inspection [9]

The report in Figure 7 was made after measuring on a CMM with a contact probe. The whole process is not so fast, and its application on all manufactured blades of serial and large-scale production is economically unprofitable.

A new request was made to speed up the entire process but to keep the reliability of the conclusion high. Figure 9 shows the same turbine blade scanned on a CMM with a

laser measuring head. In the same picture it is indicated that the total number of scanned points is over a million.

More than a million measured points is much better than half thousand measured points only if it is possible to infer something from these results. If you have no conclusion then it is completely irrelevant whether you have measured a thousand, a million, a billion or a trillion points! A new approach necessarily requires the development of new mathematical models. This is one such case.

Optical scans have many advantages compared to contact methods, but also some disadvantages. The point cloud obtained by optical scanning often has false overlaps, dislocated zones and a unwanted noise. It is necessary to remove all observed irregularities and then reorganize the point cloud according to the desired structure. Figure 8 shows this step. Only the zones of interest for the required analysis were selected. Every cross-section, was represented via the same number of uniformly spaced parametric samples of the corresponding B-spline, enabling characterization of each airfoil using same dimension vectors [10].

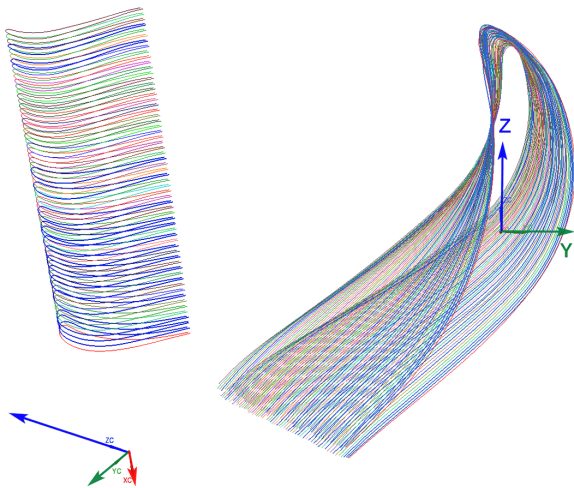


Figure 8. Turbine Blade: Reorganized points cloud

It is noticeable that the number of airfoils selected from the point cloud is much higher than the number of sections from Figure 9, but they will not be analyzed in the same way.

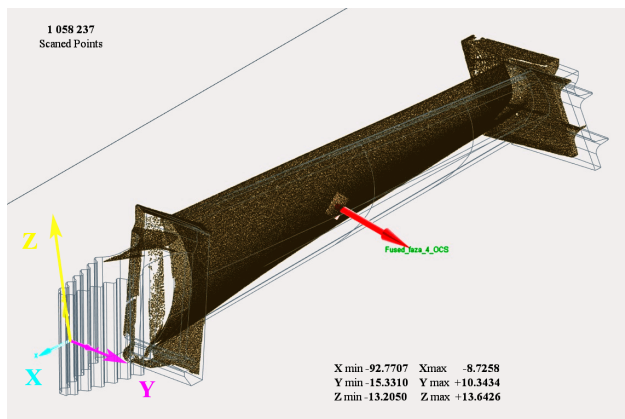


Figure 9. Turbine Blade scanned using CMM with laser

First, one of the sets of manufactured turbine blades is selected to represent the etalon piece. The selected blade is carefully and very precisely measured and analyzed, identically shown in Figure 7. This step is critical and must be done carefully and without rush. All other turbine blades will be optically scanned and that image will be compared with the image of the selected reference piece. This approach will give us a very quick answer to the question of whether the turbine blade is good or not, i.e., is its geometric image close to the reference turbine blade.

This approach is fully in line with the principles of the *Industry 4.0* concept, i.e. creating a digital twin. The approach combines production and metrological information so that they have their own digital twins for each stage of the production process, is called CPM<sup>3</sup> (Cyber-Physical Manufacturing Metrology Model), fig 10. This original concept was presented in a series of scientific papers at conferences organized by the International Academy of Production Engineering CIRP<sup>1</sup> [9]

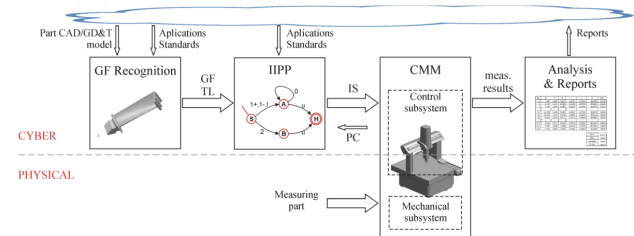


Figure 10. Structure of the CPM<sup>3</sup> concept [9].

Optical scanning generates a very large amount of data. If we add that it is multiplied with a large number of pieces, such as serial and mass production of turbine blades, it is clear that searching and processing large databases can take a lot of time even on fast computers. The described deficiency was overcome by the development of a special approach in the search of large databases [10].

In [10], a new and original concept of data curation<sup>2</sup> of large databases was proposed. The proposed methodology decomposes metrological data into a tree structure by grouping them into distance-based clusters. This approach, in comparison with traditional search methods, enables a logarithmic acceleration of the search and thus brings significant advantages.

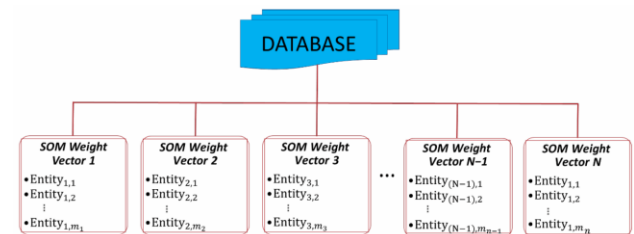


Figure 11. Database re-organization: Self-Organizing Map (SOM) [10].

<sup>1</sup> CIRP - French acronym of College International pour la Recherche en Productique

<sup>2</sup> Data curation is the process of transforming and enriching raw data into smaller, more accessible subsets.

In [10] is proposed using of growing Self-Organizing Map (SOM) based unsupervised clustering of metrology data to obtain clusters of database entries as Voronoi<sup>3</sup> sets.

For the purposes of testing the developed mathematical model, anomalies were artificially generated on the surface of the turbine blade in the zone between 2→3 [cm] from the coordinate origin, shown on Fig. 6.

Each black dot on Fig. 12 [10] corresponds to a turbine-blade cross-section, while each purple disk represents a cluster centroid in the tree-based database.

In Figure 12, it is clearly visible that the SOM centroids of the turbine blade with the faulty cross-section are displaced in relation to the centroids of the original reference turbine blade. The conclusion is clear and very reliable, this turbine blade must be rejected because its geometric characteristics do not meet the required geometric requirements.

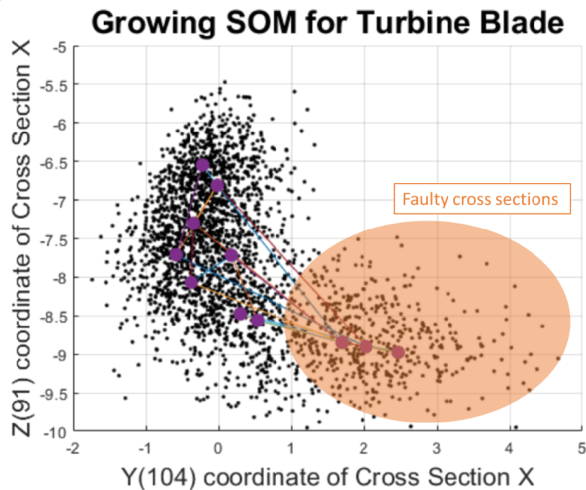


**Figure 12.** A 2-dimensional projection of CMM data

The set goal was reached, we got a quick answer to the question: accept or reject the turbine blade. For large-scale and mass production, this approach is very useful. This approach is a supplement and not a substitute for a detailed geometric inspection of the turbine blade, Fig. 9.

## 5. CONCLUSION

The primary topic of the paper is a geometric inspection of machine parts complex spatial form. Both case studies showed a diverse application of coordinate metrology of complex spatial forms: parts of smaller and larger dimensions, contact and non-contact measuring methods, small and large number of measuring points, complete and partial geometric inspection. Both case studies were applied to machine parts manufactured by AM using PBF-LB/M technology process. Geometric inspection, in both case studies, had a double role: final geometric inspection and quality management of production process of subsequent necessary machining. Both case studies

clearly indicate the necessity of coordinate metrology in all stages of the production process taking into account all AM specificities.

Product quality management as well as the final quality of the product made of PBF-LB/M technology is very complex and multidimensional. The design phases should not be considered separately from the production process. Errors incurred in the design phase, as a consequence of non-compliance with the standards, affect the total price of the product. Previous chapters have been comprehensively processed the quality topic of machine parts made in PBF-LB/M technological procedure.

## Acknowledgments

The authors thank the Ministry of Science, Technological Development and Innovation Republic of Serbia, to support in this research; Contract No. 451-03-66/2024-03/200325

## References

- [1] Thomson, William (Lord Kelvin). "Electrical Units of Measurement." Chapter. In Popular Lectures and Addresses, 73–136. Cambridge Library Collection – Physical Sciences. Cambridge University Press, 2011. First pub: 1889. DOI: <https://doi.org/10.1017/CBO9780511997242.006>
- [2] Kannan, T.R. "Design for Additive Manufacturing". Technical Report, 2013. Online: [https://www.researchgate.net/publication/269094941\\_Design\\_for\\_Additive\\_Manufacturing](https://www.researchgate.net/publication/269094941_Design_for_Additive_Manufacturing) Accessed: 23.04.2024.
- [3] Živković, Srdjan. "Production of Big Parts using MAM (Metal Additive Manufacturing) Technologies" (Lecture), Additional program during "PARTNER 2023" International Armaments and Defense Exhibition, Belgrade Serbia, 2023. DOI: 10.13140/RG.2.2.13588.48009
- [4] Malbašić Slobodan, Živković Srdjan, Nedić Bogdan, Đorđević Aleksandar, Grubić Aleksa. "Process Planning and Optimization Techniques in Additive Manufacturing". Scientific Technical Review, 2023, Vol.73, No.2, pp.33-41. doi: 10.5937/str2302033M
- [5] Malbašić Slobodan, Nedić Bogdan, Đorđević Aleksandar, Živković Srdjan, Grubić Aleksa. "Applications and Economics of Additive Metal Production Technologies". ICPEs 2023 - 39<sup>th</sup> Int. Conf. on Production Engineering of Serbia, Proc. pp.307-313. Novi Sad, Serbia, 26-27 October 2023.
- [6] Abdullah Alfaiy, Mustafa Saleh, Fawaz M. Abdullah, Abdulrahman Al-Ahmari. "Design for Additive Manufacturing: A Systematic Review". Sustainability 12(19):7936, 2020. DOI: 10.3390/su12197936.
- [7] Čirić-Kostić Snežana, Bogojević Nebojša. "Principi i primena aditivne proizvodnje". Univerzitet u Kragujevcu, Fakultet za mašinstvo i građevinarstvo u Kraljevu. ISBN 978-86-81412-05-3, 2020.
- [8] Živković Srdjan, Veljko Petrović. Automation of

<sup>3</sup> Voronoi partition is a geometric structure that divides a given space into the regions based on the distance to a set of the points called "seeds" or "sites".

- DfMA Principles in Parts and Assembly Design. Journal Advanced Quality ISSN 2217-8155. United Association of Serbia for Quality Belgrade. Vol.46 N°2, pp. 34-39. 2018. DOI: 10.25137/IJAQ.n2.v46.y2018.p34-39
- [9] Majstorović Vidosav, Stojadinović Slavenko, Živković Srdjan, Djurdjanović Dragan, Jakovljević Živana, Gligorijević Nemanja. Cyber-Physical Manufacturing Metrology Model (CPM<sup>3</sup>) for Sculptured Surfaces – Turbine Blade Application. Procedia CIRP, ISSN 2212-8271, Volume 63, 2017, Pages 658-663. DOI: 10.1016/j.procir.2017.03.093,
- [10] Sabbagh Ramin, Živković Srdjan, Gawlik Brian, Sreenivasan S.V., Stothert Alec, Majstorović Vidosav, Djurdjanović Dragan. “Organization of big metrology data within the Cyber-Physical Manufacturing Metrology Model (CPM<sup>3</sup>)”. CIRP Journal of Manufacturing Science and Technology Vol. 36, Jan. 2022, Pages 90-99. ISSN 1755-5817, Elsevier. DOI: 10.1016/j.cirpj.2021.10.009.



## RELIABILITY OF ARTIFICIAL INTELLIGENCE

SLAVKO POKORNI

Information Technology School, Belgrade, [slavko.pokorni@its.edu.rs](mailto:slavko.pokorni@its.edu.rs)

**Abstract:** The goal of this paper is to show the importance of reliability for artificial intelligence (AI), which is nowadays applying in almost every area of human life. Everything can fail, and AI is not an exception, as any other product or devices. AI also need to be reliable. The definitions of AI, reliability and some reasons for unreliability such as quality of data, small or insufficient number of training and test data, training on unreal data, nature of learning algorithms and user incompetence are analysed in this paper.

**Keywords:** reliability, artificial intelligence.

### 1. INTRODUCTION

Everything can fail, and artificial intelligence (AI) is not an exception. If AI is an attempt to replace human intelligence with machine intelligence, and human reasoning can sometimes fail, so AI can fail in a similar way [1]. If something can fail, we speak about reliability, and if it can be repaired, we speak about maintenance. Reliability is related to failures, and failures can cause losses from little to very big, for example economic and sometimes loss of life. So, reliability is important, and sometimes critical, depending of area where AI is applied (airplanes, autonomous vehicles, medical devices, etc.). It implies that reliability of AI is important in order to use it with confidence and safety, for the benefit of all people, without misuse.

Artificial intelligence is mainly realized as software, but it involves hardware, data and human. So, when we speak about AI reliability, it obviously includes hardware, software, data and human reliability.

### 2. DEFINITION OF RELIABILITY

In general, reliability is defined as the ability of an item to perform a required (expected) function under stated conditions for a stated period of time [1]. Instead of term item, in this paper we will use term product as general term, and this will include device, element or system realized in hardware, software or both. AI can also be treated as product. Reliability of AI can be defined in similar way as reliability of a product.

In [2] Reliability of Artificial Intelligence<sup>1</sup> is defined as the probability, at a certain level of confidence, that the System will successfully, without failure, perform the function for which it is intended, within the specified performance limits, during the specified duration of the tasks, when it is used in the prescribed manner and for the purpose for which it is intended, under defined load

levels, taking into account the previous system usage time.

Quantitatively, reliability is expressed in probability, and are very important in reducing downtime and operational and maintenance cost of a product. Reliability and maintenance are mutually connected. Higher reliability means less costly maintenance. There are many factors which can influence reliability. For example, reliability of hardware can change if environment changes (temperature, mechanical stresses, etc). Similarly, reliability of AI changes if data and user behaviour changes.

High reliability is very important, especially in professional equipment as military, medical or driverless cars, and it comprises hardware reliability, software reliability, and human reliability [3], and it can include AI, so reliability of AI is also important.

Calculating reliability, we essentially calculate prognostic reliability. That is why we are not talking about determination, but about reliability assessment or reliability prognostic. Reliability prognostic has been done for almost 60 years using MIL-HDBK-217, mostly for electronic hardware [4]. Reliability assessment of software is more complicated.

Reliability is building in during designing of a product, provided in production and supported in use. It is also connected with cost. More reliable product is more expensive, but more reliable product is also cheaper for maintenance.

Artificial intelligence is in essence a software but it involves hardware, data and human and reliability of AI can be defined as in [5].

Because AI is dominantly software, it is connected with software reliability. Software errors are dominantly cause of software unreliability. Software can contain errors, and errors can produce faults. Errors in software are produced by programmers, so it is important to be familiar with these errors.

<sup>1</sup> In [2] it is called System or Artificial Intelligence System.

AI can learn from human, and human knowledge can be erroneous, so it is connected with human reliability.

AI can learn from data, and data can be accidentally or intentionally corrupted, so AI can fail. Now we can speak about data reliability, and AI reliability is connected with data reliability.

Reliability is not easy to calculate or evaluate. In calculation of reliability input data is the biggest problem. Not because there is too much data, but because, sometimes, there is too little data. When we are dealing with maintenance, also the problem is more often that we do not have enough data. How many data we have about AI reliability, especially if it is new application?

### 3. DEFINITION OF AI

There is no generally accepted definition of artificial intelligence [6]. According to the Encyclopaedia Britannica dictionary [7] artificial intelligence is the ability of a digital computer or computer-controlled robot to perform tasks commonly associated with intelligent beings. According to the Merriam-Webster dictionary [8], AI is a branch of computer science dealing with the simulation of intelligent behaviour in computers, or the capability of a machine to imitate intelligent human behaviour.

Government of the Republic of Serbia ([6, 2] accepted next definition of AI, also used in [9]: “Artificial intelligence (AI) refers to systems that display intelligent behaviour by analysing their environment and taking actions – with some degree of autonomy – to achieve specific goals.”

Artificial intelligence-based systems can be purely software-based and operate in a virtual world (for example: virtual assistants, photo analysis software, web browsers, recommendation systems, speech and face recognition systems) or they can be embedded in devices - hardware (for example: advanced robots, autonomous vehicles, drones, etc.) [2, 9].

Artificial intelligence was founded as an academic and scientific discipline in the middle of fifties of the last century, and since then development has gone in different directions, being divided in sub-fields. Therefore, it is not a surprise that the definition of AI has been changed during time.

In the history of AI, there have been ups and downs, starting with the logic-based approach (during the 1950s and 1960s), the knowledge-based expert systems approach (1970s and 1980s), and the data-based approach (since 2000) years onwards - with periods of disappointment and reduced investment [6]. In the last decades, AI is defined as a study of intelligent agents - any device that precepts its environment and takes actions (by learning or using knowledge) to achieve its goals [1].

Essentially, the use of AI is an attempt to replace human intelligence with machine intelligence. Because of that, sometimes, AI is called machine intelligence. But it does not mean that AI learn just copying human. Nowadays AI

can learn in its own way. And it, maybe, gives IT a potential to outperform human (brain).

## 4. RELIABILITY OF AI

As it is mentioned before, everything can fail, and Artificial intelligence (AI) is not an exception. If AI is an attempt to replace human intelligence with machine intelligence, and human reasoning can sometimes fail, so AI can fail in a similar way. So, this is the reason of erroneous reasoning (erroneous concluding, decisioning) or wrong learning? Having that in mind, can we raise the question about the reliability of AI, or how to avoid AI to fail? [1].

If AI fails, it is unreliable, so can we trust in it?

### 4.1. Trustworthiness

This is an important question which attracted the attention of ISO/IEC. In [10], there are surveys of topics related to the so-called trustworthiness in AI systems, including the following: (1) approaches to establish trust in AI systems through transparency, explainability, controllability, etc.; (2) engineering pitfalls and typical associated threats and risks to AI systems, along with possible mitigation techniques and methods; and (3) approaches to assess and achieve availability, resiliency, reliability, accuracy, safety, security, and privacy of AI systems. In that document, trustworthiness is defined as an ability to meet stakeholders expectations in a verifiable way, including the characteristics of trustworthiness such as reliability, availability, resilience, security, privacy, safety, accountability, transparency, integrity, authenticity, quality, and usability.

It seems that trustworthiness is broader term than reliability.

In [11] under the headline “Enhancing the reliability of artificial intelligence“ is stated that “Computers that learn for themselves are with us now. As they become more common in 'high-stakes' applications like robotic surgery, terrorism detection and driverless cars, researchers ask what can be done to make sure we can trust them. “So, are they reliable? Or, can they fail? Or can we fool them?”

In [12] is discussed why deep learning AI is so easy to be fooled. An example is in a self-driving car application in a real situation. It is, however, said that it can happen in the case of sabotage as well.

There are examples of erroneous AI. From these examples we can derive some reasons for AI to fail, such as: quality of data, small or insufficient number of training and test data, training on unreal data, nature of learning algorithms, user incompetence.

### 4.2. Quality of data

Quality of data can have significant impact on the reliability of AI. What if AI learns from corrupted data or data which are corrupted on purpose (for example by an enemy)? The consequences can be different, from insignificant to catastrophic. So we need some kind of



control on the data which AI uses to learn. This problem doesn't imply not to use AI, or not to allow AI to learn from data, but to be aware of the problem in order to prevent difficult consequences.

Some examples can be found in [13], AI failures from IBM, Microsoft, Apple, and Amazon. The example from IBM happened in 2013, when IBM partnered with the University of Texas MD Anderson Cancer Center which developed a new "Oncology Expert Advisor" system with the goal to cure cancer [14].

Obviously, quality of data influence reliability. That is the reason to speak of data reliability. Data reliability refers to the completeness and accuracy of data as a measure of how well it can be counted on to be consistent and free from errors across time and sources. The more reliable data is, the more trustworthy it becomes [15].

There are authors who ask questions about potential risks, such as whether AI will pose an existential threat to humanity, or whether AI technology will be concentrated in the hands of the few [13]. But is not only question of reliability.

### 4.3. Nature of the algorithm

There is also a question raised whether AI can fail to function as expected, and the reason is because of the nature of the machine-learning algorithms on which modern AI techniques are commonly built. These algorithms are capable of learning from massive amounts of data, and once that data is internalized, they are capable of making decisions experientially or intuitively like humans. This means that for the first time, computers are no longer merely executing detailed pre-written instructions but are capable of arriving at dynamic solutions to problems based on patterns in data that humans may not even be able to perceive. This new approach comes at a price, because many of these algorithms can be black boxes, even to their creators [13]. Algorithm of AI is good if data from which this algorithm learns is good. So, again we can speak about data reliability.

### 4.4. Number and nature of data

One of the important questions is whether AI can work on a small number of data, for example, the number of failures of a product. In [16], it is concluded that model's predictive accuracy depends on the relevancy, sufficiency, and quality of the training and test data. Two questions are commonly asked with regard to failure history data: (1) How many failure events are required to train a model? And (2) How many records is considered as "enough"?

In July 2018, StatNews reviewed internal IBM documents and found that IBM's Watson was making erroneous, downright dangerous cancer treatment advice. In [12], it is concluded that, probably, the reason is because the software is trained on a small number of hypothetical cancer patients, rather than on real patient data.

Reliability is also important for security of AI (for

example protection of unauthorized access).

### 4.5. User competence

It seems to me that user competence or incompetence in using AI can also be the reason for inadequate results which AI can delivered. Important question is if human can control AI.

As a conclusion for AI reliability, or trustworthiness (which is a broader term), let us use the statement from [17]: „Having the capability to generate tremendous benefits for individuals and society, AI also gives rise to certain risks that should be properly managed,„ and „It is known that humans are biased in their decision making. Since AI systems are designed by humans, it is possible that humans inject their bias into them, even in an unintended way.“

Analysing failures of AI, can help to improve AI reliability. But on the other hand, use of AI can help to improve its reliability, and evaluate of other products, and also improve maintenance (methodology and training).

### 4.6. AI and human reliability

As we stated before AI can learn from human, and human knowledge can be erroneous. Because we can speak about human reliability, and if human is involved in AI, obviously AI reliability is connected with human reliability, because human action can influence reliability of AI.

I considered human reliability important from the beginning of my work in reliability, so human reliability is included in my textbooks and lectures for students [18, 19].

## 5. CONCLUSION

Artificial intelligence (AI) is in nowadays applying in almost every area of human life, and can has big impact. Everything can fail to function properly or as expected, and AI is not an exception, so as any other product AI must be reliable.

Some reason why AI is not reliable are inadequate quality of data used to learn, small or insufficient number of training and test data, training with unreal data, change of data, nature of learning algorithms, changes of user behaviour.

Someone must have in mind that AI is mainly software and uses data to learn.

In order to avoid situations when AI becomes unreliable, it is important to be familiar with causes of its unreliability.

To build successful AI, there is a need to be familiar with cases when AI failed in order not to make the same mistakes. Analysing failure of AI can help to improve AI reliability. Designers who want to apply AI must have in mind reliability.

If humans are biased in their decision making, this can

happen also with AI if AI learn from human.

AI is dominantly software, but can involve hardware and human, and of course data, so reliability of AI is related with software reliability, hardware reliability, human reliability and data reliability. Software reliability is usually more complex problem than hardware reliability, and AI reliability is more complex than any of these included human and data reliability.

## References

- [1] POKORNI S. *Current State of the application of Artificial Intelligence in Reliability and Maintainability*. Vojnotehnički glasnik/Military Technical Courier, 2021, Vol. 69, Issue 3, pp. 578-593, DOI: 10.5937/vojtehg69-30434, <https://doi:10.5937/vojtehg69-30434>, ISSN 0042-8469, UDC 623 + 355/359
- [2] Ethical guidelines for the development, implementation and use of reliable and responsible artificial intelligence. "Sl. glasnik RS", br. 23/2023. Available at: [http://demo.paragraf.rs/demo/combined/Old/t/2023\\_03/SG\\_023\\_2023\\_007.htm](http://demo.paragraf.rs/demo/combined/Old/t/2023_03/SG_023_2023_007.htm). (In Serbian)
- [3] POKORNI, S. *Reliability of Internet of Things*. In: 8<sup>th</sup> International Scientific Conference on Defensive Technologies OTEH 2018, Belgrade, pp.567-570, 11-12 October [online]. Available at: <http://www.vti.mod.gov.rs/oteh18/elementi/rad/027.htm>. ISBN 978-86-81123-88-4.
- [4] POKORNI, S. *Reliability prediction of electronic equipment: problems and experience*. In: 7<sup>th</sup> International Scientific Conference on Defensive Technologies OTEH 2016, Belgrade, pp.695-700, 6-7 October. ISBN 978-86-81123-82-9.
- [5] POKORNI S. *Data-driven reliability and availability of electronic equipment*, Vojnotehnički glasnik/Military Technical Courier, 2023, Vol. 71, Issue 3, pp. 769-782, DOI: 10.5937/vojtehg71-43474, <https://doi:10.5937/vojtehg71-43474>, eISSN 2217-4753, ISSN 0042-8469, UDC 623 + 355/359
- [6] Government of the Republic of Serbia. *Strategy for the Development of Artificial Intelligence in the Republic of Serbia for the period 2020-2025*. 2019. [online]. Available at: <https://www.srbija.gov.rs/tekst/en/149169/strategy-for-the-development-of-artificial-intelligence-in-the-republic-of-serbia-for-the-period-2020-2025.php>
- [7] COPELAND, B.J. *Artificial intelligence* In: Encyclopedia Britannica. London: Encyclopedia Britannica, Inc. 1998. [online]. Available at: <https://www.britannica.com/technology/artificial-intelligence>
- [8] Merriam-Webster. *Artificial intelligence*. In: *Merriam-Webster.com dictionary*. 2020. [online]. Available at: <https://www.merriam-webster.com/dictionary/artificial%20intelligence>
- [9] European Commission. 2019. *A definition of AI: Main capabilities and scientific disciplines*. Brussels: European Commission Independent High-Level Expert Group on Artificial Intelligence [online]. Available at: <https://ec.europa.eu/digital-single-market/en/news/definition-artificial-intelligence-main-capabilities-and-scientific-disciplines>
- [10] ISO. 2020. *ISO/IEC TR 24028:2020 Information technology — Artificial intelligence — Overview of trustworthiness in artificial intelligence* [online]. Available at: <https://www.iso.org/standard/77608.html?browse=tc>
- [11] University of Cambridge. *Enhancing the reliability of artificial intelligence*. 2016. [online]. Available at: <https://phys.org/news/2016-10-reliability-artificial-intelligence.html>
- [12] HEAVEN, D. *Why deep-learning AIs are so easy to fool*. Nature, 09 October 2019. [online]. Available at: <https://www.nature.com/articles/d41586-019-03013-5>
- [13] BATHAEE, Y. *The Artificial Intelligence Black Box and the Failure of Intent and Causation*. Harvard Journal of Law & Technology, 2018. 31(2) [online]. Available at: <https://jolt.law.harvard.edu/assets/articlePDFs/v31/The-Artificial-Intelligence-Black-Box-and-the-Failure-of-Intent-and-Causation-Yavar-Bathae.pdf>
- [14] BLIER, N. *Stories of AI Failure and How to Avoid Similar AI Fails*. Lexalytics, 30 January 2020. [online]. Available at: <https://www.lexalytics.com/lexablog/stories-ai-failure-avoid-ai-fails-2020>
- [15] IBM What is data reliability? Available at: <https://www.ibm.com/topics/data-reliability>
- [16] -Microsoft. *Azure AI guide for predictive maintenance solutions*. 2020. [online]. Available at: <https://docs.microsoft.com/en-us/azure/machine-learning/team-data-science-process/predictive-maintenance-playbook>
- [17] European Commission. *Draft Ethics Guidelines for Trustworthy AI*. 2018. Available at: <https://digital-strategy.ec.europa.eu/en/library/draft-ethics-guidelines-trustworthy-ai>
- [18] POKORNI S. *Reliability and maintenance of technical systems*. Military academy. Belgrade. 2002. (in Serbian)
- [19] POKORNI S. *Reliability of information systems*. Information Technology School. Belgrade. 2014. (in Serbian)



## TEST SETUP FOR QUALIFICATION OF POWER SUPPLY FOR GENIII NIGHT VISION IMAGE INTENSIFIERS

SLOBODAN PETRIČEVIĆ

School of Electrical Engineering, University of Belgrade, Belgrade, [slobodan@etf.bg.ac.rs](mailto:slobodan@etf.bg.ac.rs)

PEĐA MIHAILOVIĆ

School of Electrical Engineering, University of Belgrade, Belgrade, [pedja@etf.bg.ac.rs](mailto:pedja@etf.bg.ac.rs)

PETAR ATANASIJEVIĆ

School of Electrical Engineering, University of Belgrade, Belgrade, [petarat@etf.bg.ac.rs](mailto:petarat@etf.bg.ac.rs)

**Abstract:** *GenIII image intensifiers have been in use for decades and have undergone continuous improvements in terms of performance. Delicate matching of each individual tube with customized power supply remains workforce intensive and is one of bottlenecks in mass production. With each individual intensifier module having distinctive characteristics, achieving standardized performance in serial production is accomplished by compensating for tube individuality with programmable power supply unit. Since power supply and tube must be enclosed in a sealed package, matching is a one-time operation. For a power supply unit to be capable of matching tube variations in production, it must be capable of wide range of adjustments in polarization voltages. Thus, each power supply must be individually qualified on a dedicated test bench and must satisfy strict requirements for wide adjustment ranges. This paper presents a dedicated, custom made, test bench and its operations for testing power supplies in mass production and qualifying them for tube matching.*

**Keywords:** *Image intensifiers, power supply, GenIII.*

### 1. INTRODUCTION

Image intensifiers (II) have for several decades played a key role in night military operations providing the troops with sighting ability and situational awareness as close to daylight conditions as possible. The side enjoying such an advantage is favored in any combat scenario, but one – presence of strong artificial illumination [1]. No military is willing to dispense with this advantage making military night vision goggles (NVG) a regular part of the outfit of most modern armies. A great deal of investment has been provided for research and development of NVG since 1950s, creating at least 3 generation of devices colloquially referred to as GenI, GenII and GenIII night vision systems [2], [3]. A typical NVG assembly consists of an image intensifier, optical components and housing with battery compartment [4]. The image intensifier itself is an encapsulated package containing an image intensifier tube (IIT) and an embedded power supply unit (PSU). The IIT provides optical gain by converting photons to electrons on the photocathode (PC), amplifying the photocurrent in the microchannel plate (MCP) and converting electron current to intensified optical image on the screen (sometimes called anode). The PSU provides required power for PC, MCP and screen in the form of high voltage DC or pulsed sources ranging from -800 V on the PC to over 6 kV on the screen. Standardized IIT sizes include the 25mm and 18mm models.

However, manufacturing IIT on a large scale is a challenging task riddled with technology issues, material quality, process control and quality testing problems of all kinds. Single most important problem yet to be resolved in mass production of the IITs is large tolerance for total optical gain. Since optical gain is a function of all three supply voltages generated by the PSU, the solution to this issue is still a brute force one – the PSU is “matched” to the tube by adjusting the voltages to achieve equal gains of the final II.

In addition, the PSU is tasked with two important functions: automatic brightness control (ABC) and bright screen protection (BSP). Both are implemented with changing the MCP voltage (ABC function) or cathode voltage (BSP function) in response to screen current or cathode current. ABC maintains constant screen current that is set during the matching of the PSU with the tube and BSP operates by reducing the cathode voltage in response to high levels of cathode current. ABC requires quantitative evaluation during test since the ABC is specified as both screen brightness uniformity with cathode illumination change and screen current uniformity with cathode illumination change. BSP is not specified as a PSU parameter but is verified by measuring the cathode voltage change with cathode illumination change.

This approach places a demanding design requirement for the PSU creating and a set of requirements (happily

expressed in numbers) for adjustment range of voltages and various electrical, mechanical, and other kind of parameters. So instead of evaluating the IITs and classifying them in groups, it is the PSU task to compensate for deficiencies of each individual tube. The reason is purely economic in nature – cost of manufacturing an IIT is an order of magnitude larger than of the PSU, and every single IIT should be used, if possible, to make manufacturing economically viable.

This paper reports on a solution for testing IIT PSU units in mass production with the aim of demonstrating the difficulties associated with PSU design and testing.

## 2. THE IIT AS AN ELECTRICAL LOAD

The IIT as an electrical load for the PSU can be represented as an illumination dependent current source for the IIT cathode control, voltage dependent resistor for the MCP control (from 70 M $\Omega$  up to 150 M $\Omega$ ) and screen brightness dependent current source for the screen control. This strange combination of active and passive components creates a huge problem for the test environment mainly because of the voltage and current values typical to the PSU as seen in the table below.

**Table 1.** Voltage numeration

Name	Min value	Max value	Transient condition
Screen voltage	4500V	6000V	Overshoot to 6500V for a part of a second.
MCP voltage	300V	1300V	Varies within range depending on the cathode illumination.
Cathode voltage	-800V	+80V	For auto-gated PSU voltage pulses at frequency of several hundred Hz from -300V to +80V. For non -gated PSU DC voltage increasing with cathode illumination.
Screen current	30nA	400nA	Transient overshoot of several $\mu$ A during rapid cathode illumination change.
MCP current	2 $\mu$ A	15 $\mu$ A	Not tested, irrelevant for operation.
Cathode current	<1nA	30 $\mu$ A	Pulsed for gated PSU and DC value for non-gated PSU.

With these values in mind the test station must measure the voltages and current without loading the PSU appreciably. This is indeed a nasty problem since, for example, measuring the screen voltage requires that no more than about 10nA of current is drawn from the PSU yellow wire implying T $\Omega$  value resistor for sensing. Similar issues exist at the cathode with some additional complication of pulsed operation. Measuring  $\mu$ A and nA

currents is an issue with its own merits [5], and even more nasty in high voltage case [6] and here additionally complicated since screen and/or cathode current measurement can cause flicker on the screen.

The cathode is a problem of its own, being somewhat of an orphan regarding standards. Standards that existed for GenIII are no longer valid and their predecessor (no longer valid as well) specified the BSP. Although called a “Screen Protection” function, BSP is implemented in the cathode drive circuit. With increased cathode illumination, the cathode voltage rises (it is negative with respect to red wire and ground) and this is deliberately implemented in the PSU to reduce the cathode responsivity and the cathode current. Implementation is usually done with gigaohmic resistor placed in the PSU on the blue wire driver. This means that any test unit measuring cathode voltage must not load the cathode with a resistance of less than about 100 G $\Omega$ , otherwise the BSP will be active and cathode voltage cannot be measured.

The problem is complicated even further in auto-gated PSU units that pulses the cathode voltage to PWM modulate the cathode current. Not only they do not implement the BSP function, but at higher cathode illumination (about 1  $\mu$ A of cathode current) the pulses appear at the blue wire with peak value going into positive with respect to red wire. Given the sharp edges of pulses (around few  $\mu$ s) and large ohmic values of the cathode resistive divider, measuring these pulses is a problem.

Traditional PSU testing uses needle type floating voltmeters and amperemeters that are difficult to read accurately. For this reason, screen current meter has been designed as a separate unit with additional insulation and is not part of the main measuring unit. Insulation is of incredible importance in this setup, since any leakage into yellow or blue wire from nearby components could induce false PSU operation and flicker. Further complication arises from the need to shield sensitive amplifier inputs with faraday cage, which being made of metal, is an excellent conductor. The PSU wires must be insulated perfectly, and the points where they connect to the sensing system (terminals or connectors), require heavy shielding.

Inspite of a rather a bleak outlook, the test unit was successfully designed in the end, by sacrificing volume. If measuring sections for each terminal are separated with a gap large enough to eliminate capacitive coupling and if the terminals are insulated from the metal chassis, then it all works out somehow. Another requirement is that the room moisture is controlled to a level low enough to permit operations. Sometimes, due to leakages on the test modules, the module itself must be immersed in nitrogen. A story beyond the scope of this paper...

Functional PSU testing requires that the operator qualifies the PSU for eventual flicker, i.e., unstable screen brightness with stable cathode illumination. This phenomenon can occur for several reasons, typically if any of the three voltages generated by the PSU exhibit instability. To positively identify the PSU as the culprit,

the operator needs to see the waveforms of the voltages, so DC value of the voltages is of limited use. This of course implies that the voltage dividers measuring the high voltages must be carefully compensated and tested for proper pulsed operation [7].

Once voltage and current measurement issues in all operational conditions have been resolved, more complex PSU requirements can be evaluated such as ABC function, BSP function and others.

### 3. THE BLACK BOX

The heart of the test setup is a dedicated measuring instrument named „The Black Box “(figure 1) out of the lack of inspiration for a name that would describe its function. It is a quad high-voltage passive voltmeter combined with a low voltage voltmeter and amperemeter. This PSU high-voltage side is connected to the PSU under test via top side-colored connectors on the right and measures high voltages on blue, red, black, and yellow wires. The measurement is accomplished via a compensated resistive divider and its output is fed to an ADC inside the box and to a set of analog difference amplifiers.

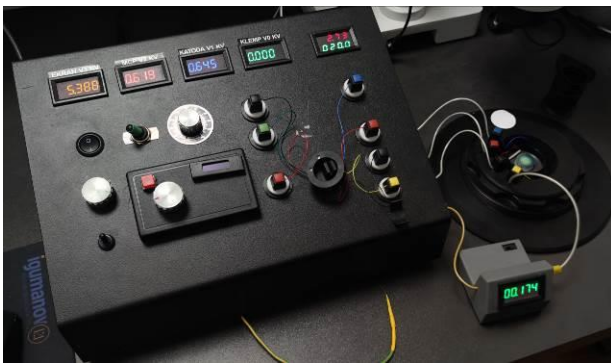


**Figure 1.** The black box

Since conventional measurement of the PSU voltage is expressed in relative values (i.e., potential difference between wires) internal analog difference amplifier creates the voltage differences as per table below:

**Table 2.** Voltage numeration

Name	V <sub>n</sub>	Voltage Difference
Screen voltage	V <sub>3</sub>	Yellow-Black
MCP voltage	V <sub>2</sub>	Black-Red
Cathode voltage	V <sub>1</sub>	Red-Blue

These voltage differences are presented on the panel meters with yellow, red, and blue digits, respectively. Additional panel meter with green digits measures the peak voltage in a gated PSU and is not part of the standard setup. ADC inside the unit converts voltage on the four wires with respect to the ground potential (black ground wire), and digital subtraction accomplishes the same result.

The low-voltage PSU side is connected to the left connector set located on the box topside with black as

PSU negative battery pin, red as PSU positive battery pin and green wire as EGC input. The dual panel meter on the right top side measures the PSU input voltage on the red wire (red in V) and PSU current consumption (green in mA) through the same red wire.

The EGC function is evaluated with a potentiometer placed left to the black connector. The potentiometer value is 100kΩ. There are several combinations of the EGC functionality of the PSU varying with the manufacturer and the product. The EGC resistance (set by the said potentiometer) can be connected to ground (black wire) or battery positive (red wire). The green switch to the potentiometer left is used to switch between these two options so that all PSU models can be evaluated.

The switch to the far left applies the power to the PSU and the potentiometer below that switch is used to set the PSU input voltage from 1.7V up to 3.7V. The PSU itself is positioned on the holder between the connectors for convenient adjustment via its integrated potentiometers.

The remaining assets on the black box topside are used for special PSU model adjustments.

The right side of the black box contains a set of four 4mm round receptacles colored in the high-voltage side colors. The IIT tube (without its PSU) is connected to the black box via double isolated white wires and module's own set of colored connectors mounted on the module holder (black recessed tube to the right). In this way all PSU can be evaluated using the same quality intensifier module and qualified.

The setup uses separate microammeter for measuring the screen current on the yellow wire that is connected between the black box right side yellow connector and image intensifier module yellow wire.

During testing it is possible to disconnect the module from the black box right side connectors and a set of fixed resistors can be connected in its place. These tests are part of the PSU procedure for evaluation.

The black box back side contains power on/off switch and DE15 connector for connection to the oscilloscope. The analog difference amplifier outputs, PSU input voltage and current consumption are available for observation on the oscilloscope.

### 4. SETUP

The black box is positioned in the middle of the test table, as seen in figure below (figure 2). The module holder is embedded in the table to the right. The transformer placed to the table far right side powers the bulbs in the illumination setup that is below the table and will be discussed later. Since PSU qualification requires careful testing for possible flicker and screen brightness issues, a microscope is required and it is located behind the module holder on a swing arm. Typical test requires eye observation of the module screen without and with microscope, so a convenient microscope mount is very

useful. Table top contains an oscilloscope (almost any 4 channel model would do) for observation of voltages and a luxmeter (model Digilux 9500). The luxmeter has its measurement head connected via a gray cable, and the head can be moved around the table and placed on the module when needed. Due to strict screen brightness uniformity requirements, human eye cannot discern the level of nonuniformity that disqualifies the PSU. So a lux meter is necessary for screen brightness tests. The paper table strapped to the table top contains a list of transformer voltages measured on the AC voltmeter atop the transformer and respective illumination levels of the cathode.



**Figure 2.** Test table topside setup

The black box unit contains a Raspberry PI computer that

acquires the ADC data and presents the voltage waveforms on the monitor (figure 3). Important values such as average voltages, peak-to-peak voltages and other values are calculated and shown on monitor for ease of use. This duplicates the oscilloscope function since occasional flicker can be traced to PSU voltage instabilities. Given that 0.1% of variation of the MCP voltage is visible by human eye in close contact with the screen, oscilloscope with 8 bit ADC cannot detect the cause of the flicker. The ADC module inside the black box uses 16 bit ADCs and can resolve these small variations on the 2K monitors, which is an important aspect of the PSU control. Simply put, observing the voltages on the oscilloscope does not guarantee that PSU voltages are stable to the required level.



**Figure 3.** PSU waveforms

Below the table there is a set of incandescent lamps (figure 4) that illuminate the cathode from below the table via a lens placed on the module holder bottom mount (not visible). The illumination surface (a diffuser) also contains a target for module resolution qualification so that resolution of the IIT in low-light and high-light conditions can be easily tested. The illumination can be covered via a hinged door to the right (barely visible) in order to prevent external light from entering the lens and illuminating the cathode. In this way a controllable cathode illumination is possible from  $10^{-4}$  Lux up to 200 Lux.



**Figure 4.** Test table bottom-side setup

The illumination setup contains cooling fan that is also powered by the same transformer so that it generates fan noise at high illumination levels only. Since the module cathodes degenerate quickly at the levels of illumination, testing is short, so noise is not a big problem.

**Table 3.** PSU Evaluation Tests

Test Type
PSU High voltage measurement in all operational conditions.
Screen current measurement in all operational conditions.
Battery Voltage compliance.
Current consumption from battery in all operational conditions.
Screen brightness uniformity change with cathode illumination change.
Screen current uniformity change with cathode illumination change.
ABC function verification.
MCP voltage step response.
Rise-on time evaluation.
Response-time evaluation.
MCP voltage change with various resistive loads.
Cathode voltage change with various resistive loads.

## 5. CONCLUSION

A solution for II PSU evaluation in mass production has been presented in this paper. The solution fits inside a 3 m<sup>2</sup> room with all instruments placed within hands reach. All the tests required for PSU qualification can be performed on this test bench within about 10 minutes. This setup eliminates one of bottlenecks in PSU production allowing for more units of equal quality to be produced.

## References

- [1] J. E. Zacher *et al.*, "Effects of image intensifier halo on perceived layout," *SPIE Def. + Commer. Sens.*, vol. 6557, p. 65570U, Apr. 2007.
- [2] A. G. V. Ltd, "DIFFERENCES BETWEEN GENERATIONS OF NIGHT VISION SYSTEMS," 2020. [Online]. Available: <https://www.agmglobalvision.eu/blog/difference-between-night-vision-generations>. [Accessed: 05-Jun-2024].
- [3] Teledyne Flir, "What's the Difference Between Gen 2 and Gen 3 Night Vision?," 2019. [Online]. Available: <https://www.flir.com/discover/ots/whats-the-difference-between-gen-2-and-gen-3-night-vision/>.
- [4] T. DEPARTMENTS OF THE ARMY, THE NAVY and M. C. AIR FORCE AND HEADQUARTERS, "PVS7 Training Manual." 2000.
- [5] W. Lin and S. A. Deng, "Research on nano-ampere current-measuring meter system," *FBIE 2009 - 2009 Int. Conf. Futur. Biomed. Inf. Eng.*, pp. 41–44, 2009.
- [6] R. Soto-Camacho *et al.*, "A Current Monitor System in High-Voltage Applications in a Range from Picoamps to Microamps," *Electron. 2021, Vol. 10, Page 164*, vol. 10, no. 2, p. 164, Jan. 2021.
- [7] A. M. Doug Mercer, "ADALM1000 SMU Training Topic 11: Frequency Compensated Voltage Dividers | Analog Devices," *Analog Dialogue*, vol. 52, no. 11, pp. 1–4, Nov. 2018.



# IMPLEMENTATION OF ZIGBEE TECHNOLOGY IN THE PROCESS OF SENSOR CALIBRATION IN WIRELESS SENSOR NETWORK SYSTEMS

IGOR MEDENICA

Elektrodistribucija Srbije d.o.o. Belgrade, Serbia, [medenicaigor@gmail.com](mailto:medenicaigor@gmail.com)

MILOŠ JOVANOVIĆ

Technical Test Center, Belgrade, Ministry of Defense Republic of Serbia, Serbia, [mjovanovic@raf.rs](mailto:mjovanovic@raf.rs)

SLOBODAN SUBOTIĆ

Technical Test Center, Belgrade, Ministry of Defense Republic of Serbia, Serbia, [slobodansubotic80@gmail.com](mailto:slobodansubotic80@gmail.com)

DRAGAN LAZIĆ

Technical Test Center, Belgrade, Ministry of Defense Republic of Serbia, Serbia, [astazu.lazic@gmail.com](mailto:astazu.lazic@gmail.com)

**Abstract:** *The compatibility of sensor functionality requires periodic calibration in an accredited laboratory. The calibration process involves temporarily disconnecting the sensor from operation, performing necessary preparations, and determining the sensor's condition. As a solution to improving the calibration process, the use of mesh networks is presented to avoid disconnecting sensors from active states. Using ZigBee technology, all sensors are represented through nodes with specific functions in the network. Information exchange occurs wirelessly among all nodes in the network, which are involved in communication with the main node (gateway). The main node serves the function of storing and processing data based on specified standards. To gain complete control over the system, observed state changes are stored in the main node's memory, which communicates with all nodes in the network during its operation. Deviations from reference sensor values are determined based on collected parameters from other nodes in the wireless sensor network. To expedite network operation, there is a need to categorize nodes into different types. Definitions of all node types are stored in a dynamic state table, with parameters defining the node type and its state. To facilitate access to all defined nodes from the dynamic state table, node types, in addition to the main node, are divided into reference and regular nodes. Reference nodes in the network do not have a constant role, and their role is separate from regular nodes to expedite communication and parameter retrieval for necessary analyses. Retrieved parameters from the state table are included in the comparison and analysis process based on node type. Obtaining results enables the identification of deviations, issues during operation, and the correctness of retrieved data compared to reference sensors.*

**Keywords:** *Sensor, calibration, ZigBee, mesh network, sensor network, gateway.*

## 1. INTRODUCTION

In current practice, wireless sensor networks are used in a variety of applications, including environmental monitoring (e.g. temperature, humidity, air quality), resource monitoring in industrial processes, infrastructure monitoring (e.g. road, bridge condition monitoring), smart agriculture, security and many others. To enhance and accelerate the deployment of communication systems between nodes, ZigBee technology is utilized, which has increasingly gained prominence as a commercial solution. Communication based on this technology allows the network to be flexible and easy to expand.

In this paper, we focus on the proposed solution for facilitating and speeding up calibration based on the mentioned technologies. The advantage of this approach is significant for large systems that have a large number of sensors.

In order to carry out all the calibration processes, the main step is to physically switch off the required sensor and transfer it to the laboratory in order to carry out the calibration under special conditions. The use of a network would facilitate the current calibration method and the sensor itself would not have to be switched off. This method streamlines the calibration process and reduces costs.

Through various researches, the concept of blind calibration has been presented which is designed for general sensor networks. The idea is to achieve great similarity in the measurements of all sensors in the network for the same purpose through this concept [1]. This method of testing does not always give correct results, but through a larger number of measurements and the inclusion of comparison with a reference sensor, this concept could be applied through a wireless network of sensors. The mesh network through various applications has shown flexibility and cost reduction [2][3]. This



network topology allows all network participants to send and receive data, thus all sensors within the sensor network can communicate with each other.

The rest of the work is organized through four sections. Section 2 introduces wireless sensor network technologies and ZigBee technologies. Section 3 shows the proposal of the system architecture and Section 4 describes the implementation of the calibration based on the proposed architecture. In Section V conclusion of the work.

## 2. WSN AND ZIGBEE

A wireless sensor network (WSN) is a self-organizing, ad hoc multi-hop network comprised of sensors distributed across a wide area [4]. It functions as a distributed real-time system where nodes possess the capability to both transmit and receive data. Consequently, a WSN facilitates the concurrent collection of physical parameters, real-time processing, and wireless communication, enabling efficient and synchronized data handling across the network.

WSN consists of multiple sensor nodes that generate sensor readings that are delivered via multi-hop paths to a specific node in the network for data collection. The node to which readings are delivered is called a sink [5].

This system has two types of nodes, a sensor node and a coordinator node. Sensor nodes have a role in the network to detect physical changes in the environment, such as temperature, humidity, and forward all collected parameters to the network. Coordinator nodes have the task of collecting all the data forwarded by the sensor nodes and forward them either to the end user or for processing [6].

ZigBee is a worldwide open standard of low-speed wireless networking based on IEEE 802.15.4. The aim of this standard is to enable [7]:

- Low cost
- Ultra-low power consumption
- Use of unlicensed radio bands
- Cheap and easy installation
- Flexible and extendable networks
- Integrated solutions for message routing

The mentioned characteristics enable quick installation of external power supplies without the need for cables due to low levels of vibration during operation.

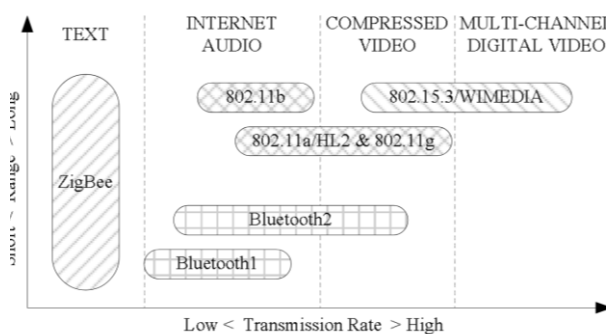


Figure 1. Wireless landscape

This technology finds its application in smart home communication, security systems and remote control and reading of devices. Compared to other wireless protocols such as Bluetooth (802.11), ZigBee exhibits a wide range in communication distance and a low transmission rate. It is characterized by fast and short transmission of text format. The figure (Figure 1) below shows wireless network protocols with an emphasis on two characteristics, wireless radio range and data transfer rate [8].

Routing a message through the network from one node to another depends on the network topology, which is divided into star, tree and mesh.

Star topology relies on a central node and all messages travel through it.

A tree topology has a main node at the top that branches into branches and leaves. In order for the message to reach the required destination, it travels up the tree and then down the chain.

The mesh topology is the most similar to the tree topology, only that the nodes have a direct connection to other nodes.

Unlike the star topology, which has a single coordinator node that distributes traffic in the network, a mesh network can communicate without the help of a coordinator. Nodes in this network serve as routers that form a flexible and reliable structure with the possibility of mobility of the end nodes of the network. Thanks to these characteristics, ZigBee has the ability to cover a large area and therefore has applications in various industries.

ZigBee technology has found its application in many fields such as smart homes and cities, agriculture, industrial production and many more. The choice of this technology for communication within the WSN system is low-cost, low-power and multifunctional sensor nodes.

Based on the mesh network structure, it is possible to communicate over long distances. One of the applications of this technology is that it can be used in testing the correct operation of sensors and testing their accuracy in operation. The previous method of checking the operation of the sensor required disconnecting it from operation and testing it in laboratory conditions. Through the wireless method of testing the correctness of sensors, costs would be reduced and the effectiveness of the system would be increased. In order for this method to work, it is necessary to predefine the types of nodes in the network, which ZigBee communication provides in its work. One of the ways is to create a dynamic node state table that has the purpose of defining all nodes in the system.

### 3. NETWORK SYSTEM ARCHITECTURE

In order to take full advantage of the advantages of ZigBee technology, the definition of node types is performed depending on the role in the system, structuring and storage of data exchanged between nodes.

#### 3.1. Types of nodes

By using a mesh network, it is necessary to introduce the definition of network nodes in order to adapt to the solution of the calibration problem within the wireless sensor network.

Nodes are divided based on their roles in the network into the main node (orange), reference (blue) and regular (green) nodes (Figure 2).

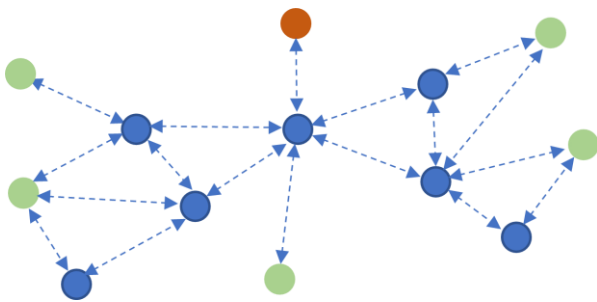


**Figure 2.** Communication between different types of nodes

The main or input node has the role of coordination in the system as well as receiving and sending data outside the network. Within the main node, information related to the state of nodes in the network and data measured through measurements on reference and regular nodes are stored.

Reference nodes are occasionally active nodes within the network that assume their role at certain time intervals. After successful measurements, they are disconnected from the network.

Regular nodes are all other nodes that have a daily function within the sensor wireless network. Through this system functioning model, their work is constant without planned disconnections from the network, as long as they provide the required functionality.

#### 3.2. Table of dynamic states

In order for communication to be uninterrupted and reliable in the network, the state of each node and the type of node it belongs to are recorded. On the basis of the above information, a decision is made about the necessary storage of parameters and the analysis thereof. The parameters are entered into the table of dynamic states, which has the following structure:

- Node address
- Node type
- Purpose/Function
- Routing time

#### - Status

Based on the routing time, an assessment is made on the need for a new node status update. The state of a node determines its activity in the network, which can be active or deactivated.

Nodes that cannot be accessed during each subsequent routing are given the status deactivated, while deactivated nodes are examined first with each pass. By definition, if a node is inactive in the network for a certain period, it is deleted from the status table.

Recognizing a new node in the network during routing, its function or type of sensor in the WSN system is recorded, the node type is basically added for regular, while in reference connection situations this type changes and the status of the node becomes active and visible in every subsequent routing.

The table is stored on the main node to facilitate subsequent data analysis because all data is available in one place.

#### 3.3. Table of sensor parameters

During dynamic state table routing through the network, nodes forward their sensor reading parameters to the master node. All measurement parameters for all sensors in the network are stored within the main node. For these needs, a table is created that records the address of the node, the type of measurement, the time of measurement and the values of the performed measurements. Based on the entered data, it is possible to follow the complete measurement history for each node in the network from the beginning of its activation. Based on the stated values of the sensors, it is possible to establish deviations in the operation of each sensor in different conditions, and based on the data from the table of dynamic states, the type of node is determined. In order for the calibration to be carried out successfully after storage, on the basis of establishing the type of node, the reference values for the selected sensors are determined, on the basis of which the calibration process is entered.

### 4. SENSOR CALIBRATION IN WSN SYSTEM

Wireless sensor networks usually consist of inferior sensors that are deeply integrated into the physical environment and as a result, the performance of the network is undermined by poor hardware and sums in data measurement [9]. Through various researches, calibration solutions have been proposed at the device level, which do not perform well in larger systems.

Through this work, a new concept of thinking within the mesh network is explained, with the definition of communication between nodes and the definition of data types in the system. Stored data within the main node contributes to tracking deviations of regular sensors in operation. With this work model, calibration includes a reference model that is defined in the system as a reference node, based on the parameters of which

comparison is made with regular nodes of the same type of purpose.

During the sensor calibration, the measurement data is stored on the main node in the network, while the regular nodes, as permanent participants in the communication, only perform their measurement function.

Reference nodes are part of the system while measuring in similar conditions based on other sensors under test. During calibration, it is possible to take one or more sensors into the process, given that the architecture explained in Section 3 allows communication with multiple sensors and that all data is related to measurements on the main node, which has recorded the complete history of a particular sensor.

In addition to this, the calibration process incorporates advanced algorithms that adjust for environmental variations and sensor drift over time. By continuously comparing the measurements of the regular sensors to those of the reference node, the system can dynamically update calibration parameters and ensure that sensor data remains accurate and reliable. This approach not only improves the overall accuracy of the sensor network but also enhances the robustness of the network by minimizing the impact of individual sensor failures or discrepancies. Thus, this calibration method represents a significant advancement in maintaining the integrity and performance of wireless sensor networks.

## 5. CONCLUSION

The presentation of the wireless calibration model in relation to the traditional one shows the increasing need for sizes and number of nodes in wireless sensor network systems. ZigBee is one of the technologies that finds its application and facilitates this access model. By defining dynamic states, assigning node types and storing data, it gives full control over the network and creates a new environment that gives the possibility of expanding functionality and opening new fields of application.

This work represents the first step in the exploration of advanced calibration techniques for wireless sensor networks. Future research will focus on extensive testing to evaluate the performance of the calibration model under various conditions. These tests will aim to identify the most efficient components of the system, pinpointing which aspects of the calibration model perform optimally and where further improvements may be needed. The insights gained from this testing phase will be crucial for refining the calibration approach, enhancing the accuracy and reliability of the sensor network, and guiding future developments in this field.

## References

- [1] BALZANO,L., NOWAK,R.: *Blind calibration of sensor networks*, Proc. of IPSN. IEEE/ACM, (2007) 79-88.
- [2] FRANCESCHINIS,M., SPIRITO,M., TOMASI,R., OSSINI,G., PIDALA,M.: *Using wsn technology for industrial monitoring: A real case*, Sensor Technologies and Applications, SENSORCOMM, (2008) 282-287.
- [3] HEILE,B.: *Emerging Standards: Where to ZigBee/UWB fit*, ZigBee Alliance, ZigBee Alliance, 2004.
- [4] KARL,H., WILLIG,A.: *Protocols and Architectures for Wireless Sensor Networks*, John Wiley & Sons, 2005.
- [5] BARONTI,P., PILLAI,P., CHOOK,W.C.V., CHESSA,S., GOTTA,A.,FUN HU,Y.: *Wireless sensor networks: A survey on the state of the art and the 802.15.4 and ZigBee standards*, Computer Communications, (2007) 1655-1695.
- [6] ONDREJ,S., ZDENEK,B., PETR,F., ONDREJ,H.: *ZigBee Technology and Device Design*, International Conference on Networking, International Conference on Systems and International Conference on Mobile Communications and Learning Technologies, IEEE, (2006) 129-139.
- [7] BAKER,N.: *ZigBee and Bluetooth strengths and weaknesses for industrial applications*, Computing & Control Engineering Journal, (2005) 20-25.
- [8] FITRIAWAN,H., MAUSA,D., ARFIN,J.,A.A., TRISANTO,A.: *Realization of Wireless Sensor Networks for Temperature and Humidity Monitoring*, Proceeding of International Conference on Electrical Engineering Computer Science and Informatics, 2015.
- [9] RAMANATHAN,N., BALZANO,L., BURT, M., ESTRIN,D., HARMON,T., HARVEY,C., JAY,J., KOHLER,E.,ROTHENBERG,S., SRIVASTAVA,M.: *Rapid Deployment with Confidence: Calibration and Fault Detection in Environmental Sensor Networks*, Technical Report CENS-TR-62, Center for Embedded Networked Sensing, 2006.



# THE ROLE OF INTELLECTUAL CAPITAL REPORTING IN THE PROCESS OF SUPPLY CHAIN INTEGRATION OF THE MILITARY TECHNICAL INSTITUTE

ALEKSANDAR SAVIĆ

Military Technical Institute, Ministry of Defense, Belgrade, [aleksandar22071993@gmail.com](mailto:aleksandar22071993@gmail.com)

MIHAJLO RANISAVLJEVIĆ

Military Technical Institute, Ministry of Defense, Belgrade

MILAN MIHAJLOVIĆ

University of Defense, Belgrade Military Academy

**Abstract:** *The Military Technical Institute (MTI) is the largest military scientific and research institution in the Republic of Serbia. It mainly realizes its supply chain from the approved budget funds of the Republic of Serbia, while a smaller part is realized from its own revenues. Her continuous work to improve non-financial performance within the supply chain as well as motivate employees to manage their supply chain integration (SCI) initiatives requires intellectual capital (IC) tracking and reporting. Analysis and reporting on IC in MTI can be done within the human, organizational and social dimensions of IC. This paper will examine the role of IC reporting and examine its impact on SCI in MTI. The aim of the paper is to determine that the monitoring and reporting of IC affects the process of SCI in MTI.*

**Keywords:** *reporting, intellectual capital, supply chain, Military Technical Institute.*

## 1. INTRODUCTION

The Military Technical Institute (MTI) is a scientific and research institution that is part of the Ministry of Defense of the Republic of Serbia. The development of weapons and military equipment, as high-tech products, is the main goal of MTI. During the past few decades, MTI has played an important role in the modernization of weapons and military equipment. The improvement of operations at MTI can be influenced by several stakeholders, including the companies with which MTI cooperates. The MTI supply chain is realized mainly from the budget of the Republic of Serbia, while a part is realized from own revenues and donations. That is why supply chain networks are usually more complex than networks of for-profit scientific research institutions.

Supply, demand and internal integration are the three constitutive aspects of supply chain integration (SCI) [1]. Although SCI is known to vary greatly from institution to institution, three types of aspects of SCI are key to improving MTI performance. MTI's ability to manage and report on human, organizational and social capital is critical to strengthening SCI. MTI, unlike for-profit institutions, is limited in terms of its organizational assets (such as an institutionalized knowledge base) and its talent management capabilities. Therefore, it is important to direct organizational and human resources in order to create a higher level capability that relies on synergy and advantage in cooperation [2].

Careful management of organizational and human capital is crucial for self-sustaining operations. SCI is considered a set of elements in operations, which can be used to help find solutions for efficiency and develop simplified processes of coordination of organizational activities inside and outside the system [3]. The empirical SCI literature shows that integration practices lead to improved operational and financial performance.

Although the benefits of SCI have already been studied and evaluated in for-profit enterprises, empirical validation of SCI in a non-profit military context is lacking. One of the contributions of this work lies in filling this gap.

## 2. INTELLECTUAL CAPITAL IN THE MILITARY TECHNICAL INSTITUTE

Individual knowledge, skills, norms and values, culture and behavior of employees, databases, methodologies, standards and procedures and licenses in MTI glass have received considerable attention as a source of competitive advantage during the last few decades. The unique term IC is used to describe these components in MTI.

Specifically, IC in MTI is considered a driver of both financial and non-financial performance. IC is one of the most important components, which contributes to MTI's achievement of the set goals. Knowledge exchange processes that cross borders are also included in this form of capital.

Social capital facilitates the actions of individuals and increases the efficiency of action. Unlike for-profit organizations in which social capital is conceived to be directly connected with SCI [12], in MTI it can be concluded that human capital and organizational capital are the building blocks of social capital. Furthermore, social capital is a key driver of SCI in MTI, as it facilitates "identification" - the process through which group members take the values or standards of other group members as their frame of reference.

Norms of social capital include individuals, who have an identity, common interests and commitment to the common good, a group. Teamwork, information exchange, joint decision-making and joint understanding are the basis for achieving a social goal [13], i.e. production and modernization of weapons and military equipment at MTI.

Human capital, manifested in the workforce, is key to finding effective solutions for strategic problem solving in MTI.

Organizational capital is the institutional knowledge that exists in MTI, which is stored in manuals, databases and reports. For example, MTI has manuals for employees, customers, suppliers, customers, donors and other foreign forces, as well as various forms and databases that store information about MTI's operations.

Finally, social capital, which is characterized by interactions between individuals, is perhaps the most critical element of MTI. The social capital of MTI enables the creation of consensus and focuses on a common goal - equipping and modernizing the Serbian Armed Forces.

### **3. SUPPLY CHAIN INTEGRATION IN THE MILITARY TECHNICAL INSTITUTE**

The SCI concept has received considerable scholarly attention in the research literature spanning more than a decade [14]. SCI is generally classified into two dimensions - internal and external integration. Internal integration involves the synchronization of information and integrative initiatives between functions within the institution. External integration, in contrast, refers to the level of cooperation of the institution with its suppliers, partners and customers [15]. Flynn, Huo and Zhao define SCI as the degree of strategic cooperation of an organization with its customers and suppliers and the management of processes within the organization. Collaboration with supply chain partners, as well as integration of functions within an institution, in several research studies have shown that SCI affects operational and financial performance [16]. Internal integration is a task in MTI, which is usually organized with management staff [17]. Resource limitations and the nature of work often do not allow for a large organizational structure, which negatively affects the work of MTI. The integration of supply takes place in each sector of MTI, which enables the Management of MTI to better plan the quantities of material assets that need to be procured in a certain period of time.

MTI's ability to coordinate distribution, shipping and inventory management tasks depends on the level of coordination with partners such as suppliers, customers, etc. The exchange of information with partners and the need for transportation and shipping capabilities determine demand integration [18]. SCI mainly focuses on information sharing, teamwork, building relationships and close ties that go beyond everyday transactions. KC, which is derived from resource-based capital (RC), indicates that knowledge is the most important strategic resource of an institution [19]. RC indicates that institutions seek valuable, rare, inimitable and non-substitutable resources to achieve competitive success [20]. Human knowledge-based resources are strategic in the sense that they bring skills, practices, knowledge and capabilities that add value to the institution [21]. MTI employees are like other employees in other institutions, but they possess specific knowledge and skills that are used to solve complex problems, regardless of the fact that they are not in profit institutions.

A review of the literature shows that SCI has primarily been examined in the context of private sector organizations and institutions. Therefore, understanding the nature and potential of the SCI of state organizations and institutions that realize social goals is a relatively under-researched area. Similar to private enterprises and MTI, as a military organization it must manage a constant flow of materials, services and information in order to achieve its objectives. In addition, MTI faces unique budgetary, infrastructure and staffing constraints, which require innovative approaches to managing operations. Compared to for-profit supply chains, the number of non-profit supply chains is much smaller, so to obtain an adequate sample size of respondents for statistical analysis, it is often necessary to collect data from a relatively large number of employees.

### **4. RESEARCH PROBLEM**

The problem of the research is to determine the existence of a difference in the degree of influence of IC reporting on SCI in MTI between people who deal with logistics (transportation, supply, maintenance, general logistics, health, infrastructure, resource protection, etc.) and people who they do not deal with the mentioned jobs.

#### **The aim of the research**

The aim of the paper is to examine the degree of impact of IC reporting on SCI in MTI, with a special emphasis on persons engaged (experimental group) and those not engaged (control group) in logistics business.

The subject of the paper is the influence of IC on SCI in MTI.

#### **Research hypotheses**

H1- There is a difference in the degree of impact of IC reporting on SCI in MTI between the "experimental" and control groups.

H2- There is a difference in the degree of impact of IC reporting on SCI in MTI between the "experimental" and

control groups in relation to gender.

H3- There is a difference in the degree of influence of IC reporting on SCI in MTI between the "experimental" and control groups in relation to age.

H4- There is a difference in the degree of influence of IC reporting on SCI in MTI among persons engaged in logistics business in relation to whether or not they are engaged in logistics business.

## 5. RESEARCH METHODOLOGY

The research belongs to the group of non-experimental research considering that the variable is not directly manipulated, but only by examining the individual difference and the connection between the variables. According to the control conditions, this research is included in the field research group. According to the purpose of the research, this research can be characterized as an explanatory research, and it is conducted for fundamental (educational) purposes. The sample consisted of a total of 48 respondents, that is, 48 employees of the Military Technical Institute, both sexes, aged from 20 to 65 years (younger age group 20 to 45 years and older age group 45 and over). The sample was divided into two groups: experimental group – 24 subjects engaged in logistics and control group – 24 subjects not engaged in logistics.

In this research, the sample is convenient. Tables 1, 2 and 3 show the distribution of the sample according to gender, age and group (experimental and control).

**Table 1.** Distribution of the sample by gender

Male	Female	Total
28 (58,2%)	20 (41,8%)	48 (100%)

**Table 2.** Distribution of the sample according to age

Younger	Older	Total
25 (52,2%)	23 (47,8%)	48 (100%)

**Table 3.** Distribution of the sample by group

Experim. group	Control group	Total
24(50%)	24(50%)	100 (100%)

The results obtained from the research were statistically processed with an adequate selection of statistical methods. Descriptive and inferential statistical analysis was used in statistical processing. Statistical processing of the data was performed using the package for statistical processing of data in the social sciences SPSS (SPSS, version 21.0). The results are tabulated.

One-factor multivariate ANOVA was used to examine the differences in the degree of influence of IC reporting on SCI in MTI between the "experimental" and control groups. The examination of differences in the degree of impact of IC reporting on SCI in MTI between the "experimental" and control groups in relation to gender was performed with the help of a two-factor multivariate

ANOVA. A two-factor multivariate ANOVA was also used to examine the differences in the degree of influence of IQ reporting on SCI in MTI between the "experimental" and control groups in relation to age. The examination of the differences in the degree of influence of IC on SCI in MTI among persons engaged in logistics business in relation to whether or not they are engaged in logistics business in percentage was carried out with the help of one-factor multivariate ANOVA. Table 4 shows the classification of variables according to the role of the research, the way of expressing values, the level of measurement and the degree of control.

**Table 4.** Classification of variables

Variable	Role in research	A way of expressing values	Measurement level	Degree of control
Gender	Independent	Categorical	Nominal	Registered
Age	Independent	Categorical	Nominal	Registered
% dealing with logistics	Independent	Categorical	Ordinal	Registered
Group of respondents	Independent	Categorical	Nominal	Registered
They deal with logistics	Independent	Categorical	Nominal	Registered
Impact of IC reporting on SCI	Independent	Numeric	Interval	Registered

Taking into account the fact that the sample size is not negligible, the obtained results should be seen as a good approximation of the results that would be valid for a much larger number of respondents. The research was conducted at the MTI in February 2024, with respondents filling out a questionnaire. The sample type is random. Respondents were tasked with answering 25 questions about the impact of IC reporting on SCI in MTI by rounding the marks on a scale of 0-4 (0 - "completely disagree", 1 - "mostly disagree" 2 - "not sure", 3 - "mostly agree", 4 - "completely agree"). By adding up the scores (summary score) for each question in the questionnaire, five categories of degree of influence are obtained: 1 - normal level (0-19), 2 - mild level (20-39), 3 - moderate level (40-59), 4 - moderately extreme level (60-79), 5 - extreme level (80-100). The reliability of the guide, estimated by Krombach coefficient  $\alpha$ , can be considered satisfactory ( $\alpha = 0.71$ ).

## 6. RESEARCH RESULTS

In order to verify the first research hypothesis, one-factor multivariate ANOVA was applied.

Table 5 shows descriptive statistics for the variable belonging to the exam group.

**Table 5.** Descriptive measures of the "experimental" and control groups of respondents

Groups of respondents	N	M	SD	SEM
Experimental group	24	1,5372	,44833	,08890
Control Group	24	,5592	,45832	,09235
Total	48	1,0274	,67095	,09641

N - number of respondents, M - average (arithmetic mean), SD - standard deviation (deviation), SEM - Standard Error of the Mean

The obtained results of the research are shown in Table 6. In this research, the degree of influence of IC reporting on SCI in MTI is a numerical variable, and the group of respondents is a categorical variable.

**Table 6.** Difference in the degree of impact of IC reporting on SCI in MTI in relation to the group of respondents

Relation	rc $\chi^2$	df	M	F	p
sum score x group	11,434	1	11,434	57,274	,00

rc $\chi^2$  - the value of the given statistic, df - number of degrees of freedom, M - average, F - statistic, p - significance level

The research revealed statistically significant differences ( $p < 0,05$ ) in the degree of influence of IC reporting on SCI in MTI between the "experimental" and control groups ( $F = 11,434$ ,  $df_1 = 1$ ,  $df_2 = 46$ ,  $H_0 = \text{rejected}$ , groups differ). Analyzing the average of the arithmetic mean of the two groups of respondents from Table 5, it can be concluded that in the "experimental group" the opinion that IC affects SCI in MTI is more prevalent. It follows that there are differences in the degree of influence of IC reporting on SCI between the "experimental" and control groups.

Differences in the degree of influence of IC reporting on SCI in MTI between the "experimental" and control groups in relation to gender

In order to check the second research hypothesis, a two-factor multivariate ANOVA was also applied.

Table 7 shows descriptive statistics for the variables gender and belonging to the group of respondents in the sample ( $N=48$ ).

**Table 7.** Descriptive measures of the degree of impact of IC reporting on SCI in MTI in relation to the respondent's gender and group affiliation

Sex of the respondent	Group of respondents	N	SD	M
Female	Experimental group	8	,48375	1,5099
	Control group	12	,58257	,6621
	Total	20	,67423	1,0105
Male	Experimental group	16	,41522	1,4299
	Control group	12	,17653	,4176
	Total	28	,64257	1,0522
Total	Experimental group	24	,42155	1,5198
	Control group	24	,43522	,5318
	Total	48	,65158	1,0299

N - number of respondents, M - average (arithmetic mean), SD - standard deviation (deviation)

The obtained results of the research are shown in Table 8. In this research, the degree of influence of IC reporting on SCI in MTI is a numerical variable, while the gender of the respondents and the groups of respondents ("experimental" and control) are categorical variables.

**Table 8.** Differences in the degree of influence of IC reporting on SCI in MTI in relation to gender between respondents of the "experimental" and control groups

Source	Sum of Squares	df	MS	F	p
Corrected Model	11,895a	3	3,921	19,963	,000
Intercept	47,985	1	47,985	244,877	,000
Sex	,125	1	,125	,699	,389
Group	10,686	1	10,686	53,819	,000
sex * group	,197	1	,197	1,125	,276
Error	8,663	44	,185		
Total	71,981	48			
Corrected Total	20,543	47			

a. R Squared = ,578 (Adjusted R Squared = ,549)

df - number of degrees of freedom, MS - arithmetic mean, F - statistic, p - significance level

H01: There is no influence of gender on the degree of influence of IC reporting on SCI in MTI.

$F(1,44) = 0,699$   $p > 0,05$  We do not reject  $H_0$ . There is no influence of gender on the degree of influence of IC reporting on SCI in MTI.

H02: There is no influence of belonging to the group ("experimental" and control group) on the degree of influence of IC reporting on SCI in MTI.

$F(1,44) = 53,819$   $p < 0,01$  We reject  $H_0$ . There is an influence of belonging to the group ("experimental" and control group) on the degree of influence of reporting on IC on SCI in MTI.

Interaction:  $F(1,44) = 1,125$   $p > 0,05$

Using a two-factor multivariate ANOVA, no statistically significant differences ( $p > 0,05$ ) were obtained in the degree of influence of IC reporting on SCI in MTI between the "experimental" and control groups in relation to gender  $F(1,44) = 1,125$   $p > 0,05$ . The null hypothesis is not rejected, that is, there are no differences in the degree of influence of IC reporting on SCI in MTI between the "experimental" and control groups in relation to gender.

Differences in the degree of influence of IC reporting on SCI in MTI between the "experimental" and control groups in relation to age

To test the third research hypothesis, a two-factor multivariate ANOVA was applied.

Table 9 shows descriptive statistics for the variables age of respondents and affiliation of respondents to the group of respondents.

**Table 9.** Descriptive measures of the degree of influence of IC reporting on SCI in MTI in relation to the age of the respondents and belonging to the group

Groups of respondent	Age of the respondents	N	SD	M
Experimental group	younger	13	,44363	1,5411
	older	11	,43526	1,4865
	Total	24	,43121	1,5187
Control group	younger	12	,54845	,5874
	older	12	,32856	,4978
	Total	24	,44029	,5322
Total	younger	25	,69155	1,0874
	older	23	,62492	,9676
	Total	48	,65766	1,0214

N - number of respondents, M - average (arithmetic mean), SD - standard deviation (deviation)

The obtained results of the research are shown in Table

10. In this research, the degree of influence of IC reporting on SCI in MTI is a numerical variable, while the age of the respondents and the groups of respondents ("experimental" and control) are categorical variables.

**Table 10.** Differences in the degree of influence of IC reporting on SCI in MTI in relation to age between subjects of the "experimental" and control groups

Source	Sum of Squares	df	MS	F	p
Corrected Model	11,520a	3	3,756	18,768	,000
Intercept	51,332	1	51,332	250,796	,000
grp	10,956	1	10,956	54,911	,000
starost	,059	1	,059	,297	,577
grp * starost	,002	1	,002	,007	,944
Error	8,802	44	,193		
Total	71,856	48			
Corrected Total	20,574	47			

a. R Squared = ,562 (Adjusted R Squared = ,533)

df - number of degrees of freedom, MS - arithmetic mean, F - statistic, p - significance level

H01: There is no influence of belonging to the group ("experimental" and control group) on the degree of influence of IC reporting on SCI in MTI.

F (1,44)= 54,911 p< 0,01 We reject H0. There is an influence of belonging to the group ("experimental" and control group) on the degree of influence of reporting on IC on SCI in MTI.

H02: There is no influence of age on the degree of influence of IC reporting on SCI in MTI.

F (1,44)= 0,297 p> 0,05 We do not reject H0. There is no effect of age on the degree of influence of IC reporting on SCI in MTI. Interaction: F(1,44) =0,007 p>0,05

Using a two-factor multivariate ANOVA, no statistically significant differences (p>0,05) were obtained in the degree of influence of IC reporting on SCI in MTI between the "experimental" and control groups in relation to age F(1,44) =0,007 p>0,05 . The null hypothesis is not rejected, that is, there are no differences in the degree of influence of IC reporting on SCI in MTI between the "experimental" and control groups in relation to age.

Differences in the degree of influence of IC reporting on SCI in MTI among persons engaged in logistics activities in relation to whether or not they engage in logistics activities

Whether there are differences in the degree of influence of IC reporting on SCI in MTI among persons engaged in logistics activities in relation to whether or not they engage in logistics activities were checked using a one-factor multivariate ANOVA.

Table 11 shows the descriptive statistics for the variable whether or not they are engaged in logistics activities in percentage on the sub-sample of respondents engaged in logistics activities (N=24).

**Table 11.** Descriptive measures of the percentage of respondents engaged in logistics work

% engaged in logistics business	N	M	SD	SEM
Low	0,21422	5	1,4800	0,40222
Middle	0,10274	15	1,3588	0,32542

Tall	0,15882	4	1,7900	0,29544
Total	0,09855	24	1,4974	0,38142

N - number of respondents, M - average (arithmetic mean), SD - standard deviation (deviation), SEM - Standard Error of the Mean

The obtained results of the research are shown in Table 12. In this research, the degree of influence of IC reporting on SCI in MTI is a numerical variable, and whether or not they are engaged in logistics business in percentage is a categorical variable.

**Table 12.** The difference in the degree of impact of IC reporting on SCI in MTI in relation to the % engaged in logistics business

Relation	rc $\chi^2$	df	M	F	p
sum score x % engag. logis.	0,378	2	0,189	1,121	0,325

rc $\chi^2$  - value of given statistic, df - number of degrees of freedom, M - average, F - statistic, p - level of significance

By applying a single-factor multivariate ANOVA, no statistically significant differences (p>0,05) were obtained in the degree of influence of IC reporting on SCI in MTI among persons engaged in logistics activities in relation to the variable of whether or not they engage in logistics activities in percentage (F = 1,121, df1 = 2, df2 = 21, Ho= groups do not differ). From this, it can be concluded that there is no difference in the degree of influence of IC reporting on SCI in MTI among persons engaged in logistics business in relation to whether they are engaged in or not engaged in logistics business in percentage.

## 7. CONCLUSION

The research results indicate that between the "experimental" and "control" groups of respondents there is a difference in the degree of influence of IC reporting on SCI in MTI (F = 11,434, df1 = 1, df2 = 46, p<0,05). From this, it is concluded that there are differences in the degree of influence of IC reporting on SCI in MTI between the "experimental" and "control" groups, i.e. that the respondents who deal with logistics business have the opinion that the impact is greater than the respondents who do not deal with logistics business.

The first research hypothesis was confirmed.

These results confirm the research findings that indicate that the degree of impact of IC reporting on SCI in MTI is higher among persons engaged in logistics activities than among the control group.

In the second research hypothesis, it is claimed that there are differences in the degree of influence of reporting on IC on SCI in MTI between the "experimental" and control groups in subjects of different gender. The results of the research show that there were no statistically significant differences (p>0,05) in the degree of influence of IC reporting on SCI in MTI between the "experimental" and control groups in relation to gender F(1,44) =1,125 p>0,05. Analyzing the first question (does gender influence the degree of influence of reporting on IC on SCI in MTI), the result is that the variable does not influence the degree of influence of reporting on IC on



SCI in MTI. Analyzing the second question (does the factor of groups of respondents influence the degree of impact of reporting on IC on SCI in MTI), the result is that there is an influence of the variable of groups of respondents ("experimental" and control group) on the degree of impact of reporting on IC on SCI in MTI. Analyzing the interaction of these two factors, it can be concluded that there are no differences in the degree of influence of IC reporting on SCI in MTI between the "experimental" and control groups in relation to gender, that is, the second research hypothesis is rejected.

The third research hypothesis related to the existence of a difference in the degree of influence of IC reporting on SCI in MTI between the "experimental" and control groups in subjects of different ages. In the research, no statistically significant differences ( $p > 0,05$ ) were obtained in the degree of influence of IC reporting on SCI in MTI between the "experimental" and control groups in relation to the age groups of the respondents. Analyzing the first question (does the factor of groups of respondents influence the degree of impact of reporting on IC on SCI in MTI), the result is that there is an influence of the variable of groups of respondents ("experimental" and control group) on the degree of impact of reporting on IC on SCI in MTI. Analyzing the second question (does the age factor influence the degree of influence of reporting on IC on SCI in MTI), the result is that there is no influence of the age variable on the degree of influence of reporting on IC on SCI in MTI. After analyzing the interaction of these two factors, it is concluded that there are no differences in the degree of influence of IC reporting on SCI in MTI between the "experimental" and control groups in relation to the age groups of the respondents, that is, the third research hypothesis is rejected.

The fourth research hypothesis refers to the existence of differences in the degree of influence of IC reporting on SCI in MTI among persons engaged in logistics activities in relation to whether or not they engage in logistics activities in percentage. The analysis of the obtained results concludes that there is no difference in the degree of influence of IC reporting on SCI in MTI among people who are engaged in logistics business in relation to whether or not they are engaged in logistics business in percentage ( $F = 1,121$ ,  $df_1 = 2$ ,  $df_2 = 21$ ,  $p > 0,05$ ). From this, it is concluded that there is no difference in the degree of influence of IC reporting on SCI in MTI among persons engaged in logistics business in relation to the percentage engaged in the mentioned business, i.e. that the percentage engaged in logistics business has no effect or influence on the degree of influence of IC reporting on SCI in MTI. The fourth research hypothesis is rejected.

## References

- [1] ABEYRATNE, S. A., MONFARED, R. P.: *Blockchain Ready Manufacturing Supply Chain Using Distributed Ledger*, International Journal of Research in Engineering and Technology, 5(9) (2016) 1-10.
- [2] BAJWA, N., PREWETT, K., SHAVERS, C. L.: *Is your supply chain ready to embrace blockchain?*, Journal of Corporate Accounting & Finance, 31(2) (2019) 1-11.
- [3] ATASEVEN C., NAIR A.: *Assessment of supply chain integration and performance relationships: A meta-analytic investigation of the literature*, International Journal of Production Economics, 185 (2017) 252–265.
- [4] SHI, R., YAN, J., SHI, A. Y., CHEN, S., REN, Z., ZHANG, J.: *A Blockchain-based Supply Chain Quality Management Framework*, The Fourteenth IEEE International Conference on e-Business Engineering, Shanghai, Kina, 2017.
- [5] KUEI, C. H., MADU, C. N., LIN, C.: *Developing global supply chain quality management systems*, International Journal of Production Research, 49(15) (2011) 4457-4481.
- [6] KWAN, S. C., YEUNG, I-K., PUN, K. F.: *Development of an assessment system for supplier quality management*, International Journal of Quality & Reliability Management, 23(7) (2006) 743-765.
- [7] SCHOENHERR, T., SWINK, M.: *Revisiting the arcs of integration: Crossvalidations and extensions*, Journal of operations management, 30(1) (2012) 99–115.
- [8] BRAUNSCHEIDEL, M. J., SURESH, N. C.: *The organizational antecedents of a firm's supply chain agility for risk mitigation and response*, Journal of Operations Management, 27(2) (2009) 119–140.
- [9] FLYNN, B. B., HUO, B., ZHAO, X.: *The impact of supply chain integration on performance: A contingency and configuration approach*, Journal of Operations Management, 28(1) (2010) 58–71.
- [10] SWINK, M., NARASIMHAN, R., WANG, C.: *Managing beyond the factory walls: Effects of four types of strategic integration on manufacturing plant performance*, Journal of Operations Management, 25(1) (2007) 148–164.
- [11] MENTZER, J. T., DEWITT, W., KEEBLER, J. S., MIN, S., NIX, N. W., SMITH, C. D., ZACHARIA, Z. G.: *Defining Supply Chain Management*, Journal of Business Logistics, 22(2) (2001) 1-25.
- [12] KUEI, C. H., MADU, C. N., LIN, C.: *Implementing supply chain quality management*, Total Quality Management & Business Excellence, 19(11) (2008) 1127-1141.
- [13] PARK, A., LI, H.: *The Effect of Blockchain Technology on Supply Chain Sustainability Performances*, Sustainability, 13(4) (2021) 1-18.



## GROUNDWATER AS AN IMPORTANT RESOURCES IN EMERGENCY SITUATIONS OF THE REPUBLIC OF SERBIA

BORIS VAKANJAC

Military Geographical Institute "General Stevan Bošković", Mije Kovačevića 5, Belgrade, [boris.vakanjac@vs.rs](mailto:boris.vakanjac@vs.rs)

RADOJE BANKOVIĆ

Military Geographical Institute "General Stevan Bošković", Mije Kovačevića 5, Belgrade, [radoje.bankovic@vs.rs](mailto:radoje.bankovic@vs.rs)

VESNA RISTIĆ VAKANJAC

University of Belgrade, Faculty of Mining and Geology, Đušina 7, Belgrade, [vesna.ristic@rgf.bg.ac.rs](mailto:vesna.ristic@rgf.bg.ac.rs)

SAŠA MILANOVIĆ

University of Belgrade, Faculty of Mining and Geology, Đušina 7, Belgrade, [sasa.milanovic@rgf.bg.ac.rs](mailto:sasa.milanovic@rgf.bg.ac.rs)

LJILJANA VASIĆ

University of Belgrade, Faculty of Mining and Geology, Đušina 7, Belgrade, [ljljana.vasic@rgf.bg.ac.rs](mailto:ljljana.vasic@rgf.bg.ac.rs)

SAŠA BAKRAČ

Military Geographical Institute "General Stevan Bošković", Mije Kovačevića 5, Belgrade, [sasa.bakrac@vs.rs](mailto:sasa.bakrac@vs.rs)

NIKOLA KOZIĆ

Military Geographical Institute "General Stevan Bošković", Mije Kovačevića 5, Belgrade, [nikola.kozic@mod.gov.rs](mailto:nikola.kozic@mod.gov.rs)

**Abstract:** Groundwater is a renewable resource wholly or partially protected from external influences (pollutants) by nature. Currently, about 75% of the population of the Republic of Serbia meets its water needs by using underground water. Hence, this water represents an essential strategic resource of our country; according to data from the Water Management Foundation of the Republic of Serbia (VOS, 2001), water from existing sources is used in quantities of about 23 m<sup>3</sup>/s. As 67.13 m<sup>3</sup>/s is the estimated potential of underground water in Serbia, we state that only 1/3 of the total available potential of these waters is in usage. Therefore, we can count on these exceptional quality underground waters in emergencies. The problem is the need to monitor these waters that need to be captured and have their intended use. Monitoring water's quantitative and qualitative parameters is necessary to determine which reserves we are talking about. Whether it is easy to reach these resources (road and electrical infrastructure), making accompanying maps using GIS tools is essential. The paper will give an example of identifying hydrogeological objects in an area, establishing monitoring of selected hydrogeological objects, and determining which maps need to be made that would be important in emergencies.

**Keywords:** groundwater, spring, monitoring, emergency situation.

### 1. INTRODUCTION

Groundwater is a water resource that, unlike surface water, is fully or partially protected from external influences and, therefore, pollution. Due to its quality, groundwater is preferred over surface waters in being used for any purpose, especially for water supply purposes [1].

We can say that the Republic of Serbia belongs to the group of countries in Europe that are richer in groundwater. The complexity of Serbia's geological structure led to specific hydrogeological conditions, so different types of aquifers are formed within them. The most significant in terms of size and, to some extent in

terms of quality are the underground water resources formed within alluvial deposits. The capacity of these aquifers is about 44 m<sup>3</sup>/s, and the biggest problem with these waters is the anthropogenic factor. More precisely, the largest settlements in the world, including in our country, are mainly located on the banks of rivers and their alluviums, so potential pollution is always present. The following water resource regarding available groundwater is karst outcrops formed within the Carpatho-Balkanides (eastern Serbia) and Internal Dinarides (western Serbia). The total capacity of these aquifers is about 14 m<sup>3</sup>/s. These are high-quality waters, and for distribution to users, they usually only need to be pre-chlorinated. Some sources are captured for the water supply needs of the local population. The karst massifs are mostly uninhabited parts of Serbia, and the existing

road infrastructure bypasses them, so potential pollutants are almost non-existent. The problem is that these resources are relatively far from big cities. The remaining estimated reserves of 9.5 m<sup>3</sup>/s are related to less renewable water resources, i.e., aquifers within tertiary sediments. Therefore, the total available underground water potential is estimated at around 67.5 m<sup>3</sup>/s [2]. It should be noted that the total discharge of all existing groundwater sources is about 23 m<sup>3</sup>/s; only 1/3 of the available resources are currently used for water supply needs [3, 4] (Fig. 1 and Table 1).

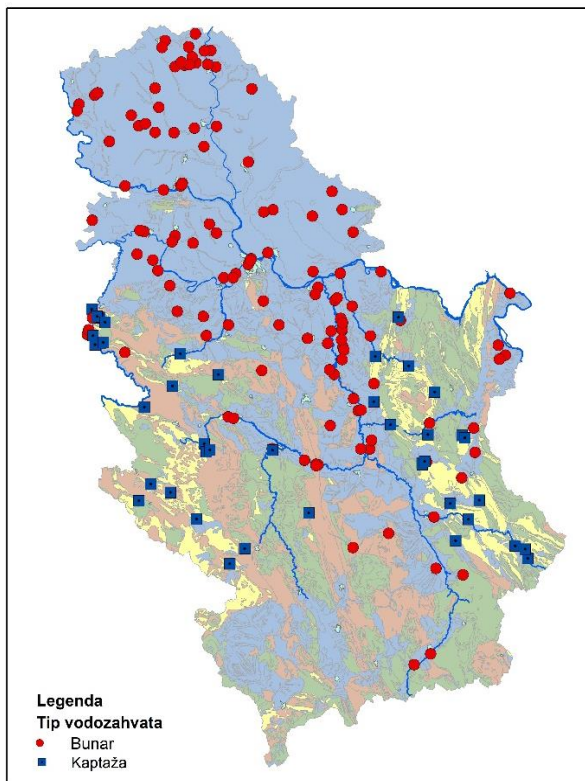


**Figure 2.** Hydrogeological map of Serbia with the positions of important springs and the method of groundwater captured water sources (wells/catchments) (taken from [1])

**Table 1.** Discharge of groundwater sources in Serbia according to the type of aquifer (m<sup>3</sup>/s) taken and modified from [1])

	AD	BAC	ND	KE	FE	sum
1	1.45	3.57	0.43	0	0	5.45
2	6.97	0.34	0.50	0.03	0	7.84
3	2.58	0	0.84	0.43	0	3.85
4	0.62	0	0.06	1.71	0	2.39
5	0.24	0	0.14	1.61	0	1.99
6	1.05	0	0.06	0.40	0.02	1.53
sum	12.91	3.91	2.03	4.18	0.02	23.08

**Note:** AD - Alluvial deposits, BAC - basic aquifer complex (AP Vojvodina), ND - Neogene deposits, KE - karst environment, FE - Fissure environment, 1 - Bačka and Banat, 2 - Srem, Mačva, Sava/Tamnava, 3 - Central

Serbia, 4 - Eastern Serbia, 5 - Southwestern Serbia, 6 - Western Serbia

It is important to note that over 75% of the inhabitants of the Republic of Serbia meet their water needs by using these waters. The importance of underground water is also indicated by the fact that Svetolik Radovanović published the book *Ground Waters (Podzemne vode)* in 1897 [5], while the Serbian Academy of Sciences asked Jovan Žujović to write the book "Supplying Villages with Water, springs and wells" which was published in 1931 [6].

Unfortunately, groundwater monitoring is still not at a satisfactory level. Although the monitoring of the underground water regime began in 1948 at 41 facilities, this number grew during the last century and reached 409 monitoring facilities (piezometers). Their arrangement, more precisely the coverage of water bodies in 2014, still needs to be improved because these observation stations mainly monitored the underground water regime of alluvial deposits. Out of 153 underground water bodies, only 34 were covered by existing piezometers. As for the qualitative properties of groundwater, their monitoring began in 1968. Currently, the situation is similar to that of quantitative parameters. Only at 32 water bodies is the regime of qualitative parameters monitored. Establishing monitoring is extremely important because, based on this data, one can gain insight into what quantities are available, what their quality is, and what the amplitudes (absolute maximum and minimum values) of the fluctuations of the selected parameters are [1, 2].

Considering the climate changes that significantly impact all water resources and, therefore, groundwater, the relationship between precipitation and groundwater is important for planning the use of these waters. In other words, the influence of the pluviographic regime on the regime of quantitative and qualitative groundwater parameters. One of the springs with the most extended monitoring series is the Mlava Spring, where the Republic Hydrometeorological Service of Serbia (RHMS) has monitored changes in the water level since 1949. Also, from 1966, flow measurements were carried out. For this reason, this spring is one of the most researched springs in Serbia, and the first hydrogeological studies were carried out by Jovan Cvijić and results was published in 1896 [7]. The investigation of this spring and a sufficiently long observation series influenced the fact that this spring was taken as a pilot area for many project including *Climate Changes and Impact on Water Supply - CCWaterS* [8]. The average yield of this spring is about 1,858 m<sup>3</sup>/s, and a negative trend of this spring is evident from 1966 to 2010 [8] (Fig. 2). With this negative trend, it can be expected that at the end of this century, the discharge average of the Mlava spring will be 0.392 m<sup>3</sup>/s [8] by applying the model for simulating the daily yield values of karst springs that were developed at the Department of Hydrogeology of the Faculty of Mining and Geology [9] and using forecast values of daily precipitation and mean daily temperatures obtained using regional climate models, for the end of this century, i.e. for 2100. year, the expected value of the discharge of this spring was

obtained in the amount of about  $1.6 \text{ m}^3/\text{s}$  [8], which does not represent such a drastic reduction in the amount of water that will be discharged from the Mlava spring (Fig. 3).

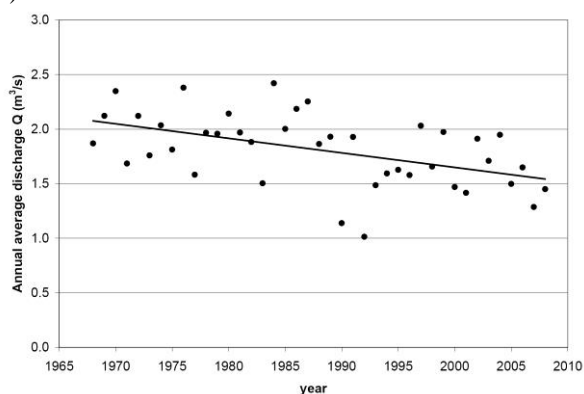


**Figure 2.** Annual discharge of Mlava spring [8]

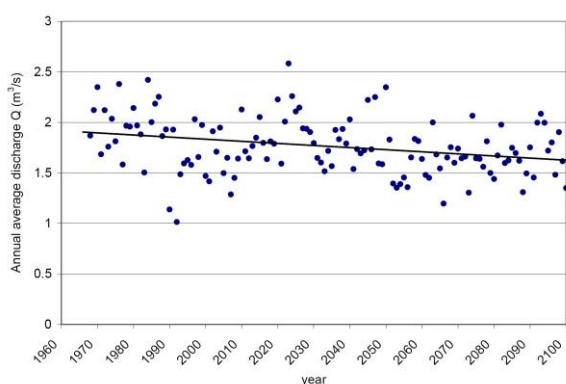


**Figure 3.** Annual average of discharges of karst spring Mlava and its trend line [8]

As  $2/3$  of underground water resources remain unused, these resources can be of great importance in emergencies as alternative drinking water sources or technical water if the water quality is not satisfactory.

## 2. METHODOLOGY

For the selected potential alternative sources, it is necessary, for a reason, to determine underground water reserves, as well as the amount of water available and its quality, to do the following:

1. Establish water level monitoring,
2. Periodically perform hydrometric measurements in the entire range of water level changes,
3. Define the flow curve - dependence of the flow as a function of the water level,
4. Perform water sampling at appropriate time intervals,
5. Provide reports for each hydrogeological object individually,
6. Produce maps of the appropriate scale with the road infrastructure presented in detail,

7. By agreement with the Republic Hydrometeorological

Service of Serbia, monitor selected hydrogeological objects.

## 3. SELECTED CATCHMENT AREAS

In the case of emergencies that can be caused by natural risks (floods, landslides, fires, droughts, earthquakes, etc.) as well as anthropogenic factors (spills of pollutants in catchments areas, war operations and others), the most common problem is drinking water as well as technical water. We cannot predict these phenomena with great certainty (exact time and place of occurrence). Therefore, we cannot adequately prepare in advance for any of the listed situations that lead to an emergency in some part or of the country's entire territory; it is necessary to have a cadastre of alternative sources to distribute water to users who need it. Information on the spatial location of possible alternative sources exists; however, the problem of researching the watershed, the quantity and quality of these waters have not been collected adequately so far, and this is of crucial importance for whether these waters can be used for drinking or not, i.e. whether it is necessary to carry out their appropriate treatment.

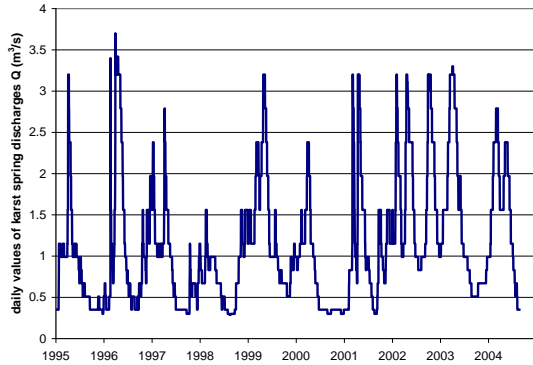
The type of spring informs whether the spring regime is stable or whether there are rapid and sudden changes in certain qualitative and quantitative parameters. Thus, for example, small discharge oscillations within the year are generally present in ascending springs, quality parameters do not change over time, and these waters are generally protected from potential pollutants. On the other hand, gravity springs have a quick reaction to precipitation, mainly rapid propagation of precipitation through the hydrogeological basin, which results in abrupt changes in discharge (sudden discharge increase and decrease) as well as changes in quality (increase in turbidity, suspended sediment, total number of bacteria, etc.) [10, 11].

Whit this reasons, for this paper, we selected three karst springs on which various institutions carried out hydrogeological research several times. Those are:

1. Jelovica spring,
2. Veliko spring and
3. Andrić spring.

Andrić spring was chosen as a typical example of an ascending spring. It drains the eastern parts of Zlatibor and is the least explored compared to the other two. At this spring, observations were made during the period when the monitoring of the discharge and Veliko spring was carried out (1995 - VIII 2004). The catchment area of Andrić spring consists of psammite-pelitic sediments of the Carboniferous age, carbonate formations of the Triassic age, diabase-chert formation of the Jurassic age and Quaternary sediments. The karst outcrop drained by this spring was formed in massive and cliff limestones of the Triassic age; its recharge is done by directly infiltrating rainwater on the exposed part of the karst collector [12]. Drainage is on the right bank of the Prištavica river via this spring. The elevation is 490 meters above sea level, and the point of spring discharges

is connected to the exit of Prišteвица from its gorge. It is located near Ravni village. The average annual runoff volume from this spring for the observation period is 1,157 m<sup>3</sup>/s. The absolute maximum was  $Q_{max}=3,417$  m<sup>3</sup>/s (April 1996), while the absolute minimum was recorded in August 1998 in the amount of  $Q_{min}=0,287$  m<sup>3</sup>/s [12] (Figure 4).



**Slika 4.** Mean daily discharge of the Andrić spring

The Veliko spring drains the southern part of the Beljanica karst massif. It is one of the major springs in the Carpathian karst of eastern Serbia. This typical gravity spring drains Tithonian age limestone massive. One of the most beautiful waterfalls has formed a few hundred meters from the discharge points, and today, it is protected as a natural monument. It was chosen as a typical representative of gravity springs. It was monitored from 1995 to 2006, with a four-month break from September to December 2004. For the CCWaterS project needs, monitoring of this spring was also established from August 2009 until the end of the project (2012). The water flows out at the bottom of a long talus between large limestone blocks at the top of a short and shallow valley. It occurs at an altitude of 415 m asl. However, during the maximum yields, the discharge zone moves to higher altitudes when the elevation of the discharge reaches a value of 445 m asl. Based on eight-hour data, it was established that on the year's level, on average, 0.584 m<sup>3</sup>/s of water flowed, with the values ranging from 0.477 m<sup>3</sup>/s (2000) to 0.762 m<sup>3</sup>/s (1997). The absolute minimum daily value of the discharge of Veliko spring was recorded from September 5 to 7, 1998, in the amount of only 57 l/s, while the maximum value was 5.6 m<sup>3</sup>/s (July 28, 1997) [13].

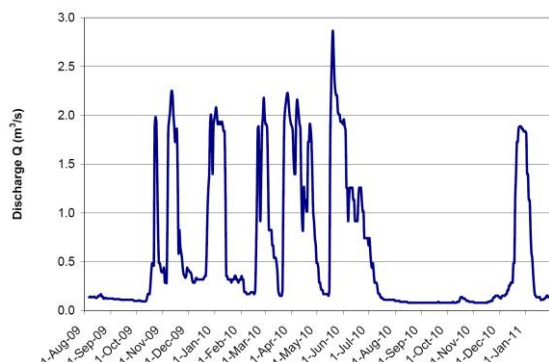


**Figure 5.** Discharge of Veliko karst spring [8]

Jelovičko spring is the largest karst spring in the southern

part of Stara Planina, i.e. Vidlič, drains carbonate rocks of the Middle Triassic age. It was chosen because there was no monitoring on it until now. This ascending spring type appears in a minor depression (doline) that is laked and occurs at the height of the bed of the Jelovička River (Figure 6). The stream formed by this spring, after only a few hundred meters, flows into the Jelovička River, and together with it, after a little less than 1 km, flows into the Dojkinačka River (catchment area of the Visočica River). Speleological diving has been carried out on several occasions to show the geometry and orientation of the channels and caverns through which the spring water moves in the discharge zone in as much detail as possible [14]. The Jelovica spring has never been systematically observed for a long time. However, due to its characteristics and importance, it would be necessary to establish constant underground water monitoring quantitatively and qualitatively. According to occasional observations of the spring made during hydrogeological research, its minimum yield falls below 80 l/s, with water temperatures of 9.5 to 12 °C. This spring belongs to the typical karst siphon spring type with deep karst channels. It is considered that the maximum yield of the hot spring is over 5 m<sup>3</sup>/s [15].



**Figure 6.** Jelovica spring (photo by V. Ristić Vakanjac)

## 4. DISCUSSION

Suppose the hydrogeological object is considered an alternative potential water source, in addition to the information on the spatial position of the hydrogeological object (coordinates and altitude). In that case, it is first necessary to establish the appropriate monitoring of quantitative parameters. If it is a spring, it is necessary to install a water meter bracket and hire an observer - a person who lives in the immediate vicinity of the selected object and who will read the water level of the water that flows out every day. If the discharge is less, a weir can be installed. If the project have good financial support, it is possible to install automatic stations - limnigraphs that can digitally record water level changes at appropriate time intervals (for example, every 5, 10, 30, 60, 120 minutes). With the establishment of water level monitoring, it is necessary to carry out hydrometric

measurements periodically and cover the entire range of water level changes (small, medium-small, medium, medium-large, and large waters). Mentioned is necessary to establish the flow curve (graphic form and analytical in tabular form). The average daily amount of runoff at the spring can be obtained based on the defined flow curve and average daily water levels.

If we are dealing with ascending springs like Andrić spring, where there are no sudden changes in the water level, the water level can be monitored once a day or, even in extreme situations, once every five days. In the case of gravity wells (Veliko spring), the time intervals for observing the water level must be shorter, maximum once a day, and preferably twice a day or every 6 hours, even less. Mentioned is especially important for springs that drain small catchments areas and where rainfall propagation occurs within 24 hours.

As the quality of the water of the potential alternative water source is also important, it is necessary to carry out water sampling for ascending springs four times a year, while the author recommends 12 times a year for gravity springs. Suppose chemical analysis results indicate significant changes in specific parameters are present. In that case, it is necessary to carry out more frequent sampling with an emphasis on parameters with a variable concentration according to the pluviographic regime of the area of interest.

After the three-year monitoring, it is necessary to perform calculations of underground water reserves, the amount of water that can be used of and its quality. According to the completed reports, the established profiles on which monitoring was carried out should become part of the observation network of the Republic Hydrometeorological Service of Serbia, which would continue with water level observations and flow measurements, and the Environmental Protection Agency should continue sampling, i.e. checking water quality.

Finally, each report should be accompanied by appropriate maps on which the positions of the hydrogeological object and the road infrastructure would be highlighted, with the help of which the object can be easily found (Figures 7, 8 and 9).

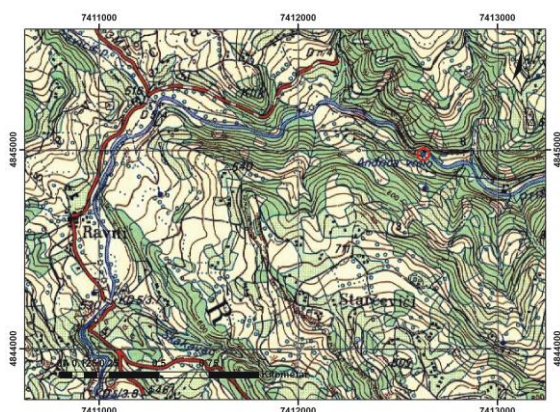


**Figure 7.** Spatial position of the Andrić spring (in red circle), raster base TK25 second edition, Military Geographical Institute “General Stevan Bošković”, part of sheet Ravni, modified

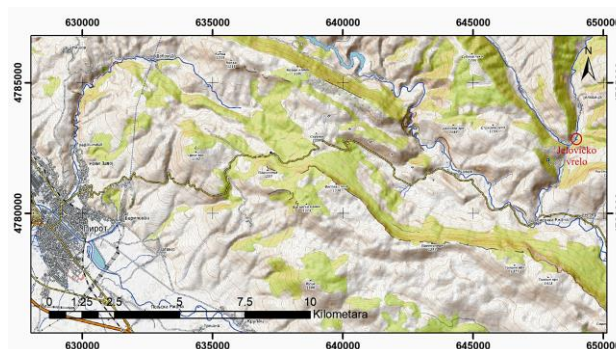


**Figure 8.** Spatial position of Jelovica spring, (in red circle), raster base © OpenStreetMaps contributors, CC-BY-SA, rendering opentopomap.org, modified

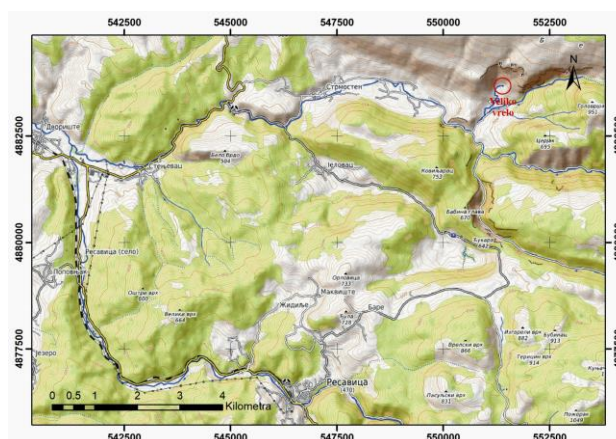


**Figure 9.** Spatial position of Veliko spring, (in red circle), raster base SAS.Planet, © OpenStreetMaps contributors, CC-BY-SA, rendering opentopomap.org, modified

## 5. CONCLUSION

Most of the water used for the water supply of the population of the Republic of Serbia is underground water. Serbia belongs to the countries of Europe that are richer in underground water. However, the research and monitoring of these resources could be more satisfactory. Today, only 1/3 of the underground water capacity is used for water supply, and the remaining 2/3, or 44.5 m<sup>3</sup>/s, mostly high-quality water, goes unused through the river network. Therefore, in this case, alternative sources of water for water supply should be searched. A good example from the recent past is the problem of water supply in the city of Užice when a lot of algae formed in Lake Vrutci, giving the lake a red colour. The appearance of cyanobacteria in the water supply system caused a ban on water use from the water supply system. An alternative solution was Sušičko spring.

As regional climate change models indicate an increase in air temperature and a decrease in precipitation, the river flows that feed the lakes will provide less water to these reservoirs. Therefore, there is a high probability that the Vrutci reservoir scenario will repeat itself in the near or distant future. Also, the mentioned climate changes predict a more significant number of extreme events (drought and floods), for which you also need to be

prepared because you don't know when or where exactly this will happen. More precisely, droughts affect the entire region, while floods can be extremely local. In these situations, it is necessary to have an alternative source.

It remains to define the hydrogeological objects that are of interest to the Republic of Serbia, to see the status of these objects (some of the mentioned are protected objects), to obtain information about the reserves and quantities of water that can be counted on, and if it is necessary to carry out appropriate construction preparations for a more straightforward approach to the object as well as easier taking of water from the hydrogeological object, and to allocate proper funds for a suitable strategic project.

## References

- [1] POLOMČIĆ,D., VASIĆ,LJ., MILANOVIĆ,S., RISTIĆ VAKANJAC,V., PETROVIĆ,B., MARINOVIĆ,V., BAJIĆ,D., HAJDIN,B., ČOKORILO ILIĆ,M., RATKOVIĆ,J.: *Vodosnabdevanje - podzemne vode i održivo upravljanje resursima*, u monografiji 50 godina Departmana za hidrogeologiju (ed. Polomčić, Živanović, Vranješ i Vasić), Izdavač RGF, ISBN 978-867352-377-4, str 67-111, 2021.
- [2] DOKMANOVIĆ,P., STEVANOVIĆ,Z.: *Projekat proširenja mreže stanica podzemnih voda u Srbiji*, Univerzitet u Beogradu, Rudarsko-geološki fakultet, Departman za hidrogeologiju, fondovska dokumentacija, 2015
- [3] GRUPA AUTORA: *Vodoprivredna osnova Srbije*, 2001
- [4] POLOMČIĆ,D., STEVANOVIĆ,Z., DOKMANOVIĆ,P., PAPIĆ,P., RISTIĆ VAKANJAC,V., HAJDIN,B., MILANOVIĆ,S., BAJIĆ,D.: *Vodosnabdevanje podzemnim vodama u Srbiji - stanje i perspektive*, Monografija: Naših 40 godina (ed. Polomčić i Ristić Vakanjac), Rudarsko-geološki fakultet, Beograd, 2011
- [5] RADOVANOVIĆ,S.: *Podzemne vode*, Srpska književna zadruga, str. 152, 1897.
- [6] ŽUJOVIĆ,J.: *Snabdevanje sela vodom, izvori i bunari*, edicija Zbirke poučnih knjiga za seoski narod, str 119, 1931.
- [7] CVIJIĆ,J.: *Izvori, tresave i vodopadi u istočnoj Srbiji*, Glas SKA, LI 18, Reprint u: Morfologija i hidrografija istočne Srbije, Sab. dela J. Cvijića, 13: 99–170, SANU i Zav. za udžb. i nast. sreds., Beograd. 1896
- [8] STEVANOVIĆ,Z., RISTIĆ VAKANJAC,V., MILANOVIĆ,S. (editors): *Climate Changes and Impacts on Water Supply*, Monografija, Univerzitet u Beogradu, Rudarsko-geološki fakultet, Beograd, pp 1-475. ISBN 978-86-7352-263-0, COBISS.SR-ID 194497804, 2012
- [9] RISTIĆ,V.: *Razvoj simulacionog modela za proračun dnevnih isticanja iz karstnih vrela*, doktorska disertacija, Rudarsko-geološki fakultet, Univerzitet u Beogradu
- [10] RISTIĆ VAKANJAC,V., GOLUBOVIĆ,R., POLOMČIĆ,D., ČOKORILO ILIĆ,M., ŠTRBAČKI,J., BAJIĆ,D., RATKOVIĆ,J., *Autocorrelation and cross-correlation analyses of total bacteria: Case study of Banja karst spring in Valjevo, Serbia*. Review of the Bulgarian geological society, Geoscience 2017, Bulgarian Geological Society, pp 145-146, ISSN 0007-3938, 2018
- [11] PEŠIĆ,M., RISTIĆ VAKANJAC,V., VAKANJAC,B., JOVANOVIĆ,K.: *Turbidity simulation for short-term predictions: case study of the karst spring Surdup (Bor, Serbia)*, Comptes rendus de l'Academie bulgare des Sciences (ed. Todor Nikolov), Vol. 69(9):1183-1194
- [12] ČOKORILO ILIĆ,M., RISTIĆ VAKANJAC,V., POLOMČIĆ,D., BAJIĆ,D., RATKOVIĆ,J., HAJDIN,B.: *Mathematical modeling to define catchment size and real evapotranspiration (case study: Andrića karst spring, Western Serbia)*, Review of the Bulgarian geological society, Geoscience 2018, Bulgarian Geological Society, pp 135-136, ISSN 0007-3938, 2018
- [13] MARINOVIĆ,V., RISTIĆ VAKANJAC,V., MILANOVIĆ,S., VASIĆ,Lj., PETROVIĆ,B., POLOMČIĆ,D., GOLUBOVIĆ,R.: *Primena autoregresionih modela za potrebe kratkoročnih prognoza isticanja karstnih vrela*, SymOpIs 23, Tara, pp 783 - 788
- [14] MILANOVIĆ,S., VASIĆ,LJ.: *Hidrogeološka istraživanja karstnih vrela – Jelovičko vrelo*, Pirotski zbornik, br 40, str. 227-241, 2015,
- [15] ČUBRILOVIĆ,P.: *Izveštaj o ispitivanju izvora opštine Pirot*. Beograd: Geozavod, Sektor za hidrogeološka i geotehnička istraživanja, 1990.



# RISK MANAGEMENT IN INDUSTRIAL SECURITY IN THE FIELD OF PRODUCTION AND TRADE OF WEAPONS AND MILITARY EQUIPMENT

NENAD KOMAZEC

University of Defense Belgrade, Military Academy, [nenadkomazec@yahoo.com](mailto:nenadkomazec@yahoo.com)

KATARINA JANKOVIĆ

Technical Test Center, Center for testing weapons and military equipment "Nikinci", [jankovickatarina95@gmail.com](mailto:jankovickatarina95@gmail.com)

MILICA MLADENOVIĆ

S4 GloSec globalna bezbednost, Belgrade, [mladenovicmilica21@yahoo.com](mailto:mladenovicmilica21@yahoo.com)

**Abstract:** *The production of weapons and military equipment represents an industrial sector that is advancing exceptionally quickly. Progress is being made in technological, personnel, and economic aspects. This rapid advancement is accompanied by technological processes, personnel selection, and results that, in many cases, exceed the real business conditions. Additionally, industrial capacities for the production of weapons and military equipment are an interesting "object" to various interested parties, in both positive and negative contexts. The risks generated in the process of producing weapons and military equipment are of a hybrid nature and can create opportunities or conditions for negative events. Industrial security recognizes the need for risk management in the production process of weapons and military equipment and materializes it through industrial security plans. Risk management in industrial security is a prerequisite for the effective prevention of events, from business disruptions to accidents with the most severe consequences. Industrial security based on risk management presupposes the production process of weapons and military equipment under conditions of acceptable risks.*

**Keywords:** *weapons and military equipment, risk management, industrial security.*

## 1. INTRODUCTION

The production and trade of weapons and military equipment represent complex and high-risk activities. These activities are classified as strategically significant for the state. Considering the importance of these activities and their profitability on a global scale, the risk of negative events with various consequences increases. States regulate the system of production and trade of weapons and military equipment through various legal solutions; however, the fact remains that these activities continue to be high-risk.

The production and trade of weapons and military equipment are monitored by intelligence services of other states as well as specific informal groups within and outside the country that engages in the production and trade of these items. An efficient system for the production and trade of weapons and military equipment involves the synchronization of numerous factors to ensure successful operation.

Technological solutions that enhance the production and trade processes of weapons and military equipment continually generate new risks. In most cases, these new risks are overshadowed by the required processes, posing a danger as they become apparent only when a problem arises.

## 2. PRODUCTION AND TRADE OF WEAPONS AND MILITARY EQUIPMENT

Considering its strategic significance for the state, the production and trade of weapons and military equipment are regulated by special laws. The legal framework for this area in the Republic of Serbia encompasses: research and development of weapons and military equipment; development and adoption of defense technologies; manufacturing, testing, overhaul, and upgrading of weapons and military equipment; demilitarization and disposal of weapons and military equipment; construction and equipping of capacities for the production of weapons and military equipment; and the creation of technical documentation [8].

The trade of weapons and military equipment within the country involves the conditions for purchasing and selling weapons and military equipment domestically, purchasing for the purpose of selling both domestically and internationally, and activities related to such purchasing and selling [8]. Thus, the overall portfolio of legal, technical, material, and spatial conditions for the sale and purchase of weapons and military equipment is defined.

As production is the process of converting raw materials or semi-finished products into finished products, namely



weapons and military equipment, it is concluded that this is a complex process involving numerous factors.

By definition, and according to legal provisions, weapons and military equipment are considered hazardous materials or products in terms of research, production, storage, maintenance, safeguarding, and use.

### 3. INDUSTRIAL SECURITY

Security, as a business function, attains high utility value in the activities of production and trade of weapons and military equipment. The need for high protection of data on processes and products, hazardous materials, and products that may be of interest to various informal groups, such as terrorist groups, makes security a priority among business functions.

Most legal frameworks define industrial security in the area of weapons and military equipment production as a system of security-protection measures and procedures that meet organizational and technical requirements for safeguarding technical documentation for the production of weapons and military equipment and other classified information. These measures also prevent the destruction or damage of production capacities, endangerment of human resources, destruction, damage, or theft of weapons and military equipment, and the disclosure of classified information about their production.

This approach, without delving into other aspects, indicates that industrial security in this area is complex and dependent on various factors. When viewed in this way, industrial security is essentially corporate security and includes all its elements. The foundation of the strategy and implementation of industrial security requirements is the industrial security plan. This plan regulates specific measures and approaches for all participants in the production and trade of weapons and military equipment.

The industrial security plan for the production of weapons and military equipment includes [8]:

1. An assessment of the vulnerability of production capacities to various external influences;
2. Security and protection measures for weapons and military equipment, production capacities, and technical documentation, and the methods of their implementation;
3. Measures and procedures to be undertaken in case of a breach of industrial security.

The basis of the industrial security plan is a variety of documents regulated by specific laws (Law on Occupational Safety and Health, Law on Fire Protection, Law on Disaster Risk Reduction and Emergency Management, Law on Environmental Protection, Law on Private Security, etc.). The essence of the industrial security plan is to define measures that ensure the safe process of production and trade of weapons and military equipment.

The core of the security philosophy is the concept of danger. Any phenomenon or interaction in the

environment that can generate a disturbance relative to the desired state of the system constitutes a danger. Lesser danger implies greater security, and vice versa. The essence is to act on the elements that constitute phenomena in the environment and thus mitigate their negative effects.

An effective way to influence system security is through risk management. Given that industrial security in the production and trade of weapons and military equipment possesses all the prerogatives of corporate security, it is possible to apply methods used in corporate security systems to manage risks.

### 4. RISK MANAGEMENT

Risk management is a complex process of identifying and assessing risks. In the area of production and trade of weapons and military equipment, risk management plays a key role in maintaining the desired level of security and control over risks. Effective risk management requires educated risk managers and resources dedicated to risk treatment. Integrating security areas enables the simplification of the risk management process.

Integrated risk management (Figure 1) allows for an overview of all factors affecting the security of protected values in the industrial security area of weapons and military equipment production and trade. It identifies potential hazards, determines the risk level for each hazard, and proposes the most efficient way to treat risks [5]. The risk assessment process (Figure 3) consists of the following phases:

1. Determining the context of risk management
2. Risk assessment
  - a. Risk identification
  - b. Risk analysis
  - c. Risk evaluation
  - d. Risk treatment
5. Monitoring and review
6. Consultation and communication:

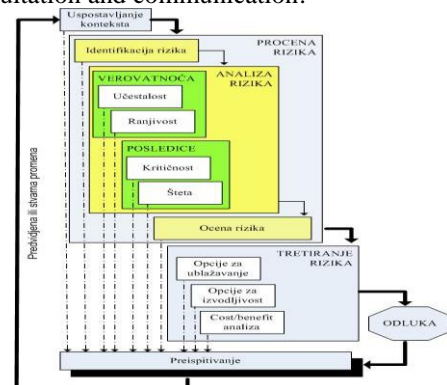


**Figure 1:** Risk Assessment Process According to SRPS A.L2.003 - Security and Resilience of Society - Risk Assessment

The risk management process is standardized and provides guidelines for handling the risk management process. Organizations are given the flexibility to adapt risk assessment to their needs in a real environment. In

practice, the templating of risk assessment is prevalent, leading to the creation of invisible risks.

**Determining the Context of Risk Assessment**

The context of risk assessment must be defined concerning external and internal factors. It needs to be set in relation to the organization's policy, culture, processes, and structure. Defining the context of risk assessment establishes the framework, scope, and criteria for the overall process [6]. In the area of protecting people, property, and operations, the main challenge is to ensure a comprehensive view of all factors that may pose potential threats to protected values.

**Risk Assessment**

Risk assessment is a comprehensive process of identifying, analyzing, and evaluating risks. It is the central process of risk management, in which a thorough examination and analysis of risks concerning identified hazards are conducted.

**Risk Identification**

The organization should ensure conditions for identifying potential hazards, i.e., sources of risk, events, or a series of circumstances, as well as their potential consequences. The primary goal of identification is to compile a realistic and comprehensive list of potential hazards based on those events and circumstances that may facilitate, hinder, or slow down the achievement of the organization's objectives. Any potential hazard not identified at this stage falls out of further analysis and remains a constant and hidden threat.

**Risk Analysis**

Risk analysis involves understanding the fundamental characteristics of risks [5]. It provides input information for risk evaluation and decisions on whether risks should be addressed and what the appropriate (most acceptable) strategies for risk treatment are. For a complete risk analysis, it is necessary to determine the likelihood of the potential hazard occurring and the consequences it may cause.

*Likelihood* is determined by the frequency of occurrence (exposure time) and the system's vulnerability, i.e., the existing level of protection, and is categorized as: impossible, unlikely, likely, almost certain, and certain.

*Consequences* are determined by the extent of possible damage and the system's criticality, i.e., the importance of individual protected values for the system, and are categorized as: minimal, minor, moderate, serious, and catastrophic. The level of risk is determined by the relationship between likelihood and consequences (Table

1)

**Table 1: Risk matrix**

Consequences \ Likelihood	Consequences				
	Minimal	Minor	Moderate	Serious	Catastrophic
Rare	1	2	3	4	5
Unlikely	2	4	6	8	10
Moderately Likely	3	6	9	12	15
Likely	4	8	12	16	20
Almost Certain	5	10	15	20	25

Risk is determined at the following levels: very low (negligible), low, moderately high, high, extremely high. Based on the risk level, risks can be classified into the following categories: first-very low, second-low, third-moderately high, fourth-high, and fifth-extremely high. By determining the risk level and category, the acceptability is assessed: risks in the first and second categories are considered acceptable, while those in the third, fourth, and fifth categories are deemed unacceptable.

**Risk evaluation**

The goal of risk evaluation is to assist in decision-making based on the results of risk analysis, and to determine which risks should be addressed and the priorities for risk treatment. Risk evaluation involves comparing the levels of risk identified during the analysis process with the risk criteria established while considering the entire context. The organization's objectives and the scope of potential circumstances should also be considered. In situations where choices need to be made between options, the decision will depend on the organization's context. Decisions should consider the broader risk context and include considerations of risk tolerance found by other organizations that the organization can benefit from. Decisions should also take legal constraints into account. If the risk level does not meet the criteria, that risk should be addressed (risk should be treated). Priority should be given to risks with the highest level.

**Risk treatment**

Risk treatment involves selecting one or more options to eliminate, reduce, or mitigate risks and implementing those options [6]. Risk treatment options do not necessarily exclude each other and may not be applicable in all circumstances. If resources for risk treatment are limited, the risk treatment plan should clearly identify the order of priority for applying individual risk treatment options. The full cost of taking and/or not taking action should be compared with budget savings. After risk treatment, decision-makers and stakeholders must be cautious about the nature and extent of the residual risk.

Residual risk should be documented and subject to control and review, and where appropriate, further treatment in line with new circumstances [2]. Risk treatment can be carried out by applying:

1. Risk mitigation options;
2. Feasibility options; and/or
3. Cost-benefit analysis.

**Risk Mitigation Options** [6] include the following:

1. Avoiding the risk by not starting or continuing the activity that would lead to the risk;
2. Seeking opportunities by starting or continuing the activity that may lead to or sustain the risk;
3. Influencing the likelihood;
4. Influencing the consequences;
5. Sharing the risk with one or more other parties; and
6. Retaining the risk, either by conscious choice or unconsciously.

#### *Feasibility options*

Each risk treatment option should be considered in stages of risk assessment. The analysis of each option must consider the cost of changing procedures or products (services) in accordance with risk treatment measures. Feasibility analysis should be conducted by competent financial bodies, and the results should be provided to the decision-maker.

#### *Cost-Benefit Analysis*

Cost-benefit analysis is the final step in conducting risk assessment concerning the undertaken risk treatment strategies. It is necessary to determine the actual cost of implementing the proposed risk treatment options and assess the financial and other costs resulting from the implementation of the proposed measures. The analysis should be conducted by competent financial bodies, and the results should be provided to the decision-maker.

#### **Control and review**

Control and review are integral parts of the risk management process [2]. Control and review should enable:

1. Adequate use of analysis results and lessons from analyzed disturbances or successes;
2. Detection of changes in the external and internal context, including changes in the risk itself, which may require reassessment of risk treatment options and priorities; and
3. Verification of whether risk control and treatment measures are effective in plans and implementation.

Actual progress in implementing risk treatment plans shows the achievement measure and can be integrated into the organization's operational management, measurement, and internal and external reporting activities. Control and review can include regular checks or controls of what is already present; it can be periodic or sudden, depending on management's assessment. Both aspects should be planned. It is not enough to rely only on occasional audits and controls.

#### **Continuous improvement of the risk management process**

Planning and implementing risk management should be one of the key competencies of every organization and its employees in the function of protecting protected values. Risk management methods and tools help each organization plan and implement specific actions and programs to raise their capabilities to the highest level and control threats [7]. Risk assessment can be applied partially or to the entire organization's operations. Horizontal integration is possible by applying specific risk management systems. All organizations should strive for the highest performance of their risk management framework relative to the importance of the decisions to be made. Continuous monitoring of activities and the state of internal and external factors, as well as the state and operations of the organization itself, is necessary. All employees and stakeholders should be involved in the risk management process. Based on control and review, decisions and conclusions should be made in the organization on how to improve the risk management framework, plan, and policy [7]. Such decisions should lead to improvements in the organization's risk management. This contributes to better management, flexibility, and accountability of the organization that applies the protection of people, property, and operations in any way.

## **5. CONCLUSION**

Industrial security is a high-risk area of economic activity that requires a comprehensive approach to monitoring, identifying, and mitigating threats to protected values in the production and trade of weapons and military equipment. Neglecting any segment of impact on hazards in the environment itself poses a danger. A pragmatic method of influencing hazards and monitoring in conditions of uncertainty is risk assessment and management. The practical applicability of risk management methods allows the production and trade of weapons and military equipment to raise the level of security of their own capacities.

In the future, the number of risks in this area will increase. Some of the reasons are: the technologization of processes, which assumes less attention to the safety of technological systems; greater danger due to the application of various new technologies in the production of weapons and military equipment; an increasing number of interested parties in the environment; the need for

higher production, which implies less implementation of measures to maintain security, etc.

Today, risk management is not practiced, which is a precondition for the occurrence of negative events. Fulfilling legal obligations is of a template nature and aims to meet the minimum legal requirements. In terms of meeting legal requirements, this makes sense because there is no threat from inspections. In terms of the effectiveness of the security system, it does not make sense, as risks are generated in the own environment, and the question is not if they will happen, but when.

### References

[1] Standard SRPS ISO 9001 - Sistemi menadžmenta kvalitetom – Osnove i rečnik

[2] Standard SRPS A.L2.001 – Društvena bezbednost – Privatno obezbeđenje - Rečnik

[3] Standard SRPS A.L2.002 - Društvena bezbednost – Privatno obezbeđenje - Zahtevi i uputstvo za ocenjivanje usaglašenosti

[4] Keković.Z., Komazec.N., Glišić.G.: Pristup metodologiji procene rizika, Žurnal za kriminalistiku i pravo, Beograd, 2009

[5] ISO TC 223/SC: Upravljanje rizicima - Uputstvo o principima i implementaciji upravljanja rizicima

[6] ASIS INTERNATIONAL: General security risk assessment guideline

[7] Drennan, L., McConnell, A, Risk and Crisis Management in the Public Sector, Routledge,

[8] Zakon o proizvodnji prometu naoružanja i vojne opreme (Sl Glasnik RS 36/2018)



## IMPROVEMENT OF PRODUCT QUALITY BY IMPLEMENTATION QFD METHODS

BRANKO VUJATOVIĆ

Center for Applied Mathematics and Electronics, Belgrade, [branko.vujatovic@vs.rs](mailto:branko.vujatovic@vs.rs)

MARIJA VUJATOVIĆ

Directorate for Telecommunications and Informatics (J-6) GS VS, Belgrade, [marija.vujatovic@vs.rs](mailto:marija.vujatovic@vs.rs)

DARKO GRUBAČ

Center for Applied Mathematics and Electronics, Belgrade, [darko.grubac@vs.rs](mailto:darko.grubac@vs.rs)

NENAD STOJANOVIĆ

Center for Applied Mathematics and Electronics, Belgrade, [nenad.m.stojanovic@vs.rs](mailto:nenad.m.stojanovic@vs.rs)

**Abstract:** *In nowadays business conditions, such as increased competition and the rapid market changes, companies can be distinguished by the quality of services resulting from analysis and matching opportunities with market requirements. One way is to use the Quality Function Deployment (QFD) method. This method has shown a significant effect in the EU countries, the USA, and especially in Japan, while in our country its use is not widespread in the quality system. From the market perspective, there are three basic product characteristics: price, quality and delivery time. These facts are used in the planning process, based on user requirements interpretation into appropriate quality characteristics for each phase of the product life cycle (marketing, planning, design, prototype development, production process testing and development, production, sales). The common goal of the entire team working on the project must be the product competitiveness on the market. This method application has led to significant improvements in solving deficiencies in planning, designing, testing and developing the production process. In this paper, we presented the QFD method application for selecting products or services that meet the quality, price, and delivery time requirements.*

**Keywords:** *QFD, product competitiveness, quality system.*

### 1. INTRODUCTION

Production engineers were the first to deal with the problems of product quality control and then quality management. The Quality Function Deployment (QFD) method was developed in Japan, more precisely in Kobe in the 1970s, in the Mitsubishi shipyard, while it later found application in other branches of industry.

The QFD method is used by:

- Toyota since 1973,
- Honda since 1979,
- Ford since 1983,
- Volvo and Saab since 1987.

Quality function deployment term originated from the Japanese words "hinshitsu kino tenkai", which refer to the methodology developed by Yoji Akao and Kogure Mizuno in Japan in 1966 [1].

The aim of the paper is to introduce the concept of QFD method through the basic principles and description of the application through a suitable example.

In the second part of the paper are described principals of the QFD method. Third part gives input data for the

further analysis. In the forth part of the paper concrete applications and basic results are given. Finally, the most important conclusions are given.

### 2. QFD METHOD - HOUSE OF QUALITY AND MATRIX

The complete and complex QFD method is based on the establishment of relationships: for each WHAT, a corresponding HOW should be found. One of the necessary conditions for the successful implementation of the QFD method is the quality composition of the QFD team.

In the paper, we have dealt with the case of choosing a printer that would enable printing on several types of materials: cardboard, stickers, used paper, hologram foils, paper, envelopes, etc., and to fulfill the requirements during the production process. The choice of the printer needed in the production process was reflected in the fact that they also meet the conditions prescribed by the tender.

There are three basic factors of the product from the point of view of the customer/market:

- price of the product,
- product quality,

- product delivery terms.

It is very important to emphasize that the implementation of the QFD method requires teamwork, but also that the composition of the team does not have to be the same through the analysis of all phases of the product life cycle. It is also very important that each phase is carried out with the highest possible quality, and in order to achieve this, members chosen for the part of the team should be professional, knowledgeable and best aware of the problem. Another important condition for the successful implementation of the QFD method is that the problem is defined clearly and in as much detail as possible.

The QFD method defines the following:

- 1) What users want – user requests related to product description and its features are collected and processed;
- 2) The importance of user preferences – emphasizing the importance of user requirements that have been gathered from direct experience with users and/or from research and
- 3) How to turn perceived user needs into a competent advantage – define engineering characteristics that represent measurable product characteristics that describe each of the functional requirements, among which identify those that bring a competent advantage.

We made the choice after complete and complex analyzes obtained using the QFD method.

The matrix of the QFD "house of quality" method consists of seven phases. Phases are shown in Figure 1 [2].

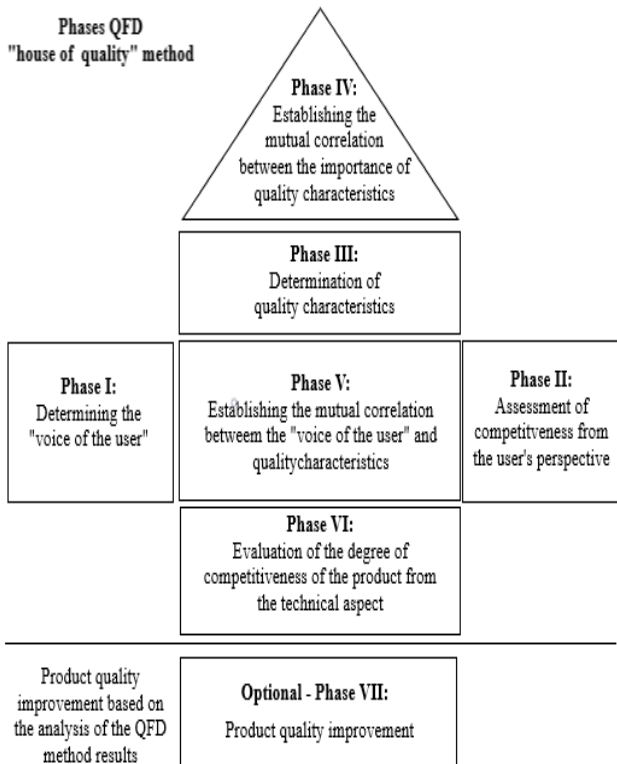


**Figure 1.** Matrix QFD - House of Quality

**Phase I: Determining the "voice of the user"**

The initial and most critical step in the process of the QFD method is determining the user's requirements in relation to the product's characteristics, and then obtaining the value of the user's importance rating.

**Phase II: Assessment of competitiveness from the user's perspective**

In this phase, competitive weaknesses and strengths of the bidder are determined.

**Phase III: Determination of quality characteristics**

In this phase, established user requirements are transformed into product quality characteristics.

**Phase IV: Establishing the mutual correlation between the importance of quality characteristics**

The roof of the "house" is designed to determine the relationships between the importance of quality characteristics.

**Phase V: Establishing the mutual correlation between the "voice of the user" and quality characteristics**

The construction of the "house of quality" continues by determining the strength of the connections between the user's voice and the quality characteristics of the product.

**Phase VI: Evaluation of the degree of competitiveness of the product from the technical aspect**

The degree of competitiveness is calculated for each quality characteristic and represents the product of the user's rating of importance and the strength of the connection between the user's voice and the product's quality characteristics.

**Phase VII: Product quality improvement**

After determining the importance of all product quality characteristics, it can be determined which characteristics should be improved first, so that further work can be concentrated on them. The phase is optional if the results are satisfactory, it does not have to be implemented.

**3. DATA PREPARATION**

Given that suppliers are not able to fully satisfy the set criteria of users, it is necessary to define which quality characteristics are more important than others.

The results collected by a structured questionnaire are shown in Table 1 through mean value and standard deviation. With a structured questionnaire, we asked future consumers to assess and define the importance of certain product characteristics by assigning them values from 1 to 5, where 1 is requirement with relatively little importance, and 5 is requirement with very significant requirement.

Before the surveying users, we conduct market research of WHAT companies offer, in order to collect technical characteristics of products from manufacturers.

This is how we arrive at the results that we need for further research, namely the mean values of the product characteristics and the standard deviation of the user's assessment of the importance of the required qualities of individual product characteristics.

We can conclude that Phase I is the most demanding phase in which the requirements of the customer and/or user, which the product needs to satisfy, are defined.

In the WHAT field, enter the characteristics of the product that are significant for satisfying the customer's and/or user's requirements.

**Table 1.** Overview of mean values and standard deviation of user ratings

Characteristics	Mean value	Standard deviation
Double-side printing	3,40	1,62
Print resolution 1200x1200 dpi	2,80	0,40
Network work	4,60	0,49
Power supply 220V/50Hz	5,00	0,00
working and spare toner in the set	4,00	0,00
Weight up to 20 kg	3,00	0,63
Touch screen and laser	1,80	0,40
Price	3,00	0,63
Warranty period 12 months	2,80	0,40
possibility of installation OS Win7, Win10	4,40	0,80
Ecological aspects: ENERGY STAR, RoHS	2,00	0,00

#### 4. APPLICATION OF THE QFD METHOD

We applied the QFD method to select a printer supplier. In order to apply the QFD method, we used: Template Traditional House of Quality, version 2.0.346.0, 11.12.2007. years [3].

The interdependence of requests is shown by values and labels:

- 1 ( $\Delta$ ) → Weak Relationship,
- 3 ( $O$ ) → Moderate Relationship and
- 9 ( $\odot$ ) → Strong Relationship.

In the first house of quality, which is shown in Figure 2, in its left part, we enter user requirements with mean values, and in the upper middle part, we enter the researched characteristics of product quality. We enter the correlation of user requirements according to product characteristics in the middle part of the quality house, with previously defined values and labels.

In the "roof" of the first house of quality, the correlation of product properties is shown, where are:

- ++ → represents a strong positive correlation,
- + → represents positive correlation,
- - → represents a negative correlation and
- -- → represents a large negative correlation and
- → if there is no correlation, then the field is left blank.

The fully filled graphic layout of the first house of quality is shown in Figure 2.

The results of the first house of quality give us information about the weighting coefficient of the HOW technical characteristics of the product for each of the listed characteristics of product quality that need to be paid attention to in the selection of the product, which are ranked by importance and shown in Table 2.

**Table 2.** Weight coefficient of HOW technical product characteristics

Weight importance	Quality characteristics
378,1	Win 7 and Win 10
321,4	Maintenance after warranty
216,8	Foil, hologram sticker, envelope, cardboard, pre-printed and rough
203,7	Touch screen and laser
202,0	Warranty period 12 months
145,4	ENERGY STAR and RoHS
48,5	Weight up to 20 kg

By analyzing the results shown in Table 2, and based on the results from the first quality house, we can get conclusion about the importance of the required qualities of certain product characteristics and the choice of products that we rank according to the concretely obtained value of the importance of the requirements for the quality characteristics of the product.

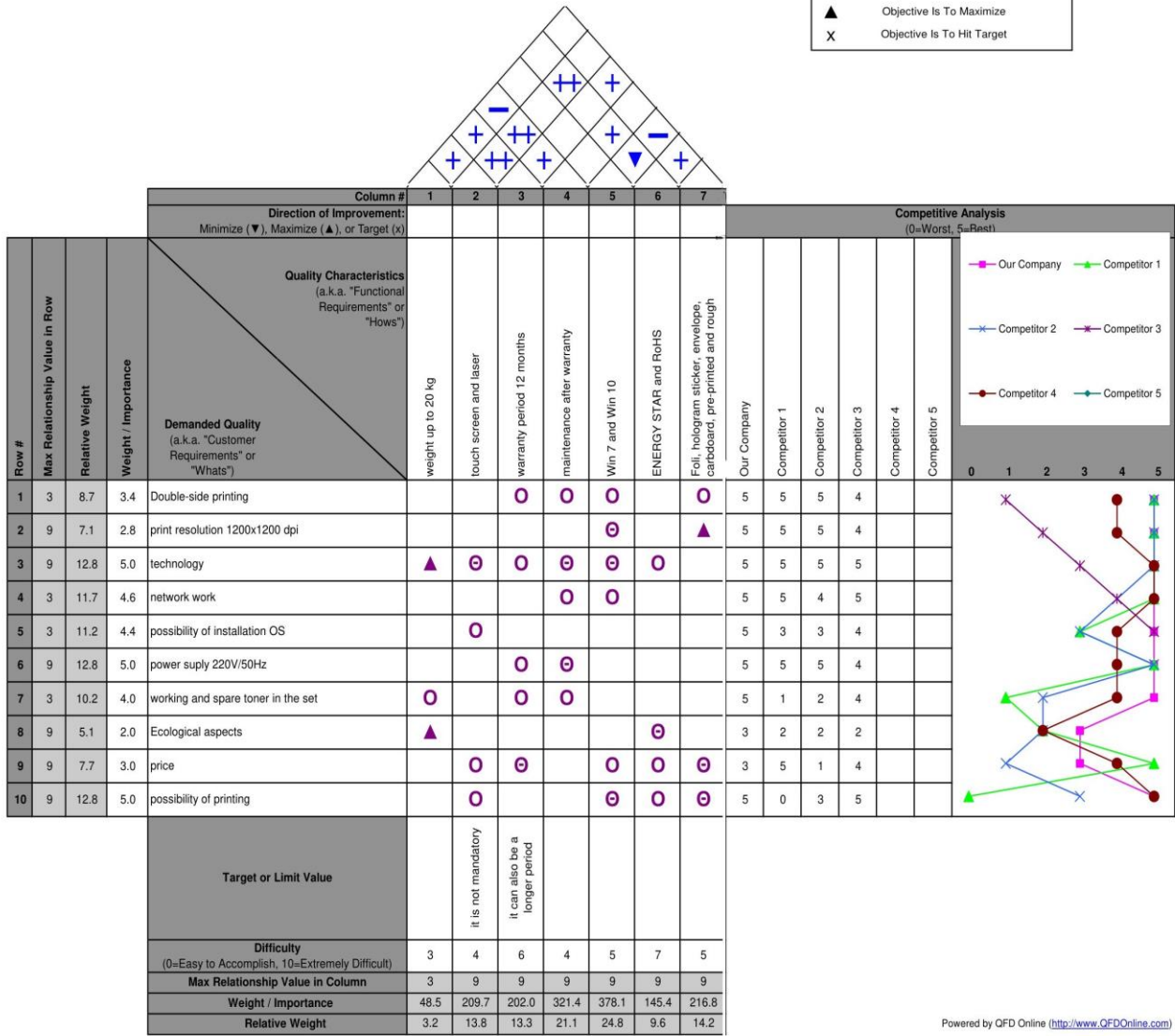
In the right part of the first quality house, we perform a comparative analysis of the bidders by evaluating the requirements users according to the weighting coefficient with the values: 1 - not suitable, 5 - extremely suitable, as well as based on the weighting coefficient of each product quality characteristic.

In the second house of quality, in the left part of the house of quality, we enter the technical characteristics of the product, and in the middle part of the user's requirements in order to determine the weight of the importance of the technical characteristics of the manufacturer's product. We enter the correlation of the technical characteristics of the product according to the user's requirements into the middle part of the quality house, with previously defined values and labels. The graphic layout of the second house of quality is shown in Figure 3.

Title: QFD METODE  
 Author: Branko Vujatovic  
 Date: 26.06.2024.  
 Notes: Izbor stampaca primenom QFD metodom  
 Korisnicki zahtevi "STA"

**Legend**

- ⊙ Strong Relationship 9
- Moderate Relationship 3
- △ Weak Relationship 1
- ⊕ Strong Positive Correlation
- + Positive Correlation
- Negative Correlation
- ▽ Strong Negative Correlation
- ▼ Objective Is To Minimize
- ▲ Objective Is To Maximize
- X Objective Is To Hit Target



Powered by QFD Online (<http://www.QFDOnline.com>)

Figure 2. The first house of quality



Title: Izbor stampaca primenom QFD metodom  
 Author: Branko Vujatovic  
 Date: 26.06.2024  
 Notes:

Legend		
⊖	Strong Relationship	9
○	Moderate Relationship	3
△	Weak Relationship	1
++	Strong Positive Correlation	
+	Positive Correlation	
-	Negative Correlation	
▼	Strong Negative Correlation	
▼	Objective Is To Minimize	
▲	Objective Is To Maximize	
X	Objective Is To Hit Target	

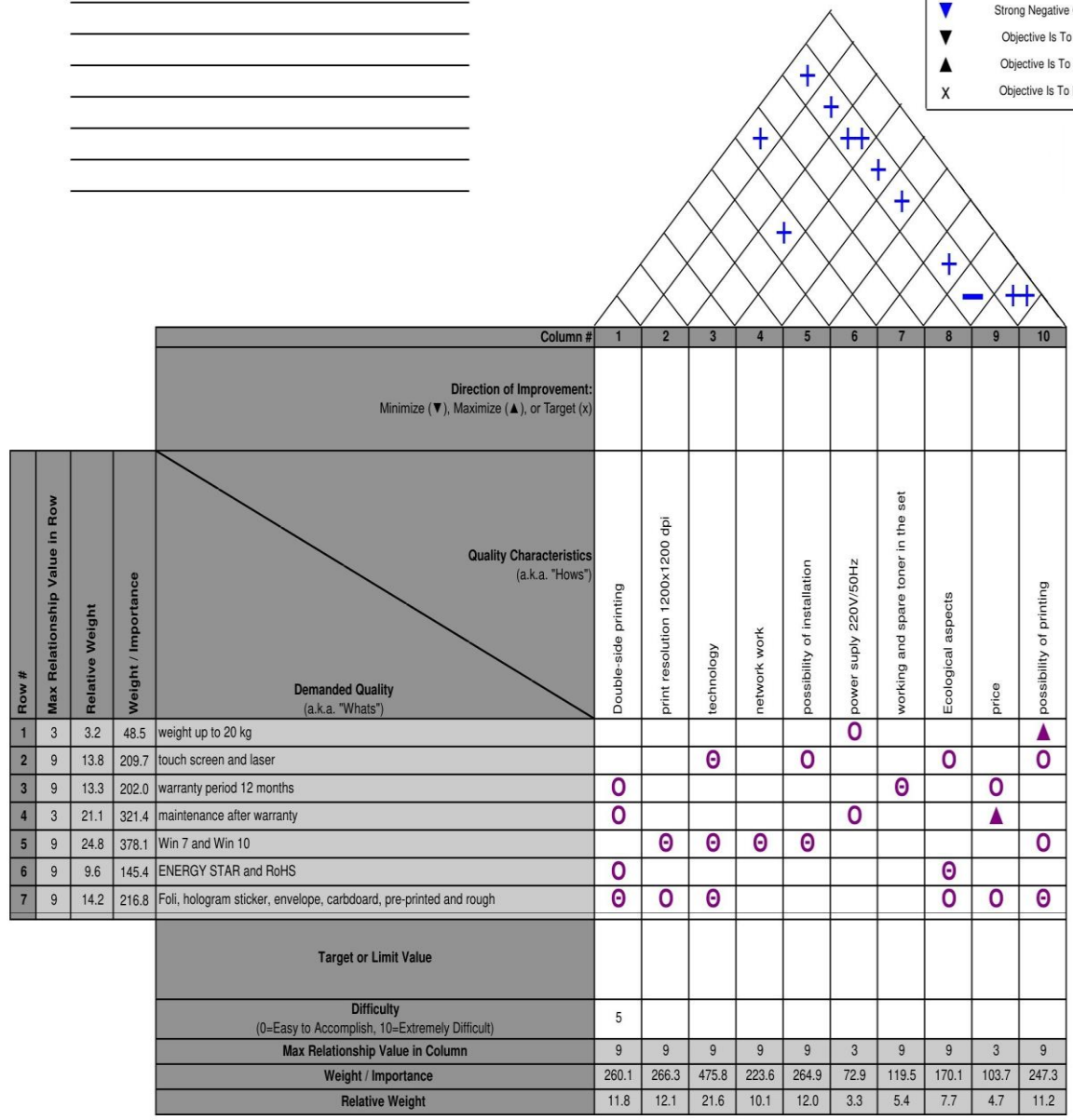


Figure 3. The second house of quality

The results of the second quality house give us information about the weight and importance of the user's request HOW for each specified characteristic of the user's request that needs to be paid attention in the selection of products, which are ranked by importance and shown in Table 3.

**Table 3.** User requirements

Weight importance	Quality characteristics
475,8	Technology
266,3	Print resolution 1200x1200 dpi
264,9	Possibility of installation
260,1	Double-side printing
247,3	Possibility of printing
223,6	Network work
170,1	Ecological aspects
119,5	Working and spare toner in the set
103,7	Price
72,9	Power supply 220V/50Hz

## 5. CONCLUSION

In our case, by applying the QFD method, we were able to select the product and the bidder that best suits our requirements and conditions of the tender procedure. We found that the QFD method can be successfully applied in

the procurement process itself, harmonizing all the necessary procedures and requirements of the successfully implemented steps applied in the QFD method.

By applying the QFD method, we obtained an objective result of the selection of bidders for the required product, which was the goal of solving and concretizing the specified request.

It can be concluded that the QFD method contains seven phases, with the fact that certain phases can be combined, and considering that the method also requires teamwork with the variability of the members by phase, by analyzing the obtained results, we get an objective choice of product or service.

Through complex and specific work, we determined individual and team results that are extremely important in order to implement this method from start to finish, in order to obtain an objective result.

the procurement process itself, harmonizing all the necessary procedures and requirements of the successfully implemented steps applied in the QFD method.

By applying the QFD method, we obtained an objective result of the selection of bidders for the required product, which was the goal of solving and concretizing the specified request.

It can be concluded that the QFD method contains seven phases, with the fact that certain phases can be combined, and considering that the method also requires teamwork with the variability of the members by phase, by analyzing the obtained results, we get an objective choice of product or service.

Through complex and specific work, we determined individual and team results that are extremely important in order to implement this method from start to finish, in order to obtain an objective result.

## References

- [1] SIVASAMY, K., ARUMUGAM, C., DEVADASAN, S. R., MURUGESH, R., THILAK, V. M. M.: *Advanced models of quality function deployment: a literature review. Quality & quantity*, 50 (2016) 1399-1414.
- [2] ISRAR, M., GANGELE, A.: *Quality function deployment methodology for product development*, International Journal of Multidisciplinary and Scientific Emerging Research, 3(2) (2014) 989-997.
- [3] *Traditional House of Quality*, version: 2.0.346.0, December 11, 2008, (at again 04.2024) <https://qfdonline.com/templates/>



## COMPARATIVE ANALYSIS OF INFORMATION SECURITY STANDARDS APPLICATION IN DIFFERENT IT SECTOR REGIONS

PREDRAG RANITOVIĆ

School of Business, Novi Sad, [predrag.ranitovic@gmail.com](mailto:predrag.ranitovic@gmail.com)

SINIŠA MITIĆ

School of Business, Novi Sad, [smitic@uns.ac.rs](mailto:smitic@uns.ac.rs)

**Abstract:** *The characteristics of the IT sector are, among other things, its global dissemination, as well as the interoperability of the Internet business models. These characteristics assume equality, uniformity of the following business concepts: work organization, business models, work technologies, work processes, communication and access processes, and human resource management. The IT sector, as a basic element of the information society, should be generally available and equally developed all over the world, as much as in highly developed rich societies as in developing countries, and also in underdeveloped countries of the world. Although the rate of growth and market expansion is a global phenomenon, what separates developed and undeveloped markets is the quality of the work done. One of the leading factors for achieving services/products of better quality is the respect of certain norms. Looking at the European Union (EU) region as a reference market with great IT potential, the prerequisite for joining the EU IT market is to meet the norms established in the EU. The growing IT market of Serbia requires harmonization with the EU IT sector, through the application of certain ISO standards, with the aim of free spreading beyond the borders of Serbia, primarily towards the EU market. The paper analyzes the process of harmonization of the IT sector of Serbia with the IT sector of the EU from the current implementation of the ISO standard perspective*

**Keywords:** *Information technologies, IT Standards, Norms, IT sector, EU IT sector, Serbian IT sector*

### 1. INTRODUCTION

The trends of development of modern society are directed towards the establishment of a state with a stable information-technological, economic and social system in which all prerequisites for development and international cooperation exist [1].

One of the basic drivers for the creation of such a system is the developed and standardised IT sector [2]. This paper analyses the standardisation process of the Serbian IT sector in terms of assessing the state of application of IT standards in Serbia compared to the application of IT standards in the EU.

The main aim of the research is to analyse the effects of application of IT standards in the IT sector of Serbia by means of comparison with the corresponding application of IT standards in the IT sector of the EU.

Specifically, the aim of our research is to analyse data related to the application of IT standards by software companies in Serbia compared to software companies from the EU, in order to find out to what extent these processes in Serbia and the EU are synchronised.

Information and communication technology systems are of special social interest, while standardisation processes improve the efficiency of information and communication technology systems [3].

Thus, research pertaining to the standardisation of information and communication technology systems represents the most modern research in the field of application of IT standards [4]. Starting from that fact, as well as from the notion that the IT sector integrates a whole series of elements essential for the development of any society, this research represents a contribution to areas that are directly or indirectly related to the development of the IT sector in Serbia, and therefore to the development of Serbia in general.

Expected contributions as well as possible application of research results are reflected in the following:

- perceiving new approaches, concepts, models and systems of application of IT standards and business of the IT sector,
- defining the functional dependence of IT standards and the IT sector,
- projecting the connection between IT standards and the IT sector,
- analysing the IT sector by observing the effects of the contribution and application of IT standards and
- acquiring new practical and theoretical knowledge in the field of application of IT standards.

## 2. ISO IT NORME

IT norms or IT standards are agreed rules by means of which functions are determined, i.e. desired or required characteristics of a certain product, process or service, in accordance with legal IT norms [5], [6], [7].

There are many different products in the world, as well as the processes that lead to their placement on the market. Any manufacturing process can in theory produce a quality product intended for the end user.

However, the user, apart from their own experience, does not have a neutral set of indicators with the help of which they could evaluate the safety, quality and value of the purchased product. In order to simplify and harmonise the evaluation process in a generally acceptable and comprehensible manner, norms or standards were introduced.

Owing to them, nowadays we can say with quite certainty how high-quality certain products or services are, that is, whether their quality justifies their price [8]. Accelerated technological changes are defined as the fourth industrial revolution leading to the so-called information society.

It requires the mobilisation of all segments of society in order to adapt to new forms of life and work, under the conditions of application of modern IT.

All this puts forward a whole series of demands for the global economy. One of the basic requirements is compliance with defined norms in the function of combining new and old aspects of business, communication, business systems, IT systems, etc.

Modern trends, which are a consequence of the application of modern forms of IT and the associated standardisation within organisations, enable far-reaching economic and social consequences.

The process of progress is spurred by technical standardisation among individuals, organisations, disciplines, and nations [9].

When it comes to IT standards, it should be noted that IT standardisation includes two elements. The first is the analysis of the IT system through the requirements of the standards of the given technical field.

The second presents an analysis of significant IT points created according to the defined requirements of the standards of a given technical area [10].

The International Organisation for Standardisation has initiated several projects to create a set of international standards for software product development [11] and published a number of international standards related to software engineering [12].

Furthermore, the European Commission presented a strategy for the development of IT standardisation for 2018 based on a study of the analysis of the state of IT in the EU for the period from 1995 to 2015 [13], [14].

This document highlights the special importance of monitoring and harmonising IT standardisation within the EU by the leading EU bodies in charge of development.

## 3. ANALYSIS OF RESULTS

The research presented in this paper is based on a sample consisting of 30 national and 30 foreign software companies from the EU.

The data were collected using electronic questionnaires compiled in two versions, in Serbian and English, which are in accordance with the technical requirements of the standard.

Processing of the obtained data and their comparative analysis was conducted with the aim of comparing the application of ISO standards in the IT sectors of Serbia and the EU.

The results of the survey, as well as the interpretation of the research results, are given below.

Through a comparative analysis of the collected responses referring to the application of ISO IT standards in the IT sectors of Serbia and the EU, we came to the following conclusions:

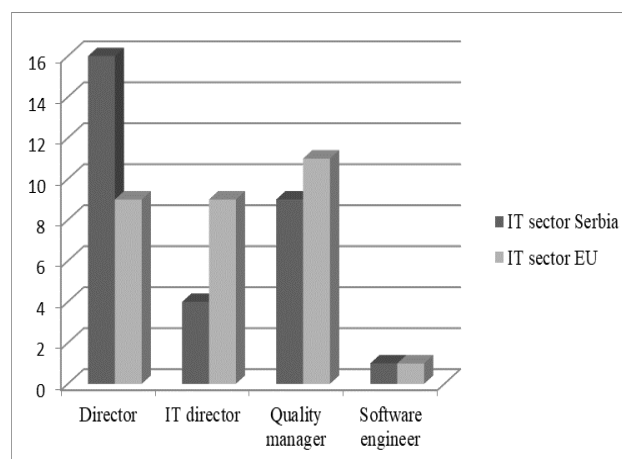


**Figure 1.** Distribution of the sample by workplace of respondents

Active participation in the electronic survey in the Serbian IT sector was mostly taken by directors, while in the EU IT sector this activity was evenly distributed between directors, IT directors and quality managers (Figure 1).

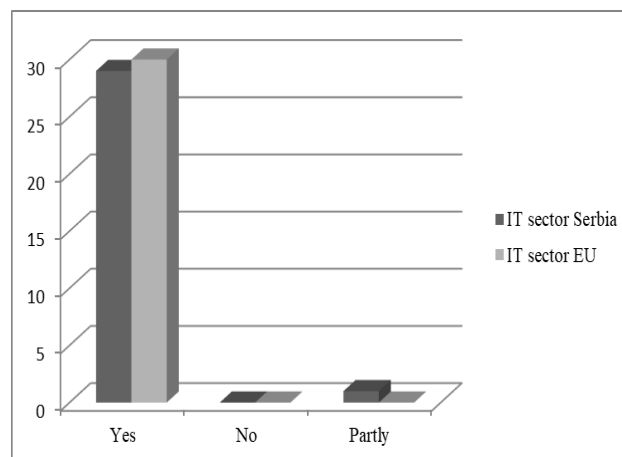


**Figure 2.** Answers the question  
Do you invest in new technologies?

Investment in new technologies is equally represented in the IT sector of Serbia as in the IT sector of the EU (Figure 2).

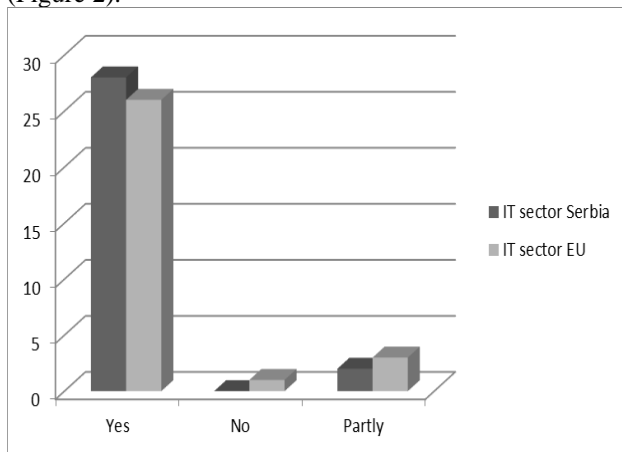


**Figure 3.** Answer the question

Are you familiar with ISO IT standards?

When it comes to knowing and adhering to ISO IT standards, the situation is similar both in Serbia and in the EU (Figure 3).

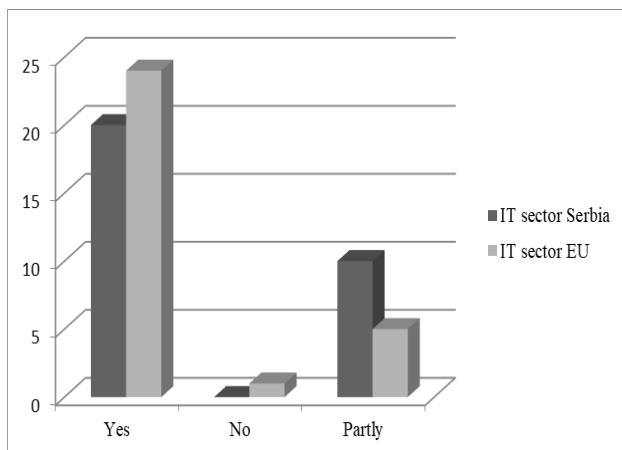


**Figure 4.** Answer the question

Do you adhere to the ISO IT standards?

Compliance with the requirements of ISO IT standards is less in the IT sector of Serbia compared to the IT sector of the EU. According to the results of the survey, the number of those who observe the ISO IT standards is significantly lower in Serbia, while, on the other hand, there are almost twice as many those who only partially comply with the requirements of ISO IT standards (Figure 4).

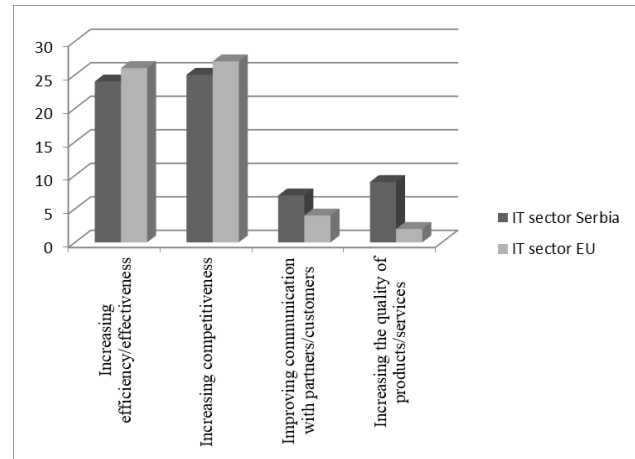


**Figure 5.** Answer the question

What are the motives for applying ISO IT standards?

The main motives for the application of ISO IT standards in the IT sectors of both areas are found primarily in increasing competitiveness and increasing efficiency/effectiveness, while improving communication with partners/customers and increasing the quality of products/services are much less prominent as motives (Figure 5).

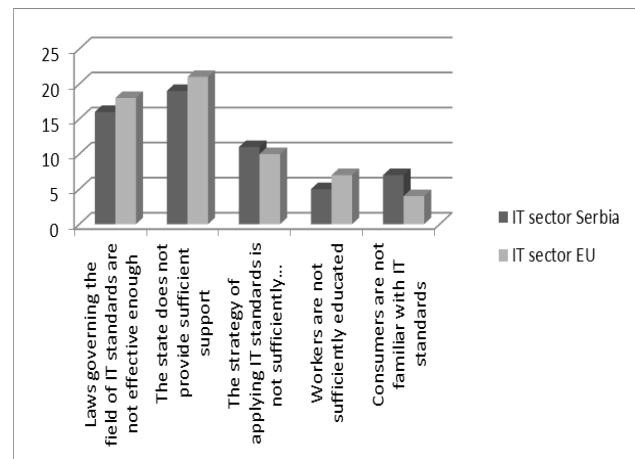


**Figure 6.** Answer the question

In your opinion, what are the obstacles to ISO IT standards application?

Obstacles to the application of ISO IT standards are proportionally expressed in the IT sectors of Serbia and the EU, where insufficient state support stands out in the first place, followed by the legal disorder in this area (Figure 6).

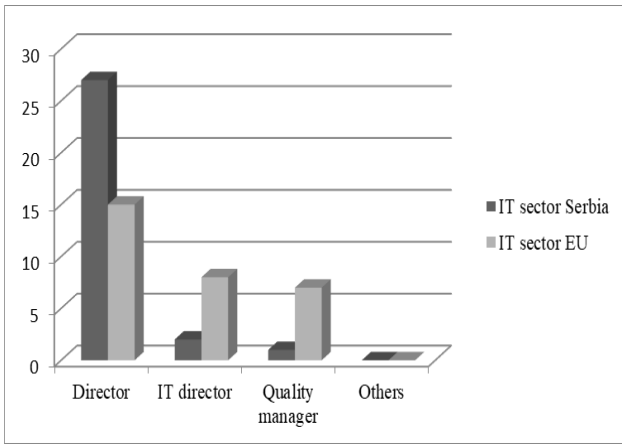


**Figure 7.** Answer the question Who approves investment in new business systems?

The approval of investments in the IT sector of Serbia is largely the responsibility of the director, while in the IT sector of the EU, in addition to the leading role of the director, the participation of the IT director as well as the quality manager is somewhat greater (Figure 7).

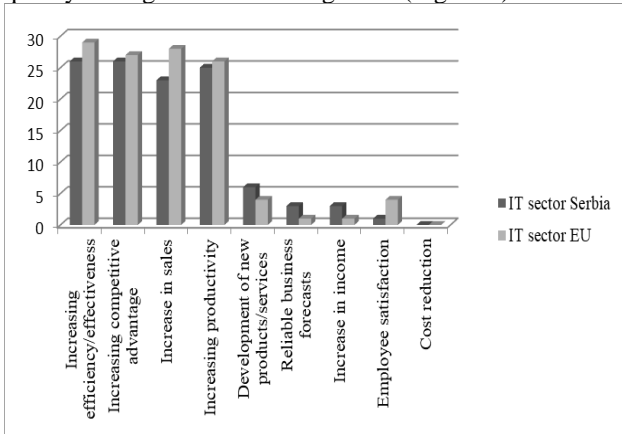


**Figure 8.** Answer the question

In your opinion, what are the benefits of ISO IT standards?

As for the basic benefits brought by the application of ISO IT standards, in both examined IT sectors, with very small deviations, the most prominent are the increase in efficiency/effectiveness, increase in sales, increase in competitive advantage and increase in productivity (Figure 8).

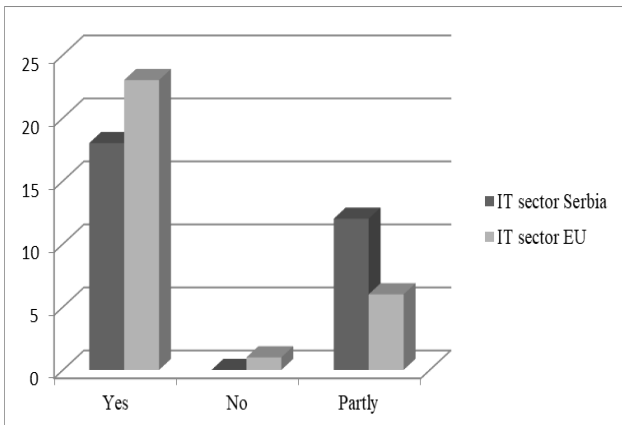


**Figure 9.** Answer the question In your opinion, do ISO IT standards affect business operation?

The opinion about the impact of ISO IT standards on business operation differs in the observed IT sectors. A positive response is more present in the IT sector of the EU, while partial influence as a response is more prevalent in the IT sector of Serbia (Figure 9).

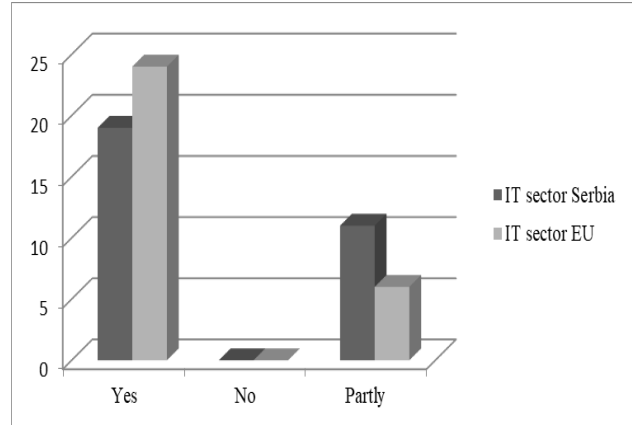


**Figure 10.** Answer the question

In your opinion, does the integration of (new) business systems and ISO IT standards bring positive business effects?

The integration of business systems and ISO IT standards in both IT sectors is characterised by positive business effects. The majority of respondents are unequivocal in their response, while a smaller number of respondents in both sectors believe that the impact of the integration of standards into business operation is only partial (Figure 10).

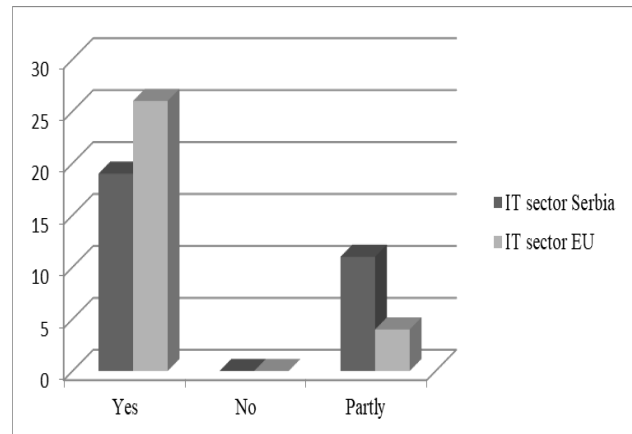


**Figure 11.** Answer the question Do you think ISO IT standards affect the efficiency and effectiveness of business operation?

The largest number of respondents in both IT sectors believe that the impact of ISO IT standards on the efficiency and effectiveness of business operation is great, while twice as many respondents in Serbia than in the EU opted for only a partial impact (Figure 11).

## 4. CONCLUSION

Based on the previous analysis, we can conclude that there is a certain conformity of the application of international technical standards in the field of information technologies in the IT sectors of the EU and Serbia, which indicates that the IT sector of Serbia is not lagging behind the IT sector of the EU in this business aspect.

Such conclusions speak in favour of the thesis of progress, growth and development of the IT sector of Serbia, harmonised with the corresponding sector of the EU, which is the first prerequisite for the free expansion of the market outside the borders of Serbia.

It is expected that this research, based on quantitative and qualitative results, will contribute to the creation of preconditions for the future greater application of IT standards in the IT sector of Serbia.

The results of the research can help to define new elements in the areas of business systems related to the implementation and application of standards in the IT sector of Serbia, based on experiences taken from the EU.

In addition, such or similar research contributes to the understanding of the importance and impact of the IT sector on the economic system of the Republic of Serbia.

## References

- [1] Delic, M., Radlovacki, V., Kamberovic, B., Maksimovic, R. M., & Pecujlija, M.: "Examining relationships between quality management and organisational performance in transitional economies", *Total quality management & business excellence*, 2014.
- [2] Delic, M., Radlovacki, V., Kamberovic, B., Vulcanovic, S., & Hadzistevec M.: "Exploring the impact of quality management and application of information technologies on organisational performance - the case of Serbia and the wider region", *Total quality management & business excellence*, 2014.
- [3] Liu, JYC., Chen, VJ., Chan, CL., Lie, T.: "The impact of software process standardization on software flexibility and project management performance: Control theory perspective", *Information and Software Technology*, 2008.
- [4] Jakobs, K.: "Standardization Research in Information Technology: New Perspectives", Retrieved from <https://www.igi-global.com/book/standardization-research-information-technology/935>, 2007.
- [5] Bakator, M., Čočkaló, D.: "Improving business performance with ISO 9001: a review of literature and business practice", *The European Journal of Applied Economics*, 2018.
- [6] Mambi, A.J.: "ICT Law Book: a source book for information and communication technologies & cyber law", Retrieved from <https://trove.nla.gov.au/work/173885389?q&versionId=189500541>, 2010.
- [7] Murray, A.: "Information Technology Law The Law and Society", Retrieved from <https://global.oup.com/academic/product/information-technology-law-9780198830559?cc=rs&lang=en&>, 2016.
- [8] Radlovacki, V., Beker, I., Majstorovic, V., Pecujlija, M., Stanivukovic, D., & Kamberovic, B.: "Quality Managers Estimates of Quality Management Principles Application in Certified Organisations in Transitional Conditions - Is Serbia Close to TQM", *Strojniški vestnik - Journal of Mechanical Engineering*, 2011.
- [9] Jakobs, K.: "Modern Trends Surrounding Information Technology Standards and Standardization Within Organizations", Retrieved from <https://www.igi-global.com/book/modern-trends-surrounding-information-technology/104754>, 2014.
- [10] Jakobs, K.: "Corporate and Global Standardization Initiatives in Contemporary Society", Retrieved from <https://www.igi-global.com/book/corporate-global-standardization-initiatives-contemporary/188331>, 2018.
- [11] Kakola, T.: "Standards initiatives for software product line engineering and management within the international organization for standardization. System Sciences", *HICSS*, 2010.
- [12] Al-Qutaish, Re.: "Measuring the software product quality during the software development life-cycle: An international organization for standardization standards perspective", *Journal of Computer Science*, 2009.
- [13] Robledo, J.C., Samoili, S., Lopez-Cobo, M.; Mas, M., Cardona, M., Femandez de Guevara, J., De Prato, G., & Righi, R.: "The 2018 Predict key facts report, European Commission", Retrieved from <http://publications.jrc.ec.europa.eu/repository/handle/JRC112019>, 2018.
- [14] 2018 Rolling Plan for ICT Standardisation



## BENFORD'S LAW IN SERVICE OF DATA QUALITY: TWO CASES OF NATURAL NUMBERS

IGOR ĐORIĆ,

Military Technical Institute, Belgrade, [allslovenac@yahoo.com](mailto:allslovenac@yahoo.com)

SLADANA VUJIČIĆ,

Faculty of Business Economics and Entrepreneurship, Belgrade, [sladjanakonto@gmail.com](mailto:sladjanakonto@gmail.com)

MIHAJLO RANISAVLJEVIĆ,

Military Technical Institute, Belgrade, [mranisan@gmail.com](mailto:mranisan@gmail.com)

**Abstract** In an era of constant, growing accumulation of information quantified numerically, the need for establishing data authenticity also increases. Identifying false, fabricated data within a mass of numbers becomes a challenge that many interested parties strive to overcome, especially investigative bodies, institutions that monitor budget spending reports, and governmental agencies overseeing financial operations in the private sector. Scientific literature suggests using a natural distribution of numbers known as Benford's Law for detecting data manipulation. This study analyzes the numbers in the collected data and their distribution according to Benford's Law. This paper processed two sets of independent data, different in volume and source of collection. The goal is to demonstrate the usefulness of data processing for faster detection of misuse, and the use of Benford's Law is proposed as an effective aid for regulatory institutions.

**Keywords:** Benford's Law, quality, data, forensics

### 1. INTRODUCTION

Data is a fundamental, raw element, an isolated unprocessed fact, which does not necessarily have meaning on its own. In Latin, "datum" means something that is given. Essentially, it refers to numbers, text, images, sounds, or any other recording. Information is derived from data that has been processed, organized, or interpreted. Information is a useful, meaningful data that can be used for decision making, understanding a situation, or solving a problem. In this work, an evaluation of the quality of numbers in that mass of data will be performed through analysis of financial data or randomly collected data.

Decision makers seek to increase their knowledge by analysing available data. Data analysis can identify trends and behaviour patterns that indicate future events or changes in the market, as well as identify risks, hazards, and irregularities in business operations. In terms of business performance, the need for control and supervision over business processes and deviations from expected results increases due to large databases.

The accuracy of data in the era of vast amounts of information expressed in numbers is increasing, along with the need to establish credibility. Discovering false, fabricated data in a mass of numbers becomes a challenge pursued by many interested parties, especially investigative authorities, institutions monitoring the expenditure of budget funds, and government authorities

overseeing financial operations. It is suggested in scientific literature to use the natural distribution of numbers known as Benford's law to detect data manipulation.

### 2. FINANCIAL FORENSIC

Data analysis is crucial because it allows for the understanding and utilization of information to improve business operations, increase transparency and security, as well as make better and more informed decisions. The system of controls and audit procedures help ensure that the organization operates in compliance with laws and regulations.

Data analysis identifies trends in business and detects patterns that indicate future events and changes in the organization or market. The available information allows for risk assessment and identification of opportunities, all towards improving strategic planning and resource allocation. Therefore, inaccurate data and fabricated information can lead the organization into inefficiencies.

Monitoring performance through control and information analysis, business processes are followed and deviations from expected results are revealed. Control helps the organization ensure compliance with relevant laws and regulations and identify potential areas for improvement. Financial data analysis can reveal unusual or suspicious transactions that indicate possible fraud or misuse.

Financial forensics is a specialized area of accounting and auditing that deals with examining financial information to detect fraud, corruption, money laundering, and other



financial irregularities. [1] Financial forensics combines accounting, auditing, law, and investigative skills. The goal is to provide evidence that can be used in legal proceedings or internal investigations. [2]

The benefits of using financial forensics include:

- detecting and preventing fraud before causing serious financial losses,
- improving business transparency and financial reporting,
- protecting the organization's reputation and promoting the building of a positive image,
- enhancing control mechanisms by implementing better control procedures to reduce the risk of future fraud,
- financial stability by providing accurate financial information crucial for decision-making.

Financial forensics is key to preserving the integrity of the organization and helps the organization recognize and respond to financial threats, ultimately aiming to achieve reliability of the financial system. It goes through several phases of implementation (Graph 1).

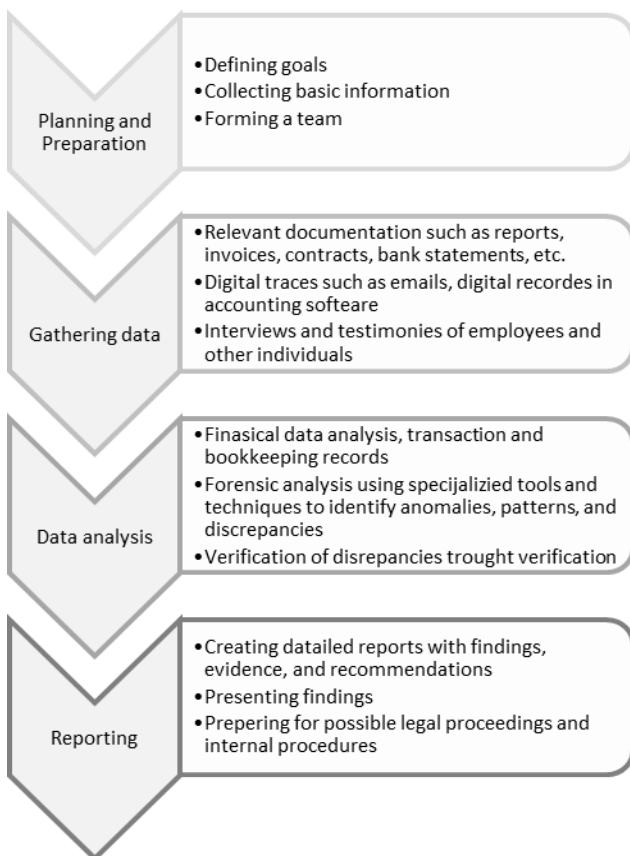


**Chart 1.** Phases of financial forensics  
Source: author

This paper focuses on data analysis using specialized methods to identify anomalies in data, for which we propose the use of Benford's Law. This law will be used in one segment of financial forensics to evaluate the data collected for analysis.

### 3. BENFORD'S LAW

Benford's Law, also known as the First-Digit Law, is a mathematical theory that predicts the distribution of first digits in many datasets. According to this law, the frequency of occurrence of a digit in the first position of a number is such that the digit 1 appears in about 30% of numbers, the digit 2 in 18% of cases, and so on logarithmically up to the digit 9 which appears in 4.6% of cases. [3]

$$P(d) = \text{Log}_{10} \left( \frac{d + 1}{d} \right), d = 1, 2, 3 \dots 9$$

The probability was discovered by American astronomer Simon Newcomb, who noticed that the pages of a logarithmic handbook with numbers 1 and 2 were more frequently used than pages with numbers 8 and 9. Physicist Frank Benford analysed 20,000 data points from various sources in 1938, more than five decades later, and confirmed the logarithmic regularity observed by Newcomb. The numbers appeared in a specific distribution. [4]

Although Benford's Law refers to the probability of the first two digits appearing in numbers, this mysterious law of nature, also known as the First-Digit Law, is still considered elusive by many experts. It is recommended in scientific literature to use this mathematical law to detect possible fraud and data manipulation in various areas of social life. [5]

Professor Mark J. Nigrini recommends using Benford's Law for detecting data fraud in the process of auditing business operations and accounting forensics. In data analysis, for larger databases, the distribution regularity can validate data authenticity, but further isolating data for fraud detection through deeper analysis is necessary for confirmation. [6]

### 4. ANALYSIS OF TWO CASES

For the purposes of this research, a comparative analysis of two sets of data was conducted to demonstrate the natural distribution of numbers. The aim was to apply Benford's model to real data and compare it with the theoretical probability of digit occurrence in a logarithmic distribution. In order to statistically express the obtained results significantly, doubts and the accuracy of the analysed data, it was necessary to examine the frequency of appearance of the first two digits through the analysis of mean absolute deviation (MAD), Kolmogorov-Smirnov test (KS statistic), and  $\chi^2$  test.

The first set of data was obtained in a way that an informal group of participants, 20 individuals, recorded random numbers in a table of 75 possible fields for number entry. The participants were not informed about the purpose of the research to avoid a subjective component and potential intention influence on the entered numbers. Two restrictions were given: the above sequence of numbers must have at least two digits and the numbers must not be repeated. The numbers entered by all participants contained 1 to 8 digits in a sequence. Out of 1500 possible numbers, participants entered 1232 on

the table form, of which 16 were unacceptable for this research, 4 numbers were decimal, 11 had only one digit, and one participant repeated a number twice in the sequence.

In Graph 2, the distribution of the first digit is shown, where a deviation in digits 7 and 9 is observed. The absolute difference in occurrence compared to Benford's distribution is 0.018 and 0.022, respectively, indicating a significant deviation in these two numbers. The analysis shows that the overall distribution follows the curve of Benford's model.

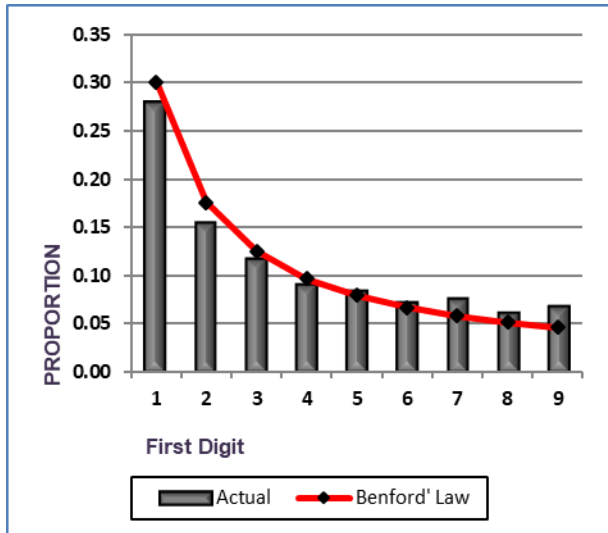


**Chart 2.** Distribution of the first digit of the first database

Chart 3. Distribution of the second digit of the first database where statistically significant deviations are observed only in digits 0 and 5.

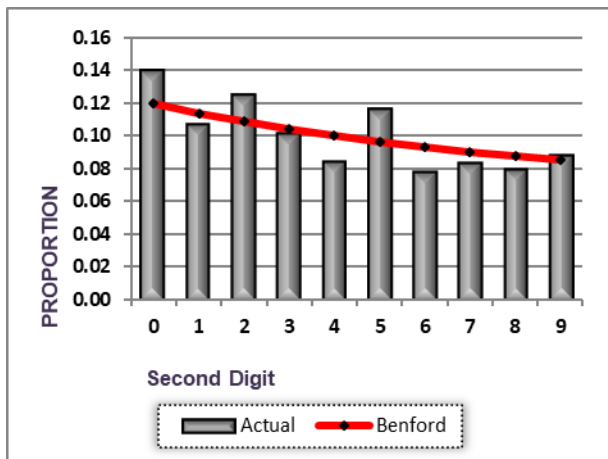


**Chart 3.** Distribution of the second digit of the first database

The reasons for the deviations in this case are not relevant, but they are used to demonstrate the natural distribution of digits in numbers as they clearly have a pattern in accordance with the Benford's model that we will use in the second group of processed data.

The second set of data was taken from the financial statements of a business entity registered in the Republic of Serbia (the name is known to the authors and is not relevant for this research) for the years 2022 and 2023.

The financial data on accounts of executed payments for the observation period were included. The issued invoices for the revenues generated by the business entity were not covered by the research.

A total of 2752 numbers were analysed. In Diagram 4, the distribution of the first digits in the included accounts is shown. The numbers with the first digits 1, 5, and 9 are significant, with a negative score for the digit 1, with an absolute deviation of -0.027, as it is currently at 27.4% compared to Benford's Law where it is expected to appear at 30.1%.

Digits 5 and 9 appear more frequently in the accounts than projected by Benford's model, so the z-test indicates deviations that significantly exceed the expected, with a value of 4.490 for digit 5 and 4.795 for digit 9.

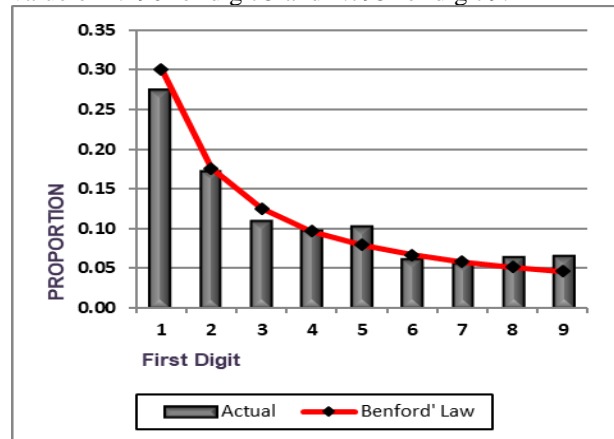


**Chart 4.** Distribution of the first digit of the second database

In the case of the second digit, as shown in Chart 5, there is a significant deviation in digits 0 and 3, and a less significant one in 1 and 9.

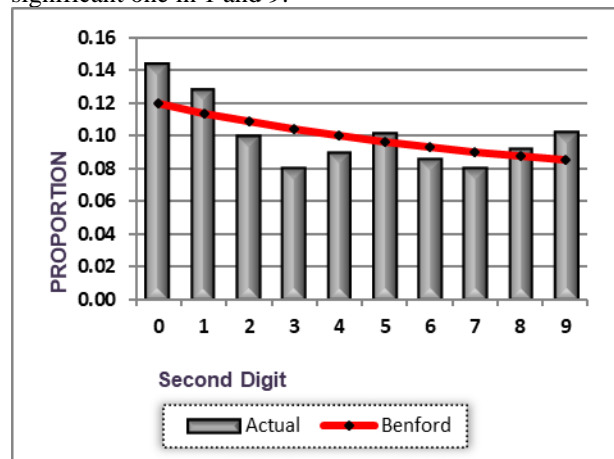


**Chart 5.** Distribution of the second digit of the second database

The deviations indicate, in the first case, specific behaviour of the subjects, and in the second case, possible deviations due to data manipulation. In both cases, the distribution of digits in numbers in the first and second positions follows Benford's model.

After identifying anomalies using Benford's law, deeper analysis requires the application of analytical and

statistical methods. In this context, regression analysis, analysis of variance, and other statistical techniques are used to identify deviations or patterns of behaviour in selected data that deviate from Benford's law. Modern mathematical-statistical models, such as neural networks and machine learning algorithms, would help in the detailed detection of anomalies for automatic identification of irregularities.

In the case of financial forensics, forensic auditing is necessary, which involves a detailed examination of all relevant financial documents and records for transactions that show significant deviations in the previous analysis. By analysing these accounts, the flow of money can be traced, and unusual or suspicious transactions can be identified.

## 5. CONCLUSION

Decision-makers and control bodies rely fully on information compiled from large amounts of data to reduce risks and threats to business activities or to conceal fraudulent activities in official reports. In this study, we analysed two types of number distributions and compared them, using Benford's Law as a tool to assess natural distributions. The results obtained in both cases satisfy Benford's distribution, indicating that the quality of data can be measured using this model.

Deviation in distribution from the perspective of financial forensics speeds up the process of processing collected data by efficiently identifying irregularities and potential fraud in a mass of data. The focus is put on data that deviates from a natural distribution, thus reducing the overall time for making conclusions. This method enables quick scanning of large data sets to identify potential areas of irregularities that require detailed investigation.

In practice, there is a serious need to assess the credibility of data used in decision-making, specifically data entered in financial reports. Since deviations from Benford's

distribution hint at irregular distribution that does not follow the probability of digits appearing in numbers, we suggest that deeper analysis should rely on additional methods or tools that would provide a clearer picture.

Further studies should focus on applying Benford's Law in combination with modern economic-mathematical models and techniques, such as machine learning and neural networks. In the context of increasingly complex data sets dependent on very complex relationships at risk of manipulation by well-organized groups and individuals in fraudulent activities in all areas of social life, quick response is important to minimize consequences and subject actors to appropriate sanctions.

Benford's Law, as a reliable mathematical tool, continues to be crucial in ensuring data integrity and accuracy in increasingly complex business and financial circumstances.

## Literature

- [1] Wells, J. T. (2014). *Principles of fraud examination*. John Wiley & Sons.
- [2] Jennings, W. L. (2022). *Fraud Investigation and Forensic Accounting in the Real World*. CRC Press.
- [3] Newcomb, S. (1881). Note on the frequency of use of the different digits in natural numbers. *American Journal of mathematics*, 4(1), 39-40.
- [4] Benford, F. (1938). The Law of Anomalous Numbers, *Proceedings of the American Philosophical Society*, 75, 551—572.
- [5] Đorić, I., Ranisavljević, M., & Kocka, Đ. (2024). Benford's law: Planning and analysis of the planned values in the defense budget. *Trendovi u poslovanju*, 12(1), 39-47.
- [6] Nigrini, M. J. (2012). *Benford's Law: Applications for forensic accounting, auditing, and fraud detection* (Vol. 586). John Wiley & Sons..



# THE NEW METHOD FOR SOLVING GAMMA-GAMMA, X-X, X-GAMMA COINCIDENCE SUMMING IN GAMMA SPECTROSCOPY

DRAGANA JORDANOV

VINCA Institute of Nuclear Sciences –Institute of National Importance for the Republic of Serbia,  
University of Belgrade, Belgrade, [djordano@vinca.rs](mailto:djordano@vinca.rs)

LASLO NADJDJERDJ

VINCA Institute of Nuclear Sciences –Institute of National Importance for the Republic of Serbia,  
University of Belgrade, Belgrade, [mappy@vinca.rs](mailto:mappy@vinca.rs)

MILENA ROSIĆ

VINCA Institute of Nuclear Sciences –Institute of National Importance for the Republic of Serbia,  
University of Belgrade, Belgrade, [mrosic@vinca.rs](mailto:mrosic@vinca.rs)

**Abstract:** *New challenges in gamma spectroscopy came with the development of experimental techniques. The new germanium detectors have an extended detector sensitivity to lower energies - BEGe (broad energy HPGe), which allows the efficient detection of X-rays generated in the processes of electronic capture and internal conversion at the same time as gamma radiation. In addition to the previous gamma-gamma, this type of detector has an additional X-X and X-gamma coincidence summation, which further complicates the problem of deconvolution of the energy spectrum. By considering and analyzing previously developed methods, a deterministic method was developed for deriving the counting rate for gamma spectra, which allows us to predict all summation peaks that occur in the spectrum. We devised a method for calculating coincident effects in gamma spectroscopy that is applicable to all radionuclides regardless of the degree of complexity of the decay scheme. This approach also allows us to determine the activity of sources directly without calibration of the detector, which is very important in metrology of radionuclides. Accordingly, based on the value of the peak area in the spectrum and knowledge of probability transitions between excited states of a nucleus, it is possible to determine the efficiency of detection together with the activity of radioactive sources. Our work also includes the successful application of the new method to radionuclides used in real experiments such as radionuclides  $^{139}\text{Ce}$ ,  $^{57}\text{Co}$ ,  $^{133}\text{Ba}$  and  $^{152}\text{Eu}$ .*

**Keywords:** *Metrology of radionuclides, Coincidence summing, Activity of source, Detector efficiency,  $^{152}\text{Eu}$ .*

## 1. INTRODUCTION

Coincidental summation is topical in international groups dealing with radionuclide metrology, i.e. gamma radiation spectrometry.

Interest in the effects of coincidental summation in gamma spectrometry is related to their influence on the accuracy of determining the efficiency of detectors and radionuclide activity.

Our goal was to find the most optimal method for calculating the effects of coincidental summation in gamma spectroscopy and we developed a new matrix method for calculating the counting rate for radionuclides in which the cascade deexcitation of the nucleus takes place simultaneously with the cascade deexcitation of the atomic shell [1-4].

Applying the analytical approach gives the problem of coincidental summation the ability to predict all the summation peaks that may appear in the spectrum.

The new method has been successfully applied to radionuclides used in real metrology. We successfully applied the new matrix method to radionuclides with a simple decay scheme. It was also applied with the same

success to the radionuclide with an extremely complex decay scheme  $^{152}\text{Eu}$  [2].

When we were working on  $^{152}\text{Eu}$ , using a new method for calculating the effects of coincidental summation, certain irregularities were noticed during the formation of probability matrices. Analyzing the calculations given in the data evaluation, which follow the tables with transition probabilities, a series of errors and omissions are observed that directly affect the values of the recommended transition intensities.

To facilitate future work in gamma spectroscopy we give in the paper, an analysis of the errors and mistakes that the evaluators have made [3].

## 2. THE NEW MATRIX METHOD

### 2.1. The matrix method for calculating coincident effects

During nuclear decay, cascading transitions emit two or more photons, in a short time interval, shorter than the resolving time of the detector, and as a result, the detector treats them as a single interaction. This leads to an

increase in counts in the summation peaks as well as a decrease in the counts in the photo peaks of the cascading photons (Figure 1.). Andreev et al.[5] have method were determines nuclear parameters, while source activities and detection efficiencies are known. We developed a method where we solve the inverse problem: knowing the nuclear parameters, we determine the unknown activities of the source and the efficiency of detection.

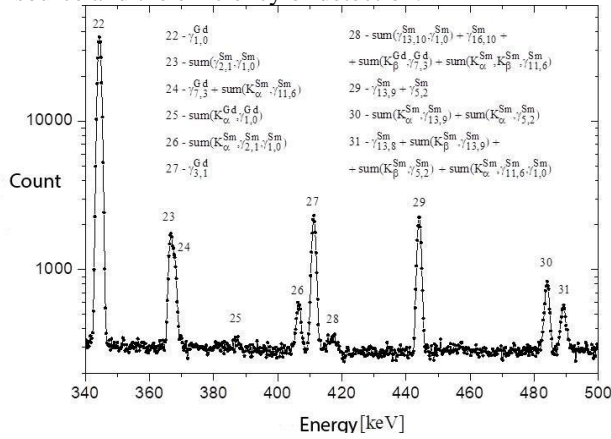


**Figure 1.** The part of the spectrum of Eu-152 where the summation peaks are shown

That is, based on the values of the peak areas in the spectrum and knowing the probabilities of transitions between the excited nucleus states, we determine the activity and efficiency. First, we modified the decay scheme for the needs of matrix formalism (Figure 2.)

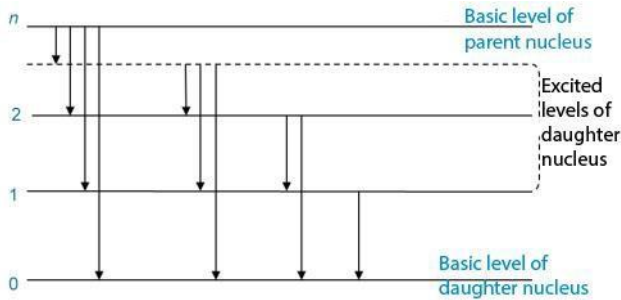


**Figure 2.** The decay scheme is modified as follows: the ground level of the parent nucleus is represented as the most excited level of the daughter nucleus and is denoted by  $n$

Then we form the transition probability matrix (stochastic, transition or probability matrix)  $X$ : transition probabilities  $x_{ij}$  from the energy level  $i$  to the  $j$  level form one square matrix of dimensions  $(n + 1) \times (n + 1)$

$$X = \begin{bmatrix} 0 & 0 & 0 & \dots & 0 \\ x_{10} & 0 & 0 & \dots & 0 \\ x_{20} & x_{21} & 0 & \dots & 0 \\ \vdots & \vdots & \vdots & \ddots & \vdots \\ x_{n0} & x_{n1} & \dots & x_{n,n-1} & 0 \end{bmatrix} \quad (1)$$

$$\sum_{i=0}^{n-1} x_{ni} = 1 \quad (2)$$

$$\sum_{j=0}^{i-1} x_{ij} = 1, \quad i = 1, \dots, n-1 \quad (3)$$

When the nucleus's decay occurs near the detector, the photons emitted in the cascade transitions can be detected. The set of all detection probabilities forms a characteristic diagram. However, it is necessary to come to an expression for the probabilities of simultaneous detection of photons during the cascade transition, i.e. the transition in several successive steps. In fact, it should only be noted that the expressions for detection probabilities are nothing but expressions for matrix elements of matrices that we have called detection probability matrices:

- Probability matrix of  $K_{\alpha}$  photon detection,  $A$ ,
- Probability matrix of  $K_{\beta}$  photon detection,  $B$ ,
- Probability matrix of gamma photon detection,  $\Gamma$ ,
- Non-detection probability matrix of any photon,  $Q$ .

Summation matrix of all detection probability matrices:

$$S = A + B + \Gamma + Q, \quad (4)$$

contains all probabilities of (non) detection of photons emitted during one-step transitions.

Analogously, the sum of all powers of the matrix  $S$  contains all the detection probabilities of photons emitted at cascade transitions in any possible number of steps:

$$\nu-1$$

$$M = \sum_{k=1}^{\nu-1} S^k = S + S^2 + S^3 + \dots + S^{\nu-1} \quad (5)$$

For the problem of coincidental summation, only complete cascade transitions are interesting, i.e. cascade transitions that start from the basic state of the parent nucleus and end with the basic state of the daughter nucleus. Therefore, instead of the whole matrix  $M$ , which contains all possible detection probabilities, for our further analysis we need only its element which is in the last,  $n$ -th row, and zero column:

$$\begin{aligned}
 [M]_{n,0} = & \overbrace{a_{n,0} e^{iE_s} + b_{n,0} e^{iE_s} + q_{n,0} e^{i0}}^{1 \text{ корпус}} + \\
 & \overbrace{\left( a_{n,n-1} e^{iE_s} a_{n-1,0} e^{iE_s} + a_{n,n-2} e^{iE_s} a_{n-2,0} e^{iE_s} + \dots + a_{n,1} e^{iE_s} a_{1,0} e^{iE_s} \right) +}^{2 \text{ корпуса}} \\
 & \overbrace{\left( a_{n,n-1} e^{iE_s} b_{n-1,0} e^{iE_s} + a_{n,n-2} e^{iE_s} b_{n-2,0} e^{iE_s} + \dots + a_{n,1} e^{iE_s} b_{1,0} e^{iE_s} \right) +} \\
 & \overbrace{\left( a_{n,n-1} e^{iE_s} \gamma_{n-1,0} e^{iE_s} + a_{n,n-2} e^{iE_s} \gamma_{n-2,0} e^{iE_s} + \dots + a_{n,1} e^{iE_s} \gamma_{1,0} e^{iE_s} \right) +} \\
 & \overbrace{\left( a_{n,n-1} e^{iE_s} q_{n-1,0} e^{i0} + a_{n,n-2} e^{iE_s} q_{n-2,0} e^{i0} + \dots + a_{n,1} e^{iE_s} q_{1,0} e^{i0} \right) +} \\
 & \overbrace{\left( b_{n,n-1} e^{iE_s} a_{n-1,0} e^{iE_s} + b_{n,n-2} e^{iE_s} a_{n-2,0} e^{iE_s} + \dots + b_{n,1} e^{iE_s} a_{1,0} e^{iE_s} \right) +} \\
 & \overbrace{\left( b_{n,n-1} e^{iE_s} b_{n-1,0} e^{iE_s} + b_{n,n-2} e^{iE_s} b_{n-2,0} e^{iE_s} + \dots + b_{n,1} e^{iE_s} b_{1,0} e^{iE_s} \right) +} \\
 & \overbrace{\left( b_{n,n-1} e^{iE_s} \gamma_{n-1,0} e^{iE_s} + b_{n,n-2} e^{iE_s} \gamma_{n-2,0} e^{iE_s} + \dots + b_{n,1} e^{iE_s} \gamma_{1,0} e^{iE_s} \right) +} \\
 & \overbrace{\left( b_{n,n-1} e^{iE_s} q_{n-1,0} e^{i0} + b_{n,n-2} e^{iE_s} q_{n-2,0} e^{i0} + \dots + b_{n,1} e^{iE_s} q_{1,0} e^{i0} \right) +} \\
 & \overbrace{\left( q_{n,n-1} e^{i0} a_{n-1,0} e^{iE_s} + q_{n,n-2} e^{i0} a_{n-2,0} e^{iE_s} + \dots + q_{n,1} e^{i0} a_{1,0} e^{iE_s} \right) +} \\
 & \overbrace{\left( q_{n,n-1} e^{i0} b_{n-1,0} e^{iE_s} + q_{n,n-2} e^{i0} b_{n-2,0} e^{iE_s} + \dots + q_{n,1} e^{i0} b_{1,0} e^{iE_s} \right) +} \\
 & \overbrace{\left( q_{n,n-1} e^{i0} \gamma_{n-1,0} e^{iE_s} + q_{n,n-2} e^{i0} \gamma_{n-2,0} e^{iE_s} + \dots + q_{n,1} e^{i0} \gamma_{1,0} e^{iE_s} \right) +} \\
 & \overbrace{\left( q_{n,n-1} e^{i0} q_{n-1,0} e^{i0} + q_{n,n-2} e^{i0} q_{n-2,0} e^{i0} + \dots + q_{n,1} e^{i0} q_{1,0} e^{i0} \right) +} \\
 & \overbrace{\left( a_{n,n-1} e^{iE_s} a_{n-1,n-2} e^{iE_s} a_{n-2,0} e^{iE_s} + \dots + a_{n,2} e^{iE_s} a_{2,1} e^{iE_s} a_{1,0} e^{iE_s} \right) +}^{3 \text{ корпуса}} \\
 & \overbrace{\left( a_{n,n-1} e^{iE_s} a_{n-1,n-2} e^{iE_s} b_{n-2,0} e^{iE_s} + \dots + a_{n,2} e^{iE_s} a_{2,1} e^{iE_s} b_{1,0} e^{iE_s} \right) +} \\
 & \dots + \\
 & \overbrace{q_{n,n-1} e^{i0} q_{n-1,n-2} e^{i0} q_{n-2,n-3} e^{i0} \dots q_{1,0} e^{i0}}^{i-1 \text{ корпуса}}
 \end{aligned}
 \tag{6}$$

Different detection events whose probabilities in the previous expression have the same argument actually belong to a group of events with the same detection outcome. All of these members contribute to the same photo peak. This finally established a connection with the energy spectrum. The normalized area below a certain peak in the energy spectrum is equal to the sum of the probabilities of detection of all events with the same outcome.

The theoretical counting rate in the corresponding photo-peak is obtained by multiplying the activity of the source, R, with the sum of the probabilities of detection of all events with the same outcome:

$$n^{Th}(E_\ell) \equiv R \sum_k p_k(E_\ell) \quad \ell = 1,2,3,\dots
 \tag{7}$$

By equating theoretical with experimental counting rate, a system of equations for counting rate in all peaks in the energy spectrum is obtained:

$$R \sum_k p_k(E_\ell) = n^{Exp}(E_\ell) \quad \ell = 1,2,3,\dots
 \tag{8}$$

that is, a system of equations based on when we determine R and all efficiencies.

### 3.EXPERIMENT

#### 3.1Equipment

One of the important characteristics of detectors for gamma radiation detection is the simultaneous detection of photons (emitted in the process of cascade deexcitation) which lead to the appearance of summation peaks (coincidental summation). Previously detectors did not detect X-rays or were removed by filters. New challenges in gamma spectroscopy came with the development of experimental techniques. The new germanium detectors have an extended detector sensitivity to lower energies - BEGe (broad energy HPGe), which allows the efficient detection of X-rays generated in electronic capture and internal conversion

processes at the same time as gamma radiation (Figure 3).

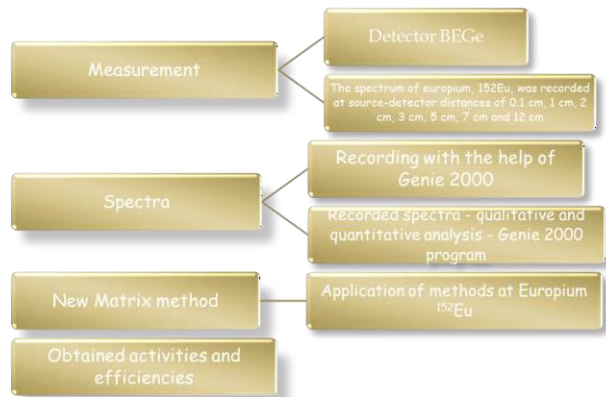


Figure 3. Extendent Range Coaxial Canberra Ge detector GX5020

Scientists have successfully developed a method for solving gamma-gamma coincidence summation. But in BEGe - in addition to the previous gamma-gamma, this type of detector has an additional X-X and X-gamma coincidence summation, which further complicates the problem of deconvolution of the energy spectrum.

#### 3.2.Experimental settings

We verified our matrix method using experimental spectra.



Point source of europium, <sup>152</sup>Eu, reference activity 7037 Bq ± 4% on the day of calibration on June 9, 1987, measured on September 27, 2011. a high-purity germanium detector with an energy range extended to lower values (Extendent Range Coaxial Canberra Ge detector GX5020. The extended energy range of this type of detector enables efficient detection of Kα and Kβ radiation. The dead time of measurement in the nearest geometry is below 3%.

After subtracting the background, the spectrum of Europium <sup>152</sup>Eu was analyzed using the Genie2000 program. The total number and area under all peaks together with their errors were determined.

The results of calculated values of activities from the

experimental spectra are shown in **Table 1**. We have a good agreement with value of activity point source from Reference Laboratory

**Table 1.** Results of measurement and calculation

Referent activity	2023 ± 81 Bq						
Spectrum number	1	2	3	4	5	6	7
The distance of the source from the detector	0.1cm	1cm	2cm	3cm	5cm	7cm	12cm
Calculated value of source activity	2070 ± 26 Bq	2083 ± 34 Bq	2076 ± 35 Bq	2142 ± 54 Bq	2088 ± 127 Bq	2169 ± 84 Bq	1882 ± 109 Bq

#### 4. CONCLUSION

With the development of experimental techniques in gamma spectroscopy, the appearance of more sensitive detectors, which can measure even lower energies, and therefore, in addition to gamma radiation and X-ray radiation, it became necessary to develop a method for calculating the coincidental effects that arise.

We have developed a method that allows us to determine an additional X-X and X-gamma coincidence summation in addition to the previous gamma-gamma. Using the data given in the transition probabilities tables, we formed, following our method, the appropriate detection probability matrix. This approach allows us to determine activity of source and efficiency of detection. The importance of the new method is that it allows us to determine the efficiency of detection and activity of radioactive sources directly without calibration of the

detector, which is very important in the metrology of radionuclides.

#### References

- [1] NADJDJERDJ L. J., JORDANOV D. J., DAVIDOVIĆ M. D., *A new matrix method for calculating coincidence summing effects for gamma spectroscopy*, Nuclear Instruments and Methods A 662 (1) (2012) 21 – 25.
- [2] JORDANOV D. J., NADJDJERDJ L. J., PUZOVIĆ J., ROSIĆ M., KOKUNEŠOSKI M., *The application of the new matrix method for calculating coincidence summing effects in the case of radionuclide with the more complex decay scheme - 152Eu*, Nuclear Instruments and Methods in Physics Research A 836 (2016) 22-29.
- [3] JORDANOV D. J., NADJDJERDJ L. J., ROSIĆ M., *Compilation of errors in nuclear parameters for radionuclide Eu-152*, Nuclear Instruments and Methods in Physics Research A 899 (2018) 49–51.
- [4] NADJDJERDJ L. J., DAVIDOVIĆ M. D., MILOŠEVIĆ M. J., JORDANOV D. J., STANKOVIĆ S. J., PRVANOVIĆ S. L., *A possible improvement of the determination of 133Ba activity and detection efficiency by the sum-peak method, by inclusion of the previously neglected transitions*, Nuclear Instruments and Methods in Physics Research A 698 (2013) 60 – 65.
- [5] Д. С. Андреев, К. И. Ерохина, В. С. Звонов и И. Х. Лемберг, *Определение эффективности регистрации  $\gamma$ -квантов в пиках энергии с помощью нуклидов со сложной схемой распада в условиях близкой геометрии*, Известия академии наук СССР сепия физическая, т. 37, (1973)1609-1612



## THE IMPACT OF DIVERSIFICATION STRATEGY ON COMPANY PERFORMANCE IN DEFENSE INDUSTRY

SRĐAN MIRKOVIĆ

Singidunum University, [srdjan.mirkovic23@singimail.rs](mailto:srdjan.mirkovic23@singimail.rs)  
Directorate for General Logistics, SMR MoD, Belgrade

MIHAJLO RANISAVLJEVIĆ,

Military Technical Institute, Belgrade, [mranisan@gmail.com](mailto:mranisan@gmail.com)

IGOR ĐORIĆ,

Military Technical Institute, Belgrade, [allslovenac@yahoo.com](mailto:allslovenac@yahoo.com)

**Abstract:** This paper explores the impact of diversification strategy on company performance through a systematic review of existing literature. Diversification strategies, which involve expanding business activities into new industries or markets, are often employed with the aim of increasing profitability and reducing risk. A significant number of studies analyze how different diversification strategies affect company performance. However, the results are often contradictory, with some studies showing a positive impact, while others indicate a negative or neutral effect. There is a lack of consensus on best practices and contextual factors that influence the success of these strategies. The paper includes studies from various industries and regions, focusing on those covered by meta-analyses on this topic. This allows for insights into different economic contexts and market conditions that affect the success of diversification strategies. The goal of the paper is to contribute to a better understanding of the complexity of diversification strategies and their impact on overall company performance, as well as in the defense industry of Serbia. The paper also highlights the importance of a contextual approach and adapting strategies to the specific conditions of the company and market.

**Keywords:** diversification, defense industry of Serbia, contextual factors, industry.

### 1. INTRODUCTION

In the modern business environment, diversification strategy has become a key aspect for many companies striving for sustainable growth and competitive advantage. Diversification involves expanding business operations into new products, services, or markets to reduce risk and increase profitability.

This paper provides a systematic review of the literature that investigates the impact of diversification strategy on company performance. The goal is to identify the key factors that contribute to the success or failure of these strategies and to consider various theoretical and empirical approaches in existing research.

The existing literature shows mixed results regarding the impact of diversification on company performance. Some authors point to positive effects, such as increased profitability and reduced risk, while others highlight negative consequences, including increased management complexity and unjustified dispersion of resources. Limitations of previous research include various methodological approaches, insufficient consideration of contextual factors, and inconsistencies in defining and measuring diversification.

The main idea of this paper is to analyze and synthesize

existing knowledge on the impact of diversification on company performance and attempt to answer the question of how different types of diversification (related and unrelated) affect company performance. What are the contextual factors that moderate this relationship? How can growth strategies be successfully applied in defense industry enterprises?

This paper contributes to the literature by providing a structured review of existing research, identifying knowledge gaps, and proposing directions for future research. It also provides practical recommendations for managers considering the implementation of diversification strategies.

### 2. GROWTH STRATEGIES

After a brief introduction to the topic, the following sections of the paper will address corporate strategies, focusing on diversification strategy and its impact on company performance. Before proceeding, it is essential to understand the basic concepts related to growth strategies, formulated by Igor Ansoff in 1957 through his matrix.

Ansoff, using market and product as criteria, defined four possible growth strategies:

1. Market Penetration Strategy
2. Product Development Strategy



3. Market Development Strategy
4. Diversification Strategy

Ansoff's matrix is still used in strategic management textbooks and represents a fundamental tool for considering possible directions for company growth.

### 2.1. Market Penetration Strategy

Market penetration strategy involves increasing sales of existing products in existing markets. This strategy is suitable when there is a quality product that meets customer needs and the market is not saturated. Although this strategy carries minimal risk, dynamic market conditions and competition may require additional measures to increase sales.

To increase market share, companies can:

1. Increase purchases from existing customers through promotional pricing, discounts, and volume discounts.
2. Attract customers from competitors through promotion and distribution.

While the market penetration strategy can bring significant benefits, it is not unlimited. The demand for the product is limited, and increasing our market share inevitably leads to a reduction in competitors' market share. This can cause price wars, which, if not resolved through acquisition or elimination of competition, can have negative consequences for the company's growth and development.

The application of the market penetration strategy in Serbian defense industry enterprises is limited by legal provisions. These enterprises face limited demand as the only customer of their products in the domestic market is the Ministry of Defense, so opportunities for increasing sales of existing products in the existing market are limited by the budget funds allocated annually for the procurement of armaments and military equipment. Despite these limitations, opportunities for increasing sales volumes to domestic and foreign customers exist, considering enterprises that operate on foreign markets on behalf of and for the state, whether they are state-owned or private enterprises licensed by the state for arms and military equipment trade.

### 2.2. Product Development Strategy

Product development strategy is applied when new or improved products can attract new customers or motivate existing ones to replace old products with new ones. This strategy is particularly effective when a product reaches maturity in its life cycle.

Successful application of the product development strategy depends on a strong research and development sector that can create innovative products.

While the product development strategy can bring significant benefits, it carries a higher risk compared to the market penetration strategy. Some research indicates that out of 50 newly developed products, only one succeeds in the market, highlighting the high level of risk and significant costs associated with research and

development.

Although limited by legal provisions and internal regulations of the Ministry of Defense, which stipulate that only organizational units of the Ministry of Defense and the Serbian Armed Forces can initiate the development of new products through their program documents, this does not prevent these enterprises from offering innovative products to the domestic and foreign markets through their development sectors. These products, due to their superior characteristics, can be imposed on the domestic market through the procurement of finished products from the domestic market and can also be of interest to foreign markets.

### 2.3. Market Development Strategy

Market development strategy involves selling existing products in new markets or new market segments. This strategy often includes minimal product modifications to comply with the regulations and conditions of the new market.

The advantage of this strategy is the possibility of growth without significant investments in research and development, but entering new markets carries risks due to different market regulations and strong competition. Although less risky than developing new products, this strategy requires careful analysis and planning.

Although Serbian defense industry enterprises face limited opportunities for selling their products in other markets, and this is only possible with special permission from the Ministry of Defense, the application of this strategy in Serbian defense industry enterprises is possible. The application of this strategy requires a detailed cost-benefit analysis, and entry into foreign markets offers enormous potential for stable growth, profitability, and reduced dependence on government orders. On the other hand, increasing serial production volumes, reducing overhead costs, and using the effects of economies of scale can lower the unit price of the product, allowing greater competitiveness of the domestic defense industry in foreign markets.

### 2.4. Diversification Strategy

Diversification strategy involves entering new business areas through the development of new products that are marketed in new markets. This strategy is the riskiest but can bring significant advantages if successfully implemented.

The basic division of diversification strategy is based on the criterion of the new business's connection to the existing one:

- ✓ **Related diversification** involves investments in new business areas closely related to the existing activity and can be horizontal or vertical.
- ✓ **Horizontal diversification** involves expanding the production program by introducing new production lines.
- ✓ **Vertical diversification** involves moving within the value chain, either backward toward raw material suppliers or forward toward distribution networks.

- ✓ **Unrelated diversification** involves investments in new business areas that have no connection with existing activities.

Diversification strategy represents an important tool for long-term growth and stability of the company, but it carries significant risks and requires careful planning.

Given that the production and trade of arms and military equipment in the Republic of Serbia are regulated by the Law on the Production and Trade of Arms and Military Equipment, which imposes specific restrictions affecting the operations of defense industry enterprises, especially concerning market conditions such as cost analysis, price determination, supply, and demand. In this context, the application of diversification strategy can improve the sustainability and competitiveness of these enterprises.

Despite being subject to legal restrictions related to the production and trade of arms and military equipment, which affect their business operations, Serbian defense industry enterprises have the opportunity to apply each of these growth strategies, considering that legal restrictions protect the interests and needs of the state for its security, without limiting initiative and managerial abilities to increase market share, develop new products, and enter foreign markets to ensure greater competitiveness, profitability, and reduced business risk.

### 3. DIVERSIFICATION STRATEGIES AND COMPANY PERFORMANCE

The impact of diversification strategy on company performance is one of the most researched topics in strategic management. However, the results are often contradictory, with some studies showing a positive impact, while others indicate a negative or neutral effect. There is a lack of consensus on the best practices and contextual factors influencing the success of these strategies.

A study (Palich et al., 2000) examines the relationship between diversification and business success through a meta-analysis of data from 55 previously published studies. The results show that moderate diversification has a greater impact on success than limited or extensive diversification. This supports a curvilinear model suggesting that the effects of diversification increase when companies move to related diversifications but decrease when moving from related to unrelated diversifications.

**Related diversification** involves participation in multiple industries using common corporate resources and achieving economies of scale. This strategy can result from operational synergies and sharing activities and resources among enterprises. There are benefits from the efficiency of the learning curve, product and process technology diffusion within the firm, and limited access to production factors necessary for operations in certain industries.

However, there are also costs associated with diversification. Managing a diverse portfolio of businesses can lead to loss of control, conflicts, and

inefficiencies in the organization. Optimal diversification thus involves balancing benefits and costs, which can vary depending on the specific circumstances of each company.

While it is suggested that both related and unrelated diversification are somewhat equal in their impact on performance, the challenges of managing a related portfolio can reduce the benefits of relatedness.

**Unrelated diversification**, on the other hand, can bring benefits such as risk reduction and dispersion and increased debt capacity.

Marginal benefits of diversification can be significant up to an optimal level, after which additional diversification can reduce overall efficiency. The study confirms the inverted U model, emphasizing the importance of finding the optimal level of diversification to achieve the best performance, although the effects of diversification are not as dramatic as previously thought, indicating that diversification may not be a key factor in achieving exceptional performance.

Research by Bausch and Pils (2009) examines the impact of related and unrelated diversification strategies on company performance, showing that both strategies are significantly associated with concurrent accounting and market performance but not with subsequent performance.

Modern theory suggests that related diversification has positive effects on performance, while unrelated diversification has negative effects on accounting and market performance. Companies with a related business portfolio can achieve benefits from transferring and exploiting business capabilities and knowledge, while companies with unrelated diversification must face high costs of organizing complex operations.

Analyses show that neither related nor unrelated diversification is significantly correlated with subsequent performance. Related diversification is positively correlated with concurrent market performance, while unrelated diversification is negatively correlated with concurrent market performance. Diversification in terms of business diversity is negatively correlated with both subsequent and concurrent performance.

The diversification strategy can have different effects on financial performance depending on the type of diversification and the time sequence of performance measurement.

Research findings emphasize several important points:

1. Measuring performance after diversification is crucial, but events during that period can distort the observation of effects;
2. Related diversification can lead to better long-term performance, while unrelated diversification can lead to poorer performance;
3. Neither related nor unrelated diversification is associated with subsequent accounting returns;
4. Industry profitability, market expectations, and risks can significantly influence the relationship between diversification and performance.

Research on the future of business groups in developed markets highlights the importance of unrelated diversification and its positive effects on company performance, especially when a certain threshold is exceeded. However, contextual factors such as the evolution of the institutional environment can affect the ability of business groups to generate value. This analysis indicates the need for precise data assessment and methodology, as well as the importance of understanding contextual factors that shape these effects.

Research (Schommer, Richter, & Karna, 2019) indicates a decrease in the level of unrelated diversification, while the levels of related diversification have increased since the mid-1990s, after an initial decline during the 1970s and 1980s. There is an improvement in the relationship between unrelated diversification and company performance over time, while the relationship between related diversification and performance has remained relatively stable. In developing economies, trends are less clear; some studies indicate a decrease in diversification with increasing institutional development, while others show that diversification remains an important strategy for firms in such markets.

By analyzing the development of diversification over time and distinguishing between related and unrelated forms of diversification through a meta-analysis covering over 60 years of research, changes in the relationship between diversification and performance were observed in the context of the evolution of diversification levels.

Increasing shareholder power, a more active market for corporate control, and a liberalized market environment have limited managers' ability to pursue potentially value-destroying conglomerate strategies. This trend led to the "deinstitutionalization" of the conglomerate form in the U.S. in the late 1980s and early 1990s, with similar trends in other Western countries, albeit at a slower pace.

Although overall levels of diversification have declined over time, the average performance of diversification may be becoming more positive.

It is believed that diversification has an inverted U-shaped relationship with company performance, considering rising costs and diminishing benefits with increasing levels of diversification.

The effects of diversification can be attributed to how resources are allocated in diversified firms, often with a bias toward good opportunities in the case of related diversification, while in highly diversified firms, resources are often allocated to poor opportunities.

Although traditionally believed that the effect of diversification on company performance follows an inverted U shape, where low levels and related diversification have positive effects on company performance, while high levels and less related types of diversification have negative effects.

There is no complete agreement on whether the strength or effects of diversification on performance change over time. The relationship between diversification and company performance depends on many factors,

including time and institutional environment. Recent research suggests that the diversification premium can vary over time, and in particular, the relative value of diversified firms can increase during recessions. Empirical research shows that diversification among large American firms has decreased since the late 1970s or early 1980s, while trends in other countries are mixed. The main factors identified that influence the decline in diversification levels are:

1. Focusing on business lines where firms have the clearest advantage over competitors;
2. Excessive diversification contributed to the decline in the competitiveness of American companies in the 1970s, and global competition forced firms to reduce the scope of their businesses to regain competitiveness;
3. Endogenous determination of optimal diversification strategy implies that firms will choose the level and type of diversification that best suits their capabilities and resources.

Results showed a continuous decline in the level of unrelated diversification over time, while levels of related diversification declined to a certain point before rising again. This suggests that the decline in overall diversification is mainly due to the reduction of unrelated diversification, with a simultaneous increase in related diversification after an initial decline.

In summary, the results partially support the hypothesis of decreasing diversification levels over time, with the decline in overall diversification mainly due to the reduction of unrelated diversification, while related diversification increased after an initial decline.

The results of this study indicate several key conclusions. First, overall levels of diversification have declined over time, with different trends for related and unrelated diversification. While unrelated diversification has declined linearly, related diversification has shown a tendency to increase again since the mid-1990s.

Second, the relationship between unrelated diversification and company performance has significantly improved over time, while the effect of related diversification has remained practically unchanged. This change in the relationship between diversification and performance suggests that conventional wisdom about the inverse relationship between diversification and company performance may not be universally applicable over time.

Third, the heterogeneity of diversification effects on performance indicates that there are no universal solutions for diversification. Decision-makers should define their diversification strategies in line with their firms' resources and capabilities and the external conditions in which they operate.

It is important to emphasize that, although the effects of unrelated diversification on performance have improved over time, this does not mean that excessive diversification is justified. Managers should carefully analyze the decision to enter a new line of business and consider each case individually.

## 4. CONCLUSION

Growth strategies represent key frameworks for the development and advancement of companies as a whole. The market penetration strategy focuses on increasing sales of existing products in existing markets and is ideal under conditions of stable demand and competitive advantage but carries risks of price wars with competitors. The product development strategy involves introducing new or improved products to existing markets. This strategy is beneficial when existing products reach maturity but requires significant investments in research and development, with a high risk of new product failure. The market development strategy involves selling existing products in new markets or new segments. This strategy allows growth without significant investments in new products but carries risks related to unfamiliarity with new markets and required marketing efforts.

The application of these strategies in Serbian defense industry enterprises is limited by legal frameworks regulating the production and trade of arms and military equipment. The main limitations for applying these strategies are reflected in the limited demand by the state, the inability to increase market share with existing products, the development of new products is conditioned by the needs and capabilities of the state, and entry into new markets is also determined by the state. Despite these limitations, Serbian defense industry enterprises have the opportunity to apply each of these growth strategies, considering that legal restrictions protect the interests and needs of the state for its own security, without limiting initiative and managerial abilities to increase market share, develop new products, and enter foreign markets to ensure greater competitiveness, profitability, and reduce business risk.

Research has shown that the effect of diversification on business performance is subject to changes depending on various institutional, economic, and managerial factors, challenging the established theoretical notion that the relationship between diversification and company performance is in the form of an inverted U. Leading research on this topic has confirmed that up to a certain limit, the impact of diversification on company performance has a linear relationship, i.e., a higher degree of diversification positively affects company performance. Beyond a certain maximum point, company performance begins to decline as the degree of diversification increases.

Diversification is a complex strategy that, instead of reducing risk, can help disperse risk by spreading it across multiple areas and reducing dependence on one field of activity. Although it can bring advantages in stability and competitive position, it can also lead to increased uncertainty and loss of focus if not carefully planned and executed.

A review of the literature on diversification strategy indicates that its impact on company performance depends on the type of diversification (related or unrelated) and the timing of performance measurement. Studies show that moderate and related diversification can

bring benefits through synergies and economies of scale, while extensive or unrelated diversification can lead to increased costs and loss of focus.

Meta-analyses of research suggest a curvilinear relationship (inverted U), where moderate diversification yields the best results. Conclusions imply that diversification is not always a key factor for success, but its effect varies depending on many factors. Unrelated diversification has continuously decreased over time, while related diversification has increased again since the mid-1990s after an initial decline. The relationship between unrelated diversification and company performance has significantly improved, while the relationship between related diversification and performance has remained stable.

The effects of diversification on performance are diverse among firms, indicating that there is no universal approach to diversification. The results suggest the need to adjust the approach to analysis and strategy according to temporal changes and market specifics, which is important for strategic management. These conclusions contribute to a better understanding of the dynamics of diversification and its effects on company performance.

The main results indicate the complexity of the relationship between diversification and company performance, where success depends on many factors, including the type of diversification, industry specifics, and internal management capacities. These findings have significant implications for theoretical models of diversification and practical management strategies.

Although Serbian defense industry enterprises operate under specific conditions that include high dependence on the state and limited market demand, the application of diversification strategy can significantly improve their competitiveness and sustainability. Diversification of products and markets, investment in new technologies, and improvement of production processes, as well as the development of civilian products, can help these enterprises better adapt to market conditions and achieve better results.

### References:

- [1] ANSOFF, I. H.: *Strategies for diversification*. *Harvard Business Review*, 35(5)(1957) 113-124.
- [2] BAUSCH, A., & PILS, F.: *Product diversification strategy and financial performance: Meta-analytic evidence on causality and construct multidimensionality*. *Review of Managerial Science*, 3(2009) 157–190.
- [3] ĐURIČIN, D., JANOŠEVIĆ, S., & KALIČANIN, Đ.: *Menadžment i strategija*. Beograd: Ekonomski fakultet, (2016) 449– 474.
- [4] KHANNA, T., & PALEPU, K.: *The future of business groups in emerging markets: Long-run evidence from Chile*. *Academy of Management Journal*, 43 (2000) 268–285.

- [5] PALICH, L. E., CARDINAL, L. B., & MILLER, C. C.: *Curvilinearity in the diversification–performance linkage: An examination of over three decades of research*. Strategic Management Journal, 21(2) (2000) 155-174.
- [6] PIERCE, J. R., & AGUINIS, H.: *The too-much-of-a-good-thing effect in management*. Journal of Management, 39(2)(2013)313-338.
- [7] SCHOMMER, M., RICHTER, A., & KARNA A.: *Does the diversification–firm performance relationship change over time? A meta-analytical review*. Journal of Management Studies, 56(1) (2019) 270-298.



## STUDY AND ANALYSIS THERMAL PERFORMANCE OF TAZA GAS POWER PLANT IN KIRKUK –IRAQ

H. J. KHALAF<sup>A</sup>, M. I. QADDOURI<sup>B</sup>

Mechanical Department/ Engineering College/Tikrit University, Tikrit-Iraq

<sup>A</sup> Email: [hameed.j.khalaf@tu.edu.iq](mailto:hameed.j.khalaf@tu.edu.iq),

<sup>B</sup>, Email: [2023mechgr3@st.tu.edu.iq](mailto:2023mechgr3@st.tu.edu.iq)

**Abstract:** In this research, the concept of energy balance was implemented in one of the gas turbine electricity generation units in Iraq (Kirkuk - Taza) K1. The design operating data is taken and compared with the data calculated in the computer model used by Engineering Equation Solutions (EES), and the validity of the model used was confirmed. The results indicate the release of a large amount of thermal energy into the atmosphere due to the open Brayton cycle, as energy losses amounted to 60% of the energy input. The results based on the data of the first unit of the station demonstrated that the theoretical efficiency of the unit is a function of the two variables, which are the temperature of the air entering the compressor and the Turbine inlet temperature: Increasing the compressor inlet temperature leads to a decrease in net power output and first-law efficiency and an increase in the specific fuel consumption rate. Increasing the turbine inlet temperature to 1°C leads to an improvement in both net power output and first-law efficiency by (0.24MW, and 0.04) %, respectively. The results also showed that cooling the air entering the compressor for 1°C leads to improving power output and first law efficiency by (0.72MW, and 0.12%), respectively, and reduces specific fuel consumption by 7.8kg/MWh..

**Keywords:** Compressor, Combustion Chamber, Fuel, Net power, Thermal efficiency.

### 1. INTRODUCTION

The Kirkuk-Taza gas station in Iraq is a significant energy provider with The three types of gas units (K1, K2, and K3) that make up the Kirkuk gas station have a design power of 260 MW, 65 MW, and 283 MW, respectively. Unit K1, equipped with a V94.3A gas turbine, compressor, combustion chamber, and turbine. A portion of the thermal energy contained in flue gas is transformed by the turbine into mechanical rotational energy, which is then transformed into electrical energy by the electrical turbogenerator. The remainder of the heat energy content of an exhaust gas can either cause thermal loss or be efficiently used in a downstream heat exchanger.[1] The natural gas turbine performance may be impacted since the unique atmospheric conditions in Iraq differ from those required by ISO(1 bar, 15 °C, and 60% relative humidity). High temperatures will reduce its power since they will cause the air's mass flow to diminish. Additionally, efficiency declines as a result of compressors needing more power in higher temperatures. The first-law in thermodynamics is applied to any analysis of a thermal system. The first law states that energy cannot be destroyed once it enters a thermal system through heat, work, or mass. However, it makes no mention of internal losses or the quality of energy that reaches the boundaries of the thermal system. Instead, it merely presents the concept of energy conservation[2]. Numerous scholars have examined and evaluated gas

power plants, in addition to the impact of temperature variations on the effectiveness and functionality of gas turbine parts. D. Pinilla Fernandez and et.[3]A study compared the performance of a gas power plant under design and actual operational conditions. Higher compressor inlet temperature led to a decrease in power output and thermal efficiency. For every 1°C rise above 15°C, thermal efficiency drops by 0.06%. Y. Koc and et.[4]An annual exergy study was performed and theoretical calculations were compared with the system's actual characteristics. For both the real and theoretical cases, the cogeneration system's maximum thermal and exergy efficiency were found to be 79.00% and 94.19%, respectively, and 83.92% and 91.64%. A.Mohapatra and et.[5] ,shows that evaporative cooling improves both The specific work of a turbine by 10.48% and the efficiency by 4.6%, while evaporative compression cooling improves the specific work of the turbine and efficiency (18.4 %) and (4.18%), respectively.

## 2. METHODOLOGY TO ENERGY ANALYSIS

The evaluation of the energy analysis for every plant component, as displayed in Figure (1), is carried out in the following manner:

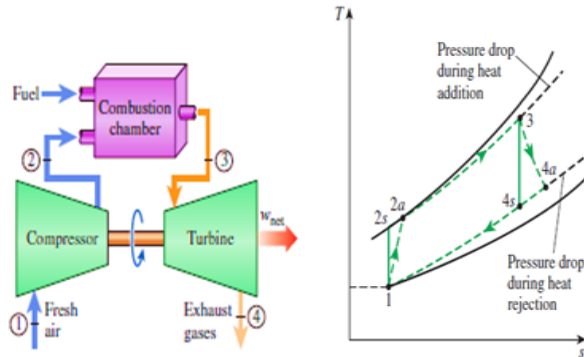


**Fig 1.** Diagrammatic representation of the gas turbine and related Brayton cycle

All the equations are from:[2],[6],[7],[8],[9].

### 2.1. Energy balance of the air compressor

The pressure ratio(rp) for an ideal cycle is as follows:

$$rp = \frac{P_2}{P_1} = \frac{P_3}{P_4} \quad (1)$$

based on the isentropic relation between pressure and temperature:

$$\frac{T_{2,is}}{T_1} = \left(\frac{P_2}{P_1}\right)^{\frac{\gamma-1}{\gamma}} = \frac{T_3}{T_4} \quad (2)$$

In states 1-2,is , the compressor processes air through an isentropic compression process, and work input per unit mass(KJ/Kg) provided by:

$$W_{1-2,is} = W_{c,is} = (h_{2,is} - h_1) = cp(T_{2,is} - T_1) \quad (3)$$

In states 1-2,a, the compressor processes air through an actual compression process, and work input per unit mass is provided by:

$$W_{1-2,a} = W_{c,a} = (h_{2,a} - h_1) = cp(T_{2,a} - T_1) \quad (4)$$

To calculate Compressor isentropic efficiency( $\eta_{c,is}$ )We apply the following relationship:

$$\eta_{c,is} = \frac{W_{c,is}}{W_{c,a}} = \frac{h_{2,is} - h_1}{h_{2,a} - h_1} = \frac{cp(T_{2,is} - T_1)}{cp(T_{2,a} - T_1)} \quad (5)$$

The work rate of the compressor (KW) can be calculated by knowing the air mass flow rate.

$$\dot{W}_{C,is} = \dot{m}_a W_{C,is} \quad (6)$$

$$\dot{W}_{C,a} = \dot{m}_a W_{C,a} \quad (7)$$

The state equation to the ideal-gas can be expressed as:

$$Pv = mRT \quad (8)$$

$$\text{But:} \quad \rho = \frac{m}{v} \quad (9)$$

The density of air can be calculated from:

$$\rho_{air} = \frac{P_1}{RT_1} \quad (10)$$

The mass flow rate of air can be obtained from:

$$\dot{m}_{air} = \rho_{air} \dot{V} \quad (11)$$

### 2.2. Energy balance of the combustion chamber(C-C)

In an ideal process, heat is added to a combustion chamber at constant pressure.

$$P_3 = P_2 \quad (12)$$

mass flow rate of flow gas( $\dot{m}_g$ ) as in the equation:

$$\dot{m}_g = \dot{m}_{air} + \dot{m}_f \quad (13)$$

The supply of heat (KW) for a cycle is provided by:

$$\dot{Q}_{in,cv} = \dot{m}_g (h_3 - h_2) = \dot{m}_g cp(T_3 - T_2) \quad (14)$$

The combustion of heat rate  $Q_{in}$  (kw) For a cycle is provided by

$$\dot{Q}_{in} = \dot{m}_f LHV \quad (15)$$

To calculate Combustion chamber isentropic efficiency( $\eta_{c,is}$ ) We apply the following relationship:

$$\eta_{cc} = \frac{\dot{Q}_{in,cv}}{\dot{Q}_{in}} \quad (16)$$

The air fuel ratio equation (AF):

$$AF = \frac{\dot{m}_{air}}{\dot{m}_f} \quad (17)$$

### 2.3. Energy balance of the turbine

In states 3-4,is , the turbine processes air through an isentropic expansion process, and Work out put (KW) provided by:

$$\dot{W}_{3-4,is} = \dot{W}_{T,is} = \dot{m}_g (h_3 - h_{4,is}) = \dot{m}_g cp(T_3 - T_{4,is}) \quad (18)$$

In states 3-4,a , the turbine processes air through an actual expansion process, and work out Put (K) is provided by

$$\dot{W}_{3-4,a} = \dot{W}_{T,a} = \dot{m}_g (h_3 - h_{4,a}) = \dot{m}_g cp(T_3 - T_{4,a}) \quad (19)$$

To calculate turbine isentropic efficiency( $\eta_{T,is}$ ) We apply the following relationship:

$$\eta_{T,is} = \frac{W_{T,a}}{W_{T,is}} \quad (20)$$

Heat rejected can be calculated by:

$$\dot{Q}_{out} = \dot{m}_g (h_4 - h_1) \quad (21)$$

### 2.4. Energy balance of the cycle

It is possible to calculate the open ideal gas turbine cycle's efficiency as:

$$\eta_1 = \frac{\text{NetWorkOutput}}{\text{HeatSupplied}} = \frac{W_T - W_C}{Q_{in}} \quad (22)$$

" The fraction of the turbine work used to drive the compressor is called the back work ratio " [2]

$$B.W.R = \frac{W_C}{W_T} \times 100\% \quad (23)$$

To estimate of the specific consumption of fuel (SFC) Kg/kw.h is as follows:

$$SFC = \frac{\dot{m}_f \times 3600}{\dot{W}_{net}} \quad (24)$$

**Table1** properties for the fuel-gas used in a gas-turbine power plant at Taza-Kirkuk.

fuel type	fuel gas	
Composition % by volume	METHANE	85.930%
	ETHANE	12.033%
	PROPANE	1.8020%
	N_BUTANE	0.1235%
	I_BUTANE	0.0790%
	N_PENTANE	0.0107%
	I_PENTANE	0.0121%
	H <sub>2</sub> S	0.0007%
LHV	37.7 MJ/m <sup>3</sup>	
DENSITY	0.6 kg/m <sup>3</sup>	

\*for ISO conditions only 100% CH<sub>4</sub> is considered

**Table 2** Siemens (SGT5-4000F, V94.3) Gas Turbine Model Specification (Standard and Predicted by the Present Thermodynamic Model).

	Standard value .[10]	Predicted by the present model	Error %
Compression ratio( rp)	17	17	-
Thermal Efficiency. %	39.8	39.77	0.07
Net power output. MW	265	264.4	0.23
Volumetric flow rate . m <sup>3</sup> /sec	555 (max.)	540	2.7
Air mass flow rate. kg/s	650 @250MW	661.8	1.82
Fuel mass flow rate. kg/s	14.5 @250MW	14.77	1.86
Firing Temperature, C <sup>0</sup>	1200-1390	1248	-
Temperature of Exhaust gas. C <sup>0</sup>	577	567	1.7

### 3.RESULTS AND DESCUSSION

All equations utilized in this study were solved using computer software "Engineering equations solving" (ESS). The values generated in the software and the standard design values for the Taza-Kirkuk gas station in ISO circumstances, where the error rate was modest and acceptable not to exceed 2%, were compared in **Table 2** of the research.

The energy distribution among the plant equipment is depicted in **Figure 2**. These distribution is limited to ISO operating conditions for full load. The energy and energy sources provided to the plant are represented by the fuel input. 40% of the energy intake is accounted for by the power output. The plant's first-law efficiency is defined by this percentage. 60% of the fuel energy is released into the atmosphere by the plant as exhaust gasses. This implies that if there is a chance to improve plant performance, it will undoubtedly occur in this area of the unit.

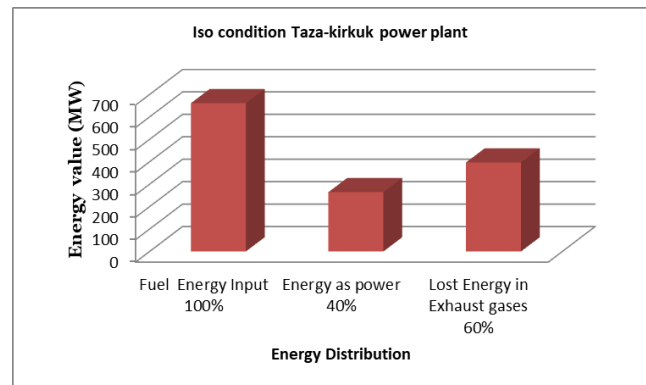


**Fig. 2** Energy (MW) Distribution in Taza-kirkuk gas turbine power plant components operating.

In **Fig. 3** The real data produced from the station and the values estimated in the software display the inverse connection between the temperature of the air entering the compressor and the power production over 2023. The greatest power production recorded in February, at 10.2 °C, was 218.9 MW for the computed data and 216.7 MW for the real data. The computed and actual data's poweroutput figures dropped to 198.129 MW and 196.88 MW, respectively, in August, when the compressor's intake air temperature was 37.8 C. The compressor requires more effort from the net because a rise in temperature causes a drop in density and an increase in specific volume. These outcomes are comparable to those seen in:[11]



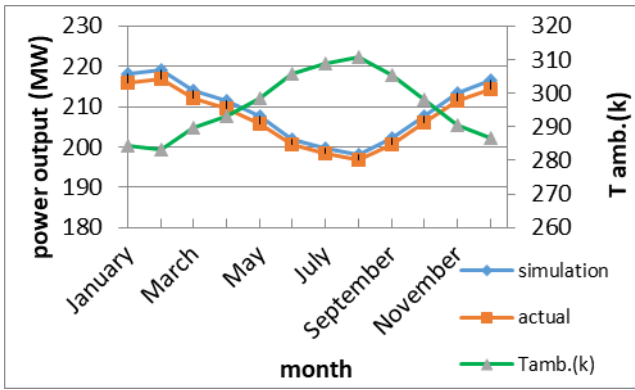


**Fig. 3** Power output with ambient temperature for 2023 (actual and simulation data).

**Fig. 4** shows demonstrates the relationship between the ambient temperature and the thermal efficiency( actual and simulation) which is the true measure of the turbine's performance, is equal to the quotient of the amount of energy produced by the fuel consumed According to equation (21),In February, at a temperature of 10.2°C, the highest thermal efficiency of the gas turbine was 36.38, 36.01 for the actual and calculated data, respectively. And in the summer, when the temperature rose to 37.8°C, the efficiency decreased to 32.7, 32.91 for the actual and calculated data, respectively These outcomes are comparable to those seen in : [12]

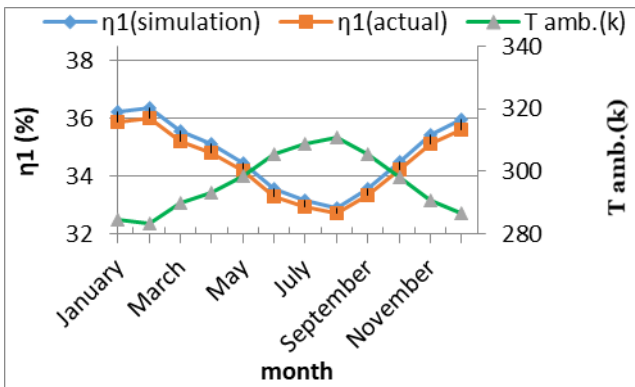


**Fig. 4** Thermal efficiency ( $\eta_1$ ) with ambient temperature for 2023 (actual and simulation data).

**Fig.5** shows the correlation between the specific fuel consumption (SFC) which is obtained in equation (24) and the air temperature entering the compressor. An increase in the compressor's intake air temperature causes the mass flow rate at the compressor input to drop at a constant compression ratio, which raises SFC. February is when the value hits (0.198,0.199) Kg/Kw.h. during the winter. It increases to (0.219, 0.22) Kg/Kw.h for (real and simulation data respectively) in the summer (August). These values are nearly identical to the ones found in:[13].

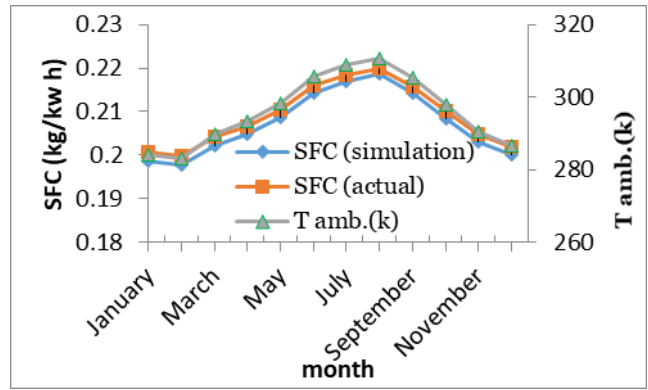


**Fig. 5** specific fuel consumption (SFC) with ambient temperature for 2023 (actual and simulation data).

When summertime temperatures are 36 °C, the compressor's air conditioning system is activated. The hottest temperatures ever recorded in 2023 happened in August, and they peaked between 10 a.m. and 2 p.m. The system operates to lower the temperature at the compressor inlet at a rate of 11.1–15.2 °C when the air temperature varies between 36 and 49 °C, according to average real readings recorded between 8 a.m. and 4 p.m. It was discovered that decreasing 1 C increases power output by (0.72, 0.75) MW and raises the first law's efficiency by( 0.12%, 0.13%) for the actual and computed data, respectively, as in Figs. 6- (a&b)

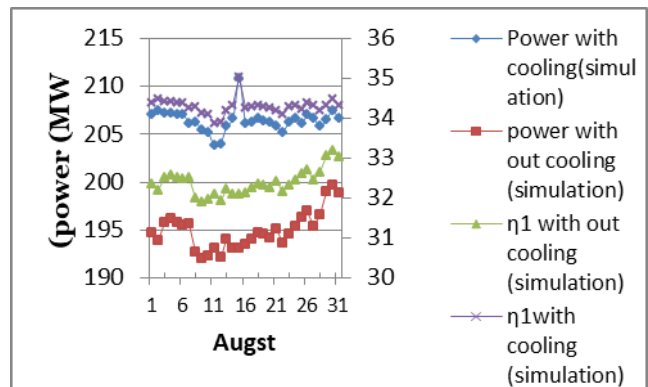


**Fig.6-a** Gas turbine net power output and  $\eta_1$  with and without cooling system for August 2023.(simulation data).

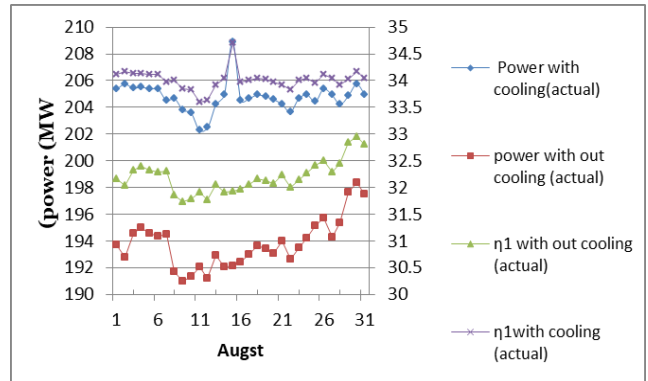


**Fig.6-b** Gas turbine net power output and  $\eta_1$  with and without cooling system for August 2023.(actual data)

**Figs.7-(a&b)** They show that the average specific fuel consumption decreases by (0.0078, 0.00815) kg/kWh for the actual and calculated data, respectively, for August, for each decrease of 1 C°.

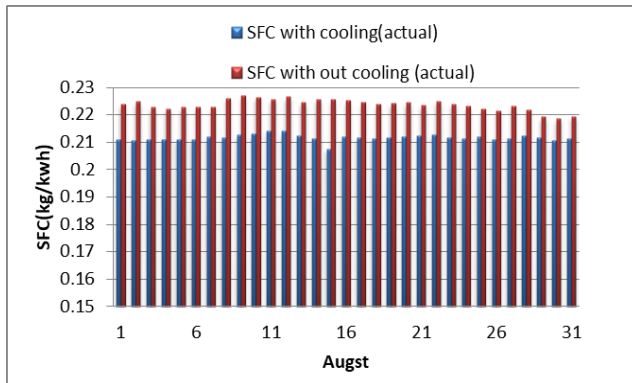


**Fig.7-a** SFC with and without cooling (actual data)

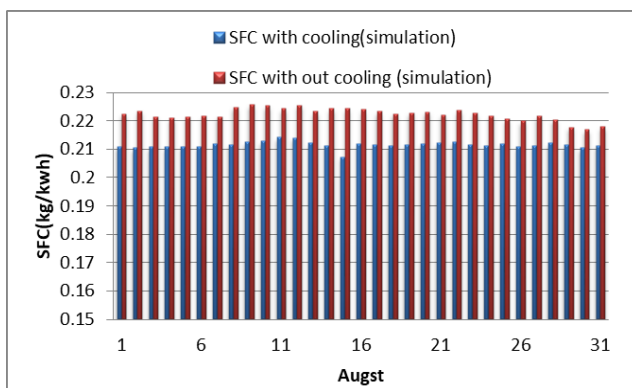


**Fig.7-b** SFC with and without cooling (simulation data).

The **Fig.8** illustrates how the first law's efficiency and net power production are directly correlated with the temperature at the inlet of the turbine. An increase of one degree Celsius in the turbine's intake temperature results in a corresponding increase of 0.24 MW and 0.04 % in net power production and efficiency.

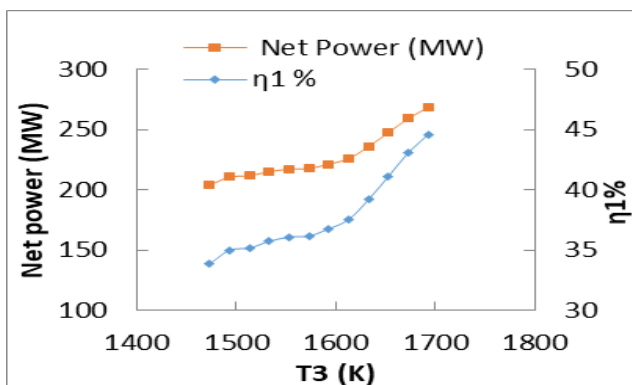


**Fig.8** Turbine inlet temperature with  $\eta_1$  and net power output during 2023 (simulation data).

## 4.CONCLUSIONS

The main conclusions of the present study could be summarized as follows:

- The energy balance in the Kirkuk-Taza gas

station was able to measure the amount of energy losses, which amounted to 396.6 megawatts (60%), which goes with the exhaust gases in the open cycle.

- A rise in the compressor inlet temperature causes the specific fuel consumption rate to rise along with a fall in net power output and first-law efficiency.
- Reducing specific fuel consumption by 7.8kg/MWh and increasing power output and first law efficiency by 0.72MW and 0.12%, respectively, are the results of cooling the compressor's intake air by 1c°
- The first law efficiency and net power production both improve by 0.24 MW and 0.04%, respectively, with a 1C° increase in the turbine inlet temperature.

## NOMENCLATURE

$C_p$  Specific heat at constant pressure(kJ/kg.K)

$h$  Specific enthalpy, (kJ/kg)

$r_p$  pressure ratio

$T$  Temperature, °C

$P$  pressure, kpa

$w$  Work, kJ/kg

$\dot{W}$  Power or work rate(kw)

$\dot{m}$  Mass flow rate, (kg/s)

$R$  Gas constant [kJ/mol – K]

$m$  mass (kg)

$v$  volume (m<sup>3</sup>)

$\dot{v}$  volumetric flow rate(m<sup>3</sup>/s)

L H V Lower heating value (kJ/kg)

$\dot{Q}$  Heat rate, (kw)

B.W.R back work ratio

SFC specific fuel consumption(kg/kw.h)

## Greek symbols

$\rho$  Density, (kg/m<sup>3</sup>)

$\gamma$  Adiabatic index

$\eta_1$  First law efficiency

## Subscripts,

$amb$  Ambient

$in$  Input

$out$  Outlet

$cc$  Combustion chamber

$c$  Compressor

$is$  Isentropic

$a$  Actual

$T$  Turbine

$f$  Fuel

$CV$  Control volume

$g$  Flue gasses

1 At compressor inlet

2 At compressor outlet

3 At gas turbine inlet

4 At exhaust

## References

- [1] E. Basics, E. Components, A. Systems, and G. T. Operation, "GTPP Biskra - Algeria Basic Training Plant Operators & Maintenance Staff," 2016.
- [2] YUNUS A. ÇENGEL and MICHAEL A. BOLES, *THERMODYNAMICS: AN ENGINEERING APPROACH, EIGHTH EDITION*. doi: 10.1007/978-94-009-4185-4\_1.
- [3] D. A. Pinilla Fernandez, B. Foliaco, R. V. Padilla, A. Bula, and A. Gonzalez-Quiroga, "High ambient temperature effects on the performance of a gas turbine-based cogeneration system with supplementary fire in a tropical climate," *Case Stud. Therm. Eng.*, vol. 26, no. April, p. 101206, 2021, doi: 10.1016/j.csite.2021.101206.
- [4] Y. Koc, O. Kose, and H. Yagli, "Exergy analysis of a natural gas fuelled gas turbine based cogeneration cycle," *Int. J. Exergy*, vol. 30, no. 2, pp. 103–125, 2019, doi: 10.1504/IJEX.2019.102162.
- [5] A. K. Mohapatra and Sanjay, "Comparative analysis of inlet air cooling techniques integrated to cooled gas turbine plant," *J. Energy Inst.*, vol. 88, no. 3, pp. 344–358, 2014, doi: 10.1016/j.joei.2014.07.006.
- [6] S. A. Salah, E. F. Abbas, O. M. Ali, N. T. Alwan, S. J. Yaqoob, and R. Alayi, "Evaluation of the gas turbine unit in the Kirkuk gas power plant to analyse the energy and exergy using ChemCad simulation," *Int. J. Low-Carbon Technol.*, vol. 17, no. April, pp. 603–610, 2022, doi: 10.1093/ijlct/ctac034.
- [7] A. Figueiró, *Advanced Gas Turbine Cycles J. H. Horlock F.R.Eng., F.R.S. Whittle Laboratory Cambridge, U.K. 2003*. 2003 An imprint of Elsevier Science AMSTERDAM \* BOSTON . HEIDELBERG . LONDON . NEW YORK OXFORD . PARIS \* zyx, 1967.
- [8] M. Shamoushaki and M. A. Ehyaei, "Exergy, economic, and environmental (3E) analysis of a gas turbine power plant and optimization by MOPSO algorithm," *Therm. Sci.*, vol. 22, no. 6PartA, pp. 2641–2651, 2018, doi: 10.2298/TSCI161011091S.
- [9] A. De Sa and S. Al Zubaidy, "Gas turbine performance at varying ambient temperature," *Applied Thermal Engineering*, vol. 31, no. 14–15, pp. 2735–2739, 2011. doi: 10.1016/j.applthermaleng.2011.04.045.
- [10] Avio, "Avio Gas Turbine Package Application Handbook," no. November, 2016.
- [11] W. S. Mohammed and A. H. M. Habbo, "The Effect of The Change In The External Environment Temperature On The Performance of Al-Qayyara Gas Station," *J. Therm. Eng.*, vol. 6, no. 3, pp. 21–25, 2020, doi: 10.14445/23950250/IJTE-V6I3P105.
- [12] A. H. Ahmed, A. M. Ahmed, and Q. Y. Hamid, "Exergy and energy analysis of 150 MW gas turbine unit," *J. Adv. Res. Fluid Mech. Therm. Sci.*, vol. 67, no. 1, pp. 186–192, 2020.
- [13] M. Elwardany, A. E. M. M. Nassib, and H. A. Mohamed, "Comparative Evaluation for Selected Gas Turbine Cycles," *Int. J. Thermodyn.*, vol. 26, no. 4, pp. 57–67, 2023, doi: 10.5541/ijot.1268823.



## DEFENSE ACQUISITIONS AND INTERNATIONAL POLITICS

MARKO JOVANOVIĆ, GORAN VUKADINOVIĆ  
SECTOR FOR MATERIEL RESOURCES MOD RS, Belgrade, [ma.markoj@gmail.com](mailto:ma.markoj@gmail.com)

**Abstract:** *This paper defines the relations between defense acquisitions and international politics in the modern framework of international relations. The goal is to explain theoretical concept in which armaments acquisition can be scientifically defined and the impact this important subject has on relations between states in the 21<sup>st</sup> century.*

**Keywords:** *defense, armament, acquisition, international politics, international relations.*

### 1. INTRODUCTION

As the first human societies started to come across each other, conflicts between them started to occur. After the first states were formed they continued to clash and the latest events in the 21<sup>st</sup> century, unfortunately, shows us that those clashes are still happening and that they will continue to happen in future. War has been and still is an important tool of international politics and states have shown numerous times that they will use their power to achieve goals even if that leads to war and other types of conflicts.

A question "What are the causes of war?" has been frequently asked among scholars, especially after the First World War when humanity was shocked by the devastation it caused. Many different theories have been researched and developed trying to explain the causes of war. For example, the First World War has started after Austro-Hungarian Empire declared war to Serbia because the Austrian Archduke, Franz Ferdinand, was assassinated in Sarajevo and this event constituted the most immediate cause of war. When we take a step back, we can conclude that causes of war were much complex and more numerous. Less than ten years before the war couple of events have happened that shook the international relations between the great powers of that time. Austro-Hungarian Empire has annexed Bosnia (Annexation crisis 1908), Germany and France clashed over the control of Morocco (The Second Moroccan Crisis 1911), etc. Geopolitical situation of that time was complex and the great powers were preparing for war, what they needed was only a spark to pursue their goals by force. The explanation of this type of behavior of the great powers was best explained in [1] by defining the theory of offensive realism which argues that anarchy of the system of international relations urges states to compete with other states in obtaining more power. No amount of power is enough because other states also have power, offensive military capabilities, and states can't be sure that others will not use their power against them. This leads to a race between the states to become the most powerful state (hegemon) and clashes, conflicts and eventually

wars will be the means used to obtain the power. We are now witnessing events across the world which confirms this theory and we can conclude that it is still valuable as a basis for research of international politics.

Bearing in mind the basic idea of the theory of offensive realism, that states are looking to obtain the biggest amount of power, and that war is not outdated as the mean to obtain power, conclusion is that states have to be prepared for war now and in the future. Obtaining military power is the most important part of the preparation for war and acquisition of defense materiel is the first step for boosting the state's military power. The goal of this paper is to define acquisition of defense materiel through term and definition, present some models of acquisition and explain the theoretical framework in which defense acquisitions can be defined in relation to international politics.

### 2. ACQUISITION OF DEFENSE MATERIEL

#### 2.1. Term and Definition

As we have already stated in the introduction, one of the goals of the state is to obtain military power and the best way to do so is through acquisition of defense materiel. There are different ways to acquire armaments for armed forces and they differ due to economic and technological development of the state. Highly developed countries have the capacity necessary to research, develop and produce defense materiel and they rely on their domestic defense industry to acquire armaments for their armed forces thus being self-sustaining in this field. Other states don't have the industrial capacity needed to produce armaments and turn to other states in order to procure defense materiel from their defense industries. Those countries with developed defense industries, after equipping their own armed forces, look into the possibilities to deliver armaments to armed forces of other states. Motives for this could be financial but when it comes to selling and buying weapons it is never strictly financial. States can spread their influence by delivering armaments to other states and sometimes their goal could

be to increase the military power of other state, that is why lucrative motives can sometimes be casted aside and states sometimes donate defense materiel to other countries.

By explaining what we mean under term acquisition of defense materiel we came closer to definition of this term. Bearing in mind that the goal of this paper is to explain the theoretical framework in which defense acquisitions can be defined in relation to international politics definition of the acquisition of defense materiel for the purpose of this paper shall exclude all those elements of the acquisition which do not include at least two states. Also, besides the procedure of equipping own armed forces, we included the procedure of equipping armed forces of other states as mentioned above. Therefore, and in order to define the main subject of this paper we will try to give concise and precise definition as follows:

"Acquisition of defense materiel represents the process of procuring or supplying defense materiel between supplying state and receiving state with the goal of equipping armed forces of the receiving state."

This definition covers different acquisition processes which include at least two states, supplier and receiver, and depending on position it can be procurement, from the receiver's point of view, or delivery, from the supplier's point of view. To further clarify this definition, it also includes delivery of armaments by the defense company from one state to another state because this process, having in mind it's sensitivity and international implications it can have, never happens without the authorization of the government of the defense company's state.

## 2.2. Acquisition models

States used to equip their armies with their own resources because conventional armament was simple to make and it was easy for the states to produce enough for their armies. Later when industrial revolution took place and technology developed fast, some states managed to keep up with the development pace and those states become suppliers while other states become receivers of defense materiel. In this paper we will explain models of acquisition when at least two states are involved and we will use different criteria to distinguish different models.

Money is the power that pushes the world forward and therefore it plays a significant role in armament acquisition processes. Therefore, we can distinguish two different models of acquisition depending on the fact if receiver state is paying for the armament or not: donation and selling. By donating defense materiel to other state and equipping its defense forces, the supplier enlarges the military power of the receiver and does not receive any financial benefits in return. Examples of donation of armaments can be found in Serbian history. During the second half of the 19<sup>th</sup> century, Serbia was preparing for the liberation from the Ottoman Empire and the Russian Empire donated 40.000 rifles to Serbia in 1862. Besides this donation, Serbian forces equipped themselves with 20.000 rifles more in 1867 and those rifles were

purchased from Russia [2]. Donation as an acquisition model still plays an important role in modern international politics. Some great powers have developed an institutional framework for donation of armaments, for example the United States of America has developed the Foreign Military Financing (FMF) program under the auspices of the United States Department of Defense. FMF allows foreign armies to request defense materiel from the United States government and after thorough procedure the US government can finance acquisition of defense materiel by foreign states through grants or loans. This type of program represents an institutional approach to donation; the procedure is strict and could last long. On the other hand, after the Ukrainian conflict has started, we witnessed through news and other open sources information that procedure for donation of defense materiel could be very prompt when the goal is to quickly improve the military capabilities of an army involved in conflict. Therefore, donation as an acquisition model can have a very high impact on the international relations between involved countries. The fact that there are no financial benefits for the supplier implicates that motives behind the donation are strictly geopolitical such as providing more military power to other state and by that helping that state defend itself or threaten its rivals. Because of its possible implications on international relations, donation firmly depends on international relations between the country donating the materiel and the country receiving the materiel, as well as the countries with complex international relations with the receiver country.

Selling and buying of the defense materiel, on the other hand, is not solely connected with the international relations of the countries. Even though there are financial motives connected with selling and buying, when it comes to armaments international politics has to be involved. For example, when buyer buys some goods, he looks for quality, good price and his goal is to receive the goods as soon as possible. Seller, on the other hand, wants to sell the goods which he can produce quickly with reasonable funding, to get the best price for them and to get the money as soon as possible. These motives are all of the economic nature and they exist in the process of selling and buying of armaments but they are accompanied by geopolitical motives. States involved in selling and buying of the defense materiel have to analyze how this selling or buying could affect their international relations. Receiving state has to analyze the market and find potential suppliers because the supplier is going to look into the effects that this transaction has on its international relations, therefore supplier will not sell armaments to every state that requests it. Some elements of international relations of the seller and the buyer highly affect their decision to sell or buy armaments. For example, the seller will closely analyze and thoroughly examine the consequences of selling weapons to the state which is at war. This could be seen as an aid to one side in conflict and could roughly impact the seller's international relations with other states involved in conflict. With this possible outcome, seller will put its geopolitics motives above its financial motives in this type of processes. Modern international relations are

influenced by international institutions such as United Nations or Security Council and these institutions have the ability to impose sanctions on states. International sanctions can also have an impact on the selling and buying of defense materiel and vice versa, acquisition of defense materiel can cause the state to undergo international sanctions. Selling armament to a state that is under sanctions or embargo and opposing the decision of international institutions can cause measures against the seller, also buying from a state that is under sanctions can cause measures against the buyer. States are reasonable actors on the world stage and they make decisions which they believe would benefit them, therefore strictly financial motives such as earning money or acquiring the best model of armament are easily overcome by higher motives in connection with international relations of the country.

Acquisition models can also be divided based on the fact what is being delivered, armament itself or the tools to produce armaments. If supplier delivers armaments, for example infantry fighting vehicles, we are talking about direct delivery. Direct delivery is the most common way of armaments acquisition and it allows the receiver state to have the weapons in its hands as quickly as possible accompanied by other materiel, spare parts, ammunition and necessary services. After direct delivery process is completed, receiver state's army has that weapon in its equipment; they have been trained to use it and to maintain it in future.

Indirect delivery, on the other hand, represents a model where supplier state transfers technology for development and production of defense materiel to receiver state or improves industrial capacities of the receiver state's industry for production of defense materiel. Indirect delivery doesn't have an immediate effect on equipping the armed forces of the receiver state but after some period of time the state receives the capability to independently produce that type of defense materiel making it independent on other state's desire to sell to it. There is also another positive effect of the indirect delivery and that is the possibility to sell that type of defense materiel to other countries in future.

Direct and indirect delivery sometimes interfere, when a country buys defense materiel that procedure can also include indirect delivery like transfer of technology. Offset is also common in defense acquisitions. Offset represents the model where buyer receives additional capacity in industrial or technological field while acquiring defense materiel. Offset is specific because the buyer does not pay additional money for increase in its capacity, but the price for offset is included in the price of acquisition. Lastly, offset is specifically defined in legislations of some countries.

Differences between direct and indirect delivery and their effect on international politics can be best observed when it comes to delivery of complex weapon systems and nuclear weapons. Indirect delivery of technology and capacities for production of complex weapon systems and nuclear weapons, thus providing receiver country with the capability to produce and use those weapons can have

higher impact on international relations. This is specifically important when it comes to nuclear weapons because direct delivery of nuclear weapons didn't happen before but there were cases of indirect deliveries of technology, dual use goods or equipment necessary for nuclear weapons production. Direct delivery of complex weapon systems to a country which is not under sanctions or at war could also raise eyebrows because it can disrupt the balance of powers, but indirect delivery always has more significant implications.

All of the models of defense acquisition mentioned before can have impact on international politics and relations but the effect depends on geopolitical situation in which the states involved in transaction are at the current moment. That is why we will try to further explain modern international relations in the following paragraphs.

### **3. MODERN INTERNATIONAL RELATIONS**

#### **3.1. Time determination**

In order to determine what modern international relations, represent we have to determine the time which is the subject of our interest in this paper. The term "modern" implicates that we are referring to something new, something happening now or in the recent past. Having in mind that the paper is written in 2024, during the first quarter of the 21<sup>st</sup> century, it is appropriate to include the 21<sup>st</sup> century in the scope of this work. Regarding the 20<sup>th</sup> century it was hard to develop international politics and international relations during this period bearing in mind the two world wars that occurred and devastated the world followed by The Cold War and the period of bipolarity in international politics. The world was divided between two great powers working against each other in a frozen conflict that affected every part of the world and international relations between the states. Even though the world was devastated by two world wars and afterwards the states tried to avoid something like that in future by forming international institutions like the United Nations, international relations were promptly disrupted and various conflicts occurred during The Cold War. When The Cold War ended, states once again tried to articulate the future international politics through institutions and international agreements aimed at avoiding conflicts and arms race and improving international relations. With this explanation provided we are determining modern international relations to include period from the end of the Cold War (December 26<sup>th</sup> 1991) until today, and with the goal to be useful in future scientific researches.

#### **3.2. Theoretical determination**

Theories are important building blocks for scholars and choosing the right theoretical path is very important when we try to reach conclusion on some topics. We have already mentioned theory of offensive realism as a structural theory of international politics which explains the offensive behavior of states. Besides this theory there are other theories which have been developed as

foundations of the science of international relations. In order to enrich the scientific research, we need to provide a framework in which the research will take place, together with starting presumptions from which the conclusions are being derived. This means that researchers need to think theoretically and apply theoretical presumptions and paradigms on which the future research shall be based. Two basic theories of the science of international relations that will be presented below are liberalism and realism with their variants.

Liberalism started to develop between the two wars as a counterpart to national-socialism which defined the priority of state in relations with an individual and advocated for the war to be valid mean for achieving goals. On the other hand, liberalism advocated for reason and moral in international relations, which liberal scientists believed could create better world in future. The ideas derived from liberal thinking were such as the idea of creating international institutions with the goal to form and protect the system of collective security. Then the idea of concluding international agreements and creating international legal tools for peaceful resolution of conflicts. Those who based their scientific work on liberalism also argued that developing economic cooperation between the countries and mutual economic dependence could lower the possibility of conflict between those states. There was also an idea that democratic states do not go to war with each other and that states which have McDonald's, a fast-food chain, do not go to war with each other. Because of the predominant idea of avoiding conflicts and wars, those ideas were sometimes described as idealistic.

Realism, on the other hand, presents a theory which accepts the fact that conflicts and wars between the states are not avoidable. States are trying to acquire the maximum amount power in the system of international relations, the same as they are trying to acquire the maximum amount of money in economic relations. There is no limit for the amount of wealth and there is no limit for the amount of power to be obtained by states. As given in [1], power is the currency of the great power politics and states compete for it. In order to obtain the maximum amount of power states interfere with each other and conflicts arise, therefore conflicts are not avoidable and wars are legitimate means of politics in international relations. This insight deriving from realism is directly in conflict with the liberal insights.

If we compare realism and liberalism, we can see there are many similarities between those two theories. Both theories are based on similar starting ideas and afterwards differ with each other regarding the conclusion on what are the causes that influence state's decisions in international politics. Basic characteristics of realism and liberalism are given in Table 1 below:

**Table 1.** Realism and Liberalism, basic characteristics

Theory	Realism	Liberalism
I	System of international politics is anarchic	
II	States are the main actors in international politics	
III	States strive to achieve their goals	
IV	States act in accordance with factors coming from the outside	States act in accordance with factors coming from the inside
V	Competition for power is the main goal	Political and economic cooperation is the main goal

When we analyze similarities and differences between those two theories, we can conclude that realists and liberals agree that international arena is anarchic and that states, as its main players, strive to achieve their goals. Then we have different conclusions on the idea why and how will states act in order to achieve their goals. When it comes to why realists point out external factors which affect the states like influence from another state and liberals emphasize internal factors like political system of that state (democracy). Another difference between realism and liberalism is on how will the states act when it comes to achieving their goals. Realists believe that the states will always compete for more power even when that means conflict with other states and liberals point out the idea that states will choose political and economic cooperation over accumulating power. Liberal theories gave different ideas to explain why and when will states opt out of accumulating power and avoid conflicts to enhance cooperation. For example, theory of liberal peace points out trade as an important factor and developed free market as a condition for peace, while theory of democratic peace argues that democracies do not go to war with each other, as we have already mentioned before. There is also an idea of neoliberal institutionalism which emphasizes the role of international institutions in keeping the peace between the states. Realists on the other hand start from the idea that every state in given circumstances will act the same and that it will pursue the maximum amount of power whenever it can no matter the political system of the state or free market. Achieving power is the main goal of every state and institutions and economic correlations will not stop the states in pursue for power, therefore conflicts are imminent. If we turn on the TV or read the news, we can see a brutal revelation that international institutions and economic correlation between the countries failed to develop peace and peaceful resolution of conflicts. Therefore, we can conclude that realism gives better basis for research of international relations in the 21<sup>st</sup> century and along with that we can conclude that realistic behavior of the states affects the subject of this paper, defense acquisitions.

When states compete for power, they try to enlarge their own military strength in order to achieve their goals easier and therefore they try to equip their forces with defense materiel through different models of acquisitions.

Realistic theories, which are based on the before mentioned assumptions, differ in definitions of what is the cause for the states to compete for power. Realism is based on the security dilemma, which is a situation in which actions taken by one entity in order to increase its own security cause reactions from other entities, which in turn lead to a decrease rather than an increase in security. The first mention of something similar to security dilemma occurred in relation with Peloponnesian war (5<sup>th</sup> century BC) when Tucidid wrote about this war and explained that Athens' growth in power generated a disturbance in Sparta, causing the war in the end. Classic realism points out the personality of humans and their inborn trait to strive for power. When a person becomes a state leader that inborn trait is carried on onto his decisions and the leader act in the way to fight for more power for his state. Thomas Hobbes, in his work *Leviathan*, wrote about the individuals and their conflicts with the idea that individuals live in an anarchy so they unite in a state in order to transfer the power to the state (*Leviathan*). But afterwards the conclusion is that conflicts and competition for power are then transferred to the states. Defensive realism argues that states have to fight for power in order to ensure their survival and when this is achieved the states try to control the situation and keep the balance of power. Offensive realism, the theory already cited in this paper, also emphasizes that the fight for power is necessary in order for the state to secure its survival. The difference between offensive and defensive realism is in the fact that offensive realism does not recognize the balance of power as a possibility. States strive to obtain the maximum amount of power no matter the fact that maybe at that moment that state is the most powerful. The goal of the state is to become hegemon, therefore the most powerful state in the world.

As explained before, our vision is that offensive realism has the best chance to explain the system of international politics now and in the future, therefore we will try to present the theory of offensive realism in more details. Basic hypotheses of offensive realism were first set by John Mearsheimer in [1]. The first hypothesis is that the system of international politics is anarchic in the way that in this system states play the most important role and that there is no higher authority above the states which can control their behavior and prevent clashes. International institutions and international agreements and other legal documents failed in creating a sustainable system of checks and balances between the states. The second hypothesis is that all states possess military power, some of them bigger amount and some of them smaller amount of it. Use of that power in order to achieve goals defined by that state can jeopardize other states. The third hypothesis is that no state can be certain of the goals defined by other states therefore it can't be certain what means will other states use in order to achieve those goals. Intentions of one state are a mystery for other states, and this is one of the best reasons why intelligence

and espionage exists. The fourth hypothesis is that the main goal of all states is assuring their own survival and with this goal states are similar to every other individual. Finally, the fifth hypothesis is that every state is a reasonable actor on the world stage taking actions which are aligned with its goals. When you take all five hypothesis or assumptions, they produce two important occurrences in international relations between the states. The first occurrence is the sense of fear and mistrust between the states which brings us back to security dilemma mentioned earlier. Because of this, states understand that the best way to ensure their survival is self-help and that the ultimate goal should be to become the hegemon, the most powerful state in the system. In order to achieve this the states not only try to upgrade their own power but they also try to minimize the power of other states and to prevent other states to become the most powerful one. If a state succeeds in this and becomes a hegemon that will ensure its survival on a long-term basis and achievement of its goals.

Because of the anarchy that rules the system of international politics, one state with the highest amount of power could define the rules and dictate the actions. This idea dictates the behavior of states in modern international relations and urges them to obtain more and more power and the most important power of them all is the military power.

#### 4. CONCLUSION

Theoretical determination of the international relations provided us with clearer view of the causes, motives and actions taken by the states. We are aware that we live in an unstable world where wars are being fought at every moment. Complex geopolitical processes have broader influence on every aspect of our lives in the 21st century than ever before. Events that happen far away across the globe transfer their effects rapidly to every corner of the world because of the relations and connections between the states and individuals. In this global world we need to pay more attention to causes and implications which occur from some events and all of the main aspects of everyday life, business, trade, cooperation etc. we have to observe from the height of globalization.

Defense acquisitions, as one of the forms of business, trade and cooperation between the states we ought to observe from the global point of view among the international relations. International relations influence defense acquisitions and defense acquisitions influence international relations and international politics. Because of these effects of the defense acquisitions, they attract more and more attention in the modern world. The first of all is political attention, defense acquisitions are always under the eye of states and their political background and effects are thoroughly observed. Media are also turning their full attention to defense acquisitions especially in the era of modern conflicts that happen today. Newspapers, magazines and TV shows report about the realized or possible acquisitions of armament and in the world dominated by internet numerous You Tube channels and forums discuss about this topic frequently. We can also say



that interest of ordinary people for this subject is increased and the possible reason why individuals are interested in this topic could be the question why is someone arming its defense forces and what could be the intentions behind that.

When we perceive that acquisition of defense materiel has become the point of interest for both media and individuals than we can undoubtedly conclude that states and international institutions are highly interested in this subject as the main actors of the international politics. After The Cold War the international institutions tried to regulate armaments acquisitions with international agreements and other legal documents. For example, Missile Technology Control Regime is an informal political understanding between states which aims to control the proliferation of defense materiel in relation to rocket technologies and it was later broadened to include unmanned vehicles and weapons of mass destruction. Then we have Treaty on Conventional Armed Forces in Europe which was negotiated and concluded between the NATO and the Warsaw Pact states with the aim to limit the conventional armed forces in Europe and to define an obligation for the member states to destroy their surplus defense materiel. Russia suspended its participation in this Treaty in 2007, in 2015 Russia halted its participation and withdrew from the Treaty in 2023. This withdrawal was followed by United States and its NATO allies suspending their participation in the Treaty. This example showed that even though many international treaties and agreements, formal and informal, were negotiated, concluded and signed but they never succeeded in establishing control over the state's actions in defense field. Even without formal withdrawal, many states violated the norms of the treaties they signed which lead us into conclusion that the system of international politics failed to define and construct the norms which will regulate this area.

When we take into the account the importance of defense acquisitions in the 21<sup>st</sup> century and the inability of international system to control this area, we can conclude that defense acquisitions will continue to influence the international relations in future. Because the war has been and will be the tool of international politics, military cooperation will be the most important form of cooperation between the countries, with defense acquisitions as the most important element of this cooperation. As it was given in [3], Machiavelli concluded in his work "The Prince" that without the force, armed force, no state can be permanent. In order to achieve its goals, the state has to obtain military power and the best way to obtain military power is through procurement of defense materiel. Acquisition of defense

materiel in today's world where the theory of offensive realism prevails allows the state to expand its political influence by increasing its military power or by increasing military power of other states. Even if the state is not at war and if it never uses war as the way to achieve its goals, defense acquisitions allows the state to expand its influence through other means, for example economic or diplomatic. Strong military power has another effect on international relations which is called deterrence. Other states will probably give up on their plans for invasion or plans to attack another state if that state has strong military power. States, as reasonable actors, will analyze the possible outcome of the planned invasion and if there is a higher chance that they are going to be defeated or to suffer losses they will give up on that idea. If a state deliver armament to another state, the strength of the receiver state will raise and its chances of deterrence will be higher. Positive effects of delivery of armaments could also be financial because defense industry is highly profitable field which can enrich the economic power of the state. There are also negative effects of defense acquisitions when delivering or acquiring of defense materiel can negatively impact international relations of involved countries.

Finally, we can conclude that effects of defense acquisitions could be highly positive or highly negative and they can quickly resonate between this far ends of the scale. The effects can start between two states but they can easily spill over on regional or even on a global level. Defense acquisitions are and will be an important tool of international politics, therefore states and institutions should try to find the way to regulate this field. Until international institutions succeed in developing the system which will be the framework for future relations between the states regarding the defense acquisitions, states need to develop their own regulatory system. This system has to include the possible effects of the acquisition of defense materiel to the state's international relations, thus giving the opportunity to the future decision makers in this field to consider this important correlation when procuring or supplying weapons.

## References

- [1] MEARSHEIMER, J.: *The Tragedy of Great Power Politics*, Čigoja štampa, Belgrade, 2009.
- [2] PERIŠIĆ, S.: *Geopolitika i Srbi*, Filip Višnjić, Belgrade, 2022.
- [3] SIMEUNOVIĆ, D.: *Teroija politike*, Udruženje nauka i društvo, Belgrade, 2002.

## INDEX OF AUTHORS

### A

15, 28, 172    Abdellah Ferfour  
 298            Adrijana Jovanović  
 560            Aleksa Grubić  
 34             Aleksa Maljević  
 006            Aleksandar Bengin  
 560, 567      Aleksandar Ćitić  
 469            Aleksandar Dimić  
 186            Aleksandar Đurić  
 15, 96        Aleksandar Kari  
 166            Aleksandar Petrovski  
 381            Aleksandar Ristić  
 656            Aleksandar Savić  
 8, 24         Aleksandar Simonović  
 289, 293      Aleksandar Stefanović  
 96, 103, 109   Aleksandra Živković  
 572, 590      Aleksija Đurić  
 258            Alen Crnalić  
 610            Amer. Alsammarraie  
 616            Amir Alsammarraie  
 578, 582, 586   Ana Alil  
 96, 114        Ana Gačić  
 433, 439, 444   Ana Matović  
 235, 452      Anđela Mitrović  
 166            Aner Behlić

### B

50, 56        Biljana Dovatov  
 43            Biljana Ilić  
 475            Biljana M. Babić  
 590            Biljana Marković  
 622            Biljana Mihajlović  
 616            Bmaki H. Zaidan  
 319, 326      Boban Bondžulić  
 369, 386      Boban Sazdić-Jotić  
 213, 222      Bojana Fidanovski  
 662            Boris Vakanjac  
 376            Boriša Jovanović  
 605            Borivoje Nedeljković  
 50, 91        Branislav Ostojić 2  
 449            Branislav Stojković  
 673            Branko Vujatović

### C

616            Cali K. A. Aljboury

### D

475            Dalibor B. Jovanović  
 15, 28, 235    Damir Jerković  
 572            Damjan Klobčar  
 480            Dana Vasiljević Radović  
 213, 263, 463   Danica Bajić  
 673            Darko Grubač  
 531, 535      Darko Janković  
 258            Darko Kuprešak  
 369            Darko Mikanović  
 381            Darko Pijević  
 531, 535      Darko Vasiljević  
 427            Dejan Djordjević  
 392            Dejan Drajić  
 381            Dejan Ivković  
 135, 207, 228   Dejan Jevtić  
 449, 518      Denis Dinić  
 449            Dijana Aksentijević  
 56            Dijana Damljanović  
 319, 326      Dimitrije Bujaković  
 357            Dimitrije Kolašinac  
 452            Dragan Adamović  
 263, 313      Dragan Knežević  
 652            Dragan Lazić  
 572, 590      Dragan Milčić  
 381            Dragan Nikolić  
 186            Dragan Stojadinović  
 332, 515      Dragan Tanasković  
 386            Dragana Bojić  
 688            Dragana Jordanov  
 596            Dragana Lazić  
 553            Dragana Vasić Aničijević  
 545            Dragica M. Minić  
 627            Dragomir Glišić  
 196            Dragoslav R. Petrović  
 550            Dunja Crnogorac  
 452            Dušan Arsić  
 114, 336      Dušan Božić  
 8             Dušan Ivković

420 Dušan Jovanović  
332, 480, 515 Dušan Nešić

## D

452 Đorđe Ivković  
39 Đorđe Jankuloski  
392, 397, 403 Đorđe Nešković

## E

433 Elmedin Biberović  
627 Esmail Ali Salem Ahmed

## F

202 Filip Stanić

## G

103, 336 Goran Dragović  
313 Goran Marjanović  
403 Goran Marković  
43 Goran Ocoljić  
006 Goran Vorotović  
704 Goran Vukadinović  
627 Gvozden Jovanović

## H

698 H. J. Khalafa

## I

475 Igor A. Pašti  
263 Igor Blagojević  
684, 692 Igor Đorić  
632 Igor Goršić  
652 Igor Medenica  
499, 504 Igor Pašti  
50, 56, 60 Ilija Nenadić  
241 Ivan Dimitrijević  
427 Ivan Garić  
8 Ivan Kostić  
131 Ivan Marić  
369 Ivan Pokrajac  
376 Ivan Tot

39 Ivan Vesić  
332 Ivana Jokić  
480 Ivana Mladenović  
135, 228 Ivana Todić  
298 Ivana Trajkovski  
74 Ivana Vasović Maksimović  
439, 444 Ivica Marjanović  
65 Ivo Obradović

## J

409 Jasmina M. Jovanović  
39, 65 Jasminka Jelisavac  
258 Jelena Gržetić  
596 Jelena Marinković  
241 Jelena Mojsilović  
605 Jelena Orelj  
39 Jelena Šobot  
246, 252 Jelena Šultans  
24 Jelena Svorcan  
307 Jelena Vidaković  
557 Jonas Mitterecker  
457 Jose F. M. L. Mariano  
560 Jovana Mandić  
357 Jovana Mihailov

## K

159, 668 Katarina Janković  
74 Katarina Maksimović  
281 Katarina Mišković  
126, 147, 531 Katarina Nestorović  
550 Konstantin Komatina  
166 Kristijan Ilievski  
357 Kristina Živanović

## L

392, 397, 403 Lara Kašca  
688 Laslo Nadjdjerdj  
109, 114 Lazar Arsić  
135 Luka Miličić

## LJ

662 Ljiljana Vasić  
545 Ljubica Radović  
65, 531, 535 Ljubiša Tomić

## M

- 698 M. I. Qaddouri  
463, 486 Maja Vitorović-Todorović  
560, 567 Maja Mladenović  
535 Maja Pagnacco  
263 Maja Radmanovac  
140, 361 Maja Rosić  
222 Marica Bogosavljević  
553 Marija Kovačević  
439, 444 Marija Matović  
439, 444 Marija Milovanović  
557 Marija Mihailović  
43 Marija Samardžić  
357 Marija Šekler  
673 Marija Vujatović  
480 Marija Vuksanović  
289, 293 Marijana Stojanović  
600, 353, 622 Marina Ilic  
70 Marina Ostojić  
126, 531, 535 Marina Simović – Pavlović  
147 Marinko Ugrčić  
449 Marko Anđelković  
56, 60 Marko Bek-Uzarov  
191 Marko Crnogorac  
452 Marko Delić  
704 Marko Jovanović  
28, 268 Marko Karić  
392, 397, 403 Marko Marković  
480 Marko Obradov  
166, 191 Marko Radovanović  
409 Marko Simić  
96, 114, 336 Marko Simonović  
409 Marko Stojanović  
186 Martin Jovanović  
228 Martin Macko  
596 Mihael Bučko  
307 Mihailo Lazarević  
86 Mihailo Zdravković  
656, 684, 692 Mihajlo Ranisavljević  
509 Mihal Đuriš  
343 Milan Blagojević  
433 Milan Gligorijević  
550 Milan Ignjatović  
596 Milan Jovanović  
656 Milan Mihajlović  
313 Milan Popović  
486 Milan R. Nikolić  
96, 103, 114 Milan Simonović  
449, 518 Milan Tanić  
235 Milan Vučković  
332 Milče M. Smiljanić  
688 Milena Rosić  
319, 326 Milenko Andrić  
80 Milenko Trifković  
469 Mileta Ristivojević  
202 Milica Ivanović  
557 Milica Košević  
545 Milica M. Vasić  
668 Milica Mladenović  
353, 600 Miljan Miletic  
475 Miloš Baljžović  
420, 427 Miloš Basarić  
553 Miloš D. Milović  
268 Miloš Filipović  
332 Miloš Frantlović  
652 Miloš Jovanović  
135, 207, 228 Miloš Marković  
126, 131, 289 Miloš Pavić  
172 Miloš Pešić  
140, 361 Miloš Sedak  
313 Miloš Simić  
636 Miloš Stepanović  
332, 480, 515 Miloš Vorkapić  
572, 590 Miodrag Milčić  
50, 86, 91 Miodrag Milenković Babić  
284 Miodrag Vračar  
222 Mirjana Dimić  
74 Mirjana Đurić  
213, 222, 241 Mirjana Krstović  
8, 34 Mirko Dinulović  
268 Mirko Karić  
74 Mirko Maksimović  
147 Miroslav Gluvačević  
493 Miroslav Papović  
392, 397, 403 Miroslav Perić  
39 Miša Živković  
235 Mladen Josijević  
392, 403 Mladen Koprivica  
213, 263 Mladen Timotijević  
319, 326 Mohammed Zouaoui Laidouni  
610 Muraja S. Slman

## N

- 298 Nada Asanović  
567 Nada Ilić  
524, 539 Nataša Pajić

43 Nataša Vujić  
 572, 590 Nataša Zdravković  
 28, 109, 235 Nebojša Hristov  
 289, 293 Nebojša Jovičić  
 545, 605 Nebojša Mitrović  
 480 Nebojša Nikolić  
 449 Negovan Ivanković  
 336, 605 Nedeljko Dučić  
 34 Nemanja Deura  
 449 Nemanja Jovanović  
 409 Nenad Galjak  
 159, 668 Nenad Komazec  
 627 Nenad Radović  
 673 Nenad Stojanović  
 70 Nikola Bogavac  
 177 Nikola Gligorijević  
 662 Nikola Kozić  
 343 Nikola Nešić  
 369, 386 Nikola Petrović  
 109, 172 Nikola Radovanović  
 307 Nikola Živković  
 103, 276, 301 Nina Mitričević

## O

24 Ognjen Peković  
 2, 8 Olivera Kostić

## P

545 Pavel Crnomarković  
 647 Peđa Mihailović  
 647 Petar Atanasijević  
 207, 228 Predrag Elek  
 332 Predrag Poljak  
 679 Predrag Ranitović

## R

276, 301 Rade Pavlović  
 415 Rade R. Božović  
 147 Rade Stančić  
 662 Radoje Banković  
 70 Radoje Zarubica  
 120 Radomir Janković  
 263 Radoslav Sirovatka  
 545, 605 Radoslav Surla  
 207 Radovan Đurović  
 475 Radovan M. Karkalić

596 Radovan Radovanović  
 152 Ranko Babić  
 166 Rexhep Mustafovski

## S

578, 582, 586 Sanja Martinović  
 553 Sanja Živković  
 268, 632 Saša Antonović  
 662 Saša Bakrač  
 258 Saša Brzić  
 632 Saša Gundelj  
 662 Saša Milanović  
 235 Saša Savić  
 469 Saša Spasenić  
 531 Saša Veselinović  
 15, 28, 268 Saša Živković  
 376 Silvana Ilić  
 679 Siniša Mitić  
 684 Slađana Vujičić  
 263 Slavica Terzić  
 246, 252 Slaviša Stojiljković  
 222, 258 Slavko Mijatov  
 643 Slavko Pokorni  
 126, 147 Slobodan Bosiljčić  
 636 Slobodan Malbašić  
 647 Slobodan Petričević  
 652 Slobodan Subotić  
 186 Snežana Jovanović  
 202 Snežana Mališić  
 369, 386 Snežana Zurovac  
 166 Sofija Ackovska  
 524, 539, 600 Sonja Bauk  
 692 Srđan Mirković  
 590 Srđan Samardžić  
 301 Srđan Savić  
 126 Srđan Stojković  
 560, 636 Srdjan Živković  
 172 Srećko Manasijević  
 596 Sreten Perić  
 469 Sreten Spasenić  
 578, 586 Stanica Nedović  
 469, 627 Stefan Dikić  
 357 Stefan Ivanović  
 336 Stefan Jovanović  
 392, 397, 403 Stefan Stanković  
 550 Stefan Tomić  
 65 Stevan Jovičić  
 74 Stevan Maksimović

241, 463 Stevan Stupar  
60 Stefan Rašić  
284 Stevo Vračar  
307 Stjepko Pišl  
172 Svetlana Stojnović

## T

463, 486 Tamara B. Vujatović-Velimirov  
475, 499, 504 Tamara D. Lazarević-Pašti  
70 Tamara Nikolić  
475, 499, 504 Tamara Tasić  
509 Tatjana Kaluđerović Radoičić  
353, 600, 622 Tatjana Marković  
578, 582, 586 Tatjana Volkov Husović  
213, 509 Teodora Stančić  
IX Thomas M. Klapötke  
258 Tihomir Kovačević  
24 Toni Ivanov  
319, 326 Touati Adli  
28 Toufik Allouche

## V

86, 91 Vanja Stefanović Gobeljić  
369 Vasilija Joksimović  
475, 499, 504 Vedran Milanković  
241 Veselin Živanović  
452 Vesna Mandić  
560, 567 Vesna Pejović  
246, 252 Vesna Petrović  
662 Vesna Ristić Vakanjac  
632 Violeta Brnin  
457 Violeta Nikolić  
475, 499, 504 Vladan Anićijević  
415 Vladimir D. Orlić  
135 Vladimir Kuzmanović  
172, 452, 469 Vladimir Milovanović  
535 Vladimir Obradović  
605 Vladimir Pavlović  
409 Vladimir Vučenov  
298 Vladimir Vukmirica  
80 Vojimir Molović  
80 Vuk Antonić  
343 Vuk Todorović  
572 Vukašin Pavlović  
622 Vukica Grković

## Ž

332 Žarko Lazić  
166 Željko Jokić  
524, 600 Željko Senić

## Z

457 Zoran Ivić  
2 Zorana Z. Dančuo  
381 Zvonko Radosavljević

SPECIAL THANKS TO



**PREDUZEĆE**

**◊ MILAN BLAGOJEVIĆ - NAMENSKA ◊ AD**

**LUČANI, SRBIJA**

